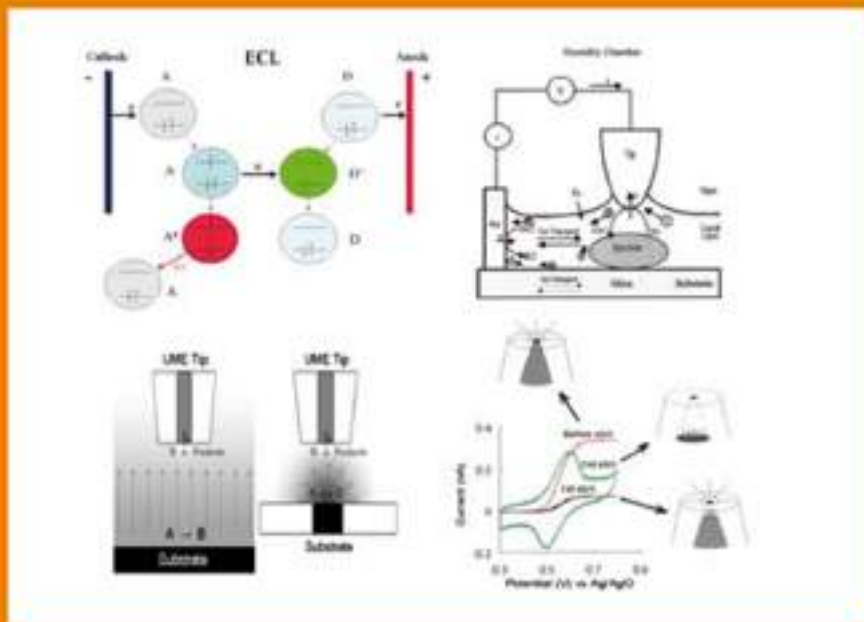




Handbook of Electrochemistry

Edited by
Cynthia G. Zoski



Handbook of Electrochemistry

This page intentionally left blank

Handbook of Electrochemistry

Cynthia G. Zoski

*New Mexico State University
Department of Chemistry and Biochemistry
Las Cruces, New Mexico, USA*



Amsterdam • Boston • Heidelberg • London • New York • Oxford
ELSEVIER Paris • San Diego • San Francisco • Singapore • Sydney • Tokyo

Elsevier
Radarweg 29, PO Box 211, 1000 AE Amsterdam, The Netherlands
The Boulevard, Langford Lane, Kidlington, Oxford OX5 1GB, UK

First edition 2007

Copyright © 2007 Elsevier B.V. All rights reserved

No part of this publication may be reproduced, stored in a retrieval system or transmitted in any form or by any means electronic, mechanical, photocopying, recording or otherwise without the prior written permission of the publisher

Permissions may be sought directly from Elsevier's Science & Technology Rights Department in Oxford, UK: phone (+44) (0) 1865 843830; fax (+44) (0) 1865 853333; email: permissions@elsevier.com. Alternatively you can submit your request online by visiting the Elsevier web site at <http://elsevier.com/locate/permissions>, and selecting *Obtaining permission to use Elsevier material*

Notice

No responsibility is assumed by the publisher for any injury and/or damage to persons or property as a matter of products liability, negligence or otherwise, or from any use or operation of any methods, products, instructions or ideas contained in the material herein. Because of rapid advances in the medical sciences, in particular, independent verification of diagnoses and drug dosages should be made

Library of Congress Cataloging-in-Publication Data

A catalog record for this book is available from the Library of Congress

British Library Cataloguing in Publication Data

A catalogue record for this book is available from the British Library

ISBN-13: 978-0-444-51958-0

ISBN-10: 0-444-51958-0

For information on all Elsevier publications
visit our website at books.elsevier.com

Printed and bound in The Netherlands

07 08 09 10 11 10 9 8 7 6 5 4 3 2 1



Preface

Electrochemistry now plays an important role in a vast number of fundamental research and applied areas. These include, but are not limited to, the exploration of new inorganic and organic compounds, biochemical and biological systems, corrosion, energy applications involving fuel cells and solar cells, and nanoscale investigations. There are many excellent textbooks and monographs, which explain the fundamentals and theory of electrochemistry. This handbook is not a textbook, however, but rather a source of electrochemical information, details of experimental considerations, representative calculations, and illustrations of the possibilities available in electrochemical experimentation. It is most closely allied with the textbook *Electrochemical Methods: Fundamentals and Applications* by Allen J. Bard and Larry R. Faulkner, second edition.

The *Handbook of Electrochemistry* is divided into five parts: Fundamentals (Chapter 1), Laboratory Practical (Chapters 2–10), Techniques (Chapters 11–14), Applications (Chapters 15–17), and Data (Chapters 18–20). Chapter 1 covers the fundamentals of electrochemistry that are essential for everyone working in this field and sets the stage for the following 19 chapters. Thus, Chapter 1 presents an overview of electrochemical conventions, terminology, fundamental equations, electrochemical cells, experiments, literature, textbooks, and specialized books. Laboratory aspects of electrochemistry are emphasized in the following nine chapters that include *Practical Electrochemical Cells* (Chapter 2), *Solvents and Supporting Electrolytes* (Chapter 3), *Reference Electrodes* (Chapter 4), *Solid Electrode Materials: Pretreatment and Activation* (Chapter 5), *Ultramicroelectrodes* (Chapter 6), *Potentiometric Ion-Selective Electrodes* (Chapter 7), *Chemically Modified Electrodes* (Chapter 8), *Semiconductor Electrodes* (Chapter 9), and *Microelectrode Arrays* (Chapter 10). Electrochemical techniques covered in this handbook range from classical experiments (Chapter 11) to *Scanning Electrochemical Microscopy* (SECM) (Chapter 12), *Electro-generated Chemiluminescence* (Chapter 13), and *Spectroelectrochemistry* (Chapter 14). These four chapters also include representative applications based on the method described. Specific electrochemical applications based on the preceding chapters illustrate the impact of electrochemistry in exploring diverse topics ranging from electrode kinetic determinations (Chapter 15), unique aspects of metal deposition (Chapter 16) including micro- and nanostructures, template deposition, and single particle deposition, and electrochemistry in small places and at novel interfaces (Chapter 17) including biological cells, single molecule electrochemistry, and electrochemistry at liquid/liquid interfaces. The remaining three chapters provide useful electrochemical data and information involving electrode potentials (Chapter 18), diffusion coefficients (Chapter 19), and methods used in measuring liquid-junction potentials (Chapter 20). The majority of the chapters were supervised by a single corresponding author. Exceptions to this are Chapters 6, *Ultramicroelectrodes*; Chapter 16, *Metal Deposition*; and Chapter 17, *Electrochemistry in Small Places and at Novel Interfaces*, where several authors contributed to different sections in a specific chapter.

I would like to thank the contributors of this handbook, colleagues in the electrochemical community, and the authors of the many papers, textbooks, and specialized books whose work is cited in this handbook and has led to the development of electrochemistry, its expansion into diverse areas, and much of the information presented in this handbook. I especially want to thank Allen J. Bard, a pioneer in electrochemistry, for his helpful comments, suggestions, advice, and unwavering encouragement during the editing of this handbook.

Cynthia G. Zoski

Contents

Preface	v
Corresponding Authors.....	xix
I Fundamentals.....	01
1 Fundamentals	03
1.1 Conventions in Electrochemistry	03
1.1.1 Potential conventions	03
1.1.2 Current conventions	06
1.2 Terminology.....	06
1.3 Fundamental Equations	08
1.3.1 Nernst equation.....	09
1.3.2 Equilibrium constant.....	09
1.3.3 Mass-transfer limited current.....	10
1.3.4 Cottrell equation	10
1.3.5 Faraday's law	11
1.4 Factors Affecting Reaction Rate and Current	11
1.4.1 Current, current density, and rate.....	11
1.4.2 Reversibility	13
1.4.3 Kinetics.....	14
1.5 Equations Governing Modes of Mass Transfer.....	17
1.5.1 Nernst–Planck equation.....	17
1.5.2 Fick's laws of diffusion.....	17
1.6 Electrochemical Cells.....	20
1.7 Cell Resistance; Capacitance; Uncompensated Resistance	22
1.8 Overview of Electrochemical Experiments	25
1.9 Electrochemistry Literature; Textbooks; Specialized Books	25
1.9.1 Electrochemical journals	26
1.9.2 Specialized texts	26
1.9.3 Review series	28
References	28
II Laboratory Practical	31
2 Practical Electrochemical Cells	33
2.1 Materials	33
2.2 General Cell Designs	33
2.2.1 Two-electrode cells	34
2.2.2 Three-electrode cells	35

2.3	Electrochemical Cells for Specific Applications	35
2.3.1	Flow-through cells	35
2.3.2	Thin-layer cells (TLCs)	41
2.3.3	Spectroelectrochemical cells	43
2.3.4	Electrochemical cells for molten salts	47
2.3.5	Attachment to a vacuum line	49
2.4	Establishing and Maintaining an Inert Atmosphere	50
	References	55
3	Solvents and Supporting Electrolytes	57
3.1	Introduction	57
3.2	Electrolyte Conductivity	58
3.3	Cells, Electrodes and Electrolytes	60
3.4	Cell Time Constants	62
3.5	Solvents	62
3.5.1	Protic solvents	63
3.5.2	Nitriles	65
3.5.3	Halogenated organics	65
3.5.4	Amides	65
3.5.5	Sulfoxides and sulfones	65
3.5.6	Ethers, carbonates, lactone	66
3.6	Salts	66
3.7	"Exotic" Electrolytes	67
3.8	Purification Procedures for some Commonly Used Solvents in Electrochemistry	68
3.8.1	Acetonitrile	69
3.8.2	Butyronitrile	69
3.8.3	Benzonitrile	69
3.8.4	Propylene carbonate	70
3.8.5	Dichloromethane	70
3.8.6	Dimethylformamide	70
3.9	Purification Procedures for some Commonly Used Salts in Electrochemistry	70
3.9.1	Tetraethylammonium tetrafluoroborate	70
3.9.2	Tetraethylammonium tetr phenylborate	70
3.9.3	Tetraethylammonium hexafluorophosphate	71
3.9.4	Tetrabutylammonium tetrafluoroborate	71
3.9.5	Tetrabutylammonium hexafluorophosphate	71
3.9.6	Lithium perchlorate	71
	References	71
4	Reference Electrodes	73
4.1	Introduction	73
4.1.1	Selecting a reference electrode	73
4.1.2	Converting between aqueous potential scales	74
4.2	Basic Components of a Reference Electrode	74
4.2.1	Body material	74
4.2.2	Top seal	74

4.2.3 Junction (4)	77
4.2.4 Active component of RE	79
4.3 Electrode Details and Fabrication	80
4.3.1 Hydrogen electrodes	80
4.3.2 Mercury electrodes (24)	86
4.3.3 Silver electrodes	92
4.3.4 Quasi-reference electrodes (QRE)	94
4.4 Junctions	95
4.4.1 Filling solutions	95
4.4.2 Salt bridges	96
4.4.3 Double-junction reference electrodes	97
4.4.4 Reference electrode impedance	97
4.5 Reference Electrodes: Nonaqueous Solvents	98
4.6 Reference Electrode Calibration	100
4.6.1 Versus a second reference electrode	100
4.6.2 Using a well-defined redox couple	100
4.7 Maintenance	102
4.7.1 Storage	103
4.7.2 Cleaning junctions	103
4.7.3 Replacing filling solutions	103
4.7.4 Regenerating the reference electrode	103
4.8 Troubleshooting	104
4.8.1 Special notes	104
References	108
5 Solid Electrode Materials: Pretreatment and Activation	111
5.1 Introduction	111
5.2 Carbon Electrodes	114
5.2.1 Highly oriented pyrolytic graphite	115
5.2.2 Glassy carbon	121
5.2.3 Pyrolyzed photoresist films (PPF)	126
5.2.4 Carbon fibers	128
5.2.5 Carbon nanotubes	133
5.2.6 Diamond films	135
5.2.7 Tetrahedral amorphous carbon (Ta-C) films	140
5.3 Metal Electrodes	143
5.3.1 Polycrystalline platinum and gold	144
5.3.2 Single-crystal platinum and gold	146
5.4 Semiconductor Electrodes	147
5.4.1 Indium tin oxide (ITO)	147
5.5 Conclusions	149
Acknowledgments	149
References	150
6 Ultramicroelectrodes	155
6.1 Behavior Of Ultramicroelectrodes	155

6.1.1	Electrode response times	156
6.1.2	Factors that influence the electrode response time	159
6.1.3	Origins of non-ideal responses	160
6.1.4	Fundamentals of faradaic electrochemistry	164
6.1.5	Origins of non-ideal faradaic responses	168
References	171
6.2	Microelectrode Applications	171
6.2.1	Electroanalysis at the micro- and nano-length scale	172
6.2.2	Spatially heterogeneous systems: biological structures	175
6.2.3	Low conductivity media	177
6.2.4	Ultrafast electrochemical techniques	180
6.2.5	AC electrokinetics	184
References	186
6.3	UME Fabrication/Characterization Basics	189
6.3.1	Platinum and gold inlaid disks $\geq 5 \mu\text{m}$ diameter	189
References	197
6.3.2	Platinum and gold inlaid disks $\geq 5 \mu\text{m}$ diameter	197
References	199
6.3.3	Laser-pulled ultramicroelectrodes	199
References	211
6.3.4	Platinum conical ultramicroelectrodes	211
References	216
6.3.5	Flame-etched carbon nanofibers	217
References	221
6.3.6	Electrochemically etched carbon fiber electrodes	221
References	226
6.3.7	Gold spherical microelectrodes	226
References	235
6.3.8	Hg microhemispherical electrodes	235
References	243
6.3.9	Clarke oxygen microelectrode	243
References	248
6.3.10	Nitric oxide microsensors	249
References	253
6.3.11	Glass nanopore electrodes	254
References	260
7	Potentiometric Ion-Selective Electrodes	261
7.1	Introduction	261
7.2	Classification and Mechanism	263
7.2.1	Phase boundary potential	263
7.2.2	Ion-exchanger-based ISEs	264
7.2.3	Neutral-ionophore-based ISEs	266
7.2.4	Charged-ionophore-based ISEs	270

7.3	Equilibrium Potentiometric Responses	273
7.3.1	The Nikolsky–Eisenman equation and phase boundary potential model.	273
7.3.2	Effect of ionic sites on selectivity	276
7.3.3	Apparently “non-Nernstian” equilibrium responses	279
7.4	Non-Equilibrium Potentiometric Responses	282
7.4.1	Mixed ion-transfer potentials.	282
7.4.2	Elimination of non-equilibrium effects in separate solutions	284
7.4.3	Effects of transmembrane ion flux on detection limit.	287
7.4.4	Non-equilibrium responses for polyion detection.	290
7.5	Conclusions	291
	References	292
8	Chemically Modified Electrodes	295
8.1	Introduction	295
8.2	Substrate Materials and Preparation	296
8.3	Modified Electrode Types	296
8.3.1	Langmuir–Blodgett	297
8.3.2	Self-assembly	300
8.3.3	Covalent attachment	305
8.3.4	Clay modified electrodes.	308
8.3.5	Zeolite modified electrodes	311
8.3.6	Sol-gel modified electrodes	314
8.3.7	Polymer modified electrodes	317
8.3.8	DNA modified electrodes	322
8.4	Conclusions and Prospects	322
	References	323
9	Semiconductor Electrodes	329
9.1	Introduction	329
9.2	Semiconductor Basics	330
9.2.1	Band theory of solids	330
9.2.2	Size quantization in semiconductors	336
9.3	Energetics of a Semiconductor	340
9.3.1	Semiconductor–electrolyte interface (SEI).	343
9.4	Semiconductor Electrodes	346
9.4.1	Electron transfer at semiconductor–electrolyte interface	346
9.4.2	Illuminated semiconductor electrodes	349
9.4.3	Cyclic voltammetry (CV) at semiconductor electrodes	351
9.4.4	Fermi-level pinning in semiconductor electrodes	355
9.4.5	Characterization of the SEI by scanning electrochemical microscopy (SECM)	358
9.5	Types of Semiconductor Electrodes	367
9.5.1	Single crystal and epitaxial film electrodes	367
9.5.2	Polycrystalline electrodes	369

9.6	Nanostructured Semiconductor Electrodes (NSSE)	374
9.6.1	Epitaxial methods for the preparation of NSSE	375
9.6.2	Preparation of particulate films	375
9.6.3	Electrochemistry on nanostructured semiconductors	377
9.6.4	Electrochemistry on suspended semiconductor nanoparticles	378
9.7	Semiconductor Electrode Applications	381
9.7.1	Solar cells	381
9.7.2	Sensors	384
	Acknowledgments.	385
	References	385
10	Microelectrode Arrays	391
10.1	Introduction	391
10.2	Classification of Microelectrode Arrays	392
10.2.1	Microelectrode designs.	392
10.2.2	Microelectrode array behavior	394
10.3	Theory: Diffusion at Microelectrode Arrays	396
10.3.1	Arrays of electrodes operating at identical potentials	396
10.3.2	Arrays of electrodes operating in generator/collector mode	400
10.4	Fabrication of Microelectrode Arrays	403
10.4.1	Mechanical methods.	404
10.4.2	Template approaches	407
10.4.3	Lithographic techniques	411
10.4.4	Etching techniques.	416
10.5	Electrochemical Characterisation of Microelectrode Arrays	418
10.5.1	Chronoamperometry and cyclic voltammetry	419
10.5.2	Scanning electrochemical microscopy	422
10.5.3	Optical microscopy	422
10.6	Conclusion and Prospects	422
	References	423
III	Techniques	429
11	Classical Experiments.	431
11.1	Introduction	431
11.2	Selected Experimental Techniques	432
11.2.1	Potential steps	432
11.2.2	Potential sweeps.	438
11.2.3	Combinations of sweeps and steps	445
11.2.4	Microelectrodes	447
11.2.5	Rotating disc electrodes	451
11.2.6	Small amplitude perturbations and impedance methods	454
11.3	Simulations	458
11.3.1	Electrochemical simulations—a few questions	458
11.3.2	Basic principles of an electrochemical simulation.	460

11.4	Troubleshooting Electrochemical Experiments: A Checklist	464
11.4.1	Checking the results	464
11.4.2	No current response	464
11.4.3	Potential shift	465
11.4.4	Currents lower than expected	466
11.4.5	Slanted voltammogram	466
11.4.6	Noisy current	466
11.4.7	Other common problems	466
	References	467
12	Scanning Electrochemical Microscopy	471
12.1	Introduction and Principles	471
12.2	Instrumentation	473
12.2.1	Basic SECM apparatus	473
12.2.2	Combining SECM with other techniques	475
12.3	Methods and Operational Modes	479
12.3.1	Amperometric methods	479
12.3.2	Potentiometric method	489
12.3.3	Imaging	497
12.4	Applications	501
12.4.1	Heterogeneous kinetics	501
12.4.2	Homogeneous chemical reactions	506
12.4.3	Catalytic activity	510
12.4.4	Surface reactivity	514
12.4.5	Patterning	519
12.4.6	Biological applications	524
	References	535
13	Electrogenerated Chemiluminescence	541
13.1	Concepts and History	541
13.2	Types of Luminescence	541
13.3	Fundamental Reactions	542
13.3.1	Ion annihilation ECL	542
13.3.2	Coreactant ECL (123)	546
13.4	Experimental Setup	554
13.4.1	Electrochemical media	554
13.4.2	Cell design and electrodes	556
13.4.3	Light detection and ECL instrumentation	560
13.5	Types of Experiments	568
13.5.1	Ion annihilation ECL: $\text{Ru}(\text{bpy})_3^{2+}$ and derivatives	568
13.5.2	Coreactant ECL of $\text{Ru}(\text{bpy})_3^{2+}/\text{TPrA}$ system in aqueous solutions	570
13.6	Applications	572
13.6.1	Applications of $\text{Ru}(\text{bpy})_3^{2+}$ ECL: determination of oxalate and organic acids	573
13.6.2	Applications of $\text{Ru}(\text{bpy})_3^{2+}$ ECL: determination of amines	574

13.6.3 Applications of Ru(bpy) ₃ ²⁺ ECL: determination of amino acids	575
13.6.4 Applications of Ru(bpy) ₃ ²⁺ ECL: determination of pharmaceuticals	576
13.6.5 Applications of Ru(bpy) ₃ ²⁺ ECL: determination of Ru(bpy) ₃ ²⁺	577
13.6.6 Applications of Ru(bpy) ₃ ²⁺ ECL in capillary electrophoresis (CE) and micro-total analysis (μ TAS)	577
13.6.7 Application of Ru(bpy) ₃ ²⁺ ECL: determination of clinical analytes	578
13.6.8 Applications of Ru(bpy) ₃ ²⁺ ECL: analytes associated with food, water, and biological agents	580
Acknowledgments	582
References	582
14 Spectroelectrochemistry	591
14.1 Introduction	591
14.2 Light Transmission and Reflection at an Electrode Surface	592
14.3 Electronic Spectroscopy	593
14.3.1 Transmittance spectroscopy and optically transparent cell materials	594
14.3.2 Thin layer spectroelectrochemistry	595
14.3.3 Spectroelectrochemistry: semi-infinite linear diffusion	601
14.3.4 Long optical pathway thin layer cells (LOPTLC)	603
14.3.5 Reflectance spectroscopy	605
14.4 Luminiscence Spectroelectrochemistry	612
14.4.1 Steady-state luminescence spectroelectrochemistry	612
14.4.2 Time-resolved luminescence spectroelectrochemistry	615
14.5 Vibrational Spectroelectrochemistry	616
14.5.1 IR spectroelectrochemistry	618
14.5.2 Raman spectroelectrochemistry	623
14.6 Outlook	632
References	633
IV Applications	637
15 Determination of Electrode Kinetics	639
15.1 Introduction to Kinetic Measurements	639
15.2 Heterogeneous Electron Transfer: Transient Methods	641
15.2.1 Linear sweep and cyclic voltammetry	641
15.2.2 Sampled-current voltammetry	644
15.2.3 Ac voltammetry	645
15.3 Heterogeneous Electron Transfer: Steady-State Methods	646
15.3.1 Steady-state voltammetry	646
15.3.2 Scanning electrochemical microscopy (SECM)	648
15.4 Processes with Coupled Homogeneous Reactions	651
15.4.1 Linear sweep and cyclic voltammetry	651
15.4.2 Scanning electrochemical microscopy (SECM)	655
15.4.3 Simulations and curve fitting	656
References	660

16 Metal Deposition	661
16.1 Electrodeposition of Nanostructures and Microstructures on Highly Oriented Pyrolytic Graphite (HOPG)	661
16.1.1 Introduction and perspective	661
16.1.2 HOPG: seeing electrodeposited metal nano- and microparticles	663
16.1.3 Brownian Dynamics simulations: understanding particle size distribution broadening	664
16.1.4 “Slow-growth” electrodeposition: dimensionally uniform metal nano- and microparticles	667
16.1.5 Electrodeposition of metal nanowires	673
References	676
16.2 Template Deposition of Metals	678
16.2.1 Introduction	678
16.2.2 Templating membranes	678
16.2.3 Template deposition of metals	686
16.2.4 Morphological and optical properties	695
16.2.5 Electrochemistry with template nanomaterials: nanoelectrode ensembles	697
16.2.6 Conclusions and prospects	704
References	706
16.3 Single Particle Deposition on Nanometer Electrodes	709
16.3.1 Introduction	709
16.3.2 Electrode selection	710
16.3.3 Electrodeposition of particles: electrokinetic vs. diffusion control	711
16.3.4 Nucleation exclusion zones: modeling particle growth	715
16.3.5 Examples of systems	717
References	717
17 Electrochemistry in Small Places and at Novel Interfaces	719
17.1 Electrochemistry in and at Single Biological Cells	719
17.1.1 Electrochemistry at the cell membrane–solution interface	719
17.1.2 Electrochemistry at lipid bilayer membranes	726
17.1.3 Electrochemistry in small drops and vials	737
17.1.4 Intracellular electrochemistry	742
17.1.5 Conclusions	744
References	746
17.2 Single Molecule Electrochemistry	749
17.2.1 Introduction	749
17.2.2 Special topics	749
17.2.3 Conclusions	783
References	783
17.3 Electrochemistry at Liquid/Liquid Interfaces	785
17.3.1 Introduction	785
17.3.2 Fundamentals	786
17.3.3 Charge transfer reactions at liquid/liquid interfaces	793
17.3.4 Methodologies and techniques	799

17.3.5 Applications	802
17.3.6 Prospects	806
Acknowledgments	806
References	806
V Data	811
18 Electrode Potentials	813
18.1 Overview	813
18.2 Estimated Potential Ranges: Aqueous and Non-aqueous Solutions	813
18.3 Standard Electrode Potentials: Aqueous Solutions	813
18.4 Formal Electrode Potentials: Aprotic Solvents	813
18.5 Formal Electrode Potentials: Common Organic Mediators	820
18.6 Electrode Potentials: Inorganic One-Electron Complexes	820
18.7 Formal Electrode Potentials: Biological Redox Species	821
18.8 Formal Electrode Potentials: Common Vitamins, Drugs, Neurochemicals	821
18.9 Abbreviations	822
18.10 Chemical Structures	825
References	827
19 Diffusion Coefficients	829
19.1 Introduction	829
19.2 Fundamental Equations	829
19.3 General Considerations	830
19.3.1 Selection of a technique	830
19.3.2 Electrode	833
19.3.3 Electrochemical system	835
19.3.4 Instrumentation	835
19.4 Electrochemical Methods	836
19.4.1 Potential step techniques (chronoamperometry)	836
19.4.2 Rotating disk electrode techniques	840
19.4.3 Potential sweep techniques	842
19.4.4 Current step techniques (chronopotentiometry)	843
19.4.5 Scanning electrochemical microscopy (SECM) techniques	844
19.5 Tables of Diffusion Coefficients	844
References	847
20 Liquid Junction Potentials	849
20.1 Types of Liquid Junctions	849
20.1.1 Interfacial potentials without electrolyte transport	849
20.1.2 Interfacial potentials with electrolyte transport	850
20.2 Transference Numbers and Conductivity	854
20.2.1 Experimental methods of determining transference number	854
20.2.2 Sample calculations of ionic transference numbers	860
20.2.3 Experimental methods of determining electrolytic conductivity	863

Contents	xvii
20.2.4 Sample calculations relating to electrolytic conductivity	864
20.2.5 Tabulation of parameters related to electrolyte conductance	866
20.3 Minimization of Liquid Junction Potentials	867
20.3.1 Balancing ionic mobilities	867
20.3.2 The salt bridge	870
20.4 Junctions of Immiscible Liquids	870
20.4.1 The non-polarisable liquid/liquid interface	870
20.4.2 The polarisable liquid/liquid interface	872
20.5 Non-Classical Electrolytes: Polymer-Based Electrolytes and Ionic Liquids.	874
References	876
<i>Subject Index</i>	879

Colour Section to be found at the end of the book

This page intentionally left blank

Corresponding Authors

<i>Shigeru Amemiya</i>	University of Pittsburgh, Pittsburgh, PA, USA
<i>Melisa D. Arning</i>	Saint Louis University, St. Louis, MO, USA
<i>John E. Baur</i>	Illinois State University, Normal, IL, USA
<i>Adam J. Bergren</i>	Iowa State University, Ames, IA, USA (present address: The University of Alberta, Edmonton, Alberta, Canada)
<i>Shaowei Chen</i>	University of California, Santa Cruz, CA, USA
<i>Madalina Ciobanu</i>	Vanderbilt University, Nashville, TN, USA
<i>David E. Cliffel</i>	Vanderbilt University, Nashville, TN, USA
<i>Stephen Creager</i>	Clemson University, Clemson, SC, USA
<i>Christophe Demaille</i>	Université Paris 7-UMR CNRS 7591, France
<i>Guy Denuault</i>	University of Southampton, UK
<i>Robert A.W. Dryfe</i>	University of Manchester, Manchester, UK
<i>Grant A. Edwards</i>	Iowa State University, Ames, IA, USA (present address: Northern Kentucky University, Highland Heights, KY, USA)
<i>Andrew G. Ewing</i>	Pennsylvania State University, PA, USA
<i>Fu-Ren F. Fan</i>	The University of Texas at Austin, Austin, TX, USA
<i>José Fernandez</i>	The University of Texas at Austin, Austin, TX, USA
<i>Robert J. Forster</i>	Dublin City University, Ireland
<i>Santosh K. Haram</i>	University of Pune, Ganeshkhind, Pune, India
<i>Katherine B. Holt</i>	The University of Texas at Austin, Austin, TX, USA (present address: University College London, London, UK)
<i>Tia E. Keyes</i>	Dublin City University, Ireland
<i>Anthony Kucernak</i>	Imperial College London, London, UK
<i>Youngmi Lee</i>	University of Tennessee, Knoxville, TN, USA
<i>Biao Liu</i>	The University of Texas at Austin, Austin, TX, USA
<i>Janine Mauzeroll</i>	Université Paris 7-UMR CNRS 7591, France (present address: Université du Québec à Montréal, Montréal, Québec, Canada)

<i>Wujian Miao</i>	The University of Southern Mississippi, Hattiesburg, MS, USA
<i>Shelley D. Minteer</i>	Saint Louis University, St. Louis, MO, USA
<i>Michael V. Mirkin</i>	Queens College – CUNY, Flushing, NY, USA
<i>Reginald M. Penner</i>	University of California, Irvine, CA, USA
<i>Marc D. Porter</i>	Iowa State University, Ames, IA, USA (present address: Arizona State University, Tempe, AZ, USA)
<i>Yuanhua Shao</i>	Peking University, Beijing, China
<i>Timothy J. Smith</i>	The University of Texas at Austin, Austin, TX, USA
<i>Keith J. Stevenson</i>	The University of Texas at Austin, Austin, TX, USA
<i>Greg M. Swain</i>	Michigan State University, East Lansing, MI, USA
<i>Sabine Szunerits</i>	Institut National Polytechnique de Grenoble, Domaine Universitaire, France
<i>Paolo Ugo</i>	University of Venice, Venice, Italy
<i>Ran Tel-Vered</i>	University of Texas at Austin, Austin, TX, USA
<i>Henry S. White</i>	University of Utah, Salt Lake City, UT, USA
<i>Nathan J. Wittenberg</i>	Pennsylvania State University, PA, USA
<i>Cynthia G. Zoski</i>	New Mexico State University, Las Cruces, NM, USA

Part One

FUNDAMENTALS

This page intentionally left blank

Fundamentals

**Madalina Ciobanu, Jeremy P. Wilburn,
Morgan L. Krim, and David E. Cliffel**

Department of Chemistry, Vanderbilt University,
Nashville, TN 37235, USA

1.1 CONVENTIONS IN ELECTROCHEMISTRY

The science of electrochemistry is concerned with electron transfer at the solution/electrode interface. Most of the basic principles and relationships, however, were described prior to the discovery of the electron by J. J. Thompson in 1893. In 1800, Alessandro Volta invented the first battery, then known as a voltaic pile, by alternating stacks of copper and zinc disks separated by paper soaked in acid solutions. With the discovery of a sustainable source of electrical current, the stage was set for the rapid development of the area of science now known as electrochemistry. By 1835, Michael Faraday had already defined the anode, cathode, electrode, electrolyte, and ion: concepts without which any definitive description of electrochemistry is virtually impossible.

The positive and negative mathematical convention for electrical charge is attributed to Benjamin Franklin (1). Charles-François de Cisternay du Fay had earlier theorized the existence of only two types of electrical charge. Du Fay had named the charge generated by rubbing a glass rod as “vitreous,” while the equivalent charge generated by rubbing amber, or resin, as “resinous.” Franklin, however, envisioned electrical charge as being attributed to the level of a single invisible fluid present inside objects (i.e., a negatively charged object had a lesser amount of this fluid and a positively charged one had an excess amount). Franklin accordingly renamed resinous charge as negative and vitreous charge positive, thereby establishing the convention that would eventually demand the electron to be defined as a negative charge.

1.1.1 Potential conventions

Although the work of Faraday had established early on the relationship between the current generated during electrolysis and the amount of generated species, the dependence of cell

potential on the concentration of electroactive species remained theoretically elusive until the advent of thermodynamics. Let us consider the following reduction reaction:



where O is the oxidized species, R is the reduced species, and n is the number of electrons exchanged between O and R. The relationship between the concentration of oxidized species [O], concentration of reduced species [R], and free energy (ΔG [J mol⁻¹]) is given as

$$\Delta G = \Delta G^0 + RT \ln \frac{[\text{R}]}{[\text{O}]} \quad (1.1.2)$$

where R is the gas constant (8.3145 J mol⁻¹ K⁻¹) and T [K] is the temperature. The critical aspect of this equation is that the ratio of reduced to oxidized species can be related to the Gibbs free energy change (ΔG), from which we can then derive the potential (E [V]):

$$\Delta G = -nFE \quad (1.1.3)$$

Here E is the maximum potential between two electrodes, also known as the open-circuit potential (OCP) or the equilibrium potential, which is present when no current is flowing through the cell, and F is Faraday's constant (1F = 96,485.3 C mol⁻¹). If the reactant and product have unit activity, and E is for the reaction in the direction of reduction (left to right in equation (1.1.1)), then equation (1.1.3) can be written as

$$\Delta G^0 = -nFE^0 \quad (1.1.4)$$

In this case, the potential is known as the *standard electrode potential* (E^0 [V]) or the *standard potential* and it relates to the *standard Gibbs free energy change* (ΔG^0 [J mol⁻¹]). It should be noted here that due to the minus sign in equation (1.1.4), all spontaneous reactions (i.e., with $\Delta G^0 < 0$) will have a positive standard electrode potential ($E^0 > 0$).

The mathematical expression describing the correlation between potential and concentration for a cell reaction is a central tenant of electrochemistry and is known as the *Nernst equation* (obtained by combining equations (1.1.2)–(1.1.4)):

$$E = E^0 + \frac{RT}{nF} \ln \frac{[\text{O}]}{[\text{R}]} \quad (1.1.5)$$

In addition to the use of the *standard potential* (E^0), reaction potentials may also be reported with the convention of *electromotive force* (*emf* or \mathcal{E} [V]). The convention of *emf* was adopted to make the calculation of cell potentials, from the combination of two half-reactions, more straightforward. For a reduction reaction, the *standard potential* and the *emf* have the same value, while for the same reaction written in the direction of oxidation (e.g., the reverse reaction), their signs are opposite. Using the example of a silver iodide cell, consider the complete cell schematic:



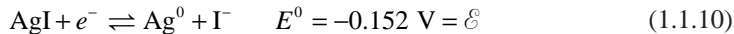
The calculation of cell potential for *emf* requires only the addition of the *emf* values for each half-reaction, while the same cell potential calculation using *standard potentials* requires the usage of the following convention:

$$E_{\text{cell}}^0 = E_{\text{cathode}}^0 - E_{\text{anode}}^0 \quad (1.1.7)$$

The anode half-reaction can be written either as a reduction (equation (1.1.8)) or as an oxidation (equation (1.1.9)):



The *standard potential* of the anodic oxidation reaction is given in equation (1.1.9), and the *standard potential* of the cathodic reduction reaction is



First, we will use the *emf* convention. The anodic reaction is an oxidation, and therefore the sign of the *standard potential* must be reversed to give the *emf*. For the cathodic reaction, however, the reaction is a reduction, and therefore the *emf* is the same as the *standard potential*. The cell *emf* would be given as

$$\mathcal{E}_{\text{cell}} = \mathcal{E}_{\text{cathode}} + \mathcal{E}_{\text{anode}} = -0.152 \text{ V} + (-0.799 \text{ V}) = -0.951 \text{ V} \quad (1.1.11)$$

The same calculation for the *standard potential* convention would be

$$E_{\text{cell}}^0 = E_{\text{cathode}}^0 - E_{\text{anode}}^0 = -0.152 \text{ V} - 0.799 \text{ V} = -0.951 \text{ V} \quad (1.1.12)$$

Therefore, the result is the same regardless of the convention used. We can also calculate the standard free energy change for the net reaction by using equation (1.1.4):

$$\Delta G^0 = -(1)F(-0.951 \text{ V}) = +91.76 \text{ kJ mol}^{-1} \quad (1.1.13)$$

The results from equations (1.1.12) and (1.1.13) indicate that this net reaction is not spontaneous; therefore it requires energy input in order to occur.

Each half-cell reaction has a specific standard potential reported as the potential of the reduction reaction vs. the normal hydrogen electrode (NHE). In an electrochemical cell, there is a half-cell corresponding to the working electrode (WE), where the reactions under study take place, and a reference half-cell. Experimentally the cell potential is measured as the difference between the potentials of the WE half-cell and the reference electrode/reference half-cell (see Chapter 4). The archetypal reference electrode is the NHE, also known as the standard hydrogen electrode (SHE) and is defined, by convention, as 0.000 V for any temperature. Although the NHE is not typically encountered due to difficulty of operation, all conventional electrodes are in turn referenced to this standard to define their absolute potential (i.e., the Ag/AgCl, 3 M KCl reference has a potential of 203 mV vs. the NHE). In practice, experimental results are either stated as being obtained vs. a specific reference electrode, or converted to potentials vs. NHE.

Numerous tables exist referencing E^0 values for the most typically encountered redox reactions (see Chapter 18). Initially these tables were derived from thermodynamic data,

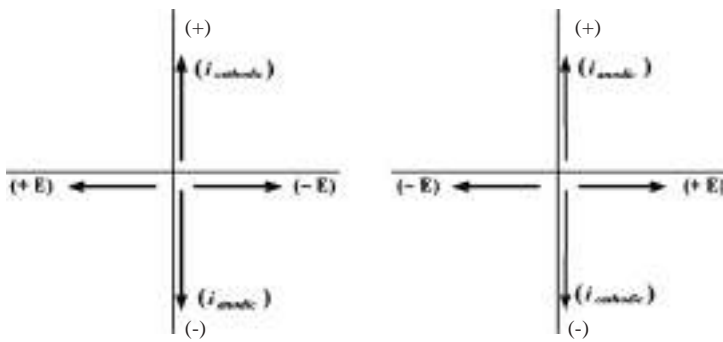


Figure 1.1 American (left) and IUPAC (right) voltammogram conventions.

and as the science has progressed these values have been confirmed in most cases via electrochemical experimentation.

1.1.2 Current conventions

As previously mentioned, Faraday initially coined the expressions ion, anode, and cathode. Faraday called the active species in his electrolysis experiments ions, using a Greek word loosely translated as wanderer. Therefore, anodic currents are generated by species (anions) diffusing (wandering) toward the anode and cathodic currents by those (cations) diffusing toward the cathode. The anode and cathode are defined by convention, with the anode always being the site of oxidation and the cathode the site of reduction. The mathematical signs of currents and potentials measured at the anode and cathode depend on the type of electrochemical cell being investigated. There are two basic classifications: cells are either galvanic, where reactions are spontaneous (such as batteries), or electrolytic where a current or potential is applied to drive a chemical reaction (see Section 1.6).

Additionally, there are two conflicting conventions dictating the graphical depiction of combined voltage/current plots, known as voltammograms (see Figure 1.1); both conventions are currently found in the literature. In both conventions, the potential is plotted on the x -axis and the current on the y -axis. In the older convention, known as the polarographic or American convention, positive potentials lie to the left of the origin and cathodic current is positive, while the International Union of Pure and Applied Chemistry (IUPAC) has adopted the opposite convention, also known as the European convention, where positive potentials are to the right of the origin, and anodic currents are positive. The American convention (positive cathodic currents and negative potentials to the right) will be used throughout this book, unless otherwise indicated.

1.2 TERMINOLOGY

The definitions provided here tend to follow the IUPAC instructions (2), where possible. Additional explanations are present, as some terms have specific meanings in electrochemistry (3).

Anode: electrode where the oxidation takes place.

Auxiliary (Counter) Electrode (CE): electrode that helps pass the current flowing through the cell; the current travels between the WE and CE; typically no processes of interest (under study) occur at the surface of CE; example: Pt wire.

Battery: one or more galvanic cells.

Cathode: electrode where the reduction takes place.

Cell Potential (E [V]): the sum of electrical potentials within an electrochemical cell that also accounts for all redox processes occurring at the electrodes.

Chronoamperometry: electrochemical methods that utilize a potential step and have the output current readings vs. time.

Electrochemical Cell: device that involves the presence of faradaic currents as a result of redox chemical reactions; it can be either a galvanic cell, when the reactions are spontaneous, or an electrolytic cell, when the reactions are non-spontaneous.

Electrochemical Mediator: the electrochemically active species with fast kinetics that will undergo a reduction or an oxidation reaction at the electrode, thus yielding a faradaic current that can give information about a kinetically slow process.

Electrode: it represents an electrical conductor/semiconductor in an electrochemical cell; in electrochemistry, it is the conductive phase where the electron transfer occurs; it can be an anode or a cathode.

Electrolytic Cell: energy-consuming device that converts electrical energy into chemical energy; it consists of at least two electrodes and an electrolyte solution; cathode is negative as compared to the anode; example: electrolysis cell.

Equilibrium Potential (E_{eq} [V]): the potential associated with an electrode when all redox processes are in equilibrium; the net current is zero under these conditions and the electrode potential is given by the Nernst equation.

Faradaic: the multitude of processes involving redox chemical reactions.

Fuel Cell: device similar to a galvanic cell used for the conversion of chemical energy into electricity, sustained by a continuous supply of chemical reactants from outside the cell; example: H₂-O₂ cell.

Galvanic (Voltaic) Cell: self-powered device that produces electricity by means of chemical energy; it is limited by the supply of the chemicals contained inside the device; it consists of two electrodes (anode and cathode) and an electrolyte solution; the cathode is positive as compared to the anode.

Half-cell: the anode or the cathode compartment of an electrochemical cell, including all reactions that occur at that particular electrode.

Half-reaction: the redox reaction that occurs in one half-cell, either at the anode or at the cathode.

Ideal Non-polarizable (Depolarized) Electrode: it is a type of electrode that does not change its potential upon passage of current; example: reference electrode.

Ideal Polarizable (Polarized) Electrode (IPE): it is a type of electrode that exhibits a large change in potential for an infinitesimal change in current; example: WE.

Interface (Junction): in an electrochemical cell, it represents the location where two distinct phases come in contact with each other: solid-liquid (electrode-solution), two liquids of different concentrations and/or compositions (reference electrode-solution), etc.

Nernstian: a reversible redox process that follows equilibria equations.

Non-faradaic: processes that follow Ohm's law; they are comprised of all processes that occur at the *electrode* (excluding chemical reactions) and account for solution conductivity and capacitive charging.

Normal/Standard Hydrogen Electrode (NHE/SHE): it is the standard *reference electrode*; all *standard potentials* are referred to *NHE*; its potential is by definition 0.000 V.

Oxidation: refers to the process in which a chemical species loses one or more electrons; it is the reverse of the *reduction*.

Oxidized Species/Oxidizing Agent/Oxidant (O): the chemical species that undergoes the *reduction*, enabling the *oxidation* of a different species.

Overpotential (η [V]): deviation of the *electrode/cell potential* from its *equilibrium value*, $\eta = E - E_{eq}$; it can be either positive or negative.

Potentiometry: electrochemical methods that utilize near zero currents and have the output potential readings vs. time, using the *Nernst equation* to find analyte concentrations.

Redox: a process that involves both a *reduction* and an *oxidation*.

Redox Couple: the chemical species that has at least two oxidation states, and thus can act either as the *reduced* or the *oxidized species* (depending on the oxidation state); example: $\text{Fe}^{3+}/\text{Fe}^{2+}$.

Reduced Species/Reducing Agent/Reducant (R): the chemical species that undergoes the *oxidation*, enabling the *reduction* of a different species.

Reduction: refers to the process in which a chemical species gains one or more electrons; it is the reverse of the *oxidation*.

Reference Electrode (RE): *electrode* that can maintain a constant potential under changing experimental conditions; the *WE* potential is referenced vs. the *RE* potential; *REs* are typically *anodes* in *electrochemical cells*; example: *NHE*.

Standard Reduction Potential (E^0 [V vs. NHE]): is defined as the potential of the *reduction half-reaction* at the *electrode*, with respect to the *NHE*; each redox couple has a fixed *standard reduction potential*.

Supporting Electrolyte: an ionic substance (typically a salt) that is present in a solution to ensure its conductivity; example: KCl. The *supporting electrolyte* reduces the migration effects in the solution; it does not undergo redox chemistry, and thus its ions are called *spectator ions*. Sometimes the *supporting electrolyte* is referred to simply as the *electrolyte*.

Voltammetry: electrochemical methods that utilize a potential ramp (e.g., increase or decrease with time) and have the output current vs. potential.

Working Electrode (WE)/Indicator Electrode: *electrode* where the *redox processes* under study occur; *WEs* are typically *cathodes*; example: ion-selective electrode or noble metal.

1.3 FUNDAMENTAL EQUATIONS

The ability to predict how a system will behave under certain conditions is very important for practicing electrochemists. In this regard, the fundamental equations described in this section can be quite useful. Let us consider the case of a simple redox process:



1.3.1 Nernst equation

The Nernst equation solves the potential of an electrochemical cell containing a reversible system with fast kinetics and it is valid only at equilibrium and at the surface of the electrode:

$$E = E^0' + \frac{RT}{nF} \ln \frac{C_O^*}{C_R^*} \quad (1.3.2)$$

$$E = E^0 + \frac{RT}{nF} \ln \frac{a_O}{a_R} \quad (1.3.3)$$

where E^0' [V] is the formal potential, E^0 [V] is the standard potential, C^* [mol L^{-1}] is the bulk concentration for the considered species, and a [mol L^{-1}] is the activity. A common assumption is to ignore the activity coefficients resulting in $E^0 = E^0'$. The formal potential in equation (1.3.2) accounts for the activity coefficients for the species O and R. The values for the formal potential (see Chapter 18) are dependent upon the nature of both the solvent and the supporting electrolyte. If we consider the reduction reaction for a platinum solution (Pt^{2+}) with a concentration of 1 mM at a solid platinum electrode:



then we are able to apply the Nernst equation to calculate the voltage drop across this system; since the reduced form is a solid, it has unity activity; the activity for very dilute solutions (1 mM) is the same as the concentration, so we can write

$$E = 1.188\text{V} + \frac{RT}{2F} \ln \frac{0.001}{1} = 1.099\text{ V} \quad (1.3.5)$$

The standard electrode potential for platinum is 1.188 V and the temperature is 25 °C. The voltage of this half-reaction is 1.1 V.

1.3.2 Equilibrium constant

The free energy change in the form of equation (1.1.4) can be related to the equilibrium constant (K), assuming unit activity for electrons:

$$\Delta G^0 = -RT \ln K \quad (1.3.6)$$

This relationship is an example of the power of electrochemistry. A single experimental measurement, such as E^0 , can be used to directly calculate K . For example, a cell consisting of a silver electrode and a silver electrode coated with solid silver iodide can be used to determine the solubility product (K_{sp}) of silver iodide. For the net chemical reaction of the cell:



since AgI is a solid, K becomes K_{sp} . Given that the cell potential is -0.951 V, that it is a one electron reaction, and from equation (1.1.4):

$$\Delta G^0 = -(1)F(-0.951\text{ V}) = (0.951\text{ V})F \quad (1.3.8)$$

The value obtained for the change in free energy can be then substituted into equation (1.3.6) and K_{sp} calculated for 25 °C as follows:

$$K_{\text{sp}} = e^{-(0.951 \text{ V})F/RT} = 8.3 \times 10^{-17} \quad (1.3.9)$$

1.3.3 Mass-transfer limited current

The expression for the mass-transfer limited current i_l [A] is given by

$$i_l = nFAMC \quad (1.3.10)$$

where C [mol cm⁻³] represents the concentration of the electrochemically active species that gets converted at the electrode; if the entire analyte gets converted, then C is equal to the initial bulk concentration of the analyte, C^* . If in equation (1.3.10) we know that the analyte ($C^* = 20$ mM) reacts completely at an electrode that has the area $A = 0.1$ cm² in a process that involves the transfer of $n = 2$ electrons, and that the solution is stirred in such a manner that the mass-transfer coefficient $m = 0.01$ cm sec⁻¹, we can then calculate the value for the mass-transfer limiting current $i_l = 4$ mA.

1.3.4 Cottrell equation

The Cottrell equation is derived from Fick's second law of diffusion (Section 1.5) and predicts the variation of the current in time, when a potential step is applied under conditions of large overpotential. For this equation to be valid the current must be limited by diffusion of the analyte to the electrode surface, and thus the solution has to be unstirred. The overpotential at which the reaction is driven must be large enough to ensure the rapid depletion of the electroactive species (O) at the electrode surface, such that the process would be controlled by the diffusion to the electrode. This equation is most often applied to potential step methods (e.g., chronoamperometry; see Chapter 11):

$$i(t) = \frac{nFAD_O^{1/2}C_o}{\pi^{1/2}t^{1/2}} \quad (1.3.11)$$

where D_O [cm² sec⁻¹] is the diffusion coefficient for the species O, and A [cm²] is the electrode area.

In an unperturbed solution, when a potential step is applied that causes a surface reaction to occur, the current decays according to the Cottrell equation. One application is the determination of the diffusion coefficient for an electrochemically active species O, with the initial concentration of 0.1 M, that undergoes a single electron reduction at a 1 mm diameter electrode. The current decays to a diffusion limited current of 68 µA after 2 sec. When applying the Cottrell equation it is important to note that the concentration has to be converted to mol cm⁻³ (in our case 0.1 M corresponds to 10⁻⁴ mol cm⁻³). The electrode area is 7.85 × 10⁻³ cm², and the value for the diffusion coefficient can be calculated as 5 × 10⁻⁶ cm² sec⁻¹.

1.3.5 Faraday's law

Faraday's law correlates the total charge, Q [C], passed through a cell to the amount of product, N [mol]:

$$Q = nFN \quad (1.3.12)$$

where F is Faraday's constant, $F = 96,485.3 \text{ C mol}^{-1}$, and n is the number of electrons transferred per mole of product. Faraday's law can be used in many applications, such as electrogravimetry (to find the amount of substance deposited at an electrode) and coulometry (to find the total amount of electricity required for complete electrolysis of a compound); it can also be used for finding the number of electrons implicated in an electrolytic process. In order to reduce one mole of a generic reactant according to equation (1.3.1) ($n = 1$), we need to pass through the cell a total charge equal to $9.65 \times 10^4 \text{ C}$.

When we pass a 2 A current for 3 h through a solution containing copper ions, we are able to collect 7.11 g of pure copper. We can now find what was the oxidation state of the copper ions in the initial solution. The total charge passed through the solution is $21,600 \text{ C}$. Upon converting the mass of copper into moles (0.11 moles), we can use equation (1.3.12) to find $n = 2$. Thus our starting solution contained Cu^{2+} ions.

1.4 FACTORS AFFECTING REACTION RATE AND CURRENT

1.4.1 Current, current density, and rate

In order to grasp what is taking place in an electrochemical reaction, the concept of current and how the current changes when a stimulus is applied must be understood. The current is equal to the change in charge with time, or

$$i = \frac{dQ}{dt} \quad (1.4.1)$$

where i [A] is the faradaic current, t [sec] is the time, and Q [C] is the charge given by Faraday's law (equation (1.3.12)).

Chemical reactions can be either *homogeneous* or *heterogeneous*. The first type occurs in a single phase, and its rate is uniform everywhere in the volume where it occurs:

$$\text{Rate} [\text{mol sec}^{-1}] = \frac{dN}{dt} \quad (1.4.2)$$

Heterogeneous reactions occur at the electrode-solution interface, and they are characteristic of electrochemistry. While the expression for the reaction rate is similar to equation (1.4.2), it depends upon the area of the electrode, A [cm^2], or the area of the phase boundary where the reaction occurs:

$$\text{Rate} [\text{mol sec}^{-1} \text{ cm}^{-2}] = \frac{i}{nFA} = \frac{j}{nF} \quad (1.4.3)$$

where j [A cm^{-2}] is the current density. In order to compare processes that take place at electrodes of varying size, the rate of reaction has to be normalized for the area of the electrode (equation (1.4.3)). The size of the electrode is crucial to the amount of product created in a bulk electrolysis experiment, for example. For a one electron reaction, with 0.1 moles of reactant that gets converted into product for 1 h at an electrode of 1 cm^2 area, we can calculate the charge $Q = 9.6 \times 10^3 \text{ C}$, the current $i = 2.7 \text{ A}$, and the current density $j = 2.7 \text{ A cm}^{-2}$. From equation (1.4.3) we can then obtain the reaction rate: $28 \mu\text{mol sec}^{-1} \text{ cm}^{-2}$.

There are four major factors that govern the reaction rate and current at electrodes: (i) mass transfer to the electrode surface; (ii) kinetics of electron transfer; (iii) preceding and ensuing reactions; (iv) surface reactions (adsorption). The slowest process will be the rate-determining step. Let us consider the case of the simple reaction:



This reaction may be considered as a set of equilibria involved in the migration of the reactant to the electrode, the reaction at the electrode, and the migration of the product away from the electrode surface into the bulk of the solution (Figure 1.2).

For this reaction to proceed, O is required to move from the bulk solution near the electrode surface. This aspect of the mechanism is related to mass transfer and is governed by equations such as Fick's laws of diffusion and Nernst–Planck. Mass transfer from the bulk solution towards the electrode surface could limit the rate of the reaction (Section 1.5).

When all of the processes leading to the reaction are fast, this leaves the electron transfer reaction as the limiting factor. The measurement of fast electron transfer rates is still limited by the non-faradaic time constant for the electrode, τ [sec]:

$$\tau = R_s C_d \quad (1.4.5)$$

where R_s [Ω] is the solution resistance and C_d [F] is the double layer capacitance. In a potential step experiment, if $R_s = 1000 \Omega$ and $C_d = 10 \mu\text{F}$, we can calculate the time constant $\tau = 10 \text{ msec}$. The double layer charging will be complete (95%) in a time frame equal to 3τ (30 msec for our example) (3). For the same type of potential step experiment, the variation of the non-faradaic current, i_{nf} [A], in time, t [sec], is given by

$$i_{\text{nf}} = \frac{E}{R_s} e^{-t/R_s C_d} \quad (1.4.6)$$

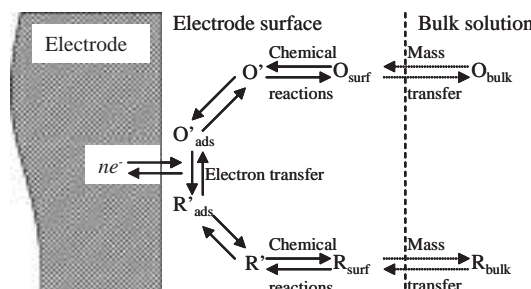


Figure 1.2 Processes involved in an electrode reaction (adapted from reference (3), with permission).

where E [V] is the magnitude of the potential step. The expression of the current from equation (1.4.6) indicates that the reaction cannot proceed faster than τ . One way to measure faster electron transfer kinetics is to increase the solution conductivity by lowering R_s . In voltammetry/amperometry this is accomplished by using a three-electrode cell instead of a two-electrode cell (Section 1.7).

In a potential sweep experiment (see Chapter 11) the output is the current, which accounts for both the faradaic and non-faradaic processes. Since the scan rate, v [V sec⁻¹] is known, it is possible to calculate the non-faradaic current, i_{nf} [A]:

$$i_{nf} = vC_d \quad (1.4.7)$$

For an electrode with $A = 0.2$ cm² and a capacitance of $15 \mu\text{F cm}^{-2}$, we can calculate $C_d = 3 \mu\text{F}$. If this electrode is employed in a potential sweep experiment where the scan rate is 10 mV sec^{-1} , then the corresponding non-faradaic current (equation (1.4.7)) is 30 nA .

The oxidized species from Figure 1.2 might undergo a chemical reaction preceding the reaction at the electrode surface. The coupled preceding chemical equilibrium can have a dramatic effect and is critical to understanding the system. If the electron transfer at the electrode is fast while the preceding chemical equilibrium is slow, then the slow chemical reaction is the *rate-determining step* and has the largest influence on the faradaic current. Also, a similar examination of reactions that occur after a fast electron transfer may provide information about the system under study (see Chapter 15).

Reactions involving changes in the electrode surface also affect the rate of the reaction. These reactions include adsorption, desorption, and crystallization. They are able to affect the system by changing the electrolyte-electrode interface, and thereby changing the electrochemical behavior of the electrode. When the electroactive species is directly adsorbed onto the surface of an electrode, the effect of “pre-concentrating” the reactant species makes them instantly available at the electrode. In a voltammetry experiment, this would lead to a curve whose shape is not affected by diffusion (Chapter 11).

1.4.2 Reversibility

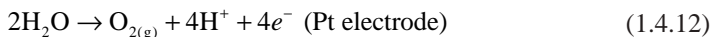
Reversibility is a key concept when dealing with electrochemical reaction mechanisms. An electrochemical cell is considered *chemically reversible* if reversing the current through the cell reverses the cell reaction and no new reactions or side products appear:



An electrochemical cell is considered *chemically irreversible* if reversing the current leads to different electrode reactions and new side products. This is often the case if a solid falls out of solution or a gas is produced, as the solid or gaseous product may not be available to participate in the reverse reaction. When a solid zinc electrode is oxidized in an acidic system with a platinum electrode the following two reactions take place:



When this system is reversed, by the application of a potential with a greater magnitude than the cell potential with the opposite bias, a different set of reactions occur, rendering this system chemically irreversible:



The concept of *thermodynamic reversibility* is theoretical. It applies to adiabatic changes, where the system is always at equilibrium. An infinitesimal change causes the system to move in one particular direction, resulting in an infinitesimal response; the analogy in electrochemistry is that a small change in potential could result in the reversal of the electrochemical process. In electrochemistry, the researcher is concerned with *practical reversibility*. In reality electrochemical processes occur at finite rates, and as long as the experimental parameters are set in a manner that allows for the reversal of the reaction to regenerate the original species, the processes are deemed *practically reversible*. For these systems the Nernst equation (equation (1.3.2)) holds true at all times.

1.4.3 Kinetics

1.4.3.1 Overpotential

For a non-spontaneous cell reaction to occur, an overpotential, η [V], must be applied. The extent to which the reaction is driven beyond the equilibrium potential, E_{eq} [V], is

$$\eta = E - E_{\text{eq}} \quad (1.4.13)$$

In order to deposit a metal ion, such as Pt^{2+} , from a solution at a certain rate, without consideration of ion concentration and the surface effects at which the deposition occurs, an application of a potential, i.e., $E = 2$ V, greater than the $E_{\text{eq}} = 1.2$ V, is necessary. In this case $\eta = 0.8$ V.

1.4.3.2 Butler–Volmer Equation

The Butler–Volmer equation can be used to predict the current that results from an overpotential when mass-transfer limitations are eliminated. Let us consider the case of a simple reduction reaction (Butler–Volmer always assumes that $n = 1$):



where k_f [cm sec^{-1}] and k_b [cm sec^{-1}] are the heterogeneous rate constants for the forward reduction and backward oxidation electrode reactions, respectively. The final form of the Butler–Volmer equation (equation (1.4.25)) predicts the current of a system as a function of the overpotential in a well-stirred cell. The overall current, i [A], can be viewed as the difference of the cathodic (reduction) current, i_c [A], and the anodic (oxidation) current, i_a [A]:

$$i = i_c - i_a \quad (1.4.15)$$

Each of the currents is proportional to their corresponding heterogeneous rate constant:

$$i_c = FAk_f C_o(0,t) \quad (1.4.16)$$

$$i_a = FAk_b C_R(0,t) \quad (1.4.17)$$

where F is Faraday's constant, A [cm^2] is the area of the electrode, and $C_j(x,t)$ [mol cm^{-3}] is the concentration of species j at the distance x [cm] from the electrode at the time t [sec]. Here we are considering reactions at the electrode surface, therefore $x = 0$. The forward and reverse rate constants can be written as a function of the standard heterogeneous rate constant, k^0 [cm sec^{-1}]:

$$k_f = k^0 e^{-\gamma f(E-E^0)} \quad (1.4.18)$$

$$k_b = k^0 e^{(1-\gamma)f(E-E^0)} \quad (1.4.19)$$

where the coefficient $f = F/(RT)$ and the transfer coefficient, γ , is a dimensionless parameter with values between 0 and 1, and is often estimated to be 0.5.

By dividing the expressions for the rate constants from equations (1.4.18) and (1.4.19) we obtain a relation that governs all models of electrode kinetics, not only for equilibrium cases (3):

$$\frac{k_b}{k_f} = e^{f(E-E^0)} = e^{-(E-E^0)/kT} \quad (1.4.20)$$

where k [J K^{-1}] is Boltzmann's constant.

By combining equations (1.4.15) – (1.4.19), the current of the reaction may be described by the complete *current–potential characteristic*:

$$i = FAk^0 [C_o(0,t)e^{-\gamma f(E-E^0)} - C_R(0,t)e^{(1-\gamma)f(E-E^0)}] \quad (1.4.21)$$

This equation is the basis for all accounts of heterogeneous electrode kinetics, including the expression for the *Butler–Volmer equation*.

When an electrochemical cell is at equilibrium there is no net current, because the system contains a cathodic current balanced by an equal and opposite anodic current:

$$i_0 = i_a = i_c \quad (1.4.22)$$

where i_0 [A] is the exchange current and can be written as

$$i_0 = FAk^0 C_o^{*(1-\gamma)} C_R^{*\gamma} \quad (1.4.23)$$

where C_j^* [mol cm^{-3}] is the bulk concentration for the j species. The exchange current can be derived experimentally from Tafel plots (Figure 1.3). Equation (1.4.23) can be used for calculating the standard heterogeneous rate constant. If the exchange current is determined to be 15 μA at a 1 mm^2 electrode in a solution where the concentrations of both the oxidized and reduced forms are 0.1 M, then $k^0 = 1.6 \times 10^{-4} \text{ cm sec}^{-1}$.

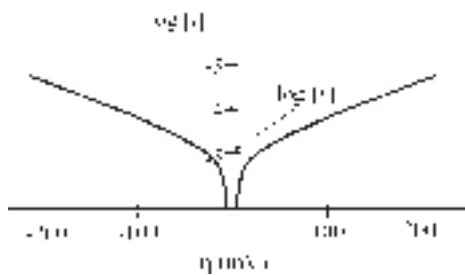


Figure 1.3 Tafel plot (adapted from reference (3), with permission).

From equations (1.4.21) and (1.4.23) we can obtain the *current–overpotential equation*:

$$i = i_0 \left[\frac{C_O(0,t)}{C_O^*} e^{-\alpha f \eta} - \frac{C_R(0,t)}{C_R^*} e^{(1-\alpha)f \eta} \right] \quad (1.4.24)$$

where η [V] is the overpotential. With efficient mass transfer the concentrations of the bulk solution and the solution at the electrode surface ($x = 0$) are equal and the *current–overpotential equation* (equation (1.4.24)) reduces to the *Butler–Volmer equation*:

$$i = i_0 \left[e^{-\alpha f \eta} - e^{(1-\alpha)f \eta} \right] \quad (1.4.25)$$

This equation can be used to predict the current when the mass-transfer limitation is eliminated. In a well-stirred solution diffusion to the electrode is no longer the limiting factor in the experiment. In a cell at 25 °C, if $\alpha = 0.5$ and $i_0 = 10 \mu\text{A}$, for an overpotential of 200 mV the resultant current calculated with equation (1.4.25) is 0.49 mA.

1.4.3.3 Tafel equation

The Tafel equation links the applied overpotential to the current, i [A], that passes through the circuit:

$$\eta = \frac{RT}{\alpha F} \ln i_0 - \frac{RT}{\alpha F} \log i \quad (1.4.26)$$

In equation (1.4.26), the y -axis intercept at no overpotential can be used to calculate the exchange current, i_0 [A]. Tafel equation can be written in a very simple form as

$$\eta = a + b \log i \quad (1.4.27)$$

where a and b are constants that can be easily inferred from equation (1.4.26). A graphic representation of $\log |i|$ vs. η is known as a *Tafel plot*. The utility of equation (1.4.27) is limited by the reverse reaction and diffusion. When the overpotentials are small (<50 mV), the slope increases because the backward reaction becomes greater than 1% of the forward reaction, changing the relative concentrations at the electrode surface (equation (1.4.24)). When very large overpotentials (>few hundred mV) are applied, the slope of the line can deviate below the prediction of the Tafel equation because of mass-transfer limitations.

Tafel plots are composed of an anodic branch for positive overpotentials and a cathodic branch for negative overpotentials. The slope of the linear region on the Tafel plot (between 50 mV and very large overpotentials) can be used to calculate α , the transfer coefficient:

$$\text{reduction slope} = \frac{-\alpha F}{2.3RT} \quad (1.4.28)$$

$$\text{oxidation slope} = \frac{(1-\alpha)F}{2.3RT} \quad (1.4.29)$$

If the slope is 8.46, then at 25 °C the transfer coefficient $\alpha = 0.5$. Tafel plots can also be used to calculate exchange current from the y-intercept of the Tafel regions. From Figure 1.3, $\log |i_0| = -5$, and thus $i_0 = 10 \mu\text{A}$.

1.5 EQUATIONS GOVERNING MODES OF MASS TRANSFER

Mass transfer can be accomplished in three different ways and/or a combination of these modes: (a) *migration*—movement of charged particles in an electric field; (b) *diffusion*—movement of species against a concentration gradient; (c) *convection*—movement of species induced by stirring or density gradients. The more modes of mass transfer are present concurrently, the more complicated the equations that describe them are.

1.5.1 Nernst–Planck equation

The Nernst–Planck equation below relates the unidirectional (x) flux of a species j to diffusion, migration, and convection:

$$J_j(x) = -D_j \frac{\partial C_j(x)}{\partial x} - \frac{z_j F}{RT} D_j C_j \frac{\partial \phi(x)}{\partial x} + C_j v(x) \quad (1.5.1)$$

↑ ↑ ↑
 1st term 2nd term 3rd term

where $J_j(x)$ [mol cm⁻² sec⁻¹] is a one-dimensional flux for species j at distance x [cm] from the electrode; D_j [cm² sec⁻¹], z_j , and C_j [mol cm⁻³] are the diffusion coefficient, the charge, and the concentration for the species j , respectively; $v(x)$ [cm sec⁻¹] is the rate with which a volume element moves in solution; $\partial C_j(x)/\partial x$ is the concentration gradient; and $\partial \phi(x)/\partial x$ is the potential gradient along the x -axis. In equation (1.5.1), the first term is concerned with the diffusion and is, in fact, Fick's first law (equation (1.5.2)), the second term accounts for the migration of the species in the solution, and the last term represents the convection of the solution.

1.5.2 Fick's laws of diffusion

Fick proposed two laws of diffusion in solution. These equations describe the relation between the flux of a substance and its concentration as a function of both time and position.

The first law describes the flux of a species, O, as a function of the change in its concentration, C_O [mol cm⁻³], with distance, x [cm], from an electrode, at a time t [sec]:

$$-J_O(x,t) = D_O \frac{\partial C_O(x,t)}{\partial x} \quad (1.5.2)$$

where $J_O(x,t)$ [mol cm⁻² sec⁻¹] is the flux of species O, and D_O [cm² sec⁻¹] is the diffusion coefficient. The second law relates the change in concentration with time to the change in flux with position:

$$\frac{\partial C_O(x,t)}{\partial t} = D_O \left(\frac{\partial^2 C_O(x,t)}{\partial x^2} \right) \quad (1.5.3)$$

From the point of view of an experimentalist that has to interpret data, it is desirable to reduce the complexity of the equations that govern the mass transfer. This can be accomplished by minimizing the effects of convection, for example, by using quiescent conditions (not stirring). Migration can be reduced by adding a supporting electrolyte to the solution to carry the current and to minimize R_s and $(\partial\phi/\partial x)$; the appropriate supporting electrolyte should be inert and present in high concentration (ca. 100 times greater than the concentration of the analyte).

Alternatively, the solution can be stirred so fast that the flux J becomes a function of convection only. Under constant stirring,

$$v(x) = m \quad (1.5.4)$$

where m [cm sec⁻¹] is the mass-transfer coefficient, and it represents the speed with which the species j gets at the surface of the electrode. Thus,

$$J = mC_j \quad (1.5.5)$$

The flux can also be written as

$$J = \frac{1}{A} \frac{dN}{dt} \quad (1.5.6)$$

where A is the area of the electrode. Since

$$\frac{dN}{dt} = \frac{i}{nF} \quad (1.5.7)$$

we can combine equations (1.5.5)–(1.5.7) to get the expression for the mass-transfer limiting current i_l [A],

$$i_l = nFAmC \quad (1.5.8)$$

The mass-transfer coefficient can be quantified for particular applications, such as the rotating disk electrode (see Chapters 11 and 19):

$$m = 0.62D^{2/3}\omega^{1/2}v^{-1/6} \quad (1.5.9)$$

where ω [sec⁻¹] is the angular frequency of rotation and ν [cm² sec⁻¹] is the kinematic viscosity; and for an ultramicroelectrode of radius r_0 , at steady state,

$$m = \frac{4D}{\pi r_0} \quad (1.5.10)$$

Mass transfer occurs before charge transfer (Figure 1.2), and we always have both processes occurring. The slower of the two processes is the rate-limiting step. If the applied potential has small values, then the charge transfer is going to be slow and will become the limiting factor; in this case we can often totally neglect the contribution of the mass transport. However, if the applied potential is high, then the charge transfer is very fast, and the mass transfer is the rate-limiting step. At low potentials, we can write the following expression for the current:

$$i = FAk_f C_o \quad (1.5.11)$$

where the reaction rate k (Section 1.4) has the same units as m . Whichever of the two is the smallest governs the reaction. If $k < m$, we are kinetically limited and apply equation (1.5.11); if $k > m$, then we are mass-transfer limited and apply equation (1.5.8).

The mass-transfer limiting current, which is by definition independent of potential, can be also written as

$$i_l = \frac{nFADC^*}{\delta} \quad (1.5.12)$$

where δ [cm] is the thickness of the Nernst diffusion layer. The values for δ are in the range 10⁻³–10⁻¹ cm (4). Equations (1.5.8) and (1.5.12) are practically the same because $m = D/\delta$.

If the mass transfer is governed by diffusion, then

$$\delta = \sqrt{\pi Dt} \quad (1.5.13)$$

From equations (1.5.12) and (1.5.13), for a diffusion-controlled unidirectional process, the current i will decrease with time, as shown by *Cottrell equation*:

$$i(t) = \frac{nFAD^{1/2}C^*}{\pi^{1/2}t^{1/2}} \quad (1.5.14)$$

Equation (1.5.13) enables the calculation of the period that takes for a molecule of analyte to wander a certain distance. If the diffusion coefficient for the analyte is 5 × 10⁻⁶ cm² sec⁻¹, then it will take 6.4 sec to wander 0.01 cm.

If in equation (1.5.14) we know that $i = 1$ mA, $n = 1$, $D = 5 \times 10^{-6}$ cm² sec⁻¹, $A = 0.1$ cm², and $\delta = 10$ μm, then we are able to calculate $C = 21$ mM. Cottrell equation enables many electrochemical techniques by relating the current in a directly proportional manner to the concentration of the electrochemically active species.

1.6 ELECTROCHEMICAL CELLS

Electrochemical cells (see Chapter 2) are divided into two sub-types, galvanic and electrolytic. Galvanic cells are those whose reactions are spontaneous ($\Delta G < 0$) when the electrodes are connected via a conductor (i.e., a copper wire), while an electrolytic cell requires a potential in excess of its OCP to be applied in order to drive an electrochemical process (e.g., non-spontaneous, $\Delta G \geq 0$). In order to better describe the composition of an electrochemical cell, a notation system has been devised to represent both the individual components of the cell and the phases in which they reside. A comma separates components that exist within the same phase in this system, and phase boundaries are represented by a single slash mark. Phase boundaries that possess a potential that is considered to be a negligible component of the overall cell potential (i.e., a salt bridge) are depicted with a double slash. The activities or concentrations of all species should also be specified, and the cell is always written from the anode (at left) to the cathode (at right). For example, a copper plating *electrolytic cell* comprised from copper and platinum electrodes immersed in an aqueous solution containing H_2SO_4 and $CuSO_4$ (Figure 1.4) would be written as



If the cell contained two divided chambers linked by a KCl salt bridge, with the first containing the platinum electrode in $CuCl_2$ and the second containing the copper electrode in HCl , it would then be written as



Electrolytic processes are used by the pharmaceutical industry (electrochemical synthesis) and heavily by the metal-refining industry where they represent the only currently utilized means of production of aluminum from alumina ore. These industrial electrolytic processes, by some estimates, use a significant fraction of the electricity produced worldwide today (5).

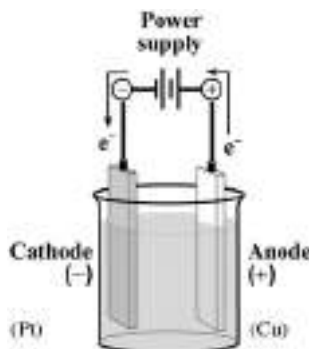


Figure 1.4 An electrolytic electrochemical cell. (for colour version: see colour section at the end of the book).

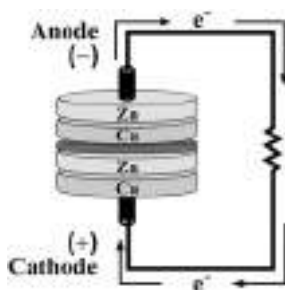
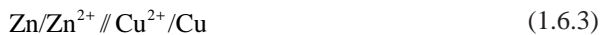


Figure 1.5 A galvanic electrochemical cell. (for colour version: see colour section at the end of the book).

The schematic depiction of Volta’s battery (Section 1.1), which is composed of stacked copper and zinc disks separated by paper soaked in an acidic solution (Figure 1.5), could be represented as



This is an example of a *primary (non-rechargeable) cell*. Other types of important galvanic cells include *secondary (rechargeable) cells* and *fuel cells*. It should be noted that when a *secondary galvanic cell* is being recharged, it becomes an *electrolytic cell*, because a potential is being applied in order to reverse the direction of the spontaneous electrochemical reaction.

While it may suffice to describe the electrodes of a galvanic cell as simply an anode or cathode, electrodes in electrolytic cells are called on to perform more specialized roles. In order to differentiate the electrodes, they are labeled according to their specific role in the cell: the working electrode (WE), the reference electrode (RE), and the counter electrode (CE), also known as the auxiliary electrode. The use of these labels helps to avoid confusion since in some experiments, where the direction of current flow reverses periodically, the WE and CE alternate between acting as anode and cathode.

The WE, typically a cathode, is generally where the reaction of interest occurs. Typical WEs (see Chapters 5 and 6) include the noble metals (especially gold and platinum), carbon (including pyrolytic carbon, glassy carbon, carbon paste, nanotubes, and vapor-deposited diamond), liquid metals (mercury and its amalgams), and semiconductors (indium-tin oxide, Si, see Chapter 9). WEs can be chemically modified (see Chapter 8) in order to increase their sensitivities toward specific species (i.e., become chemical sensors) or to decrease the potential required to drive a particular reaction (i.e., catalysis).

Regardless of whether an electrolytic cell is of the two-electrode or three-electrode configuration, it must contain a reference electrode, typically classified as an anode. The RE (see Chapter 4) is composed of a system of phases, which retain an essentially constant composition, and therefore provides a stable potential by which the WE potential can be monitored. The phases present in REs undergo reversible redox processes at a very high rate, enabling them to rapidly adjust to changes in the solution’s ionic activity, but leaving them sensitive to the passage of large current densities. For some systems, where there are no major fluctuations of ionic activity, a noble metal electrode (e.g., a platinum wire) may

be substituted for the reference electrode. In this case, the substitute is referred to as a quasi-reference electrode.

Since REs can be damaged by the presence of large current densities and may lose their ideal non-polarizable behavior, a three-electrode configuration is often used. The third electrode, called the CE/auxiliary electrode, is provided as a current sink to shunt excess current away from the RE. The CE is generally chosen to be inert under the reaction conditions (i.e., a large-area noble metal electrode such as platinum is common), and may be placed in a separate cell joined by a sintered glass frit for experiments where very large currents are generated.

1.7 CELL RESISTANCE; CAPACITANCE; UNCOMPENSATED RESISTANCE

Two types of current may flow in an electrochemical cell, faradaic and non-faradaic. All currents that are created by the reduction and/or oxidation of chemical species in the cell are termed faradaic currents. Faradaic currents may be described by the following equation:

$$\frac{dQ}{dt} = \frac{d}{dt}(nFN) = nF \frac{dN}{dt} \quad (1.7.1)$$

where Q [C] is the charge, t [sec] is the time, n is the number of electrons transferred, F is Faraday's constant, and N is the number of moles reacted. All other current is deemed non-faradaic in nature, and is directly related to Ohm's law:

$$i = \frac{V}{R} = \frac{V}{Z} \quad (1.7.2)$$

where i [A] is the current, V [V] is the potential, R [Ω] is the resistance, and Z [Ω] is the impedance. While the resistance is applicable when considering Ohm's law in an electrical circuit, the application to an electrochemical cell requires the usage of impedance, which includes elements of resistance and capacitance.

In order to describe the effects of resistance and electrode capacitance in electrochemical cells, it is useful to introduce the concept of the ideal polarizable electrode (IPE). The IPE (Figure 1.6) is one that will not pass any charge across the solution/metal interface when the potential across it is changed. The behavior of the IPE then mimics that of a capacitor in an electrical circuit, with the one difference being that the capacitance of an

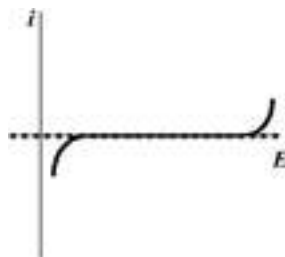


Figure 1.6 The ideal polarizable electrode in theory (dashed line) and in practice (solid line).

IPE will be dependent on the potential placed across it, while for a normal capacitor it will not. In Figure 1.6 the dashed line depicts how close a real electrode can come to behaving as an IPE over a limited potential range. Above and below that range, the real electrode will begin to pass a charge. Therefore within that specific potential range, the real electrode will mimic the IPE and behave as a capacitor.

The electrode/solution interface itself is thought of as an *electrical double layer* composed of the electrical charge at the surface of the electrode itself and the charge of the ions disbursed in the solution at a small distance from the electrode surface. This double layer is formed when a potential is applied to the electrode and causes a *charging current* (non-faradaic current) to pass through the cell. The solution half of the double layer can be thought of as being made up of distinct sub-layers (Figure 1.7). The first layer consists of solvent molecules and specifically adsorbed (desolvated) ions. The locus of the electrical centers of this layer is termed the boundary of the *inner Helmholtz plane* (IHP) and lies at a distance of χ_1 from the electrode surface. The second layer consists of solvated ions. Since these ions are completely surrounded by solvent molecules, they may approach no closer than χ_2 and the locus of the electrical charges from these ions is known as the *outer Helmholtz plane* (OHP). Ions that remain solvated are termed non-specifically adsorbed, and may only approach up to the OHP. The interactions of non-specifically adsorbed ions with the electrode surface only involve long-range electrostatics and are independent of chemical properties. The ionic species in this plane are less compact than the IHP and are disbursed in a three-dimensional region called the *diffuse layer*, which extends well into the bulk of the solution.

During most electrochemical experiments, only the reaction occurring at one electrode, usually the WE, is of interest. In these cases, an IPE is paired with an electrode whose behavior approaches that of an ideal non-polarizable electrode (e.g., an RE). When the potential is measured between the WE (IPE) and the RE, there will be a voltage drop observed that is equivalent to iR_s , as given by Ohm's law:

$$V = iR = iR_s \quad (1.7.3)$$

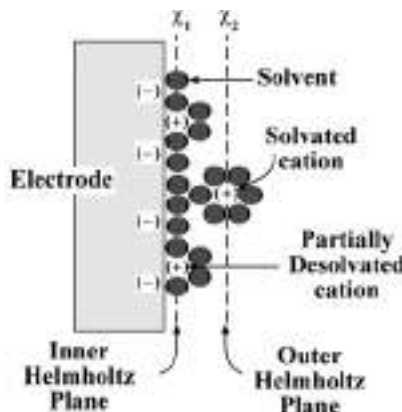


Figure 1.7 The electrical double layer (adapted from reference (3), with permission). (for colour version: see colour section at the end of the book).

where i [A] is the current passing through the cell and R_s [Ω] is the solution resistance. For systems where iR_s is small ($< 1\text{--}2 \text{ mV}$) a two-electrode system may be used. If iR_s is larger, a two-electrode cell may still be used, but it will require a smaller current. The usage of an ultramicroelectrode (UME, Chapter 6), with diameter $< 50 \mu\text{m}$, will result in a drastic decrease in current. Currents measured in systems with UMEs are typically in the nA–pA ($10^{-9}\text{--}10^{-12} \text{ A}$) range. Therefore, with a UME even non-polar solvents can be utilized without breaking the 2 mV barrier (R_s of $2 \text{ M}\Omega$ and i of 1 nA give 2 mV of potential drop).

For cases where iR_s cannot be kept below 2 mV, a three-electrode cell must be used. Usually potentiometric applications employ two-electrode cells, whereas three-electrode cells improve results for voltammetry and amperometry. The third electrode is a CE and is used as a current sink for the cell (Figure 1.8). In the three-electrode cell, the majority of the current passes between the WE and the CE, which lowers the potential drop resulting from iR_s measured between the RE and the WE, but does not completely eliminate it. If the cell is pictured as a potentiometer (Figure 1.9), the solution resistance (R_s) can be split into two components, termed the *compensated resistance* (R_c) and the *uncompensated resistance* (R_u), one of which (R_c) can be eliminated from the measurement based on the positioning of the RE. By positioning the RE as close as possible to the WE, a majority of R_s can be eliminated. In some cases (e.g., where an organic solvent is used) the total resistivity of the solution cannot be minimized sufficiently through the placement of the RE, due to the low conductivity (i.e., higher R_s) of the solvent itself. In these cases ultramicroelectrodes are generally required, since their very much smaller area greatly reduces the current, which reduces the overall value of iR_s .

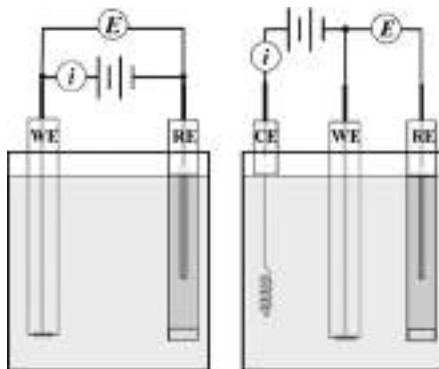


Figure 1.8 Schematic representation of two-electrode (left) and three-electrode (right) electrochemical cells. (for colour version: see colour section at the end of the book).

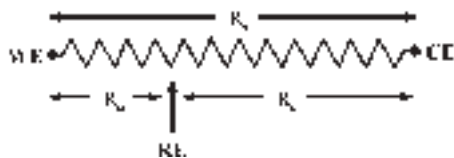


Figure 1.9 Schematic representation of an electrochemical cell as a potentiostat.

1.8 OVERVIEW OF ELECTROCHEMICAL EXPERIMENTS

The electrochemical techniques can be divided into two major groups: *static* ($i = 0$) and *dynamic* ($i \neq 0$) (6). *Potentiometry* is a *static* method, and it measures the rest potential vs. time; the most common applications in *potentiometry* are the use of ion-selective electrodes and pH meters. The *dynamic* methods comprise mostly all the other electrochemical techniques (3). Table 1.1 lists the most commonly used methods among this group.

1.9 ELECTROCHEMISTRY LITERATURE; TEXTBOOKS; SPECIALIZED BOOKS

The scope of this book is to outline the basic theories and concepts that may be encountered by a researcher in the course of basic electrochemical experimentation. This section

TABLE 1.1

General classification of electrochemical dynamic methods

Controlled Potential	Potential Step	Amperometry	Chronoamperometry; Double Potential Step Chronoamperometry						
			Chronocoulometry; Double Potential Step Chronocoulometry						
			Sampled Current Voltammetry; Differential Pulse Voltammetry; Square Wave Voltammetry						
	Potential Sweep	Voltammetry	Stationary	Linear Scan Voltammetry					
				Cyclic Voltammetry					
			Hydro-dynamic	Stirred Solution/ Flow Cell					
				Rotating Disk Electrode; Rotating Ring-Disk Electrode					
			Anodic Stripping Voltammetry (Stationary/Hydrodynamic)						
	Constant Potential	Bulk Electrolysis	Stirred Solution Flow Electrolysis						
Controlled Current	Chronopotentiometry		Constant-Current Linearly Increasing Current Current Reversal Cyclic						
			Coulometry						
			Coulometric Titrations						
			Electrolysis						
Controlled Charge	Charge Step	Coulostatic Methods							
Impedance Techniques	ac Voltammetry (ac Polarography)								
	Electrochemical Impedance Spectroscopy								

aims to serve as an introduction to a few of the types of literature (published in English) that may be relied upon to provide additional assistance to those researchers. There are a few key scientific journals that focus exclusively on electrochemistry, and those will be listed here along with their publishers. Also included are publications that, while not exclusively focusing on electrochemistry, often include significant articles on the science. Additionally, there is a well-established pool of review series and more specialized texts that give a far more in-depth consideration of specific electrochemical principles than is the goal of this book. The lists here are intended as a starting place, and as always should supplement, rather than replace, a search of current scientific literature.

1.9.1 Electrochemical journals

- Analytical Chemistry (1947-), ACS Publications.
- Bioelectrochemistry (1974-), Elsevier.
- Electroanalysis (1989-), Wiley.
- Electrochemical and Solid State Letters (1998-), The Electrochemical Society.
- Electrochemistry Communications (1999-), Elsevier.
- Electrochimica Acta (1959-), Elsevier.
- Journal of the American Chemical Society (1879-), ACS Publications.
- Journal of Applied Electrochemistry (1971-), Kluwer Academic Publishers.
- Journal of Electroanalytical Chemistry and Interfacial Chemistry (1959–1992), Journal of Electroanalytical Chemistry (1992-), Elsevier.
- Journal of the Electrochemical Society (1902-), The Electrochemical Society.
- Journal of Physical Chemistry (1896–1996, after 1997 Journal of Physical Chemistry B), ACS Publications.
- Journal of Solid State Electrochemistry (1997-), Springer-Verlag.
- Langmuir (1985-), ACS Publications.
- Solid State Ionics (1980-), Elsevier.

1.9.2 Specialized texts

1.9.2.1 General

- W. J. Albery, *Electrode Kinetics*, Clarendon Press, Oxford, 1975.
- A. J. Bard, L. R. Faulkner, Eds., *Electrochemical Methods: Fundamentals and Applications*, 2nd ed., John Wiley and Sons: New York, 2001.
- J. O'M. Bockris, S. U. M. Khan, *Surface Electrochemistry: A Molecular Level Approach*, Plenum Press: New York, 1993.
- J. O'M. Bockris, A. K. N. Reddy, *Modern Electrochemistry*, 2nd ed., Plenum Press: New York, 1998, 2 volumes
- J. O'M. Bockris, S. U. M. Khan, *Quantum Electrochemistry*, Plenum Press: New York, 1979.
- P. A. Christensen, A. Hamnett, *Techniques and Mechanisms in Electrochemistry*, Blackie Academic and Professional: New York, 1994.
- B. E. Conway, *Theory and Principles of Electrode Processes*, Ronald Press: New York, 1965.
- E. Gileadi, *Electrode Kinetics for Chemists, Chemical Engineers, and Materials Scientists*, VCH: New York, 1993.

- H. H. Girault, *Analytical Electrochemistry*, EPFL-Press: Lausanne, Switzerland, 2004.
- J. Goodisman, *Electrochemistry: Theoretical Foundations, Quantum and Statistical Mechanics, Thermodynamics, the Solid State*, Wiley: New York, 1987.
- C. H. Hamann, A. Hamnett, W. Vielstich, *Electrochemistry*, Wiley-VCH: Weinheim, Germany, 1997.
- G. Hodes, *Electrochemistry of Nanomaterials*, Wiley-VCH: Weinheim, Germany, 2001.
- D. J. G. Ives, G. J. Janz, *Reference Electrodes: Theory and Practice*, Academic Press: New York, 1961.
- K. Izutsu, *Electrochemistry in Nonaqueous Solutions*, Wiley-VCH: Weinheim, Germany, 2002.
- J. Koryta, J. Dvorak, L. Kavan, *Principles of Electrochemistry*, 2nd ed., Wiley: New York, 1993.
- H. Lund, O. Hammerich, *Organic Electrochemistry*, Marcel Dekker: New York, 2001.
- D. A. MacInnes, *The Principles of Electrochemistry*, Dover: New York, 1961.
- R. Memming, *Semiconductor Electrochemistry*, Wiley-VCH: Weinheim, Germany, 2001.
- P. M. S. Monk, *Fundamentals of Electroanalytical Chemistry*, Wiley: New York, 2001.
- J. S. Newman, *Electrochemical Systems*, 2nd ed., Prentice-Hall: Englewood Cliffs, NJ, 1991.
- K. B. Oldham, J. C. Myland, *Fundamentals of Electrochemical Science*, Academic Press: San Diego, 1994.
- A. J. L. Pombeiro, C. Amatore, Eds., *New Trends in Molecular Electrochemistry*, Marcel Dekker: New York, 2004.
- P. H. Rieger, *Electrochemistry*, 2nd ed., Chapman and Hall: New York, 1994.
- I. Rubinstein, Ed., *Physical Electrochemistry: Principles, Methods, and Applications*, Marcel Dekker: New York, 1995.
- W. Schmickler, *Interfacial Electrochemistry*, Oxford University Press: New York, 1996.
- J. Wang, *Analytical Electrochemistry*, 2nd ed., John Wiley and Sons: New York, 2000.
- P. Zanello, *Inorganic Electrochemistry: Theory, Practice, and Applications*, Royal Society of Chemistry: Cambridge, England, 2003.

1.9.2.2 Methodology

- R. N. Adams, *Electrochemistry at Solid Electrodes*, Marcel Dekker: New York, 1969.
- A. J. Bard, *Electrogenerated Chemiluminescence*, Marcel Dekker: New York, 2004.
- C. M. A. Brett, A. M. O. Brett, , *Electrochemistry: Principles, Methods, and Applications*, Oxford University Press: UK, 1993.
- P. Delahay, *New Instrumental Methods in Electrochemistry*, Interscience: New York, 1954.
- Z. Galus, *Fundamentals of Electrochemical Analysis*, 2nd ed., Wiley: New York, 1994.
- E. Gileadi, E. Kirowa-Eisner, J. Penciner, *Interfacial Electrochemistry: An Experimental Approach*, Addison-Wesley: Reading, MA, 1975.
- P. T. Kissinger, W. R. Heineman, Eds., *Laboratory Techniques in Electroanalytical Chemistry*, 2nd ed., Marcel Dekker: New York, 1996.
- J. J. Lingane, *Electroanalytical Chemistry*, 2nd ed., Interscience: New York, 1958.
- D. D. Macdonald, *Transient Techniques in Electrochemistry*, Plenum Press: New York, 1977.
- C. K. Mann, K. K. Barnes, *Electrochemical Reactions in Nonaqueous Systems*, Marcel Dekker: New York, 1970.
- D. T. Sawyer, A. Sobkowiak, J. L. Roberts, Jr., *Electrochemistry for Chemists*, 2nd ed., John Wiley and Sons: New York, 1995.
- F. Scholz, Ed., *Electroanalytical Methods: Guide to Experiments and Applications*, Springer: New York, 2002.
- F. Scholz, U. Schroeder, R. Gulaboski, *The Electrochemistry of Particles and Droplets Immobilized on Electrode Surfaces*, Springer: New York, 2004.

Southampton Electrochemistry Group, *Instrumental Methods in Electrochemistry*, Ellis Horwood: Chichester, UK, 1985.

P. Vanysek, Ed., *Modern Techniques in Electroanalysis*, Wiley: New York, 1996.

1.9.2.3 Data

- A. J. Bard, R. Parsons, J. Jordan, Eds., *Standard Potentials in Aqueous Solution*, Marcel Dekker: New York, 1985.
- B. E. Conway, *Electrochemical Data*, Elsevier: Amsterdam, 1952.
- A. L. Horvath, *Handbook of Aqueous Electrolyte Solutions: Physical Properties, Estimation, and Correlation Methods*, Ellis Horwood: Chichester, UK, 1985.
- G. J. Janz, R. P. T. Tomkins, *Nonaqueous Electrolytes Handbook*, Academic Press: New York, 1972, 2 volumes.
- L. Meites, P. Zuman, *Electrochemical Data*, Wiley: New York, 1974.
- L. Meites, P. Zuman, et al., *CRC Handbook Series in Organic Electrochemistry*, CRC Press: Boca Raton, FL, 1977–1983, 6 volumes.
- L. Meites, P. Zuman, et al., *CRC Handbook Series in Inorganic Electrochemistry*, CRC Press: Boca Raton, FL, 1980–1988, 8 volumes.
- R. Parsons, *Handbook of Electrochemical Data*, Butterworths: London, 1959.
- J. F. Zemaitis, D. M. Clark, M. Rafal, N. C. Scrivner, *Handbook of Aqueous Electrolyte Thermodynamics: Theory and Applications*, Design Institute for Physical Property Data: New York, 1986.

1.9.3 Review series

- A. J. Bard (from Vol. 19 with I. Rubinstein), Eds., *Electroanalytical Chemistry*, Marcel Dekker: New York, 1966–2004, 22 volumes.
- A. J. Bard et al., Eds., *Encyclopedia of Electrochemistry*, Wiley-VCH: Germany, 2002–2007, 11 volumes.
- A. J. Bard, H. Lund, Eds., *Encyclopedia of the Electrochemistry of the Elements*, Marcel Dekker: New York, 1973–1986, 16 volumes.
- B. E. Conway et al., Eds., *Modern Aspects of Electrochemistry*, Plenum Press: New York, 1954–2004, 38 volumes.
- P. Delahay, C. W. Tobias (from Vol. 10, H. Gerischer, C. W. Tobias), Eds., *Advances in Electrochemistry and Electrochemical Engineering*, Wiley: New York, 1961–1984, 13 volumes.
- H. Gerischer, C. W. Tobias, Eds., *Advances in Electrochemistry and Electrochemical Engineering*, Wiley-VCH: Weinheim, Germany, 1990–1997, 5 volumes.
- Specialist Periodical Reports, *Electrochemistry*, G. J. Hills (Vols. 1–3), H. R. Thirsk (Vols. 4–7), and D. Pletcher (Vols. 8–10) Senior Reporters, The Chemical Society: London, 1968–1985, 10 volumes.
- E. Steckhan, Ed., *Electrochemistry (Topics in Current Chemistry)*, Springer: New York, 1987–1997, 6 volumes.
- E. Yeager, J. O'M. Bockris, B. E. Conway et al., Eds., *Comprehensive Treatise of Electrochemistry*, Plenum Press: New York, 1984, 10 volumes.
- E. Yeager, A. J. Salkind, Eds., *Techniques of Electrochemistry*, Wiley-Interscience: New York, 1972–1978, 3 volumes.

REFERENCES

1. D. E. Roller, R. Blum, *Physics: Electricity Magnetism and Light*, Holden-Day: San Francisco, 1982, Vol. 2.

2. A. D. McNaught, A. Wilkinson, IUPAC, *Compendium of Chemical Terminology: IUPAC Recommendations*, Blackwell Science: Oxford, England; Malden, MA, USA, 1997.
3. A. J. Bard, L. R. Faulkner, *Electrochemical Methods: Fundamentals and Applications*, Wiley: New York, 2001.
4. E. Gileadi, *Electrode Kinetics for Chemists, Chemical Engineers, and Materials Scientists*, VCH: New York, 1993.
5. United States Energy Information Administration, Office of Energy Markets, EIA-846, 1998 *Manufacturing Energy Consumption Survey*, 1998.
6. P. T. Kissinger, W. R. Heineman, *Laboratory Techniques in Electroanalytical Chemistry*, Marcel Dekker: New York, 1984.

This page intentionally left blank

Part Two

LABORATORY PRACTICAL

This page intentionally left blank

- 2 -

Practical Electrochemical Cells

Shaowei Chen

Department of Chemistry and Biochemistry, University of California,
Santa Cruz, CA 95064, USA

2.1 MATERIALS

There are a variety of materials that can be used to make electrochemical cells. The most common ones include glass (Pyrex and quartz), Teflon, Kel-F, and Nylon. A practical consideration in selecting these materials is that the materials should be easily processable, inert to the electrochemical reactions, and cost-effective. For most electrochemical reactions, a Pyrex glass cell is used because it is easy to make and glass is generally a very low cost material. However, when the reaction involves media that are corrosive to glass (e.g., high pH, hydrofluoride, etc.), Teflon, Kel-F, Nylon or other plastic materials should be used instead. In the presence of some organic solvents, however, the plastic materials might decompose leading to contamination and hence interference in sensitive measurements. It should also be noted that in the presence of some strong acids, sometimes Nylon may not be stable and therefore glass should be the material of choice.

2.2 GENERAL CELL DESIGNS

The exact design of an electrochemical cell varies with the specific needs of an experiment. On the laboratory scale, typically if the amount of analytes is not a concern, a 25–50 mL cell (or even larger) can be used for the sake of convenience. With limited quantities of samples, a solution volume of a few mL is reasonable. Even smaller volumes of sample solutions (say, <μL) are also possible. However, in these cases, electrodes of ultrasmall dimensions (UMES, see Chapter 6) will have to be used and aligned properly. Complication in the current/potential measurements might occur as a result from solution resistance (see Chapters 1 and 3) and heterogeneity of the electrolyte solutions. These may render data analysis difficult and sometimes ambiguous.

In this chapter, we will describe several examples of electrochemical cell designs for a variety of systems and applications in a research laboratory. It should be noted that the

overview is not intended to be exhaustive. Rather, it provides some illustrating examples where one may adapt or modify the fundamental principles for their specific needs. The readers may refer to other reviews for more information (1).

2.2.1 Two-electrode cells

Two-electrode cells (see Chapter 1) consist of a working electrode and a reference electrode. Since the potential of the working electrode is monitored relative to the reference electrode, the potential of the reference electrode must be maintained at a constant value. In other words, the reference electrode must behave as an ideal nonpolarized electrode with current passing between working and reference electrodes. Classically, two-electrode cells have been used in polarographic studies with a dropping mercury electrode (DME) as the working electrode and a large mercury pool as the reference (Figure 2.1). These two electrodes are aligned concentrically. Since the area of the pool is substantially large compared to that of the DME electrode, the pool is considered unpolarized and hence a reasonably good reference for potential control (though of an unknown potential). Another issue that one has to bear in mind is the solution resistance (R_s) and consequently the iR_s drop. Typically in these polarographic measurements, $i < 10 \mu\text{A}$ and $R_s < 100 \Omega$ and hence $iR_s < 1 \text{ mV}$, which is negligible. For more resistive systems such as nonaqueous media, one can use a very small electrode (for instance, an ultramicroelectrode, see Chapter 6) to keep a very low current profile, on the order of nA. With such a current scale, solution resistance within the range of $\text{k}\Omega$ to $\text{M}\Omega$ can still be acceptable.

Two-electrode cells have also been used in measurements of the solid-state electronic conductivity of nanoparticles and other materials. A typical cell is a concentric tubular structure with an inner dimension on the order of a few mm where a pair of disk-shaped electrodes can be plugged in and sandwich the electrolyte confined within a tubular interior (Figure 2.2). To maintain good contact between the electrode and the electrolyte, the two electrodes have to be pressed in where the interelectrode distance can be accurately

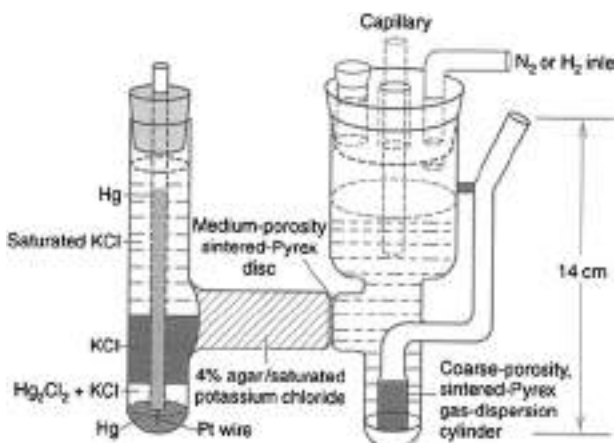


Figure 2.1 Two-electrode cell for polarography (2, 3).



Figure 2.2 Two-electrode cell for solid-state conductivity measurements. (for colour version: see colour section at the end of the book).

measured by a micrometer scale. Therefore, the cell materials should be able to sustain a relatively high mechanical pressure. Materials with good mechanical toughness such as Kel-F are generally a good choice; glass is generally too brittle, while Nylon and Teflon are too soft. To maintain the electrode positions during experimental measurements, some screw threads can be machined onto the electrodes and the interior of the electrochemical cell such that hand tightening may be good enough to achieve a satisfactory contact between the electrode and the electrolyte.

2.2.2 Three-electrode cells

Three-electrode cells (see Chapter 1) are the most commonly used setup in electrochemical studies, especially when the cell resistance is relatively high. In this configuration, the potential of the working electrode is still monitored relative to the reference potential; however, the current passes between the working electrode and a separate auxiliary (counter) electrode. Since no (or little) current passes to the reference electrode (see Chapter 4), it approaches ideal nonpolarizability and is hence a reliable reference for potential control. Experimentally, the tip of the reference electrode is placed as close as possible to the working electrode in order to minimize (uncompensated) solution resistance where control of the voltammetric current scale will also be critical, as mentioned above. The position of the reference tip should not interfere with the mass transfer of electrolyte species. Two typical configurations are shown in Figure 2.3. Generally the cell constitutes three compartments that can be separated by a glass frit with medium porosity (top panel). The glass frits are used to reduce the interference of electrochemical reactions at the counter electrode and yet allow electrical conductivity. Generally, the center compartment contains the supporting electrolyte and the redox molecules, whereas in the two side compartments only the supporting electrolyte is added. An additional opening can be added for degassing purposes (details below). In cases where no substance is produced at the counter electrode via electrolysis that can reach the working electrode, a frit separator is not necessary (bottom panel).

2.3 ELECTROCHEMICAL CELLS FOR SPECIFIC APPLICATIONS

2.3.1 Flow-through cells

Flow-through cells involve a continuous feeding of sample solution and hence can be used for real-time detection and monitoring. The exact configuration varies with the specific needs of an experiment. Figure 2.4 shows some typical cell arrangements (e.g., thin-layer cell (TLC) and wall-jet cell) and electrode geometries including tubular electrodes, planar

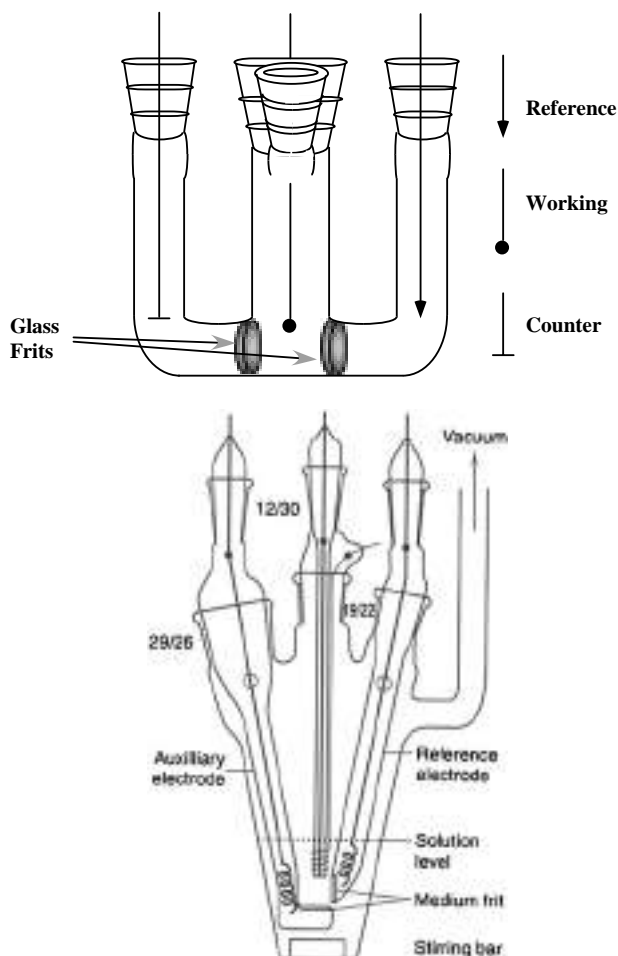


Figure 2.3 Three-electrode electrochemical cells. Three-compartment cell with (top panel) and without (bottom panel) glass frits (3, 4). (for colour version: see colour section at the end of the book).

electrodes with parallel flow, planar electrodes with perpendicular flow, and wall-jet electrodes. Flow cells can be in two- or three-electrode configurations.

Figure 2.5 shows a two-electrode flow cell with reticulated vitreous carbon (RVC) as the working electrode. There are a wide variety of electrode materials for flow cell applications ranging from microconical platinum, to platinum grid, to gold micromesh, to graphite packing, etc. In this configuration, the sample solution is fed through the cell under a constant flow and a steady-state current is measured. It should be noted that here the reference electrode is isolated from the sample solution by a cation-exchange membrane and the internal filling solution is also replaced continually. The immediate advantage of such a design is drastic simplification of instrumentation and accurate and precise measurements of low concentrations of analytes.

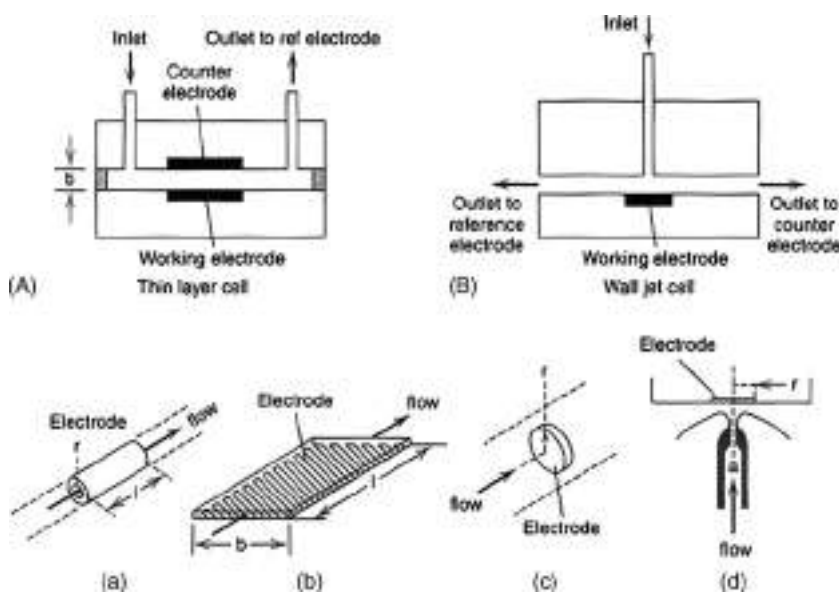


Figure 2.4 Typical cell arrangements and electrode geometries for electrochemical flow cells. Top: (A) thin-layer cell, (B) wall-jet cell. Bottom: Various electrode geometries: (a) tubular electrode, (b) planar electrode with parallel flow, (c) planar electrode with perpendicular flow, (d) wall-jet electrode (5, 6).

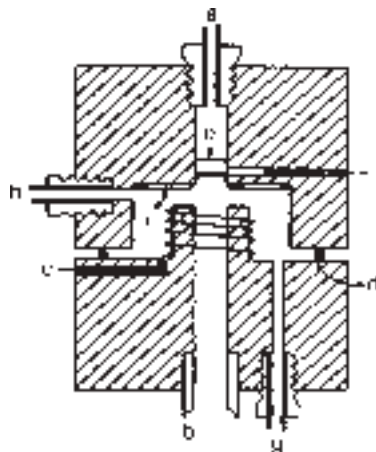


Figure 2.5 Flow-through cell with RVC electrode and reference electrode. a, sample solution inlet; b, sample solution outlet (Tygon); c, lead to reference electrode; d, O-ring; e, RVC electrode, one disk shown; f, cation exchange membranes; g, reference solution inlet; h, reference solution outlet; i, lead to working electrode (7).

In a three-electrode configuration, the flow direction is typically parallel to the working electrode surface; the working electrode is placed opposite to the auxiliary electrode in the walls of the thin flow channel. Thus, the current density across the electrode is not significantly influenced by iR drop due to the low impedance between the electrodes. The performance can be further enhanced by using parallel or series working electrodes, as shown in Figure 2.6. Such flow cells can be used as detector cells in liquid chromatography (Figure 2.7), where there can be at least two configurations: (a) the auxiliary and reference electrodes can be placed downstream from the working electrode; (b) the working and auxiliary electrodes are facing each other across the flow channel and the reference electrode is placed downstream.

In other systems, the flow is perpendicular to and centered on the electrode surface. The main advantage is to reduce the dead volume and enhance the mass transfer to the working electrode surface. An example is shown in Figure 2.8 and such a configuration has been used as a detector in microbore chromatography. For bulk electrolysis, perpendicular flow cells have also been used with a working electrode of large surface area (Figure 2.9).

Flow cells can also be equipped with dual working electrodes that serve as the generator and collector electrodes. The working principle is similar to that of a rotating ring-disk

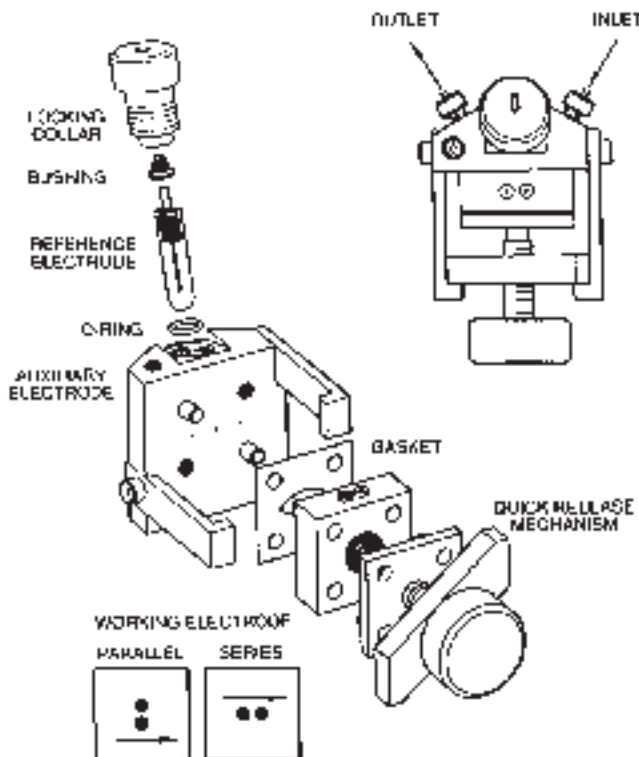


Figure 2.6 Cross-flow cell design with parallel or series working electrodes (8).

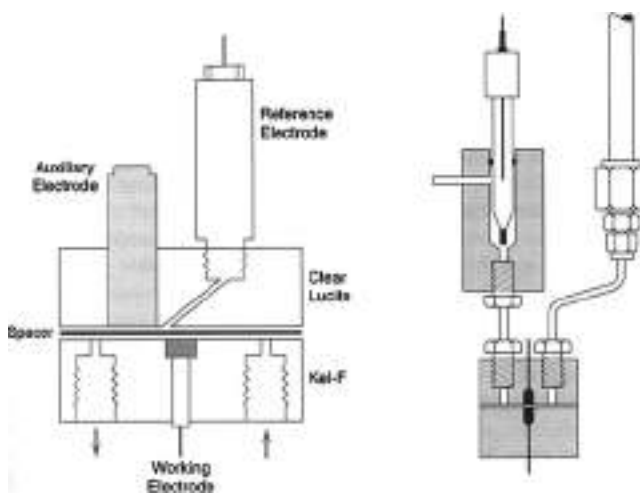


Figure 2.7 Thin-layer LC detector cells. *Left:* Cell with auxiliary and reference electrodes in thin-layer portion downstream from working electrode (9). *Right:* Cell with working and auxiliary electrodes facing each other and reference electrode downstream in flow channel (10, 11).

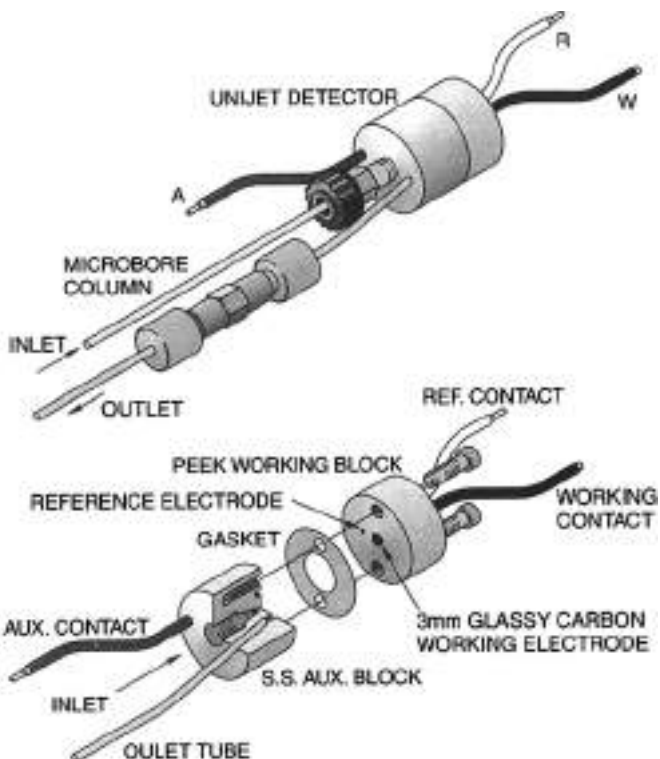


Figure 2.8 Radial flow thin-layer electrochemical cell for microbore chromatography (8).

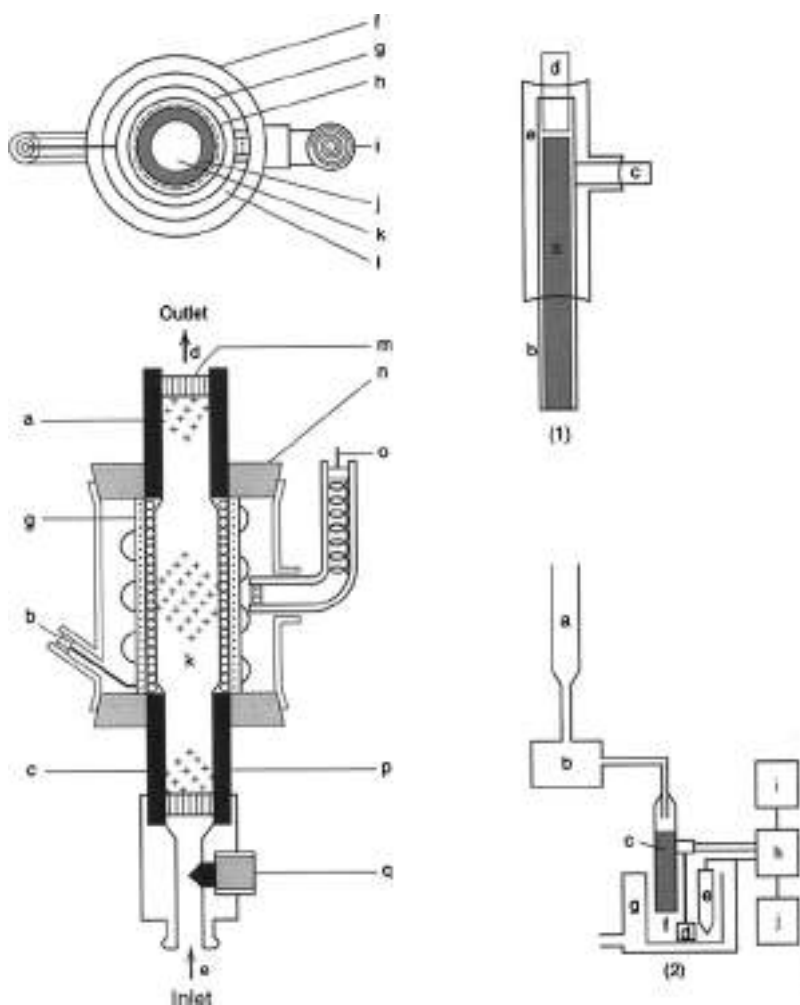


Figure 2.9 Flow electrolytic cells. *Left:* cell utilizing glassy carbon granule working electrode (k), silver auxiliary electrode (g), Ag/AgCl reference electrode (o, i) with porous glass separator (h). Other components are (a, c) lead for working electrode; (b) lead to auxiliary electrode; (d) solution outlet; (e) solution inlet; (f) glass or plastic tube; (j, p) porous carbon tube; (l) saturated KCl solution; (m) silicon rubber (12). *Right:* cells with reticulated vitreous carbon (RVC). (1): (a) RVC cylinder, (b) heat shrink tube, (c) graphite rid sidearm, (d) glass tube, (e) glass and epoxy support. (2) Schematic diagram of complete apparatus. (a) Solution reservoir, (b) pump, (c) RVC electrode, (d) platinum electrode, (e) saturated calomel electrode (SCE) reference electrode, (f) downstream reservoir, (g) run-over collector, (h) potentiostat, (i) recorder, and (j) digital voltmeter (13, 14).

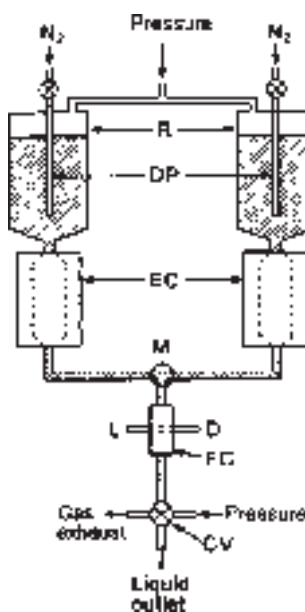


Figure 2.10 (a) Schematic representation of a dual-electrode flow cell. (b) Actual complete dual electrode flow assembly. Solution flows by gravity from upper reservoir. For greater clarity, the “O-ring joint” portion of the cell with the dual working electrodes is shown in exploded form. A close-up view of this portion with the porous silver electrodes is shown in (c) (15, 16).

electrode. A setup is shown in Figure 2.10 where the two electrodes are large beds of glassy carbon particles.

It is anticipated that, in comparison with the two-electrode counterpart, the three-electrode design will provide better control of electrode potential and voltammetric detection in reaction media of high resistance and high currents.

2.3.2 Thin-layer cells (TLCs)

Thin-layer cells (TLCs) typically involve a micrometer-thick (2–100 μm) layer of electrolyte solution that is confined at the electrode surface (the above-mentioned thin-layer flow cell is one example). This confinement can be created by two working electrodes that face each other (twin-electrode mode) or a working electrode facing a flat barrier (single-electrode mode), as shown in Figure 2.11. Since the cell thickness is generally smaller than the diffusion layer thickness, mass transfer within the layer can be ignored. Therefore, the reaction is akin to bulk electrolysis, but within a confined interfacial environment. The thickness of the solution layer can be accurately adjusted and measured by a micrometer scale. For the twin-electrode (generator–collector) configuration, ideally, the two working

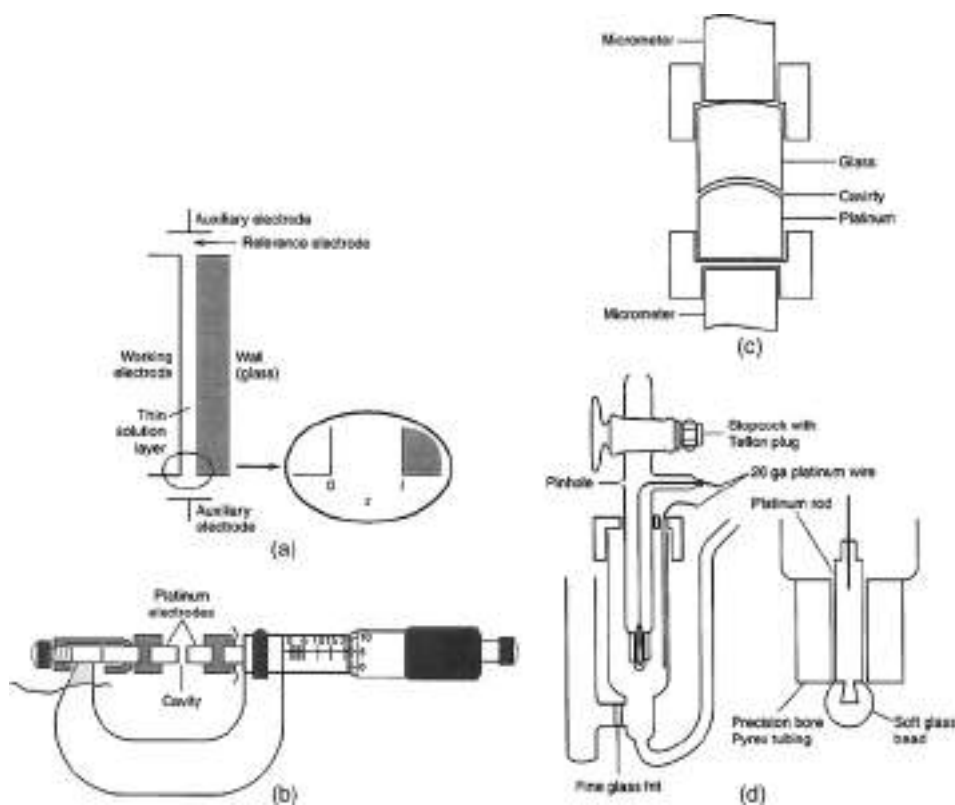


Figure 2.11 (a) Schematic diagram of a single-electrode thin-layer cell. (b) Micrometer, twin-electrode thin-layer cell with adjustable solution layer thickness. (c) Close-up of electrode portion for single-electrode configuration of (b). (d) Capillary-wire single electrode thin-layer electrode (17, 18).

electrodes are of the same geometric area and positioned concentrically facing each other. The bottom electrode is embedded in the cell housing with the electrode surface at the same level as the compartment bottom. The entire housing can be attached to the stationary end of a micrometer scale (by a set screw, for instance). The top electrode is attached to the moving piston of the micrometer scale. A lid can be put on the cell chamber for enclosure purpose. In the center there is an opening for the top working electrode and two small holes are drilled for electrical contacts for the reference and counter electrodes (an additional one can be made for deaerating purpose). It is important that the electrode surfaces are flat and ideally should parallel to each other. In addition, the thin-layer area is generally kept much larger than that of the working electrodes to minimize mass transfer effect from the edge. Since the counter electrode is generally placed outside the thin-layer portion, a rather significant resistive drop may occur between the working electrode and the counter electrode which may complicate the distributions of electrode potential and current density.

The cell can be made of Teflon, Kel-F, or Nylon with electrical contacts to the electrodes achieved by set screws. This type of setup generally works very well for aqueous electrochemical systems. For volatile organic media, leaking and evaporation of solvents will be an issue. One possible solution is to put the entire cell setup inside a housing container that is saturated with the respective solvent.

2.3.3 Spectroelectrochemical cells

Spectroscopic measurements can be carried out concurrently with electrochemical control (see Chapter 14), with each technique providing complementary information about the chemical systems of interest. These studies mainly involve two modes, transmission and reflection, and the measurements can be *in situ* or *ex situ*. In transmission experiments, the typical setup involves a light beam passing through the working electrode. One can then, for example, measure the optical absorbance as a function of electrochemical potentials. Figure 2.12 shows one of these cells used in UV-vis measurements. One can also use a quartz cuvette as the electrochemical cell inside which the three electrodes are placed. Here the (quasi)reference and counter electrodes are placed at the corners of the cuvette while the working electrode is typically made of materials of optical transparency so that it will not interfere with the optical pathway. There are a variety of electrodes that are optically transparent, including indium-tin oxide (ITO), gold or platinum minigrids, and ultrathin gold films (e.g., <50 nm) deposited onto a glass substrate. Figure 2.13 shows

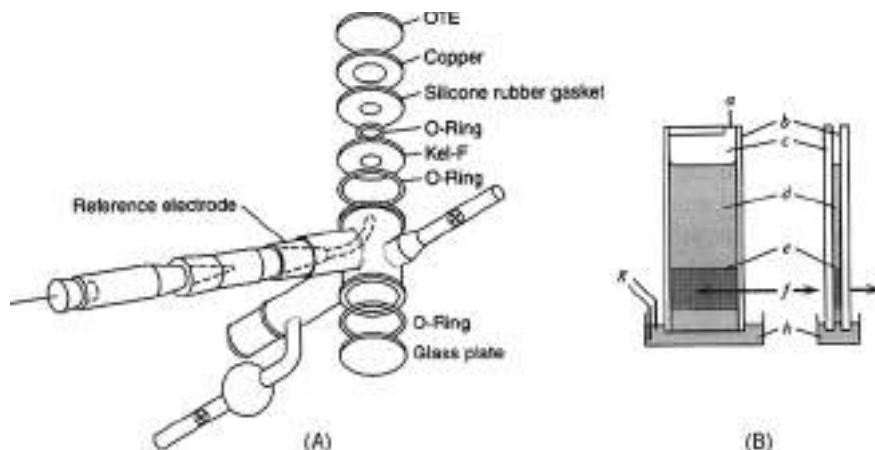


Figure 2.12 (A) Cell for transmission spectroelectrochemistry involving semi-infinite linear diffusion. Light beam passes along vertical axis (19). (B) Optically transparent thin-layer system: front and side views. (a) Point of suction application in changing solutions; (b) Teflon tape spacers; (c) 1 × 3 in. microscope slides; (d) test solution; (e) gold minigrid, 1 cm height; (f) optical beam axis; (g) reference and auxiliary electrodes; and (h) cup containing test solution (20, 21).

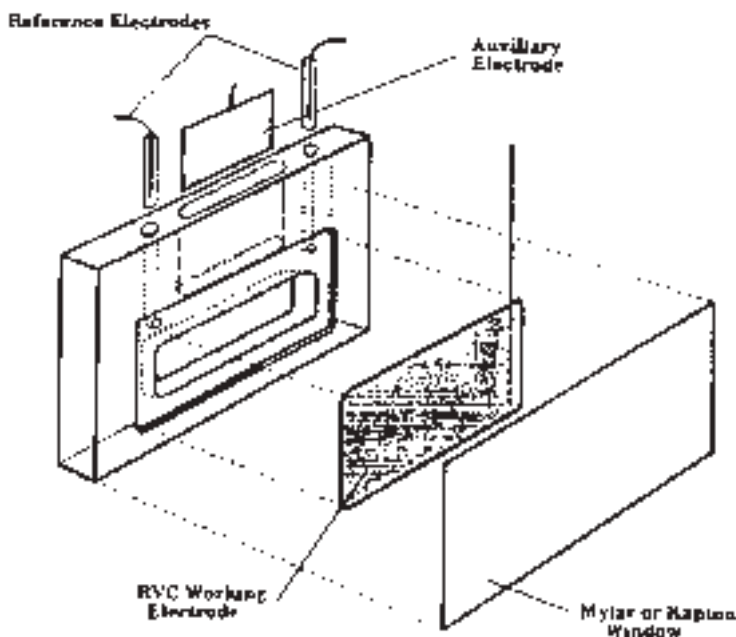


Figure 2.13 Assembly of sandwich-type optically transparent electrochemical cell for EXAFS spectroelectrochemistry (22).

a sandwich-type electrochemical cell for extended X-ray absorbance fine structure (EXAFS) spectroelectrochemistry where the cell body is of MACOR and the working electrode is RVC.

One may recognize that there exists a concentration gradient of the reaction product at the electrode surface. This might complicate the quantitative spectroscopic evaluation. In combination with the flow cells described above, one can design a spectroelectrochemical flow cell for continuous monitoring of the sample solutions, where the concentration of the electrogenerated species can be maintained uniform in the solution. The feeding of the solution is through a thin channel between a working electrode and a counter electrode and is controlled by an outside pump. Figure 2.14 depicts a representative stop-flow spectroelectrochemical setup.

In the reflection mode, typically specular reflectance is measured on the electrode surface. It is anticipated that the variation of the surface structure (e.g., surface adsorption, phase transitions, etc.) will result in appreciable changes in the reflectivity properties. One can thus correlate the structural characteristics gleaned from spectroscopic measurements with electrochemical results. Figure 2.15 shows a cell assembly for internal reflection spectroelectrochemistry. Several spectroscopic techniques have been used, such as infrared, surface plasmon resonance, and X-ray based techniques (reflectivity, standing wave, etc.). Figure 2.16 depicts a cell setup for (A) infrared spectroelectrochemistry (IR-SEC) and (B) surface X-ray diffraction.

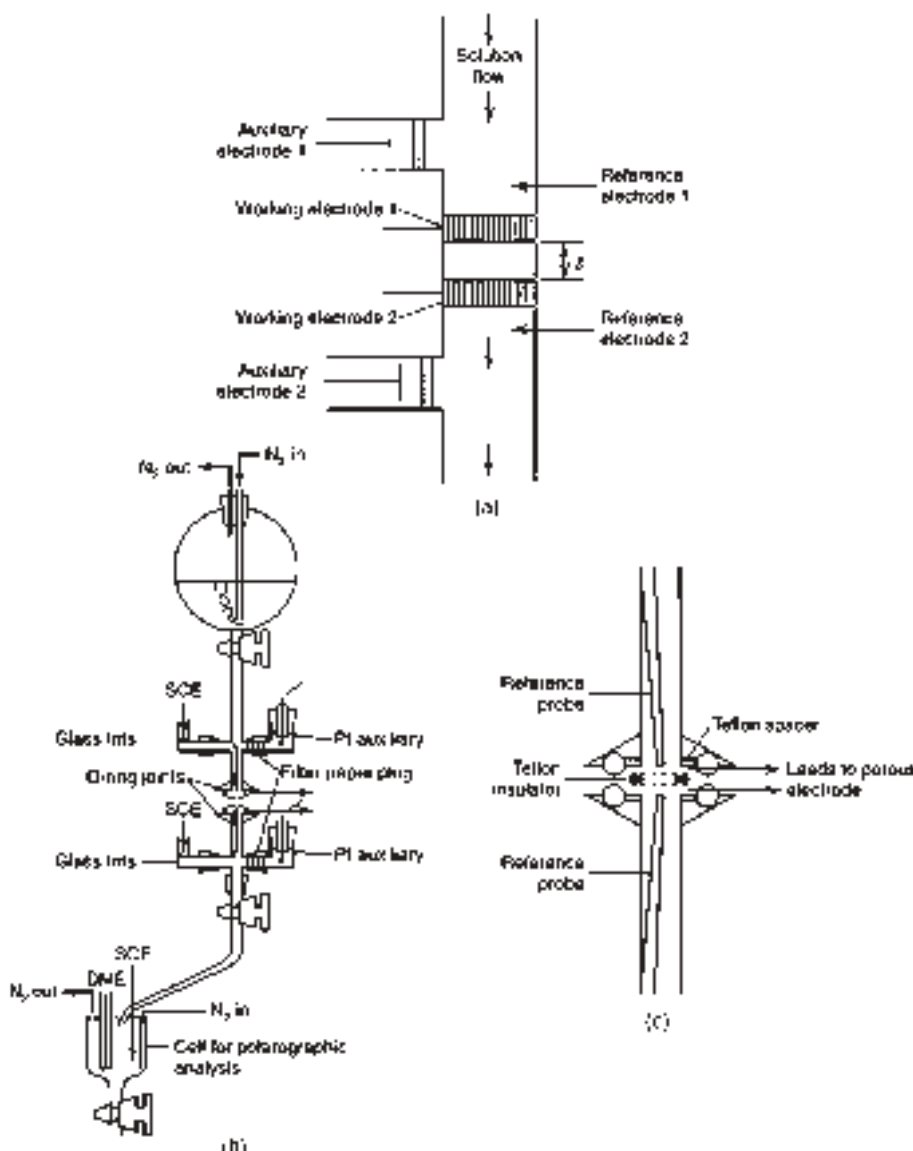


Figure 2.14 A stopped-flow optical absorption cell equipped with two column-type cells for rapid electrolysis. R, solution reservoir; DP, N₂ gas bubbling; EC, electrochemical cell for flow electrolysis; M, mixer; FC, flow-type optical absorption cell; L, light beam; D, photodetector, CV, control valve (23, 24).

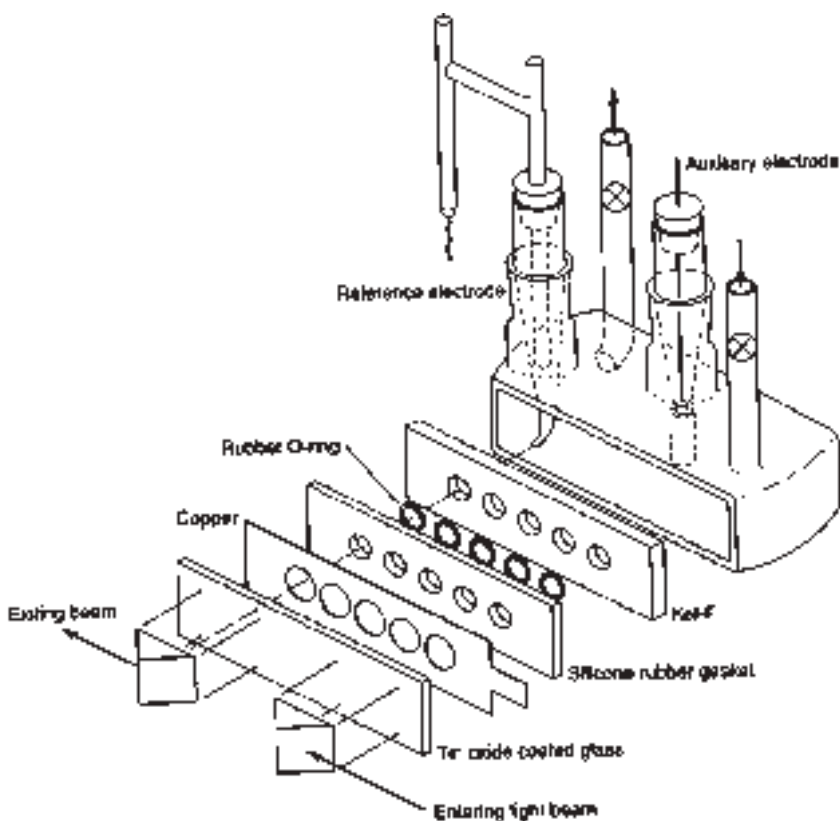


Figure 2.15 Cell assembly for internal reflection spectroelectrochemistry (25, 26).

In these studies, generally a very thin layer of solution is used to cover the electrode surface in order to minimize the reflective effect of the solvent and to make electrical contacts. On top of this solution layer, a Mylar film is used to enclose the solution to prevent solvent vaporization. The general principle of cell design is quite similar to that of TLCs described above except that the top cover of the cells must be spectroscopically transparent (for instance, replaced by a Mylar film here).

Electrochemical measurements can also be coupled with mass spectrometry. Figure 2.17 shows a schematic diagram of the apparatus for differential electrochemical mass spectrometry (DEMS). Here the chamber connected directly to the electrochemical cell and the mass spectrometer (MS) is pumped differentially by turbo pumps PA and PB. Electrolysis products are passed into the ionization chamber (i), analyzed in the quadrupole mass filter (ii), and detected with either a Faraday cup (iii) or electron multiplier (iv). Such DEMS measurements can be used *in situ* to identify electrolysis products. This may lead to an understanding of the electron-transfer reaction mechanism and optimization of the reaction process.

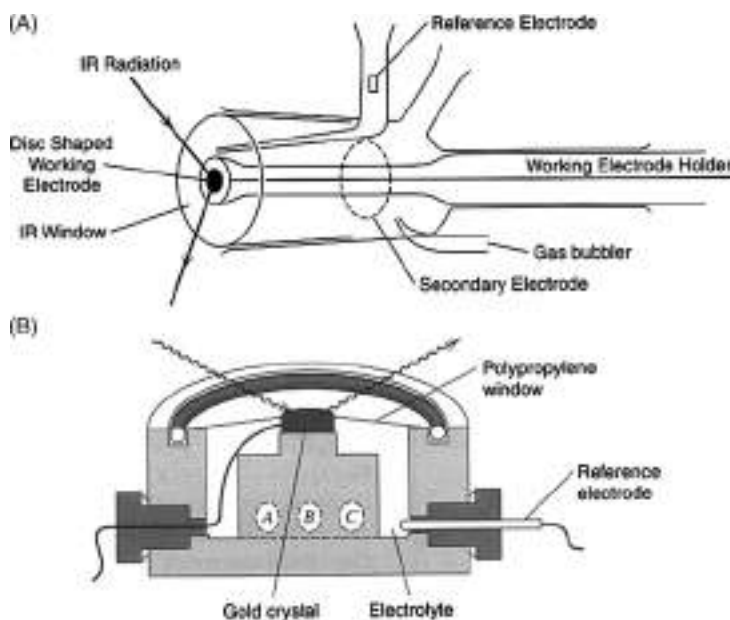


Figure 2.16 Spectroelectrochemical cells for (A) IR-SEC (27) and (B) X-ray diffraction experiments. In (B) a single-crystal gold electrode is used with a thin layer of solution held between the polypropylene window and the electrode. The window is held in place by an O-ring that clamps it to the Kel-F cell body. A and C are electrolyte ports and B is the counter electrode (28).

Electron paramagnetic resonance (EPR) spectroscopy has also been coupled with electrochemical measurements where radical species are involved in the electrochemical reactions. Figure 2.18 shows a cell for simultaneous electrochemical-EPR studies. The EPR measurements can be *ex situ* where the radicals are formed outside of the spectrometer (Figure 2.19). In addition, in combination with the flow cell design described above, one can also use electrochemical-EPR technique to monitor the generation of free radicals in a continuous stream of solutions (Figure 2.20).

2.3.4 Electrochemical cells for molten salts

Molten salts (or ionic liquids) represent a unique class of electrochemical systems. These materials may be corrosive, moisture- or oxygen-sensitive, and/or with a high melting temperature. All these factors must be taken into account in the design of electrochemical cells for molten salt research. Figure 2.21 depicts two gas-tight Pyrex glass electrochemical cells for use with moderate-melting molten salts. Figure 2.22 demonstrates a setup for high-melting molten salts. Typically, in these cell setups, additional provision must be made for temperature measurements and control (through a thermocouple or thermistor). More comprehensive reviews regarding cell designs for molten salts can be found in the literature (37, 38).

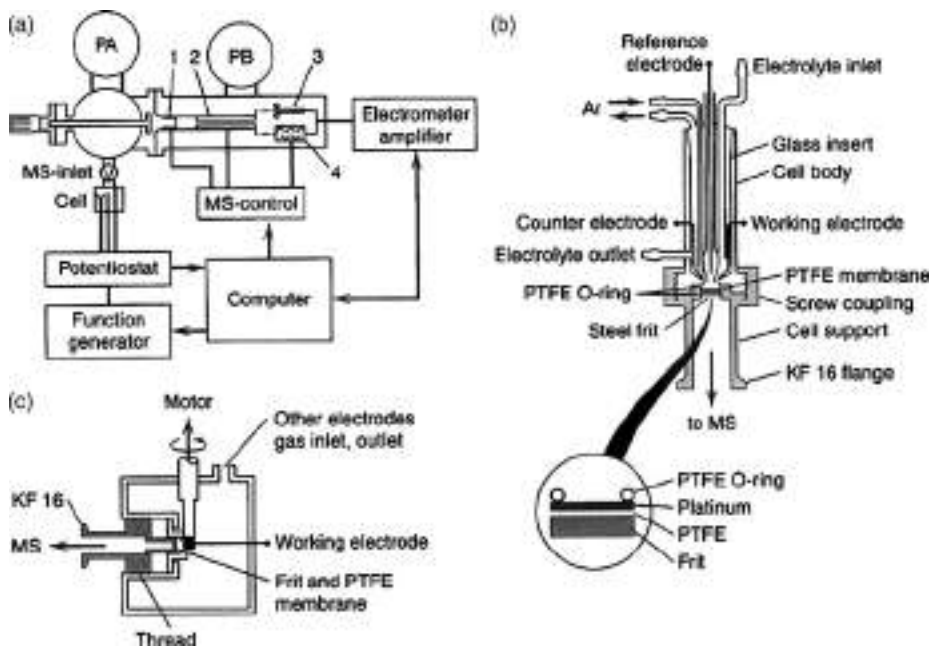


Figure 2.17 Top left: (a) schematic diagram of apparatus for DEMS. Right: (b) electrochemical cell for on-line mass spectrometry with a porous electrode. Electrode show is Pt with Teflon (PTFE)-treated glass frit (29). Bottom left: (c) electrochemical cell with a rotating cylinder electrode and sampling with separate inlet to MS (30, 31).

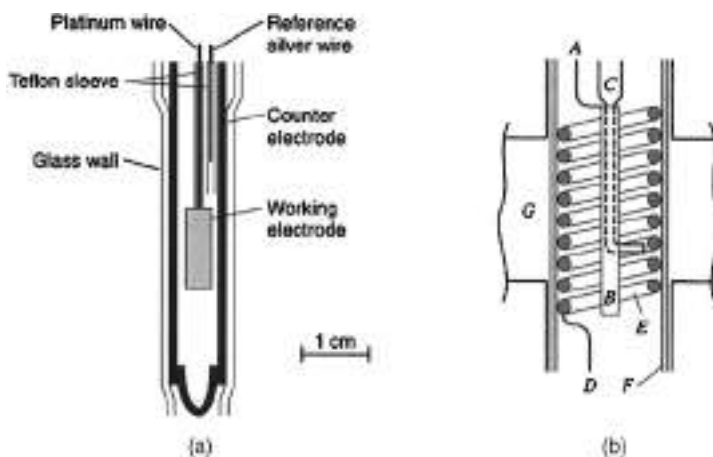


Figure 2.18 Cells for simultaneous electrochemical-EPR experiments. (a) Flat cell with platinum working and tungsten auxiliary electrodes for use in a rectangular cavity (32). (b) Cell with a helical gold working electrode (E) that forms the center conductor of a coaxial cylindrical microwave cavity (G). A, auxiliary electrode lead; B, central platinum auxiliary electrode; C, Luggin capillary for reference electrode; D, working electrode lead; F, quartz tube (33).

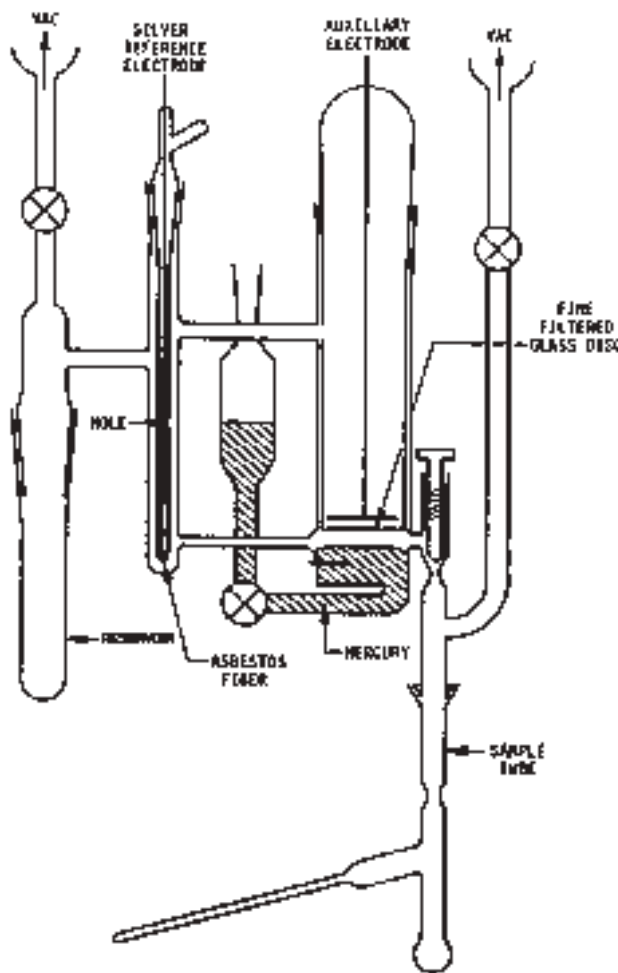


Figure 2.19 Cell used for generation of radicals outside the spectrometer for EPR detection (34).

2.3.5 Attachment to a vacuum line

For electrochemical systems that are sensitive to air and/or moisture, the cells are typically attached to a vacuum line. Here the solution is bubbled with a dry inert gas of ultrahigh purity (e.g., Ar, N₂, etc.) to remove dissolved oxygen. The cell is then attached to a vacuum line or introduced into a glove box to prevent back-contamination. Figure 2.23A shows a simple vacuum cell that consists of two glass units with a three-electrode configuration, which have been used extensively in preliminary work and for elevated-temperature studies with molten scintillator dyes as solvents (39). Figure 2.23B depicts a similar vacuum cell but with several additional features including an attached sidearm chamber for

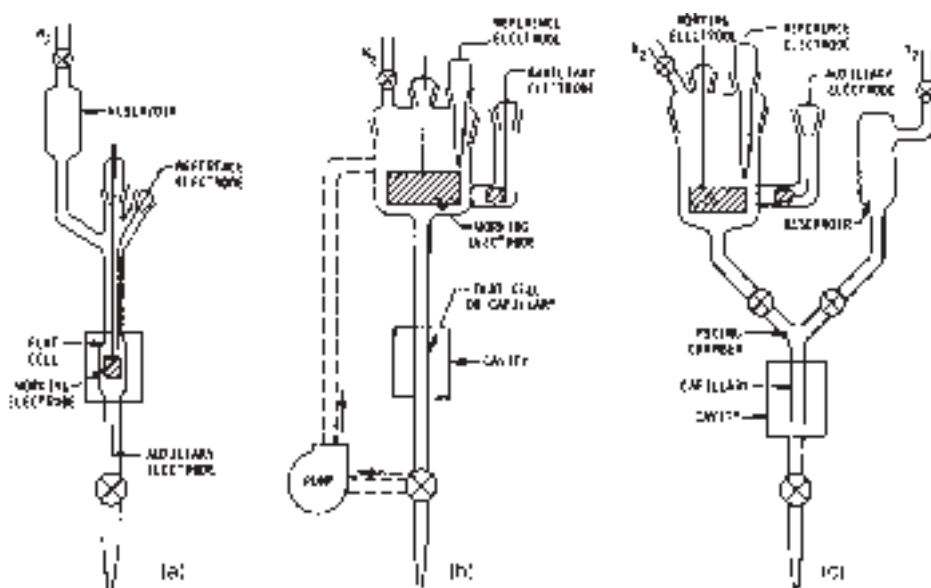


Figure 2.20 EPR-electrochemical cells for flowing electrolysis: (a) gravity-flow system with internal generation; (b) recirculating electrolyte with external generation; (c) flow-mixing cell to study kinetics of reactions with electrochemically generated radicals (35).

freeze-pump-thaw cycles, a microelectrode as the working electrode and a macroelectrode for bulk electrolysis (4, 42). For extremely air-sensitive compounds, one can add an internal Al_2O_3 drying column into the vacuum electrochemical cell.

For quantitative electrochemical studies, one would like to be able to adjust the solution concentration. This can be achieved by using a cell shown in Figure 2.24 where one can control the addition of a certain amount of solution by attaching to the electrochemical cell a buret or a graduated ampule, for example.

Vacuum cells have also found use in spectroelectrochemical studies. Here, optically transparent electrodes may have to be used. Figure 2.25 shows a schematic setup of a vacuum spectroelectrochemical cell that can be used in UV-vis spectral measurements, for example. Attachments to a main vacuum line and a solution ampule can also be accommodated.

2.4 ESTABLISHING AND MAINTAINING AN INERT ATMOSPHERE

In many electrochemical studies, an inert atmosphere is needed to prevent the interference of the oxygen reaction at the electrode surface. Typically ultra-high-purity (UHP) nitrogen or argon is used. Nitrogen is less expensive, whereas the density of argon is greater than that of air and hence provides a better protection layer over the electrochemical solution. The inert gas must be saturated with the pure solvent used in preparing the reaction solution

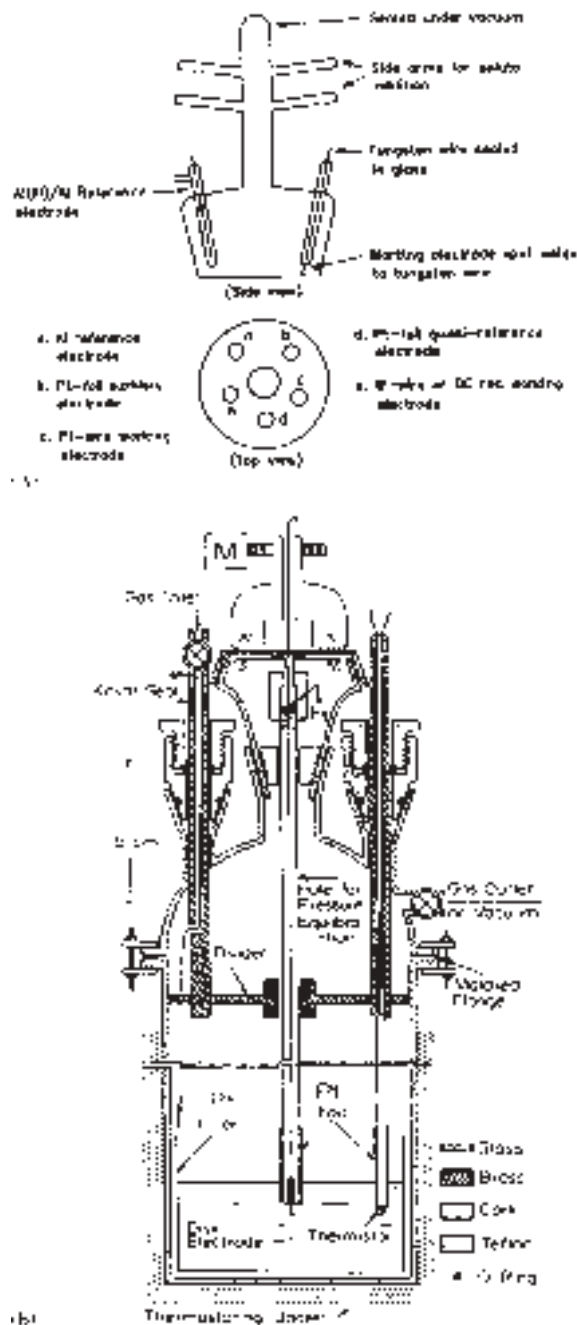


Figure 2.21 Gas-tight Pyrex glass electrochemical cell for use with (A) moderate-melting molten salts (35) and (B) gas-tight cell with a magnetically coupled drive for rotating-disk electrode voltammetry in moderate-melting salts (36).

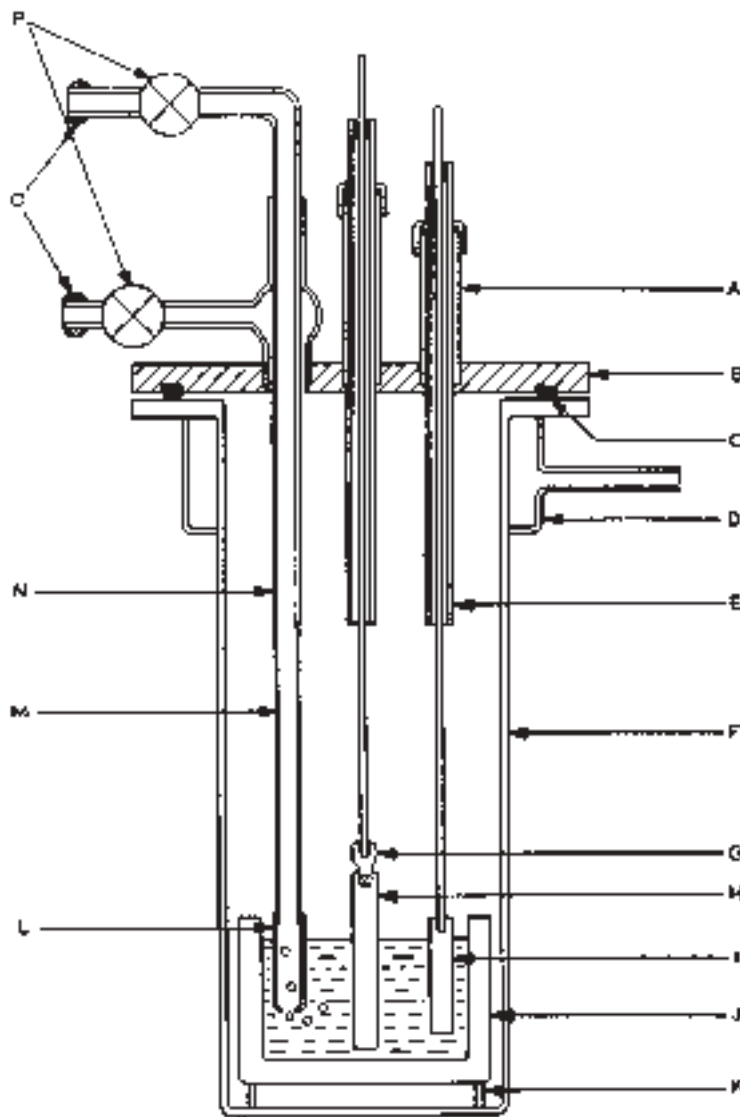


Figure 2.22 Cell used for high-melting alkali metal fluorides: (A) tube with screw cap, (B) brass head, (C) Viton O-ring, (D) cooling jacket, (E) Pyrex glass support tube, (F) cell body made from nickel or Inconel, (G) stainless-steel conductor block, (H) graphite or tungsten cathode, (I) graphite anode, (M) stainless steel tube, (N) Pyrex glass gas inlet tube, (O) ball joint, (P) vacuum valves (37).

such that the loss of solvent during degassing can be minimized. This is particularly important when dealing with volatile organic media. In practice, the solution is bubbled with the inert gas for at least 20 min by inserting the tubing into the solution. Then the tubing is withdrawn from the solution with a separation of a few mm above the solution surface. In

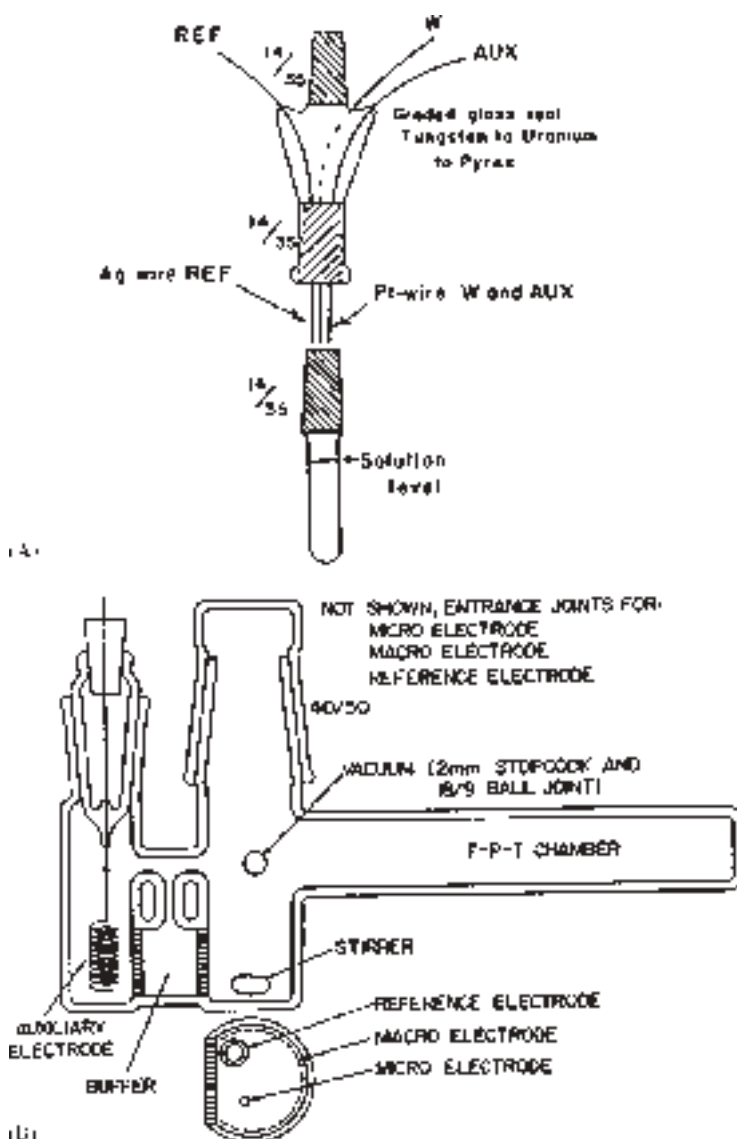


Figure 2.23 (A) Simple vacuum electrochemical cell that is suitable for direct freeze-pump-thaw of the solution. It is very useful for rapid exploratory experiments under vacuum (40). (B) Vacuum electrochemical cell with freeze-pump-thaw chamber (41).

so doing, an inert atmosphere is maintained within the reaction compartment. One can increase the efficiency of protection by reducing the exposure of the reaction compartment to the outside atmosphere, for instance, by sealing the opening with parafilm or Teflon tapes (but make sure to have a small leak so that pressure will not be built up inside the

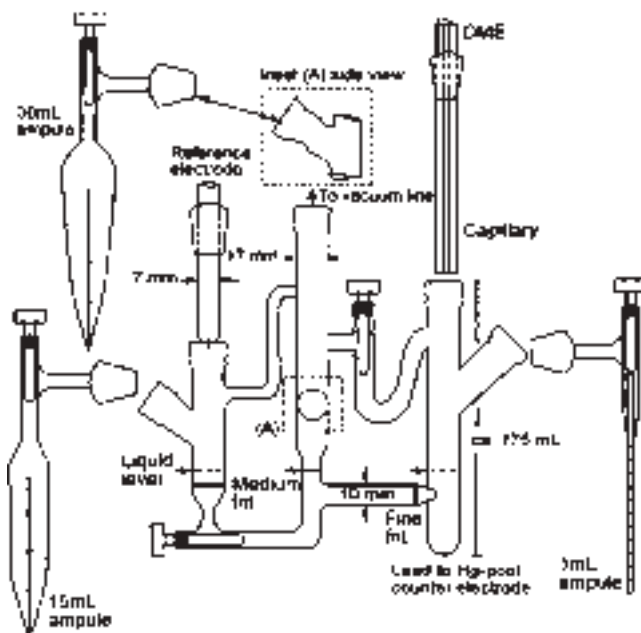


Figure 2.24 Vacuum electrochemical cell and assorted glassware that allows for concentration-dependent electrochemical studies using a dropping mercury electrode (43).

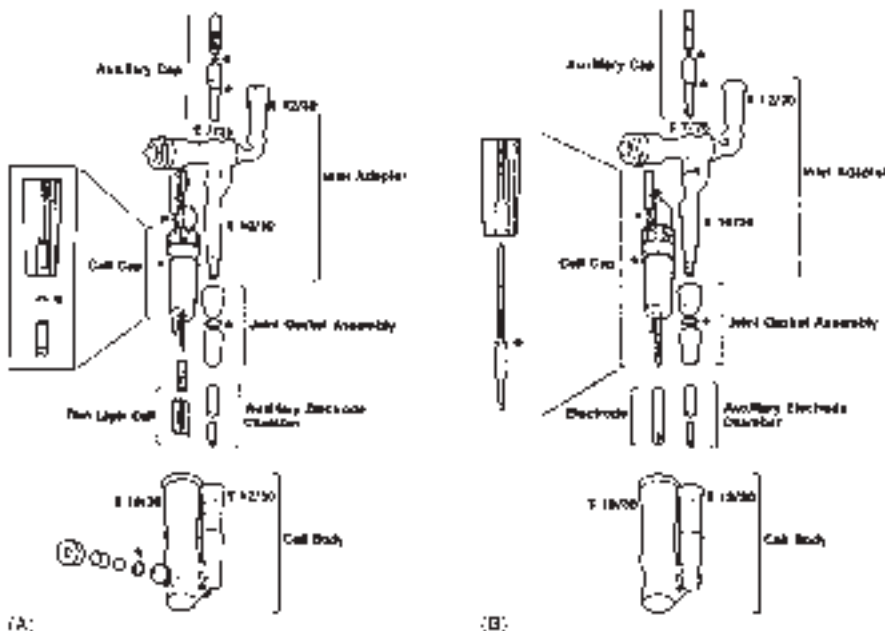


Figure 2.25 Vacuum electrochemical cells (A) vacuum spectroelectrochemical cell that contains an optically transparent thin-layer electrode (OTTLE) and (B) electrochemical cell assembly (44).

reaction chamber). Another concern is the choice of tubing used in the setup. For aqueous solutions, generally most synthetic tubings (Nylon, Teflon, etc.) are acceptable. For organic solutions, care must be taken to make sure that the tubing is inert in the solvent to prevent the interference in electrode reactions. This is particularly important in *in situ* spectroscopic studies such as fluorescence or infrared measurements. Therefore, it is always helpful if one can do a control experiment prior to any new setup.

REFERENCES

1. F. M. Hawkridge, in *Laboratory Techniques in Electroanalytical Chemistry*, 2nd ed., P. T. Kissinger, W. R. Heineman, Eds., Marcel Dekker: New York, 1996.
2. L. Meites, *Polarographic Techniques*, 2nd ed., Wiley-Interscience: New York, 1965.
3. A. J. Bard, L. R. Faulkner, *Electrochemical Methods*, 2nd ed., John Wiley & Sons: New York, 2001, p. 26.
4. A. Demortier, A. J. Bard, *J. Am. Chem. Soc.* **95**, 3495 (1973).
5. H. Gunasingham, B. Fleet, *Electroanal. Chem.* **16**, 89 (1989).
6. A. J. Bard, L. R. Faulkner, *Electrochemical Methods*, 2nd ed., John Wiley & Sons: New York, 2001, p. 448.
7. W. J. Blaedel, J. Wang, *Anal. Chem.* **51**, 799 (1979).
8. S. M. Lunte, C. E. Lunte, P. T. Kissinger, in *Laboratory Techniques in Electroanalytical Chemistry*, 2nd ed., P. T. Kissinger, W. R. Heineman, Eds., Marcel Dekker: New York, 1996.
9. J. A. Wise, W. R. Heineman, P. T. Kissinger, *Anal. Chim. Acta* **172**, 1 (1985).
10. Bioanalytical Systems, Inc.
11. A. J. Bard, L. R. Faulkner, *Electrochemical Methods*, 2nd ed., John Wiley & Sons: New York, 2001, p. 449.
12. T. Fujinaga, S. Kihara, *CRC Crit. Rev. Anal. Chem.* **6**, 223 (1977).
13. A. N. Strohl, D. J. Curran, *Anal. Chem.* **51**, 353 (1979).
14. A. J. Bard, L. R. Faulkner, *Electrochemical Methods*, 2nd ed., John Wiley & Sons: New York, 2001, p. 442.
15. J. V. Kenkel, A. J. Bard, *J. Electroanal. Chem.* **54**, 47 (1974).
16. A. J. Bard, L. R. Faulkner, *Electrochemical Methods*, 2nd ed., John Wiley & Sons: New York, 2001, p. 447.
17. A. T. Hubbard, F. C. Anson, *Electroanal. Chem.* **4**, 129 (1970).
18. A. J. Bard, L. R. Faulkner, *Electrochemical Methods*, 2nd ed., John Wiley & Sons: New York, 2001, p. 453.
19. N. Winograd, T. Kuwana, *Electroanal. Chem.* **7**, 1 (1974).
20. W. R. Heinman, B. J. Norris, J. F. Goelz, *Anal. Chem.* **47**, 79 (1975).
21. A. J. Bard, L. R. Faulkner, *Electrochemical Methods*, 2nd ed., John Wiley & Sons: New York, 2001, p. 681.
22. L. R. Sharp, W. R. Heineman, R. C. Elder, *Chem. Rev.* **19**, 705 (1990).
23. M. Oyama, K. Nozaki, T. Nagaoka, S. Okazaki, *Bull. Chem. Soc. Jpn.* **63**, 33 (1990).
24. M. Oyama, K. Nozaki, S. Okazaki, *Anal. Chem.* **63**, 1387 (1991).
25. N. Winograd, T. Kuwana, *J. Electroanal. Chem.* **23**, 333 (1969).
26. A. J. Bard, L. R. Faulkner, *Electrochemical Methods*, 2nd ed., John Wiley & Sons: New York, 2001, p. 694.
27. A. Bewick, K. Kunimatsu, B. S. Pons, J. W. Russel, *J. Electroanal. Chem.* **160**, 47 (1984).
28. J. McBreen, in *Physical Electrochemistry*, I. Rubinstein, Ed., Marcel Dekker: New York, 1995, Chap. 8.

29. B. Bittins-Cattaneo, E. Cattaneo, P. Konigshoven, W. Vielstich, *Electroanal. Chem.* **17**, 181 (1991).
30. S. Wasmus, E. Cattaneo, W. Vielstich, *Electrochim. Acta* **35**, 771 (1990).
31. A. J. Bard, L. R. Faulkner, *Electrochemical Methods*, 2nd ed., John Wiley & Sons: New York, 2001, p. 721.
32. I. B. Goldberg, A. J. Bard, *J. Phys. Chem.* **75**, 3281 (1971).
33. R. D. Allendoerfer, G. A. Martinchek, S. Bruckensteine, *Anal. Chem.* **47**, 890 (1975).
34. I. B. Goldberg, T. M. McKinney, in *Laboratory Techniques in Electroanalytical Chemistry*, 2nd ed., P. T. Kissinger, W. R. Heineman, Eds., Marcel Dekker: New York, 1996.
35. C. L. Hussey, in *Laboratory Techniques in Electroanalytical Chemistry*, 2nd ed., P. T. Kissinger, W. R. Heineman, Eds., Marcel Dekker: New York, 1996.
36. P. G. Zambonin, *Anal. Chem.* **41**, 868 (1969).
37. S. H. White, in *Molten Salt Techniques*, D. G. Lovering, R. J. Gale, Eds., Plenum: New York, 1983, Vol. 1, Chap. 2.
38. F. Lantelme, D. Inman, D. G. Lovering, in *Molten Salt Techniques*, R. J. Gale, D. G. Lovering, Eds., Plenum: New York, 1984, Vol. 2, Chap. 5.
39. C. P. Keszthelyi, A. J. Bard, *J. Electrochem. Soc.* **95**, 2395 (1973).
40. N. E. Tokel, C. P. Keszthelyi, A. J. Bard, *J. Am. Chem. Soc.* **94**, 4872 (1972).
41. V. Katovic, M. A. May, C. P. Keszthelyi, in *Laboratory Techniques in Electroanalytical Chemistry*, 2nd ed., P. T. Kissinger, W. R. Heineman, Eds., Marcel Dekker: New York, 1996.
42. A. J. Bard, *Pure. Appl. Chem.* **25**, 379 (1971).
43. J. L. Mills, R. Nelson, S. G. Shore, L. B. Anderson, *Anal. Chem.* **43**, 157 (1971).
44. E. A. Blubaugh, L. M. Doane, *Anal. Chem.* **54**, 329 (1982).

– 3 –

Solvents and Supporting Electrolytes

Stephen Creager

Department of Chemistry, Clemson University, Clemson,
SC 29634, USA

3.1 INTRODUCTION

All electrochemical reactions and phenomena occur in a medium, usually a solvent containing dissolved ions (often called the supporting electrolyte or just the electrolyte) which are mobile and able to support current flow. The properties of this medium (which we will call the solvent–electrolyte combination, or sometimes the electrolyte for short) are critically important to any electrochemical experiment. A medium containing mobile ions must exist between the electrodes in an electrochemical cell to allow for control and/or measurement of the electrode potential in the cell, which is required in nearly all electrochemical experiments. A medium with good solvating power is needed to dissolve reactants and products from the electrode reaction, and one with reasonably low viscosity is often needed to allow for rapid transport of reactants and products to and from electrodes. Finally, a medium with low reactivity, or at least with a specific desired reactivity, is needed that will be compatible with oxidizing and reducing electrodes and with reactive species which might be created at electrodes, for any of a wide variety of reasons including analysis, synthesis, energy conversion, or simply the novelty of making a new species for the first time and studying its properties.

This chapter will focus on the properties of some solvent–electrolyte combinations that are commonly used in electrochemical science. Many excellent reviews exist on the properties of solvents and solvent–electrolyte combinations for use as media for performing electrochemical experiments (1–5) and we will not attempt to present a comprehensive review of this material. Rather, we present a discussion focusing on some critical aspects of solvent and electrolyte properties as they relate to electrochemical science, along with some select data on particular solvent and electrolyte combinations that are commonly used. We also include some suggested methods for purifying commonly used solvents and electrolytes. Our purpose is to present a chapter that will provide the reader with some intuition regarding the factors that can be important in selecting a suitable solvent–electrolyte combination for a particular application or experiment, and some practical guidance for preparing and using selected solvents and electrolytes.

© 2007 Elsevier B.V. All rights reserved.

Handbook of Electrochemistry

Edited by C.G. Zoski

3.2 ELECTROLYTE CONDUCTIVITY

One of the most important qualities that a medium must possess to be useful in electrochemical science is an ability to support current flow. Electrochemical reactions always produce or consume ions at electrodes, and the electrolyte provides the pathway for ions to flow between and among electrodes in the cell to maintain charge balance. The ability of a phase to support current flow by motion of charged particles (ions in an electrolyte) when an electric field exists within the phase is called the conductivity, usually abbreviated as κ . Conductivity has units of $\text{ohm}^{-1} \text{ cm}^{-1}$, sometimes called siemens cm^{-1} . Conductivity is a property of a phase or material; for an electrolyte phase of uniform cross-section of area A and length L , whose electrical resistance is R , the ionic conductivity is given by $\kappa = (1/R)(L/A)$. Conductivity is the inverse of resistivity, usually abbreviated as ρ , with units of ohm cm. Representative values for ionic conductivity for some commonly used solvent-electrolyte combinations in electrochemistry are presented in Table 3.1.

A full consideration of all the factors affecting ionic conductivity in electrolytes is beyond the scope of this chapter. Even so, it is worthwhile to consider, in a simplified way, the factors affecting ionic conductivity to gain an understanding of how the conductivity of various solvent-electrolyte combinations depends on the solvent and electrolyte properties.

Ionic conductivity in electrolytes depends on two main factors: (i) the concentration of free charge carriers (ions) and (ii) the ability of the charge carriers (ions) to move in an electric field. Obviously, charge carriers tend to be present at high concentration when the concentration of dissolved salt in an electrolyte phase is high, and in general more concentrated salt solutions are expected to exhibit higher conductivities. This expectation is generally true, and fails only at very high salt concentrations near the solubility limit where the properties of electrolyte phases change drastically mainly due to the limited availability of solvent. For example, the room-temperature ionic conductivity of an aqueous lithium chloride solution increases monotonically with concentration to reach a peak value of $0.17 \text{ ohm}^{-1} \text{ cm}^{-1}$ for a 20 wt.% solution (approximately 5.3 M) but then decreases to a value of $0.15 \text{ ohm}^{-1} \text{ cm}^{-1}$ for a 30 wt.% solution (approximately 8.3 M) (7). This fact may be understood by noting that in a 30 wt.% aqueous lithium chloride solution there are only 2.7 water molecules present for each ion which is not enough to form a proper salvation shell for each ion. Also the viscosity of highly concentrated salt solutions can be large, which can limit ion mobility and yield diminished conductivity.

Electrolytes may be broadly considered in two groups: the strong electrolytes and the weak electrolytes. Strong electrolytes are electrolytes that are normally fully dissociated into ions when dissolved. A good example is sodium chloride in water. Weak electrolytes are electrolytes that normally exist in a partially dissociated state such that some portion, often a large portion, of the dissolved electrolyte exists in an uncharged form, usually a neutral molecule. A good example of a weak electrolyte is acetic acid in water. A 0.1 M solution of acetic acid in water is only about 1% dissociated into protons and acetate ions, with approximately 99% of the acetic acid being present as neutral molecules. This fact makes the conductivity of an acetic acid solution much less than would be expected if one assumed full dissociation of the acid into free protons and acetate ions. Normally, the electrolytes chosen for making solvent-electrolyte combinations for use in electrochemical experiments are strong electrolytes. All the electrolytes in Table 3.1 are strong electrolytes.

Table 3.1

Selected ionic conductivity values for solvent–electrolyte combinations

Solvent	Electrolyte	Electrolyte concentration (M)	Temperature (°C)	Conductivity (ohm ⁻¹ cm ⁻¹)	Reference
Water	HCl	6.0	25	0.84	(6)
Water	HCl	1.0	25	0.33	(6)
Water	HCl	0.1	25	0.039	(6)
Water	H ₂ SO ₄	0.53	25	0.21	(7)
Water	H ₂ SO ₄	0.10	25	0.048	(7)
Water	KCl	1.05	25	0.11	(7)
Water	KCl	0.1	25	0.013	(6)
Water	LiClO ₄	0.1	25	0.0089	(6)
Acetonitrile	TEAClO ₄	1.0	25	0.050	(8)
Acetonitrile	TEAClO ₄	1.0	22	0.026	(9)
Acetonitrile	TEAClO ₄	0.1	22	0.0084	(9)
Acetonitrile	TEABF ₄	1.0	25	0.056	(8)
Acetonitrile	TEAPF ₆	1.0	25	0.055	(8)
Acetonitrile	TEACF ₃ SO ₃	1.0	25	0.042	(8)
Acetonitrile	TBAClO ₄	1.0	22	0.023	(9)
Acetonitrile	TBAPF ₆	1.0	25	0.031	(8)
Acetonitrile	LiPF ₆	1.0	25	0.050	(8)
Acetonitrile	LiCF ₃ SO ₃	1.0	25	0.0097	(8)
Dimethyl-formamide	TBABF ₄	1.0	25	0.0145	(10)
Propylene carbonate	TBABF ₄	1.0	25	0.0074	(8)
Propylene carbonate	TBAPF ₆	1.0	25	0.0061	(8)
Dichloro-methane	TBAClO ₄	1.0	22	0.0064	(9)
Dimethoxy-ethane	TBABF ₄	1.0	25	0.0044	(10)
Tetrahydro-furan	TBABF ₄	1.0	25	0.0027	(10)
Butyronitrile	TBAPF ₆	0.3	25	0.0079	(11)
Dichloro-methane	TBAPF ₆	0.1	Ambient	0.0014	(12)
Trifluoro-toluene	TBAB(C ₆ F ₅) ₄	0.1	Ambient	0.0013	(12)
Tetrahydro-furan	TBAPF ₆	0.1	Ambient	0.0005	(12)

One factor that can limit the free ion concentration in a strong electrolyte solution is ion pairing, whereby free ions associate with ions of opposite charge to make electrically neutral ion pairs that do not contribute to the conductivity. Ion pairing differs from the process described above for weak electrolytes because the bonding in an ion pair is entirely electrostatic, whereas that in most weak electrolytes involves formation of covalent molecular bonds. Ion pairing may be understood as a competition between the energy of electrostatic

attraction of two oppositely charged ions toward each other, which serves to keep the ion pair together, and the thermal energy in the medium, which serves to break the ion pair apart. A full consideration of the theory of ion pairing is beyond the scope of this chapter and the reader is referred to some excellent references for a more thorough treatment (13, 14). Even so, it is useful to consider some predictions from theory regarding how ion pairing should depend upon solvent and electrolyte properties. The Bjerrum theory of ion pairing, which is the earliest and simplest such theory, predicts that ion pairing will be greatest when the salt concentration is high, the salt ions are small and have high charge, the temperature is low, and the solvent permittivity (dielectric constant) is low. These predictions are generally borne out in experiments. For example, in a potassium chloride solution in water (dielectric constant = 78) at ambient temperature the extent of ion pairing is reported to be so low as to be undetectable, whereas in a 0.1 M solution of KCl in methanol solvent (dielectric constant = 32.6) approximately 32% of the KCl is reported to exist as K^+Cl^- ion pairs, and for a similar solution in acetic acid solvent (dielectric constant = 6.2) over 99.9% of the dissolved KCl is reported to exist in an ion-paired state (14). In solvents of low dielectric constant the effect can be particularly strong; for example, Koryta reports that a 3×10^{-5} M solution of tetraisopentylammonium nitrate in water shows no evidence of ion pairing whereas in a similar solution of dioxane, which has a dielectric constant of 2.2, the concentration of free nitrate ions is reduced to the very low value of 8×10^{-12} M (14). In general, ion pairing may be considered to occur to only a small extent in most aqueous electrolyte solutions, but it can be quite substantial for electrolyte solutions in organic solvents with low dielectric constants, e.g. free ions are thought to be nearly absent in electrolyte solutions in solvents with dielectric constants below approximately 5 (14).

The ability of free ions to move in an electric field is described in terms of the ion mobility, abbreviated u_i for an ion i . Ion mobility is the velocity that an ion attains per unit of electric field. Considering an ion as a charged sphere and the solvent as a continuum fluid, the ion mobility for an ion i is given by the equation $u_i = |z_i|e/(6\pi\eta r_i)$ where z is the ion charge, e the electronic charge, η the solvent viscosity, and r the ion radius. We see from this equation that ion mobilities (and therefore electrolyte conductivities) are expected to be highest for highly charged small ions in solvents of low viscosity. This is generally true, and solvents of very high viscosity (e.g., dimethylsulfoxide (DMSO) and benzonitrile) tend to be less widely used when rapid mass transfer is important.

An interesting trade-off arises when considering the effect of ion size on electrolyte conductivity. Large ions would appear to be disfavored due to their low mobility. However, large ions can sometimes be more easily solvated than small ions, especially in low-polarity solvents for which ion solvation energies are likely to be low and salts of small, highly charged ions are often insoluble. Salts of large ions are also less prone to undergo ion-pairing interactions in such solvents. Thus, especially in low-polarity solvents, it is often necessary to use salts of very large ions despite their low ion mobility.

3.3 CELLS, ELECTRODES, AND ELECTROLYTES

Current flow between electrodes in electrochemical cells occurs through the electrolyte phase and is described in terms of a solution resistance for the electrolyte between the electrodes. The magnitude of this resistance depends on the ionic conductivity of the electrolyte, as

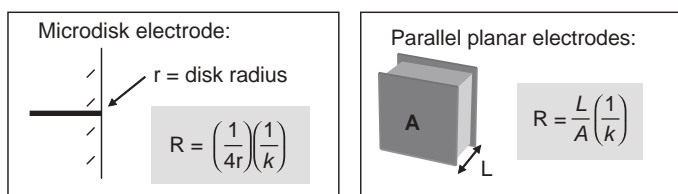


Figure 3.1 Relationships between solution resistance and cell geometry for two limiting cases of electrodes in contact with electrolytes. (for colour version: see colour section at the end of the book).

Table 3.2

Calculated solution resistance values for microdisk and planar electrodes in contact with electrolytes

Microdisk configuration		Parallel plane configuration	
r_{disk} (cm)	R_{sol} (ohm) ^a	d_{space} (cm)	R_{sol} (ohm) ^a
1	5	10	200
0.1	50	1	20
0.01	500	0.1	2
0.001	5000	0.01	0.2

^aSolution resistances were calculated assuming an electrolyte conductivity of 0.05 ohm⁻¹ cm⁻¹.

described above, and also on the geometric arrangement of electrodes in the cell. We consider here the effect of electrode and cell geometry on the solution resistance in the cell.

The dependence of solution resistance on cell and electrode geometry is complicated for the general case and requires integration over the full three-dimensional geometry of the cell for a rigorous solution. Although such treatments are beyond the scope of this chapter, it is useful to consider some limiting cases. Figure 3.1 presents two such cases: one for a disk electrode embedded in an insulator and immersed in an electrolyte phase, and the other for a pair of parallel planar electrodes with an electrolyte phase interposed between them. The figure includes equations for estimating the solution resistance using only the electrolyte conductivity and parameters relating to electrode size and spacing for the calculation.

Table 3.2 presents some calculated values of solution resistance for various combinations of electrode size and spacing with reasonable assumptions for electrolyte conductivity. We see that for the microdisk configuration solution, resistance increases with decreasing electrode size, and that for the parallel planar electrode configuration, resistance decreases with decreasing spacing. Calculations of this sort can be useful when trying to evaluate ohmic losses associated with uncompensated solution resistance in cells in which a net current flows. Ohmic losses are of approximate magnitude $I \times R$ where I is the cell current and R the solution resistance. A more thorough treatment must consider how current depends on electrode geometry, which is a rich subject that is considered in more depth in Chapters 6, 11, and 19 of this handbook. For the present, we note only that ohmic losses usually represent a source of error in attempts to control and/or measure the potential of a working electrode relative to a reference electrode while current is flowing. It is usually desirable to keep such losses as low as possible, and one way to achieve this is to use electrolytes having conductivity as high as possible.

3.4 CELL TIME CONSTANTS

Simple electrochemical cells have characteristic time constants associated with them. The cell time constant may be thought of as the time it takes for the electrical double layer at a polarizable working electrode to be charged or discharged. A simple cell may be considered as a series combination of the solution resistance and a double-layer capacitance, and the time constant for such a combination is simply the product of the resistance and the capacitance. It is instructive to consider the magnitudes of cell time constants for some simple cells in common electrolytes. Using the resistance values in Table 3.2 for microdisk electrodes, and making the reasonable assumption that the specific capacitance of a working electrode is approximately $20 \mu\text{F cm}^{-2}$, we readily calculate that the time constant for a 1 mm radius disk electrode in contact with a $0.05 \text{ ohm}^{-1} \text{ cm}^{-1}$ electrolyte is approximately 30 μsec , and that for a 10 μm radius disk electrode is approximately 0.3 μsec . These values represent lower limits on the timescale over which methods involving current flow at electrodes may be used to study dynamics associated with electrode reactions.

The use of solvent–electrolyte combinations having low ionic conductivity will result in substantial increases in cell time constant. Thus, another reason for using electrolytes with high conductivity is that doing so allows for more rapid control of applied potential at electrodes, which allows for study of more rapid chemical dynamics in cell reactions.

3.5 SOLVENTS

Many organic liquids (in addition to water) have been used as solvents for electrochemical experiments, and many excellent reviews exist on the properties of solvents and solvent–electrolyte combinations for use as media for performing electrochemical experiments (1–5). We will not attempt a comprehensive review of this collected material here. Rather, we present a brief discussion of the solvent properties that are especially relevant for the use of solvents in electrochemical experiments, followed by a discussion focusing on a few solvents that are commonly used in electrochemistry.

There is no such thing as a “universal solvent” for electrochemistry, any more than there is a universal solvent for any other type of chemistry. The solvent properties that are most important are dictated by the application and can vary widely. Even so, it is possible to focus on a few groups of solvent properties that are particularly important for applications in electrochemistry. One important property is the ability of a solvent to dissolve and dissociate salts to achieve a reasonably high ionic conductivity. We have seen that there are problems associated with the use of solvents that do not have adequate ionic conductivity. The ability of a solvent to dissolve and dissociate salt is in fact a special case of a more general solvent property, which is the solvating power of the solvent. Except in special cases such as electrodeposition or electrochemically induced precipitation, it is usually desired that solvents solvate the reactants and products in electrochemical reactions. Solvents are often chosen for their ability to do this.

The other general solvent property category that is often especially important in electrochemistry is reactivity, including acidity/basicity, nucleophilicity/electrophilicity, redox, polarity, and many other types of reactivities which are limited only by the chemistry one

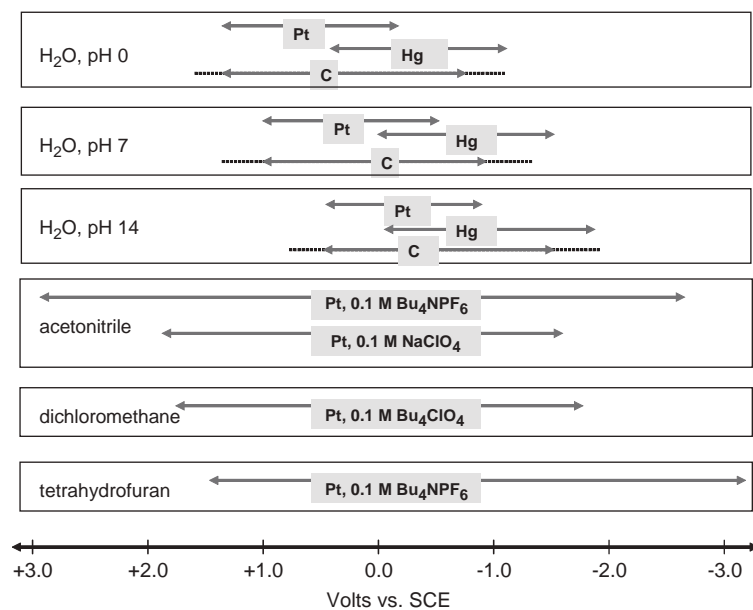


Figure 3.2 Potential limits for some selected combinations of solvent, electrolyte, and working electrode. Data compiled from Rieger, *Electrochemistry*, 2nd edition, Chapman & Hall, New York, 1994; Bard and Faulkner, “*Electrochemical Methods*”, Wiley, New York, 1980; and Rocklin, in “*A Practical Guide to HPLC Detection*”, D. Parriott, Ed., Academic Press, San Diego, 1993, Chapter 6. (for colour version: see colour section at the end of the book).

is attempting to perform on the solvent. Susceptibility to oxidation or reduction is especially important in electrochemistry since the solvent is often in contact with electrodes that are held at very oxidizing and/or reducing potentials, and at which highly oxidized and/or reduced species are produced. Figure 3.2 presents a summary of selected potential limits for some common combinations of solvent, electrolytes, and electrode. Other factors that can be important include liquid range, optical properties, volatility, toxicity, and cost. Table 3.3 presents a summary of selected properties of a few commonly used solvents in electrochemistry, and Figure 3.3 presents the structures of some of these solvents, grouped so as to highlight the structural similarities between and among various solvents.

3.5.1 Protic solvents

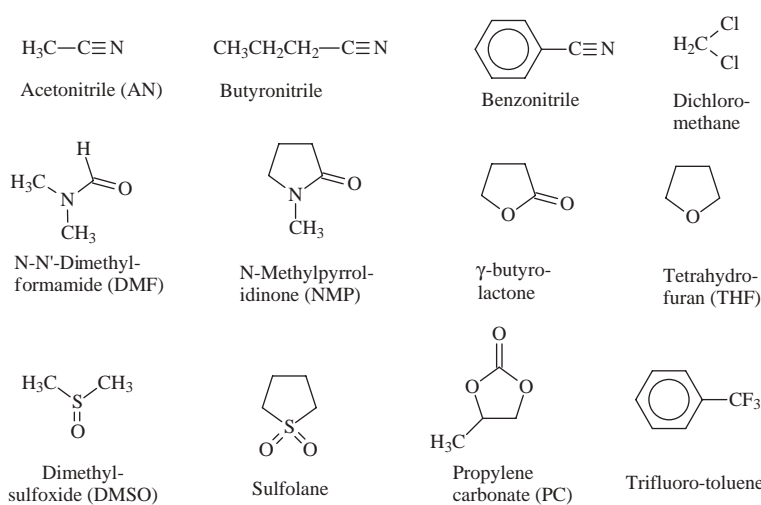
The common protic solvents for electrochemistry are water and the lower alcohols such as methanol and ethanol. All protic solvents are prone to proton reduction to yield hydrogen gas, and they are used for reductive electrochemistry only with electrodes such as mercury or carbon for which proton reduction is kinetically slow, or in circumstances where a species of interest is added with the intent that it be protonated or that it reacts with solvent in a desired way. Of course, much electrochemistry is performed in water due to its ubiquity in the natural world and its excellence as a solvent for salts.

Table 3.3

Properties of some commonly used solvents in electrochemistry (6)

Common name	Molecular weight (g mol ⁻¹)	Freezing point (°C)	Boiling point (°C)	Density (g cm ⁻³)	Viscosity (centipoise)	Dielectric constant (DC)	Dipole moment
Water	18.02	0.0	100.0	0.997	0.890	80.1	1.85
Methanol (MeOH)	32.04	-97.5	64.6	0.791 ²⁰	0.544	33.0	1.70
Acetone	58.08	-94.7	56.1	0.785 ²⁵	0.306	21.0	2.88
Acetonitrile (AN)	41.05	-43.8	81.7	0.786 ²⁰	0.369	36.6	3.92
Butyronitrile	69.11	-111.9	117.6	0.794 ²⁰	0.553	24.8	3.9
Benzonitrile	103.12	-14.0	191.1	1.009 ¹⁵	1.267	25.9	4.18
Dichloromethane	84.93	-97.2	40.0	1.327 ²⁰	0.413	8.93	1.6
<i>N,N'</i> -dimethyl-formamide (DMF)	73.09	-60.5	153	0.945 ²⁵	0.794	38.3	3.82
<i>N</i> -methyl-pyrrolidinone (NMP)	99.13	-23.1	202	1.023 ²⁵	-	32.6	4.1
γ -Butyrolactone	86.09	-43.6	204	1.130 ²⁰	-	39.0	4.27
1,2-dimethoxy-ethane (glyme)	90.12	-69.2	84.5	0.864 ²⁵	0.455	7.3	-
Tetrahydrofuran (THF)	72.11	-108.44	65	0.883 ²⁵	0.456	7.52	1.75
Dimethylsulfoxide (DMSO)	78.13	17.89	189	1.101 ²⁵	1.987	47.2	3.96
Sulfolane	120.17	27.6	287.3	1.272 ¹⁸	-	43.3	4.8
Propylene carbonate (PC)	102.09	-48.8	242	1.205 ²⁰	-	66.14	4.9
Trifluoro-toluene	146.11	-29.0	102.1	1.188 ²⁰	-	9.22	2.86

Note: Superscript numbers represents the temperature, in degree celsius, at which the density was measured.

**Figure 3.3** Structures of organic solvents commonly used in electrochemistry.

3.5.2 Nitriles

The organic nitriles acetonitrile, butyronitrile, and benzonitrile are widely used in electrochemistry. They offer a quite favorable combination of good organic solvating power from their hydrocarbon character, and high polarity from the polar nitrile group. The nitrile group is not easily oxidized or reduced and nitriles are not strongly acidic or basic, which gives them excellent stability under both oxidizing and reducing conductions in electrochemical cells. They are good general-purpose aprotic organic solvents for electrochemistry. Acetonitrile is also fully miscible with water, and can be useful for studies in which a mixed solvent system is desired for solubility and/or reactivity reasons.

3.5.3 Halogenated organics

Halogenated organic solvents such as dichloromethane and dichloroethane, and in some cases *ortho*-dichlorobenzene (e.g., fullerenes) and trifluorotoluene, have excellent solvating power for a wide range of organic and organometallic compounds and, as such, they have been widely used as electrochemical solvents. Their use has declined in recent years due to concerns about their toxicity and the disposal of halogenated solvents, which certainly limits their use in any large-scale application. Still, for research applications they present a good compromise between polarity and organic solvating power and they are still widely used. Halogenated solvents will in general be subject to electro-reduction, which can limit their use in situations involving generation of powerful reducing agents or application of highly reducing potentials. They are good choices for oxidative electrochemistry.

3.5.4 Amides

Organic amide solvents such as dimethylformamide (DMF) and *N*-methylpyrrolidinone (NMP) are good choices when a polar, high-boiling solvent is desired. These solvents are often useful for dissolving polar organic molecules that do not dissolve in water or in conventional organic solvents. They are also often used to dissolve polar polymers, in part because they can be heated to quite high temperatures before boiling. DMF can be difficult to purify since it decomposes slightly at its normal boiling point to produce small amounts of dimethylamine. NMP is a cyclic analog of DMF that is a good all-purpose polar organic solvent.

3.5.5 Sulfoxides and sulfones

Dimethylsulfoxide (DMSO) and sulfolane are also good choices when a polar, high-boiling solvent is desired. DMSO has a quite high viscosity that limits transport rates and ionic conductivities, but it is also quite polar and dissolves many salts and organic compounds easily. Sulfolane is among the highest boiling organic solvents that can be used for electrochemical studies, and is therefore useful for high-temperature electrochemical studies.

3.5.6 Ethers, carbonates, lactone

Tetrahydrofuran (THF) and 1,2-dimethoxyethane (glyme) are the most commonly used ether solvents in electrochemistry. They are very inert, especially toward reducing conditions. They are fairly non-polar (low dielectric constants), which can make dissolving electrolytes and achieving high conductivity in salt solutions in these solvents difficult. Organic carbonates such as propylene carbonate (PC) and ethylene carbonate (EC), and lactones such as γ -butyrolactone are especially good choices for lithium salts such as LiPF₆, LiTriflate, and LiTFSI, which are all widely used in lithium battery technology. They have not been widely used for other applications in electrochemistry but they should be well suited for such applications.

3.6 SALTS

The number of salts that are widely used as supporting electrolytes in electrochemical experiments is surprisingly small, considering how many salts are known. This is particularly true of organic solvents, which are not normally considered as good solvents for salts and for which salts must usually have substantial organic characteristics to be soluble. To a certain extent, the anions and cations in such salts may be considered separately since both species are generally stable and in most cases the anions and cations may be “mixed and matched” to produce the desired salt.

Figure 3.4 presents structures of some cations and anions that are the components of commonly used salts for preparing organic electrolytes. By far, the most commonly used cations

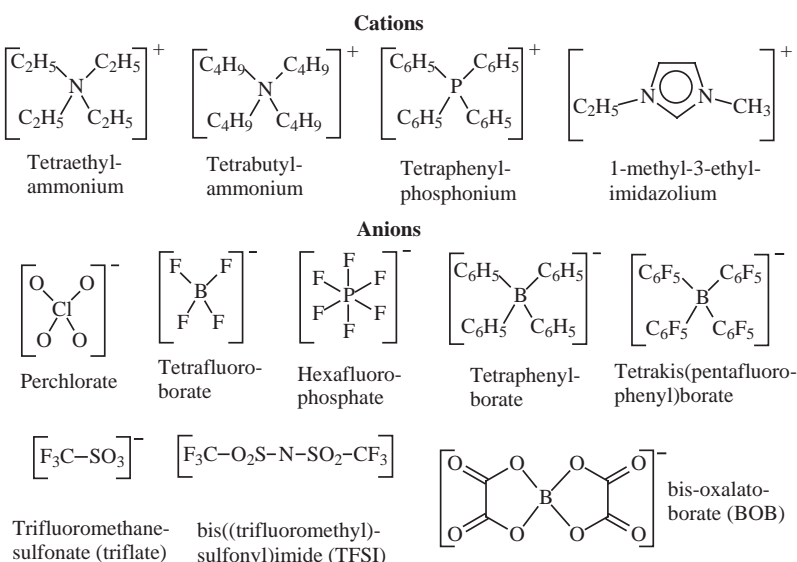


Figure 3.4 Anions and cations of salts commonly used in electrochemistry.

are the tetra-alkylammonium ions; their organic character combined with their relatively low electroreductive reactivity makes them well suited for use in electrochemical experiments. Tetraethylammonium (TEA) and tetrabutylammonium (TBA) ions are the most widely used. There is more diversity among the anions. Perchlorates have been widely used in the past but their use is discouraged today due to explosion hazard concerns. Tetrafluoroborate and hexafluorophosphate salts are excellent replacements for perchlorates and are widely used. Tetraphenylborate salts are also suitable, as are salts based on the tetrakis-(pentafluorophenyl)borate anion which is an extremely unreactive, non-coordinating anion with good solubility in low-reactivity solvents such as trifluorotoluene (12). Finally, lithium salts of fluorosulfonates such as triflate, fluorosulfonimides such as bis[(trifluoromethyl)sulfonyl]imide (TFSI), and borates such as bis-oxaloborate (BOB) are being developed for use in lithium battery technology. These anions are attractive because they are resistant to electro-oxidation and reduction and they dissolve in organic solvents to produce electrolytes with high conductivity, which should make them useful in a variety of electrochemical experiments.

3.7 “EXOTIC” ELECTROLYTES

It is useful to compare the properties of the solvent–electrolyte systems we have considered so far with those of some more “exotic” electrolytes, meaning electrolytes with unusual properties not found in conventional electrolytes. Table 3.4 presents a compilation of ionic conductivities of some electrolytes that are extreme in some ways. The first four entries illustrate that an otherwise conventional electrolyte, TBAPF₆ in butyronitrile, can

Table 3.4

Ionic conductivity values for some “exotic” electrolytes

Medium	Electrolyte	Electrolyte concentration (M)	Temperature (°C)	Conductivity (ohm ⁻¹ cm ⁻¹)	Reference
Butyronitrile	TBAPF ₆	0.2	0	0.0033	(15)
Butyronitrile	TBAPF ₆	0.2	-40	0.0016	(15)
Butyronitrile	TBAPF ₆	0.2	-80	0.0004	(15)
Butyronitrile	TBAPF ₆	0.2	-120	0.00002	(15)
Nafion 1100 EW	Fluorosulfonate	1 (approx.)	25	0.06–0.08	(16, 17)
PC/EC/polyacrylonitrile gel	LiTFSI, LiTriflate, LiPF ₆	5–15 wt.%	30	0.001–0.005	(18)
Polyethylene-glycol-dimethylether (350 MW) with fumed silica additive	LiTFSI	1 (approx.)	30	0.0025	(19)
Polyethylene oxide	LiTFSI, LiTriflate, LiClO ₄	8–15 wt.%	50	0.0001–0.0002	(20)
Imidazolium BF ₄ /PF ₆ /TFSI/ionic liquids		3–6	Ambient	0.010–0.001	(21)

be used at ultralow temperatures. Combinations of butyronitrile with various halogenated organic solvents have been used to produce liquid electrolytes that can be used at temperatures as low as -160°C (or 113 K) (15). Low-temperature electrochemistry can be useful for a variety of purposes including slowing down very fast reactions to capture reactive intermediates, measuring activation energies as part of a mechanistic study, or even for studying phenomena such as magnetism or superconductivity that are manifested only at very low temperature.

The next entry is for Nafion, a proton-conducting fluorosulfonic acid ionomer material which in membrane form is widely used in PEM fuel-cell technology. The conductivity value quoted is for a fully hydrated membrane at an ambient temperature. Note that the conductivity is less than that of a comparable aqueous acid solution, for example 0.5 M sulfuric acid, but by a factor of only 3–4. Heavily hydrated Nafion membranes contain a lot of water, and consequently they behave a lot like aqueous acid solutions. The next three entries are for various gel and solid-polymer electrolytes containing lithium salts. All these material are membranes; some contain some potentially volatile solvents, while others do not. Conductivities for these materials are low relative to true liquid solvents but they are still well within the range of usable values for electrochemical experiments. The semi-solid character of these materials, combined with their near-zero volatility (for solid-polymer electrolytes which do not contain volatile solvents), makes them suitable for use under high-vacuum conditions which makes them potentially useful for fabrication of electrochemical devices which are targeted for use in vacuum or under conditions which could otherwise result in solvent loss by evaporation.

The last entry in Table 3.4 is for a series of room-temperature ionic liquids based on combinations of imidazolium cations with hexafluorophosphate, tetrafluoroborate, and fluorosulfonimide anions. These materials are interesting because they contain only ions (e.g., no volatile or uncharged components). Room-temperature ionic liquids based on chloroaluminate anions with various organic cations have also been described (22). Conductivity values are perhaps surprisingly low for these materials considering that they contain only ions at relatively high concentrations. This fact probably reflects the relatively large size of the ions, the still somewhat high viscosity of the ionic liquids, and some degree of ion association/pairing. Still, the low volatility, low reactivity, low water solubility, and relatively high ionic conductivity of these ionic liquids make them attractive for use in electrochemical studies where the complete absence of a volatile and/or reactive solvent is desired.

3.8 PURIFICATION PROCEDURES FOR SOME COMMONLY USED SOLVENTS IN ELECTROCHEMISTRY

It is difficult to generalize about the need for solvent and electrolyte purification or the best procedures to follow in a particular application. Common impurities in nearly all organic solvents and electrolytes are water and oxygen, which can be present in commercial materials in concentrations ranging from zero to a few millimolar depending on the source of the material. The nature and amounts of other impurities are highly dependent on the particular material in question. In general, care should be taken to ensure that solvent and

electrolytes are free from impurities when highly reactive species are being used or generated at electrodes which could react with impurities and/or when impurities in the solvent/electrolyte could contaminate an electrogenerated product that is being collected. Problems can be particularly acute when concentrations of electroactive species are low (e.g., less than millimolar) since under such conditions, solvent and electrolyte impurities can be present at concentrations greater than that of the component being studied. Whenever possible, the best policy is often to use solvents and electrolytes from commercial sources in the best purity available, and to adopt additional purification procedures if initial experiments suggest that the materials in as-received form are not adequate for the task in hand.

Many procedures for purifying solvents and electrolytes have been described in the original literature. Some excellent compilations have also appeared; one that this author has found to be particularly useful is "Purification of Laboratory Chemicals", in the fifth edition, by Armarego and Chai (23). This volume is an update of the volume of the same name, originally authored by Perrin and Armarego (24). Many of the procedures described below are summaries of the procedures that appear in this volume. The interested reader is encouraged to consult the book by Armarego and Chai for further details and references to the original literature.

3.8.1 Acetonitrile

Acetonitrile is available commercially in sufficiently high purity for routine applications. Common contaminants in commercial acetonitrile are water, acetamide, ammonia, and ammonium acetate. Removal of water by shaking with silica gel or 4 Å molecule sieves, or with activated alumina (activated by heating at 250 °C for 4 h) is effective. Subsequent treatment with calcium hydride until hydrogen evolution stops, followed by fractional distillation over calcium hydride, provides an acceptably pure solvent. Calcium sulfate and calcium chloride are reported to be ineffective as drying agents for acetonitrile, and distillation using phosphorous oxide (P_2O_5) as drying agent is discouraged because use of excess P_2O_5 can cause formation of an orange polymer. Storage over activated 3 Å molecular sieves is recommended to keep water levels low following purification.

3.8.2 Butyronitrile

Treatment with concentrated HCl is recommended to remove isonitriles, followed by drying over potassium carbonate and fractional distillation. Further drying over activated alumina is effective for removing water.

3.8.3 Benzonitrile

The same treatment described above for butyronitrile is also effective for benzonitrile, with the single difference that the fractional distillation is recommended to be performed under reduced pressure (boiling point 69 °C/10 torr).

3.8.4 Propylene carbonate

Common contaminants in commercial PC include propylene oxide, carbon dioxide, propanediols, allyl alcohol, ethylene carbonate, and water. Purification may be accomplished by percolation through 5 Å molecular sieves (activated by treatment at 350 °C for 14 h under argon), followed by distillation under vacuum and storage under molecular sieves.

3.8.5 Dichloromethane

A rapid treatment involves reflux over solid calcium hydride followed by fractional distillation and storage over 4 Å molecular sieves. A more comprehensive and effective procedure involves treatment with concentrated H₂SO₄ until the acid layer remains colorless, followed by washing with water, aqueous base (carbonate, bicarbonate, or hydroxide solution), and water again, followed by drying over CaCl₂ and distillation over CaSO₄, CaH₂, or P₂O₅, gives material of acceptable purity. Storage over 4 Å molecular sieves helps keep water levels down. Dichloromethane should be stored in brown bottles to prevent photolysis by ambient light.

3.8.6 Dimethylformamide

Dimethylformamide (DMF) decomposes slightly via a process which is catalyzed by strong acids or bases, so such materials should be avoided during purification. A recommended procedure is to use a preliminary drying step with CaSO₄, MgSO₄, silica gel, or type 4 Å molecular sieves, followed by vacuum distillation and storage over 3 or 4 Å molecular sieves.

3.9 PURIFICATION PROCEDURES FOR SOME COMMONLY USED SALTS IN ELECTROCHEMISTRY

Most of the following salts are available from commercial sources in the indicated form and may be used as received for routine applications. The following purification procedures are recommended when very pure materials, free from all undesirable impurities including water, are needed.

3.9.1 Tetraethylammonium tetrafluoroborate

Recrystallization from a 5:1 mixture of ethyl acetate/hexane, or from methanol/diethyl ether, followed by storage under vacuum at 95 °C for 48 h.

3.9.2 Tetraethylammonium tetr phenylborate

Recrystallization from aqueous acetone followed by drying at 60 °C under vacuum for several days.

3.9.3 Tetraethylammonium hexafluorophosphate

Recrystallization from hot water.

3.9.4 Tetrabutylammonium tetrafluoroborate

Recrystallization from water or aqueous ethanol, or ethyl acetate/pentane, or pure ethyl acetate with cooling in dry ice to induce precipitation, followed by drying at 80 °C under vacuum.

3.9.5 Tetrabutylammonium hexafluorophosphate

Recrystallization from aqueous ethanol, or from absolute ethanol, followed by drying in vacuum at 70 °C for 10 h.

3.9.6 Lithium perchlorate

Recrystallization from water or aqueous methanol, followed by heating at 170–180 °C in an air oven (vacuum is also suitable) to remove waters of hydration. Subsequent crystallization from acetonitrile is also suggested to improve purity.

REFERENCES

1. A. J. Fry, in *Laboratory Techniques in Electroanalytical Chemistry*, 2nd ed., P. T. Kissinger, W. R. Heineman, Eds., Marcel Dekker: New York, 1996.
2. D. T. Sawyer, A. Sobkowiak, J. L. Roberts, in *Electrochemistry for Chemists*, 2nd ed., Wiley: New York, 1995.
3. C. J. Janz, R. P. T. Tompkins, *Nonaqueous Electrolytes*, Academic Press: New York, 1972 and 1974, Vols. I and II.
4. C. K. Mann, in *Electroanalytical Chemistry*, A. J. Bard, Ed., Marcel Dekker: New York, 1969, Vol. 3, p. 57.
5. H. Lund, in *Organic Electrochemistry*, 3rd ed., H. Lund, M. M. Baizer, Eds., Marcel Dekker: New York, 1991.
6. D. R. Lide, Ed., *CRC Handbook of Chemistry and Physics*, 85th ed., CRC Press: Boca Raton, FL, 2004.
7. R. C. Weast, Ed., *CRC Handbook of Chemistry and Physics*, 60th ed., CRC Press: Boca Raton, FL, 1980.
8. M. Ue, K. Ida, S. Mori, *J. Electrochem. Soc.* **141**, 2989 (1994).
9. K. M. Kadish, J. Q. Ding, T. Malinski, *Anal. Chem.* **56**, 1741 (1984).
10. H. O. House, E. Feng, N. P. Peet, *J. Org. Chem.* **36**, 2371 (1971).
11. L. K. Safford, M. J. Weaver, *J. Electroanal. Chem.* **331**, 857 (1992).
12. R. J. Lesuer, C. Buttolph, W. E. Geiger, *Anal. Chem.* **76**, 6395 (2004).
13. J. O. M. Bockris, A. K. N. Reddy, *Modern Electrochemistry*, Plenum: New York, 1970, Vol. 1, p. 251.

14. J. Koryta, J. Dvorak, L. Kavan, *Principles of Electrochemistry*, 2nd ed., John Wiley & Sons: Chichester, 1993, p. 23.
15. S. Ching, J. T. Mcdevitt, S. P. Peck, R. W. Murray, *J. Electrochem. Soc.* **138**, 2308 (1991).
16. G. Pourcelly, C. Gavach, in *Proton Conductors. Solids, Membranes, and Gels-materials and Devices*, P. Colombari, Ed., Cambridge University Press: Cambridge, UK, 1992.
17. Y. Stone, P. Ekdunge, K. Simonsson, *J. Electrochem. Soc.* **143**, 1254 (1996).
18. H. S. Choe, B. G. Carroll, D. M. Pasquariello, K. M. Abraham, *Chem. Mater.* **9**, 369 (1997).
19. H. J. Walls, P. S. Fedkiw, T. A. Zawodzinski, S. A. Khan, *J. Electrochem. Soc.* **150**, E165 (2003).
20. A. Vallee, S. Besner, J. Prud'homme, *Electrochim. Acta* **37**, 1579 (1992).
21. A. B. McEwen, H. L. Ngo, K. Lecompte, J. L. Goldman, *J. Electrochem. Soc.* **146**, 1687 (1999).
22. T. A. Zawodzinski, R. A. Osteryoung, *Inorg. Chem.* **27**, 4383 (1988).
23. W. L. F. Armarego, C. L. L. Chai, *Purification of Laboratory Chemicals*, 5th ed., Butterworth Heinemann: Amsterdam, 2003.
24. D. D. Perrin, W. L. F. Armarego, *Purification of Laboratory Chemicals*, 3rd ed., Pergamon Press: Oxford, UK, 1988.

Reference Electrodes

Timothy J. Smith and Keith J. Stevenson

The University of Texas at Austin, USA

4.1 INTRODUCTION

The composition of a good reference electrode (RE) must remain effectively constant, unvarying for the duration of an experiment, in order to provide a stable potential for controlled regulation of the working electrode (WE) potential. The chosen RE should be an ideal nonpolarizable electrode (1), i.e., its potential does not change regardless of current flow through the RE. The reaction at the RE should be reversible, permitting a potential to be calculated from the Nernst equation, as well as have the capability to recover its potential after a current stress. This requires that the RE act as a source or a sink for small currents due to imperfections in potentiostat or galvanostat design without displaying a change in its potential throughout the duration of the experiment.

4.1.1 Selecting a reference electrode

Many considerations must be weighed in choosing a suitable RE for an experiment. Proper experimental design must prevent incompatible species present in the electrolyte from reacting with the RE materials. For instance, an ionic species with poor solubility can precipitate in the frit, clogging the RE, and thus increasing the junction potential. Additionally, species that are in the electrochemical cell can interfere with the performance of an RE by poisoning the controlling redox process (i.e., H₂ catalysis), or increase the solubility of the reference couple (i.e., Ag|AgCl). Cell conditions such as pressure and temperature must also be considered in choosing the appropriate RE for a particular experiment as the equilibrium of the redox couple is dependent on these parameters. Time requirements can allow the use of a less robust RE, permitted that the RE is stable over the duration of the measurement. One option that allows for flexibility in the selection of an RE is the incorporation of a double junction, or a salt bridge, to separate the RE from the WE. Nonetheless, several different RE varieties are available for use in electrochemical experiments. In the following, we describe common elements for the construction of a stable RE and provide tips for their calibration and maintenance.

4.1.2 Converting between aqueous potential scales

It is often useful to compare experimentally measured cell potentials. A useful conversion chart is provided in Table 4.1 for conversions between reference scales.

4.2 BASIC COMPONENTS OF A REFERENCE ELECTRODE

All REs consist of four essential parts: body, top seal, junction, and active component of the electrode. Many of these elements are interchangeable and can be tailored to meet a variety of experimental conditions. However, the active component is what defines the reference potential.

4.2.1 Body material

The material selected for the tube or body of the RE must withstand the usage requirements for the electrode as well as the fabrication process. This typically precludes the use of plastics for most hydrogen electrodes as well as the use of glass (and Vycor) for extreme alkaline or hydrofluoric acid (HF) solutions. Table 4.2 lists the general chemical stability of some commonly used materials.

4.2.2 Top seal

The presence of a seal at the top of an RE will affect the performance of the RE in several ways. An air-tight, leak-proof seal is used to retain H₂ in some varieties of hydrogen electrodes and can both reduce the flow of filling solution through the junction at the base of an RE and eliminate filling solution evaporation. A leaky seal will have the opposite effect and should only be used with saturated filling solutions.

- (a) *Platinum–glass seal.* A platinum–glass seal (3) can be made using flint (soft) glass and a propane torch. Borosilicate glass (i.e., Pyrex) used with platinum requires a hotter flame and produces a poor seal. If required, this type of seal should be made with assistance from an experienced glass blower. The platinum glass seal should be leak proof. Two examples of this type of seal are shown in Figure 4.1A.
- (b) *Polymer cap.* A polymer cap can be made using a metal wire that is force fit into a machined piece of Teflon or other polymer where it can be fit to the inside diameter (male cap) or outside diameter (female cap) of a glass or polymer body as shown in Figure 4.1B. This type of seal can be made leak proof with the addition of an o-ring to the Teflon end piece. Care must be taken so that high forces are not placed on the inside diameter of a glass tube, due to the stresses that can be created from the cutting of the tube. Fire polishing can create a poorly tolerated hole that is difficult to make leak proof. For electrodes where a vent is required to produce a “leaky reference” electrode, this type of seal can be made to meet these requirements. This type of seal simplifies refilling the RE by functioning as a filling port.

Table 4.1

Aqueous RE potential scale conversions

Electrode description		Hydrogen	Mercury				Silver chloride			
			Calomel		Sulfate	Oxide				
<i>To convert</i>	<i>From→To</i>	NHE or SHE	SCE	SSCE	NCE	MSRE	1M NaOH	Saturated KCl/NaCl	3M KCl/NaCl	
	Hydrogen	NHE or SHE	0	-0.241	-0.236	-0.280	-0.640	-0.098	-0.197	-0.209
Mercury	Calomel	SCE	+0.241	0	+0.005	-0.039	-0.399	+0.143	+0.044	+0.032
		SSCE	+0.236	-0.005	0	-0.044	-0.404	+0.138	+0.039	+0.027
		NCE	+0.280	+0.039	+0.044	0	-0.360	+0.182	+0.083	+0.071
	Sulfate	MSRE	+0.640	+0.399	+0.404	+0.360	0	+0.542	+0.443	+0.431
		1M NaOH	+0.098	-0.143	-0.138	-0.182	-0.542	0	-0.099	-0.111
	Oxide	Saturated KCl/NaCl	+0.197	-0.044	-0.039	-0.083	-0.443	+0.099	0	-0.012
Silver chloride	3M KCl/NaCl	+0.209	-0.032	-0.027	-0.071	-0.431	+0.111	+0.012	0	

NHE: Normal Hydrogen Electrode ($a_{H^+} = 1$); SHE: Standard Hydrogen Electrode ($a_{H^+} = 1$); SCE: Saturated Calomel Electrode (saturated KCl); SSCE: Saturated Salt Calomel Electrode (saturated NaCl); NCE: Normal Calomel Electrode (1 M KCl); MSRE: Mercury(I) Sulfate Reference Electrode (saturated K_2SO_4).

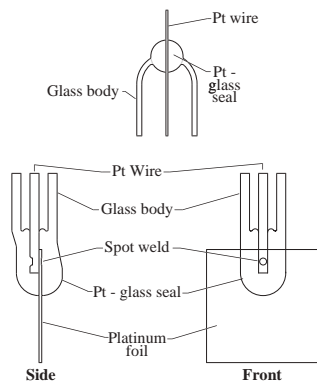
Table 4.2

Solvent compatibility chart (2)

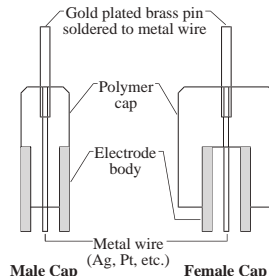
Body material	Acids		Bases	Organics						
	Organic	Inorganic		Aromatics	Ketones	Aldehydes	Ethers	Amines	Halogenated	Aliphatic
Halogenated										
Polytetrafluoro-ethylene	PTFE	A	A	A	A	A	A	A	A	A
Perfluoro (ethylene-propylene) copolymer	Teflon® FEP	A	A	A	A	A	A	A	A	A
Polychlorotri-fluoroethylene	Teflon® PCTFE	A	A	A	A	A	B	A	B	A
Fluoroelestomer	Kel-F® Viton®	B	B	B	A	C	B	C	B	A
Polyolefins										
Polypropylene	PP	B	B	A	C	B	B	C	A	B
Polyethylene	LDPE	B	B	B	C	B	B	B	B	B
	HDPE	B	B	B	C	B	B	B	B	B
Polyacetal	Delrin®	C	C	C	A	A	A	B	B	A

A: acceptable; B: not all members of class acceptable; C: not acceptable.

A. Platinum - glass seals



B. Polymer caps



C. Wire - epoxy seal

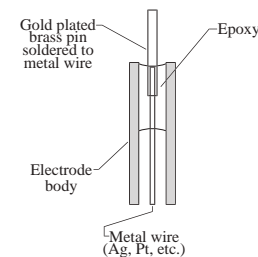


Figure 4.1 Reference electrode top seal types: (A) platinum–glass seals; (B) polymer caps; (C) wire–epoxy seal.

- (c) *Wire–epoxy seal.* The wire–epoxy seal, shown in Figure 4.1C, is a simple, quick, and inexpensive seal for REs. This type of seal is leak proof, but concerns should be raised about any volatiles emitted or leached from the epoxy that could be electroactive or coat the active surface of the electrode. This seal can make changing the filling solution difficult, requiring removal of the junction unless a filling port is built into the RE.

4.2.3 Junction (4)

The junction separates the internal filling solution of the RE from the external electrolyte of the electrochemical cell. In some instances, no junction is used due to the similarity between filling solution and the electrolyte in the electrochemical cell. In others, a double junction is used to prevent mixing of incompatible species between the RE and electrochemical cell. Junctions are covered in more detail in Section 4.4.

- (a) *Vycor, polyethylene, or Teflon frit.* The frit material can be sealed to the body material with heat shrink tubing. The recovery temperature of the heat shrink must be low enough that no damage is done to the frit material during the sealing process. This type of junction is shown in Figure 4.2A.
- (b) *Ceramic junction.* A ceramic frit can be sealed into a glass RE body using standard glass blowing techniques. The ceramic must be held tightly in the glass with no spaces on the sides of the ceramic, otherwise solutions will bypass the ceramic. This type of junction, shown in Figure 4.2B, typically has a very low leak rate.
- (c) *Glass wool, cellulose pulp, or agar.* Glass wool or other junction material can be filled or wedged into a restricted end of the RE body as shown in Figure 4.2C. The leak rate can be adjusted by changing both the type and the density of the material.

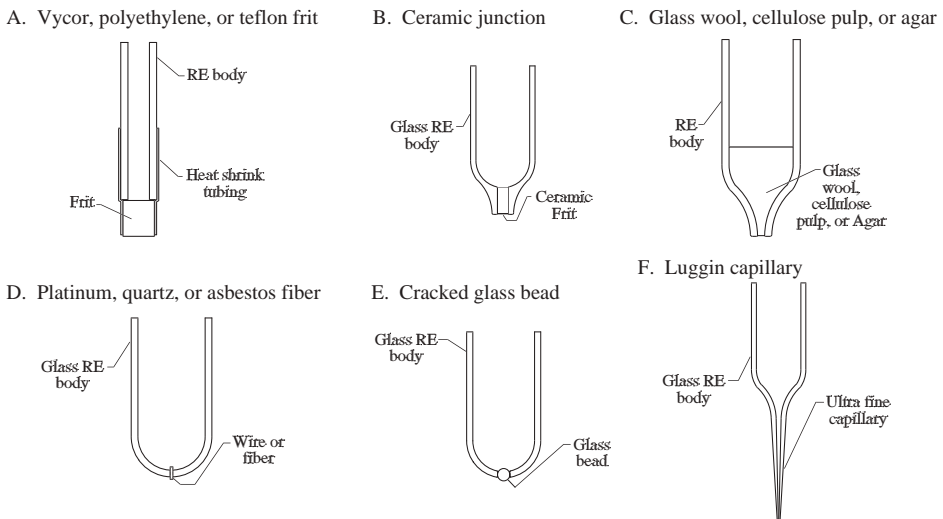


Figure 4.2 Reference electrode junction types: (A) Vycor, polyethylene, or Teflon frit; (B) ceramic junction; (C) glass wool, cellulose pulp, or agar; (D) platinum, quartz, or asbestos fiber; (E) cracked glass bead; (F) Luggin capillary.

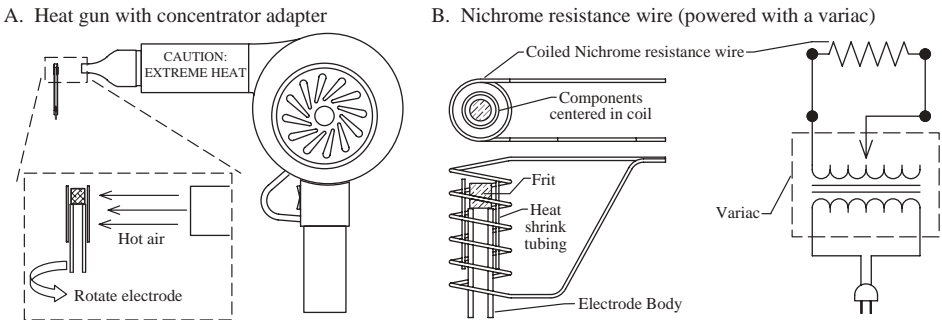


Figure 4.3 Suggested methods to shrink heat shrink tubing: (A) heat gun with concentrator adapter; (B) nichrome resistance wire (powered with a variac).

- (d) *Platinum wire, quartz, or asbestos fiber.* An imperfect seal (5) can be created between the fiber or wire and the glass body of the RE. This serves as a leak through which the filling solution can interact with the electrolyte of the electrochemical cell. This type of junction is shown in Figure 4.3D.
- (e) *Cracked glass bead.* Fusing a glass bead to a hole in a glass RE body using a torch, and then initiating a crack at the interface, will create a cracked glass bead junction. This type of junction is shown in Figure 4.2E.

- (f) *Luggin capillary.* A Luggin capillary, shown in Figure 4.2F, can be constructed by pulling a fine capillary at the end of a glass electrode body. The diameter of the capillary will determine how fast the filling solution leaks out of the RE.

4.2.3.1 Sealing junctions to the RE body with heat shrink tubing

Heat shrink tubing can be recovered to its minimum diameter through the careful exposure to heat. This can be accomplished with an oven, hot air gun, or a coil of nichrome wire. Care must be taken so that the filling solution is not heated excessively as localized boiling could occur, creating high pressure inside the electrode. Excessive heat can also cause the heat shrink to become brittle, or melt the frit, closing the pores and destroying its functionality. Several types of heat shrink tubing that are commercially available are listed in Table 4.3, and methods to apply heat to shrink the tubing are shown in Figure 4.3.

4.2.4 Active component of RE

The active component of an RE defines the baseline potential that is developed by the RE. The details of this RE component are illustrated in Figure 4.4 and are discussed in the following sections of this chapter.

Table 4.3

Heat shrink recovery data

Heat shrink polymer	Recovery temperature ± 5% (°C)	
Teflon® (6)	PTFE	340
	FEP	190
Fluoroelastomer (7)	Viton®	175
Polyolefin (6)	Polyolefin	100

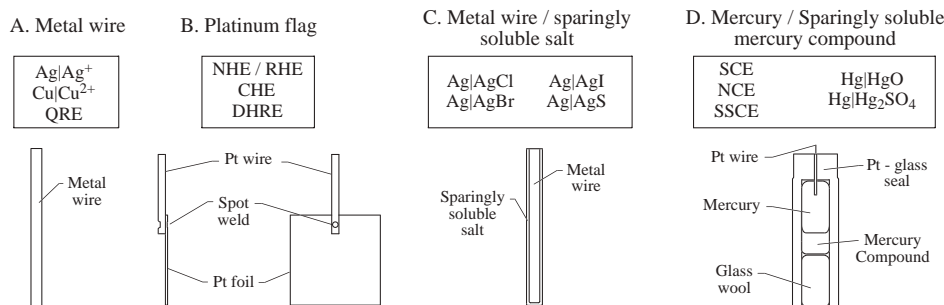
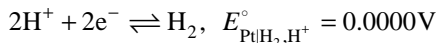


Figure 4.4 Reference electrode active component: (A) metal wire; (B) platinum flag; (C) metal wire/sparingly soluble salt; (D) mercury/sparingly soluble mercury compound.

4.3 ELECTRODE DETAILS AND FABRICATION

4.3.1 Hydrogen electrodes

Controlling redox process:



The Normal Hydrogen Electrode (NHE) or Standard Hydrogen Electrode (SHE) is the standard reference point for standard electrochemical reduction potentials, with its potential, E° , assigned as 0.0000 volts (V) at all temperatures by convention. By definition, the hydrogen must be at 1 atm pressure and the activity of hydronium ions equal to 1. These requirements are difficult to attain experimentally, and lower concentrations of acid are often used, as well as a slightly higher pressure of hydrogen gas, due to experimental necessity. As such, the hydrogen RE deviates from the defined potential of 0.0000 V, but is calculable using the Nernst equation, expressed in the following form:

$$E_{\text{Pt}|\text{H}_2,\text{H}^+} = E_{\text{Pt}|\text{H}_2,\text{H}^+}^\circ + \frac{RT}{F} \ln \frac{a_{\text{H}}}{\sqrt{P_{\text{H}_2}}} \quad (4.1)$$

$$P_{\text{H}_2} = P_{\text{barometric}} - P_{\text{H}_2\text{O}} + (4.2 \times 10^{-5})h \quad (4.2)$$

where h is the depth of delivery of the H_2 supply to solution (in mm), $P_{\text{barometric}}$ the barometric (atmospheric) pressure (in atm), and $P_{\text{H}_2\text{O}}$ the partial pressure of water vapor that can be estimated for dilute solutions as the same as pure water. Values are listed in Table 4.4.

4.3.1.1 Active component for hydrogen electrodes

The active body of an NHE is typically a platinized platinum foil, but it can be any material that catalyzes hydrogen. Other alternatives include platinized gold foil, palladized gold, or platinum foils. Palladium is sometimes used for the catalyst due to the increased ability of hydrogen to permeate into bulk palladium compared with platinum. This can be advantageous since palladium can be presaturated with hydrogen prior to measurement, removing the need for a hydrogen gas supply. Unplatinized platinum surfaces can be used, but they remain active only for a short duration, typically a few hours. The platinum deposit should not be too heavy, otherwise a sluggish electrode will result (10).

Table 4.4

Partial pressure of water vapor from 0 to 100 °C (9)

t (°C)	$P_{\text{H}_2\text{O}}$ (atm)	t (°C)	$P_{\text{H}_2\text{O}}$ (atm)	t (°C)	$P_{\text{H}_2\text{O}}$ (atm)
0	6.0330×10^{-3}	30	4.1900×10^{-2}	70	0.30768
10	1.2120×10^{-2}	40	7.2849×10^{-2}	80	0.46754
20	2.3082×10^{-2}	50	0.12183	90	0.69200
25	3.1276×10^{-2}	60	0.19671	100	1

$$P_{\text{H}_2\text{O}} = (1 \times 10^{-8})t^4 - (3 \times 10^{-7})t^3 + (4 \times 10^{-5})t^2 + (1 \times 10^{-4})t + 7 \times 10^{-3}.$$

Table 4.5

	Platinization recipes		
	I	II	III
Chloroplatinic acid	0.072 M (3.5%)	0.072 M (3.5%)	0.042 M (2%)
Lead acetate trihydrate	1.3×10^{-4} M (0.005%)	1.3×10^{-4} M (0.005%)	–
Hydrochloric acid	–	2 M	2 M
Current density (mA/cm ²)	30	30	10–20
Deposition time (min)	5	5	10–20
Deposit color	Very black	Very black	Light gray to golden
Reference	Bates (13)	Feltham and Spiro (14)	Hill and Ives (15)

Note: Stirring is required for all recipes.

(a) Electrode preparation

Cleaning a platinum substrate (11). The platinum substrate is soaked in 50% aqua regia (1:3 concentrated HNO₃ + HCl) for several minutes, and then rinsed in distilled water. Next, it is placed in concentrated nitric acid for several minutes, and then again washed in distilled water. Just prior to platinization, the platinum substrate is cycled between –1.0 and 0 V (vs. NHE) in dilute sulfuric acid (~0.1 M).

Platinizing substrate. Several methods are available for platinization of electrodes. The first two include lead in the recipe, the addition of which serves as an additive that leads to a blacker deposit, and allows for good adhesion to the substrate. If lead in the deposit is a problem, it can be removed (12) by soaking in an aerated 1 M perchloric acid solution for 24 h. The last method does not contain lead, and results in a gray to golden deposit. Any of the three methods listed in Table 4.5 are acceptable for hydrogen electrode fabrication.

(b) Storage

Platinized electrodes should be stored in distilled water and not left to sit in air as this quickly destroys the catalytic activity and necessitates replatinization.

(c) Renewal

Platinized electrodes can be renewed by removal of previous platinization with 50% aqua regia, followed by cleaning and fresh platinization as described above.

4.3.1.2 H₂ purification and presaturation (16)

The purity of the hydrogen supply will affect the potential of the electrode by poisoning the catalyst sites (CO and CO₂) or changing the reactions taking place at the catalyst (O₂). Purification of an H₂ supply can be accomplished with a series of filters, including O₂ and CO₂ removal. A particle filter should also be included in the purification train.

(a) O₂ removal

Recombination catalyst. A recombination catalyst is used to recombine O₂ impurities with H₂ to form H₂O. One example is the platinum catalyst that operates at room temperature and is available commercially.

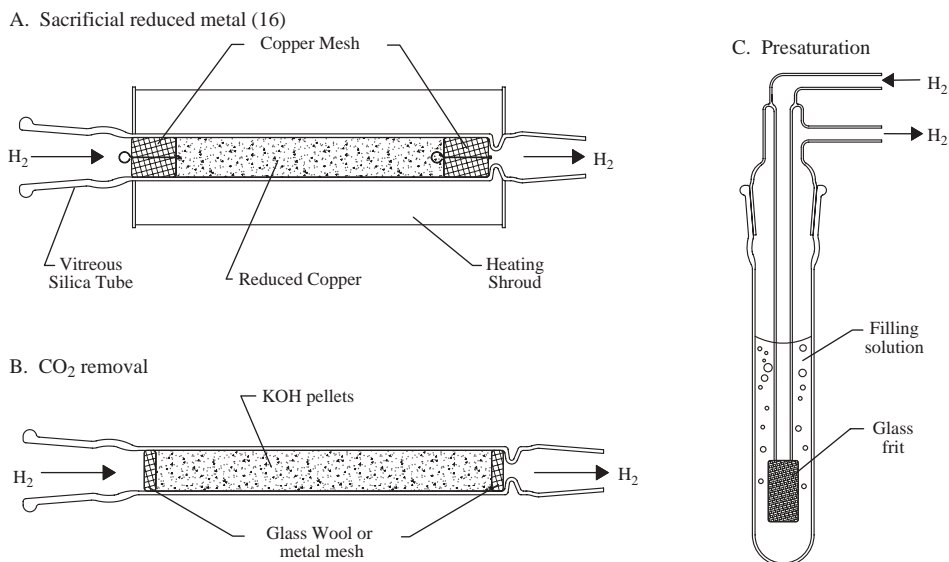


Figure 4.5 H_2 purification and presaturation: (A) sacrificial reduced metal (16); (B) CO_2 removal; (C) presaturation.

- Sacrificial reduced metal.* A sacrificial metal filler is oxidized in the presence of oxygen, trapping the O_2 as a solid metal oxide. Typically, these must be operated at higher temperatures to promote faster kinetics, such as reduced copper that requires an operating temperature of between 450 and 700 °C. An example configuration is shown in Figure 4.5A.
- (b) CO_2 removal
The removal of CO_2 from an H_2 gas stream can be accomplished with a glass tube packed with KOH pellets, as shown in Figure 4.5B. This works best if used after a recombination-type O_2 removal system because the H_2O present in the effluent increases the solubility of CO_2 into the thin layer of water on the KOH pellets.
- (c) Presaturation
If dry H_2 is used for an RE, the bubbling gas will slowly increase the concentration of the electrolyte due to the H_2O that is dissolved in the exiting H_2 stream. To minimize this, the H_2 gas stream can be presaturated prior to introduction into the RE by bubbling it through a chamber filled with the same electrolyte as that in the electrode, as shown in Figure 4.5C.

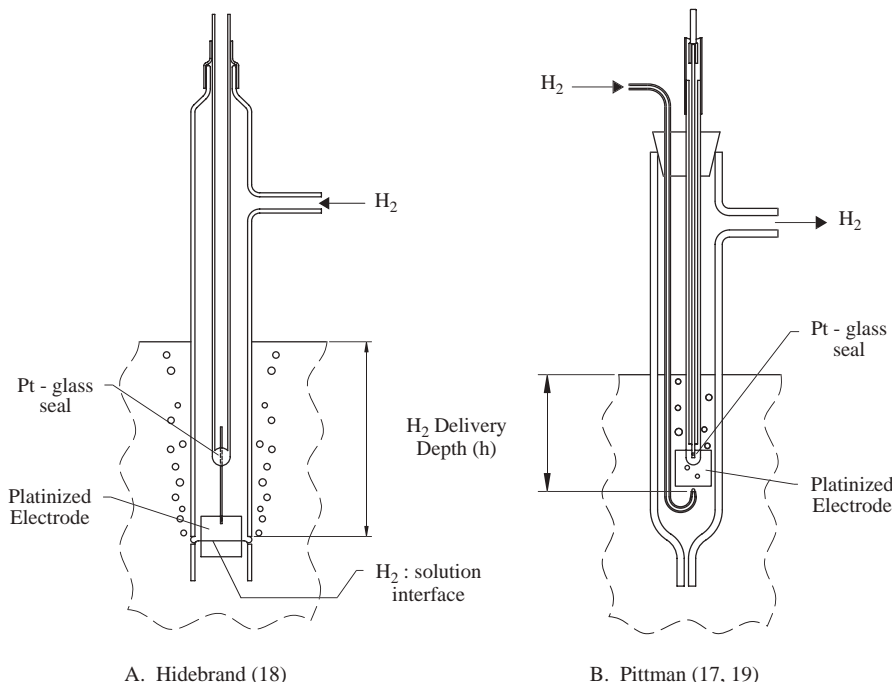
4.3.1.3 Normal Hydrogen Electrode (NHE) and Reversible Hydrogen Electrode (RHE)

(a) Filling solutions

NHE. By definition, the NHE should have a hydronium ion activity of unity, and a partial pressure of hydrogen gas of 1 atm. Being experimentally difficult to attain, other concentrations and pressures are typically used, and the potential is corrected for these conditions using the equations listed above. Table 4.6 lists the activity of H^+ for dilute HCl solutions at 25 °C.

Table 4.6Mean molal activity coefficients of $\text{HCl}_{(\text{aq})}$ at 25 °C (20)

m_{HCl} (mol/kg)	γ_{\pm}	a_{H^+}	b_{HCl} (mol/kg)	γ_{\pm}	a_{H^+}
0.001	0.9650	9.650×10^{-4}	0.005	0.9280	4.640×10^{-3}
0.002	0.9519	1.904×10^{-3}	0.010	0.9040	9.040×10^{-3}

**Figure 4.6** Normal Hydrogen Electrode and Reversible Hydrogen Electrode designs (17): (A) Hildebrand (18); (B) Pittman (17, 19).

RHE. The RHE is assembled directly in an electrochemical cell, with the electrolyte in the cell as the RE filling solution. This necessitates the calculation of the potential from the Nernst equation using the pH of the cell solution and the applied H_2 partial pressure (Figure 4.6).

4.3.1.4 Convenient Hydrogen (CHE)/Self-Contained Hydrogen (SCHE) Electrodes

The Convenient Hydrogen Electrode (21) (CHE) or the Self-Contained Hydrogen Electrode (22) (SCHE) is an RE with a hydrogen bubble contained within the electrode body that replaces the hydrogen gas supply required for typical hydrogen REs. The thin layer of solution drawn by capillary action onto the platinized electrode surface quickly

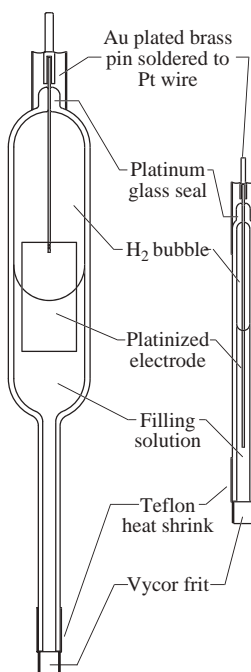


Figure 4.7 Convenient Hydrogen Electrode.

saturates the active surface of the electrode with H₂, mimicking the action of bubbling gas near an electrode in the NHE. This electrode is stable for several weeks and is easily refilled with hydrogen. This electrode makes no effort to exclude oxygen, so the potential will deviate several millivolts from the NHE, requiring calibration with another RE. This electrode is very useful for studies in acids, especially fuel cell studies, where counter ions such as chloride can poison the catalyst being studied. One key advantage of a CHE is that its size can be tailored to meet experimental requirements. The H₂ can either be electrolytically generated within the electrode or filled from an external H₂ gas supply. Two different CHE electrodes are shown in Figure 4.7.

(a) Electrode preparation

Platinization. Platinization should be carried out as described for the NHE, producing a light gray platinized surface.

(b) Filling solution (other filling solutions possible)

0.05–0.5 M H₂SO₄.

0.1–1 M NaOH.

Works best between pH 0–2 and 12–14; other pHs may need to be buffered to increase the current sink/source capability of the RE.

(c) H₂ filling

Hydrogen can be bubbled into the electrode with a Teflon or glass tube connected to an H₂ gas supply. Alternatively, making the CHE negative with respect to an

inert counter electrode (CE) can generate H₂, taking care that the CE is sufficiently separated from the CHE so as to prevent excess O₂ from entering the electrode body. During electrolytic hydrogen generation, any restrictive junction must be removed from the electrode, due to the possibility of dangerous pressures being created by the generation of gas in a confined space.

(d) Junction exceptions

In some experimental situations, no junction is used, especially with microscale REs (μ REs). When using the CHE in alkaline solutions of pH > 8, a VYCOR® frit cannot be used, as it will dissolve.

4.3.1.5 Dynamic Hydrogen Reference Electrode (DHRE)

The Dynamic Hydrogen Reference Electrode (23) (DHRE) functions by producing H₂ and O₂ at a pair of electrodes, using the H₂-producing electrode as a reference potential. This potential will deviate from the NHE due to the overpotential applied for the H₂ generation. The electrode pair is vertically separated (1 cm) with the upper electrode producing O₂ (positive) with respect to the lower H₂-producing electrode. The H₂-producing electrode is typically platinized, to reduce the overpotential required to produce a stable potential. The electrodes can be microfabricated so long as the electrodes are separated sufficiently to prevent diffusion of O₂ from one electrode to the H₂-producing electrode within the experimental time frame. One type of DHRE is shown in Figure 4.8.

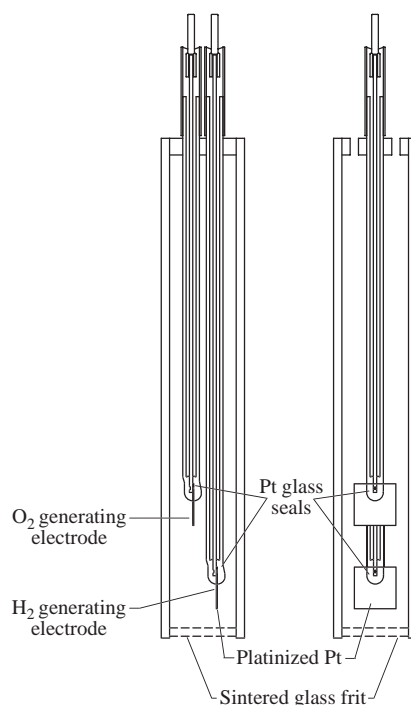
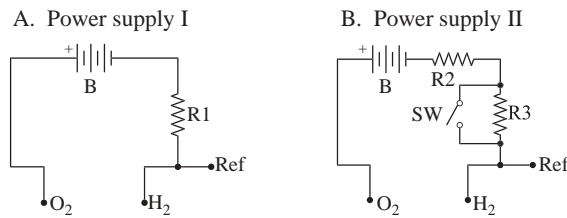


Figure 4.8 Dynamic Hydrogen Electrode.



Example values for a 1cm² surface area electrode:

$$B=45V, R1=45k\Omega, R2=5k\Omega, R3=40k\Omega$$

Figure 4.9 DHRE power supply circuits: (A) power supply I; (B) power supply II.

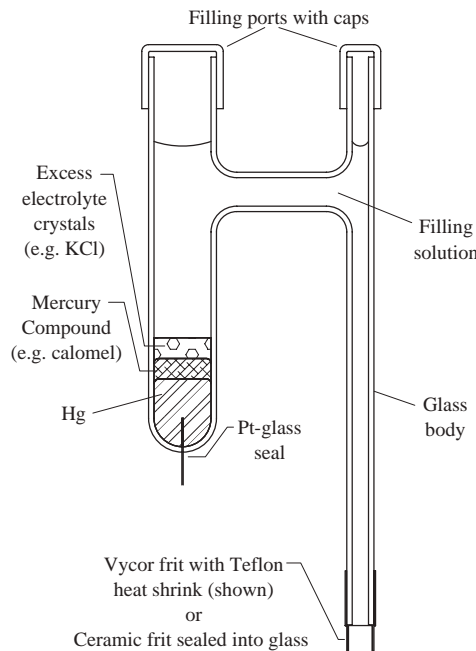
- (a) *Active components.* Two electrodes are required for this RE. The H₂-generating electrode should be platinized platinum, and the O₂ can be any inert electrode, but is often platinum. These electrodes can be reduced in size from the macroscale 1 cm² platinum flag electrodes to UMEs. Care must be taken so that the O₂ generated does not readily diffuse to the H₂ electrode, otherwise the potential will change.
- (b) *Platinization.* Platinization should be carried out as with the NHE to produce either a thin light gray coating or a thick black coating.
- (c) *Power circuit.* The DHRE requires a constant-current power supply to support the electrolysis of both O₂ and H₂. Care should be taken that the current does not deviate during the experiment, otherwise the reference potential will drift. A stable DC power supply capable of delivering 1–10 mA/cm² of constant current (see below) should be used to prevent drift. With a 1 mA/cm² current source (Figure 4.9A), the potential should stabilize after approximately 20 min to the H₂ reference potential. To reduce the time required for stabilization, a switch can be used (Figure 4.9B) that first supplies 10 mA/cm² current for 10 min, and then can be switched to 1 mA/cm² current for constant operation during the electrochemical experiment.

4.3.2 Mercury electrodes (24)

Mercury REs are formed with mercury in its purified, liquid form, along with a sparingly soluble mercury salt (i.e., mercury(I) chloride, mercury(I) sulfate, or mercury(II) oxide). Because mercury is easy to purify through distillation, it is easy to reuse and forms a consistent surface, adding to the ability to create REs repeatedly. Due to environmental concerns, mercury electrodes are less favored today. Two modern styles of mercury REs are shown in Figure 4.10.

- (a) Hg purification
Mercury is available in >99.9999% purity levels commercially, removing the need for purification in the laboratory as was required in the past.
- (b) Glass considerations
The glass in the mercury-containing portion of the RE should be made hydrophobic, thus eliminating solvent entrapment on the sides of the mercury and the possibility of

- A. Larger volume mercury pool; must be rigidly held for stable potential



- B. Smaller volume mercury pool; less sensitive to electrode movement

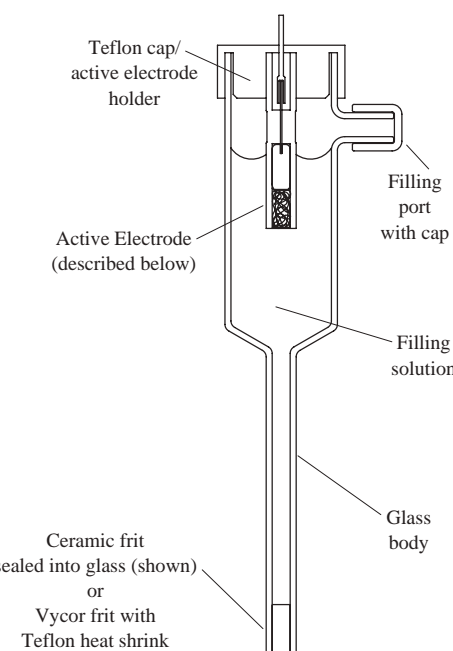


Figure 4.10 Basic Mercury Reference Electrode designs: (A) larger volume mercury pool, must be rigidly held for subtle potential; (B) smaller volume mercury pool, less sensitive to electrode movement.

producing a sluggish or erratic RE. This treatment can cause problems with a platinum glass seal requiring an alternate electrode design or in the least care should be taken so that the glass in the vicinity of the platinum wire or at a Pt/glass seal is not treated.

Hydrophobic glass treatment. Clean dry glass should be heated to 100 °C, before being filled with 1% Dow-Corning Silicone Fluid No. 200 in CCl₄. The glass should then be emptied, drained, and baked at 300 °C for 2 h, before being thoroughly extracted with CCl₄ to remove any unbonded silicone (25). Other commercial treatment procedures are available.

4.3.2.1 Saturated Calomel Electrode (SCE)

Controlling redox process:



Mercury|mercury(I) chloride (*also mercurous chloride or calomel*), abbreviated as Saturated Calomel Electrode (SCE), is the most widely used mercury RE (26). The preparation of this electrode, especially the purity of the mercury and the method of addition of mercury(I) chloride to the mercury, strongly affects the performance and potential exhibited. This RE can be very reproducible if produced and handled carefully. The potential of

the mercury(I) chloride RE is defined by the chloride concentration in the filling solution, and can be calculated as shown below:

$$E_{\text{Hg}|\text{Hg}_2\text{Cl}_2} = E_{\text{Hg}|\text{Hg}_2\text{Cl}_2}^{\circ} - \frac{RT}{F} \ln a_{\text{Cl}^-} \quad (4.3)$$

This electrode displays hysteresis upon heating and cooling (27), and it is not recommended that the electrode be used above 70 °C. Temperature effects are discussed in Section 4.8.1.3.

(a) Electrode preparation

Mercury preparation. No special preparative steps are required if mercury of sufficient purity is used.

Hg₂Cl₂ preparation. High-purity Hg₂Cl₂ is available commercially, or it can be produced by chemical precipitation as described below. The Hg₂Cl₂ must be a finely divided powder (0.1–5 µm) to produce a well-behaved RE.

Hg/Hg₂Cl₂ electrode preparation (see Figure 4.11). Method I (28). On adding the Hg₂Cl₂ to the dry mercury; it will rapidly form a pearly skin on the surface. Once the surface is completely covered, the addition of Hg₂Cl₂ is stopped, otherwise the electrode will be sluggish. This interface must be prepared prior to the introduction of filling solution for a stable potential to develop.

Method II (29). Hg and Hg₂Cl₂ should be ground together with a few drops of KCl filling solution using a mortar and pestle to form a paste. The paste should be placed in the tube, in direct contact with the Pt wire. About 1 cm thick paste should be used.

(b) Filling solution

SCE—saturated KCl.

SSCE—saturated NaCl.

NCE—1N KCl.

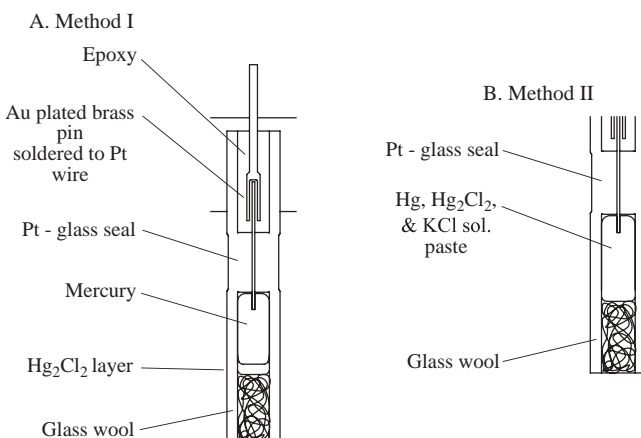


Figure 4.11 SCE active electrode body: (A) method I; (B) method II.

(c) Hg_2Cl_2 preparation

Chemical precipitation (30). About 1 g of reagent-grade mercury(I) nitrate dihydrate, $\text{Hg}_2(\text{NO}_3)_2 \cdot 2\text{H}_2\text{O}$, should be mixed with 200 μl of concentrated nitric acid and ~ 20 ml of water. Add this solution dropwise for 2 min into a covered beaker containing approximately 100 ml of 0.1 M HCl, using a magnetic stir bar to continuously stir the solution. After the addition is completed, stir the suspension for an additional hour. Allow the precipitate to settle, decant the supernatant solution, and repeat this twice to completely rinse the precipitate. Filter the precipitated mercury(I) chloride with a sintered glass crucible, rinsing quickly with four portions of cold distilled water, and then transfer it to a vacuum desiccator. It is important that the HCl used be free from traces of other halogens, otherwise the mercury(I) chloride produced will be contaminated with other mercury(I) halides, resulting in an RE with a mixed potential.

Electrochemical production. Electrochemically prepared Hg_2Cl_2 can be produced (30) in a similar fashion as HgSO_4 described in the next section, but it is less stable than chemically precipitated material and therefore its preparation is not discussed further.

4.3.2.2 Mercury Sulfate Reference Electrode (MSRE)

Controlling redox process:



Mercury|mercury(I) sulfate (*also mercurous sulfate*), abbreviated as Mercury Sulfate Reference Electrode (MSRE), is the second (26) most used mercury RE after SCE. The construction of the MSRE is similar to that of the SCE, although it is less sensitive to the purity of the mercury. The reproducibility (31) of the MSRE is second only to the NHE, and given the absence of chloride ion in the construction of the MSRE, it has found use in systems with sensitivity to chloride content. The reference potential of the MSRE is calculated as follows:

$$E_{\text{Hg}|\text{HgSO}_4} = E_{\text{Hg}|\text{HgSO}_4}^\circ - \frac{RT}{F} \ln a_{\text{SO}_4^{2-}} \quad (4.4)$$

(a) Electrode preparation

Mercury preparation. No special preparative steps are required if mercury of sufficient purity is used (31).

Hg_2SO_4 preparation. High-purity Hg_2SO_4 is available commercially, can be produced electrochemically, or by chemical precipitation as described below.

$\text{Hg}/\text{Hg}_2\text{SO}_4$ electrode preparation (32) (*Figures 4.12 and 4.13*). Approximately 2.5 mm thick layer of Hg_2SO_4 should be coated on the mercury before flushing out the assembly five times with the filling solution. To equilibrate, the RE should sit overnight in fresh filling solution.

(b) Filling solution.

Saturated K_2SO_4 or ≥ 1 M H_2SO_4 —dilute solutions exhibit poor reversibility (33).

(c) Mercury(I) sulfate production (32, 34)

Mercury(I) sulfate must be prepared, washed, and stored in acid as hydrolysis occurs in neutral solutions. The details for its preparation are described below.

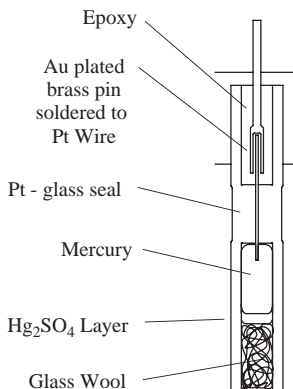


Figure 4.12 MSRE active electrode body.

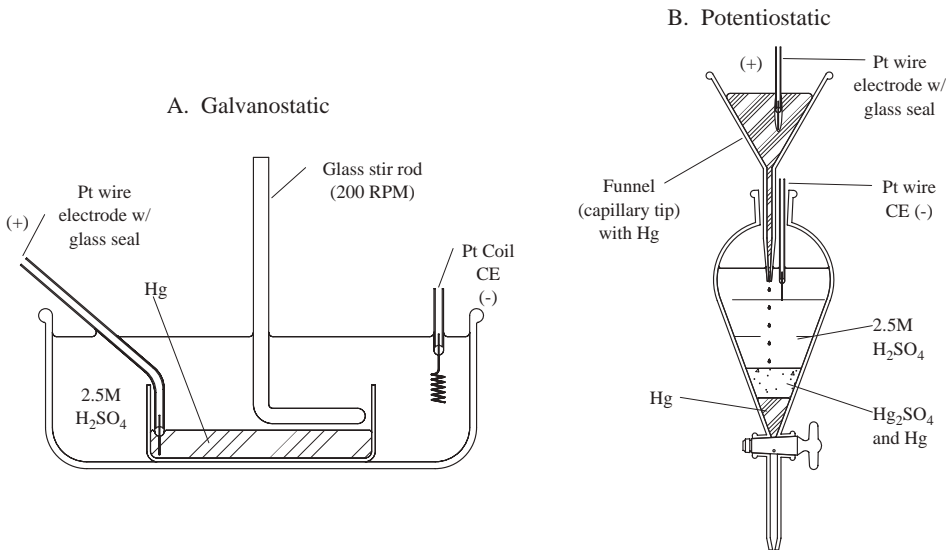


Figure 4.13 Electrochemical Hg_2SO_4 preparation: (A) galvanostatic; (B) potentiostatic.

Electrochemical preparation. Galvanostatic (see Figure 4.13A). Mercury can be oxidized in 2.5 M H_2SO_4 by applying a current density of 40 mA/cm² between an Hg pool electrode and a platinum coil CE. The setup, depicted in Figure 4.13A, consists of a glass stirrer that is positioned so as to not agitate the Hg pool electrode, but to keep the Hg_2SO_4 in suspension and allow for mixing. This method will produce 1–1.2 g of Hg_2SO_4 per cm³ Hg. The Hg_2SO_4 is gray and contains finely divided mercury.

Potentiostatic (see Figure 4.13B). Mercury can also be oxidized using a dropping Hg electrode created by employing a funnel filled with Hg. As shown in Figure 4.13B, the Hg is dropped into 2.5 M H_2SO_4 at an applied potential of 2 V. The Hg_2SO_4 produced is gray and contains finely divided mercury as above.

Chemical precipitation. Mercury(I) sulfate can be prepared in a similar fashion as mercury(I) chloride (31). First, about 1 g of reagent-grade mercury(I) nitrate dihydrate, $\text{Hg}_2(\text{NO}_3)_2 \cdot 2\text{H}_2\text{O}$, is moistened with 200 μl of concentrated nitric acid and dissolved in 20 ml of water. This solution is then added dropwise for 2 min into a covered beaker containing approximately 100 ml of 1 M H_2SO_4 while using a magnetic stir bar to continuously stir the solution. After addition, the suspension should be stirred for an hour. The precipitated mercury(I) sulfate is rinsed in a sintered glass crucible with ample cold 1 M H_2SO_4 , and then stored in ≥ 1 M H_2SO_4 , protected from light. Chemically precipitated mercury(I) sulfate can be recrystallized (35) by first dissolving the Hg_2SO_4 in concentrated sulfuric acid in the presence of Hg. This solution is then added dropwise to an excess of absolute methanol causing the mercury(I) sulfate to precipitate. The mercury(I) sulfate that is precipitated is white. The precipitate is washed 20 times employing decantation. Again, the Hg_2SO_4 should be stored in ≥ 1 M H_2SO_4 and protected from light.

4.3.2.3 Mercury(II) oxide reference electrode (Hg/HgO)

Controlling redox process (36):



The mercury(II) oxide (mercuric oxide) RE is limited to use in highly alkaline solutions due to the stability of the oxide. While mercury(II) oxide is the only stable oxide, it can exist as either red or yellow powders that differ in solubility (37). The potential of the mercury(II) oxide RE is independent of the electrolyte, but depends on the activities of both OH^- and H_2O (36). The potential can be calculated as follows (36):

$$E_{\text{Hg}|\text{HgO}} = E_{\text{Hg}|\text{HgO}}^\circ - \frac{RT}{F} \ln \frac{a_{\text{OH}^-}}{\sqrt{a_{\text{H}_2\text{O}}}} \quad (4.5)$$

This electrode is stable for several days and reproducible to ± 0.1 mV (38).

(a) Electrode Preparation

Mercury Preparation. No special preparative steps are required if mercury of sufficient purity is used.

HgO preparation. Method I. Either high-purity mercury(II) oxide (available to 99.999% purity commercially) or reagent-grade mercury(II) oxide that is thoroughly extracted with water on a steam bath (39) can be used. Note: Yellow oxide will equilibrate more slowly than red oxide.

Method II (39). The mercury(II) oxide can also be produced by the ignition of mercury(II) nitrate that has been carefully crystallized. The mercury(II) oxide must be washed before use.

Hg/HgO electrode preparation (39) (see Figure 4.14). The RE is assembled similarly to the SCE but with an alkaline solution, typically saturated $\text{Ca}(\text{OH})_2$, as the filling solution.

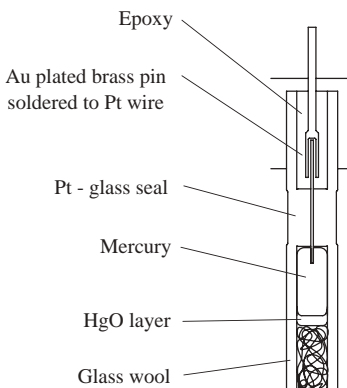


Figure 4.14 Hg|HgO active electrode body.

- (b) Filling solution
Saturated Ca(OH)₂.

4.3.3 Silver electrodes

4.3.3.1 Silver/silver chloride reference electrode (Ag|AgCl)

Controlling redox process:



The silver–silver chloride RE is the most regularly used RE due to its simplicity, inexpensive design, and nontoxic components (40). The simplicity of the Ag|AgCl RE lends itself to microfabrication as well as incorporation into sensors. The potential is calculated as follows:

$$E_{\text{Ag}|\text{AgCl}} = E_{\text{Ag}|\text{AgCl}}^\circ - \frac{RT}{F} \ln a_{\text{Cl}^-} \quad (4.6)$$

- (a) Electrode preparation (Figure 4.15)

High-purity silver wire (>99.999% Ag) preparation. High-purity silver wire will have an oxide on its surface that must be removed before use. This can be accomplished by dipping (41) the wire in 0.1 M HNO₃ for a few seconds. The wire should be rinsed with 18 MΩ cm water prior to use in subsequent steps.

Anodic AgCl coating (42). The freshly cleaned silver wire can be chloridized by placing it in a compartmentalized cell containing 0.1–1 M HCl or KCl and applying 0.4 mA/cm² current for 30 min. The coated wire should be washed with 18 MΩ cm water and soaked for 1–2 days in 18 MΩ cm water. The color of the AgCl should be sepia (dark brown with a reddish tint) if chloridized in the absence of light or pale tan to brown if chloridized while exposed to a light source. After washing, the coating color will range from pink to a shade of plum.

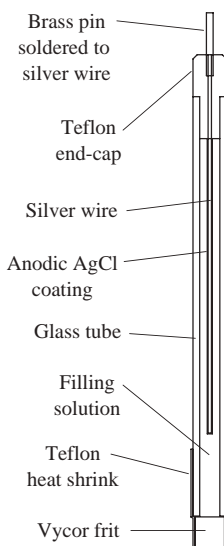


Figure 4.15 Ag|AgCl electrode.

(b) Filling solution

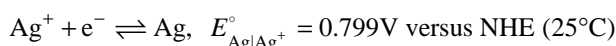
KCl—saturated, 3.5 M, 3 M.

NaCl—saturated, 3.5 M, 3 M HCl—dilute.

Saturated KCl should be presaturated with AgCl due to higher solubility of AgCl (43).

4.3.3.2 Silver/silver cation reference electrode (Ag/Ag⁺)

Controlling redox process:



This RE is typically used as a nonaqueous RE with AgNO₃ and a supporting electrolyte dissolved in MeCN or other organic solvents as the filling solution. The potential can be calculated as follows (44):

$$E_{\text{Ag}|\text{Ag}^+} = E_{\text{Ag}|\text{Ag}^+}^\circ + \frac{RT}{F} \ln \alpha_{\text{Ag}^+, \text{solv}} m_{\text{Ag}^+} \gamma_{\text{Ag}|\text{Ag}^+, \text{solv}} \quad (4.7)$$

where $\alpha_{\text{Ag}^+, \text{solv}}$ is the degree of ionization of Ag in the solvent, m_{Ag^+} the molality of Ag⁺, and $\gamma_{\text{Ag}|\text{Ag}^+, \text{solv}}$ the molal ionic activity coefficient of Ag⁺ in the solvent.

There may be variability in the potential of the RE prepared with different solvents due to differences in the degree of ionization of the silver ion in each solvent. The potential of a 10 mM AgNO₃ in MeCN is reported (45) as 0.3 V versus SCE_{aq}. This RE cannot be used in solvents that are readily oxidized by Ag⁺ (46).

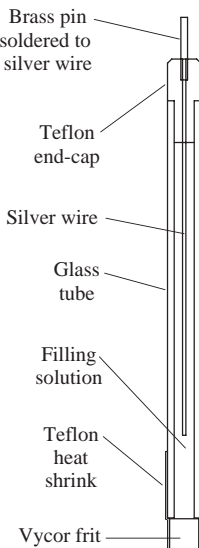


Figure 4.16 $\text{Ag}|\text{Ag}^+$ electrode.

(a) Electrode preparation (Figure 4.16)

High-purity silver wire (>99.999% Ag) preparation. See $\text{Ag}|\text{AgCl}$ preparation procedure.

(b) Filling solution

A range of filling solutions is used with the $\text{Ag}|\text{Ag}^+$ RE. Typical solutions are listed below:

Silver ion source: 10 mM or 0.1 M AgNO_3 .

Solvents: acetonitrile, propylene carbonate, dimethyl formamide, or dimethyl sulfoxide.

Supporting electrolyte: 0.1 M tetrabutylammonium perchlorate (TBAP), or same as that used in electrochemical cell.

4.3.4 Quasi-reference electrodes (QRE)

A quasi-reference electrode (QRE) is a general phrase for any poorly defined or unpoised RE. A QRE typically consists of an inert metal wire such as platinum or gold. A silver wire can also be used, so long as silver ions do not interfere with the measurements. The potential should ideally be steady, but the actual potential is not predictable if it is unpoised. Some methods to circumvent the ill-defined potential are to compare the potential to a conventional RE, or to include an electrochemical couple as an internal standard (see Section 4.6.2). A QRE is a low-impedance RE, but is also a polarizable electrode.

4.4 JUNCTIONS

As previously mentioned, the primary task of the junction on an RE is to separate the filling solution of the RE from the electrolyte of the electrochemical cell. If the two solutions being separated contain either electrolytes with different mobilities, or the same electrolyte in different solvents, a junction potential will develop. The potential drop (ΔV) that is developed across the junction is the product of the impedance (Z) of the junction and the ion flux (or current, i) that flows through it, according to Ohms Law ($\Delta V = iZ$). Experimentally, it is best to minimize the junction potential, and to ensure that it remains constant during any experiment. The current that the RE experiences is typically limited by the potentiostat input impedance in its electrometer and is typically beyond the control of the experimenter. Additionally, the impedance of the junction is controlled by the pore size and density of the material as well as the nature of the electrolytes on either side of the junction. To minimize the potential drop for any given junction, the electrolytes on either side should have similar ionic mobilities, which are listed in Table 4.7.

When using a high-flow rate junction, the impedance is effectively decreased, but the amount of filling solution that can interact with the sample increases, requiring careful design, and sometimes a compromise. Some data on common frit materials are shown in Table 4.8.

4.4.1 Filling solutions

When choosing (54) a filling solution for an RE, several factors must be considered. The filling solution should not react with any species in the electrochemical cell, or interfere with the measurement in any way. While difficult to do in highly acidic or basic solution due to the high mobilities of hydroxyl and hydronium ions, it is best to match the

Table 4.7

Ionic mobilities of various ions calculated for infinite dilution at 25 °C (47)

Cations	Mobility (cm ² /(V sec))	Anions	Mobility (cm ² /(V sec))
H ⁺	3.625×10^{-3}	OH ⁻	2.05×10^{-3}
K ⁺	7.619×10^{-4}	Cl ⁻	7.912×10^{-4}
Na ⁺	5.193×10^{-4}	Br ⁻	8.13×10^{-4}
Li ⁺	4.010×10^{-4}	I ⁻	7.96×10^{-4}
NH ₄ ⁺	7.61×10^{-4}	NO ₃ ⁻	7.404×10^{-4}
1/2 Ca ²⁺	6.166×10^{-4}	OAc ⁻	4.24×10^{-4}
		ClO ₄ ⁻	7.05×10^{-4}
		1/2 SO ₄ ²⁻	8.27×10^{-4}
		HCO ₃ ⁻	4.610×10^{-4}
		1/3 Fe(CN) ₆ ³⁻	1.047×10^{-3}
		1/4 Fe(CN) ₆ ⁴⁻	1.145×10^{-3}

Note: The mobility is the limiting velocity of the ion in an electric field of unit strength (48).

Table 4.8

Common frit materials

Type	Pore size	Impedance (saturated KCl)	Leak rate ^a (μl/h)	Compatibility issues
Vycor (49, 50)	4 nm	500 Ω	Modest	Not compatible with strong bases, HF
Polyethylene (51)	–	–	–	Used in strongly basic solutions
Ceramic (52)	–	1000 Ω	3–30	Can be used in strong bases; avoid precipitates and colloids
Ceramic/ conductive polymer (53) composite	Pores filled with conductive polymer	500 Ω– 2.7 kΩ	7.4 × 10 ⁻⁴ to 5.7 × 10 ⁻⁵	Resistant to strong acids, alkalis, and organic solvents

^aThe leak rate is dependent on several factors in addition to the porosity of the junction, including the height of solution over the frit, the pressure on this solution, as well as the depth that the junction is immersed and the pressure on that solution.

mobilities of anionic and cationic species, minimizing the junction potential. Due to the difficulty in balancing all these parameters, it is sometimes necessary to use a salt bridge or a double-junction RE, minimizing both electrolyte interactions and the potential across the junctions.

4.4.2 Salt bridges

Salt bridges are used to both minimize and stabilize the junction potential between solutions of different compositions as well as minimizing any cross-contamination between solutions. One vital consideration in setting up a salt bridge between different solvents is ensuring that the electrolyte in the bridge is soluble in both and interferes with species in neither. Typical electrolytes (55) for salt bridges include KNO_3 , KCl , NaSO_4 , and NH_4NO_3 . In some cases, the electrolyte in a salt bridge is gelled to reduce cross-contamination while maintaining a high conductivity. This is described in more detail below.

(a) Gelling an electrolyte (56)

Aqueous. A 4% agar solution can be used to gel an electrolyte by first dissolving the agar in hot water and adding the electrolyte salt. The hot agar solution is then transferred to the target vessel by pouring it, drawing it in with a vacuum, forcing it in with slight backpressure such as with a syringe, or by using pipette. It is extremely important that bubbles are not trapped in the gelled material, creating breaks in the ion flow path. The agar solution is then permitted to cool to room temperature, forming a gel. This procedure is equally useful to gel the electrolyte in an RE, salt bridge, or double-junction RE, but is not recommended for bridging from an aqueous to an organic solution.

Organic. Methylcellulose can be used as a gelation agent in pyridine and possibly other organic solutions. This is done by adding 5 g of methylcellulose to 100 ml of a 0.5 M solution of LiClO_4 in pyridine. This will produce a colorless, transparent, and conductive electrolyte gel.

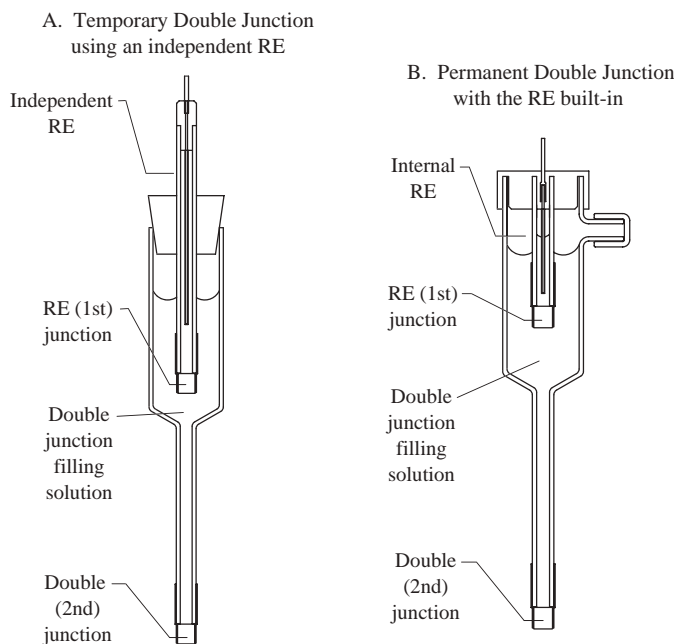


Figure 4.17 Double junctions: (A) temporary double junction using an independent RE; (B) permanent double junction with the RE built-in.

4.4.3 Double-junction reference electrodes

A double-junction RE incorporates a salt bridge into the RE design, typically to improve the compatibility of the electrolytes in the filling solution with those in the electrochemical cell. Chloride-containing electrodes are often isolated from an electrochemical cell due to the contamination and catalyst-poisoning potential of chloride ions. This is easily done using a K_2SO_4 solution between the two junctions. Two types of double junctions are shown in Figure 4.17.

4.4.4 Reference electrode impedance

The impedance of an RE can be measured with any potentiostat with built-in electrochemical impedance spectroscopy (EIS) capabilities or with the addition of a separate frequency response analyzer (FRA). One method is described below.

(a) Measuring the impedance of an RE (57)

The RE and an inert CE of sufficient size are placed in a beaker containing electrolyte. The RE is connected to the WE terminal of the potentiostat, and the CE is connected to both the RE and the CE terminals. An impedance scan is set up from at least 10 kHz down to 1 Hz, with no DC potential (V_{DC}) applied ($V_{DC} = V_{OCP}$, where V_{OCP} is open circuit potential) and an AC waveform (V_{AC}) of 5–10 mV amplitude.

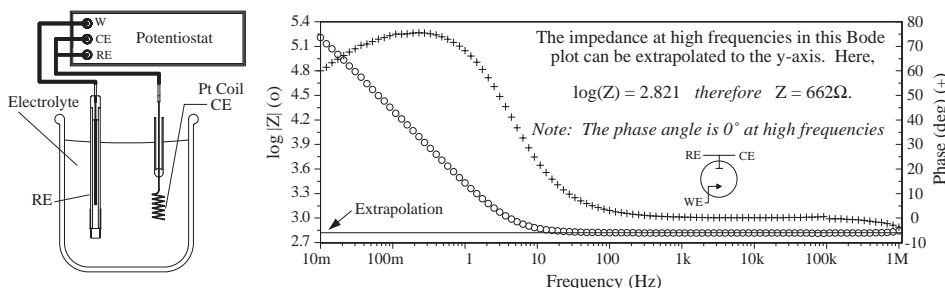


Figure 4.18 Measuring the impedance of a reference electrode.

Caution: If V_{DC} is set to any potential other than the open circuit potential, appreciable current can flow, possibly destroying the RE! The impedance at high frequencies is the impedance of the RE. At these frequencies, there should only be a real component to the impedance, and no imaginary components (the phase angle should be at or near 0°). The interpretation of sample data is shown in Figure 4.18 with a diagram of setup required for this measurement.

4.5 REFERENCE ELECTRODES: NONAQUEOUS SOLVENTS

Nonaqueous solvent systems introduce additional considerations into the process of selecting an RE for electrochemical measurements. There are relatively few REs designed for these systems, with most based on exotic formulations specific to the electrochemical system of study. Due to space constraints, only the $\text{Ag}|\text{Ag}^+$ RE is described here. In certain circumstances, aqueous REs can be used, but the electrolyte must be soluble in the nonaqueous solvent. In some cases, alternative filling solutions (58) for aqueous $\text{Ag}|\text{AgCl}$ or SCE REs can be used, such as aqueous lithium chloride or quaternary ammonium chloride. Another possible solution for using an aqueous RE in a nonaqueous solution is through the use of a salt bridge or a double-junction RE. Both tetraethylammonium picrate and tetra-*n*-butylammonium tetraphenylborate ($\text{NBu}_4^+\text{BPh}_4^-$) are nearly equitransferent in many organic solvents (59) and either can be used within a salt bridge.

One caveat to using aqueous REs in nonaqueous solvents is that the potential measurements carried out cannot be related (59) from solvent to solvent even though the same RE is used. This is due to the difference in junction potentials that exist between systems. The acceptability of various REs in different solvents is summarized in Table 4.9.

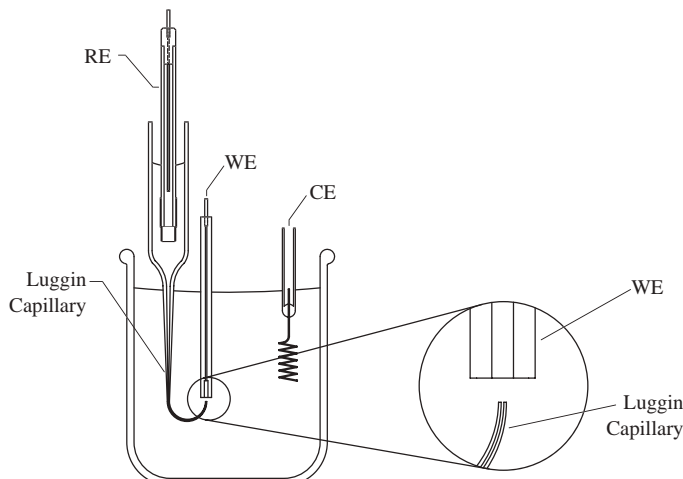
As described in Section 4.3.3.2, the $\text{Ag}|\text{Ag}^+$ RE can be used with a variety of organic solvents. Using the same solvent in the RE filling solution as in the electrochemical cell will minimize the junction potential of the RE. The limitations of this electrode are that only solvents in which a silver salt is soluble and not oxidized by the Ag^+ can be used. Similar to the difficulty in comparing potentials between different solvents using aqueous

Table 4.9

Reference electrodes for use in dipolar aprotic solvents (58, 60)

RE	Acetonitrile	Propylene carbonate	Dimethyl formamide	Dimethyl sulfoxide
Pt H ₃ O ⁺ , H ₂	S	S	S	NR
Ag Ag _{solv} ⁺	S	S	S	S
Ag AgCl	NR	NR	NR	NR
Ag AgCl	S	S	S	S
Hg Hg ₂ Cl ₂	NR	NR	NR	NR
Hg Hg ₂ Cl ₂	S	S	S	S
Li Li(OH ₂) ₄ ⁺		S	S	S

S: satisfactory stability and reproducibility; NR: not recommended (unstable and/or not reproducible); the symbol '||' denotes a salt bridge.

**Figure 4.19** Luggin capillary placement.

REs, this RE suffers the same limitation. One solution to this problem is calibration of the RE using internal standards as described in Section 4.6.2. In some cases with nonaqueous solvents, solubility limitations provide reduced conductivity in the electrochemical cell resulting in large uncompensated resistances between the RE and WE. One way to reduce the uncompensated resistance is to use a Luggin capillary to sample the electrochemical cell in the vicinity of the WE by placing the outlet of the Luggin capillary in close proximity to the WE. To prevent shielding of the WE, the minimum distance between the Luggin capillary and the WE should be no closer than two times (61) the diameter of the WE. The placement of the capillary with respect to a WE is shown in Figure 4.19.

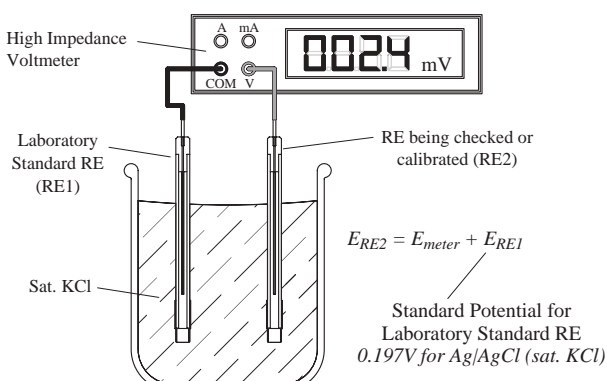
4.6 REFERENCE ELECTRODE CALIBRATION

4.6.1 Versus a second reference electrode

The potential of all REs should be checked periodically. This is easily accomplished by using a high-impedance voltmeter and a second RE that is held as a laboratory standard (62), shown in Figure 4.20. This laboratory-standard RE should be a well-behaved RE, such as Ag|AgCl (saturated KCl), and maintained in the laboratory solely for the purpose of calibration. This will prevent any questions as to fouling, clogging, or contamination and will give confidence in the calibrations conducted. To calibrate an RE or check its potential, both the RE in question and the laboratory-standard RE are placed in a common electrolyte of high conductivity (e.g., saturated KCl) that is maintained at a constant temperature. The standard RE is connected to a common meter, and the voltage of the RE in question is read. If the potential takes a long time to settle, the RE must be evaluated and possibly rebuilt, as the junction is likely clogged. An RE evaluated in this way is considered acceptable if its potential is within a few mV of the accepted standard potential. The two electrodes should not be left connected to the voltmeter or the potentiostat, as described below, for any extended duration since to measure the potential, a small, nonzero current must flow.

4.6.2 Using a well-defined redox couple

A well-defined redox couple can be used to calibrate an RE or as an internal standard in electrochemical experiments. The reference redox couple must be stable for the duration of the measurement, and must exhibit a repeatable potential in the system used. A good reference redox couple (63) for nonaqueous, and some carefully controlled aqueous systems, is the ferrocene/ferrocenium ($\text{Fc}|\text{Fc}^+$) couple at 0.5–10.0 mM concentration. Standard reduction potentials, E° , for various solvents (64) are listed in Table 4.10. Other couples can be found in References (64–66).



Additional Note: A potentiostat* can also be used to check reference electrode potentials

Connect RE1 to RE
Connect RE2 to WE
Monitor the potential (vs. time)

Do not connect the CE, turn the cell on, or attempt to control the current or potential

*not all potentiostats provide the capability to track the potential vs time in the software.

Figure 4.20 Calibration of a reference electrode with a second reference electrode.

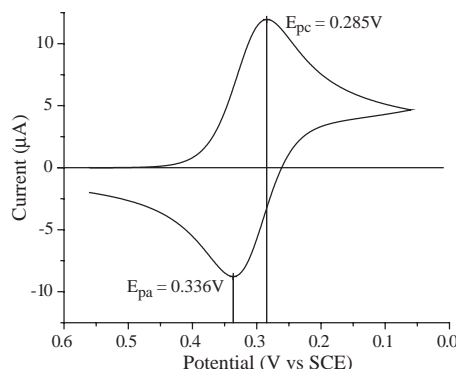
Table 4.10

Suggested reference redox systems (65)

Solvent ^a	$E_{\text{Fc} \text{Fc}^+, \text{solvent}}^\circ$ (V versus NHE) (66)
Ferrocene ferrocenium	
H ₂ O	0.40
MeCN	0.69
DMF	0.72
Py	0.76
Me ₂ SO	0.68

Note: Other reference redox systems include: Rb/Rb⁺ and Fe(bpy)₃²⁺/Fe(bpy)₃³⁺ (where bpy: 2,2'-bipyridine).

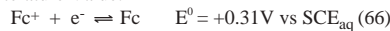
^aUnstable in some organics due to decomposition.



$$E_{1/2} = \frac{E_{\text{pc}} + E_{\text{pa}}}{2}$$

$$E_{1/2} = \frac{0.285\text{V} + 0.336\text{V}}{2} = 0.311\text{V}$$

Literature Value:



Experimental value is the same as the literature value.

Figure 4.21 Calibration of an RE using a well-defined redox couple (67).

4.6.2.1 Verifying the potential of an RE with a well-defined redox couple

In addition to checking the reference potential with a second RE, an RE can be checked using a well-defined redox couple. This is done by running a cyclic voltammogram (CV) and comparing the $E_{1/2}$ value to that which is expected of the redox couple, as shown in Figure 4.21. As when checking an RE versus a laboratory-standard RE, agreement between calculated and experimental $E_{1/2}$ within a few mV for the reference couple indicates an acceptable RE.

4.6.2.2 Defining potentials with a well-defined redox couple as an internal standard (68)

Internal standards are routinely used in analytical measurements to aid in the quantification of analyte signals in chromatography, or as reference energy standards in NMR. An internal standard can be used in electrochemistry as a reference potential standard in circumstances that an RE alone does not provide an adequately known reference potential in a particular system. This may be the case if a QRE (Section 4.3.4) is used or if large junction potentials are encountered within an electrochemical cell, as with an aqueous RE in a

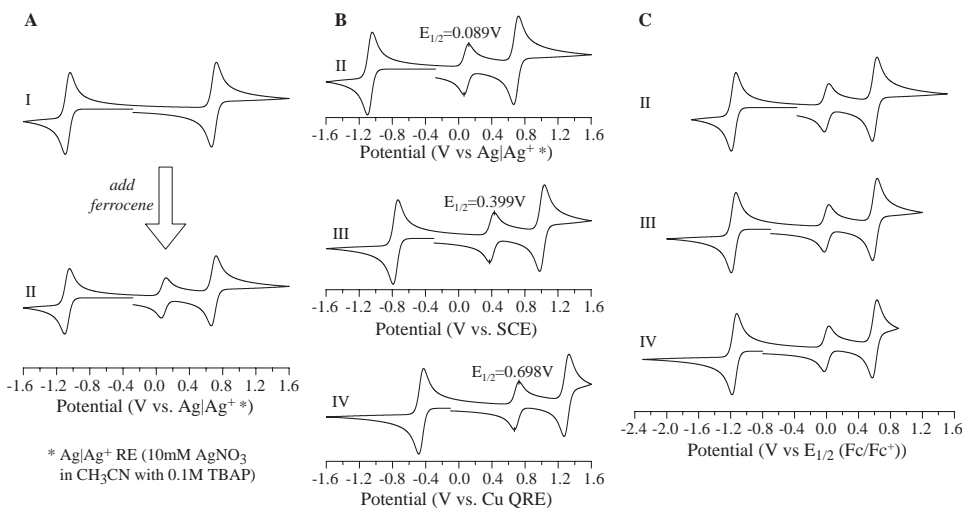


Figure 4.22 (A–C) Calculating a potential scale with an internal standard.

nonaqueous system (Section 4.5). In either case, a well-defined redox couple can be used as an internal standard. The redox potential ($E_{1/2}$) of the internal standard should be well separated from the electrochemical system under study, and should not chemically interfere. Care must also be taken that no electrode fouling or inactivation occurs from the use of the internal standard.

Figure 4.22 demonstrates how to calculate a potential scale with an internal standard using a sample system of 5 mM Ru(acac)₃ in CH₃CN with 0.1 M TBAP as a supporting electrolyte. Initially (Figure 4.22A), a CV is acquired without internal standard (plot I), and then a measured amount of ferrocene is added and an additional CV is collected (plot II). This verifies the sufficient separation between analyte and internal standard peaks, as well as provides a simple way to distinguish which peak belongs to the internal standard. The half-wave potential ($E_{1/2}$) can be calculated for the internal standard as demonstrated in Figure 4.21. This is shown in Figure 4.22B for the same system with ferrocene added as an internal standard versus three different REs. The experimental potential scale can then be adjusted such that the $E_{1/2}$ of the reference couple is used as a 0 V reference point on the potential axis. Figure 4.22C shows the potential scales of each CV normalized to the experimentally determined $E_{1/2}$ value of the ferrocene internal standard, demonstrating that with this technique, the peaks line up regardless of the RE used, so long as the RE is stable for the duration of the experiment.

4.7 MAINTENANCE

All REs need to be rebuilt or regenerated several times during their life, but with careful handling and proper storage conditions, the time between rebuilding cycles can be maximized. Even with the utmost care, junctions will clog, current will pass, and filling

solution will become contaminated. This section provides information on proper storage and maintenance of REs.

4.7.1 Storage

The majority of REs should be stored in solutions that are the same as the filling solution (e.g., SCE in saturated KCl). The manufacturers of some specialty REs provide directions with the RE. Storage solutions for REs with nonsaturated filling solutions should be protected from evaporative losses, otherwise the concentration of the filling solution will increase through diffusion with the storage solution. An RE should never be permitted to dry out. Certain REs are light sensitive ($\text{Ag}|\text{AgCl}$ and MSRE) and should be shielded from light sources for maximum life.

4.7.2 Cleaning junctions

Junctions can become clogged through several means including precipitation within the junction, plugging the pores with colloids from sample solutions, proteins binding within the pores, and organic contamination. Using an RE in an incompatible electrolyte such as K^+ with ClO_4^- will form an insoluble salt, clogging the junction. Due to the colorless nature of Vycor, it will typically change color when contaminated, turning yellowish when contaminated with organics and even brown with severe organic contamination followed by heating. In many cases, it is possible to renew a clogged junction, whereas for others, it must be replaced. In the simplest cases, a precipitated salt can be dissolved out, otherwise the contamination must be digested. When cleaning a junction, attention must be paid to both the junction material and the contaminant, otherwise the junction may be dissolved along with the contamination. Several junction cleaning methods are described in Table 4.11.

4.7.3 Replacing filling solutions

Through normal use of an RE, the filling solution and the electrolyte of the electrochemical cells with which it is used will diffuse together, diluting and contaminating each other. This requires that the filling solution of any RE be changed periodically, the frequency of which is dependent on the actual usage of each RE. When changing the filling solution, the replacement solution should have the proper concentration for the RE (i.e., $\text{Ag}|\text{AgCl}$ (saturated KCl) the filling solution should be saturated with KCl and AgCl.) The introduction of air bubbles upon introducing the new filling solution should be avoided, and removed if inadvertently introduced.

4.7.4 Regenerating the reference electrode

When required, most REs can easily be refreshed with new filling solution or a new frit, but in some cases, the entire electrode must be rebuilt. The possible actions for each RE are summarized in Table 4.12.

Table 4.11

Junction cleaning procedures

Before cleaning	Before the washing procedure, the RE filling solution must be removed, and if possible, the active portion of the RE should be removed from the electrode body or the frit removed from the electrode body and cleaned alone, to prevent any contamination or reactions from destroying the RE	
Cleaning	Contaminant	Procedure
	Proteins (69)	Soak in a 0.1 M HCl and 1 wt% pepsin solution followed by thorough rinsing with deionized water
	Silver sulfide (70)	Soak in a 0.1 M HCl and 7.5 wt% thiourea solution followed by thorough rinsing with deionized water
	Organic (49) (i.e., yellowed Vycor)	Soak the frit in a strong oxidizing solution (e.g., 30% H ₂ O ₂ or concentrated HNO ₃ with a few crystals of KClO ₃ or NaClO ₃) heated to 100 °C until any color disappears. The frit should then be washed thoroughly with deionized water
After cleaning	After cleaning, the junction and/or RE body should be rinsed with filling solution to remove all traces of the cleaning solutions, and the RE rebuilt and refilled	

Table 4.12

Renewal and regeneration possibilities for reference electrodes

Electrode	Possible actions for regeneration
NHE or SHE	Replace filling solution; if H ₂ supply is bad, replace; replatinize electrode
CHE	Replace filling solution and/or junction; refill with H ₂ ; replatinize electrode
DHRE	Replace filling solution; if no bubbles or low current, replace power supply and/or replatinize H ₂ electrode
SCE, MSRE, Hg HgO	If new filling solution and/or new junction do not work, electrode must be rebuilt using new or repurified mercury and the appropriate mercury salt. See appropriate section above
Ag AgCl	If new filling solution and/or new junction do not work, rechloridize the silver wire. This is accomplished by first removing the old AgCl by soaking in concentrated NH ₄ OH, and then following the same procedure as building an new RE, outlined in Section 4.3.3.1
Ag Ag ⁺	Replace filling solution and/or junction; clean Ag wire

4.8 TROUBLESHOOTING**4.8.1 Special notes****4.8.1.1 High-frequency effects**

The impedance of an RE, particularly if large, can have undesired effects in electrochemical experiments (Table 4.13). This is especially true for high-frequency or high-speed

Table 4.13

Troubleshooting reference electrodes

Problem	Cause	Solution
Incorrect potential	Filling solution is not at the correct concentration, or species that diffused into the RE are interfering with the redox couple in the RE	Replace filling solution
	Clogged frit	Clean or replace frit as it may be clogged with insoluble salts Do not polish the junction of an RE. You will only embed polishing media and ground pieces of frit material in the frit
	Sparingly soluble salt is completely dissolved (i.e., silver wire in Ag AgCl looks like silver)	Replate if Ag AgCl RE. Rebuild if Hg-based RE
Sluggish (potential appears to change or settle over time of experiment)	Clogged frit	Clean or replace frit
	Platinization too thick	Remove old platinization; replatinize the electrode
	Mercury salt too thick	Rebuild RE with new or repurified Hg and new mercury salt
Erratic and/or sluggish	Bubble on frit	Tap or flick RE to remove bubbles
Noisy voltammetry Discontinuity in EIS	RE impedance too high	Use a double RE (high-frequency shunt)

measurements. This can show itself as a noise in most methods, and as a discontinuity in EIS measurements at high frequency. Figure 4.23A shows a bode plot of an EIS measurement displaying this characteristic discontinuity between frequencies of 100 kHz and 1 MHz.

The discontinuity occurs even with an RE with very low impedance ($\sim 600 \Omega$). Problems of this type can be addressed using a double RE, or a high-frequency shunt. This is created using a typical RE connected in parallel with a capacitor and a platinum wire that is placed directly in the electrochemical cell, as shown in Figure 4.24. Its purpose is to pass high frequencies directly into the cell solution, effectively bypassing the RE with a high-pass filter. This double RE used in the same experiment described above in place of the solitary RE is shown in Figure 4.23B. Notice that the discontinuity at high frequencies disappears when the shunt is incorporated.

In fast-sweep rate cyclic voltammetry, an RE with high impedance can cause noise to be superimposed onto the CV due to a slowed potentiostat response, as well as contributions from environmental noise sources (71). This effect is shown in Figure 4.25 with CVs at 10 V/sec in a solution of 0.59 mM Co(III)(Salen)⁺ in DMF with 0.1 M NBu₄PF₆ as a supporting electrolyte. Potentiostat sensitivity settings of both 10⁻⁴ A/V (Figure 4.25A)

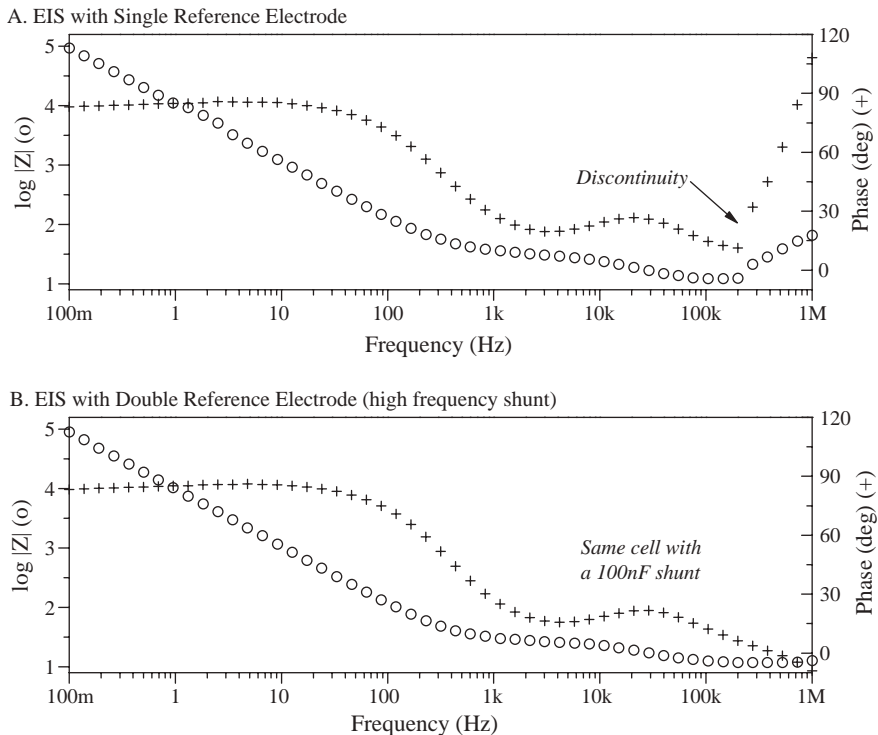


Figure 4.23 High-frequency reference electrode impedance problems in electrochemical impedance spectroscopy. EIS with (A) single reference electrode and (B) double reference electrode (high-frequency shunt).

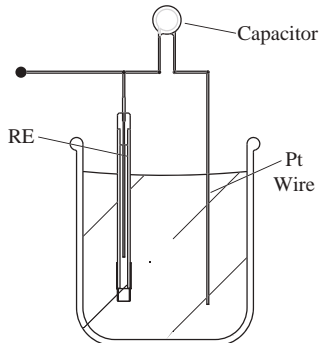


Figure 4.24 Double reference electrode.

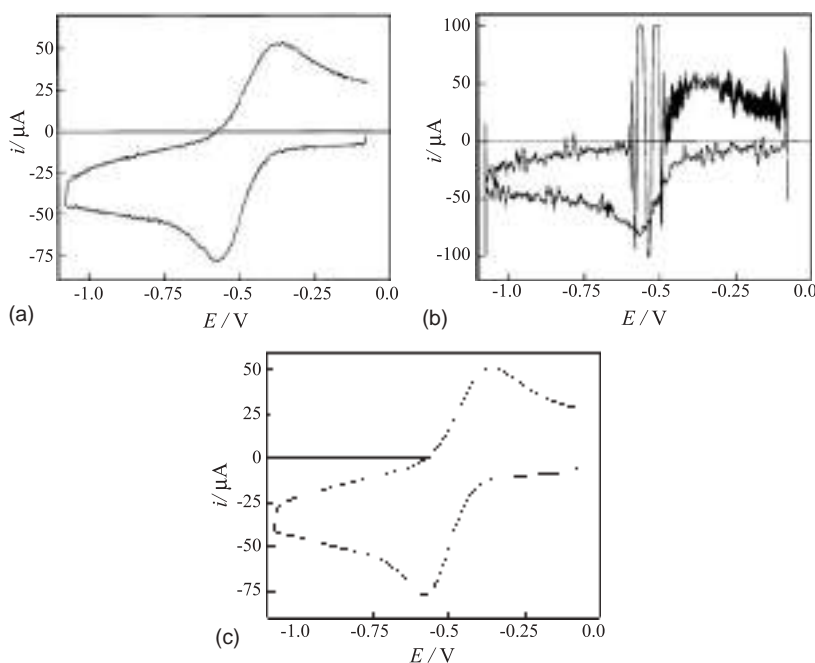


Figure 4.25 (A–C) Effect of high RE impedance on fast-scan rate CV. [Reprinted with permission from reference (71). Copyright 1994, Bioanalytical Systems, Inc.]

and 10^{-5} A/V (Figure 4.25B) result in noisy data. The incorporation of a double RE, as described above, produces a less noisy CV, shown in Figure 4.25C.

4.8.1.2 Microscale reference electrodes

In many cases, modern electrochemists are probing systems where classical REs are much too large. Microscale reference electrodes (μREs) are now being used, such as with solid-state REs incorporated into biosensors. These μREs are typically miniaturized versions of the classical electrodes that utilize novel solutions to attain the size required, usually using polymer films for both the electrolyte and the junction material. The most popular in the literature is the $\text{Ag}|\text{AgCl}$ μRE using either thick- or thin-film polymer methods to create a mixed polymer–electrolyte and an additional polymer layer that serves as a membrane junction. Simonis *et al.* (72) recently compared thin- versus thick-film techniques for the $\text{Ag}|\text{AgCl}$ μRE . In addition to the $\text{Ag}|\text{AgCl}$ μRE , $\text{Ag}|\text{Ag}^+$ μREs have been described (73), and general methods for the miniaturization of REs through the use of micromachining techniques are presented by Suzuki (74). The DHRE could also be miniaturized using standard microfabrication techniques.

4.8.1.3 Temperature effects on reference electrode potentials

Using an RE at a temperature other than standard temperature (25°C) requires a correction to be made to the potential due to differences in solubility and activity of the components

Table 4.14

Temperature-dependent potentials

RE	Equation (valid for 0–100 °C for calomel; 0–95 °C for Ag AgCl; 0–60 °C MSRE)
SCE (75)	$E = 0.2412 - 6.61 \times 10^{-4}(t - 25) - 1.75 \times 10^{-6}(t - 25)^2 - 9.0 \times 10^{-10}(t - 25)^3$
NCE (75)	$E = 0.2801 - 2.75 \times 10^{-4}(t - 25) - 2.50 \times 10^{-6}(t - 25)^2 - 4 \times 10^{-9}(t - 25)^3$
Ag AgCl (76)	$E = 0.23659 - 4.8564 \times 10^{-4}t - 3.4205 \times 10^{-6}t^2 - 5.869 \times 10^{-9}t^3$
MSRE (33)	$E = 0.63495 - 7.8144 \times 10^{-8}t - 4.2689 \times 10^{-11}t^2$

of the RE. The SHE is defined as 0.0000 V at all temperatures, so no correction is required. Listed in Table 4.14 are temperature correction formulas for Ag|AgCl, NCE, SCE, and MSRE REs. It has been recommended (29) that calomel-based electrodes should not be used above 70 °C for long durations.

REFERENCES

1. A. J. Bard, L. R. Faulkner, *Electrochemical Methods*, 2nd ed., John Wiley & Sons: New York, 2001, p. 22.
2. Compiled with data obtained from: Chemical Resistance Data. [Online]. Available at: <http://www.tank-depot.com/engineerdata/chemicalres.pdf>. Accessed 7 Sept. 2004. Quick Reference Polymer Solvent Compatibility Chart. [Online]. Available at: <http://www.upchurch.com/TechInfo/polymerInfo.asp>. Accessed 7 Sept. 2004. Spill Prevention Guidance Document, Appendix E: Chemical/Material Compatibility Matrix. [Online]. Available at: http://enviro.nfesc.navy.mil/ps/spillprev/appx_e_chem.pdf. Accessed 7 Sept. 2004. Dupont Dow Elstomers. Viton Brochure. [Online]. Available at: <http://www.dupont-dow.com/literature/viton/090017a28008d688.pdf>. Accessed 10 Sept. 2004. Cole-Parmer: Chemical Resistance Database. [Online]. Available at: <http://www.coleparmer.com/techinfo/ChemComp.asp>. Accessed 12 Sept. 2004.
3. R. Barbour, *Glassblowing for Laboratory Technicians*, Pergamon Press: Oxford, 1978, pp. 122–131.
4. E. P. Serjeant, in *Potentiometry*, E. P. Serjeant, Ed., John Wiley & Sons: New York, 1984, p. 111.
5. D. T. Sawyer, A. Sobkowiak, J. L. Roberts Jr., *Electrochemistry for Chemists*, 2nd ed., John Wiley & Sons: New York, 1995, p. 179.
6. Zeus Industrial Products, Heat Shrink Tubing—Recovery Information. [Online]. Available at: <http://www.zeusinc.com/heatshrink.asp>. Accessed 4 Oct. 2004.
7. 3M™ Heat Shrink Tubing Selection Guide. [Online]. Available at: http://www.3m.com/market/electrical/elpd/oem/pdf/heat_shrink_tubing_guide.pdf. Accessed 29 Sept. 2004.
8. H. Galster, *pH Measurement Fundamentals, Methods, Applications, Instrumentation*, VCH: Weinheim, 1991, p. 68.
9. L. Haar, J. S. Gallagher, G. S. Kell, *NBS/NRC Steam Tables*, Hemisphere Publishing: New York, 1984.
10. G. J. Hills, D. J. G. Ives, in *Reference Electrodes*, D. J. G. Ives, G. J. Janz, Eds., Academic Press: New York, 1961, p. 107.
11. *Ibid.*, p. 106.

12. A. M. Feltham, M. Spiro, *Chem. Rev.* **71**, 177 (1971). R. G. Bates, *Determination of pH Theory and Practice*, 2nd ed., John Wiley & Sons: New York, 1973, p. 292.
13. R. G. Bates, *ibid.*, p. 291.
14. A. M. Feltham, M. Spiro, *op. cit.*, p. 193.
15. G. J. Hills, D. J. G. Ives, *op. cit.*, pp. 106–108.
16. G. J. Hills, D. J. G. Ives, *op. cit.*, pp. 93.
17. G. J. Hills, D. J. G. Ives, *op. cit.*, p. 99.
18. J. H. Hildebrand, *J. Am. Chem. Soc.* **35**, 847 (1913).
19. R. W. Pittman, unpublished, 1959.
20. G. J. Hills, D. J. G. Ives, *J. Chem. Soc.* 318 (1951).
21. S. Gong, J. Lu, Y. Heqing, *J. Electroanal. Chem.* **436**, 291 (1997).
22. F. G. Will, *J. Electrochem. Soc.* **133**, 454 (1986).
23. J. Giner, *J. Electrochem. Soc.* **111**, 376 (1964).
24. G. J. Hills, D. J. G. Ives, in D. J. G. Ives, G. J. Janz, Eds., *op. cit.*, Chapter 3. J. Newman, K. E. Thomas-Alyea, *Electrochemical Systems*, 3rd ed., John Wiley & Sons: New York, 2004, p. 137.
25. G. J. Hills, D. J. G. Ives, in D. J. G. Ives, G. J. Janz, Eds., *op. cit.*, p. 136.
26. J. Newman, K. E. Thomas-Alyea, *op. cit.*, p. 139.
27. H. Kahlert, in *Electroanalytical Methods*, F. Scholz, Ed., Springer-Verlag: Berlin, 2002, p. 266.
28. G. J. Hills, D. J. G. Ives, in D. J. G. Ives, G. J. Janz, Eds., *op. cit.*, p. 132.
29. E. P. Serjeant, *op. cit.*, p. 99.
30. G. J. Hills, D. J. G. Ives, in D. J. G. Ives, G. J. Janz, Eds., *op. cit.*, p. 135.
31. D. J. G. Ives, F. R. Smith, in D. J. G. Ives, G. J. Janz, Eds., *op. cit.*, p. 403.
32. *Ibid.*, p. 405.
33. *Ibid.*, p. 404.
34. G. A. Hulett, *Phys. Rev.* **32**, 257 (1911).
35. D. J. G. Ives, F. R. Smith, in D. J. G. Ives, G. J. Janz, Eds., *op. cit.*, p. 406.
36. Research Solutions and Resources. Hg/HgO Reference Electrode. [Online]. Available at: <http://www.consultrsr.com/resources/ref/hgopotl.htm>. Accessed 15 Oct. 2004.
37. D. J. G. Ives, in D. J. G. Ives, G. J. Janz, Eds., *op. cit.*, p. 335.
38. J. Newman, K. E. Thomas-Alyea, *op. cit.*, p. 140.
39. D. J. G. Ives, in D. J. G. Ives, G. J. Janz, Eds., *op. cit.*, p. 336.
40. H. Kahlert, *op. cit.*, p. 268.
41. J. M. Thomas, *J. Chem. Ed.* **76**, 97 (1999).
42. D. T. Sawyer, A. Sobkowiak, J. L. Roberts Jr., *op. cit.*, p. 189. G. J. Janz, in D. J. G. Ives, G. J. Janz, Eds., *op. cit.*, p. 205.
43. D. T. Sawyer, A. Sobkowiak, J. L. Roberts Jr., *op. cit.*, p. 190.
44. G. J. Hills, in D. J. G. Ives, G. J. Janz, Eds., *op. cit.*, p. 438.
45. L. Meites, Ed., *Handbook of Analytical Chemistry*, McGraw Hill: New York, 1963, Section 5.
46. D. T. Sawyer, A. Sobkowiak, J. L. Roberts Jr., *op. cit.*, p. 201.
47. A. J. Bard, L. R. Faulkner, *op. cit.*, p. 68, and references cited therein.
48. *Ibid.*, p. 66.
49. Corning, VYCOR® Brand Porous Glass 7930 Data Sheet. [Online]. Available at: http://www.corning.com/lightingmaterials/images/Vycor_7930.pdf. Accessed 8 Sept. 2004.
50. Koslow Scientific. Porous Vycor. [Online]. Available at: <http://www.koslow.com/vycor.html>. Accessed 8 Sept. 2004.
51. Princeton Applied Research, <http://www.princetonappliedresearch.com>.
52. D. T. Sawyer, A. Sobkowiak, J. L. Roberts Jr., *op. cit.*, p. 180.
53. WPI Dri-Ref Reference Electrodes. [Online]. Available at: http://www.wpiinc.com/WPI_Web/Biosensing/Dri-Ref.html. Accessed 18 Oct. 2004.

54. D. T. Sawyer, A. Sobkowiak, J. L. Roberts Jr., *op. cit.*, p. 181.
55. H. Kahlert, *op. cit.*, p. 274.
56. D. T. Sawyer, A. Sobkowiak, J. L. Roberts Jr., *op. cit.*, pp. 182–184.
57. Gamry Instruments. Reference Electrode Impedance Check. [Online]. Available at: http://www.gamry.com/App_Notes/ReferenceElectrodes/Reference_Impedance_Check.htm. Accessed 28 Oct. 2004.
58. D. T. Sawyer, A. Sobkowiak, J. L. Roberts Jr., *op. cit.*, p. 200.
59. *Ibid.*, p. 182.
60. J. N. Butler, Advances in Electrochemistry and Electrochemical Engineering, in *Electrochemistry*, P. Delahay, Ed., John Wiley & Sons: New York, Vol. 7, 1970.
61. A. J. Bard, L. R. Faulkner, *op. cit.*, p. 27.
62. H. Kahlert, *op. cit.*, pp. 276–277.
63. *Ibid.*, pp. 270–271.
64. A. Tagni, T. Hayashi, *Ferrocenes*, VCH: Weinheim, 1995.
65. A. J. Bard, L. R. Faulkner, *op. cit.*, p. 812, and references cited therein.
66. D. T. Sawyer, A. Sobkowiak, J. L. Roberts Jr., *op. cit.*, p. 203, and references cited therein.
67. R. D. Williams, University of Texas at Austin, simulated data.
68. R. R. Gagné, C. A. Koval, G. C. Lisensky, *Inorg. Chem.* **19**, 2854 (1980).
69. H. Kahlert, *op. cit.*, p. 276.
70. H. Galster, *op. cit.*, p. 114.
71. B. Gollas, B. Krauss, B. Speiser, H. Stahl, *Curr. Seps.*, **13**, 42 (1994). A. W. Bott, *Curr. Seps.* **14**, 64 (1994).
72. A. Simonis, H. Luth, J. Wang, M. J. Schoning, *Sens. Acuators B* **103**, 429 (2004).
73. M. Ciobanu, J. P. Wilburn, I. Nicholas, P. Ditavong, D. A. Lowy, *Electroanalysis* **14**, 989 (2002).
74. H. Suzuki, *Chem. Sens.* **13**, 55 (1997).
75. G. J. Hills, D. J. G. Ives, in D. J. G. Ives, G. J. Janz, Eds., *op. cit.*, p. 161.
76. G. J. Janz, in D. J. G. Ives, G. J. Janz, Eds., *op. cit.*, p. 189.

— 5 —

Solid Electrode Materials: Pretreatment and Activation

Greg M. Swain

Department of Chemistry, Michigan State University,
East Lansing, MI 48824-1322, USA

5.1 INTRODUCTION

Solid electrodes have been a mainstay in electroanalytical chemistry for nearly five decades now (1). For a solid material to function as an electrochemical electrode, it must possess several characteristics: electrical conductivity, chemical and electrochemical stability over a wide range of conditions, rapid electron transfer for a wide variety of redox systems, and reproducible electrical, microstructural, and chemical properties. Table 5.1 lists some desirable electrode properties for materials used in electroanalytical measurements. A challenge with making high-quality electroanalytical measurements is reproducibly controlling the electrode's physicochemical properties in such a way as to achieve a low background current and a rapid rate of electron transfer for the target analyte. Electrodes exhibiting these properties are referred to as being "active" or in an "activated state". Activation is accomplished by a process known as electrode pretreatment, which involves conditioning the surface morphology, microstructure, and chemistry in a manner that promotes low background current and rapid reaction kinetics (both electron and proton transfer) with a redox analyte dissolved in solution or confined to the surface.

Electrochemical reactions are heterogeneous in nature with the reaction kinetics being controlled by the properties of the electrode–electrolyte interface and the concentration of reactant available at this interface. Therefore, the physical, chemical, and electronic properties of the electrode surface are of paramount importance. Several factors will influence the electron-transfer kinetics for a redox system: (i) type of electrode material, (ii) surface cleanliness, (iii) surface microstructure, (iv) surface chemistry, and (v) electronic properties (e.g., charge carrier mobility and concentration, which can be potential dependent for some semiconducting electrodes). Of course, if the solid is not a good electrical conductor (low charge carrier mobility and/or carrier concentration), then the current flow will be limited and the material will have drawbacks for electrochemical measurements. With the exception

Table 5.1

Material and electrochemical properties of an ideal electrode

High electrical conductivity
Hard and durable
Homogeneous microstructure throughout the bulk
Reproducible physical, chemical, and electronic properties
Good chemical inertness
Low and stable background current
Morphological and microstructural stability over a wide potential range
Rapid electron-transfer kinetics for a wide range of redox systems
Easily fabricated, shaped, and inexpensive in cost

of the electronic properties, the extent to which any one of the above-listed factors influences the electrochemical reaction kinetics very much depends on the particular redox system (2–8). The effectiveness of the pretreatment for a particular redox system also depends on the electrode material. For example, the same pretreatment applied to two different electrode materials often results in different levels of activation for each toward the same redox system. Surface cleanliness is a critical property for every electrode and all redox systems. For example, it is highly unusual for a researcher to simply take an electrode out of laboratory storage and use it as it is to make a high-quality measurement. This is because contaminants from the air adsorb onto the surface, particularly carbon materials, and block sites for electron transfer. This leads to complete electrode blocking and, at the very least, an increased electron-tunnelling distance and/or alteration in the local double-layer structure. Air oxidation of the surface can also occur producing a change in the surface chemistry, wettability, and microstructure. Furthermore, every electrode has a past history of use that affects its performance. Therefore, every electrode needs to be first pretreated in order to make it ready for the electrochemical measurement. Pretreatments activate the electrode by some combination of surface cleaning, alteration of the exposed microstructure (i.e., edge plane exposure), and manipulation of the surface chemistry (i.e., introduction of surface carbon–oxygen functionalities).

Every pretreatment protocol should have some sort of surface cleaning as its first step, although it should be pointed out that the apparent heterogeneous electron-transfer rate constant, k_{app}° , for some redox systems is more strongly influenced by surface cleanliness than other factors. For instance, k_{app}° for $\text{Fe}(\text{CN})_6^{3-/4-}$ can decrease by orders of magnitude (10^{-2} – 10^{-5} cm sec $^{-1}$) for an unclean compared to a clean electrode surface (2–8). In contrast, k_{app}° for $\text{Ru}(\text{NH}_3)_6^{3+/2+}$ might decrease by only a factor of 5–10 for the same unclean surface (2–8). The rate constants are referred to as “apparent (app)” because they are often not corrected for electric double-layer effects (so-called Frumkin effects). As I have already mentioned, oxidation reactions can occur, particularly with carbon electrodes, that will alter the electrode surface chemistry and even the microstructure if severe enough. These oxidation reactions occur during exposure to the ambient air or can be potential-induced. Depending on the redox system, surface oxidation can accelerate or decelerate the rate of electron transfer. Incorporating oxygen makes electrode surfaces more polar and hydrophilic and, consequently, more wettable with water. It also makes them more susceptible to molecular adsorption involving polar adsorbates whether the molecule be a contaminant or the redox analyte under study. When reaction intermediates or products adsorb, active sites on the electrode may be blocked. At the very least, molecular adsorption creates a prior

Table 5.2

Common redox analytes: relative effect of factors on the heterogeneous electron-transfer rate constant

Redox analyte	Cleanliness	Microstructure	Surface chemistry
Ru(NH ₃) ₆ ^{3+/2+}	Weak	Weak	Weak
Chlorpromazine	Weak	Weak	Weak
Methyl viologen	Weak	Weak	Weak
IrCl ₆ ^{2-/3-}	Weak	Weak	Weak
Ferrocene	Weak	Weak	Weak
Ferrocene carboxylic acid	Weak	Weak	Weak
Fe(CN) ₆ ^{3-/4-}	Strong	Strong	Strong
Ascorbic acid	Strong	Strong	Minor
Catechol	Strong	Strong	Strong
Fe ^{3+/2+}	Strong	Strong	Strong
Eu ^{3+/2+}	Strong	Strong	Strong

history that can be carried over to the next measurement if the electrode is not properly cleaned. Table 5.2 shows some of the common redox systems used to probe the electrochemical activity of electrode materials, along with a listing of the relative influence of surface cleanliness, microstructure, and chemistry on k_{app}° for each. In summary, factors, such as the surface microstructure, surface oxides, adsorption strength, and surface cleanliness, influence k_{app}° for all redox systems to varying extents. The challenge is to reproducibly pretreat an electrode in a manner that activates it for the particular redox system under study.

Extensive research has been conducted over the years within the electroanalytical community in an effort to understand how solid electrodes are “activated” by pretreatment. Many pretreatment protocols have been established that can reproducibly activate various electrode materials. These include mechanical polishing, vacuum heat treatment, laser-based thermal treatment, electrochemical polarization, radio-frequency plasma treatment, and microwave plasma treatment. The ability to reproducibly activate macrosized electrodes results, to a large degree, because the surface can be polished prior to treatment. Polishing removes the effects of the electrode’s past history and allows a particular pretreatment to be performed on a fresh surface. Thus, polishing is often the first step in any pretreatment protocol. A prerequisite for performing high-quality electrochemical measurements is the preparation of an electrode with reproducible physical, chemical, and electronic properties. It is very easy, even for the novice, to pretreat an electrode and improve k_{app}° from say 10^{-5} to 10^{-3} cm sec⁻¹, but difficult to achieve large rate constants of $>10^{-2}$ cm sec⁻¹. Great care and attention must be given to how an electrode is pretreated if one intends to use it in a high-quality electroanalytical measurement.

The commonly used pretreatment protocols for activating solid electrodes are reviewed in this chapter. Specifically, the pretreatment of carbon, metal, and semiconductor electrodes (thin conducting oxides) is discussed. Details of how the different electrode materials are produced, how the particular pretreatment works, and what effect it has on electron-transfer kinetics and voltammetric background current are given, since these factors determine the electroanalytical utility of an electrode. Issues associated with cell design and electrode placement (Chapter 2), solvent and electrolyte purity (Chapter 3), and uncompensated ohmic resistance (Chapter 1) are discussed elsewhere in this book. This

chapter is divided into three main sections: carbon electrodes (highly oriented pyrolytic graphite (HOPG), glassy carbon, pyrolyzed photoresist films, fibers, nanotubes, diamond films, and tetrahedral amorphous carbon (Ta-C) films), metal electrodes (Pt and Au), and semiconductor electrodes (indium tin oxide (ITO)). Since carbon is widely employed in electroanalysis, a significant portion of this chapter is devoted to it. The various types of high-surface-area carbon powders used as catalyst support materials, for example, are not discussed as these materials typically are not used in electroanalysis.

5.2 CARBON ELECTRODES

Carbon is the most commonly used electrode material in electroanalytical chemistry and it is available in a variety of microstructures: graphite, glassy carbon, carbon fiber, nanotube, amorphous powders, and diamond. The electrochemical properties of many of these carbon types are discussed in the seminal book by Kinoshita (9). Some carbon electrode types (e.g., glassy carbon) have been studied and used extensively for ~40 years now. Even so, there are still incompletely understood points about the structure–performance relationship and how this relationship affects electrochemical activity. Details of this research history are given in monographs by McCreery (10–12). Carbon exists in two distinct crystalline structures: diamond and graphite. The diamond crystal is cubic and the carbon atoms are arranged in a tetrahedral configuration with sp^3 -hybridized bonding between them. This strong covalent bonding makes diamond the hardest known substance. For this reason, two commercial applications of diamond are as a grit for abrading and polishing metals and as a coating for cutting tools. Graphite consists of a hexagonal structure with the carbon atoms arranged in a trigonal configuration of sp^2 -hybridized bonding. This atomic arrangement leads to the formation of layer planes or graphene sheets with a spacing of 3.354 Å. Strong covalent bonding exists between the atoms within the graphene sheet (*a*-axis). Unlike diamond though, weak van der Waals forces exist between the layer planes to hold them together (*c*-axis). It is because of these weak interactions that the graphene sheets can slide across one another, making the material a good lubricant. There are permutations of the graphitic microstructure that characterize other types of sp^2 carbon electrode materials. For instance, when the in-plane dimension of the graphene sheets is small (i.e., high fraction of crystallite edges) and the spacing between them is large, this carbon is categorized as amorphous (e.g., powders, glassy carbon, etc.). Amorphous films of diamond also exist with mixtures of sp^3 - and sp^2 -bonded carbon, such as Ta-C. There is also a more exotic form of carbon known as the “buckyball” or fullerene that was discovered in 1985. The “buckyball” resembles a soccer ball in shape and contains 60 carbon atoms (C_{60}) in a spherical structure consisting of 20 hexagons and 12 pentagons arranged on the surface. The discovery has led to an expansion of research on C_{60} and variations of this structure (e.g., nanotubes) (13). The important take-home message is that carbon electrode materials possess different microstructures and surface chemistries depending on the type and how each was processed. As a consequence, the electrochemical properties can vary from material to material. Of all the solid electrodes utilized in electroanalytical chemistry, carbon materials are probably the most challenging and problematic from this perspective.

5.2.1 Highly oriented pyrolytic graphite

Highly oriented pyrolytic graphite (HOPG) is a special type of carbon that is analogous to a single-crystal metal (1, 9–12). It is prepared by exposing pyrolytic graphite, a material formed from the decomposition of hydrocarbon gases on a heated surface, to high pressure and temperature. It is composed of a lamellar arrangement of condensed polycyclic aromatic planes (i.e., graphene sheets) stacked in a slightly staggered fashion. The material is turbostratic, which means that the graphene sheets are rotationally disordered (i.e., random angular orientations to one another) and the alternating ABAB...stacking pattern of single-crystal graphite (that is produced naturally) is observed only over short distances along the *c*-axis. The interplanar spacing generally ranges from 3.35 to 3.39 Å. Organized arrangements of these graphene sheets are termed crystallites with the dimensional parameters L_c (stacking height), L_a (layer plane width), and d (interplanar distance). L_a is the mean size of the graphitic microcrystallite along the *a*-axis that always lies in the plane of the hexagonal lattice. L_c refers to the coherence length of the graphene sheet stacking in a direction perpendicular to L_a . Knowledge of these parameters, obtained from X-ray diffraction measurements, is usually sufficient to predict many of the material properties. An exposed hexagonal surface that is perpendicular to the *c*-axis is referred to as a basal plane whereas a cut surface parallel to the *c*-axis is called an edge plane. Raman spectroscopy is a useful tool for characterizing the microstructure of carbon materials, in particular, for examining the edge/basal plane ratio (14–16). The spectrum for the low-defect material (i.e., primarily basal plane exposed) has a single sharp peak at 1582 cm^{−1} (so-called G band), which has been assigned to an E_{2g} or a lattice “ring breathing” mode. Such a spectrum is seen for materials with large L_a and L_c parameters. The E_{2g} peak broadens and shifts to a higher frequency with decreasing L_a and L_c . If the graphene sheets are separated by intercalants (e.g., staging), a shoulder can develop on the 1582 cm^{−1} peak that is upshifted to ca. 1620 cm^{−1}. When L_a is decreased (i.e., significant edge plane is exposed), a new peak develops at 1360 cm^{−1} (the so-called D band). This peak correlates with the presence of edge plane density and the 1360/1580 cm^{−1} relative peak intensity ratio scales proportionally with $1/L_a$ (i.e., decreasing microcrystallite size) (14–16). The 1360 cm^{−1} band has been assigned to an A_{1g} mode and arises from a breakdown of the selection rules for optical excitation of phonons in the graphite lattice caused by the termination of the extended graphene sheets. As a consequence, new vibrational modes, including A_{1g} , become active. The important take-home message is that the 1360 cm^{−1} band correlates with microstructural disorder.

The reason HOPG is analogous to a single-crystal metal is because of the ordered arrangement of the carbon atoms within a graphene sheet. Each carbon atom is bonded to three others in the layer plane. The distance between neighboring carbon atoms is 1.42 Å, which is very close to the C–C bond distance in benzene. In addition to being well ordered, the surface is atomically smooth over relatively large dimensions (micrometers), making the material quite useful for studying electrochemical reactions, molecular adsorption, and potential-induced microstructural degradation at the atomic level. Physically, its stiffness along the *a*-axis is due to the strong σ bonds between the carbon atoms. However, the material is held together along the *c*-axis by weak van der Waals forces acting on the layer planes. Electronically, the material is also anisotropic because of the extended π -electron system. The material has metallic conductivity along the *a*-axis and semiconducting to

semimetallic conductivity along the *c*-axis. For example, the electrical conductivity is on the order of 10^5 ($\Omega \text{ cm}$) $^{-1}$ along the *a*-axis and 10^3 ($\Omega \text{ cm}$) $^{-1}$ along the *c*-axis, producing an anisotropy factor about 100, or so (10–12, and references therein).

The background current for the relatively defect-free basal plane is typically low within the working potential window with values $<5 \mu\text{A cm}^{-2}$ (8, 10–12). This is because of the characteristically low double-layer capacitance, C_{dl} , of $1\text{--}5 \mu\text{F cm}^{-2}$ (8, 10–12). The more defective the basal plane is, the greater the $1360/1580 \text{ cm}^{-1}$ Raman peak intensity ratio and the background current are. The magnitude of the peak ratio correlates with the fraction of edge plane exposed, hence the microstructural disorder. Gewirth and Bard used STM to characterize the types of defects native to the basal plane (17). The adsorption of polar molecules is generally weak on the basal plane with the adsorption enthalpy and coverage scaling with the amount of exposed edge plane and the increased carbon–oxygen functionality that exists there. Molecular adsorption tends to be much stronger on this surface for both chemical and electronic reasons (10–12, 18–20). HOPG has some very well-established electrochemical characteristics with the activity of the edge plane sites differing greatly from the basal plane sites (1, 8, 10–12). Microstructurally, chemically, and electronically, the edge plane sites are unique. Therefore, depending on the exposed microstructure and the particular redox system under study, the electrochemical properties of HOPG can be quite varied.

5.2.1.1 Layer plane cleavage

Since HOPG is a soft, microstructurally ordered material, some conventional pretreatment methods are typically not employed. For instance, one does not usually mechanically polish the electrode because of the microstructural damage this would introduce. The microstructural changes and the corresponding alterations of surface chemistry would have a significant impact on the magnitude of the background current, the extent of molecular adsorption, and k_{app}° for those redox systems that are “surface sensitive”. A very good way to achieve a clean basal plane, without microstructural damage, is to carefully cleave the layer planes. The scotch tape method is one of the means to accomplish this. In this method, one simply presses a piece of Scotch™ tape across the surface of HOPG and then carefully lifts the tape, peeling away graphene sheets. Another cleavage method involves the use of a sharp knife blade to remove the graphene sheets. For this and all pretreatments, gloves should be worn and the electrode should be handled with tweezers to avoid contamination. As long as either of these methods is performed carefully, minimal damage to the basal plane will result. The basal plane surface is fragile and also susceptible to damage during physical manipulation and mounting in the electrochemical cell. In order to conduct electrochemical measurements on a low-defect basal plane, an o-ring is often used with gentle pressure to define the area exposed to the solution. Care should be taken to avoid damaging the surface during handling and mounting. The two AFM images in Figure 5.1 show a surface after a careful cleavage (left) with no evident damage over a $5 \times 5 \mu\text{m}^2$ area and a surface (right) with some layer plane damage (i.e., cleavage plane). This is a useful first step in any pretreatment protocol for this electrode material.

5.2.1.2 Solvent cleaning

Exposure to clean organic solvents is another useful method for cleaning the HOPG surface without introducing alterations in the surface microstructure and chemistry. It is often

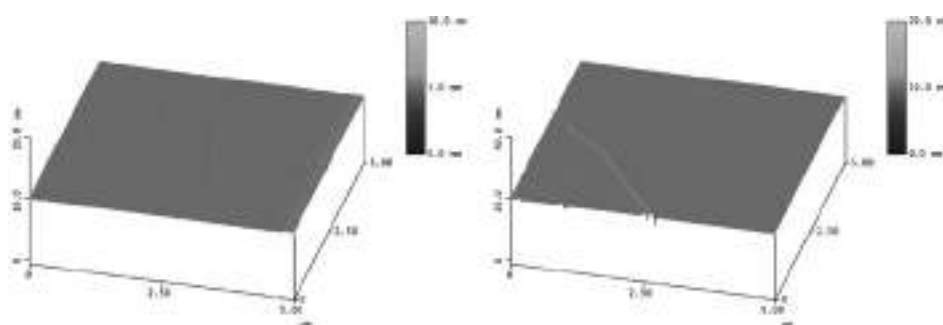


Figure 5.1 Atomic force micrographs of the basal plane of HOPG after (left) careful layer plane cleavage and (right) damaging cleavage leaving a fracture plane. (for colour version: see colour section at the end of the book).

applied in conjunction with layer plane cleavage. In fact, all the pretreatments for HOPG discussed here are often performed with layer plane cleavage as the first step. This pre-treatment method works by dissolving and/or desorbing adsorbed contaminants from the surface (21). An exposure time of 20–30 min is usually sufficient. Solvent cleaning can be performed on the entire electrode or on the electrode surface when mounted in the electrochemical cell. Several different solvents can and should be used including acetonitrile, isopropanol, dichloromethane, and toluene. The type of solvent required for activation ultimately depends on the molecular structure of the admolecule or contaminant on the surface. In other words, the solvent should be selected for its solubilizing power of the admolecule(s). The solvent should also be purified by distillation and stored over activated carbon (AC) prior to use because reagent-grade solvents often contain impurities that may adsorb on and contaminate the electrode surface (21). The large surface area of suspended AC particles provides numerous sites for the preferential adsorption of solvent and/or impurities, thereby removing the latter from the solvent. Effective solvent clean-up can usually be achieved after exposing the distilled solvent to AC for 2 days. The use of “clean” organic solvents is critical for the success of this activation method. Care should be taken to avoid transferring the AC in the solvent to the electrochemical cell containing the HOPG, or any other electrode for that matter. This is usually accomplished by filtering. If the particle transfer occurs, the carbon will contact the surface and change the electrode’s behavior. No new active sites are created by this pretreatment. Existing ones are simply cleaned and made ready for electron transfer. This is a general pretreatment applicable for all electrodes and for all redox systems.

5.2.1.3 Laser activation

This pretreatment can be used to activate HOPG for electron transfer and it can be damaging or non-damaging to the surface microstructure, depending on the conditions (10, 11, 22). Through a combination of active site generation and surface cleaning, short intense laser pulses *in situ* can increase k_{app}^o for several redox systems (e.g., $\text{Fe}(\text{CN})_6^{3-/-4-}$, dopamine, and ascorbic acid) by several orders of magnitude. In this treatment, short (ca. 10 nsec) and intense (ca. 10–100 MW cm⁻²) pulses of light from a Nd:YAG or N₂ laser are applied to

the HOPG surface immersed in a supporting electrolyte solution. If the incident power density is low ($<50 \text{ MW cm}^{-2}$), then microstructural alterations of the basal plane do not occur and the pretreatment simply heats the electrode surface. This “heat treatment” activates the electrode by desorbing contaminants and exposing “clean” existing edge plane. However, at power densities $>50 \text{ MW cm}^{-2}$, the basal plane microstructure is altered, leading to the formation of new edge plane sites. These microstructural changes are manifested in an increase in the $1360/1580 \text{ cm}^{-1}$ Raman peak intensity ratio. Increased surface roughening, background current, and molecular adsorption also occur as a consequence of increased microstructural disorder. If this pretreatment is performed *in situ*, then a clean edge plane is exposed and k_{app}° for $\text{Fe}(\text{CN})_6^{3-4-}$ can increase from $<10^{-5}$ to ca. $10^{-1} \text{ cm sec}^{-1}$ (10, 11, 22). In solution, limited surface oxide formation occurs at these newly exposed edge plane sites if the applied potential is maintained below about +1.0 V vs. SCE. However, once exposed to the laboratory atmosphere, the laser-activated surface tends to be quite reactive and surface oxygen is incorporated at the newly formed edge plane. This pretreatment can both clean existing active sites and create new ones, depending on the conditions. As stated, the most active regions on HOPG for electron transfer, and other sp^2 carbons, are generally associated with the graphitic edge plane.

5.2.1.4 Heat treatment

Heat treatment activates HOPG by desorbing contaminants and/or removing chemisorbed oxygen from the exposed edge plane sites, depending on the temperature. This pretreatment is effective at cleaning and producing low-oxide carbon surfaces. For best results, the pretreatment should be performed under the clean conditions of high vacuum ($<10^{-6}$ Torr); however, activation can also be achieved if the treatment is conducted under a thorough inert gas purge. Surface carbon–oxygen functional groups will populate any exposed edge plane and defect sites. Contaminant adsorption, particularly polar molecules, will be strongest near these sites. Heating the electrode to about 500 °C in the absence of oxygen is effective at desorbing contaminants and exposing a clean surface. The electrode will still retain much of the surface oxygen as these functional groups do not decompose at a significant rate until temperatures $>500 \text{ }^{\circ}\text{C}$ (23). A treatment time of 10–30 min is usually sufficient for cleaning. If higher temperatures are employed, the carbon–oxygen functional groups will decompose (CO and CO_2 evolution) and this can lead to pitting and exposure of new edge planes. The pretreatment needs to be performed under vacuum or an inert gas atmosphere if a clean, low-oxygen surface is desired. If significant levels of oxygen are present in the gas phase during heat treatment, then surface oxidation and corrosion (gasification) will occur. The morphological and microstructural changes associated with gas-phase oxidation of HOPG have been reported by Beebe and coworkers (24). The heat-treated HOPG surface will be deactivated by contaminant adsorption and reaction with the atmosphere after short-term exposure to the air, so electrochemical measurements should be made immediately after treatment for best results.

5.2.1.5 Electrochemical polarization

Although altering both the surface microstructure and the chemistry, electrochemical polarization can be used to activate HOPG. Anodic polarization, depending on the severity,

can clean the surface, create new edge plane, and introduce surface oxygen. The 1360/1580 cm⁻¹ Raman peak intensity ratio is a useful indicator of the microstructural disorder and XPS can be used to quantify the level of surface oxygen. Of all the pretreatments used to activate HOPG, electrochemical polarization has the most dramatic effect on surface microstructure and chemistry (10–12). Generally, the background current and the extent of molecular adsorption track the fraction of edge plane exposed. k_{app}° for some redox systems (e.g., ascorbic acid and Fe(CN)₆^{3-/4-}) increases by several orders of magnitude after electrochemical polarization. For example, the surface-sensitive Fe(CN)₆^{3-/4-} has a k_{app}° value of ca. 10⁻⁵ cm sec⁻¹ on a low-defect basal plane surface and a value of ca. 10⁻² cm sec⁻¹ on the same surface after anodic polarization (8, 10–12, 25). The extent of microstructural damage depends on the charge passed at the particular applied potential. Exposure of edge plane increases both the density of electronic states in the vicinity of the site and the surface oxygen content (8, 10–12, 25). The increased density of electronic states necessarily means that a different double-layer structure exists at these sites. This may lead to a greater potential drop locally, hence faster electron-transfer kinetics. Increasing the surface oxygen content can result in the acceleration of electron-transfer rates if specific functional groups are involved in the redox reaction mechanism (26). An important point to remember about pretreatment methods such as electrochemical polarization is that they can affect more than one electrode property (e.g., electronic structure, surface oxides, wettability, etc.) and this makes it difficult to elucidate structure–function relationships.

The mechanism of edge plane formation during anodic polarization in mild acid has been studied by McCreery and coworkers (25, 27) using *in situ* Raman spectroscopy. They found that the first step is separation of the graphene sheets due to the interlayer incursion of solvent molecules and/or intercalated anions. The extent of anion intercalation depends on the electrolyte composition, specifically the anion type, ionic strength, existing defect density on the basal plane surface, and the applied potential. The important potential is actually the applied potential relative to the point of zero charge. The second step involves fracturing of the graphene sheets, a process by which the new edge plane is exposed. Solvent and/or anion intercalation, driven by the positive potentials used for polarization, produces microstructural strain. Eventually, the strain gets large enough to fracture the layer planes because they can no longer bend and flex. This fracturing exposes the new edge plane and increases the local density of electronic states and the surface oxygen content.

There are many electrochemical pretreatment protocols reported in the literature. Potentiostatic, potentiodynamic, and galvanostatic methods have been used. An excellent method for electrochemically pretreating HOPG is potential cycling between -0.5 and 1.5 V vs. SCE in 0.1–1 M KNO₃ at 50 mV sec⁻¹. Anodic potential limits below ~1.0 V produce “minor” microstructural alterations and minimal surface oxidation, whereas potential limits >1.5 V lead to “severe” damage and extensive oxygen incorporation (25–28). In general, one needs to balance the need for active site generation (e.g., edge plane formation) with the consequential effects listed above that can have a limiting effect on the electroanalytical utility of the electrode.

The severity of the polarization depends on the anodic potential limit. The electrochemical oxidation of HOPG at positive potentials (>1.5 V) has been studied by numerous groups. For example, Gewirth and Bard used *in situ* scanning tunneling microscopy to

study the basal plane of HOPG during potentiodynamic polarization in 0.1 M H₂SO₄ (17). They proposed that a graphite oxide layer forms following a nucleation and growth process. The early stages of potential cycling between 0 and 1.8 V vs. AgQRE produced roughened and apparently oxidized regions of the surface with lower barrier height than the untreated surface. Continued potential cycling caused further roughening and expansion of the oxidized regions to completely cover the surface. Similar observations were made by Zhang and Wang (29). Goss *et al.* studied the oxidation of HOPG in 1.0 M KNO₃ using *in situ* atomic force microscopy, and found that potential cycling to potentials between 1.5 and 2.0 V SSCE produced isolated surface blisters (30). The outermost layer of the blister was found to be the top-most graphene sheet, whereas the interior of the blister contained graphite oxide. The authors proposed that following potential-dependent intercalation of electrolyte anions and solvent, blisters form as a result of electrolytic gas evolution at subsurface active sites with accompanying graphite oxide formation. The initially formed graphite intercalation compound subsequently oxidizes water or carbon to form graphite oxides. The surface oxides can be problematic in some electrochemical measurements. For example, the voltammetric background current increases and peaks develop in the 0–0.5 V vs. SCE range at acidic pH when redox-active surface carbon–oxygen functional groups are present. The redox-active functional groups are of the quinone/hydroquinone type (20, 31, 32). Their presence can interfere with the electrochemical measurement of the redox analytes at low concentration by causing a reduction in the signal-to-background (S/B) ratio for the measurement. The background voltammetric peaks associated with the redox-active oxygen functional groups shift with pH (-59 mV dec^{-1}) (20, 31, 32).

The increased carbon–oxygen functional group content produced by electrochemical polarization has been correlated with increased rates of electron transfer for some redox systems. For example, Kepley and Bard showed that the k_{app}° value for the quinone/hydroquinone redox couple tracked the thickness of the oxide layer formed by severe anodic polarization (33). McCreery and coworkers reported that k_{app}° for the Fe^{3+/2+} redox system can be increased by orders of magnitude when surface oxygen is incorporated at the edge plane sites on the HOPG surface, particularly carbonyl functional groups (26). These authors, as well as others, have proposed that the electrochemical polarization mechanism involves the creation of oxygen functional groups that act as electron- and/or proton-transfer mediators. Oxygen functional groups can impact upon electrochemical reactions directly or indirectly. They can directly affect the reaction kinetics and mechanism by providing (i) specific reaction or adsorption sites for a particular redox system and (ii) sites that facilitate proton exchange with those redox systems that undergo proton transfer. The functional groups can indirectly affect the reaction kinetics by providing sites for contaminant adsorption from the solution. Furthermore, the increased electrode reaction kinetics might not be due to the oxygen functional groups at all, but rather due to the increased density of electronic states that accompanies the edge plane formation, sites at which the oxides form (2–5, 22). The carbon–oxygen functional groups can impact the structure of the electric double layer. The nature of water interaction with a hydrophobic basal plane and a hydrophilic, oxygen-containing edge plane site will be different. Some of the functional groups that can form are not electroactive but are acidic in nature and undergo deprotonation. This ionization alters the charge on the surface of the electrode and leads to pH-dependent k_{app}° for some redox

systems. For example, carboxylic acid functional groups can form during polarization with a pK_a of ca. 4.5. Deprotonation of these groups occurs at pH values above the pK_a , creating increased negative surface charge. For electrochemically treated glassy carbon, and the same should hold true for HOPG, Deakin *et al.* observed that the k^o for anionic redox systems ($\text{Fe}(\text{CN})_6^{3-/4-}$ and $\text{IrCl}_6^{2-/3-}$) decreased with increasing solution pH (i.e., increasing negative surface charge) (31). The opposite behavior was seen for the cationic redox systems ($\text{Ru}(\text{NH}_3)_6^{3+/2+}$). Blurton looked at the surface chemistry changes of low-porosity graphite during potentiodynamic polarization in H_2SO_4 (34). It was observed that multiple anodic and associated cathodic peaks develop in the 0–1.5 V vs. SHE window, which were attributed to redox-active quinone/hydroquinone functional groups. Panzer and Elving also studied the surface chemistry of pyrolytic graphite during potentiodynamic polarization in aqueous and non-aqueous media (35). Generally speaking, from all the published work with HOPG, applied potentials of 1.5 V or greater are needed to expose new edge plane sites. The formation of these sites leads to an increase in k_{app}^o for some surface-sensitive probes such as $\text{Fe}(\text{CN})_6^{3-/4-}$. Rate constant increases from 10^{-5} to 10^{-2} cm sec $^{-1}$ should accompany new edge plane formation.

5.2.2 Glassy carbon

Glassy carbon (GC), also referred to as vitreous carbon, is the most commonly used carbon electrode for electroanalysis (10–12). It is available in variety of architectures including rods, disks and plates. Unlike HOPG and other graphites, GC is hard and microstructurally isotropic (the same in all directions). It is impermeable to gases and liquids and has slightly lower electrical and thermal conductivity (9–12, 36, 37). The material is prepared by heat treating polyacrylonitrile (PAN) or phenolic resin under pressure at temperatures between 1000 and 3000 °C. The heat treatment is often applied slowly over days and causes expulsion of non-carbon atoms. This produces a conjugated carbon microstructure. The original polymer backbone stays largely intact, preventing the formation of extended graphitic domains (9–12, 36, 37). The resulting microstructure is a complex one of interwoven graphitic ribbons with L_a and L_c values of ca. 50 and 15 Å, respectively (9–12, 36, 37). The accepted model for the GC microstructure is the one proposed by Jenkins and Kawamura (37). The interwoven sp^2 carbon ribbon gives rise to mechanical hardness, so the material is polishable and impermeable to gases and liquids. The density of GC (ca. 1.5) is less than HOPG, indicating that the material contains some void space (nanoporosity). Since the material is impermeable to gases and liquids, the voids are small and unconnected. Two peaks are present in the Raman spectrum for GC at 1350 and 1580 cm $^{-1}$ with the ratio of the two reflecting the extent of microstructural disorder. Typical 1350/1580 cm $^{-1}$ peak intensity ratios are in the 1.3–1.5 range. The material possesses a complex surface chemistry consisting of various types of carbon–oxygen functional groups at the graphitic edge plane sites (9–12).

5.2.2.1 Mechanical polishing

The surface of GC, like other solid electrodes, is gradually deactivated during exposure to the atmosphere or during electrochemical use (38, 39). Therefore, periodic pretreatment is

necessary. The most common method for activating GC is mechanical polishing. As indicated above, polishing is often a first step in any activation protocol. Polishing serves to renew the surface by cleaning, removing the effect of past history, and exposing a fresh microstructure. Since GC possesses an isotropic microstructure, a similar edge-to-basal plane ratio is always exposed after conventional polishing. Polishing should be performed under ultraclean conditions if the highest “activity” is to be achieved. Numerous polishing procedures have been reported in the literature. A good protocol to follow is the one described by Kuwana and coworkers (39, 40). In their method, the electrode is polished using successively smaller sizes of alumina on a smooth glass plate. Deagglomerated alumina powders work best in sizes from 1.0 down to 0.05 μm . The alumina is slurried in ultrapure water to make a paste. The electrode should be polished using circular motions with an even force applied. Starting from the largest grit size, the electrode should be polished and then carefully cleaned by (i) rinsing with ultrapure water and (ii) ultrasonication in the same medium for about 15 min. The GC should be placed in a clean beaker, submerged in ultrapure water and covered during the ultrasonic cleaning. Eventually, a mirror-like finish should be obtained, hence the name glassy carbon. The electrode should be used immediately after the polishing, or any pretreatment for that matter, for best results. k_{app}° for a surface-sensitive redox system like $\text{Fe}(\text{CN})_6^{3-/\text{4}-}$ should be at least in the high $10^{-2} \text{ cm sec}^{-1}$ range if the electrode surface is adequately cleaned and renewed.

Polishing is damaging to the material because the mechanical abrasion breaks carbon–carbon bonds. Polishing debris (e.g., a carbon and alumina microparticle layer), if not removed by thorough cleaning, will remain on the surface and affect the electrochemical properties (41). Oxygen is generally incorporated during the pretreatment as the dangling carbon bonds created on the surface readily react with oxygen in the air or from the water. Low-oxygen surfaces can be created if the polishing is done in an anaerobic environment. For example, McCreery and coworkers have produced low-oxygen GC by polishing in deoxygenated hexane (42). Unlike HOPG, the GC microstructure is isotropic and homogeneous throughout the bulk so that the same disordered microstructure is present regardless of how many layers are removed by polishing.

5.2.2.2 Solvent cleaning

Exposure to clean organic solvents is a useful method for activating GC without introducing new microstructure and surface chemistry. Usually, this pretreatment is applied in conjunction with mechanical polishing. Such is the case for the other pretreatment methods described herein for GC. As discussed above, this pretreatment method works by dissolving and/or desorbing adsorbed contaminants from the surface, generating clean edge plane (i.e., active sites) (21). Exposure times of 20–30 min are usually sufficient. Several different solvents can be used including acetonitrile, isopropanol, dichloromethane, or toluene. The solvents should be purified by distillation prior to use. AC should also be added to the distilled solvent for additional purification (21). k_{app}° for a surface-sensitive redox system like $\text{Fe}(\text{CN})_6^{3-/\text{4}-}$ should be at least in the high $10^{-2} \text{ cm sec}^{-1}$ range if the electrode surface is adequately cleaned and renewed.

5.2.2.3 Vacuum heat treatment

Vacuum heat treatment can be used to renew and activate GC (43, 44). As discussed above, this pretreatment method cleans the surface by desorbing contaminants from “active” sites and creates a low-oxygen surface by decomposing carbon–oxygen functionalities as CO and CO₂. Vacuum heat treatment generally does not alter the surface morphology or microstructure. The heat treatment is best performed under high-vacuum conditions (<10⁻⁶ Torr). Heating the electrode to about 500 °C in the absence of oxygen is effective at desorbing contaminants. The electrode will still retain much of the surface oxygen as these functional groups do not decompose at a significant rate until temperatures >500 °C are reached. Treatment times from 10 to 30 min are usually sufficient. If higher temperatures are employed, ca. 1000 °C, then the carbon–oxygen functional groups will decompose (CO and CO₂ evolution) causing some minor pitting and new edge plane exposure. In general, this pretreatment activates the surface for electron transfer, lowers the background current, and reduces the surface functionality. k_{app}° for a surface-sensitive redox system like Fe(CN)₆^{3-/4-} should be at least in the high 10⁻² cm sec⁻¹ range if the electrode surface is adequately cleaned.

5.2.2.4 Laser activation

Through a mechanism of contaminant desorption, this pretreatment activates GC for electron transfer (45). Short (ca. 10 nsec) and intense (ca. 10–100 MW cm⁻²) pulses of light from a Nd:YAG or N₂ laser are applied while the electrode is immersed in a supporting electrolyte solution. Surface heating occurs as a result of the laser light being absorbed by the carbon. The heating causes the desorption of contaminants from the surface, particularly from the active edge plane, and this leads to improved rates of electron transfer for most redox systems. Since GC is a microstructurally isotropic electrode material, laser activation generally does not alter the microstructure by creating new edge plane, as is the case for HOPG. k_{app}° for a surface-sensitive redox system like Fe(CN)₆^{3-/4-} should be at least in the high 10⁻² cm sec⁻¹ range if the electrode surface is adequately cleaned.

5.2.2.5 RF plasma treatment

Treatment in an RF plasma can be used to activate GC (46). Small RF plasma cleaners are available (e.g., Harrick Scientific) for treating electrodes at powers up to about 100 mW and pressures in the 100 mTorr range. The plasma chamber is attached to a mechanical rough pump, and sometimes also to an oil diffusion pump, in order to maintain a reduced pressure. A short 10–15 min treatment in an Ar plasma (10–100 mTorr) is useful for cleaning GC and this involves a sputtering type of mechanism in which energetic argon ions (Ar⁺) collide with the surface. The electrode surface tends to be roughened after the plasma treatment. If the treatment is performed in a relatively oxygen-free gas environment, then the surface oxygen content is usually decreased as compared to the typical oxygen content for a freshly polished electrode. RF plasma treatment can also be used to chemically modify the GC surface (46). For example, researchers have incorporated surface oxygen by exposing GC to an oxygen or water/oxygen plasma (46). The alterations in the electrode surface chemistry and microstructure can range from mild to severe depending on the plasma conditions (e.g., gas phase, power, pressure, and duration).

5.2.2.6 Hydrogen plasma treatment

GC surfaces prepared in air and/or used in aqueous environments have edge plane and defect sites that are terminated with surface oxides of varying type and coverage (8, 10–12). The heterogeneous distribution of these functional groups can be a cause for significant variability in the electrochemical response for some redox systems and can generally lead to poor response stability. Some of these oxides are redox-active (e.g., quinone/hydroquinone couple) and others are electroinactive but ionizable (e.g., carboxylic acid). Both types of functional groups give rise to pH-dependent voltammetric and amperometric background current over a wide potential range. Several approaches have been employed for removing surface oxides from sp^2 carbon electrodes including high-vacuum heat treatment (43, 44) and mechanical polishing in an anaerobic environment (42). A relatively new pretreatment, and one analogous to vacuum heating, is hydrogen plasma treatment (47–49). Hydrogenated glassy carbon (HGC) is prepared by exposing GC to a hydrogen microwave plasma or to hydrogen gas activated by passage over a heated metal (e.g., tungsten) filament. Atomic hydrogen, not molecular hydrogen, is the principal reactant that chemisorbs at the exposed edge plane and leads to the replacement of terminal oxygen functional groups (47–49). This treatment is fundamentally different from vacuum heat treatment or mechanical polishing in an anaerobic environment because it not only removes the surface oxides but also stabilizes the surface carbon atoms by forming strong covalent C–H bonds. The hydrogenated surfaces are low in oxygen content (atomic oxygen-to-carbon ratio (O/C) < 0.02), as determined by X-ray photoelectron spectroscopy (XPS), and hydrophobic with a water contact angle $> 65^\circ$. In fact, the oxygen content remains low even during air exposure for weeks due to the stability of the C–H bonds (49). Based on static secondary ion mass spectrometry (SIMS) results, it was proposed that the hydrogenated surface is composed of aliphatic hydrocarbon moieties (e.g., CH_3 , C_3H_3 , C_2H_5 , C_3H_5 , etc.) rather than simply hydrogen, as the chemisorption of atomic hydrogen not only replaces terminal oxygen groups but also causes ring opening reactions that lead to the formation of surface hydrocarbon moieties (48). Figure 5.2 shows a proposed surface structure for HGC.

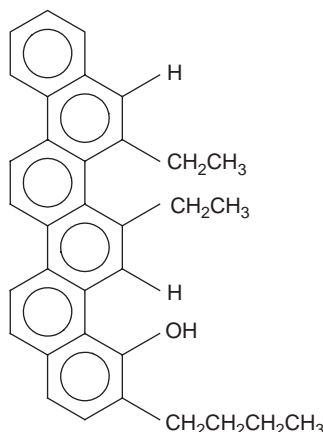


Figure 5.2 Proposed surface chemistry of hydrogenated glassy carbon (48).

HGC exhibits lower voltammetric background current, comparable electrochemical activity for several redox systems, enhanced S/B ratios, and improved response stability compared with freshly polished (i.e., oxygenated) GC. Cyclic voltammetric investigations revealed relatively rapid electrochemical reaction kinetics for $\text{Fe}(\text{CN})_6^{3-/\text{4}-}$ and $\text{Ru}(\text{NH}_3)_6^{3+/\text{2}+}$, and slightly slower kinetics for dopamine and 4-methylcatechol. Very sluggish kinetics were found for $\text{Fe}^{3+/\text{2}+}$. For example, k_{app}° of $0.01\text{--}0.03 \text{ cm sec}^{-1}$ were determined for $\text{Fe}(\text{CN})_6^{3-/\text{4}-}$ and $\text{Ru}(\text{NH}_3)_6^{3+/\text{2}+}$, whereas slightly lower values of $\sim 5 \times 10^{-3} \text{ cm sec}^{-1}$ were found for dopamine and 4-methylcatechol (48). Significantly lower rate constants of $\sim 3 \times 10^{-5} \text{ cm sec}^{-1}$ were seen for $\text{Fe}^{3+/\text{2}+}$ (48). The low k_{app}° for $\text{Fe}^{3+/\text{2}+}$ was attributed to the absence of mediating carbonyl functional groups on the HGC surface (26, 50). The electrode response for all five redox analytes was extremely stable even after a 3-month period of air exposure. This reflects how resistive this hydrophobic surface is to deactivation (fouling) via contaminant adsorption. Further evidence for the lack of molecular adsorption (polar molecules) was revealed from chronocoulometric measurements performed with anthraquinone-2,6-disulfonate (2,6-AQDS) (51). AQDS strongly physisorbs at high coverages on the polar, oxygenated GC (51, 52). However, negligible adsorption was detected on HGC. These results demonstrate that hydrogenation is a suitable modification method for producing an active, stable, and low-oxide GC surface.

5.2.2.7 *Electrochemical polarization*

Electrochemical polarization, depending on the conditions, can improve the surface cleanliness, alter the surface microstructure, and/or change the surface chemistry. Numerous methods have been reported in the literature. Electrochemical pretreatment is best performed in conjunction with mechanical polishing and/or solvent cleaning. For many electroactive species, polarizing GC anodically at potentials from 1.5 to 2.0 V vs. Ag/AgCl is required for activation. Generally, anodic and cathodic polarization applied in unison provide the highest degree of activation. For example, a protocol used by our group to reproducibly activate GC is 5 min of potential cycling between -1.0 and 1.5 V vs. SCE (50 mV sec^{-1}) in 0.1 M phosphate buffer, pH 2, or 0.1 M HClO_4 . This would be categorized as a “mild” pretreatment as only minor changes in background current are observed. There are also other protocols that work well for activation. The effectiveness of a particular pretreatment method for activating an electrode very much depends on the redox system under study. Engstrom described the activation of GC for several different redox systems using potential step anodization ($0.5\text{--}2.0$ V vs. SCE) followed by cathodization (0 to -0.5 V) in 0.1 M $\text{KNO}_3 + 0.01 \text{ M}$ phosphate buffer, pH 7 (53). It was proposed that three different surface conditions exist on the electrode during the course pretreatment: (i) the inactive state that results from some combination of inadequate surface cleanliness and/or minimal functional group coverage, (ii) the active surface after anodization with the oxidized form of the oxide layer and (iii) the active surface after cathodization with the reduced form of the oxide layer. Wang and Lin applied short-duration (5–60 sec) potential steps to anodic potentials between 1.0 and 2.5 V followed by steps to cathodic potentials between -1.0 and -2.0 V vs. SCE (54). The potential excursions required for activation depended on the particular redox system (e.g., phenol and uric acid). The activation was performed in neutral phosphate buffer or 1 M NaCl. Wightman and coworkers described

the activation of GC by an anodic potential step to +1.4 V vs. SCE in citrate buffer, pH 5.2, for 20 min (55). The electrode activity was assessed using $\text{Fe}(\text{CN})_6^{3-/4-}$ and ascorbic acid. There are other potentiostatic, potentiodynamic, and galvanostatic pretreatments reported (56–59). The paper by Beilby *et al.* discusses the influence of the anodic and cathodic potentials, the ionic strength and pH of the supporting electrolyte, and the length of time of the oxidation or reduction on the degree of activation (59).

5.2.3 Pyrolyzed photoresist films (PPF)

Thin films of sp^2 -bonded carbon can be produced by pyrolyzing photoresist layers. These films (PPF) are an attractive alternative to thick-film electrodes because of their smoothness and amenability to patterns. Kinoshita and coworkers were the first to report on the electrochemistry of PPF (60). McCreery and coworkers examined the formation, microstructure, chemical properties, and electrochemical behavior of these thin films in detail, and are using the material as an electrode for molecular electronic assemblies (61–64). This is a new form of conductive carbon, so a complete understanding of the interrelationship between the microstructure, surface chemistry and electrochemical properties has yet to be fully developed. In general, PPF is an electrically conducting material ($\sim 5 \times 10^{-3} \Omega \text{ cm}$) that possesses a microstructure much like that of GC, but is low in surface oxygen. Presumably, some of the carbon atoms at the exposed edge plane are terminated by hydrogen during the pyrolysis. One of the most practical properties of PPF is its near-atomic smoothness as the surface roughness is on the order of 0.5 nm over square micrometer dimensions (61–64).

PPF is produced by spin coating a thin layer of photoresist onto a clean and smooth substrate, such as Si or quartz. Multiple coatings can be applied to control the final film thickness, which is usually a few micrometers. The coated substrate is then baked in an oven under atmospheric conditions at approximately 90 °C for 30 min. This step cures the photoresist layer. The substrate can then be cut into smaller pieces, if required, for placement in a tube furnace for pyrolysis. A quartz tube furnace is used for this purpose with a forming gas of 95% N₂ + 5% H₂ continuously flowing at approximately 100 sccm (61–64). The main purpose of the forming gas is to keep oxygen from reacting with the hot carbon surface. If oxygen is present then significant carbon gasification will occur. The pyrolysis is conducted by slowly raising the temperature (10 °C min⁻¹) from ambient to 1000 °C and then holding it there for 60 min. The samples are then cooled to room temperature under the constant flow of the forming gas. Film shrinkage occurs due to decomposition of the photoresist and gas evolution. The shrinkage occurs primarily in the film thickness and not so much in the lateral film dimensions. Weight loss and densification also occur during the pyrolysis. About 70% loss of the initial dry weight is typical. The weight loss, though, depends on the heat treatment temperature and, at least at low temperatures, results from the evolution of H₂O, CO, CO₂ and other gaseous decomposition products. Film densification and aromatization occur at the higher heat treatment temperatures.

The microstructure and surface chemistry of PPF have been studied as a function of the pyrolysis temperature (62–64). Raman spectra for PPF reveal the characteristic bands of sp^2 carbon at ~ 1358 and $\sim 1580 \text{ cm}^{-1}$. The “D” (1358 cm^{-1}) and “G” (1580 cm^{-1}) bands

have been studied extensively and the peak area or intensity ratio (1358/1580) has been correlated with the extent of microstructural disorder (i.e., fraction of exposed edge plane) (62–64). The spectrum for PPF resembles that for glassy carbon. Typical 1358/1580 peak intensity ratios are 1.2–1.5, reflective of a relatively disordered microstructure. The bands narrow with increasing heat treatment temperature suggestive of more microstructural ordering. In terms of the surface chemistry, PPF is generally low in surface oxygen ($O/C = ca. 2\%$) after pyrolysis and somewhat resistant to oxidation in air. McCreery and coworkers have shown, for example, that PPF slowly incorporates oxygen during exposure to the atmosphere over a 2-h period at room temperature, as indicated by an XPS-determined O/C that increases to only about 6% (62–64). The low-oxygen content of PPF is much like that of HGC (47–49). More remains to be learned about how the surface microstructure and chemistry change as a function of the electrode potential.

Clean PPF films possess a low C_{dl} , 5–10 $\mu F\text{ cm}^{-2}$, and exhibit relatively rapid electron-transfer kinetics for several outer-sphere redox systems. For instance, k_{app}^o in the low to mid $10^{-2}\text{ cm sec}^{-1}$ range is observed for $\text{Ru}(\text{NH}_3)_6^{3+/2+}$, chlorpromazine and $\text{Fe}(\text{CN})_6^{3-/4-}$ (62–64).

5.2.3.1 Mechanical polishing

Even though the adhesion of the PPF to the substrate is generally strong, pretreatment by mechanical polishing is not practical. The films are relatively thin and soft, so polishing with even a 0.05 μm diameter alumina grit would cause significant roughening and destruction of the PPF layer.

5.2.3.2 Solvent cleaning

PPF is probably best and most easily activated by solvent cleaning. As described above, soaking the electrode for 20–30 min in isopropanol (cleaned by distillation and exposure to AC) is effective at cleaning the surface without causing any roughening or microstructural damage (21). This pretreatment effectively dissolves site-blocking contaminants from the surface, particularly from the regions around the edge plane. The pretreatment only affects the surface cleanliness and does not alter the electronic properties, surface microstructure, or surface chemistry. Solvent cleaning is a good starting point for the activation of PPF.

5.2.3.3 Heat treatment

Heat treatment can be used to remove surface oxygen and clean the PPF surface. The electrodes are heat treated during the pyrolysis but the effects of past use can only be removed by a postgrowth heat treatment. For optimum results, the treatment is best performed under high-vacuum ($<10^{-6}$ Torr) conditions. Heating the electrode to about 500 °C in the absence of oxygen should be effective at desorbing contaminants. The surface oxygen content, which is low to begin with, will be retained as these functional groups do not decompose at significant rates until temperatures >500 °C are reached. Treatment times from 15 to 30 min are usually sufficient. If higher temperatures are employed, the carbon–oxygen functional groups will decompose (CO and CO₂ evolution) possibly leading to pitting and new edge plane site exposure. Due to differences in thermal expansion coefficient, heat

treatment at high temperature might result in film delamination from the substrate. Therefore, care should be taken to perform the heat treatment at a temperature where the PPF film is physically and chemically stable on the substrate surface. As is the case for all other heat-treated carbon electrodes, electrochemical measurements with treated PPF should be made immediately after treatment.

5.2.3.4 *Electrochemical polarization*

Depending on the severity of the conditions, electrochemical polarization can cause surface roughening and microstructural damage, as well as oxygen incorporation. An advantage of the PPF is its atomic smoothness. In most instances, one would not want to pretreat the electrode by severe electrochemical anodization (>1.5 V) or cathodization because of the microstructural damage that would be caused. McCreery and coworkers have studied the stability and surface chemistry of PPF during electrochemical polarization. The material was found to behave in much the same manner as GC during mild potentiodynamic cycling in 0.2 M HClO_4 between -0.5 and 1.5 V vs. Ag/AgCl (61–64). As the number of cycles was increased, the O/C increased, resulting in faster $\text{Fe}^{3+/2+}$ electron-transfer kinetics. They also examined the electrode after constant potential polarization in 0.1 M H_2SO_4 at $+1.8$ V for 1 min. Significant oxygen incorporation and microstructural damage occurred as reflected by an increase in C_{dl} to $>50 \mu\text{F cm}^{-2}$. If polarization is to be employed as a pretreatment, then mild conditions (<1.5 V) should be used.

5.2.4 Carbon fibers

Carbon fibers are classified as microelectrodes (Chapter 6) because of their small size. Typical diameters range from 1 to 40 μm . Microelectrodes offer advantages over conventional macroelectrodes in electroanalytical measurements in terms of (i) a lower background current (i.e., double-layer charging) due to a smaller exposed area, (ii) a smaller size that enables measurements to be made with high spatial resolution, (iii) a faster response time because of a shorter RC time constant, which enables measurements to be made with high temporal resolution and (iv) the ability to make measurements in resistive media due to low ohmic (iR) potential losses (65, 66). The fast response time of microelectrodes allows measurement of redox systems with large k° . For example, k_{app}° for redox systems has been found to be in excess of 1 cm sec^{-1} (67).

Carbon fibers are manufactured from several starting materials including rayon, PAN, pitch, and lignin, with all materials possessing different chemical compositions. Fibers can also be produced by gas-phase deposition from a carbon precursor. A wide variety of synthesis and heat treatment procedures exist for the preparation and post-treatment of the fibers. For this reason, fibers are available with different exposed microstructures and surface chemistries. One has to be cognizant of this when selecting a fiber for a particular electroanalytical application. One way to classify carbon fibers is in terms of the temperature employed for their production. Generally, as the pyrolysis temperature increases, the fiber becomes more enriched with carbon and the microstructure becomes more “graphitized” or ordered. The three general classifications are (i) partially carbonized fibers at temperatures near 500 °C with up to 90 wt % carbon, (ii) carbonized fibers at temperatures between 500

and 1500 °C with 91–99 wt % carbon, and (iii) graphitized fibers at temperatures between 2000 and 3000 °C with >99 wt % carbon (68). The microstructure and surface chemistry can vary considerably from fiber type to type, depending on the source material and the fabrication procedures, and this will have a significant impact on the electrochemical properties. Furthermore, many commercial fibers receive a final surface treatment to improve their adhesion with binders in carbon–carbon composite materials. Removal of such coatings is necessary prior to electrochemical use. The most commonly used fibers in electroanalytical chemistry are the microstructurally disordered types (PAN and pitch). These fiber types have an inherently high fraction of exposed edge plane, and therefore a high active site density.

Carbon fiber microelectrodes can be used in either a disk or a microcylinder geometry. The fiber is usually sealed or insulated with pulled glass or polymeric coatings (65, 66, 69). A disk geometry is one in which the fiber is cut flush with the insulation material. A microcylinder geometry is one in which the fiber protrudes some distance (hundreds of micrometers or more) beyond the end of the insulation. Like every other type of carbon electrode, the basic electrochemical properties of carbon fibers depend on their exposed microstructure and chemical composition. Untreated fibers usually exhibit sluggish electron-transfer kinetics for most redox systems, as evidenced by poorly shaped voltammetric i – E curves. As with other carbon electrodes, pretreatment is usually a prerequisite for carbon fiber microelectrode use. The background current, C_{dl} , and the extent of molecular adsorption are strongly influenced by the exposed microstructure and surface chemistry, which are affected by the pretreatment method. These factors track the fraction of edge plane exposed, as determined from the Raman 1360/1580 peak intensity ratio, as well as the surface oxygen content. The more graphitic the exposed microstructure is, the lower C_{dl} (2–10 $\mu\text{F cm}^{-2}$) is and the lower the background voltammetric current and surface oxygen content are. Recall that C_{dl} for the basal plane of HOPG is low (i.e., in the 1–5 $\mu\text{F cm}^{-2}$ range). Increased C_{dl} results, at least in part, from a higher density of electronic states at the exposed edge plane sites. This translates into a greater potential-dependent excess surface charge that is counterbalanced by greater ion accumulation and solvent dipole orientation on the solution side of the interface. The background voltammetric current increases because of the larger C_{dl} , but there can also be a contribution from pseudocapacitance associated with electroactive surface carbon–oxygen functionalities. As discussed above, the redox-active functional groups undergo electron transfer in the 0–0.5 V range (acidic solution) and their presence is manifested in a larger background current. The study of carbon fibers is challenging because they often consist of multi-phase microstructures; this means that one orientation is present on the surface, whereas another is present in the core. In addition, the fragility of the fiber, at least in the microcylinder geometry, precludes any polishing to clean and renew the surface. The anisotropic microstructure and inability to polish the surface can make response reproducibility with carbon fibers a challenge.

Figures 5.3a–e show representations of different carbon fiber microstructures (68). The fiber microstructure can be determined by Raman spectroscopy and X-ray diffraction, as discussed above for HOPG and glassy carbon. Carbon fibers come in several different microstructures, as indicated above. A concentric arrangement of the graphene sheets exists in Figure 5.3a (circumferentially orthotropic) with primarily exposed basal plane. This fiber has a single-phase microstructure that is observed for vapor-grown fibers. The physical and chemical properties of such fibers have been previously discussed (70).

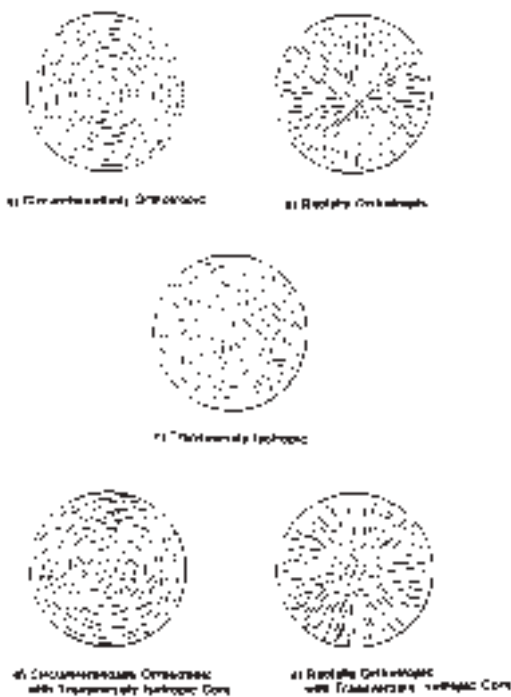


Figure 5.3 Representations of different carbon fiber microstructures.

A center void occurs because of the large energies required to bend the graphene sheets into smaller circumferences.

Figures 5.3b (radially orthotropic) and 5.3c (transversely isotropic) show single-phase microstructures. The graphene sheets are well ordered in a radial alignment with a large portion of exposed graphitic edge plane in one microstructure. A more random distribution of the graphene sheets is seen in the other with an isotropic distribution of both edge and basal plane throughout.

Diagrams of a two-phase microstructure are shown in Figures 5.3d (circumferentially orthotropic with an isotropic core) and 5.3e (radially orthotropic with an isotropic core). The exterior of the fiber has a high degree of basal character with the graphene sheets circumferentially oriented in one microstructure. The thickness of the concentric layers is less than that for the fiber type shown in Figure 5.3a. The fiber core has a random distribution of graphene sheets similar to that for glassy carbon. There is a gradual transition from the ordered surface structure to the disordered core. This fiber is an example of an onion-skin exterior and a random-core interior. The other type has an ordered radial alignment of the graphene sheets at the exterior and a more random, isotropic distribution in the core.

5.2.4.1 Mechanical polishing

Carbon fibers in a microcylindrical geometry are too fragile to be polished. However, a fiber in a disk geometry can be polished in a manner similar to that for GC. The same ultraclean

polishing conditions described above for GC should be employed. Care should be taken to avoid damaging the insulation layer. This means a special jig needs to be constructed to hold the microelectrode in a fixed position, if polishing by hand. Alternately, a special microelectrode beveler with a micromanipulator/electrode holder can be used. It is important that all polishing debris be removed from the electrode surface by copious rinsing and ultrasonic cleaning. To avoid damaging the end of the electrode during cleaning, it should not be allowed to “bounce” on the bottom of the solution container. It is best to suspend the microelectrode in the sonicated solution during cleaning. At least for the disk geometry, polishing is a useful first step for electrode activation. One must remember, though, that polishing can roughen the surface and alter the exposed microstructure, particularly for the fiber types with more ordered surface microstructures.

5.2.4.2 Solvent cleaning

Exposure to clean organic solvents can be useful for cleaning and activating carbon fibers. Several different solvents can be used to clean the electrode surface including acetonitrile, isopropanol, dichloromethane, and toluene. The solvents should first be distilled for purification. Reagent-grade solvents often contain impurities at levels that can cause significant electrode deactivation. AC can be added to the distilled solvents for additional purification. Soak times of 20–30 min are usually adequate. The solvent cleaning can also be performed by Soxhlet extraction.

5.2.4.3 Heat treatment

Achieving an ideal carbon fiber reference surface for studies of electrode structure–function is difficult to achieve. Another good method for cleaning carbon fibers without significantly altering the microstructure is high-vacuum heat treatment. Heating the surface in the UHV (10^{-9} Torr) to temperatures near 1000 °C for 30 min causes impurities to desorb and surface oxygen functional groups to decompose. Therefore, this pretreatment cleans the surface by desorbing contaminants and removes surface carbon–oxygen if the temperature is high enough (71). Swain, under the direction of Kuwana, studied the activation of different carbon fiber types by heat treatment (72). The heat-treated fiber surfaces are low in surface oxygen as the carbon–oxygen functionalities decompose between 500 and 900 °C (71, 72). However, the loss of surface oxygen creates dangling bonds on the surface that quickly react in the atmosphere when brought out of the vacuum chamber for use. Therefore, electrochemical measurements should be performed as soon as possible after removal from the chamber. Alternately, the heat treatment can be performed in a quartz tube furnace, carefully purged with nitrogen or argon, at a temperature of ca. 400–800 °C for 30 min. It is more difficult to remove trace levels of oxygen from the tube furnace than in the high vacuum; carbon oxidation and gasification can be a problem. Heat treatment in a tube furnace, if the temperature is kept low, ~400 °C, results in a clean surface but not one that is as low in oxygen as is achieved by vacuum heat treatment. In general, heat treatment is a good starting point for the activation of any carbon fiber type as it produces a clean and low-oxygen surface.

5.2.4.4 *Laser activation*

Laser treatment is useful for cleaning and activating carbon fibers without altering the microstructure or surface chemistry, at least if the treatment is performed under mild conditions (i.e., low incident laser power). Strein and Ewing used a pulsed N₂ laser operating at 337 nm to activate a carbon fiber microdisk electrode (73). The treatment works by both heating the surface (absorbed light), resulting in the desorption of contaminants and creation of new edge plane (e.g., active sites). The extent of edge plane formation depends on the pulse power density, pulse duration, as well as the native fiber microstructure. If significant new edge plane is exposed, then k_{app}^o for different redox systems will increase as will the background voltammetric current and the surface oxygen content.

5.2.4.5 *Electrochemical polarization*

Electrochemical pretreatment is the most common method for activating carbon fibers. There are many electrochemical pretreatment methods reported in the literature. It is best to apply the pretreatment to a clean and reproducibly conditioned surface for best results. Such a surface can be obtained by mechanical polishing (disk electrodes only), solvent cleaning, or vacuum heat treatment. Usually, electrochemical pretreatment involves anodic polarization in acidic, neutral, or basic media with the magnitude of the potential, the time, and the medium being critical parameters. The polarization can be performed potentiostatically, potentiodynamically, or galvanostatically. Mild polarization in acid (<1.5 V) can be used to activate the more disordered fibers when only surface cleaning and minimal oxidation are desired. Severe polarization (>1.5 V) can be used to activate more ordered fibers by creating new edge plane. As a consequence of the edge plane formation, the background voltammetric current, the surface oxygen content, and molecular adsorption will increase. A few representative examples are given below.

Gonon and coworkers demonstrated that the response of a pyrolytic carbon fiber can be dramatically improved by immersing the fiber in a phosphate-buffered saline (PBS) solution (0.2 g L⁻¹ KCl, 0.2 g L⁻¹ KH₂PO₄, 0.047 g L⁻¹ MgCl₂, 8 g L⁻¹ NaCl, and 1.15 g L⁻¹ Na₂HPO₄, pH 7.4) and alternating the potential between 0 and 3 V vs. Ag/AgCl at a frequency of 70 Hz and a duration of 20 sec (74). This is a rather severe treatment (the so-called French-fry method) that improved the sensitivity, reversibility, and selectivity of this particular fiber type for catecholamines. An interesting feature of the treated electrode was its ability to resolve the voltammetric oxidation of catechols from ascorbic acid. Ewing *et al.* activated PAN-based carbon fibers by potentiodynamic cycling between 0 and 1.8 V vs. SCE at 250 V sec⁻¹ in pH 7.4 citrate–phosphate buffer (75). The duration of the cycling can be varied from several minutes to several tens of minutes. The anodic limit is well into the oxygen evolution regime at this solution pH so that microstructural and chemical changes (i.e., increasing the surface oxygen content) occur. The electrode sensitivity and reproducibility for various redox systems (e.g., catecholamines) were improved after pretreatment. Kovach *et al.* treated carbon fibers in a microcylinder geometry by potentiodynamic cycling between 0 and 3 V vs. SCE in phosphate buffer, pH 7.4, for 20 sec (76). This was followed by potentiostating the electrode at 0 V in the buffer solution for 30–60 min. The latter was noted to improve the response stability. Again, the anodic limit is well into the oxygen evolution regime at this solution pH so that microstructural

and chemical changes occur. Many reported pretreatments for carbon fibers involve anodic potential excursions of ~3 V (74, 76–78), which according to Adams and coworkers is “overkill” for surface oxidation as a significant portion of the current passed goes toward oxygen evolution (79). Adams and coworkers found that milder electrochemical polarization was also effective at activating carbon fibers. They reported two protocols, both in pH 7.4 PBS solution: (i) potentiodynamic cycling from 0 to 2.6 V vs. Ag/AgCl for 30 sec and (ii) potentiodynamic cycling from 0 to 1.3 V vs. Ag/AgCl for 30 sec. These are two recommended methods for activating most fiber types. The authors demonstrated that electrochemical polarization increases the electrode sensitivity toward catechols but decreases the response time and they recommended that future applications of pretreated fibers include experimental checks of the electrode response time.

5.2.5 Carbon nanotubes

These are new and interesting members of the carbon electrode family offering unique mechanical and electronic properties combined with chemical stability (80–82). So far, they have not been used extensively in electroanalytical chemistry but this is likely to change in the near future. Carbon nanotubes are formed as two structures: multi-walled (MWNT) and single-walled (SWNT) (82). MWNTs are composed of concentric and closed graphene tubules, each with a rolled-up graphene sheet. A range of diameters can be produced from a few to about 30 nm. The majority of the research in this field over the years has utilized MWNTs because of the difficulty in producing phase-pure and oriented SWNTs. An SWNT is made of a single graphite sheet rolled seamlessly with a diameter of 1–2 nm. SWNTs are usually arranged in a regular pattern of bundles that consist of tens to hundreds of tubes in contact with each other. Nanotubes can be grown in a “spaghetti mesh-like” arrangement or in an ordered array or network (82). An interesting property relevant to electrochemistry is the fact that the material can possess either metallic or semi-conducting electrical properties depending on the diameter and lattice helicity.

As discussed by Dai and others, nanotubes can be synthesized by arc discharge, laser ablation, and chemical vapor deposition (CVD) methods (82). The first two employ a solid-state precursor as the carbon source and involve vaporization at high temperatures (thousands of degrees centigrade). These well-established methods produce high-quality nanotube structures, despite the by-products that are formed. CVD utilizes a hydrocarbon source gas and a metal catalyst particle as a “seed” for nanotube growth. Growth by CVD occurs at lower temperatures (500–1000 °C) than the arc discharge or laser ablation methods. The preparation of the catalyst is a critical step in the nanotube growth. Catalysts have been prepared as thin metal layers, thin metal salt layers, and dispersed nanoparticles (83). Fe, Co, and their alloys with Mo are used as catalysts (82, 83). Both SWNTs and MWNTs can be produced by all three methods. Great progress has been made in recent years, particularly by the CVD method, producing SWNTs with high crystallinity and perfection.

Carbon nanotubes can be grown on conducting Si, Au, Pt, and glass. The first three substrates are useful for making nanotubes into electrochemical electrodes. There are three ways nanotubes have been configured as an electrochemical electrode. First, nanotubes have been made into the equivalent of a carbon paste electrode by dispersion into mineral

oil and cast into a Teflon cavity. Valentini *et al.* found that a mixture of 60% nanotube (by mass) and 40% mineral oil produced an electrode with good electrochemical properties (84). Second, the “spaghetti mesh-like” arrangement of nanotubes can be physically attached to an electrode surface. Luo *et al.* cast a network of SWNTs on a glassy carbon electrode (84). This was accomplished by dispersing 1 mg of nanotubes in *N,N*-dimethylformamide. Approximately 10 µL of this dispersion was dropped on the glassy carbon electrode and the solvent evaporated. The electrochemical response of this electrode, however, contains a contribution from both the nanotubes and the underlying support electrode. Third, an individual nanotube or bundle can be fabricated into a microelectrode. Crooks and coworkers reported the electrochemical behavior of a single nanotube, attached to a conducting wire and insulated with polyphenol (85). The use of this carbon type in electroanalytical chemistry is so new that there is not a wealth of literature yet available on pretreatment methods and their efficacy.

5.2.5.1 *Chemical oxidation*

Because of their structure, carbon nanotube electrodes are not amenable to conventional pretreatment. The material is too fragile for mechanical polishing and heat treatment would likely not be practical due to the way nanotube electrodes are formed (paste electrode or physically contacted to another electrode). Laser activation could be used but, so far, this pretreatment method has not been studied. One of the challenges faced while working with nanotubes is their purification after growth. Nanotubes are routinely submitted to various chemical and physical treatments to remove graphitic nanoparticle, amorphous carbon, and metal catalyst impurities (82). Chemical oxidation is often used for this purpose and therefore can serve as a pretreatment method. Purification of the nanotubes is a critical step in their application, so much work has gone into developing appropriate cleaning and dispersing treatments. In one method reported by Valentini *et al.*, the authors oxidized the nanotubes in a tube furnace at 400 °C in flowing air for 1 h (84). This was followed by exposure of the nanotubes to 6 M HCl for 4 h under ultrasonic agitation. The nanotubes were then washed with ultrapure water before being placed in 2 M HNO₃ for 20 h under ultrasonic agitation. The final step involved a copious rinse with ultrapure water. This chemical oxidation removes amorphous carbon and metal catalyst impurities and introduces significant carbon–oxygen functionalization at the exposed edge plane and defect sites.

5.2.5.2 *Electrochemical polarization*

Potentiodynamic and potentiostatic methods can also be used to activate nanotubes. Similar to chemical oxidation, electrochemical pretreatment can effectively remove impurities and cause the creation of carbon–oxygen functional groups at the exposed edge plane and defect sites. The same authors reported on an electrochemical pretreatment that involved potentiostating the electrode at +1.7 V vs. Ag/AgCl in pH 7 phosphate buffer for 3 min followed by 3 min at –1.5 V (84). Both the chemical and electrochemical oxidations improved the electrode response (smaller voltammetric ΔE_p and larger i_p values) for Fe(CN)₆^{3–/4–}, serotonin, and caffeic acid.

5.2.6 Diamond films

Electrically conducting diamond is a new type of carbon electrode material that is beginning to find widespread use in electroanalysis (86–88). The material possesses properties superior to other forms of carbon that include (i) low and stable background current over a wide potential range, (ii) wide working potential window in aqueous media, (iii) relatively rapid electron-transfer kinetics for several redox systems without conventional pretreatment, (iv) weak molecular adsorption, (v) dimensional stability and corrosion resistance, and (vi) optical transparency. The material is now available from several commercial sources and is not overly expensive, as commonly perceived (89).

Diamond is often grown as a thin film on a conducting substrate, such as highly doped Si, Mo, W, or Ti, using one of the several methods: microwave plasma, hot-filament or combustion flame-assisted CVD. The most common method is microwave plasma CVD. One reason for this is the commercial availability of such reactor systems. While the mechanism of film growth is somewhat different from method to method, all serve to activate a carbonaceous source gas producing a growth precursor in close proximity to the substrate surface (90). A typical CVD reactor consists of the growth chamber and equipment associated with the particular activation method (e.g., microwave power source) as well as various accessories, such as mass flow controllers for regulating the source gas, a throttle exhaust valve and controller for regulating the system pressure, a pumping system, temperature measurement capability, and the gas handling system for supplying the source gases. A block diagram of a typical CVD system is shown in Figure 5.4. The same reactor design can be used for growing carbon nanotubes, for example. In the case of microwave-assisted CVD, the microwave energy from the generator is directed to, and focused within,

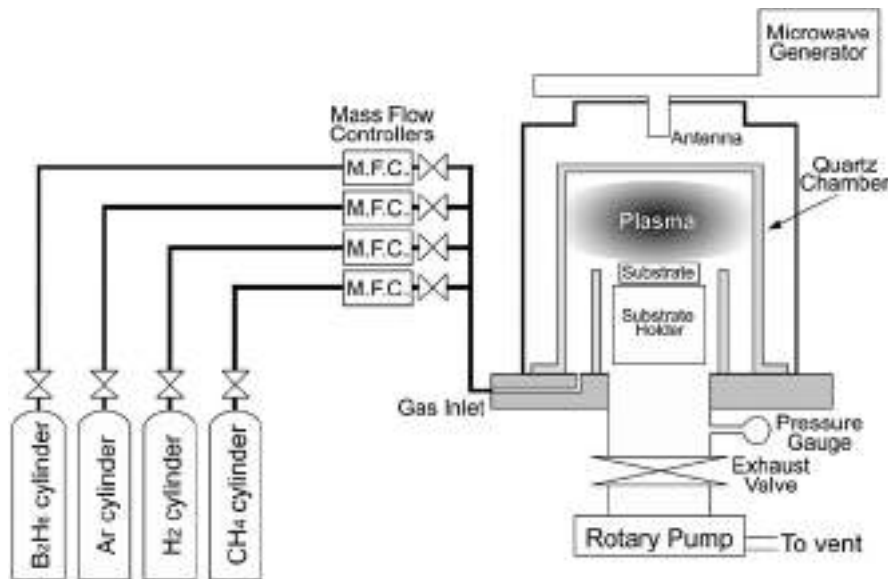


Figure 5.4 Block diagram of a typical microwave plasma CVD reactor.

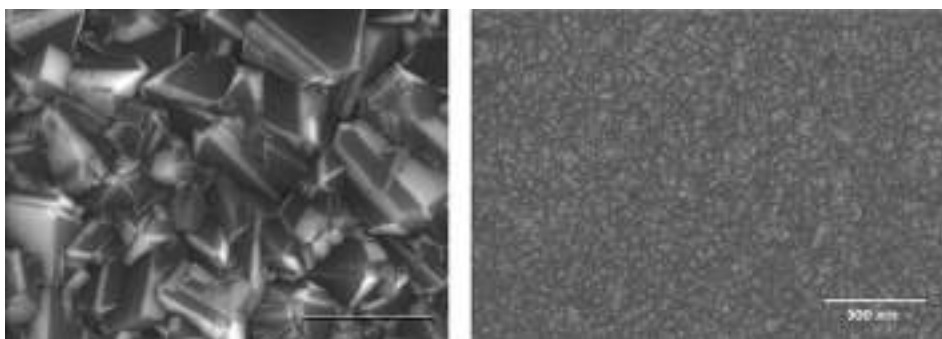


Figure 5.5 SEM images of (left) a boron-doped microcrystalline (scale bar = 2 μm) and (right) a boron-doped nanocrystalline (scale bar = 500 nm) diamond thin film grown on Si.

a quartz cavity producing a spherically shaped, glow-discharge plasma directly above the substrate. The substrate can be positioned either outside of (few mm), or immersed within, the intense discharge region. The plasma is where the reactive species involved in the diamond growth are formed. The key deposition parameters to control are the source gas composition, microwave power, system pressure, and substrate temperature.

There are two types of synthetic diamond thin film routinely produced: microcrystalline and nanocrystalline (91, 92). The classification of these two film types is based on their nominal crystallite size and morphology. Figure 5.5 shows SEM images of the two types of boron-doped diamond deposited as thin films on Si. High-quality microcrystalline diamond films are deposited from CH_4/H_2 source gas mixtures with volumetric ratios of 0.3–1.0%, microwave powers of 0.8–1 kW, pressures of 35–65 Torr, and substrate temperatures of 700–800 °C. Under these conditions, $\text{CH}_3\cdot$ is the primary growth precursor. The added hydrogen serves several critical functions: (i) abstraction of hydrogen from chemisorbed methyl groups on the growing film surface thereby producing active sites for carbon addition, (ii) activation of reactive methyl radicals in the gas phase by hydrogen abstraction, (iii) passivation of dangling bonds on the growth surface, which is important for minimizing reconstruction from sp^3 to sp^2 bonding, and (iv) gasification of any sp^2 -bonded, non-diamond carbon impurity that forms on the growth surface. It can be seen from the image that microcrystalline films are well faceted with crystallite sizes on the order of a few micrometers, or greater, in lateral dimension. The individual crystallites are randomly oriented and there tends to be significant twinning. A grain boundary is present at the junction between two or more crystallites, which has structural, chemical, and electronic properties that are different from the grains.

One way high-quality nanocrystalline diamond films are deposited is from CH_4/Ar source gas mixtures using a volumetric ratio of 0.5–1.0% with little or no added hydrogen, microwave power of 0.8–1 kW, pressure of 130–160 Torr, and substrate temperature of 700–800 °C. Gruen and coworkers discovered some years ago that phase-pure nanocrystalline diamond can be grown from hydrogen-poor CH_4/Ar gas mixtures (93–103). The most remarkable difference in films grown using hydrogen-poor gas mixtures, compared with those grown from conventional hydrogen-rich mixtures, is the nanocrystallinity and

smoothness (rms roughness \sim 10–30 nm over large areas) of the former, as can be seen in the SEM image shown above. Noble or inert gas addition to hydrogen-rich plasmas (e.g., 0.5% CH_4/H_2) enhances the growth rate of films by increasing the $\text{CH}_3\cdot$ and atomic hydrogen concentrations in the plasma. The low excitation energy of inert gases, such as Ar or Xe, results in a plasma discharge with a higher electron density, and this leads to the higher levels of $\text{CH}_3\cdot$ and $\text{H}\cdot$. There is a fundamental change in the plasma chemistry, growth mechanism, growth rate, and film properties as one transitions from a hydrogen-rich to a hydrogen-poor plasma. In particular, hydrogen-poor plasmas have a high concentration of carbon dimer, C_2 , which serves as both the primary growth and the nucleation species. The nanocrystallinity is a result of a growth and nucleation mechanism involving the insertion of C_2 into surface C–H bonds. Apparently during growth, there is sufficient hydrogen from the CH_4 to minimize surface reconstruction to an sp^2 -bonded phase. The C_2 addition is believed to occur by a two-step growth mechanism (93–103). A C_2 molecule approaches the unreconstructed monohydride surface and inserts into a C–H bond. The C_2 molecule then rotates to insert its other carbon into a neighboring C–H bond on the surface. A C_2 molecule then inserts into an adjacent C–H bond, parallel to the newly inserted C_2 dimer. The original state of the surface is recovered by the formation of a bond between carbon atoms in the adjacent surface dimers. Very high rates of heterogeneous renucleation are observed on the order of 10^{10} cm^{-2} , and the resulting films consist of randomly oriented, phase-pure grains of diamond with well-delineated grain boundaries (93–103). Nanocrystalline films produced in Ar-rich plasma possess a very fine, uniform grain size (3–5 nm is typical for high-quality ultrananocrystalline diamond) and a small but non-negligible amount of sp^2 -bonded carbon at the abrupt grain boundaries.

The instantaneous nucleation density during diamond growth on untreated, smooth non-diamond substrates is generally low. Therefore, substrate pretreatment is a prerequisite for achieving thin continuous films. A common substrate preparation involves either mechanical polishing with small-diameter diamond powder (0.01–1 μm) suspended in ethanol or ultrasonication in a diamond powder/solvent suspension. For example, with the latter, the diamond powder can be suspended in ethanol and the ultrasonic agitation performed in this medium. Either pretreatment results in the formation of scratches and defects, as well as the dispersion of some embedded diamond particles over the surface. Subsequent substrate washing to remove polishing debris and clusters of diamond particles from the surface is critical. The washing typically involves sequential ultrasonic cleanings in organic solvents (isopropanol, acetone, and methanol). Enhancement of the instantaneous heterogeneous nucleation density results from both the physical defects introduced and the dispersed diamond seed particles.

A number of tools are useful for characterizing the physical and chemical properties of diamond thin films including scanning electron microscopy, Raman spectroscopy, X-ray diffraction, X-ray photoelectron spectroscopy, conductivity-probe atomic force microscopy, and near-edge X-ray absorption spectroscopy. Detailed characterization of diamond electrodes has been reported in the literature. Raman spectroscopy is particularly useful. A sharp first-order phonon mode at 1332 cm^{-1} is seen for diamond. The line width is inversely related to the defect density (phonon scattering) and the line position can reflect tensile or compressive stress within the film (104, 105). Scattering intensity also is present in the 1500 – 1560 cm^{-1} range when the film contains non-diamond carbon impurity. This

impurity is not graphitic but possesses a mixed sp^2 and sp^3 bonding. The scattering cross-section for the non-diamond carbon is approximately 50 times greater than that for diamond, so Raman spectroscopy is particularly sensitive to the presence of non-diamond carbon impurity (106). The ratio of the $1332/1580\text{ cm}^{-1}$ bands is reflective of the film quality. The higher this ratio, the lower the film quality. This is manifested in a higher voltammetric background current, a narrower working potential window, and a greater molecular adsorption (107, 108). The Raman spectral features for microcrystalline and nanocrystalline films are quite different, and the spectral features, particularly for the microcrystalline films, can change depending on the boron-doping level (109–111).

Diamond is one of the mother nature's best electrical insulators. In order to have sufficient electrical conductivity for electroanalytical measurements ($<0.1\text{ }\Omega\text{ cm}$ or $>10\text{ S cm}^{-1}$), diamond films must be doped. The most common dopant is boron with doping levels in the $1 \times 10^{19}\text{ cm}^{-3}$ range, or greater, being the norm. The introduction of boron imparts p-type electrical properties to the film. Other dopants have also been used, such as nitrogen, phosphorous, and sulfur, but all suffer from either low solubility or high activation energy (90). The boron can be added to the source gas mixture in the form of B_2H_6 or $\text{B}(\text{CH}_3)_3$. B_2H_6 is the preferred gas as $\text{B}(\text{CH}_3)_3$ not only adds boron to the source gas mixture but also extra carbon. This extra carbon can alter the film morphology and decrease the quality. The electrically active boron is that which substitutionally inserts into the growing lattice. The films are rendered electrically conducting through incorporation of boron dopant atoms during deposition, although the electrical conductivity depends in a complex manner on lattice hydrogen, defects, and dangling bonds, in addition to the doping level. For example, films can be doped as high as 10^{21} cm^{-3} with little alteration of the morphology or microstructure. Typical film resistivities are $<0.05\text{ }\Omega\text{ cm}$, carrier concentrations are 10^{19} cm^{-3} , or greater, and carrier mobilities are in the $0.1\text{--}10\text{ cm}^2\text{ V}^{-1}\text{ sec}^{-1}$ range. Thus far, there has been little study of how to activate diamond electrodes for electron transfer. Actually, one of the interesting features of this electrode material is the fact that pretreatment is usually not required to achieve an “activated” electrode. The most active surface tends to be the hydrogen-terminated one.

5.2.6.1 Mechanical polishing

As mentioned above, most pretreatments of carbon electrodes initially involve mechanical polishing to remove contaminant layers and expose a fresh surface. Due to its hardness, mechanical polishing of diamond is not practical in this sense. Contaminant layers can be removed but a fresh surface will not be exposed. The polishing also likely causes the rupture of the surface carbon–hydrogen bonds leading to the incorporation of surface oxygen. If polishing is performed, then a thorough cleaning is necessary to remove all the polishing debris prior to use, particularly the alumina powder. Extensive ultrasonic cleaning in clean organic solvents (isopropanol and acetone) and ultrapure water is useful for this purpose.

5.2.6.2 Acid washing and rehydrogenation

Diamond electrodes tend to be quite “active” for electron transfer without pretreatment, at least for some outer-sphere redox systems. Exposure to the laboratory atmosphere does not deactivate this electrode like it does other sp^2 carbons (39). As deposited diamond

electrodes exhibit relatively rapid heterogeneous electron-transfer rate constants for several redox systems (91, 92). It is our experience that in cases where pretreatment is required, the most active diamond electrodes are produced by a two-step procedure: (i) acid washing and (ii) hydrogen plasma treatment. The acid washing involves soaking the electrode for 30 min each in a 3:1 (v/v) HNO_3/HCl solution and a 30% (v/v) H_2O_2 solution. The solutions are warmed to about 50 °C. Copious rinsing with ultrapure water is performed after each solution exposure. Exposure to these oxidizing solutions removes chemical contaminants, metal impurities, and adventitious non-diamond carbon impurity from the surface. Oxygen is also incorporated as the surface becomes much more hydrophilic. XPS-determined O/C atomic ratios increase from ~0.002 to 0.15. After water rinsing, the electrodes are transferred to the CVD reactor for a 15–30 min hydrogen plasma treatment (atomic hydrogen). This treatment removes the surface oxygen by incorporating hydrogen. The resulting film is low in surface oxygen and it is hydrophobic. In order to retain the hydrogen surface termination, the films must be slowly cooled in the presence of atomic hydrogen by lowering the power and pressure over a 5–15 min period until the electrode surface temperature is below 400 °C. Typical heterogeneous electron-transfer rate constants range from 0.02 to 0.2 cm sec⁻¹ for redox systems such as $\text{Fe}(\text{CN})_6^{3-/4-}$, $\text{Ru}(\text{NH}_3)_6^{3+/2+}$, and $\text{IrCl}_6^{2-/3-}$ (91, 92).

5.2.6.3 Solvent cleaning

Diamond thin-film electrodes in our laboratory are routinely cleaned by soaking in distilled isopropanol for 20 min prior to use. While no detailed study has been performed yet, it is presumed that the solvent exposure cleans the diamond surface by desorbing and/or dissolving contaminants. A controlled study of the effect of solvent cleaning on the electrochemical response of diamond is needed; however, it is expected that this pretreatment will be an effective, non-destructive one for activating diamond electrodes, when necessary.

5.2.6.4 Heat treatment

Although not studied as yet either, heat treatment is expected to be an effective, non-destructive method for activating diamond electrodes, if performed under the appropriate conditions. Heat treatment of boron-doped diamond cleans the surface by desorbing adsorbed contaminants, but it also can alter the electronic properties. It is expected that adsorbed contaminants would possess low activation energies for desorption; therefore, low heat treatment temperatures should be needed for cleaning. Temperatures of 250–500 °C for 30 min, either in high vacuum or a quartz tube furnace under an inert gas atmosphere, should be adequate. Exposure to this temperature is also sufficient to desorb subsurface hydrogen, which has been shown to function as a charge carrier and increase the electrical conductivity in semiconducting diamond (112–114). This reduces the number of charge carriers in the surface region. However, this carrier density is orders of magnitude lower than that arising from the substitutionally inserted boron, so little change in the electrical conductivity is expected. In contrast, heat treatment at these temperatures is also sufficient to desorb hydrogen from B–H complexes on the surface. The interacting hydrogen functions as an electron donor and compensates the boron acceptor (115). This compensation leads to a reduction in the carrier concentration. Destruction of these

complexes is expected to increase the active carrier concentration and, consequently, the film conductivity.

At heat treatment temperatures in the 700–900 °C range, the desorption of contaminants and the surface terminating hydrogen will also occur. This will create dangling bonds on the surface, which will result in surface reconstruction to form sp^2 -bonded clusters and/or introduce surface oxygen once exposed to the atmosphere. For this reason, heat treatment of diamond at these high temperatures should be avoided.

5.2.6.5 *Electrochemical polarization*

Potentiostatic and potentiodynamic polarizations in either strong acid or base have been investigated, to a limited extent, as a pretreatment. Unlike most sp^2 carbon electrodes, electrochemical pretreatment does not alter the diamond microstructure, if the film quality is high, but does change the surface chemistry, causing the incorporation of oxygen. So far, there has been no controlled, systematic study of the effect of electrochemical polarization on the electron-transfer kinetics for different redox systems, so the full extent of the activation method is unknown. What has been reported is (i) converting from a hydrogen to an oxygen surface termination improves the electrode response stability toward some redox systems and (ii) in the case of adsorbed reaction products (e.g., phenol oxidation), anodic polarization can remove these adsorbed contaminants presumably by complete oxidation to CO_2 with $OH\cdot$ being the reactive species. One example of a severe anodic polarization applied to a microcrystalline diamond electrode was reported by Fujishima and coworkers (116). It involved potentiostating the electrode at 2.6 V vs. SCE for 4 min in pH 2 Britton–Robinson buffer. A total anodic charge of 720 mC cm^{-2} was passed. The pretreatment presumably did not alter the microstructure or crystallinity, but did increase the surface oxygen content.

5.2.7 **Tetrahedral amorphous carbon (Ta-C) films**

The use of conducting diamond as an electrochemical electrode has stimulated recent interest in the study of diamond-like carbons (DLCs) as electrode materials. Amorphous carbon thin films (0.1–20 μm thick) with a mixed sp^2 - and sp^3 -bonded microstructure can be produced by several deposition methods. These films, depending on their microstructure, can have hardness, strength, and chemical inertness close to that of crystalline diamond, yet be produced as a smooth and relatively stress-free film at low temperatures (<200 °C). These kinds of amorphous films include a variety of DLCs and Ta-C, which is sometimes referred to as amorphous diamond. In general, these materials have local bonding that falls between that for graphite and diamond—a mixed sp^2 (threefold coordinated) and sp^3 (fourfold coordinated) microstructure. Films can contain hydrogen or be relatively hydrogen-free, depending upon the growth conditions. The type of microstructure formed very much depends on the film deposition conditions. While their study as electrochemical electrodes is a relatively recent research undertaking, DLC and Ta-C films have been used for a number of years as wear- and corrosion-resistant coatings for cutting tools (89, 117–121).

The hardness of these coatings can be tailored from something comparable to graphite up to diamond by controlling the ratio of the sp^3 to sp^2 carbon–carbon bonding and the hydrogen content in the film. This is accomplished by adjusting the deposition conditions. The coating of stainless steel, electrically conducting Si, and other temperature sensitive materials (e.g., Ti and Al alloys, plastics, etc.) is rather commonplace nowadays. Not only do the film hardness and coefficient of friction depend on the microstructure and hydrogen content, but so do the electrical properties. The deposition of DLC films with a high level of sp^3 bonding (>80%) is possible when the carbon ions used for growth have kinetic energies in the range of 30–600 eV. Based on the pioneering work with mass selected ion beams (MSIB), DLC formation on substrates is understood by the subplantation model of Lifshitz and coworkers (122, 123) and Robertson (123). In general, DLC films are deposited from ionized carbon plasmas. Ta-C is a specific type of DLC material that is very low in hydrogen content and possesses high hardness and density.

Ta-C films can be produced by pulsed laser, vacuum-arc, laser-arc, and high-current-arc deposition (117–123). Common to all four methods is the use of a high-purity graphite target and the formation of energetic carbon ions with kinetic energies in the 30–600 eV range. These ions are accelerated toward the substrate in the presence of an electric field and they penetrate into the superficial atomic layers (subplantation model) (122, 123). There they produce a highly compressive stress, which promotes sp^3 -hybridized bonding. The deposition is carried out under high-vacuum conditions to minimize loss of carbon ion kinetic energy by interaction with residual gas species. The required conditions for Ta-C deposition are the combination of sufficient carbon particle kinetic energy and low deposition temperature. A common problem with the arc deposition methods is particle emission (e.g., clusters of carbon atoms and other impurities) from the cathode. These particles can get incorporated into the deposited film and disturb the film growth. Therefore, filtering techniques have been developed to isolate the primary growth species from the impurities during deposition. Typically, ion filtration is accomplished using electromagnetic fields (122, 123).

Ta-C films can be viewed as nanostructured or nanocomposite materials. The electrical conductivity depends on the extent of sp^2 -bonded carbon in the microstructure. Amorphous DLC films with high sp^3 carbon content are poor electrical conductors and therefore have limited application as electrochemical electrodes. The sp^2 carbon content has to be increased to make the films more electrically conducting. The microstructural disorder and composition (e.g., hydrogen and sp^2 carbon fraction) affect the electrical conductivity. One way this is accomplished is through ion bombardment. During ion bombardment, the sp^3 carbon bonding is gradually converted into an sp^2 -bonded phase. Growing, clustering, and ordering of the sp^2 carbon domains occur during this process, as revealed by Raman spectroscopy (122–125). The extent of structural rearrangement depends on the ion energy and dose, but the change in electrical resistivity can vary from the original 10^8 to $10^{-3} \Omega \text{ cm}$ (122, 123). The ions can either be carbon, in which case no impurity is added, or others, such as nitrogen.

The electrochemical properties of electrically conducting Ta-C films have not yet been extensively studied. In fact, there have only been a couple of literature citations. Yoo *et al.* studied the electrochemical behavior of nitrogen-incorporated Ta-C thin-film electrodes (118). A low background current and a wide working potential window (>3 V) in aqueous

media were reported. Cyclic voltammetric studies of $\text{Ru}(\text{NH}_3)_6^{3+/2+}$ and Co(III)-sepulchrate revealed electrochemical reversibility at par with that of highly boron-doped diamond electrodes. In addition, the electrochemical reversibility of the Cl_2/Cl^- and quinone/hydroquinone redox systems was better than that observed for highly boron-doped diamond. Evstafeeva *et al.* performed electrochemical impedance measurements on Ta-C films annealed at 700–900 °C in vacuum or ion implanted with C^+ ions (118). $\text{Fe}(\text{CN})_6^{3-/4-}$ was used as the redox test system to evaluate electrode activity. The authors observed that both the vacuum heat treatment and the ion implantation imparted electrochemical activity to inactive Ta-C films. There has simply not been enough work yet with this form of carbon to know how different pretreatments affect the electrochemical response. The following provides some speculation as to how this material might best be prepared for use in electroanalytical measurements.

5.2.7.1 *Mechanical polishing*

Like diamond, polishing is not practical due to the material hardness. There would simply be no new carbon exposed, but contaminant layers would be removed from the surface. There would also likely be some surface oxygen incorporation if the polishing is performed in the ambient.

5.2.7.2 *Solvent cleaning*

Solvent cleaning, as applied to other carbon electrodes, is expected to be an effective, non-damaging method of electrode pretreatment. Several different solvents can be used to clean the electrode surface including acetonitrile, isopropanol, dichloromethane, and toluene. The solvents should first be distilled for purification. Reagent-grade solvents often contain impurities at levels that can cause significant electrode deactivation. AC can be added to the distilled solvents for additional purification. Soak times of 20–30 min should be adequate. The solvent cleaning can also be performed by Soxhlet extraction.

5.2.7.3 *Heat treatment*

Heat treatment, depending on the conditions, is expected to be effective at both desorbing contaminants and improving the electrical conductivity. Low-temperature heat treatment in an inert atmosphere or in vacuum at temperatures <500 °C should be effective at desorbing contaminants. Care should be taken to minimize the presence of oxygen as significant gasification will occur at this temperature. Heat treatment at higher temperatures might also desorb hydrogen from the lattice, thereby improving the electrical conductivity as the loss of hydrogen leads to the formation of sp^2 -bonded carbon (π states).

5.2.7.4 *Electrochemical polarization*

Electrochemical polarization might also be a useful pretreatment method, but this remains to be determined. Surface oxygen would certainly be incorporated during such a treatment but the extent of morphological and microstructural alteration would depend on the sp^3/sp^2 fraction of the film. The more sp^2 -bonded carbon there is, the greater is the

extent of morphological and microstructural degradation expected. Conditions, such as those described for activating glassy carbon, would likely be useful for Ta-C films. For example, potentiodynamic cycling in 0.1 M KNO₃ between -0.5 and +1.8 V vs. SCE would introduce some surface carbon–oxygen functionality and possibly clean the surface. In summary, the activation of this type of carbon films remains an open area for research.

5.3 METAL ELECTRODES

A wide choice of solid metal electrodes exists for use in electroanalysis including platinum, gold, nickel, and palladium. Of these, platinum and gold are the most commonly used. In general, metal electrodes exhibit fast electron-transfer kinetics for many redox systems and possess a relatively wide anodic potential window. The cathodic window for some, such as platinum, is more limited due to hydrogen evolution. The background voltammetric i – E curves for metals usually are characterized by a larger overall current per geometric area than that for carbon electrodes and exhibit features or peaks associated with the formation and reduction of surface oxides, and the adsorption and desorption of H⁺ and other ions. Metals have a larger C_{dl} than most carbon electrodes and this contributes to the larger background current. The presence of the surface oxides, for example, can alter the electrode reaction kinetics and mechanism for certain redox systems and this can lead to variability in the electroanalytical measurement. Due to the specific adsorption of anions, the heterogeneous electron-transfer rate constant for some redox systems at metal electrodes is quite sensitive to the electrolyte composition, more so than for carbon. For instance, anions such as Cl⁻, Br⁻, I⁻, CN⁻, S²⁻, etc., show a strong tendency to adsorb on metal surfaces. The adsorption can block sites involved in the electrochemical reaction and alter both the reaction kinetics and the mechanism (126).

Metal electrodes can come in either bulk or thin-film form. This discussion will focus on the thin-film forms of platinum and gold. The fabrication and characterization of thin-film metal electrodes have been comprehensively described by Anderson and Winograd (127), so only a brief discussion is given herein. In general, thin films of a metal can be formed on a variety of substrates by vacuum evaporation, DC and RF sputtering, screen printing and CVD. Common substrates are glass (soda-lime and quartz), silicon, and mica. The substrates should possess a relatively smooth morphology with low surface roughness. The preparation of the substrate is a key step in the formation of well-adhering, electrically conducting and optically transparent (if needed for the application) films. Cleaning is a critical step in the substrate preparation that is sometimes overlooked. A common procedure for cleaning glass or oxide-coated silicon involves boiling in an aqueous detergent solution, rinsing with ultrapure water, followed by degreasing with clean organic solvents, such as isopropanol or methanol. When the surface is clean, distilled water will run off the surface as a continuous sheet and not bead up in the form of droplets. Mica is best prepared by cleaving the layer planes with tape or a sharp knife, which results in the exposure of a clean basal plane. The cleaning step should be performed immediately prior to film deposition.

5.3.1 Polycrystalline platinum and gold

As mentioned above, several methods can be used to deposit thin-film metal electrodes. Vacuum evaporation is performed at reduced pressures (ca. 10^{-6} Torr or lower). Deposition in the high vacuum is necessary to ensure that the mean free path of the evaporated growth species is long enough to reach the substrate. Evaporation is accomplished by melting a piece of the metal that is attached to a conductive support. This enables the metal to be resistively heated. Electron beam heating is also sometimes used. The key to keeping the deposited film chemically pure is the high-vacuum environment.

DC or RF sputtering is closely related to the cleaning process for activating electrodes described above. An electrical discharge is maintained between two electrodes, one of which is the material to be deposited (i.e., target), or a glow-discharge plasma is formed in the vicinity of the target. Both types of discharge can be formed in the presence of low-pressure (~ 10 mTorr) argon gas. Energetic argon ions (cations) are formed and accelerated into the negatively biased target. The ions gain kinetic energy and momentum from the accelerating bias voltage (approximately a few kV). Momentum is transferred to the target material causing the ejection of atoms or ions that deposit on the substrate with relatively high velocities. DC sputtering is best for electrically conducting targets, whereas the RF method is more useful for depositing films from insulating targets. Sputtered films often have better adhesion to the substrate than do evaporated films. This is because of the greater physical force with which they are deposited. Unlike evaporative deposition, sputter deposition methods can be carried out at lower temperatures. However, the films are not deposited in the high vacuum, so the chemical purity of the sputtered films can be lower than that of evaporated films.

The screen-printed approach for depositing thin films of metal has become popular in recent years. This approach is especially useful for producing multiple electrodes on a substrate or electrode array structures. Patterns are photolithographically formed on a screen, whose mesh contains open and blocked zones. An ink containing the metal of interest is applied to the screen and forced through the open zones onto the substrate using a squeegee blade. Once the solvent has been evaporated (air dry or an oven cure), the electrode is ready for use. In the CVD approach, molecules of a volatile precursor are transported in a carrier gas to a heated substrate. The compounds reach the substrate and react to form the desired metal film.

Both platinum and gold films are routinely deposited by vacuum deposition, sputtering, and screen-printing techniques. Macrosized electrodes can be formed or microlithography can be used to produce arrays of metal microelectrode structures. Adhesion layers are often used to produce well-adhering films. The best adhesion layers tend to be formed from metals (particularly the transition metals) that readily form oxides. The metal atoms deposited can then form covalent bonds with the oxide substrate lattice while simultaneously alloying with the metal film. Both chemical processes contribute to anchor the metal film to the substrate. In the case of gold, a thin chromium layer ($\sim 5\text{--}50$ nm) is deposited on the substrate first prior to the metal deposition. Key for electrochemical applications is the burial of the chromium layer. This means that the gold films need to be >200 nm thick. Treatments have been designed to selectively remove chromium contaminant atoms from the gold surface. These include chemical etching in a $\text{Ce}(\text{SO}_4)_2/\text{HNO}_3$ solution or electrochemical etching.

In the case of platinum, chromium is also used as an adhesion layer as are niobium and titanium (128). For this metal, chemical treatments have also been developed for the removal of adhesion layer contaminants (129).

Often the final step in the growth of thin-film electrodes is annealing. The electrical resistivity of thin films of gold and platinum is usually greatly improved by annealing in either air or high vacuum. The annealing probably works by causing the coalescence of islands of metal on the surface into a more continuous film. Typical annealing temperatures are in the 400–700 °C range, sufficiently low so as to not cause the metal film evaporate.

5.3.1.1 *Mechanical polishing*

Bulk platinum and gold electrodes can be prepared for use by mechanical polishing in a manner similar to that described for GC. In order to achieve the most rapid electron-transfer kinetics, one needs to polish under ultraclean conditions. The electrode should be polished using successively smaller sizes of alumina on a smooth glass plate (38–41). Deagglomerated alumina powders work best in sizes from 1.0 down to 0.05 μm. The alumina is slurried in ultrapure water to make a paste. The electrode should be polished using circular motions with an even force applied. Starting from the largest grit size, the electrode should be polished and then carefully cleaned by (i) rinsing with ultrapure water and (ii) ultrasonication in the same medium for about 15 min. The metal electrode should be placed in a clean beaker, submerged in ultrapure water, and covered during the ultrasonic cleaning. Eventually, a mirror-like finish should be obtained. The electrode should be used immediately after the polishing, or any pretreatment for that matter, for best results. Polishing metal film electrodes is often not possible due to the thinness of these layers and the mechanical damage caused by polishing. As is the case for many types of carbon, the pre-treatment of platinum and gold often involves two steps with the first being polishing. This can be followed up by laser irradiation, vacuum heat treatment, solvent cleaning, or electrochemical polarization. As is the case for carbon electrodes, several surface-sensitive and -insensitive redox systems should be used to assess the electrode activity after pretreatment.

5.3.1.2 *Heat treatment*

Vacuum heat treatment can be used to clean the electrode surface by causing the desorption of contaminants. Performing the treatment in the high vacuum ($>10^{-6}$ Torr) in the 400–900 °C range is sufficient for cleaning and activating both platinum and gold. For example, surfaces of single-crystal Au(III) can be atomically ordered and cleaned by vacuum heat treatment up to temperatures of 900 °C, as evidenced by low-energy electron diffraction (LEED) and auger electron spectroscopy (AES) (130, 131). The heat treatment can be performed in the high vacuum or in a tube furnace with an inert atmosphere, such as N₂ or Ar gas. Since this environment is not as clean as the vacuum, it is supposed that the degree of activation, as measured by the k_{app}° for different redox systems, would not be as high as that for the vacuum treatment.

5.3.1.3 *Solvent cleaning*

Solvent cleaning or solution soaking should also be effective at activating the metal electrodes, although one must be careful about the molecular adsorption of some solvent types

on the surface. This adsorption could block sites and deactivate the electrode. For metals, one should stay away from aromatic solvents and use only distilled and AC-cleaned isopropanol or dichloromethane. It is beneficial to complete the solvent cleaning by soaking the electrode in warm ultrapure water for about 30 min. In some cases, simply prolonged exposure to an acid solution is sufficient to clean metal surfaces. For example, platinum can be cleaned by simply soaking for 0.5–2 h in highly concentrated sulfuric acid of ultra-high purity ($>1\text{ M H}_2\text{SO}_4$).

5.3.1.4 Laser activation

Laser irradiation has been used by McCreery and coworkers to activate platinum electrodes (132). This involves applying pulses from a Nd:YAG laser (1064 nm) to the electrode immersed in a supporting electrolyte solution. The laser beam diameter is a few mm and output powers of 5–100 MW cm⁻² can be employed. Importantly, the activation was performed in the presence of a few mM of CN⁻ anion. Several researchers have reported that CN⁻ stabilizes k_{app}° for Fe(CN)₆^{3-/4-} by forming an adlayer that prevents electrode deactivation. The deactivation is caused by the decomposition of Fe(CN)₆^{3-/4-} on the bare platinum surface. McCreery and coworkers showed that laser irradiation of platinum exposed to the air in the presence of 5 mM KCN + 1 M KCl produced k_{app}° of 0.5 cm sec⁻¹, or greater. It is presumed that similar laser irradiation of gold would activate this surface for electron transfer as well by a surface cleaning mechanism. However, one would want to avoid contacting the gold with CN⁻ due to the formation of soluble AuCN₄⁻² (i.e., corrosion).

5.3.1.5 Electrochemical polarization

A common method for cleaning platinum and gold electrodes is potential cycling in 0.1 M H₂SO₄ between the oxygen and the hydrogen evolution regimes. This process serves to oxidize contaminants at potentials where the metal oxide layer forms or where water discharge commences (OH[•] radical generation). The potential range for cycling is different for each metal and depends on the pH. For example, the cycling potential window for platinum in acidic media (pH 1) would be between -0.2 and 1.5 V vs. Ag/AgCl. Both metals form stable oxide layers on the anodic potential cycle prior to oxygen evolution that can be fully reduced to the bare metal during the cathodic sweep. Surface roughening occurs during such a cycling treatment and this can influence some measurements, particularly those in which the redox reaction involves an adsorbed state (e.g., oxygen reduction) (133). It should be noted that gold is susceptible to corrosion in the presence of Cl⁻, so care should be taken when using chloride-containing supporting electrolytes.

5.3.2 Single-crystal platinum and gold

Polycrystalline gold and platinum electrodes can be converted into clean, well-ordered single-crystal electrodes by heating the respective wires in an H₂ + O₂ flame. This is the so-called Clavilier method (134–137). Such electrodes are prepared by melting one end of a pure wire (1 mm diameter)—a zone-refining process. The crystallinity of the bead is usually

indicated by faceting that develops. These facets possess well-defined terrace-step structures extending over a large area, as evidenced by STM (138, 139). The single-crystal bead with (1 1 1) facets is oriented by the laser beam deflection method, sealed in epoxy and polished down with alumina grit. The metal is thoroughly solvent cleaned by both rinsing and ultrasonication with the electrode suspended in the solution. Sometimes a heat treatment in an $H_2 + O_2$ flame is performed to remove polishing debris and surface damage. As a final treatment, the electrode is flame annealed and quickly quenched to expose the clean, ordered surface. This is accomplished by heating the metal in an H_2 flame for several seconds and then quickly quenching it in ultrapure water that is purged with H_2 . This is done by having the quenching solution, in a special cell, right below the flame so that the electrode always is exposed to a reducing environment. This cools the electrode to room temperature in an H_2 environment. The electrode is then transferred to an electrochemical cell for use with the surface covered and protected with a droplet of ultrapure water.

5.4 SEMICONDUCTOR ELECTRODES

5.4.1 Indium tin oxide (ITO)

Indium tin oxide (ITO) is a tin-doped In_2O_3 -based n-type wide-bandgap semiconductor (140–144). The two dominant markets for this and other transparent conducting oxides are architectural applications (e.g., energy efficient windows) and flat panel displays. ITO, in particular, has been used extensively for many years in spectroelectrochemical measurements that involved a combined electrochemical and spectroscopic measurement. It is generally thought that the structure of ITO tracks that of the bixbyite lattice with tin incorporated substitutionally for indium to create n-type doping (145). Its attractive properties include high electrical conductivity ($10^{-5} \Omega \text{ cm}$), high optical transparency in the visible (85%), good physical and chemical properties (at least under some conditions), and strong adhesion to many kinds of substrates. For many years, $In_xSn_{1-x}O_2$ and ZnO were the transparent, conducting oxides of focus. However, in recent years, the perception that these materials are sufficient for many applications has begun to change. This is a consequence of the acknowledgement of the limitations of existing materials as well as the realization that new materials can pave the way for new and improved devices (141). Recent work has begun to explore new binary and ternary oxide combinations, including $CdSnO_4$, $ZnSnO_4$, and $ZnIn_2O_5$ (141). It should be mentioned that these new oxides have not yet been used extensively in electroanalysis but may in the future.

The two most common ways of preparing transparent, conducting oxides are RF and DC-magnetron sputtering from an appropriate target. ITO films are often deposited by RF cathode sputtering of a 90% SnO_2 –10% In_2O_3 sintering target in moderate vacuum (10^{-6} Torr) (142). Glass, quartz, and Si are the common substrates. The structural properties, surface roughness, optical transmission, and transport properties of low-temperature-deposited films will depend on the power density, total pressure, oxygen partial pressure flow rate, substrate bias, and anode-to-cathode distance (142). ITO films can also be deposited by DC-magnetron sputtering at room temperature using 10 W of power

and a total pressure of 20 mTorr (0.05% oxygen in argon) (140). Of course, the target must be of an appropriate composition.

5.4.1.1 Mechanical polishing

Polishing the thin-film electrodes is not practical due to the thinness of these layers and the mechanical damage caused by polishing.

5.4.1.2 Solvent cleaning

ITO is probably best activated by solvent cleaning. As described above, soaking the electrode for 20–30 min in isopropanol, cleaned by distillation and exposure to AC, should be effective at cleaning the surface without causing any roughening, bulk oxide reduction, or microstructural damage (21). This pretreatment works by dissolving site-blocking contaminants from the surface. Importantly, the pretreatment only affects the surface cleanliness and does not alter the electronic properties, surface microstructure, or surface chemistry. Solvent cleaning is both an end treatment as well as a good starting point for the further pretreatment of ITO. ITO is stable during exposure to methanol, toluene and hexane but unstable in dichloromethane (146). Upon exposure of ITO to this solvent, isolated film dissolution was observed, which caused an increase in the resistivity and optical transparency.

Another cleaning routinely used is washing the ITO surface with a solution of Triton X-100 (a surfactant) and water (140, 144). Other surfactant solutions might also be used for washing the surface. This is followed up by ultrasonic washing in ultrapure water and ethanol for at least 10 min each.

Donley *et al.* referred to an ITO surface cleaned by the detergent solution as “as received”. They also reported four additional pretreatment/cleaning procedures that were designed to affect both the level of adventitious carbon and the control of the coverage of hydroxide on the surface (140). They adapted a *piranha treatment* that consisted of three steps: (i) heating the ITO in a 10 mM NaOH solution for 4 h at 80 °C, (ii) soaking the ITO in piranha solution (4:1 H₂SO₄/H₂O₂) for 1 min, and (iii) heating the ITO to 160 °C for 2 h. The ITO was rinsed with copious amounts of ultrapure water between each step.

The same authors reported an *RCA treatment* that involved heating the ITO in a 1:1:5 solution of NH₄OH/H₂O₂/H₂O for 30 min at 80 °C. This was followed by a thorough rinsing with ultrapure water and drying with a stream of nitrogen gas.

5.4.1.3 RF plasma treatment

Cleaning by an air plasma treatment can be accomplished using a standard Harrick plasma cleaner (Model PDC-32G) at 60 W and 100–200 mTorr for 15 min. The samples should first be solvent cleaned as described above.

5.4.1.4 Heat treatment

ITO can also be cleaned and activated by vacuum heat treatment. The treatment should be performed in a vacuum that is relatively free of residual oxygen. Relatively low temperatures should be used to avoid desorbing the ITO film from the substrate or decomposing

it. For example, Chaney and Pehrsson cleaned ITO surfaces by heat treatment in UHV at 50 °C (143). Treatment times of 15–30 min should be sufficient. To the best of our knowledge, there has been no systematic study of the effect heat treatment has on the optical, electrical, or electrochemical properties of ITO.

Another similar pretreatment involves argon-ion sputtering for 45 min at 750 eV in the UHV using an argon gas pressure of 10^{-7} Torr (140). These conditions were selected to remove the adventitious carbon and surface hydroxides but not to cause extensive oxide reduction or lattice damage. Before either of these treatments, the samples should first be solvent cleaned as described above.

5.4.1.5 *Electrochemical polarization*

In general, electrochemical polarization can cause surface and bulk chemical changes in ITO as well as significant morphological and microstructural damage. Therefore, this pretreatment is not recommended. The effects of electrochemical polarization on the electrical and optical properties of ITO have been reported (146). In general, anodic polarization in strong acid (1 M HNO₃) or base (1 M NaOH) causes extensive film roughening and some isolated film loss from quartz substrates. Cathodic polarization causes metal reduction and this leads to reduced optical throughput.

5.5 CONCLUSIONS

The field of electroanalytical chemistry is as vibrant as ever today. New platforms for detection and sensing are being developed for a wide variety of chemically, biologically, and environmentally important analytes, and many of these involve some sort of electrochemical signal transduction. At the heart of any electroanalytical method is the working or indicator electrode. These methods are made possible by the unique nature of the specific working electrode material, namely the electronic, structural, and chemical properties. With few exceptions, electrode pretreatment is required for top analytical performance. If the electrode is to be activated optimally and reproducibly, one must have a good understanding of how the above-listed properties are affected by the particular pretreatment method. The goal of any pretreatment is to improve the electron transfer kinetics for the target analyte and to reduce the background signal. This chapter described some of the commonly used protocols for pretreating carbon, metal, and semiconductor electrodes. If a sensitive, reproducible, and stable electrode response is desired, then one must apply the appropriate pretreatment with an understanding of how the pretreatment affects the electrode's physical, chemical, and electronic properties.

ACKNOWLEDGMENTS

The financial support for our work with carbon electrodes over the years from the National Science Foundation, Department of Energy (Office of Energy Science), National Institutes of Health (HLB), and the National Aeronautics and Space Administration is

most appreciated. Some of the work described herein was performed by a talented and enthusiastic group of graduate students (Qingyun Chen, Jishou Xu, Michael Granger, Jian Wang, Maggie Witek, Matt Hupert, Shannon Haymond, Jason Stotter, Prerna Sonthalia, Grace Muna, Jason Bennett, Elizabeth McGaw, Jinwoo Park, and Yang Song).

REFERENCES

1. R. N. Adams, *Electrochemistry at Solid Electrodes*, Marcel Dekker, Inc.: New York, 1968.
2. K. R. Kneten, R. L. McCreery, *Anal. Chem.* **64**, 2518 (1992).
3. K. Kneten-Cline, M. T. McDermott, R. L. McCreery, *J. Phys. Chem.* **98**, 5314 (1994).
4. P. Chen, M. A. Fryling, R. L. McCreery, *Anal. Chem.* **67**, 3115 (1995).
5. P. Chen, R. L. McCreery, *Anal. Chem.* **68**, 3958 (1996).
6. A. Fischer, Y. Show, G. M. Swain, *Anal. Chem.* **76**, 2553 (2004).
7. M. C. Granger, M. A. Witek, J. Xu, J. Wang, M. A. Hupert, A. Hanks, M. D. Koppang, J. E. Butler, G. Lucazeau, M. Mermoux, J. W. Strojek, G. M. Swain, *Anal. Chem.* **72**, 3793 (2000).
8. R. Bowling, R. T. Packard, R. L. McCreery, *Langmuir* **5**, 683 (1989).
9. K. Kinoshita, *Carbon: Electrochemical and Physicochemical Properties*, Wiley: New York, 1988.
10. R. L. McCreery, "Carbon Electrodes: Structural Effects on Electron Transfer Kinetics", in *Electroanalytical Chemistry*, A. J. Bard, Ed., Marcel Dekker, Inc.: New York, 1991, Vol. 17, pp. 221–374.
11. R. L. McCreery, "Carbon Electrode Surface Chemistry", in *Neuromethods, Vol. 27: Voltammetric Methods in Brain Systems*, A. Boulton, G. Baker, R. N. Adams, Eds., Humana Press Inc.: New York, 1995, pp. 1–26.
12. R. L. McCreery, "Electrochemical Properties of Carbon Surfaces", in *Interfacial Electrochemistry*, A. Wieckowski, Ed., Marcel Dekker, Inc.: New York, 1999, pp. 631–647.
13. R. F. Curl, R. E. Smalley, *Science* **242**, 1017 (1988).
14. F. Tunistra, J. L. Koenig, *J. Chem. Phys.* **53**, 1126 (1970).
15. Y. Wang, D. C. Alsmeyer, R. L. McCreery, *Chem. Mater.* **2**, 557 (1990).
16. J. R. Dennison, M. Holtz, G. M. Swain, *Spectroscopy* **11**, 38 (1996).
17. A. A. Gewirth, A. J. Bard, *J. Phys. Chem.* **92**, 5563 (1988).
18. M. T. McDermott, R. L. McCreery, *Langmuir* **10**, 4307 (1994).
19. J. Xu, Q. Chen, G. M. Swain, *Anal. Chem.* **70**, 3146 (1998).
20. B. D. Bath, H. B. Martin, R. M. Wightman, M. R. Anderson, *Langmuir* **17**, 7032 (2001).
21. S. Ranganathan, T.-C. Kuo, R. L. McCreery, *Anal. Chem.* **71**, 3574 (1999).
22. R. J. Rice, R. L. McCreery, *Anal. Chem.* **61**, 1637 (1989).
23. D. T. Fagan, T. Kuwana, *Anal. Chem.* **61**, 1017 (1989).
24. F. Stevens, L. A. Kolodny, T. P. Beebe, Jr., *J. Phys. Chem. B* **102**, 10799 (1998).
25. R. J. Bowling, R. T. Packard, R. L. McCreery, *J. Am. Chem. Soc.* **111**, 1217 (1989).
26. C. A. McDermott, K. R. Kneten, R. L. McCreery, *J. Electrochem. Soc.* **140**, 2593 (1993).
27. D. C. Alsmeyer, R. L. McCreery, *Anal. Chem.* **64**, 1528 (1992).
28. R. C. Engstrom, *Anal. Chem.* **54**, 2310 (1982). R. J. Bowling, R. L. McCreery, C. M. Parr, R. C. Engstrom, *Anal. Chem.* **61**, 2763 (1989).
29. B. Zhang, E. Wang, *Electrochim. Acta* **40**, 2627 (1995).
30. C. A. Goss, J. C. Brumfield, E. A. Irene, R. W. Murray, *Anal. Chem.* **65**, 1378 (1993).
31. M. R. Deakin, K. J. Stutts, R. M. Wightman, *J. Electroanal. Chem.* **182**, 113 (1985).
32. P. L. Runnels, J. D. Joseph, M. J. Logman, R. M. Wightman, *Anal. Chem.* **71**, 2782 (1999).
33. L. J. Kepley, A. J. Bard, *Anal. Chem.* **60**, 1459 (1988).

34. K. F. Burton, *Electrochim. Acta* **18**, 869 (1973).
35. R. E. Panzer, P. J. Elving, *J. Electrochem. Soc.* **119**, 864 (1972).
36. P. J. F. Harris, *Philos. Mag.* **84**, 3159 (2004).
37. G. M. Jenkins, K. Kawamura, *Nature* **231**, 175 (1971).
38. S. Bruckensteiner, J. W. Sharkey, J. Y. Yip, *Anal. Chem.* **57**, 368 (1985).
39. I.-F. Hu, D. H. Karweik, T. Kuwana, *J. Electroanal. Chem.* **188**, 59 (1985).
40. G. W. Hance, T. Kuwana, *Anal. Chem.* **59**, 131 (1987).
41. B. Kazee, D. E. Weisshaar, T. Kuwana, *Anal. Chem.* **57**, 2736 (1985).
42. P. Chen, R. L. McCreery, *Anal. Chem.* **68**, 3958 (1996).
43. K. J. Stutts, P. M. Kovach, W. G. Kuhr, R. M. Wightman, *Anal. Chem.* **54**, 1632 (1983).
44. D. T. Fagan, I.-F. Hu, T. Kuwana, *Anal. Chem.* **57**, 2759 (1985).
45. M. Poon, R. L. McCreery, *Anal. Chem.* **58**, 2745 (1986).
46. C. W. Miller, D. H. Karweik, T. Kuwana, *Anal. Chem.* **53**, 2319 (1981).
47. R. DeClements, G. M. Swain, T. Dallas, M. Holtz, R. D. Herrick, III, J. L. Stickney, *Langmuir* **12**, 6578 (1996).
48. Q. Chen, G. M. Swain, *Langmuir* **14**, 7017 (1998).
49. T.-C. Kuo, R. L. McCreery, *Anal. Chem.* **71**, 1553 (1999).
50. M. C. Granger, G. M. Swain, *J. Electrochem. Soc.* **146**, 4551 (1999).
51. J. Xu, Q. Chen, G. M. Swain, *Anal. Chem.* **70**, 3146 (1998).
52. M. T. McDermott, R. L. McCreery, *Langmuir* **10**, 4307 (1994).
53. R. C. Engstrom, *Anal. Chem.* **54**, 2310 (1982).
54. J. Wang, M. S. Lin, *Anal. Chem.* **60**, 499 (1988).
55. R. M. Wightman, M. R. Deakin, P. M. Kovach, W. G. Kuhr, K. J. Stutts, *J. Electrochem. Soc.: Electrochem. Sci. Technol.* **131**, 1578 (1984).
56. J. Wang, L. D. Hutchins, *Anal. Chim. Acta* **167**, 325 (1985).
57. D. C. Thortnon, K. T. Coby, V. A. Spendel, J. Jordan, A. Robbat, Jr., D. J. Rustrom, M. Gross, G. Ritzler, *Anal. Chem.* **57**, 150 (1985).
58. J. Mattusch, K.-H. Hallmeier, K. Štulil, V. Pacákova, *Electroanalysis* **1**, 405 (1989).
59. A. L. Beilby, T. A. Sasaki, H. M. Stern, *Anal. Chem.* **67**, 976 (1995).
60. J. Kim, X. Song, K. Kinoshita, M. Madou, R. White, *J. Electrochem. Soc.* **145**, 2314 (1998).
61. S. Ranganathan, R. L. McCreery, S. Majji, M. Madou, *J. Electrochem. Soc.* **147**, 277 (2000).
62. S. Ranganathan, R. L. McCreery, *Anal. Chem.* **73**, 893 (2001).
63. N. E. Hebert, B. Snyder, R. L. McCreery, W. G. Kuhr, S. A. Brazil, *Anal. Chem.* **75**, 4265 (2003).
64. R. P. Kalakodimi, A. M. Novak, R. L. McCreery, *Chem. Mater.* **17**, 4939 (2005).
65. R. M. Wightman, *Anal. Chem.* **53**, 1125A (1981).
66. R. M. Wightman, *Science* **240**, 415 (1988).
67. C. Amatore, A. Jutand, F. Pfluger, *J. Electroanal. Chem.* **218**, 361 (1987).
68. I. N. Ermolenko, I. P. Lyubliner, N. V. Gulko, *Chemically Modified Carbon Fibers*, VCH: Germany, 1990.
69. K. T. Kawagoe, J. B. Zimmerman, R. M. Wightman, *J. Neurosci. Methods* **48**, 225 (1993).
70. G. C. Tibbets, *Carbon* **27**, 745 (1989).
71. D. T. Fagan, T. Kuwana, *Anal. Chem.* **61**, 1017 (1989).
72. G. M. Swain, *Activation Studies of Carbon Fiber Electrodes*, Ph.D. Dissertation, University of Kansas, 1991.
73. T. Strein, A. G. Ewing, *Anal. Chem.* **63**, 194 (1991).
74. F. G. Gonon, C. M. Fombarlet, M. J. Buda, J. F. Pujol, *Anal. Chem.* **53**, 1386 (1981).
75. A. G. Ewing, M. A. Dayton, R. M. Wightman, *Anal. Chem.* **53**, 1842 (1981).
76. P. M. Kovach, M. R. Deakin, R. M. Wightman, *J. Phys. Chem.* **90**, 4612 (1986).
77. G. M. Swain, T. Kuwana, *Anal. Chem.* **63**, 517 (1991).

78. G. M. Swain, T. Kuwana, *Anal. Chem.* **64**, 565 (1992).
79. J.-X. Feng, M. Brazell, K. Renner, R. Kasser, R. N. Adams, *Anal. Chem.* **59**, 1863 (1987).
80. S. Iijima, *Nature* **349**, 315 (1982).
81. D. N. Futaba, K. Hata, T. Yamada, K. Mizuno, M. Yumura, S. Iijima, *Phys. Rev. Lett.* **95**, 056104 (2005).
82. H. Dai, *Acc. Chem. Res.* **35**, 1035 (2002).
83. K. Mizuno, K. Hata, T. Saito, S. Ohshima, M. Yumura, S. Iijima, *J. Phys. Chem. B* **109**, 2632 (2005).
84. F. Valentini, A. Amine, S. Orlanducci, M. L. Terranova, G. Palleschi, *Anal. Chem.* **75**, 5413 (2003).
85. J. K. Campbell, L. Sun, R. M. Crooks, *J. Am. Chem. Soc.* **121**, 3779 (1999).
86. G. M. Swain, "Electroanalytical Applications of Diamond Electrodes", in *Thin Film Diamond II*, C. Nebel, J. Ristein, Eds., Elsevier: New York, 2004, pp. 121–148, Chapter 4.
87. G. M. Swain, "Electrically Conducting Diamond Thin-Films: Advanced Electrode Materials for Electrochemical Technologies", in *Electroanalytical Chemistry*, A. J. Bard, I. Rubinstein, Eds., Marcel Dekker, Inc.: New York, 2004, Vol. 22, pp. 182–277.
88. D. Knigge, P. Kaur, G. M. Swain, "Recent Trends in the Chemical Modification of sp² and sp³ Bonded Carbon Electrodes", in *Encyclopedia of Electrochemistry*, A. J. Bard, M. Stratmann, Eds., Wiley-VCH, 2005, Vol. 10.
89. J. C. Angus, C. E. Hayman, *Science* **241**, 913 (1988).
90. F. G. Celi, J. E. Butler, *Annu. Rev. Phys. Chem.* **42**, 643 (1991).
91. A. E. Fischer, Y. Show, G. M. Swain, *Anal. Chem.* **76**, 2553 (2004).
92. Y. Show, M. A. Witek, P. Sonthalia, G. M. Swain, *Chem. Mater.* **15**, 879 (2003).
93. Q. Chen, D. M. Gruen, A. R. Krauss, T. D. Corrigan, M. A. Witek, G. M. Swain, *J. Electrochem. Soc.* **148**, E44 (2001).
94. D. M. Gruen, *MRS Bull.* **23**, 32 (1998).
95. D. M. Gruen, *Annu. Rev. Mater. Sci.* **29**, 211 (1999).
96. T. G. McCauley, D. M. Gruen, A. R. Krauss, *Appl. Phys. Lett.* **73**, 1646 (1998).
97. P. C. Redfern, D. A. Horner, L. A. Curtiss, D. M. Gruen, *J. Phys. Chem.* **100**, 11654 (1996).
98. D. Zhou, D. M. Gruen, L. C. Qin, T. G. McCauley, A. R. Krauss, *J. Appl. Phys.* **84**, 1981 (1998).
99. D. Zhou, T. G. McCauley, L. C. Qin, A. R. Krauss, D. M. Gruen, *J. Appl. Phys.* **83**, 540 (1998).
100. S. Jiao, A. Sumant, M. A. Kirk, D. M. Gruen, A. R. Krauss, O. Auciello, *J. Appl. Phys.* **90**, 118 (2001).
101. S. Bhattacharyya, O. Auciello, J. Birrell, J. A. Carlisle, L. A. Curtis, A. N. Goyette, D. M. Gruen, A. R. Krauss, J. Schlueter, A. Sumant, P. Zapol, *Appl. Phys. Lett.* **79**, 1441 (2001).
102. J. Birrell, J. A. Carlisle, O. Auciello, D. M. Gruen, J. M. Gibson, *Appl. Phys. Lett.* **81**, 2235 (2002).
103. J. Birrell, J. E. Gerbi, O. Auciello, J. M. Gibson, D. M. Gruen, J. A. Carlisle, *J. Appl. Phys.* **93**, 5606 (2003).
104. W. A. Yarbrough, R. Messier, *Science* **247**, 688 (1990).
105. M. Mermoux, B. Marcus, G. M. Swain, J. E. Butler, *J. Phys. Chem. B* **106**, 10816 (2002).
106. D. S. Knight, W. B. White, *J. Mater. Res.* **4**, 385 (1989).
107. M. C. Granger, J. Xu, J. W. Strojek, G. M. Swain, *Anal. Chim. Acta* **397**, 145 (1999).
108. J. A. Bennett, J. Wang, Y. Show, G. M. Swain, *J. Electrochem. Soc.* **151**, E306 (2004).
109. L. H. Robins, E. N. Farabaugh, A. Feldman, *J. Mater. Res.* **5**, 2456 (1990).
110. P. Gonon, E. Gheeraert, A. Deneuville, F. Fontaine, L. Abello, G. Lucaleau, *J. Appl. Phys.* **78**, 7059 (1995).
111. J. W. Ager, III, W. Walukiewicz, M. McCluskey, M. A. Plano, M. I. Landstrass, *Appl. Phys. Lett.* **66**, 616 (1995).
112. H. J. Looi, L. Y. S. Pang, A. B. Molloy, F. Jones, J. S. Foord, R. B. Jackman, *Diam. Relat. Mater.* **7**, 550 (1998).

113. F. Maier, M. Riedel, B. Mantel, J. Ristein, L. Ley, *Phys. Rev. Lett.* **85**, 3472 (2000).
114. A. Denisenko, A. Aleksov, A. Pribil, P. Gluche, W. Ebert, E. Kohn, *Diam. Relat. Mater.* **9**, 1138 (2000).
115. J. Chevallier, B. Theys, A. Lusson, C. Grattepain, A. Deneuville, E. Gheeraert, *Phys. Rev. B* **58**, 7966 (1998).
116. E. Popa, H. Notsu, T. Miwa, D. A. Tryk, A. Fujishima, *Electrochem. Solid-State Lett.* **2**, 49 (1999).
117. U. Stephan, Th. Frauenheim, P. Blaudeck, G. Jungnickel, *Phys. Rev. B* **49**, 1 (1994).
118. K. Yoo, B. Miller, R. Kalish, X. Shi, *Electrochem. Solid-State Lett.* **2**, 233 (1999). Yu. E. Evstefeeva, Yu. V. Pleskov, A. M. Kutsay, I. Bello, *Russ. J. Electrochem.* **41**, 772 (2005).
119. G. Fanchini, S. C. Ray, A. Tagliaferro, *Diam. Relat. Mater.* **12**, 891 (2003).
120. J. Benedikt, R. V. Woen, S. L. M. Van Mensfoort, V. Perina, J. Hong, M. C. M. Van de Sanden, *Diam. Relat. Mater.* **12**, 90 (2003).
121. D. A. LaVan, R. F. Padera, T. A. Friedmann, J. P. Sullivan, R. Langer, D. S. Kohane, *Biomaterials* **26**, 465 (2005).
122. O. Kutsay, I. Bello, Y. Lifshitz, C. W. Lam, W. Y. Luk, S. T. Lee, X. Meng, V. Kremnican, *Diam. Relat. Mater.* **12**, 2051 (2003).
123. W. Y. Luk, O. Kutsay, I. Bello, Y. Lifshitz, C. W. Lam, X. Meng, S. T. Lee, *Diam. Relat. Mater.* **13**, 1427 (2004). J. Robertson, *Diam. Relat. Mater.* **14**, 942 (2005).
124. A. C. Ferrari, J. Robertson, *Philos. Trans. R. Soc. Lond.: Ser. A* **362**, 2477 (2004).
125. S. Piscanec, F. Mauri, A. C. Ferrari, M. Lazzeri, J. Robertson, *Diam. Relat. Mater.* **14**, 1078 (2005).
126. M. P. Soriaga, *Prog. Surf. Sci.* **39**, 325 (1992).
127. J. L. Anderson, N. Winograd, "Film Electrodes", in *Laboratory Techniques in Electroanalytical Chemistry*, 2nd ed., P. T. Kissinger, W. R. Heineman, Eds., Marcel Dekker, Inc.: New York, 1996, p. 333.
128. A. J. Bard, J. A. Crayston, G. P. Kittlesen, T. Varco Shea, M. S. Wrighton, *Anal. Chem.* **58**, 2321 (1986).
129. M. Josowicz, J. Janata, M. Levy, *J. Electrochem. Soc.* **135**, 112 (1988).
130. F. Wagner, P. Ross, *Surf. Sci.* **160**, 305 (1985).
131. T. Yamada, N. Batina, K. Itaya, *Surf. Sci.* **335**, 204 (1995).
132. M. Poon, R. L. McCreery, *Anal. Chem.* **59**, 1615 (1987).
133. S. Motoo, N. Furuya, *J. Electroanal. Chem.* **172**, 339 (1984).
134. J. Clavilier, R. Fame, G. Guisret, R. Durand, *J. Electroanal. Chem.* **107**, 211 (1980). J. Chavilier, *ibid.* **107**, 211 (1980).
135. J. Clavilier, D. Armand, B. L. Wu, *J. Electroanal. Chem.* **135**, 159 (1982).
136. J. Clavilier, A. Rhodes, K. El Achi, M. A. Zamakhchori, *J. Chim. Phys.* **88**, 1291 (1991).
137. J. Clavilier, R. Albalat, R. Gomes, J. M. Orts, J. M. Feliu, *J. Electroanal. Chem.* **360**, 325 (1993).
138. S. Tanaka, S.-L. Yau, K. Itaya, *J. Electroanal. Chem.* **396**, 125 (1995).
139. L. Wan, S.-L. Yau, G. M. Swain, K. Itaya, *J. Electroanal. Chem.* **381**, 105 (1991).
140. C. Donley, D. Dunphy, D. Paine, C. Carter, K. Nebesny, P. Lee, D. Alloway, N. R. Armstrong, *Langmuir* **18**, 450 (2002).
141. D. S. Ginley, C. Bright, *MRS Bull.* **8**, 15 (2000).
142. D. Vaufrey, M. B. Khalifa, J. Tardy, C. Ghica, M. G. Blanchin, C. Sandu, J. A. Roger, *Semicond. Sci. Technol.* **18**, 253 (2003).
143. J. A. Chaney, P. E. Pehrsson, *Appl. Surf. Sci.* **180**, 214 (2001).
144. N. R. Armstrong, A. W. C. Liu, M. Fujihira, T. Kuwana, *Anal. Chem.* **48**, 741 (1976).
145. P. A. Cox, W. R. Flavell, R. G. Egddell, *J. Solid-State Chem.* **68**, 340 (1987).
146. J. Stotter, Y. Show, S. Wang, G. M. Swain, *Chem. Mater.* **17**, 4880 (2005).

This page intentionally left blank

– 6 –

Ultramicroelectrodes

6.1 BEHAVIOR OF ULTRAMICROELECTRODES

Robert J. Forster and Tia E. Keyes

National Centre for Sensor Research, School of Chemical Sciences,
Dublin City University, Ireland

Ultramicroelectrodes (UMEs) are electrodes with characteristic dimensions on the micrometer or sub-micrometer scale. Faster double-layer charging, reduced ohmic loss, and high mass-transport rates have allowed them to revolutionize thermodynamic, kinetic, and electroanalytical measurements (1, 2). These properties have pushed the boundaries of electrochemistry into small length scales, nanosecond timescales, hydrodynamic applications, and environments, such as liquid CO₂ and single biological cells that are not possible using conventional-sized electrodes (3, 4). The currents observed at microelectrodes typically lie in the pA to nA range, which is several orders of magnitude smaller than those observed at conventional macroelectrodes, where the radius is usually several millimeters. These reduced currents are a key element in the successful application of microelectrodes:

- **Unusual media:** Traditionally, electrochemistry suffered relative to spectroscopy because electrochemical measurements could be made only in highly ionic conducting solutions. This restriction arose because resistance between the working or sensing electrode and the reference electrode limited the precision with which the applied potential could be accurately controlled. The small electrolysis currents observed at microelectrodes often completely eliminate these ohmic effects.
- **Small volumes:** Electrochemical methods offer significant advantages over spectroscopy when working with small reactions volumes (e.g., as found in biochips and capillary electrophoresis separation systems). Electron transfer occurs at an electrode surface and the limits of detection are not compromised by a small sample volume. This property contrasts with absorption spectroscopy where the signal intensity depends directly on the path length. Moreover, electrochemistry does not require an optical waveguide to deliver the interrogating light (absorption) or collect the resulting

signal (emission) making the approach less costly to implement in mass diagnostic devices for analytes, such as glucose (diabetes). From a biological perspective, voltammetric measurements have been successfully performed in picoliter vials allowing single cells to be interrogated and reactions to be monitored in extremely small volumes (see Chapter 17).

- **Short timescales:** Many electrochemical events, such as electron and proton transfers, ligand exchanges, isomerizations, and ejection of leaving groups, occur on the microsecond and nanosecond time domains. To achieve a meaningful insight into these redox processes, it must be possible to measure rate constants under a wide range of experimental conditions, such as driving force, temperature, etc. However, conventional electrochemical methods cannot fulfil this role as they are restricted to millisecond, or longer, timescales. Thus, although modern laser-based spectroscopy has provided a powerful new insight into chemical processes that occur on femtosecond timescales, it is only recently that it has been possible to reach megavolts per second scan rates in cyclic voltammetry. For a solution phase reactant, this scan rate corresponds to a time resolution of a few tens of nanoseconds. This capability allows standard potentials and reaction rates of short lifetime intermediates (e.g., electronically excited states) in molecular electrochemistry. Moreover, high-speed electron transfer dynamics (e.g., of self-assembled monolayers) can be measured.

In Sections 6.1 and 6.2, we look in detail at the fundamental properties of microelectrodes, consider some of the practical aspects of using microelectrodes and discuss the experimental factors that influence the choice of electrode size.

6.1.1 Electrode response times

First, we consider the properties of a microelectrode in contact with a solution of pure electrolyte in the absence of a dissolved or immobilized redox active analyte. The objective is to understand the fundamental behavior of microelectrodes in the absence of an electroactive analyte and to discuss strategies for optimizing the electrode's temporal response. The existence of the double-layer capacitance (see Chapter 1) at the working electrode complicates electrochemical measurements at short timescales. Figure 6.1.1.1 is an equivalent circuit of an electrochemical cell where Z_F is the faradaic impedance corresponding to the

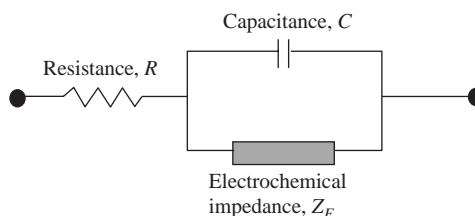


Figure 6.1.1.1 Equivalent circuit for an electrochemical cell and associated electrochemical process.

electrochemical reaction. In seeking to make transient measurements, the electrochemical cell must respond to the applied potential waveform much more rapidly than the process one is seeking to measure. However, the potential across a capacitor cannot be changed instantaneously and the double-layer capacitance must be charged through the solution resistance to change the potential across the faradaic impedance.

The time constant for this charging process is given by equation (6.1.1.1):

$$RC = \frac{\pi r_0 C}{4\kappa} \quad (6.1.1.1)$$

where R is the cell resistance (Ω), C is the total interfacial capacitance (F), r_0 is the electrode radius (cm) and κ is the conductivity of the solution ($S\ cm^{-1}$). The RC time constant is typically hundreds of microseconds for a conventional millimeter-sized electrode placing a lower limit on the useful timescale of the order of several milliseconds. The use of UMEs with critical dimensions in the micron and even nanometer range has opened new possibilities for fast kinetic studies because of the greatly diminished capacitance of these ultrasmall probes.

For an electrode immersed in a dilute solution of supporting electrolyte that does not contain any electroactive species, a charging current, i_c , will flow following a potential step according to equation (6.1.1.2):

$$i_c(t) = \Delta E / R \exp(-t / RC) \quad (6.1.1.2)$$

where ΔE is the magnitude of the potential step.

Figure 6.1.1.2 shows the chronoamperometric (current–time) response for a $10\ \mu m$ radius platinum microelectrode where the supporting electrolyte is aqueous $0.1\ M\ LiClO_4$. This figure shows that current flows for approximately $10\ \mu sec$ due to double-layer

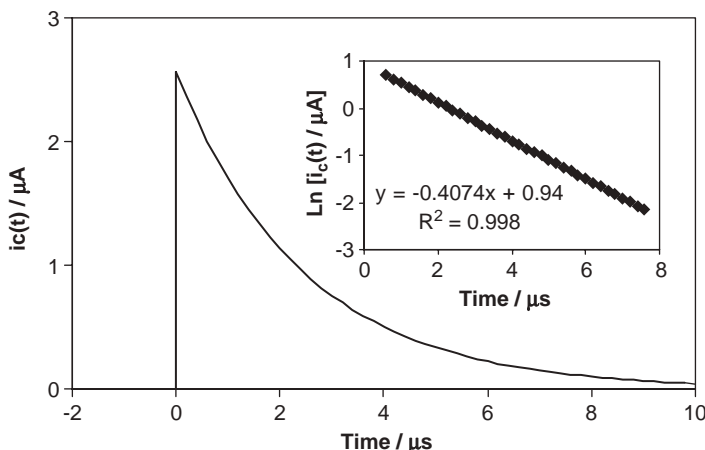


Figure 6.1.1.2 Current–time transient for a $10\text{-}\mu m$ radius platinum microelectrode in contact with an aqueous solution of $0.1\ M\ LiClO_4$ as supporting electrolyte following a potential step from 0.000 to $0.050\ V$. The inset shows the corresponding semi-log current vs. time plot.

charging. Every electrochemical measurement has a lower timescale limit that is imposed by the RC cell time constant (i.e., the product of the solution resistance, R , and the double-layer capacitance, C , of the working electrode). Meaningful electrochemical data can only be extracted at timescales that are longer than the cell time constant, typically 5–10 times the RC time constant (5). Therefore, an important objective when seeking to make transient measurements is to minimize the cell time constant.

Equation (6.1.1.2) indicates that a semi-log plot of the capacitive current vs. time should be linear with slope $1/RC$ and intercept $\ln \Delta E/R$ thus allowing the cell resistance and electrode capacitance to be determined. For the experiment illustrated in Figure 6.1.1.2, a linear semi-log plot is observed indicating that there is a single response time characterizing the electrochemical cell. This behavior is consistent with a clean, unmodified electrode surface and a well-constructed electrode (Section 6.1.3). The measured resistance and capacitance for this $10\text{ }\mu\text{m}$ radius platinum microelectrode are $19,500 \pm 780\text{ }\Omega$ and $1.5 \pm 0.1 \times 10^{-10}\text{ F}$, respectively.

As discussed in detail by Newman (6) and described by equation (6.1.1.3), the solution resistance for a disk-shaped UME is inversely proportional to the electrode radius:

$$R = \frac{1}{4\kappa r_0} \quad (6.1.1.3)$$

Equation (6.1.1.3) shows that R increases as the electrode radius decreases. Taking the conductivity of aqueous 0.1 M LiClO_4 as 1.28 S m^{-1} , equation (6.1.1.3) predicts a theoretical resistance of $19,530\text{ }\Omega$, which is entirely consistent with the experimental result. The resistance can be a useful diagnostic of problems with the electrochemical cell (e.g., as discussed in Section 6.1.3). Surface films and imperfect seals can cause R to increase significantly. An important feature of equation (6.1.1.3) is that changes in the cell resistance with decreasing electrode radius do not have the desired effect of reducing the RC cell time constant.

Altering the potential that is applied to an electrode causes the charge on the metal side of the interface to change and some reorganization of the ions and solvent dipoles in the double layer on the solution side of the interface will occur. This process causes electrons to flow into or out of the surface giving rise to the charging or capacitive response. The double-layer capacitance for a disk-shaped UME is proportional to the area ($A = \pi r_0^2$ for an inlaid disk UME) of the electrode surface and is given by:

$$C = AC_d = \pi r_0^2 C_d \quad (6.1.1.4)$$

where C_d is the specific double-layer capacitance of the electrode. Thus, shrinking the size of the electrode causes the interfacial capacitance to decrease with decreasing r_0^2 . The capacitance determined from the data shown in the inset of Figure 6.1.1.2 is 150 pF . Taken in conjunction with a microscopic area of the $10\text{ }\mu\text{m}$ radius microelectrode of $3.8 \times 10^{-6}\text{ cm}^2$ (roughness of 1.2), this specific capacitance yields an area normalized value of $39.5\text{ }\mu\text{F cm}^{-2}$. This value is typical of that found for a clean platinum surface in contact with a dilute aqueous electrolyte. Surface contamination (e.g., by adventitious organic adsorbates) causes the interfacial capacitance to decrease by as much as a factor of two.

6.1.2 Factors that influence the electrode response time

6.1.2.1 Electrode size

Equation (6.1.1.1) suggests that the electrode response time should decrease with decreasing electrode radius. Figure 6.1.2.1 shows how the RC cell time constant measured in 0.1 M LiClO₄ depends on the radius of platinum microdisk electrodes. Consistent with equation (6.1.1.1), as the electrode radius decreases from 25 to 1 μm , the cell time constant decreases linearly from approximately 2 μsec to 80 nsec. The slope of the best-fit line is consistent with equation (6.1.1.1) where the double-layer capacitance is about 40 $\mu\text{F cm}^{-2}$. Moreover, the intercept is approximately 4.3 nsec indicating that the stray capacitance (Section 6.1.3.3) of these microelectrodes is very small. Thus, cell time constants of tens of nanoseconds can be achieved with UMEs of micron radii.

6.1.2.2 Electrolyte concentration

The overall cell resistance influences the cell time constant. Therefore, decreasing the resistance of the solution, through which the faradaic and charging currents must flow, will decrease the cell time constant. Figure 6.1.2.2 illustrates the decrease in cell time constant that is observed for a 5- μm radius platinum microdisk as the solution conductivity is systematically varied by changing the supporting electrolyte concentration from 0.05 to 2.0 M. As predicted by equation (6.1.1.1), this figure shows that a linear response is obtained and the specific double-layer capacitance is estimated as $41.7 \pm 2.1 \mu\text{F cm}^{-2}$ over this range of supporting electrolyte concentrations. Figures 6.1.2.1 and 6.1.2.2 indicate that microdisk electrodes can be manufactured that respond ideally to changes in the

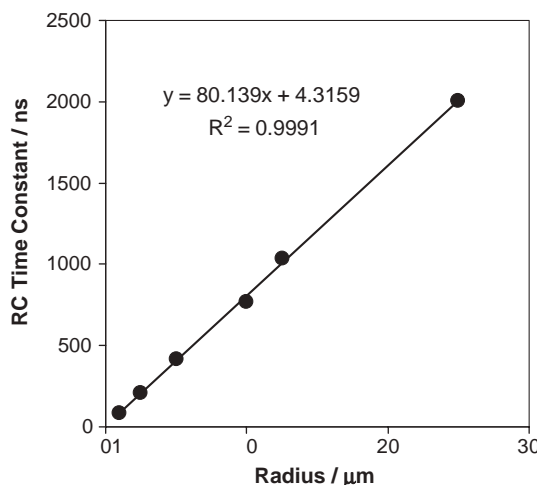


Figure 6.1.2.1 Relationship between the RC cell time constant and the radius of platinum microdisks where the supporting electrolyte is 0.1 M HCl. Cell time constants were measured using chronoamperometry conducted on a microsecond to sub-microsecond timescale by stepping the potential from 0.200 to 0.250 V vs. Ag/AgCl.

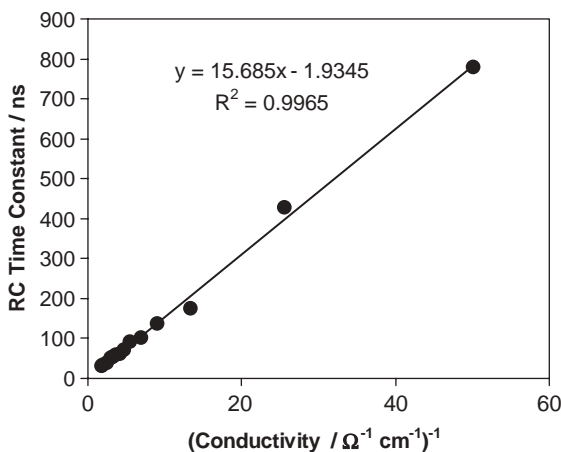


Figure 6.1.2.2 Relationship between the *RC* cell time constant of a 5-μm radius platinum microdisk and the reciprocal of the solution conductivity. Cell time constants were measured using chronoamperometry conducted on a microsecond to sub-microsecond timescale by stepping the potential from 0.200 to 0.250 V vs. Ag/AgCl.

applied potential at timescales as short as 30 nsec. Experiments performed in more conducting solutions (e.g., highly concentrated acids) indicate that *RC* cell time constants as short as 5 nsec can be achieved.

However, there are a number of practical problems associated with the design and fabrication of microelectrodes that cause micron-sized electrodes to have *RC* time constants that greatly exceed those predicted by equation (6.1.1.1).

6.1.3 Origins of nonideal responses

6.1.3.1 Electrode geometry problems

A challenge in this field is to reproducibly manufacture perfect microdisk electrodes. This is especially difficult when the radius of the microwire is less than 2 μm. Figure 6.1.3.1 illustrates some the most common structural nonidealities that can occur. Figure 6.1.3.1B illustrates an elliptical electrode caused by the wire sealing at an angle within the insulator. Figure 6.1.3.1C shows a protruding, irregular cylindrical electrode caused either by insufficient mechanical polishing or because the electrode material is very much softer than the insulator. In contrast, when the electrode material is soft (e.g., gold), it is possible to polish the working electrode to a lower level than the surrounding insulator thus creating a recessed electrode in which the opening in the insulator is of same size (Figure 6.1.3.1D), or larger than the microdisk size (Figure 6.1.3.1E). Figure 6.1.3.1F illustrates the imperfect seals that can result when heat-sealing microwires within an insulator (e.g., glass), if the thermal coefficients of expansion of the insulator and wire are not closely matched. Similarly, failure to adequately clean both the insulators and microwires can lead to imperfect seals. Table 6.1.3.1 indicates the changes in the resistance and capacitance expected for each of these nonideal electrode geometries.

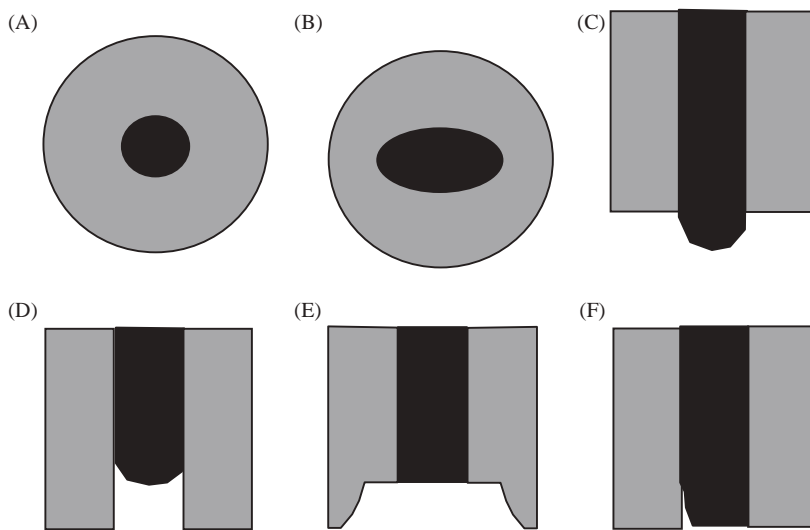


Figure 6.1.3.1 Different shapes of ultramicroelectrodes (UMEs). (A) A perfect microdisk electrode. (B) A conical disk-type planar UME due to sealing of the microwire at an angle relative to the insulating shroud. (C) An irregular cylindrical protruding from the insulator. (D) A recessed microdisk electrode. (E) A recessed electrode in which the cavity in the insulator is large than the microwire. (F) A leaky UME due to an imperfect wire-insulator seal.

Table 6.1.3.1

Effect of nonideal microelectrode geometry on resistance and capacitance^a

Geometry	R (Ω)	C ($\mu\text{F cm}^{-2}$)	Comment
Elliptical (1B)	↗	↑	Capacitance increases but resistance decreases relative to ideal due to increased electrode area.
Protruding (1C)	↘	↑	Capacitance increases relative to ideal due to increased effective electrode area.
Microcavity/lagooned (1D)	↑	→	Resistance typically increases significantly relative to ideal due to difficulties of ion mass transport within pore.
Recessed (1E)	↑	→	Resistance may increase moderately but diagnostic abilities of chronoamperometry are limited.
Imperfect seal (1F)	↑	↑	Resistance and capacitance both very significantly larger than ideal.

^aA common feature of nonideal geometry is that the capacitive current–time response following a potential step fails to decay according to a single exponential.

6.1.3.2 Surface impurities

For electrodes with radii in the micrometer range, scanning electron microscopy (SEM) provides a useful insight into the geometry of the structure formed. However, surface charging is often a difficulty even when the electrode itself is grounded and for smaller

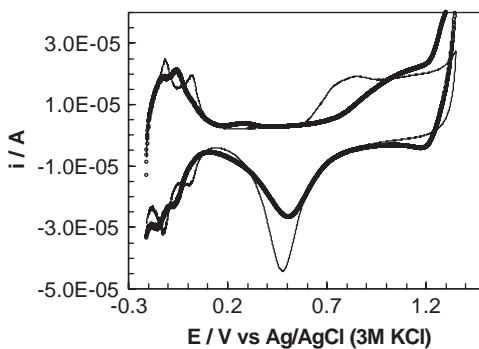


Figure 6.1.3.2 Cyclic voltammograms for a polished platinum microelectrode. The solid black line is obtained in 0.5 M H₂SO₄ (99.999%). The thick line/open circles show the effect of chloride contamination at a nanomolar concentration. Note that reduction currents are negative and oxidation currents positive in this figure.

microelectrodes, it may be necessary to destructively dissolve the insulator to expose the microwire. Even when it has been established that a close to ideal geometry microelectrode has been created, the observed resistance and capacitance behavior may deviate significantly from that predicted by theory. In particular, imperfect surface cleanliness (e.g., due to adventitiously adsorbed organics) can cause lower capacitance values and nonsingle exponential current–time transients to be observed. Electrochemical cleaning by cycling in dilute sulfuric acid represents a useful approach to producing pristine surfaces in an experimentally accessible way. Figure 6.1.3.2 illustrates two cyclic voltammograms for a 10 μm radius platinum microelectrode when electrochemically cycled in 0.1 M H₂SO₄ to create an oxide monolayer that is subsequently reduced. It is important to restrict the potential window and to avoid excessive cycling so as to prevent bulk oxidation of the metal. The microscopic or “real” area of the electrode can be determined by measuring the charge passed during the reduction of the surface oxide monolayer at approximately 0.600 V or the hydrogen adsorption/desorption peaks at approximately −0.200 V. To produce a clean electrode surface, the purity of the electrolyte significantly affects the voltammetry obtained. As illustrated in Figure 6.1.3.2, in 99.999% pure sulfuric acid, well-defined oxide monolayer formation and reduction, double layer, and hydrogen adsorption and desorption regions are observed. However, the presence of chloride even at nanomolar concentrations (e.g., arising from electrolyte leakage from the reference electrode) makes the oxide monolayer formation ill-defined, shifts the hydrogen adsorption/desorption potentials, and causes the double-layer region (expected between approximately 0.08 and 0.20 V) to be either significantly diminished or totally absent.

6.1.3.3 Experimental setup: stray capacitance

One cause of a nonideal response is stray capacitance within the electrochemical system that may arise from the electrode itself, the leads, or the electrical connections. Stray capacitance will increase the cell time constant as described by equation (6.1.3.1).

$$RC = \frac{1}{4\kappa r}(\pi r_0^2 C_0 + C_{\text{Stray}}) \quad (6.1.3.1)$$

where C_{stray} is the stray capacitance. Although it depends on the microelectrode design and the experimental setup, this stray capacitance is typically between a few pF and several tens of pF. The cell time constant observed in these circumstances depends strongly on the relative magnitudes of the double layer and stray capacitances. At a normal-size electrode, the stray capacitance is negligible compared with the double-layer capacitance, and therefore, does not significantly affect the observed cell time constant. However, when the magnitude of the double-layer capacitance is reduced by shrinking the size of the electrode to micron and sub-micron dimensions, the stray and double-layer capacitances can become comparable. For example, taking a typical value of $40 \mu\text{F cm}^{-2}$ as the specific double-layer capacitance for a platinum electrode in contact with 1 M aqueous electrolyte solution, the double-layer capacitance of a 1 mm radius disk will be approximately 1 μF . This value is very significantly larger than the pF stray capacitance found in a typical electrochemical experiment. However, for a 1- μm radius microdisk, the interfacial capacitance will decrease by six orders of magnitude to approximately 1 pF. Therefore, stray capacitance of even a few pF will cause the observed RC time constant to increase significantly beyond the minimum value dictated by double-layer charging alone. This increased cell time constant will cause the transient response characteristics of the electrodes to become nonideal. Thus, an objective in implementing ultrafast transient techniques is to minimize the stray capacitance.

Two major sources of stray capacitance are: (i) the capacitance of the cell leads and capacitive coupling between leads, and (ii) the microelectrode itself. By using high-quality cable of minimum length (e.g., by mounting the current-to-voltage converter directly over the electrochemical cell) and by avoiding the use of switches as far as possible, stray capacitance from the electrochemical system can be minimized. However, the importance of good microelectrode fabrication and design should not be overlooked. For example, if there is a small imperfection in the seal between the insulator and the electrode material, then solution leakage will cause the RC cell time constant to increase massively and the faradaic response may become obscured by charging/discharging processes. Moreover, using silver epoxy or mercury to make the electrical connection between the microwire and a larger hook-up wire can cause the RC cell time constant to increase dramatically (7, 8). This increase arises because the electronically conducting mercury/glass insulator/ionically conducting solution junctions cause significant stray capacitance. It is important to note that these effects may only become apparent in high-frequency measurements.

6.1.3.4 Ohmic effects

When faradaic and charging currents flow through a solution, they generate a potential that acts to weaken the applied potential by an amount, iR , where i is the total current. This is an undesirable process that leads to distorted voltammetric responses. It is important to note that, as described by equation (6.1.1.3), the cell resistance *increases* with *decreasing* electrode radius. Thus, the ohmic drop is not reduced at microelectrodes relative to macroelectrodes because of reduced resistance. However, the capacitive or double-layer charging current depends on the electrode area or r_0^2 . Similarly, for reversible redox reactions under semi-infinite diffusion control, the faradaic current depends on the electrode area. This sensitivity to area means that the currents observed at microelectrodes are typically six orders of magnitude smaller than those observed at

macroelectrodes. These small currents often completely eliminate ohmic drop effects even when working in organic solvents. For example, the steady-state current observed at a 5- μm radius microdisk is approximately 2 nA for a 1.0-mM solution of ferrocene. Taking a value of 0.01 $\Omega^{-1} \text{ cm}^{-1}$ as the specific conductivity, then equation (6.1.1.3) indicates that the resistance will be of the order of 50,000 Ω . This analysis suggests that the iR drop in this organic solvent is a negligible 0.09 mV. In contrast, for a conventional macroelectrode, the iR drop would be of the order of 5–10 mV. Under these circumstances, distorted current responses and shifted peak potentials would be observed in cyclic voltammetry.

It is useful at this point to discuss the effect of experimental timescale on the iR drop observed at microelectrodes. In the following section, we discuss how the diffusion field at microelectrodes depends on the characteristic time of the experiment. In general, at short times, the dominant mass transport mechanism is planar diffusion and the microelectrode behaves like a macroelectrode. Therefore, at short times, the current i decreases with decreasing electrode area (r_0^2). As the resistance increases with decreasing electrode radius rather than electrode area, the product iR decreases with decreasing electrode radius in short timescale experiments. Thus, beyond the reduced iR drop because of low currents, decreasing the electrode radius from say 1 mm to 10 μm decreases the ohmic iR drop observed at short times by a factor of 100. In contrast, at long experimental timescales, the faradaic current depends directly on the radius making the product iR independent of the electrode radius and a constant value, which is inversely proportional to the solution conductivity.

6.1.4 Fundamentals of faradaic electrochemistry

Oxidation or reduction of a redox-active species at an electrode surface generates a concentration gradient between the interface and the bulk solution. This redox process requires electron-transfer across the electrode/solution interface. The rate at which electron transfer takes place across the interface is described by the heterogeneous electron-transfer rate constant, k . If this rate constant is large, then diffusional mass transport will control the current observed. Our objective is to describe how these diffusion fields evolve in time and then to look at experimental parameters that influence the ideality of the response. The experiment of interest involves stepping the potential from an initial value where no electrode reaction occurs, to one where electrolysis proceeds at a diffusion-controlled rate. We consider the case of a spherical electrode of radius r_s placed in a solution that contains only supporting electrolyte and a redox-active species of concentration C^* . The concentration gradient at the electrode surface is obtained by solving Fick's second law in spherical coordinates:

$$\frac{\partial C(r,t)}{\partial t} = D \left[\frac{\partial^2 C(r,t)}{\partial r^2} + \frac{2}{r} \frac{\partial C(r,t)}{\partial r} \right] \quad (6.1.4.1)$$

The boundary conditions for the potential step experiments described above are:

$$\lim_{r \rightarrow \infty} C(r,t) = C^\infty$$

$$C(r,0) = C^\infty$$

$$C(r,t) = 0 \text{ for } t > 0$$

where r is the distance from the center of the sphere, D is the diffusion coefficient for the redox active species, and C is the concentration as a function of distance r and time t .

Equation (6.1.4.1) can be solved using Laplace transform techniques to give the time evolution of the current, $i(t)$, subject to the boundary conditions described. Equation (6.1.4.2) is then obtained:

$$i(t) = \frac{nFADC^\infty}{r_s} + \frac{nFAD^{1/2}C^\infty}{\pi^{1/2}t^{1/2}} \quad (6.1.4.2)$$

where n is the number of electrons transferred in the redox reaction, F is Faraday's constant, and A is the geometric electrode area.

Equation (6.1.4.2) shows that the current response following a potential step contains both time-independent and time-dependent terms. The differences in the electrochemical responses observed at macroscopic and microscopic electrodes arise because of the relative importance of these terms at conventional electrochemical timescales. It is possible to distinguish two limiting regimes depending on whether the experimental timescale is short or long.

6.1.4.1 Short times

At sufficiently short times, the thickness of the diffusion layer that is depleted of reactant is much smaller than the electrode radius and the spherical electrode appears to be planar to a molecule at the edge of this diffusion layer. Under these conditions, the electrode behaves like a macroelectrode and mass transport is dominated by linear diffusion to the electrode surface as illustrated in Figure 6.1.4.1A.

At these short times, the $t^{-1/2}$ dependence of the second term in equation (6.1.4.2) makes it significantly larger than the first and the current response induced by the potential step initially decays in time according to the Cottrell equation (Chapter 11):

$$i(t) = \frac{nFAD^{1/2}C^\infty}{\pi^{1/2}t^{1/2}} \quad (6.1.4.3)$$

Figure 6.1.4.2 shows the relationship that exists between the range of useable scan rates and electrode radius subject to the condition that ohmic drop is negligible and that the dominant mass transport regime is linear diffusion (9).

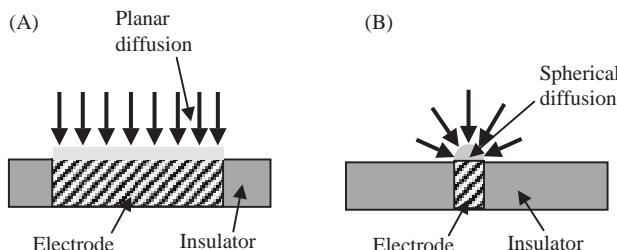


Figure 6.1.4.1 Diffusion fields observed at microelectrodes. (A) Linear diffusion observed at short times. (B) Radial (convergent) diffusion observed at long times.

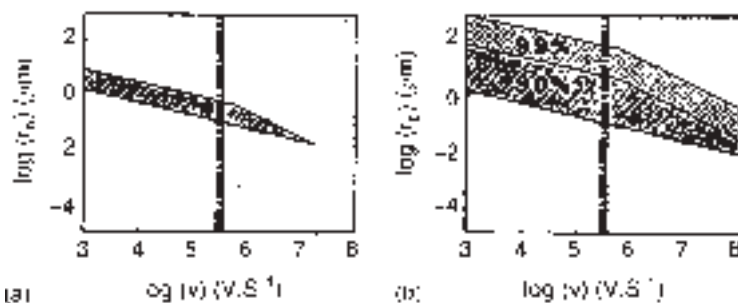


Figure 6.1.4.2 Theoretical limitations on ultrafast cyclic voltammetry. The shaded area between the slanted lines represents the radius that a microdisk must have if the ohmic drop is to be less than 15 mV and distortions due to nonplanar diffusion account for less than 10% of the peak current. (a) Without iR drop compensation by positive feedback, and (b) with 90 and 99% ohmic drop compensation. The dotted area in (a) and (b) represent the regions where transport within the double layer affects the voltammetric response. Limits are indicative and correspond approximately to a 5-mM anthracene solution in acetonitrile, 0.3 M tetrafluoroborate as supporting electrolyte. [Reproduced by permission of Marcel Dekker from C. Amatore, *Electrochemistry at Microelectrodes*, I. Rubenstein, Ed., 1995, Chapter 4, p. 198.]

6.1.4.2 Long times

At long times, the transient contribution given by the second term of equation (6.1.4.3) has decayed to the point where its contribution to the overall current is negligible. At these long times, the spherical character of the electrode becomes important and the mass transport process is dominated by radial (spherical) diffusion as illustrated in Figure 6.1.4.1B.

The current attains a time-independent steady-state value given by equation (6.1.4.4) for a spherical electrode.

$$i_{ss} = \frac{nFADC^\infty}{r_s} = 4\pi nFDC^\infty r_s \quad (6.1.4.4)$$

The steady-state response arises because the electrolysis rate is equal to the rate at which molecules diffuse to the electrode surface.

As “short” and “long” times are relative terms, it is useful to determine the times over which transient and steady-state behaviors will predominate and how this time regime is affected by the electrode radius.

This objective can be achieved by considering the ratio of the transient to steady-state current contributions (equations (6.1.4.3) and (6.1.4.4), respectively). This analysis gives a dimensionless parameter $(\pi Dt)^{1/2}/r_s$ that can be used to calculate a lower time limit at which the steady-state contribution will dominate the total current to a specified extent. For example, one can calculate the time required for the steady-state current contribution, i_{ss} , to be 10 times larger than the transient component, i_t . Taking a typical value of D as $1 \times 10^{-5} \text{ cm}^2 \text{ sec}^{-1}$ for an aqueous solution, for an electrode of radius 5 mm, the experimental timescale must be longer than 80 sec. Therefore, steady state is not observed for

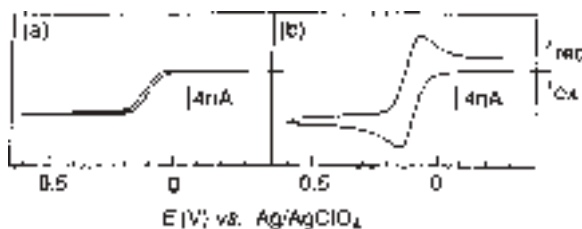


Figure 6.1.4.3 Effect of scan rate on the cyclic voltammetry of 1.0 mM ferrocene at a 6.5- μm gold microdisk where the supporting electrolyte is 0.1 M tetrabutyl ammonium perchlorate in acetonitrile. (a) Scan rate is 0.1 V sec^{-1} ; (b) scan rate is 10 V sec^{-1} . [Reproduced with permission from J. O. Howell, R. M. Wightman, *Anal. Chem.* **56**, 524 (1984). Copyright 1984, American Chemical Society.]

macroelectrodes at the tens of mV sec^{-1} timescale typical of conventional cyclic voltammetry experiments. However, reducing the electrode radius by a factor of a thousand to 5 μm , means that a steady-state response can be observed for times longer than 80 μsec . As the steady-state current becomes more dominant with increasing time, steady-state responses are easily observed for microelectrodes in electrochemical experiments run at conventional timescales. Figure 6.1.4.3A shows the sigmoidal-shaped responses that characterize steady-state mass transfer in slow scan-rate cyclic voltammetry. In contrast, at short experimental timescales (high scan rates), peaked responses (Figure 6.1.4.3B) similar to those observed at conventional macroelectrodes are seen. There is no theoretical barrier to observing steady-state behavior for any size of the electrode. However, for conventional millimetre dimensioned macroelectrodes, the time taken ($>10,000$ sec) is far too long to be experimentally practical. Moreover, unintentional convection (e.g., because of building vibrations) will play an important role in the mass transport process at these long timescales.

The preceding analysis considered a spherical electrode because its surface is uniformly accessible, and a simple closed-form solution to the diffusion equation exists (10). The microdisk is the most widely used geometry, but derivation of rigorous expressions describing their experimental response is complicated because the surface is not uniformly accessible. For disks, electrolysis at the outer circumference of the disk diminishes the flux of the electroactive material to the center of the electrode. However, microdisk and microring geometries share the advantage of spherical microelectrodes in that quasi-spherical diffusion fields are established in relatively short periods of time. The steady-state limiting current obtained from these rigorous derivations is given by:

$$i_{ss} = \gamma nFDC * r_0 \quad (6.1.4.5)$$

where γ is a shape parameter, which is 4 for a disk electrode. Consistent with equation 6.4.4.4, γ is 4π for a spherical electrode and 2π for a hemispherical electrode.

Observing a steady-state response depends on all the electrode dimensions being small, not just the radius, and is, therefore, not achieved for every geometry at the timescales considered above. For example, band electrodes whose thickness is in the micrometer range, but whose length is several millimeters, do not exhibit true steady-state responses.

However, a high analyte flux to the ends of the band often makes it possible to observe a pseudo-steady-state condition in a practical sense.

Radial diffusion gives very high rates of mass transport to the electrode surface with a mass transport coefficient of the order of D/r . Therefore, even at rotation rates of 10^4 rpm, convective transport to a rotating macroelectrode is smaller than diffusion to a 1- μm microdisk. The high flux at a microelectrode means that one does not observe a reverse wave under steady-state conditions (Figure 6.1.4.3A), because the electrolysis product leaves the diffusion layer at an enhanced rate.

6.1.5 Origins of nonideal faradaic responses

6.1.5.1 Electrode area effects

Capacitive currents are generated by events occurring within very small distances from an electrode surface and their magnitude is controlled by the microscopic area of the electrode. In most electrochemical experiments designed to probe the redox properties of solution phase reactants, the timescale of the measurement is often such that the diffusion layer is several times larger than the critical dimension (e.g., radius) of the microelectrode. For example, the depletion layer thickness, δ , can be estimated as:

$$\delta = (\pi D t)^{1/2} \quad (6.1.5.1)$$

where D is the diffusion coefficient of the electroactive species ($\text{cm}^2 \text{ sec}^{-1}$) and t is the experimental timescale (sec). Given a characteristic diffusion coefficient of $10^{-5} \text{ cm}^2 \text{ sec}^{-1}$, equation (6.1.5.1) reveals that the depletion layer thickness will exceed the 10 μm radius of a typical microelectrode within approximately 32 msec, which corresponds to a scan rate slower than approximately 0.8 V sec $^{-1}$ in cyclic voltammetry (see Chapter 11). Typically, electrodes are prepared by mechanical polishing using small particle size (0.05 μm) alumina or diamond paste and the microscopic area can be a factor of two larger than the geometric one. Therefore, at the timescales usually used in electrochemical experiments, the depletion layer thickness will be much larger than the scale of roughness of a polished electrode and the electrode appears flat to molecules approaching the electrode surface.

The short RC time constants possible with microelectrodes facilitates electrochemical measurements at short timescales. For example, in a chronoamperometry experiment conducted at a nanosecond timescale, the depletion layer thickness will be of the order of a few hundred nanometers thick, which may be comparable with the length scale of the surface roughness. Under these circumstances, the depletion layer will tend to follow the structural contours of the microscopically rough surface and the area of the depletion layer will generally be larger than the geometric area. Such effects are important for electrodes partially covered by a blocking layer (e.g., due to poor fabrication) with pinholes through which the electroactive species may access the electrode surface. At short timescales, the diffusion layer thickness is small compared with the size of the active region and a depletion region will be established at each active region. The area of the overall diffusion field is the sum of the geometric areas of the individual active spots. At longer times, the

individual depletion zones begin to extend beyond the active regions, and linear diffusion is augmented by a radial component. For sufficiently long reaction times, the individual depletion layers become much thicker than the distances between the active regions and a single merged depletion layer covering the entire electrode surface (i.e., both active and inactive regions) is formed. The current response is now once again controlled by semi-infinite linear diffusion and the current magnitude is controlled by the geometric area of the electrode. Similar evolutions in the diffusion field from semi-infinite linear to radial and back to semi-infinite linear are observed when using a lithographically defined microelectrode arrays (see Chapter 10) consisting of an ensemble of nonindependently addressable electrodes or when the electrode is a composite material based on immobilizing conducting particles (e.g., graphite) within an insulating phase (e.g., a polymer) (see Chapters 10 and 16).

6.1.5.2 Surface contamination

The electron transfer kinetics (see Chapters 1 and 15), and current response of redox-active species can be dramatically affected by the surface condition of the working electrode. This sensitivity to surface contamination arises because the rate of heterogeneous electron transfer decreases exponentially with increasing distance. Pretreatment of the electrode surface is often necessary to obtain reproducible results. Typically, a microelectrode is polished with successively smaller particle size abrasive (e.g., 12.5, 5, 1, 0.3, and 0.05 μm alumina or diamond paste) so as to achieve a mirror finish. The progression of polishing should always proceed from coarse to fine abrasive, with thorough rinsing and a change of polishing pads between each step. Fabric pads attached to glass plates are typically used as the platform onto which the polishing suspensions are applied. Thorough rinsing is required after each polishing and the electrodes polished using 0.05 μm alumina should be ultrasonically cleaned in deionized water for a few minutes, to remove any residual alumina.

Although mechanical polishing may provide a sufficiently clean electrode for many applications, cleaner surfaces can be produced by treating the surface with piranha solution or through electrochemical cleaning. Piranha solutions are used to remove organic residues from substrates, particularly in microfabrication labs. The traditional piranha solution is a 3:1 mixture of sulfuric acid and 30% hydrogen peroxide. The solution may be mixed before application or directly applied to the material, applying the sulfuric acid first, followed by the peroxide. (*Caution: Piranha solutions are extremely energetic and may result in explosion or skin burns if not handled with extreme caution.*) Electrochemical cleaning represents a useful alternative and provided that care is taken with the potential limits and the number of cycles to prevent surface roughening, it not only generates clean surfaces but also provides the microscopic area. In a typical application, the electrode is cycled in 0.1 M HClO_4 by cycling between potential limits chosen to initially oxidize, and subsequently to reduce the surface of the platinum electrode. The potential is then held in the double-layer region to ensure complete reduction of any surface oxide and desorption of the hydrogen. After use, it may be sufficient to rinse the electrode surface with water and/or methanol, followed by air drying to remove adsorbed species and to ensure that the working electrode is in pristine condition. Otherwise, repolishing may be required.

6.1.5.3 Instrumental challenges

A challenge in using microelectrodes is the ability to measure very low currents (down to femto ampere, 10^{-15} A). Measuring small currents is a particular challenge when the experimental timescale is short (e.g., tens of nanoseconds are accessible using micrometer dimensioned electrodes). For example, taking values of 100 μM and $1 \times 10^{-5} \text{ cm}^2 \text{ sec}^{-1}$ for the concentration and diffusion coefficient, respectively, the steady-state current is of the order of 200 pA for a 5- μm radius microdisk. As described by equation (6.1.4.4), the magnitude of this current will decrease with decreasing electrode radius and femtoampere currents (i.e., approximately 6000 electrons transferred per second!) will be observed for a 10-nm radius electrode. Thus, in some microelectrode experiments, potentiostats work close to the capabilities of contemporary electronics.

Consider the equivalent circuit shown in Figure 6.1.5.1 in which the objective is to measure the cell impedance given by Z_{cell} .

This circuit includes several components associated with both the electrochemical cell itself and measuring electronics. For example, the parasitic resistance and capacitance (e.g., arising from leads, switches, etc.) in the cell are described by $R_{p,\text{cell}}$ and $C_{p,\text{cell}}$, respectively, while the stray input resistance and capacitance of the measurement circuit are denoted as R_{in} and C_{in} , respectively. In the ideal current measurement circuit, R_{in} is infinite, while C_{in} and I_{in} are zero and all the current generated in the cell flows through the resistance of the measuring circuit, R_m . To measure the small currents generated at microelectrodes, R_m needs to be large (hundreds of k Ω to many M Ω). With an ideal cell and voltage source, $R_{p,\text{cell}}$ is infinite and $C_{p,\text{cell}}$ is zero and all of the current flowing into the current measurement circuit is due to Z_{cell} . The voltage developed across R_m is measured by the meter as V_m and Z_{cell} and is given by:

$$Z_{\text{cell}} = E_s R_m / V_m \quad (6.1.5.2)$$

As described by equation (6.1.5.2), the contribution from the electrode resistance to Z_{cell} increases with decreasing electrode radius and the total cell impedance can become very large. The precision with which high-impedance measurements can be made is limited for several reasons including: (a) current measurement circuits always have nonzero input capacitance, (b) an infinite input resistance cannot be achieved with real

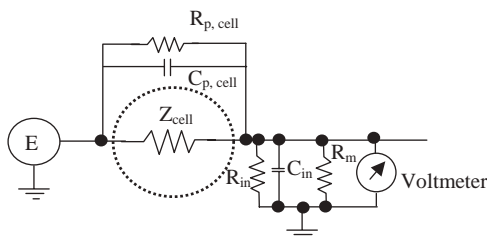


Figure 6.1.5.1 Equivalent circuit of the electrochemical cell and potentiostat measuring circuit incorporating nonideal elements.

circuits, and (c) the amplifiers used in the meter need a small but tangible input current, i.e., $I_{in} > 0$. For example, the best commercially available input amplifiers have input currents of around 50 fA, making it impossible to make absolute current measurements (DC signal) of low fA currents. Also, as discussed in Section 6.1.5c, the cell, potentiostat, and leads all contribute to parasitic resistance and capacitance components. In particular, the stray capacitance reduces the frequency or time domain over which meaningful electrochemical data can be obtained. In seeking to push the boundaries of time and media in which electrochemical measurements can be performed, fundamental physics is now influencing the experimental outcome. For example, Johnson noise associated with thermal agitation of electrons gives rise to a random fluctuation in the voltage across the resistor terminals, which may limit ultrahigh frequency, short timescale, and measurements.

REFERENCES

1. R. J. Forster, *Chem. Soc. Rev.* **23**, 289 (1994).
2. J. Heinze, *Angew. Chem. Int. Ed. Engl.* **32**, 1268 (1993).
3. B. B. Katemann, A. Schulte, E. J. Calvo, M. Koudelka-Hep, W. Schuhmann, *Electrochim. Commun.* **4**, 134 (2002).
4. J. C. Eklund, A. M. Bond, *Adv. Phys. Org. Chem.* **31**, 1 (1999).
5. A. J. Bard, L. R. Faulkner, *Electrochemical Methods: Fundamentals and Applications*, Wiley: New York, 1980.
6. J. J. Newman, *Electrochim. Soc.* **113**, 501 (1968).
7. D. O. Wipf, A. C. Michael, R. M. Wightman, *J. Electroanal. Chem.* **15**, 269 (1989).
8. L. R. Faulkner, M. R. Walsh, C. Xu, in *Contemporary Electroanalytical Chemistry*, A. Ivaska, Ed., Plenum Press: New York, 1990, p. 5.
9. W. J. Bowyer, E. E. Engelman, D. H. Evans, *J. Electroanal. Chem.* **67**, 262 (1989).
10. C. Amatore, B. Fosset, *Anal. Chem.* **68**, 4377 (1996).

6.2 MICROELECTRODE APPLICATIONS

The properties and applications of microelectrodes, as well as the broad field of electroanalysis, have been the subject of a number of reviews. Unwin reviewed the use of dynamic electrochemical methods to probe interfacial processes for a wide variety of techniques and applications including various flow-channel methods and scanning electrochemical microscopy (SEM), including issues relating to mass transport (1). Williams and Macpherson reviewed hydrodynamic modulation methods and their mass transport issues (2). Eklund et al. reviewed cyclic voltammetry, hydrodynamic voltammetry, and sonovoltammetry for assessment of electrode reaction kinetics and mechanisms with discussion of mass transport modelling issues (3). Here, we focus on applications ranging from measurements in small volumes to electroanalysis in electrolyte free media that exploit the unique properties of microelectrodes.

6.2.1 Electroanalysis at the micro- and nano-length scale

Microelectrodes have played an important role in the movement of analytical chemistry toward small-volume techniques as well as real time and spatially resolved measurement-techniques. The advantages of microelectrodes are exploited in many areas of electroanalysis, including environmental, biomedical, and material science areas. It is now possible to obtain electrochemical information at length scales ranging from meters to micrometers and even nanometers (4). As illustrated in Figure 6.2.1.1, microelectrochemistry is a rapidly developing field that forms interdisciplinary bridges from fundamental science to medicine, corrosion research, microelectronics, and biology.

The small physical size of microelectrodes allows the dimension of the electrochemical cell to be dramatically reduced allowing direct measurements to be performed in nanoliter and even picoliter volumes.

6.2.1.1 Electrochemical cells

Figure 6.2.1.2 illustrates the range of electrochemical cells that have been developed for microelectrochemical measurements. Significant features include the cell volume, distance of the electrodes, electrolyte flow, and optical transparency. For example, scanning electrochemical microscopy (SECM, see Chapter 12) is performed in a macroscopic cell, but the

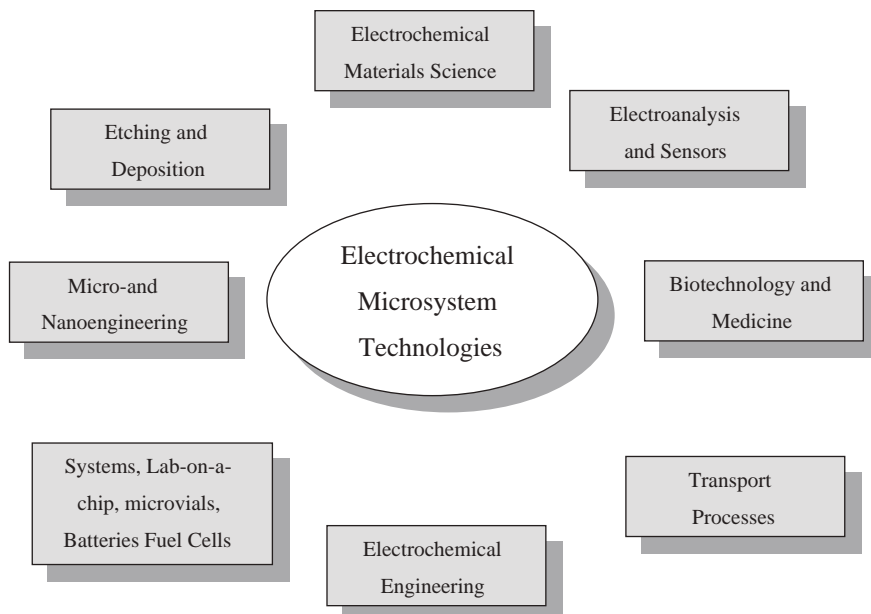


Figure 6.2.1.1 Electrochemical microsystem technologies with connections to and applications in electrochemical materials science, microengineering, electrochemical engineering, and biology and medicine.

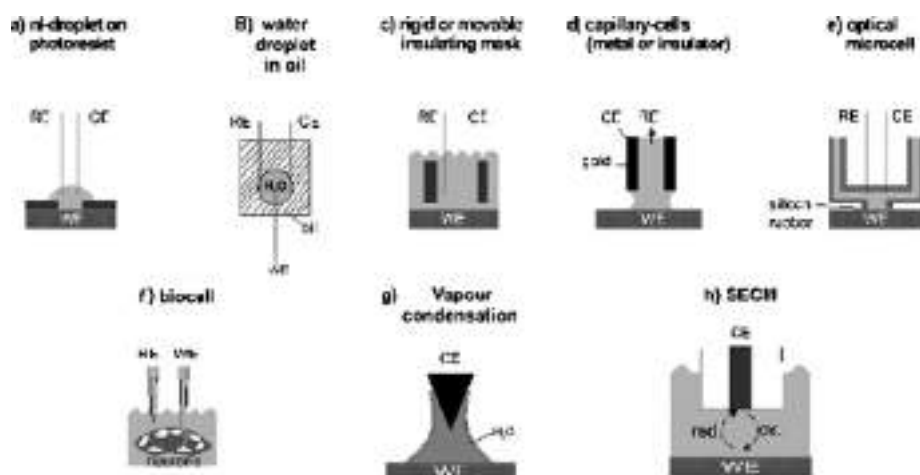


Figure 6.2.1.2 Cell constructions for microelectrochemical experiments: (a) water droplet on a photoresist electrode (8, 9); (b) water droplet in oil (10); (c) movable mask (11); (d) scanning droplet or capillary cell (12); (e) optical microcell (13); (f) biological cell (14); (g) vapour condensation cell with two electrodes or ‘electrochemical nano cell’ (15) and (h) SECM (16). [Reprinted from J. W. Schultze, A. Bressel, *Electrochimica Acta*, **47**, 3 (2001). Copyright (2001) with permission from Elsevier.]

local resolution is achieved by limitation of diffusion. Microelectrodes formed using lithographic techniques in which the electrode is surrounded by a hydrophobic photoresist can be used to perform electrochemical measurements in nanoliter volumes by wetting the electrode surface and introducing counter and reference electrodes into the nanoliter drop (16). Various modifications of the capillary cell and the optical microcell have been described and are similar in concept to a movable mask (10, 11). Perhaps, the smallest two-electrode electrochemical cell is that created by vapor condensation between a substrate and an SPM-tip (5) and has proven to be useful in the creation of nanodimensional structures (e.g., through “dip-pen nanolithography”). Beyond nanolithography, Bard and Fan developed an approach to detect single redox molecules using a piezoelectric positioner to move a microelectrode toward a large counter electrode to create a microvolume electrochemical cell (6). When a redox active molecule is moved from bulk solution into the microvolume defined by the two electrodes, it can be repeatedly electrolyzed to generate a measurable current. Transport of the electroactive species was dictated by Brownian motion causing the events to be infrequent.

Another approach to confining the volume is to use vials that have picoliter volumes (7). These can be fabricated with lithographic techniques. Electrochemical experiments using a standard reduction–oxidation couple, ferrocene–carboxylic acid, have been performed in volumes as small as 1 pL. Peak-shaped voltammetry and an increase in the current on the reverse wave of the cyclic voltammogram are observed in the voltammetric response when ultrasmall volumes (16 pL or less) are used. This deviation from bulk microelectrode behavior is observed only at slower scan rates in the smaller microvials. The voltammetric behavior in the small-volume experiments depends on the scan rate, vial size, and analyte concentration. A physical model based on restriction of analyte in these well-defined

microenvironments is proposed to explain the differences in current compared with that predicted by microelectrode theory in bulk solutions.

Irrespective of the sample volume, the amount of sample probed in an electrochemical experiment depends on the timescale. This sensitivity arises because, for solution phase reactants, diffusion is typically the dominant mode of mass transport. When the response is under semi-infinite linear diffusion control, the thickness of the diffusion layer, δ , is given by equation (6.1.5.1). Taking a typical diffusion coefficient of $1 \times 10^{-5} \text{ cm}^2 \text{ sec}^{-1}$ in aqueous solution, equation (6.1.5.1) indicates that for a conventional electrochemical experiment employing an electrode of 3 mm diameter and an electrolysis time of 1 sec, a volume of approximately $10 \mu\text{L}$ will be electrolyzed. In contrast, for a $5\text{-}\mu\text{m}$ radius microelectrode and a $50\text{-}\mu\text{sec}$ electrolysis time, the volume will be less than 30 fL .

This approach can be exploited to monitor reactions involving single molecules. For example, Wightman and co-workers investigated electrochemiluminescent reactions involving individual reactant pairs (17). Their approach was to use $50 \mu\text{sec}$ potential steps at a $5\text{-}\mu\text{m}$ radius microelectrode to electrolyze a few femtoliters of 9,10-diphenylanthracene so as to generate a small population of radical anions. By allowing these radical anions to diffuse into a solution containing the radical cation of the same molecule, singlet excited states of 9,10-diphenylanthracene were created. This electronically excited state then decays back to the ground state by emission. Because of the low concentrations involved, these reactions are seen as individual light producing events.

6.2.1.2 Analytical applications

Microelectrodes have been used in combination with classical analytical techniques, such as anodic stripping voltammetry (ASV) to determine the concentration of a wide range of analytes, especially metal ions (18, 19). However, here we focus on more contemporary approaches that modify the surface of the microelectrode to produce sensors.

Cholesterol is a major structural component of the mammalian cell plasma membrane that regulates fluidity and permeability. It is a key component in signal transduction among cells, as well as in the immune response, cell infection, and cell surface polarity. Complete elucidation of the pathways governing the initial steps in atherogenesis requires the development of microscopic sensors capable of following the dynamics of intracellular cholesterol trafficking to and from the plasma membrane. Devadoss and Burgess (20) have probed the steady-state detection of cholesterol in the plasma membrane of a single cell using lipid bilayer-modified microelectrodes incorporating cholesterol oxidase. Their single-cell approach uses a platinum microelectrode modified with a lipid bilayer membrane containing cholesterol oxidase in which the steady-state electrode response appears to correlate with the cholesterol content of the cell plasma membrane. As shown in Figure 6.2.1.3, positioning the electrode directly adjacent to the cell (within $\sim 1 \mu\text{m}$ or partially touching) produces an intermediate response, while contacting the cell with some force yields maximum current. The response observed adjacent to the cell may reflect detection of cholesterol efflux (i.e., solution-phase cholesterol). The apparent steady-state responses suggest that cholesterol oxidation is not limited by lateral diffusion of cholesterol in the plasma membrane to the electrode contact site (i.e., no current decay for depletion is observed).

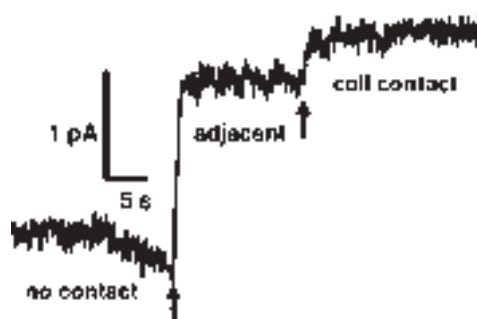


Figure 6.2.1.3 Amperometric data for detection of cellular cholesterol at a microelectrode ($11.5\text{ }\mu\text{m}$ diameter) modified with a lipid bilayer membrane containing cholesterol oxidase. No contact: baseline data; no cholesterol detection. Adjacent: data for positioning the electrode within $\sim 1\text{ }\mu\text{m}$ of (or partially touching) the plasma membrane. Cell contact: data for contacting the oocyte plasma membrane. Arrows approximate the times of changing electrode position. The buffer is 0.1 M sodium phosphate, pH 6.5. The electrode potential is 800 mV vs. NHE. [Reproduced with permission from A. Devadoss, J. D. Burgess, *J. Am. Chem. Soc.* **126**, 10214 (2004). Copyright 2004, American Chemical Society.]

6.2.2 Spatially heterogeneous systems: biological structures

In biological systems, chemical events of interest are often restricted to the interior or exterior surfaces of single cells. To provide useful information about *in vivo* biochemistry, these measurements must be performed with a high degree of spatial and temporal resolution as well as a high degree of sensitivity and selectivity (21). Spectroscopic techniques, such as fluorescence microscopy, magnetic resonance imaging, ion-mass spectrometry, and even X-ray emission imaging can provide useful information about the two-dimensional structure of biosystems. However, they are typically restricted to high analyte concentrations, millimeter rather than micrometer resolution and slow ($>\text{msec}$) time responses.

The mammalian brain (22) represents an extraordinarily challenging environment. At every level of organization, the brain is temporally and spatially heterogeneous: neuronal structures of differing sizes (from nanometer to meter) communicate with each other at timescales ranging from the microseconds to hours or days. Structurally, the brain contains small nuclei, such as the suprachiasmatic nucleus as well as larger nuclei that are not structurally homogeneous (e.g., the laminar structures of the cortex and hippocampus are well documented). When the objective is to elucidate the structure–function relationship of these structures, the ability to make spatially resolved measurements with microprecision is paramount. Thus, the spatial region that the chemical probe samples need to have dimensions similar to those expected for the phenomena of interest. Also, the concentrations of species present are nonuniform and the concentration of a target molecule is frequently higher close to its release site than it is in the surrounding tissue. Although the local concentration may be easily measurable, the total number of molecules in the small volume may be quite low (e.g., there are only 30,000 molecules in 50 fL of a $1\text{ }\mu\text{M}$ solution). For this reason, analysis in heterogeneous structures demands both high spatial resolution and a high mass, as opposed to concentration and sensitivity (23).

Another consequence of performing analysis at short length scales is that random processes (e.g., Brownian motion in response to a concentration gradient) can cause the instantaneously measured concentration to vary significantly from the time-averaged value. For example, equation (6.1.5.1) shows that diffusion will not significantly perturb the measured concentration over a sample interval of 1 cm for several hundred seconds. In contrast, if the concentration is measured only over 1 μm , diffusion will change the “sample” composition within a millisecond. Thus, electroanalysis becomes possible at short length scales only with the short response times of microelectrodes. It is important to note that amperometry consumes the target molecule (through oxidation or reduction) thus altering the chemical microenvironment and creating a driving force for molecular diffusion. In addition, the newly created species can interact with the sample. It is also frequently difficult to relate the measured current to concentration because of the challenge of replicating the heterogeneous nature of the sample during calibration.

Investigations elucidating neurotransmitter release have revealed the location and dynamics of neurotransmitter release through exocytotic events. A challenge in this field is to avoid fouling of the electrode surface through adsorption and carbon-fiber microelectrodes are frequently used. Neurotransmitter release occurs at short timescales making fast-scan cyclic voltammetry a powerful tool to temporally resolve neurotransmitter release. A disadvantage of electrochemistry is that the voltammetric response of each analyte is a significant fraction of the available potential window that rarely exceeds 1.5 V in aqueous media. Therefore, the task of resolving individual neurochemicals benefits greatly from advanced data analysis techniques. Wightman and co-workers evaluated the ability of cyclic voltammograms recorded at fast scan rates to resolve neurochemicals when analyzed by principal component regression (24). In their approach, a calibration set of 30 cyclic voltammograms was constructed from nine different substances at a variety of concentrations. The set was reduced by principal component analysis, and it was found that 99.5% of the variance in the data could be captured with five principal components. This set was used to evaluate cyclic voltammograms obtained with one or two compounds present in solution. In most cases, satisfactory predictions of the identity and concentration of analytes were obtained. Chemical dynamics were also resolved from a set of fast-scan cyclic voltammograms obtained with the electrode implanted in a region of a brain slice that contains dopaminergic terminals. Following stimulation, principal component regression of the data resolved the changes in dopamine and pH that were evoked. In a second test of the method, vesicular release was measured from adrenal medullary cells and the data were evaluated with a calibration set composed of epinephrine and norepinephrine. Cells that secreted one or the other were identified. Overall, the results show that principal component regression with appropriate calibration data allows resolution of substances that give overlapping cyclic voltammograms.

The utility of combining electrochemical and spectroscopic detection has also been demonstrated. Xin and Wightman demonstrated simultaneous detection of catecholamine exocytosis and calcium-ion release from single bovine chromaffin cells with a dual amperometric/calcium-selective dye-bound fluorescence sensor and demonstrated that catecholamine and calcium release were temporally and spatially correlated (25). In microelectrode measurements, individual exocytotic events associated with neurotransmitter release appear as spikes with the area of the amperometric spikes providing a

coulometric measure of the number of molecules released from each secretory event. On an average, the spikes from chromaffin cells yield an attomole of material. Despite the tiny amount of materials released, the signals are robust due to the small volume. However, because of diffusional dispersion, the concentration spikes are transient and are diluted to negligible values within a few milliseconds.

Microelectrode structures have been created that mimic aspects of brain function. Amatore and coworkers have described assemblies of paired microband electrodes that behave like a neuronal synapse (26). The generator electrode in these devices mimics a synaptic terminal, and the collector electrode functions as a postsynaptic membrane. These artificial synapses can be designed in several configurations to perform Boolean logical operations, such as AND or OR operations.

6.2.2.1 Reactive surfaces and bioelectronics

A number of successful bioelectronic devices have been created that exploit microelectrode technology. These include the cochlear implant and peripherally implantable stimulators (27). Other devices including retinal or cortical implants are less developed and not yet applicable. A challenge in this field is to engineer microelectrode surfaces so that they are both biocompatible and can be used to direct cell adhesion and growth (e.g., to stimulate nerve growth across an interrupted neuronal pathway).

Controlling the interfaces between cells and solid substrates is an important objective (28–30) that impacts areas as diverse as microfluidic, lab-on-a-chip separations, cellular biology, and tissue engineering. Modified surfaces offer excellent possibilities for real progress, most notably using molecular self-assembly to create low-defect density surfaces of controlled charge, hydrophobicity, and chemical reactivity (e.g., with respect to biomolecule binding (31–33)). Nishizawa recently described a strategy for the real-time local manipulation of the cell-adhesive properties of a substrate in the presence of attached living cells (34, 35). The strategy involves rapid switching of the cytophobic nature of albumin-coated substrates to a cell-adhesive surface by exposing it to an oxidizing agent, such as hypobromous acid. The oxidizing agent can be generated electrochemically at the tip of a microelectrode to create arbitrary cellular micropatterns. It is also possible to guide cellular growth and migration on substrates during cultivation. Figure 6.2.2.1 shows that the culturing of HeLa cells depends on the scanning height above the reactive surface. Approaches of this kind that facilitate the spatially controlled growth of individual cells will simplify bioassays based on cellular motility as well as contribute to cell and tissue engineering by creating micropatterned cocultures of different kinds of cell types.

6.2.3 Low conductivity media

Theoretical and practical applications of voltammetry in low ionic strength solutions have been reviewed by Ciszkowska and Stojek (36). Here, we present a selective overview of the importance of the area and the increased range of media that are now amenable to electrochemical investigation with microelectrodes.

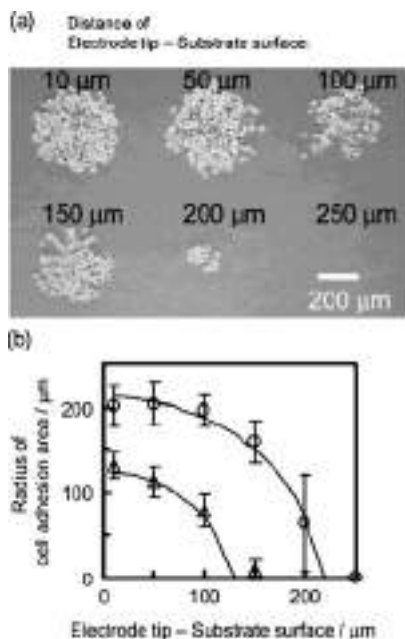


Figure 6.2.2.1 Size of cellular adhesion area at various distances between the electrode tip and the substrate surface during the electrochemical treatment. (a) Phase contrast micrograph of HeLa cells cultured for 24 h on the BSA-coated glass substrate, which was pretreated by a Br – oxidation pulse of 30 sec at the tip–surface distance indicated in the micrograph. (b) Plots of the radius of the cell adhesion area versus the distance of electrode tip–substrate surface for the electrolysis periods of 10 sec (4) and 30 sec (O). Error bars for the plots were calculated from the standard deviation of at least four cellular patterns. Solid curves were calculated assuming a diffusion-limited surface reaction. [Reproduced with permission from H. Kaji, K. Tsukidate, T. Matsue, M. Nishizawa, *J. Am. Chem. Soc.* **126**, 15026 (2004). Copyright 2004, American Chemical Society.] (for colour version: see colour section at the end of the book).

6.2.3.1 Voltammetry in the absence of deliberately added electrolyte

Voltammetry in highly pure water without added electrolyte is now well established (37–41). The ability to perform stripping analysis of metals without the need to add potentially contaminating supporting electrolyte is an important application (37). Ciszkowska and Osteryoung (38) have probed the voltammetric reduction of three metal cations: thallium, cadmium, and lead in solutions of various salts (TlNO_3 , Tl_2SO_4 , $\text{Cd}(\text{NO}_3)_2$, $\text{Pb}(\text{NO}_3)_2$, and CdSO_4), containing either no supporting electrolyte or where LiClO_4 or $\text{Ca}(\text{NO}_3)_2$ were added at various concentrations. The influence of migration was studied for a wide range of concentrations of the electroactive species and supporting electrolyte. As predicted by theory (39), the ratio of the limiting current, i_l , to the diffusion limited current, i_d , was 1.5 and 2 in solutions with and without excess supporting electrolyte, for the reduction of Tl^+ cation in the solutions with mono- and divalent anions.

6.2.3.2 Voltammetry in pure liquid organics

White and coworkers pioneered the use of microelectrodes in neat organic liquids and their theoretical interpretation (40–47). The low dielectric constant of these materials usually means that supporting electrolyte is often added to avoid catastrophic ohmic effects. A very low level of electrolyte, which results in a support ratio not higher than 0.001, helps to lower the ohmic potential drop and permits well-defined voltammetric waves to be obtained. Voltammograms were obtained for redox processes of several organic compounds, including nitrobenzene (40, 41), 4-cyanopyridine (42), aniline and pyrrole (48), acetonitrile (49), simple alcohols (50), dimethylsulfoxide (51), and DMF (52). Because the analyte concentration is so high in these experiments, water and other impurities do not influence the observed responses to any great extent.

A characteristic feature of voltammetry of pure organics is the formation of a microlayer of an ionic liquid at the electrode surface. This microlayer forms at the wave plateau, where the concentration of the substrate drops to zero and the charged product is neutralized by a counterion. For an oxidation reaction at potentials sufficiently negative of $E^{\circ'}$, the mole fraction of the analyte is 1. For potentials sufficiently positive of $E^{\circ'}$, the molar fraction of both the product and counterion is 0.5. This change in relative concentrations leads to a specific type of convection called diffusion-engendered convection (42). This thin layer of ionic liquid also leads to strong changes in the viscosity of media, which change both the activities of all species close to the electrode surface and their diffusion coefficient. These layers can be very stable especially for the electrooxidation of simple alcohols, and the electroreduction of nitrobenzene. In extreme situations, precipitation may occur at the electrode surface. White and coworkers have used interferometry (44) and voltammetry at elevated pressure (45) to probe the interfacial structure in these systems. These careful studies allow the pressure dependence of molecular transport to be investigated and have demonstrated that the interfacial layer can be compressed (45). The presence of this interfacial layer complicates the interpretation of voltammetric peak or steady-state currents because the diffusion coefficient of the analyte within the microlayer will be significantly different from that found in dilute solution. Ragsdale and White (47) used the Cullinan–Vignes equation to predict the reduction wave height of nitrobenzene in acetonitrile over a wide range of compositions. The deviations of experimental data from theoretical predictions for mole fractions of nitrobenzene less than 0.4 allowed self-association of the solution components to be detected.

6.2.3.3 Complexation equilibria

Traditionally, voltammetric investigations of complexation suffered relative to spectroscopy because of the need to add an excess of supporting electrolyte. A high concentration of electrolyte can cause contamination or can compete with the analyte of interest in the complexation reaction itself. The high ionic strength can cause the activity of the analyte to deviate significantly from its concentration. The ability to perform electrochemical measurements without deliberately adding supporting electrolyte may extend the range of analyte/ligand concentrations that can be investigated.

Palys and coworkers extended the work of Myland and Oldham (53) and developed a theoretical model that describes the steady-state microelectrode response for a wide range

of complexes that are inert on the experimental timescale (54). The theory shows that the steady-state limiting current depends on the type of complexation equilibrium, the type of the change in the reactant charge number, and the complex formation constant. The theory provides a good description of the experimental data found for the complexation of europium(III) with 1,4,8,11-tetraazacyclotetradecane (cyclam) in a 4:1 mixture (v/v) of methanol and dimethylsulfoxide. The influence of the concentration of the electroinert ionic species on the limiting currents was also considered. For cases where migration contributes significantly to the transport, relationships between the measured steady-state limiting currents and β are given in the form of fitted equations.

Stojek and co-workers (55) found that in the case of neutral ligands, the shift of the half wave potential caused by the formation of the complex has the same magnitude in solutions with and without supporting electrolyte. For charged ligands, it is possible to find a value for the ligand/reactant concentration ratio above which migrational effects can be neglected. This behavior allows the classic analytical approaches to be applied to charged ligands. This approach was applied to experimental results obtained for Tl^+ with 18-crown-6 ligand in water without addition of supporting electrolyte.

6.2.4 Ultrafast electrochemical techniques

Ultrafast electrochemical techniques provide information about the kinetics and thermodynamics of redox processes that occur at sub-millisecond or nanosecond timescales. This short timescale is achieved either by making very rapid transient measurements or by using ultrasmall probes to achieve high rates of diffusion under steady-state conditions. Microelectrodes play pivotal roles in both approaches. Electrochemistry has several advantages over spectroscopy in that it provides *direct* information about electron transfer and coupled chemical reactions. In transient measurements, decreasing the lower accessible timescale depends critically on fabricating ultramicroelectrodes (UMEs) that continue to respond ideally as their critical dimension (e.g., the radius of a microdisk) decreases. The principal difficulty with transient approaches that use extremely short duration potential perturbations is ohmic drop as a small diffusion layer corresponds to a large concentration gradient, and so the current is large. The second difficulty is to produce microelectrodes with extremely short response times. It is now possible to assemble microelectrodes that respond to changes in applied potential within less than a few nanoseconds. In steady-state approaches, ultrasmall probes are required to make short timescale measurements. Various approaches that yield “nanodes” (i.e., electrodes of nanometer dimension) have been developed but the production of well-characterized nanodes remains a challenge.

6.2.4.1 Transient techniques

In transient electrochemical measurements involving a solution phase redox couple, one seeks to create a competition between the reaction of interest, electron transfer at the electrode surface or coupled homogeneous steps, and diffusion of the species to and from the electrode surface (56).

(a) Heterogeneous electron transfer dynamics

At short times, the diffusion layer thickness is much smaller than the microelectrode radius and the dominant mass transport mechanism is planar diffusion. The heterogeneous electron transfer dynamics of a diverse range of organic and inorganic species have been investigated using transient techniques. For example, cyclic voltammetry of the anthracene/anthracene anion radical has been used extensively as a reference system for characterizing new electrodes or instruments. This focus arises because the aromatic nature of the molecule leads to very small changes in the bond lengths and bond angles (i.e., the Marcus inner sphere reorganization energy is small (57)) thus causing the heterogeneous electron transfer rate constant to be large. Wightman (58) has studied this reaction using cyclic voltammetry at scan rates up to 10^5 V sec $^{-1}$ and good agreement between the predictions of the Nicholson and Shain theory and experiment was found after correcting for the nonspherical nature of the microdisk used.

Despite the many elegant investigations that have been conducted on heterogeneous electron transfer dynamics of solution phase reactants, the magnitude of the diffusion-controlled current at short times ultimately places a lower limit on the accessible timescale. For diffusive species, the thickness of the diffusion layer, δ , is defined as $\delta = (\pi D t)^{1/2}$ (equation (6.1.5.1)) and is, therefore, proportional to the square root of the polarization time, t . One can estimate that the diffusion layer thickness is approximately 50 Å if the diffusion coefficient is 1×10^{-5} cm 2 sec $^{-1}$ and the polarization time is 10 nsec. Given a typical bulk concentration of the electroactive species of 1 mM, this analysis reveals that only 10,000 molecules would be oxidized or reduced at a 1-μm radius microdisk under these conditions. The average current for this experiment is only 170 nA, which is too small to be detected with low nanosecond time resolution.

Therefore, to probe the dynamics and energetics of ultrafast heterogeneous electron transfer dynamics, this diffusion limitation must be eliminated. One successful approach to achieving this objective is to use self-assembled or spontaneously adsorbed monolayers. When immobilized on an electrode surface, the electroactive species no longer needs to diffuse to the electrode to undergo electron transfer. Moreover, the electroactive species is preconcentrated on the electrode surface. For example, in the situation considered above, there will be approximately 1.7×10^{-20} mol of electroactive material within the diffusion layer. Given that the area of a 1-μm disk is approximately 3.1×10^{-8} cm 2 , this translates into an “equivalent surface coverage” of about 5.4×10^{-13} mol cm $^{-2}$. In contrast, the surface coverage, Γ , observed for dense monolayers of adsorbates is typically more than two orders of magnitude larger with coverages of the order of 10^{-10} mol cm $^{-2}$ being observed. This higher concentration gives rise to much larger currents that are easier to detect at short timescales. As exemplified by the work of Chidsey (59), Abruña (60), Faulkner (61), and Finklea (62), electroactively adsorbed monolayers have been developed that exhibit close to ideal reversible electrochemical behavior under a wide variety of experimental conditions of timescale, temperature, solvent, and electrolyte.

(b) Homogeneous chemical kinetics

The decrease in the lower accessible time limit possible using microelectrodes has important implications for probing the dynamics of rapid homogeneous chemical reactions.

Bimolecular reactions in solution cannot proceed faster than the rate at which molecules come into close contact. Thus, bimolecular rate constants cannot exceed the diffusion limited rate constant that is of the order of 10^9 – 10^{10} M $^{-1}$ sec $^{-1}$ in most organic solvents. As the characteristic time of cyclic voltammetry is RT/Fv , where v is the scan rate, experiments performed at MV sec $^{-1}$ scan rates allow kinetic information, such as lifetimes that are close to the diffusion limit, to be obtained (63). As illustrated in Figure 6.2.4.1, Wightman (64) has shown that the irreversible response observed for the oxidation of anthracene at slow scan rates becomes fully reversible at a scan rate of 10^4 V sec $^{-1}$. This behavior is opposite to that expected when heterogeneous electron transfer is slow and suggests that the cation radical undergoes a following chemical reaction. The ability to make the voltammetric response reversible means that the formal potentials of highly reactive species can be accurately measured.

The kinetics and mechanism of homogeneous reactions following the reduction of NAD $^+$ and synthetic analogues continue to be investigated. Several reaction mechanisms have been observed for NAD $^+$ analogues, with molecules containing at least one hydrogen at the 4-position (i.e. direct analogues of NAD $^+$) typically undergoing a dimerisation reaction (65). The effect of changing the substitution pattern on the mechanism and kinetics of the homogeneous solution reactions of electrogenerated 1-methyl-carbamidopyridinyl radicals has been investigated. Fast-scan cyclic voltammetry (CV) and double potential

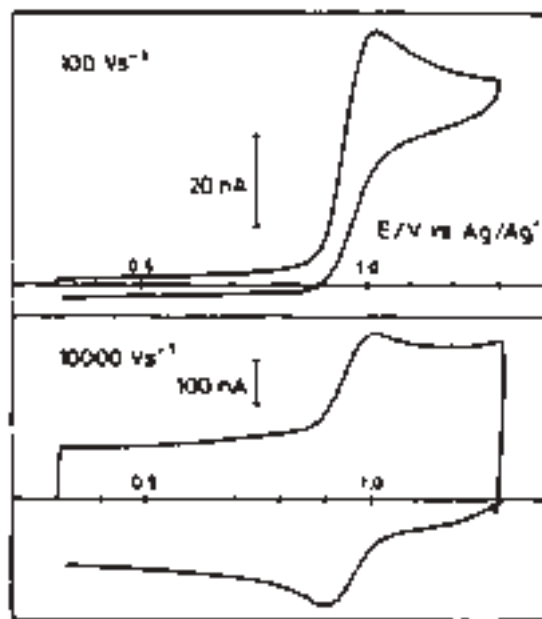


Figure 6.2.4.1 Effect of scan rate on the voltammetric response observed at a 5- μ m platinum microdisk for the oxidation of 2.36 mM anthracene in DMF containing 0.6 M tetraethyl ammonium perchlorate. [Reproduced with permission from J. O. Howell, R. M. Wightman, *J. Phys. Chem.* **88**, 3915 (1984). Copyright 1984, American Chemical Society.]

step chronoamperometry (DPSC) conducted on a microsecond timescale reveal that 1-methyl-3-carbamidopyridinyl radicals react via a dimerisation mechanism involving direct coupling of the electrogenerated neutral radicals at a rate of approximately $1.6 \pm 0.1 \times 10^7 \text{ M}^{-1} \text{ sec}^{-1}$ in DMF. The 1-methyl-4-carbamidopyridinyl and 1-methyl-3,4-dicarbamidopyridinyl radicals react via a pH-dependent ECE-DISP1 mechanism, where E, C and DISP denote electron transfer, following chemical and disproportionation reactions, respectively.

6.2.4.2 Steady-state electrochemistry

Under steady-state conditions, the time required for diffusion, t_D , is *not* related to the actual duration of the experiment as the diffusion layer thickness depends only on the radius. Under these conditions, t_D is approximately equal to r_0^2/D . This property has a profound impact on the size of microelectrodes required to make measurements at a steady state. Given a typical diffusion coefficient of $10^{-5} \text{ cm}^2 \text{ sec}^{-1}$, microelectrodes with radii less than 30 nm are required to address sub-microsecond timescales. In using steady-state methods to determine kinetic parameters for fast reactions, experimental conditions are chosen so that there is mixed control by kinetics and diffusion. Aoki (66), Fleischmann (67), and Oldham (68) have addressed this issue and provided several equivalent approaches for analyzing experimental current–voltage curves. Bard and coworkers (69) developed an approach for determining kinetic parameters of simple quasi-reversible electron transfer reactions. In principle, only the one-quarter ($E_{1/4}$), one-half ($E_{1/2}$), and three-quarters ($E_{3/4}$) potentials from a single steady-state voltammogram are required, although more precise values of k° and α can be obtained by fitting the full voltammogram. The analysis is independent of the electrode area and the concentration of the electroactive species, which improves the reliability of the analysis.

Parameters describing the kinetics of heterogeneous electron transfer for several solution phase redox active molecules have been reported and a representative sample is given in Table 6.2.4.1. These data show that the rate of electron transfer across the electrode/solution interface is influenced by the identity of the redox couple. These variations reflect differences in the reaction adiabaticity and activation barriers that exist for the individual systems. However, even for a single species, a considerable range of k° values are observed (e.g., for the archetypal reversible couple ferrocene, reported k° values range from 0.09 to 220 cm sec^{-1}). Reasons for these discrepancies include electrode fabrication protocol, purity of the ferrocene, solvent and electrolyte, and the method used to analyze the data. For high ferrocene concentrations, the electrode becomes pacified by an insoluble layer. Electrode surface blocking impedes diffusion and causes a nonproportional increase in current with increasing ferrocene concentration. Even for a standard electrochemical test system, considerable care must be taken over all aspects of the experiment, chemicals, electrode fabrication, experimental setup, as well as data collection and analysis if accurate kinetic parameters are to be obtained.

(a) Homogeneous chemical kinetics

Steady-state measurements are important in studies of chemical reactivity. Steady-state measurements using electrodes of different radii provide insight into the kinetics of

Table 6.2.4.1

Rate constants for heterogeneous electron transfer determined using steady-state methods

Analyte	Electrode ^a	k° (cm sec ⁻¹)	Reference
Anthracene	Au ring $\Delta r = 0.09 \mu\text{m}$; $r = 5 \mu\text{m}$	3.33 ± 0.05	(70)
$(\text{C}_6\text{H}_6)\text{Cr}(\text{CO})_3^+$	Pt, $25 \mu\text{m}$	≥ 0.3	(71)
$(\text{CpCOOCH}_3)_2\text{C}_6\text{O}^+$	Pt, $23 \text{\AA} - 4.7 \mu$	130 ± 70	(72)
Cytochrome <i>c</i>	C, $6.3 \mu\text{m}$	> 0.4	(73)
9,10-Diphenylanthracene	Au ring $\Delta r = 90 \mu\text{m}$; $r = 5 \text{ mm}$	5.7 ± 0.1	(70)
Ferrocene	Au ring $\Delta r = 0.09 \mu\text{m}$; $r = 5 \mu\text{m}$	0.09 ± 0.005	(70)
	C, $6 \mu\text{m}$	2.3 ± 0.8	(74)
	Pt, $0.3 - 25 \mu\text{m}$	≥ 6	(75)
	Pt, $1 \mu\text{m}$	> 2	(76)
	Pt, $16 \text{\AA} - 2.6 \mu\text{m}$	220 ± 120	(72)
Fe(OEP)(<i>N</i> -Melm) ₂ ⁺	Pt, $1 - 25 \mu\text{m}$	0.4	(77)
	Pt, $0.5 - 12.5 \mu\text{m}$	0.38	(78)
	Pt, $1 - 25 \mu\text{m}$	0.35	(77)
Fe(TPP) (Hlm) ₂ ⁺	Pt, $1 - 25 \mu\text{m}$	0.5	(77)
Fe (TPP) py ₂ ⁺	Pt, $1 - 25 \mu\text{m}$	0.6	(77)
MV ^{2+(F)}	Pt, $22 \text{\AA} - 0.21 \mu\text{m}$	170 ± 90	(72)
Naphthalene	Au ring $\Delta r = 0.2 \mu\text{m}$; $r = 20.5 \mu\text{m}$	0.88 ± 0.02	(70)
Oxygen	Pt, $12.7 - 250 \mu\text{m}$	0.63 ± 0.05	(79)
Ru (NH ₃) ₆ ³⁺	Au, $5 \mu\text{m}$	0.076	(80)
	Pt, $1.3 - 4.6 \mu\text{m}$	0.26 ± 0.13	(72)
	Pt, $11 \text{\AA} - 11.1 \mu\text{m}$	79 ± 44	(72)
Tetracyanoethylene	Au ring $\Delta r = 0.2 \mu\text{m}$; $r = 20.5 \mu\text{m}$	0.15 ± 0.01	(70)
Tetracyanoquinodi-ethane	Au ring $\Delta r = 0.2 \mu\text{m}$; $r = 20.5 \mu\text{m}$	0.23 ± 0.01	(70)
Zn(TPP)	Pt, $1 - 25 \mu\text{m}$	> 1	(77)

^aDimension given is the radius of a microdisk electrode unless otherwise stated.

homogeneous reactions where the limiting current density depends on the magnitude of the homogeneous rate constant. Coupled chemical (C) and electron transfer (E) reactions (e.g. CE mechanisms, catalytic follow-up processes, as well as reactions involving disproportionation (DISP)) have been characterized. However, reactions such as chemical reactions that follow electron transfer (EC) mechanisms cannot be investigated in the same way as the current density is not influenced by the following chemical reaction. In these circumstances, the homogeneous reaction does not affect the height or shape of the reversible steady-state voltammogram. As indicated in Figure 6.2.4.2, the position of the wave on the potential axis depends on the homogeneous reaction rate and kinetic information can be obtained by probing how $E_{1/2}$ depends on the electrode radius.

6.2.5 AC electrokinetics

Electrochemical investigations are found in the areas of molecular electronics and nanotechnology. Electrochemistry can be used to produce and characterize clean surfaces (e.g., electrochemical cleaning of metals). It can direct the assembly and structure of supramolecular assemblies (e.g., by using self-assembled or spontaneously adsorbed

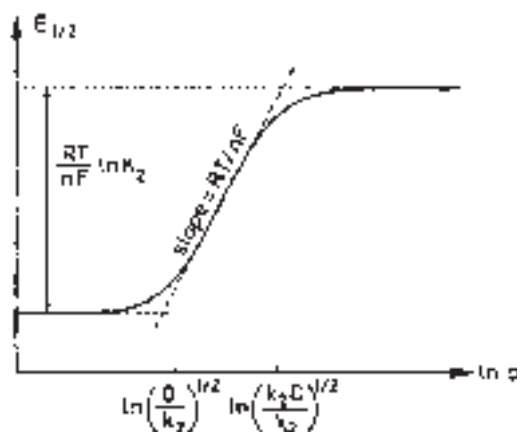


Figure 6.2.4.2 Dependence of $E_{1/2}$ for an EC reaction on the logarithm of the electrode radius. [Reproduced from K. B. Oldham, *J. Electroanal. Chem.* **313**, 3 (1991). Copyright (1991) with permission from Elsevier.]

monolayers). It can address molecular components (e.g., by switching their oxidation state). It can read their state (e.g., through measurements of the open circuit potential). Microelectrodes offer the possibility of selecting and moving nanometer dimensioned objects with precision by using AC electrokinetics. AC electrokinetics offers advantages over scanning-probe methods of nanoparticle manipulation in that the equipment used is simple, inexpensive, and has no moving parts, relying entirely on the electrostatic interactions between the particle and the dynamic electric field. There is a theoretical evidence that as manufacturing technology further improves, single particles considerably smaller than presently studied using AC electrokinetics may be manipulated.

AC electrokinetics uses an electric field created between two or more microelectrodes to induce a dipole within a cell, particle or macromolecule. With a suitable electrode design, a variety of motions including attraction, repulsion, and rotation can be induced by changing the nature of the dynamic field. These forces may be viewed as an electrostatic equivalent to optical tweezers (81) and optical spanners (82) in that they exert translational and rotational forces on a body due to the interaction between a body and an imposed field gradient. AC electrokinetic techniques, such as dielectrophoresis (83) and electrorotation (84) have been utilized for many years for the manipulation, separation, and analysis of cellular-scale particles. Recent advances in semiconductor manufacturing technology have enabled researchers to develop electrodes for manipulating macromolecules as small as 9 kDa using both attractive (85) and repulsive AC electrostatic forces and to concentrate 14 nm beads from solution (86). Trapping of single particles such as viruses and 93 nm diameter latex spheres in contactless potential energy wells (87) has also been demonstrated.

An application of AC electrokinetic phenomena is the preconcentration of a target molecule within a small volume. Crooks and coworkers (88) have achieved enrichment factors for DNA exceeding 100 using channels that are 5 mm in length, require only a single homogeneous analyte phase, and avoid complex microfluidic designs. The approach

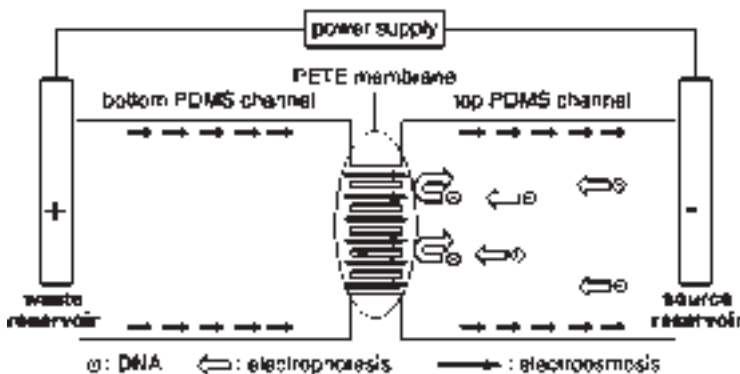


Figure 6.2.5.1 Diagram of a microfluidic concentrator. The three-dimensional microfluidic system consists of a nanoporous polyester membrane sandwiched between two poly(dimethylsiloxane) blocks, each containing a single fluidic channel (100 μm wide, 25 μm deep, and 5 mm long). [Reproduced with permission from J. Dai, T. Ito, L. Sun, R.M. Crooks, *J. Am. Chem. Soc.* **125**, 13026 (2003). Copyright 2003, American Chemical Society.]

appears versatile and should be applicable to any charged molecule or object. As illustrated in Figure 6.2.5.1, their approach relies on exerting spatial control over the electrokinetic velocity of the analyte. The electro-osmotic (eo) velocity of the buffer solution in one region of a microfluidic system opposes the electrophoretic (ep) velocity of the analyte in a second region. This results in ep transport of DNA to a location where the ep and eo velocities are equal and opposite, and DNA concentrates at this location.

When a forward bias (negative potential in the source reservoir) was applied between the electrodes, the concentration of DNA is apparent within 30 sec and reaches an enrichment factor of 11 within approximately 1 min. When the bias is reversed, DNA immediately transports through the PETE membrane indicating that concentration is not a consequence of physical blocking or size exclusion, and is trapped in the left channel (Figure 6.2.5.1) by the same balance of ep and eo velocities that were initially responsible for concentration in the right channel. This enrichment method is conceptually distinct from field-amplification stacking, isotachophoresis, micelle sweeping, size exclusion, and solid-phase extraction, but it is conceptually linked to a recent report in which micrometer-scale beads were trapped within a microfluidic channel by opposing pressure-driven flow and eo flow (89).

REFERENCES

1. P. R. Unwin, *J. Chem. Soc., Faraday Trans.* **94**, 3183 (1998).
2. D. E. Williams, J. V. Macpherson, in *Comprehensive Chemical Kinetics*, R. G. Compton, G. Hancock, Eds., Elsevier: Amsterdam, 1999, pp. 369–438.
3. J. C. Eklund, A. M. Bond, J. A. Alden, R. G. Compton, *Adv. Phys. Org. Chem.* **32**, 1 (1999).
4. R. Kashyap, M. Gratzl, *Anal. Chem.* **70**, 1468 (1998).
5. H. Sugimura, T. Uchida, N. Kitamura, H. Masuhara, *Appl. Phys. Lett.* **63**, 1288 (1993).
6. F.-R. F. Fan, A. J. Bard, *Science* **267**, 871 (1995).
7. R. A. Clark, A. G. Ewing, *Anal. Chem.* **70**, 1119 (1998).

8. A. Michaelis, S. Kudelka, in *New Trends in Electrochemical Technology Series*, Gordon and Breach: London, 2001, Vol. 2, p. 160.
9. S. Kudelka, J. W. Schultze, *Electrochim. Acta* **42**, 2817 (1997).
10. M. M. Lohrengel, *Electrochim. Acta* **42**, 3265 (1997).
11. J. W. Schultze, V. Tsakova, *Electrochim. Acta* **44**, 3605 (1999).
12. A. W. Hassel, M. M. Lohrengel, *Electrochim. Acta* **42**, 3327 (1997).
13. A. Vogeland, J. W. Schultze, *Electrochim. Acta* **44**, 3751 (1999).
14. J. W. Deitmer, W. R. Schlue, A. Pfluegers, *Arch. Eur. J. Physiol.* **397**, 195 (1983).
15. H. Bloeß, G. Staikov, J. W. Schultze, *Electrochim. Acta* **47**, 335 (2001).
16. M. V. Mirkin, B. R. Horrocks, "Electrochemical Microsystem Technologies", in *New Trends in Electrochemical Technology Series*, J. W. Schultze, T. Osaka, M. Datta, Eds., Gordon and Breach: London, 2001, Vol. 2.
17. M. M. Collinson, R. M. Wightman, *Science* **268**, 1883 (1994).
18. M. L. Tercier, J. Buffle, *Electroanalysis* **5**, 187 (1993).
19. G. A. Daniele, M. Mazzocchin, *Anal. Chim. Acta* **273**, 3 (1993).
20. A. Devadoss, J. D. Burgess, *J. Am. Chem. Soc.* **126**, 10214 (2004).
21. R. M. Wightman, P. Runnels, K. Troyer, *Anal. Chim. Acta* **400**, 5 (1999).
22. P. L. McGeer, J. C. Eccles, E. G. McGeer, *Molecular Neurobiology of the Mammalian Brain*, Springer, 1987.
23. S. A. Brazill, S. E. Bender, N. E. Hebert, J. K. Cullison, E. W. Kristensen, W. G. Kuhr, *J. Electroanal. Chem.* **531**, 119 (2002).
24. M. L. Heien, M. A. Johnson, R. M. Wightman, *Anal. Chem.* **76**, 5697 (2004).
25. Q. Xin, R. M. Wightman, *Anal. Chem.* **70**, 1677 (1998).
26. C. Amatore, L. Thouin, J. Warkocz, *Chem. Eur. J.* **5**, 456 (1999).
27. G. M. Clark, *Cochlear Implants: Fundamentals and Applications*, Springer Verlag: New York, 2003.
28. A. Folch, M. Toner, *Annu. Rev. Biomed. Eng.* **2**, 227 (2000).
29. Y. Ito, *Biomaterials* **20**, 2333 (1999).
30. J. Shim, T. F. Bersano-Begey, X. Zhu, A. H. Tkaczyk, J. J. Linderman, S. Takayama, *Curr. Top. Med. Chem.* **3**, 687 (2003).
31. C. S. Chen, M. Mrksich, S. Huang, G. M. Whitesides, D. E. Ingber, *Science* **276**, 1425 (1997).
32. A. Brock, E. Chang, C. Ho, P. LeDuc, X. Jiang, G. M. Whitesides, D. E. Ingber, *Langmuir* **19**, 1611 (2003).
33. J. Lahann, M. Balcells, T. Rodon, J. Lee, I. S. Choi, K. F. Jensen, R. Langer, *Langmuir* **18**, 3632 (2002).
34. H. Kaji, M. Kanada, D. Oyamatsu, T. Matsue, M. Nishizawa, *Langmuir* **20**, 16 (2004).
35. H. Kaji, K. Tsukidate, T. Matsue, M. Nishizawa, *J. Am. Chem. Soc.* **126**, 15026 (2004).
36. M. Ciszkowska, Z. Stojek, *J. Electroanal. Chem.* **466**, 129 (1999).
37. J. Widera, W. H. Steinecker, G. E. Pace, J. A. Cox, *J. Appl. Electrochem.* **33**, 121 (2003).
38. M. Ciszkowska, J. M. Osteryoung, *Anal. Chem.* **67**, 1125 (1995).
39. J. B. Cooper, A. M. Bond, K. B. Oldham, *J. Electroanal. Chem.* **331**, 877 (1992).
40. R. A. Malmsten, H. S. White, *J. Electrochem. Soc.* **133**, 1067 (1986).
41. R. A. Malmsten, C. P. Smith, H. S. White, *J. Electroanal. Chem.* **215**, 223 (1986).
42. R. B. Morris, K. F. Fischer, H. S. White, *J. Phys. Chem.* **92**, 5306 (1988).
43. J. D. Norton, S. A. Anderson, H. S. White, *J. Phys. Chem.* **96**, 3 (1992).
44. Q. Li, H. S. White, *Anal. Chem.* **67**, 561 (1995).
45. K. J. Stevenson, H. S. White, *J. Phys. Chem.* **100**, 18818 (1996).
46. S. C. Paulson, N. D. Okerlund, H. S. White, *Anal. Chem.* **68**, 581 (1996).
47. S. R. Ragsdale, H. S. White, *J. Electroanal. Chem.* **432**, 199 (1997).
48. R. L. McCarley, M. Morita, K. O. Wilbourn, R. W. Murray, *J. Electroanal. Chem.* **245**, 321 (1988).

49. J. Cassidy, S. B. Khoo, S. Pons, M. J. Fleischmann, *J. Phys. Chem.* **89**, 3933 (1985).
50. M. Ciszkowska, Z. Stojek, *J. Electroanal. Chem.* **344**, 135 (1993).
51. M. Koncka, Z. Stojek, *Electroanalysis* **7**, 1010 (1995).
52. J. Gadomska, Z. Stojek, *Electroanalysis* **10**, 307 (1998).
53. J. C. Myland, K. B. Oldham, *J. Electroanal. Chem.* **347**, 49 (1993).
54. M. Palys, Z. Stojek, M. Bos, W. van der Linden, *Anal. Chim. Acta* **337**, 5 (1997).
55. M. J. Palys, H. Sokolowska, Z. Stojek, *Electrochim. Acta* **49**, 3765 (2004).
56. M. I. Montenegro, in *Research in Chemical Kinetics*, R. G. Compton, G. Hancock, Eds., 1994, Vol. 2, p. 1.
57. R. A. Marcus, *J. Chem. Phys.* **43**, 679 (1965).
58. J. O. Howell, R. M. Wightman, *Anal. Chem.* **56**, 524 (1984).
59. C. E. D. Chidsey, *Science* **251**, 919 (1991).
60. D. Acevedo, H. D. Abruña, *J. Phys. Chem.* **95**, 9590 (1991).
61. R. J. Forster, L. R. Faulkner, *J. Am. Chem. Soc.* **116**, 5444 (1994).
62. H. O. Finklea, D. D. Hanshew, *J. Am. Chem. Soc.* **114**, 3173 (1992).
63. C. A. Amatore, A. Jutand, F. Pflüger, *J. Electroanal. Chem.* **218**, 361 (1987).
64. J. O. Howell, R. M. Wightman, *J. Phys. Chem.* **88**, 3915 (1984).
65. P. Hapiot, J. Moiroux, J. M. Savéant, *J. Am. Chem. Soc.* **112**, 1337 (1990).
66. K. Aoki, K. Tokuda, H. Matsuda, *J. Electroanal. Chem.* **235**, 87 (1987).
67. M. Fleischmann, S. Bandyopadhyay, S. Pons, *J. Phys. Chem.* **89**, 5537 (1985).
68. K. B. Oldham, C. G. Zoski, *J. Electroanal. Chem.* **256**, 11 (1988).
69. M. V. Mirkin, A. J. Bard, *Anal. Chem.* **64**, 2293 (1992).
70. A. Russell, K. Repka, T. Dibble, J. Ghoroghchian, J. Smith, M. Fleischmann, C. Pitt, S. Pons, *Anal. Chem.* **58**, 2961 (1986).
71. C. G. Zoski, D. A. Sweigart, N. J. Stone, P. H. Rieger, E. Mocellin, T. F. Mann, D. R. Mann, D. K. Gosser, M. M. Doeffer, A. M. Bond, *J. Am. Chem. Soc.* **110**, 2109 (1988).
72. R. M. Penner, M. J. Heben, T. L. Longin, N. S. Lewis, *Science* **250**, 1118 (1990).
73. F. N. Büchi, A. M. Bond, *J. Electroanal. Chem.* **314**, 191 (1991).
74. A. Owlia, J. F. Rusling, *Electroanalysis* **1**, 141 (1989).
75. A. M. Bond, T. L. E. Henderson, D. R. Mann, T. F. Mann, W. Thormann, C. G. Zoski, *Anal. Chem.* **60**, 1878 (1988).
76. J. Daschbach, D. Blackwood, J. W. Pons, S. Pons, *J. Electroanal. Chem.* **237**, 269 (1987).
77. Y. Zhang, C. D. Baer, C. Camaiioni-Neto, P. O'Brien, D. A. Sweigart, *Inorg. Chem.* **30**, 1682 (1991).
78. K. B. Oldham, C. G. Zoski, A. M. Bond, *J. Electroanal. Chem.* **248**, 467 (1988).
79. B. R. Scharifker, P. Zelenay, J. O'M. Bockris, *J. Electrochem. Soc.* **134**, 2714 (1987).
80. A. J. Bard, M. V. Mirkin, P. R. Unwin, D. O. Wipf, *J. Phys. Chem.* **96**, 1861 (1992).
81. J. Prikulis, F. Svedberg, M. Kall, J. Enger, K. Ramser, M. Goksor, D. Hanstorp, *Nano Lett.* **4**, 115 (2004).
82. N. B. Simpson, K. Dholakia, L. Allen, M. J. Padgett, *Opt. Lett.* **22**, 52 (1997).
83. T. B. Jones, *Electromechanics of Particles*, Cambridge University Press: Cambridge, UK, 1995.
84. U. Zimmermann, G. A. Neil, *Electromanipulation of Cells*, CRC Press, 1996.
85. M. Washizu, S. Suzuki, O. Kurosawa, T. Nishizaka, T. Shinohara, *IEEE Trans. Ind. Appl.* **30**, 835 (1994).
86. T. Müller, A. Gerardino, T. Schnelle, S. G. Shirley, F. Bordoni, G. DeGasperis, R. Leoni, G. Fuhr, *J. Phys. D: Appl. Phys.* **29**, 340 (1996).
87. M. P. Hughes, *Phys. Med. Biol.* **12**, 3639 (1998).
88. J. Dai, T. Ito, L. Sun, R. M. Crooks, *J. Am. Chem. Soc.* **125**, 13026 (2003).
89. G.-L. Lettieri, A. Dodge, G. Boer, N. de Rooij, E. Verpoorte, *Lab Chip* **3**, 34 (2003).

6.3 UME FABRICATION/CHARACTERIZATION BASICS

6.3.1 Platinum and gold inlaid disks $\geq 5 \mu\text{m}$ diameter

*Fu-Ren F. Fan¹, Jose Fernandez¹, Biao Liu¹,
Janine Mauzeroll², and Cynthia G. Zoski³*

¹Department of Chemistry and Biochemistry, The University of Texas at Austin, Austin, Texas 78712-0165, USA

²Laboratoire d'Electrochimie Moléculaire, Université Paris,
7-UMR CNRS 7591, France

³Chemistry Department, New Mexico State University, Las Cruces,
NM 88011, USA

6.3.1.1 Introduction

The fabrication of ultramicroelectrodes (UMEs) has been reviewed (1–3) and involves several steps. First, the end of a glass capillary is sealed such that a conical shape is obtained. A straight 25, 10, or 5 μm diameter metal wire is then positioned at the bottom of the sealed borosilicate glass capillary and put under vacuum for 30 min. The capillary is slowly sealed onto the wire using a heated resistor coil. The sealed wire is then electrically connected to a larger wire using a conducting silver epoxy. The connected tip is placed in the oven at 120 °C overnight to cure the epoxy.

This procedure can also be applied to 5 and 10 μm platinum and gold wires (where the use of soft glass capillaries is sometimes preferred). For smaller tips (1–2 μm diameter), a Wollaston wire (a metal wire covered by a silver layer) is first placed in weak nitric acid solution to dissolve the silver layer prior to sealing the tip (Section 6.3.2). A laser puller can also be used with small diameter quartz capillaries to make submicron size electrodes (Section 6.3.3). Such sealing techniques require much practice and patience.

UME tip fabrication also includes electrode polishing, sharpening, and characterization. The voltammetric behavior of the electrode is recorded to evaluate the quality of the glass/metal seal and the tip radius and that value is compared with the one observed optically. Conducting and insulating approach curves using scanning electrochemical microscopy (SECM) (see Chapter 12) can also be acquired and fitted to theory to determine the radius of the UME and the thickness of the insulating glass.

6.3.1.2 Sealing the capillary tube

Take a clean and dry Pyrex (borosilicate) glass capillary (at least 15 cm long to manipulate in a flame, inner diameter 1 mm, outer diameter 2 mm). The precleaned capillary should be moisture- and dust free so as to avoid bad sealing of the glass onto the wire. Polluting substances and water can lead to bubble formation next to the wire as the glass is melted. To circumvent this, the glass capillaries can be soaked in 1:10 diluted HNO₃, rinsed with copious amounts of distilled water, oven dried, and stored in an enclosed vial.

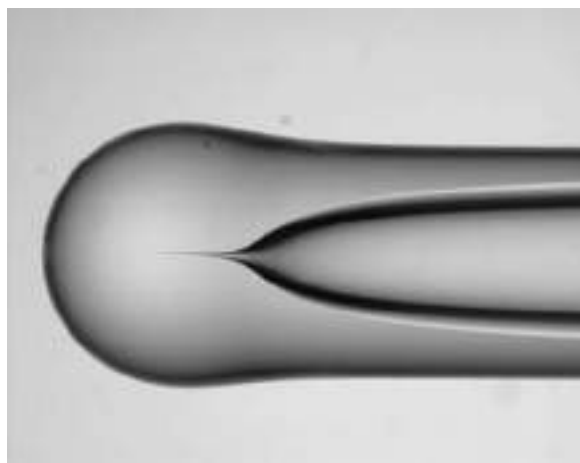


Figure 6.3.1.1 The end of a sealed glass capillary with an internal conical shape.

Use a gas/oxygen flame to seal one end of the glass capillary. Choose an adequate flame temperature, which is not too hot to avoid bending the glass. Rotate the capillary continuously on the side of the flame to obtain a conical shape (Figure 6.3.1.1). This shape must be obtained to adequately place the Pt wire in the capillary.

Check the capillary under a microscope and make sure that it is completely sealed at the base. Cut the glass capillary to about 5 cm length using a file.

6.3.1.3 Manipulating the platinum wire

Now that the capillary is sealed and shows a conical shape, a straight Pt wire must be inserted at the bottom of the capillary into the crack of the cone. Straightening the wire and positioning it is a time-consuming work and it is possible that you might have to take the wire out, straighten it several times before getting the desired results.

Using gloves, cut a piece of approximately 1.5 cm of hard (i.e., not annealed) platinum wire (5, 10, or 25 μm diameter, 99.9% purity) and rinse with acetone. The gloves are necessary to prevent finger oils from contaminating the wire.

Carefully straighten the wire with your fingers and without twisting it on a white piece of paper. This can be done by rolling the wire on a sheet of white glossy paper with a finger or the flat side of a wooden ruler. This might take several attempts.

Bring the straight wire to the edge of the paper and introduce the wire into the sealed glass capillary. At this point, special care must be taken not to bend the wire. The wire must go in straight. The use of tweezers tends to crimp the end of the wire making it difficult to fall into the glass capillary properly.

Position the wire at the bottom of the capillary in the crack of the cone (Figure 6.3.1.2) by gently tapping the capillary on the bench top. If the capillary is tapped too forcefully against the bench, the wire can sometimes bounce out of the capillary or curl up at the end. Checking under an optical microscope, the wire should be aligned as shown in Figure 6.3.1.2. If this

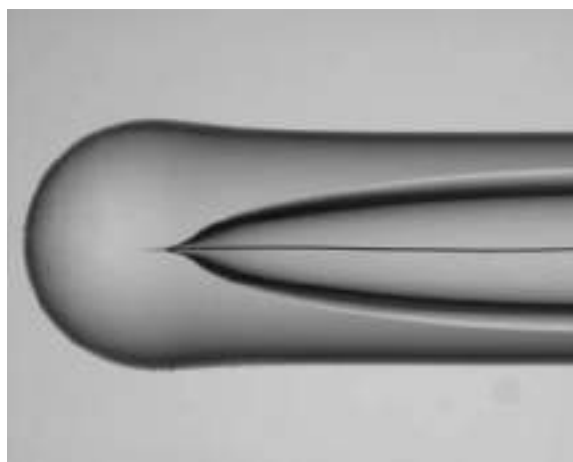


Figure 6.3.1.2 The 25 µm Pt wire is inserted at the base of the cone and remains straight. (for colour version: see colour section at the end of the book).

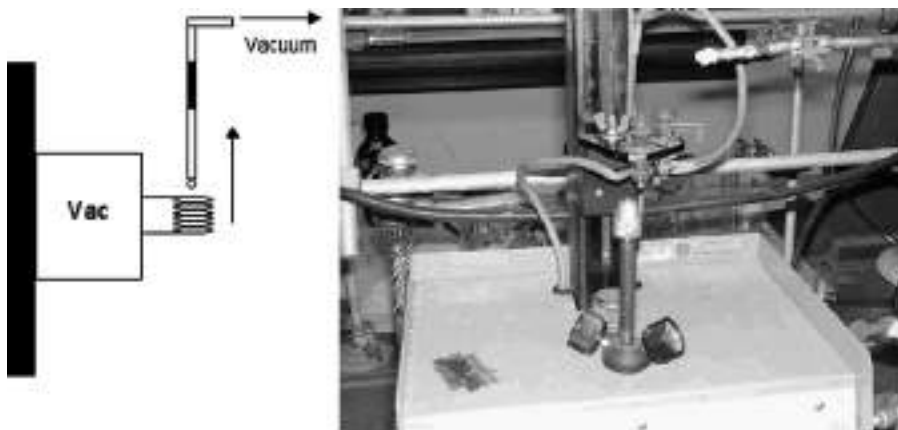


Figure 6.3.1.3 Left-hand side: Diagram of the setup where the capillary is aligned with the resistor coil. Right-hand side: Picture of the sealing setup.

is not the case, then the glass/wire assembly can be dropped through an approximately 10 cm glass tube of larger diameter, resting on a layer of Kimwipes to cushion the fall. Approximately 2 or 3 falls should align the wire in the capillary. If this does not center the wire, then it is often easiest to remove the wire from the capillary and start again.

6.3.1.4 Sealing the electrode

To seal the Pt wire into the glass capillary, a setup like that shown in Figure 6.3.1.3 is used. It is composed of a Nickel–Chromium resistor coil (gauge 18) that can be electrically

heated up to 800 °C. By turning the screw on the right-hand side of the vertical metal support, the coil can be moved vertically.

The power supply is an old pipette puller that has a 2.5-A fuse, a 120-V output, and a maximum power of 300 W. The Nickel–Chromium wire has a thickness of approximately 1 mm. It is coiled to a length of about 1 cm, with five or six turns, and an inner and outer diameter of 5 and 7 mm, respectively. The alligator clip above the coil is used to hold the glass capillary and help to align it perpendicularly to the bench top.

Connect the capillary tube to a vacuum line by inserting it into rubber tubing and clamping it to the alligator clip shown in sealing setup in Figure 6.3.1.3. Align the tip such that the capillary is perpendicular to the bench top and at the center of the resistor coil as depicted in Figure 6.3.1.3 on the left-hand side. If the capillary is not in the center of the coil and is closer to the sides, it will cause the capillary to bend during sealing. Take the time to make a good alignment and to move the coil up and down the capillary.

There should be a T joint between the UME capillary and the vacuum pump. Before turning on the vacuum, check that the T joint is in the closed position such that the capillary is not yet directly connected to the vacuum line. Turn on the vacuum. *Slowly* turn the T joint to the open position. This must be done slowly in order not to displace the Pt wire.

Leave the capillary under vacuum for 30 min. If the pump used is bad or the evacuation time is too short, air bubbles occur during the sealing process.

Center the glass capillary in the coil with the bottom of the capillary just inside the coil. This means that the bottom of the tip should be approximately 1 mm (or one coil diameter) inside the coil.

Turn on the power. The color of the coil should be orange yellow and not bright yellow. Leave the capillary at the bottom of the coil for 20 min so that the volatile compounds and residual moisture are evacuated.

Move the coil up the glass capillary very slowly to assure a proper sealing. Take steps of 1 mm every 5 min to seal approximately 1 cm of the capillary tube. Using a Kimwipe placed behind the capillary, make sure that the glass does not seal past the wire. Also, be very careful not to bump the setup while manipulating. If the glass capillary touches the hot sides of the coil, the process has to be repeated from the start.

Turn the power supply and vacuum off. Wait for the glass capillary to cool down. Remove the glass capillary and check under the microscope (Figure 6.3.1.4) to make sure that the wire has been properly sealed.

Once sealed, electrical contact between the Pt wire and a lead wire must be made. Using a hypodermic syringe (for example, a 3-ml syringe with a 22 G1.5 gauge needle works best for this size glass capillary), inject a premixed silver epoxy mixture (Epotek) into the glass capillary around the sealed wire. The epoxy must be inserted all the way down where the Pt wire is sealed. Next introduce a conductive wire (30AWG wire for this size capillary) into the tube and put the electrode in the oven (120 °C) overnight (i.e., for 10–12 h) to cure the epoxy.

6.3.1.5 Polishing the electrode

A small amount of 5-min epoxy should be patched between the connection wire and the end of the capillary to restrict the strain put on the connection wire. Allow to dry.

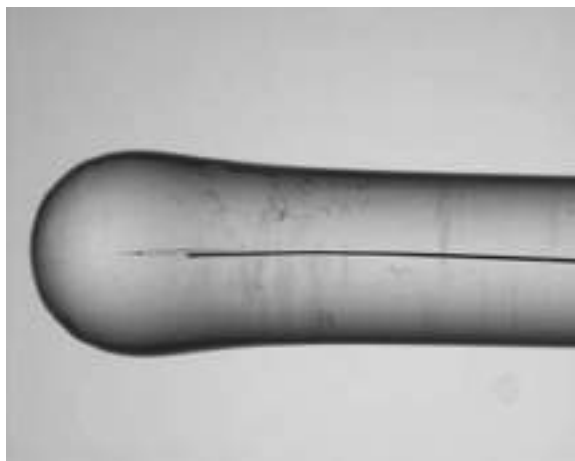


Figure 6.3.1.4 Sealed 25 μm Pt wire in a Pyrex capillary. A small air-pocket is observed at the beginning of the wire but the rest of the body is properly sealed. This is not unusual and can be shaved off during the polishing steps. (for colour version: see colour section at the end of the book).



Figure 6.3.1.5 Polishing wheel.

To polish the electrode, a polishing wheel can be used as shown in Figure 6.3.1.5. Sandpaper or micropolishing cloths are put at the center of the wheel. The lower speed levels of the polishing wheel are used to polish the electrodes.

Using sandpaper (Buehler, 400 or higher grit sandpaper), remove the glass from the bottom of the tip until the sealed platinum wire is exposed and observe under a microscope (Figure 6.3.1.6). Using water on the sandpaper while polishing sometimes reduces the strain on the glass.

Polish the tip by gradually increasing the grit size of the sandpaper (400, 600, 800, 1200). Try to maintain the electrode as vertical as possible so that the tip stays completely

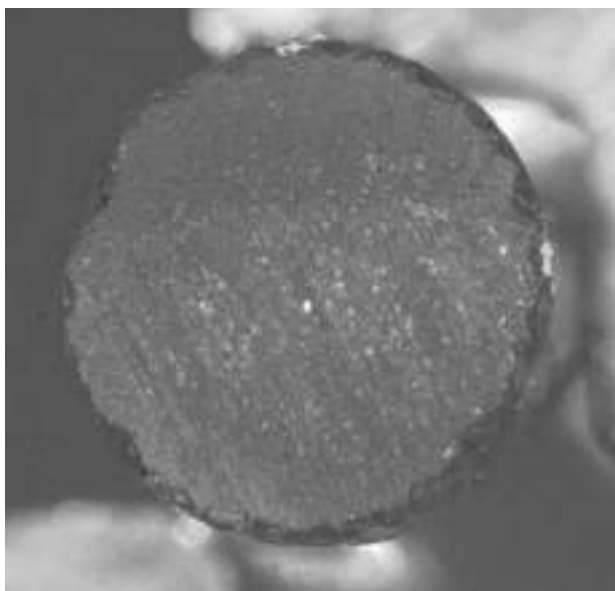


Figure 6.3.1.6 Polished capillary exposing the 25 μm Pt wire at the center. (for colour version: see colour section at the end of the book).

flat. Observe the polishing progress under the microscope. Always wash the surface of the electrode with Milli-Q water before changing from one sandpaper grit to another.

Use polishing cloth (Buehler) and solutions of alumina with different particle size (typically 1.0, 0.30, and 0.05 μm) to perform the final polishing. Always go from the larger grain size to the smallest one and use a different polishing cloth for each alumina size grain. The polishing cloths can be reused (as they are quite expensive). Make sure to wash the electrode surface extensively between alumina solutions. Decrease the particle size gradually and check under the microscope. A smooth surface must be obtained, as shown in Figure 6.3.1.7.

6.3.1.6 Checking the glass/metal seal

A steady-state voltammogram is recorded to check the seal between the glass capillary and the Pt wire. No matter how good the tip looks under the microscope, a steady-state voltammogram where the reverse scan retraces the forward scan, as shown in Figure 6.3.1.8, must be obtained. A solution of FcOH (1 mM in 0.1 M KCl) and a scan rate of 20 mV sec^{-1} were used in recording the voltammogram.

The initial potential was set to -0.2 V vs. Ag/AgCl , the reversal potential to 0.5 V , the final potential to -0.2 V , the initial scan polarity to positive, the scan rate to 0.02 V sec^{-1} , and the current sensitivity to $1 \times 10^{-8} \text{ A}$.

If the steady-state voltammogram does not resemble that in Figure 6.3.1.8, one has two choices: to throw away the tip or to repeat the polishing again to remove more glass to find a better sealed segment of electrode. The most common cause for electrode failure is unsuccessful sealing.

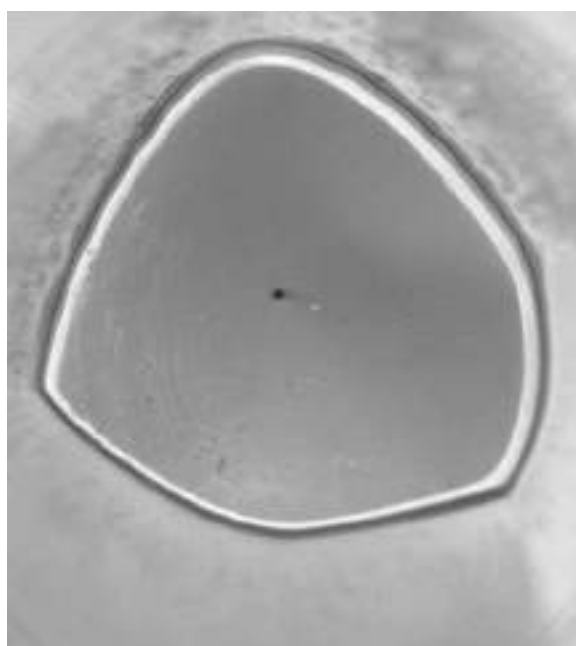


Figure 6.3.1.7 Smoothly polished 25 μm Pt UME that has been slightly sharpened.

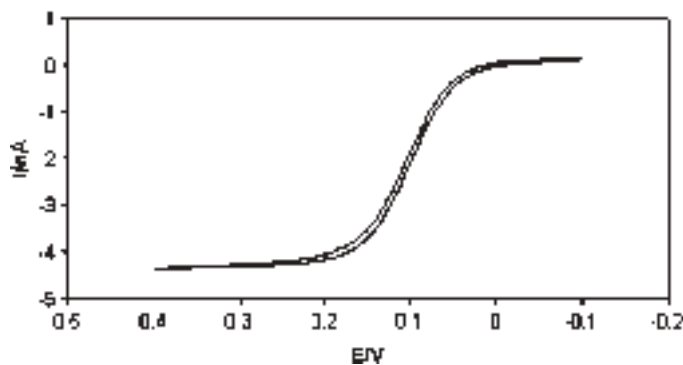


Figure 6.3.1.8 Steady-state voltammogram at a 25- μm diameter Pt disk UME in a solution of 1 mM ferrocenemethanol (FcOH) in 0.1 M KCl electrolyte. The potentials are given with respect to Ag/AgCl.

If the CV is satisfactory, the quantitative behavior of the tip can be checked by back calculating the radius of the electrode using the theoretical expression for the steady-state current. The steady-state current, i_{ss} ($\text{A} = \text{coulombs sec}^{-1}$), for a microdisk electrode can be expressed as:

$$i_{ss} = 4nFDaC^* \quad (6.3.1.1)$$

where n is the number of electrons involved in the electrochemical reaction ($n = 1$ eq. mol $^{-1}$), F is the Faraday's constant (96,485 C eq. $^{-1}$), D is the diffusion coefficient of the reacting species (for FcOH: $D = 7 \times 10^{-6}$ cm 2 sec $^{-1}$), C^* is the bulk concentration of the species (1×10^{-6} mol cm $^{-3}$), and a is the radius of the electrode (in cm).

From the optical measurements, we know that the radius of the electrode should be 12.5×10^{-4} cm. The value extracted from the voltammogram using equation 6.3.1.1 should be very close to that value.

When micron or sub-micron size electrodes are used, it can sometimes be very difficult to optically define the radius of the electrode. It is thus useful to use available analytical expressions to determine these values (as in equation 6.3.1.1) or to monitor decreases in electrode active area as a result of adsorption processes (4).

6.3.1.7 Electrode sharpening

Electrode sharpening of the glass insulator surrounding the metal electrode is necessary in scanning probe techniques, such as SECM (see Chapter 12), in experiments where small volumes of solution are used, and in those where the electrode is inserted into small places, such as in biological cells. The goal of electrode sharpening is to reduce the ratio of the diameter of the (metal + glass) to the diameter of the metal to 10 or less, with 2–5 being optimum. Thus, the ratio of the diameter of (metal + glass) to the diameter of the metal is the so-called RG value. The process of electrode sharpening is very individualistic. However, we describe a general method below and encourage the experimentalist to make modifications. It is important to emphasize that if a UME is fabricated for routine purposes, then a larger $RG \approx 20$ is adequate for equation (6.3.1.1) to be valid. Electrode polishing also becomes easier because one can see under an optical microscope if the metal has become recessed in the glass, such that the polishing material collects around the metal/glass seal. This is much harder to see if the metal is surrounded by glass of infinite RG.

Electrode sharpening begins with the use of 800-grit sandpaper on a polishing wheel. Hold the electrode at about a 45° angle while rotating the electrode in your fingers. Check on the RG value frequently under a microscope that is equipped with a measurement grid in the eyepiece. When $RG \approx 20$, change to 1200-grit sandpaper and continue using the polishing wheel, but stop more frequently to check under the microscope. At about $RG = 10$, it is advisable to sharpen the electrode manually on the 1200-grit paper with frequent trips to the microscope.

Desirable final shapes of the electrode tip are shown in Figure 6.3.1.9.

Depending on how one does the final polishing, the overall appearance of the tip can be different as seen in Figure 6.3.1.9. On the left-hand side, $0.3\text{ }\mu\text{m}$ alumina was used to finish sharpening the tip. This yields a much smoother glass rim that is often hard to photograph and gives the appearance of a recessed disk. The use of a 1200-grit sandpaper on the right-hand side yields a more defined edge that is easier to observe. Using sandpaper is faster, but requires more skill because it is more likely that the electrode area will be scratched up by glass debris or that the side of the Pt wire will be exposed.

Again, there is no one way of sharpening a UME tip and many people end up developing a method that works best for their skill and applications.

Before collecting experimental data, it is always a good practice to repolish the electrode manually with $0.05\text{ }\mu\text{m}$ alumina and to record a steady-state voltammogram of the tip, which

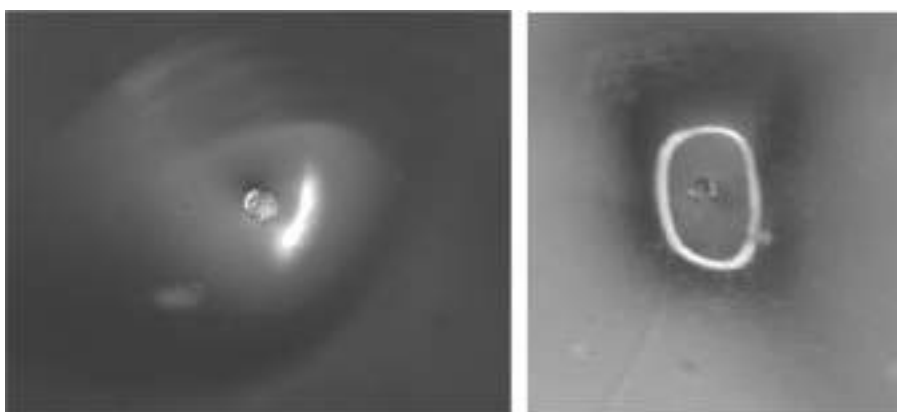


Figure 6.3.1.9 Left-hand side: 25 μm Pt tip with RG = 4; right-hand side: 25 μm Pt tip with RG = 3.

should look like that shown in Figure 6.3.1.8. It is important to note that when polishing with alumina particles greater than 0.05 μm or with grit paper, the RG value will increase. Thus, one needs to be constantly aware of the condition of the microelectrode that is being used.

REFERENCES

1. C. Amatore, in *Physical Electrochemistry: Principles, Methods and Applications*, I. Rubinstein, Ed., Marcel Dekker, Inc.: New York, 1995, p. 131.
2. R. M. Wightman, D. O. Wipf, *Electroanal. Chem.* **15**, 267 (1988).
3. F.-R. F. Fan, C. Demaille, in *Scanning Electrochemical Microscopy*, A. J. Bard, Ed., Marcel Dekker: New York, 2001, p. 75.
4. A. J. Bard, L. R. Faulkner, *Electrochemical Methods: Fundamentals and Applications*, 2nd ed., Wiley, 2001, pp. 569–571.

6.3.2 Platinum and gold inlaid disks $\leq 5 \mu\text{m}$ diameter

Biao Liu

Department of Chemistry and Biochemistry, The University of Texas at Austin, Austin, Texas 78712-0165, USA

6.3.2.1 Fabrication with Wollaston wire

The fabrication of disk-shaped Pt or Au microelectrodes of diameter less than 5 μm is similar to that described in Section 6.3.1 but employs a Wollaston wire (Goodfellow Metals, Cambridge, UK), i.e., a metal wire covered by a 50- to 100- μm silver coating (1, 2). The fabrication process is diagrammed in Figure 6.3.2.1. A 2-cm long Pt or Au Wollaston wire is inserted into one end of a 1-mm inner diameter glass capillary (Pyrex or soft glass) such

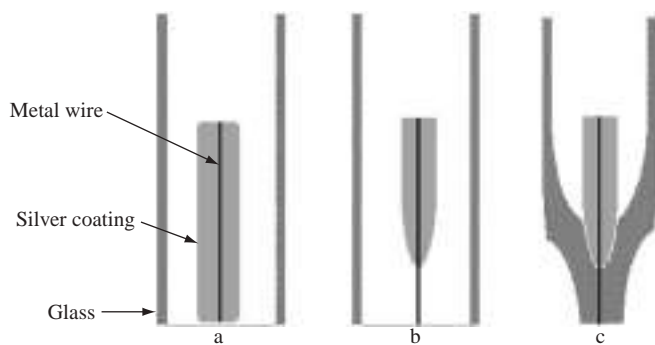


Figure 6.3.2.1 Schematic of Pt or Au UMEs with Wollaston wires. (a) Insert a 2-cm long Pt or Au Wollaston wire into one end of a glass capillary. (b) Remove the silver coating with 50% nitric acid. (3) Seal the wire into glass and polish it.

that one end of the metal wire is flush with the capillary opening. This end is then dipped into a 50% nitric acid solution to dissolve the silver coating. The quantity of nitric acid solution that fills the capillary by capillary action is controlled by judicious finger placement on the top end of the capillary so that about 3–5 mm of the metal wire is exposed. The nitric acid solution is then removed by placing the end of the capillary filled with nitric acid on a piece of filter paper or on a Kimwipe. The exposed wire must be thoroughly washed with distilled water to assure complete removal of the nitric acid. This typically requires approximately 20 separate flushings with water in the capillary by capillary action and subsequent removal via a Kimwipe. The glass capillary/wire assembly is then dried in an oven at 100 °C for 2 h. Extreme care must be taken during the dissolution of the silver coating and the washing procedure because the exposed wire is very fragile and easily broken.

The wire is secured in position by melting the glass tip of the capillary around the etched wire using a gas/oxygen flame, and then sealed into the glass using a heating coil by the same procedure as described in Section 6.3.1. It is essential that the junction between the bare and silver-coated section of the wire is sealed to prevent breakage of the wire during the use of the electrode. The electrical connection and polishing of the sealed wire are carried out by the same procedure as described in Section 6.3.1.

6.3.2.2 Fabrication with commercial pipette pullers

An alternative procedure for fabricating disk-shaped UMEs less than 5 µm diameter involves pulling metal wires into a glass capillary with the use of a commercial pipette puller (3–5) (see Section 6.3.3 for more detail). A 2-cm piece of wire with a diameter of 25 or 50 µm is inserted into a 10-cm long borosilicate or quartz capillary (1.2 mm outer diameter and 0.3 mm inner diameter) such that the wire is placed in the middle part of the capillary. It is important that microwire be classified as *annealed* and not hard be used. A laser-based pipette puller (P-2000, Sutter Instrument Co., Novato, CA) is used to pull the metal/glass assembly together. Usually two pulling programs are necessary. The first program is used to pull the glass capillary so that a firm connection between the glass and the platinum is formed. When the second program is run, the metal wire is pulled simultaneously with the glass leading to

a drastic decrease in its diameter and a simultaneous tight seal of the metal within the glass capillary. Both radii of the metal and surrounding glass can be controlled by changing the parameters of the pulling program, e.g., the temperature of heating and the strength of pulling.

Immediately after pulling, the platinum core may be covered with glass and must be exposed. In order to obtain disk-shaped UMEs, the pulled UME can be polished using a micropipette beveller (e.g., Sutter BV-10) equipped with a micromanipulator. The micro-manipulator is used to move the pulled UME toward a slowly rotating abrasive disk covered with 0.05- μm alumina. The axis of the pulled UME is kept perpendicular to the plane of the abrasive rotating disk. The diameter of the exposed platinum wire increases with the length of polishing. Optical microscopy is used to check the polished UME and the polishing is stopped when a desired size is obtained. UMEs with diameter of 1–3 μm can be obtained using this procedure. Nanometer-sized electrodes can also be obtained if the polishing is carefully controlled (see Section 6.3.3).

Once fabricated, the UMEs can be characterized using SEM and steady-state voltammetry as described in Section 6.3.1. If the UMEs are used as SECM tips, the size and the shape of the tips can be evaluated using SECM (6) as described in Chapter 12.

REFERENCES

1. R. M. Wightman, D. O. Wipf, in *Electroanalytical Chemistry*, A. J. Bard, Ed., Marcel Dekker: New York, 1989, Vol. 15, p. 267.
2. A. J. Bard, F.-R. Fan, M. V. Mirkin, in *Electroanalytical Chemistry*, A. J. Bard, Ed., Marcel Dekker: New York, 1994, Vol. 18, p. 243.
3. B. D. Pendley, H. D. Abruna, *Anal. Chem.* **62**, 782 (1990).
4. Y. H. Shao, M. V. Mirkin, G. Fish, S. Kokotov, D. Palanker, A. Lewis, *Anal. Chem.* **69**, 1627 (1997).
5. B. B. Katemann, W. Schuhmann, *Electroanalysis* **14**, 22 (2001).
6. A. J. Bard, M. V. Mirkin, Eds., *Scanning Electrochemical Microscopy*, Marcel Dekker: New York, 2001.

6.3.3 Laser-pulled ultramicroelectrodes

Janine Mauzeroll¹ and Robert J. LeSuer²

¹Laboratoire d'Electrochimie Moléculaire, Université Paris,
7-UMR CNRS 7591, France

²Department of Chemistry and Physics, Chicago State University,
Chicago, IL 60628

6.3.3.1 Introduction

This section discusses the fabrication of microelectrodes with diameters of a few micrometers to tens of nanometers using a laser-pulled technique. The methods discussed focus on the fabrication of platinum (Pt) ultramicroelectrodes (UMEs) sealed in

quartz, although the concepts can be readily applied to other glass/metal combinations. A general review of UME fabrication has been presented (1) and several publications have demonstrated the utility of laser-pulled tips (2, 3). This section provides a comprehensive description of laser-pulled UME fabrication, highlighting key steps and providing insight into trouble spots. The many parameters used in making laser-pulled UMEs add a significant amount of complexity but provide a comparable amount of flexibility in the final shape of the UME.

6.3.3.1 Microelectrode fabrication

(a) Equipment requirements (4)

The most important tool for fabricating pulled microelectrodes is a micropipette puller. A popular micropipette puller used for scanning electrochemical microscopy (SECM) microelectrodes is the Sutter Instrument (Novato, CA, <http://www.sutter.com/>) P-2000 CO₂ laser puller. A laser puller, which in 2004 cost approximately \$13k, has several advantages over resistance-based pulling systems. The most relevant of them to microelectrode fabrication are the ability to heat quartz and better control the heat distribution. Metal wire (Goodfellow) typically used is 25 µm in diameter though other diameters can be used. Platinum wire can be purchased in two different forms: hard or annealed. Annealed wire is generally softer and can be pulled at lower temperatures than hard Pt wire. However, hard Pt wire is easier to manipulate and is less likely to be damaged by mechanical stress. The parameters given below were designed for pulling annealed wire, but optimizations for hard wire configurations will be discussed as well.

Quartz capillaries (Sutter Instrument, Co.) with an outer diameter (OD) of 1 mm and inner diameter (ID) of 0.3 mm are preferred. Softer glass can be used, and must be used, if the microelectrode puller is based on resistance heating. The ID of the capillary will influence both the ability to position the wire properly and the thickness of the insulating glass sheath surrounding the metal surface of the UME. Sutter claims that their capillaries maintain a constant OD/ID ratio throughout the pull when making micropipettes. It is not clear how this translates to the construction of a UME as the wire is sealed into the glass capillary prior to pulling. Ideally, one would prefer a small OD/ID ratio as this means less insulating sheath will need to be removed during the polishing and beveling steps. However, for capillaries with the same OD, a thicker wall provides extra electrode stability as well as a smaller hole through which to align the axis of the microwire with that of the capillary.

Additional equipment includes a vacuum pump for evacuating the capillary prior to sealing along with vacuum tubing of appropriate size. After the electrode is pulled, contact can be made between the microwire and an electrode lead with either premixed silver epoxy, mercury, or a concentrated electrolyte solution. Additional larger capillaries as well as quick setting epoxy may be used to reinforce the microelectrode prior to exposing and polishing. To expose the UME wire with either sharpening or beveling, either commercial instruments (WPI or Sutter) or home built designs can be used. The basic necessities for polishing and beveling UMEs include: a method to rotate the electrode; a flat surface to apply polishing cloths of varying abrasiveness (600 or higher grit sandpaper, micropolishing cloths, 0.05 µm alumina slurries and diamond pastes, all of which can be supplied by

Buehler, Lake Bluff, IL); a method to manipulate the plane of the polishing surface; and a microscope or other method to facilitate viewing the UME tip. An optical microscope is a necessity for monitoring the various stages of pulled UME construction.

(b) Capillary and wire preparation

All materials should be handled with gloves and kept free of dust and debris to eliminate sealing of contaminants into the glass along with the microwire. Capillaries can be cleaned with a dilute (10% v/v) nitric acid solution, rinsed with water, and allowed to dry thoroughly in an oven. Pt wire can be cleaned with either dilute nitric acid or organic solvents (acetone and hexanes) followed by a rinse with high purity ($18 \text{ M}\Omega \text{ cm}$) water and a thorough drying. The next step is to straighten the microwire to be inserted into the center of the capillary. One to two centimeters of microwire should be carefully straightened by rubbing along the axis of the microwire. One should avoid twisting the microwire or introducing other mechanical stress that may result in breaks in the pulled microelectrode. Hard wire twists and bends less but requires more power in the pulling step to generate a useable UME. Using a stiff wire small enough to fit into the capillary, the Pt microwire is then positioned into the middle of the capillary so that, ideally, two symmetric microelectrodes can be produced from a pull.

(c) Wire sealing

After positioning the microwire into the center of a capillary, it is placed into the puller and a vacuum is attached to each end of the capillary (Figure 6.3.3.1). A vacuum is applied to the capillary for up to 30 min to remove residual moisture and to minimize bubble formation in the glass during the sealing. The safety shield of the P-2000 is not designed to support the vacuum tubes that are connected to the end of the capillary to be pulled. However, it is possible to apply a vacuum to the capillary without interfering with the safety mechanisms of the pipette puller and it is strongly encouraged that the reader contacts the manufacturer before diverging from recommended instrument use. To insure that the instrument exerts no pulling force on the capillary during the sealing step, stoppers (which can be home built or purchased from Sutter) are placed on each of the pulling sleds (Figure 6.3.3.2a). When the capillary is sufficiently evacuated, a heating program is applied to seal several millimeters of the microwire into the quartz. Of the five variables available on the P-2000 laser puller, only the heating power (H) and filament (F) are important for the sealing step. Two sets of parameters have been used successfully by the authors. With a heating power set to 900, the filament size is set to 4; or heating power and filament can be set to 925 and 15, respectively. The difference between the two programs lies in the amount of wire that will be sealed in the glass. For filament 15, the laser scans slowly over 8 mm of the capillary. A filament of 4 scans the laser over 6.5 mm of the capillary more quickly. The amount of metal sealed into glass will influence the length of the taper formed during the pull. In both cases, the heating program was applied for 50 sec, followed by a 25-sec cooling time. A total of five heating/cooling cycles were performed to insure a proper seal (Figure 6.3.3.2b). Schuhmann (3) reports that much lower heating can be used successfully (H: 775; F: 5) with five cycles of 40 sec heating and 20 sec cooling. The sealing and pulling parameters are influenced by the wear and tear of individual instruments. Thus, when optimizing the sealing step, one should monitor the extent of a

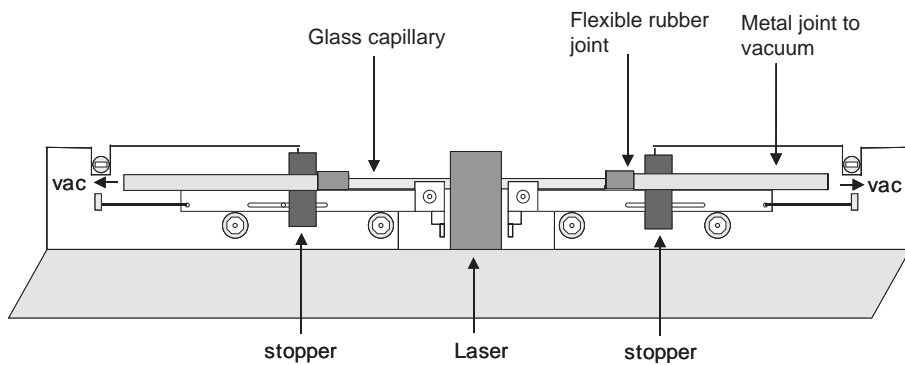


Figure 6.3.3.1 Diagram of the P-2000 laser-puller setup for the fabrication of Pt laser-pulled UME. The secured quartz capillary is connected via a rubber joint to a machine metal tube that is connected to a vacuum pump with a Y-joint. Two homemade stoppers are added to the sleds of the puller.

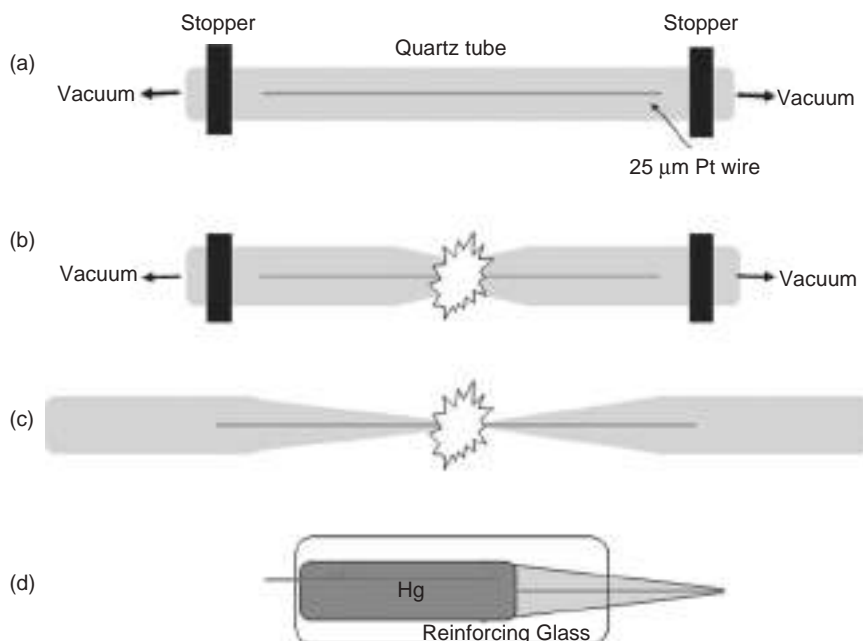


Figure 6.3.3.2 Diagram of the sealing and pulling protocol for the fabrication of Pt laser-pulled UME. (a) The straight Pt wire is inserted into the quartz capillary. The capillary is installed in the puller and connected to a vacuum. The sleds have been secured using stoppers. (b) The sealing program is run five times. (c) The pulling program is applied following the removal of vacuum and stoppers. (d) The pulled tips are electrically connected and strengthened with a larger diameter glass capillary.

seal after each cycle to minimize the amount of heating time required, because prolonged heating cycles could result in damage to the puller.

(d) Wire pulling

The P-2000 uses five parameters to conduct a pull. The heating power, H, is the amount of heat applied to the capillary. Filament, F, can be 1 of 16 values that determines the length of capillary heated as well as the speed at which the laser is scanned (Table 6.3.3.1). For a given H, slower scan speeds and smaller scan lengths result in greater heating of the capillary. Velocity, V, determines the point at which the glass has reached the desired temperature based on changes in glass viscosity. Once the velocity is achieved, the laser is shut off. On the P-2000, the magnitude of this value is counterintuitive; a higher value for velocity means the laser will shut off when the glass reaches a lower temperature. Delay, D, is the time between the laser shutting off and the hard pull. A delay of 127 indicates that the hard pull will trigger when the laser is shut off. Values above 127 (to a maximum of 255) indicate the millisecond delay between shutting off the laser and the hard pull. Values lower than 127 allow the user to initiate the pull with the laser still on. Pull, P, is the force exerted on the capillary to create the UME. With the exception of the delay, all of the parameters have units that are not easily translated into physical quantities. Each parameter has an important effect on the shape of the microelectrode and these are summarized in Table 6.3.3.2.

Optimization of a pulling program requires patience, practice, and a bit of luck. The efficiency of UME fabrication using this technique is rarely more than 60% and when every step is taken into consideration, is typically much less. Under ideal conditions, one capillary should produce two identical microelectrodes. However, small imbalances in the pulling solenoids or imprecise calibration of the laser scanning results in less than ideal behavior.

Table 6.3.3.1

Filament number corresponding to the scan length and scan speed of the laser for the Sutter P-2000

Speed	Length (mm)				
	1.5	1.9	4.5	6.5	8
Fast	1	2	3	4	5
medium	6	7	8	9	10
slow	11	12	13	14	15

Table 6.3.3.2

Effect of pulling parameter on the shape of the pull

Parameter	Increase	Decrease
Heat	Smaller tip; longer taper	Larger tip; shorter taper
Velocity	Smaller tip	Larger tip
Pull	Smaller tip; longer taper	Longer tip; shorter taper

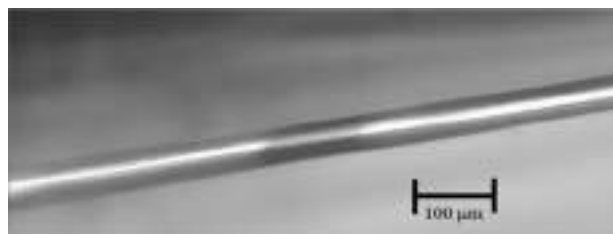


Figure 6.3.3.3 Optical micrographs of a break in the Pt wire, which occurred during the pulling step. Small cracks likely appear where the pulling force is exerted on a cooled portion of the electrode.

When attempting to optimize a pulling program, one should start with one of the programs listed here or a program suggested by the manufacturer that closely resembles the desired dimensions. Only one parameter should be adjusted at a time (for the P-2000, Sutter recommends changing values other than F in intervals of 5). The P-2000 reports the time required to pull the UME, and this value can be diagnostic of the success of the pull. To maximize the reproducibility of a parameter set, the values should be adjusted such that a pull takes between 4 and 6 sec to complete.

Two very similar procedures have been used by the authors with similar success. The first performs the pull within 25 sec of the final heating step, such that the quartz has not completely cooled prior to the pull. The laser is turned off, the vacuum tubes removed from the capillary and the stoppers removed from the pulling sleds followed by a pull using the parameters: *Heat*: 875; *Filament*: 2; *Velocity*: 130; *Delay*: 150; *Pull*: 200. This procedure results in electrode tapers of 3–5 mm and metal disk diameters from 200 nm to 4 μm. Alternatively, the sealed capillary can be cooled to room temperature prior to executing a pull using the parameters: *Heat*: 875; *Filament*: 2; *Velocity*: 50; *Delay*: 120; *Pull*: 200. This method results in electrodes with tapers of roughly 1 cm and electrodes as small as 3 nm diameter have been fabricated.

It is important to inspect a pulled UME to insure continuity of the Pt wire. Oftentimes, small cracks from 1 to 100 μm will occur. These cracks typically occur either where the glass begins to taper or at the very tip of the UME and are most likely due to a section of Pt wire being pulled when it has cooled too much. Cracks at each of these locations can be avoided by systematically optimizing the pulling parameters (Figure 6.3.3.3). When a crack is at the start of a taper, the glass surrounding that portion of wire likely absorbs much of the heat from the laser and the Pt microwire does not melt sufficiently. Either a smaller velocity or higher heat value can be used to supply more heating to the capillary at this stage of the pull. When the crack occurs at the tip of the UME, the wire has cooled too much toward the end of the pull, and the delay between the hard pull and the laser shut off trigger should be lowered. Note that by changing these values, the shape of the UME will change as well, so parameters should be changed only enough to eliminate the break in the Pt wire.

(e) Electrical connection and reinforcement

Connection of an electrode lead to the unsealed Pt wire can be made with mercury, silver epoxy, or a concentrated electrolyte solution. Mercury is the easiest material for

making electrical contact but can easily be displaced and results in loss of contact. An electrolyte solution can be used for making electrical contact but problems related to a shift in electrode potentials and the possibility of solution evaporation over time can occur. Silver epoxy provides a solid contact with the least amount of capacitance. However, delivery of the epoxy into a small capillary is challenging. To deliver mercury into a 0.3-mm ID capillary, a long syringe was custom made from HPLC-like needles that could fit onto a typical disposable syringe (SGE Inc., Austin, TX). We have had the most success with Hg contacts and Schuhmann (3) reports good results with silver epoxy. To provide additional stability, the UME can then be sealed in a larger, reinforcing glass tube using 5-min epoxy. This step is sometimes avoided since it is critical that the axis of the UME be parallel to the reinforcement tube. However, rotation of the UME/reinforcement tube while the epoxy dries gives a satisfactory result. Figure 6.3.3.2 summarizes the four steps of UME fabrication using a laser puller.

(f) *Exposing the metal surface*

The authors used a home built beveller to expose the Pt disk and sharpen the UME; however, commercial bevellers are available (WPI or Sutter). Generally, solid-surface bevellers use a high quality lapping film that is widely used in the fiber optics industry and can be easily replaced if the abrasive is damaged or saturated with glass particles. Other models rely on optically-flat mirrored glass disks, wetted with an abrasive slurry to bevel fluid-filled microelectrodes that are commonly used in microinjection applications. In the former case, the beveller spins at 4000 rpm to provide sufficient cutting force to produce a sharp, uniform tip in a very short time. The latter model spins at 60 rpm and is said to be preferred for pipettes that are 1 μm or less. Fluid-filled pipettes are hollow and much more delicate than pulled tips and so in designing our home-built system, we elected to work with high spin rates so that a minimum amount of time would be needed to expose and shape the tips. Only one touch to the polishing cloth is necessary to change the surface of the electrode and the least amount of manipulation is desirable.

The home-built beveller consisted of a rotating-disk electrode combined with a flat surface that could be translated up and down and tilted (Figure 6.3.3.4a). To expose the Pt surface, the UME is wrapped in Teflon tape, placed in a rotating-disk electrode setup (Pine Instrument, Co., Grove City, PA) and rotated at 5000 rpm. The desired polishing material is applied onto a flat surface, which is brought in contact with the rotating UME. Touching the tip of the UME to the abrasive surface can be observed as an oscillation of the long quartz end. This procedure is repeated until a reasonable CV response is obtained. The procedure is repeated with various polishing materials, typically starting with wet 1200 grit sandpaper and finishing with 0.05 μm alumina on a polishing cloth, until the CV response of the UME is ideal (Figure 6.6.3.4b).

Alternatively, the exposing step can be performed using hydrofluoric acid (2). Unlike polishing, HF etching will produce a conical or cylindrical UME. Although this may cause complications in the quantitative analysis of data, a protruding metal tip minimizes the difficulties of crashing the insulating sheath into a surface, and precise knowledge of zero tip/substrate distance can be obtained. Very small UMEs have been obtained by dipping a pulled tip in 49% HF solution for 3 sec three times (Figure 6.3.3.5). Concentrated HF solutions dissolve quartz very quickly, especially on UMEs with taper thicknesses less than

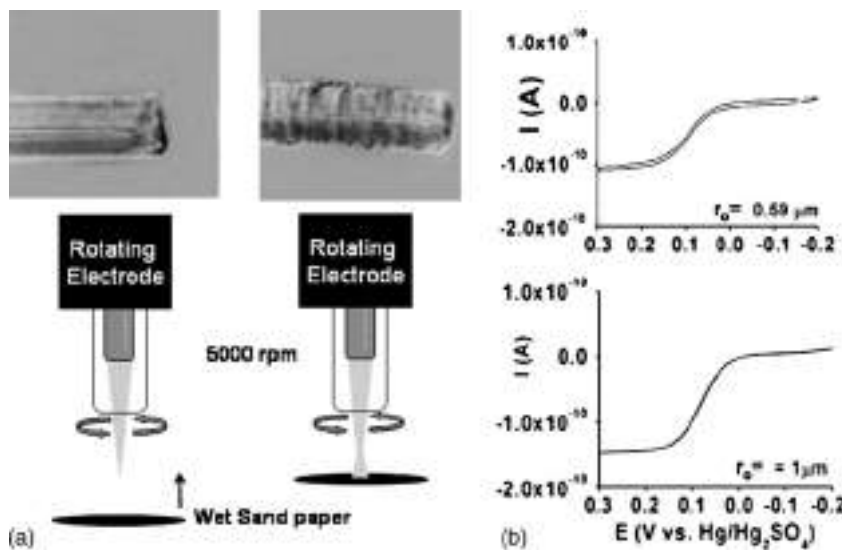


Figure 6.3.3.4 (a) Exposing the Pt surface using a homebuilt beveller. (b) Voltammetric response of exposed tips in 1 mM ferrocenemethanol/0.1 M KCl.

1 μm . Very little work has been done with HF etching of UMEs. However, as the SECM theory for conical tips has been developed (5), this method should be explored as a viable alternative to mechanical polishing.

(g) Sharpening and etching

The final step in making an UME for SECM techniques is also the most challenging. The goal is to remove enough of the insulating glass sheath from the tip of the electrode such that the diameter of the sheath is (ideally) less than 10 times the diameter of the metal disk. Like sharpening a pencil, quartz surrounding the exposed Pt disk can be removed by polishing the UME at an angle. A flat surface with fine grit (600+) sandpaper is tilted and brought into contact with the UME. Unlike exposing the metal surface, where a UME slightly off the rotation axis was advantageous, UME sharpening requires the tip to be on the rotation axis in order to avoid asymmetry in the sharpening and, worse, breaking of the UME. Quartz tapers are surprisingly flexible and can withstand a small amount of bending, thus allowing contact between the tip and the abrasive surface to be observed (Figure 6.3.3.6a). UMEs sharpened in this way result in insulating sheath diameters that are approximately 10–20 times larger than the disk diameter (Figure 6.3.3.6b).

6.3.3.2 Microelectrode characterization

(a) Voltammetry

Voltammetric techniques are used in analyzing the qualities of a new UME as discussed in Section 6.3.1. Slow scan ($<100 \text{ mV sec}^{-1}$) linear sweeps should result in a scan rate

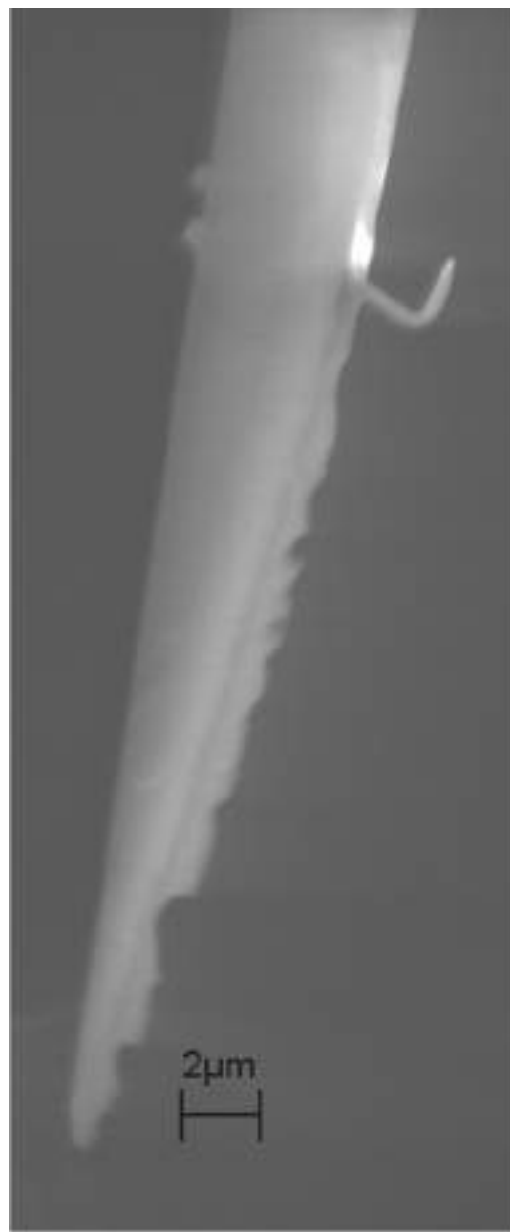


Figure 6.3.3.5 Scanning electrochemical micrograph (SEM) of an etched HF UME. Etching of a sealed Pt UME in concentrated HF for several seconds can provide electrodes with very small RGs. However, the etching process is not easily controlled and can yield nonideal results.

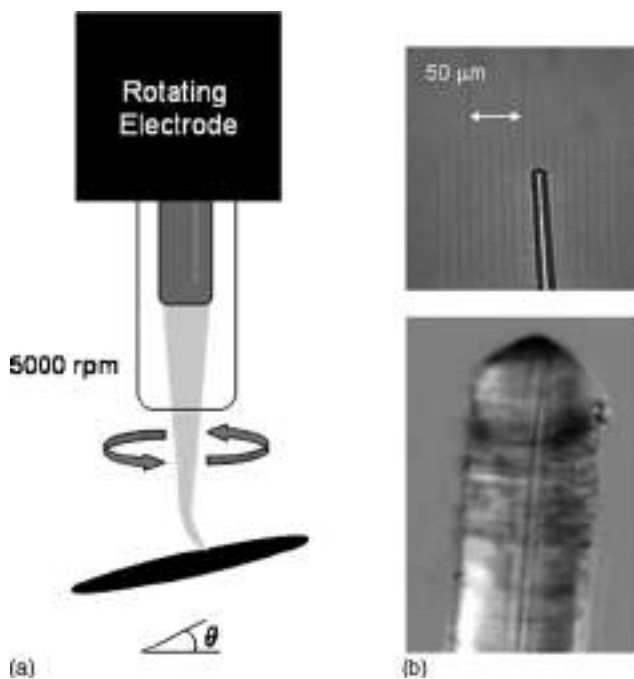


Figure 6.3.3.6 (a) Sharpening of the exposed Pt UME using the homebuilt beveller. (b) Optical micrographs of a sharpened UME.

independent sigmoidal curve with a current height equal to nFr_0DC^* where n is the number of electrons transferred, F is the Faraday constant, r_0 is the radius of the disk, D is the diffusion coefficient, and C^* is the concentration of the electroactive component in solution. Ideal voltammetric behavior consists of a steady-state plateau in the forward portion of the potential sweep and a reduced capacitive hysteresis on the return portion of the sweep. As seen in Figure 6.3.3.4b, pulled-laser UMEs behave like ideal UMEs in terms of retraceability, reduced capacitance, and stability of the steady-state current. In electrochemical studies where small analyte concentrations are of interest, these tips are well suited (6). These electrodes maintain a well-shaped sigmoidal behavior even at high scan rates and the lack of background current indicates that the electrodes are tightly sealed.

Measuring the resistance between a UME and an indium/gallium alloy is an alternative method of estimating the electrode surface area of a UME (2). This method has been incorporated into some commercial bevellers for monitoring exposure of the UME disk during polishing. However, this method has the disadvantage of contaminating the electrode with the alloy.

Neither voltammetry nor resistance methods can easily differentiate between planar and nonplanar geometries, and other techniques need to be used in order to fully characterize a UME. Two other techniques, SECM (see Chapter 12) and scanning electron microscopy (SEM), help to differentiate between an inlaid disk, recessed, and conical-shaped UMEs.

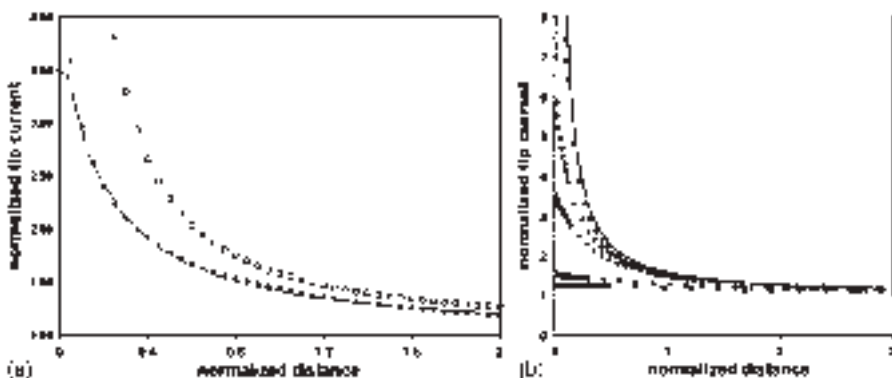


Figure 6.3.3.7 (A) Steady-state current–distance curves for mercury/Pt (25 μm diameter) hemispherical tip (line) as compared with theoretical behavior of a planar disk (\square) and hemispherical (\bullet). [Reproduced with permission from J. Mauzeroll, E. A. Hueske, A. J. Bard, *Anal. Chem.* **75**, 3880–3889 (2003). Copyright 2003, American Chemical Society.] (B) Steady-state current–distance curves for a “lagooned” tip over a planar conductive substrate corresponding to different values of the parameter l/a (where l is the depth of metal recession and a is the tip radius) and the analogous working curve for a disk-shaped tip. l/a : 10 (\square), 5 (\blacksquare), 1 (\bullet), 0.5 (\circ), and 0.1 (Δ). The upper curve was computed for a disk-shaped tip from equation S11 of reference (2). [Reproduced with permission from Y. Shao, M. V. Mirkin, G. Fish, S. Kokotov, D. Palanker, A. Lewis, *Anal. Chem.* **69**, 1627 (1997). Copyright 1997, American Chemical Society.]

Feedback mode SECM experiments (Figure 6.3.3.7a) can distinguish between different UME geometries of conventional size (7–13). In the case of laser-pulled tips, present SECM theory can also distinguish between inlaid and noninlaid geometry (Figure 6.3.3.7b). The feedback current response for a recessed and a convex geometry (hemispherical, conical, and spherical) will both result in a lower normalized current response than that of the inlaid geometry (2). In positive feedback mode, the recessed geometry will yield a positive feedback response when slightly recessed and what appears to be kinetically controlled behavior when deeply recessed. It will also have a maximum current related to the contact of the glass opening with the metal surface and the sealing of the microcavity. The convex geometries will yield positive feedback and present a short circuit current when put in contact with the conductive substrate.

SEM can be used to “visually” inspect UMEs (Figure 6.3.3.8). Images allow one to determine the approximate diameter and geometry of a UME as well as to determine the electrode RG and observe if the disk is centered in the quartz. The biggest difficulty in obtaining suitable SEM images is that the large amount of insulating material surrounding a small, conductive disk sometimes results in a significant amount of distortion due to charging of the quartz sheath.

6.3.3.3 Microelectrode maintenance and storage

Maintenance of UMEs is a misnomer because the time it takes to “repair” a nonfunctioning electrode can be better spent fabricating a new UME. However, broken or fouled



Figure 6.3.3.8 Scanning electron micrographs of 50-nm radius conductive Pt disk somewhat displaced toward the edge of the 1- μm radius glass ring. [Reproduced with permission from Y. Shao, M. V. Mirkin, G. Fish, S. Kokotov, D. Palanker, A. Lewis, *Anal. Chem.* **69**, 1627 (1997). Copyright 1997, American Chemical Society.]

UMEs can be cut to larger diameters (2–5 μm) and used as conventional electrodes for many months. Electrodes can be stored dry, typically on a glass slide or taped to some other surface to protect the fragile tip, or they can be stored in distilled water to minimize contamination from air pollutants. Unlike larger (25 μm diameter) microelectrodes, polishing is not a suitable cleaning method unless an increase in the electrode area is acceptable. UMEs on the order of 1 μm diameter and larger can, in principle, be polished and sharpened by hand without increasing the electroactive area. Fouled UMEs can sometimes be cleaned electrochemically via cycling through the potential window of 0.5 M H₂SO₄ for 20 min (14). It is also possible to renew a UME by bathing it in the vapor of refluxing HNO₃ followed by electrochemical reduction of the PtO surface (15). One should note, however, that with very small UMEs, the formation of an oxide layer and its subsequent removal can result in the active surface becoming recessed.

6.3.3.4 Conclusions

This section has described the fabrication of sub 100 nm electrodes based on a laser-pulling technique. Because laser-pulled UMEs with an inlaid disk geometry require a mechanical sharpening step, micrometer to submicrometer dimensions might be the practical limit for electrodes fabricated with this technique. If an inlaid disk is not a requirement, the lower limit of electrode size can be extended to the 10 nm region by using HF-etching techniques to expose a conical surface.

The push towards nanometer sized electrodes brings with it challenges in some of the fundamental assumptions made in electrochemistry as discussed in reference (16).

REFERENCES

1. A. J. Bard, M. V. Mirkin, *Scanning Electrochemical Microscopy*, Marcel Dekker, Inc.: New York, 2001.
2. Y. Shao, M. V. Mirkin, G. Fish, S. Kokotov, D. Palanker, A. Lewis, *Anal. Chem.* **69**, 1627 (1997).
3. B. B. Katemann, W. Schuhmann, *Electroanalysis* **14**, 22 (2002).
4. The companies listed are those that have been used by the authors, but their inclusion in this chapter is neither an endorsement nor a statement that they are the only companies that provide such services.
5. C. G. Zoski, B. Liu, A. J. Bard, *Anal. Chem.* **76**, 3646 (2004).
6. J. Mauzeroll, A. J. Bard, *Proc. Natl. Acad. Sci. USA* **101**, 7862 (2004).
7. M. V. Mirkin, F. R. F. Fan, A. J. Bard, *J. Electroanal. Chem.* **328**, 47 (1992).
8. C. Demaille, M. Brust, M. Tionsky, A. J. Bard, *Anal. Chem.* **69**, 2323 (1997).
9. Q. Fulian, A. C. Fisher, G. Denuault, *J. Phys. Chem. B* **103**, 4387 (1999).
10. Q. Fulian, A. C. Fisher, G. Denuault, *J. Phys. Chem. B* **103**, 4393 (1999).
11. Y. Selzer, D. Mandler, *Anal. Chem.* **72**, 2383 (2000).
12. C. G. Zoski, M. V. Mirkin, *Anal. Chem.* **74**, 1986 (2002).
13. N. J. Gray, P. R. Unwin, *Analyst* **125**, 889 (2000).
14. B. Liu, A. J. Bard, M. V. Mirkin, S. E. Creager, *JACS* **126**, 1485 (2004).
15. R. N. Adams, *Electrochemistry at Solid Electrodes*, Marcel Dekker, Inc.: New York, 1969.
16. C. Amatore, in *Physical Electrochemistry: Principles, Methods and Applications*, I. Rubinstein, Ed., Marcel Dekker, Inc.: New York, 1995, p. 131.

6.3.4 Platinum conical ultramicroelectrodes

Biao Liu

Department of Chemistry and Biochemistry, The University of Texas at Austin, Austin, Texas 78712-0165, USA

6.3.4.1 Introduction

Conical-shaped ultramicroelectrodes (UMEs) are of special interest in connection with the imaging of surfaces, in kinetic studies, in probing thin films, and in probing minute environments, such as single cells. The most common fabrication procedure is by the etching of platinum wire or carbon fibers followed by coating with an insulating material except at the apex of the electrode. In this section, the fabrication of both blunt and sharp conical electrodes are discussed.

6.3.4.2 Blunt conical UMEs

Pt conical UMEs are constructed from 25 μm or 50 μm diameter Pt or Pt–Ir wires. A 2-cm length of Pt wire is connected to a conductive wire with silver epoxy (Epotek, H20E, Epoxy Technology, Inc., Billerica, MA). The ensemble is then enclosed in a glass capillary, which

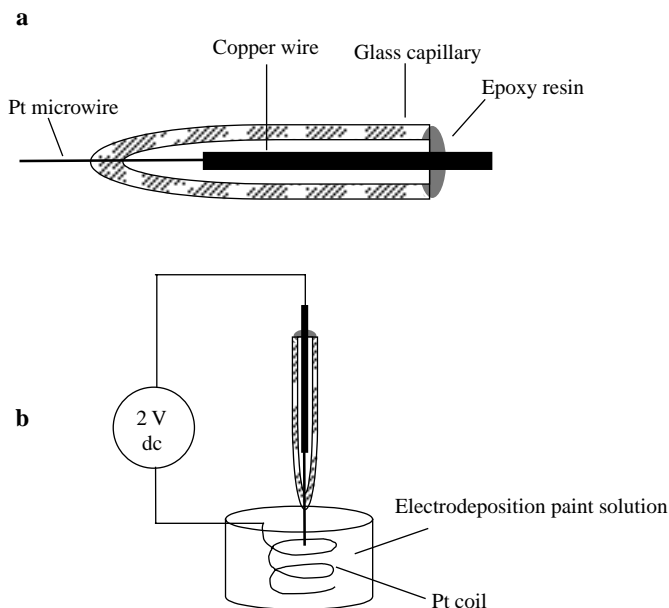


Figure 6.3.4.1 Schematic of the setup for the fabrication of Pt conical UMEs. (a) A Pt wire is sealed into glass capillary. (b) The etched wire is insulated with electrophoretic paint.

has first been drawn to a fine point using a pipette puller, such that ~5 mm of the microwire is protruding. The Pt wire is sealed in the glass capillary by melting the glass tip of the capillary around the wire using a heating coil or by heating over a gas/oxygen flame (Figure 6.3.4.1).

The Pt wire is then electrochemically etched in a solution containing saturated CaCl_2 (60% by volume), H_2O (36% by volume), and concentrated HCl (4% by volume) (1). Other etching solutions, such as concentrated NaNO_2 (2, 3), NaCN , or NaOH (4, 5) can also be used. About 2 mm of the wire is immersed in the solution. An alternating voltage of ~5 V rms is applied between the Pt wire and a large area carbon plate electrode using a Variac transformer. As the etching proceeds at the air/solution interface, bubbles form at the Pt/solution interface. The Variac transformer is switched off immediately upon cessation of bubbling as the top part of the electrode in air loses contact with the solution. The electrode shape at this point is not perfectly conical and has a longer sharp protrusion from the tip (i.e., the etched wire is very sharp). This is “trimmed” by turning the Variac transformer back on and very rapidly immersing the tip into the etching solution for very short (<1 sec) periods several times. Repeated “trimming” may be necessary to get a desired aspect ratio of the conical electrode. After “trimming”, the wire is thoroughly rinsed with deionized water. The etched wire is then dipped for ~3 sec in a 3:1 $\text{HCl}:\text{HNO}_3$ solution to clean the Pt surface, washed with copious amounts of deionized water, and then dried in an oven at 110 °C for 2 h.

The etched conical Pt tips are then coated with an insulating material, except at the apex of the tip. A number of coating procedures have been reported in the literature,

including RF sputtering of insulating materials (6), dipping the tip in a varnish (7, 8) or molten paraffin (9), and translating the tip through a molten bead of glass (5, 10), poly(α -methylstyrene) (5), or apiezon wax (4, 11) held on a heated support. The etched Pt UMEs have also been coated by electrodepositing insulating layers onto the metal surface (2, 3, 12–15).

A commonly used anodic electrophoretic paint consists of poly(acrylic acid) (PAAH) with an excess of base added to make it water-soluble by deprotonation of the acidic groups thus forming the PAA^- species. Prior to use, the anodic paint is diluted with water (1:15 by volume). The etched wire is immersed in the dilute aqueous paint solution and positioned in the center of a Pt coil (0.5 mm diameter), as shown in Figure 6.3.4.1b. A dc potential of ~2 V is applied between the etched wire and the Pt coil until the current reaches a steady state (after ~30 sec). The anodic current flow produces a local pH decrease at the electrode surface, induced by water oxidation, and generates water insoluble PAAH that deposits onto the etched metal surface. The insulated electrode is removed from solution and dried at 150 °C for 3 min. During heat curing, the insulating layer shrinks so that the sharp end of the tip is exposed, while the shaft of the tip is completely insulated. Usually, the entire coating procedure is repeated one or two times with more dilute anodic paint solution (1:20 by volume) to insure any pinholes formed in the first curing are sealed. The exposed end of the conical electrodes prepared using the approach described above is usually nanometer sized.

6.3.4.3 Sharp conical UMEs

Recently, an approach has been developed to prepare micrometer-sized conical Pt electrodes (16). In this method, the conical Pt microelectrodes are constructed from 25 μm diameter Pt wire. The Pt wire is electrochemically etched as described above. Working under an optical microscope, the etched Pt wire is inserted into one end of a pulled glass capillary with an inner diameter of ~20 μm such that the sharp end of the Pt tip is flush with the capillary opening, which is then melted around the Pt wire by using a gas/oxygen flame. The glass capillary is placed on the stage of an optical microscope, and the etched wire is inserted into the capillary until the sharp end of the wire is flush with the capillary opening. The inserting process is monitored under the optical microscope. The 20- μm diameter glass capillary is prepared by pulling a borosilicate glass tube (O.D. = 1.0 mm, I.D. = 0.58 mm) with a micropipette puller (Model P-2000, Sutter Instrument Co.). A one-line program can be used in the pulling with the parameters: Heat = 300, Filament = 4, Velocity = 35, Delay = 200, and Pull = 0.

Careful control of the flame temperature and heating time is critical to obtaining a well-sealed tip. Thus, the Pt tip/capillary assembly is held in the cone part of the flame near the nozzle outlet for ~2 sec. The melted glass retracts from the tip on cooling, giving conical Pt electrodes with the base radius of the cone of \approx 5–10 μm and the cone height of \approx 10–20 μm , as shown in Figure 6.3.4.2.

Once fabricated, the conical electrodes can be characterized by scanning electron microscopy (SEM), transmission electron microscopy (TEM), steady-state voltammetry (SSV), and scanning electrochemical microscopy (SECM) (see Chapter 12).

The conical UMEs are first characterized by steady-state voltammetry to get an estimate of the radius from the limiting current. When using steady-state voltammetry in this way,

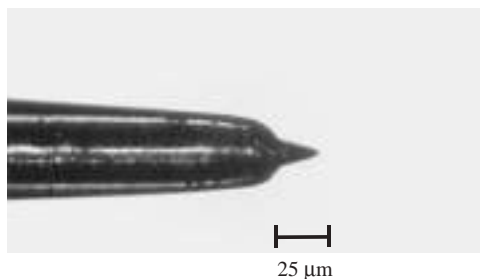


Figure 6.3.4.2 The optical image of a micrometer-sized conical Pt electrode. (The photo was provided by the Electrochemistry Laboratory of the Department of Chemistry and Biochemistry, University of Austin at Texas.)

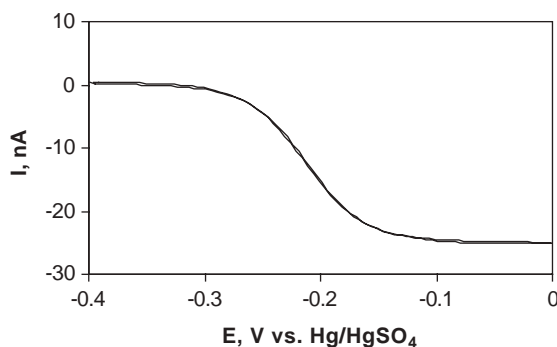


Figure 6.3.4.3 Steady-state voltammogram of a conical Pt tip in an aqueous solution contained 1 mM ferrocenemethanol and 0.1 M KCl. The potential scan rate was 20 mV sec⁻¹.

well-characterized systems having rapid heterogeneous electron transfer are used. Commonly used aqueous systems include the oxidation of ferrocenemethanol and the reduction of ruthenium hexamine. Figure 6.3.4.3 shows a typical CV obtained at a conical Pt. In steady-state voltammetry at UMEs, the current–potential curve is sigmoidal in shape. The voltammetric response for a well-insulated UME shows little hysteresis on the return scan. Large hysteresis on the return scan is an indication that the sweep rate is too fast, or that there is a poor seal between the insulator and metal wire. The apparent electrochemical radius of the electrode is calculated from the diffusion-limited plateau current, i_{lim} , assuming a hemispherical or disk geometry.

$$i_{\text{lim}} = 2\pi nFDC * r_o \quad (\text{hemisphere}) \quad (6.3.4.1)$$

$$i_{\text{lim}} = 4nFDC * r_o \quad (\text{disk}) \quad (6.3.4.2)$$

where n is the number of electrons, F is Faraday's constant, D is the diffusion coefficient, C^* is the bulk concentration of electroactive species, and r_o is the radius of a hemisphere or a disk. Using these equations, the electrode radius for a specific UME geometry can be determined and compared with values obtained from electron microscopy images.

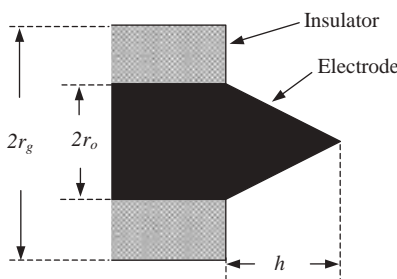


Figure 6.3.4.4 The schematic of a finite conical electrode.

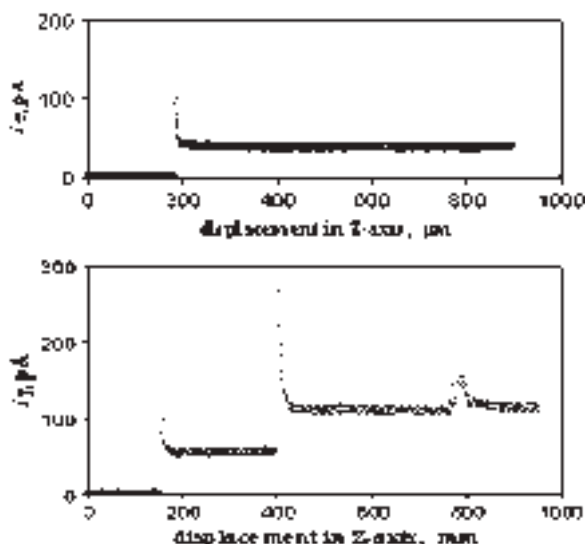


Figure 6.3.4.5 The electrochemical approach curves of a Pt UME insulated with electrophoretic paint to an air/solution interface. (a) Electrode insulation is good. (b) Electrode insulation is poor. The solution contained 10 mM $\text{K}_3\text{Fe}(\text{CN})_6$ and 0.1 M KCl. The tip potential was 0.1 V vs. Ag/AgCl. (The data was from the Electrochemistry Laboratory of the Department of Chemistry and Biochemistry, University of Austin at Texas.)

SEM and TEM have also been used for the characterization of conical UMEs. From SEM or TEM images, one can obtain an estimate of the radius of the electrode as well as the radius of the insulating material (2, 17). The side-view images can also provide information regarding whether the metal or fiber is in the plane of, recessed within, or protruding from the insulating material.

SECM has proven to be a valuable tool for the characterization of conical UMEs to obtain the geometrical parameters of a UME, including the insulating sheath (11, 16, 18, 19). Electrode characterization with SECM is based on approach curve measurements of a UME tip current, i_T , as a function of the tip–substrate separation, d , over either a

conducting or insulating substrate (refer to Chapter 12 for the theory and application of SECM). The SECM approach curves depend on the ratio of the base radius of the cone (r_o) to the height of the cone (h) and on the thickness of the insulating sheath ($\text{RG} = r_g/r_o$, where r_g is the radius of the insulating sheath, Figure 6.3.4.4). The shape parameters of a conical electrode, including r_o , h , and RG can be obtained by fitting experimental SECM approach curves to theoretical ones (16).

SECM can also be used to gain information about the quality of the insulation on the conical tips. An approach curve is obtained at the air/solution interface, where the solution contains a redox mediator such as $\text{Fe}(\text{CN})_6^{3-}$. The potential sufficient to reduce $\text{Fe}(\text{CN})_6^{3-}$ is applied to the tip and the tip current is monitored as the tip is moved from air into the aqueous ferricyanide solution. Figure 6.3.4.5a shows the air/solution approach curve for a finite conical tip insulated with anodic paint. No current flows until the tip first enters the solution, where the current then rises sharply in an UME transient, which decays to a constant steady-state current value. This constant value is maintained as more of the tip is immersed in solution. Figure 6.3.4.5a indicates that the tip is completely insulated with only the very end of the tip uncovered. In contrast, a poorly insulated tip showed leaks along the sides as more of the tip is immersed into the solution (Figure 6.3.4.5b). The tip current increases stepwise as more of the tip enters the solution. This behavior is an indication of pinholes in the insulating film.

REFERENCES

1. F. R. F. Fan, C. Demaille, in *Scanning Electrochemical Microscopy*, A. J. Bard, M. V. Mirkin, Eds., Marcel Dekker: New York, 2001, pp. 75–110.
2. C. J. Slevin, N. J. Gray, J. V. Macpherson, M. A. Webb, P. R. Unwin, *Electrochim. Commun.* **1**, 282 (1999).
3. J. L. Conyers, H. S. White, *Anal. Chem.* **72**, 4441 (2000).
4. L. A. Nagahara, T. Thundat, S. M. Lindsay, *Rev. Sci. Instrum.* **60**, 3128 (1989).
5. R. M. Penner, M. J. Heben, N. S. Lewis, *Anal. Chem.* **61**, 1630 (1989).
6. T. Abe, K. Itaya, I. Uchida, *Chem. Lett.* 399 (1988).
7. A. A. Gewirth, D. H. Craston, A. J. Bard, *J. Electroanal. Chem.* **261**, 477 (1989).
8. C. M. Vitus, S. C. Chang, M. J. Weaver, *J. Phys. Chem.* **95**, 7559 (1991).
9. B. Zhang, E. Wang, *Electrochim. Acta* **39**, 103 (1994).
10. R. M. Penner, M. J. Heben, T. L. Longin, N. S. Lewis, *Science* **250**, 1118 (1990).
11. M. V. Mirkin, F.-R. F. Fan, A. J. Bard, *J. Electroanal. Chem.* **328**, 47 (1992).
12. C. E. Bach, R. J. Nichols, H. Meyer, J. O. Besenhard, *Surf. Coatings Technol.* **67**, 139 (1994).
13. B. W. Mao, J. H. Ye, X. D. Zhuo, J. Q. Mu, Z. D. Fen, Z. W. Tian, *Ultramicroscopy* **42–44**, 464 (1992).
14. K. Potje-Kamloth, J. Janata, M. Josowicz, *Ber. Bunsenges. Phys. Chem.* **93**, 1480 (1993).
15. T. G. Strein, A. G. Ewing, *Anal. Chem.* **64**, 1368 (1992).
16. C. G. Zoski, B. Liu, A. J. Bard, *Anal. Chem.* **76**, 3646 (2004).
17. J. J. Watkins, J. Chen, H. S. White, H. D. Abruna, E. Maisonnaute, C. Amatore, *Anal. Chem.* **75**, 3962 (2003).
18. Y. H. Shao, M. V. Mirkin, G. Fish, S. Kokotov, D. Palanker, A. Lewis, *Anal. Chem.* **69**, 1627 (1997).
19. J. V. Macpherson, P. R. Unwin, *Anal. Chem.* **72**, 276 (2000).

6.3.5 Flame-etched carbon nanofibers

Ran Tel-Vered

Department of Chemistry and Biochemistry, The University of Texas at Austin, Austin, Texas 78712-0165, USA

6.3.5.1 Introduction

Of the more prominent advantages in the preparation of flame-etched carbon fiber electrodes are that they can be easily obtained at minimal cost and with short fabrication times (1, 2). Moreover, their preparation involves only benign materials, avoiding the need for corrosive substances and high voltages that are often used in wet-etching techniques. Following flame etching and electrophoretic insulation, the radius of curvature of the carbon fiber at the apex ranges between several tens to less than 200 nm, primarily depending on variations in the etching time, flame temperature, and the exact position of the tip in the flame.

6.3.5.2 Probe preparation

Borosilicate tubes (Sutter Instrument Co., Novato, CA) of 1.0 mm outer diameter and 0.58 mm inner diameter are immersed in 0.5 M HNO₃ for 15 min and sonicated for 10 min in deionized water. The tubes are then pulled using a laser pipet puller (Model P-2000, Sutter Instrument Co.), employing the following pulling parameters: heat = 385, filament = 4, velocity = 30, delay = 150, and pull = 0. This yields micropipet tips with inner diameters of approximately 20 μm and tapers that are approximately 0.5 cm in length. Approximately 1 cm of a 10-μm diameter carbon fiber (Strem Chemicals, Newburyport, MA) is attached to one end of a straight Ni–Cr wire using a small amount of silver epoxy and cured in an oven for 45 min at 100 °C. The wire/fiber assembly is then manually inserted into the top of the micropipet and pushed through so that approximately 3 mm of the fiber protrudes from the micropipet tip. At that point, epoxy cement is applied for sealing the other side of the capillary to form a stable connection between the Ni–Cr wire and the glass. The capillary is then sealed around the carbon fiber using a cool low oxygen natural gas flame by inserting the pipet tip into the flame for approximately 0.5 sec. To ensure hermetic seals, the tips are immersed in DI water and then examined with an optical microscope. At this stage, tips that show a slight intake of water are resealed in the flame whereas electrodes that show slight bending caused by the flame treatment are discarded. The part of the carbon fiber that protrudes from the glass pipet is then flame etched in an oxygen-rich (bright blue color) natural gas flame to a length of 50 μm or less (Figure 6.3.5.1). During this step, it is very important to etch the carbon alone, without melting the glass seal. This is done by a very slow manual approach of the fiber to the vicinity of the outer region at the base of the flame (Figure 6.3.5.2) and periodic observation by optical microscopy to monitor the progress of etching. An orange glow from the carbon fiber indicates that etching is proceeding. Insulation of the etched carbon fiber is carried out by

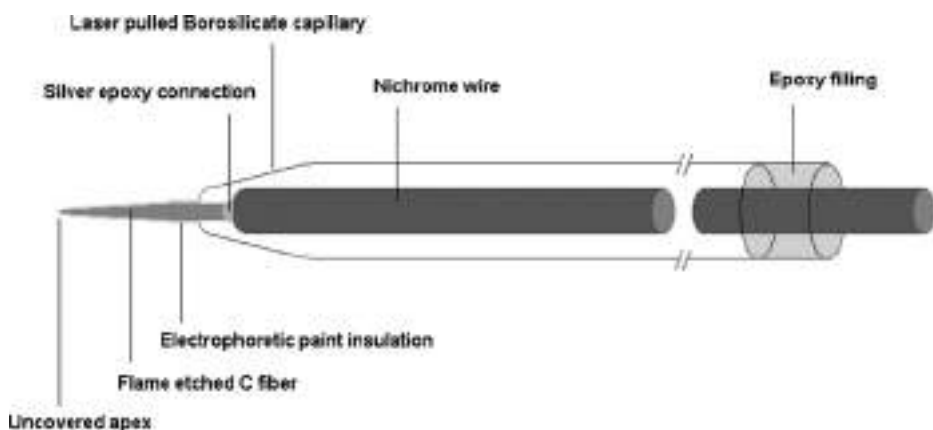


Figure 6.3.5.1 Schematic drawing of a flame-etched carbon nanofiber electrode.

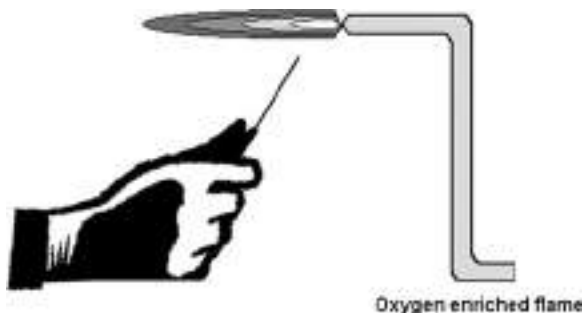


Figure 6.3.5.2 Slow, manual approach of the fiber to the outer region at the base of the flame.

using anodic electrophoretic paint (Glassophor ZQ 84-3225 from BASF, Münster, Germany). The etched fiber is immersed into a 1:20 solution of the paint in water and a Pt coil surrounding the tip serves as the reference/auxiliary electrode. A dc potential of 2.2 V is applied to the carbon electrode for 40 sec, typically showing a gradual decrease in the oxidation current from several tens of nanoamperes to a steady value of 0.2–1.0 nA, depending on the length of the etched fiber. The electrode assembly is then washed with DI water and heated at 150 °C for 3 min, allowing the deposited paint polymer film to fuse and shrink while exposing the tip apex (3). The entire deposition and heating process is repeated once more to ensure good insulation of the fiber. A typical oxidation current during the second deposition is in the range of tens of picoamperes.

6.3.5.3 Tip characterization

To probe for pinholes in the electrophoretic paint insulation, the carbon nanofiber electrodes are tested with a scanning electrochemical microscope (SECM, see Chapter 12)

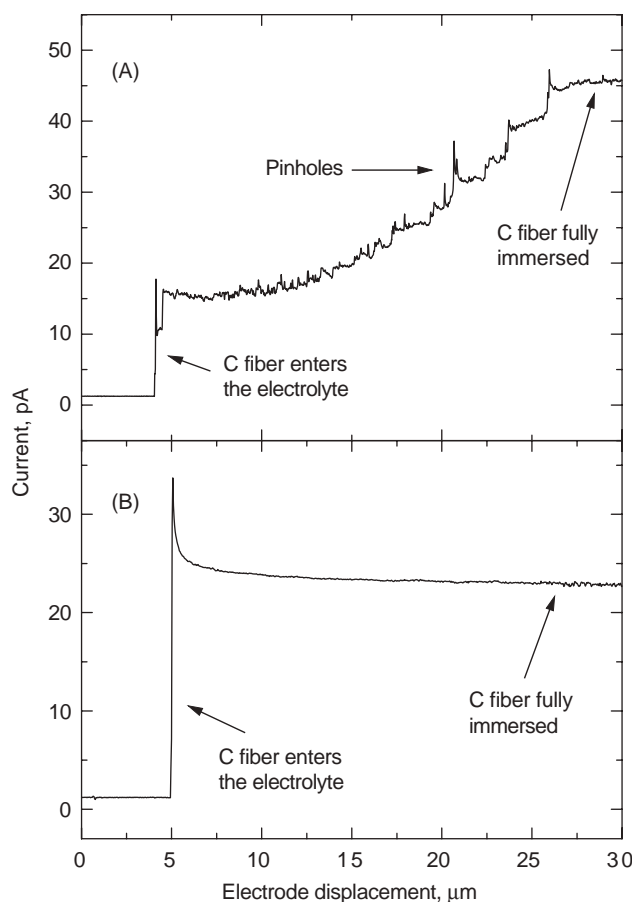


Figure 6.3.5.3 Approach from air into liquid for a flame-etched carbon nanofiber with (A) and without (B) pinholes. The electrolyte is 1 mM ferrocenemethanol (FcOH) in 0.1 M KCl. Tips are held at 0.35 V vs. Ag/AgCl. Approach rate: 200 nm sec⁻¹.

amperometric technique known as approach into liquid (4). Figure 6.3.5.3 presents an example for both properly (A) and poorly (B) insulated tips. The carbon tip is positioned in air approximately 500 μm above the surface of a 1-mM ferrocenemethanol (FcOH) in 0.1 M KCl solution and polarized to 0.35 V vs. Ag/AgCl where a steady-state FcOH oxidation current is expected to occur when exposed parts of carbon are in contact with the electrolyte solution. In the next stage, the tip is slowly (200 nm sec^{-1}) lowered toward the solution, until an initial touch between the exposed carbon apex and the electrolyte is achieved as indicated by a combined faradaic/charging current jump. The tip is further scanned down until no increase in the measured current can be detected, corresponding to a full immersion inside the solution. As the tip is held above the mediator's oxidation potential, any current spikes along the scanned path can be attributed to pinholes in the



Figure 6.3.5.4 SEM image of a carbon nanofiber after insulation with electrophoretic paint. Beam energy is 5.00 kV and the focal distance is 11 mm.

electrophoretic paint layer. It is important to note that although the occurrence of pinholes decreases sharply by flame etching the carbon fiber to only a few micrometers in length; and that in most cases, no holes are detected even at very slow scans, tiny pinholes can still be undetectable due to the small currents associated with their size.

Scanning electron microscopy (SEM) is effective in characterizing the geometry, radius, and shape of the flame-etched carbon nanofiber. Figure 6.3.5.4 shows a hemispherical tip apex supporting a radius of curvature of nearly 150 nm. In practice, smaller tips down to $r = 50$ nm can be fabricated depending on variations in the etching time, flame temperature, and the exact position of the tip in the flame. For a properly insulated tip (such as the one in Figure 6.3.5.3A), a comparison between the visible radius (r_{vis}) measured by SEM and the steady state electrochemically evaluated radius (r_{ec}) measured by cyclic voltammetry at a slow scan rate in the presence of a Nernstian redox mediator, shows a good correlation with the equation for a hemisphere with an error of less than 10%, and hence:

$$r_{\text{vis}} \sim r_{\text{ec}} = i_{\text{ss}} / 2\pi n F D_o C_o^* \quad (6.3.5.1)$$

where D_o is the diffusion coefficient of the mediator species, C_o^* is the mediator bulk concentration, and i_{ss} is the steady-state diffusion limiting current.

The good agreement between the radii measured by the different methods indicates that for properly insulated fibers, most of the electroactive area is concentrated at the very end of the apex and that the contribution of undetected pinholes to total faradaic current is negligible. Furthermore, the correlation between the radii is useful in evaluating the aspect ratio (H) at the nanofiber apex. A closer look at Figure 6.3.5.4 shows a radius of curvature that is nearly 150 nm. As the tip starts to broaden right from its apex, this geometry corresponds to an aspect ratio of approximately $H = 0.5$ or less. Such carbon nanofiber tips are especially useful for electrochemically probing surfaces, as they possess a conical

geometry that facilitates closer approach to the substrate and maintain high sensitivity to redox feedback currents in accordance with the small H value.

REFERENCES

1. T. G. Stein, A. G. Ewing, *Anal. Chem.* **64**, 1368 (1992).
2. W. H. Huang, D. W. Pang, H. Tong, Z. L. Wang, J. K. Cheng, *Anal. Chem.* **73**, 1048 (2001).
3. C. J. Slevin, N. J. Gray, J. V. Macpherson, M. A. Webb, P. R. Unwin, *Electrochim. Commun.* **1**, 282 (1999).
4. Y. Lee, A. J. Bard, *Anal. Chem.* **74**, 3626 (2002).

6.3.6 Electrochemically etched carbon fiber electrodes

Anthony Kucernak

Department of Chemistry, University of Tennessee, Knoxville,
TN 37996, USA

6.3.6.1 Introduction

Etched insulated carbon fiber electrodes can be prepared from a suitable source of graphitized carbon fibers (e.g., PANEX®33 CF, 95% Carbon, Zoltek Corporation, MO, USA), copper wire, colloidal graphite (e.g., type G303 from Agar Scientific Ltd., UK), and a cathodic electrophoretic paint (e.g., Clearclad HSR, from LVH Coating Ltd., UK). Etching of the electrodes requires a variable voltage AC source (50 Hz, 1–10 V_{ac}), an AC current meter capable of measuring in the μ A range and a suitable linear translation stage. Insulation of the electrode requires a DC power supply (0–20 V), linear translation stage, microscope, and oven. Testing of electrodes requires a high-gain low-noise potentiostat.

The processes involved in the production of these electrodes involve mounting the carbon fibers, etching them to produce a sharp tip, and subsequent insulation of the tip so that only the very end of the tip is exposed (1, 2). Testing of the electrode is then performed to determine whether there are any pinholes in the insulation.

6.3.6.2 Preparation and etching of electrodes

Individual single fibers of about 5–6 mm in length are attached to one end of a 1-mm diameter copper wire with a drop of colloidal graphite. The mounted fiber can then be left to cure in air at room temperature for several hours. Prior to etching of the fiber, it is successively rinsed with ethanol and water. A linear translation stage is prepared with a screw connector so that the mounted carbon fiber can be affixed to the stage via the copper wire. The screw connector also provides electrical contact to the power supply. The configuration is displayed in Figure 6.3.6.1. The mounted fiber is then gently translated into the etching solution (0.01 M NaOH) with about 0.5–1 mm of the fiber immersed. A 50-Hz

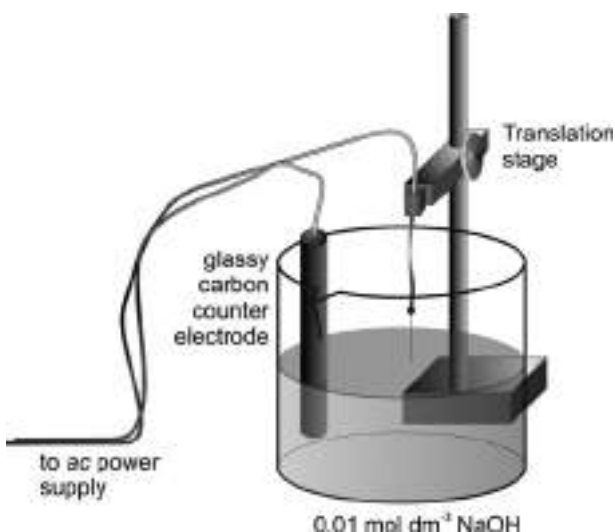


Figure 6.3.6.1 Schematic diagram of the experimental configuration used to etch the mounted carbon fiber electrodes.

AC voltage is then applied between the mounted fiber and a glassy carbon rod auxiliary electrode for a defined period.

The magnitude of the applied AC voltage and its duration has a critical effect on the shape of the resultant tip, as does the source of carbon fiber. In order to produce good electrodes, the cone-angle of the tip should be around 30° – if the angle is much smaller, then the tip will be overly fragile and liable to break during handling. If the cone angle is much larger, then it becomes difficult during the insulation process to prevent the end of the electrode from being coated. In general, three different etching regimes can be characterized as shown in Figure 6.3.6.2.

When the applied potential is too high (Figure 6.3.6.2(a), $V_{\text{applied}} = 8 \text{ V}_{\text{ac}}$), etching of the carbon proceeds at a very fast rate ($i \sim 70 \mu\text{A}$) accompanied by significant amounts of gas evolution. The measured current quickly decays away and the resulting electrode shows a severely pitted and etched end without any tapering of the fiber. If the applied potential is reduced (Figure 6.3.6.2(b), $V_{\text{applied}} = 5 \text{ V}_{\text{ac}}$), the measured AC current is significantly reduced ($i \sim 5\text{--}15 \mu\text{A}$) and the etching proceeds predominantly at the electrolyte/air interface, leading initially to a fiber with a “neck” in it. Etching of the immersed portion of the fiber appears to be quite slow. If etching is allowed to continue, eventually the neck becomes so narrow that the immersed section of the fiber drops off, and the current becomes very small. At still lower applied potentials (Figure 6.3.6.2(c), $V_{\text{applied}} = 3 \text{ V}_{\text{ac}}$), etching occurs much more slowly ($i \sim 2\text{--}6 \mu\text{A}$), but homogeneously distributed along the entire length of the fiber, leading initially to a significantly thinned carbon electrode. These thin carbon electrodes are quite fragile, and easily destroyed. Continued etching leads to eventual total dissolution of the carbon except for a sharp tip formed at the electrolyte/air interface. Tips produced at either of the lower potentials typically have radius of curvatures $<50 \text{ nm}$ and are suitable for the subsequent steps.

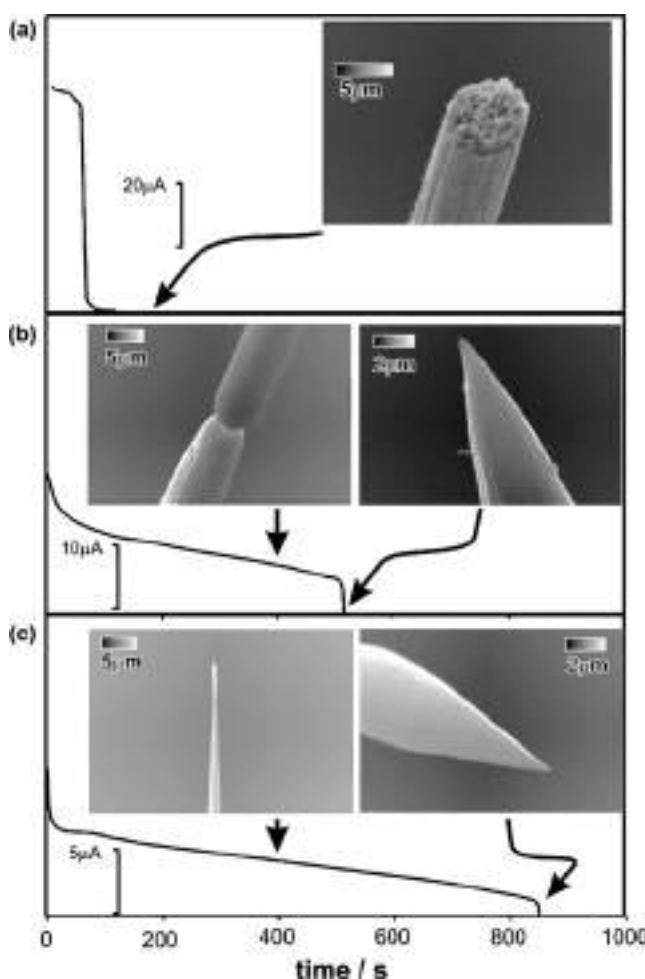


Figure 6.3.6.2 Variation of AC current with time and SEM images of the different tip morphologies obtained at different times during the etching of Zoltek PANEX®33 CF carbon fibers in 0.01 M NaOH as a function of applied AC voltage. (a) 8 V_{ac}; (b) 5 V_{ac}; (c) 3 V_{ac}.

After etching, the fibers are rinsed with water to remove any residual alkaline solution and left to dry prior to the insulation step.

6.3.6.3 Insulation of etched carbon fiber electrodes

The insulation process involves two separate stages: electrophoretic deposition of paint onto the tip surface followed by a curing step at high temperatures during which the paint particles fuse together. As some shrinkage of the deposited film will occur accompanying the heating process, the insulating film tends to retract slightly from the tip apex, allowing the surface of the tip apex to be exposed in a natural and spontaneous way without the need

for any manual intervention. This is a major advantage of the electrophoretic deposition process in making nanometer-sized electrodes compared with other insulating techniques. However, the shrinkage process also brings about some complexities. To be able to expose the tip end during the heating stage, a thin paint layer must be deposited. Otherwise, a fully insulated electrode would be produced even after the subsequent heating stage. In contrast, if the coating layer is too thin, pinholes tend to be left in the film, probably caused by rough protrusions on the surface of the fiber. These additional pinholes will provide an additional faradaic current contribution, bringing about uncertainties in the voltammetric response.

Cathodic electrophoretic paint is the preferred polymeric material used to insulate the carbon fibers as the negative potentials required for deposition avoid any possibility of further oxidative dissolution of the carbon fiber. The usual approach for electrophoretic deposition is to suspend the article being coated in an appropriate suspension of polymer particles and polarising the item versus a secondary electrode.

A modification of this process allows the formation of a tapering deposit of polymer particles so that after the curing process, the shaft of the carbon electrode is coated by a relatively thick layer of polymer, whereas closer to the tip, the polymer layer becomes thinner. The modification of the process involves immersing the carbon electrode in the electrophoretic solution and translating the entire electrode so that the tip of the electrode almost breaks the surface. As shown in Figure 6.3.6.3(a), the tip apex remains in contact with the solution by a very thin liquid meniscus. Such an arrangement will lead to virtually no deposition on the very end of the tip, and an increase in deposition density moving away from the tip. Figure 6.3.6.3(b) shows an overhead photomicrograph taken with side illumination. Light reflects off the meniscus, and produces a small bright patch where the meniscus exists.

A deposition voltage of 5–7 V employed for 60–90 sec is used during the first deposition. Subsequent deposition steps employ the same potential and a deposition time of 20–40 sec. A glassy carbon auxiliary electrode was used, and again, no effect of auxiliary electrode position was obvious. After deposition, spray rinsing is used to remove any loose solution from the fiber. The copper-fiber assembly is then heated at ~195 °C for about 30 min to let the deposited film cure. This heat cure process hardens the film and fuses the resin particles together forming an insulating film. Repeated deposition and cure steps are performed to obtain electrodes with smaller effective radii. Typically two deposition/curing cycles are performed to produce relatively large electrodes, and up to five cycles are performed to produce carbon electrodes with the smallest active surface area.

The final step is to seal the copper-fiber assembly into a glass tube with epoxy resin. Only the insulated carbon fiber should be allowed to protrude from the epoxy sealed glass tube. Electrodes may be re-used and have lifespans of a few weeks.

6.3.6.4 Testing of insulated carbon fiber electrodes

Assuming that the exposed portion of the electrodes fabricated above possess a hemispherical shape, then the diffusion-limited current is expected to follow (3):

$$i_d = 2\pi n F D C^* r_{\text{eff}} \quad (6.3.6.1)$$

where D and C^* are respectively the diffusion coefficient and the bulk concentration of electroactive species in the electrolyte, r_{eff} is the effective radius of the electrode, and n is

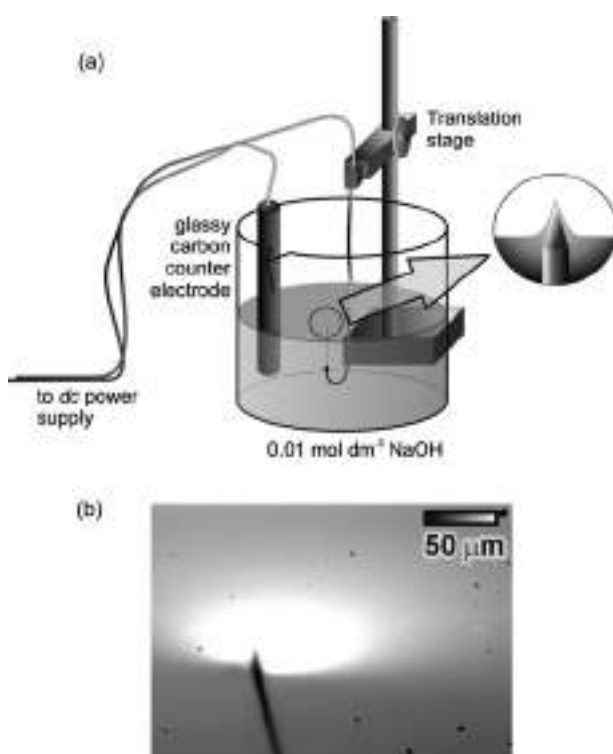


Figure 6.3.6.3 (a) Schematic diagram of the “inverted deposition” configuration used during the electrophoretic deposition of insulator onto the etched carbon electrode. (b) Photomicrograph of surface of electrophoretic paint showing the carbon fiber disappearing into the solution and the extent of the meniscus (white disk) made visible by illumination parallel to the surface of the paint solution.

the number of electron involved in the electrode reaction. Thus, the value of r_{eff} can be determined from the measured steady-state limiting current in the presence of excess supporting electrolyte by using equation (6.3.6.1) with the known values of D , C^* , and n .

The quality of the coating of the electrode may be assessed in a nondestructive manner by measuring the diffusion limited current response as a function of the extent of immersion of the electrode into a suitable electrolyte solution. An example is shown in Figure 6.3.6.4, which displays two overlapping cyclic voltammograms for an insulated carbon fiber electrode with an effective radius of 4.3 nm inserted only ~5–10 μm and inserted 3 mm into an electrolyte containing 0.01 M K_3FeCN_6 + 0.5 M KCl. The absence of any difference between the two scans suggests that there are no defects in the insulation along the shaft of the electrode.

A more destructive approach to assessing the quality of the coating may be performed by polarising the electrode in an electrolyte containing a suitable metal salt (e.g., 0.005 M CuSO_4) at a potential at which metallic copper will deposit, and examining the electrode under an SEM after the electrode has been removed. The presence of any defects will be evident by the obvious growth of copper deposits at sites away from the tip.

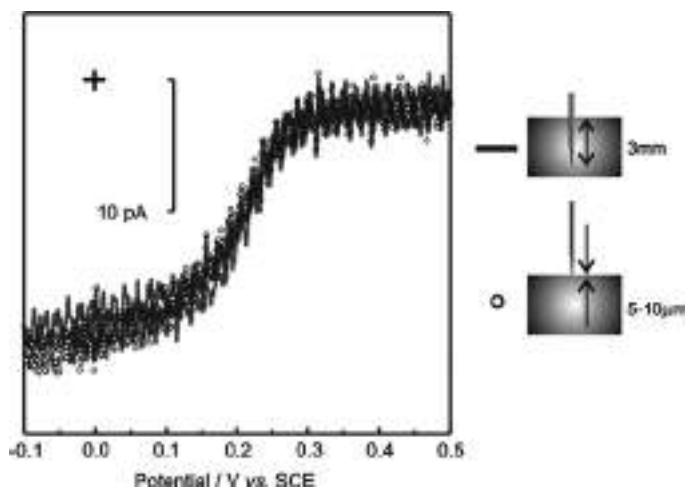


Figure 6.3.6.4 Comparison of the cyclic voltammograms for the reduction of 0.01 M $K_3Fe(CN)_6$ in 0.5 M KCl on a carbon electrode with an effective radius of 4.3 nm as a function of the distance the electrode is immersed into the solution. ○: 5–10 μm ; —: 3 mm. $dE/dt = 0.05$ V sec $^{-1}$.

REFERENCES

1. S. L. Chen, A. Kucernak, *Electrochim. Commun.* **4**, 80 (2002).
2. S. Chen, A. Kucernak, *J. Phys. Chem. B* **106**, 9369 (2002).
3. M. I. Montenegro, M. A. Queiros, J. L. Daschbach, *Microelectrodes: Theory and Applications*, Kluwer Academic Press: Dordrecht, The Netherlands, 1991.

6.3.7 Gold spherical microelectrodes

Christophe Demaille

Laboratoire d'Electrochimie Moléculaire, Université Paris
7-UMR CNRS 7591, France

6.3.7.1 Spherical microelectrodes: self-assembly of gold nanoparticles

(a) Fabrication technique

This original ultramicroelectrode (UME) fabrication technique, developed by Bard and coworkers (1a,b), makes use of the finding of Schiffenbacher and coworkers (2) who showed that, in the presence of dithiol linkers, gold nanoparticles self-assemble to form an electrically conductive gold-like material. By confining the dithiol linker molecules inside the micrometer-sized tip of a glass micropipette, that was then immersed into a solution of gold nanoparticles, the dithiol–nanoparticle encounter could be restricted to the very tip of

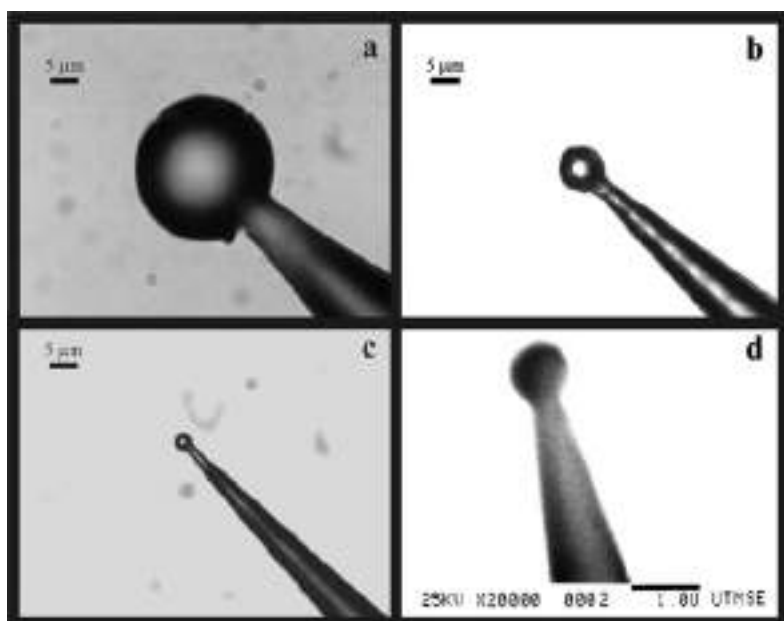


Figure 6.3.7.1 Optical (a–c) and scanning electron (d) microscope images of spherical gold UMEs self-assembled at the very tip of micropipettes. The horizontal scale bar in (d) represents 1 μm . Electrode diameters: (a) 26 μm , (b) 8 μm , (c) 3 μm , and (d) 0.9 μm . (Reprinted with permission from reference (1a), Copyright © 1997 American Chemical Society.)

the micropipette, thus limiting the growth of the self-assembled material to this region. This method was observed to result in the formation of perfectly spherical structures at the micropipette tip, as seen in Figure 6.3.7.1.

The complete self-assembly process of the spherical gold microstructures is represented schematically in Figure 6.3.7.2 and is described in detail below.

Quartz capillaries are pulled to form micropipettes having a tip orifice of a size ranging from 0.1 to 1 μm depending on the pulling conditions, using for example, a Sutter Instrument (Novato, CA) P2000 laser puller. The micropipette is then immersed in a 1,9-nonanedithiol solution in 2-propanol for ~1 h in order to fill the micropipette tip with a small amount of the dithiol solution. The micropipette is then thoroughly rinsed with toluene and immersed in a toluene solution containing octylammonium-protected ~8-nm gold nanoparticles prepared as described by Schiffrin and coworkers (2). The sphere then self-assembles at the tip of the capillary in ~2 h with the final diameter depending on the dithiol concentration and on the micropipette size. As a rule of thumb, the sphere diameter ranged from 2 to 20 times the micropipette tip diameter for dithiol concentrations ranging, respectively, from 1 to 5 mM. Spheres of a diameter ranging from 1 to 30 μm can be reproducibly assembled by this technique. Larger spheres can be produced but they tend to become mechanically unstable. Submicrometer-sized spheres can also be assembled but only with a low yield.

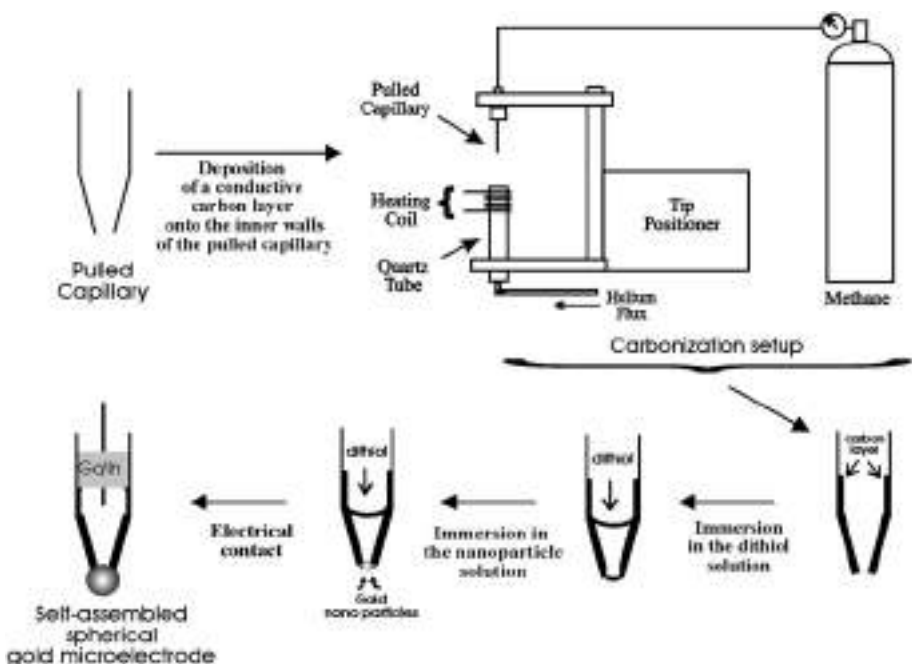


Figure 6.3.7.2 Schematic representation of the self-assembled spherical gold UME fabrication technique. (Adapted with permission from reference (1a,b)).

To use the self-assembled spheres as UMEs, electrical contact has to be established between the sphere and the macroscopic end of the supporting micropipette. The solution proposed by Bard and coworkers (1c) was to coat the inner walls of the pulled micropipette by a thin layer of pyrolytic carbon extending from the top to the very tip of the capillary. This carbon film deposition technique was adapted from previous work (3). The carbonization setup, presented in Figure 6.3.7.2, was constructed for better control of the carbon film quality and is used as follows. The micropipette, held in a gas-chromatography ferrule, is filled with methane under high pressure (240–500 psi) and introduced into a quartz tube heated to ~1000 °C. The quartz tube is continuously flushed with helium to avoid methane combustion. The heat source originally proposed was a Bunsen-burner (3), but it can be conveniently replaced by a Nichrome wire coil (1c). For a given micropipette size, the appropriate pressure is the one for which methane bubbles start to come out from the micropipette when immersed in water. A better quality film is formed when oxygen is pumped out from the micropipette before filling with high-pressure methane. Deposition of a thin conducting carbon film onto the inner walls of the capillary occurs when the micropipette is introduced into the quartz tube and passed *slowly* back and forth through the heated zone. This ensures that the interior of the micropipette is properly coated while the micropipette tip is still open. To gain better control of the carbonizing process, the motion of the micropipette into the heated tube can be controlled via the use of a mechanical positioner. Carbon-coated micropipettes are then used in the

sphere assembly process detailed above. A small amount of gallium indium eutectic, introduced from the macroscopic side of the micropipette, establishes the final connection between the carbon layer and the biasing circuit, as shown in Figure 6.3.7.2.

(b) Electrochemical behavior: self-assembled spherical UMEs

Although it has been demonstrated that the nanoparticles maintain their individualities within the self-assembled spheres (1a,b), the electrochemical behavior of the self-assembled UMEs is similar to that of UMEs made of bulk gold. In particular, voltammetric peaks corresponding to gold oxide formation/reduction (4) were recorded at the self-assembled spherical UMEs in acidic media. Integration of the gold oxide reduction peak yielded an electrode surface roughness of 1.0, which confirmed the remarkable smoothness of the self-assembled spheres. The use of the self-assembled spherical structures as UMEs was tested both in aqueous solution and in acetonitrile. In both cases, ideally shaped reversible steady-state cyclic voltammograms (5a) (Section 6.1) were recorded, as shown in Figure 6.3.7.3.

Recording of such well-defined voltammetric signals, especially in nonaqueous solvent, together with the fact that this ideal behavior was maintained even at the highest scan rate explored (10 V sec^{-1}), shows that the self-assembled spherical UMEs are not porous and are tightly sealed to the supporting glass capillary surface.

Self-assembled spherical electrodes have been successfully used as SECM amperometric probes both in positive and negative feedback modes (1a,b) (Chapter 12). A very close tip–substrate separation could be attained due to the great smoothness of the self-assembled structures.

The self-assembled spherical electrodes have a fabrication success rate over 70%. In some instances, the presence of a golden conducting film adjacent to the sphere was seen on the outside wall of the micropipette tip. This thin film could be removed by

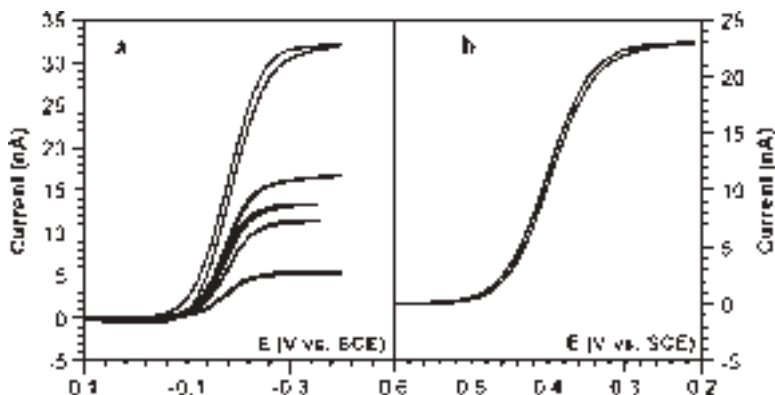


Figure 6.3.7.3 Cyclic voltammograms recorded at self-assembled gold UMEs. (a) In a 7.5-mM aqueous solution of hexaaminoruthenium (III) chloride, 1 M KCl electrolyte. UME diameters (top to bottom): 10, 5, 4, 3, and 1.7 μm . (b) In a 6.5-mM solution of tetracyanoquinodimethane in acetonitrile, 0.1 M tetrabutylammonium tetrafluoroborate electrolyte. UME diameter: 6 μm . (Reprinted with permission from reference (1a), Copyright © 1997 American Chemical Society.)

briefly dipping the micropipette tip in a dilute aqua-regia solution ($\text{HNO}_3/\text{HCl}/\text{H}_2\text{O}$ 1:3:10, caution! highly corrosive solution!). The self-assembled spherical electrodes were observed to be quite robust and could be handled without any particular caution. Indeed, when used as SECM probes, these microelectrodes even survived brief contacts with a hard substrate surface. Fall-out of the sphere from the supporting glass capillary has been observed, but only as a result of very harsh handling. Self-assembled gold UMEs have been stored in air for at least a week without any loss of their mechanical stability (6).

6.3.7.2 Submicrometer-sized spherical electrodes produced by spark-induced melting

(a) Fabrication technique

In this technique developed by Abbou et al. (7), a spark-discharge of controlled intensity is used to melt the tip of a sharpened (etched) gold microwire, which balls-up instantaneously upon cooling. Extremely smooth spherical structures of controllable sizes, ranging from 0.1 to 1 μm in diameter, can be formed in this way (Figure 6.3.7.4).

Successive steps for the fabrication of gold spherical UMEs from these preformed structures are summarized graphically in Figure 6.3.7.5.

(b) Sharpening the tip of a gold microwire by electrochemical etching

Sharpened gold microwires, the starting material for this technique, are produced by electrochemical etching of commercial gold microwires (60 μm in diameter) in a saturated CaCl_2 :water:ethanol solution (10:40:5 v:v:v), under a DC-voltage of +7 V. Etching is complete in ~2 min and results in giving the extremity of the microwire a smooth conical aspect.

(c) Spark-induced melting of the tip of the etched gold microwire

The diameter of the gold sphere ultimately formed at the tip of the etched microwire depends on the intensity of the spark-discharge, which can be controlled by the use of the spark-generating setup presented in Figure 6.3.7.6.

The electronic circuit shown in Figure 6.3.7.6 was designed to generate a *single* high-voltage pulse of an amplitude as high as 6 kV required to trigger the arc discharge. Most of the electronic components necessary to built such a high-voltage generating circuit can

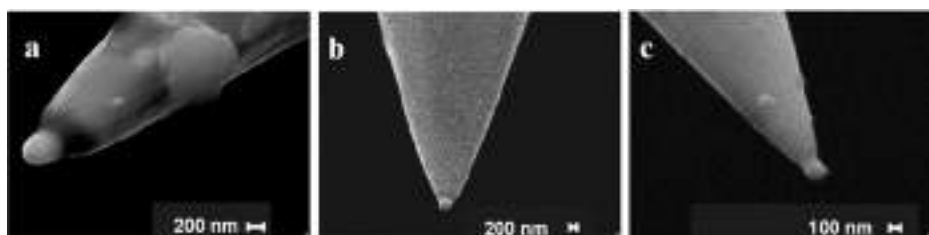


Figure 6.3.7.4 Scanning electron microscopy images of spherical gold UMEs formed by spark-induced localized melting of the tip of etched gold microwires. To form the submicrometer spheres shown, the spark-generator (Figure 6.3.7.6) was operated in an open-circuit configuration with the following settings: $R = 0$, $d_s = 0.5 \text{ mm}$, the shielding gas was air (a) or helium (b and c). (Adapted with permission from reference (1). Copyright © 2002 American Chemical Society.)

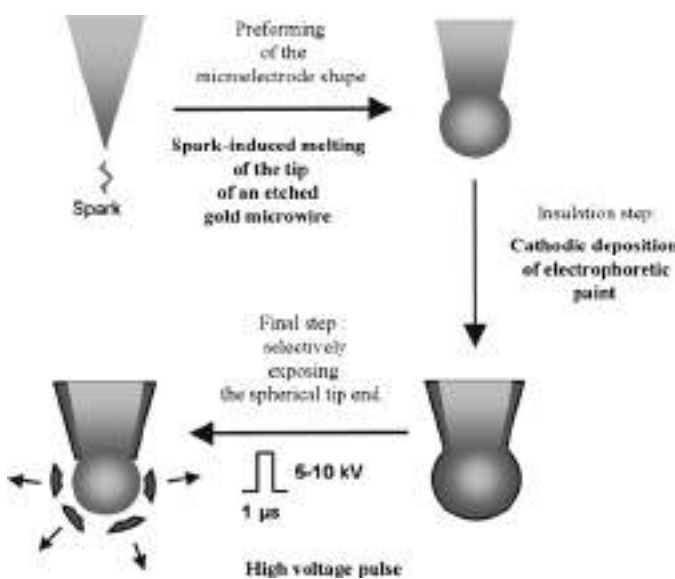


Figure 6.3.7.5 Schematic representation of the technique to fabricate submicrometer-sized spherical gold electrodes.

be found in commercial electric gas-lighters. The sharpened gold wire, as the anode, is connected to the low-voltage terminal of the circuit while a sharpened tungsten wire, used as a cathode, is connected to the high-voltage (−) terminal. Using the home-made positioning apparatus shown in Figure 6.3.7.6b, the gold microwire can be positioned exactly facing the tungsten wire. The spark-discharge intensity can be controlled by varying both the distance, d_s , separating the extremities of the gold and the tungsten wires, and the value of the resistance, R , in series with the cathode. The smaller the value of d_s , and conversely, the higher the value of R , the smaller the diameter of the sphere formed. It was shown that for d_s values of ~1 mm, spheres of a diameter ranging from ~10 μm to a few μm s were formed when R was increased from 1 to 500 $\text{k}\Omega$. It was observed that spheres as small as ~1 μm in diameter could reliably be formed for $d_s \sim 0.5$ mm and $R \sim 1$ $\text{M}\Omega$. Submicrometer-sized spheres could only be formed when the setup was used in an *open-circuit* configuration; that is, when the gold wire was disconnected from the electronic setup, while d_s was kept at ~0.5 mm and R set to zero. A further decrease of the sphere diameter could be obtained by continuously blowing helium within the inter-electrode gap during the spark generation. Helium has a much larger thermal conductivity than air, so that more heat is driven away from the wire and very small spheres, of a diameter of ~100 nm, were then observed to form. To use the spheres as microelectrodes, the body of the gold microwire must be insulated. This was achieved by electrophoretic deposition of an insulating cathodic paint as described below.

(d) Insulation of the gold microwire

The gold microwire, bearing the preformed sphere at its tip, is immersed in a solution containing cathodic electrophoretic paint (BASF, Cathodip™ FT83-0250) diluted in a

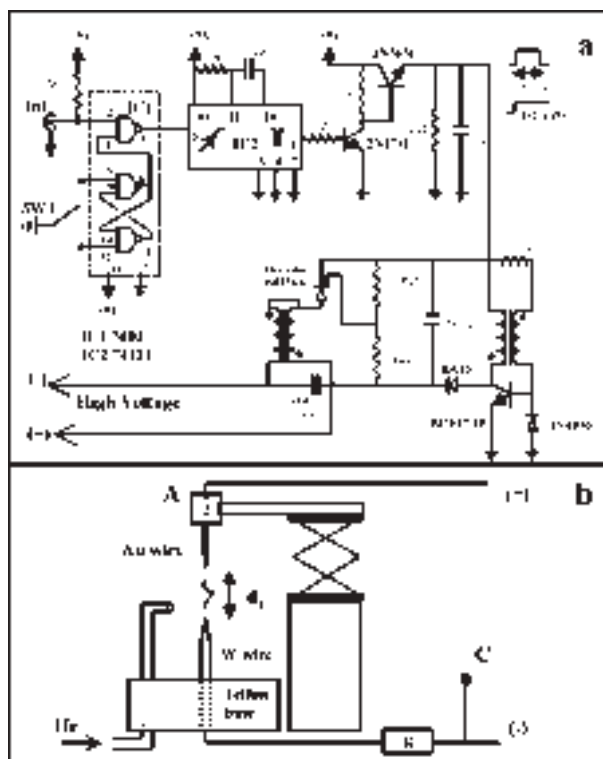


Figure 6.3.7.6 Schematic diagram of the high-voltage single pulse/spark generator setup. (a) Schematics of the electronic circuit of the high-voltage single pulse generator. (b) Diagram of the microwire positioning setup. The configuration shown is the closed-circuit configuration used to perform spherical microstructures at the end of etched gold microwires. In the open-circuit configuration, the gold wire is disconnected from the (+) terminal in point A. When this setup is used for the selective exposure of UMEs, the painted microwires are connected in point C and the resistance R is short-circuited. (Reprinted with permission from reference (1). Copyright © 2002 American Chemical Society).

1:1 (v:v) ratio by water, and acidified by 3 mM acetic acid. The gold microwire is then connected to a potentiostat as the cathode of a two-electrode configuration, the anode being a platinum coil. The potential of the microwire is scanned from 0 to -5 V at a rate of 50 mV sec $^{-1}$ to trigger deposition of the paint. At such a negative potential, protons are reduced and the ensuing local pH rise causes the deprotonation of the NH $_3^+$ moieties borne by the polymer chains composing the cathodic paint that then precipitate onto the gold microwire surface. After deposition, the gold microwire is rinsed with water and placed in an oven heated to 180 °C for 20 min. This thermal curing step results in the cross-linking of the amine-bearing chains by diisocyanate linkers also present in the paint composition. When the painted gold microwires were characterized in an aqueous solution of ferrocenedimethanol by cyclic voltammetry, no faradaic current was recorded. This behavior was observed for more than 80% of the painted wires and demonstrates that the cured paint

layer forms a perfectly insulating coating over the entire surface of the gold microwire. A technique to selectively expose only the preformed spherical extremity of the microwires follows below.

(e) Selective exposure of the spherical end of the microwire

This technique makes use of the same spark-generating setup described above, but the gold microwire connected to the (+) terminal of the setup is here a sacrificial microwire, whereas the microwire to be exposed is connected to the high-voltage (-) terminal of the setup in point C of Figure 6.3.7.6(b), i.e., in *parallel* to the spark-generating circuit. The spark is thus generated between the tungsten and the sacrificial gold wire *and not* at the painted microwire. However, being connected to the high-voltage terminal of the setup, the painted microwire experiences the same sudden high-voltage pulse as the tungsten cathode does. The highest voltage experienced by the painted microwire can be controlled by varying the interelectrode spacing d_s ; the smaller d_s the lower the voltage reached. Typical values of d_s in the 0.5–2 mm range translate to an applied voltage of 1.5–6 kV. It was observed that, once subjected to this high-voltage pulse, painted microwires systematically exhibited sigmoidal-shaped cyclic voltammograms typical of UMEs (5a) (Figure 6.3.7.7).

The high-voltage pulse resulted in exposure of a small portion of the insulating film covering the microwire. The size of the exposed area, as determined from the plateau current of the steady-state voltammogram (5b), corresponds to the diameter of the spherical tip-end of the microwire, as measured from SEM images. In addition, when a spherical microelectrode, fabricated as described above, was used to reduce Fe^{2+} ions in solution, the resulting iron deposit was observed to grow exclusively onto the spherical tip-end of

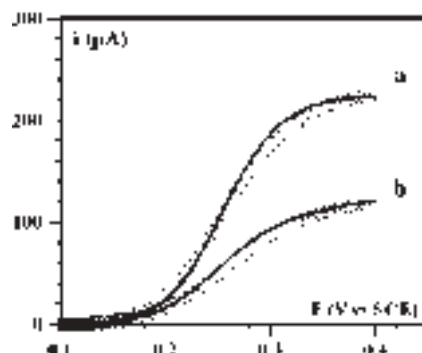


Figure 6.3.7.7 Cyclic voltammetry of ferrocenedimethanol at submicrometer-sized spherical gold UMEs produced by spark-induced melting of the tip of etched gold microwires. The cyclic voltammograms (a and b) were recorded, respectively, at the UMEs shown in the SEM pictures (a and b) of Figure 6.3.7.4. From the value of the plateau currents, the UME diameters were estimated to be of (a) 250 nm and (b) 150 nm. The scan rate was of 20 mV sec⁻¹. The forward and backward traces of each voltammogram are perfectly superimposable at this scan rate. The open circles correspond to the fit of the whole voltammogram using the equation given in the text and the following parameter values: $E^\circ = 235$ mV vs. SCE, $D = 7.4 \times 10^{-6}$ cm² sec⁻¹, $k_s = 0.4$ cm sec⁻¹, $\alpha = 0.5$. Ferrocenedimethanol is at a concentration of 1 mM in 0.1 M KH_2PO_4 .

the microelectrode. All of the above conclusively show that the high-voltage pulse method actually results in *selectively* exposing the preformed spherical tip-end of the microwires. The physical reasons behind such remarkable selectivity is not absolutely clear. It is thought that the high electric field created at the very end of the microwire blows away the insulating paint covering the spherical structure. This process seems to be facilitated by the bottle-neck shape of the extremity of the preformed electrodes (Figure 6.3.7.4) as much poorer results were obtained with nonpreformed (simply etched and painted) microwires.

(f) Electrochemical characterization of spherical gold UMEs

From the value of the plateau current i_{ss} of the cyclic voltammograms recorded in an aqueous solution of ferrocenedimethanol, the radius r_o of the submicrometer-sized spherical gold UMEs could be obtained using the expression: $i_{ss} = 4\pi FDC^*r_o$, where D is the diffusion coefficient of ferrocenedimethanol and C^* is its concentration (Section 6.1) (5b). The cyclic voltammograms were fitted using the theoretical expression for steady-state voltammograms at spherical UMEs (5a).

$$i = \frac{i_{ss}}{1 + \exp[-F(E - E^\circ)/RT] + (D_0/r_0k_s)\exp[-\alpha F(E - E^\circ)/RT]} \quad (6.3.7.1)$$

where k_s and E° are, respectively, the heterogeneous electron transfer rate constant and standard potential of ferrocenedimethanol (7). The good fit obtained (Figure 6.3.7.7, open circles) demonstrates the ideal voltammetric behavior of the spherical submicrometer-sized gold UMEs.

Another interesting aspect of the cyclic voltammetric response recorded at these spherical gold UMEs is the absence of hysteresis between the forward and backward traces of the voltammograms. This is indicative of the relatively low capacitance of the microelectrodes resulting from the good insulating property of the reticulated paint film. A typical value of ~ 5 pF was reported for the capacitance of the spherical UMEs. This value is low enough for the capacitive charging current not to interfere with the cyclic voltammetry signals for scan rates as high as a few volts per second. It was also reported that the UMEs could be used in a large potential window, ranging from -1.2 to $+1.7$ V/SCE in a pH 4.4 aqueous solution without damaging the insulating coating film. The spherical UMEs can be fabricated as described with an overall success yield of $\sim 60\%$. The microelectrodes can be stored in air for as long as a year without any degradation of their electrochemical behavior (8).

This fabrication technique was also successfully applied to combined AFM-SECM probes (7, 9). Following a reported technique (10), the gold microwire was bent to a right angle ~ 1 mm away from one of its ends while its other end was flattened between stainless-steel plates. The flattened part of the microwire serves as a flexible AFM cantilever arm while its short extremity is converted into a spherical microelectrode following the method described above. The AFM-SECM experiments using these combined probes, confirmed the ideal behavior of the spherical gold microelectrodes formed by the spark-method.

REFERENCES

1. (a) C. Demaille, M. Brust, M. Tsionsky, A. J. Bard, *Anal. Chem.* **69**, 2323 (1997); (b) F.-R. F. Fan, C. Demaille, in *Scanning Electrochemical Microscopy*, A. J. Bard, M. V. Mirkin, Eds., Marcel Dekker: New York, 2001, pp. 81–91; (c) *Ibid*, pp. 94–99.
2. (a) M. Brust, D. Bethell, D. J. Schiffrin, C. J. Kiely, *Adv. Mater.* **7**, 795 (1995); (b) D. Bethell, M. Brust, D. J. Schiffrin, C. J. Kiely, *J. Electroanal. Chem.* **409**, 137 (1996).
3. (a) Y.-T. Kim, D. M. Scarnulis, A. G. Ewing, *Anal. Chem.* **58**, 1782 (1986); (b) D. K. Y. Wong, L. Y. F. Xu, *Anal. Chem.* **67**, 4086 (1995).
4. D. A. J. Rand, R. Woods, *J. Electroanal. Chem.* **31**, 29 (1971).
5. (a) M. V. Mirkin, A. J. Bard, *Anal. Chem.* **64**, 2293 (1992); (b) C. Amatore, in *Physical Electrochemistry. Principles, Methods and Applications*, I. Rubinstein, Ed., Marcel Dekker: New York, 1995, pp. 131–208.
6. A. J. Bard, M. Brust, C. Demaille, M. Tsionsky, Unpublished results (1995).
7. J. Abbou, C. Demaille, M. Druet, J. Moiroux, *Anal. Chem.* **74**, 6355 (2002).
8. J. Abbou, C. Demaille, Unpublished results (2004).
9. J. Abbou, C. Demaille, A. Anne, *J. Am. Chem. Soc.* **126**, 10095 (2004).
10. (a) J. V. Macpherson, P. R. Unwin, *Anal. Chem.* **72**, 276 (2000); (b) J. V. Macpherson, M. A. Webb, P. R. Unwin, *Anal. Chem.* **73**, 550 (2001).

6.3.8 Hg microhemispherical electrodes

Janine Mauzeroll

Laboratoire d'Electrochimie Moléculaire, Université Paris,
7-UMR CNRS 7591, France

6.3.8.1 Introduction

The Hg/Pt ultramicroelectrodes (UMEs) described here are hemispherical in shape and can be used in both electrochemical and scanning electrochemical studies (scanning electrochemical microscopy (SECM), Chapter 12 of this handbook) when it is necessary to work in negative potential regions where proton reduction occurs at Pt. Examples include the detection of Tl(I) as a surrogate for K(I) in studies of ion transport through channels in membranes (1, 2) or in studies where a very negative redox couple, like methyl viologen, is needed.

This section describes the deposition and characterization of a Hg hemisphere on Pt UMEs (3). Two methods of fabricating hemispherical Hg/Pt UMEs are described: electrodeposition from an inorganic mercury solution or from controlled contact of the Pt UME with a mercury drop. Electrochemical characterization can be performed using linear sweep voltammetry, amperometry (see Chapter 11) and SECM feedback experiments (see Chapter 12).

6.3.8.2 Importance of the choice of substrate

Ideally, the solid support should be easily wet by and have a low solubility in mercury. In the case of glassy carbon, the surface is poorly wet leading to the formation of scattered

mercury droplets (4). For metals like gold, platinum and silver, the formation of inter-metallic compounds at the base metal can occur. Thermal evaporation experiments have shown that the formation of inter-metallic species leads to a potential window that extends to less negative potentials than that of the hanging mercury drop electrode (HMDE) (5). Since the dissolution of Pt is hindered by the presence of surface oxides, Pt supports can still be used in voltammetric studies following the deposition of a sufficiently thick mercury layer (6). Also, in the case of a Hg–Au amalgam UME, Mandler and coworkers (7) have demonstrated the use of such probes in SECM studies of surface reactions catalyzed by Pt. Another possible substrate material is iridium. Osteryoung and coworkers fabricated and studied Ir (8) and Ir/Pt (9) alloy-based mercury UMEs. They are very useful for electrochemical studies but are more brittle than Pt UMEs.

6.3.8.3 Hg/Pt hemispherical UME fabrication by electrodeposition

The solid support for the Hg hemisphere is a conventional Pt UME as reported in detail in Section 6.3.1 of this Handbook and other published work (10).

(a) Solutions

To deposit mercury onto a Pt UME, a 10 mM $\text{Hg}_2(\text{NO}_3)_2$ (J.T. Baker Chem. Co., Phillipsburg, NJ) in 0.1 M KNO_3 solution acidified to 0.5% with HNO_3 is used. Following deposition, cyclic voltammetry and SECM characterization experiments use 1 mM in cobalt sepulchrate trichloride (Aldrich), hexamineruthenium (III) chloride (Strem Chem., Newbury Port, MA), or methyl viologen (Aldrich) redox couples. The supporting electrolyte used is formed by 0.1 M KCl solutions buffered by a 1:1 molar ratio of $\text{NaH}_2\text{PO}_4/\text{Na}_2\text{HPO}_4$ of total concentration of 0.01 M at pH 7. All solutions are prepared with Milli-Q (Millipore Corp.) reagent water and degassed with Ar for 30 min prior to all experiments.

(b) Instruments

A CHI Model 900 scanning electrochemical microscope (CH Instruments, Austin, TX) can be used to control UME tip potentials, obtain approach curves and monitor the tip to underlying substrate distance. Voltammetric and SECM experiments can be performed either with the SECM head in a glove bag under positive pressure or the SECM cell covered with parafilm and in the presence of an argon blanket. Where SECM characterization is not possible, any potentiostat can be used to deposit and characterize the Hg/Pt UME.

(c) Reaction cell

To monitor mercury deposition *in situ*, a microscope reaction cell can be used. The working Pt UME and counter electrode are inserted through a hole at the base of the cell while the reference electrode is positioned in a side compartment as shown in Figure 6.3.8.1. Once mounted on an optical microscope equipped with a water immersion objective (Olympus FLxw40), a camera and personal computer can then be used to record images of the mercury deposition.

(d) In-situ mercury deposition

Mercury is deposited onto a Pt UME from a $\text{Hg}_2(\text{NO}_3)_2$ solution in a three-electrode setup and controlled by a potentiostat. A 1 mm Pt wire serves as a counter electrode and a fritted

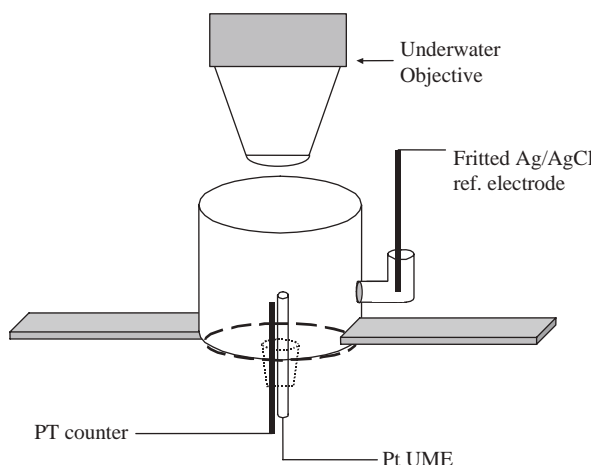


Figure 6.3.8.1 Experimental setup for the formation of Hg/Pt hemispherical UME by electrodeposition from a $\text{Hg}_2(\text{NO}_3)_2$ solution with 0.1 M KNO_3 acidified to 0.5% with HNO_3 as supporting electrolyte. This glass cell was joined at the base with a microscope slide. The underwater objective was lowered into solution and the deposition curve recorded during a 300 sec potential step of -0.1 V vs. Ag/AgCl. Reprinted with permission from reference (3). Copyright, the American Chemical Society.

Ag/AgCl electrode serves as a reference electrode. The deposition curve is recorded during a 300 sec potential step of -0.1 V vs. Ag/AgCl. In the first stages of deposition, a very thin layer of inter-metallic species (Pt_2Hg) is formed (5). This is followed by the spontaneous formation of mercury nuclei (Figure 6.3.8.2a) close to the edge of the Pt/glass interface where the current density is the highest (11). With time, the nuclei coalesce until a full hemisphere is formed. This coalescence alters the surface area of the electrode and leads to indentations in the current deposition curves (Figure 6.3.8.2b). These results are consistent with previously reported work (7).

(e) Hg/Pt hemispherical UME characterization: voltammetry

The electrochemical behavior and stability of a Hg UME is evaluated using linear sweep voltammetry. After mercury deposition, proton reduction shifts to more negative potentials from that seen at bare Pt by about 800 mV (Figure 6.3.8.2c). Dirty or damaged electrodes only shift the potential by about 200 mV and show prewaves characteristic of Pt micro arrays. Clean UMEs with a thick mercury deposit, however, are well behaved.

Proton reduction at Pt is catalyzed by methyl viologen. Electrochemical studies of this couple in aqueous media must, therefore, be performed at a mercury electrode. The methyl viologen voltammogram at the Hg UME is well behaved (Figure 6.3.8.3a) and confirms good coverage of the Pt disk.

The change in geometry from a disk to a hemisphere can be observed by the change in limiting current in voltammograms of $\text{Ru}(\text{NH}_3)_6^{3+}$ (Figure 6.3.8.3a). This follows theoretical equations of the steady-state current at microelectrodes (see Section 6.1 in Chapter 6 of this handbook) where the ratio of the limiting current of a disk UME (12)

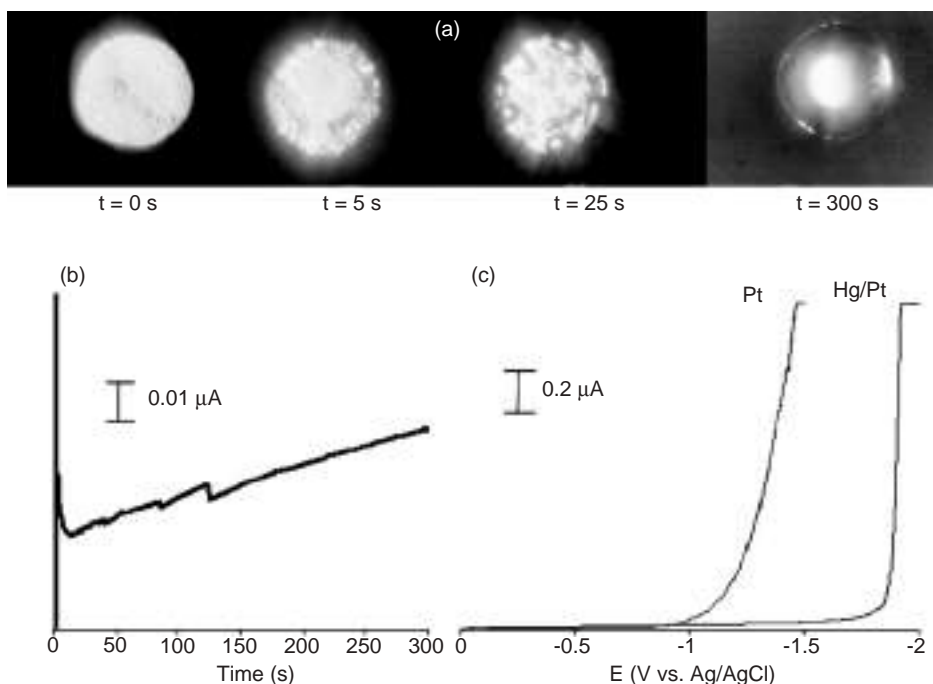


Figure 6.3.8.2 Characterization of a $25\text{ }\mu\text{m}$ Hg/Pt hemispherical UME. (a) In-situ micrographs of mercury deposition (0–300 sec) from a 10 mM $\text{Hg}_2(\text{NO}_3)_2$ solution with 0.1 M KNO_3 supporting electrolyte acidified to 0.5% with HNO_3 . (b) The deposition curve recorded during a 300 sec potential step of -0.1 V vs. Ag/AgCl . A 1 mm Pt wire served as the counter electrode and a fritted Ag/AgCl electrode served as the reference electrode. (c) Current potential curves at Pt and Hg/Pt UMEs in 0.1 M KNO_3 . Reprinted with permission from reference (3). Copyright, the American Chemical Society.

and that of a hemispherical UME is close to $\pi/2$. The observed change of steady-state current ($i_h/i_d = 1.47$) from the Pt UME to the Hg UME is close to this value for $\text{Ru}(\text{NH}_3)_6^{3+}$, confirming the near hemispherical geometry of the UME. A similar increase in the steady-state ratio ($i_h/i_d = 1.57$) was observed for cobalt sepulchrate trichloride (Figure 6.3.8.3a). Thus, both the optical and voltammetric analyses confirm the hemispherical geometry of the UME.

(f) Hg/Pt hemispherical UME characterization: SECM

Theory (13, 14) and applications of SECM are discussed in Chapter 12. Relevant here is the effect of UME tip geometry on SECM approach curves as shown in Figure 6.3.8.3b–d. Approach curves to a Hg/Pt hemispherical UME are compared with those at a Pt disk for three redox couples and the comparison demonstrates the reduced sensitivity of the Hg/Pt hemispherical UMEs relative to Pt disk electrodes in terms of SECM feedback experiments. The Hg/Pt experimental approach curves are consistent with an analytical approximation

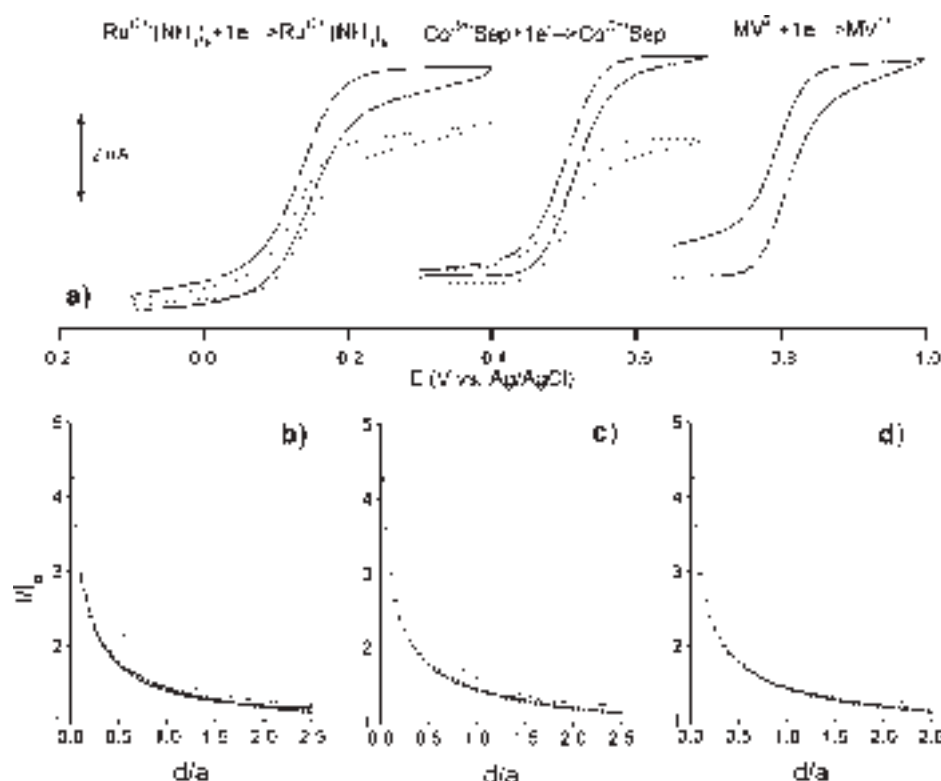


Figure 6.3.8.3 (a) Voltammetric behavior of the 25 μm (--) Pt UME and (solid line) Hg/Pt hemispherical UMEs in 1 mM $\text{Ru}(\text{NH}_3)_6\text{Cl}_3$, cobalt sepulchrate trichloride, and methyl viologen in 0.1 M KNO_3 . (b) Positive feedback SECM fitting of the (\square) finite disk theory, (\blacklozenge) hemispherical disk theory, and (line) experimental results for the 1 mM $\text{Ru}(\text{NH}_3)_6\text{Cl}_3$. (c) Positive feedback SECM fitting of the (\square) finite disk theory, (\blacklozenge) hemispherical disk theory, and (line) experimental results for the 1 mM cobalt sepulchrate trichloride in 0.1 M KNO_3 . (d) Positive feedback SECM fitting of the (\square) finite disk theory, (\blacklozenge) hemispherical disk theory, and (line) experimental results for the 1 mM methyl viologen. Reprinted with permission from reference (3). Copyright, the American Chemical Society.

for positive feedback ($\pm 1\%$) (normalized current vs. distance) for a hemispherical UME developed by Selzer and Mandler (15):

$$\frac{i_T}{i_{T,\infty}} = 0.873 + \ln(1+L^{-1}) - 0.20986 \exp\left[-\frac{L-0.1}{0.55032}\right] \quad (6.3.8.1)$$

where i_T is the tip current, $i_{T,\infty}$ is the steady-state current when the tip is far from the substrate and L is the ratio of the tip to substrate spacing (d) and the active electrode radius (12.5 μm) (i.e., $L = d/r_0$). The response is significantly different from that reported for a disk UME (16):

$$\frac{i_T}{i_{T,\infty}} = 0.68 + \frac{0.7838}{L} + 0.3315 \exp\left[-\frac{1.0672}{L}\right] \quad (6.3.8.2)$$

Previously reported studies of gold spherical UMEs prepared by self-assembly of gold nanoparticles (17) show similar behavior (see Section 6.3.7).

6.3.8.4 Hg/Pt hemispherical UME fabrication by contact to a mercury pool

(a) Solution

The supporting electrolyte used is identical to that in the first protocol. The redox couples used for electrochemical characterization are 2 mM hexamineruthenium (III) chloride (Strem Chem., Newburyport, MA) and 0.1 mM Tl(I) nitrate (Aldrich). All solutions are prepared using Milli-Q (Millipore Corp.) reagent water and degassed with Ar for 30 min prior to all experiments.

(b) Instruments

A CHI Model 900 scanning electrochemical microscope (CH Instruments, Austin, TX) can be used to control UME tip potentials, obtain approach curves and to approach a Pt UME to a mercury pool. Similar results can be achieved with a micromanipulator and an independent potentiostat.

(c) In-situ mercury deposition

A Hg/Pt UME can be formed by applying -1.1 V vs. Hg/Hg₂SO₄ (Radiometer, Copenhagen, Denmark) at a Pt UME and contacting it with the mercury (Bethlehem Instr., Hellertown, PA) of an HDME (Metrohm Instr., Herisau, Switzerland) or a Hg pool in phosphate buffer (Figure 6.3.8.4a).

(d) Hg/Pt hemispherical UME characterization: voltammetry

As shown in Figure 6.3.8.4b, a 0.5 V overpotential for hydrogen evolution is observed in deaerated phosphate buffer (pH = 7) following Hg deposition onto Pt. The response shown in Figure 6.3.8.4b suggests full coverage of Pt by Hg. The extension of the potential window allows the detection of Tl(I) electrochemistry at the Hg/Pt UME (Figure 6.3.8.4c). The voltammogram shows a stable steady-state current for the Tl(I) reduction and a characteristic stripping peak for the oxidation of the Tl amalgam.

(e) Hg/Pt hemispherical UME characterization: SECM

Hg/Pt hemispherical UME show positive feedback with Ru(NH₃)₆²⁺ when approaching an HMDE (Figure 6.3.8.5) or a Hg pool. The experimental approach curves fit theory developed by Selzer and Mandler (15) for a hemispherical UME as described in Section 6.3.8.2. Reproduction of the voltammetric and SECM characterization confirms the equivalency of the two methods used to form Hg/Pt hemispherical UMEs.

In SECM experiments, the close approach of the disk UME is often hampered by the insulating sheath, which may strike the substrate due to misalignment of the tip. The protrusion of the active electrode area as in the mercury hemisphere permits an uninhibited approach and a better estimation of the true zero distance.

6.3.8.5 Microelectrode maintenance and storage

Once formed, the mercury hemisphere is firmly attached to the Pt substrate and can withstand washing; however, it cannot be stored in air and left to dry. When dry, the hemisphere

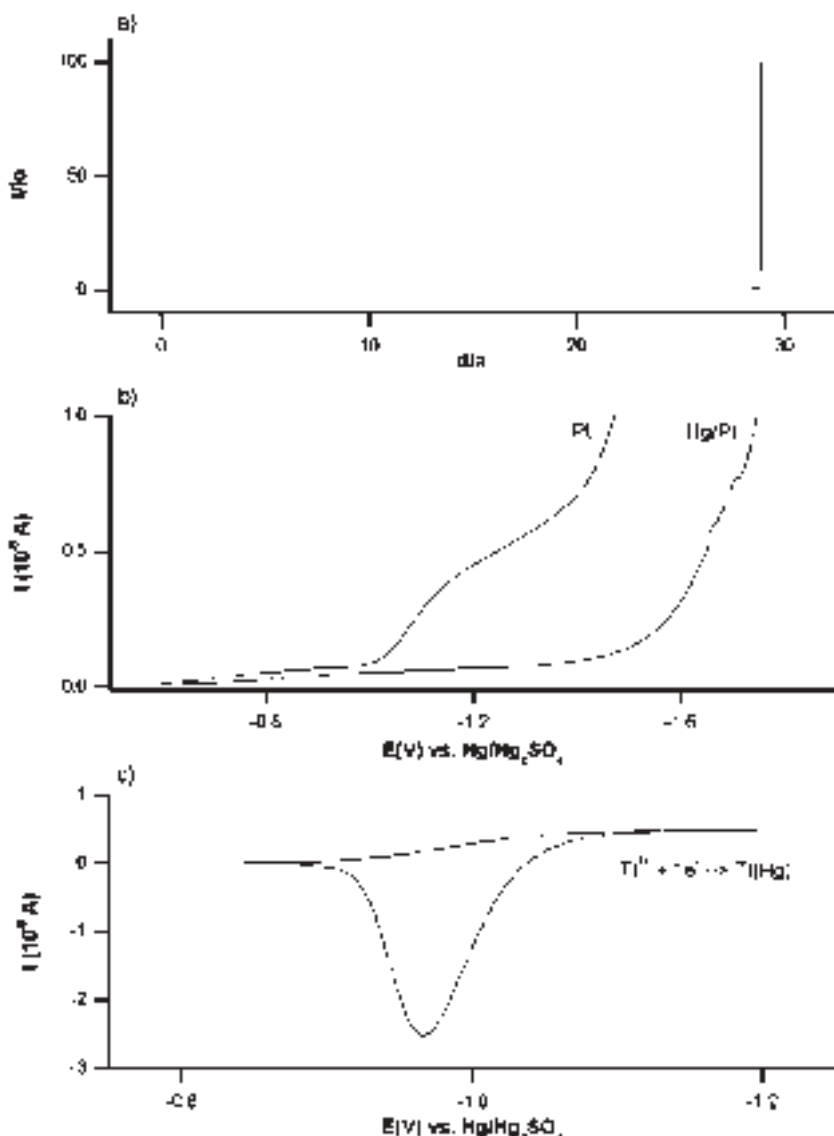


Figure 6.3.8.4 Formation and characterization of the Hg/Pt hemispherical submarine UME. (a) The Pt submarine electrode in phosphate buffer ($\text{pH} = 7$) as it approached the HMDE while poised at -1.1 V vs. $\text{Hg}/\text{Hg}_2\text{SO}_4$. Upon contact with the HMDE, a hemispherical mercury layer is deposited onto the Pt UME. (b) Hydrogen evolution at Pt and Hg/Pt submarine UME in phosphate buffer. (c) Voltammogram of the 10^{-4} M Tl(I) at the Hg/Pt submarine electrode in phosphate buffer. Reprinted with permission from reference (2). Copyright the American Chemical Society.

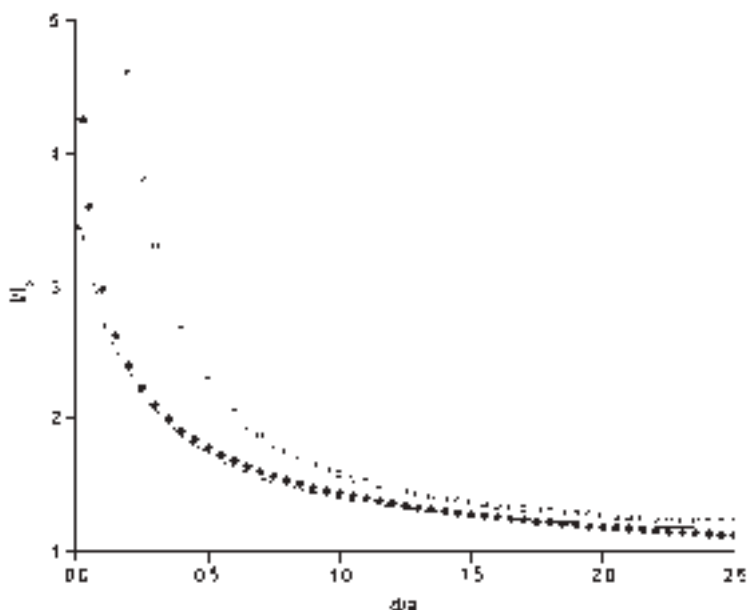


Figure 6.3.8.5 Positive feedback SECM curve fitting of (line) Hg/Pt hemispherical submarine UME approach curve to (♦) hemispherical SECM theory and (□) disk SECM theory for a 2 mM hexamineruthenium chloride solution in phosphate buffer (pH = 7). The Hg/Pt hemispherical UME approached an HMDE. Reprinted with permission from reference (2). Copyright the American Chemical Society.

shrinks and sometimes exposes Pt as a result of surface tension changes. Hg UMEs should therefore be stored in a degassed potassium nitrate solution.

The main limitation of Hg/Pt UMEs is their reusability. For studies where the redox couples do not adhere to the mercury or form an amalgam, electrochemical cycling and storage in PBS is sufficient. In cases where amalgam formation is important, no amount of cycling is able to completely remove all traces of amalgam. Many times, it is easier to mechanically polish the UME to remove the mercury and expose a fresh Pt surface. In SECM studies, where mechanical polishing implies an increase in RG, this cleaning method can become cumbersome.

6.3.8.6 Conclusions, limitations and prospects

Hg/Pt hemispherical UMEs can be fabricated by two methods which produce identical UMEs and characterized using optical and electrochemical instrumentation. Voltammograms are well behaved and the extension of the potential window to more negative potentials facilitates the use of mediators such as methyl viologen. Approach curves recorded over conductors for different redox couples show good agreement with hemispherical theory (3).

These electrodes can be used in voltammetric, amperometric, and SECM studies in negative potential regions where proton reduction occurs at Pt. They are also very smooth and

easily adaptable to stripping voltammetry studies. Their positive potential region is limited by stripping (oxidation) of the mercury deposit.

REFERENCES

1. M. Rueda, I. Navarro, G. Ramirez, F. Prieto, C. Prado, A. Nelson, *Langmuir* **15**, 3672 (1999).
2. J. Mauzeroll, M. Buda, A. J. Bard, F. Prieto, M. Rueda, *Langmuir* **18**, 9453 (2002).
3. J. Mauzeroll, E. A. Hueske, A. J. Bard, *Anal. Chem.* **75**, 3880 (2003).
4. H. P. Wu, *Anal. Chem.* **66**, 3151 (1994).
5. Z. Yoshima, *Bull. Chem. Soc. Jpn.* **1981**, 556 (1981).
6. K. R. Wehmeyer, R. M. Wightman, *Anal. Chem.* **57**, 1989 (1985).
7. Y. Selzer, I. Turyan, D. Mandler, *J. Phys. Chem. B* **103**, 1509 (1999).
8. J. Golas, Z. Galus, J. Osteryoung, *Anal. Chem.* **59**, 389 (1987).
9. C. Wechter, J. Osteryoung, *Anal. Chim. Acta* **234**, 275 (1990).
10. F.-R. F. Fan, C. Demaille, in *Scanning Electrochemical Microscopy*, A. J. Bard, Ed., Marcel Dekker: New York, 2001, p. 75.
11. B. Sharifer, G. J. Hills, *J. Electroanal. Chem.* **130**, 81 (1981).
12. R. M. Wightman, D. O. Wipf, *Electroanal. Chem.* **15**, 267 (1988).
13. A. J. Bard, F.-R. F. Fan, J. Kwak, O. Lev, *Anal. Chem.* **61**, 132 (1989).
14. J. M. Davis, F.-R. F. Fan, A. J. Bard, *J. Electroanal. Chem. Interfacial Electrochem.* **238**, 9 (1987).
15. Y. Selzer, D. Mandler, *Anal. Chem.* **72**, 2383 (2000).
16. M. Arca, A. J. Bard, B. R. Horrocks, T. C. Richards, D. A. Treichel, *Analyst* **119**, 719 (1994).
17. C. Demaille, M. Brust, M. Tsionsky, A. J. Bard, *Anal. Chem.* **69**, 2323 (1997).

6.3.9 Clarke oxygen microelectrode

Katherine B. Holt

Department of Chemistry and Biochemistry, The University of Texas at Austin, Austin, Texas 78712-0165, USA

6.3.9.1 Introduction

Platinum and carbon ultramicroelectrodes (UMEs) are commonly used to determine the concentration of dissolved oxygen in solution, by measuring the current for the reduction of oxygen (1, 2). However, difficulties with signal stability are often encountered, associated with interference by other electroactive species, or poisoning of the electrode surface by adsorbed impurities. These problems can be overcome by covering the electrode with a membrane that is permeable to oxygen but not to other solution species, as first proposed by Clarke in his design for the membrane oxygen electrode (3–6). If both working and counter electrodes are placed behind the membrane, with electrochemical contact maintained through a thin layer of immobilized electrolyte, then measurements of oxygen concentration in the gas phase are possible. The use of an UME tip as the basis for a Clarke

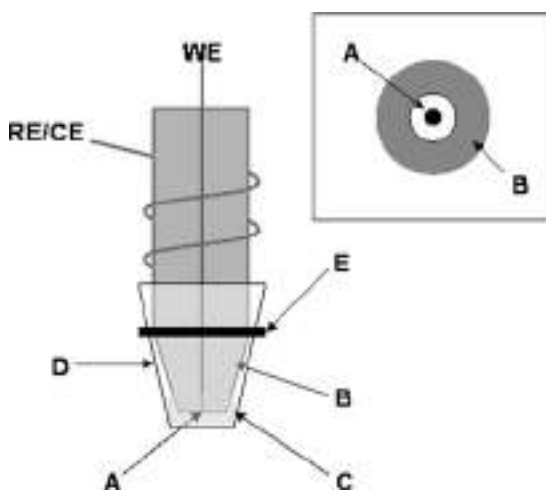


Figure 6.3.9.1 Schematic diagram of membrane UME-based oxygen sensor: (A) 25 μm diameter disk Pt working electrode sealed in glass; (B) Ag layer acting as reference/counter electrode; (C) electrolyte layer forming electrolytic contact between working and reference electrodes; (D) 10 μm thick high density polyethylene (HDPE) membrane; (E) rubber o-ring. Inset: bottom view of electrode surface; (A) 25 μm diameter disk Pt working electrode sealed in glass; (B) Ag paint creating a ring reference/counter electrode. [Reprinted with permission from M. Carano, K. B. Holt, A. J. Bard, *Anal. Chem.* **74**, 5071 (2003). Copyright 2003. The American Chemical Society.]

membrane electrode allows the gas-phase measurement of oxygen concentration to be extended to scanning electrochemical microscopy (SECM, see Chapter 12) (7).

6.3.9.2 Construction and electrochemical response of Clarke UME

(a) Construction

The fabrication of the Clarke UME is illustrated schematically in Figure 6.3.9.1. It consists of a 25 μm Pt disk working electrode sealed in glass with a silver coating on the outside of the glass acting as a reference/counter electrode. Electrochemical contact between the two electrodes is made possible by a thin electrolyte layer maintained behind an oxygen-permeable membrane pulled over the tip and held in place with an o-ring.

(b) UME oxygen sensor

The basis of the electrode is a 25 μm diameter Pt wire sealed in glass by the procedure described in Section 6.3.1 and elsewhere (8). For use in SECM, the electrode is sharpened to a tip using sandpaper to reduce the RG to values of 3–4. It is important that a thin membrane can be pulled tightly over the tip without tearing, so care must be taken during sharpening that the glass edges remain relatively smooth. After sharpening, a layer of silver paint (GC Electronics) is applied to the outside of the glass from the tip to approximately two-thirds of the length of the electrode. The electrode is placed in a 110 °C oven for 1 h to evaporate the solvents from the silver paint solution. Contact is made to the silver layer by coiling a wire around the body of the electrode and then painting over the wire with

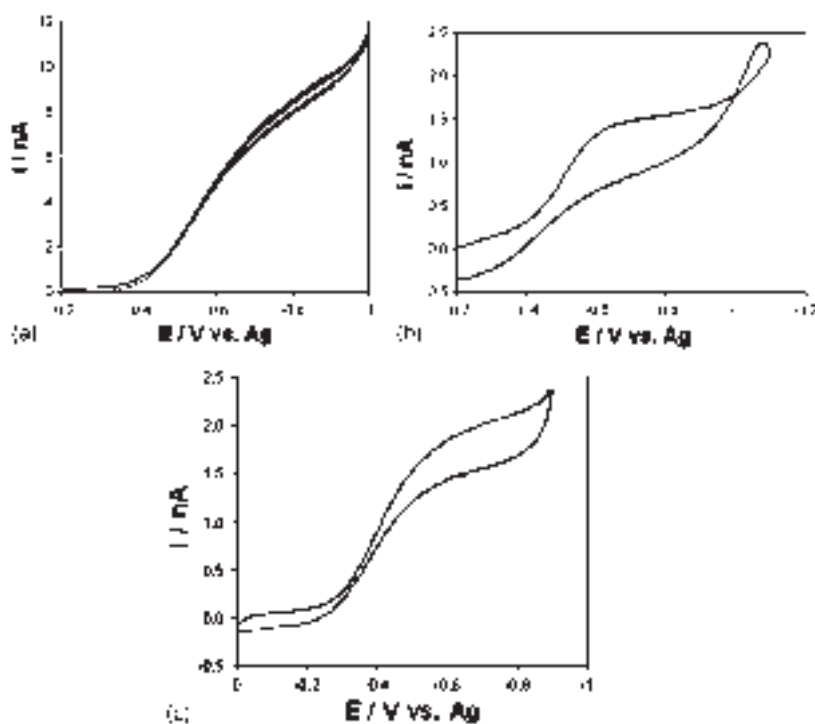


Figure 6.3.9.2 (a) Typical CV (scan rate 0.2 V sec^{-1}) for the reduction of oxygen in air-saturated 0.2 M pH 7 PBS at a bare $25 \mu\text{m}$ Pt disk–Ag ring UME, after 10 min continuous cycling; (b) CV (scan rate 0.2 V sec^{-1}) for the reduction of oxygen in air-saturated 0.2 M NaNO_3 solution for $25 \mu\text{m}$ Pt disk–Ag ring UME covered with $10 \mu\text{m}$ thick HDPE membrane containing drop of 0.2 M pH 7 PBS electrolyte; (c) CV (scan rate 0.2 V sec^{-1}) for the reduction of oxygen in air for $25 \mu\text{m}$ Pt disk–Ag ring UME covered with a $10 \mu\text{m}$ thick HDPE membrane containing drop of 0.2 M pH 7 PBS electrolyte. [Reprinted with permission from M. Carano, K. B. Holt, A. J. Bard, *Anal. Chem.* **74**, 5071 (2003). Copyright 2003. The American Chemical Society.]

silver paint. The electrode is left overnight in the oven to ensure all solvents are evaporated from the silver paint. Before use, the tip is polished thoroughly with 1, 0.3 and $0.05 \mu\text{m}$ alumina to remove any silver paint in contact with the Pt disk working electrode.

The most important factor in operation of an oxygen electrode is that a reproducible limiting current for oxygen reduction is obtained which does not deteriorate over time. For this reason, reproducible and stable cyclic voltammograms (CVs) for the bare electrode should be obtained in solution before the membrane electrode is constructed. Repeated cycling in the oxygen reduction region, from 0 V to -1.2 V vs. Ag/AgCl should result in a stable oxygen reduction current after 20 min, as shown in Figure 6.3.9.2a. Formation of surface oxides by electrochemical oxidation should be avoided. Typically, oxygen reduction currents of $\sim 10 \text{ nA}$ should be obtained for a $25 \mu\text{m}$ diameter disk electrode in an air-saturated solution (oxygen concentration = 0.27 mM , $D_s = 2 \times 10^{-5} \text{ cm}^2 \text{ sec}^{-1}$).

(c) Electrolyte

Any inert aqueous electrolyte solution is suitable for use in a Clarke electrode (4–6). There may be some benefits to using a buffered electrolyte solution because the product of the four-electron reduction of oxygen is the hydroxide ion, which causes a localized shift in pH at the electrode surface during use. However, satisfactory behavior is obtained using unbuffered solutions.

The electrolyte layer should be reduced to the smallest possible thickness, dictated by the roughness of the tip surface and the stretching of the membrane. However, the layer should not be too thin, as it is essential to maintain good electrochemical contact between the working and reference electrodes and also to allow the efficient removal of the hydroxide ion products from the surface of the cathode. The thickness of the electrolyte layer may be estimated by adding a redox active species to the electrolyte layer and performing SECM approach curves (see Chapter 12) to an insulator. An estimate of electrolyte layer thickness of 20–60 µm was obtained for a typical Clarke UME using this technique (7).

The lifetime of the electrolyte layer, that is the time before the composition changes due to the build up of hydroxide ions, depends on the rate at which oxygen is reduced. Probes with cathodes of UME dimensions, producing currents in the nA range, will typically have a longer electrolyte life than probes using cathodes of macro-dimensions, with a similar electrolyte thickness. In this case, it was found that the Clarke UME behaved reproducibly, without changing the membrane or electrolyte, for up to 8 h. If deactivation begins to occur, or if the oxygen reduction current becomes unstable, then the membrane and electrolyte layer should be replaced and the Pt electrode repolished.

(d) Membrane

Membranes suitable for use in a Clarke electrode must be readily permeable to oxygen, but not to species that interfere with the oxygen reduction process. They should also be largely nonpermeable to water molecules so that the integrity of the electrolyte layer is maintained when used in the gas phase. Typical membrane materials used for Clarke electrodes include polytetrafluoroethylene (PTFE), polyethylene, polystyrene, collodion and polyvinyl chloride (4, 5). Thicknesses generally range from 10 to 50 µm. For the Clarke UME, a 10 µm thick high density polyethylene (HDPE) membrane was used, as it is commonly available, being the constituent of most supermarket plastic bags. A square of 30 mm × 30 mm was cut and a drop (0.5–1 µL) of electrolyte placed in the center. The tip was placed in contact with the electrolyte drop and the membrane pulled around the tip and secured using a rubber o-ring. The membrane must be pulled tightly against the surface of the working electrode; however care must be taken not to tear the membrane during this procedure. The solution and gas-phase CVs for oxygen reduction in air-saturated solution and in air should then be recorded to ensure the integrity of the membrane.

The response time, τ , of the electrode is the time taken for 99% of the current change on alteration of oxygen concentration and can be calculated according to the equation (5):

$$\tau = 0.53z_m^2/D_m \quad (6.3.9.1)$$

where z_m is the thickness of the membrane and D_m is the diffusion coefficient of the oxygen through the membrane. Assuming a 10 µm thick membrane, with $D_m = 1 \times 10^{-7} \text{ cm}^2 \text{ sec}^{-1}$

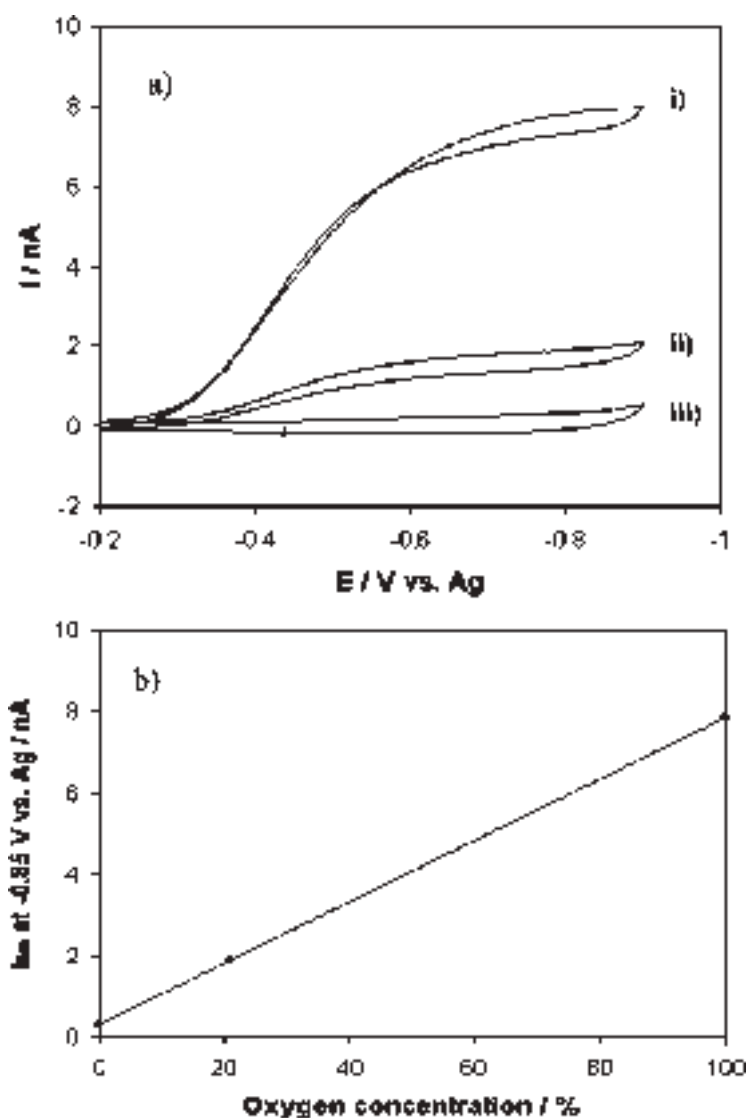


Figure 6.3.9.3 (a) Cyclic voltammograms (scan rate 0.05 V sec^{-1}) in the gas-phase for the reduction of oxygen at $25 \mu\text{m}$ Pt disk–Ag ring UME with $10 \mu\text{m}$ thick HDPE membrane and 0.1 M pH 7 PBS electrolyte in: (i) 100% oxygen; (ii) air (20.9% oxygen); and (iii) argon (0% oxygen). (b) Calibration plot for the relationship between tip current at -0.85 V and gas-phase oxygen concentration for a $25 \mu\text{m}$ Pt disk–Ag ring UME with $10 \mu\text{m}$ thick HDPE membrane and 0.1 M pH 7 PBS electrolyte. [Reprinted with permission from M. Carano, K. B. Holt, A. J. Bard, *Anal. Chem.* **74**, 5071 (2003). Copyright 2003. The American Chemical Society.]

in the gas phase, a value of $\tau = 5$ sec is obtained. In contrast, the UME response time without a membrane is ~ 70 ms, as given by the expression $\tau = r^2/D_s$, where r is the radius of the electrode. The increase in response time for the Clarke UME should be taken into consideration for time-dependent applications.

6.3.9.3 Typical electrochemical behavior of Clarke UME

If the membrane is pulled tightly against the electrode and there are no holes, a CV similar to that in Figure 6.3.9.2b should be obtained for a Clarke UME, in air-saturated solution ($[O_2] = 0.27$ mM). Compared with the CV obtained without a membrane, in the same solution (Figure 6.3.9.2a), the oxygen reduction current is smaller, due to the reduced diffusion coefficient of oxygen through the membrane. For a 25 μm disk electrode with a 10 μm thick HDPE membrane, limiting currents of 1.5–2 nA are typical for oxygen reduction in an air-saturated solution. This corresponds to a diffusion coefficient, $D_{m,s}$, for oxygen through the membrane in solution, of $1 \times 10^{-6} \text{ cm}^2 \text{ sec}^{-1}$. The exact value of the limiting current will vary according to the tightness of the membrane and thickness of the electrolyte layer, but should be of this order. Currents closer to 10 nA indicate a hole in the membrane, or that the membrane is too loose.

Figure 6.3.9.2c shows a typical CV for a Clarke UME in air. The limiting current is ~ 2 nA, corresponding to diffusion coefficient of oxygen through the membrane in the gas phase, $D_{m,a}$, of $1 \times 10^{-7} \text{ cm}^2 \text{ sec}^{-1}$. Limiting currents of the order of 10 nA indicate that diffusion through the membrane is not rate-limiting and that the membrane is too loose, or has a hole. The limiting currents obtained indicate that different diffusion coefficients are obtained for oxygen diffusion through the HDPE membrane in solution and in the gas phase. Diffusion of oxygen through the membrane is actually faster when the electrode is used in the solution phase, which may be attributed to water incorporation into the membrane polymer matrix (9). It is therefore important to calibrate the electrode according to the medium in which it will be used. Figure 6.3.9.3a shows typical oxygen reduction CVs obtained for the Clarke UME in the gas phase, at (i) 100% oxygen flow, (ii) 20.9% oxygen (air) and (iii) 0% oxygen (100% argon). Figure 6.3.9.3b shows the limiting current of the CVs at -0.85 V vs. Ag plotted against oxygen concentration, showing that a linear response is obtained. For use in the solution phase, the membrane electrode should be calibrated using degassed, air-saturated and oxygen-saturated solutions.

Several unique complications are encountered when using a Clarke UME as a SECM tip (7). Increased response time of the membrane UME and convection in the gas phase mean that conventional approach curves cannot be obtained. In addition, care must be taken during imaging not to touch the substrate surface with the membrane, as changes to the tip current are then observed, due to deformation of the membrane and electrolyte layer.

REFERENCES

1. C. Lee, J. Kwak, A. J. Bard, *Proc. Natl. Acad. Sci. USA.* **87**, 1740 (1990).
2. B. R. Horrocks, G. Wittstock, in *Scanning Electrochemical Microscopy*, A. J. Bard, M. V. Mirkin, Eds., Marcel Dekker: New York, 2001, p. 490.
3. L. C. Clark, *T. Am. Soc. Art. Int. Org.* **2**, 41 (1956).

4. M. L. Hitchman, in *Measurement of Dissolved Oxygen*, P. J. Elving, J. D. Winefordner, Eds., I. M. Kolthoff, Ed. Emeritus, John Wiley & Sons: New York, 1978.
5. I. Fatt, *The Polarographic Oxygen Sensor: Its Theory of Operation and Its Application in Biology, Medicine and Technology*, CRC Press: Cleveland, OH, 1976.
6. J. Linek, V. Vacek, J. Sinuke, P. Benes, "Measurement of Oxygen by Membrane-Covered Probes", in *Ellis Horwood Series in Analytical Chemistry*, Ellis Horwood: New York, 1988.
7. M. Carano, K. B. Holt, A. J. Bard, *Anal. Chem.* **74**, 5071 (2003).
8. A. J. Bard, F. -R. F. Fan, M. V. Mirkin, in *Electroanalytical Chemistry*, A. J. Bard, Ed, Marcel Dekker: New York, 1994; Vol. 18, pp 243–373.
9. H. Yasuda, W. Stone, *J. Polym. Sci.* **4**, 1314 (1966).

6.3.10 Nitric oxide microsensors

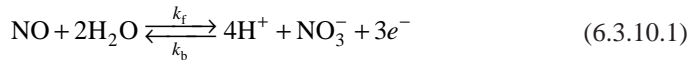
Youngmi Lee

Department of Chemistry, University of Tennessee, Knoxville,
TN 37996, USA

Nitric oxide (NO) had been considered nothing more than toxic gas (e.g., air pollutant) until its physiological functions were discovered in the 1980s (1). NO (enzymatically produced within mammalian cells) plays critical roles in vasodilatation (1), inhibition of platelet adhesion and activation (2), mediation of anti-tumor activities (3, 4), and neurotransmission (5). Quantitative measurement of NO at biological levels is challenging not only because biological cells generate a trace-amount of NO, but also because NO decays relatively fast to form nitrite (NO_2^-) and/or nitrate (NO_3^-) by reaction with NO scavengers (e.g., oxygen, hemoglobin)(6). Electrochemical detection with the use of a NO microsensor is advantageous for real-time quantitative analysis of NO generated from its sources (e.g., biological samples as well as synthesized materials which generate NO). The small dimension of a NO microsensor allows one to estimate the local concentration of NO in close proximity to the NO source (7). The fabrication and characterization of planar amperometric NO microsensors and electrochemical NO measurements using the NO microsensors are discussed in this section.

6.3.10.1 Electrochemical detection of NO

Nitric oxide can be electrochemically oxidized to nitrite and then to nitrate via a three-electron transfer reaction. The overall reaction is:



The oxidation of NO to nitrite and the subsequent oxidation of nitrite to nitrate cannot be clearly discriminated due to their similar oxidation potentials (8). To detect NO electrochemically, the complete three-electron oxidation of NO to nitrate (at ca. 0.9 V vs. Ag/AgCl) at the surface of a working electrode is accomplished (9, 10) amperometrically

by polarizing the working electrode at a constant potential sufficient for the complete oxidation of NO to nitrate. The oxidation current is directly proportional to NO concentration.

Electrochemical oxidation of NO at the surfaces of novel electrode materials (e.g., platinum, gold, glassy carbon, carbon fiber) is known to be kinetically slow. However, accelerated electron-transfer kinetics of NO oxidation have been reported for a variety of chemically modified electrodes with polymeric metalloporphyrin films (11, 12) and platinized Pt (13). These electrodes require less positive potentials for NO oxidation to nitrate ($\sim 0.65 - 0.75$ V vs. Ag/AgCl) and generate higher current (5–10 fold) than bare metal electrodes.

To fabricate NO sensors, chemically modified electrodes are commonly covered with an additional membrane layer. This increases the selectivity for NO by cutting off other easily oxidized and interfering species. A variety of membranes (e.g., cellulose acetate (14, 15), Nafion (16)) have been used to modify the surface of working electrodes via electropolymerization or classic dip coating methods.

6.3.10.2 Fabrication of NO microsensors

NO sensors based on chemically modified electrodes have been reported to exhibit both enhanced electrode kinetics and larger currents compared with bare solid electrodes. Wire-type NO microsensors have also been widely used due to their larger sensing areas (17). In fact, most commercially available NO microsensors are of the wire-type. However, it is the planar configuration of sensors that is essential in gaining access to concentration profiles of analytes (especially for unstable analytes) as a function of distance from a source. Amperometric NO microsensors have been thoroughly reviewed (18). Despite the advantage of a planar configuration, few NO microsensors of this type have been reported.

Planar NO microsensors are constructed similarly to the planar metal disk microelectrodes commonly used in scanning electrochemical microscopy (SECM, see Chapter 12). The working electrodes are prepared as follows: (i) The metal (e.g., Pt) disk electrode is encased in glass and the surrounding glass sheath reduced as described in Section 6.3.1 and in reference (19). The bare metal electrode is then chemically modified to enhance the kinetics for electrochemical oxidation of NO on its surface.

For a platinized Pt-based Clark-type NO microsensor (13), the surface of a bare Pt disk electrode is electrochemically platinized by cyclic voltammetry in a platinizing solution (3% chloroplatinic acid in water). As the potential is scanned (from +0.6 to -0.35 V vs. Ag/AgCl) using cyclic voltammetry (see Chapter 11), Pt(IV) ions are electroplated on the bare Pt disk electrode to create a porous and roughened electrode surface. The platinized Pt electrode has a larger active surface area as demonstrated by the larger recorded currents and lower detection limits for NO measurements compared with bare Pt electrodes as shown in Figure 6.3.10.1.

In this Clark-type NO microsensor, a PTFE gas permeable membrane was used for selectivity specific to NO. A capillary structure with the bottom end simply covered with a thin PTFE gas permeable membrane (~ 30 μm thick) was used as an outer sleeve of the sensor. A platinized Pt working electrode with a Ag wire reference electrode coiled around its glass sheath was inserted into the outer sleeve filled with an internal solution (aqueous 30 mM NaCl and 0.3 mM HCl solution as recommended by Shibuki) to optimize kinetics of NO oxidation at the platinum working electrode of the NO gas sensor (20). The Pt

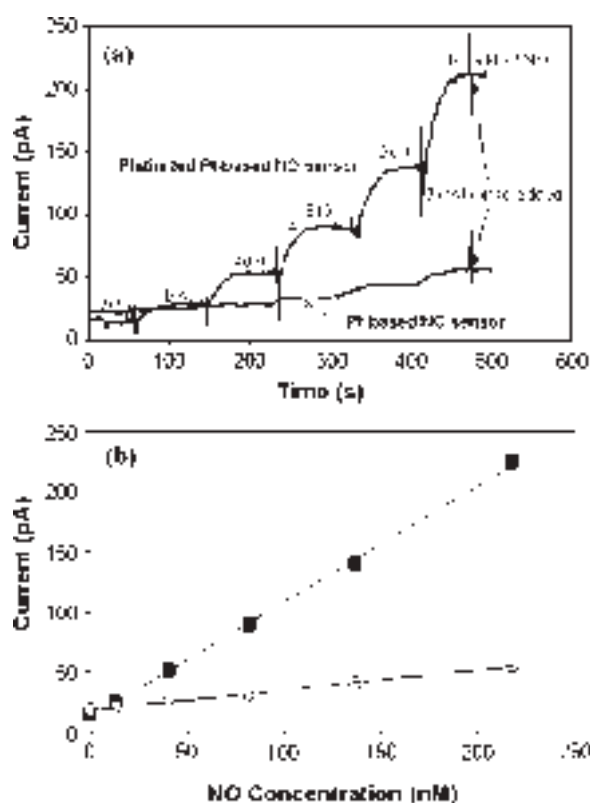


Figure 6.3.10.1 (a) Typical dynamic response curves for bare Pt-based NO microsensors and platinized Pt-based NO microsensors; (b) Corresponding calibration curves for bare Pt-based NO microsensors (■) and platinized Pt-based NO microsensors (○). [Reprinted with permission from Y. Lee, B. K. Oh, M. E. Meyerhoff, *Anal. Chem.* **76**, 545–553 (2004). Copyright 2004, American Chemical Society.]

electrode was pushed smoothly toward the PTFE membrane to cause the inner working electrode to protrude from the end plane of the outer sleeve without tearing the membrane. Therefore, the dimension of the NO microsensor is the sum of the inner electrode diameter and the membrane thickness.

Other types of planar NO microsensors include Pt microelectrodes chemically modified by electrodeposition of metalloporphyrin-like nickel(II) complexes. For example, tetrasulfonated phthalocyanine tetrasodium (NiTSPc) was electrodeposited on the bare electrode surface by repetitive cyclic voltammetry (21). Alternatively, electrode functionalization using nickel(4-*N*-tetramethyl)pyridyl porphyrin (NiTmPyP) as an electrocatalyst was also carried out by applying multiple pulses in differential pulse amperometry (22). In this case, the electrocatalyst was entrapped in a NO selective polymer network of a negatively charged acrylic acid resin that prevented access by anionic interfering species.

6.3.10.3 Characterization of NO microsensors

Effective NO sensors have high selectivity for NO, good sensitivity (low detection limit), linearity, fast response times, and long-term stability. These features can be evaluated using dynamic sensor response curves in which the sensor current (proportional to the concentration of NO) is recorded at a constant working electrode potential (sufficient to oxidize NO to nitrate) while a given amount of NO standard solution is successively added to the stirred deaerated background solution. The NO standard solution is prepared by bubbling NO gas into the same kind of deaerated solution as the sample background solution (assuming a concentration of NO in this saturated solution of 1.9 mM (23)).

The sensitivity (in A/M) and the linear dynamic range for any given sensor are determined from calibration curves (i.e., plots of the steady-state currents from the dynamic response curves vs. the corresponding NO concentrations). Typical dynamic response curves and calibration curves are shown in Figure 6.3.10.1. Compared with sensors based on a bare Pt electrode, NO sensors based on a platinized Pt electrode have significantly improved sensitivity. The stability of a NO sensor is tested through the reproducibility of calibration curves obtained with time. Electrochemically stable sensors should generate similar and reproducible calibration curves in repeated measurements regardless of sensor operating time. The selectivity of a NO sensor is determined by monitoring sensor responses in the presence of interfering species which can be easily oxidized at the redox potential for NO. For example, in the same experimental setup used for obtaining NO dynamic response curves, sensor currents are monitored in the presence of varying amounts of possible interferents (e.g., dopamine, ascorbic acid, nitrite, etc.) instead of NO added into the solution. No (or little) response of the NO sensor to the addition of these species verify the selectivity of the sensor exclusively for NO. Lastly, response times are calculated as the time required to reach a certain percentage (e.g., 90%) of the steady-state response currents when NO concentration changes. The response time depends primarily on the thickness of the membrane covering the bare or platinized Pt electrode. Fast response times are essential for real-time detection of unstable analytes with short life-time (like NO). Therefore, it is important to fabricate NO sensors with thin gas permeable membranes.

6.3.10.4 Bulk vs. surface NO measurements

When the concentration of an analyte is constant (i.e., the analyte molecules are homogeneously distributed) through a sample solution, a sensor generates an identical signal (only proportional to the analyte concentration) regardless of its location in the solution. [Note that the sensor should be positioned away from the container walls so that mass transport of analytes to the sensor is unhindered.] In contrast, the position of a sensor becomes a key factor when the concentration of an analyte is highly location dependent as in measurements of NO generated from biological samples (e.g., mammalian endothelial cells) or NO releasing materials. Because the life-time of NO is relatively short, positioning an NO microsensor near the surface of its source is crucial to detecting NO before it decays. Recently, it was reported that NO-microsensor signals measured over endothelial cells were a function of the distances between the sensor and the surfaces of NO generating cells (22). In fact, a higher current was measured at a shorter distance over the same cells.

This result indicates that the distance of the sensor from the NO source plays an important role in quantitative measurements of NO.

The effect of the size of a sensor on the levels of NO detected near the surface of its source has been investigated (13). A larger sensor exhibited a higher signal even at the same distance from the surface of the same NO releasing samples. The higher signal also occurred in NO sensors having different insulating sheath sizes but with an equal electrode area. This result was attributed to a NO trapping effect where the large insulating sheath of a large sensor prevents free diffusion of NO generated from the sample, thus leading to falsely elevated NO local concentrations near the large NO sensor (relative to levels at the same distance when no sensor was present). Therefore, the sensor distance from NO sources and the sensor size and geometry must be known for accurate NO measurements near NO generating samples.

REFERENCES

1. L. J. Ignarro, G. M. Bugga, K. S. Wood, R. E. Byrns, G. Chaudhuri, *Proc. Natl. Acad. Sci. USA* **84**, 9265–9269 (1987).
2. M. W. Radomski, R. M. J. Palmer, S. Moncada, *Proc. Natl. Acad. Sci. USA* **87**, 5193–5197 (1990).
3. C. F. Nathan, J. B. Hibbs, *Curr. Opin. Immunol.* **3**, 65–70 (1991).
4. J. M. Langrehr, R. A. Hoffman, J. R. Lancaster, R. L. Simmons, *Transplantation* **55**, 1205–1212 (1993).
5. A. Ohta, H. Takagi, T. Matsui, J. Hamai, S. Iida, H. Esumi, *Neurosci. Lett.* **158**, 33–35 (1993).
6. D. D. Thomas, X. Liu, S. P. Kantrow, J. R. Lancaster, *Proc. Natl. Acad. Sci. USA* **98**, 355–360 (2001).
7. M. Feelish, J. Stamler, Eds., *Methods in Nitric Oxide Research*, John Wiley: Chichester, 1996.
8. J. T. Maloy, A. J. Bard, R. Parsons, T. Jordan, Eds., *Standard Potentials in Aqueous Solution*, Marcel Dekker: New York, 1985, Chap. 7.
9. F. Bedioui, S. Trévin, J. Devynck, *Electroanalysis* **8**, 1085–1091 (1996).
10. F. Bedioui, N. Villeneuve, *Electroanalysis* **15**, 5–18 (2003).
11. T. Malinski, Z. Taha, *Nature* **358**, 676–678 (1992).
12. S. Trévin, F. Bedioui, J. Devynck, *Talanta* **43**, 303–311 (1996).
13. Y. Lee, B. K. Oh, M. E. Meyerhoff, *Anal. Chem.* **76**, 545–553 (2004).
14. A. Meulemans, *Neurosci. Lett.* **171**, 89–93 (1994).
15. A. Cserey, M. Gratzel, *Anal. Chem.* **73**, 3965–3974 (2001).
16. F. Bedioui, S. Trévin, J. Devynck, *J. Electroanal. Chem.* **377**, 295–298 (1994).
17. A. Dickson, J. Lin, J. Sun, M. Broderik, H. Fein, X. Zhang, *Electroanalysis* **16**, 640–643 (2004).
18. F. Bedioui, N. Villeneuve, *Electroanalysis* **15**, 5–18 (2003).
19. A. J. Bard, F. -R. Fan, J. Kwak, O. Lev., *Anal. Chem.* **61**, 132–138 (1989).
20. K. Shibuki, *Neurosci. Res.* **9**, 69–76 (1990).
21. A. Pailleret, J. Oni, S. Reiter, S. Isik, M. Etienne, F. Bedioui, W. Schuhmann, *Electrochim. Commun.* **5**, 847–852 (2003).
22. S. Isik, M. Etienne, J. Oni, A. Biochi, A. Reiter, W. Schuhmann, *Anal. Chem.* **76**, 6389–6394 (2004).
23. D. R. Lide, Ed., *Handbook of Chemistry and Physics*, CRC Press, Inc.: Boca Raton, Ann Arbor, Boston, 1990–1991.

6.3.11 Glass nanopore electrodes

Bo Zhang, Gangli Wang, and Henry S. White

Department of Chemistry, University of Utah, Salt Lake City,
UT 84112, USA

6.3.11.1 Introduction

The truncated conical-shaped glass nanopore electrode (for brevity, hereafter referred to as a “glass nanopore electrode” or GNE) comprises a Pt microdisk electrode sealed at the bottom of a conical-shaped pore in glass (1). The radius of the pore orifice can be varied between 5 nm and 1 μm . The GNE was developed as a structurally simple platform for nanopore-based sensors and for investigating molecular transport through orifices of nanoscale dimensions.

Fabrication of a GNE, depicted in Figure 6.3.11.1, involves four general steps: (i) electrochemically etching a small diameter Pt wire to produce a sharp tip with a radius of curvature of a few nanometers; (ii) sealing the sharpened Pt tip into a glass capillary; (iii) polishing the capillary until a Pt nanodisk is exposed; and (iv) electrochemically etching the exposed Pt to produce a truncated cone-shaped nanopore in glass, the bottom of the pore defined by a Pt microdisk electrode. Each step can be performed in an electrochemical laboratory without any specialized equipment.

Owing to the conical shape of the pore, transport of redox molecules from the bulk solution to the electrode surface, Figure 6.3.11.2, is largely determined by the solution resistance in vicinity of the pore orifice (2). This geometry-based localization of the pore resistance to the orifice, originally described by Martin and coworkers (3, 4), suggests that transport selectivity can be achieved by chemical modification of the interior glass surface near the pore orifice. Two additional advantages are associated with the conical shape

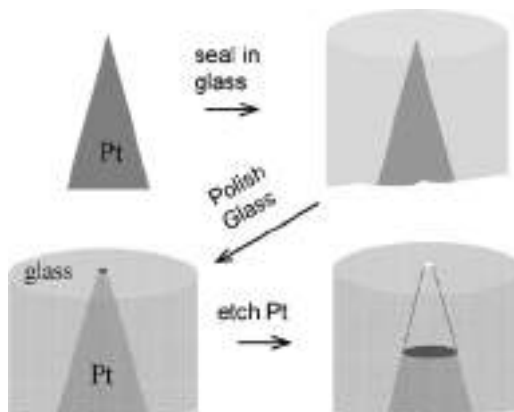


Figure 6.3.11.1 Fabrication of a GNE.

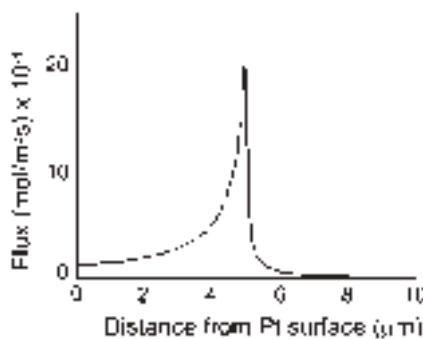


Figure 6.3.11.2 Flux as a function of position at a GNE. Note that the flux reaches a maximum value at the pore orifice, rather than at the electrode surface. This behavior is a result of the diffusion resistance being localized at the pore orifice (5).

pore. First, higher ionic conductance can be achieved with conical-shaped pores relative to straight cylindrical pores, without sacrificing the ability to localize the resistance to the pore orifice. Second, the steady-state flux of molecules (or ionic conductivity) in a conical-shaped pore is *independent of the pore depth* for pores that have a depth $>20\times$ the orifice radii (2). This characteristic is advantageous in the fabrication of nanopores. As with other types of micro- and nanometer-scale electrodes, the GNE can be used for quantitative measurements in highly resistive solution without suffering from prohibitive Ohmic potential losses (5).

6.3.11.2 Fabrication (6)

Fabricating a nanopore in glass, Figure 6.3.11.1, is primarily limited by the initial sharpness of the Pt tip and the ability to expose a very small Pt disk by polishing the glass.

(a) Pt tip preparation

A 25- μm diameter Pt hard wire (Alfa-Aesar, 99.95%), about 4 cm in length, is attached to a stiff W wire using Ag conductive epoxy. The W/Pt wire is then carefully inserted into a glass capillary, leaving \sim 2 cm of the Pt wire out of the capillary. The end of the Pt wire (\sim 1 cm) is immersed vertically into a 15% CaCl_2 solution prepared from a 1:1 (v/v) mixture of H_2O and acetone and an ac voltage of 3 V is applied between the Pt tip and a larger Pt wire, resulting in vigorous bubbling at the Pt tip. The ac voltage is removed as the bubbling ceases, indicating complete etching of the wire to the solution/air interface. The sharpened Pt tips were cleaned by rinsing in H_2O , EtOH, and piranha solution. Tips prepared by this method were found by transmission electron microscopy to have radii of curvature of \sim 50 nm. The tips were further sharpened by electropolishing in dilute H_2SO_4 using the procedure described by Libioulle *et al.* (7). The etched Pt tip is inserted into 0.1 M H_2SO_4 solution and positive 15 V pulses (vs. a large Pt electrode) of 16 μs duration were applied using a homemade waveform generator at a repeating frequency of 4 kHz for \sim 1 sec. A -1.1 V dc voltage is then applied to the Pt wire for \sim 60 sec to reduce any remaining surface oxide. This two-step electropolishing process is repeated three times. Pt tips

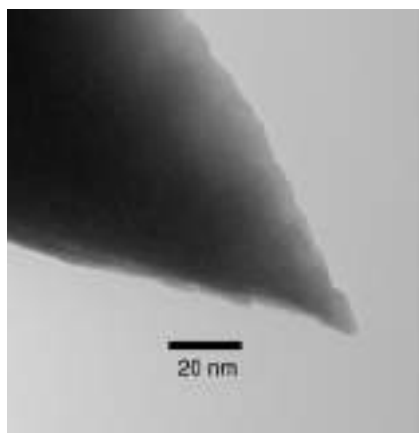


Figure 6.3.11.3 Sharpened Pt wire with ~2 nm tip radius (8).

with apex radii less than 20 nm, Figure 6.3.11.3, as measured by transmission electron microscopy, are obtained by this method.

(b) Sealing the Pt tip in glass

Soda-lime (Warner Instruments Inc., i.d. = 0.75 mm; o.d. = 1.65 mm) and Pb-doped Corning 8161 glass (Warner Instruments Inc., i.d. = 1.10 mm; o.d. = 1.50 mm) capillaries were chosen based on their low softening temperature (700 and 604 °C, respectively), electrical properties, and thermal expansion coefficients (6, 8). The softening temperatures of these glasses are ~1100 °C lower than the melting point of Pt (1769 °C), allowing the Pt tip to be sealed without melting. Following step (i), the W/Pt wire is pulled back into the capillary, leaving ~5 mm of glass extending past the Pt tip. The glass capillary is inserted into the center of a ceramic tube without touching the tube, and the outside of the ceramic tube is heated using a H₂–O₂ torch. During heating, the glass capillary is rotated slowly by hand, allowing the softened glass to collapse around the end of the sharpened Pt wire. Approximately 3 mm of solid glass extends past the end of the Pt tip.

(c) Exposing the Pt nanodisk

The glass-sealed Pt electrodes are sanded using 400, 800, 1200 grit papers until the glass gap between the Pt tip and its mirror image, viewed under an optical microscope (40×) is less than ~1 μm. The electrode is then polished on microcloth wetted with an aqueous slurry of 50 nm aluminum oxide power (Alfa Aesar) containing 0.1 M KCl. An electrical continuity measurement employing a simple electrical circuit is used to determine when the dc resistance between the W wire extending from the top of the capillary and the wetted polishing cloth decreased below ~2 GΩ (8). Electrode radii (*a*) are determined at this point by measuring the diffusion-limited voltammetric current (*i*_d) for the oxidation of 5 mM ferrocene (Fc) in CH₃CN, using the equation $i_d = 4nFDC^*a$, where *n* is the number of electrons transferred, *F* is Faraday's constant, and *D* is the diffusion coefficient of Fc ($2.4 \times 10^{-5} \text{ cm}^2 \text{ sec}^{-1}$). An example is shown in Figure 6.3.11.4. For larger electrodes (*a* > 75 nm), the electrochemical measurement yields values that are within 20% of values

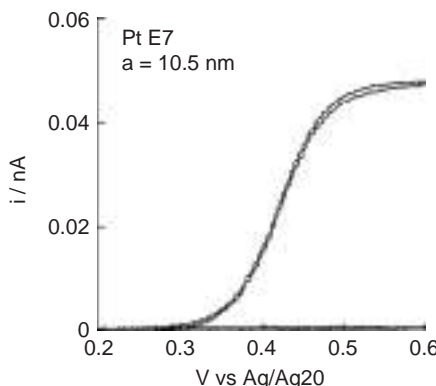


Figure 6.3.11.4 Voltammetric response of a 10.5-nm radius Pt nanodisk electrode corresponding to the oxidation of ferrocene in acetonitrile. Also shown is the i – V response prior to exposing the Pt disk.

determined by scanning electron microscopy (SEM). The radii of smaller nanodisks are difficult to measure by SEM due to surface charging of the glass surface.

(d) Etching the Pt disk to create a pore

The Pt surface of the nanodisk electrode is electrochemically etched in a 15% CaCl_2 solution ($\text{pH} \sim 5.5$) with the entire cell placed in an ultrasonic bath to increase the rate of transport of the etching products out of the pore. A 5 V ac voltage is applied between the Pt nanoelectrode and a Pt wire counter. Large nanodisk electrodes (>100 nm) required significantly shorter etching times (10–20 sec) than smaller nanodisk electrodes (<50 nm, 5–20 min) to generate a pore in the glass with a depth at least $10\times$ the pore orifice radius. The electrode is then rinsed with water.

6.3.11.3 Characterization of GNEs (2)

Determination of the GNE geometry requires experimental measurement of at least three of the four geometrical parameters shown in Figure 6.3.11.5: the pore depth (d), orifice radius (a), microdisk radius at the pore base (a_p), and the pore half-cone angle (θ).

(a) Pore orifice radius

The value of a is also equal to the radius of the Pt disk prior to etching the Pt to generate the pore. The disk radius is determined by measuring the steady-state diffusion-limited current in a solution containing millimolar concentrations of a redox-active molecule. The accuracy in determining a based on i_d depends on whether the geometry of the pore walls after etching faithfully reproduces the shape of the original Pt wire surface. Scanning electron microscopy images have shown that the orifice radius is within 20% of the original Pt disk radius after etching the Pt.

(b) Half-cone angle

Values of θ are determined to within 1° by optical and electron microscopy of the etched Pt wire prior to sealing it in glass. The angle θ is constant except at the very apex of the sharpened wire. Limitations of a varying θ near the tip of the wire have been discussed (2).

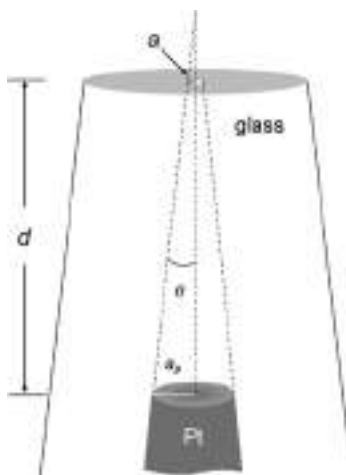


Figure 6.3.11.5 Geometrical parameters of a GNE (2).

(c) Radius of Pt disk at the bottom of the pore

At sufficiently high scan rates in a voltammetric experiment, the current becomes limited by planar diffusion of redox molecules initially present in the pore and adjacent to the Pt surface. The voltammetric response of the GNE is identical to that of a shielded macroscopic planar electrode in this limit (2). The value of a_p is determined from the slope of a plot of the voltammetric peak current, i_p , versus the square root of scan rate, $v^{1/2}$, according to the expression:

$$i_p = 2.69 \times 10^5 n^{3/2} D^{1/2} C^* v^{1/2} \pi a_p^2 \quad (6.3.11.1)$$

(d) Pore depth

A value of d is obtained by geometry if a , θ , and a_p are previously measured by the above methods. Alternatively, at intermediate scan rates, the GNE behaves as a thin-layer electrochemical cell, exhibiting symmetrical cathodic and anodic voltammetric peaks corresponding to redox molecules initially present in the pore. This thin-layer cell response is superimposed on the steady-state diffusion current (equation (6.3.11.3), presented below in Section 6.3.11.4) and the peak current is approximated by:

$$i_p = i_{\text{lim}} + \frac{n^2 F^2 v}{4RT} C_b V_p \quad (6.3.11.2)$$

where R is the gas constant, T is absolute temperature, and V_p is the pore volume. If any pair of geometrical parameters is known (e.g., θ and a_p), then d can be computed from the value of V_p obtained from a linear plot of i_p versus v .

6.3.11.4 Voltammetric response of GNEs

The transient and steady-state voltammetric responses of GNEs have been analyzed by simulation, theory, and experiment (1, 2). An approximate analytical expression for the diffusion-limited steady-state current at a GNE, i_{lim} , is given by equation (6.3.11.3):

$$i_{\text{lim}} = 4nFaDC^* \left[\frac{(1 + (d/a)\tan\theta)}{(4d/a\pi) + (1 + (d/a)\tan\theta)} \right] \quad (6.3.11.3)$$

where all variables and constants are defined above. Equation (6.3.11.3) is derived from the general definition of the limiting current, $i_{\text{lim}} = nFC^*/R_{\text{MT}}$, where R_{MT} is the steady-state mass-transfer (diffusion only) resistance comprising the internal pore resistance, R_{in} , and the external solution resistance, R_{ex} . The latter is equivalent to the mass-transport resistance at a disk electrode, $R_{\text{ex}} = 1/4Da$. For small cone angles, $\theta < 20^\circ$, the pore resistance can be approximated as $R_{\text{in}} = d/Da\pi(a + d \tan\theta)$ with reasonable accuracy (<5% error), which, when combined with the above expression for R_{ex} and R_{MT} , yields equation (6.3.11.3).

In the limit $d \rightarrow 0$, the GNE geometry reduces to that of a disk electrode of radius a and equation (6.3.11.3) reduces to:

$$i_{\text{lim}}^{d=0} = 4nFaDC^*, \quad (6.3.11.4)$$

the well-known expression for the steady-state limiting current at a disk-shaped electrode. Conversely, in the limit $d \rightarrow \infty$, corresponding to a very deep pore, equation (6.3.11.3) reduces to:

$$i_{\text{lim}}^{d \rightarrow \infty} = 4nFaDC^* \left[\frac{\tan\theta}{4/\pi + \tan\theta} \right] \quad (6.3.11.5)$$

A key prediction of equation (6.3.11.5) is that $i_{\text{lim}}^{d \rightarrow \infty}$ is independent of d , a consequence of the radial divergent flux within a conical-shaped pore. For typical values of θ obtained in preparing GNEs ($\sim 10^\circ$), the current (equation (6.3.11.1)) asymptotically approaches the depth-independent value (equation (6.3.11.5)) when the pore depth is at least 20× greater than the radius of the pore orifice. For instance, for a pore with a 20-nm radius orifice, any pore depth greater than ~400 nm will yield a similar value of the steady-state limiting current. Experimental measurements of i_{lim} as a function of d confirm the behavior predicted by the above set of equations (2).

Figure 6.3.11.6 shows typical behavior of a GNE with a 74-nm radius orifice (including the voltammetric response of the nanodisk electrode *prior to* etching the Pt to create a pore). Etching the pore to micrometer depths results in an ~75% decrease in the steady-state current relative to the unetched nanodisk electrode, in quantitative agreement with equation (6.3.11.5) using the measured value of $\theta \sim 10^\circ$. This current reflects the rate at which ferrocene diffuses across the pore orifice (mol sec^{-1}). When the same GNE is re-etched to create an even deeper pore, the voltammetric response displays a “thin-layer” shape, corresponding to oxidation of the ferrocene molecules initially within the pore. The thin-layer response of the GNE can be exploited to detect very small numbers of

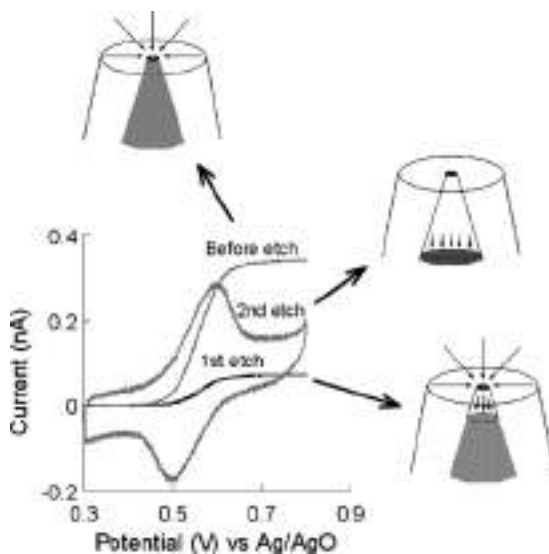


Figure 6.1.11.6 Voltammetric response of a GNE in a 5 mM ferrocene/acetonitrile solution as a function of pore depth. The radius of the Pt nanodisk prior to etching is 74 nm. All curves were recorded at 10 mV sec^{-1} .

molecules contained within the pore. Finite-element simulations of the transient voltammetric response have also been reported and are in good agreement with experimental observations (1, 2).

REFERENCES

1. B. Zhang, Y. Zhang, H. S. White, *Anal. Chem.* **76**, 6229 (2004).
2. B. Zhang, Y. Zhang, H. S. White, *Anal. Chem.* **78**, 477 (2006).
3. S. Lee, Y. Zhang, H. S. White, C. C. Harrell, C. R. Martin, *Anal. Chem.* **76**, 6108 (2004).
4. E. A. Heins, Z. S. Siwy, L. A. Baker, C. R. Martin, *Nano Lett.* **5**, 824–1829 (2005).
5. Y. Zhang, B. Zhang, H. S. White, *J. Phys. Chem.* **110**, 1768 (2006).
6. The fabrication of glass GNEs is rapidly evolving at the time of this writing. The description presented here is adapted from reference (2) and from: G. Wang, B. Zhang, J. R. Wayment, J. M. Harris, H. S. White, unpublished results, University of Utah, 2006.
7. L. Libioulle, Y. Houbion, J. -M. Gilles *Rev. Sci. Instrum.* **66**, 97 (1995).
8. B. Zhang, J. Galusha, G. Wang, R. J. White, E. N. Ervin, R. Jones, C. Cauley, H. S. White, A. J. Bergren, unpublished results, University of Utah, 2006.

- 7 -

Potentiometric Ion-Selective Electrodes

Shigeru Amemiya

Department of Chemistry, University of Pittsburgh, 219 Parkman Avenue,
Pittsburgh, PA 15260, USA

7.1 INTRODUCTION

Potentiometric ion-selective electrodes (ISEs) are one of the most important groups of chemical sensors. The application of ISEs has evolved to a well-established routine analytical technique in many fields, including clinical and environmental analysis, physiology, and process control. The essential part of ISEs is the ion-selective membrane that is commonly placed between two aqueous phases, i.e., the sample and inner solutions that contain an analyte ion. The membrane may be a glass, a crystalline solid, or a liquid (1). The potential difference across the membrane is measured with two reference electrodes positioned in the respective aqueous phases

reference electrode 2 || sample solution | membrane | inner solution || reference electrode 1
(cell 1)

Under equilibrium conditions, the measured potential (or emf of the cell), E , can be expressed as

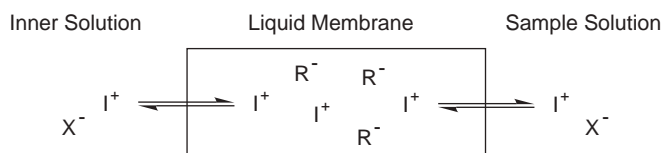
$$E = E_I^0 + \frac{RT}{z_I F} \ln a_I^W \quad (7.1.1)$$

where z_I is the charge of the analyte ion, I , a_I^W is its activity in the sample solution, and the constant term, E_I^0 , is unique for the analyte and also includes the sum of the potential differences at all the interfaces other than the membrane/sample solution interface. This well-known “Nernst” equation for ISEs represents their unique response properties, i.e., Nernstian responses, where the sensor signal, E , is proportional to logarithm of the analyte activity rather than the activity itself. The slope in an E versus $\ln a_I^W$ (or more commonly $\log a_I^W$) plot is used for identification of the analyte based on the charge. A wide range of the analyte activity can be determined because of the logarithmic dependence of the

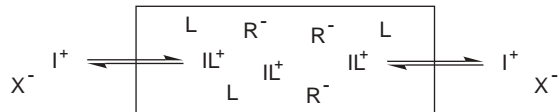
potential on the analyte activity. Moreover, a very low analyte activity can be determined only by measuring the potential difference rather than detecting a very small signal. A well-known example is a glass membrane pH electrode, which has a detection limit of down to 10^{-12} M for H^+ .

How can we create such a membrane for a wider range of analytes? The most successful approach is to use ion-selective liquid membranes (2, 3). The liquid membranes are hydrophobic and immiscible with water, and most commonly made of plasticized poly(vinyl chloride). The selectivity is achieved by doping the membranes with a hydrophobic ion (ionic site) and a hydrophobic ligand (ionophore or carrier) that selectively and reversibly forms complexes with the analyte (Figure 7.1). Whereas the technique has been well established experimentally since the 1960s, it is only recently that the response mechanisms are fully understood. In this chapter, principles of liquid membrane ISEs will be introduced using simple concepts of ion-transfer equilibrium at water/liquid membrane interfaces. Non-equilibrium effects on the selectivity and detection limits will also be discussed. This information will enable practitioners of ISEs to better optimize experimental conditions and also to interpret data. Additionally, examples of ISEs based on commercially available ionophores are listed. More comprehensive lists of ionophore-based ISEs developed so far are available in recent IUPAC reports (4–6).

(A) Ionophore-Free Ion-Exchanger Electrode



(B) Neutral-Ionophore-Based Electrode



(C) Charged-Ionophore-Based Electrode

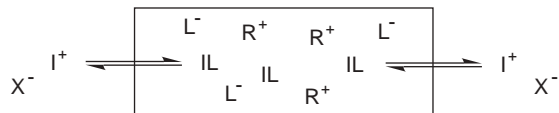
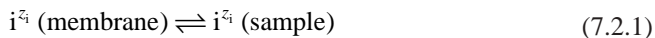


Figure 7.1 Schematic view of the equilibrium between sample, ion-selective membrane, and inner filling solution (cell 1). The cation-selective membranes are based on (A) cation exchanger (R^-), (B) electrically neutral ionophore (L) and anionic sites (R^-), and (C) charged ionophore (L^-) and cationic sites (R^+). The aqueous solutions contain an analyte cation (I^+) and its counter anion (X^-). Adapted from reference (2).

7.2 CLASSIFICATION AND MECHANISM

7.2.1 Phase boundary potential

Potentiometric responses of liquid membrane ISEs depend on a change in the phase boundary potential at the membrane/sample solution interface, which is controlled by bulk equilibrium (7). When an ion, i , with charge z_i is transferred across the interface between the sample and membrane phases, the ion-transfer reaction is defined as



Under equilibrium conditions between the two phases, the electrochemical potentials of the ion in the sample and membrane phases, $\bar{\mu}_i^W$ and $\bar{\mu}_i^M$, respectively, is equal

$$\bar{\mu}_i^M = \bar{\mu}_i^W \quad (7.2.2)$$

which is equivalent to

$$\mu_i^{M,0} + RT \ln a_i^M + z_i F \phi^M = \mu_i^{W,0} + RT \ln a_i^W + z_i F \phi^W \quad (7.2.3)$$

where a_i^W and a_i^M are the ion activities in the sample and membrane phases, respectively, $\mu_i^{W,0}$ and $\mu_i^{M,0}$ are the standard chemical potentials of the ion in the respective phases, and ϕ^W and ϕ^M are the inner potentials in the respective phases. Rearrangement of equation (7.2.3) gives the phase boundary potential, $\Delta_w^M \phi$, as a function of the ion activities

$$\Delta_w^M \phi = \frac{RT}{z_i F} \ln \frac{k_i a_i^W}{a_i^M} \quad (7.2.4)$$

with

$$\Delta_w^M \phi = \phi^M - \phi^W \quad (7.2.5)$$

$$k_i = \exp \left[-\frac{RT(\mu_i^{M,0} - \mu_i^{W,0})}{z_i F} \right] \quad (7.2.6)$$

where k_i is the so-called single ion distribution coefficient. Equations (7.2.1) and (7.2.4) for the ion-transfer reactions are counterparts of the half reaction and the Nernst equation for redox reactions at liquid/solid electrode interfaces, respectively.

To obtain a Nernstian response to the ion, its membrane activity must be constant and independent of the sample activity so that equation (7.2.4) can be simplified to

$$\Delta_w^M \phi = \text{constant} + \frac{RT}{z_i F} \ln a_i^W \quad (7.2.7)$$

where the constant term is $(RT/z_i F) \ln(k_i/a_i^M)$. The activity term of equation (7.2.7) is the origin of the activity term of equation (7.1.1) for Nernstian responses. Also, the constant

term of equation (7.1.1) includes that of equation (7.2.7) so that, in an E versus $\log a_i^W$ plot, not only the response slope but also the intercept depends on the transferred ion, which is an expression of the ion selectivity. In any potentiometric experiment, the sample solutions of an analyte ion (primary ion) also contain its counter ions and, in most cases, its co-ions (interfering ions). Nernstian responses can be obtained when the primary ion is the only major ion that is selectively transferred across the interface between the two phases as demonstrated below.

7.2.2 Ion-exchanger-based ISEs

Since the sample solutions always contain similar concentrations of an analyte ion and its counter ions, the primary requirement for Nernstian responses is selective membrane permeability for the analyte against the aqueous counter ions. The selectivity can be obtained simply by doping a membrane with ionic sites that have a charge opposite to that of the analyte. This type of membrane electrode based on ionic sites is called ion-exchanger-based ISEs or more specifically, ionophore-free ion-exchanger-based ISEs because any liquid membrane ISE has an ion-exchange capability for Nernstian responses. Table 7.1

Table 7.1

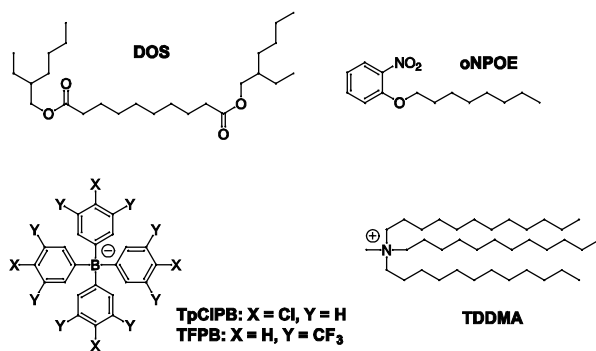
Membrane compositions and selectivity coefficients of ion-exchanger-based ISEs

Ion	Membrane composition ^a	$\log k_{I,J}^{\text{pot}, b}$	Method	Reference
Na^{+c}	DOS (66.15), PVC (33.40), NaTFPB (0.45)	$\text{H}^+, (0.8); \text{K}^+, (0.5); \text{Ag}^+, (0); \text{N}(\text{CH}_3)_4^+, (1.6); \text{Mg}^{2+}, (-2.2); \text{Ca}^{2+}, (-2.2); \text{Cu}^{2+}, (-2.2); \text{Cd}^{2+}, (-2.2)$	FIM	(9)
Cl^{-c}	oNPOE (66), PVC (33), TDDMACl (1)	$\text{F}^-, -1.8; \text{Br}^-, 1.3; \text{I}^-, 3.3; \text{HCO}_3^-, -1.4; \text{NO}_2^-, 1.1; \text{NO}_3^-, 2.0; \text{SCN}^-, 3.8; \text{ClO}_4^-, 5.1; \text{acetate}^-, -1.5; \text{SO}_4^{2-}, -1.6$	SSM	(10)

^aThe weight percentages of ionic site, plasticizer, and PVC are given in parentheses.

^bUnbiased selectivity coefficients are given in parentheses.

^cThe selectivity coefficients were determined for another primary ion (Pb^{2+} and NO_2^- for the cation- and anion-exchange electrodes) and then recalculated for the present ion.



lists examples of the electrodes and the structures of representative ionic sites and membrane plasticizers. Cation selectivity against anions can be obtained by doping a membrane with an analyte salt of a tetraphenylborate derivative as an anionic site, whereas anion selectivity can be obtained by doping a membrane with an analyte salt of a lipophilic tetraalkylammonium as a cationic site.

When a membrane doped with anionic sites is in contact with an aqueous solution of I^+X^- , I^+ is exchanged across the interface (Figure 7.1A). The aqueous counter ion is excluded from the membrane phase because of the “common ion” effect. Transfer of an aqueous counter ion into the membrane phase must be followed by simultaneous transfer of the analyte so that the electroneutrality is maintained in the two phases. The salt-extraction process can be defined as



Also, the equilibrium reaction can be quantified by salt-partitioning constant, K_p , as defined by

$$K_p = k_I k_X = \frac{a_I^M a_X^M}{a_I^W a_X^W} \quad (7.2.9)$$

The high membrane concentration of the analyte as a counter ion of the ionic sites shifts the equilibrium such that the aqueous counter ion is excluded from the membrane. Thus, the concentration of the aqueous anion in the cation-selective membrane doped with anionic sites is negligible in the charge balance in the membrane phase

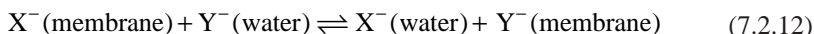
$$[I^+]_M = [R^-]_M + [X^-]_M \approx [R^-]_M \quad (7.2.10)$$

where brackets indicate the membrane concentration of the species. Since the membrane concentration of the analyte is fixed by the concentration of the anionic site, the phase boundary potential given by equation (7.2.4) depends only on the analyte activity in the sample solution, resulting in a Nernstian response.

While ion-exchanger-based ISEs provide a very high selectivity against the counter ions of an analyte, a drawback is the lack of the selectivity against the co-ions. The selectivity against interfering co-ions is primarily determined by hydrophobicity of the ions as quantified by k_i . It is well known that selectivity of anion-exchanger-based ISEs among inorganic anions follows so-called Hofmeister series



This selectivity sequence means that, for example, Cl^- in the membranes can be easily replaced with more hydrophobic anions. When it is completely replaced with another anion, the phase boundary potential becomes independent of the sample activity of Cl^- and is determined by that of the interfering anion. The ion-exchange equilibrium is defined as



with the ion-exchange equilibrium constant, K_E

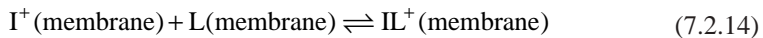
$$K_E = \frac{k_Y}{k_X} = \frac{a_X^W a_Y^M}{a_X^M a_Y^W} \quad (7.2.13)$$

When Y^- is more hydrophobic than X^- , $k_Y > k_X$, so that K_E is >1 . In the sample solution containing both X^- and Y^- , X^- can be more easily replaced by Y^- at higher activity of Y^- and lower activity of X^- . Because of this selectivity mechanism, ion-exchanger-based electrodes were developed mostly for hydrophobic ions such as organic ions and drugs for pharmaceutical applications (8).

7.2.3 Neutral-ionophore-based ISEs

Selectivity of ion-exchanger-based ISEs can be modified by adding an electrically neutral ionophore to the membranes (Figure 7.1B). Examples of ISEs based on commercially available neutral ionophores are summarized in Table 7.2. The neutral-ionophore-based electrodes were first developed using an antibiotic such as valinomycin as a K^+ -selective ionophore (K^+-1). In addition to naturally occurring ionophores, many neutral ionophores were synthesized for alkaline cations, alkaline earth cations, heavy metal ions, and inorganic anions.

When a membrane containing anionic sites is doped with a cation-selective neutral ionophore, the cationic analyte in the membrane phase forms complexes with the ionophore



where the formation constant, β , is given by

$$\beta = \frac{a_{IL}^M}{a_I^M a_L^M} \quad (7.2.15)$$

When the formation constant is large enough and the membrane contains an excess amount of the free ionophore, the complexation reaction proceeds completely so that most analytes in the membrane are in the complexed form. Therefore, the charge balance in the membrane phase can be simplified as

$$R_T = [I^+]_M + [IL^+]_M \approx [IL^+]_M \quad (7.2.16)$$

where R_T is the total concentration of ionic sites (anionic sites in this example). Also, combination of the mass balance equation for the ionophore with equation (7.2.16) gives the membrane concentration of the free ionophore as

$$[L]_M = L_T - [IL^+]_M \approx L_T - R_T \quad (7.2.17)$$

Table 7.2

Membrane compositions and selectivity coefficients of ISEs based on commercially available neutral ionophores and their complexation constants

Ion	Membrane composition ^a	$\log k_{I,J}^{\text{pot}b}$	Method	$\log \beta (n)^c$	Reference
H ⁺	H ⁺ -1 (1), PVC (30), oNPOE (69), KTpCIPB (70)	Li ⁺ , -6.9; Na ⁺ , -5.6	FIM	—	(13)
Li ⁺	Li ⁺ -1 (1), oNPPE/TEHP ^d (70), PVC (28), KTpCIPB (71)	H ⁺ , -2.6; Na ⁺ , -2.5; K ⁺ , -2.4; Rb ⁺ , -1.5; Cs ⁺ , -1.2; NH ₄ ⁺ , -2.4; Mg ²⁺ , -4.1; Ca ²⁺ , -3.8; Sr ²⁺ , -3.9; Ba ²⁺ , -3.7	SSM	5.33 (1)	(14)
Li ⁺	Li ⁺ -2 (2.5), PVC (33), oNPOE (66), KTpCIPB (15)	H ⁺ , -2.6; Na ⁺ , -1.9; K ⁺ , -3.2; Rb ⁺ , -3.1; Cs ⁺ , -3.8; NH ₄ ⁺ , -3.8; Mg ²⁺ , -2.4; Ca ²⁺ , -1.0; Sr ²⁺ , -0.9; Ba ²⁺ , -1.1	SSM	10.40 (1)	(15)
Na ⁺	Na ⁺ -1 (0.66), o-NPOE (70), PVC (28), KTpCIPB (50)	H ⁺ , -2.2; Li ⁺ , -2.5; K ⁺ , -2.0; Cs ⁺ , -2.1; NH ₄ ⁺ , -2.7; Mg ²⁺ , -2.9; Ca ²⁺ , -2.6	SSM (FIM) ^e	10.27 (1)	(16)
Na ⁺	Na ⁺ -2 (1), o-NPOE (65), PVC (33), KTpCIPB (11)	H ⁺ , -0.8; K ⁺ , -1.5; Mg ²⁺ , -3.8; Ca ²⁺ , -1.6	SSM	10.91 (2)	(17)
K ⁺	K ⁺ -1 (1.2), DOS (65), PVC (33), NaTFPB (60)	Na ⁺ , -4.1 (-4.5); Mg ²⁺ , -5.2 (-7.5); Ca ²⁺ , -5.0 (-6.9)	SSM	10.10 (1)	(18)
K ⁺	K ⁺ -2 (2), oNPOE (33), PVC (65), KTpCIPB (70)	Li ⁺ , -3.8; Na ⁺ , -3.2; NH ₄ ⁺ , -2.1; Mg ²⁺ , -5.0; Ca ²⁺ , -4.5	SSM	10.04 (1)	(19)
Cs ⁺	Cs ⁺ -1 (0.4), PVC (33.2), oNPOE (66.3), KTpCIPB (62)	Li ⁺ , -3.3; Na ⁺ , -2.1; K ⁺ , -3.2; Rb ⁺ , -0.8; Rb ⁺ , -1.0; Mg ²⁺ , -3.0; Ca ²⁺ , -3.5	SSM	—	(20)
NH ₄ ⁺	NH ₄ ⁺ -1 (3), PVC (30), BEHS (66.5), KTpCIPB (25)	Li ⁺ , -3.5; Na ⁺ , -2.4; K ⁺ , -1.0; Rb ⁺ , -1.5; Cs ⁺ , -2.4; Mg ²⁺ , -4.0; Ca ²⁺ , -3.8; Sr ²⁺ , -3.6; Ba ²⁺ , -4.0	SSM	—	(21)
Mg ²⁺	Mg ²⁺ -1 (1), PVC (33), oNPOE (65), KTpCIPB (50)	H ⁺ , +6.5; Li ⁺ , -0.9; Na ⁺ , -2.3; K ⁺ , -1.2; Rb ⁺ , -0.6; Cs ⁺ , +0.3; Ca ²⁺ , +1.5; Sr ²⁺ , +0.3; Ba ²⁺ , +0.3	SSM	13.84 (3)	(22)
Mg ²⁺	Mg ²⁺ -2 (2), oNPOE (66), PVC (32), KTpCIPB (100)	Li ⁺ , -3.6; Na ⁺ , -3.0; K ⁺ , -1.4; Rb ⁺ , -0.5; Cs ⁺ , +0.6; NH ₄ ⁺ , -2.0; Ca ²⁺ , -2.5; Sr ²⁺ , -2.9; Ba ²⁺ , -2.3	SSM	—	(23)
Ca ²⁺	Ca ²⁺ -1 (0.46), oNPOE (66), PVC (33), NaTFPB (50)	Na ⁺ , -3.4 (-8.3); K ⁺ , -3.8 (-10.1); Mg ²⁺ , -4.6 (-9.3)	SSM	29.2 (3)	(24)

(Continued)

Table 7.2 (Cont.)

Ion	Membrane composition ^a	$\log k_{i,j}^{\text{pot}}{}^b$	Method	$\log \beta (n)^c$	Reference
Ca^{2+}	$\text{Ca}^{2+}\text{-}2$ (1), oNPOE (64), PVC (34.5), KTpClPB (69)	$\text{H}^+, -4.4; \text{Li}^+, -2.8; \text{Na}^+, -3.4;$ $\text{K}^+, -3.8; \text{Mg}^{2+}, -4.4$	SSM	24.54 (2)	(25)
Ca^{2+}	$\text{Ca}^{2+}\text{-}3$ (2), oNPOE (66), PVC (32), KTpClPB (100)	$\text{H}^+, -3.7; \text{Li}^+, -4.1; \text{Na}^+, -4.1; \text{K}^+, -4.5; \text{Rb}^+, -4.2;$ $\text{Cs}^+, -4.0; \text{NH}_4^+, -4.2; \text{Mg}^{2+}, -5.0; \text{Sr}^{2+}, -1.0;$ $\text{Ba}^{2+}, -2.0$	SSM	—	(23)
Ba^{2+}	$\text{Ba}^{2+}\text{-}1$ (1), PVC (33), oNPOE (66), KTpClPB (65)	$\text{H}^+, -1.6; \text{Li}^+, -3.2; \text{Na}^+, -2.7; \text{K}^+, -2.7; \text{Rb}^+, -2.9;$ $\text{Cs}^+, -2.9; \text{NH}_4^+, -3.2; \text{Mg}^{2+}, -7.8; \text{Ca}^{2+}, -1.8;$ $\text{Sr}^{2+}, -0.2$	SSM	—	(26)
Cu^{2+}	$\text{Cu}^{2+}\text{-}1$ (1.2), PVC (57.2), oNPOE (34.3), KTpClPB (24)	$\text{Na}^+, -2.7; \text{K}^+, -2.3; \text{Mg}^{2+}, -3.6; \text{Ca}^{2+}, -3.6;$ $\text{Sr}^{2+}, -3.7; \text{Mn}^{2+}, -2.5; \text{Ni}^{2+}, -3.2; \text{Co}^{2+}, -4.0;$ $\text{Zn}^{2+}, -2.2 \text{ Cd}^{2+}, -4.4; \text{Pb}^{2+}, -0.7$	FIM	—	(27)
Ag^+	$\text{Ag}^+\text{-}1$ (1.1), DOS (66), PVC (32), KTpClPB (29)	$\text{Na}^+, -3.4 (-6.2); \text{K}^+, -3.3 (-5.7); \text{Ca}^{2+}, -4.0 (-8.0);$ $\text{Pb}^{2+}, -4.3 (-6.0); \text{Cu}^{2+}, -4.1 (-7.7)$	SSM	—	(24)
Pb^{2+}	$\text{Pb}^{2+}\text{-}1$ (1.57), DOS (66.15), PVC (33.40), NaTFPB (34)	$\text{H}^+, (-7.5); \text{Na}^+, (-7.5); \text{K}^+, (-6.9); \text{Ag}^+, f (9.5);$ $\text{N}(\text{CH}_3)_4^+, (-6.5); \text{Mg}^{2+}, (-13.9); \text{Ca}^{2+}, (-13.1);$ $\text{Cu}^{2+}, (-4.0); \text{Cd}^{2+}, (-6.3)$	SSM	—	(9)
Pb^{2+}	$\text{Pb}^{2+}\text{-}2$ (1.24), DOS (66.15), PVC (33.40), NaTFPB (17)	$\text{H}^+, (4.4); \text{Na}^+, (3.5); \text{K}^+, (4.5); \text{Ag}^+, (21.8);$ $\text{N}(\text{CH}_3)_4^+, (6.7); \text{Mg}^{2+}, (-1.7); \text{Ca}^{2+}, (-1.1);$ $\text{Cu}^{2+}, (0.3); \text{Cd}^{2+}, (-0.3)$	SSM	—	(9)
Cl^-	$\text{Cl}^-\text{-}1$ (2), DOS (65), PVC (33), TDDMACl (1)	$\text{F}^-, -5.2; \text{Br}^-, -0.7; \text{I}^-, -0.7; \text{HCO}_3^-, -4.7;$ $\text{NO}_3^-, -2.5; \text{SCN}^-, -0.3; \text{ClO}_4^-, -0.2; \text{acetate}^-, -5.2;$ $\text{salicylate}^-, -0.8; \text{SO}_4^{2-}, -5.5; \text{HPO}_4^{2-}, -5.2$	SSM	—	(28)
CO_3^{2-}	$\text{CO}_3^{2-}\text{-}1$ (9.7), DOS (59.0), PVC (2 9.5), TDDMACl (13.8)	$\text{Cl}^-, -5.0; \text{Br}^-, -3.6; \text{NO}_3^-, -1.8; \text{SCN}^-, 0.5;$ $\text{salicylate}^-, 3.6; \text{SO}_4^{2-}, -5.0; \text{HPO}_4^{2-}, -5.0$	SSM	—	(29)

^aThe weight percentages of ionophore, plasticizer, and PVC are given in parentheses. The amount of ionic sites is in mol% relative to the ionophore.

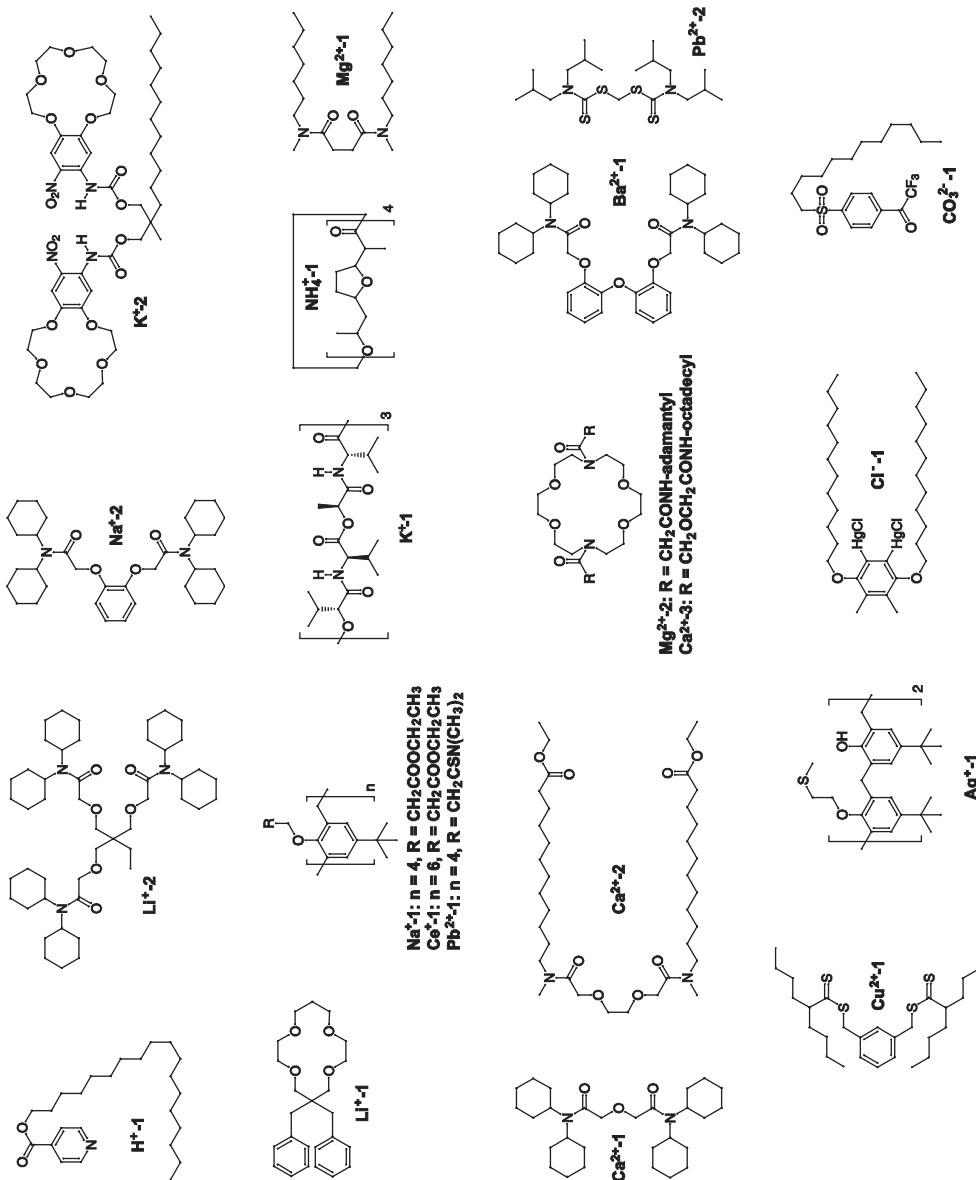
^bUnbiased selectivity coefficients are given in parentheses.

^cData from reference (30). n is the assumed stoichiometry.

^d98:2 mixture of o-nitrophenyl phenyl ether and tris(2-ethylhexyl)phosphate.

^eSSM for monocations and FIM for dications.

^fObtained with oNPOE.



where L_T is the total concentration of the ionophore. Since the membrane contains both free and complexed ionophores, the free analyte concentration in the membrane phase is buffered to be low and independent of the sample composition. Combination of equations (7.2.15)–(7.2.17) gives the free analyte concentration, and subsequently its activity as

$$a_I^M = \frac{\gamma_{IL}^M R_T}{\beta \gamma_L^M (L_T - R_T)} \quad (7.2.18)$$

where γ_{LM}^M and γ_L^M are the membrane activities of the complexes and the free ionophore, respectively. The sample-independent membrane activity results in the Nernstian response to the analyte ion. Moreover, because of the complexation process, the analyte in neutral-ionophore-based membranes is more stabilized than that in ion-exchanger-based membranes. The lower free analyte activity in the membrane phase shifts the ion-exchange equilibrium (see equation (7.2.12) for anions) such that the analyte is not exchanged with an interfering ion at a lower analyte activity or at a higher interfering-ion activity in the sample solution, leading to higher selectivity for the analyte.

While selective complexation makes the membrane more permeable to the analyte ion than the co-ions, selectivity against counter ions in neutral-ionophore-based membranes is achieved by ionic sites, not by the ionophore. In fact, the ionophore-analyte complexation decreases the free analyte activity in the membrane to enhance the salt extraction into the membrane phase, which may result in counter-ion interference due to Donnan exclusion failure (7). Although the PVC matrix has inherent negative sites as an impurity (11), the concentration is so low that the anionic sites were initially introduced in cation-selective ISEs based on neutral ionophores to suppress the counter-ion interference (12).

7.2.4 Charged-ionophore-based ISEs

Another way to improve selectivity against interfering co-ions is to use electrically charged ionophores. Commercially available charged ionophores and selectivity of the ISEs based on them are listed in Table 7.3. This system appears to be an ion-exchanger-based membrane based on the ionic sites that form a complex with an analyte selectively. For example, Ca^{2+} -selective electrodes based on organophosphate compounds are well-known examples of charged-ionophore-based ISEs although they have also been called ion-exchanger-based electrodes because of the ion-exchange capability. In this case, the charged ionophore provides selectivity for Ca^{2+} against both anions and other cations simultaneously. Another important class of charged ionophores is positively charged metalloporphyrins for anions (31). For example, membranes doped with a chloride salt of $\text{Mn}(\text{III})$ protoporphyrin respond selectively to Cl^- , which is due to selective coordination of Cl^- to the positively charged metal center.

Despite the dual selectivity inherent to the charged ionophores, they have been studied much less than neutral ionophores, limiting the number of examples. This is partially because of the belief that the membranes with charged ionophores are less suited for potentiometric ISEs than those with neutral ones (32), which turned out to be wrong only recently. When a membrane is doped only with an electrically neutral complex of a

Table 7.3

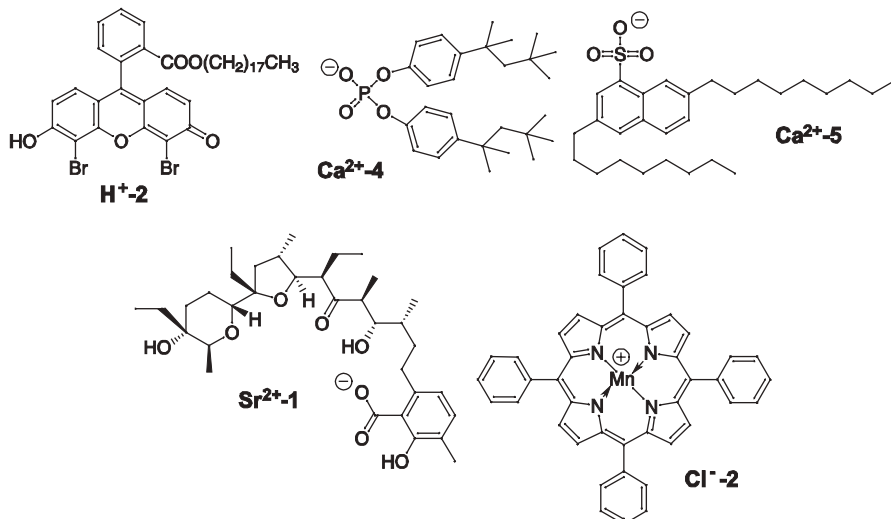
Membrane compositions and selectivity coefficients of ISEs based on commercially available charged ionophores

Ion	Membrane composition ^a	$\log k_{\text{I,J}}^{\text{pot}}$	Method	Reference
H ⁺	H ⁺ -2 (0.7), PVC (33), oNPOE (66), TDDMACl (50)	Li ⁺ , -9.6; Na ⁺ , -9.5; K ⁺ , -9.4	FIM	(34)
Ca ²⁺	Ca ²⁺ -4 (1), DOPP (66), PVC (33)	H ⁺ , 0.2; Li ⁺ , -1.2; Na ⁺ , -2.0; K ⁺ , -2.3; Rb ⁺ , -2.2; Cs ⁺ , -2.4; NH ₄ ⁺ , -1.6; Mg ²⁺ , -1.6; Ba ²⁺ , -1.6; Sr ²⁺ , -0.9	SSM	(35)
Ca ²⁺	Ca ²⁺ -5 (1), DOS (65), PVC (33), TDDMACl (48)	H ⁺ , 1.0; Li ⁺ , -1.6; Na ⁺ , -1.4; K ⁺ , -1.1; Rb ⁺ , -1.1; Cs ⁺ , -1.1; NH ₄ ⁺ , -0.9	SSM	(35)
Sr ²⁺	Sr ²⁺ -1 (1.2), PVC (33), oNPOE (65), KTpClPB (50)	Mg ²⁺ , -4.9; Ca ²⁺ , -3.5; Ba ²⁺ , 0.8	SSM	(36)
Cl ⁻	Cl ⁻ -2 (5), NPOE (90), 1-decanol (4), TDDMATpBCIPB (1) ^b	Br ⁻ , 0.3; I ⁻ , 1.3; NO ₂ ⁻ , 0.5; NO ₃ ⁻ , -0.9; ClO ₄ ⁻ , 1.5; acetate ⁻ , -3.7; SO ₄ ²⁻ , -5.9	SSM	(37)
NO ₂ ⁻	NO ₂ ⁻ -1 (1), ^c NPOE (65), PVC (33), KTpClPB (36.6)	F ⁻ , -3.9; Cl ⁻ , -3.7; Br ⁻ , -3.3; I ⁻ , -2.2; HCO ₃ ⁻ , -3.7; NO ₃ ⁻ , -3.5; SCN ⁻ , 0.2; ClO ₄ ⁻ , -2.2; acetate ⁻ , -3.8; SO ₄ ²⁻ , -4.1	SSM	(10)

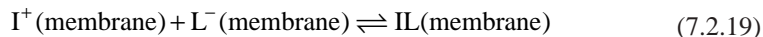
^aThe weight percentages of ionophore, plasticizer, and PVC are given in parentheses. The amount of ionic sites is in mole percent relative to the ionophore.

^bUsed as a supporting electrolyte so that the weight percentage is given in the parentheses.

^cThe ionophore structure is given in Figure 7.6.



negatively charged ionophore and a cationic analyte, the complex partially dissociates in the membrane



The reaction can be quantified with a formation constant as defined by equation (7.2.15) for neutral ionophores. In contrast to the neutral ionophore system, free charged ionophore does not exist in excess in the membrane so that complex dissociation is enhanced. With a sufficiently large formation constant, the analyte activity in the membrane phase is given as

$$a_I^M = \sqrt{\frac{\gamma_{IL}^M \gamma_I^M L_T}{\gamma_L^M \beta}} \quad (7.2.20)$$

The analyte activity depends only on the square root of the formation constant rather than the constant itself, which contrasts with the case of neutral ionophores. While the constant analyte activity in the membrane phase results in a Nernstian response, the membrane activity is relatively high and uncomplexed analytes are available for exchange with an interfering ion.

It was recently found that use of ionic sites in charged-ionophore-based ISEs improves the selectivity against interfering co-ions by providing excess free ionophores (10, 33). Figure 7.1C illustrates a charged-ionophore-based membrane that contains a salt of a cationic site and the charged ionophore in addition to the ionophore-analyte salt. Since the ionophore interacts weakly with the cationic site, the salt of the cationic site dissociates efficiently. Excess free ionophore provided from the ionic-site salt shifts the complexation equilibrium in equation (7.2.19) such that the ionophore-analyte complexation is enhanced. With the assumption that the ionophore-ionic-site salt dissociates completely, the charge and mass balances in the membrane phase are given as

$$[L^-]_M = R_T \quad (7.2.21)$$

$$L_T = [L^-]_M + [LM]_M \quad (7.2.22)$$

Combination of equations (7.2.21) and (7.2.22) with an expression for the formation constant gives the membrane activity of the free analyte as

$$a_I^M = \frac{\gamma_{IL}^M (L_T - R_T)}{\beta \gamma_L^M R_T} \quad (7.2.23)$$

With the ionic sites, most analyte is in the complexed form so that the membrane activity is not only independent of the sample solution but also very low. Equation (7.2.23) with the buffering effect by ionophore is very similar to equation (7.2.18) for neutral ionophores. Therefore, charged-ionophore-based membranes must be doped with ionic site to improve the selectivity against interfering co-ions. In this specific example, the charge sign of ionic sites is opposite to that of the ionophore, which is not always the case (34).

Charge sign of ionic sites significantly affects the selectivity of charged-ionophore systems as discussed in Section 7.3.2.

7.3 EQUILIBRIUM POTENTIOMETRIC RESPONSES

7.3.1 The Nikolsky–Eisenman equation and phase boundary potential model

Most ionophores form complexes not only with the analyte ion but also with the aqueous co-ions. Interference by co-ions is a major origin of experimental errors in the analysis. The Nernst equation (7.1.1), however, does not describe the contribution of the interfering ions to the measured potential. Traditionally, the influence of the interfering ions on the potentiometric responses has been described using the Nikolsky–Eisenman equation (38)

$$E = E_I^0 + \frac{RT}{z_I F} \ln \left(a_I + \sum_{I \neq J} k_{IJ}^{\text{pot}} a_J^{z_I/z_J} \right) \quad (7.3.1)$$

where k_{IJ}^{pot} is the selectivity coefficient for the analyte ion, I, against an interfering co-ion, J, and a_I and z_J are the sample activity and charge of the interfering ion. In a solution containing no interfering ion, equation (7.3.1) is equivalent to the Nernst equation (7.1.1) for the ion. Also, with only an interfering ion in a solution, equation (7.3.1) can be simplified to a Nernst equation for the interfering ion as

$$E = E_J^0 + \frac{RT}{z_J F} \ln a_J \quad (7.3.2)$$

with

$$E_J^0 = E_I^0 + \frac{RT}{z_I F} \ln k_{IJ}^{\text{pot}} \quad (7.3.3)$$

Therefore, the selectivity coefficient can be determined by potential measurements in separate solutions containing only the analyte or interfering ion (Figure 7.2A: the separate solution method, SSM). With potentials E_I and E_J at sample activities of the respective ions, a_I (SSM) and a_J (SSM), or with the intercepts of the E versus $\log a$ plots, the selectivity coefficient is given as

$$k_{IJ}^{\text{pot}} = \frac{a_I(\text{SSM})}{a_J(\text{SSM})^{z_I/z_J}} \exp \left[\frac{z_I F(E_J - E_I)}{RT} \right] = \exp \left[\frac{z_I F(E_J^0 - E_I^0)}{RT} \right] \quad (7.3.4)$$

Importantly, the potentials must be measured in activity ranges in which the electrode responses are Nernstian to the ions (39). While this requirement for equilibrium conditions

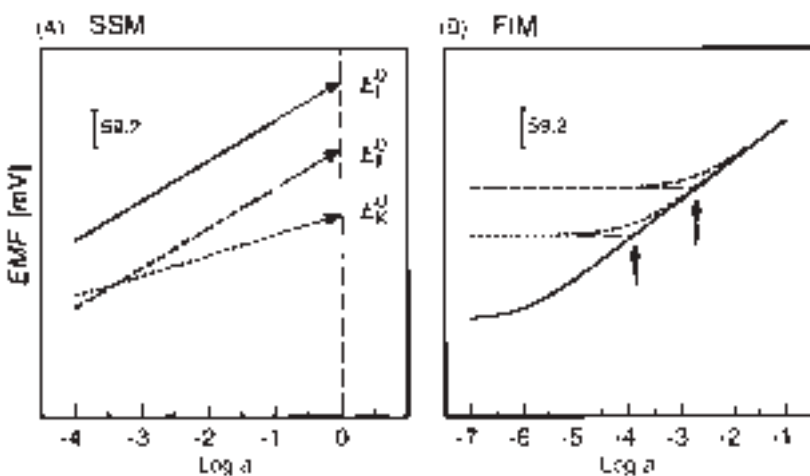


Figure 7.2 Representation of the separate solution method (A; SSM) and fixed interference method (B; FIM) under equilibrium conditions. Solid lines, response to monovalent primary ion; dashed and dotted lines, monovalent and divalent interfering ions, respectively. In the case of the FIM, the arrows indicate the detection limit. From reference (39). Copyright 2000 American Chemical Society.

can be checked experimentally, it is not always satisfied because of the non-equilibrium effects as discussed in Section 7.4.

The selectivity coefficient can also be determined by measuring the cell potentials at different analyte concentrations in the presence of a fixed concentration of an interfering ion (Figure 7.2B: the fixed interference method, FIM). In this case, the Nernstian response at high analyte activities is represented by equation (7.1.1). The constant potential at low analyte activities is determined by the interfering ion, whereas the Nernstian response to the interfering ion at the fixed activity should be confirmed in additional experiments (39). Linear extrapolations of these responses at high and low activities result in a cross point, which is defined as a detection limit. The selectivity coefficient can be obtained as

$$k_{IJ}^{\text{pot}} = \frac{a_I(\text{DL})}{a_J(\text{FIM})^{z_I/z_J}} \quad (7.3.5)$$

where $a_I(\text{DL})$ is the analyte activity at the detection limit and $a_J(\text{FIM})$ is the fixed activity of the interfering ion.

Despite the wide use of the Nikolsky–Eisenman equation and the selectivity coefficients, it is not so obvious whether this equation is valid when both analyte and interfering ions significantly contribute to the phase boundary potentials (for example, near the detection limit in Figure 7.2B). The equation was originally derived under equilibrium conditions for ions with the same charge number (specifically, $z_I = z_J = 1$) and then extended empirically (40). The experimental potentiometric responses in mixed ion solutions may deviate from the Nikolsky–Eisenman equation when the (1) experimental

conditions are not at equilibrium and (2) empirically extended equation is not valid, i.e., when the charge numbers are different.

To address the theoretical limitation of the Nikolsky–Eisenman equation, a more general description of the equilibrium responses of liquid membrane ISEs in mixed ion solutions was proposed (41). The model is based on phase boundary potentials under an equilibrium exchange of an analyte and an interfering co-ion at the membrane/sample solution interface. With ionophore-based membranes, the ion-exchange process is followed by complexation of the ions with an ionophore, where free ionophore was assumed to be always present in excess to simplify the model. The charge of the ions was not fixed so that their effect on the potentiometric responses can be addressed by the model. Under equilibrium conditions, the model demonstrated that the Nikolsky–Eisenman equation is valid only for ions with the same charge ($z_I = z_J$). The selectivity coefficient, however, can still be used in the new model to quantify the potentiometric responses in the mixed ion solution. For example, the potentiometric responses to a monovalent cation in the presence of a divalent cation are given as

$$E = E_I^0 + \frac{RT}{F} \ln \left[\frac{a_I}{2} + \frac{1}{2} \sqrt{a_I^2 + 4a_J(k_{IJ}^{\text{pot}})^2} \right] \quad (7.3.6)$$

Figure 7.3 shows potentiometric responses to Na^+ in the presence of Ca^{2+} as obtained with an Na^+ -selective electrode based on a neutral ionophore (Na^+ -2). Equation (7.3.6) fits the

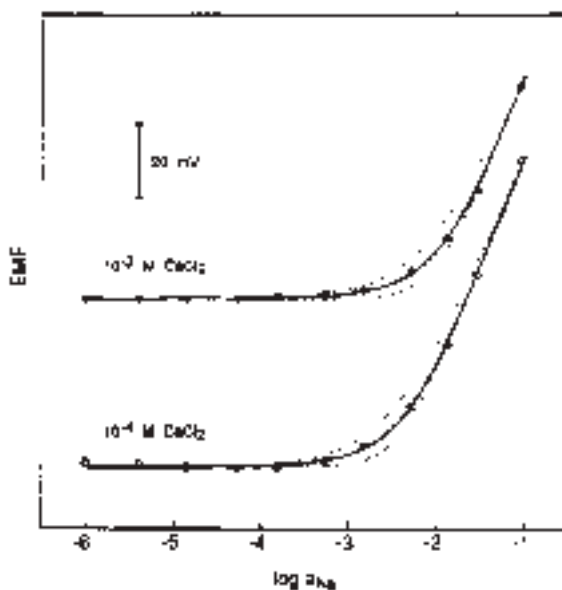


Figure 7.3 Sodium calibration curves in a background of 0.001 or 0.0001 M CaCl_2 , for an Na^+ -selective electrode based on a membrane of Na^+ -2 in DOS/PVC (2:1, w/w). Solid line according to equation (7.3.6); dotted lines according to Nicolsky–Eisenman equation (7.3.1) when Na^+ (upper curve) or Ca^{2+} (lower curve) is assumed to be the primary ion. From reference (41). Copyright 1994 American Chemical Society.

experimental responses better than the Nikolsky–Eisenman equation. More recently, the model was extended to describe the simultaneous responses for any number of monovalent, divalent, and trivalent ions (42).

7.3.2 Effect of ionic sites on selectivity

Besides hydrophobicity of ions and stability of their ionophore complexes, the concentration and charge of the ionic sites in the membrane phase also affect the ion selectivity of ionophore-based ISEs. This effect was first found for neutral-ionophore-based ISEs (14, 43), then for charge-ionophore-based ISEs (10, 33), and most recently implemented in an equilibrium phase boundary potential model generalized for both systems with primary and interfering ions of any charges and their complexes of any stoichiometries (34).

In ionophore-based ISEs, the analyte ion must be buffered to achieve a low and sample-independent membrane activity for a selective Nernstian response. This condition is satisfied when the membranes contain both free and complexed ionophores (Figure 7.4A: ionophore-based response mechanism). The membrane responds to an ion, i , on the basis of an ionophore-based mechanism when the concentration and charge of ionic sites satisfy the following relationship based on mass and charge balances in ionophore-based membranes (34):

$$-\frac{|z_i|}{z_i} \left(z_L + \frac{z_R R_T}{L_T} \right) < \frac{|z_i|}{n_i} \quad (7.3.7)$$

where z_L and z_R are the charges of the ionophore and the ionic sites, respectively, and n_i is the stoichiometry of the ionophore–ion complexes. Otherwise, free ionophore in the membrane is depleted by complexation with the ion so that the potentiometric responses become independent of the complexation process and are determined by the excess free ions as in the case of ionophore-free ion-exchanger electrodes (Figure 7.4B: ionophore-independent mechanism).

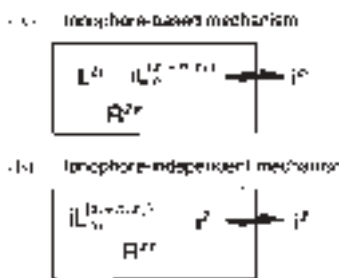


Figure 7.4 Schematic diagram of the major components in membranes that respond according to (A) an ionophore-based mechanism and (B) an ionophore-independent mechanism. In the latter case, the membranes contain a high concentration of free analyte ions but no significant concentration of free ionophore. The boxes designate the membrane phases: i , the primary or interfering ion; R^{z_R} , the lipophilic ionic site; L^{z_L} , the ionophore; and $iL^{\frac{z_i}{n_i}+n_i z_L}$, the $1:n_i$ complexes of the ion with the ionophore. From reference (34). Copyright 2000 American Chemical Society.

mechanism). Also, the response mechanism of the same membrane to an interfering ion depends on the charge and complexation stoichiometry of the ion. When $|z_J|/n_J \geq |z_I|/n_I$, equation (7.3.7) is satisfied simultaneously for primary and interfering ions so that the membrane responds to both ions on the basis of an ionophore-based mechanism, where the ionic sites do not affect the selectivity significantly. With $|z_J|/n_J < |z_I|/n_I$, the membrane responds to the analyte and interfering ions on the basis of ionophore-based and ionophore-independent mechanisms, respectively, when the following equation is satisfied:

$$\frac{|z_J|}{n_J} < -\frac{|z_I|}{z_I} \left(z_I + \frac{z_R [R_T]}{[L_T]} \right) < \frac{|z_I|}{n_I} \quad (7.3.8)$$

When $|z_J|/n_J < |z_I|/n_I$, the selectivity can be dramatically improved by optimizing the concentration and charge of ionic sites to satisfy equation (7.3.8). Figure 7.5 shows the effect of anionic sites on the Mg^{2+} selectivity of a neutral-ionophore-based ISE as determined by the SSM (14). The selectivity coefficients strongly depend on the membrane concentration of the anionic sites and result in optimum values against most ions with 120 mol% anionic sites relative to the ionophore concentration. With 1:1 complexes between the ionophore and Mg^{2+} , a large amount of the free ionophore is available for the ion in the membrane with 120 mol% anionic sites, i.e., ionophore-based mechanism. Ca^{2+} and

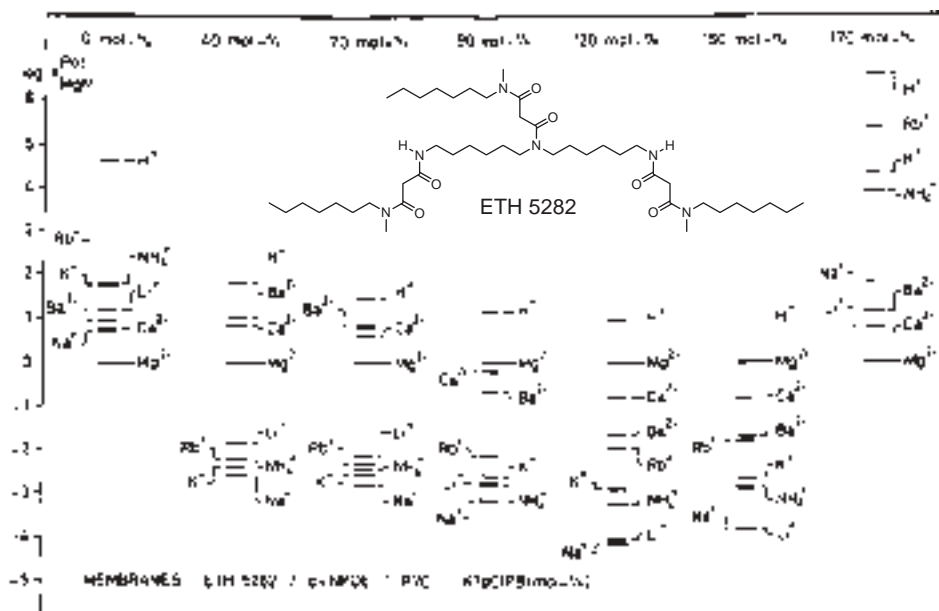


Figure 7.5 Selectivity coefficients, $\log k_{Mg}^{pot}$, of liquid membranes containing neutral ionophore ETH 5282 and oNPOE as the membrane solvent as determined by the SSM. From reference (14). Copyright 1991 American Chemical Society.

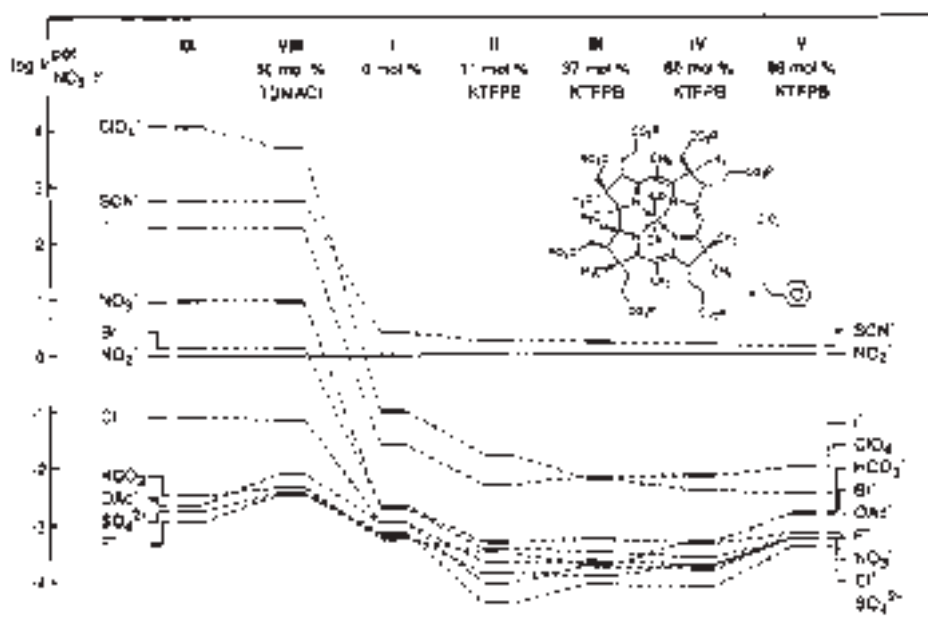


Figure 7.6 Selectivity coefficients, $\log k_{\text{NO}_3^-}^{\text{pot}}$ of liquid membranes containing charged ionophore NO_2^- -1 and oNPOE as the membrane solvent as determined by the SSM. The membrane IX is based only on an anion exchanger TDDMA. Selectivity coefficients of the membranes III and IX are also listed in Tables 7.3 and 7.1, respectively. From reference (10). Copyright 1994 American Chemical Society.

Ba^{2+} , however, form 1:2 complexes so that the free ionophore in the same membrane is depleted in contact with the separate solutions containing these ions. Since the interfering ions remain partially uncomplexed in the membrane phase, the electrode responds to the interfering ions on the basis of an ionophore-independent mechanism.

The effect of ionic sites on the selectivity is more complicated for charged ionophores because not only the concentration but also the charge of the sites affects the selectivity. Figure 7.6 shows the effects of ionic sites on the selectivity of NO_2^- -selective electrodes based on a positively charged ionophore (NO_2^- -1). As discussed in Section 7.2.4, addition of anionic sites improves the selectivity by increasing free ionophore concentration in the membrane. Most anions coordinate to the metal center of the ionophore for 1:1 complexation so that the selectivity coefficient depends slightly on the site concentration. Free anions are introduced by doping a membrane with cationic sites, resulting in a selectivity similar to that of ionophore-free anion-exchanger electrodes. In this example, $|z_I|/n_I = |z_J|/n_J$ so that the membranes function on the basis of the same mechanism (ionophore-based or ionophore-independent mechanism) to the primary and interfering ions. This example supports that charged ionophores require ionic sites of opposite charge (10, 33), which is not always true (34).

Figure 7.7 shows selectivity coefficients for Sr^{2+} against other alkaline earth cations as obtained with an electrode based on lasalocid (Sr^{2+} -1) as a negatively charged ionophore.

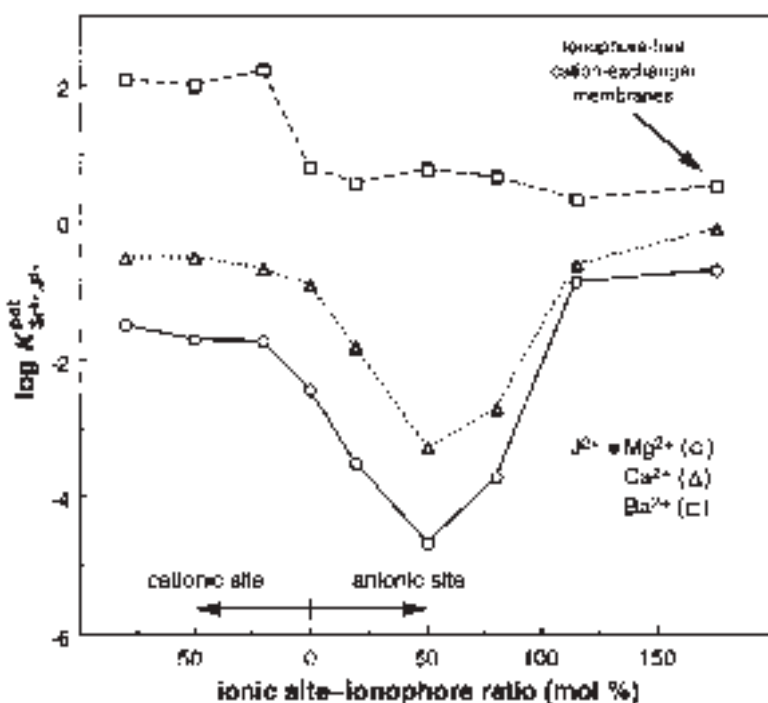


Figure 7.7 Selectivity coefficients, $\log k_{\text{Sr}^{2+}}^{\text{pot}}$, as determined with the SSM for oNPOE-PVC (2:1, w/w) membranes based on lasalocid ($\text{Sr}^{2+}-1$) and ionic sites. Selectivity coefficients of the membranes with 50 mol% anionic sites are also listed in Table 7.3. From reference (34). Copyright 2000 American Chemical Society.

As predicted by the generalized mode (34), the highest selectivity was achieved by addition of anionic sites rather than cationic sites. Also, the selectivity coefficients against Ca^{2+} and Mg^{2+} give the minimum values as observed with an Mg^{2+} -selective electrode based on a neutral ionophore, suggesting difference of complexation stoichiometry among the divalent cations. The selectivity dependence on the concentration and charge of ionic sites can be explained by formation of 1:1 and 1:2 complexes for the analyte and interfering ions, respectively. Importantly, the concentration and charge of ionic sites that give the highest selectivity can be calculated (14, 34), even when each analyte and interfering ion forms more than one type of complexes with different stoichiometries (34).

7.3.3 Apparently “non-Nernstian” equilibrium responses

The Nikolsky–Eisenman equation and a more general phase boundary model discussed in Section 7.3.1 are based on a common assumption that a well-defined amount of a free ionophore is always present in the membrane, implying that the membrane always functions on the basis of an ionophore-based mechanism. As discussed in Section 7.3.2, however, the

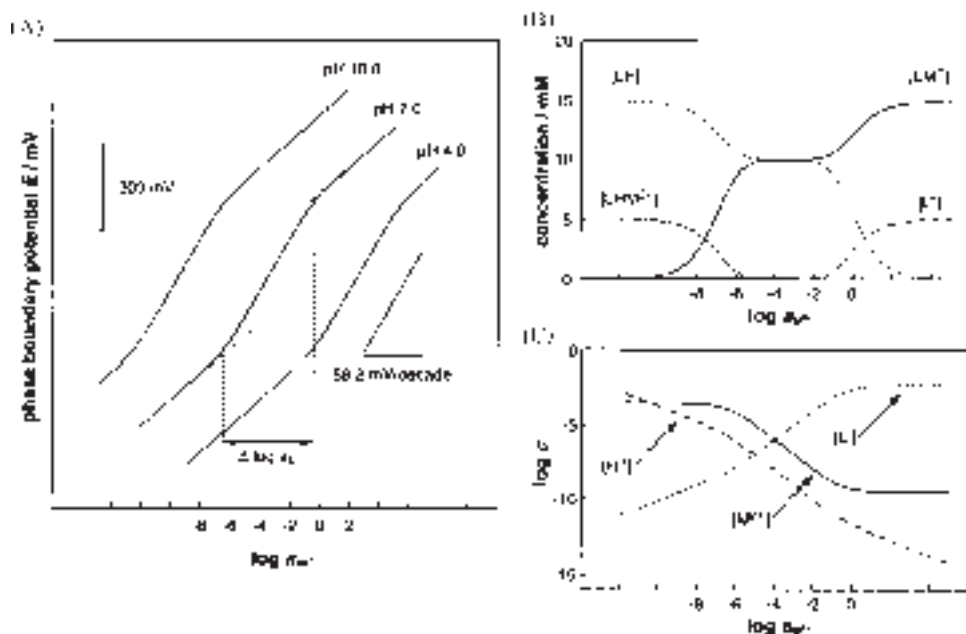


Figure 7.8 (A) Calculated phase boundary potentials as a function of the activity of a divalent cation in the sample solution for a membrane with an acidic ionophore and anionic sites. Responses are shown for sample solutions of pH 4.0, 7.0, and 10.0. Calculated equilibrium concentrations of (B) the deprotonated ionophore, L^- , and its complexes, LH , LM^+ , and LHM^{2+} , and (C) the deprotonated ionophore and the free primary ion, M^{2+} , and hydrogen ion, H^+ , in the membrane phase for pH 7.0. From reference (44). Copyright 1998 American Chemical Society.

concentration and charge of ionic sites can be such that the free ionophore can be depleted for some ions. Recently, potentiometric responses of the latter systems in mixed ion solutions were studied theoretically and experimentally to establish a novel response mechanism where equilibrium potentiometric responses can be apparently “non-Nernstian” in a wide activity range (44–46).

The apparently “twice-Nernstian” responses of ISEs based on acidic ionophores (Figure 7.8A) are the first examples of apparently “non-Nernstian” responses that could be explained on the basis of equilibrium phase boundary potentials (44). In this system, the acidic ionophores such as lasalocid ($Sr^{2+}-1$) in their deprotonated form, L^- , can bind both to dications, M^{2+} , as primary ions and to H^+ ions as secondary ions. With the assumption of 1:1 complexes for both ions and equilibrium exchange of the ions at the membrane/sample interface, the potentiometric response was demonstrated to depend simultaneously on the two ions over several orders of magnitude of the sample primary-ion activity in pH-buffered solutions. In the “twice-Nernstian” response region, the ionophores in the complexed forms with H^+ and M^{2+} are present simultaneously, whereas free ionophores are depleted (Figure 7.8B). The free M^{2+} concentration in the membrane phase is inversely proportional to the sample activity (Figure 7.8C), which results in a

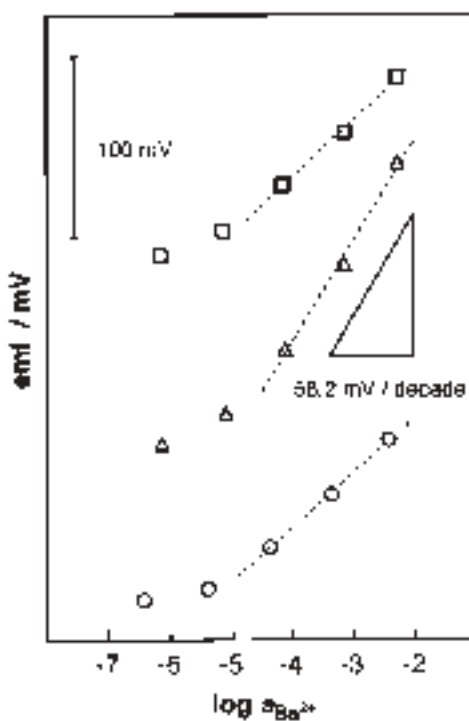


Figure 7.9 Potentiometric responses to Ba^{2+} as obtained with oNPOE-PVC (2:1, w/w) membranes based on lasalocid ($\text{Sr}^{2+}-1$) and 50 mol% KTpCIPB: (□) pH 2.0 (10 mM HCl), (Δ) pH 4.0 (1 mM $(\text{CH}_3\text{COO})_2\text{Mg}/\text{HCl}$), and (○) pH 7.0 (0.1 M Tris/HCl). The three response curves have been shifted vertically for enhanced clarity. From reference (44). Copyright 1998 American Chemical Society.

response slope twice as large as the Nernstian slope. This result contrasts to conventional Nernstian responses of ionophore-based ISEs, for which the membrane activity of the free primary ion is buffered with the ionophore and remains sample-independent. As predicted theoretically, these ISEs gave Nernstian, apparently twice-Nernstian, and again Nernstian responses to the primary dication when samples of high, intermediate, and low pH were used, respectively (Figure 7.9).

Analogously, apparently “super-Nernstian” responses to monoanions as observed with metalloporphyrin-based ISEs were shown to result from the formation of OH^- -bridged metalloporphyrin dimers in the ISE membranes (31, 45). Apparently super-Nernstian responses to F^- with slopes from -70 to -85 mV/decade were obtained with membranes based on Ga(III)octaethylporphyrin and anionic sites, which were quantitatively explained as responses co-determined by F^- as the primary ion and OH^- ions as the secondary ion with 1:1 and 1:2 complexation stoichiometry, respectively.

More recently, a generalized phase boundary potential model that describes apparently “non-Nernstian” equilibrium responses of ionophore-based ISEs was developed (46). The model predicts that ionophore-based ISEs can give three types of apparently non-Nernstian

equilibrium responses, i.e., apparently “super-Nernstian”, “sub-Nernstian”, and “inverted-Nernstian” responses (response slopes with a sign opposite to that of the conventional Nernstian responses). The response slopes depend on the charge numbers of the primary and secondary ions and on the stoichiometries of their complexes with the ionophore

$$\frac{\partial E}{\partial \log a_I^W} = \frac{RT \ln 10}{z_I F} \left(\frac{1}{1 - n_I z_J / n_J z_I} \right) \quad (7.3.9)$$

where $n_I z_J \neq n_J z_I$. The generalized model also revealed other requirements for apparently “non-Nernstian” equilibrium responses such as binding site and formation constants of the ionophore, and the concentration and charge of the ionic sites.

7.4 NON-EQUILIBRIUM POTENTIOMETRIC RESPONSES

7.4.1 Mixed ion-transfer potentials

ISEs are operated under open circuit condition, where no significant current flows. When a Nernstian response is obtained, only one ion is exchanged significantly between the membrane and sample phases so that there is no net current carried by the ion at the interface. In contrast, when co-extraction of the analyte and its aqueous counter ion (Donnan exclusion failure) or exchange of the analyte and its interfering co-ion occurs at the interface, the partial current carried by each ion, I_i , may become significant. The partial currents, however, cancel each other so that the total current at the interface, I , is zero

$$I = \sum_i I_i = 0 \quad (7.4.1)$$

The non-equilibrium ion-exchange processes can cause deviation of the potentiometric responses from those predicted by the Nikolsky–Eisenman equation and the equilibrium phase boundary potential model.

The non-equilibrium effects on potentiometric responses can be described using the concept of mixed ion-transfer potential (47). When ion transfers at a sample solution/membrane interface are fast enough, a local equilibrium at the interface is always achieved. The salt-extraction and ion-exchange processes, however, induce concentration polarization of the ions near the interface so that the potential is determined by the interfacial ion concentration as

$$E_{\text{mix}} = E_i^0 + \frac{RT}{z_i F} \ln \frac{\gamma_i^{W,S} c_i^{W,S}}{\gamma_i^{M,S} c_i^{M,S}} \quad (7.4.2)$$

where E_{mix} is the mixed ion-transfer potential, E_i^0 is a constant term unique for the ion, $c_i^{W,S}$ and $c_i^{M,S}$ are the ion concentrations at the water and membrane sides of the interface, respectively, and $\gamma_i^{W,S}$ and $\gamma_i^{M,S}$ are the activity coefficients of the ion at the respective

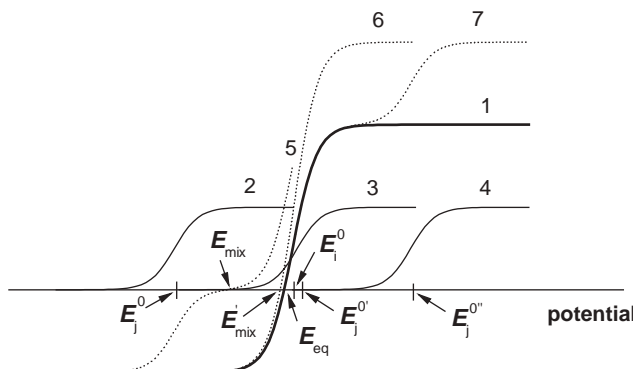


Figure 7.10 Schematic representation of the partial current versus potential curves for the transfer of primary ion, I (curve 1), and interfering ions, J, with different E_J^0 values (curves 2–4) across the sample solution/membrane interfaces. Curves 5–7 represent the total current versus potential relationships corresponding to curves 2–4, respectively. The curves are calculated using equations (7.4.2) and (7.4.3). See also reference (47).

sides of the interface. The interfacial concentrations are related to the partial current carried by the ion, which can be obtained under steady-state diffusion layer approximation as

$$\frac{I_i}{z_i FA} = \frac{D^W}{\delta^W} (c_i^{W,S} - c_i^W) = - \frac{D^M}{\delta^M} (c_i^{M,S} - c_i^M) \quad (7.4.3)$$

where A is the interfacial area, D^W and D^M are the diffusion coefficients of the ion in the sample and membrane phases, respectively, δ^W and δ^M are the thickness of the steady-state diffusion layers in the respective phases, and c_i^W and c_i^M are the bulk concentrations of the ion in the respective phases.

Consider an ion-exchanger-based membrane doped with a salt of a cationic analyte and an anionic site, which is in contact with a sample solution containing both the analyte and an interfering cation. Under steady-state conditions, combination of equations (7.4.2) and (7.4.3) for the analyte ion gives the partial current versus potential relationship based on transfer of the analyte ion between the membrane and sample phases as illustrated by curve 1 in Figure 7.10. The potential at zero current in the curve, E_{eq} , corresponds to the equilibrium potentiometric response of the membrane in the absence of the interfering ion in the sample solution. Also, the partial current versus potential relationship is obtained for transfer of the interfering ion from the sample solution to the membrane phase as represented by curves 2–4 depending on hydrophobicity of the ion. Because of the zero-current condition, the measured potential must be such that the partial current carried by the interfering ion exactly cancels current carried by the analyte. Therefore, in the presence of the interfering ion, the measured potential shifts from the equilibrium potential to a mixed ion-transfer potential (see curves 5–7).

The concept of this mixed ion-transfer potential was recently extended to quantify the non-equilibrium responses of neutral-ionophore-based ISEs (48). Figure 7.11 shows the

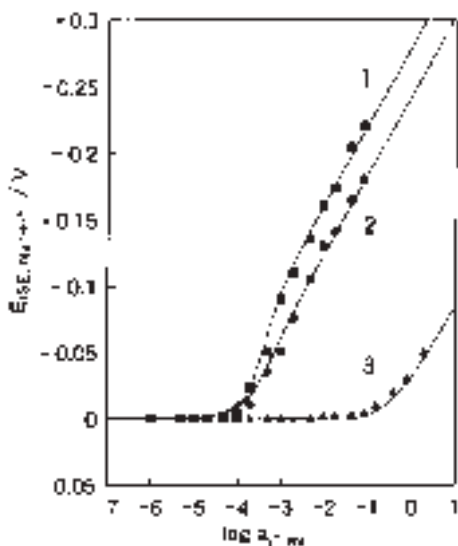


Figure 7.11 Potentiometric responses of Na^+ -ISE to (■) Rb^+ , (●) K^+ , and (▲) Li^+ in sample solutions containing 1 mM Na^+ . The membrane is a nitrobenzene solution of 0.05 M dibenz-18-crown-6 and 1 mM NaTFPB as a neutral ionophore and anionic sites, respectively. Solid lines represent theoretical curves. From reference (48).

effect of the interfering ions on the potentiometric responses in a solution containing a fixed concentration of the analyte Na^+ . When 10^{-4} to 10^{-3} M Rb^+ is added to the sample solution as a more preferred interfering ion, the potential increases from the equilibrium potential determined by Na^+ , resulting in a super-Nernstian response (curve 1). In this activity region, the analyte ion in the membrane is significantly replaced with the interfering ion so that the potential is based on mixed ion-transfer potentials. Since the interfering ion is significantly depleted at the sample side of the interface, the measured potential is lower than the equilibrium potential as extrapolated from the Nernstian response at higher interfering-ion activities. In contrast, addition of a more discriminated Li^+ gives a sub-Nernstian response even in a high activity range (curve 3), where Na^+ in the membrane phase is only partially replaced with Li^+ . Good fits of the experimental potentials with the theoretical ones demonstrate usefulness of this concept for quantifying the non-equilibrium effects on the potentiometric responses.

7.4.2 Elimination of non-equilibrium effects in separate solutions

Liquid membranes are usually soaked in an analyte solution, which is high in activity, overnight before measurements so that all exchangeable ions in the membranes are replaced with the analyte ion for a Nernstian response. This process is called conditioning. When a membrane conditioned in an analyte solution is in contact with the separate solution of an

interfering ion, the ion-exchange process at the interface may cause a non-equilibrium effect. The membranes give sub-Nernstian or no responses to highly discriminated ions, where the responses to the discriminated ions are masked by the analyte ion released from the membranes. Therefore, the selectivity coefficients thus determined are upper limits rather than those determined thermodynamically.

The non-equilibrium effects on the selectivity determination can be eliminated by measuring the bi-ionic potential in the following cell (49, 50):



where the membrane compositions are the same except for the exchangeable ions given in parentheses. With this cell, the measured potential is the difference between the equilibrium phase boundary potentials at the left and right membrane/solution interfaces as determined by distributions of ions I and J, respectively, as far as the liquid junction potential between the two membranes is negligibly small. Therefore, an unbiased selectivity coefficient can be obtained directly from the measured potential difference, $E_I - E_J$, using equation (7.3.4) for the SSM, where the analyte and interfering-ion activities correspond to those in the solutions at the left- and right-hand sides of the cell, respectively.

On the basis of a similar concept, a more simple method was proposed for determination of unbiased selectivity coefficients (24). With this method, a membrane is conditioned in a solution of a highly discriminated ion rather than the highly preferred analyte ion so that the membrane gives a Nernstian response to the discriminated ion. Then, the potentiometric responses to a less discriminated ion are measured. Whereas a super-Nernstian response based on a mixed ion-transfer potential may be observed in a lower activity region, completion of the ion-exchange process at the interface at higher activities results in a Nernstian response. The procedure is carried out in the rigid sequence of exposure of the membranes to the ions of interest from a highly discriminated one to a highly preferred one, allowing a determination of the unbiased selectivity coefficients against a series of the ions. Figure 7.12 shows the potentiometric responses of K^+ -selective membranes based on a neutral ionophore valinomycin ($\text{K}^+ \text{-} 1$), which were conditioned in a KCl solution and in an NaCl solution. When conditioned in highly discriminated Na^+ , the membrane gives Nernstian responses to all ions (even to more discriminated Ca^{2+} and Mg^{2+}) so that the selectivity coefficients can be determined under equilibrium conditions by the SSM. In contrast, the membrane conditioned in a K^+ solution gives almost no response to the discriminated ions because of the non-equilibrium effect.

Importantly, the unbiased selectivity coefficients are thermodynamically meaningful. When an interfering ion, such as tetraethylammonium ion for cation-selective electrodes, does not bind to an ionophore, the selectivity coefficient for an ion of interest against such an interfering ion can be used to determine the formation constant of the ion–ionophore complexes (9). For example, when a neutral ionophore forms $1:n_i$ complexes with an ion, i, and does not bind to an interfering ion, j, the formation constant is given as

$$\beta_{n_i} = \frac{k_{ij}^{\text{pot}}(\text{IE})}{k_{ij}^{\text{pot}}(L)(L_T - n_i R_T / z_i)^{n_i}} \quad (7.4.4)$$

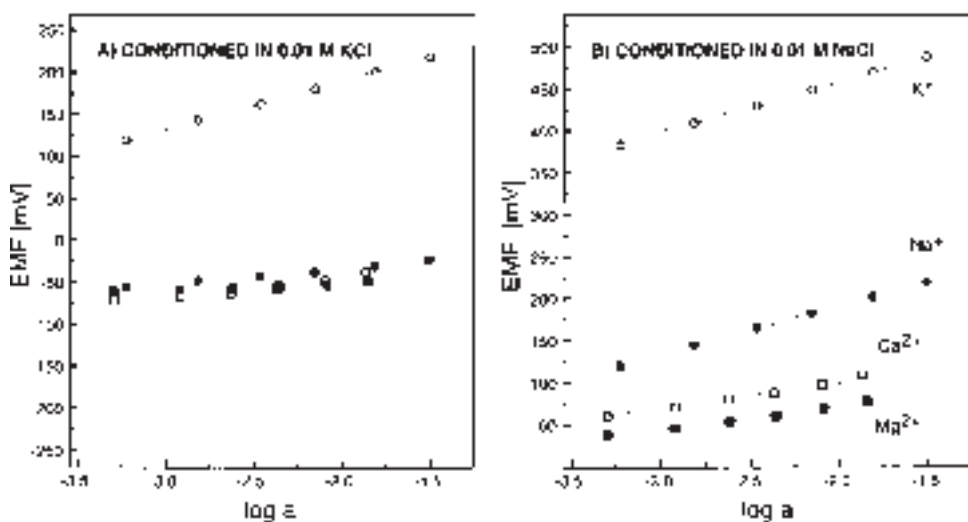
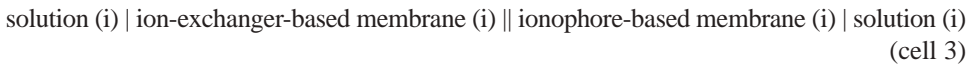


Figure 7.12 Potentiometric responses of liquid membranes based on valinomycin (K^+ -1) and NaTFPB conditioned in (A) 0.01 M KCl and (B) 0.01 M NaCl to (\circ) K^+ , (\bullet) Na^+ , (\blacksquare) Mg^{2+} , and (\square) Ca^{2+} . Dotted lines with Nernstian response slopes of 58.4 and 29.2 mV for monovalent and divalent cations, respectively. From reference (2). Copyright 1997 American Chemical Society.

where $k_{ij}^{pot}(IE)$ and $k_{ij}^{pot}(L)$ are the unbiased selectivity coefficients as obtained with an ion-exchanger-based membrane and an ionophore-based membrane, respectively, which contain the same concentration of ionic sites.

Formation constants can also be determined by measuring the potential of the following cell (51):



Whereas the potential is transient because of the gradual mixing of the membrane components, the initial potential is directly related to the formation constants without requirement of a reference ion. Assuming the same ionophore and ion as equation (7.4.4), the formation constant is given by

$$\beta_{n_i} = \frac{\exp(z_i F E_M / RT)}{(L_T - n_i R_T / z_i)^{n_i}} \quad (7.4.5)$$

where E_M is the potential of cell 3 with the same aqueous solutions measured using the same reference electrodes. This technique is called the sandwich method and can be used to determine equilibrium constants for complexation, ion-exchange, and salt-partitioning processes (51, 52).

Table 7.4.

Formal complex formation constant, $\log\beta_n$, and stoichiometries, n , of ionophore–ion complexes in PVC membranes^a

Ion	Pb ²⁺ –1 ^b		Pb ²⁺ –2 ^{b,c}		K ⁺ –1 ^d		K ⁺ –2 ^d	
	$\log\beta_n$	n	$\log\beta_n$	n	$\log\beta_n$	n	$\log\beta_n$	n
Li ⁺	–	–	–	–	(6.74) ^e	(1) ^e	4.22	1
Na ⁺	3.1	1	<3	1	(6.65) ^e	(1) ^e	6.00	1
K ⁺	<3	1	<3	1	9.95	1	8.10	1
Ag ⁺	–	–	12.6	1	–	–	–	–
Pb ²⁺	15.9	1	<3	1	–	–	–	–
Cu ²⁺	12.1	1	<3	1	–	–	–	–
Cd ²⁺	10.0	1	<3	1	–	–	–	–

^aThe ionophore structures are given in Table 7.2.

^bDetermined using a reference ion in DOS/PVC membranes.

^cThe ionophore is also known as a Ag⁺ ionophore because of its strong binding with Ag⁺.

^dDetermined by the sandwich method in DOS/PVC membranes.

^eDetermined using two ionophores. From reference (53).

The formation constants determined so far for representative neutral ionophores and the primary ions are listed in Table 7.2. Also, Table 7.4 lists the formation constants for both primary and interfering ions and reveals the very high complexation selectivity of the ionophores.

7.4.3 Effects of transmembrane ion flux on detection limit

Potentiometric responses of liquid membrane ISEs can be explained in most cases by considering ion-transfer processes only across the membrane/sample solution interfaces. It, however, was recently found that ion flux across the bulk membrane affects the interfacial processes and subsequently determines the detection limit (54, 55). When the analyte concentration in the sample solution is very low, a much higher analyte concentration in the inner solution drives the analyte flux from the inner solution to the sample solution. Therefore, the analyte activity at the sample side of the interface is determined not by the sample concentration but by the transmembrane ion flux. The analyte flux can be balanced by the flux of the aqueous counter ion from the inner solution to the sample solution (Figure 7.13A), maintaining the electroneutrality in the membrane and the two aqueous phases. Also, the counter flux of the interfering co-ion from the sample solution to the inner solution can balance the analyte flux (Figure 7.13B and C).

Pretsch and co-workers demonstrated for the first time that a detection limit of liquid membrane ISEs can be as low as the picomolar range by controlling the transmembrane flux (54). Figure 7.14 shows the responses of the same Pb²⁺-selective electrodes with different inner solution compositions. When Pb²⁺ is buffered in the inner solution containing EDTA, the detection limit can be improved by almost five orders of magnitudes down to $\sim 10^{-12}$ M. The low Pb²⁺ concentration in the inner solution suppresses the co-extraction

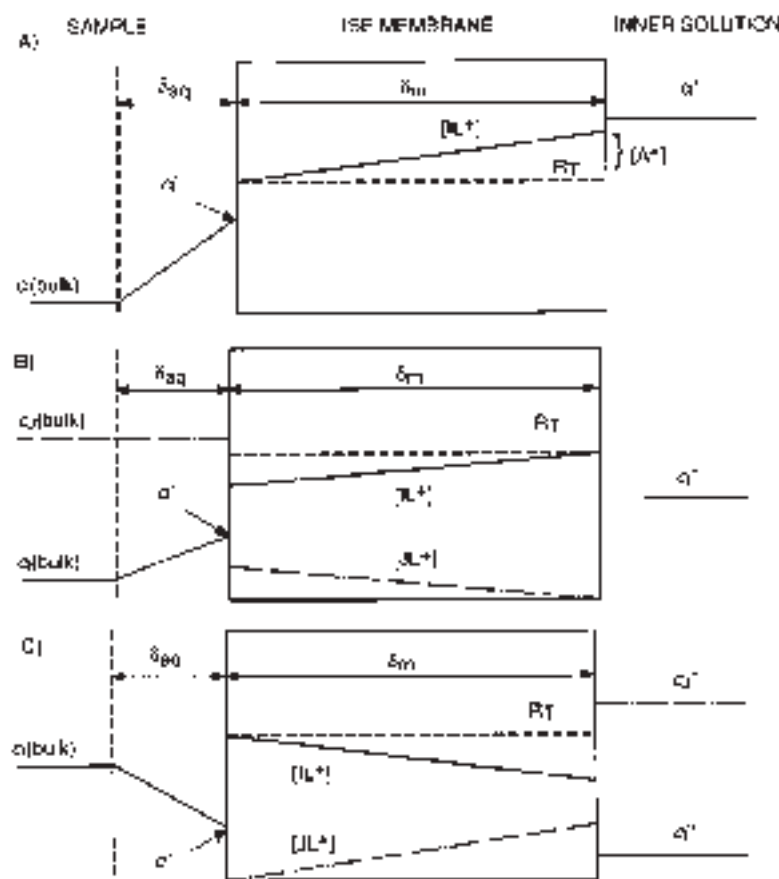


Figure 7.13 Schematic representation of the processes influencing the lower detection limit of ISEs based on an ionophore (L) forming 1:1 complexes with the monovalent primary (I^+) and interfering ions (J^+). Gradients are generated in the aqueous Nernstian phase boundary (thickness δ_{aq}) because of (A) co-extraction of I^+ and A^- from the inner solution and (B and C) partial exchange of primary ions by interfering ones at the sample and reference side, respectively. From reference (55). Copyright 1999 American Chemical Society.

at the inner solution side of the membrane, decreasing the Pb^{2+} flux directed to the sample solution. A high Na^+ concentration in the inner solution further decreases the membrane concentration of Pb^{2+} at the side of the inner solution by ion exchange, resulting in dramatic improvement of the detection limit. An improvement of detection limit was also observed for an interfering ion Na^+ . The subsequent Nernstian response to Na^+ allows determination of the unbiased selectivity coefficient.

So far, detection limits of liquid membrane ISEs for Pb^{2+} , Cd^{2+} , Ag^+ , Ca^{2+} , K^+ , NH_4^+ , ClO_4^- , and I^- have been improved to nanomolar and picomolar levels (56). The transmembrane ion flux at a Pb^{2+} -selective membrane was directly detected using scanning electrochemical microscopy (57). Potentiometric ISEs, however, are a passive

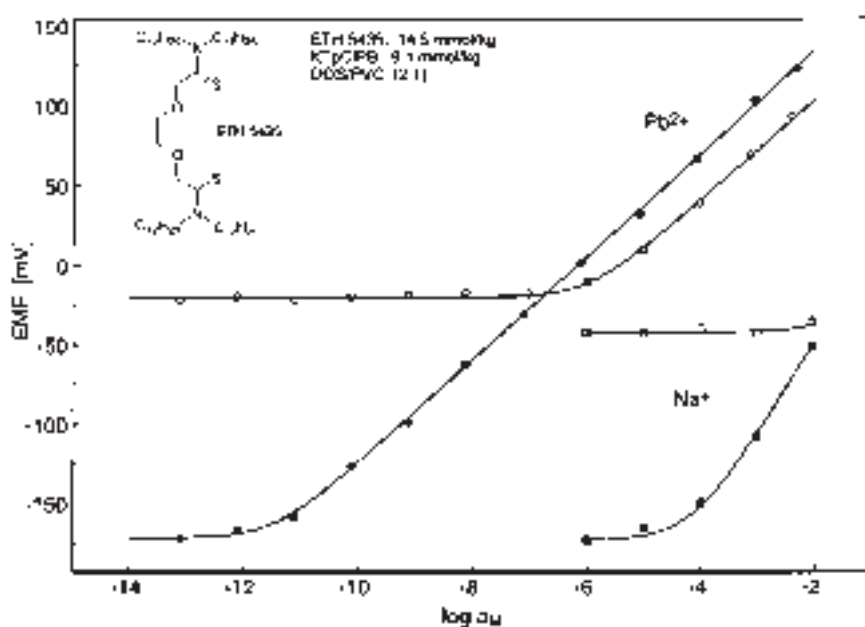


Figure 7.14 Response of two Pb²⁺ ISEs with the same membrane but different internal electrolytes. Conventional (empty symbols): 1:1 mixture of 10⁻³ M PbCl₂ and 0.1 M MgCl₂. New (full symbols): 1 mL of 0.1 M Pb(NO₃)₂ in 100 mL of 0.05 M EDTA-Na₂; measured pH 4.34. Calculated activities: 10⁻¹² M Pb²⁺ and 10⁻¹ M Na⁺. From reference (54). Copyright 1997 American Chemical Society.

electrochemical sensor so that control of the transmembrane flux is a challenging task. An optimum composition of the inner solution strongly depends on the sample composition (55). When the transmembrane flux of an analyte toward the inner solution becomes much larger than the analyte flux sustainable from the bulk sample solution to the interface, the analyte is completely depleted at the sample side of the interface (Figure 7.13C), where the phase boundary potential becomes insensitive to the analyte in a low sample activity range and then changes only at higher activities, resulting in a super-Nernstian response. Besides optimization of the membrane and inner solution compositions, detection limits were lowered by suppressing the transmembrane ion flux by applying an external current (58) or by enhancing the analyte flux to the membrane surface with a rotating-electrode configuration (59) though more instrumentation is necessary.

Effects of the transmembrane flux on the detection limits were also studied theoretically (60). The phase boundary potential model in mixed ion solutions as discussed in Section 7.3.1 was extended by implementing the steady-state transmembrane flux to demonstrate that the detection limit of a highly selective electrode, $c_1(\text{DL})$, is given approximately as

$$c_1(\text{DL}) = \sqrt{\frac{q[R_T]}{z_1} k_{IJ}^{\text{pot}} c_J^W} \quad (7.4.6)$$

with

$$q = \frac{D^M \delta^W}{\delta^M D^W} \quad (7.4.7)$$

where $z_I = z_J$, δ^M is approximated to be equal to the membrane thickness, and $k_{IJ}^{\text{pot}} c_J \ll q[R_T]/z_I \approx 10^{-6}$ M for highly selective electrodes. Comparison of the detection limit under the transmembrane ion flux conditions given by equation (7.4.6) with that under equilibrium conditions given by equation (7.3.5) reveals that the non-equilibrium effect worsens the detection limit, i.e.,

$$\frac{c_I(\text{DL})}{c_I^{\text{eq}}(\text{DL})} = \sqrt{\frac{q[R_T]}{z_I k_{IJ}^{\text{pot}} c_J}} > 1 \quad (7.4.8)$$

where $c_I^{\text{eq}}(\text{DL})$ is the detection limit under equilibrium conditions as given by equation (7.3.5) with activity coefficients of 1. Therefore, elimination of the transmembrane flux will improve the detection limit to the thermodynamically determined one. A possible approach is the use of solid-contact ISEs where a membrane is directly mounted on a solid electrode without an inner solution so that the major source of the transmembrane ion flux is eliminated. Although establishment of a reliable electrical contact at the membrane/electrode interface is challenging, there are a few examples of solid-contact ISEs with nanomolar detection limits (61). Potentiometric measurements under complete two-phase equilibrium will be an idealistic condition not only for practical application with a low detection limit but also for fundamental characterization of the membrane equilibrium.

7.4.4 Non-equilibrium responses for polyion detection

While selectivity and detection limit are biased by the non-equilibrium effects, it is interesting to point out that liquid membrane ISEs for polyions were successfully developed by taking advantage of mixed ion-transfer potentials (62). Two typical examples of the electrodes are those for heparin and protamine. Heparin is a highly sulfated polysaccharide (M_r 5000–25,000), which is extensively used as an anticoagulant in many medical procedures for prevention of blood clotting, especially during open heart surgery. Protamine is a naturally occurring polycationic protein rich in arginine (M_r ~4500), which is used to neutralize the anticoagulant activity of heparin. These electrodes are based on membranes doped with an anion-exchanger tridodecylmethylammonium (TDDMA) for heparin or with a negatively charged ionophore dinonylnaphthalene sulfonate (Ca^{2+} -5) for protamine. Equilibrium partitioning of such multiply charged ions between the membrane and aqueous phases results in a very small potential change as predicted by the Nernst equation (Figure 7.15). However, a non-equilibrium ion-exchange process between a polyion in the aqueous phase and a counter ion of the ion-exchanger sites in the membrane phase causes a large potential change, resulting in a non-equilibrium super-Nernstian

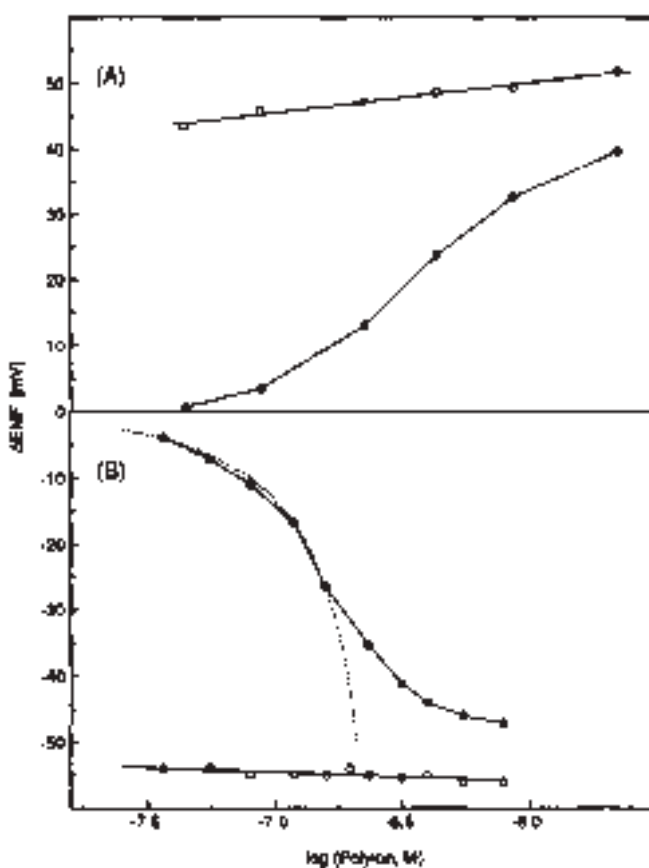


Figure 7.15 Potentiometric responses of (A) protamine and (B) heparin sensors in 0.12 M NaCl solution at different response times: (●) 5 min and (○) 24 h. The membranes were composed of 66 wt% PVC, 32.5 wt% plasticizer (oNPOE and DOS for respective polyions), and 1.5 wt% ion exchangers (Ca^{2+} -5 and TDDMA, respectively). Dotted line, theoretical curve. From reference (62). Copyright 1994 American Chemical Society.

response. This classical response mechanism based on mixed ion-transfer potentials turned out to be analytically useful for detection of biological polyions even beyond protamine and heparin. Moreover, rotating-electrode potentiometry was first developed for the polyion sensors to improve the detection limit (63), where a higher ion flux from the bulk sample solution to the membrane surface is achieved by reducing the diffusion layer thickness.

7.5 CONCLUSIONS

Development of various ionophores in the last four decades has allowed detection of more than 60 analyte ions with liquid membrane ISEs (3). Recent progress in the theory of liquid

membrane ISEs has clarified the response mechanisms so that several long-standing problems of practical importance in the field have been solved. Potentiometric responses in mixed ion solutions can be explained and quantified under both equilibrium and non-equilibrium conditions. The effect of ionic sites on the potentiometric response is fully understood so that the optimum membrane compositions for the highest selectivity can be predicted theoretically. Most impressively, finding and controlling the transmembrane ion flux now allows detection of trace amounts of ions at the picomolar level by ion-selective potentiometry.

These theoretical advances have led to the development of potentiometric methods for quantifying fundamental membrane processes. The stoichiometry of the ionophore–ion complexation in the membrane phase can be determined by studying the effects of ionic sites on potentiometric selectivity. Such a study also reveals whether an ionophore serves as a neutral or a charged ionophore (64). Formation constants of the complexes with the corresponding stoichiometry can be determined from the unbiased selectivity coefficients or more directly by the sandwich method. Quantitative information about the complexation processes in the membranes, which eventually limits practical performances of the electrodes, will be useful for future design of selective ionophores.

Non-equilibrium processes at the sample/membrane interface and across the bulk membrane bias the selectivity and detection limits of the electrodes. Elimination of these non-equilibrium effects by operating the electrodes under complete equilibrium conditions will be of both practical and fundamental significance. While non-equilibrium responses are useful for potentiometric polyion-selective electrodes, it is not obvious whether potentiometry based on mixed ion-transfer potentials is a better transduction mechanism than amperometry/voltammetry based on selective polyion transfer (65, 66). Ion-transfer electrochemistry at polarized liquid/liquid interfaces is introduced in Chapter 17 of this handbook.

REFERENCES

1. W. R. Fawcett, *Liquids, Solutions, and Interfaces: From Classical Macroscopic Descriptions to Modern Microscopic Details*, Oxford University Press: New York, 2004.
2. E. Bakker, P. Bühlmann, E. Pretsch, *Chem. Rev.* **97**, 3083 (1997).
3. P. Bühlmann, E. Pretsch, E. Bakker, *Chem. Rev.* **98**, 1593 (1998).
4. Y. Umezawa, P. Bühlmann, K. Umezawa, K. Tohda, S. Amemiya, *Pure Appl. Chem.* **72**, 1851 (2000).
5. Y. Umezawa, K. Umezawa, P. Bühlmann, N. Hamada, H. Aoki, J. Nakanishi, M. Sato, K. P. Xiao, Y. Nishimura, *Pure Appl. Chem.* **74**, 923 (2002).
6. Y. Umezawa, P. Bühlmann, K. Umezawa, N. Hamada, *Pure Appl. Chem.* **74**, 995 (2002).
7. R. P. Buck, E. Lindner, *Acc. Chem. Res.* **31**, 257 (1998).
8. V. V. Cosofret, R. P. Buck, *Crit. Rev. Anal. Chem.* **24**, 1 (1993).
9. A. Ceresa, E. Pretsch, *Anal. Chim. Acta* **395**, 41 (1999).
10. U. Schaller, E. Bakker, U. E. Spichiger, E. Pretsch, *Anal. Chem.* **66**, 391 (1994).
11. A. Van den Berg, P. D. van der Wal, M. Skowronksa-Ptasinska, E. J. R. Sudholter, D. N. Reinhoudt, P. Bergveld, *Anal. Chem.* **59**, 2827 (1987).
12. J. H. Boles, R. P. Buck, *Anal. Chem.* **45**, 2057 (1973).
13. U. Oesch, Z. Brzozka, A. Xu, B. Rusterholz, G. Suter, H. V. Pham, D. H. Welti, D. Ammann, E. Pretsch, W. Simon, *Anal. Chem.* **58**, 2285 (1986).

14. R. Eugster, P. M. Gehrig, W. E. Morf, U. E. Spichiger, W. Simon, *Anal. Chem.* **63**, 2285 (1991).
15. M. Bochenska, W. Simon, *Mikrochim. Acta* **III**, 277 (1990).
16. T. Grady, A. Cadogan, T. McKittrick, S. J. Harris, D. Diamond, M. A. McKervey, *Anal. Chim. Acta* **336**, 1 (1996).
17. M. Huser, P. M. Gehrig, W. E. Morf, W. Simon, E. Lindner, J. Jeney, K. Tóth, E. Pungor, *Anal. Chem.* **63**, 1380 (1991).
18. E. Bakker, *J. Electrochem. Soc.* **143**, L83 (1996).
19. E. Lindner, K. Tóth, J. Jeney, M. Horvath, E. Pungor, I. Bitter, B. Agai, L. Toke, *Mikrochim. Acta* **I**, 157 (1990).
20. A. Cadogan, D. Diamond, M. R. Smyth, G. Svehla, M. A. McKervey, E. M. Seward, S. J. Harris, *Analyst* **115**, 1207 (1990).
21. D. Siswanta, H. Hisamoto, H. Tohma, N. Yamamoto, K. Suzuki, *Chem. Lett.* 945 (1994).
22. M. V. Rouilly, M. Badertscher, E. Pretsch, G. Suter, W. Simon, *Anal. Chem.* **60**, 2013 (1988).
23. K. Suzuki, K. Watanabe, Y. Matsumoto, M. Kobayashi, S. Sato, D. Siswanta, H. Hisamoto, *Anal. Chem.* **67**, 324 (1995).
24. E. Bakker, *Anal. Chem.* **69**, 1061 (1997).
25. U. Schefer, D. Ammann, E. Pretsch, U. Oesch, W. Simon, *Anal. Chem.* **58**, 2282 (1986).
26. M. W. Laubli, O. Dinten, E. Pretsch, W. Simon, F. Vogtle, F. Bongardt, T. Kleiner, *Anal. Chem.* **57**, 2756 (1985).
27. S. Kamata, H. Murata, Y. Kubo, A. Bhale, *Analyst* **114**, 1029 (1989).
28. M. Rothmaier, U. Schaller, W. E. Morf, E. Pretsch, *Anal. Chim. Acta* **327**, 17 (1996).
29. C. Behringer, B. Lehmann, J.-P. Haug, K. Seiler, W. E. Morf, K. Hartman, W. Simon, *Anal. Chim. Acta* **233**, 41 (1990).
30. Y. Qin, Y. Mi, E. Bakker, *Anal. Chim. Acta* **421**, 207 (2000).
31. L. Gorski, E. Malinowska, P. Parzuchowski, W. Zhang, M. E. Meyerhoff, *Electroanalysis* **15**, 1229 (2003).
32. W. E. Morf, *The Principles of Ion-Selective Electrodes and of Membrane Transport*, Elsevier: New York, 1981.
33. V. V. Egorov, V. A. Repin, T. A. Ovsyannikova, *J. Anal. Chem.* **47**, 1235 (1992).
34. S. Amemiya, P. Bühlmann, E. Pretsch, B. Rusterholz, Y. Umezawa, *Anal. Chem.* **72**, 1618 (2000).
35. Y. Mi, C. Green, E. Bakker, *Anal. Chem.* **70**, 5252 (1998).
36. U. Schaller, E. Bakker, E. Pretsch, *Anal. Chem.* **67**, 3123 (1995).
37. P. C. Hauser, N. D. Renner, A. P. C. Hong, *Anal. Chim. Acta* **295**, 181 (1994).
38. G. G. Guilbault, R. A. Durst, M. S. Frant, H. Freiser, E. H. Hansen, T. S. Light, E. Pungor, G. Rechnitz, N. M. Rice, T. J. Rohm, W. Simon, J. D. R. Thomas, *Pure Appl. Chem.* **48**, 127 (1976).
39. E. Bakker, E. Pretsch, P. Bühlmann, *Anal. Chem.* **72**, 1127 (2000).
40. Y. Umezawa, K. Umezawa, H. Sato, *Pure Appl. Chem.* **67**, 508 (1995).
41. E. Bakker, R. V. Meruva, E. Pretsch, M. E. Meyerhoff, *Anal. Chem.* **66**, 3021 (1994).
42. M. Nägele, E. Bakker, E. Pretsch, *Anal. Chem.* **71**, 1041 (1999).
43. P. C. Meier, W. E. Morf, M. Läubli, W. Simon, *Anal. Chim. Acta* **156**, 1 (1984).
44. S. Amemiya, P. Bühlmann, Y. Umezawa, *Anal. Chem.* **70**, 445 (1998).
45. E. D. Steinle, S. Amemiya, P. Bühlmann, M. E. Meyerhoff, *Anal. Chem.* **72**, 5766 (2000).
46. S. Amemiya, P. Bühlmann, K. Odashima, *Anal. Chem.* **75**, 2997 (2003).
47. T. Kakiuchi, M. Senda, *Bull. Chem. Soc. Jpn.* **57**, 1801 (1984).
48. Y. Yoshida, M. Matsui, K. Maeda, S. Kihara, *Anal. Chim. Acta* **374**, 269 (1998).
49. G. M. Shean, *J. Membr. Sci.* **2**, 133 (1977).
50. S. Koizumi, T. Imato, N. Ishibashi, *J. Membr. Sci.* **132**, 149 (1997).
51. Y. Mi, E. Bakker, *Anal. Chem.* **71**, 5279 (1999).

52. Y. Qin, E. Bakker, *Anal. Chem.* **74**, 3134 (2002).
53. E. Bakker, E. Pretsch, *Anal. Chem.* **70**, 295 (1998).
54. T. Sokalski, A. Ceresa, T. Zwickl, E. Pretsch, *J. Am. Chem. Soc.* **119**, 11347 (1997).
55. T. Sokalski, T. Zwickl, E. Bakker, E. Pretsch, *Anal. Chem.* **71**, 1204 (1999).
56. E. Bakker, E. Pretsch, *Anal. Chem.* **74**, 420A (2002).
57. R. E. Gyurcsanyi, E. Pergel, R. Nagy, I. Kapui, B. T. T. Lan, K. Toth, I. Bitter, E. Lindner, *Anal. Chem.* **73**, 2104 (2001).
58. K. Pergel, R. E. Gyurcsanyi, K. Toth, E. Lindner, *Anal. Chem.* **73**, 4249 (2001).
59. T. Vigassy, R. E. Gyurcsanyi, E. Pretsch, *Electroanalysis* **15**, 1270 (2003).
60. A. Ceresa, A. Radu, S. Peper, E. Bakker, E. Pretsch, *Anal. Chem.* **74**, 4027 (2002).
61. J. Sutter, E. Lindner, R. E. Gyurcsanyi, E. Pretsch, *Anal. Bioanal. Chem.* **380**, 7 (2004).
62. B. Fu, E. Bakker, J. H. Yun, V. C. Yang, M. E. Meyerhoff, *Anal. Chem.* **66**, 2250 (1994).
63. Q. S. Ye, M. E. Meyerhoff, *Anal. Chem.* **73**, 332 (2001).
64. E. Bakker, E. Malinowska, R. D. Schiller, M. E. Meyerhoff, *Talanta* **41**, 881 (1994).
65. Y. Yuan, S. Amemiya, *Anal. Chem.* **76**, 6877 (2004).
66. J. Guo, Y. Yuan, S. Amemiya, *Anal. Chem.* **77**, 5711 (2005).

— 8 —

Chemically Modified Electrodes

Grant A. Edwards, Adam Johan Bergren, and Marc D. Porter

Iowa State University, Ames, IA 50011, USA

8.1 INTRODUCTION

Electrode surfaces are modified in a quest to render an electrochemical function either not possible or difficult to achieve using conventional electrodes. Targeted improvements include increased selectivity, sensitivity, chemical and electrochemical stability, as well as a larger usable potential window and improved resistance to fouling. Furthermore, electrodes with tailored surfaces enhance fundamental studies of interfacial processes. Therefore, the need for improved electrode performance and logically designed interfaces is rapidly growing in many areas of science.

The definition of a chemically modified electrode (CME) is: a conducting or semiconducting material that has been coated with a monomolecular, multi-molecular, ionic, or polymeric film (termed adlayer; see Figure 8.1) which alter the electrochemical, optical, and other properties of the interface (1, 2). The conductive and semiconductive substrates are derived from conventional electrode materials (see Chapter 5), while the adlayers are widely diverse in their origins and properties. This diversity extends or enhances the range and scope of electrochemical techniques.

Ideally, the properties of the adlayer impart a predictable function to the electrode. Recent improvements in surface characterization techniques enable a molecular-level understanding of modified interfaces. These techniques, coupled with electrochemical characterizations, not only provide a means to verify the function, but also serve as a basis for refinements of the modification strategy to further enhance its performance.

The extensive nature of electrode modification procedures prevents a comprehensive description of all types of modified electrodes, their uses, and the techniques used to characterize them. This chapter therefore focuses on providing the reader with concepts central to electrode modification through several examples of established systems. Specialized reviews are noted in each section, where appropriate; these and topical texts (3–10) should be consulted for more detailed information.

© 2007 Elsevier B.V. All rights reserved.

Handbook of Electrochemistry

Edited by C.G. Zoski

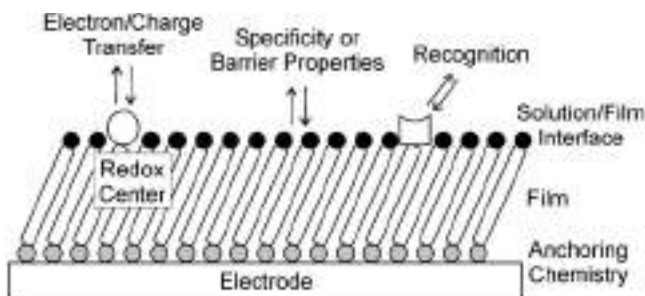


Figure 8.1 Generic illustration of a modified electrode. The film (or adlayer) is anchored to a conventional electrode to enhance performance or achieve a specialized function.

8.2 SUBSTRATE MATERIALS AND PREPARATION

The substrate is the platform electrode that supports the adlayer. Commercially available or custom fabricated substrates can be used. While any conventional electrode material can serve as a substrate, some materials are more convenient to modify. Of the conductive metals, Au, Ag, and Pt are the most commonly modified (11). These surfaces benefit from the ease with which reproducible and clean surfaces can be produced and maintained in the laboratory environment. Carbon electrodes (12, 13) are also commonly employed for similar reasons. Other metals and semiconductors are used less frequently, but are nonetheless high-profile materials (4, 5).

In most electrode preparation schemes, the electrode surface is treated before modification to provide reproducible surface attributes. These procedures often involve conventional electrode treatments (see Chapter 5), with adaptations or additions where needed. The pretreatment is critical: the electrochemical behavior of a derivatized electrode is often sensitive to small variations in the substrate properties (e.g., crystallinity, roughness, chemical functionality). Thus, preparation procedures must frequently be refined through trial and error to achieve the desired performance. On the other hand, the function of the electrode can often be fine-tuned by changing pretreatment variables, enhancing the versatility of a modification scheme.

Specific functional groups may also be necessary for some modification strategies. In these cases, pretreatment methodologies can include steps designed to create a high population of active sites on the substrate surface. Likewise, requirements of adlayer characterization methods may require specific substrate properties. For example, atomically smooth surfaces are preferable for high-resolution scanning tunneling microscopic (STM) characterizations of adlayer structures. Thus, the intended application of the modified electrode, requirements of surface characterization techniques, and the modification chemistry often direct the choice of substrates and pretreatment procedures.

8.3 MODIFIED ELECTRODE TYPES

Modified electrodes can be classified by the film–substrate attachment method (e.g., physisorption, chemisorption, and covalent attachment) and film composition (e.g., clays,

zeolites, sol-gels, polymer, and DNA). Choice of modification methods and film identity stems from the demand of the end-application. Multiple combinations of attachment methodologies and film compositions may be realized. The anchoring mechanisms, structural characteristics, and electrochemical uses of some example systems are discussed within this section.

8.3.1 Langmuir-Blodgett

The Langmuir-Blodgett (L-B) assembly technique (8, 14, 15) offers a versatile way to prepare a modified electrode. L-B layers are created by transferring organized monomolecular films from a liquid phase in a Langmuir trough onto a solid support. Attractive non-covalent interactions hold the film in a cohesive unit on the electrode surface. However, the weak nature of these forces limits adlayer stability.

L-B films are useful in biological studies, as they can easily be prepared to act as mimics of lipid membranes. Thus, modified electrodes of this type are often used in studies of transport phenomena (16) and enzyme activity. These electrodes are also often used as molecular recognition sensors (17–20) and in molecular electronics (20–22).

8.3.1.1 Structural description and preparation

Langmuir-Blodgett films are formed by the deposition of a Langmuir film onto a solid substrate. Langmuir films are composed of an organized monolayer of amphiphilic molecules at a liquid/gas interface. These molecules, by virtue of possessing a hydrophobic tail and a hydrophilic head, are spontaneously oriented at a liquid/gas interface. For example, a sparingly water-soluble amphiphile spread onto an aqueous phase results in partial solubilization of the head group, while the hydrophobic tail group extends partially into the gaseous phase to minimize the free energy of the system. The resulting film is depicted in Figure 8.2. Some amphiphiles commonly used in the construction of Langmuir films are given in Table 8.1. Films with mixed composition can be prepared by spreading mixtures of amphiphiles onto a common solvent (20, 23). Homogeneous or phase segregated films result from the chemical properties of the molecules spread at the interface.

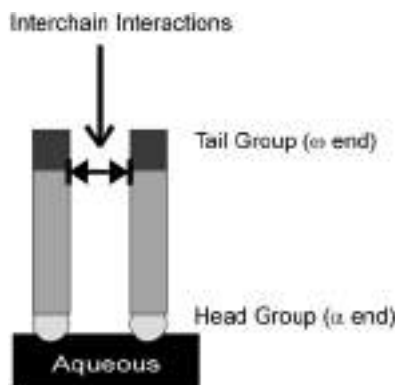


Figure 8.2 Diagram of a Langmuir film (only two molecules are shown for clarity).

Table 8.1Functionalized aliphatic amphiphiles used to form Langmuir-Blodgett films^a

Molecule	Formula	Attributes
Acids	$C_nH_{2n+1}COOH$	Easy to vary n
Alcohols	$C_nH_{2n+1}OH$	Difficult to form L-B layers
Esters	$C_nH_{2n+1}COOR$	Form monolayers and multilayers
Amides	$C_nH_{2n+1}CONH_2$	Form alternating multilayers
Amines	$C_nH_{2n+1}NH_2$	Alternate with acids
Nitriles	$C_nH_{2n+1}CN$	

^aOther examples include aromatics, heterocycles, highly conjugated molecules (dyes), porphyrins, phthalocyanines, fullerenes, polymers and biological compounds (phospholipids, pigments, peptides, and proteins).

Source: Adapted from reference (8) with the permission of Cambridge University Press.

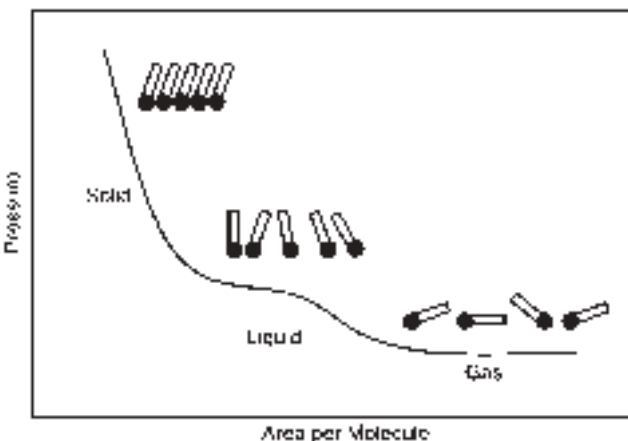


Figure 8.3 Two-dimensional phase diagram of a Langmuir film. Reproduced from: K. Kolasinski, *Surface Science: Foundations of Catalysis and Nanoscience*, John Wiley & Sons, Ltd.: Chichester, 2002. Copyright 2002 by John Wiley & Sons, Limited. Reproduced with permission.

After a desired composition (single- or multi-component) is achieved, lateral pressure is applied to increase the two-dimensional film concentration. In practice, pressure is applied using a moveable barrier in a Langmuir trough. As the film is compressed, the system goes through a series of phase transitions, as shown in Figure 8.3. At the end of the compression cycle, a highly ordered two-dimensional film is formed.

After creation of the compressed film, it can be transferred to an electrode surface. The characteristics of the substrate can tremendously affect the quality of the resulting Langmuir-Blodgett film (20), and dictate how the initial layer is transferred. Figure 8.4 depicts a common film transfer method, where a hydrophilic substrate is vertically lifted through a Langmuir film. The attractive forces between the surface and the head groups result in transfer of the layer, such that the film physisorbs on the electrode surface. These

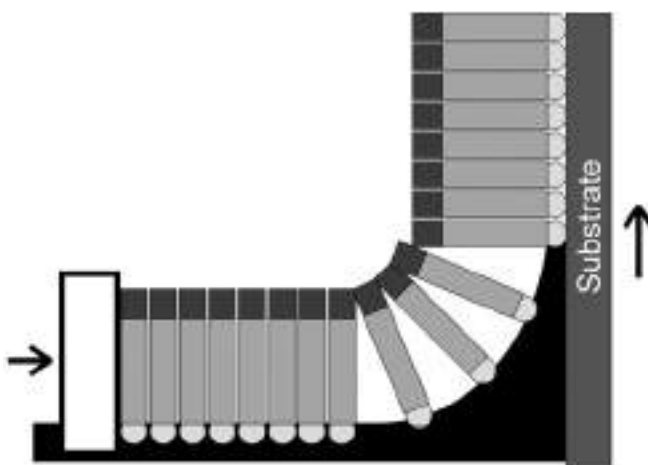


Figure 8.4 Receding deposition of an L-B film. Adapted from reference (8) with the permission of Cambridge University Press.

forces are often sufficient to exclude solvent molecules from the interface between the solid support and the film. Upon careful transfer, the electrode-supported adlayer retains the packing density and orientation of the precursor Langmuir film.

Extending deposition transverses the substrate downwards from the gas phase through the Langmuir film into the liquid layer, orienting the head groups away from the surface. Conversely, the example shown in Figure 8.4 is termed receding deposition; as the substrate is withdrawn from the liquid, hydrophilic head groups are deposited directly onto the substrate surface. Multiple layers can be deposited by repeated cycles in which the substrate is raised and/or lowered through the Langmuir film.

Complex layer architectures can be developed using different deposition cycles. Figure 8.5 shows some examples of layers that can be created, where X, Y, Z, and A-B-A types are represented. X-type films are created by repeated extending deposition, resulting in head-to-tail orientation of molecules in adjacent layers. Z-type layers are formed from successive receding deposition cycles. Alternating extending and receding deposition results in a Y-type film, orienting the monomolecular layers in a head-to-head and tail-to-tail configuration. Mixed multilayers (termed A-B-A layers) are deposited using more than one amphiphile, and a multiple tank trough, with a variety of possible structural features.

8.3.1.2 Overall characteristics

The power of the L-B technique is the vast array of possible layer types and orientations. However, the forces that hold the film in a coherent unit on the substrate surface consist of van der Waals interactions. These forces are much smaller than those resulting in chemical bond formation. Thus, L-B layers may not be stable for long periods of time or in harsh environments. Moreover, specialized equipment is required to create them, and special care must be taken to ensure reproducible and well-ordered films. This approach is particularly demanding with respect to high-purity reagents and liquids, and surface preparation procedures.

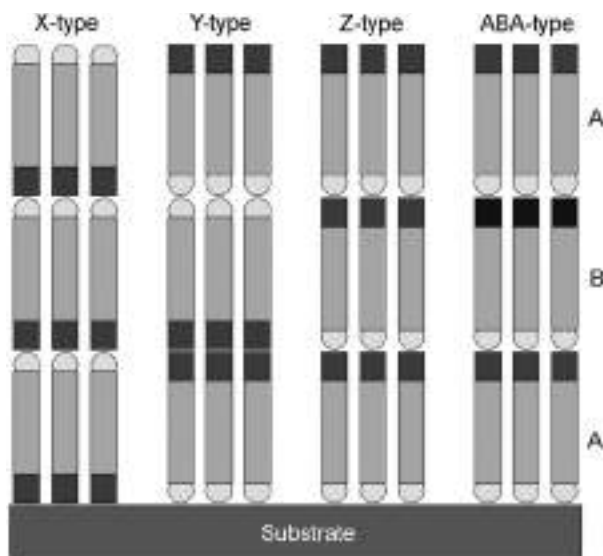


Figure 8.5 Langmuir-Blodgett film types. Adapted from reference (8) with the permission of Cambridge University Press.

8.3.1.3 Applications

L-B films often resemble lipid membranes. Thus, electrodes modified with these layers are particularly relevant as mimics in studies of biological functions, including transport phenomena (16), enzyme activity (20), and molecular recognition (17–20, 22). Finally, the ability to control the thickness of an L-B layer on the nanometer scale is well-suited for studies of molecular electronics and nanotechnology (20–22).

8.3.2 Self-assembly

Modification of a substrate surface by spontaneous adsorption (24), now more commonly referred to as self-assembly, is one of the most utilized modification pathways. These films are typically bound to the substrate by chemisorption; however, intermolecular forces within the film are also important. Chemisorption is the strong adsorption of a molecule onto a surface through the spontaneous formation of a chemical bond (1). This chemical bond forms between a functional group in the molecule and a site on the electrode. Monomolecular layers prepared by chemisorption are known as self-assembled monolayers (SAMs). These adlayers can be used to impart the desired function to the electrode directly, or can serve as a foundation for more complex electrode architectures.

8.3.2.1 Structural description and preparation

A schematic illustration of a SAM is shown in Figure 8.6. Chemisorption occurs through the head group, or α -end. A spacer chain separates the head group from the tail group,

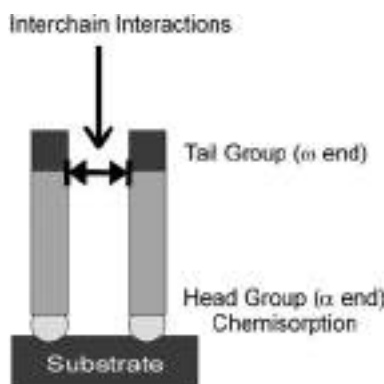


Figure 8.6 Schematic of a self-assembled monolayer. Adapted from reference (6) with permission.

or ω -end. The head group is responsible for the largest energetic contribution to self-assembly, while the tail group strongly influences interfacial properties. The microscopic structure of the film is dependent on the forces acting between the spacer chain and tail groups, and include dispersive (or van der Waals), electrostatic, and steric interactions. Densely packed layers are formed when the spacer chains and tail groups maximize attractive forces and have comparable van der Waals radii. Less dense and more disordered adlayers may also form as a consequence of repulsive interactions, mismatches in packing radii, and/or registry with the substrate, but are still suitable for a wide range of studies.

SAMs are created by exposure of an adsorbate precursor (liquid or vapor) to a suitable substrate. Usually, the substrate is immersed in a dilute solution (10^{-4} – 10^{-3} M) for a pre-determined time (seconds to days) after which the electrode is removed, rinsed copiously with neat solvent, and dried before use. Mixed monolayers can be formed by the simultaneous deposition of multiple precursors from the same solution. However, caution must be exercised since the solution concentration ratio usually does not reflect the resulting surface composition.

Many sulfur-containing functional groups chemisorb onto metal electrodes (11, 25–30). For example, thiols and disulfides spontaneously adsorb on gold. Thiols also chemisorb at silver, copper, platinum, and mercury; however, gold is by far the commonly used substrate electrode due to its relative inert nature. Several examples of SAMs that have been reported in the literature are listed in Table 8.2. A detailed discussion of an example (alkanethiolates on gold) is given below.

8.3.2.2 Formation and structure of alkanethiolates on gold

Alkanethiolates on gold ($\text{Au-S-(CH}_2\text{)}_n\text{-X}$) serves as an ideal system for demonstrating the important concepts and techniques used in the fabrication, characterization, and application of SAM-based modified electrodes. There are many excellent examples of their application in practical and fundamental areas related to electroanalytical and surface chemistry

Table 8.2

Examples of modifying layers formed by chemisorption

Molecule	Electrode material
RSH	Au (29), Ag (31), Pt (4), Cu (30), Hg (32)
RSSR'	Au (26)
RSR'	Au (33)
R ₃ P	Zr (34, 35)
RNC	Au (36–40), Pt (41), Cu (36)
RCOOH	Ag (6), Al ₂ O ₃ (6)
R(OArCH(NH ₂) ₂) ₂	Au (42)
Silanes	Hydroxylated surfaces (6, 43)

Note: A more extensive table could be found in reference (25).

(6, 43, 44). However, the adsorption mechanism and the resulting structural details of these adlayers are complicated (45, 46).

The assembly mechanism of alkanethiols onto gold from the liquid phase (45–55) and the vapor phase (56) has been investigated using scanning tunneling microscopy (STM) and other techniques. A generalized mechanism is illustrated in Figure 8.7. The adsorption process is characterized by two distinct stages. The first stage results from the affinity of the thiol head group for the Au surface, driving the formation of a disordered layer with sub-monolayer coverage, as depicted in Figure 8.7A–C. During this stage, the surface becomes saturated with molecules having an average orientation parallel to the surface; the layer does not reach its full thickness. The second stage, shown in Figure 8.7D–E, proceeds over a longer time scale, and is driven by interactions (van der Waals forces) between the spacer chain and tail groups. These lateral interactions orient the molecules more perpendicular to the surface, allowing the coverage and thickness to increase to packing density limits. This combination of head-group binding and intermolecular forces leads to an equilibrium structure characterized by high packing density (formation of a full monolayer), molecular ordering (all-trans zigzag conformation of sequences with the alkane chains), and stability.

Although SAMs are capable of forming dense adlayers, many subtle variables, especially during the early stages of formation (57, 58), can result in the variation of the microscopic film structure. These differences can significantly alter the behavior of the electrode.

SAMs are stable within an extended potential window: –0.8 to +0.8 V vs. Ag/AgCl (59). However, the pH of the solution can alter these limits. Nevertheless, the positive limit is defined by oxidation of the adlayer. Furthermore, electrochemical experiments have revealed that upon cathodic potential sweeps, a surface wave is observed that corresponds to the one-electron reduction of a complete monolayer of thiolates (60). The film packing density can be determined from integration of the peak current obtained upon reductive desorption. Moreover, insights into the structural features and formation mechanism is available from reductive desorption data (59). This desorption process limits the cathodic potential possible for SAM modified electrodes.

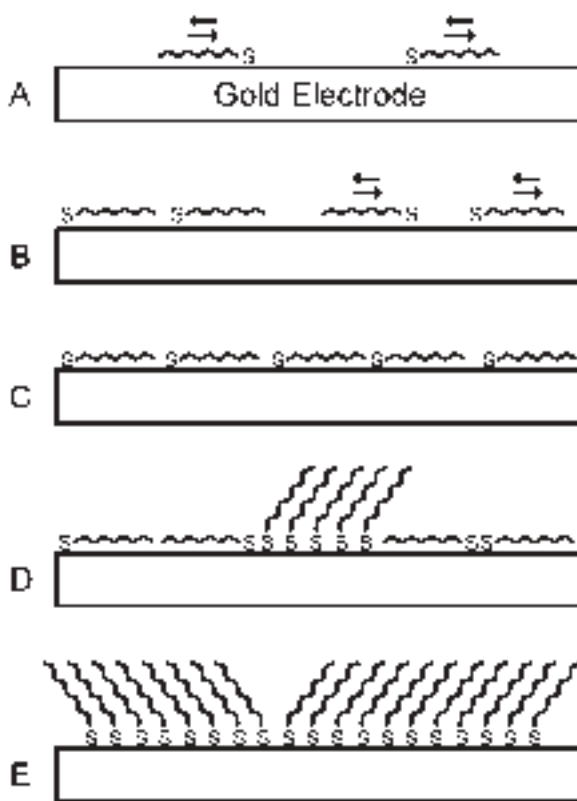


Figure 8.7 Illustration of the self-assembly mechanism of alkanethiols onto gold. Adapted from reference (56) with permission. Copyright 1996 AAAS.

Extensive surface characterizations have been applied to alkanethiolates on gold. For instance, X-ray photoelectron spectroscopy (XPS) has been used to identify the electronic state of the adsorbed sulfur atom as a thiolate (26) with a partial charge of -0.2 (61). STM has also been used extensively to interrogate the resulting adlayer structure. The binding site of the sulfur head-group has been speculated to occur at threefold hollow sites at Au(111), forming a $(\sqrt{3} \times \sqrt{3})R30^\circ$ adlayer, as shown in Figure 8.8 (62, 63). There are also numerous studies indicating more complicated lattice structures, showing that perhaps, many different structures are possible (43).

8.3.2.3 Overall characteristics

The main limitation of self-assembly is the requirement of a specific functional group that will drive assembly onto the substrate of interest. Moreover, the rational design and formation of tailored mixed systems are complicated by an interwoven multi-step assembly mechanism. Fortunately, these limitations could be overcome on most occasions, and self-assembly allows facile control of interfacial properties at the molecular level (64).

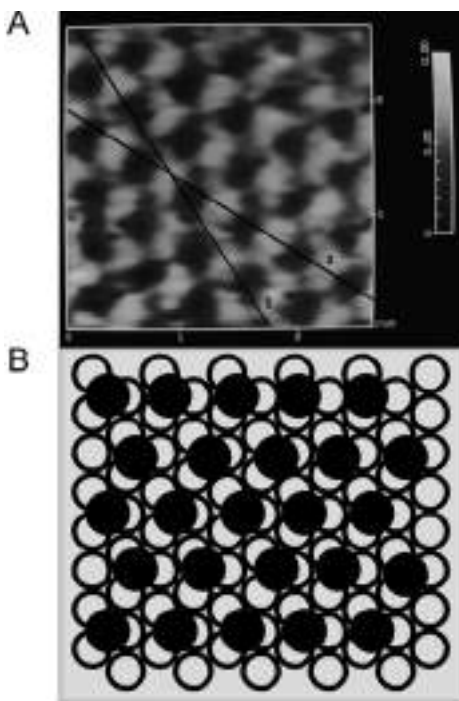


Figure 8.8 (A) STM image of ethanethiolate on Au(111). (B) Representation of the $(\sqrt{3} \times \sqrt{3})R30^\circ$ overlayer structure of a thiolate monolayer. Open circles represent Au atoms while filled circles represent S atoms (not to scale). Adapted from reference (63) with permission. Copyright 1991 American Chemical Society.

Although SAM precursors are amphiphilic molecules, as in L-B films, SAMs are more stable due to the specific nature of chemisorption. Thus, the preparation of SAMs is much more facile and the resulting adlayers are more stable. Functionalities can also be introduced into the adlayer that allows for further modification of the interface. Therefore, SAMs are attractive as coatings in many applications.

8.3.2.4 Applications

SAMs are widely used in electrochemistry to block access of solution-based molecules (11). A well-defined thickness between the substrate surface and redox couple is provided by SAMs with electroactive tail groups (11, 65–72). The spacer chain is used to hold the redox center away from the surface of the electrode, enabling studies of long-range heterogeneous electron transfer.

The use of SAMs as a facile way to attach other functionalities to the electrode surface has been exploited in the development of chemical sensors (44, 45). Functionalities presented at the electrode easily modulate the selectivity of the electrode surface for an analyte of interest. Cyclodextrins, calixarenes, and other molecules with size and shape specificity

can be tethered to the surface of the SAMs lending chemical specificity to the electrode surface (73, 74). SAM modified electrodes are also utilized in biomimetics (45), studies of interfacial phenomenon (25), nanotechnology (25), and molecular electronics (45).

8.3.3 Covalent attachment

By taking advantage of traditional synthetic chemistry, surface-based functional groups can be modified through the formation of new chemical bonds (4, 5, 75). These covalent attachment schemes are used to modify the surface of an electrode. The reactions used for derivatization are determined by the identity of the chemical components on the electrode surface. Therefore, the choice of the modifier must account for the reactivity of the target surface site.

Covalent anchoring can result in stable, reusable modified electrodes. However, adlayer stability is not guaranteed (especially for organosilane linkages) and increased robustness may be offset by the complicated preparation required for many covalent modification schemes. Moreover, highly organized layers are often difficult to achieve, and reproducibility of the fine structure of the layer can be limited.

8.3.3.1 Overall description and electrode pretreatment

A variety of functional groups exist on the surface of many common electrode materials. Enrichment of these groups is normally required to realize acceptable reactive site population (4, 5). Additional activation steps can be employed to increase the efficiency of coupling (i.e., by converting the functional group to a more reactive form). The enrichment and activation steps can be accomplished in a single step, or may require multiple steps. Figure 8.9 illustrates common covalent electrode modification schemes.

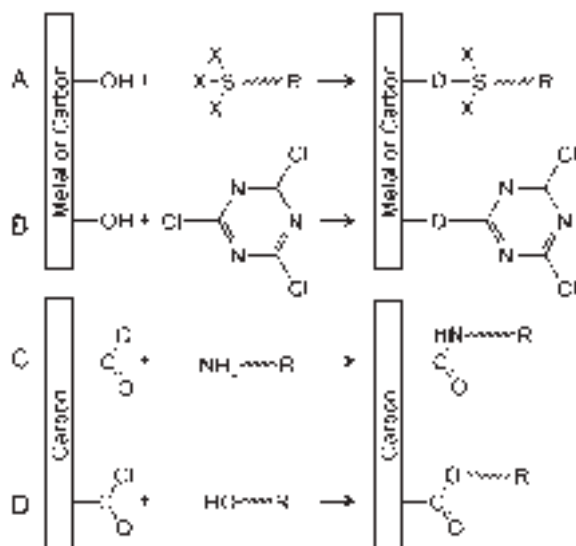


Figure 8.9 Covalent modification schemes (4, 5, 76).

8.3.3.2 Covalent modification of carbon electrodes

Considering the scope of organic chemistry, carbon electrodes are an obvious choice as a substrate for covalent anchoring schemes (5). The bulk of carbon electrode materials are extended networks of fused aromatic rings (see Chapter 5). The terminal surface region of the network is often rich in reactive sites. Oxygen-containing functional groups (i.e., carboxylic acids and alcohols) and sp^2 hybridized carbon atoms have been exploited in covalent modification strategies (5).

There are two categories of covalent modification schemes for carbon electrodes: (1) chemical and (2) electrochemically assisted. Common functional groups on carbon electrodes include carboxylic acids, alcohols, and ketones. Most chemical methods employ carboxylic acid or hydroxyl groups, while electrochemically assisted modification can occur by direct reactions with aromatic surface carbon atoms.

(a) Chemical reactions at carbon

Organosilane chemistry can be used to anchor modifying layers to any hydroxyl-containing moiety, as shown in Figure 8.9A. Thus, organosilanes are commonly used to modify carbon electrodes. In practice, dense hydroxyl group populations are formed by reduction of acids. The silane can be used directly as the adlayer or serve as a linker molecule.

Although silane chemistry provides a very versatile method for modification of carbon electrode surfaces, it is difficult to obtain ordered layers with well-defined thickness (see Figure 8.10). Moreover, these layers show poor reproducibility and stability, and thus far have mainly been used in fundamental studies (43).

Hydroxyl groups can also be reacted with cyanuric chloride (76–79), as shown in Figure 8.9B. Each cyanuric chloride moiety has three reactive sites, which can be used for

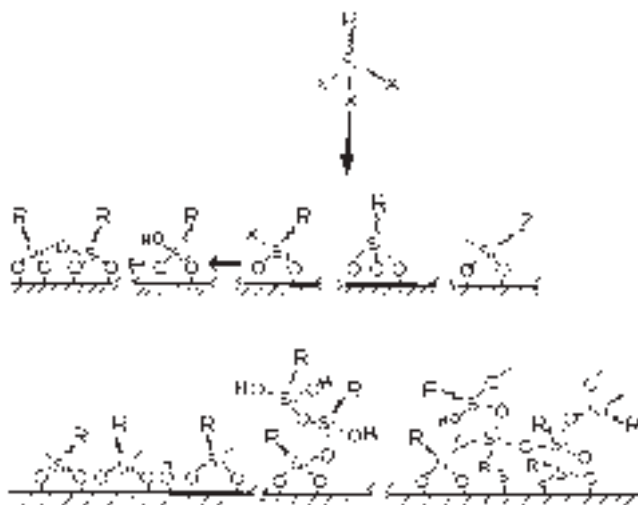


Figure 8.10 Organosilane reactions with metal oxide surfaces. Reproduced from reference (5) with permission. Copyright 1984 Marcel Dekker, Inc.

immobilization. This leaves one or two reactive sites for the formation of an adlayer of amines, alcohols, Grignard reagents, or hydrazines (5).

On the other hand, carboxylic acid groups, due to their rich synthetic chemistry and natural occurrence on carbon electrode surfaces, are often used in covalent anchoring of adlayers onto carbon electrodes. The surface density of carboxylic acid groups can be increased by heating the electrode in air or by oxygen plasma treatment (77). To increase the efficiency of the reaction between surface sites and amines or alcohols, the carboxylic acids are often converted to acid chlorides (e.g., using thionyl chloride). After activation, these surfaces can be further reacted with amines and alcohols to allow attachment of other functional groups or electrode-modifying layers (Figure 8.9C–D). Often, these reactions are used to tether electroactive groups to the surface, and the resulting systems are used in electron transfer studies (5).

(b) *Electrochemically assisted reactions at carbon*

A powerful strategy to covalently derivatize carbon electrodes with monolayers and multilayers utilizes electrochemical reactions (75). Electron transfer is used to activate a heterogeneous chemical reaction. The adlayer is formed after generating the highly reactive species by oxidation or reduction of the solution-based molecule or a surface-based functional group. In most electrochemically assisted modification schemes, the reaction involves a carbon radical.

Electrochemically assisted modification of carbon electrodes has been accomplished by oxidation of amines (80, 81) and arylacetates (82), reduction of aryl diazonium salts (83), and anodization (oxidation) in a solution with alcohols (75). Of these schemes, reduction of diazonium salts, shown in Figure 8.11, provides a particularly convenient pathway for carbon electrode modification.

The electrochemical reduction of aryl diazonium salts is generally carried out in acetonitrile or acid solutions (75). This method allows diverse functionality (84, 85), and the possibility of monolayers or multilayers (86, 87). Although a high adlayer coverage can be obtained (88), the blocking efficiency depends on the details of the modification procedures (89). The convenience and diversity offered by diazonium reduction have led to the application of this modification procedure in areas ranging from studies of electron transfer kinetics (90), molecular electronics (91), sensor design (92), and even in the chemical modification of carbon stationary phases in liquid chromatography (93).

8.3.3.3 *Covalent modification of metal electrodes*

Many different metals can be electrochemically oxidized, providing a high density of hydroxyl groups (4, 5). Organosilane and cyanuric chloride chemistry can be utilized to

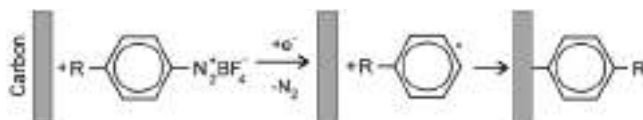


Figure 8.11 Reaction scheme for covalent attachment by phenyldiazonium reduction. Adapted from reference (75) with permission.

modify oxidized metal surfaces as shown in Figure 8.9A–B, analogous to carbon electrodes (10, 43).

8.3.4 Clay modified electrodes

Clays possess many properties that make their use as electrode modifiers intriguing. These features include abundance, low cost, diversity, high chemical stability, negligible toxicity, and pliability (94–98). The diversity stems from differences in chemical composition, charge, size, and major associated ions (95). Clays can also withstand highly oxidizing environments and temperatures (98). Therefore, they are often used as electrode modifiers when the experiments demand harsh conditions where the integrity of other adlayers would be compromised. Perhaps most importantly, the structural composition of clays imparts functions that are particularly amenable to electrochemistry. An overview of the chemical and physical characteristics is necessary to understand their utility in electrochemistry.

8.3.4.1 Structural description

Clays are abundant throughout the world; approximately 4250 distinct clay minerals have been identified (98), of both natural and synthetic origin. Clays are phyllosilicate minerals, so-called because of their sheet-like (1:20 thickness:length) structure (99). The sheets (phyllo) consist of aluminosilicate networks composed of silicon oxide tetrahedra (SiO_4) or aluminum oxide octahedra (AlO_6). These sheets form layers (platelets) when oxygen atoms are shared between two or more adjacent sheets, and can combine in various ways to form many different types of clays.

Clays are categorized by a tetrahedral:octahedral numbering system. A 1:1 layer is composed of one tetrahedral sheet linked to one octahedral sheet. 2:1 layers are also common, where one octahedra is sandwiched between two tetrahedral sheets (99). Some of the common clay materials are presented in Table 8.3.

Clay platelets may be dispersed or stacked in pseudo-crystalline arrangements. Regular groupings of layers in face-to-face, edge-to-face, or edge-to-edge configurations (and combinations of these) result (96) in crystals having grain sizes in the colloidal range (<2 μm) (99). Cohesive van der Waals and electrostatic forces hold the grains together when present in a modifying layer on the substrate. The surface of a platelet contains oxygen or hydroxide groups, imparting a hydrophilic nature to the region between two platelets. Therefore, this region can swell and accommodate water molecules (98).

The number of different clays is greatly extended by replacement of the Al^{3+} or Si^{4+} cations in the crystalline lattice (i.e., Mg^{2+} , Fe^{2+} , or Li^+ for Al^{3+}) (98). Usually, the replacement cations are less positively charged, resulting in an inherent excess negative charge on each platelet. Exchangeable cations, on the other hand, such as Na^+ and Ca^{2+} , reside in the aqueous interlayer region, neutralizing the excess negative charge and electrostatically binding the platelets. Thus, the cation-exchange capacity (CEC) of clays is generally large. The natural occurrence of anion-exchange clays is far more infrequent than cation-exchange clays. However, anion-exchanged clays have been prepared synthetically. An outline of the different types of clay is presented in Table 8.3.

Table 8.3

Clay materials commonly used to modify electrodes

	Tet:Oct	Name
Cation-exchange	1:1	Kaolinite
		Halloysite
	2:1	Prototype montmorillonite
		Montmorillonite
		Nontronite
		Illite
		Hectorite
		Laponite
		Saponite
		Vermiculite
Anion exchange	2:1	Chlorite
	0:1	Brucite
		Hydrotalcite
		Layered double hydroxide

Source: Adapted from reference (95) with permission.

8.3.4.2 Pretreatment

Before immobilization on the substrate, the clay must be treated to ensure uniform and predictable properties. Naturally occurring clays contain particulate and chemical impurities. Moreover, the native ionic species in the interlayer region may vary, requiring different procedures to realize effective and reproducible ion-exchange properties. Pretreatment steps also influence the conductivity and porosity of the clay.

The heterogeneity inherent in natural clays can be overcome by simple treatments. The following procedure is described by Bard and Mallouk (96), while similar treatments involving freeze drying have been presented (94, 100). First, large particles are removed by decanting an aqueous suspension of the clay. The decanted suspension is stirred in a concentrated (1 M) solution of NaCl for 48 h to ensure Na^+ is the major interlayer ion. This solution is centrifuged and washed, then dialyzed to remove excess electrolyte. Finally, a last centrifugation step is used to ensure the solution contains particles under 0.2 μm in diameter. Other impurities can be removed by procedures that are more specialized. Iron oxide, for example, can be removed from the interlayer region by dithionite and citrate treatments (96) without disturbing the iron content of the crystalline lattice.

Pillared clays are prepared by intercalation of bulky cations (e.g., $[\text{Al}_{13}\text{O}_4(\text{OH})_{28}]^{3+}$) to provide a fixed spacing between platelets (96). A well-defined interlayer spacing (between 10 and 20 Å) is adjustable by changing the cation identity. Pillared clays are utilized to provide a regular cavity size, allowing the incorporation of molecular guests of specific size.

8.3.4.3 Immobilization

The plastic nature of clays makes their immobilization onto a solid substrate electrode straightforward: spin-coating, drop-casting, and screen-printing techniques have all been successfully implemented (97, 98). Covalent attachment using silane linkages has also

been reported (95). Other, less common methods include Langmuir-Blodgett film transfer and electrophoretic deposition, and have resulted in hybrid films (films containing other amphiphilic molecules), and extremely smooth films, respectively (97). Drop-casting and spin-coating are the most commonly reported techniques for immobilizing clays on electrodes (96). However, clay materials are also often utilized in composite carbon paste electrodes (97). It is important to note that the electrolyte identity and concentration, and the solvent in which the clay is dissolved prior to deposition affect the structure of the film (94–96), and therefore the function of the resulting electrode.

8.3.4.4 Applications

Clay modified electrodes are used in fundamental studies of electron transfer, and in the construction of sensor devices. The ionic aqueous environment in the interlayer region is highly amenable to electrochemical processes. Furthermore, this environment is controllable and fairly innocuous, allowing many different species to retain their activity. Molecular recognition, chemical catalysis, electrocatalysis, and preconcentration of analyte molecules are all applications of this class of modified electrodes. A condensed list of clay modified electrodes is given in Table 8.4. Reference (96), Table 6.1 on pages 280–281 contains a more comprehensive list.

The ion-exchange properties of clay materials lead to several practical applications. The analytical signal results from heterogeneous electron transfer between electroactive ions and the substrate. This signal arises from the permeation of electroactive molecules through the clay layer to the underlying electrode. Thus, electroactive ions (e.g., dissolved metals) can be preconcentrated through ion-exchange, and quantified with high sensitivity and selectivity using stripping voltammetry (98). Analytes that do not appreciably permeate the clay film can be determined by a mediation reaction.

Neutral molecules can also be incorporated into clay materials by taking advantage of their sorption properties. The mild environment of the interlayer region provides an ideal matrix for biologically active molecules. Thus, biosensors can be constructed by incorporation of enzymes into the film (98). The enzyme can then act as a mediator for the target biomolecule.

Table 8.4

Electrochemical uses of clay modified electrodes

Electrode materials	Analyte	Benefits
Glucose oxidase in nontronite on GC	Glucose	Stable, reusable, reduced interference
Nafion-coated nontronite on GC	Methyl viologen	Reduced interference
Nafion-coated nontronite on GC	Uric acid, dopamine	Reduced interference
Mercury-plated nontronite on GC	Cu ²⁺ , Zn ²⁺	Enhanced selectivity
Cellulose acetate membrane with montmorillonite or nontronite	[Cu(NH ₃) ₄] ²⁺	Trace analysis of Cu ²⁺
Screen-printed nontronite	Codeine, amitole, purine bases	FIA and voltammetry
Nontronite stabilized catalyst	Dopamine	LOD 0.54 nM

Source: Information adapted from reference (98).

Finally, the properties of the solution should be considered. Competition between electrolyte cations and analyte molecules for ion-exchange sites within the film make high concentrations of electrolyte undesirable. Moreover, small variations in the electrolyte concentration can have a large effect on the interlayer spacing of the clay material. pH also affects the stability and electrochemical response of the film. Furthermore, some solvents may degrade the film. For example, polar organic molecules are known to intercalate, dramatically changing the interlayer spacing in some clays (96).

8.3.5 Zeolite modified electrodes

A class of aluminosilicates called zeolites offer a number of chemical, physical, and structural characteristics that merit use as electrode modifiers (7, 101–106). The chemical composition of zeolites is similar to that of clays; however, zeolites are three-dimensional aluminosilicate crystals rather than two-dimensional sheet structures. This distinction imparts unique chemical and physical properties that can be exploited for preconcentration, size and shape selectivity, and catalysis. However, molecules that can be incorporated into zeolites are more limited due to spatial constraints of the zeolite cavity.

8.3.5.1 Structural description

A zeolite is an inorganic molecule consisting of a base matrix of aluminosilicates arranged in a three-dimensional crystal (107–112). They have high ion-exchange capacities due to charge excesses inherent in their structure. The distinguishing feature of zeolites is the three-dimensional framework, which results in channels and cages of molecular dimensions. These apertures act as molecular sieves, allowing the passage of small, appropriately shaped molecules. Once within a zeolite, chemical reactions are often facilitated through geometric confinement. That is, the molecule or molecules are forced into a configuration that increases their reaction probability. These combined properties (ion-exchange, size and shape selectivity, and catalytic activity) are particularly useful in electrochemistry.

The basis of the three-dimensional structure of zeolites is the framework of tetrahedral silicon and aluminum oxide rings shown in Figure 8.12. Bridging oxygen atoms are shared between the silicon and aluminum atoms in variable ratios, giving rise to diversity in the types of ring structures that can be formed. These rings come together in the third dimension because of the extended tetrahedral bonding scheme. Therefore, different ring structures result in different cage dimensions and geometries. Figure 8.13 depicts structures of four zeolite types, exemplifying the porous, cage-like openings with dimensions on the molecular scale. Approximately 40 different naturally occurring zeolites have been discovered (96).

The structure of the $\text{AlO}_2/\text{SiO}_2$ network induces a fixed negative charge at each Al atom (see Figure 8.12). Associated cations maintain electroneutrality, with common species being Na^+ , K^+ , Ca^{2+} , Mg^{2+} , H^+ , NH_4^+ , and some organic cations (96); these cations are exchangeable. The strong acid nature, arising from terminal hydroxyl groups at the crystal faces (104), is key to the catalytic activity of zeolite–acid catalyzed reactions.

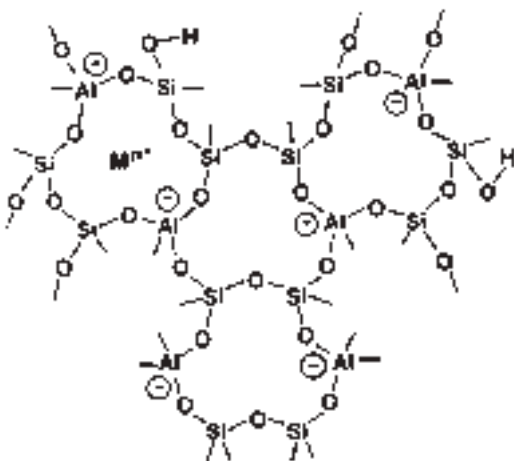


Figure 8.12 Chemical structure of an aluminosilicate zeolite, illustrating the Al-O-Si network, the terminal hydroxyl groups, and the fixed anionic sites (with charge compensating cations). Reproduced from reference (104) with permission.

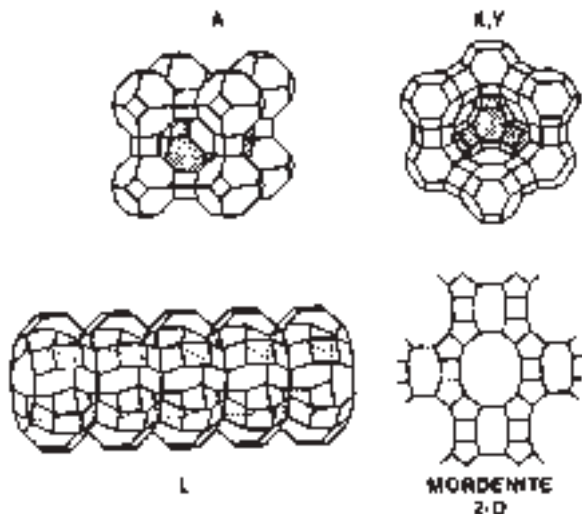


Figure 8.13 Three-dimensional representations of the framework structure of zeolite types A, XY, L, and a two-dimensional framework structure of mordenite. The vertices of lines in the above structures indicate the Si or Al atoms, with bridging oxygen slightly displaced from the lines. Reproduced from reference (102) with permission. Copyright 1990 American Chemical Society.

Expansive efforts to identify new zeolites have been driven by their importance in industrial applications (112). The most prominent industrial use is cracking of crude oil. These efforts have resulted in the preparation of numerous synthetic zeolites. There are five broadly defined classes of synthetic zeolites, as outlined in Table 8.5.

Table 8.5

Classes of zeolites (reference (96))

Abbreviation	Name	General structure
AlSiO ₄	Aluminosilicate	AlSiO ₄
AlPO ₄	Aluminophosphate	AlPO ₄
SiPO ₄	Silicoaluminophosphate	SiPO ₄
AlPO ₄	Metal-containing aluminophosphate	AlPO ₄
SiPO ₄	Metal-containing silicoaluminophosphate	SiPO ₄

^aDoped with Li, Be, Mg, or transition elements.

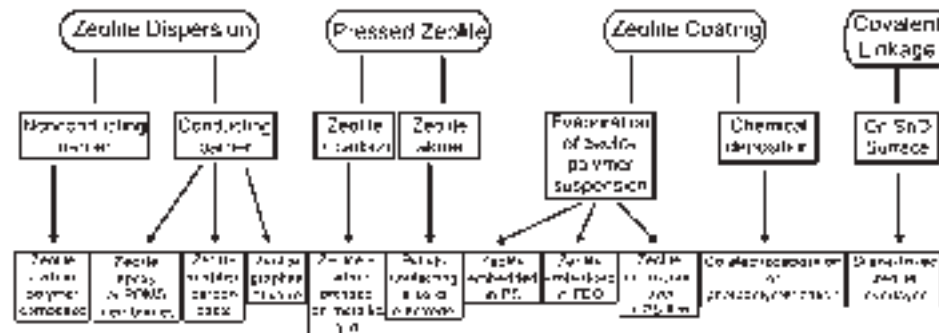


Figure 8.14 Strategies applied to prepare zeolite modified electrodes. (PDMS: polydimethylsiloxane; PS: polystyrene; PEO: polyethylene oxide). Reproduced from reference (106) with permission.

8.3.5.2 *Immobilization*

Many different procedures for modification of electrode surfaces by zeolites have been proposed (106). In practice, fabrication of zeolite modified electrodes is complicated by at least two factors: first, zeolites are electrically insulating, and second, immobilization of the film by physical or chemical bonding is difficult. Most successful zeolite modification schemes employ composites, where polymers or conductive powders are used as a matrix to support the zeolite. In any successful scheme, electroactive analyte molecules and counter-ions must be able to undergo rapid mass transport within the zeolite-based film.

Four different strategies for immobilizing zeolites on the surface of an electrode can be identified (106). The desired zeolite can be: (1) dispersed within a solid matrix; (2) compressed onto a conductive substrate; (3) embedded in a polymeric film; or (4) covalently anchored. Figure 8.14 outlines these broad approaches and the many different possible electrode structures. Further elaboration on these immobilization schemes can be found in Tables I and II of references (102) and (106), respectively. These references also contain specific examples of preparation procedures for zeolite modified electrodes.

Table 8.6

Applications of zeolite modified electrodes

(1) Molecular recognition
Molecular discrimination
Self-assembled multi-component systems
(2) Charge and mass transport characterization
Ion-exchange
Diffusion (analytes and counter-ions)
Electron transfer mechanisms
Intrazeolite effects
(3) Electroanalysis
Amperometry (preconcentration, indirect detection)
Potentiometry (membranes)
(4) Electrocatalysis
Mediation by exchanged species
Encapsulated species
Dispersion electrolysis
(5) Batteries
Reactant hosts
Dispersion electrolysis

Source: Reproduced from reference (104) with permission.

8.3.5.3 Applications

The unique three-dimensional aluminosilicate crystalline lattice of zeolites gives rise to three intriguing characteristics (104). These characteristics are: high cation-exchange capacity, sensitive molecular recognition (size and shape selectivity), and good catalytic activity. These properties give rise to the use of zeolite modified electrodes in sensor development, and electrocatalysis (106). These and other applications are outlined in Table 8.6. More detailed descriptions can be found in recent reviews (7, 96, 102–106), with extensive lists compiled by Rolison (Table II in (102)) and Walcarius (Tables 1 and 3 in (105) and Table 1 in (106)).

8.3.6 Sol-gel modified electrodes

Amorphous sol-gel materials have become increasingly appealing as electrode modifiers in the past 20 years (113). The initial interest in these materials was based on applications of their optical characteristics (silica, zirconia, and other transparent oxides) (113). As electrochemists sought convenient methods for combining different metal oxides in a crystalline product, their interest in sol-gel materials was sparked.

Sol-gel materials possess attractive properties which can be exploited as electrode modifiers in electrochemical detection schemes (114, 115). These properties include: high adsorption capacity, acid/base functionality, and thermal stability. Moreover, the inclusion of functional groups, enzymes, and proteins in sol-gels is easily achieved, expanding the possible applications.

8.3.6.1 Structural description

The term sol-gel is used to describe a broad class of solid structures created through gelation of a colloidal suspension (i.e., sol) (113). Upon dehydration, a xerogel, or “dry gel” state forms. Subsequent heat treatment can be used to remove unreacted organic residues, increase stability and density, or introduce crystallinity (113).

The chemical composition of sol-gels is typically a basic inorganic oxide. A common example of a sol-gel is silica gel, which has particular utility as stationary phase supports in chromatographic columns. The sol-gel materials used for electrode modification are typically created from two different classes of material: inert and redox active. Many different types of sol-gels are derived from these classes, as outlined in Table 8.7 (113).

The first class, inert inorganic sol-gels, are not redox active (e.g., silica, alumina, and zirconia) (113). In the gel form these materials have a large surface area, high ion-exchange capacity (due to surface hydroxyls), and exhibit good adhesion to metal oxide and ceramic supports.

The second class of sol-gels contains redox-active metal oxides, such as tungsten oxide, vanadium pentoxide, manganese oxide, and other transition metal oxides. Moreover, many n-type semiconductors such as zinc oxide, barium titanate, and titanium dioxide can be used in this class (113). The structures of these gels are sensitive to the pH and oxidation state of the precursors. Many redox-active sol-gels exhibit electrochromism (different oxidation states exhibit different colors, allowing spectroscopic determination of redox states). These gels can also accommodate the reductive insertion of lithium and other moieties.

Introduction of guest species into class one and two sol-gels can be accomplished through a variety of techniques (113), including chemical reactions and impregnation schemes. These procedures yield many different types of sol-gels that can be classified

Table 8.7

Classification of sol-gel materials and attributes relevant to electrode modification

Sol-gel classes	Attributes
(1) Inert, inorganic materials (2) Redox-active metal oxides	Electroinactive (silica, alumina, and zirconia) Electroactive (vanadium pentoxide, manganese oxide, tungsten oxide, etc.)
Modified sol-gel types	Definition
Organic–inorganic hybrids (i) Covalently bound (ii) Doped (iii) Impregnated (iv) Intercalated	Inclusion of organic functionalities Creation of sol-gel-C bond during/after formation of gel Molecules incorporated in the sol starting solution (large-scale catalysts or electrode modifiers) Adsorption or precipitation of organic compounds onto prepared gels Materials are placed into a swelled gel that are encapsulated upon dehydration
Macroscopic and microscopic inclusion	Encapsulated unicellular microorganisms, whole cells, and powders

Source: Information adapted from reference (113).

(113) as outlined in Table 8.7. The different methods for modification of class one and two sol-gels are outlined below.

Sol-gel networks can be further modified by covalently linking molecules to the matrix. These linkages can be added before or after sol-gel formation. To introduce the modifier before formation, it is important that the bond between the precursor and modifier be resistant to attack by the reactive groups of the precursor involved in gel formation. Carbon–silicon bonds are typically used for this purpose. Alternatively, the gel can be derivatized after formation, through a wider range of steps (e.g., using silanes) with direct covalent attachment to the sol-gel matrix by inorganic or organic reactions. Moreover, by combination of these two approaches, a functionalized precursor can be designed for secondary reactions with other types of molecules.

Compounds can be introduced into the gel network by entrapment (113). Doping involves the addition of a molecular guest to the sol-gel precursor solution. Alternatively, the gel may be modified by impregnation after formation by precipitation–adsorption or intercalation into the oxide network by swelling agents. When modifying the gel with small molecules, care must be exercised because doping, impregnation, and intercalation procedures often result in electrodes with guests that are prone to loss through leaching. Therefore, these techniques are more useful for immobilization of large catalysts or organic modifiers (113).

In addition to molecular guests, macroscopic species can be used to form composite materials, using the sol-gel as a matrix. To this end, conductive powders and other species have been incorporated in sol-gels (113). These large-scale objects are usually captured in the network during gel formation. Electrodes with unique qualities can be fabricated using these procedures. For example, a gel doped with conductive carbon particles results in a carbon paste-like electrode, having the electrochemical activity of carbon in conjunction with the robust mechanical characteristic of the sol-gel material. Furthermore, metal particles or conductive polymers can be used to increase the redox activity of the resulting electrode. Polymers can be incorporated by initiating a polymerization reaction within a preformed sol-gel matrix, introduction of a preformed polymer during gelation, or concurrent polymerization and polycondensation.

8.3.6.2 *Immobilization*

In constructing a sol-gel modified electrode, thin films may be necessary due to the insulating properties of the gel (115). Thus, they are often fabricated by growing a thin film on the substrate. For such cases, sol-gels with high adhesion characteristics are ideal (most sol-gels adhere to metal, metal oxide, and semiconducting electrode materials). When necessary, more robust linkages can be formed by covalent bonding through silane chemistry. Incorporation of charge mediators, chromophores, organometallic catalysts, preconcentration agents, ionophores, and active proteins into the sol-gel matrix provide the basis for the function of the electrode.

To overcome the limitations of conductivity, bulk-modified sol-gels can be used (113). These electrodes incorporate conductive materials into the gel. The resulting structures are able to serve as a carbon-paste-like electrode (see Chapter 5). The sol-gel backbone is solid-like, providing a mechanically robust and convenient electrode embodiment.

This property is combined with the attributes of the conductive elements incorporated in the gel, allowing many novel functions to be realized.

8.3.6.3 Applications

The properties of sol-gels that are useful in electroanalysis include abrasion and corrosion resistance, ionic conductivity, optical transparency, and electrochromism. These, along with the ease with which sol-gels can be constructed with variable chemical composition have led to their use in electrocatalysis (116), sensing, and as robust reference electrodes (113). Other applications are summarized in references (113, 115). Table 1 in (115) includes an in-depth list of useful sol-gel modified electrodes.

8.3.7 Polymer modified electrodes

The extended nature of a polymer network provides many opportunities for enhancing electroanalytical measurements and enabling studies of long-range interfacial phenomena. The relative thickness of a polymeric film allows a high number of active sites on the electrode surface, increasing utility in sensor design (117–120) and fundamental studies (4). For example, polymer modified electrodes can be used to study extended charge transport phenomena or electron transfer mediation reactions (121–123).

These modifiers are classified by the type of polymer (5). To this end, four classes are identified: redox, ion-exchange, conductive, and nonconductive, as shown in Figure 8.15. The first three classes of polymers are able to participate in electron transfer events; the distinction between them lies in the mode of electron-transport that dominates their observed behavior, as shown in Figure 8.16 (4). Nonconducting polymers are used to create selective physical barriers or for surface passivation (118).

A variety of methods exist for immobilization of polymeric films on substrate surfaces. These can be divided into two broad classes: coating a preformed polymer or polymerization-deposition. A dissolved polymer can be adsorbed onto a substrate by drop-casting, dip-coating, or spin-coating (124). Alternatively, a polymerization reaction can be initiated with the electrode immersed in the monomer solution to create a polymer-coated substrate.

Anchoring of polymer films is accomplished through the same forces that immobilize other films. They are easily physisorbed, due to high molecular weight and hydrophobicity. Therefore, as long as these interactions are not altered, for example, by a strong solvent for the polymer, the film remains stable. A synopsis of the characteristics, construction, and uses of each of the four classes of polymer modified electrodes follows.

8.3.7.1 Redox polymers

Redox polymers and co-polymers contain redox-active molecules covalently incorporated into the polymer. Each redox site is capable of exchanging electrons with other sites within the polymer or guests, as shown in Figure 8.17A. Only those sites in close proximity to the solution–polymer interface typically participate in electron transfer with solution-based redox couples. However, electron transfer with the substrate only occurs at immobilized sites in close proximity to the polymer–substrate interface. Thus, an analytical signal is

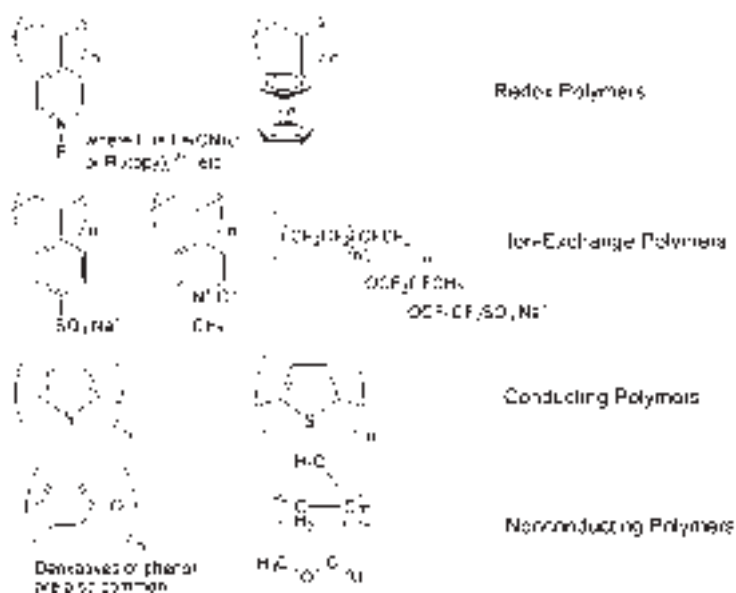


Figure 8.15 Examples of common polymers used to modify electrodes.

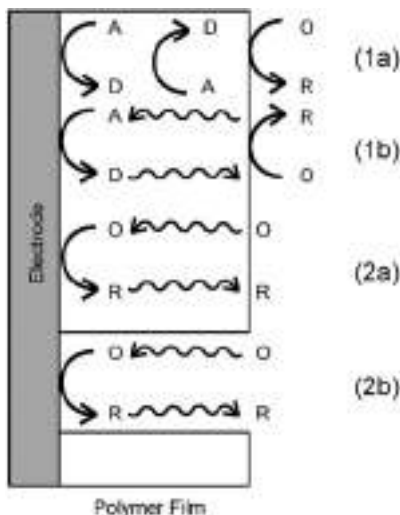


Figure 8.16 Illustration of four electron-transfer modes in polymer modified electrodes. Polymers containing redox molecules (where $A + e = D$) can mediate electrons to a solution-based analyte (where $O + e = R$) through an electron hopping mechanism (1a), or by diffusion of free redox molecules within the film (1b). Permeable polymer layers, on the other hand, provide a suitable chemical environment for diffusion of O through the layer (2a) or contain channel/pinholes where electron-transfer occurs (2b). This material is adapted with permission from: A. J. Bard, *Integrated Chemical Systems: A Chemical Approach to Nanotechnology*; John Wiley & Sons, Inc.: New York, 1994. Copyright 1994 John Wiley & Sons, Inc.

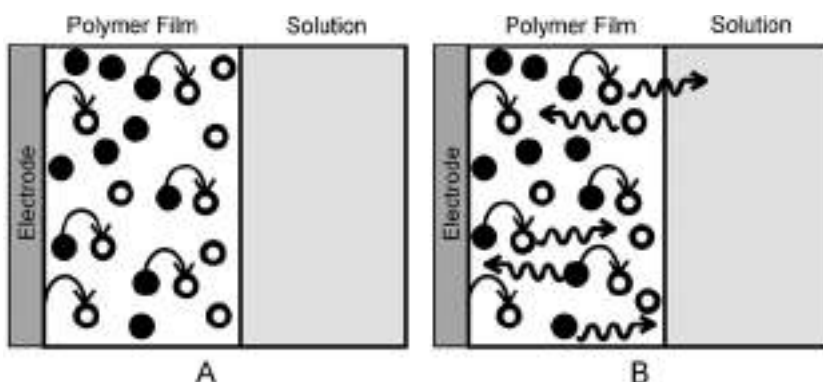


Figure 8.17 Schematic representation of the processes that take place in a redox-containing polymer film consisting of (A) a redox polymer and (B) an ion-exchange polymer filled with free redox molecules. Filled circles depict the reduced form of the couple and open circles the oxidized form. Smooth arrows show electron-transfer events between the two forms, and wavy arrows indicate diffusional processes. This material is adapted from reference (4) with permission. Copyright 1992 John Wiley & Sons, Inc.

derived from electrons that are effectively shuttled by electron hopping through the polymer film. The extended nature of this electron hopping network has contributed greatly to our understanding of neural networks and other biological systems (122).

The synthesis of redox polymers is generally performed before deposition (124). First, a polymer is synthesized by condensation or addition polymerization with at least one monomer that is redox-active. The polymer is immobilized on the substrate by dip-coating, drop-casting, or spin-coating. These procedures must be carefully applied if homogeneous and pinhole free films are needed.

Redox polymers can also be covalently coupled to a substrate surface (5). A preformed polymeric film is covalently bound to the substrate by reaction of active sites on the surface and functional groups within the polymer. The main advantage of this second synthetic route is the stability provided by tethering the polymer.

Electron transfer events within this class of modified electrodes involve the transformation of a molecule between stable oxidation states; therefore, transport of counter-ions within the film must be realized to maintain electroneutrality. Electron hopping between the redox centers is often rate-limited by ion transport. Although control of the spacing of redox centers within the polymer may provide experimental advantages, ion transport limitations must be overcome. As a result, only when closely spaced, fast-reacting redox sites reside in the film, will significant extended electron hopping be observed.

The main drawback of redox polymer electrodes, both in fundamental studies and in chemical analysis, stems from the difficulty in controlling the concentration and spatial organization of redox sites within the film (4). The main use of redox polymer modified electrodes has been in fundamental studies of electron transfer mechanisms. These electrodes are also used as electrochemical sensor devices, but on a much more limited scale (117). Many of these limitations are overcome by the use of ion-exchange polymers, as outlined below.

8.3.7.2 *Ion-exchange polymers*

A powerful and elegant way to overcome the limitations encountered in redox polymers makes use of ion-exchange polymers (5). This class of modified electrode can be constructed using any polymer with ion-exchange properties by exchanging the native counter-ion for an appropriately charged electroactive ion. This ion will serve as the electron transfer site within and on the surface of the film. The result is a layer with the ability to transport electrons as illustrated in Figure 8.17B.

In contrast to redox polymers, the electroactive molecules can diffuse between the ion-exchange sites on the polymer, resulting in a number of advantages. The polymer backbone need not flex for effective electron transfer like a redox polymer film, and therefore, occurs at a much faster rate. The concentration of redox sites in the film can be easily controlled through the ion-exchange process. Furthermore, the requirements of the redox molecule are greatly relaxed (any redox-active ion can be used). However, the active ion is prone to leaching from the ion-exchange polymer. This complication usually can be overcome by dosing the contacting solution with a small amount of the associated ion.

The preparation of ion-exchange redox polymer modified electrodes usually involves two steps. A preformed ion-exchange polymer (e.g., Nafion®) is immobilized on the electrode surface through drop-casting, spin-coating, or dip-coating. The desired redox ion (carrying the appropriate charge) is ion-exchanged into the polymer. Thus, variation of the polymer identity allows cationic or anionic redox molecules to be used.

The ease of preparation and the variety of electron active ions make ion-exchange polymers amenable to fundamental studies of electron transfer mechanisms. The systematic variation of the concentration (effective density) of redox sites within a coating has been useful in the construction of electron hopping models (4). These models are based on the apparent rate of electron diffusion through the film. Because the redox centers are able to diffuse within the polymer, the apparent rate is related to two parameters: redox molecule diffusion and the rate of electron self-exchange.

Ion-exchange polymers on electrode surfaces can also be used to perform practical tasks, such as preconcentration of ionic analyte molecules, and electron transfer mediation.

8.3.7.3 *Electrically conductive polymers*

The third class of polymer modified electrodes includes those derived from electrically conductive polymers. These materials have special structural properties (such as highly conjugated π -bonds) that facilitate the conduction of electrons through delocalized electronic bands (125). The electron transfer mechanism, therefore, occurs by movement of electrons through overlapping and unoccupied electronic energy states. Conductive polymers have several positive attributes, especially related to their synthesis and application.

The intrinsic conductivity of many conductive polymers is typically in the semiconducting range (10^{-14} – $10^2 \Omega^{-1} \text{ cm}^{-1}$). The polymer is often doped to increase conductivity into the range associated with metallic materials (1 – $10^5 \Omega^{-1} \text{ cm}^{-1}$) (126). Doping is accomplished by injection of positive or negative charge using chemical reagents or

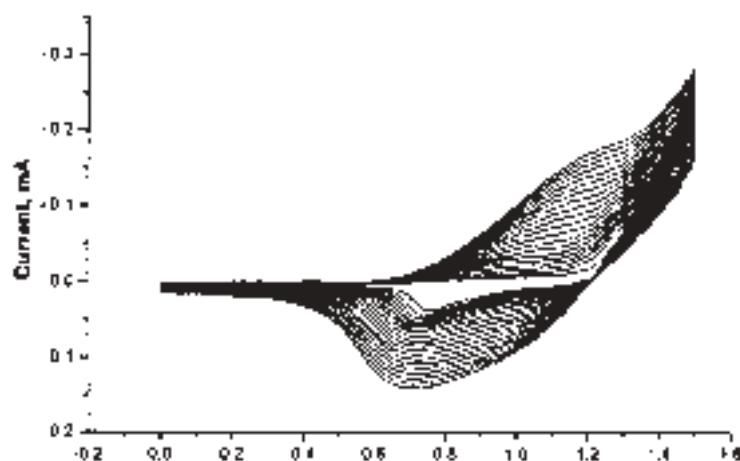


Figure 8.18 Cyclic voltammogram of 0.010 M fluorene in 0.20 M tetrabutylammonium tetrafluoroborate in acetonitrile at a Pt working electrode, scan rate 100 mV s⁻¹. Reproduced from reference (127) by permission of The Electrochemical Society, Inc.

electrochemical reactions (126), creating charge-carriers in the form of excess electrons or holes. Small ions are also incorporated during doping to maintain electroneutrality.

Although conductive polymers can be made by a variety of methods, electropolymerization is by far the most convenient method in constructing a polymer modified electrode. The polymerization proceeds by an electrochemical reaction at the electrode surface, resulting in immobilization of a polymer film. For example, Figure 8.18 shows current-potential curves for electropolymerization of fluorene. The peaks in each curve show the deposition of an additional layer of polyfluorene (127). The peak currents during electropolymerization of different types of polymer can increase or decrease with each subsequent scan depending on the electron transfer characteristics of the polymer and the deposition rate (127, 128).

The advantages offered by electropolymerization stem from the versatility and convenience provided by direct reaction of the monomer at the electrode surface. Moreover, after formation on the electrode surface, charge injection (doping) is easily controlled and optimized using potential programs and/or changing the electrolyte identity (126). Other advantages include facile, reproducible control over film thickness and the ability to use diverse electrode geometries and form thick films (up to ~1 μm) (126). The solution conditions required for the synthesis are unusually mild, allowing entrapment of biological molecules while retaining their activity (126).

The most common use for conductive polymer modified electrodes has been in the construction of sensor electrodes. These can be very selective and sensitive, and made to enhance the analysis of many different molecular entities. Thus, many different inorganic, organic, and biological species have been targeted (117).

8.3.7.4 Nonconductive polymers

Nonconducting polymers are not involved in electron transfer reactions, and therefore are partially or totally passivating. However, these polymers are useful in constructing permselective films. These films are deposited on substrate surface by the same methods as other polymers: dip-coating, spin-coating, drop-casting, or electropolymerization. The most elegant and useful approach to construct a highly selective modified electrode using a nonconducting polymer film is molecular imprinting.

The distinguishing feature of molecularly imprinted polymer films stems from the addition of a recognition molecule to the polymerization solution (129–131). During the reaction of monomer, the recognition molecule becomes trapped within the newly formed polymer. After polymerization, the recognition molecule is removed, resulting in structural voids having a structure that is complementary to the recognition molecule (129). Although imprinted polymer modified electrodes can be made using a nonconductive polymer template, the imprinting process is a generic one; any type of polymer can, in principle, be used.

The synthetic protocols needed to produce imprinted polymers are not trivial. However, successful construction of an imprinted polymer modified electrode is extremely rewarding: obtaining sites having affinities comparable to antibodies may be possible (129). Unlike current biorecognition elements, the selectivity of the imprinted layer remains high in a variety of environments. This stability results from the robust nature of the polymeric material. Recently, combinatorial approaches are being utilized for optimization of synthetic protocols in order to overcome synthetic challenges of creating these films (129, 131).

8.3.8 DNA modified electrodes

Deoxyribonucleic acid (DNA) is increasingly used for molecular recognition purposes (132–134). Electrodes modified with DNA, therefore, are useful in the construction of electroanalytical sensors. Analytes, including carcinogens, drugs, and mutagenic pollutants with high binding affinities for DNA, will be important in testing water, food, soil, and plant samples. Electroactive molecules may be detected directly upon binding to DNA bound at the electrode surface. Indirect detection of electroinactive molecules may be accomplished by monitoring changes in the signal attributed to the bound DNA (134). Sensors can also be used to detect gene sequences (134) such as mutations associated with human diseases. Further information on DNA modified electrodes, including fabrication (i.e., immobilization of DNA using many of the techniques discussed above) and application can be found in references (134–142).

8.4 CONCLUSIONS AND PROSPECTS

The properties of chemically modified electrodes that have driven their development include: increased selectivity and sensitivity, chemical and electrochemical stability, larger usable potential windows, and resistance to fouling. Chemically modified electrodes will

remain important tools in applied and fundamental science. This area has blossomed upon development of a molecular-level understanding of the synthesis and characterization of interfacial architectures. This will continue as new and improved surface characterization techniques are developed. However, challenges remain in the successful construction of modified electrodes; especially needed are advances in our understanding of the subtleties of adlayer formation processes and the related fundamental electron transfer mechanisms.

REFERENCES

1. R. A. Durst, A. J. Bäumner, R. W. Murray, R. P. Buck, C. P. Andrieux, *Pure Appl. Chem.* **69**, 1317–1323 (1997).
2. W. Kutner, J. Wang, M. L'Her, R. P. Buck, *Pure Appl. Chem.* **70**, 1301–1318 (1998).
3. C. R. Martin, C. A. Foss, Jr., “Chemically Modified Electrodes”, in *Laboratory Techniques in Electroanalytical Chemistry*, 2nd ed., P. T. Kissinger, W. R. Heineman, Eds., Marcel Dekker, Inc.: New York, 1996.
4. R. W. Murray, “Molecular Design of Electrodes Surfaces”, in *Techniques of Chemistry*, J. William H. Saunders, A. Weissberger, Eds., John Wiley and Sons, Inc.: New York, 1992, Vol. 22.
5. R. W. Murray, “Chemically Modified Electrodes”, in *Electroanalytical Chemistry*, A. J. Bard, Ed., Marcel Dekker, Inc.: New York, 1984, Vol. 13, pp. 191–368.
6. A. Ulman, *An Introduction to Ultrathin Organic Films From Langmuir-Blodgett to Self-Assembly*, Academic Press: San Diego, 1991.
7. A. Walcarius, “Implication of Zeolite Chemistry in Electrochemical Science and Applications of Zeolite-Modified Electrodes”, in *Handbook of Zeolite Science and Technology*, S. M. Auerbach, K. A. Carrado, P. K. Dutta, Eds., Marcel Dekker, Inc.: New York, 2003, pp. 721–783.
8. M. C. Petty, *Langmuir-Blodgett Films: An Introduction*, Press Syndicate of the University of Cambridge: New York, 1996.
9. D. H. Karweik, C. W. Miller, M. D. Porter, T. Kuwana, “Prospects in the Analysis of Chemically Modified Electrodes”, *Surface Analysis*, 1982, 89–119, American Chemical Society Conference Proceedings.
10. J. A. Cox, M. E. Tess, T. E. Cummings, *Rev. Anal. Chem.* **15**, 173–223 (1996).
11. H. O. Finklea, “Electrochemistry of Organized Monolayers of Thiols and Related Molecules on Electrodes”, in *Electroanalytical Chemistry: A Series of Advances*, A. J. Bard, I. Rubinstein, Eds., Marcel Dekker, Inc.: New York, 1996, Vol. 19, pp. 109–335.
12. R. L. McCreery, K. K. Cline, “Carbon Electrodes”, in *Laboratory Techniques in Electroanalytical Chemistry*, 2nd ed., P. T. Kissinger, W. R. Heineman, Eds., Marcel Dekker, Inc.: New York, 1996.
13. R. L. McCreery, “Carbon Electrodes: Structural Effects on Electron Transfer Kinetics”, in *Electroanalytical Chemistry*, A. J. Bard, Ed., Marcel Dekker, Inc.: New York, 1984, Vol. 17, pp. 191–368.
14. K. B. Blodgett, *J. Am. Chem. Soc.* **56**, 495 (1934).
15. K. B. Blodgett, *J. Am. Chem. Soc.* **57**, 1007–1022 (1935).
16. A. Mälkiä, P. Liljeroth, K. Kontturi, *Anal. Sci.* **17**, i345–i348 (2001).
17. J. Gong, X. Lin, *Electrochim. Acta* **49**, 4351–4357 (2004).
18. M. Ferreira, L. R. Dinelli, K. Wohnrath, A. A. Batista, O. N. Oliveira, Jr., *Thin Solid Films* **446**, 301–306 (2004).
19. T. Miyahara, K. Kurihara, *J. Am. Chem. Soc.* **126**, 5684–5685 (2004).
20. G. G. Roberts, *Adv. Phys.* **34**, 475–512 (1985).

21. L. M. Goldenberg, M. C. Petty, A. P. Monkman, *J. Electrochem. Soc.* **141**, 1573–1576 (1994).
22. L. M. Goldenburg, *J. Electroanal. Chem.* **379**, 3–19 (1994).
23. M. K. Ram, N. S. Sundaresan, B. D. Malhotra, *J. Phys. Chem.* **97**, 11580–11582 (1993).
24. A. T. Hubbard, *Chem. Rev.* **88**, 633–656 (1988).
25. J. C. Love, L. A. Estroff, J. K. Kriebel, R. G. Nuzzo, G. M. Whitesides, *Chem. Rev.* **105**, 1103–1169 (2005).
26. C. D. Bain, H. A. Biebuyck, G. M. Whitesides, *Langmuir* **5**, 723–727 (1989).
27. R. G. Nuzzo, D. L. Allara, *J. Am. Chem. Soc.* **105**, 4481–4483 (1983).
28. R. G. Nuzzo, F. A. Fusco, D. L. Allara, *J. Am. Chem. Soc.* **109**, 2358–2368 (1987).
29. M. D. Porter, T. B. Bright, D. L. Allara, C. E. D. Chidsey, *J. Am. Chem. Soc.* **109**, 3559–3568 (1987).
30. P. E. Laibinis, G. M. Whitesides, D. L. Allara, Y.-T. Tao, A. N. Parikh, R. G. Nuzzo, *J. Am. Chem. Soc.* **113**, 7152–7167 (1991).
31. M. M. Walczak, C. Chung, S. M. Stole, C. A. Widrig, M. D. Porter, *J. Am. Chem. Soc.* **113**, 2370–2378 (1991).
32. A. Demoz, D. J. Harrison, *Langmuir* **9**, 1046–1050 (1993).
33. E. B. Troughton, C. D. Bain, G. M. Whitesides, R. G. Nuzzo, D. L. Allara, M. D. Porter, *Langmuir* **4**, 365–385 (1988).
34. T. E. Mallouk, H. Lee, L. J. Kepley, H.-G. Hong, S. Akhter, *J. Phys. Chem.* **92**, 2597–2601 (1988).
35. T. E. Mallouk, H. Lee, L. J. Kepley, H.-G. Hong, *J. Am. Chem. Soc.* **110**, 618–620 (1988).
36. U. B. Steiner, W. R. Caseri, U. W. Suter, *Langmuir* **8**, 2771–2777 (1992).
37. A. C. Ontko, R. J. Angelici, *Langmuir* **14**, 1684–1691 (1998).
38. A. C. Ontko, R. J. Angelici, *Langmuir* **14**, 3071–3078 (1998).
39. M. J. Robertson, R. J. Angelici, *Langmuir* **10**, 1488–1492 (1994).
40. K.-C. Shih, R. J. Angelici, *Langmuir* **11**, 2539–2546 (1995).
41. J. J. Hickman, C. Zou, D. Ofer, P. D. Harvey, M. S. Wrighton, P. E. Laibinis, C. D. Bain, G. M. Whitesides, *J. Am. Chem. Soc.* **111**, 7271–7272 (1989).
42. F. Auer, B. Sellergren, A. Swietlow, A. Offenhauser, *Langmuir* **16**, 5936–5944 (2000).
43. A. Ulman, *Chem. Rev.* **96**, 1533–1554 (1996).
44. S. Flink, F. C. J. M. van Veggel, D. N. Reinhoudt, *Sensors Update* **8**, 3–19 (2001).
45. F. Schreiber, *J. Phys.: Condens. Matter* **16**, R881–R900 (2004).
46. N. Sandhyarani, T. Pradeep, *Int. Rev. Phys. Chem.* **22**, 221–262 (2003).
47. N. Camillone, III, *Langmuir* **20**, 1199–1206 (2004).
48. G. Hahner, C. Wöll, M. Buck, M. Grunze, *Langmuir* **9**, 1955–1958 (1993).
49. D. Qu, M. Morin, *J. Electroanal. Chem.* **524–525**, 77–80 (2002).
50. C.-J. Zhong, N. T. Woods, G. B. Dawson, M. D. Porter, *Electrochim. Commun.* **1**, 17–21 (1999).
51. R. Subramanian, V. Lakshminarayanan, *Electrochim. Acta* **45**, 4501–4509 (2000).
52. M. Cohen-Atiya, D. Mandler, *J. Electroanal. Chem.* **550–551**, 267–276 (2003).
53. W. Pan, C. J. Durning, N. J. Turro, *Langmuir* **12**, 4469–4473 (1996).
54. D. S. Karpovich, G. J. Blanchard, *Langmuir* **10**, 3315–3322 (1994).
55. C. D. Bain, G. M. Whitesides, *J. Am. Chem. Soc.* **111**, 7164–7175 (1989).
56. G. E. Poirier, E. D. Pylant, *Science* **272**, 1145–1148 (1996).
57. M. Byloos, H. Al-Maznai, M. Morin, *J. Phys. Chem. B* **105**, 5900–5905 (2001).
58. J. H. Teuscher, L. J. Yeager, H. Yoo, J. E. Chadwick, R. L. Garrell, *Faraday Discuss.* **107**, 399–416 (1997).
59. C. A. Widrig, C. Chung, M. D. Porter, *J. Electroanal. Chem.* **310**, 335–359 (1991).

60. M. M. Walczak, D. D. Popenoe, R. S. Deinhammer, B. D. Lamp, C. Chung, M. D. Porter, *Langmuir* **7**, 2687–2693 (1991).
61. C.-J. Zhong, R. C. Brush, J. Andregg, M. D. Porter, *Langmuir* **15**, 518–525 (1999).
62. C. E. D. Chidsey, D. N. Loiacono, *Langmuir* **6**, 682–691 (1990).
63. C. A. Widrig, C. A. Alves, M. D. Porter, *J. Am. Chem. Soc.* **113**, 2805–2810 (1991).
64. C.-J. Zhong, M. D. Porter, *Anal. Chem.* **67**, 709A–715A (1995).
65. C. Miller, P. Cuendet, M. Grätzel, *J. Phys. Chem.* **95**, 877–886 (1991).
66. C. Miller, M. Grätzel, *J. Phys. Chem.* **95**, 5225–5233 (1991).
67. S. Terrettaz, A. M. Becka, M. J. Traub, J. C. Fettinger, C. J. Miller, *J. Phys. Chem.* **99**, 11216–11224 (1995).
68. A. M. Becka, C. J. Miller, *J. Phys. Chem.* **96**, 2657–2668 (1992).
69. A. M. Becka, C. J. Miller, *J. Phys. Chem.* **97**, 6233–6239 (1993).
70. J. F. Smalley, S. W. Feldberg, C. E. D. Chidsey, M. R. Linford, M. D. Newton, Y.-P. Liu, *J. Phys. Chem.* **99**, 13141–13149 (1995).
71. J. J. Sumner, K. S. Weber, L. A. Hockett, S. E. Creager, *J. Phys. Chem. B* **104**, 7449–7454 (2000).
72. K. Weber, L. Hockett, S. Creager, *J. Phys. Chem. B* **101**, 8286–8291 (1997).
73. F. Davis, C. J. M. Stirling, *Langmuir* **12**, 5365–5374 (1996).
74. M. Weisser, G. Nelles, G. Wenz, S. Mittler-Neher, *Sens. Actuators, B* **38–39**, 58–67 (1997).
75. A. J. Downard, *Electroanalysis* **12**, 1085–1096 (2000).
76. A. M. Yacynych, T. Kuwana, *Anal. Chem.* **50**, 640–645 (1978).
77. J. F. Evans, T. Kuwana, *Anal. Chem.* **49**, 1632–1635 (1977).
78. J. F. Evans, T. Kuwana, M. T. Henne, G. P. Royer, *J. Electroanal. Chem.* **80**, 409–416 (1977).
79. A. W. C. Lin, P. Yeh, A. M. Yacynych, T. Kuwana, *J. Electroanal. Chem.* **84**, 411–419 (1977).
80. B. Barbier, J. Pinson, G. Desarmot, M. Sanchez, *J. Electrochem. Soc.* **137**, 1757–1764 (1990).
81. R. S. Deinhammer, M. Ho, J. W. Andregg, M. D. Porter, *Langmuir* **10**, 1306–1313 (1994).
82. C. P. Andrieux, F. Gonzalez, J.-M. Savéant, *J. Am. Chem. Soc.* **119**, 4292–4300 (1997).
83. M. Delamar, R. Hitmi, J. Pinson, J. M. Savéant, *J. Am. Chem. Soc.* **114**, 5883–5884 (1992).
84. J. K. Kariuki, M. T. McDermott, *Langmuir* **15**, 6534–6540 (1999).
85. P. Allongue, M. Delamar, B. Desbat, O. Fagebaume, R. Hitmi, J. Pinson, J.-M. Savéant, *J. Am. Chem. Soc.* **119**, 201–207 (1997).
86. J. K. Kariuki, M. T. McDermott, *Langmuir* **17**, 5947–5951 (2001).
87. F. Anariba, S. H. DuVall, R. L. McCreery, *Anal. Chem.* **75**, 3837–3844 (2003).
88. Y.-C. Liu, R. L. McCreery, *J. Am. Chem. Soc.* **117**, 11254–11259 (1995).
89. A. J. Downard, M. J. Prince, *Langmuir* **17**, 5581–5586 (2001).
90. H.-H. Yang, R. L. McCreery, *Anal. Chem.* **71**, 4081–4087 (1999).
91. F. Anariba, J. K. Steach, R. L. McCreery, *J. Phys. Chem. B* **109**, 11163–11172 (2005).
92. A. J. Downard, A. D. Roddick, A. M. Bond, *Anal. Chim. Acta* **317**, 303–310 (1995).
93. J. A. Harnisch, D. B. Gazda, J. W. Anderegg, M. D. Porter, *Anal. Chem.* **73**, 3954–3959 (2001).
94. A. Fitch, *Clays and Clay Minerals* **38**, 391–400 (1990).
95. S. M. Macha, A. Fitch, *Mikrochim. Acta* **128**, 1–18 (1998).
96. A. J. Bard, T. Mallouk, “Electrodes Modified with Clays, Zeolites, and Related Microporous Solids”, in *Molecular Design of Electrode Surfaces*, R. W. Murray, Ed., John Wiley & Sons, Inc.: New York, 1992, Vol. XXII, pp. 271–312.
97. Z. Navrátilová, P. Kula, *Electroanalysis* **15**, 837–846 (2003).
98. J.-M. Zen, A. S. Kumar, *Anal. Chem.* **76**, 205A–211A (2004).

99. B. Velde, Ed., *Clay and the Environment: Origin and Mineralogy of Clays*, Springer-Verlag: Berlin, 1995.
100. P. K. Ghosh, A. J. Bard, *J. Am. Chem. Soc.* **105**, 5691–5693 (1983).
101. M. D. Baker, C. Senaratne, *Anal. Chem.* **64**, 697–700 (1992).
102. D. R. Rolison, *Chem. Rev.* **90**, 867–878 (1990).
103. D. R. Rolison, C. A. Bessel, *Acc. Chem. Res.* **33**, 737–744 (2000).
104. D. R. Rolison, R. J. Nowak, T. A. Welsh, C. G. Murray, *Talanta* **38**, 27–35 (1991).
105. A. Walcarius, *Electroanalysis* **8**, 971–986 (1996).
106. A. Walcarius, *Anal. Chim. Acta* **384**, 1–16 (1999).
107. J. Dwyer, A. Dyer, *Chem. Ind. (7)*, 237–240 (1984).
108. J. Dwyer, *Chem. Ind. (7)*, 258–269 (1984).
109. A. Dyer, *Chem. Ind. (7)*, 241–245 (1984).
110. L. V. C. Rees, *Chem. Ind. (7)*, 252–257 (1984).
111. R. P. Townsend, *Chem. Ind. (7)*, 246–251 (1984).
112. J. M. Newsam, *Science* **231**, 1093–1099 (1986).
113. O. Lev, Z. Wu, S. Bharathi, V. Glezer, A. Modestov, J. Gun, L. Rabinovich, S. Sampath, *Chem. Mater.* **9**, 2354–2375 (1997).
114. M. M. Collinson, A. R. Howells, *Anal. Chem.* **72**, 702A–709A (2000).
115. A. Walcarius, *Electroanalysis* **10**, 1217–1235 (1998).
116. Q. Wang, G. Lu, B. Yang, *Langmuir* **20**, 1342–1347 (2004).
117. B. Adhikari, S. Majumdar, *Prog. Polym. Sci.* **29**, 699–766 (2004).
118. M. Yuqing, C. Jianrong, W. Xiaohua, *Trends Biotechnol.* **22**, 227–231 (2004).
119. J.-K. Park, P. H. Tran, J. K. T. Chao, R. Ghodadra, R. Rangarajan, N. V. Thakor, *Biosens. Bioelectron.* **13**, 1187–1195 (1998).
120. A. Ciszewski, G. Milczarek, *Talanta* **61**, 11–26 (2003).
121. M. Kavanoz, H. Gülcen, A. Yıldız, *Turk. J. Chem.* **28**, 287–297 (2004).
122. C. E. D. Chidsey, R. W. Murray, *Science* **231**, 25–31 (1986).
123. L. R. Faulkner, *Chem. Eng. News* **62**, 28–45 (1984).
124. A. J. Bard, L. R. Faulkner, *Electrochemical Methods: Fundamentals and Applications*, 2nd ed., John Wiley & Sons, Inc.: New York, 2001.
125. H. S. Nalwa, *Handbook of Organic Conductive Molecules and Polymers*, John Wiley & Sons, Inc.: New York, 1997.
126. J.-C. Vidal, E. García-Ruiz, J.-R. Castillo, *Microchim. Acta* **143**, 93–111 (2003).
127. H. S. Sharma, S.-M. Park, *J. Electrochem. Soc.* **151**, E61–E68 (2004).
128. S. Sadki, P. Schottland, N. Brodie, G. Sabouraud, *Chem. Soc. Rev.* **29**, 283–293 (2000).
129. S. A. Piletsky, A. P. F. Turner, *Electroanalysis* **14**, 317–323 (2002).
130. M. C. Blanco-López, S. Gutiérrez-Fernández, M. J. Lobo-Castañón, A. J. Miranda-Ordieres, P. Tuñón-Blanco, *Anal. Bioanal. Chem.* **378**, 1922–1928 (2004).
131. K. Haupt, K. Mosbach, *Chem. Rev.* **100**, 2495–2504 (2000).
132. N. D. Popovich, H. H. Thorp, *Electrochem. Soc. Interface* **11**, 30–34 (2002).
133. M. E. Napier, C. R. Loomis, M. F. Sistare, J. Kim, A. E. Eckhardt, H. H. Thorp, *Bioconjugate Chem.* **8**, 906–913 (1997).
134. M. Mascini, I. Palchetti, G. Marrazza, *Fresenius J. Anal. Chem.* **369**, 15–22 (2001).
135. T. G. Drummond, M. G. Hill, J. K. Barton, *Nat. Biotechnol.* **21**, 1192–1199 (2003).
136. M. Fojta, *Electroanalysis* **14**, 1449–1463 (2002).
137. J. J. Gooding, *Electroanalysis* **14**, 1149–1156 (2002).
138. E. Katz, I. Willner, J. Wang, *Electroanalysis* **16**, 19–44 (2004).
139. F. Lucarelli, G. Marrazza, A. P. F. Turner, M. Mascini, *Biosens. Bioelectron.* **19**, 515–530 (2004).

140. E. Palacek, M. Fojta, M. Tomschik, J. Wang, *Biosens. Bioelectron.* **13**, 621–628 (1998).
141. H. H. Thorp, *Trends Biotechnol.* **21**, 522–524 (2003).
142. J. Wang, G. Rivas, X. Cai, E. Palecek, P. Nielsen, H. Shiraishi, N. Dontha, D. Luo, C. Parrado, M. Chicharro, P. A. M. Farias, F. S. Valera, D. H. Grant, M. Ozsoz, M. N. Flair, *Anal. Chim. Acta* **347**, 1–8 (1997).

This page intentionally left blank

Semiconductor Electrodes

Santosh K. Haram

Department of Chemistry, University of Pune, Ganeshkhind,
Pune 411007, India

9.1 INTRODUCTION

Electrochemistry with semiconductor electrodes represents an interesting and highly interdisciplinary area of science—especially in physical chemistry. It involves concepts of physics including band structure, zone theory, and charge transport as well as chemical concepts including electroics, photochemistry, surface chemistry, catalysis, and Marcus theory. Semiconductor electrodes have been used in a variety of applications including liquid junction solar cells, photolytic splitting of water, pollutants and organic molecules, semiconductor processing, and sensor technology.

It is instructive to examine first the historical evolution of this field. The use of a semiconductor as an electrode in an electrochemical cell was first demonstrated by E. Becquerel in 1839. He observed a photovoltaic effect when AgCl electrode was illuminated with UV light. The ‘Becquerel effect’ was not clearly understood until 1954, when researchers from Bell Laboratories studied photoelectrochemistry on Ge single crystals. They demonstrated that photochemical reactions occurring at Ge electrodes are affected substantially by the impurity levels in Ge. Based on these experiments and the zone theory that was developing at that time, the Becquerel effect was modeled as a photoinduced charge separation at the AgCl–liquid interface. The effect was further tested with other semiconductor electrodes such as Si, GaAs, GaP, CdS, CdSe, ZnS, ZnSe, ZnTe, TiO₂, SrTiO₃, and Ta₂O₅. Electron transfer theories were also rapidly evolving during this period, starting from homogeneous systems at heterogeneous metal–electrolyte interfaces leading, in turn, to semiconductor–electrolyte junctions.

Until the early 1970s, the work was fundamental in nature and mainly of academic interest. The report by Fujishima and Honda (1) in 1972 describing photoassisted splitting of H₂O to H₂ and O₂ on TiO₂, however, suggested the possibility of using semiconductor electrodes in converting solar energy into the chemical/electric energy. Electrolysis of water using sunlight is extremely attractive because (a) the hydrogen evolved can be stored more easily than either electricity or heat and (b) it is non-polluting, renewable, inexhaustible,

and very flexible with respect to conventional fuel alternatives. This report was published during a period when the entire world was, for the first time, experiencing soaring gasoline prices due to fossil fuel depletion. This led to an intense interest in understanding the semiconductor–electrolyte interface (SEI) pertaining to renewable energy sources and remains an active area of research. The goal is to discover an ideal SEI, which can deliver an efficiency of about 15% without fouling the electrodes. To date, there has been limited success due to the inverse relationship between photocorrosion and efficiency. Oxide semiconductors such as TiO_2 and ZnO are stable against photocorrosion to some extent but deliver poor efficiency due to a wide band gap. Sulfides and selenides are more efficient due to an optimum band gap but are unstable under sunlight.

Despite the limited success of semiconductor electrodes in solving energy problems, they provide an interesting alternative to traditionally used working electrode materials in electrochemical investigations. An important advantage of semiconductor electrodes is that the electrochemical response can be varied extensively by simply changing the impurity levels, surface treatments, or surface adsorption. In this way, semiconductor electrodes have a major edge over conventional metal electrodes where the properties of a given metal electrode are less easily controlled. This property of semiconductor electrodes has potential applications in developing sensors.

The photoelectrochemistry of semiconductor electrodes will not be the focus of this chapter due to the thousands of articles and reviews available in the literature. Instead, the semiconductor as an electrode in the ‘dark’ will be discussed. The journey begins with zone theory, which addresses the energetics of semiconductors. Next is the interface between the semiconductor and electrolyte, which is described using Gerischer’s model. We then enter the solution side and use the Marcus theory to explain the distribution of energy states associated with solvent reorganization energy. We discuss how electrochemical techniques such as cyclic voltammetry (CV, see Chapter 11) and scanning electrochemical microscopy (SECM, see Chapter 12) can be used to deduce the energetics of the interface and kinetics of electron transfer, respectively. We describe measurements on suspended quantized semiconductor particles by simple electrochemical methods. We also describe various methods of preparing semiconductor electrodes.

9.2 SEMICONDUCTOR BASICS

9.2.1 Band theory of solids

The properties of semiconductor electrodes and their differences compared with metal electrodes can be understood by examining their electronic structure. Semiconductors are unique in their electronic properties due to their band structure. The origin of the energy bands is generally discussed using *band or zone theory*, where the motion of a single electron in the crystal lattice is considered. It is assumed that there is no interaction between individual electrons or between the electrons and lattice points (the potential energy is zero). Therefore, the model is sometimes referred to as the *nearly free electron model*.

The time-dependent Schrödinger equation for a *free electron* is written as

$$-\frac{\hbar^2}{2m_e} \nabla^2 \Psi(x, y, z) = E \cdot \Psi(x, y, z) \quad (9.2.1)$$

where m_e is rest mass of a free electron, E is the kinetic energy, Ψ is a single electron wave function, and $\nabla^2 = \partial^2/\partial x^2 + \partial^2/\partial y^2 + \partial^2/\partial z^2$. The solution for equation (9.2.1) is given by

$$\Psi_k(r) = \frac{1}{\sqrt{V}} \cdot e^{i \cdot k \cdot r} \quad (9.2.2)$$

where $r = (x, y, z)$ is the position vector and k is the wave vector given by $k^2 = k_x^2 + k_y^2 + k_z^2$. The multiplier, $1/\sqrt{V}$, is a normalization constant that accounts for the presence of the electron in the volume element, V . Based on the *de Broglie wavelength* (2) associated with microscopic particles, the linear momentum and kinetic energy of the electron in a single crystal can be expressed in terms of k by the expressions

$$\mathbf{P} = \hbar \cdot \mathbf{k} \quad (9.2.3)$$

and

$$E(k) = \frac{\hbar^2 k^2}{2 \cdot m_0} \quad (9.2.4)$$

where $\hbar = h/2\pi$ and h is Planck's constant. A plot of energy $E(k)$ vs. k is given in Figure 9.1a, where the relationship is essentially parabolic and the allowed energy values are distributed *continuously* from zero to infinity. In a real crystal, however, electrons interact with the periodic potential field, $U(\mathbf{r})$, created by orderly arranged ions in the lattice such that

$$U(\mathbf{r}) = U(\mathbf{r} + \mathbf{R}) \quad (9.2.5)$$

where \mathbf{R} is the unit vector. In this situation, the electron wave scatters on these lattice points. It is analogous to the diffraction of X-rays on a periodic lattice governed by Bragg's law. The electronic waves, which satisfy Bragg's condition, scatter on the lattice points and cannot propagate in the lattice. It leads to the formation of forbidden energy gaps in the

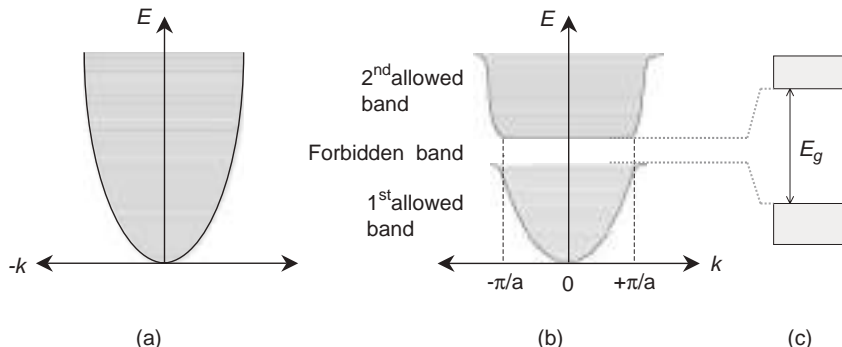


Figure 9.1 (a) Plot of energy E vs. wave vector k for the free electron, which suggests that the electron can acquire any value of energy or all transitions are allowed. (b) The effect of scattering of the electron at periodic lattice points, which gives rise to gaps of forbidden energy levels. Lower hashed area within $\pm\pi/a$ is called the first allowed band or *first Brillouin zone*, where a is the lattice constant along the ' a ' direction in the crystal. Upper hashed area is called the *second Brillouin zone*. (c) More familiar band structure for a solid. It is a plot of electronic energy vs. distance.

band, called *band gaps*. The region in the k space between $\pm\pi/a$ has allowed energy states and is called the *first Brillouin zone*. It is shown in Figure 9.1b. A more familiar picture of the band structure to the chemist is depicted in Figure 9.1c where an average value of the energy along three axes vs. distance in arbitrary unit is plotted. The electrons are filled in these allowed bands similar to the filling of electrons in the atomic and molecular orbitals. The probability that an electron can occupy a particular energy level E is governed by Fermi–Dirac statistics and is expressed as

$$f(E) = \frac{1}{1 + e^{(E-E_F)/k_B T}} \quad (9.2.6)$$

where E_F refers to the *Fermi level*. From a chemist's point of view, E_F represents an electrochemical potential of electrons ($\bar{\mu}_e$) in the solid. k_B is the Boltzmann constant. The probability distribution function $f(E)$ as a function of E at various temperatures is plotted in Figure 9.2a. In a solid, the energy states are not distributed uniformly throughout the energy values. Rather, the number of states per unit volume (i.e., density of states) increases with increasing energy value. The density of (available) states in an energy interval dE as a function of E is given by (3)

$$g(E)dE = \frac{4\pi}{h^3} (2m)^{3/2} E^{1/2} dE \quad (9.2.7)$$

which is plotted in Figure 9.2b. The product of equations (9.2.6) and (9.2.7) will lead to the following expression that represents the density of occupied states:

$$N(E)dE = F(E) \cdot g(E) dE \quad (9.2.8)$$

The function is plotted in Figure 9.2c and represents the density of states within the energy interval dE . The hashed area represents the density of occupied states. Depending on the

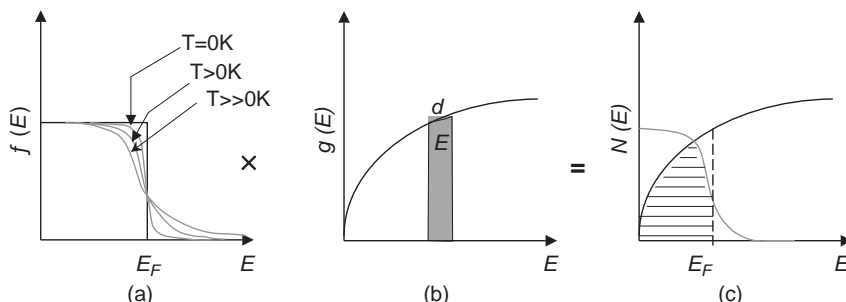


Figure 9.2 (a) Fermi–Dirac distribution function for a single electron at various temperature values. E and E_F are the energy of the allowed states and Fermi energy, respectively. (b) Density of state (DOS) as a function of energy. It represents density of available states in the energy interval dE and at energy E . (c) When Fermi–Dirac distribution function blends with density of available states, one gets density of occupied states shown as hashed area. Please note the position of E_F , below which all the states are occupied and above all the states are empty.

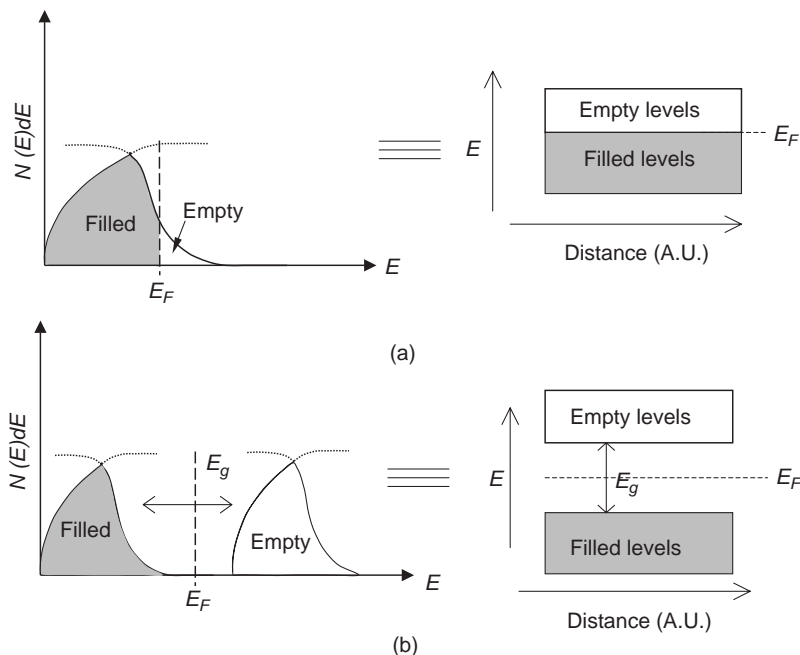


Figure 9.3 Band structure of (a) metal and (b) semiconductor. Left-hand side illustrations in both cases are a more explicit depiction of band theory. Right-hand side illustrations are more familiar and approximate.

number of valence electrons available and the probability distribution ($f(E)$), the bands can be either partially or completely filled. Materials with partially filled bands are classified as metals. If the band is completely filled and the immediate higher energy band is empty, then the material has properties of either an insulator or a semiconductor. These possibilities are shown in Figure 9.3.

For semiconductors (and insulators), the completely filled lower band is called the valence band (VB) and the higher energy band immediately above it is called the conduction band (CB). The average energy gap between these two bands is called the *band gap* (E_g). Based on equation (9.2.8), the density of energy states above the CB edge E_c is given by

$$N_c = \frac{8\sqrt{2\pi}}{h^3} (m_e^*)^{3/2} (E - E_c)^{1/2} \quad (9.2.9)$$

Similarly, the density of states below the VB edge E_v is given by

$$N_v = \frac{8\sqrt{2\pi}}{h^3} (m_h^*)^{3/2} (E - E_v)^{1/2} \quad (9.2.10)$$

where m_e^* and m_h^* are effective masses¹ of an electron and a hole in the crystal, respectively. For semiconductors ($E_g \leq \text{ca. } 1 \text{ eV}$), thermal energy at room temperature ($k_B T$) is sufficient to promote a few electrons from the VB to the CB. The corresponding density of electrons in the CB (n) and density of holes in the VB (p) are given by

$$n = N_c \exp\left(-\frac{E_c - E_{F,n}}{k_B T}\right) \quad (9.2.11)$$

and

$$p = N_v \exp\left(-\frac{E_v - E_{F,p}}{k_B T}\right) \quad (9.2.12)$$

where $E_{F,n}$ and $E_{F,p}$ are corresponding Fermi energies of electrons and holes, respectively. At equilibrium, the Fermi levels of electrons and holes are equal. That is

$$E_{F,n} = E_{F,p} = E_F \quad (9.2.13)$$

which leads to

$$n = n_0; \quad p = p_0 \quad (9.2.14)$$

where n_0 and p_0 are the respective densities of electrons in the CB and holes in the VB at equilibrium. Substituting the equilibrium condition described in equation (9.2.14) into equations (9.2.11) and (9.2.12) leads to

$$n_0 p_0 = N_c N_v \exp\left(\frac{E_c - E_v}{k_B T}\right) = n_i^2 \quad (9.2.15)$$

At room temperature (300 K), the equation simplifies to

$$n_i = p_i \approx 2.5 \times 10^{19} \exp\left(-\frac{E_g}{2k_B T}\right) \quad (9.2.16)$$

The mobility of electrons in the CB and holes in the VB imparts conductivity to the semiconductor as illustrated in Figures 9.4a and b. This type of semiconductor is called an '*intrinsic*' semiconductor.

Electron–hole pairs can also be introduced by substitution of acceptor and donor atoms by a process called *doping*. These 'doped' semiconductors are called *extrinsic* semiconductors.

¹The effective mass of an electron in a crystal is given as $m_e^* = \hbar^2 / (d^2 E / dk^2)$, which is different from the rest mass of an electron, m_e . The equation suggests that the mass of an electron in the crystal changes with the curvature of the Brillouin zone (Figure 9.1b). For most of the values of k , $m_e^* = m_e$. However, near the edges of the zone, i.e., $k = \pm n\pi/a$, m_e^* differs considerably from m_e . At the bottom of the zone, $(d^2 E / dk^2)$ is positive and the effective mass is positive. At the top of the zone, $(d^2 E / dk^2)$ is negative and the effective mass is negative. Physically, it represents an exchange of momentum with the lattice as the moving electron gets retarded near the Brillouin zone boundaries.

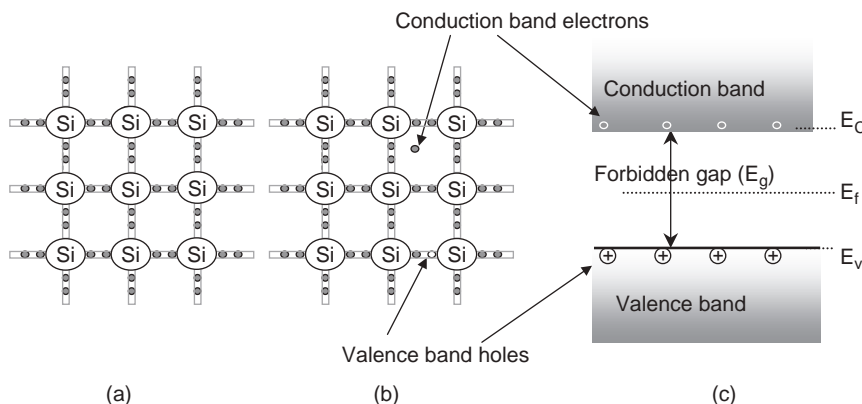


Figure 9.4 Two-dimensional representation of crystal structure of an intrinsic semiconductor such as Si crystal. The original tetrahedral structure is oversimplified to a square one for clarity. Dark spots in the sketch illustrate shared valence electrons among Si atoms and form covalent bonds. (a) Situation at 0 K where no ionization takes place. (b) At higher temperature, valence electrons gain sufficient energy and are delocalized, which form the holes in the VB. (c) Energy diagram for the intrinsic semiconductor crystal. Mobility of holes in VB and the electrons in CB imparts conductivity to the intrinsic semiconductor crystal.

For example, if Si crystal is doped with P, As, or Sb atoms (group V elements), donor states are created in the band gap. For a moderately doped semiconductor (ca. $N_D = 10^{-14}$ donor atoms per cm^3), these states lie ca. 0.02–0.03 eV below the CB. Thus, even at room temperature, these states get fully ionized by promoting electrons into the CB. The presence of electrons in the CB is due not only to their promotion from the VB but also from the ionized donor states. Thus, the overall density of electrons in the CB due to doping is given by

$$n = (n_0 N_D)^{1/2} \exp\left(-\frac{E_D}{2k_B T}\right) \quad (9.2.17)$$

where E_D is the energy gap between donor states and E_c ; it has a magnitude of approximately 0.02–0.03 eV at room temperature as Figures 9.5a and b illustrate. The density of electrons in the CB is increased compared with the density of holes in the VB. The observed conductivity is attributed to CB electrons, which are called *majority carriers*. Such a material is called an *n-type semiconductor*.

If Si crystal is doped with trivalent impurity atoms (e.g., B, Al, Ga, and In), then the acceptor levels are introduced into the band gap approximately 0.02–0.03 eV above the VB. Thus, the electrons from the VB get promoted to the acceptor levels, leaving holes behind. The overall density of holes in the VB is given by

$$p = (p_0 N_A)^{1/2} \exp\left(-\frac{E_A}{2k_B T}\right) \quad (9.2.18)$$

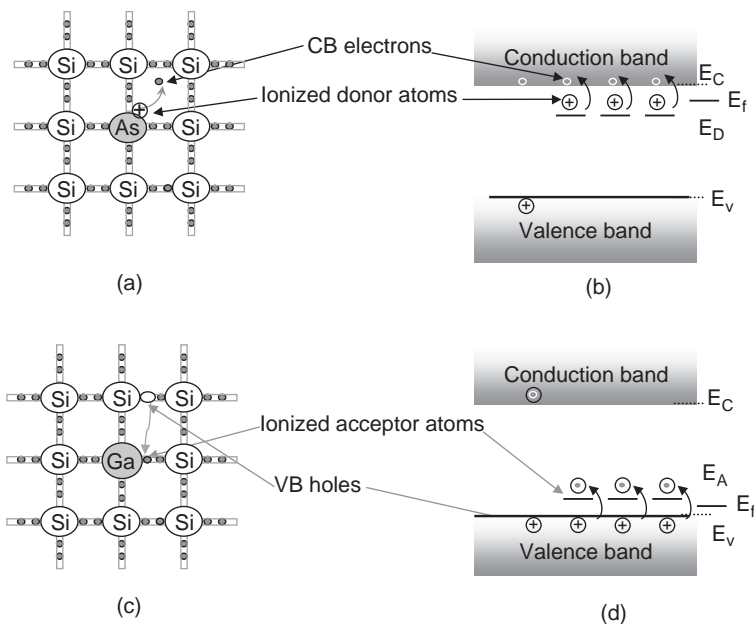


Figure 9.5 (a) Two-dimensional representation and (b) corresponding energy bands for n-doped Si. An extra valence electron from As atom is ionized and occupies the CB of Si. Similarly, (c) and (d) are respective illustrations for p-doped Si. Valence electron from Si occupies the vacancy created (acceptor levels) at Ga atoms, thus leaving a hole in the VB for conduction. Note the shift in position of the Fermi level (E_F) due to doping.

where E_A is the energy gap between acceptor states and E_V ; it is approximately 0.02–0.03 eV at room temperature as shown in Figures 9.5c and d. In this case, there are more holes in the VB than electrons in the CB. Thus, the holes are majority carriers and electrons are the minority carriers. The material is referred to as a *p-type semiconductor*.

9.2.2 Size quantization in semiconductors

It is generally assumed that the electronic properties of a semiconductor are independent of crystal size. However, recent studies have shown that if the particle size of the semiconductor is less than approximately 10 nm, then many of their physicochemical properties appear to be substantially different from analogous properties of a bulk material. This is because the electrons and holes are confined in the region of space defined by potential barriers that are comparable to or smaller than their respective *de Broglie* wavelengths so that allowed energy states become discrete (or quantized). This effect is referred to as the size quantization effect (SQE) or the quantum size effect. SQE is also observed in the noble metals (4). For semiconductors, the critical dimension for SQE depends upon the effective masses of the electrons (m_e^*) and the holes (m_h^*). For example, for $m^* \sim 0.05$, the critical dimension is approximately 30 nm. Thus, for semiconductors, SQE is observed in

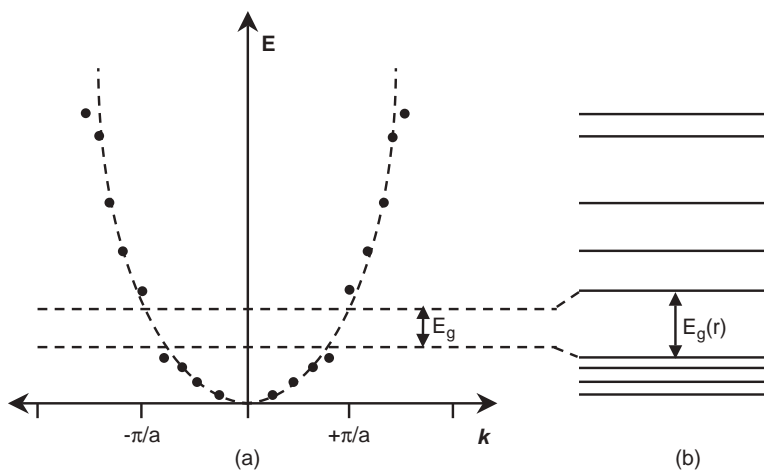


Figure 9.6 (a) Schematic plot of the energy E vs. wave vector k for the electron confined in a size-quantized semiconductor crystal. The dark dots over the parabola indicate the discrete and allowed energy values for the transition. (b) The band structure in the form of discrete energy states that suggest ‘molecular-like states’ for the size-quantized particles. E_g indicates the band gap for the bulk semiconductor, whereas $E_g(r)$ indicates energy separation between the highest occupied molecular orbital (HOMO) and the lowest unoccupied molecular orbital (LUMO) in the case of size-quantized particles, where $E_g(r) > E_g$.

the nanometer size regime and the particles are called nanoparticles or size-quantized particles. The band structure for the semiconductor in its size-quantized state is illustrated in Figure 9.6. As can be seen, the energy bands observed in a bulk semiconductor (Figure 9.1b) are replaced by discrete states, which leads to a dramatic change in its electronic properties. Currently, there is intense scientific and technological interest in size-quantized semiconductor structures. This is because electronic properties such as optical, catalytic, electrical, and redox potentials can be tuned and manipulated in fascinating ways by controlling the dimension, rather than just the chemical composition alone.

SQE is modeled similarly to the ‘particle in a box problem’, in which the smaller the ‘box’, the larger is the lower energy eigen value. The correlation for energy states between bulk material and corresponding size-quantized particle is schematically depicted in Figure 9.7.

It suggests that on decreasing the particle size, the energy of the first electronic transition of the semiconducting material shifts toward higher energy, which can be measured by using UV-vis absorption spectra. The blue shift in the absorption peak as a function of size for CdSe size-quantized particles (5) is shown in Figure 9.8. Furthermore, phase transition pressure, melting point, optical, optoelectronic, catalytic, and magnetic properties of *nanomaterials* differ from those of bulk solids and also from the molecular species from which they are made. Chemists can view this as a *giant molecule* or a new state of matter.

Two models have been used to explain SQE in the case of semiconductor nanoparticles. The first model is an effective mass approximation (6–11) developed for relatively larger particles. The second model assumes a tight-binding framework for well-defined small

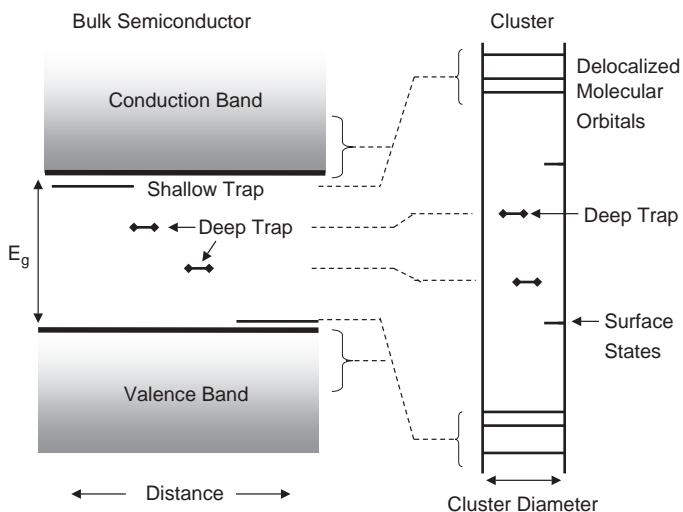


Figure 9.7 Spatial electronic state correlation diagram relating cluster states to bulk crystal states. Adapted from reference (6).

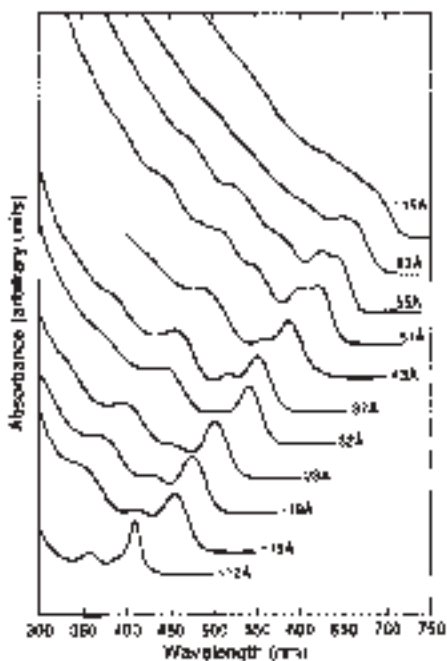


Figure 9.8 UV-vis spectra recorded for various sizes of trioctylphosphine oxide (TOPO)-capped CdSe clusters dispersed in hexane. Blue shift in the absorption edge is due to a larger separation between electronic states with decrease in particle diameter. Reprinted with permission from reference (5). Copyright 1993, American Chemical Society.

clusters (12). In the effective mass approximation, the electrons and holes are considered to be trapped in the spherical potential well. It is characterized only by a continuum of a solid having a dielectric constant ϵ . Electrons and holes are considered to be well separated from each other and uncorrelated. Variational methods (13) have been employed to solve the resulting Hydrogenic Hamiltonian. The ground-state energy of the *exciton* (minimum energy required to produce the electron–hole pair) is given by (11)

$$E_d = \frac{2\hbar^2\pi^2}{d^2} \left[\frac{1}{m_e^*} + \frac{1}{m_h^*} \right] - \frac{3.572e^2}{\epsilon d} - \frac{0.124e^4}{\hbar^2\epsilon^2} \left[\frac{1}{m_e^*} + \frac{1}{m_h^*} \right]^{-1} \quad (9.2.19)$$

where m_e^* and m_h^* are the respective effective masses of the electron and the hole, and d and ϵ refer to the diameter and dielectric constant of the semiconductor particles, respectively. The effective mass approximation gives a good understanding of the blue shift of the optical absorption threshold. However, it fails in the case of small crystallites due to the oversimplified description of the crystal potential.

A better description of the band structure for nanoparticles can be obtained by considering the tight-binding framework model (12). In this model, the atomic structure of a solid is implicitly considered. The energy levels are obtained by using the semi-empirical tight-binding theory. The energy levels and wave functions are, respectively, the eigen values and eigen vectors of the Hamiltonian matrix \mathbf{H} . Its bases are either atomic orbitals or a linear combination (hybridization) of them. The numerical calculation results obtained for CdS and ZnS nanocrystallites are summarized in Figures 9.9a and b, respectively.

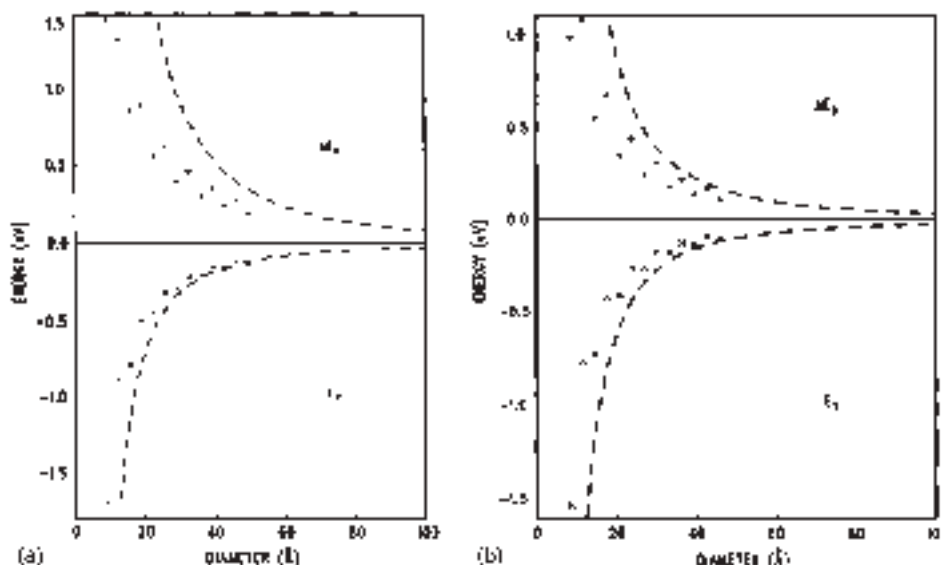


Figure 9.9 (a) Variation of band edge as a function of diameter of CdS clusters. The origin is taken as bulk values. The variational results are represented as ‘+’ in the figure. $\Delta E_c = E_c - 2.5$ eV(+). The dashed curves are the results of the effective mass approximation. (b) Similar results for ZnS cluster. $\Delta E_c = E_c - 3.7$ eV(+). Reprinted with permission from reference (12). Copyright 1989 by the American Physical Society.

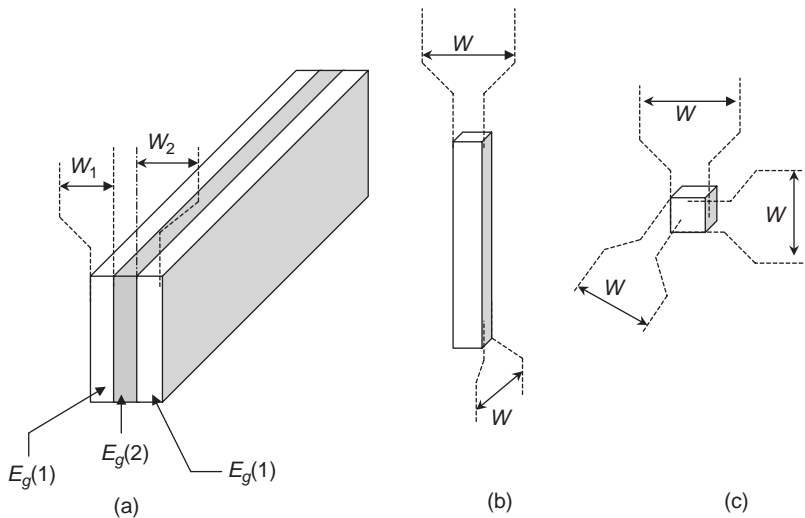


Figure 9.10 Three quantization configurations in semiconductors. (a) Confinement of charge carriers in ‘two dimensions’ called a quantum well. A narrow band gap ($E_g(2)$) is sandwiched between two wide band gap ($E_g(1)$) semiconductors. The charged carriers are trapped in a two-dimensional potential well. (b) Confinement of charge carriers in ‘one dimension’ called quantum wires. (c) Confinement of charge carriers in ‘zero dimension’ called quantum dots. ‘w’ represents width of confined direction, which is of the order of 1–20 nm. Adapted from reference (14).

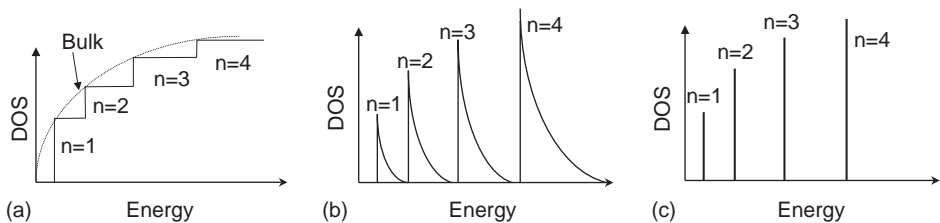


Figure 9.11 The density of electronic states (DOS) as a function of energy for three size regimes: (a) quantum well—DOS is a step function, (b) quantum wire, and (c) quantum dots. For the quantum wire, DOS distribution is in between a quantum well and quantum dots.

Semiconductor nanoparticles that arise due to the confinement of electrons/holes in zero spatial dimension are called quantum dots. Quantum wires and quantum films or wells arise when the charge carriers in the corresponding semiconductor are confined in one or two spatial dimensions. These dimensional confinements and corresponding density of states are illustrated in Figures 9.10 and 9.11, respectively.

9.3 ENERGETICS OF A SEMICONDUCTOR

Key factors in the utilization of semiconductor electrodes in electrochemical cells and devices are (a) knowledge of the relative location of the energy levels in the

semiconductor and solution and (b) understanding the role of surface states in the charge transfer. Two important parameters are the *Fermi level* (E_F) of the semiconductor and the corresponding electrochemical potential ($\bar{\mu}_{e,\text{redox}}$) of electrons in solution. The Fermi level was introduced in Section 9.2. From equation (9.2.6), the probability of finding an electron at $E = E_F$ is found to be 1/2. Thus, the Fermi level can also be defined as the energy level where the probability of an electron occupying it is one half. The probability of occupying levels above E_F is 0 and below E_F is 1. In case of an intrinsic semiconductor, E_F is expressed as

$$E_F = \frac{3}{4} k_B T \ln\left(\frac{m_h^*}{m_e^*}\right) + \frac{E_C + E_V}{2} \quad (9.3.1)$$

At absolute zero, the first term in equation (9.3.1) vanishes and

$$E_F \approx \frac{E_C + E_V}{2} = \frac{E_g}{2} \quad (9.3.2)$$

Thus, E_F lies about midway in the forbidden region as illustrated in Figure 9.4c. The position of E_F also depends upon the relative density of electrons and holes. For example, for the case of an n-type semiconductor ($N_D \approx 10^{15} \text{ cm}^{-3}$), E_F lies midway between E_c and E_D . Similarly, for the case of a p-type semiconductor, E_F lies midway between E_V and E_A , as illustrated in Figures 9.5b and d. From a chemist's point of view, E_F is simply the electrochemical potential of the electron in a given phase (in the present context, it is a semiconductor phase) that is expressed as

$$E_F^\alpha = \bar{\mu}_e^\alpha = \mu_e^\alpha - e\phi^\alpha \quad (9.3.3)$$

where μ_e^α and ϕ^α are the chemical potential and the inner potential² of an electron in phase α , respectively. It is measured in electron volts (eV) with reference to the energy of an electron in a vacuum, which is assumed to be zero. Similarly, the electrochemical potential of electrons in a dilute redox solution is given by

$$\bar{\mu}_{e,\text{redox}} = \mu_{e,\text{redox}}^0 + k_B T \ln\left(\frac{[O]}{[R]}\right) \quad (9.3.4)$$

where [O] and [R] are the concentrations of oxidized and reduced species, respectively. Redox potentials are expressed with reference to the normal hydrogen electrode (NHE) whose reduction potential is the assigned standard of 0.0 V at all temperatures.³ In order to compare the energetics of a redox reaction with those of a semiconductor, we need to

²Inner potential ϕ is defined as the work done to bring a unit positive charge from the vacuum level to the phase α electric force field ε . Thus, $\phi = \int_{-\infty}^{(x,y,z)} \varepsilon(x, y, z) dz$.

³Standard free energy change of formation ($\Delta_f^\circ G$) for a hydrogen atom from ions is assumed to be zero at all temperatures. It implies that $E^\circ(H_2(1 \text{ atm})/\text{H}^+(a = 1)) = 0.0 \text{ V}$ with $\Delta_f^\circ G = -nFE^\circ$.

express $\bar{\mu}_{e,\text{redox}}$ on a vacuum or absolute scale. As discussed, $\bar{\mu}_{e,\text{redox}}$ of a redox system is equivalent to the Fermi level $E_{F,\text{redox}}$; that is

$$E_{F,\text{redox}} = \bar{\mu}_{e,\text{redox}} \quad (9.3.5)$$

On an absolute scale, it is given by

$$E_{F,\text{redox}} = E_{\text{ref}} - eU_{\text{redox}} \text{ (in eV)} \quad (9.3.6)$$

where U_{redox} is the redox potential in volts vs. NHE and E_{ref} is the energy of the reference electrode vs. this absolute scale. The standard reduction potential of the NHE (0.0 V) is accepted to be equivalent to -4.5 eV on an absolute scale (15).

$$E_{F,\text{redox}} = -4.5 \text{ eV} - eU_{\text{redox}} \quad (9.3.7)$$

The position of bands of various semiconductors using the vacuum and electrochemical scales is shown in Figure 9.12. In fact, this is an important bridge between semiconductor physics and electrochemistry. For example, Si has $E_F = -4.8$ eV on a vacuum scale. The corresponding value with reference to NHE in solution is $+0.3$ V.

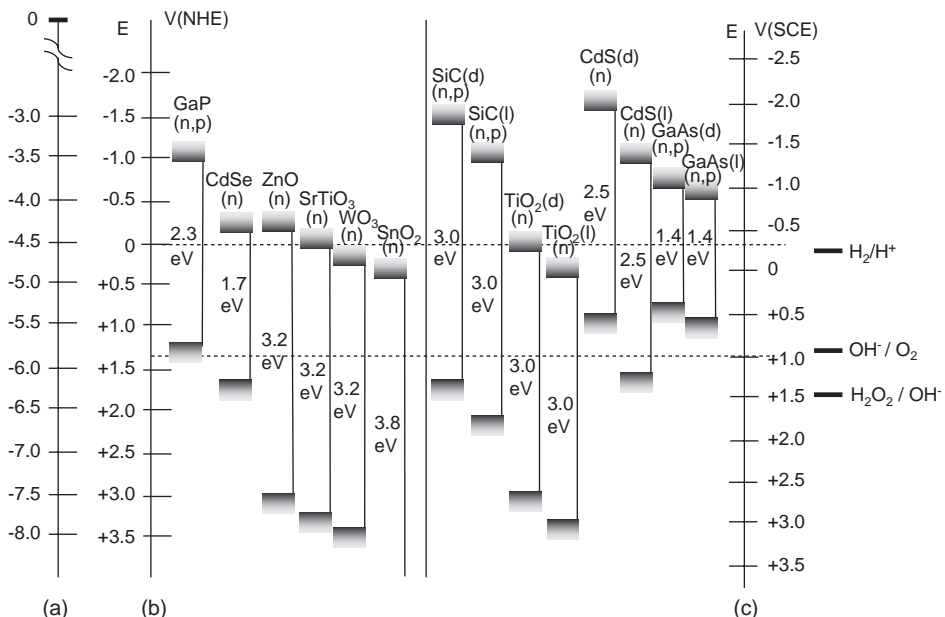


Figure 9.12 Position of energy bands of various semiconductors with respect to vacuum and electrochemical scales (adapted from reference (14)). The scale marked as (a) is for the vacuum scale. The scale marked as (b) is for the normal hydrogen electrode (NHE) scale and the scale marked as (c) is for saturated calomel electrode (SCE) scale.

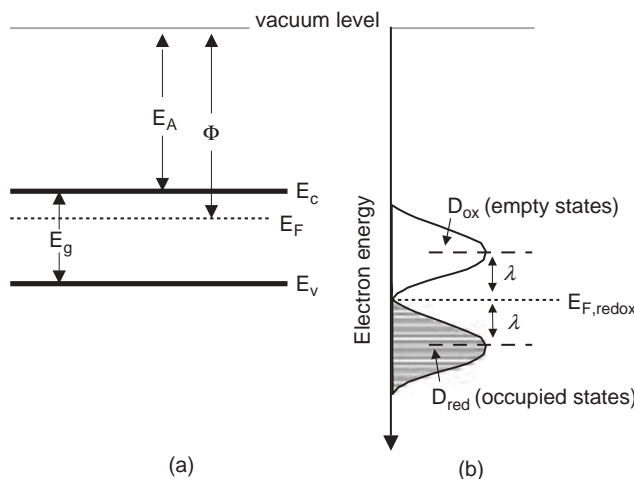


Figure 9.13 (a) Energy levels in the semiconductor. E_A and Φ stand for the electron affinity and work function of the semiconductor, respectively. (b) Energy distribution of occupied and unoccupied states of a redox couple. Adapted from reference (14).

A redox couple will also have a distribution of energy levels similar to semiconductors. These were first described by Gerischer (16, 17) in terms of a Gaussian-type distribution function, which is given by

$$D_{\text{ox}} = \exp \left[-\frac{(E - E_{F,\text{redox}} - \lambda)^2}{4k_B T \lambda} \right] \quad (9.3.8)$$

and

$$D_{\text{red}} = \exp \left[-\frac{(E - E_{F,\text{redox}} + \lambda)^2}{4k_B T \lambda} \right] \quad (9.3.9)$$

where D_{ox} and D_{red} are the distribution functions for oxidized and reduced species, respectively. λ is the solvent reorganization energy from electron transfer theory (18). A detailed picture of energy levels of semiconductor bands and a distribution of occupied and unoccupied states for a redox couple are given in Figure 9.13.

9.3.1 Semiconductor-electrolyte interface (SEI)

When the semiconductor and redox solution are brought in contact with each other, their Fermi levels must match at equilibrium. If they differ initially, then charge transfer must take place between these phases to eliminate the disparity in their Fermi levels. For example, if

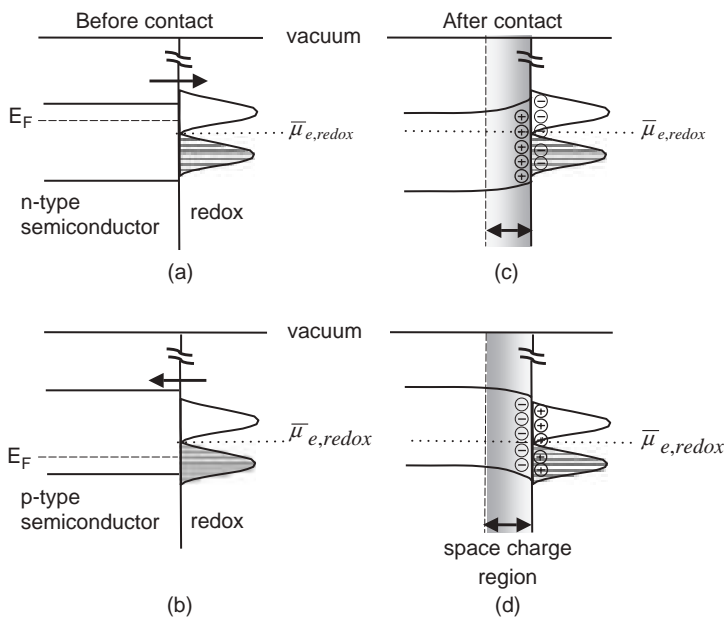


Figure 9.14 Energetics of the semiconductor–electrolyte interface, when n- and p-type semiconductors are brought in contact with the redox couple having $\bar{\mu}_{e,\text{redox}}$ in between the band gaps. (a and b) The situations before contact. (c and d) The situations after contact. Arrows shown in (a) and (b) show the direction of electron flow before equilibrium is established.

E_F of an n-type semiconductor lies above the $\bar{\mu}_{e,\text{redox}}$ of the solution as shown in Figure 9.14a, then to remove the difference in Fermi energies, the electrons will flow from the semiconductor to the solution side.

Thus, the semiconductor will acquire a positive charge and the solution will become negatively charged as shown in Figure 9.14c. Similarly, a p-type semiconductor will acquire a negative charge with respect to the solution as shown in Figure 9.14d. In the case of moderately doped semiconductors, the density of states available on the surface is not sufficient to accommodate these excess charges. Therefore, charges will be distributed inside the semiconductor region at a distance on the order of approximately 10–1000 nm. This region is called the *space charge region*. The resultant electric field in the space charge region affects the local energy of the electrons. Thus, the electrochemical potential of electrons in the semiconductor is different near the space charge region than that of the bulk of the semiconductor. It appears as *band bending* in the Gerischer diagram.

Thus, if charge separation occurs in this region, electrons in the CB will have a tendency to ‘roll down’ into the bulk. At the same time, holes in the VB will ‘bubble out’ on the surface. Thus, the space charge region is responsible for charge separation at the SEI. The potential difference created between the bulk of the semiconductor and the interface due to band bending is called the barrier height ($\Delta\phi$). It is depicted in Figure 9.15. There will also be a potential gradient toward the solution side due to the Helmholtz layer as shown in Figure 9.16.

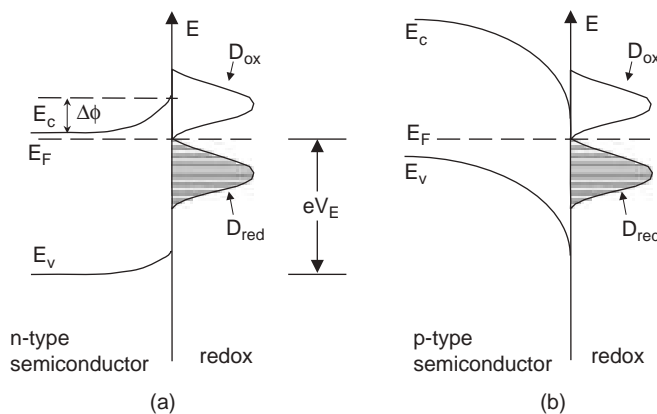


Figure 9.15 Details of the semiconductor-electrolyte interface for (a) n-type and (b) p-type semiconductors. $\Delta\phi$ represents the barrier height. Adapted from reference (14).

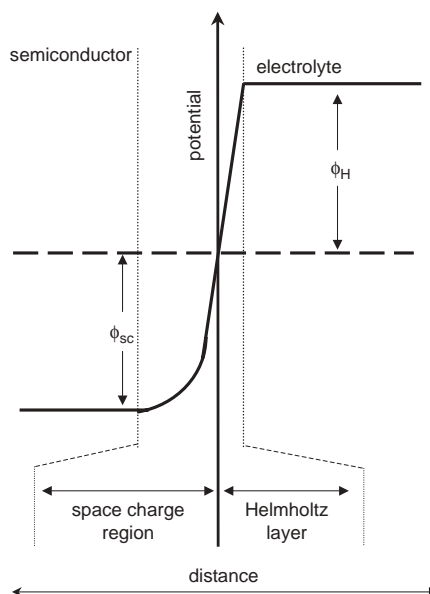


Figure 9.16 Potential distribution across the SEI. ϕ_{sc} and ϕ_H are potential drops across space charge and Helmholtz regions, respectively. Adapted from reference (14).

Thus, the SEI can be modeled as two parallel plate capacitors in series. Because the value of the space charge region capacitor is generally smaller than that of the Helmholtz layer, it dominates the overall capacitance of the SEI.

One of the important advantages in using a semiconductor as an electrode is that the energetics of the SEI can be modulated by applying a potential bias.

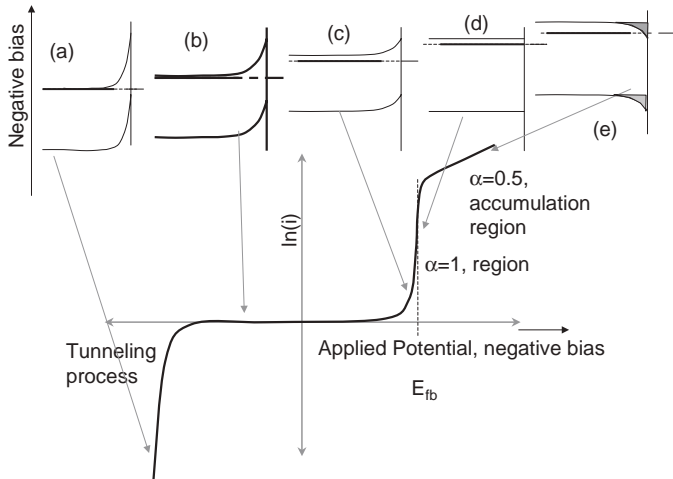


Figure 9.17 Effect of applied potential on the structure of the SEI. The corresponding current-voltage curve is also shown for n-type semiconductor. The negative bias increases from left to right side of the figure. Situation (a) occurs at extremely positive bias from E_{fb} . The flow of current is attributed to the tunneling process, when diode *breaks down*. In situations (b) and (c), the electron transfer takes place, overcoming the barrier height, which progressively reduces with more and more negative bias. Situation (d) is an unique one at which bands become flat and current increases exponentially. Further increase in the negative bias leads to inverted bands and semiconductor starts behaving like a metal.

Figure 9.17 shows the effect of an applied bias on the structure of the SEI. On applying a negative bias to an n-type semiconductor, $\Delta\phi$ is reduced and at a particular value of EMF, it is eliminated completely. The applied potential at which no space charge region exists is called a *flat-band potential* E_{fb} , which is related to the barrier height by the expression

$$-\Delta\phi = E - E_{fb} \quad (9.3.10)$$

The capacitance of the space charge region C_{sc} can be related to $\Delta\phi$ by the *Mott–Schottky* equation

$$\frac{1}{C_{sc}^2} = \left(\frac{2}{e\epsilon\epsilon_0 N_D} \right) \left(-\Delta\phi - \frac{kT}{e} \right) \quad (9.3.11)$$

Thus, a plot of $1/C_{sc}^2$ vs. applied potential E (a *Mott–Schottky plot*) can be used to determine the E_{fb} of the SEI.

9.4 SEMICONDUCTOR ELECTRODES

9.4.1 Electron transfer at semiconductor–electrolyte interface

An observed current in an electrochemical cell is usually viewed as charge transfer across the electrode–solution interface. Consequently, it is not necessary to use individual electrons

or holes in theoretical calculations. The electron transfer can be modeled as an adiabatic process (19, 20) in which an ‘electron cloud’ interacts with an electron acceptor (cloud) in a solution (redox); that is, the (symmetrically) favorable configuration in terms of spatial and angular momentum compatibility is achieved on matching the energy levels.

In the case of metallic electrodes (e.g., Pt), the observed cathodic current for the reaction



at a given potential E is given by

$$i \approx nFAk'_t C_o(x=0) \quad (9.4.2)$$

where n and F are the number of electrons involved in elementary steps and Faraday’s constant, respectively, A is the area of the electrode and $C_o(x=0)$ is the surface concentration of the oxidized species O. k'_t is the heterogeneous rate constant (cm s^{-1}) of the electron transfer, which is an exponential function of E and the transfer coefficient (α). In metals, the electron density near the Fermi level is very high compared with the concentrations of O and R. Therefore, there is hardly any change in electron density at steady state so that the rate of electron transfer is often limited by the surface concentration of ions and it follows pseudo-first-order kinetics.

In the case of a semiconductor electrode, densities of electrons and holes are limited. Therefore, the current is often governed by the density of the charge carriers (17) that can be treated as individual reactants. Thus, in the case of charge transfer across an SEI, a bimolecular heterogeneous rate constant must be considered. Unlike metals, the charge transfer can follow two different pathways.⁴ It can occur by electron transfer from the CB to O and by electron transfer from R to the VB. The latter case is viewed as a transfer of holes from the VB to R as illustrated in Figure 9.18. Unlike a metal electrode, its concentration can be varied over a wide range by simply controlling the applied potential E .

Consider the SEI as shown in Figure 9.14 where $\bar{\mu}_{e,\text{redox}}$ of ions lies between E_{VB} and E_{CB} . The semiconductor electrode is immersed in a well-stirred solution so that the

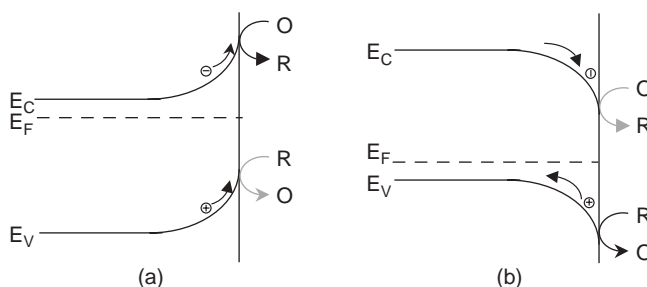


Figure 9.18 Electron transfer reaction at SEI in dark for (a) n-type and (b) p-type semiconductors. Faint arrows indicate that the process is less dominating.

⁴In this model, complications often arise in the charge transfer due to surface states. These states lie between the VB and CB and are not considered.

current is not limited by the mass transfer of ions in the solution. In the dark, the electron transfer will be dominated by the majority carriers in the semiconductor. Thus, in case of an n-type semiconductor, there are excess electrons (from the donor states) in the CB compared with the holes present in the VB. The transfer of electrons from the CB to O in solution will proceed at a higher rate than the electron transfer from R to the holes in the VB. Thus, the reduction of O will take place in solution. Since the electrons need to overcome $\Delta\phi$ in order to pass current in the forward direction, a net cathodic current will flow according to

$$i = nFAk_f n_{sc} C_o (x = 0) \quad (9.4.3)$$

where k_f ($\text{cm}^4 \text{ sec}^{-1}$) is the bimolecular heterogeneous rate constant for the forward reaction (reduction) and n_{sc} (cm^{-3}) is the density of electrons in the space charge region. Similarly, for the p-type semiconductor, oxidation of R would be the most favorable process. Similar to equation (9.4.3), the net anodic current for given potential is expressed as

$$i = nFAk_b p_{sc} C_R (x = 0) \quad (9.4.4)$$

where k_b ($\text{cm}^4 \text{ sec}^{-1}$) is the heterogeneous rate constant for the backward reaction (oxidation) and p_{sc} (cm^{-3}) is the density of holes in the space charge region. This represents the situation where no external bias is applied to the interface and the system is driven by the barrier height ($\Delta\phi$). At equilibrium, both rates will be equal and no net current will flow at the SEI.

When an EMF (E) is applied to the electrode, the heterogeneous rate constants (k_f and k_b) will vary with E according to the Butler–Volmer equations

$$k_f = k^\circ \exp \left[-\frac{\alpha F(E - E^\circ)}{RT} \right] \quad (9.4.5)$$

and

$$k_b = k^\circ \exp \left[\frac{(1-\alpha)F(E - E^\circ)}{RT} \right] \quad (9.4.6)$$

where E° is the formal reduction potential of the redox O/R couple and k° is the standard rate constant that can be related to the exchange current density i_0 at the interface. Its value depends upon the overlap of the electronic wave function of the semiconductor and the redox couple (21). The higher the overlap, the more facile are the kinetics and the faster is the charge transfer. The heterogeneous rate constants k_f or k_b depend upon the potential drop ($\Delta\phi'$) at the Helmholtz layer across the SEI, which may change with applied potential.⁵ It follows that the quantity $(E - E^\circ)$ can be replaced by $\Delta\phi'$ in equations (9.4.5) and (9.4.6). Thus, these equations are applicable to both metal and semiconductor electrodes.

⁵This is a property of the interface at the solution side and is therefore applicable to metal electrodes also.

Unlike metals, semiconductors have a space charge region. Therefore, the applied potential will affect the composition of the space charge region through the equations

$$n_{sc} = N_D \exp\left[-\frac{F(E - E_{fb})}{RT}\right] \quad (9.4.7)$$

and

$$p_{sc} = N_A \exp\left[\frac{F(E - E_{fb})}{RT}\right] \quad (9.4.8)$$

Here again, $(E - E_{fb})$ is equal to the amount of band bending that is also the barrier height ($\Delta\phi$). The applied bias changes the magnitude of the barrier height and thus controls the current in the cell. This is analogous to the current through a metal–semiconductor Schottky barrier (22). Under these conditions, variation of E mainly affects n_{sc} and p_{sc} in an n- and a p-type semiconductor, respectively. This means that the slope of a plot of $\ln(i)$ vs. E will be RT/F that implies that $\alpha = 1$ (23). For an n-type semiconductor, if E is made more negative than E_{fb} , then the electrons accumulate at the semiconductor surface, called an *accumulation layer*. In this situation, n_{sc} is no longer a function of E , which was earlier governed by equation (9.4.7). Thus, the applied potential will change k_f as per equation (9.4.3); that is, there will be a change in potential drop in the Helmholtz region ($\Delta\phi'$). Semiconductor electrodes essentially behave like a metal with $\alpha \approx 1$. Similar arguments are applicable to a p-type semiconductor when a potential more positive than that of E_{fb} is applied. If we substitute equations (9.4.5) and (9.4.7) into equation (9.4.3) and plot a Tafel plot, it would typically follow the function as shown in Figure 9.17. In this illustration, current is assumed to be purely faradaic and not limited by mass-transfer processes. Thus, in using semiconductor electrodes experimentally, the density of charge carriers is controlled as function of potential; this feature is lacking in metal electrodes.

9.4.2 Illuminated semiconductor electrodes

Consider the situation of an SEI between an n-type semiconductor electrode and redox couple, which we have discussed in Section 9.3. On illuminating this interface with a light having photon energy ($h\nu$) greater than the band gap (E_g) of the semiconductor,⁶ a transition of electrons from the VB to the CB will occur, leaving behind holes in the VB. The *charge pairs* generated in the bulk of the semiconductor will eventually neutralize each other and the energy will dissipate in terms of heat (lattice vibrations).

However, the charge pairs generated near the SEI experience a potential gradient due to the space charge region. The electrons promoted in the CB *experience* the lower energy in

⁶The feasibility of excitation of an electron from the VB to the CB is allowed if the angular momenta of the photon and electron are conserved during excitation. The semiconductor is then called a direct band gap semiconductor. For example, CdS, CdSe, GaAs, InP, etc., are direct band gap semiconductors, whereas Si is an indirect band gap semiconductor.

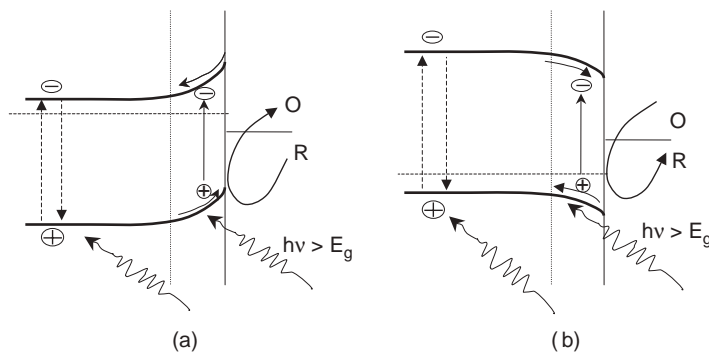


Figure 9.19 n-Type semiconductor-electrolyte interface under the illumination. (a) Charge pair generated in the bulk gets eventually annihilated and generates heat. (b) Charge pair generated in the space charge region gets separated from each other due to the potential gradient. Holes *bubbled out* at the interface can oxidize the redox R into O . Thus, net oxidation reaction will take place at the SEI of n-type semiconductor on illumination.

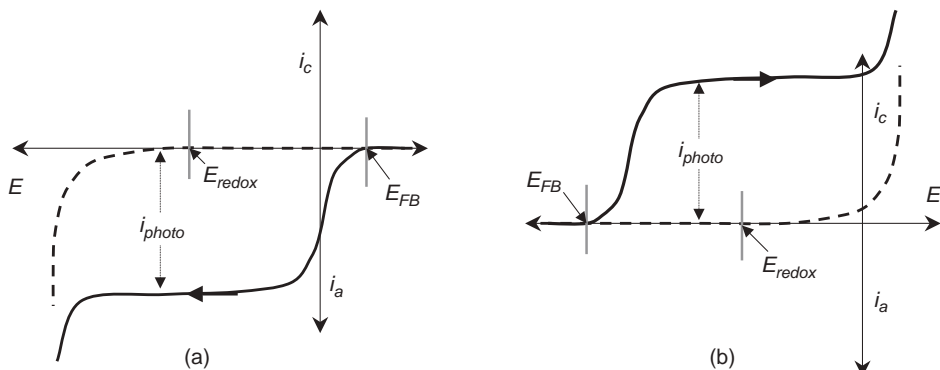


Figure 9.20 i - v curve for semiconductors/redox junction in dark (dotted line) and on illumination (hard line) for (a) n-type semiconductor, which on illumination leads to photoanodic current, and (b) p-type semiconductor, which on illumination leads to photocathodic current. The onset for photocurrents in both the diagrams suggests the flat-band potential, E_{fb} .

the bulk of the semiconductor and thus ‘roll back’ into the bulk. In contrast, holes experience an opposite force field and thus ‘bubble out’ at the interface. The situation is demonstrated in Figure 9.19. The holes, which are ‘surfaced’ at the SEI, have an effective redox potential equal to that of the VB edge and thus oxidize R into O . The electrons travel in the semiconductor bulk and proceed into the external circuit, which eventually reduces O at the counter electrode. Thus, in the case of an n-type semiconductor, the reduction will be facilitated in the dark. However, on illumination, oxidation is prevalent. Therefore, irradiation of an n-type semiconductor promotes an oxidation reaction called *photo-oxidation* at the semiconductor surface. The corresponding steady-state current–potential curves are drawn in Figure 9.20.

9.4.3 Cyclic voltammetry (CV) at semiconductor electrodes

Cyclic voltammetry (please see Chapter 11) (24) has been extensively used to probe the behavior of SEI in the dark and under illumination. Bard and co-workers (21, 25–27), Wrighton and co-workers (28, 29), Lewis and co-workers (30, 31), and Chazalviel *et al.* (32) have carried out pioneering work in this field. These studies unambiguously demonstrated the use of CV to deduce critical parameters of SEI including, for example, E_V , E_c , and E_{fb} . In Section 9.4.1, it was demonstrated that a change in EMF at a semiconductor electrode results in a large change in the density of charge carriers at an SEI. Only the redox couples, which are energetically closer to the VB and CB, are expected to undergo charge transfer. For example, Laser and Bard (21) recorded CVs with a single-crystal TiO_2 electrode in redox couples chosen such that their E_{redox} accommodates the entire potential window from the VB to the CB.

The various redox couples used in this experiment and their potentials on TiO_2 and Pt are listed in Table 9.1. The idea was to judge the position of energy bands based on the reversibility of the CV for redox couples of known potentials. Based on these results, three

Table 9.1

Electrochemical data for redox couples

	Pt	TiO_2	
	E_0 (V vs. SCE)	E_{pc}	E_{pa} (V vs. SCE)
$\text{Ru}(\text{bipy})_3^{3+}$	+1.3	+0.36	None
	-1.3	-1.34	-1.27
	-1.49	-1.52	-1.46
	-1.73	-1.77	-1.70
$\text{Th}\cdot^+$	+1.23	+0.40	None
10-MP \cdot^+	+0.82	+0.28	None
TMPD \cdot^+	+0.22	-0.31	None
$\text{Ox-1}\cdot^+$	-0.42	-0.80	None
	-1.30	-1.65	None (adsorption probe)
<i>p</i> -BQ	-0.52	-1.00	None
	-1.64 (irreversible)	-1.89	None
$\text{Ru}(\text{TPTZ})_2^{3+}$	-0.81	-0.90	-0.72
	-0.97	-1.09	-0.88
	-1.63	-1.76	-1.55
	-1.88	-2.03	-1.83
AQ	-0.94	-1.12	Some oxidation beginning at ca. -0.90
	ca. -1.61 (quasi-reversible)	-1.84	-1.44
DBM	-1.55	-1.68	-1.44
9,10-DPA	-1.84	-1.93	-1.74
A	-1.94	-2.06	-1.80

Reprinted with permission from reference (33). Copyright 1975, American Chemical Society.

^aAbbreviations used in this table: Th, thianthrene; 10-MP, 10-methylphenothiazine; TMPD, *N,N,N',N'*-tetramethyl-*p*-phenylenediamine; Ox-1, oxazine-1; *p*-BQ, *p*-benzoquinone; AQ, anthraquinone; DBM, dibenzoylmethane; 9,10-DPA, 9,10-diphenylanthracene; A, anthracene.

potential regions were identified: (a) a region positive to approximately -0.8 V, where a redox couple, which is reversible at platinum, becomes totally irreversible at TiO_2 . In some cases, the reduction wave was shifted by about 1 V more negative compared with that recorded on platinum. However, on illumination of the SEI, quasi-reversibility was observed. (b) In the second potential region, negative to about -0.8 V, there is no change in the redox profile on TiO_2 . The reduction of all redox couples on TiO_2 is reversible, similar to that recorded on a Pt electrode. (c) In the third potential region, redox couples that reduce at potentials positive of 0.4 V on platinum are reduced between $+0.3$ and $+0.4$ V at TiO_2 irrespective of their reduction potentials on Pt.

The redox reaction observed in the first potential region between approximately -0.8 and $+0.3$ V is attributed to electron transfer through a rectifying junction; this explains the irreversibility of the CV curve and the quasi-reversibility observed under illumination. This behavior indicates that the redox potentials of the chosen redox couple are within the band gap region. The behavior of the CV more negative than -0.8 V can be attributed to the formation of an accumulation layer and metallic behavior of the semiconductor. This behavior indicates that the redox potential is above E_C . The CV behavior in the third potential region positive of $+0.4$ V is attributed to the mediation of electron transfer through the surface state. Based on these results, the suggested band diagram for TiO_2 electrode is depicted in Figure 9.21.

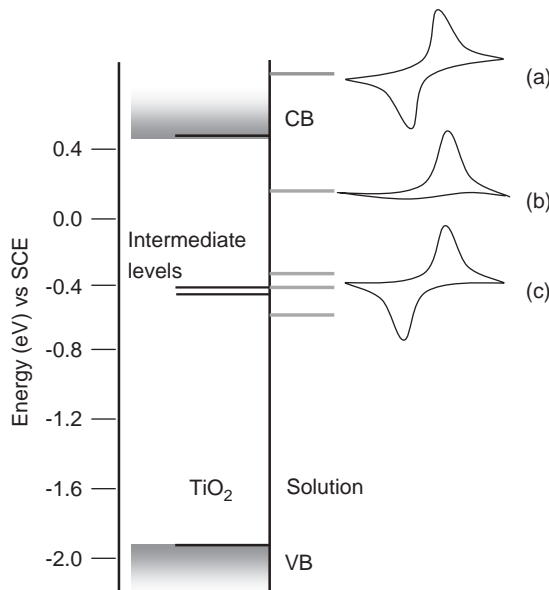


Figure 9.21 Band diagram for n-type single-crystal TiO_2 electrode based on CV measurements. (a) CV recorded for redox having redox potential above E_C . Reversibility of CV indicates metallic behavior of the electrode. (b) CV recorded for a redox having redox potential below E_C . Irreversibility of CV indicates rectifying nature of the junction. (c) Same CV for redox couples having redox potentials negative to ca. -0.3 V, indicating electron transfer through the surface states in this potential region.

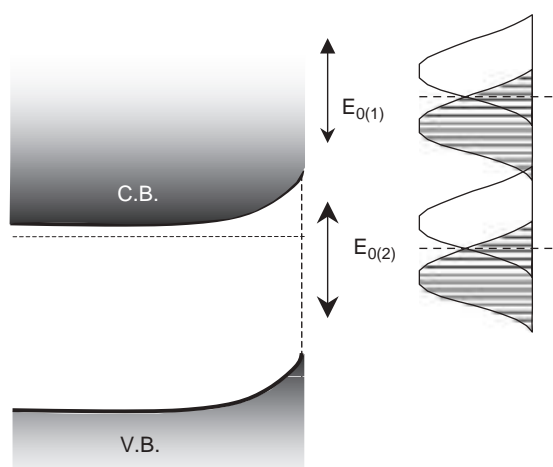


Figure 9.22 Determination of flat-band potential by CV. Reversible redox couple with two-electron transfer systems is chosen such that $E_{0(1)}$ lies in the CB and $E_{0(2)}$ lies in the band gap.

Thus, with the help of voltammetric experiments in a judiciously chosen redox couple, one can pinpoint various energy states in the bulk as well as on the surface of the semiconductor. This model was further supported by CV results obtained on WSe₂ in aqueous solution (34, 35), GaAs in molten salt (36), Si, n-type ZnO, CdS, and GaP electrodes in acetonitrile (21), and CdS, GaP, GaAs, and p-type Ge in *N,N'*-dimethylformamide (37).

To obtain information about the energetics of semiconductor electrodes using CV, it is not necessary to have a series of redox couples whose E_{redox} are distributed in the entire band structure. In fact, one can pinpoint the flat-band position E_{fb} by recording CVs for just one redox couple having two-electron systems, A⁺/A and A²⁺/A¹⁺, with respective redox potentials $E_{0(1)}$ and $E_{0(2)}$, such that these potentials lie above and below E_C . The situation is sketched in Figure 9.22.

A typical result reported (38) on an n-MoS₂ electrode with redox couples BF and TMPD⁷ is depicted in Figure 9.23. Note that both TMPD and BF exhibit two reversible one-electron waves at Pt as shown in Figures 9.23a and c. However, at MoS₂ in the dark, there is one reversible wave under the same condition and at the same potential as at Pt (refer to Figures 9.23b and d).

This situation indicates that the electrode is degenerated at that potential and behaves like a metal. The second oxidation wave appears on illumination, which was not seen in dark. As discussed in Section 9.4.2, photo-oxidation at an n-type semiconductor is prevalent if the redox potential lies within the band gap. Thus, the second wave observed upon illumination was assigned to the oxidation of TMPD⁺ to TMPD²⁺ or BF⁺ to BF²⁺. Quite interestingly for BF, the CVs recorded in the dark and under illumination are separated by approximately 0.20 V. The onset of a photocurrent for both TMPD and BF is at

⁷BF and TMPD refer to biferrocene and N,N,N',N'-tetramethyl-p-phenylenediamine, respectively.

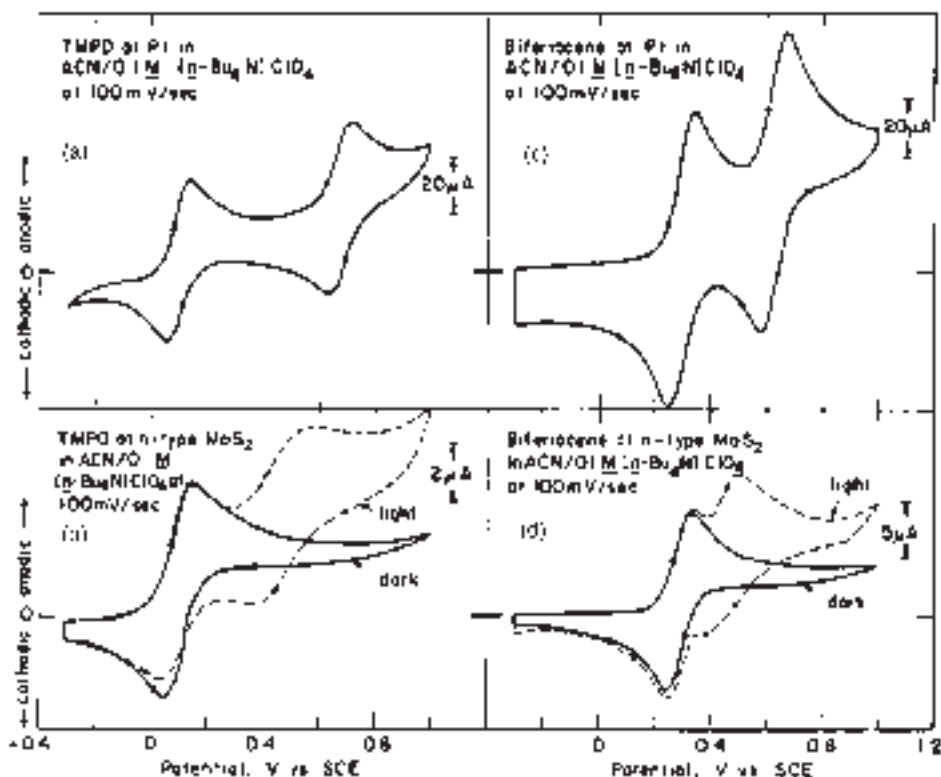


Figure 9.23 Comparison of CV for TMPD (a and b) and biferrocene (c and d) at Pt and MoS₂ (dark or illuminated). Illumination was with 632.8-nm light at 50 mW cm⁻². Reprinted with permission from reference (38). Copyright 1979, American Chemical Society.

approximately +0.3 V. Thus, one can bracket E_{FB} between 0.3 and 0.5 V where a second wave appears on illumination.

Though CV has been extensively used to probe the SEI, there are very few papers that describe the analytical theory for the CV response of a semiconductor electrode in the dark as well under illumination. Of the few, the prominent one is developed by Lewis and co-workers, where analytical solutions have been proposed for a redox couple that is adsorbed on the surface (30) as well as one having diffusion freedom (31) in solution. The model was later supported by relevant experiments (39). The equivalent circuit used for the simulation is shown in Figure 9.24.

The additional circuit elements account for the effect of capacitance (C_d) at the electrode-solution interface, background current (I_Z), and solution resistance (R_s). Figure 9.25 represents some of the results that were compared with simulated CVs obtained for an Si electrode in 1.2 mM Me₂CoCp₂PF₆ (redox)/1.0 M TEABF₄ (supporting electrolyte) in acetonitrile in an electrochemical cell having a Pt counter electrode and at various illumination periods. As can be seen, there is an excellent agreement between simulations and experiments.

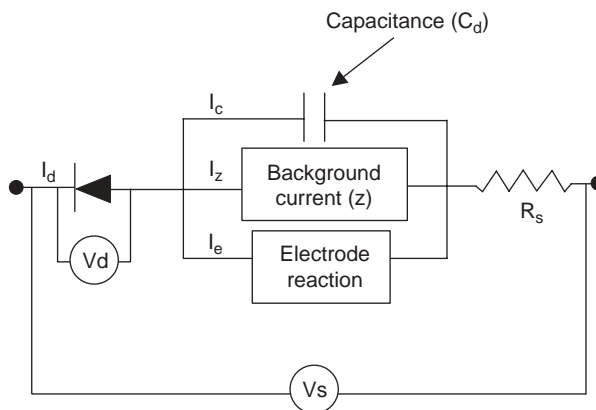


Figure 9.24 The equivalent circuit used as a model for the ideal semiconductor–liquid interface, including the effects of capacitance at the metal electrode–solution interface (C_d), background current (Z), and series resistance losses in the electrolyte (R_s). Adapted from reference (39).

9.4.4 Fermi-level pinning in semiconductor electrodes

Most of the results discussed in Section 9.4.3 have been explained on the basis of a simple model for an ideal SEI, which was first proposed by Gerischer (16). In the model, the redox system in solution is considered to have fluctuating energy levels (distribution functions, clarify with Figure 9.13) described by Marcus (19). The band structure of the interface will be decided by bulk energy levels of the semiconductor and redox couple. Charge transfer takes place between the semiconductor and redox states by tunneling through Helmholtz layers. However, as seen in Section 9.4.3 with the TiO_2 /redox system, identical CVs were observed over a particular potential range irrespective of the redox potential. This suggests that there are states on the surface⁸ that are involved in the charge transfer. If these states are present in the band gap, then the charge transfer will be preferentially mediated by a surface state as illustrated in Figure 9.26.

The energetics of the SEI will now be driven by surface states rather than by the bulk state of the semiconductor. In such a situation, the barrier height (or band bending), which can be changed by choosing the appropriate redox couple (41), is now more sensitive to the parameters as a result of surface pretreatment, cleaning of the surface, adsorption, etc. It appears as if the Fermi level of a semiconductor is ‘pinned’ at the given energy. The phenomenon is called *Fermi-level pinning*. Historically, this phenomenon is reported for a semiconductor/metal Schottky barrier in which surface states of the semiconductor give rise to a fixed barrier height, independent of the metal (42, 45). It has

⁸The surface of any solid is energetically different from that of the bulk. This is due to a variety of reasons including unsatisfied valence of surface atoms, formation of oxide layers, and adsorption of foreign atoms and molecules. It amounts to a different set of energy states at the surface than that of the bulk, which are called surface energy states or simply ‘surface states’.

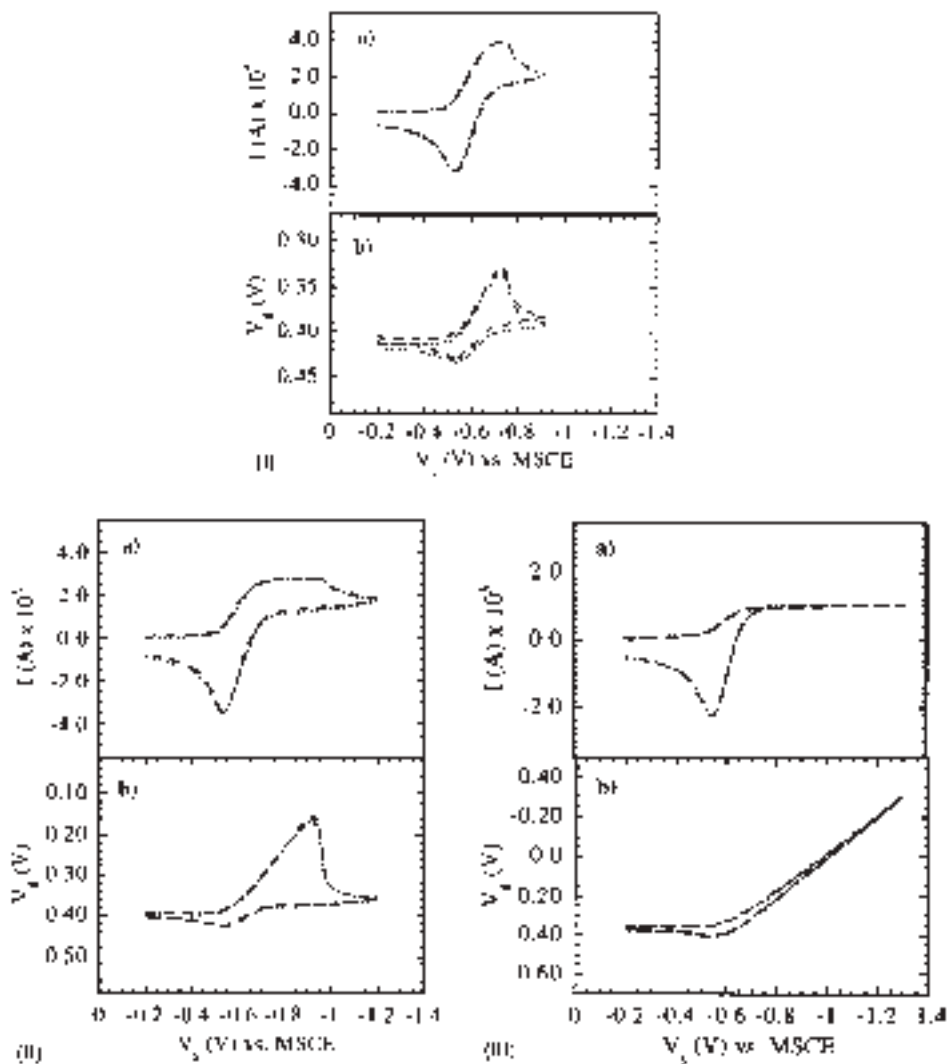


Figure 9.25 Experimental (dash) and simulated (dotted) cyclic voltammograms of n-Si photodiode at various levels of illumination (various values of light-induced current (I_L)). At (I) $I_L = 4.40 \times 10^{-5}$ A, (II) $I_L = 2.80 \times 10^{-5}$ A, and (III) $I_L = 1 \times 10^{-5}$ A. All figures with label (a) are I - V curves and label (b) are plots of voltage drop across photodiode (V_d) as a function of applied voltage V_s vs. SCE. Reprinted with permission from reference (39). Copyright 1998, American Chemical Society.

been further identified in the case of various semiconductors including GaAs (26, 46), Si (32, 40), n-CdSe (47), and n-CdS (48) in solutions. These investigations suggest that ionic semiconductors (large band gap oxides) give more ideal behavior (41) than the covalent (e.g., GaAs) and elemental semiconductors (e.g., Si) do. Thus, the observed Fermi energy pinning can be unambiguously attributed to the surface states. Note that

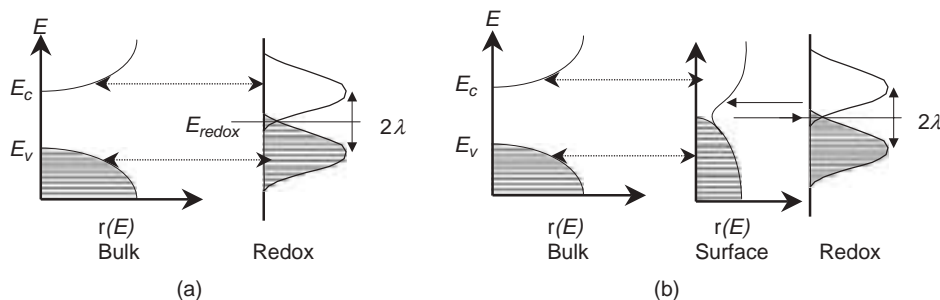


Figure 9.26 Schematic diagrams for energy vs. density of states for semiconductor-electrolyte interface (SEI). (a) An ideal interface described by Gerischer's model, where direct transfer of charge between bulk energy states of semiconductor and redox takes place, and (b) transfer of charge mediated through surface states. The hashed curves represent filled states. λ represents solvent reorganization energy from Marcus theory. Adapted from reference (40).

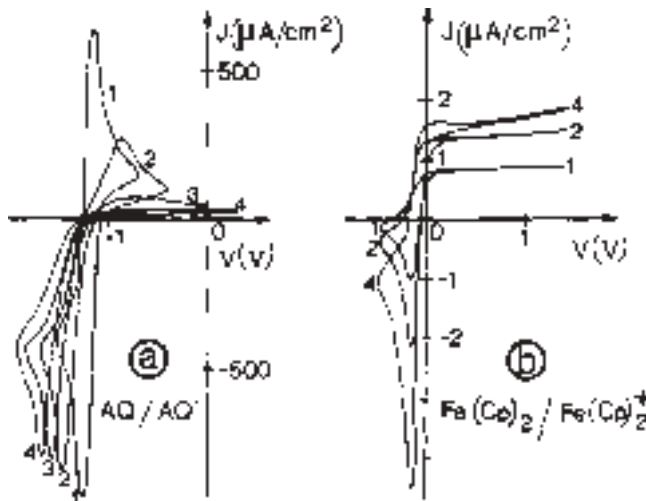


Figure 9.27 CVs for two representative redox systems (a) AQ/AQ^- and (b) $\text{Fe}(\text{Cp})/\text{Fe}(\text{Cp})^+$ at different durations of immersion, t : (1) $t = 5$ min, (2) $t = 30$ min, (3) $t = 1$ h, and (4) $t = 2$ h. The increase of the cathodic peak in part (b) is due to the increase of the (initially zero) ferricinium concentration upon potential cycling. Reprinted with permission from reference (32). Copyright 1981, American Chemical Society.

due to the dynamic nature of the SEI interface, the surface constituents may change with time; this amounts to time-dependent electrochemical behavior.

Consider the following example. Figure 9.27 shows a CV recorded on an n-Si electrode immersed in acetonitrile with two redox couples: anthraquinone and its monoanion (AQ/AQ^-) and ferrocene/ferrocenium ($\text{Fe}(\text{Cp})_2/\text{Fe}(\text{Cp})_2^{1+}$). In this experiment, care was taken in the experimental set-up so that once the electrode was introduced into the cell, it was not further exposed to the external atmosphere. Thus, effects due to surface oxidation

were minimized. As shown in Figure 9.27a, the electrochemistry of AQ/AQ^- initially gives a reversible CV similar to that obtained on a Pt electrode; this is indicative of a complete non-rectifying junction. As time passes (from curves 1 to 4 in Figure 9.27), the anodic peak reduces and finally disappears completely (curve 4) and the junction becomes rectifying. A similar observation was also found for the $\text{Fe}(\text{Cp})_2/\text{Fe}(\text{Cp})_2^{1+}$ couple (refer to Figure 9.27b). Interestingly, the photocurrent measurements carried out with these and various other redox couples exhibited the conversion of the barrier height to a single value ($\Delta\phi \approx 0.7 \text{ eV}$), irrespective of the redox potential of the couples. All of these results suggest a change in the interface with immersion time in solution from a *non-pinning* to a completely *pinned regime*, and the behavior can be attributed to a change in the surface properties due to adsorption. This behavior has also been reported in the case of CdS (49), GaAs (50), InP (29, 51), and CdTe (52) electrodes.

9.4.5 Characterization of the SEI by scanning electrochemical microscopy (SECM)

Scanning Electrochemical Microscopy (SECM) (53) is an electroanalytical technique that has been used to study the kinetics of electron transfer in a variety of substrates (54–58). However, there are very few reports about its use in investigating the SEI (23, 59–64). A detailed description of SECM is given in Chapter 12. There are also many review articles that deal extensively with this technique (65–68).

In short, SECM is a scanning probe technique similar to STM or atomic force microscopy (AFM). A tip current arises due to an electrochemical reaction (faradaic process) at an ultra-microelectrode (UME) tip (see Chapter 6). The tip generally consists of a Pt wire of diameter between 1 and 25 μm that is sealed in a glass capillary and polished to get a flat electrode surface. A typical voltammogram recorded on a UME is shown in Figure 9.28b. It is a sigmoidal, steady-state current–potential curve without any hysteresis.

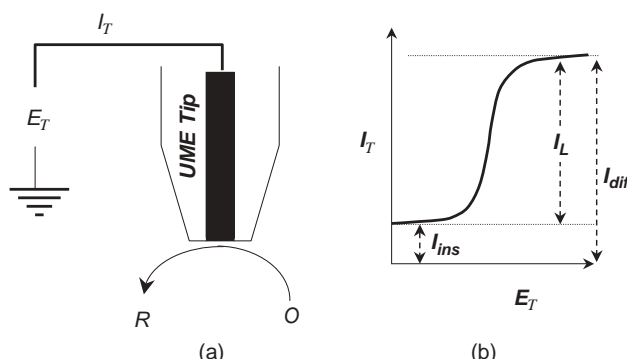


Figure 9.28 (a) An electrochemical reaction occurring at UME and (b) a corresponding voltammetric response. E_T and I_T stand for applied tip potential and measured tip current, respectively. I_L stands for limiting current.

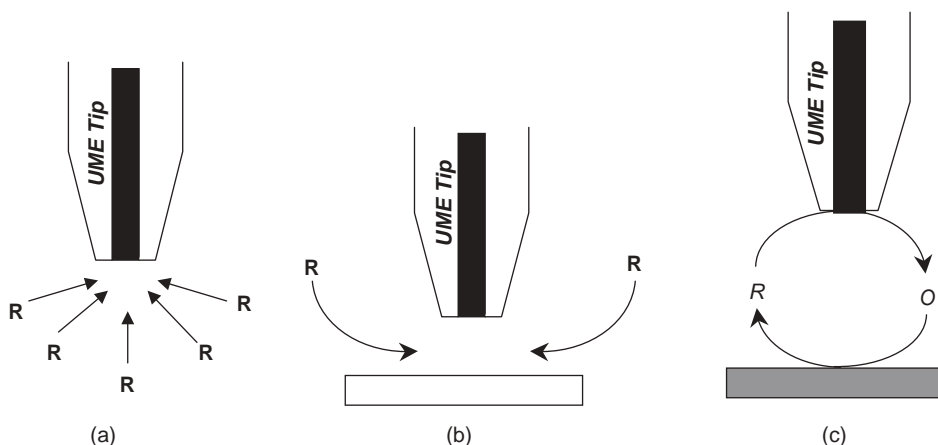


Figure 9.29 Feedback modes of SECM operations. The UME tip is poised at a potential E_T such that R will oxidize to O. (a) UME is freely hanging in the redox solution, $i_T = i_{T,\infty}$; (b) UME near the insulating substrate, the diffusion is blocked, called negative feedback, $i_T < i_{T,\infty}$; (c) UME near the conducting substrate, positive feedback from the substrate as O gets reduced back to R that leads to $i_T > i_{T,\infty}$.

To study the kinetics of electron transfer, SECM can be operated in two modes: a feedback mode (53, 69) and a substrate generation-tip collection mode (53). In the feedback mode, a mediator redox couple is required to probe the interface. The tip is poised to a potential well above E_{redox} . The steady-state current observed due to hemispherical diffusion of O toward the tip is expressed as (Figure 9.29a)

$$i_{T,\infty} = 4nFD_0C_0^*a \quad (9.4.9)$$

where a is radius of the tip. When a tip poised with a potential $>E_{\text{redox}}$ is brought very close (dimension on the order of the radius of the UME tip) to a substrate (in our case, the substrate is the semiconductor), then the diffusion of species O to the substrate will be blocked (Figure 9.29b), leading to a corresponding decrease in the tip current i_T .

A plot of tip current vs. distance between the tip and the substrate is called an approach curve and the decrease in current due to the blocking of diffusion to the tip is called *negative feedback*. In certain situations, R is regenerated back to O by the substrate as shown in Figure 9.29c. The result is a large flux of O to the tip and a corresponding increase in the tip current. Thus, the current at the tip increases as a function of its distance d from the substrate and the rate at which O is regenerated at substrate. This is called *positive feedback*. Typically, blocked diffusion is observed over an insulating substrate while positive feedback is observed over a conducting substrate when the kinetics of the redox process are reversible. Intermediate values of i_T are observed when electron transfer at the substrate is limited. In such situations, it is possible to deduce the rate constant of the charge transfer reactions.

Conventional techniques have limitations in studies of electron transfer kinetics at an SEI. In transient techniques such as CV, parallel processes such as electrode corrosion, charging of the double layer, and interference of IR drop contribute significantly to the

measured current as the electrode is poised to a desired potential. Hence, there is often a lack of agreement between an observed i - E curve and a proposed theory. Any attempt to use a low concentration of a redox couple to reduce the IR drop is likely to increase the contribution of the electrode corrosion current to the measured current. Steady-state voltammetric measurements with rotating disk electrodes (RDE) (23), wall jet electrodes (70, 71), or UMEs overcome these difficulties to some extent but it is very difficult to use semiconductors in an inlaid disk configuration.

These limitations can be overcome by SECM. One of the important advantages of SECM is that the tip does not need to be a semiconductor. Therefore, any semiconductor electrode can be probed using a Pt UME tip, for example. Since very small currents are measured at the UME tip, the IR drop is minimal. Additionally, the UME tip quickly reaches a steady state due to the small area of the electrode so that effects due to double layer charging are avoided. Because the UME tip is poised at a potential specific to the redox couple used, corrosion processes taking place at semiconductor electrode do not contribute to the tip current.

In the SECM feedback mode, the tip can be used to generate a high local concentration of a mediator. For example, if the semiconductor electrode is expected to reduce O to R from a solution of reduced species R, then the species O can be generated locally near the semiconductor surface underneath the tip by poising the tip at a sufficiently positive potential as shown schematically in Figure 9.30a.

If the semiconductor electrode does not reduce O to R, then the current at the tip will decrease due to blocked diffusion. The resulting tip current vs. distance approach curve can be fitted to the equation for an approach over an insulator. If the semiconductor substrate is poised to a potential sufficiently negative (E_S), then R is regenerated on the surface and the tip current increases. A typical plot of tip current (i_T) vs. substrate potential (E_S) is shown in Figure 9.30b. At intermediate values of E_S , the tip current may be limited by the heterogeneous rate constant (k_{et}) involved in the electron transfer reaction at the substrate.

The total tip current, i_T , can be expressed as the sum of the current due to the diffusion of O in the gap between the tip and the semiconductor surface, i_{ins} , and the feedback current due to regeneration of R at the substrate in the gap, i_{fb} (23)

$$i_T = i_{ins} + i_{fb} \quad (9.4.10)$$

The current component i_{fb} is the current at substrate i_s . Thus,

$$i_s = i_{fb} \quad (9.4.11)$$

Therefore, the flux or mass transport rate ($\text{mol s}^{-1} \text{cm}^{-2}$) at the semiconductor substrate is given by

$$m_o = \frac{i_s}{nFAC_o^*} = \frac{i_T - i_{ins}}{nFAC_o^*} \quad (9.4.12)$$

where C_o^* is the bulk concentration of the redox molecule. For a uniformly accessible electrode, the current due to an irreversible electron transfer is given by

$$i = \frac{nFAC_o^* m_o}{1 + (m_o / k)} \quad (9.4.13)$$

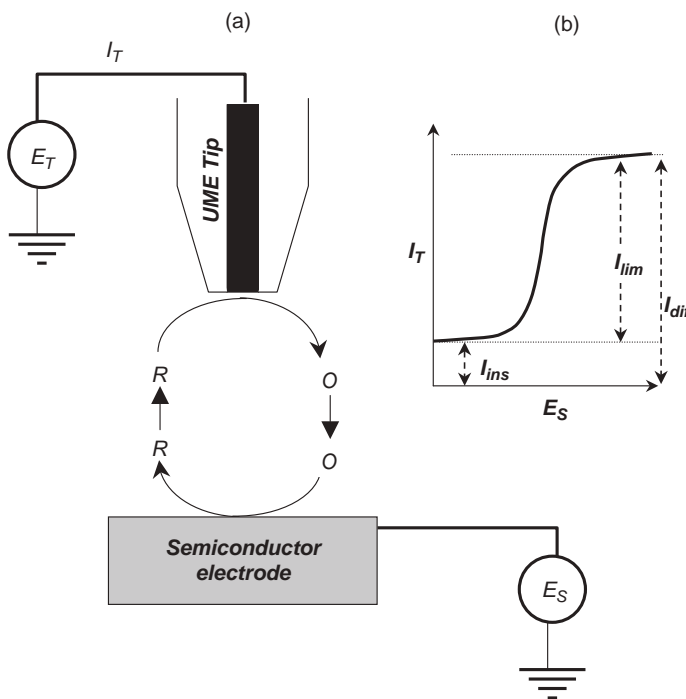


Figure 9.30 Schematics of the feedback SECM for measurements of electrochemical heterogeneous rate constant at semiconductor electrode. (a) UME tip is poised at positive potential, so that R will get oxidized to O at diffusion control rate. When the tip is closed to the substrate surface, O may get re-reduced at semiconductor electrode, depending on the potential at which semiconductor electrode is polarized (E_s). Thus, I_T depends upon rate of reduction of O on semiconductor surface. (b) A steady-state irreversible voltammogram (I_T vs. E_s).

where k is the electrochemical heterogeneous rate constant that follows Butler–Volmer kinetics according to

$$k = k_0 \exp\left[\frac{\alpha nF(E - E^{\circ'})}{RT}\right] \quad (9.4.14)$$

where α is transfer coefficient and $E^{\circ'}$ is the formal redox potential. Thus, the heterogeneous rate constant for a reaction taking place at semiconductor electrodes can be determined from SECM feedback approach curves.

Figure 9.31 shows a typical steady-state voltammogram ($i_T - E_S$) reported by Bard and co-workers (23) for the oxidation of $\text{Ru}(\text{NH}_3)_6^{2+}$ on p-WSE₂ in 0.5 M Na_2SO_4 . A UME tip was poised more negative than the $E_{1/2}$ (-0.23 V vs. saturated calomel electrode (SCE) in Na_2SO_4) of $\text{Ru}(\text{NH}_3)_6^{2+/3+}$ so that $\text{Ru}(\text{NH}_3)_6^{3+}$ generated at the p-WSe₂ semiconductor is reduced to $\text{Ru}(\text{NH}_3)_6^{2+}$ on the Pt tip.

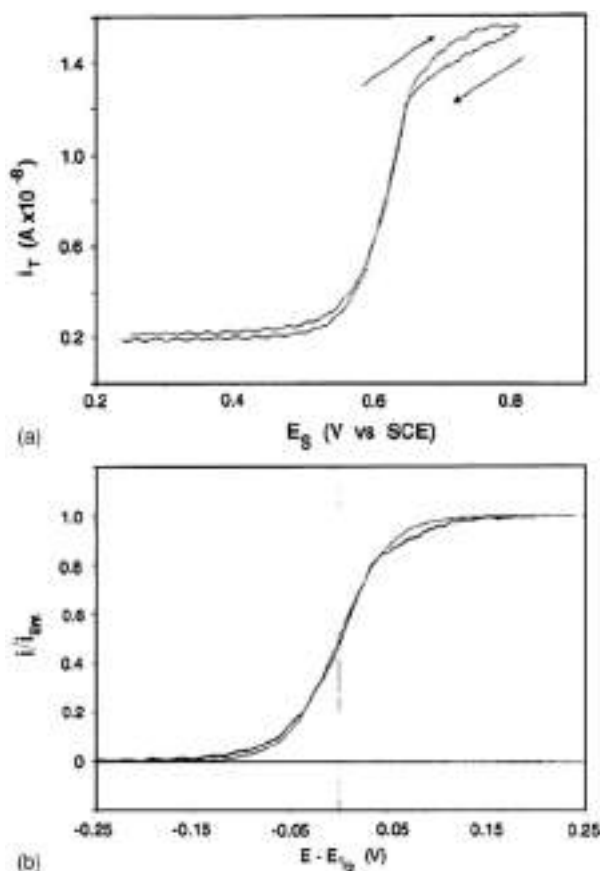


Figure 9.31 Kinetic voltammograms (i_T vs. E_s) for the oxidation of $\text{Ru}(\text{NH}_3)_6^{2+}$ on p-WSe₂ in 0.5 M Na₂SO₄. The tip was 10-μm diameter platinum and the concentration of $\text{Ru}(\text{NH}_3)_6^{2+}$ in the bulk solution was 4.78 mM. (a) A raw data and (b) a fitted voltammogram (bold line is experimental). Reprinted with permission from reference (23). Copyright 1994, American Chemical Society.

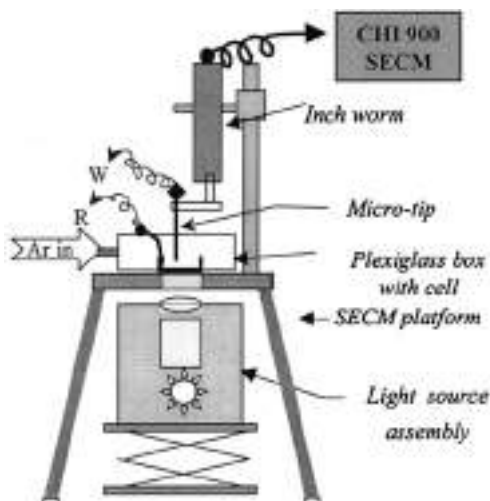
The potential of the substrate, i.e., p-WSe₂, was scanned from a region where $\text{Ru}(\text{NH}_3)_6^{2+}$ is not oxidized (below +0.66 V vs. SCE, which is the V_{FB} of p-WSe₂) to a potential region where the accumulation layer forms. As can be seen in Figure 9.31a, there is a transition from a low-current to a high-current regime at ca. +0.6 V, which fits very well to the theory (refer to Figure 9.31b). The m_0 and k_{et} values estimated for various redox concentrations are listed in Table 9.2.

SECM in the feedback mode has also been used to study the photoelectron transfer kinetics at an illuminated CdS/MV^{2+/1+} interface (63). The set-up used for these measurements is shown in Figure 9.32. In these experiments, CdS films were back-illuminated in the solution of a redox species (e.g., MV¹⁺) and a hole scavenger (e.g., triethanolamine (TEOA)). The Pt tip was poised for the oxidation of MV¹⁺, which is reduced back to MV¹⁺

Table 9.2Kinetic data for the oxidation of $\text{Ru}(\text{NH}_3)_6^{2+}$ on p-WSe₂/0.5 M Na₂SO₄

$\text{Ru}(\text{NH}_3)_6^{2+}$ (mM)	m_o (cm sec ⁻¹)	$E_{1/2} - E^{\circ'}$ (V)	k^o (10 ⁻¹⁶ cm sec ⁻¹)	K_{et} (10 ⁻¹⁷ cm ⁴ sec ⁻¹)
4.8	0.038	0.846	1.9	6.5
4.8	0.046	0.850	1.9	6.6
4.8	0.046	0.852	1.8	6.1
4.8	0.046	0.850	1.9	6.6
4.8	0.042	0.858	1.3	4.4
4.8	0.023	0.831	2.0	6.9
4.8	0.019	0.825	2.1	7.2
2.8	0.046	0.861	1.3	4.3
2.8	0.046	0.862	1.2	4.2
1.7	0.048	0.855	1.7	5.7
1.7	0.048	0.855	1.7	5.7
1.0	0.049	0.859	1.4	4.9
1.0	0.051	0.855	1.8	6.0
1.0	0.050	0.859	1.5	5.1
1.7 ± 0.6^a				5.7 ± 1.0^a

Reprinted with permission from reference (23). Copyright 1994, American Chemical Society.

^aMean value.**Figure 9.32** The set-up used for PET-SECM measurements. CdS film was back-illuminated. The cell was enclosed in the Plexiglas box. The positive pressure of Ar was always maintained in the box throughout the experiment in order to avoid air oxidation of MV¹⁺. Adapted from reference (63).

on the illuminated CdS film. Figures 9.33 and 9.34 show approach curves recorded for various light intensities and TEOA concentrations, respectively. As expected, there is a transition of the approach curve from insulating to conducting behavior on increasing either the light intensity or the TEOA concentration.

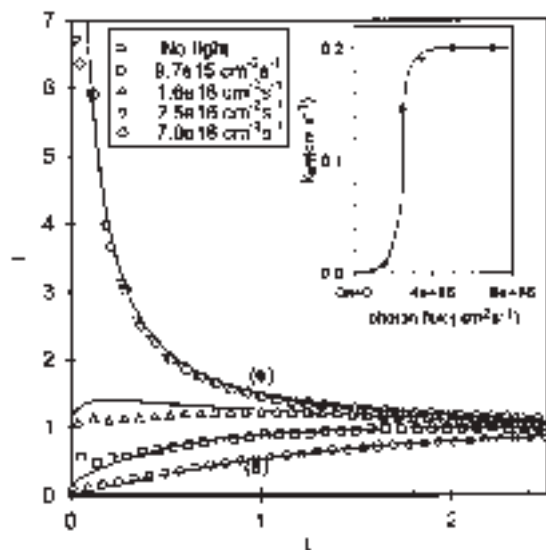


Figure 9.33 Approach curves recorded at various light intensities on CdS film in 0.1 mM MV^+ as a redox, 50 mM TEOA as a hole scavenger, and 0.1 M KCl supporting electrolyte in an inert atmosphere. (a) In the dark and (e) high intensity of illumination. The values of photon flux are given in the box. The solid lines are fitting to theory at various values of k_{eff} . The inset depicts a plot of k_{eff} vs. photon flux. The hyperbolic nature of the curve was attributed to the mass-transfer limit reached at high photon flux. The actual k_{eff} could be higher than 0.2 cm sec^{-1} at higher illumination at those intensities. Reprinted with permission from reference (63). Copyright 2001, American Chemical Society.

SECM in the *substrate generation and tip collection mode* (72) has been used for the estimation of spatially localized active sites on semiconductor electrodes (60, 61, 73). In this mode, electroactive species are generated by a redox reaction at the substrate and detected by a UME probe either amperometrically or potentiometrically. A typical set-up used for these kinds of experiments is given in Figure 9.35.

The corresponding SECM images obtained by these measurements are given in Figure 9.36a.

A local current density as large as 0.14 A cm^{-2} was observed for the oxidation of Br^- , which is four orders of magnitude higher than the average current density. These data also suggested that sites smaller than ca. 10 μm diameter are the most active for oxidation. Similar work has also been reported for Ta_2O_5 electrodes (60). Figure 9.37 shows the SECM image obtained for the oxidation of I^- on a Ta_2O_5 substrate. These results again suggest that a small cluster provides the most active site for the oxidation of I^- .

In another set of novel SECM experiments, a ZnO microelectrode (ca. 50 μm) was used as the UME tip instead of platinum and used to record steady-state voltammograms in various redox couples. The rates of electron transfer between the semiconductor tip and redox species such as ferricinium (FC^+), dimethyl-ferricinium (diM^+), and decamethyl-ferricinium (DM^+) have been estimated (64). Figure 9.38 shows steady-state voltammograms recorded with a 100- μm diameter ZnO microelectrode in various concentrations of diM^+ .

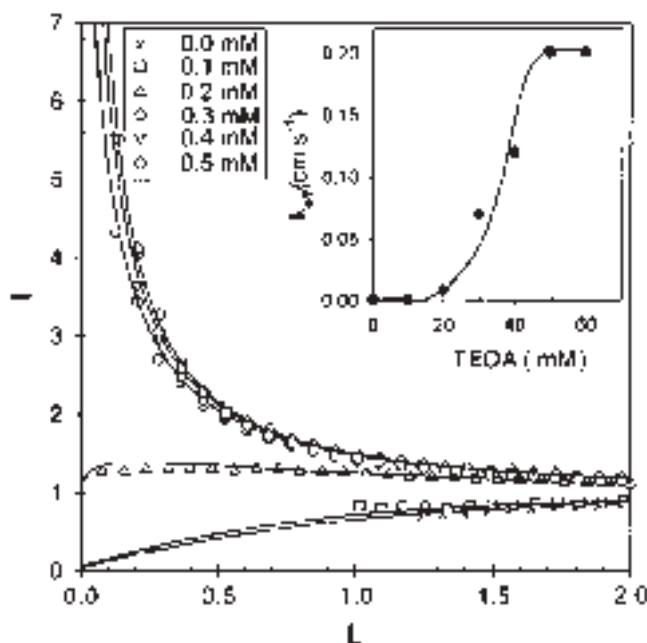


Figure 9.34 Approach curves recorded at various TEOA concentrations. $[\text{MV}^+]$ 0.1 mM in 0.1 M KCl. The solid lines are fitting to theory at various values of k_{eff} . The inset depicts a plot of k_{eff} vs. [TEOA]. Reprinted with permission from reference (63). Copyright 2001, American Chemical Society.

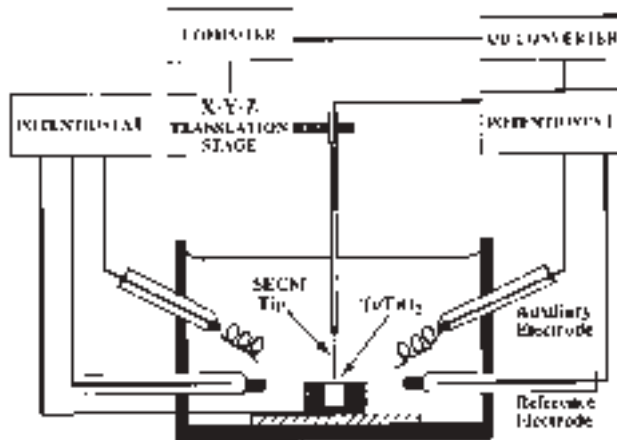


Figure 9.35 SECM set-up described in reference (71) for the determination of spatial distribution of active sites on semiconductor electrodes. Substrate potential (E_s) and the tip potential (E_T) were controlled independently by bi-potentiostat. Redox species generated on substrate were collected using UME tip, which is raster over surface by x - y piezo. The contrast is generated by the tip current i_T measured at (x, y) coordinates. Reprinted with permission from reference (73). Copyright 1998, American Chemical Society.

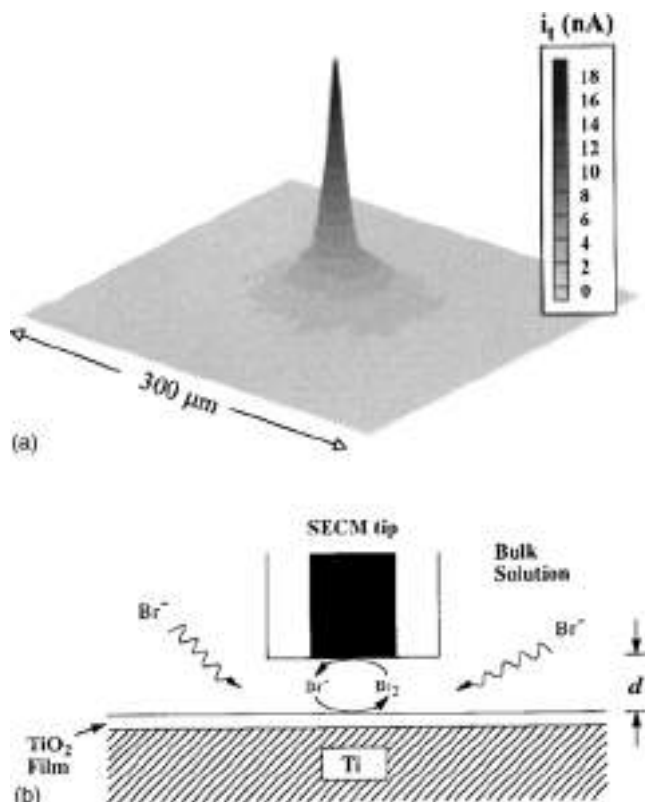


Figure 9.36 (a) $300 \times 300 \mu\text{m}$ SECM image of the electroactive site in a solution containing 50 mM KBr and 10 mM H₂SO₄. The potential of Ti/TiO₂ electrode (E_s) was held at 1.5 V to oxidize Br⁻. The potential of SECM tip (E_T) was held at 0.0 V, sufficiently negative to reduce Br₂ at the mass-transport limited rate. SECM tip was scanned at a height, d , of 5 μm above Ti/TiO₂ electrode. The image was recorded after the current at Ti/TiO₂ electrode had decayed to a steady-state value. (b) Schematics depicting SECM tip positioned above an oxide-covered Ti electrode. The tip radius and tip-to-Ti electrode separation are drawn approximately to scale. TiO₂ film (ca. 65 Å) is much thinner than drawn. Reprinted with permission from reference (73). Copyright 1998, American Chemical Society.

The steady-state current densities obtained from these data can then be approximately related to rate constants by the expression

$$j = Fk_{et}[\text{diM}^+] = Fk_0(e_{sf})[\text{diM}^+] \quad (9.4.15)$$

where k_{et} and k_0 are the pseudo-first-order rate constant (cm sec^{-1}) and the bimolecular rate constant ($\text{cm}^4 \text{ sec}^{-1}$), respectively, and e_{sf} is the surface concentration of electrons that is related to E_{fb} by the following relationship:

$$e_{sf} = N_d \exp \left[\frac{(E - E_{fb})e}{k_B T} \right] \quad (9.4.16)$$

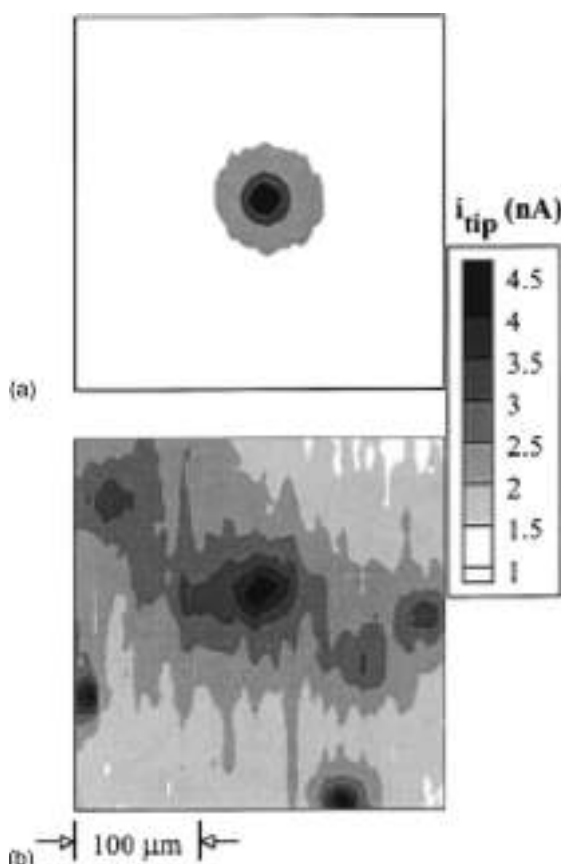


Figure 9.37 Representative SECM images ($300 \times 300 \mu\text{m}$) of $\text{Ta}/\text{Ta}_2\text{O}_5$ electrode in a solution containing 10 mM KI and $0.1 \text{ M K}_2\text{SO}_4$. The dark regions correspond to sites of high activity for the oxidation of I^- at $\text{Ta}/\text{Ta}_2\text{O}_5$ electrode: (a) an isolated site and (b) a cluster of sites. Four-micrometer radius SECM tip was scanned at $10 \mu\text{m s}^{-1}$ at a tip-to-surface separation, $d = 5 \mu\text{m}$, $E_T = 0.0 \text{ V}$, and $E_s = 1.0 \text{ V}$ vs. Ag/AgCl . Reprinted with permission from reference (59). Copyright 1999, American Chemical Society.

where E is the applied bias to the ZnO UME. A plot of the log of current density vs. applied potential is expected to be a straight line and the extrapolation at $E = E_{\text{fb}}$ gives values of k_0 as shown in Figure 9.39. These have been estimated to be 4×10^{-18} and $7 \times 10^{-23} \text{ cm}^4 \text{ s}^{-1}$, respectively, at $E = E_{\text{fb}}$.

9.5 TYPES OF SEMICONDUCTOR ELECTRODES

9.5.1 Single crystal and epitaxial film electrodes

The theory for semiconductor electrodes discussed in the previous sections is applicable to materials having long-range order in the lattice, as demonstrated by single-crystal material

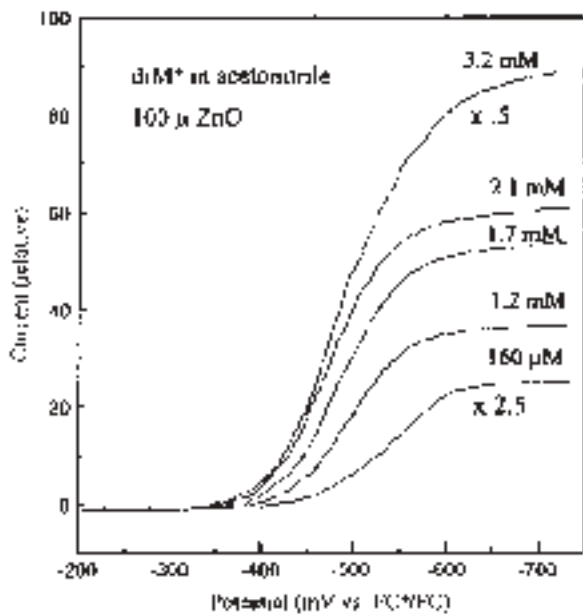


Figure 9.38 An example of a concentration study is given here for diM⁺ in which [diM⁺] is increased from 0.16 to 3.2 mM. The plateau current at a 100- μ m diameter ZnO electrode was found to be linear with [diM⁺] and the range of $E_{1/2}$ values was within 30 mV of the average of 510 mV, indicating that the rate constant did not change significantly with concentration. Reprinted with permission from reference (64). Copyright 2000, American Chemical Society.

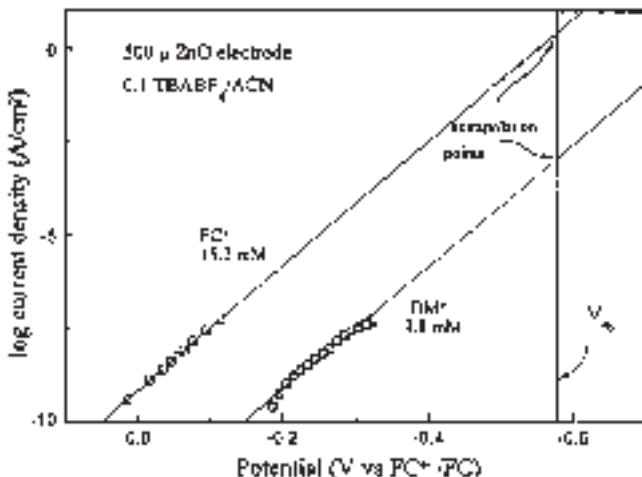


Figure 9.39 A plot of log of current density at steady state vs. applied bias at various concentrations of FC⁺ and DM⁺ on 500 μ m ZnO electrode. The reduction current is extrapolated to V_{fb} and k° is extracted from the result by the use of equations (9.4.15) and (9.4.16). Reprinted with permission from reference (64). Copyright 2000, American Chemical Society.

and epitaxial films. Their interfacial properties are spatially uniform and reproducible. Thus, many equations describing the transport and transfer of charges in them can be applied with accuracy. Layered metal dichalcogenide (LMD) semiconductors such as MoS_2 , WSe_2 , and SnSSe_2 , however, have anisotropic crystallographic properties that strongly influence the bulk and surface properties of the electrodes. Nevertheless, the molecularly smooth, chemically inert, and reproducible van der Waals surface of LMDs can easily be obtained by simply piling of the upper few layers with the help of adhesive tapes (34).

It is often difficult to obtain single crystals of semiconductors except for a few such as Si, GaAs, and InP that are routinely used by electronic industries. In a few cases, it is possible to grow a film of a few atomic layers thickness on the substrate with matching lattice parameters; these are called epitaxial layers. Techniques such as molecular beam epitaxy (MBE) and metal organic chemical vapor deposition (MOCVD) have been employed (74–77) for this purpose. It is also possible to grow a thick film (up to few micrometers) with long-range ordering; this is a semiconductor single-crystal membrane (78).

One of the important limitations in using single-crystal and epitaxial films as electrodes is that they are very expensive to prepare. Therefore, most of the studies have been undertaken with polycrystalline electrodes.

9.5.2 Polycrystalline electrodes

It is relatively easier to prepare electrodes of many semiconducting materials in which the size of the individual crystallites is small with respect to the diffusion length of the charge carriers. These charge carriers get scattered across the boundaries of the crystallites, called *grain boundaries*, and this poses a serious limitation in applying the Gerischer model for charge transfer. Additionally, the efficiency of charge transport is greatly compromised so that quantification of the electronic properties of the polycrystalline semiconductor electrodes is often difficult. Despite this problem, the preparation and characterization of polycrystalline electrodes have been intensely investigated. The rationale for this interest is the low-cost preparation of polycrystalline electrodes with a large surface area. The following sections describe methods of fabricating such electrodes.

9.5.2.1 Electrochemical deposition of semiconductor films

Electrochemical deposition has emerged as a powerful tool for growing high-quality semiconductor films (79) and nanostructures on a suitable substrate. Recent efforts have been focused on achieving atomic-level control on the growth process, which leads to the formation of well-ordered, epitaxial deposits of the desired material. Various baths used for electrodeposition of semiconductor films are listed in Table 9.3.

For chalcogenide films, a suitable complex of metal ions and selenium (H_2SeO_3) or a sulfur source is allowed to reduce simultaneously. The role of the complexing agent is twofold: (a) it avoids the reaction between the precursors in the bulk solution and (b) it helps in shifting the reduction potential of the metal ions to an optimum value so that one

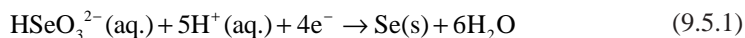
Table 9.3

Chemical bath conditions reported for deposition of semiconductors

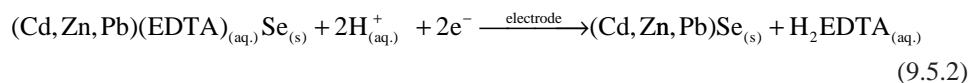
Films	Bath	Substrate	Potential/current	Bath temperature	References
CdSe	50 mM Cd(ClO ₄) ₂ + 5 mM Se in DMSO	Mica, Au	Galvanostatic	90–140 °C	(80–82)
CdSe	50 mM CdSO ₄ or CdCl ₂ + 0.3 M SeO ₂	Ti, Ni	Potentiostatic	R.T.	(83)
Cu ₂ O	CuSO ₄ + NaOH + lactic acid	Cu	Galvanostatic	R.T.	(84)
ZnO	Zn(NO ₃) ₂ + tetra-sulfonated metallothiocyanine	ITO	Potentiostatic	70 °C	(85)
CdS	CdCl ₂ + S in DMSO	ITO	Galvanostatic	R.T.	(86)
Ge	GeI ₄ in ionic liquids	Pt	Potentiostatic	R.T.	(87)
Ag ₂ Se	AgNO ₃ + KSCN + SeO ₂	ITO	Potentiostatic	R.T.	(88)
CuInSe ₂	CuCl + InCl ₃ + KSCN	Au	Potentiostatic	R.T.	(89)
PbSe	Lead acetate + SeO ₂	ITO	Potentiostatic	R.T.	(90)

R.T.: room temperature.

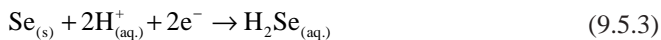
can bring both potentials to a value that facilitates simultaneous reductions. Plausible steps in the electrochemical reactions include



where due to proton involvement in the mechanism, an acidic pH facilitates the reaction



where Se formed on the electrode may also get reduced further through the mechanism



One of the major obstacles in electrodeposition of high-quality films of binary semiconductors is that one of the constituent elements may get plated simultaneously, leading to non-stoichiometric films. Thus, subsequent heat treatment is necessary to produce a film of acceptable quality. This problem can be overcome by sweeping the potential between a range where both constituents are reduced. For example, in the deposition of CdSe films, the potential was swept between –0.4 and –0.8 V vs. SCE in a low concentration of Se, which led to stoichiometric films. Using this technique, one can control the thickness of the film up to a few monolayers (83). By choosing the appropriate substrate and under-potential for deposition, it is possible to achieve an epitaxial growth of a semiconductor nanostructure called electrochemical atomic-layer epitaxy (ECALE) (91). The advantage of this method is that several kinds of structurally well-ordered thin films of compound semiconductors such as GaAs, CdTe, CdSe, and ZnS can be deposited.

Though it is relatively easy to carry out the electrodeposition from an aqueous bath, its major disadvantage is the narrow potential window available for the deposition. This problem has been overcome by carrying out the deposition in non-aqueous solvents. Moreover, elemental S and Se have the desired solubility in solvents such as *N,N*-dimethylformamide (DMF) and dimethyl sulfoxide (DMSO). Baranski and Fawcett were first to report the electrodeposition of CdSe films using non-aqueous baths of DMF (92) and DMSO (93). Non-aqueous solvents are also known to result in a deposition having nanocrystalline form (82). Use of cadmium salts having anions with adsorbing properties (such as Cl^- and Br^-) has been reported to result in deposition of CdSe nanoparticles (94). Precise control over bath temperature is known to control the size of the nanoparticles (82).

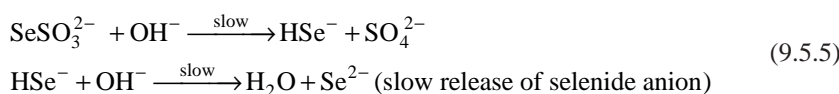
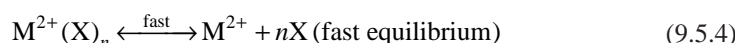
Besides non-aqueous solvents, it is possible to use room-temperature ionic liquids (RTILs) as media for electrodeposition (87). RTILs are fused organic salts that are in the liquid state at room temperature. They possess a wide range of liquid temperatures, in some cases higher than 400 °C, and have intrinsically useful characteristics including negligible vapor pressure, a wide liquid range and thermal stability, high ionic conductivity, and a large electrochemical window (95). Endres *et al.* demonstrated the electrodeposition of elemental semiconductors such as Ge films and nanoparticles in RTIL, namely 1-butyl-3-methylimidazolium hexafluorophosphate (87, 96).

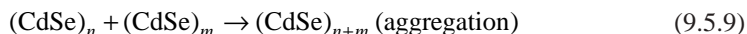
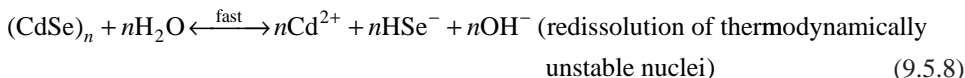
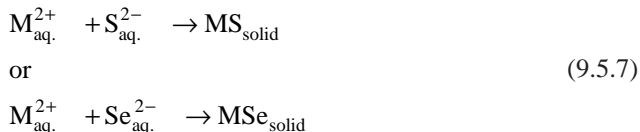
9.5.2.2 Electroless deposition of semiconductor films

Electroless deposition (ED) or chemical bath deposition (CBD), in general, consists of a spontaneous deposition of films on a conducting or an insulating substrate by carrying out a redox reaction in solution. These techniques have been known for hundreds of years for silvering mirrors. CBD has also been used for a long time to deposit semiconducting films. Various group II–VI materials such as lead, zinc, and cadmium chalcogenides in the form of films have been prepared routinely by this method. There are many review articles that describe this method (74, 75, 97, 98) in detail.

The basis of the CBD method is the slow release of anions (sulfide or selenides) with free metal ions (Cd^{2+} , Zn^{2+} , or Pb^{2+}) into a solution such that their concentration just exceeds the solubility product of semiconductor. In the bath, a low concentration of the cations is maintained by their complexation with ligands such as TEOA and/or ammonia. The anions are formed by hydrolysis of thiourea, in the case of sulfide, or hydrolysis of selenosulfate or selenourea, in the case of selenides. The material is precipitated due to a super-saturation condition when the concentration of sulfide/selenide anions exceeds the solubility product of CdS/Se .

A general reaction scheme for the deposition of group II–VI semiconductor films is as given below (98–101):





The rate-determining step in this series of plausible reactions is probably the slow release of selenide or sulfide by equation (9.5.5). Sulfide/selenide anions are consumed by two different mechanisms: one by nucleation and the other by growth of existing nuclei. The second step (i.e., growth) seems to be energetically more favorable.

AFM investigations of the electroless deposited CdS film on mica (102) suggest that the film can also be formed by ion-by-ion deposition on the substrate. This is in addition to the usually accepted notion of precipitation of clusters on the substrate that are already formed in the solution by homogeneous precipitation. Three plausible mechanisms are illustrated in Figure 9.40. In our experience, the film formed by deposition of clusters is powdery or chalky (refer to the mechanism illustrated in Figure 9.40b), and can be wiped off by tissue paper.

The ion-by-ion deposition growth, however, leads to an adherent mirror-like film, which cannot be pulled off even by a scotch adhesive tape. Ion-by-ion deposition methods have also been demonstrated for tandem deposition of CdS and ZnS thin films and Zn_{1-x}Cd_xS composites (103) on conducting glass. The effects of chelating agent, pH, and type of counter anions on the quality of ion-by-ion deposition have also been investigated (104).

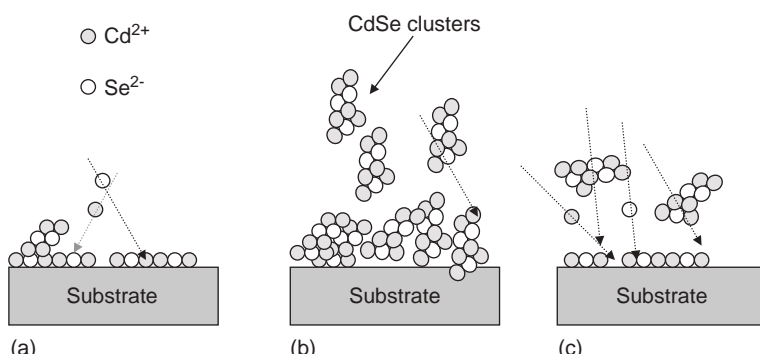


Figure 9.40 Three speculated mechanisms for the formation of semiconductor films by ED method: (a) ions are adsorbed on the substrate one by one, heterogeneous precipitation; (b) some of the clusters formed in the solution are deposited on the substrate; (c) mixed mechanism.

It is possible to use the substrate as one of the precursors. Deposition of thin films of Cu_{2-x}Se has been carried out by reacting a Cu substrate or a Cu film electrodeposited on Pt or Ti with H_2SeO_3 at an acidic pH (105, 106).

(a) Electroless deposition bath for the preparation of CdS and ZnS films

Various baths have been proposed for the ED of CdS thin films (98, 100, 103). As described in Section 9.5.2.2, a complex of Cd^{2+} ions is allowed to react with sulfide ions formed by the hydrolysis of thiourea. In principle, Na_2S or H_2S can also be used as the sulfurating agent but the reaction proceeds so fast that the deposition results in a powdery deposit. A typical protocol used by many authors for the deposition of CdS thin films on borosilicate- and indium tin oxide (ITO)-coated glasses is as follows:

One hundred and fifty milliliters, 0.2 M TEOA is mixed with 10 mL, 0.1 M cadmium acetate solution in a 250 mL reagent bottle. After stirring for about 30 min, 10 mL of 0.2 M thiourea is added. The solution is stirred for approximately 10 min. One milliliter of 30% NH_4OH solution is added to the bath. All of the contents are then transferred into a preheated (60 °C) and thermostated crystallization dish with a lid. Prior to the addition, about eight precleaned glass slides are arranged vertically in PTFE, with a ring-shaped holder having vertical notches. The solution is stirred continuously during the deposition. After an hour, the substrates are withdrawn and transferred immediately to preheated (60 °C) distilled water to avoid peeling of the films due to the thermal shock. After cooling to room temperature, the films are rinsed with a copious amount of distilled water and dried under vacuum.

The quality of the films is strongly dependent on the cleaning and pretreatment of the substrates. Prior to deposition, the glass slides are etched with *Piranha* solution.⁹ ITO-coated slides are cleaned with a solution of 2 M KOH in 2-propanol. After cleaning, these are stored in distilled water. In our experience, acidic surfaces do not give a desired deposition. We observed that etched slides soaked overnight in ammonia solution lead to a uniform deposit. So far, the reason is not clearly understood. Hydroxyl groups formed on the surface possibly lead to the formation of $\text{Cd}(\text{OH})_2$ on the surface that, perhaps, acts as nucleation center (97). ZnS films can also be prepared using a similar strategy. Various baths used for these films have been reported by O'Brien and McAleese in detail (97).

(b) Electroless deposition bath for the preparation of CdSe films

CdSe films are deposited by reacting Cd^{2+} ions with Se^{2-} ions that are generated *in situ* by the hydrolysis of Na_2SeSO_3 in ammonium hydroxide. Ammonium ions in the solution also act as complexing agents that facilitate the slow release of Cd^{2+} ions in the solution (99). Better results are obtained by using separate complexing agents such as amines. The protocol suggested by Hodes (98) for the ED of CdSe is as follows:

Two milliliters of 0.5 M Cd^{2+} is diluted with approximately 3.4 mL of distilled water. To this, 2.1 mL of 0.7 M potassium salt of nitrilotriacetic acid (KNTA)-complexing agent is

⁹Mixture of 30% H_2O_2 and concentrated H_2SO_4 in 1:3 ratio. Extreme precaution is necessary in handling the solution. Experiments should not be done without a proper fume-hood.

added. The pH of the solution is adjusted to 8 and 5 mL of 0.2 M Se (Na_2SeSO_3) is added to it. After stirring, the solution is transferred to the thermostated bath containing pre-cleaned slides and the deposition is carried out as described previously.

Na_2SeSO_3 is prepared by refluxing Se metal powder with concentrated Na_2SO_4 solution (107). Typically, to prepare a 50 mM solution of Na_2SeSO_3 , 0.0987 g of Se powder is refluxed with 0.5 g Na_2SO_4 in 20 mL distilled water in a round bottom flask fitted with an air condenser for 3–4 h. An excess concentration of Na_2SO_4 is necessary to prevent decomposition of Na_2SeSO_3 back into Se and Na_2SO_4 . After cooling down, the solution is filtered and diluted to 25 mL in a standard measuring flask. This solution should be used immediately for the synthesis.

9.6 NANOSTRUCTURED SEMICONDUCTOR ELECTRODES (NSSE)

The effect of size quantization on the electronic properties of semiconductors, discussed in Section 9.2.2, demonstrates that semiconductor electrodes made of nanostructured particles are of great practical interest. Based on size quantization, these films can be categorized into: (a) thin semiconductor films deposited or epitaxial growth on a substrate where the SQE is due to the space confinement in two dimensions (i.e., a quantum well) and (b) particulate films of size-quantized nanoparticles that may be several micrometers thick; their properties are due to the combined effect of film and isolated size-quantized particles. Both the situations are illustrated in Figure 9.41.

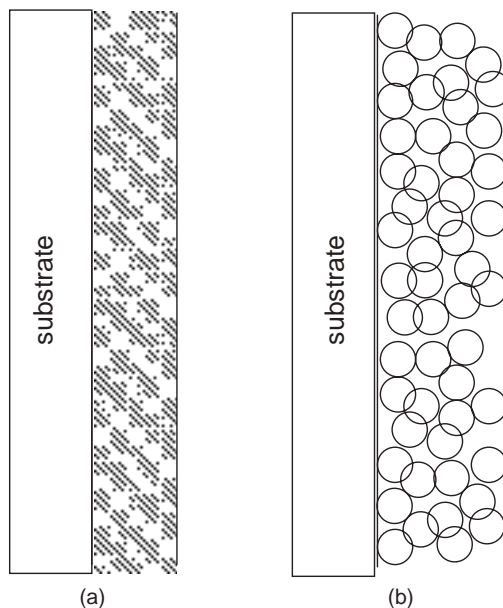


Figure 9.41 Types of nanostructured semiconducting films: (a) quantum well prepared by epitaxial growth in nanometer thickness and (b) particulate film in micrometer thickness.

9.6.1 Epitaxial methods for the preparation of NSSE

Nozik and Memming have worked extensively on the electrochemistry and photoelectrochemistry of quantum well semiconductor electrodes (14). As discussed in Section 9.5.1, the quantum wells are produced by either MBE or MOCVD method. Both of these techniques are capable of creating epitaxial layers exhibiting quantum size effects. Their properties can be varied by film thickness, interfacial abruptness, and crystalline perfection.

In MBE, ultra-high vacuum chambers are outfitted with a number of evaporation cells. Each cell has a shutter to control the molecular flux. The molecular beam can be pulsed within 0.1 sec and the growth rate can be controlled within a few Å sec⁻¹. During the growth, the substrate temperature is maintained at ca. 500–700 °C. Atomic species most commonly used include Al, In, Sb, Be, Ge, Se, Te, Cd, Hg, Zn, Mn, Pb, and Si. The most common quantum well electrodes produced by MBE are the III–V semiconductors binary and ternary compounds. Some II–VI quantum well structures have also been prepared.

MOCVD is used only to prepare III–V semiconductors. Using this method, the group III metals are introduced in the form of their organometallic vapors. Each reacts with the gaseous precursors of non-metalloid group V components of the desired semiconductor compound to form a crystalline, epitaxial film on a hot substrate. For example, Ga, Al, and In are commonly introduced in the form of their trimethyl compounds. As and P are introduced in the form of arsine or tetrabutylarsine and phosphine or tetrabutylphosphine, respectively. Organometallics are introduced in the reaction chamber by passing hydrogen gas at a controlled flow rate through liquid organometallics. The single-crystal substrate is kept on the graphite block preheated at 650–750 °C.

9.6.2 Preparation of particulate films

Nanocrystalline particulate films, which exhibit pronounced quantum size effects in three dimensions, are of great interest due to applications in solar cell (108–112) and sensor (57, 113–115) applications. They exhibit novel properties due to not only the SQE manifested by individual nanoparticles but also the total surface area. Unlike MBE and MOCVD methods used to prepare quantum well electrodes, these electrodes can be prepared by conventional chemical routes described in Section 9.5.2.2. For example, II–VI semiconductor particulate films were prepared by using low concentrations of precursors and by controlling the temperature of the deposition bath. Hodes demonstrated the SQE for CdSe thin films deposited by an electroless method (98). The blue shift in the spectra of CdSe films has been demonstrated to be a function of bath temperature. As described in Section 9.5.2.1, electrodeposition of semiconductors in non-aqueous solvents leads to the formation of size-quantized semiconductor particles. On a single-crystal substrate, electrodeposition methods result in epitaxial growth (116, 117), and demonstrate quantum well properties.

Nanoparticles can be ‘anchored’ on a substrate by forming covalent bonds between the substrate and the capped nanoparticles. For example, ITO glass can be modified by (3-mercaptopropyl)trimethoxysilane (MPTMS), which leads to the formation of thiol

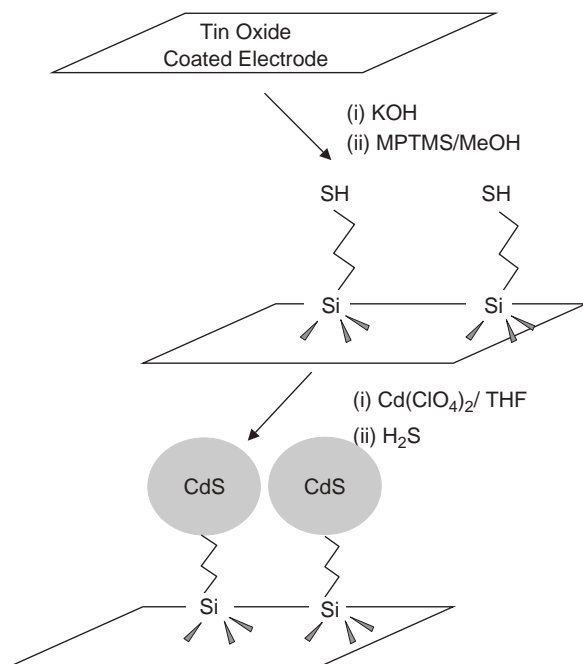


Figure 9.42 Schematic for surface modification of ITO glass with (3-mercaptopropyl)trimethoxysilane (MPTMS) followed by anchoring of CdS nanoparticles to the pendant thiol group. Adapted from reference (118).

pendants on the glass surface (118–120). Nanoparticles can be anchored to ITO glass through these pendants, as shown in Figure 9.42.

Similar work has been reported by Bard and co-workers where CdS nanoparticles were attached to a gold substrate using hexanedithiol (121). Using this method, it is possible to deposit multilayers that form an addressable three-dimensional quantum dot structure. Template methods have been used to deposit semiconductors of various shapes and sizes. For example, Li demonstrated the use of anodic aluminum oxide (AAO) templates to deposit CdS nanowires with a large aspect ratio (122).

Fendler's group recognized that semiconductor nanoparticle films can be synthesized by exposing a fatty acid monolayer complex of Cd^{2+} ions to gases (123, 124) such as H_2S . These films are called Langmuir–Blodgett (LB) films; they can be transferred to a suitable substrate for further characterization and use. The LB technique was further refined by Pan *et al.* to form LB films with CdS nanorods (125). Yoneyama and co-workers reported the fabrication of two-dimensional organized CdS nanoparticle films by cross-linking 2-aminoethanol-capped CdS nanoparticles with glutaraldehyde prior to their transfer to the substrate (126), as shown in Figure 9.43.

Coulombic interaction between capped particles can be used to organize the particles on the substrate (127–129). In one such example, polyacrylate-capped CdS nanoparticles were synthesized and assembled layer by layer on poly(diallyldimethylammonium chloride)

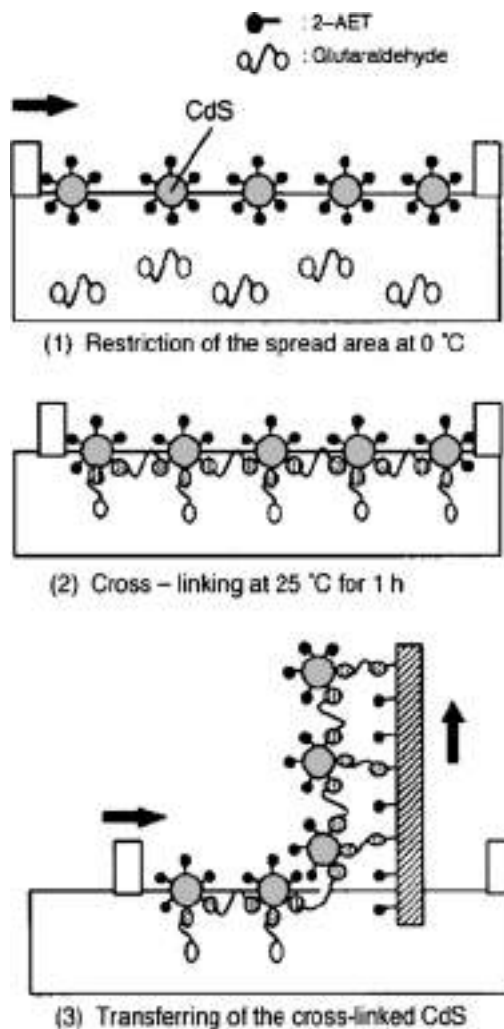


Figure 9.43 Schematic illustration of two-dimensional cross-linking of 2-aminoethanethiol-capped CdS nanoparticles spread on air–water interface that is transferred on suitable substrate. Reprinted with permission from reference (126). Copyright 1999, American Chemical Society.

coated on various substrates by virtue of the coulombic attraction between the negatively charged polyacrylate surface of the particles and cationic polyelectrolyte on a substrate. It is depicted schematically in Figure 9.44.

9.6.3 Electrochemistry on nanostructured semiconductors

Electrochemistry on nanostructured semiconductors may be classified according to the mode of charge transfer between the nanophase materials, the substrate, and the redox couple. The

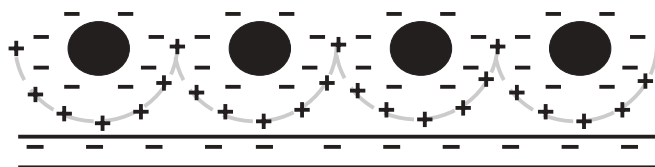


Figure 9.44 A schematics for coulombic interaction between particles and support; negatively charged polyacrylate-capped Q-CdS embedded in positively charged polyelectrolyte. Adapted from reference (127). Copyright 2001, American Chemical Society.

electrochemistry involved in charge transfer between an electrode modified with semiconductor nanoparticles and a redox couple in solution is similar to that discussed in Section 9.4 for bulk materials. A series of papers published by Gratzel and co-workers (109, 110), Liu and Kamat (130), Hodes (98, 117), and Fendlar and co-workers (62) report the electrochemistry of particulate films including TiO₂, ZnO, CdS, and CdSe pertaining to photoelectrochemical (PEC) applications.

Studies on charge transfer between addressable semiconductor nanoparticles and redox couples are quite novel. Riley and co-workers reported PEC measurements on CdS nanoparticles ‘tailored’ to ITO glass by a covalent linkage (118) as shown in Figure 9.42. A plot of photocurrent vs. the wavelength of light, called an action spectrum, recorded on these devices as a function of the size of the nanoparticles is shown in Figure 9.45. This group further investigated the kinetics of charge transfer between well-addressed tailored particles and the redox couple by electrochemical impedance spectroscopy and photocurrent transient measurements (119, 120).

9.6.4 Electrochemistry on suspended semiconductor nanoparticles

Photoelectrochemical (PEC) measurements on small semiconductor particles are of interest because of their possible applications in photocatalysis in addition to being a fundamental probe to study photolytic and electron transfer reactions at interfaces. The energetics of the particles differ, however, from the bulk. For extremely small particles, the Fermi level shifts to more negative values due to the quantum size effect. With slightly larger particles, photogenerated electrons can have energy that is different from that of the CB edge E_c of the bulk semiconductor in contact with the same solution. Thus, measurements of the energetics of dispersed particles are very important in deciding whether a given particle is in a position to reduce or oxidize the species in the solution. One of the ways to measure these properties is to collect the photogenerated electrons at an inert metal electrode immersed in the particle dispersion. The potential of the electrode can be adjusted such that it will be in position to collect the electrons, which will give an idea about the redox properties of the electrons photogenerated on the particles. Such a measurement carried out on a TiO₂ suspension is shown in Figure 9.46, where the onset of the anodic photocurrent suggests the position of the Fermi level in the particles.

These types of measurements have been confirmed for various semiconductor dispersions (27, 131–133) including TiO₂, In₂O₃, SnO₂, CdS, WO₃, and Fe₂O₃, and demonstrated that the

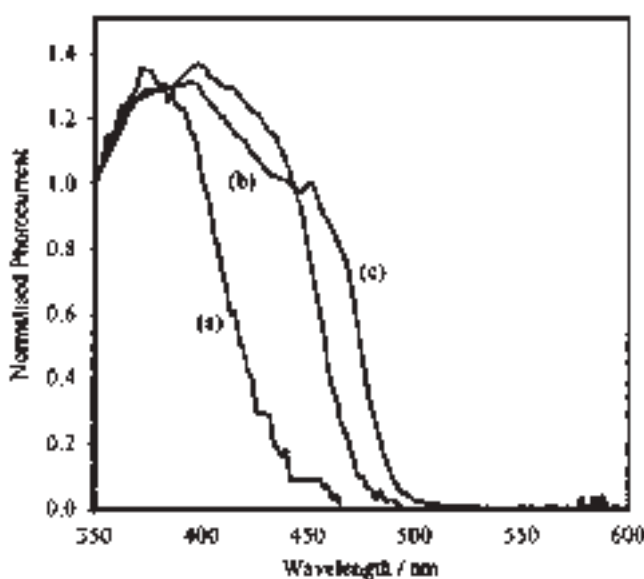


Figure 9.45 A plot of normalized photocurrent vs. wavelength of illumination, called action spectrum for CdS nanoparticle-modified ITO glass electrode. Particle size of CdS increases from (a) 2 nm and (b) 4 nm to (c) 10 nm diameter. The onset of action spectra shows red shift as a function of size, which is in concordance with the SQE. From reference (118). Reproduced by permission of The Royal Society of Chemistry.

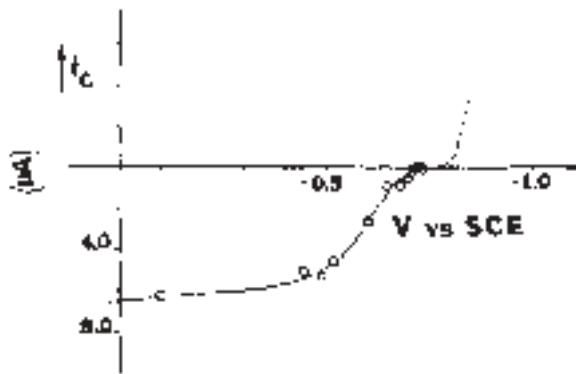


Figure 9.46 Photocurrent voltage response of suspended TiO_2 particles at In_2O_3 electrode. The anodic photocurrent indicates the electron transfer from the particles to electrode. From the onset, the potential for the photogenerated electrons was estimated to be -0.46 V vs. NHE. Reprinted with permission from reference (27). Copyright 1981, American Chemical Society.

Fermi level of particles is a function of irradiation intensity. The photo-onset potentials were shifted toward more negative values as a function of the photon flux. These experiments were supported by a blue shift of the absorption peak in the UV-vis spectra measured immediately after a high-intensity flash (134). This phenomenon is known as the ‘Burstein shift’ (135). Various potentials were applied to dispersions on an optically transparent electrode,

and the UV-vis spectra were recorded as a function of applied potentials (136). The change in absorption values was observed after a certain critical potential. It was observed that as particle size decreases, the critical potential shifts toward more and more negative values. These measurements were attributed to the quantum size effect.

The energetics of these particles have also been studied by CV and differential pulse voltammetry (127). The cyclic voltammograms recorded on alkylthiolate-capped PbS nanoparticles (3 nm diameter) in acetonitrile (137) are shown in Figure 9.47.

The peaks observed in the CVs were attributed to the redox reactions occurring due to the electrochemical decomposition of the PbS particles. For example, quasi-reversible cathodic peaks marked as I, II, and III were attributed to the reduction of PbS to Pb. The anodic peaks marked IV and V were attributed to the anodic stripping of deposited lead. The CVs recorded on Q-CdS particles in DMF however gave a cathodic and anodic peaks at extreme potential values as shown in Figure 9.48.

The peak positions marked as A1 and C1 were found to be shifted with particle diameter as shown in Figure 9.49.

In fact, there is a direct correlation between potential separation between peaks A1 and C1 and the observed band gap for various size particles. It is summarized in Table 9.4.

Based on these results, peak A1 is attributed to electron transfer from the highest occupied molecular orbital (HOMO) to the electrode and peak C1 is attributed to electron transfer from the electrode to the lowest unoccupied molecular orbital (LUMO), thus introducing the concept of ‘electrochemical band gap’ for semiconductor nanoparticles. Such a band gap was also observed earlier for extremely small metal nanoparticles (4). The decomposition of compound semiconductor particles on charge transfer poses a serious limitation on these studies, which was overcome by carrying out these measurements on

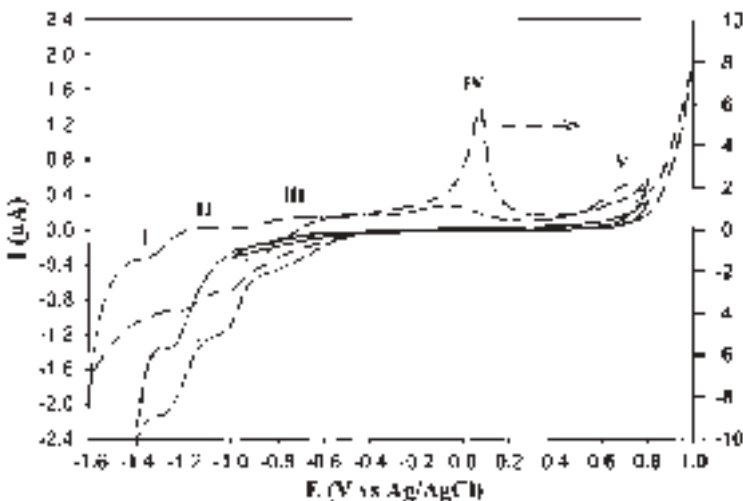


Figure 9.47 CVs recorded on hexanethiol-capped PbS nanoparticles in acetonitrile. Peaks marked (I), (II), and (III) are attributed to the reversible reduction of PbS. Anodic peaks marked (IV) and (V) are attributed to the oxidation and stripping of Pb from the electrode. Reprinted with permission from reference (137). Copyright 2000, American Chemical Society.

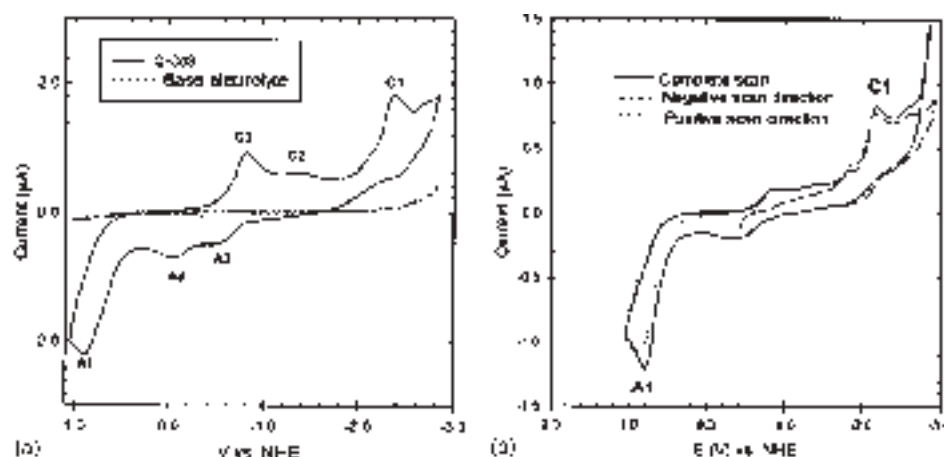


Figure 9.48 CVs recorded on thioglycol-capped CdS nanoparticles in DMF: (a) in full potential range and (b) at various starting potentials which suggests that peaks C1 and C2 are due to oxidation product from A1 and the peaks A2 and A3 are due to reduction products from C1. Reprinted with permission from reference (138). Copyright 2001, American Chemical Society.

elemental semiconductor nanoparticles such as Si (139). Differential pulse voltammograms (DPV) recorded on Si nanoparticles in DMF are shown in Figure 9.50.

Reversible peaks at about +0.09 and -0.7 V were attributed to the transfer of electrons from the HOMO and the LUMO to the electrode. The separation between these two peaks matches very well with the band gap obtained by spectroscopic methods. The reversibility of these peaks suggests that elemental semiconductor nanoparticles such as Si do not decompose on charge transfer. The peaks observed in the range -0.7 to -2.3 V are attributed to quantum double layer charging (140, 141), which is commonly observed in the case of monolayered protected clusters (MPCs).

9.7 SEMICONDUCTOR ELECTRODE APPLICATIONS

Semiconductor electrodes show electronic properties different from those of metal electrodes due to the space charge region present at SEI. The electric field gradient in the space charge region facilitates the separation of charge pairs generated at the SEI. This property of the SEI leads to numerous applications of semiconductor electrodes in the field of solar energy conversion (130, 131) and in sensor (132, 133) applications. Attention will be focused on the basic principles behind the use of semiconductor electrodes in these applications.

9.7.1 Solar cells

Solar cell applications can be broadly classified into two types: (a) photolytic or photoassisted conversion including the oxidation of water to H_2 and O_2 or decomposition of

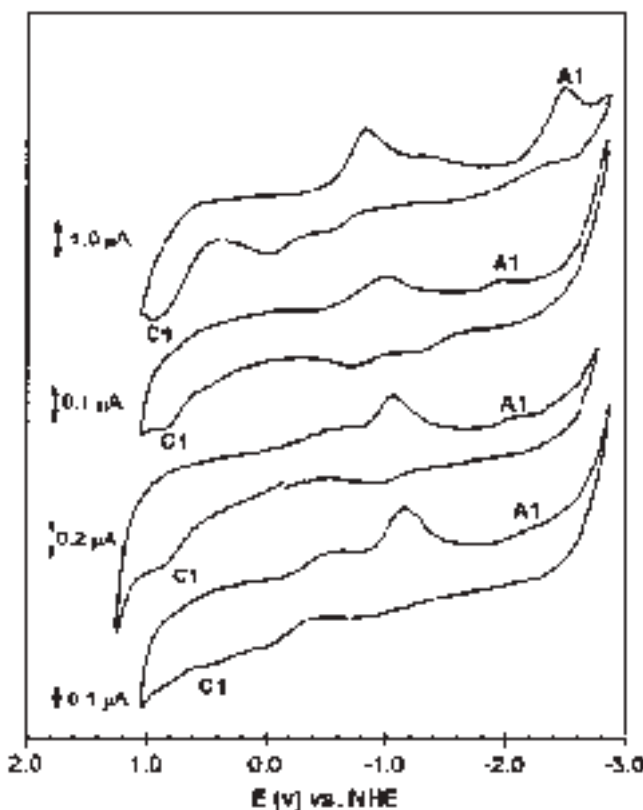


Figure 9.49 CVs recorded on various sizes of thioglycol-capped CdS nanoparticles. As the particle size increases from top to bottom, the separation between A1 and C1 decreases. Reprinted with permission from reference (138). Copyright 2001, American Chemical Society.

Table 9.4
Correlation of optical and electrochemical band gaps for fractions I–IV

Fraction	ΔE (V) ^a	ΔE (V) ^b	Band gaps ^c (eV)	Size ^d (nm)
I	^e	2.63	3.06	4.5
II	2.47	2.98	3.10	4.3
III	2.53	2.88	3.13	4.2
IV	2.96	3.39	3.23	3.9

ΔE refers to the peak separation between A1 and C1. Reprinted with permission from reference (138). Copyright 2001, American Chemical Society.

^aC1–A1 peak separation at 10 mV s⁻¹.

^bC1–A1 peak separation at 100 mV s⁻¹.

^cEstimated from UV–vis absorption peaks.

^dEstimated from electronic spectra.

^ePeak not well defined.

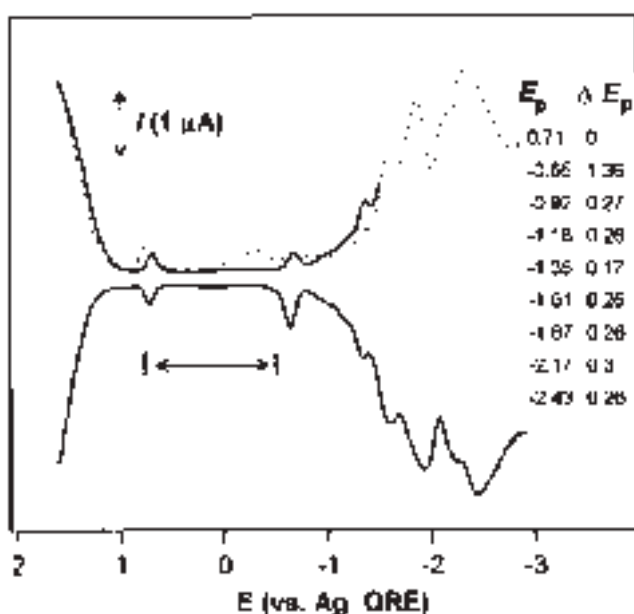


Figure 9.50 Differential pulse voltammogram (DPV) recorded on 1.74 nm Si nanoparticles. The reversible peaks near +0.09 and -0.7 V are attributed to the electron transfer through HOMO and LUMO of Si NPs. Reprinted with permission from reference (139). Copyright 2002, AAAS.

organic pollutants (142, 143) and (b) conversion of solar energy into electric energy using PEC solar cells or wet-photovoltaic cells.

The basic principle in both types is based on charge separation at the depletion semiconductor-electrode interface. As discussed in Section 9.3.1, in the case of direct band gap semiconductors, if the incident photon energy is higher than the band gap, the electrons are promoted into the VB by creating holes in the CB. The charge pairs generated in the depletion region are separated under the influence of the electric field gradient. For example, in the case of n-type semiconductors, holes will ‘bubble out’ at the SEI and can be used to carry out a desired oxidation. Electrons will travel through the semiconductor bulk, pass through the external circuit, and can be used to carry out a desired reduction at the counter electrode as shown in Figure 9.51a. Thus, a semiconductor electrode can be effectively used as a photocatalyst in carrying out photoassisted chemical conversion.

In PEC solar cells, the redox molecules used are reversibly oxidized and reduced at the semiconductor electrode and counter electrode. The current flowing through the external circuit can be used to drive a load and the device will effectively convert solar into electrical energy as shown in Figure 9.51b. Unfortunately, the decomposition potentials of most semiconductors lie in their own band gaps, leading to photocorrosion of the semiconductor surface, and put a question mark on the use of these devices. Oxide semiconductors such as TiO_2 and ZnO are more stable against photocorrosion but they absorb only in the UV region and are thus less efficient for terrestrial applications.

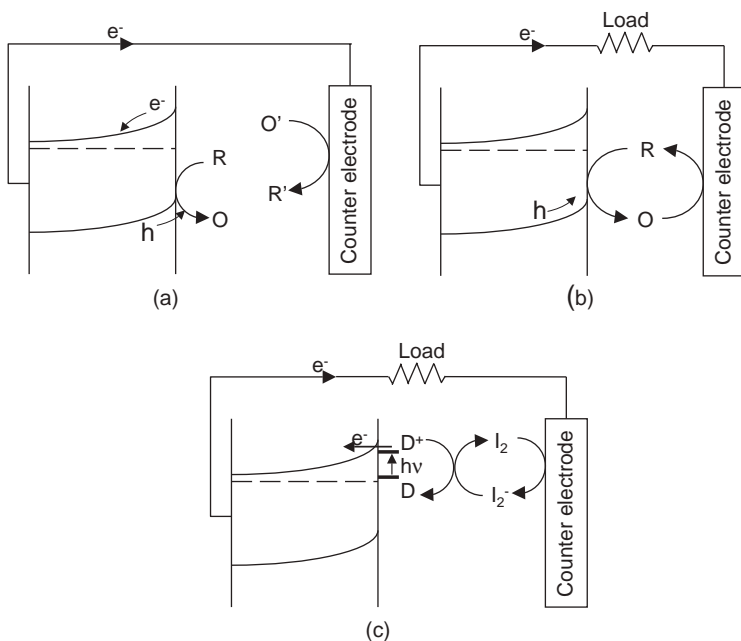


Figure 9.51 Schematics of (a) photochemical cell, where two different molecules undergo redox reaction, which leads to the photoassisted decomposition of molecules; (b) PEC solar cell, where same redox gets reduced and oxidized reversibly at photoelectrode and counter electrode, and thus net conversion of light into the electricity; (c) dye-sensitized PEC solar cell. The light is absorbed by dye molecule (D) and in an excited state, it injects the electron to CB. Electron travels through external circuit and reduces the mediator molecule, for example, I_2 into I_2^- . I_2^- reduces D^+ and the dye is regenerated for next electron transfer.

This problem is partially solved by sensitizing the electrode with a dye that absorbs in the visible region as illustrated in Figure 9.51c. Upon photoexcitation, the dye molecule injects a photoelectron in the CB that rolls down into the bulk semiconductor, passes through the external circuit, and reduces the redox mediator at the counter electrode. The reduced form of the mediator may diffuse and reduce the oxidized dye that completes the cycle. TiO_2 -based PEC cells are more efficient when particulate films are used; these are referred to as ‘Gratzel cells’. Among the various dyes explored for this purpose, ruthenium bipyridine complexes and their analogs have proven to be most efficient. However, these are not economically viable due to the cost of ruthenium, and thus have not yet been commercialized.

9.7.2 Sensors

The surface chemistry of semiconductors in sensor applications has been reviewed by Ellis and co-workers (144). Here, the basic principles behind the use of semiconductor

electrodes as sensors are discussed. The origin of the transduction mechanism of semiconductor electrodes can be realized using the band structure of the interface. It is characterized by not only E_C , E_V , and E_F positions on the surface but also surface states present in the band gap. The molecule to be sensed will interact with these energy levels by the processes of adsorption and desorption. These can influence the rate of surface recombination, producing observable changes in the electrical or optical properties of semiconductors. For example, the surface states present in the band gap are an efficient mediator for non-radiative recombination, leading to low photoluminescence (PL) yields for most ‘pinned’ systems. An adsorption-induced shift in the energy position of surface traps away from the band gap can produce an increase in the semiconductor PL intensity. For the n-type semiconductor, adsorbed donors can effectively return the surface-trapped charge to the semiconductor bulk, thereby reducing the surface electric field at the depletion layer. It may cause a contraction of its width so that both the PL intensity and the bulk conductance are expected to increase.

The depletion region of the semiconductor is not only an insulating layer but also relatively non-emissive and hence commonly referred to as a ‘dead layer’. If we oversimplify the semiconductor interface into a near-surface non-emissive zone and an underlying emissive zone, then the adsorption-induced PL behavior is quantitatively related to changes in the thickness of the dead layer according to

$$\frac{PL_0}{PL_x} = \exp(-\alpha' \Delta X) \quad (9.7.1)$$

where PL_0 and PL_x are initial and adsorption-induced PL intensities, respectively. α' is the semiconductor absorptivity, corrected for self-absorption, and ΔX is the resulting change in dead layer thickness from D_0 , the initial dead layer thickness, to D_x in the presence of adsorbate (145, 146). Based on a similar argument, adsorption of acceptors should decrease PL yield and conductance. If the thickness of the semiconductor film approaches the width of the depletion layer, a measurable change in the conductivity of the sample can be used as a method of analyte detection.

ACKNOWLEDGMENTS

The author wishes to thank Dr. Nanda, S. Haram, Mr. Shaukatali N. Inamdar, and Pravin P. Ingole for proof-reading and drawing the schemes.

REFERENCES

1. A. Fujishima, K. Honda, *Nature* **37**, 238 (1972).
2. D. A. McQuarrie, *Quantum Chemistry*, Viva Book Private Limited: New Delhi, 2003.
3. C. Kittel, *Introduction to Solid State Physics*, Vth ed., Wiley Eastern Limited: New Delhi, 1976.
4. S. Chen, R. S. Ingram, M. J. Hostetler, J. J. Pietron, R. W. Murray, T. Gregory Schaaff, J. T. Khouri, M. M. Alvarez, R. L. Whetten, *Science* **280**, 2098 (1998).

5. C. B. Murray, D. J. Norris, M. G. Bawendi, *J. Am. Chem. Soc.* **115**, 8706 (1993).
6. L. E. Brus, *J. Phys. Chem.* **90**, 2555 (1986).
7. L. E. Brus, *J. Chem. Phys.* **79**, 5566 (1983).
8. L. E. Brus, *J. Chem. Phys.* **80**, 4403 (1984).
9. R. Rossetti, J. L. Ellison, J. M. Gibson, L. E. Brus, *J. Chem. Phys.* **80**, 4464 (1984).
10. S. V. Nair, S. Sinha, K. C. Rustagi, *Phys. Rev. B* **35**, 4098 (1897).
11. Y. Kayanuma, *Solid State Commun.* **59**, 405 (1986).
12. P. E. Lippens, M. Lannoo, *Phys. Rev. B* **39**, 10935 (1989).
13. I. N. Levine, *Quantum Chemistry*, 5th ed., Pearson Education: Singapore, 2000.
14. A. J. Nozik, R. D. Memming, *J. Phys. Chem.* **100**, 13061 (1996).
15. H. Reiss, A. Heller, *J. Phys. Chem.* **89**, 4207 (1985).
16. H. Gerischer, *J. Phys. Chem.* **27**, 48 (1961).
17. H. Gerischer, *J. Phys. Chem.* **95**, 1356 (1991).
18. R. A. Marcus, *J. Phys. Chem.* **94**, 1050 (1990).
19. R. A. Marcus, *J. Chem. Phys.* **24**, 966 (1956).
20. R. A. Marcus, *Can. J. Chem.* **37**, 138 (1959).
21. D. Laser, A. J. Bard, *J. Am. Chem. Soc.* **80**, 459 (1976).
22. V. L. Rideout, *Thin Solid Films* **48**, 261 (1978).
23. B. R. Horrocks, M. V. Mirkin, A. J. Bard, *J. Phys. Chem.* **98**, 9106 (1994).
24. R. Nicholson, I. Shain, *Anal. Chem.* **36**, 706 (1964).
25. P. A. Kohl, A. J. Bard, *J. Am. Chem. Soc.* **99**, 7531 (1977).
26. F.-R. F. Fan, A. J. Bard, *J. Am. Chem. Soc.* **102**, 3676 (1980).
27. W. W. Dunn, Y. Aikawa, A. J. Bard, *J. Am. Chem. Soc.* **103**, 3456 (1981).
28. A. Aruchamy, M. S. Wrighton, *J. Phys. Chem.* **84**, 2848–2854 (1980).
29. R. N. Dominey, N. S. Lewis, M. S. Wrighton, *J. Am. Chem. Soc.* **103**, 1261 (1981).
30. P. G. Santangelo, G. M. Miskelly, N. S. Lewis, *J. Phys. Chem.* **92**, 6359 (1988).
31. P. G. Santangelo, G. M. Miskelly, N. S. Lewis, *J. Phys. Chem.* **93**, 6128 (1989).
32. J. N. Chazalviel, T. B. Truong, *J. Am. Chem. Soc.* **103**, 7447 (1981).
33. S. N. Frank, A. J. Bard, *J. Am. Chem. Soc.* **97**, 7427 (1975).
34. F.-R. F. Fan, H. S. White, B. L. Wheeler, A. J. Bard, *J. Am. Chem. Soc.* **102**, 5142 (1980).
35. J. A. Baglio, G. S. Calabrese, D. Jed Harrison, E. Kamieniecki, A. J. Ricco, M. S. Wrighton, G. D. Zoski, *J. Am. Chem. Soc.* **105**, 2246 (1983).
36. P. Singh, K. Rajeshwar, J. DuBow, R. Job, *J. Am. Chem. Soc.* **102**, 4676 (1980).
37. L.-S. R. Yeh, N. Hackerman, *J. Phys. Chem.* **82**, 2719 (1978).
38. L. F. Schneirneyer, M. S. Wrighton, *J. Am. Chem. Soc.* **101**, 6496 (1979).
39. P. G. Santangelo, M. Lieberman, N. S. Lewis, *J. Phys. Chem. B* **102**, 4731 (1998).
40. J. N. Chazalviel, *J. Electrochem. Soc.* **129**, 963 (1982).
41. M. L. Rosenbluth, N. S. Lewies, *J. Phys. Chem.* **93**, 3735 (1989).
42. J. Bardeen, *Phys. Rev.* **71**, 717 (1947).
43. C. A. Mead, W. G. Spitzer, *Phys. Rev. A* **134**, 713 (1964).
44. W. G. Spitzer, C. A. Mead, *J. Appl. Phys.* **34**, 3061 (1963).
45. S. Kurtin, T. C. McGill, C. A. Mead, *Phys. Rev. Lett.* **22**, 1433 (1969).
46. A. J. Bard, A. B. Bocarsly, F.-R. F. Fan, E. G. Walton, M. S. Wrighton, *J. Am. Chem. Soc.* **102**, 3671 (1980).
47. B. L. Wheeler, N. Hackerman, *J. Phys. Chem.* **92**, 1601 (1988).
48. S. Nakabayashi, A. Kira, *J. Phys. Chem.* **95**, 9961 (1991).
49. M. Bruening, E. Moons, D. Cahen, A. Shanzer, *J. Phys. Chem.* **99**, 8368 (1995).
50. S. Bastide, R. Butruille, D. Cahen, A. Dutta, J. Libman, A. Shanzer, L. Sun, A. Vilan, *J. Phys. Chem. B* **101**, 2678 (1997).

51. N. Prokopuk, N. S. Lewis, *J. Phys. Chem. B* **108**, 4449 (2004).
52. S. Tanaka, J. A. Bruce, M. S. Wrighton, *J. Phys. Chem.* **85**, 3778 (1981).
53. A. J. Bard, F.-R. F. Fan, J. Kwak, O. Lev, *Anal. Chem.* **61**, 132 (1989).
54. F.-R. F. Fan, M. V. Mirkin, A. J. Bard, *J. Phys. Chem.* **98**, 1475 (1994).
55. O. D. Uitto, H. S. White, *Anal. Chem.* **73**, 533 (2001).
56. D. T. Piercet, A. J. Bard, *Anal. Chem.* **65**, 3598 (1993).
57. B. R. Horrocks, D. Schmidtke, A. Heller, A. J. Bard, *Anal. Chem.* **65**, 3605 (1993).
58. Y. Selzer, D. Mandler, *J. Phys. Chem. B* **104**, 4903 (2000).
59. S. B. Basame, H. S. White, *Anal. Chem.* **71**, 3166 (1999).
60. S. B. Basame, H. S. White, *Langmuir* **15**, 819 (1999).
61. S. B. Basame, H. S. White, *J. Phys. Chem.* **99**, 16430 (1995).
62. X. K. Zhao, L. L. McCormick, J. H. Fendler, *Chem. Mater.* **3**, 922 (1991).
63. S. K. Haram, A. J. Bard, *J. Phys. Chem. B* **105**, 8192 (2001).
64. S. Rodman, M. T. Spitler, *J. Phys. Chem. B* **104**, 9438 (2000).
65. L. A. Bottomley, J. E. Courty, P. N. First, *Anal. Chem.* **68**, 185R (1996).
66. M. A. Poggi, E. D. Gadsby, L. A. Bottomley, *Anal. Chem.* **76**, 3429 (2004).
67. A. J. Bard, F.-R. Fan, M. V. Mirkin, in *Electroanalytical Chemistry*, A. J. Bard, Ed., Marcel Dekker: New York, 1994, Vol. 18, p. 243.
68. A. J. Bard, F.-R. F. Fan, M. V. Mirkin, *Physical Electrochemistry: Principles, Methods and Applications*, I. Rubinstein, Ed., Marcel Dekker: New York, 1995.
69. A. J. Bard, D. O. Wipf, *J. Electrochem. Soc.* **138**, 469 (1991).
70. C. A. Koval, J. B. Olson, *J. Phys. Chem.* **92**, 6726 (1988).
71. J. V. Macpherson, P. R. Unwin, *Anal. Chem.* **71**, 4642 (1999).
72. R. D. Martin, P. R. Unwin, *Anal. Chem.* **70**, 276 (1998).
73. S. B. Basame, H. S. White, *J. Phys. Chem. B* **102**, 9812 (1998).
74. K. L. Chopra, *Thin Film Phenomena*, McGraw Hill Book Company: New York, 1969.
75. K. L. Chopra, R. C. Kainthla, D. K. Pandya, A. P. Thakoor, in *Physics of Thin Films*, G. Hass, M. H. Francombe, J. L. Vossen, Eds., Academic Press: New York, 1982, Vol. 12, p. 201.
76. K. L. Chopra, S. Major, D. K. Pandya, *Thin Solid Films* **102**, 1 (1983).
77. H. Kikimoto, *J. Cryst. Growth* **95**, 360 (1989).
78. K. C. Lee, *J. Electrochem. Soc.* **95**, 360 (1990).
79. D. K. Roe, L. Wenzhao, H. Gerischer, *J. Electroanal. Chem. Interface Electrochem.* **136**, 323 (1982).
80. I. Ruach-Nir, Y. Zhang, R. Popovitz-Biro, I. Rubinstein, G. Hodes, *J. Phys. Chem. B* **107**, 2174 (2003).
81. Y. Golan, L. Margulis, I. Rubinstein, G. Hodes, *Langmuir* **8**, 3, 749 (1992).
82. D. Xu, G. Guo, Yuguo Guo, Y. Zhang, L. Gui, *J. Mater. Chem.* **13**, 360 (2003).
83. A. M. Kressin, V. V. Doan, J. D. Klein, M. J. Sailor, *Chem. Mater.* **3**, 1015 (1991).
84. J. Barton, A. Vertegel, E. Bohannan, J. Switzer, *Chem. Mater.* **13**, 952 (2001).
85. T. Yoshida, M. Tochimoto, D. Schlettwein, D. Wohrle, T. Sugiura, H. Minoura, *Chem. Mater.* **11**, 2657 (1999).
86. M. Lawrence, J. Dodelet, *J. Phys. Chem.* **89**, 1395 (1985).
87. F. Endres, *Phys. Chem. Chem. Phys.* **3**, 3165 (2001).
88. R. Chen, D. Xu, G. Guo, Y. Tang, *J. Mater. Chem.* **12**, 1437 (2002).
89. M. Kemell, M. Ritala, M. Leskela, *J. Mater. Chem.* **11**, 668 (2001).
90. H. Saloniemi, T. Kanniainen, M. Ritala, M. Leskela, R. Lappalainen, *J. Mater. Chem.* **8**, 651 (1998).
91. T. Torimoto, A. Obayashi, S. Kuwabata, H. Yasuda, H. Mori, H. Yoneyama, *Langmuir* **16**, 5820 (2000).

92. A. S. Baranski, W. R. Fawcett, *J. Electrochem. Soc.* **127**, 766 (1980).
93. A. S. Baranski, W. R. Fawcett, K. Gatner, A. C. McDonald, J. R. McDonald, *J. Electrochem. Soc.* **130**, 579 (1983).
94. Y. Mastai, D. Gal, G. Hodes, *J. Electrochem. Soc.* **147**, 1435 (2000).
95. B. M. Quinn, Z. Ding, R. Moulton, A. J. Bard, *Langmuir* **18**, 1734 (2002).
96. F. Endres, S. Z. E. Abedin, *Chem. Commun.* **8**, 892 (2002).
97. P. O'Brien, J. McAleese, *J. Mater. Chem.* **8**, 2309 (1998).
98. G. Hodes, *Isr. J. Chem.* **33**, 95 (1993).
99. D. R. Pratt, M. E. Langmuir, R. A. Boudreau, R. D. Rauh, *J. Electrochem. Soc.* **28**, 1627 (1981).
100. T. L. Chu, S. S. Chu, N. Schultz, C. Wang, C. Q. Wu, *J. Electrochem. Soc.* **139**, 2443 (1992).
101. F. Zhou, P. R. Unwin, A. J. Bard, *J. Phys. Chem.* **96**, 4917 (1992).
102. M. L. Breen, J. T. Woodward, D. K. Schwartz, A. W. Apblett, *Chem. Mater.* **10**, 710 (1998).
103. Y. F. Nicolau, M. Dupuy, M. Brunel, *J. Electrochem. Soc.* **137**, 2915 (1990).
104. M. Sasagawa, Y. Nosaka, *Phys. Chem. Chem. Phys.* **3**, 3371 (2001).
105. S. K. Haram, K. S. V. Santhanam, *Thin Solid Films* **238**, 21 (1994).
106. S. K. Haram, K. S. V. Santhanam, M. Neumann-Spallart, C. Levy-Clement, *Mater. Res. Bull.* **27**, 1185 (1992).
107. B. Pejova, M. Najdoskia, I. Grozdanova, S. K. Deyb, *Mater. Lett.* **43**, 269 (2000).
108. H.-Y. Byun, R. Vittal, D. Y. Kim, K.-J. Kim, *Langmuir* **20**, 6853 (2004).
109. A. J. McEvoy, M. Gratzel, in *Encyclopedia of Electrochemistry*, B. Stratman, Ed., Wiley-VCH: Weinheim, Germany, 2002, Vol. 6, p. 397.
110. A. Z. M. Zukalova, L. Kavan, Md. K. Nazeeruddin, P. Liska, M. Grätzel, *Nano Lett.* **5**, 1789–1792 (2005).
111. D. B. Mitzi, *J. Mater. Chem.* **14**, 2355 (2004).
112. J. Bisquert, A. Zaban, P. Salvador, *J. Phys. Chem. B* **106**, 8774 (2002).
113. O. Chyan, J.-J. Chen, F. Xu, J. A. Sees, L. H. Hall, *Analyst* **125**, 175 (2000).
114. A.-M. L. Nickel, F. Seker, B. P. Ziemer, A. B. Ellis, *Chem. Mater.* **13**, 1391 (2001).
115. J. Karlsson, M. Armgarth, S. Odman, I. Lundstrom, *Anal. Chem.* **62**, 542 (1990).
116. R. Liu, A. A. Vertegel, E. W. Bohannan, T. A. Sorenson, J. A. Switzer, *Chem. Mater.* **13**, 508 (2001).
117. B. Alperson, H. Demange, I. Rubinstein, G. Hodes, *J. Phys. Chem. B* **103**, 4943 (1999).
118. S. Drouard, S. G. Hickey, D. J. Riley, *Chem. Commun.* **1**, 67 (1999).
119. S. G. Hickey, D. J. Riley, *J. Phys. Chem. B* **103**, 4599 (1999).
120. S. G. Hickey, D. J. Riley, E. J. Tull, *J. Phys. Chem. B* **104**, 7623 (2000).
121. K. Hu, M. Brust, A. J. Bard, *Chem. Mater.* **10**, 1160 (1998).
122. Y. Li, D. Xu, Q. Zhang, D. Chen, F. Huang, Y. Xu, G. Guo, Z. Gu, *Chem. Mater.* **11**, 3433 (1999).
123. X. K. Zhao, Y. Yuan, J. H. Fendler, *J. Chem. Soc., Chem. Commun.* **18**, 1248 (1990).
124. X. K. Zhao, J. H. Fendler, *J. Phys. Chem.* **95**, 3716 (1991).
125. Z. Y. Pan, G. J. Shen, L. G. Zhang, Z. H. Lu, J. Z. Liu, *J. Mater. Chem.* **7**, 531 (1997).
126. T. Torimoto, N. Tsumara, M. Miyake, M. Nishisawa, T. Sakata, H. Mori, H. Yoneyama, *Langmuir* **15**, 1853 (1999).
127. L. I. Halaoui, *Langmuir* **17**, 7130 (2001).
128. Y. Sun, E. Hao, X. Zhang, B. Yang, J. Shen, L. Chi, H. Fuchs, *Langmuir* **13**, 5168 (1997).
129. S. S. Shankar, S. Chatterjee, M. Sastry, *Phys. Chem. Commun.* **6**, 36 (2003).
130. D. Liu, P. V. Kamat, *J. Phys. Chem.* **97**, 10769 (1993).
131. T. Sagara, Y. Aikawa, M. Sukigara, *J. Phys. Chem.* **91**, 1173 (1987).
132. C.-Y. Liu, A. J. Bard, *J. Phys. Chem.* **93**, 3232 (1989).
133. J. K. Leland, A. J. Bard, *J. Phys. Chem.* **91**, 5076 (1987).

134. C.-Y. Liu, A. J. Bard, *J. Phys. Chem.* **93**, 7749 (1989).
135. E. Burstein, *Phys. Rev.* **93**, 632 (1954).
136. P. Hoyer, H. Weller, *Chem. Phys. Lett.* **221**, 379 (1994).
137. S. Chen, L. A. Truax, J. M. Sommers, *Chem. Mater.* **12**, 3864 (2000).
138. S. K. Haram, B. M. Quinn, A. J. Bard, *J. Am. Chem. Soc.* **123**, 8860 (2001).
139. Z. Ding, B. M. Quinn, S. K. Haram, L. E. Pell, B. A. Korgel, A. J. Bard, *Science* **296**, 1293 (2002).
140. D. T. Miles, R. W. Murray, *Anal. Chem.* **75**, 1251 (2003).
141. J. F. Hicks, A. C. Templeton, S. Chen, K. M. Sheran, R. Jasti, R. W. Murray, *Anal. Chem.* **71**, 3703 (1999).
142. T. L. Villarreal, R. G. Mez, M. Neumann-Spallart, N. Alonso-Vante, P. Salvador, *J. Phys. Chem. B* **108**, 15172 (2004).
143. A. Heller, *Acc. Chem. Res.* **28**, 503 (1995).
144. F. Seker, K. Meeker, T. F. Kuech, A. B. Ellis, *Chem. Rev.* **100**, 2505 (2000).
145. A. A. Burk, P. B. Johnson, A. B. Ellis, *J. Appl. Phys.* **59**, 1621 (1986).
146. K. Mettler, *Appl. Phys.* **12**, 75 (1977).

This page intentionally left blank

– 10 –

Microelectrode Arrays

Sabine Szunerits¹ and Laurent Thouin²

¹LEPMI, UMR CNRS/INPG/UJF 5631, ENSEEG, Institut National Polytechnique de Grenoble, Domaine Universitaire, 38042 Saint Martin d'Hères, France

²Ecole Normale Supérieure, Département de Chimie, UMR CNRS 8640 Pasteur, 24 rue Lhomond, 75231 Paris Cedex 05, France

10.1 INTRODUCTION

The behavior of microelectrodes (radius smaller than 50 µm) differs from conventional-sized electrodes (radius 1 mm or greater) in that nonlinear diffusion is the predominant mode of transport. This difference in mass transport from the bulk solution toward the electrode has several important implications that make microelectrodes very attractive in many areas of electroanalytical chemistry. These include reduced ohmic potential drop, a decreased time constant, a fast establishment of steady-state signals, and an increased signal-to-noise ratio.

Since the beginning of the 1980s (1, 2), the development of microfabrication techniques has allowed these electrodes to become widely used even though the benefits of the properties of small electrodes was recognized much earlier. Microelectrodes have thus been employed for those applications demanding electrochemistry in restricted volumes, in solutions of high resistance as well as in short-time regimes (1, 2). For a more detailed discussion about microelectrodes, see Chapter 6.

It was around the same time that the first reports on microelectrode arrays appeared. Both experimental and theoretical works (3–27) have demonstrated the advantages of such electrode assemblies, which result from the specific mass transport of electroactive materials or diffusion regimes taking place at their interface. These include the following:

- (1) As long as the microelectrodes in the array do not interact with each other, a steady-state current is monitored at long times. This regime is a characteristic of the spherical or hemispherical diffusion achieved at individual electrodes of the array.
- (2) In conditions where individual diffusion layers overlap, the array may be considered as a single macroelectrode at which planar diffusion occurs.

- (3) Arrays of microelectrodes exhibit higher signal-to-noise ratios than macroelectrodes having an equivalent surface area. Lower current detection limits can be achieved that are important for electrochemical detectors in measuring small quantities of materials.
- (4) Interactions between individual electrodes in the arrays permit regeneration of electroactive substances through redox cycling or collection of very unstable intermediates.

Owing to these advantages, miniaturized electrochemical sensors for probing electroactive species at particular microscopic locations are in demand. This miniaturization is particularly important for diverse applications in biology where *in situ* measurements on living organisms are of interest. The aim of this chapter is to give a comprehensive understanding of the different types of microelectrode arrays (random, ordered, paired, etc.) and a general classification scheme based on their operating mode or electrochemical properties. An overview of the diverse methods employed to construct microelectrode arrays together with some recent areas where microelectrode arrays have been used will be presented. The specific properties of microelectrode arrays can, however, not be understood without a fundamental understanding of the diffusion on microelectrode arrays. A basic discussion around these phenomena will be given.

10.2 CLASSIFICATION OF MICROELECTRODE ARRAYS

The shapes of the electrodes in the array are limited mainly by the way the array is fabricated and by one's imagination. Microelectrode arrays are classified according to the design of the array and the function/use of the array.

10.2.1 Microelectrode designs

Individual electrodes in an array may assume a disordered (random) or periodical arrangement. Random microelectrode arrays are characterized by a statistical distribution of electrodes that may be of identical or dissimilar dimension and shape. Ordered microelectrode arrays generally consist of an ensemble of electrodes of identical dimensions with a periodic arrangement.

10.2.1.1 Random microelectrode arrays

The main advantage of such arrays (Figure 10.1A) is the ease with which they can be fabricated. They are mostly formed by sealing single metal wires (Pt, Au, Ag, Cu, Ni, etc.) or conducting carbon fibers into an insulating matrix, such as glass or an epoxy resin. The disadvantage is that they are geometrically ill-defined and, therefore, do not permit a clear comparison with theoretical predictions. The ill-defined spacing between conducting surfaces can lead to overlapping diffusion layers. Electrode dimensions and interelectrode distances ranging from tenths of angstroms to micrometers are possible.

One of the first random microelectrode arrays reported consisted of sealing a bundle of individually conducting carbon fibers into epoxy (29). This array consisted of five layers of 20 electrodes where each electrode had a radius of 5 μm . Each disk was located at least six diameters from its nearest neighbor electrode so that diffusional cross-talk between

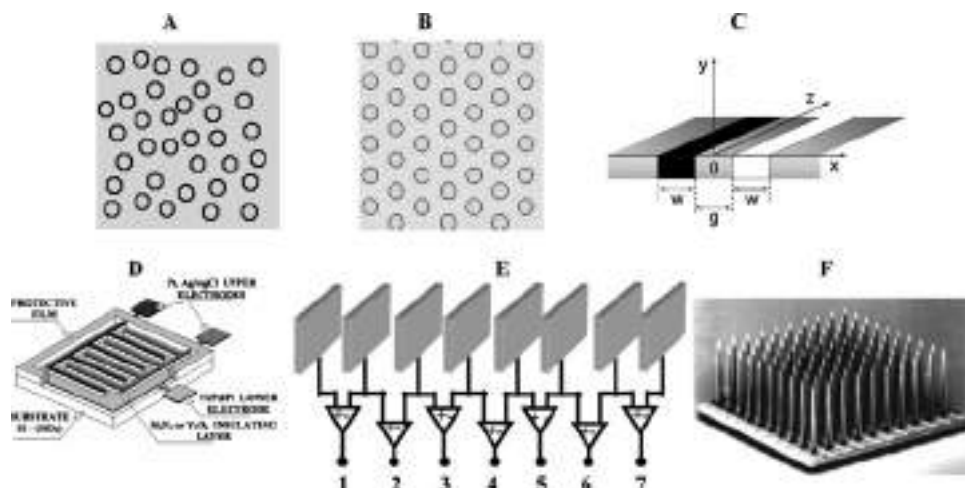


Figure 10.1 Classification of microelectrodes: (A) random array, (B) ordered array, (C) paired electrode, schematic representation of a double band assembly, (D) interdigitated array, schematic presentation of IDA electrodes vertically arranged (E) linear array, (F) three-dimensional array, Utah electrode array (reprints from reference (28)). (for colour version: see colour section at the end of the book).

disks did not occur. This array has proven to be advantageous as a flow rate independent amperometric detector.

A recent addition to this class of arrays is the construction of self-assembling arrays. Statistical arrays of microspheres with random radii have been realized by depositing mercury on an inactive substrate (30, 31) or by partial covering of a conducting electrode by a monolayer of insulating organic film (32, 33). In the same way, arrays of disk electrodes of a few hundred angstroms diameter have been made from polymeric membranes. The irradiation and local polymerization of the membranes led to the formation of transmembrane pores of calibrated dimensions in which platinum or gold were deposited (7, 18, 20). Opto-electrochemical microring arrays based on the deposition of gold around optical fibers (34–36) have recently been reported.

10.2.1.2 Ordered microelectrode arrays

The design of microelectrode arrays with well-defined geometries is largely preferred for electroanalytical, biological, as well as theoretical purposes. An ordered microelectrode array configuration, where each electrode in the array is regularly spaced with respect to another is shown in Figure 10.1B. A notable advantage of ordered arrays is their ability to be fabricated using silicon technology procedures, such as photolithography, which also accommodates bulk fabrication. The most common electrode materials are gold deposited on silica substrates, but platinum, iridium, and diamond have also been used. These devices do not endure mechanical pretreatment (polishing and removal of some coating on the electrode) but this is a minor problem, as their high interelectrode reproducibility and inexpensive nature permits disposability. Still, high-quality ordered microelectrode arrays are not easy to be fabricated and found. Regular arrays with well-defined geometries generally consist of parallel band

electrodes or disk electrodes arranged in a hexagonal array. These two geometries are preferred because their symmetry allows modeling of diffusion at these assemblies. Specific geometries have included an ensemble of microdisks sealed in a hexagonal or a square array (37–47), or parallel microbands of identical nature or alternatively polarized as an anode or a cathode. This latter configuration is generally known as paired electrodes (48–58) (Figure 10.1C) or as interdigitated electrode arrays (Figure 10.1D) (16, 20, 24, 27, 59–83).

A popular variation of ordered microelectrode arrays is the two-dimensional array (Figure 10.1E) (84) where the diffusion properties extend in two dimensions rather than three dimensions. Linear arrays with up to 16 electrodes have been reported and used for the investigation of anatomical muscle properties (85) and for basic and applied studies of the neuromuscular system (84).

10.2.1.3 Three-dimensional microelectrode arrays

This geometry has found wide application in biosensing and in recording electrical neural signals from nervous systems. Planar microelectrode arrays are not advantageous for acute tissue slice experiments. However, by using three-dimensional electrodes, it is possible to monitor the electrical activity of the tissue directly after placing it onto the electrodes. The geometry of the electrodes improves the penetration into the tissue slice, thereby reducing the distance between the active cells and the electrode. These arrays have a cylindrical structure (Figure 10.1F) and are mostly based on the etching of silicon wafers. Another configuration of a three-dimensional microelectrode array is based on the etching of optical fiber bundles and covering the surface with gold (36, 86). McKnight *et al.* have recently reported the fabrication and characterization of a microarray of individually addressable vertically aligned carbon nanofiber electrodes (87).

10.2.2 Microelectrode array behavior

Microelectrode arrays can be classified according to the way the array is operating.

10.2.2.1 Microelectrode arrays as amplifiers

If all of the microelectrodes in the array are polarized at the same potential, higher currents per unit area are possible (88). The signal-to-noise ratio of each individual electrode can be preserved and this so-called amplification effect is maintained as long as no overlap between individual diffusion layers occurs. Amplification remains effective at long times if the interelectrode spacings are at least 10 times larger than the radius of an individual microelectrode on the array. For a microelectrode of 5 μm radius, a minimal spacing of 50 μm would be necessary (88, 89).

10.2.2.2 Individually addressable arrays

Identical or different potentials can be applied to each electrode in an individually addressable array allowing multiparametric analysis while avoiding diffusional cross-talk. The development of an individually addressable microelectrode array places sophisticated demands on microfabrication technology. The conventional way to individually address each electrode of an array is to connect an electrode line to a corresponding bonding pad

at the end of a circuit chip (39, 90, 91). The electrochemical measurements are then carried out on each electrode either simultaneously, or sequentially. When carried out sequentially, however, recording a complete cyclic voltammogram on a 64 individually addressable microelectrode array can take up to 3 h (92) depending on the scan rate.

Simultaneous current measurements are possible using integrated circuits (ICs) where the addressing hardware is built onto each microelectrode array chip (40, 93). Such an approach was recently reported in which 64 individually addressable gel-integrated Hg-plated Ir-based microelectrodes were used (46, 94). The IC is based on a double multiplexing system and a single potentiostat. This was the first system reported allowing simultaneous recording of complete voltammograms for a large number of individually addressable microelectrodes with fast dynamic techniques, such as square wave anodic stripping voltammetry. This probe has been used for real-time, high spatial resolution concentration profile measurements at interfaces (46). The use of complementary metal oxide semiconductor (CMOS) technology (42, 95, 96), the major type of transistor set nowadays (97), permits local amplification just behind the electrodes to significantly decrease the electrode density. The main drawback of the standard CMOS technology is that it uses aluminum alloys as the metallic layer. This alloy shows limited stability in physiological solutions and is not biocompatible; therefore, it is not a suitable electrode material for biologically oriented investigations. However, by modifying the electrode surfaces, these arrays can be adapted for studies in biological media. Such an approach was reported by Berdondini *et al.* who electrolessly deposited gold from gold cyanide plating solutions (98).

10.2.2.3 Generator/collector scheme

Although all efforts in the individually addressable configuration are put into avoiding interactions between the electrodes in the array through overlap of individual diffusion layers, cross-talk in the collector/generator mode between closely spaced electrodes is the basic principle of their functioning. The simplest configuration for a generation/collection scheme is the paired electrode configuration mentioned above (Figure 10.1C). The intermediate generated on one electrode (the generator), diffuses to the other electrode (the collector), where it can be regenerated to the reactant initially present in bulk solution (Figure 10.2). In contrast to the rotating disk electrode where the regenerated species is swept into the bulk solution, the regenerated species at the collector electrode can diffuse back to the generator electrode and participate in the redox cycle again. The recycling or feedback between the paired electrodes results in amplifying the generator current far above the value it would have were the collector electrode disconnected (51, 53). Band electrodes are mostly used for the generator/collector mode and are fabricated generally by a sandwich method (48, 51–57).

A more sophisticated version of the paired electrode is the interdigitated array electrode (IDA). The IDA is an outgrowth of lithographic microfabrication technology (16, 20, 24, 27, 59–74, 76–83). The IDA consists of a series of parallel microband electrodes in which alternating microbands are connected together forming a set of interdigitated electrode fingers (Figure 10.1D). Typical dimensions of an individual microband “finger” are 100–200 nm in height, 1–10 µm in width and 5–10 mm in length. The typical interfinger separation (gap) is 1–10 µm. The potential of each finger set of electrodes can be controlled independently of the other relative to that of a reference electrode. The gap between the “fingers” is small enough so that for a sufficiently long electrolysis, diffusional coupling can

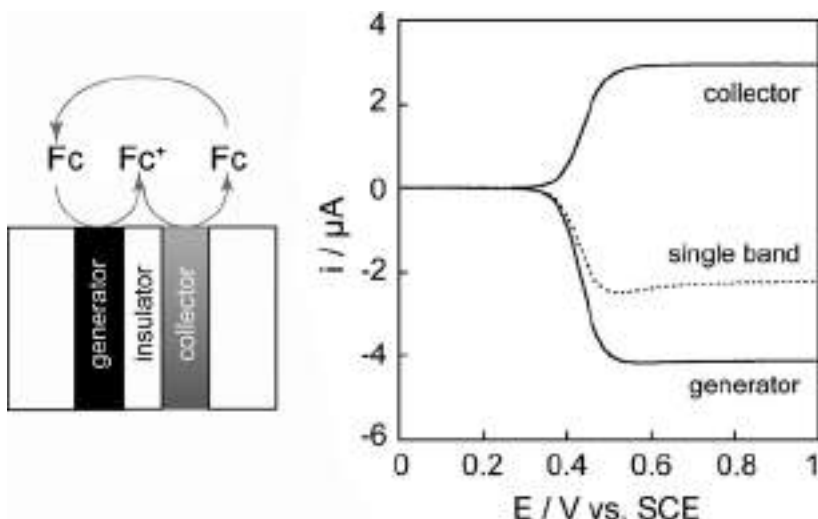


Figure 10.2 Generator/collector scheme: oxidation of 2 mM ferrocene (Fc) in 0.1 M $n\text{Bu}_4\text{BF}_4$ /CH₃CN. Dashed line: single band experiment (only one electrode is biased). Solid lines: generator/collector experiment with $E_{\text{collector}} = 0$ V/SCE. Band width, $w = 5$ μm ; gap width, $g = 2.5$ μm ; and scan rate, $v = 0.1$ V sec⁻¹.

occur between fingers and a collector/generator scheme similar to a paired electrode is set (Figure 10.2). With interdigitated electrodes, the small gap dimensions and the use of an array rather than a single generator/collector electrode pair results in very large collection efficiencies (larger than 0.98), which give the IDA an advantage in detecting trace amounts of electroactive species.

10.3 THEORY: DIFFUSION AT MICROELECTRODE ARRAYS

A quantitative description of mass transport to microelectrode arrays must take into account possible interactions between the diffusional fields of individual microelectrodes. The major complication arises from the difficulty in describing and modeling these interactions, which depend on the way the microelectrodes are arranged within the array but also on the way, the array is being operated.

10.3.1 Arrays of electrodes operating at identical potentials

When each electrode in the array is operating at the same potential, the overall response of the electrode array depends on two parameters: the density of the electrode distribution and the relative dimensions of the electrodes with regard to the thickness of the diffusion layer, δ , developing at each active element of the array. In other words, for a given array geometry, its electrochemical behavior will be strongly dependent on the time scale of the electrochemical perturbation (21, 26).

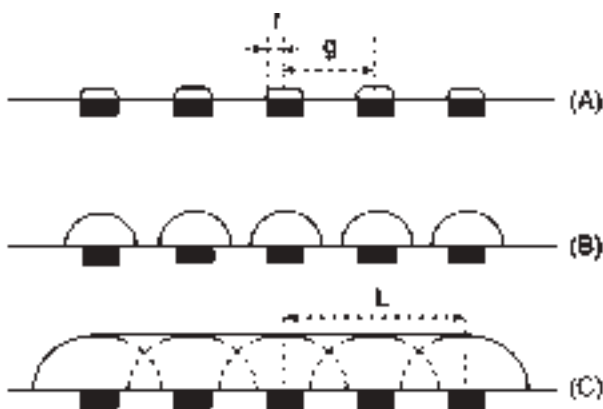


Figure 10.3 Schematic representation of diffusion layers of concentration profiles developing at arrays of electrodes at different times of the electrochemical perturbation: (A) planar diffusion at short times, (B) hemispherical or cylindrical diffusion at intermediate times, and (C) planar diffusion and overlap of individual diffusion layers at longer times.

When the duration of the experiment is sufficiently short for the diffusion layer to be small with respect to the radius r of the electrodes, planar diffusion is observed at each electrode and the current monitored at the array is proportional to the sum of geometric areas S^{el} of the individual active elements (Figure 10.3A). Under these conditions, the detected current is given by the well-known Cottrell equation:

$$(Dt)^2 \ll r, \quad i = \frac{nFS^{\text{el}}DC^*}{\sqrt{\pi Dt}} \quad (10.1)$$

At longer times, the individual diffusion layers become larger than the electrode dimensions and a transition regime occurs whose characteristics depend on the distance d separating two active elements of the array. When this distance is relatively large in comparison to the size of the diffusion layers, steady-state or quasi-steady-state diffusion takes place at each element depending on their shape (Figure 10.3B). The current is still equal to the sum of the currents at each active element but is proportional to the total active area S^{el} with a proportionality factor, which depends on the shape of the electrodes. This factor is introduced by $\delta(r)$, which is the equivalent diffusion layer thickness at each electrode under steady-state regime:

$$r \ll (Dt)^2 \ll d, \quad i = \frac{nFS^{\text{el}}DC^*}{\delta(r)} \quad (10.2)$$

This relation is only valid when the distance d separating the electrodes is much larger than their dimensions. If this is no longer the case, the diffusion layers developing at adjacent electrodes interpenetrate each other before reaching the steady- or quasi-steady-state diffusion regime observed separately at each element. The overlap of individual diffusion layers results in an apparent global diffusion layer that extends over the array in a planar diffusion regime (Figure 10.3C). In this condition, the array behaves like a large electrode

having an area equal to the geometric area of the entire array S^{array} , including the total active area S^{el} and insulating zones S^{insul} (i.e., $S^{\text{array}} = S^{\text{el}} + S^{\text{insul}}$):

$$d \ll (Dt)^2 \ll L, \quad i = \frac{nFS^{\text{array}}DC^*}{\sqrt{\pi Dt}} \quad (10.3)$$

The situation where no diffusional overlap occurs presents a major interest for independently addressable arrays. At short times, the electrodes behave independently and the array performs like a simple current amplifier. This amplification is small compared with that achieved by classical electronic means. At long times, the current corresponds to an electrode of a dimension equal to that of the entire array. As the noise in electrochemical experiments is related to the capacity of the conductor and thus proportional to its surface area, the signal-to-noise ratio under these conditions is improved by a factor equal to $S^{\text{array}}/S^{\text{el}}$. This ratio can be improved up to two orders of magnitude and even more with the present technologies developed in nanolithography. This great advantage has been used for low current detection in the design of electrochemical detectors adapted for chromatography purposes (15, 83, 99).

Another advantage concerns heterogeneous electron transfer kinetics at such electrode interfaces. When the size of the active elements and distances separating the sites are small compared with the diffusion layer thickness, nonlinear diffusion is confined to a layer, which is adjacent to the array surface. As a result, considerable torsions of flux lines occur near each active element and the local rate of diffusion is drastically enhanced compared with that occurring far from the array surface where linear diffusion prevails (14). Even though the array behaves like a larger electrode, high diffusion rates may be generated locally on the arrays while keeping a relatively low overall diffusion rate. One must note that if the array is considered as a single large electrode at which planar diffusion occurs, the evaluation of the heterogeneous kinetics will be strongly affected, leading to an underestimation of the electron transfer rate (see Section 10.5.1). The same applies to fast homogeneous kinetics for which the kinetic layers are smaller than the distance separating two electrodes in the array (14).

All the limiting behaviors and their transitions described above have been observed experimentally at electrode arrays (19, 29, 74, 100–103). These situations have been treated theoretically for cases in which the active areas are uniform in size and situated in regular arrays (3, 9, 10, 13, 22, 104–106). Some differences have been observed among the calculations especially in the description of diffusion regimes at intermediate times, while the separate diffusion fields merge into a single larger field. It is only during this critical interval that the currents or diffusion regimes depend on the way the electrodes are arranged in the array. At shorter times, the electrodes behave as if they were individually separated and at longer times, the individual active areas are no longer distinguishable. The problem in dealing with mass transport to arrays of electrodes arises from the coupling between the expansion in three dimensions of the individual diffusion layers and the two-dimensional distribution of the electrodes in the array. The earliest theories of diffusion at arrays of electrodes have been developed to analyze the electrochemical responses at partially blocked surfaces of large electrodes (5, 9, 14, 101, 107, 108). Rigorous solutions of diffusion at statistical arrays are obviously impossible

and are generally adapted from those estimated at regular arrays by the introduction of statistical corrections (22, 108, 109). This is why the problem has been most frequently undertaken with microelectrodes packed in regular arrays. The common approach is to approximate the surface of the array as an ensemble of independently performing diffusion domains. The electrodes are supposed to be distributed in a regular two-dimensional lattice (square or hexagonal lattice form) with elements considered as the base of semi-infinite unit cells. Because of symmetry considerations, there is no flux of species at the boundary between the unit cells. Simplification of the problem is usually achieved with this construction by using a cylindrical geometry (Figure 10.4). Results have been obtained analytically (9, 105) and numerically (3, 10, 13, 104, 106, 107). Analytical solutions of the models give accurate results but appear limited to the semi-infinite diffusion regime at short and long time ranges (see Section 10.5.1). Good agreement between experimental data and results based on simulations were reported over the entire time regime taking into consideration the transient character of radial diffusion by explicit finite-difference techniques (10) and using the hopscotch algorithm (106). The transition from spherical to planar diffusion at arrays of electrodes has also been treated as the overlap of equivalent diffusion zones in the case of square, hexagonal, and random arrays (22). The analytical expressions show that the current is significantly reduced if the distribution of microelectrodes is random as compared with when the microelectrodes are regularly distributed. More recently, the diffusion processes for a finite number of active elements have been investigated with regular (110, 111) or arbitrary distributions (112), in thin layer cells (110) or taking into account convection influences of the solution (111).

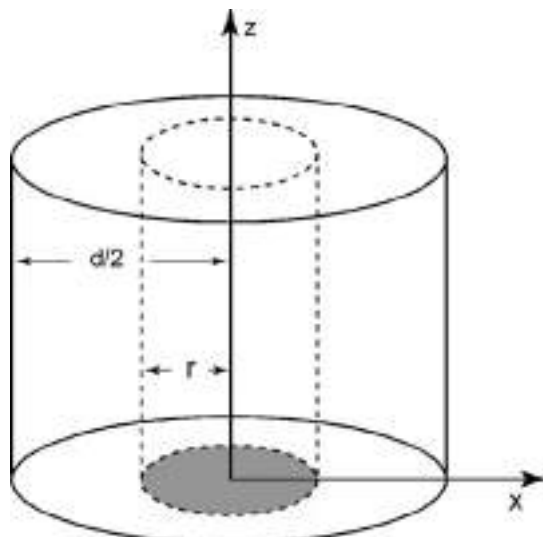


Figure 10.4 Approximate model of individual elements in arrays of electrodes with cylindrical coordinates. The electrode surface is represented in gray and insulating surface in white.

10.3.2 Arrays of electrodes operating in generator/collector mode

The intrinsic difficulties of modeling diffusion at arrays of electrodes are increased in the generator/collector mode because the transport equations must be solved numerically rather than analytically. The discontinuities between electrodes and insulators are amplified as the two adjacent electrodes interact with each other leading to cross talk at their immediate borders. Moreover, the communication between each electrode involves long-distance diffusional pathways, which connect the electrodes by their opposite borders. As a consequence, all numerical techniques have to deal with fine space grids between the electrodes to describe precisely the diffusion pathways at distances exceeding the electrode dimensions. The problem must be solved simultaneously at two different scales depending on the distance z from the array surface. For these reasons, simulations performed in real space are extremely difficult to handle as they require grid spaces perfectly adapted to the problem under investigation with a large number of points or nodes to be treated together. In an effort to reduce the number of grid elements required, simulations at electrodes arrays have employed exponential space grids (54, 74) or particular grid discretization (77) with the advantage of producing a high grid density in the vicinity of the electrodes without a dramatic increase in the overall number of elements required for the simulation of the complete diffusion layer. However, one major disadvantage is that the grid lines do not follow the actual lines of flux to the electrode surface especially at the edges of the electrodes where they are strongly curved. Moreover, it is impossible to define precisely a single grid accounting for the time-dependent shape of the concentration profiles.

An alternative to these difficulties consists of performing simulations in a nonreal space, which leads to linearization of isoconcentration and flux lines. The use of a conformal map is particularly useful and adapted for modeling diffusion at these assemblies. In many cases, it provides a simple way to estimate the steady-state currents for each type of electrode (26). This method has been used to describe analytically the current at interdigitated arrays (24, 76). In addition, the Schwarz–Christoffel transformation (Figure 10.5) allows the best change of space according to the geometry of the assemblies and time scale of experiments (27, 48, 51–53, 77, 113). Looking at a compromise between the simplicity of the transformed space and ease of formulations, it is possible to convert the real space into a conformal space, which affords a set of isoconcentration lines that is considerably more regular (Figure 10.6). Beyond the ease of calculations, these transformations allow simple comparisons or equivalences to be made between the different types of arrays. Indeed, it has been demonstrated for symmetry reasons that configurations like double-band, triple-band, and interdigitated electrodes have equivalencies (53). The nature of the original configuration is reflected only by the relative sizes of distance separating the electrodes and electrode dimensions. Nonetheless, the nature of the exact configuration is reflected through the rapidity with which the quasi-steady-state or steady-state regime is achieved.

Conformal mapping techniques often allow explicit analytical equations to be formulated for steady-state currents observed at electrode arrays in a generator/collector mode (48, 52, 53, 114). The steady-state regime is experimentally the most useful regime in these operating conditions. Under steady-state conditions, the enhanced cross-talk between electrodes leads to a reduced diffusional flux of species toward the solution as time proceeds. A steady-state regime is rapidly reached in the generator/collector mode in

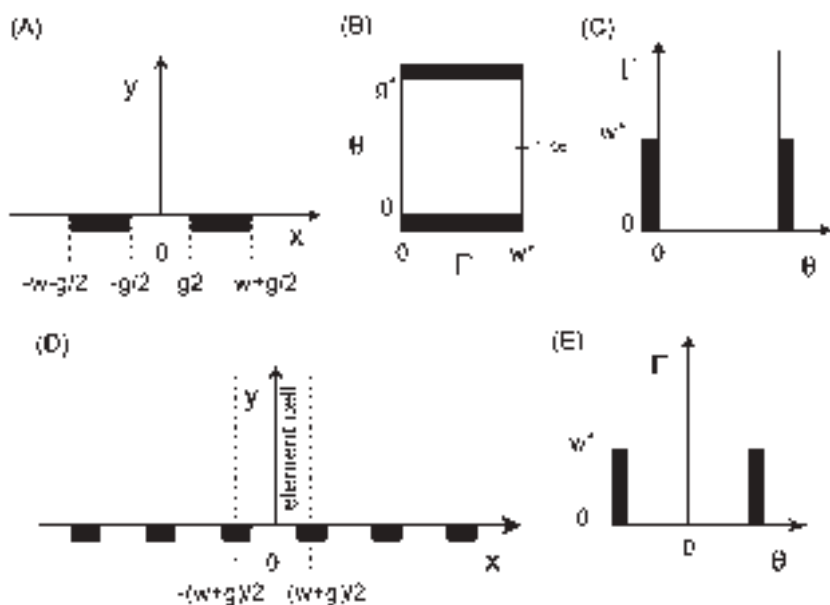


Figure 10.5 Schematic representation of band electrodes in real space and after Schwarz-Christoffel transformations. Double-band assembly in real space (A) and conformal space (B, C) for steady-state (B) and non-steady-state (C) conditions. Interdigitated array of band electrodes in real space (D) and conformal space (E).

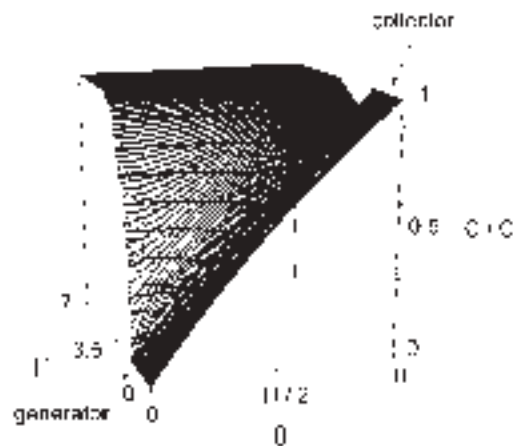


Figure 10.6 Theoretical concentration profiles calculated in the conformal space of a double-band assembly (Figure 10.3C) operating in generator/collector mode in near-steady-state conditions. $w/g = 1$ and $g/2(Dt)^{-1/2} = 0.1$. C^* is the bulk concentration of the reactant in solution.

contrast to arrays of electrodes operating at the same potential. The greater the feedback and collection efficiency between the electrodes, the more rapid is the approach to the steady state. The conformal space also allows effective numerical simulations to be performed under non-steady-state conditions whenever planar diffusion is significantly altered by nonplanar diffusion. Under non-steady-state conditions, the grid lines do not necessarily follow those of the conformal map, but the map is advantageous over other configurations as it more closely approximates the actual grid. A smaller number of nodes are necessary to obtain a numerical solution with the accuracy required. These conformal techniques also allow the effect of electrode perturbation on the electrochemical response to be evaluated for simple geometries. It has been demonstrated for double-hemicylindrical electrodes that these effects are no longer negligible when the resulting heights of the electrodes from the insulating plane become comparable to their widths or to the distance separating the electrodes (114).

All the descriptions above clearly show the strong correlation between collection efficiency, feedback, and steady-state character of the currents detected at electrode arrays. This can be established more rigorously by analyzing the response at a paired-electrode assembly operating in a generator/collector mode. The cross-talk between the two electrodes is characterized by two parameters: the collection efficiency $\text{coll}(t)$ and the amplification factor $\text{ampl}(t)$, with $\text{coll}(t) = i_c/i_g$ and $\text{ampl}(t) = i_g/i_b$. The currents i_c , i_g , and i_b are, respectively, the currents at the collector, generator, and single electrode (i.e., when the second electrode is not connected). The collection efficiency reflects the capture yield of species at the collector that were produced at the generator. The amplification factor is related to the feedback of species from the collector to the generator. The relationship between these two parameters depends on the configuration of the assembly and is a function of time (Figure 10.7A). The collection and amplification factors increase with time and tend toward a steady-state limit theoretically ($1/\text{ampl}(\infty) = 0$ and $\text{coll}(\infty) = 1$), which is not easily reached experimentally due to the diffusional escape of species toward the solution. It is noteworthy that even if the steady-state limit is never achieved experimentally for

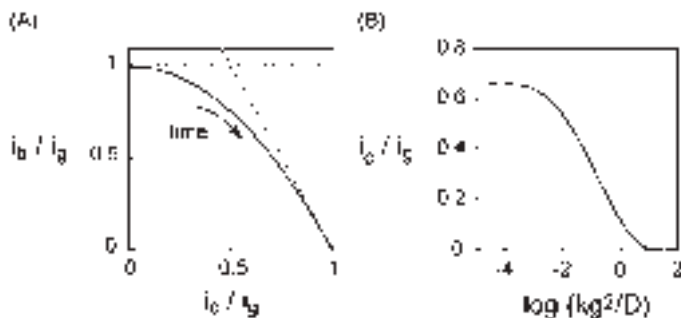


Figure 10.7 Double-band assembly operating in generator/collector mode. (A) Relationship between feedback ($1/\text{ampl}(t) = i_b/i_g$) and collection efficiency ($\text{coll}(t) = i_c/i_g$) in absence of a chemical reaction. (B) Effect of a chemical reaction (EC mechanism) on the collection efficiency as a function of kg^2/D . $w/g = 2$ and $g/2(Dt)^{-1/2} = 0.005$. k is the first-order rate constant of the chemical reaction.

micrometric arrays, an intermediate regime is attained. In these conditions, a simple relation exists between $\text{coll}(t)$ and $\text{ampl}(t)$:

$$\text{coll}(t) = 1 - \eta / \text{ampl}(t) \quad (10.4)$$

with $\eta = 0.5$ for a double-band assembly (113), $\eta = 0.25$ for a triple-band configuration (one generator flanked by two collectors) (31) and even smaller for an interdigitated array. The η value accounts for the extent of diffusional escape toward the solution according to the configuration of the assembly. It thus reflects the time dependence or rapidity in which the steady-state regime is achieved. Indeed, this regime is approached faster for an interdigitated array whereas it remains a virtual limit for a double-band configuration of micrometric size.

The collection efficiency is related to the geometry of the assembly itself but depends also on the lifetime of species produced at the generator. Indeed, one of the main interests of these assemblies is their capability to address kinetic problems. When this lifetime exceeds the time required to diffuse between the two electrodes, the collection efficiency is thus maximal according to the configuration of the assembly. In contrast, when the generated species is no longer stable, the collection efficiency tends to be zero. In this case, the temporal notion is replaced by a spatial notion linked to the dynamics of diffusion taking place between the electrodes. This is true whatever the geometry of the assembly provided that the duration of the experiment is sufficiently long for the diffusion layer developing at the generator to extend over the collector. The collection efficiency is thus a function that compares the relative values of lifetime with the time of flight over the distance separating the two electrodes (Figure 10.7B). Under these conditions, experimental determinations of rate constants or electrochemical mechanism need preliminary working curves to be established with respect to the configuration and geometry of the device (27, 53). This remains valid even if the generator/collector mode is employed in an electroanalytical approach for diffusion layer titrations in which the reactant is produced at the generator and reacts with the target analyte. As the collection efficiency is very sensitive to the heterogeneous kinetics of electron transfer at the generator (49), the need for analytical measurements to proceed with quantitative simulation appears to be obvious. Moreover, the array and especially the distance between the generator and collector must be adapted to the kinetics under investigation. Indeed, for the majority of molecules, the diffusion coefficient is equal to $D \approx 10^{-5} \text{ cm}^2 \text{ sec}^{-1}$, which means that a lifetime of 1 ms requires formally a interelectrode distance of about 1 μm (Figure 10.7B).

10.4 FABRICATION OF MICROELECTRODE ARRAYS

Numerous methods for fabricating microelectrode arrays have been devised depending on the type of array required (6, 20, 35, 41, 49, 62, 63, 65, 115–134).

Low-aspect-ratio (ratio of the height of the microelectrode divided by its lateral dimension is larger than 0.2) microelectrode arrays are fabricated using conventional silicon-based microfabrication technologies, such as lithographic techniques to yield arrays of thin films of metallic or carbon electrodes on a silicon substrate. These arrays often have limited stability and life times as a result of defects in the metal layer; poor resistance to corrosion is

observed together with subsequent swelling and delamination of the metal layers. These microfabricated arrays are typically fragile and cannot be cleaned using conventional cleaning methods, for example, polishing, washing with solvents, and sonication. They are mostly cleaned using reactive ion etching with oxygen plasma.

High-aspect-ratio (ratio of the height of the microelectrode divided by its lateral dimension is larger than 2) microelectrode arrays are mostly fabricated using silicon micromachining, silicon microfabrication, or techniques involving bundling of multiple metal wires. These arrays are mostly designed to penetrate brain tissue to permit highly localized electrical stimulation and/or recording signals from neural tissue. These arrays are more robust compared with arrays formed by lithography and the surface is rather easy to clean. However, solid wire electrode arrays do not have more than a handful of electrodes in the array. The Utah Electrode Array contains about 100 electrodes but is less prone to delamination.

10.4.1 Mechanical methods

A variety of methods have been used in fabricating microdisk electrodes (see Chapter 9). One of the most successful methods is that in which a wire is sealed in glass and the surface is subsequently polished (or etched away) until the electrode is revealed (135). The manufacturing of microdisk arrays is based on the same technique as for simple electrodes. Although lithographic methods or silicon technology are the preferred ways in industry for the mass fabrication of ordered arrays, these techniques are not always accessible to most analytical users of microelectrodes. There is thus demand for the availability of inexpensive, conventionally manufactured microelectrodes. These processes, which are mostly mechanical methods, are at present limited due to the poor reproducibility of the manufacturing methods. Mechanical methods, summarized in Figure 10.8, can be classified according to how the array is constructed. A major limitation is that a careful polishing technique has to be employed. Otherwise, the electrodes have a tendency to recess below the surface of the insulating sheet leading to voltammograms that are slightly different from those for a perfectly coplanar electrode. Careful design is essential to ensure that the diffusion layers at each microelectrode do not interfere with others.

10.4.1.1 Wire techniques

One of the current technologies involves sealing conducting wires (gold, platinum, and carbon fibers) into an insulating material (epoxy resin and glass tube), which is resistant to water and some organic solvents, such as acetonitrile and methanol (Figure 10.8A) (29, 65, 90, 117, 137). Electrical contact between the metal wires is made by using silver epoxy resin. This method was used by Schwarz *et al.* (137), in developing microelectrode arrays of gold and platinum with different numbers of single electrodes in the array. They showed that the construction of disk as well as band microelectrode arrays is possible using this mechanical method. The ordered arrays were constructed by clamping the metal wires on an H-shaped body made of bronze. The wires are fixed in notches with fixed internal distance of 120–130 µm between the single wires. Then the wires are put into a mould and

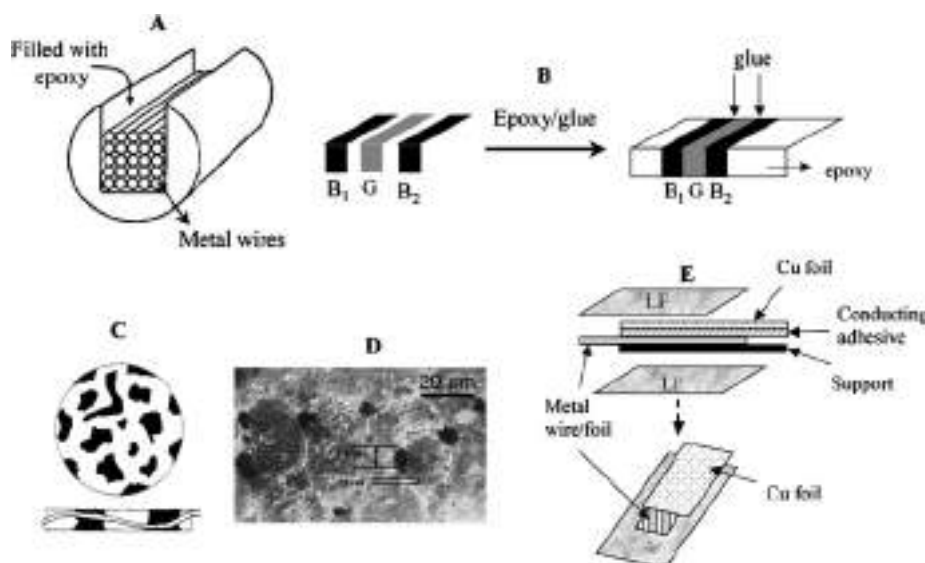


Figure 10.8 Construction principles of microelectrode arrays: (A) wire technique, (B) sandwich method, (C) composite formation (reprint with permission from reference (15)), and (D) Sonochemical formation, electrical micrograph with permission from reference (136).

epoxy resin is poured in to give a cube-shaped epoxy resin body. Arrays of disks as well as band electrodes were constructed in this way.

Band electrodes were formed by pressing gold foils with resin-impregnated glass silk fabric, as the insulation layer, at temperatures of 120–150 °C (137). The distance between the bands is 120 µm and the length of the bands is 600 µm with 2 mm width. The electrodes are provided with an electrical connector at the end of the contact cap. The radii of the sensor surfaces are 2 mm, with complete lengths of 25 mm.

Carbon fibers have been used for array construction because they are more rigid than gold. The construction of carbon fiber arrays consisting of five layers of 20 electrodes was introduced by Caudill *et al.* (29) and used as a flow rate independent amperometric detector. Sleszynski *et al.* (25) reported the design of ensembles based on reticulate vitreous carbon embedded in epoxy resin.

10.4.1.2 Sandwich method

Sandwich techniques (Figure 10.8B) are ideal for the construction of double-band assemblies (53, 113). The schematic of a double-band electrode is seen in Figure 10.1C. An insulator (Mylar film of 2.5 µm thickness, insulating gap) is placed between two sheets of platinum foil (5 µm) and the entire assembly inserted between two pieces of soft glass (about 3 mm thick and 8 mm width). Each layer of this sandwich is sealed with a small amount of epoxy resin, before firmly pressing into position. After hardening of the epoxy, each platinum foil was independently connected to an electrical copper lead with silver epoxy. This assembly can be glued into a glass tube (1 cm internal diameter).

The cross-section of this assembly can be exposed by saw yielding an assembly of two-paired microband electrodes.

An inexpensive and general method for the construction of microelectrode arrays is based upon thermal lamination of metal foils, which is very similar to the sandwich technique described before (138). The polyester/polyethylene laminating foil used is resistant to DMSO as well as to DMF. Electrical connections to the foil have been established either by spot welding a thin metal wire contact to the foil or by using a piece of copper foil with a conducting adhesive on one side. Gold, platinum, and silver microbands were fabricated in this way in addition to disks ranging from 10 to 125 μm . A linear array of microdisk electrodes was prepared by laminating two gold meshes (Figure 10.8E).

10.4.1.3 Formation of compositions (composite electrodes)

Ke-I graphite electrodes are composite electrodes with islands of graphite particles in a sea of Ke-I (13). Each island of graphite is in effect a microelectrode, each separated from other microelectrodes by insulating regions of Ke-F. The electrode surface is thus considered to consist of an array of microelectrodes (Figure 10.8C). It can be considered as a partially blocked solid carbon electrode. The electrode can be fabricated by mixing graphite (particle size of less than 1 μm) with Ke-F (150–450 μm particle size) with a mortar and pestle. This mixture was put into a vacuum chamber to remove the air from the composite and heated to 300–325 °C for 5 min. As the pressure increased, the heater turned off resulting in the composite pellet, which was mounted on a glass tube and sealed in place with epoxy. The dimensions of active and inactive sites on the electrode surface can be adjusted by varying the Ke-I particle size and carbon content. The graphite particles incorporated in an inert binder were found to exhibit microelectrode character in the range of 5–25% graphite. These electrodes are widely used as oxidative working electrodes in flowing streams because of their favorable noise and detection limit.

Another composite electrode is constructed by filling the voids of reticulated vitreous carbon with nonconductive epoxy to produce two-dimensional electrode materials (25). Reticulated vitreous carbon has been used as a three-dimensional highly porous electrode material and has been used in flowing systems as well as in thin slices as an optically transparent electrode.

Electrodes constructed of a single piece of material, such as reticulated vitreous carbon, have the advantage of good electrical contact to each conducting surface, but possess the attendant disadvantage that the magnitude of the interdistance spacing between the electrodes is limited by the requirement that the material be dimensionally stable. Microcellular foams made out of carbonized poly(acrylonitrile) (PAN) foams have been shown to be advantageous as the interelectrode spacing increases as the void fraction of the foam also increases. These foams are prepared via a thermally induced phase separation that allows control of density, pore size, and large void volume (97%). By incorporating an insulator into this matrix, an array can be made of average conducting particle size of 1 μm and smaller (139). Cylindrical samples of PAN foams were fashioned by using a simple drill press. The drill was suspended over a lab jack where the sample was placed. As the jack was raised, the drill slowly turned cutting the fragile foam structure. Filling of the foam with epoxy was accomplished in a vacuum through capillary action.

10.4.1.4 Sonochemical fabrication

Arrays can also be fabricated by sonochemical ablation of polydiamidobenzene ultra thin films deposited on gold-coated glass slides (136). These electrodes were then immersed in a beaker containing distilled water and sonicated for an hour using a 25-kHz sonic bath. The sonic bath employed 12 transducers geometrically arranged and bonded to the base of the stainless steel tank. 1,2-Diaminobenzene dihydrochloride can be electropolymerized at conductive surfaces via a two-electron process to form essentially defect-free insulation polymer films of less than 100 nm thickness. The rational underpinning of this work is that sonochemical ablation of thin insulation polymer films at electrode surfaces may expose localized areas each of which can act as localized microelectrodes and collectively as a microelectrode array. Ultrasound in the kHz range passing through solvents, such as water causes thermal agitation and localized hotspots of up to several hundreds to a few thousand K. This in turn gives rise to the formation of superheated vapor bubbles, which are cooled by the solvent at ambient temperature and asymmetrically implode with the ejection of micro-jets of solvents at speeds of up to several hundreds msec⁻¹. This micro-jet can cause the shattering of hard brittle solids. Soft polymer may, however, be ablated by such jets. A SEM image for a 60-sec sonicated electrode assembly is shown in Figure 10.8D showing the cavitations of the polymer surface. The size of the cavities are about $3 \pm 1 \mu\text{m}$ or sub-micron diameter.

10.4.2 Template approaches

A general template method for preparing nanomaterials has been investigated by Martin and others for the formation of micro- and nanoelectrode arrays (140). The method entails synthesis of the desired metal (or polymer, protein, semiconductor, carbon nanowire) within the cylindrical and monodisperse pores of a membrane or another porous material (Figure 10.9) (see also Section 16.2 in Chapter 16).

Both acid anodized aluminum (alumite membrane) (141, 142) and nuclear track-etched membranes have been used as a template. The nuclear track-etched membranes are prepared by irradiation/chemical etching (143) and contain linear, cylindrical pores of nearly uniform pore diameter. This ensures that the holes in the template are circular and approximately of the same diameter. More recently, porous nano-channel glass (144), and etched wafers of micro-channel plate glass have served as templates (125). The advantage of using porous membranes as templates can be found in their function as arrays of microelectrodes. They exhibit small potential drops, which make the electrochemical measurements possible when

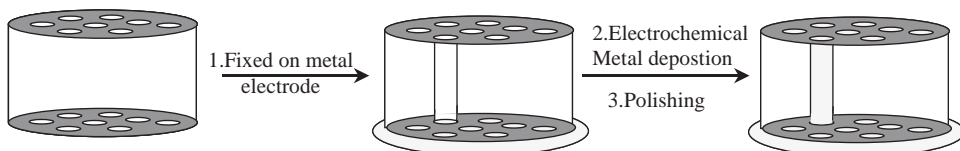


Figure 10.9 Schematic diagram of the procedure used to prepare the microelectrode array using templates. (for colour version: see colour section at the end of the book).

a low-concentration electrolyte is used. Furthermore, membranes with pore radii ranging from 6 μm to 50 Å and pore densities, ranging from 1×10^5 pores cm^{-2} to about 6×10^8 are commercially available allowing the formation of arrays with a broad range of element radii. The ability to control the length of the electrodes formed in the template is another important feature of the template method. The length of the wire can be controlled by varying the deposition time (electrochemical plating method) or by varying the thickness of the template in the electroless plating approach. The template technique is so advanced that gold metal wires as small as 80 Å in diameter can be produced (142).

The fabrication of these arrays presents three challenges:

- (1) Preparation of the porous template
- (2) Electrodeposition of the metal within the hollow parts of the template
- (3) Final preparation of the array following electrodeposition

One of the earliest applications of the template method was to prepare ensemble microscopic (7, 18) and nanoscopic electrodes (116, 141). Such electrodes were prepared by electrochemically depositing noble metals within the pores of the commercially available polymeric filtration membranes. The fabrication of a microelectrode “ensemble” based on the electrochemical deposition of platinum into the pores of a track-etched microporous polycarbonate host membrane was first shown in 1987 by Charles Martin (7). The word ensemble was used to describe the final device because the elements in the device are not evenly spaced. The procedure is simple, and requires only routine and inexpensive electrochemical instrumentation. It was ultimately found that electroless plating allowed for more uniform metal deposition (116). Both plating methods are important for the fabrication of the array, and further considerations continue in the following.

10.4.2.1 *Electrochemical plating method*

Electrodeposition of metallic wires throughout the void spaces of porous nanostructure templates was first shown by Possin in 1970 (145), who developed an electrochemical synthesis method for producing different single metal wires in a 15- μm thick mica wafer with the density of the pores in the order of 10^4 pores cm^{-2} . As the membranes employed have cylindrical pores of uniform diameter a micro- as well as nanometer-sized cylinder or fibril of the desired material is obtained in each pore (7, 146–150).

To electrodeposit metal throughout the channels of the template, the porous material is mounted on a metal-coated glass substance; typically, a metal-coated glass slide (Figure 10.9). The slide provides support for the template and the metal coating on the slide provides the electrical connection needed to drive the electrodeposition. The templates are often coated on one side with a thin metal layer (100 nm of titanium, platinum, or gold) through sputtering in the vacuum at an angle of 45° with respect to the plane of the wafer. This allows the metal to deposit uniformly on the edges of the template as well as a short distance into the channels. These metalized templates adhere well to the glass and provide a surface from which the electrodeposited metal can grow. Ideally, the metal film should completely occlude the channel ends, providing a continuous conducting surface in the channels. Large channels ($>1 \mu\text{m}$) cannot be efficiently occluded by sputtering

layers of metal from which wire growth can be initiated. The template can be bound to the metal-coated slide using epoxy applied around the periphery: a light downward force applied to the center of the template during the epoxy step followed by curing to ensure that the template maintains good electrical contact. Electrodeposition is often enhanced at elevated temperatures and the solutions are often chemically harsh. Thus, a hard, inert epoxy is needed to withstand harsh conditions. Electrodeposition of gold, platinum, silver, copper, nickel, rhodium, and cobalt in templates has been reported (7, 125, 141, 142, 145, 150–152) as well as deposition of polymer (149), semiconductors (153), and carbon (154) into these templates.

10.4.2.2 Electroless metal deposition

Electroless deposition of metals is based on the deposition and reduction of metallic ions (reducing agents are formaldehyde, hydrazine, hydroxylamine) (155–158) from a solution to a surface without applying an electrical potential (159). The key feature of the electroless deposition process is that gold deposition begins at the pore wall. The advantage of the electroless method is that the surface to be coated does not need to be electrochemically conductive. The key requirement of an electroless deposition bath of this type is to arrange the chemistry such that the kinetics of homogeneous electron transfer from the reducing agent to the metal ion is slow. This is essential because otherwise the metal ion would simply be reduced in the bulk solution. A catalyst that accelerates the rate of metal-ion reduction is thus applied to the surface to be coated. In this way, metal ions are reduced only at the surface and the surface becomes coated with the desired metal.

Electroless deposition of various metals into templates was pioneered by Martin who also showed that more uniform metal films are obtained as thicker metal layers are formed (116). Furthermore, the electroless deposition chemistry allows routine fabrication of gold disk electrode arrays, in which the disk can have a diameter as small as 10 nm. To make the electroless deposition process compatible with the membrane chemistry, a “sensitizer” (Sn^{2+}) was first applied to the surface of the membrane, by simply immersing the membrane in a solution of SnCl_2 /trifluoroacetic acid (0.026/0.07 M) (Figure 10.10).

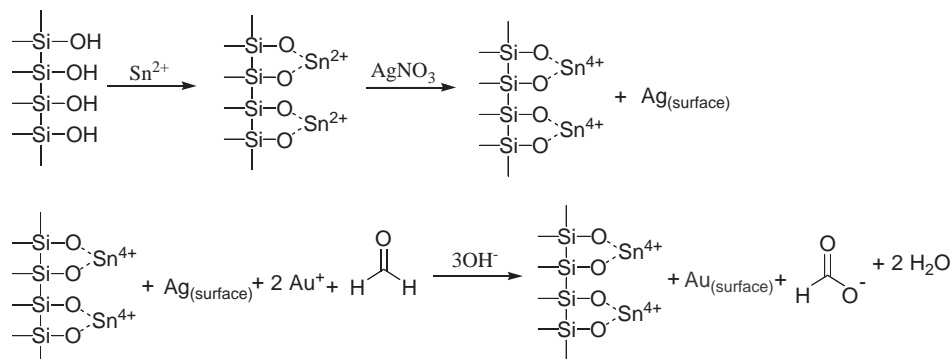
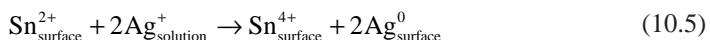


Figure 10.10 Schematic diagram of the electroless procedure used to deposit gold into templates.

The Sn^{2+} sensitized polycarbonate membrane is then activated by immersion in an aqueous solution of AgNO_3 for some minutes. This causes a redox reaction in which the surface-bound Sn^{2+} is oxidized to Sn^{4+} and the Ag^+ is reduced to elemental Ag together with some silver oxide. As a result, the pore walls become coated with discrete nanoscopic Ag particles. A gold-coated membrane can be obtained by immersing it into a Au plating bath ($\text{Na}_3\text{Au}(\text{SO}_3)_2$) (commercially available from Technic Inc., Craston, RI: OROMERSE SO Part B) in the presence of formaldehyde and Na_2SO_3 . The Ag particles are galvanically displaced by gold as gold is the more noble material. Furthermore, the silver particles show excellent catalytic sites for the oxidation of formaldehyde:



Another way of filling the pores of a template with conducting material is filling its pores with carbon paste (18). This is, however, really difficult to do and takes a long time and a lot of patience. The carbon paste was prepared by mixing Carbopack C powder (particle size diameter is 150–180 μm) with vacuum grease using a glass mortar and pestle, which also reduced the size of the carbon particles to 100–300 nm in diameter. By rubbing the paste into the pores of the membrane, after first removing the poly(vinylpyrrolidine) wetting agent by ultrasonication of the membrane in glacial acetic acid, until the carbon paste began to leak out from the opposite side of the membrane. This procedure was repeated and placed onto the surface of a macrosized carbon paste electrode and held in place with a rubber O-ring (Figure 10.11).

Recently, electroless deposition of gold on optical fibers forming ring microelectrodes was reported by Szunerits and Walt (35, 36). Hundreds of gold-coated and -insulated optical fibers were bundled together in a coherent way to form an opto-electrochemical ring electrode array (Figure 10.12). The advantage of microelectrode arrays were thus combined with the imaging properties offered by optical fiber bundles providing users with two levels of control and selectivity. Much of the work on this opto-electrical device has been performed using electrochemiluminescence (ECL) (refer to Chapter 13) as the detection method.

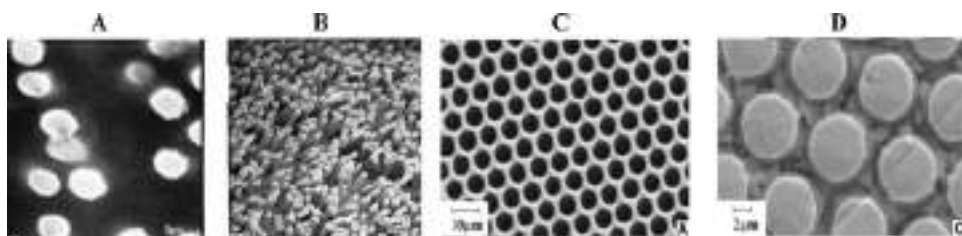


Figure 10.11 Electron micrograph of (A) the surface of an microelectrode array prepared from a microporous polycarbonate host membrane (diameter of 1 μm) (reprint with permission from reference (7)); (B) Pt fibrils obtained after the polycarbonate host membrane is dissolved away from the microelectrode array (reprint with permission from reference (7)); (C) SEM micrograph of the surface of a microchannel glass wafer etched but unfilled (reprint with permission from reference (125)); (D) etched and with Rh-filled array (125) (reprint with permission from reference (125)).

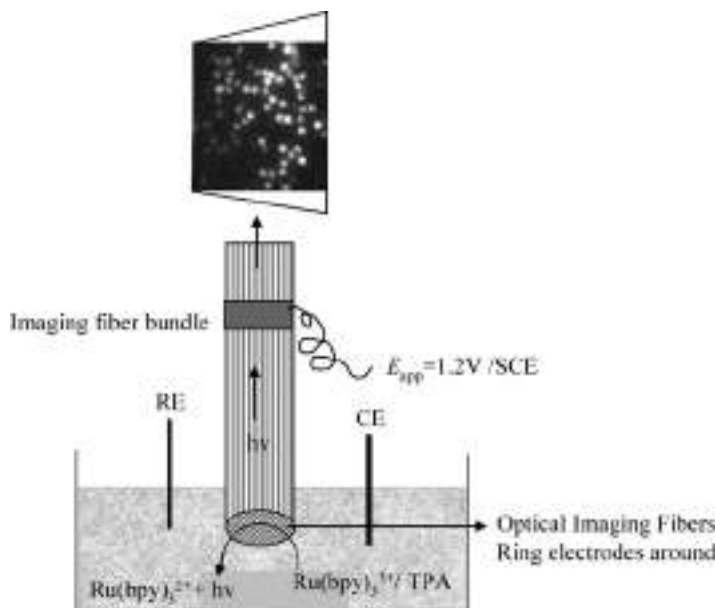


Figure 10.12 Electrochemiluminescence (ECL) imaging using an opto-electrochemical microring array. (for colour version: see colour section at the end of the book).

10.4.3 Lithographic techniques

Lithographic methods have the advantage of being highly controllable and reproducible over mechanical and template approaches. Fabrication of highly sophisticated electrode geometries is a possibility that has been utilized only to a limited extent so far. Lithography, in general, is a technique that transfers a copy of a master pattern onto the surface of a solid material, such as a silicon wafer, and advances in lithographic techniques can be found in the comprehensive literature (160, 161). Photolithography and soft lithography with reactive ion etching have been widely used for the fabrication of electrode arrays and will be discussed in more detail here.

10.4.3.1 Photolithography (*lift off and reactive ion etching*)

The most widely used form of lithography is photolithography. This is partly because of the fact that in the ICs industry, pattern transfer from masks onto thin films is accomplished almost exclusively via photolithography. Photolithographic methods all share the same operational principle: exposure of an appropriate material to electromagnetic radiation (near UV: 350–500 nm, Mercury lamps; deep UV: 150–300 nm, KrF excimer laser, X-ray, soft X-ray (EDU)) introduces a latent image into the material as a result of a set of chemical changes (usually a change in solubility) in its molecular structure. The resolution of photolithography increases as the wavelength of the light used for the exposure decreases. With 193 nm light from an ARF eximer laser and synthetic fused silica lenses,

patterns as small as 150 nm are achieved (162). However, it has been pointed out that photolithographically produced electrodes are difficult to resurface by means of polishing (163). One should keep in mind that the procedure of polishing electrodes between measurements is out of the question when it comes to practical applications, such as process monitoring or in situ investigations.

Three steps are important for the success of photolithography and for forming micro-electrode arrays:

- (1) Photo mask design
- (2) Photoresist step
- (3) Development

(a) *Photo mask design*

Although a scanned aperture can be used to write arbitrary patterns, the predominant use of photolithography is in replicating a pattern on a mask into a layer of photoresist. Such a mask, also called photo mask, is either a nearly optical flat glass, which is transparent to near UV or a quartz plate, transparent to deep UV covered with a metal absorber pattern (about 800 Å thick chromium layer). Such a mask is either placed in physical contact with the resists (contact mode), or an image of the mask is reduced and projected into the resists with an optical system (projection mode).

(b) *Photoresist step*

In addition to advances in the physics and engineering of new light sources and projection optics, clear designs for the chemistries of the photoresist have been critical to the success of photolithography. Photoresists must meet several rigorous requirements: high sensitivity, high contrast, good etching resistance, good resolution, easy processing, high purity, minimal solvent use, low cost, and a high glass transition temperature, T_g . Most resists are amorphous polymers. At temperatures above the glass transition temperature, these polymers exhibit viscous flow with motion of the polymer chain segments. At a temperature below T_g , the motion of the segments is halted and the polymer behaves as a glass rather than as a rubber. Thus, heating the resists film above the T_g enables the film to anneal into its most stable energetic state, the rubber state. Here, the solvent easily can be removed from the polymer matrix through soft-bake. The photoresist is dispensed from a vicious solution of the polymer into the wafer laying on a wafer plate in a resist spinner.

The principle components of photoresists are a polymer, a sensitizer, and a casting solvent. During radiation, the polymer changes structure. The solvent allows spin coating and thin layer formation on a wafer surface. Sensitizers control the chemical reactions in the polymeric phase. There are two types of resists: positive and negative resists. We talk about a positive resist when the photochemical reaction during exposure weakens the polymer by rupture or scission of the main and side polymer chains. The exposed resists become more soluble in developing solutions. The development rate for the exposed resist is larger than for the unexposed one. A negative resist is where the reaction strengthens the polymer by random cross-linking, thus, becoming less soluble. The best known positive photoresist is poly(methylmethacrylate) (PMMA). PMMA becomes soluble through chain scission under deep UV illumination with the maximal sensitivity at 220 nm. Negative photoresists are mostly based on cross-linking of polymer chains, rendering the exposed

parts of the resist insoluble. One negative resist commonly used is a bis(aryl)azide rubber resist, whose matrix is cyclized poly(*cis*-isoprene). Upon photolysis, this resist loses nitrogen and generates a highly reactive nitrene, which undergoes a series of reactions that result in the cross-linking of the resin. New types of resists include polyimides, polyamic acids, photosensitive polyimide precursors, SU-8 (an epoxy-based transparent photoresist). All the resists are deposited through spin coating, which is of primary importance to the effectiveness of pattern transfer.

(c) Development

The development of the resin to form microelectrode arrays is mostly based on the “lift-off process” (164). A solvent dissolves the remaining soluble positive photoresist underneath the metal, starting at the edge or lip of the unexposed photoresist and lift off the metal in the process (Figure 10.13). When the photoresist is removed, all metal on top of the photoresist strip strips off automatically while metal on the top of the photoresist lines stays.

Photolithographically patterned gold microelectrodes have been used extensively (165). Pishko *et al.* reported recently the fabrication of glucose, lactate, and pyruvate sensor arrays by depositing electrostatically complexed monolayers on lithographically patterned individually addressable, gold microelectrodes. Standard photolithographic techniques combined with metal deposition were used to fabricate gold arrays of both SiO₂/Si and flexible Mylar substrates.

Reaction Ion Etching is another possibility for the development of photolithographically treated surfaces (Figure 10.14). It is based on insulating a silicon wafer by growing a high-quality silicon dioxide (SiO₂) layer. A semiconductor interface like silicon is often

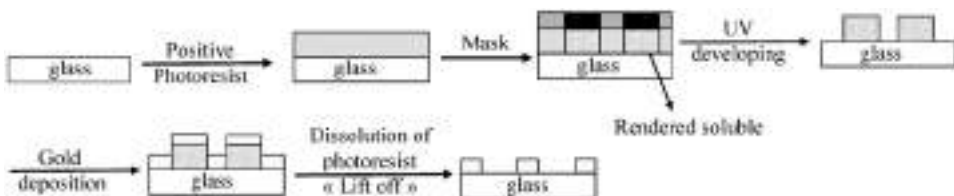


Figure 10.13 Gold microelectrode array made using photolithography (positive resin) and lift off. (for colour version: see colour section at the end of the book).

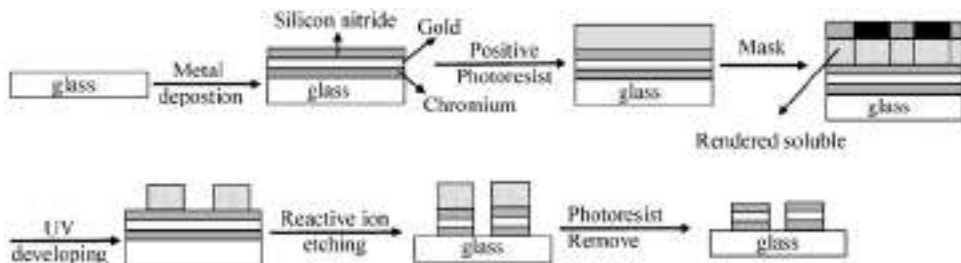


Figure 10.14 Photolithography and reactive ion etching. (for colour version: see colour section at the end of the book).

preferred over glass as it is perfectly flat and withstands the subsequent processing steps. Onto the SiO_2 , a thin metal film (10–100 nm) is deposited followed by deposition of an insulating film, Si_3N_4 , on top of the metal using plasma chemical vapor deposition (CVD). This multilayer surface is modified with a photoresist, covered with a photomask, exposed to UV light, and developed. The area, which is not protected with resin, is exposed to reactive ion etching to etch away the top insulator and the metal. The advantage of reactive ion etching is that the patterns have extremely sharp and vertical steps.

10.4.3.2 Other lithographic techniques (X-ray, electron-beam, ion-beam)

The improvement in optical resolution can be achieved either by increasing the numerical aperture or by reducing the wavelength of the illuminating light. This is a consequence of equation 10.7. The theoretical resolution of an optical system for projection printing is limited by Rayleigh diffraction:

$$R = k_1 \lambda / \text{NA} \quad (10.7)$$

where λ is the wavelength of the illumination system, NA is the numerical aperture of the lens system, and k_1 is a constant dependent on the imaging technology and process control but typically must be >0.7 for adequate production yield.

The most likely technology to push beyond photolithography is X-ray lithography. X-ray lithography is superior to optical lithography because of the use of shorter wavelength and a very large depth of focus. UV photons are scattered at all interfaces, leading to standing waves and proximity effects, X-rays are absorbed but do not scatter. Furthermore, in comparison to electron lithography and ion-beam lithography, no charged particles are directly involved thus eliminating the need for the use of vacuum. There are, however, two major limitations. One is the low sensitivity of the photoresists (PMMA, PGMA (poly(glycidyl methacrylate-co-ethyl acrylate))) to X rays as well as the high cost of sufficiently bright X-ray sources. The second is the mask making, which basically consists of a pattern of X-ray absorbing materials (like gold) on a substrate transparent to X-rays (Ti, Si, SiC, BE). Structures of about 30 nm are now routinely fabricated (161).

Methods based on writing with particles (electrons or ions) rather than photons accomplish the same task. Focused electron beams (electron beam lithography), beyond observing samples as in scanning electron microscopy (SEM) or transmission electron microscopy (TEM), can be used to form patterned nanostructures in an electron sensitive resist film, such as PMMA (166). Interaction of the electron beam with the resist causes local changes in its solubility, and in the case of PMMA, the electrons induce local chain scission and formation of micropores that cause the material to be soluble in a developer, such as methylisobutyl ketone and 2-propanol (164). Some of its attractive features are that no mask is needed, that precise control of the energy to a resist-coated wafer (0.0005 nm for 50 keV) is possible, the ability to register accurately over small areas of a wafer, a large depth of focus because of continuous focusing over topography. However, electrons also need to be held in vacuum and scatter in solids, limiting practical resolution to dimensions greater than 10 nm.

In contrast, ion-beam lithography has a better resolution than electron beam lithography because the secondary electrons produced by an ion beam are of lower energy and have a shorter diffusion range so that hardly any back scattering occurs. The ion-beam spot has the

smallest possible size and is reaching 8 nm. It offers direct writing and masking fabrication opportunities. Ions (H^+ , He^{2+} , Ar^+) react with the substrate allowing a greater variety of surface modifications, such as patterned doping.

10.4.3.3 Soft lithography

Soft lithography is the collective name for a set of lithographic techniques: replica modeling (REM), micromolding in capillaries (MIMIC), microtransfer molding (μ TM), solvent-assisted micromolding (SAMIM), near-field conformal photolithography using an elastomeric phase-shifting mask (which has been developed as an alternative to photolithography and replication technology for micro- and nanofabrication), and microcontact printing (μ CP). These techniques have in common the use of a patterned elastomer as the mold/stamp/mask (Figure 10.15) to generate/transfer patterns on solid interfaces. The elastomer usually used is poly(dimethoxysiloxane) (PDMS). Soft lithography offers immediate advantages over photolithography in applications where patterning of nonplanar substrates or large area patterning are the main concerns. For an excellent review on soft lithography, see Xia *et al.* (161). μ CP has also been used for the construction of microelectrode arrays.

(a) Soft lithography: microcontact printing

The technique of μ CP is a routine way of fabricating chemical patterns with micrometer dimensions (161, 167, 168). Being a “dry” process, it only involves transient contact between a gold surface and an inked “stamp”. No liquid drops are present that might influence the quality of the film. μ CP has mainly been developed with self-assembled monolayers (SAM) of alkanethiolates on gold (169), silver (170), and copper (171). The procedure for carrying out μ CP is rather simple and is shown in Figure 10.15 together with the formation of the stamp.

The technique requires stamps generated by casting PDMS against a “master” consisting of a surface having the desired pattern in low relief (this gives a low relief pattern on the surface (Figure 10.15). The master can be fabricated photolithographically in thin PMMA films supported on silicon wafers, provided the mask required for photolithography is available (167). Chrome mask generation is too expensive and slow to make this method practical for exploratory work requiring microfabrication. “Rapid prototyping”, a technique for the generation of masks developed by Whitesides is an alternative. It uses high-resolution printing to make photo masks generating lines of 20–50 μ m width (172). Another method that does not require the generation of conventional photo masks and is



Figure 10.15 Schematic procedure for micro-contact printing. (for colour version: see colour section at the end of the book).

capable of resolution higher than rapid prototyping is laser ablation of thin polymer films (173). Whitesides has developed an inexpensive bench top technique for the fabrication of PDMS stamps using laser ablation of dye-doped thin polymer films with a low power visible laser yielding features as small as 1 μm . The PDMS stamp is then inked with an appropriate solution, often an alkanethiol, because it forms a very stable and organized monolayer on gold (174). This chemically modified stamp is brought into contact with the gold substrate as seen in Figure 10.15, and the ink molecules are transferred to those regions of the substrate that contact the stamp. The success of μCP relies on the conformal contact between the stamp and the surface of the substrate, on the rapid formation of highly ordered monolayers (<1 sec), and on the autophobicity of the SAM, which effectively blocks the reactive spreading of the ink across the surface. Another advantage of microcontact patterning is that it is a parallel method and SAMs can be formed over relatively large surfaces in a single process. It is thus a useful tool for the fabrication of microelectrode arrays. Figure 10.16 shows a variety of micropatterns on gold using μCP . Figure 10.16A shows the friction force image of a microelectrode array formed using hexadecylmercaptane ($(\text{HS}(\text{CH}_2)_{15}\text{CH}_3)$ stamped using μCP onto gold (41). The key point of SAM-based microelectrodes is that the closely packed SAM terminated with hydrophobic functional groups can efficiently block electron transfer and mass transfer between the gold substrate and the redox couple in solution.

10.4.5 Etching techniques

A number of subtractive and/or additive processes, where material is removed/added to a device in a selective manner, precede lithographic processes. One way of removing material for the construction of electrode arrays is through etching. Reactive-ion etching has

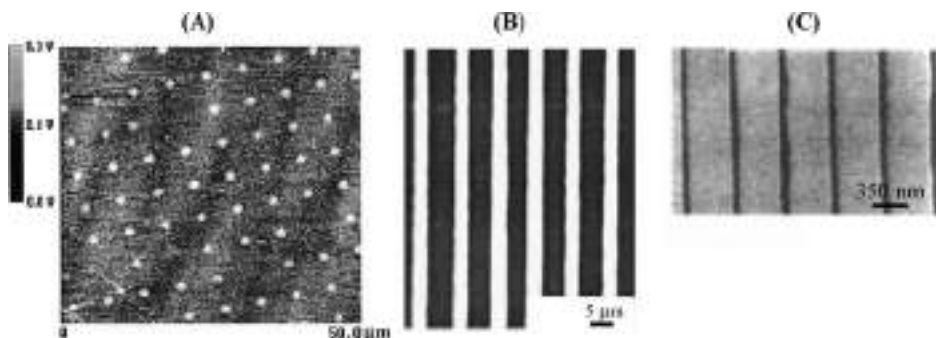


Figure 10.16 Microcontact printing (μCP): (A) friction force image of the prepared SAM-based microelectrode array 1 μm in diameter and 5 μm in pitch (41); (B) optical micrograph of lines patterned by stamping hexadecanethiol onto gold, followed by selective etching of gold. The patterns were generated by stamping hexadecanethiol onto a gold surface, followed by selective etching of the gold. Stamps used in generating these patterns were obtained via ablation through an objective (80 \times) and with a laser scan rate of 10 mm min^{-1} , power 10 mW. The white regions correspond to the unetched gold (167), and (C) array of 35 nm trenches fabricated in gold by μCP with hexadecanethiol (175).

been discussed. However, subtractive etching techniques range from wet etching, electrochemical etching, photo-electrochemical etching to focused ion-beam milling, plasma etching, laser machining, ultrasonic drilling, and mechanical methods (160).

Chemical etching has been widely used for the fabrication of three-dimensional microelectrode arrays. These kinds of electrode array configurations have been widely used to explore and assess intracortical brain activity (176). It is widely accepted that the cerebral cortex provides the easiest access to motor intent and sensory perception and is thus an attractive region for interfacing potential future devices for restoring neurological functions lost due to degenerative muscular diseases, strokes, or spinal cord injury (177). Much is still unknown about the generation of different motor behaviors, but it has been recognized that for clinical applications of such “brain-machine” interfaces, the activities of hundreds of thousands of neurons must be simultaneously sampled. A three-dimensional electrode array allows capturing neural signals from a collection of recording sites with a pre-selected spatial distribution. Two well-known approaches include the development of microelectrode arrays at the University of Utah (178, 179) and at the University of Michigan (180). Fofonoff reported the fabrication of a three-dimensional array by electrical discharge machining followed by chemical etching (181). To reduce the dimensions of the micromachined array, it was placed into a hot HCl bath heated close to its boiling point (Figure 10.17A). Electroplating with gold followed by platinum and final electrical insulation into parylene formed an array of platinum-coated electrodes (Figure 10.17B).

A rather different approach for the fabrication of three-dimensional electrode arrays is based on the use of optical imaging fiber arrays. An imaging fiber array has thousands of individual optical fibers (diameter of 3–4 μm) melted and drawn together in a coherent way. This imaging fiber can be used as a platform for the construction of a three-dimensional electrode array through chemical etching of the optical fibers. In the case of a silica fiber, the optical fiber is chemically etched in one-step procedure by dipping the fiber array into a solution of hydrofluoric acid (160) and ammonium fluoride (NH_4F) buffer (34, 182). The fiber's etch rate is dependent on the dopant concentration in the fiber and the concentration of the acid solution. In the case of the fibers used by Walt *et al.*, etching occurs at different rates between the pure SiO_2 of the fiber cladding and the GeO_2 doped SiO_2 of the core (Figure 10.17B1). The chemical reaction of SiO_2 and GeO_2 with HF acid can be summarized by reactions (10.8)–(10.10). The fluorosilicic acid (H_2SiF_6)

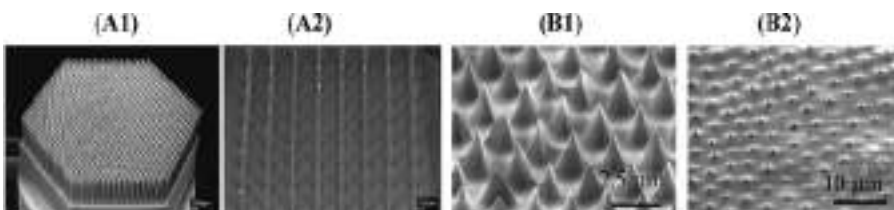
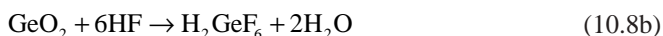


Figure 10.17 Microelectrodes array formed through chemical etching. (A1) SEM of an 1141-electrode titanium alloy electrode array, (A2) SEM image of a parylene-coated assembly of platinum-coated electrodes (181), (B1) SEM of an etched optical imaging fiber bundle, and (B2) SEM of a with gold covered and with electrophoretic paint insulated microelectrode array (with permission from reference (34)).

and the hexafluorogermanic acid (H_2GeF_6) is produced either directly (reactions (10.8a) and (10.8b)) or as outlined by reactions (10.9)–(10.11).



If an ammonium fluoride buffered etching solution is used, there is a further possible dissolution step involved, which arises from the involvement of ammonium ionized from the solution (reactions (10.11a) and (10.11b)).



It is the difference in the solubility of the resultant $(NH_4)_2SiF_6$ and $(NH_4)_2GeF_6$, which leads to the difference in etching rates between the core and cladding. The tip cone angle is thus primarily a function of the etching solution and the GeO_2 doping level of the fiber core, while the temperature, the type, and concentration of the acid used, and the etching time are crucial for the optical and geometrical characteristics (such as cone angle and aperture diameter) of the tips formed. An ordered array of individual microelectrodes (6 μm center-to-center spacing) was fabricated by coating such a chemically etched imaging fiber bundle with gold and insulating the base of the fiber array with an electrophoretic paint. Electrophoretic paints have been shown to be useful for the fabrication of microelectrodes (183, 184). The electrophoretic paint consists mainly of two types of resins: polyacrylates and polyurethanes, where the cross-linking reaction is between the isocyanate group on the urethane resins and the hydroxyl groups in the polyacrylates. The principle mechanism of deposition is by depletion of hydrogen ions at the cathode via application of a positive DC voltage between the cathode (fiber bundle) and the anode (Cu wire). The resulting increase in pH destabilizes the cationic resin emulsion and the resin loses the colloidal condition and deposits onto the cathodic surface. Curing the fiber subsequently at 200 °C results in the shrinking of the deposited film and insures that the tip apex is not covered (Figure 10.17B2).

10.5 ELECTROCHEMICAL CHARACTERISATION OF MICROELECTRODE ARRAYS

Microelectrode arrays are generally characterized using a combination of voltammetry, SEM, and atomic force microscopy (185, 186). In addition to these techniques, other methods are reported which have been shown to be important in characterizing *in situ* the

electrochemical reactivities of ensembles of microelectrodes operating at the same potential or addressed individually.

10.5.1 Chronoamperometry and cyclic voltammetry

For a microelectrode array, chronoamperometric responses are complex and depend on the time frame of the experiment and the limiting behaviors described in section 10.3.1 (26). In the case of a regular ensemble of electrodes, the general trend of the chronoamperometric response is well known. At short times, the array behaves as individual electrodes and the response to a potential step shows planar diffusion (Cottrellian behavior with dependence of the current as $1/\sqrt{\tau}$) since no interference from overlapping diffusion occurs. At longer times, this behavior changes to a mixed regime where hemispherical diffusion prevails and this regime is finally converted again to one of planar diffusion. In this last case, the diffusion layers fully overlap and the entire array behaves as a macroelectrode whose area is equal to the total geometric surface area (see Section 10.3.1).

An analytical expression for the current was provided by Shoup and Szabo (106) for an infinite number of microdisk interfaces operating at the same potential in a hexagonal array:

$$f(\tau, \theta) = \frac{i}{4nFrDC^*} = \frac{\sqrt{\pi}}{2\sqrt{\tau}} + \frac{\pi}{4} + \left(1 - \frac{\pi}{4}\right) \exp\left[\frac{-B\theta^2(3-2\theta)}{\sqrt{\tau}}\right] - \exp\left[-\frac{\frac{\sqrt{\pi}}{2}\left(\frac{\theta}{1-\theta}\right) + B\left(1-\frac{\pi}{4}\right)\theta^2(3-2\theta)}{\sqrt{\tau}}\right] \left(1 + \frac{3\sqrt{\pi}}{2\tau} \frac{\theta^3}{(1-\theta)}\right)^{-1} \quad (10.12)$$

where τ is the dimensionless time with $\tau = 4Dt/r^2$, θ the array coverage with $\theta = (2r/d)^2$, r the radius of the microdisks, d the center-to-center distance between microdisks, and B a constant equal to 0.7823. At short times, the predicted currents follow the Cottrell equation given for linear diffusion to the area of a single microdisk (i.e., πr^2), while at longer times, they converge to the Cottrell equation corresponding to linear diffusion to the total geometric area (i.e., $\pi d^2/4$). The characteristic time corresponding to a nonlinear to a linear transition from when diffusion layers overlap depends on both the size of the individual microelectrodes and their packing in the array as well as on the diffusion coefficient of redox species. This time t_c can be evaluated by (106)

$$t_c = \frac{(d/2 - r)^2}{6D} \quad (10.13)$$

However, equation 10.13 is not always experimentally appropriate (187) and gives only a crude estimation of the transition time t_c when individual diffusion layers begin to overlap according to the packing density of the array. Similar results have been also derived from a simple analytical approach to hexagonal, square, and random arrays (21). It must be emphasized that all these approaches remain valid over a specific range of parameters

resulting from particular assumptions or approximations (see Section 10.3.1). For example, numerical simulations of chronoamperometric responses of infinite arrays (110) showed that equation 10.12 was valid only for values of θ exceeding 0.9. The electrochemical properties depend strongly on the way the microelectrodes are packed as arrays of recessed microelectrodes behave differently from arrays of inlaid electrodes in the short and medium time domains (110).

The interpretation of the response of an assembly of microelectrodes to a cyclic voltammetric waveform is more complicated than in the case of chronoamperometry. When applied to microelectrode arrays, it is mainly used in the steady-state limit. From an electroanalytical point of view, the major issue is to choose an appropriate scan rate v to ensure steady-state diffusion at the array interface. If the scan rate is not properly chosen, a peak-shaped voltammogram is observed whose characteristics can be derived only from simulations (188). Figure 10.18 shows simulated cyclic voltammograms obtained at an infinite number of microdisks ($r = 10 \mu\text{m}$) in a hexagonal array with d/r ranging from 3 to 100 and d ranging from 20 to 1000 μm .

Two characteristic polarization curves can be observed. In the case of high d/r ratios, a sigmoidal shape is related to the individual microdisk electrode behavior (hemispherical diffusion). As in the case of low d/r ratios, a peak-shaped voltammogram is obtained corresponding to linear diffusion. For intermediate d/r ratios, a mixed diffusion

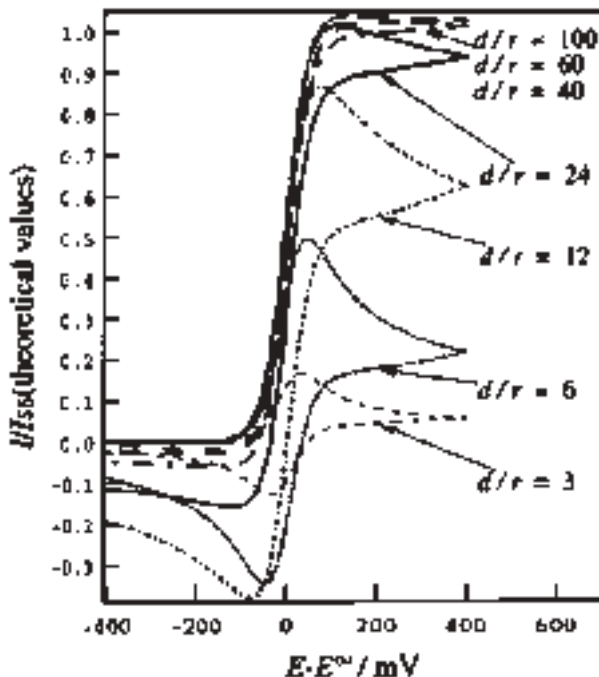


Figure 10.18 Simulated cyclic voltammograms obtained at an infinite number of microdisks in a hexagonal array having various interelectrode (center-to-center) distance, d . $d/r = 3-100$, $v = 10 \text{ mV sec}^{-1}$, $r = 10 \mu\text{m}$, $D = 10^{-7} \text{ cm}^2 \text{ sec}^{-1}$ (with permission from reference (188)).

regime takes place where the current slowly increases with d/r and the peak separation widens. Moreover, the peak-to-peak separation becomes larger in the same way as when the apparent electron transfer process is lowered, even if a Nernstian system is assumed during simulation. The characteristic scan rate v from which a steady-state voltammogram is observed can be easily derived from equation 10.12 as the equivalency in voltammetry between time and scan rate is straightforward (i.e., $t_c = RT/Fv$). This behavior has been predicted by Amatore *et al.* (14) for charge transfer at partially blocked electrodes (see Section 10.3.1). The shapes and characteristics of the voltammograms can be deduced from a zone diagram (Figure 10.19), which defines four main domains where different characteristic behaviors are encountered. Vertical frontiers delimit the linear and spherical diffusion fields. From the upper side to the lower side, a distinction is made between voltammograms exhibiting either a fast electron transfer or an apparent quasi-irreversible electron transfer. This zone diagram shows clearly the strong influence of the fractional coverage or packing density of the array on the apparent standard rate constant of the electrochemical reaction. It can be easily derived for a hexagonal array of microdisk electrodes with the assumption of disk inactive sites rather than hexagonal ones (188).

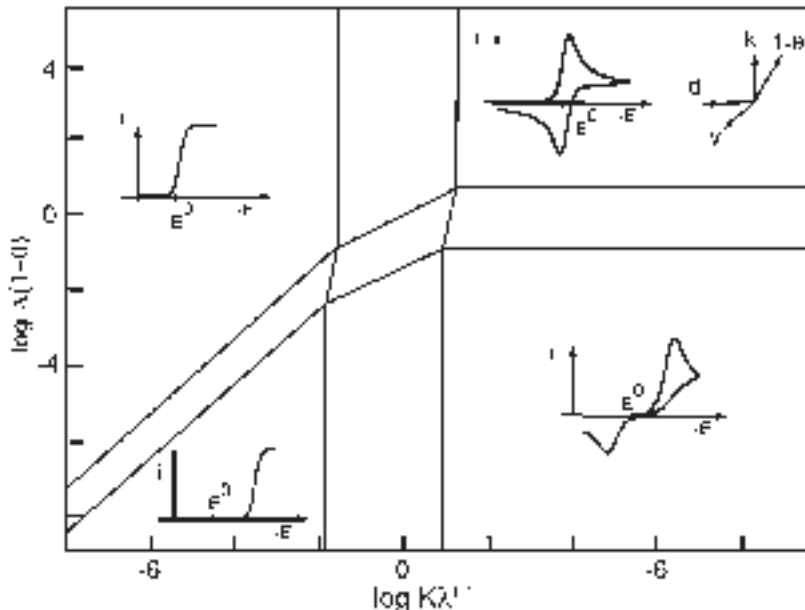


Figure 10.19 Zone diagram representing the main characteristics of cyclic voltammograms as a function of two dimensionless parameters, $K\lambda^{1/2}$ and $\Lambda(1-\theta)$ with $K\lambda^{1/2} = [(1-\theta)/\theta][(8D/d^2)\theta^{-1}(1-\theta)^{-1}/\ln[1+0.27(1-\theta)^{-1/2}]]^{1/2}t_c^{1/2}$ and $\Lambda(1-\theta) = k(t_c/D)^{1/2}(1-\theta)$. θ represents the fractional coverage of the insulating sites and is defined as $\theta = S_{ins}/(S_{ins} + S_{act})$ with S_{ins} and S_{act} the insulating and electroactive surface areas, respectively. k is the standard rate constant for the electron transfer at the active site. $t_c = RT/Fv$ with v the scan rate. Adapted from reference (14).

10.5.2 Scanning electrochemical microscopy

Scanning electrochemical microscopy (SECM) is commonly used to characterize different substrates and microelectrodes as well as to image their interfaces (189). For a more detailed discussion about SECM see Chapter 12. In comparison to conventional microscopies, this method gives valuable information regarding the conductivity, connectivity, and reactivity of microelectrode arrays (190). It can be used not only to map microelectrode arrays or track patterns but also to determine at the same time the integrity of the insulator coatings. Different SECM modes can be used depending on whether the microelectrodes in the array and the tips used for imaging the surface are reciprocally biased or unbiased. The feedback and the substrate generation/tip collection (SG/TC) modes of SECM were found to address each of these issues (190). The features of these two SECM modes have found to be particularly useful when random microelectrode arrays are being fabricated and characterized.

10.5.3 Optical microscopy

Information about the geometry, homogeneity, and morphology of array surfaces may be obtained from scanning methods, like AFM, STM, SECM, or SEM. However, these methods are not capable of giving direct evidence of the electrochemical activities of microelectrodes in arrays. Except for SECM, one way to overcome this difficulty is to detect optically the ECL initiated on each microelectrode. Indeed, by placing the microelectrode array under an optical microscope fitted with a high sensitivity CCD camera, ECL images can be acquired from the focal plane, which are directly correlated to the electrochemical activities of each microelectrode of the array (34). Furthermore, according to the mechanism of the ECL reaction involved, the size of the individual diffusion layers can be evaluated from the size of the ECL spots, which in turn, gives an estimation of the electrode dimension. The resolution achieved by this method allows the imaging of sub-micrometer electrodes.

Another way to characterize the electrochemical activity of microelectrode arrays is to map the electroactive species generated at each electrode by confocal Raman spectroscopy. Indeed, the use of confocal signal detection enables Raman spectroscopic measurements of very small sample volumes (even down to a few μm^3). Applied to a microelectrode array, it provides a statistical picture of the distribution of active sites on the array (60). As in the case of SECM, these two optical methods are particularly useful to verify if individual diffusion layers do not overlap and if the microelectrodes in the array are diffusely independent, particularly for random microelectrode arrays.

10.6 CONCLUSION AND PROSPECTS

Microelectrode arrays have been widely discussed in the literature from theoretical and practical viewpoints and these have led to a better understanding of typical characteristics encountered during their operation. Such devices offer advantages in a number of areas of

investigation. The main achievement in recent years has been the development of reliable methods for fabricating microelectrode arrays. The availability of these methods should open the field for further studies and development of novel applications in physical electrochemistry, imaging science, analytical science, and within the medical and biosensing fields.

Current research is also directed at decreasing the dimensions of the individual electrodes in the array in order to produce nanoelectrode arrays. In these nanoelectrode arrays, the critical dimension is decreased to the same order as the thickness of the electrical double layer or the molecular size of redox species, and the experimental behavior starts to deviate from extrapolations of behavior at larger electrodes. This point may be viewed as the separation point between nanoelectrodes and microelectrodes arrays (191).

REFERENCES

1. M. A. Dayton, J. C. Brown, K. J. Stutts, R. M. Wightman, *Anal. Chem.* **52**, 946 (1980).
2. R. M. Wightman, *Science* **240**, 415 (1980).
3. J. Cassidy, J. Ghoroghchian, F. Sarfarazi, J. J. Smith, S. Pons, *Electrochim. Acta* **31**, 629 (1986).
4. R. Cieslinski, N. Armstrong, *Anal. Chem.* **51**, 565 (1979).
5. O. Contamin, E. Levart, *J. Electroanal. Chem.* **136**, 259 (1982).
6. L. J. Magee, J. Osteryoung, *Anal. Chem.* **61**(18), 2124 (1989).
7. R. M. Penner, C. R. Martin, *Anal. Chem.* **59**, 2625 (1987).
8. S. G. Weber, *Anal. Chem.* **61**, 295 (1989).
9. T. Gueshi, K. Tokuda, H. Matsuda, *J. Electroanal. Chem.* **89**, 247 (1978).
10. H. Reller, E. Kirowaeisner, E. Gileadi, *J. Electroanal. Chem.* **138**(1), 65 (1982).
11. H. Reller, E. Kirowaeisner, E. Gileadi, *J. Electrochem. Soc.* **131**(3), C110 (1984).
12. H. Reller, E. Kirowaeisner, E. Gileadi, *J. Electroanal. Chem.* **161**(2), 247 (1984).
13. D. E. Weisshaar, D. E. Tallman, *Anal. Chem.* **55**, 1146 (1983).
14. C. Amatore, J. M. Saveant, D. Tessier, *J. Electroanal. Chem.* **147**(1–2), 39 (1983).
15. J. L. Anderson, K. K. Whiten, J. D. Brewster, T.-Y. Ou, W. K. Nonidez, *Anal. Chem.* **57**, 1366 (1985).
16. A. Aoki, T. Matsue, I. Uchida, *Anal. Chem.* **62**(20), 2206 (1990).
17. K. Aoki, *J. Electroanal. Chem.* **270**, 35 (1989).
18. I. F. Cheng, C. R. Martin, *Anal. Chem.* **60**, 2163 (1988).
19. I. F. Cheng, L. D. Whiteley, C. R. Martin, *Anal. Chem.* **61**(7) 762 (1989).
20. C. E. Chidsey, B. J. Feldman, C. Lundgren, R. W. Murray, *Anal. Chem.* **58**(3), 601 (1986).
21. B. J. Scharifker, in *Microelectrodes: Theory and Applications*, M. I. Montenegro, M. A. Queiros, J. L. Daschbach, Eds., NATO ASI Series Kluwer Academic Publishers: Dordrecht, 1991, Vol. 4, p. 227.
22. B. R. Scharifker, *J. Electroanal. Chem.* **240**, 61 (1988).
23. B. R. Scharifker, *J. Electroanal. Chem.* **458**(1–2), 253 (1998).
24. B. J. Seddon, H. H. Girault, M. J. Eddowes, *J. Electroanal. Chem.* **266**, 227 (1989).
25. N. Sleszynski, J. Osteryoung, M. Cartier, *Anal. Chem.* **56**(2), 130 (1984).
26. C. Amatore, in *Physical Electrochemistry*, I. Rubinstein, Ed., Marcel Dekker: New York, 1995, p. 131.
27. T. A. Postlethwaite, J. E. Hutchison, R. Murray, B. Fosset, C. Amatore, *Anal. Chem.* **68**(17), 2951 (1996).

28. G. Kindlman, R. A. Normann, A. Badi, J. Bigler, C. Keller, R. Coffey, G. M. Jones, C. R. Johnson, *BISTI 2003 Symposium, Digital Biology: The Emerging Paradigm*, www.bisti.nih.gov/2003 meeting (2003).
29. W. L. Caudill, J. O. Howell, R. M. Wightman, *Anal. Chem.* **54**, 2532 (1982).
30. P. Bindra, A. P. Brown, M. Fleischmann, D. Pletcher, *J. Electroanal. Chem.* **58**, 31 (1975).
31. P. Bindra, J. Ulstrup, *J. Electroanal. Chem.* **140**, 131 (1982).
32. E. Sabatini, I. Rubinstein, *J. Phys. Chem.* **91**, 6663 (1987).
33. E. Sabatini, I. Rubinstein, R. Maoz, J. Sagiv, *J. Electroanal. Chem.* **219**, 365 (1987).
34. S. Szunerits, J. M. Tam, L. Thouin, C. Amatore, D. R. Walt, *Anal. Chem.* **75**(17), 4382 (2003).
35. S. Szunerits, D. R. Walt, *Anal. Chem.* **74**(7), 1718 (2002).
36. S. Szunerits, D. R. Walt, *Chemphyschem* **4**(2), 186 (2003).
37. A. Chovin, P. Garrigue, P. Vinatier, N. Sojic, *Anal. Chem.* **76**(2), 357 (2004).
38. M. DeAbreu, W. C. Purdy, *Anal. Chem.* **59**(1), 204 (1987).
39. H. Ecken, S. Ingebrandt, M. Krause, D. Richter, M. Hara, A. Offenhauser, *Electrochim. Acta* **48**, 3355 (2003).
40. G. C. Fiaccabruno, M. Koudelkahep, S. Jeanneret, A. Vandenberg, N. F. Derooij, *Sens. Actuat. B Chem.* **19**(1-3), 675 (1994).
41. H. X. He, Q. G. Li, Z. Y. Zhou, H. Zhang, S. F. Y. Li, Z. F. Liu, *Langmuir* **16**(25), 9683 (2000).
42. F. Heer, W. Franks, A. Blau, S. Taschini, C. Ziegler, A. Hierlemann, H. Baltes, *Biosens. Bioelectron.* **20**, 358 (2004).
43. Y. Iwasaki, O. Niwa, M. Morita, H. Tabei, P. T. Kissinger, *Anal. Chem.* **68**(21), 3797 (1996).
44. S. P. Kounaves, W. Deng, P. R. Hallock, G. T. A. Kovacs, C. W. Storment, *Anal. Chem.* **66**(3), 418 (1994).
45. H. J. Lee, C. Beriet, H. H. Girault, *J. Electroanal. Chem.* **453**, 211 (1998).
46. J. Pei, M. L. Tercier-Waeber, J. Buffle, G. C. Fiaccabruno, M. Koudelka-Hep, *Anal. Chem.* **73**, 2273 (2001).
47. B. J. Seddon, C. F. Wang, W. F. Peng, X. J. Zhang, *J. Chem. Soc.-Faraday Trans.* **90**(4), 605 (1994).
48. C. Amatore, C. Sella, L. Thouin, *J. Phys. Chem. B* **106**(44), 11565 (2002).
49. I. B. Svir, A. I. Oleinick, R. G. Compton, *J. Electroanal. Chem.* **560**(2), 117 (2003).
50. C. Amatore, M. Belotti, Y. Chen, E. Roy, C. Sella, L. Thouin, *J. Electroanal. Chem.* **573**, 333 (2004).
51. C. Amatore, L. Thouin, J.-S. Warkocz, *Chem. Eur. J.* **5**(2), 456 (1999).
52. I. A. Arkoub, C. Amatore, C. Sella, L. Thouin, J. S. Warkocz, *J. Phys. Chem. B* **105**(37), 8694 (2001).
53. B. Fosset, C. A. Amatore, J. E. Bartelt, A. C. Michael, R. M. Wightman, *Anal. Chem.* **63**(4), 306 (1991).
54. T. V. Shea, A. J. Bard, *Anal. Chem.* **59**(17), 2101 (1987).
55. C. Amatore, A. R. Brown, *J. Am. Chem. Soc.* **118**, 1482 (1996).
56. J. E. Bartelt, M. R. Deakin, C. A. Amatore, R. M. Wightman, *Anal. Chem.* **60**, 2167 (1988).
57. H. A. O. Hill, N. A. Klein, I. S. M. Psalti, N. J. Walton, *Anal. Chem.* **61**, 2200 (1989).
58. R. G. Compton, B. A. Coles, J. J. Gooding, A. C. Fisher, T. I. Cox, *J. Phys. Chem.* **98**, 2446 (1994).
59. J. H. Thomas, S. K. Kim, P. J. Hesketh, H. B. Halsall, W. R. Heineman, *Anal. Biochem.* **328**(2), 113 (2004).
60. L. J. Yang, Y. B. Li, G. F. Erf, *Anal. Chem.* **76**(4), 1107 (2004).
61. J. Senior, A. Shah, C. Monteux, V. De Biasi, *J. Pharm. Biomed. Anal.* **24**(5-6), 843 (2001).
62. R. Kurita, H. Tabei, Z. M. Liu, T. Horiuchi, O. Niwa, *Sens. Actuat. B Chem.* **71**(1-2), 82 (2000).
63. R. M. Blanchard, A. R. Noble-Luginbuhl, R. G. Nuzzo, *Anal. Chem.* **72**(7), 1365 (2000).
64. O. Niwa, R. Kurita, Z. M. Liu, T. Horiuchi, K. Torimitsue, *Anal. Chem.* **72**(5), 949 (2000).
65. M. P. Nagale, I. Fritsch, *Anal. Chem.* **70**(14), 2902 (1998).

66. M. Morita, O. Niwa, T. Horiuchi, *Electrochim. Acta* **42**(20–22), 3177 (1997).
67. M. Morita, O. Niwa, *Nat. Rev.* **8**(2), 77 (1996).
68. S. Hoshino, O. Niwa, H. Tabei, M. Takahashi, M. Morita, *Denki Kagaku* **64**(3), 195 (1996).
69. O. Niwa, *Electroanalysis* **7**(7), 606 (1995).
70. M. Paeschke, U. Wollenberger, C. Kohler, T. Liseck, U. Schnakenberg, R. Hintsche, *Anal. Chim. Acta* **305**(1–3), 126 (1995).
71. O. Niwa, T. Horiuchi, H. Tabei, *J. Electroanal. Chem.* **367**(1–2), 265 (1994).
72. O. Niwa, M. Morita, H. Tabei, *Electroanalysis* **6**(3), 237 (1994).
73. O. Niwa, H. Tabei, *Anal. Chem.* **66**(2), 285 (1994).
74. A. J. Bard, J. A. Crayston, G. P. Kittlesen, T. V. Shea, M. S. Wrighton, *Anal. Chem.* **58**(11), 2321 (1986).
75. J. A. Alden, M. A. Feldman, E. Hill, F. Prieto, M. Oyama, B. A. Coles, R. G. Compton, P. J. Dobson, P. A. Leigh, *Anal. Chem.* **70**(9), 1707 (1998).
76. K. Aoki, M. Morita, O. Niwa, H. Tabei, *J. Electroanal. Chem.* **256**, 269 (1988).
77. K. Aoki, M. Tanaka, *J. Electroanal. Chem.* **266**, 11 (1989).
78. B. J. Feldman, R. W. Murray, *Anal. Chem.* **58**(13), 2844 (1986).
79. B. J. Feldman, R. W. Murray, *Inorg. Chem.* **26**, 1702 (1987).
80. O. Niwa, M. Morita, H. Tabei, *Anal. Chem.* **62**(5), 447 (1990).
81. O. Niwa, Y. Xu, H. B. Halsall, W. R. Heineman, *Anal. Chem.* **65**, 1559 (1993).
82. O. Niwa, M. Morita, *Anal. Chem.* **68**(2), 355 (1996).
83. L. E. Fosdick, J. L. Anderson, *Anal. Chem.* **58**(12), 2481 (1986).
84. R. Merletti, D. Farina, M. Gazzoni, *J. Electromyogr. Kinesiol.* **13**, 37 (2003).
85. T. Masuda, H. Miyano, T. Sadoyama, *Electroencephalogr. Clin. Neurophysiol.* **56**, 597 (1983).
86. S. Szunerits, P. Garrigue, J.-L. Bruneel, L. Servant, N. Sojic, *Electroanalysis* **15**, 548 (2003).
87. T. E. McKnight, A. V. Melechko, D. W. Austin, T. Sims, M. A. Guillorn, M. L. Simpson, *J. Phys. Chem. B* **108**(22), 7115 (2004).
88. S. Fletcher, in *Microelectrodes: Theory and Applications*, M. I. Montenegro, M. A. Querios, J. L. Daschbach, Eds., Kluwer: Dordrecht, 1991, p. 342.
89. S. Fletcher, M. D. Horne, *Electrochem. Commun.* **1**(10), 502 (1999).
90. P. Connolly, G. R. Moores, W. Monaghan, J. Shen, S. Britland, P. Clark, *Sens. Actuat. B* **6**, 113 (1992).
91. D. W. Deer, C. W. Toblas, *J. Electrochem. Soc.* **134**, 369 (1987).
92. M. G. Sullivan, H. Utomo, P. J. Fagan, M. D. Ward, *Anal. Chem.* **71**, 4369 (1999).
93. T. Livache, H. Bazin, P. Caillat, A. Roget, *Biosens. Bioelectr.* **13**, 629 (1998).
94. C. Berloment, M.-L. Tercier, J. Buffe, G. C. Fiaccabrino, M. Koudelka-Hep, *Anal. Chim. Acta* **329**, 203 (1996).
95. Q. Bai, K. D. Wise, *Trans. Biomed. Eng.* **48**(8), 911 (2001).
96. J. J. Pancrazio, J. P. P. Bey, D. S. Cuttino, J. K. Kusel, D. A. Borkholder, K. M. Shaffer, G. T. A. Kovacs, D. A. Stenger, *Sens. Actuat. B* **53**, 179 (1998).
97. N. H. E. Weste, K. Eshraghian, *Principles of CMOS VLSI Design*, Addison Wesley: Reading, MA, 1994.
98. L. Berdondini, P. D. van der Wal, N. F. de Rooij, A. Koudelka-Hep, *Sens. Actuat. B Chem.* **99**(2–3), 505 (2004).
99. L. E. Fosdick, J. L. Anderson, T. A. Baginski, R. C. Jaeger, *Anal. Chem.* **58**, 2750 (1986).
100. K. Aoki, J. Osteryoung, *J. Electroanal. Chem.* **125**, 315 (1981).
101. T. Gueshi, K. Tokuda, H. Matsuda, *J. Electroanal. Chem.* **101**, 29 (1979).
102. W. Thormann, P. v. d. Bosch, A. M. Bond, *Anal. Chem.* **57**(14), 2764 (1985).
103. K. Tokuda, T. Gueshi, H. Matsuda, *J. Electroanal. Chem.* **102**(1), 41 (1979).

104. E. Levart, D. Schauermann, E. Contamin, M. Etman, *J. Electroanal. Chem.* **70**, 117 (1976).
105. J. Lindemann, R. Landsberg, *J. Electroanal. Chem.* **30**, 79 (1971).
106. D. Shoup, A. Szabo, *J. Electroanal. Chem.* **160**(1–2), 19 (1984).
107. B. A. Brookes, T. J. Davies, A. C. Fisher, R. G. Evans, S. J. Wilkins, K. Yunnus, J. D. Wadhawan, R. G. Compton, *J. Phys. Chem. B* **107**, 1616 (2003).
108. T. J. Davies, B. A. Brookes, A. C. Fisher, K. Yunnus, S. J. Wilkins, P. R. Greene, J. D. Wadhawan, R. G. Compton, *J. Phys. Chem. B* **107**, 6431 (2003).
109. A. Szabo, R. Zwanzig, *J. Electroanal. Chem.* **314**, 307 (1991).
110. C. Beriet, R. Ferrigno, H. H. Girault, *J. Electroanal. Chem.* **486**(1), 56 (2000).
111. W. E. Morf, *Anal. Chim. Acta* **330**(2–3), 139 (1996).
112. S. D. Kolev, J. H. M. Simons, W. E. Vanderlinden, *Anal. Chim. Acta* **273**(1–2), 71 (1993).
113. B. Fosset, C. Amatore, J. Bartelt, R. M. M. Wightman, *Anal. Chem.* **63**, 1403 (1991).
114. A. I. Oleinick, I. B. Svir, C. Amatore, *J. Electroanal. Chem.* **553**, 49 (2003).
115. T. Horiuchi, O. Niwa, M. Morita, *J. Electroanal. Chem.* **142**(9), L146 (1995).
116. V. P. Menon, C. R. Martin, *Anal. Chem.* **67**, 1920 (1995).
117. M. P. Nagale, I. Fritsch, *Anal. Chem.* **70**, 2908 (1998).
118. D. M. Odell, W. J. Bowyer, *Anal. Chem.* **62**(15), 1619 (1990).
119. M. Ohtani, T. Sunagawa, S. Kuwabata, H. Yoneyama, *J. Electroanal. Chem.* **396**, 97 (1995).
120. J. L. Anderson, L. A. Coury, J. Leddy, *Anal. Chem.* **70**(12), 516R (1998).
121. O. T. Guenat, J.-F. Dufour, P. D. van der Wal, W. E. Morf, N. F. de Rooij, M. Koudelka-Hep, *Sens. Actuat. B* **105**, 65 (2005).
122. J. J. Hickman, C. Zou, D. Ofer, P. D. Harvey, M. S. Wrighton, *J. Am. Chem. Soc.* **111**, 7271 (1989).
123. S. K. Kim, P. J. Hesketh, C. Li, J. H. Thomas, H. B. Halsall, W. R. Heinemann, *Biosens. Bioelectr.* **20**, 887 (2004).
124. G. P. Kittlesen, H. S. White, M. S. Wrighton, *J. Am. Chem. Soc.* **106**, 7389 (1984).
125. C. D. Merritt, B. L. Justus, *Chem. Mater.* **15**(13), 2520 (2003).
126. E. W. Paul, A. J. Ricco, M. S. Wrighton, *J. Phys. Chem.* **89**, 1441 (1985).
127. B. J. Seddon, M. J. Eddowes, A. Firth, A. E. Owen, H. H. J. Girault, *Electrochim. Acta* **36**(5–6), 763 (1991).
128. G. Sreenivas, S. S. Ang, I. Fritsch, W. D. Brown, G. A. Gerhardt, D. J. Woodward, *Anal. Chem.* **68**(11), 1858 (1996).
129. K. D. Sternitzke, R. L. McCreery, *Anal. Chem.* **62**(13), 1339 (1990).
130. H. Suzuki, *Electroanalysis* **12**(9), 703 (2000).
131. K. Tsunozaki, Y. Einaga, T. N. Rao, A. Fujishima, *Chem. Lett.* **5**, 502 (2002).
132. H. S. White, G. P. Kittlesen, M. S. Wrighton, *J. Am. Chem. Soc.* **106**, 5375 (1984).
133. H. P. Wu, *Anal. Chem.* **65**(11), 1643 (1993).
134. H. Xiong, J. D. Guo, K. Kurihara, S. Amemiya, *Electrochem. Commun.* **6**(6), 615 (2004).
135. R. M. Wightman, D. O. Wipf, in *Electroanalytical Chemistry*, A. J. Bard, Ed., Marcel Dekker: New York, 1989, Vol. 15, p. 267.
136. A. C. Barton, S. D. Collyer, F. Davis, D. D. Gornall, K. A. Lawa, E. C. D. Lawrence, D. W. Mills, S. Myler, J. A. Pritchard, M. Thompson, S. P. J. Higson, *Biosens. Bioelectr.* (2004).
137. J. Schwarz, H. Kaden, U. Enseleit, *Electrochem. Commun.* **2**, 606 (2000).
138. P. J. Welford, J. Freeman, S. J. Wilkins, J. D. Wadhawan, C. E. W. Hahn, R. G. Compton, *Anal. Chem.* **73**, 6088 (2001).
139. B. K. Davis, S. G. Weber, A. P. Sylwesert, *Anal. Chem.* **62**, 1000 (1990).
140. C. R. Martin, *Science* **266**, 1961 (1994).
141. G. L. Hornay, C. J. Patrissi, C. R. Martin, *J. Phys. Chem. B* **101**, 1548 (1997).
142. W. E. Williams, N. Giordano, *Rev. Sci. Instrum.* **55**, 410 (1984).

143. R. L. Fleischer, P. B. Price, R. M. Walker, *Nuclear Tracks in Solids*, University of California Press: Berkeley, CA, 1975.
144. P. P. Ngugen, D. H. Pearson, R. J. Tonucci, K. Babcock, *J. Electrochem. Soc.* **145**, 247 (1998).
145. G. E. Possin, *Rev. Sci. Instrum.* **41**, 772 (1970).
146. K. Hiruma, M. Yazawa, T. Katsuyama, K. Ogawa, K. Haraguchi, M. Koguchi, H. Kakibayashi, *J. Appl. Phys.* **77**, 447 (1995).
147. C. A. Huber, T. E. Huber, M. Sadoqi, J. A. Lubin, S. Manalis, C. B. Prater, *Science* **263**, 800 (1994).
148. C. R. Martin, *Adv. Mater.* **3**, 457 (1991).
149. C. R. Martin, *Acc. Chem. Res.* **28**, 61 (1995).
150. Y.-L. Tai, H. Teng, *Chem. Mater.* **16**, 338 (2004).
151. J. C. Hulteen, K. B. Jirage, C. R. Martin, *J. Am. Chem. Soc.* **120**, 6603 (1998).
152. S. Valizadeh, J. M. George, P. Leisner, L. Hultman, *Electrochim. Acta* **47**(6), 865 (2001).
153. B. B. Lakshmi, C. J. Patrissi, C. R. Martin, *Chem. Mater.* **9**, 2544 (1997).
154. S. A. Miller, V. Y. Young, C. R. Martin, *J. Am. Chem. Soc.* **123**, 12335 (2001).
155. P. C. Hidberg, P. F. Nealey, W. Helbig, G. M. Whitesides, *Langmuir* **12**, 5209 (1996).
156. Z. Hou, S. Dante, N. Abbott, P. Stroeve, *Langmuir* **15**, 3011 (1999).
157. S. Metzger, R. Resch, B. E. Koel, M. E. Thompson, A. Madhukar, A. A. G. Requicha, P. Will, *Langmuir* **17**, 1713 (2001).
158. A. Vaskelis, in *Coating Technology Handbook*, D. Satas, A. A. Tracton, Eds., Marcel Dekker: New York, 2001, p. 213.
159. G. O. Marryor, J. B. Hajdu, *Electroless Plating: Fundamentals and Applications*, American Electroplates and Surface Finishing Society: Orlando, FL, 1990, p. 29.
160. M. Madou, *Fundamentals in Microfabrication*, CRC Press: Boca Raton, FL, 1997.
161. Y. Xia, J. A. Rogers, K. E. Paul, G. M. Whitesides, *Chem. Rev.* **99**, 1823 (1999).
162. M. Hibbs, R. Kunz, M. Rothschild, *Solid State Technol.* **38**, 69 (1995).
163. M. Samuelsson, M. Atmgarth, C. Nylander, *Anal. Chem.* **63**(9), 931 (1991).
164. W. M. Moreau, *Semiconductor Lithography: Principles and Materials*, Plenum: New York, 1988.
165. A. F. Revzin, K. Sirkar, A. Simonian, A. V. Pishko, *Sens. Actuat.* **B81**, 359 (2002).
166. W. Xu, J. Wong, C. C. Cheng, R. Johnson, A. Scherer, *J. Vac. Sci. Technol. B* **13**(6), 2372 (1995).
167. B. A. Grzybowski, R. Haag, N. Bowden, G. M. Whitesides, *Anal. Chem.* **70**, 4645 (1998).
168. A. Kumar, G. M. Whitesides, *Appl. Phys. Lett.* **63**, 2002 (1993).
169. A. Kumar, H. Biebuyck, G. M. Whitesides, *Langmuir* **10**, 1495 (1994).
170. Y. Xia, E. Kim, G. M. Whitesides, *J. Electrochem. Soc.* **143**, 10790 (1996).
171. Y. Xia, E. Koim, M. Mrksich, G. M. Whitesides, *Chem. Mater.* **8**, 601 (1996).
172. D. Quin, Y. Xia, G. M. Whitesides, *Adv. Mater.* **8**, 917 (1996).
173. M. A. Roberts, J. S. Rossier, P. Bercier, H. Girault, *Anal. Chem.* **69**, 2035 (1997).
174. A. Ulman, *Chem. Rev.* **96**, 1553 (1996).
175. H. A. Bibuyck, N. B. Larsen, E. Delamarche, B. Mitchel, *IBM J. Res. Dev.* **41**, 159 (1997).
176. M. A. Nicolelis, *Nature* **409**, 403 (2001).
177. Donoghue, *Nat. Neur. Rev.* **5**, 1085 (2002).
178. K. E. Jones, P. K. Campbell, R. A. Normann, *Ann. Biomed. Eng.* **20**, 423 (1992).
179. P. J. Rousche, R. A. Normann, *IEEE Trans. Biomed. Eng.* **7**, 56 (1999).
180. A. Hoogerwerf, K. Wise, *IEEE Trans. Biomed. Eng.* **41**, 1136 (1994).
181. T. A. Fofonoff, S. M. Martel, N. G. Hatsopoulos, J. P. Donoghue, I. W. Hunter, *IEEE Trans. Biomed. Eng.* **51**, 890 (2004).
182. P. Pantano, D. R. Walt, *Rev. Sci. Instrum.* **68**(3), 1357 (1997).
183. C. J. Slevin, N. J. Gray, J. V. Macpherson, M. A. Webb, P. R. Unwin, *Electrochem. Commun.* **1**, 282 (1999).

184. J. L. Conyers, H. S. White, *Anal. Chem.* **72**, 4441 (2000).
185. M. Wittkampf, K. Cammann, M. Amrein, R. Reichelt, *Sens. Actuat. B* **40**, 19 (1997).
186. R. Feeney, J. Herdan, M. A. Nolan, S. H. Tan, V. V. Tatasov, S. P. Kounaves, *Electroanalysis* **10**, 89 (1998).
187. W. S. Baker, R. M. Crooks, *J. Phys. Chem. B* **102**, 10 041 (1998).
188. H. J. Lee, C. Beriet, R. Ferrigno, H. H. Girault, *J. Electroanal. Chem.* **502**(1–2), 138 (2001).
189. A. J. Bard, M. V. Mirkin, *Scanning Electrochemical Microscopy*, Marcel Dekker: New York, 2001.
190. C. Zoski, N. Simjee, O. Guenat, M. Doudelka-Hep, *Anal. Chem.* **76**, 62 (2004).
191. C. Zoski, *Electroanalysis* **14**, 1041 (2002).

Part Three

TECHNIQUES

This page intentionally left blank

Classical Experiments

Guy Denuault, Maciej Sosna, and Kirsty-Jo Williams

School of Chemistry, University of Southampton,
Southampton, SO17 1BJ, UK

11.1 INTRODUCTION

This chapter focuses on a selection of key electrochemical techniques, chosen because they constitute the majority of experiments carried out in most laboratories, including research laboratories. Some less common methods have been included purely for pedagogical reasons, e.g. double potential step since it is one of the simplest reversal techniques. *Classical experiments* are broadly defined as those commonly found on commercial instruments, namely potential steps, potential sweeps, sweep and step combinations, AC impedance, microelectrodes and rotating disc electrodes. A section on numerical simulations is included since the availability of commercial software widens access to the powers of modelling. The chapter concludes with guidelines for troubleshooting electrochemical experiments, especially voltammetric ones, with conventional and microelectrodes. Many techniques including controlled current, polarography, hydrodynamic (e.g. flow cells) and spectroelectrochemical methods were considered to be too exotic and have been left out. With Part I of this handbook providing a solid theoretical background, this chapter only covers a brief reminder of the theoretical principles for each experiment considered.

Electrochemical experiments are always conducted under diffusion-controlled mass transport. This is achieved by (1) adding a large concentration of electrolyte to suppress the migration of ions due to the electrical field between the working and counter electrodes, (2) avoiding natural convection by completing the experiment under 30 s, (3) using controlled hydrodynamics to limit the diffusion layer thickness or (4) using microelectrodes to yield a true steady-state diffusion-controlled current before the onset of natural convection. Hence, all the cases presented involve the diffusion of the reactant towards and of the product away from the electrode. Unless stated otherwise, the model system considered is the one electron reduction of O to R where both are soluble and only O is initially present in solution. The theory is initially covered for diffusion control then extended to include the effect of electron transfer kinetics. Where appropriate, the effects of coupled chemical reactions are mentioned but not developed.

11.2 SELECTED EXPERIMENTAL TECHNIQUES

11.2.1 Potential steps

11.2.1.1 Principles

This section presents a selection of equations used in interpreting and predicting the experimental response of a simple electrochemical reaction to a step change in potential. For complete derivations and information on more complex systems, e.g. coupled chemical reactions, the reader should consult references (1–3).

In chronoamperometry, one observes the current–time behaviour of an electrochemical system after a potential step in a still solution. Consider a system where species O is electroinactive at E_i and the potential of the electrode is stepped to E_f (Figure 11.1a), where O is reduced in a simple charge transfer reaction: $O + e^- \rightarrow R$.

E_f is chosen so that the concentration of O at the electrode surface remains zero. The current (Figure 11.1b) is only due to the diffusion of O towards the electrode as illustrated in Figure 11.1c. The theoretical expression for the evolution of the concentration profile is obtained by solving Fick's second law of diffusion with appropriate boundary conditions. To derive the solution, one often uses the Laplace transform (2). For a planar electrode:

Mass transport equation:

$$\frac{\partial C_O(x,t)}{\partial t} = D_O \frac{\partial^2 C_O(x,t)}{\partial x^2} \quad (11.2.1)$$

Initial condition:

$$C_O(x \geq 0, 0) = C_O^* \quad (11.2.2)$$

Boundary conditions:

$$C_O(\infty, t > 0) = C_O^* \quad (11.2.3)$$

$$C_O(0, t > 0) = 0 \quad (11.2.4)$$

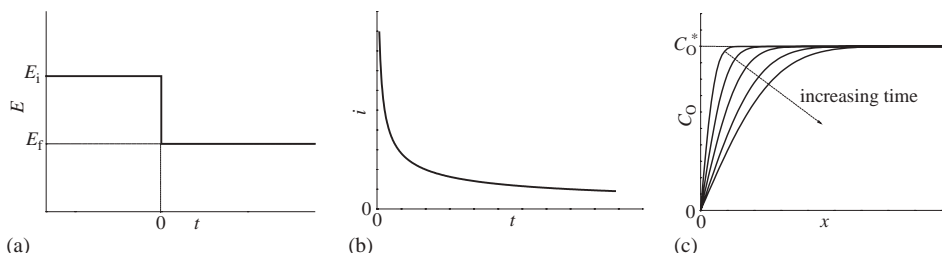


Figure 11.1 Potential step experiment to a planar electrode: (a) potential waveform, (b) current response and (c) concentration profile in the vicinity of the electrode.

Concentration profile:

$$C_o(x, t) = C_o^* \left[1 - \operatorname{erfc} \left(\frac{x}{2(D_o t)^{1/2}} \right) \right] \quad (11.2.5)$$

Current definition:

$$i(t) = FAD_o \frac{\partial C_o(x, t)}{\partial x} \Big|_{x=0, t>0} \quad (11.2.6)$$

Current transient:

$$i(t) = \frac{FAD_o^{1/2} C_o^*}{\pi^{1/2} t^{1/2}} \quad (11.2.7)$$

For a spherical electrode:

Mass transport equation:

$$\frac{\partial C_o(r, t)}{\partial t} = D_o \left(\frac{\partial^2 C_o(r, t)}{\partial r^2} + \frac{2}{r} \frac{\partial C_o(r, t)}{\partial r} \right) \quad (11.2.8)$$

Initial condition:

$$C_o(r \geq r_0, 0) = C_o^* \quad (11.2.9)$$

Boundary conditions:

$$C_o(\infty, t > 0) = C_o^* \quad (11.2.10)$$

$$C_o(r_0, t > 0) = 0 \quad (11.2.11)$$

Concentration profile:

$$C_o(r, t) = C_o^* \left[1 - \frac{r_0}{r} \operatorname{erfc} \left(\frac{r - r_0}{2(D_o t)^{1/2}} \right) \right] \quad (11.2.12)$$

Current definition:

$$i(t) = FAD_o \frac{\partial C_o(r, t)}{\partial r} \Big|_{r=r_0, t>0} \quad (11.2.13)$$

Current transient:

$$i(t) = \frac{FAD_o^{1/2} C_o^*}{\pi^{1/2} t^{1/2}} + \frac{FAD_o C_o^*}{r_0} \quad (11.2.14)$$

Equation (11.2.7) is known as the Cottrell equation (4) and a typical current transient is shown in Figure 11.1b. For spherical electrodes, the current transient (11.2.14) contains a steady-state term accounting for the effect of radial diffusion. This term will dominate at larger t when the Cottrell term tends to zero and the current reaches a steady-state value. The time required to establish the steady state is a function of the electrode radius. The smaller the electrode, the sooner the radial diffusion term becomes dominant (see Section 11.2.4 in this Chapter and Section 2.4 in Chapter 2, and Chapters 6 and 19 on Microelectrodes). To test whether the current response is controlled by diffusion, one plots i vs. $t^{-1/2}$. For both geometries, the graph should be linear but its intercept will be zero for a planar electrode and equal to the steady-state current for a spherical electrode. For planar electrodes, the current is therefore expected to decay to zero at long times. In practice, this cannot be observed because of the onset of natural convections after 30 s.

Equations (11.2.7) and (11.2.14) were derived assuming that E_f was such that the surface concentration of O was zero. The Nernst equation (11.2.15) predicts the ratio of surface concentrations of O and R in terms of the electrode potential and it is thus possible to predict the current for any value of the potential between E_i and E_f .

$$E = E^{0'} + \frac{RT}{F} \ln \left(\frac{C_o(0,t)}{C_R(0,t)} \right) \quad (11.2.15)$$

For planar electrodes and spherical electrodes at short times:

$$i = \frac{1}{1 + \xi^2 \theta} \times \frac{FAD_o^{1/2} C_o^*}{\pi^{1/2} t^{1/2}} \quad (11.2.16)$$

For spherical electrodes under steady-state conditions:

$$i_d = \frac{1}{1 + \xi^2 \theta} \times \frac{FAD_o C_o^*}{r_0} \quad (11.2.17)$$

where

$$\xi = \left(\frac{D_o}{D_R} \right)^{1/2} \quad (11.2.18)$$

$$\theta = \exp \left[\frac{F}{RT} (E - E^{0'}) \right] \quad (11.2.19)$$

The expressions given above assumed that the electron transfer kinetics was very fast. Those given in Table 11.1 consider the case where the current is controlled by both mass transport and kinetics. Hence, the forward and reverse rates of electron transfer are taken into account.

Table 11.1

Chronoamperometric responses for kinetically limited one electron electrochemical reactions

$$\text{Irreversible Planar} \quad i = FAk_f C_o^* \exp\left(\frac{k_f^2 t}{D_o}\right) \operatorname{erfc}\left(\frac{k_f t^{1/2}}{D_o^{1/2}}\right) \quad (11.2.20)$$

$$\text{Spherical} \quad i = FAk_f C_o^* \left[\left(1 + \frac{D_o}{k_f r_0} \right) \exp\left(\frac{k_f^2 t}{D_o}\right) \operatorname{erfc}\left(\frac{k_f t^{1/2}}{D_o^{1/2}}\right) - \frac{D_o}{k_f r_0} \right] \quad (11.2.21)$$

$$\text{Quasi-reversible Planar} \quad i = FAk_f C_o^* \exp(H^2 t) \operatorname{erfc}(Ht^{1/2}), \quad \text{for } C_{R(t=0)}^* = 0 \quad (11.2.22)$$

$$i = FA(k_f C_o^* - k_b C_R^*) \exp(H^2 t) \operatorname{erfc}(Ht^{1/2}), \quad \text{for } C_{R(t=0)}^* \neq 0 \quad (11.2.23)$$

$$\text{Spherical}^1 \quad i = FAk_f C_o^* \left[\left(1 + \frac{D^{1/2}}{r_0 H'} \right) \exp(H'^2 t) \operatorname{erfc}(H't^{1/2}) - \frac{D^{1/2}}{r_0 H'} \right],$$

for $C_{R(t=0)}^* = 0$ (11.2.24)

$$i = FA(k_f C_o^* - k_b C_R^*) \left[\left(1 + \frac{D^{1/2}}{r_0 H'} \right) \exp(H'^2 t) \operatorname{erfc}(H't^{1/2}) - \frac{D^{1/2}}{r_0 H'} \right],$$

for $C_{R(t=0)}^* \neq 0$ (11.2.25)

¹D=D_O=D_R.

where the forward and backward electron transfer rate constants are given by

$$k_f = k^0 \exp\left(-\frac{\alpha F(E - E^0)}{RT}\right) \quad (11.2.26)$$

$$k_b = k^0 \exp\left(\frac{(1-\alpha)F(E - E^0')}{RT}\right) \quad (11.2.27)$$

with

$$H = \frac{k_f}{D_o^{1/2}} + \frac{k_b}{D_R^{1/2}} \quad \text{and} \quad H' = \frac{k_f + k_b}{D^{1/2}} - \frac{D^{1/2}}{r_0}$$

The expression $\exp(\lambda^2)\operatorname{erfc}(\lambda)$, where $\operatorname{erfc}(\lambda)$ is the complementary error function (5), is represented by a power series of λ . Retaining only its linear terms, it reduces to $1 - 2\lambda/\pi^{1/2}$, which in turns simplifies equation (11.2.20) to

$$i = FAk_f C_o^* \left(1 - \frac{2k_f t^{1/2}}{\pi^{1/2} D_o^{1/2}} \right) \quad (11.2.28)$$

The equation predicts a linear variation of i with $t^{-1/2}$ from which the value of k_f can be derived. As $\operatorname{erfc}(\lambda)$ strongly depends on λ , k_f restricts the validity of equation (11.2.28).

In general, the larger the k_f , the shorter is the time over which equation (11.2.28) is accurate.

It is worth reiterating that all the equations given above are for mass transport by diffusion alone. Therefore, experimental responses will deviate from the predicted ones at long times because of natural convection (vibration, thermal and density gradients) or forced convection if using a rotating disc electrode. Moreover, at short times, the experiment will be affected by the charging of the double layer. The charging current i_c occurs in parallel to the faradaic current and contributes to the overall current response; see Section 11.2.6. It decays exponentially with time (equation (11.2.29)) and its magnitude depends on the solution resistance R_Ω and the double layer capacity C_d which is directly proportional to the electrode surface area. Ninety-five percent of the charging is completed in $3\tau_c$, where τ_c is the time constant for charging (equation (11.2.30)):

$$i_c = \frac{\Delta E}{R_\Omega} \exp\left(-\frac{t}{R_\Omega C_d}\right) \quad (11.2.29)$$

$$\tau_c = R_\Omega C_d \quad (11.2.30)$$

11.2.1.2 Double potential steps

The double potential step method (6) is included in this chapter as it underpins many other reversal techniques designed to study the stability of the product. Its principle is rather simple and it is a good stepping stone before tackling cyclic voltammetry. The potential is stepped to a value E_1 where species R is formed at a diffusion-controlled rate, and then, after a time τ , to a more anodic value E_2 where R is oxidised (Figure 11.2a).

The current response for the first step (Figure 11.2b) is treated as shown in Section 11.2.1.1. For the reverse step, however, the initial conditions have to be derived from the concentration profile of R at time τ . The calculation of the response is complex and often treated as a superposition of two signals (7–13). In the simplest case where both reactions are diffusion-controlled, the $i(t)$ relationships are:

$$i = \frac{FAD_O^{1/2}C_O^*}{\pi^{1/2}t^{1/2}}, \quad \text{for } 0 < t < \tau \quad (11.2.7)$$

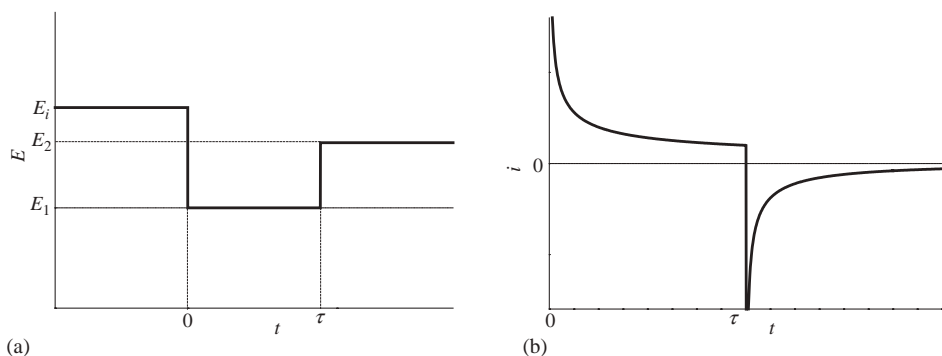


Figure 11.2 Double potential step experiment: (a) potential waveform and (b) current response.

$$i = FAD_O^{1/2} C_O^* \left\{ \frac{1}{[\pi(t - \tau)]^{1/2}} - \frac{1}{(\pi t)^{1/2}} \right\}, \quad \text{for } t > \tau \quad (11.2.31)$$

Additional theories are available for complex systems, including cases where one or both reactions are kinetically controlled (8, 12) or where a homogeneous reaction follows the electrode reaction (14).

11.2.1.3 Bulk electrolysis

Unlike most electroanalytical techniques where the amount of substance consumed or produced at the electrode is not appreciable, bulk electrolysis significantly alters the bulk concentration. This requires a large electrode surface area (A) to solution volume (V) ratio and very efficient mass transport conditions. Usually electrolysis is carried out under potentiostatic conditions by stepping the potential from a value where no faradaic current is observed to one where the reaction is mass transport-controlled. The $i(t)$ equations for a potential step apply but require corrections for the bulk concentration, C_O^* , as it evolves with time. Considering the model reaction $O + ne^- \rightarrow R$, the current transient is obtained by equating the current at a time t of the step (11.2.32) with the current indicating the rate of consumption of O (assuming 100% efficiency) (equation (11.2.33)). The evolution of the bulk concentration with time is derived (equation (11.2.34)) and using equation (11.2.32), the corresponding current transient is given by equation (11.2.35). Integration of the current (often done in real time with an electronic integrator) yields the charge (equation (11.2.36)), where Q^0 is the charge at the end of the electrolysis (equation (11.2.37)). This is the most useful information since it provides the value of n . Q^0 may be determined from the charge transient (Figure 11.3a) or from the intercept of the straight line obtained when plotting $i(t)$ vs. $Q(t)$ (Figure 11.3b), since the current and charge transients are linearly related (equation (11.2.38)).

$$i(t) = nFAM_O C_O^*(t) \quad (11.2.32)$$

$$i(t) = -nF \left(\frac{dN_O}{dt} \right) = -nFV \left(\frac{dC_O^*(t)}{dt} \right) \quad (11.2.33)$$

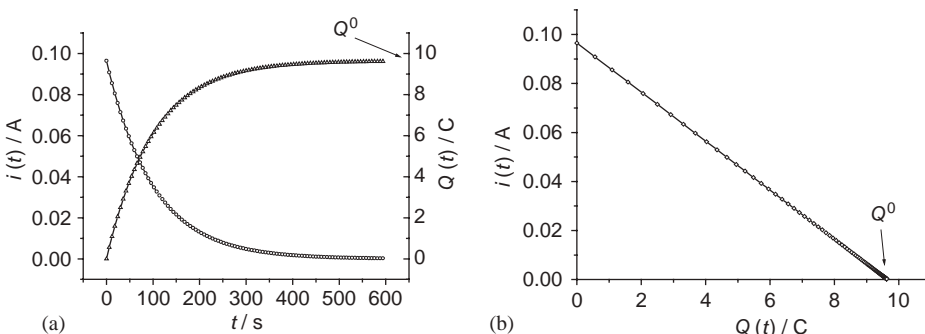


Figure 11.3 Controlled potential bulk electrolysis: (a) current and charge transients and (b) current vs. charge plot used to determine Q^0 .

$$C_o^*(t) = C_o^*(0) \exp\left(-\frac{m_o A}{V} t\right) \quad (11.2.34)$$

$$i(t) = nF A m_o C_o^*(0) \exp\left(-\frac{m_o A}{V} t\right) \quad (11.2.35)$$

$$Q(t) = Q^0 \left(1 - \exp\left(-\frac{m_o A}{V} t\right)\right) \quad (11.2.36)$$

$$Q^0 = nF V C_o^*(0) \quad (11.2.37)$$

$$Q(t) = nF V C_o^*(0) - \frac{V}{A m_o} i(t) \quad (11.2.38)$$

Typical applications of bulk electrolysis include the determination of n or of the total amount of species present (e.g. by electrogravimetry), small-scale preparative electrosynthesis and electroseparation. In addition, any deviation in the linearity of $\ln(i(t))$ vs. t or $Q(t)$ vs. $i(t)$ indicates complexity in the reaction mechanism (e.g. coupled reactions).

11.2.2 Potential sweeps

11.2.2.1 Principles

In potential sweep methods, the current is recorded while the electrode potential is changed linearly with time between two values chosen as for potential step methods. The initial potential, E_1 , is normally the one where there is no electrochemical activity and the final potential, E_2 , is the one where the reaction is mass transport controlled. In linear sweep voltammetry, the scan stops at E_2 , whereas in cyclic voltammetry, the sweep direction is reversed when the potential reaches E_2 and the potential returned to E_1 . This constitutes one cycle of the cyclic voltammogram. Multiple cycles may be recorded, for example, to study film formation. Other waveforms are used to study the formation and kinetics of intermediates when studying coupled chemical reactions (Figure 11.4c).

Choosing the waveform parameters is the most important step when preparing the experiment. The starting and reversal potentials determine the driving force for electron transfer and the oxidation state of the species involved. Appropriate choice of the potentials will

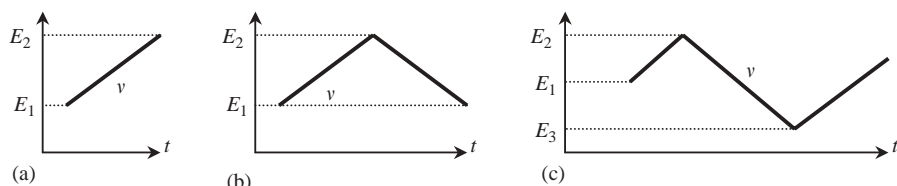


Figure 11.4 Waveforms used in linear sweep (a) and cyclic voltammetry (b and c). E_1 , E_2 and E_3 are the starting and reversal potentials while v is the scan rate.

thus determine whether a species is formed or consumed, and whether the reaction is under kinetic or mass transport control. The potential scan rate sets the timescale of the experiment, e.g. with coupled homogeneous reactions, the value of v will determine whether intermediates are formed or consumed and to what extent. Typically v ranges from a few mV sec^{-1} to a few V sec^{-1} , although this upper limit can easily be extended to a few kV s^{-1} with microelectrodes; see Section 11.2.4.

Voltammetric methods produce current–voltage curves with features characteristic of the reaction mechanism and kinetic conditions. Combining this with the ease of changing the waveform parameters, cyclic voltammetry is nearly always the first technique used to study a new system. It is particularly useful for assessing reaction mechanisms, even when there are additional complications such as coupled homogeneous reactions, or surface adsorption. These techniques also provide quantitative information as will be shown below with a selection of theoretical expressions.

When first looking at a system with cyclic voltammetry, it is useful to carry out qualitative experiments. Typically, E_1 , E_2 , v , pH and C_0^* are varied systematically and the difference in the shape of the voltammogram is analysed. Points to note are the number of peaks present, the shape, size (peak current) and position (peak potential) of the peaks. By monitoring how each of these varies, it is possible to derive mechanistic and kinetic information.

11.2.2.2 Classical cyclic voltammetry

The cyclic voltammogram for a diffusion-controlled electron transfer reaction on an inert planar electrode is shown in Figure 11.5. Its shape derives from the evolution of the

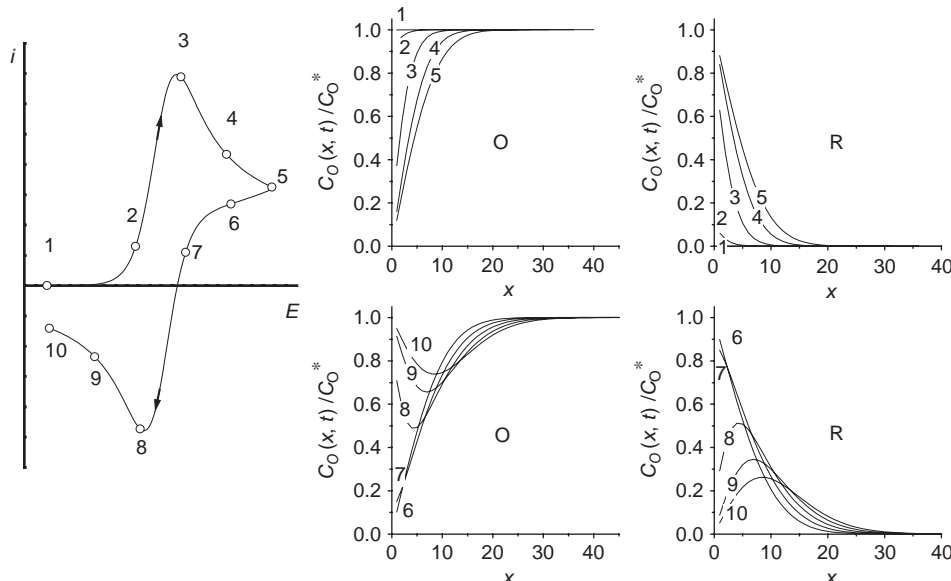


Figure 11.5 Cyclic voltammogram and corresponding O and R concentration profiles for diffusion to a planar electrode. Numbers on the concentration profiles correspond to the numbered points on the voltammogram.

concentration profiles resulting from the potential sweep and planar diffusion. Changing the electrode potential produces new surface concentrations for O and R and induces their diffusion between the bulk and the electrode. From Fick's first law of diffusion, the current is proportional to the gradient of concentration at the electrode surface. To illustrate the relationship between the concentration profiles and the current–voltage curve, selected points along the voltammogram have been linked to their corresponding concentration profile (Figure 11.5).

For points 1–7, species O is consumed at the electrode and a reduction current is observed, whereas for points 8–10, O is regenerated by oxidation of R and an oxidation current is observed. Note that the change of sign in the current is directly related to the inversion of the concentration gradient for O at the electrode surface: the gradient is positive for points 1–7 and negative for points 8–10. For additional theoretical background readers should consult Chapters 6 in reference (1), 6 in reference (2), 6 in reference (3) and 10 in reference (15).

One of the key features of the voltammogram is the peak height. For a planar diffusion-controlled case, the peak current is given by:

$$i_p = 0.4463 \frac{n^{3/2} F^{3/2}}{R^{1/2} T^{1/2}} A D_O^{1/2} C_O^* v^{1/2} \quad (11.2.39)$$

This equation, known as the Randles–Sevcik equation, predicts that the peak current is proportional to the square root of the sweep rate. This is analogous to the inverse square root of time dependence found with potential steps (equation (11.2.7)). Therefore, a plot of i_p vs. $v^{1/2}$ should be linear, pass through the origin and have a gradient from which the diffusion coefficient may be estimated. Below is a list of the diagnostic criteria used to characterise a reversible voltammogram:

$$i_p \propto v^{1/2} \quad (11.2.40)$$

$$E_p \text{ is independent of } v \quad (11.2.41)$$

$$\Delta E_p = E_{pa} - E_{pc} = \frac{59}{n} \text{ mV at 298 K} \quad (11.2.42)$$

$$|E_p - E_{p/2}| = \frac{59}{n} \text{ mV at 298 K} \quad (11.2.43)$$

$$\left| \frac{i_{pa}}{i_{pc}} \right| = 1 \quad (11.2.44)$$

The shape of the voltammogram changes significantly when the rate of mass transport overcomes the rate of electron transfer (Figure 11.6). When the mass transfer coefficient is comparable to the rate constant for electron transfer, the voltammogram is almost identical to the diffusion-controlled one (Figure 11.5). However, when the mass transfer coefficient is increased, i.e. at large values of v , the voltammogram becomes drawn out. The

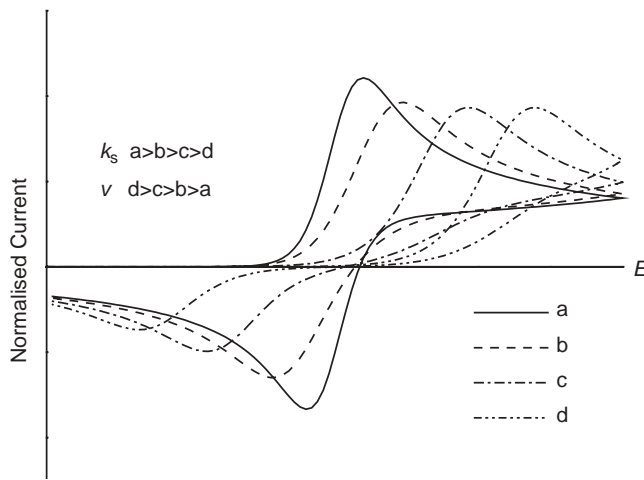


Figure 11.6 Voltammograms under kinetic control. The current scale has been normalised to illustrate either the effect of changing the sweep rate for a given electron transfer rate constant or changing the electron transfer rate constant for a given sweep rate. (a) The mass transfer coefficient is smaller than the electron transfer rate constant. (b–d) The mass transfer coefficient is increasingly larger than the electron transfer rate constant.

peaks broaden and the peak separation increases because a greater overpotential is needed to achieve the same rate of electron transfer.

As the rate of mass transport increases, the reverse peak becomes less and less pronounced. In the limit of a very slow rate of electron transfer, a case known as an irreversible system, the reverse peak disappears. Below are diagnostic criteria used to characterise an irreversible voltammogram:

$$i_{p,c} \propto v^{1/2} \quad (11.2.45)$$

$$\text{No reverse peak} \quad (11.2.46)$$

$$E_{p,c} \text{ shifts to higher overpotentials as } v \text{ increases} \quad (11.2.47)$$

$$|E_p - E_{p/2}| = \frac{48}{\alpha n} \text{ mV at } 25^\circ\text{C} \quad (11.2.48)$$

11.2.2.3 Potential sweep experiments in the steady state

In cases where the mass transport conditions reach a steady state, e.g. with a microelectrode where spherical diffusion dominates (Section 11.2.4) or with a rotating disc electrode where hydrodynamic convection controls the diffusion layer thickness (Section 11.2.5), the current–voltage curve takes the form of a sigmoidal wave (Figure 11.7). The voltammogram is described by equation (11.2.49) when the kinetics are reversible. If however the

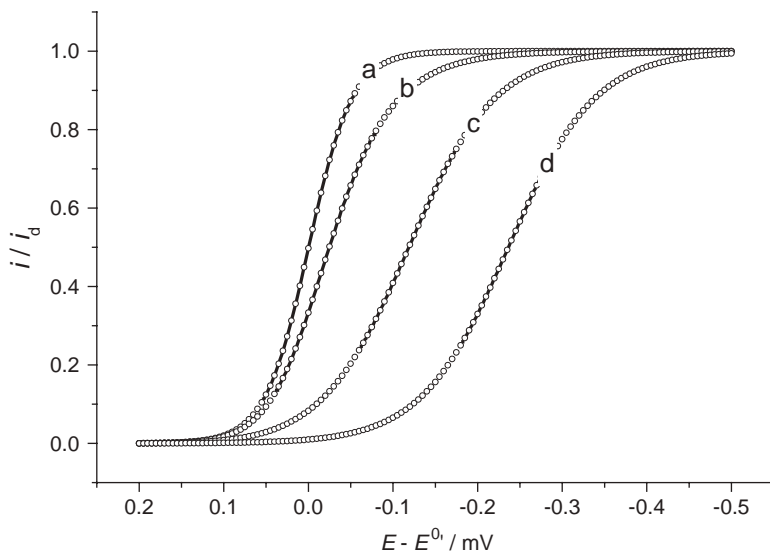


Figure 11.7 Steady-state voltammograms under different kinetic regimes: (a) reversible, (b) quasi-reversible and (c and d) totally irreversible.

kinetics of electron transfer become limiting, then the current–voltage curve is said to be quasi-reversible or even irreversible and is described by equation (11.2.50):

$$i = \frac{i_d}{1 + (D_O/D_R) \exp((F/RT)(E - E^{0'}))} \quad (11.2.49)$$

$$i = i_d \frac{k_f}{m_O + k_f + k_b(D_O/D_R)} \quad (11.2.50)$$

where k_f and k_b , respectively, the forward and reverse electron transfer rate constants, are both functions of the electrode potential as defined in equations (11.2.26) and (11.2.27). Both i_d , the mass transport-controlled limiting current, and m_O , the mass transfer coefficient for O, depend on the technique used.

When the standard rate constant for electron transfer k^0 is very small, k_f and k_b are also both very small. Moreover, k_b becomes negligible as the electrode potential is made increasingly negative to drive the reduction of O. In this case, the voltammogram is said to be totally irreversible and equation (11.2.50) reduces to equation (11.2.51). After substitution of k_f and further rearrangement, the potential is expressed in terms of the current (equation (11.2.52)):

$$i = i_d \frac{k_f}{m_O + k_f} \quad (11.2.51)$$

$$E = E^{0'} + \frac{RT}{\alpha F} \ln \left(\frac{k^0}{m_O} \right) + \frac{RT}{\alpha F} \ln \left(\frac{i_d - i}{i} \right) \quad (11.2.52)$$

Thus, a plot of the electrode potential against $\ln((i_d - i)/i)$ should be linear and yield the values of α and k^0 .

The shape of the current–voltage curve is easily analysed with the Tomeš criteria:

$$\text{if } |E_{3/4} - E_{1/4}| = \frac{56.4}{n} \text{ mV at } 25^\circ\text{C}, \text{ then the voltammogram is reversible} \quad (11.2.53)$$

$$\text{if } |E_{3/4} - E_{1/4}| = \frac{51.4}{\alpha n} \text{ mV at } 25^\circ\text{C}, \text{ then the voltammogram is irreversible} \quad (11.2.54)$$

Steady-state voltammograms also reflect the mechanism and kinetics of coupled chemical reaction (16) but this is outside the scope of this chapter. For additional material, readers should consult Chapter 5 in references (2) and reference (17).

11.2.2.4 Potential sweep experiments involving adsorbed species

Potential sweep experiments are very sensitive to redox reactions involving adsorption of a reactant or a product. The cyclic voltammetry where both O and R are adsorbed on the electrode surface is different to that when both are in solution. This is because there is no mass transport step to consider. The typical shape of a cyclic voltammogram for an ideal Nernstian electron transfer with the Langmuir isotherm describing adsorption (only short-range repulsive interactions between the adsorbates) is shown in Figure 11.8. It consists of two symmetrical peaks, where the charges (the areas under the peaks) for oxidation and reduction are equal as all the adsorbed species undergo reduction/oxidation. The current peaks and decays to zero because there is a fixed amount of reactant present. The charged

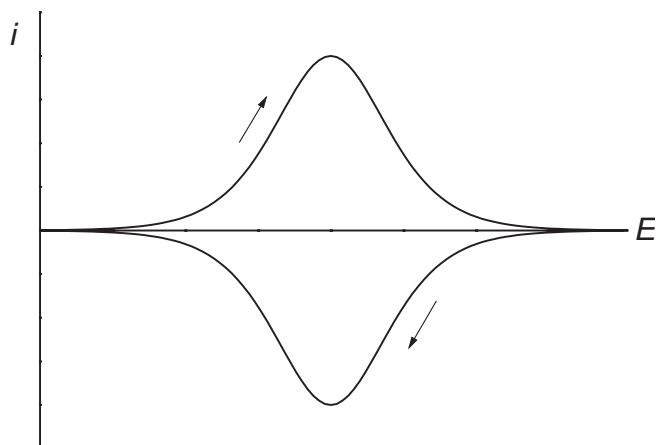


Figure 11.8 Cyclic voltammogram for a redox process with O and R adsorbed on the electrode surface.

passed must remain constant. Therefore, if the scan rate is increased, the peak current must also increase as shown by the following expression:

$$i_p = \frac{n^2 F^2}{4RT} v A \Gamma_O^* \quad (11.2.55)$$

where Γ_O^* is the maximum coverage for species O.

The list below shows the characteristic features of a cyclic voltammogram involving an ideal Nernstian adsorption with Langmuir isotherm:

$$\Delta E_p = 0 \quad (11.2.56)$$

$$i_{p,a} = -i_{p,c} \quad (11.2.57)$$

$$Q_a = -Q_c \quad (11.2.58)$$

$$\Delta E_{p/2} = 3.53 \frac{RT}{nF} = \frac{90}{n} \text{ mV at 298 K} \quad (11.2.59)$$

The shape of the peaks is indicative of the nature of the interactions between the adsorbates and other isotherms have been used to model these interactions (18). Similarly, the position of the peaks along the potential axis is indicative of the reversibility of the electron transfer process. The larger the ΔE_p , the more irreversible is the electron transfer. For additional information on these effects, see Chapter 14 in reference (2).

Quantitatively, the voltammetric response of reactions involving adsorption is remarkably sensitive and without any special effort or experimental precautions, the voltammogram indicates the reduction or oxidation of a very small number of molecules, as low as a fraction of a monolayer. Qualitatively, the position and shape of the peaks give a signature, the voltammetric fingerprint, of the surface processes (Figure 11.9). Overall, this makes potential sweep experiments highly suited to the study of redox processes with adsorption steps.

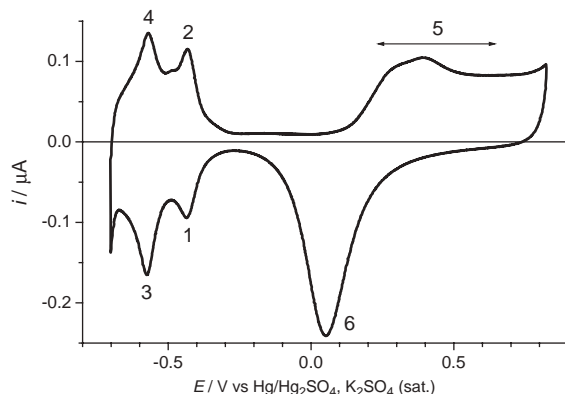


Figure 11.9 “Fingerprint” voltammogram for a high surface area Pt electrode in H_2SO_4 . (1 and 2) Strong hydrogen adsorption/desorption, (3 and 4) weak hydrogen adsorption/desorption and (5 and 6) formation/reduction of Pt oxides.

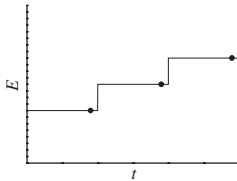
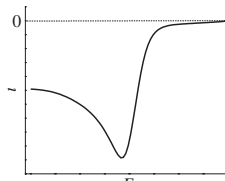
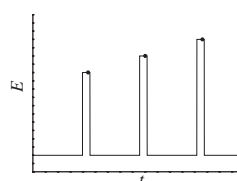
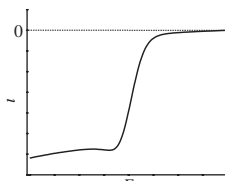
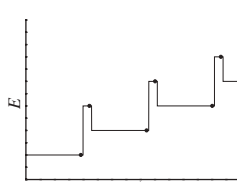
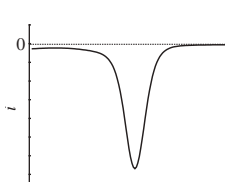
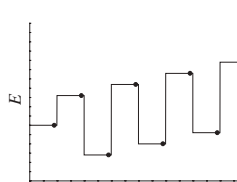
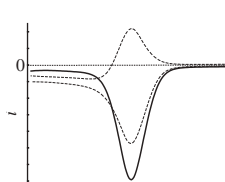
11.2.3 Combinations of sweeps and steps

11.2.3.1 Pulse voltammetry

Methods employing complex potential waveforms involving combinations of sweeps and steps evolved from polarography, mainly to improve detection limits. They were particularly advantageous in Dropping Mercury Electrode (DME) experiments, where a continuous charging current resulting from the drop growth is observed. The move to the Static Mercury Drop Electrode (SMDE) eliminates this requirement. Applied to stationary electrodes, pulsed voltammetric methods yield significant enhancements. The most important pulse voltammetric techniques together with key references are presented in Table 11.2.

Table 11.2

Potential waveforms and typical current responses for selected techniques

Technique	Potential waveform	Current response	References
Staircase voltammetry (SCV)			(19, 20)
Normal pulse voltammetry (NPV)			(20–23)
Differential pulse voltammetry (DPV)			(20, 22–25)
Square wave voltammetry (SWV)			(20, 24, 26–31)

The dot indicates the time when the current is sampled. The current response is that for the reduction of a reversible redox couple.

All four methods can be considered as fixed potential techniques with the current being sampled after the potential has remained constant for sufficiently long time, typically 40 msec. Discrimination against charging current is thus achieved by sampling the current just before the end of the pulse (or the end of the step for a staircase), where the charging current is negligible compared to the faradaic component. DPV and SWV further improve the sensitivity by subtracting current values sampled at two different times. SWV combines advantages of the other three and offers significant improvements. The result is a voltammetric response akin to a Gaussian, characterised by an excellent suppression of background current and yielding improved quantitative information with a wider range of timescales.

11.2.3.2 Stripping analysis

Stripping techniques extensively described by Wang (32) are used in quantitative determination and speciation in particular of metals and metal complexes. The procedure involves a pre-electrolysis step followed by a potential sweep to strip the pre-concentrated species of interest (Figure 11.10). Depending on the nature of the analyte, different modes of stripping analysis are used. The most common is *Anodic Stripping Voltammetry* (ASV), employing an SMDE or a Mercury Film Electrode (MFE). The main application of this method is the analysis of metal ions and the pre-electrolysis step allows detection in very diluted solutions (down to 10^{-11} M). Metal cations are reduced forming an amalgam and subsequently oxidised by means of potential sweep (LSV or DPV). A typical stripping response is shown in Figure 11.10b.

The amount of metal is calculated from the charge under the stripping peak. Using standard addition or calibration, this amount can be related to the concentration of the metal ion in the analyte. For this, all parameters—pre-concentration potential and time, stirring conditions, temperature and quantity of Hg—should remain constant throughout the calibration and be identical to those used with the sample.

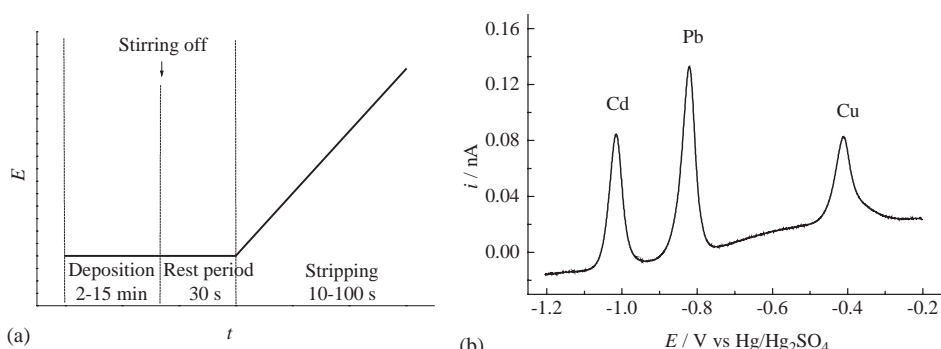


Figure 11.10 (a) Potential waveform for a typical ASV experiment and (b) anodic stripping analysis in 0.1 M NaClO_4 solution containing 0.2 mM Cu^{2+} , 0.25 mM Pb^{2+} and 0.25 mM Cd^{2+} . The stripping was performed by LSV at $v = 10 \text{ mV s}^{-1}$ on an Hg film microdisc electrode.

Potentiometric Stripping Analysis is an alternative for metal ions analysis. As with ASV, the pre-electrolysis is carried out under potential-controlled conditions. Amalgamated metals are subsequently stripped by either applying a controlled anodic current or addition of an oxidising agent to the solution (e.g. dissolved oxygen). The resulting chronopotentiogram presents stripping plateaus corresponding to the different metals. These plateaus are qualitatively identified using the Nernst equation for each $M^{n+}/M(Hg)$ couple. The quantitative analysis can be facilitated by differentiating the E vs. t curve yielding a peak-shaped response.

Cathodic Stripping Voltammetry (CSV) can be used to detect organic and inorganic compounds. An anodic potential is applied during the pre-concentration step and the compound of interest forms an insoluble salt with mercury. Stripping is carried out with a potential sweep towards negative potentials.

Adsortive Stripping Voltammetry broadens even more the range of species that can be analysed by the stripping techniques. It often offers a significant improvement in sensitivity and selectivity of metal ions analysis. The principle of the method is the formation of surface-active metal complex which is subsequently adsorbed and undergoes reduction at the electrode surface. The electrochemical process may involve the ligand as well as the metal centre. The method is also suitable for numerous important organic compounds (polycyclic hydrocarbons, nucleic acids and drugs). For different species, either cathodic or anodic stripping can be utilised. While very useful for trace analysis, the technique has limitations for higher concentrations due to the limited number of adsorption sites at the electrode surface.

11.2.4 Microelectrodes

The practical characteristics of microelectrodes are discussed in Chapter 6 of this handbook; hence, this section is restricted to a brief theoretical background followed by a discussion of key experiments where microelectrodes have made significant improvements.

Microelectrodes are defined as electrodes having at least one dimension small enough that their properties are a function of this size (33). This characteristic dimension (radius, width or thickness depending on geometry) must be smaller than circa 50 μm , otherwise the electrode behaves like a conventional electrode. Three key electrochemical properties are significantly affected by the size of the electrode: (1) the mass transport regime, (2) the charging of the double layer and (3) the ohmic drop in solution. Only two geometries will be considered: spherical microelectrodes because of their simple theory and microdisc electrodes because they offer the best compromise between ease of fabrication, robustness and “friendly” theoretical treatment.

11.2.4.1 The mass transport regime

Diffusion to a microelectrode is notably different than that to a conventional electrode, including mm-size electrodes. For a simple fast electron transfer process, the application of a potential step from a value where no current flows to one where the reaction is diffusion controlled produces different diffusion regimes. At short times, the diffusion layer is very thin relative to the electrode. Diffusion to and from the electrode is planar (irrespective of

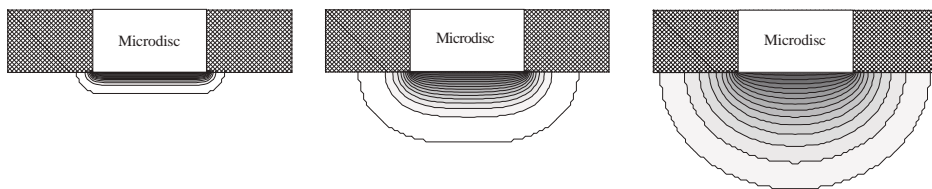


Figure 11.11 Diffusion regimes following a potential step to a microdisc electrode. From left to right: planar diffusion at short times, transition from planar to quasi-hemispherical, and then hemispherical diffusion at long times.

the electrode geometry) and the microelectrode behaves like a conventional electrode. As time increases, the diffusion layer thickness becomes comparable, and then larger than the dimensions of the electrode. The diffusion regime evolves from planar to spherical (quasi-hemispherical for a microdisc) (Figure 11.11) and yields a steady-state rate of mass transport to the electrode. So in contrast to the constant planar diffusion regime observed with large electrodes, a microelectrode shifts from planar to spherical diffusion. This, of course, depends on the characteristic dimension of the electrode. Below 50 µm, the microelectrode can fully develop its diffusion layer without influence from natural convection. Larger electrodes produce thicker diffusion layers which soon become affected by natural convection. In this case, the steady rate of mass transport observed is greater than that for diffusion alone.

11.2.4.2 Double layer charging

Because microelectrodes have a very small electroactive area, the time required to charge or discharge the double layer is very short. Hence, a great property of microelectrodes is to significantly improve the discrimination against charging current. Reliable recordings of the faradaic current can be made at times shorter than those with a conventional electrode and this has opened the application of voltammetric and chronoamperometric experiments to the sub-millisecond timescale.

11.2.4.3 Ohmic drop

Due to their small size, the faradaic current flowing to microelectrodes typically ranges from a few pA to a few nA. In contrast, the resistive drop is small because most of it occurs very close to the microelectrode (e.g. within a few radii for a spherical or microdisc electrode). This is in contrast with large electrodes where the resistive drop continually increases with distance between the working electrode and the reference electrode. Taking these two effects into account, the ohmic drop due to the passage of the current in the solution is much reduced and the distortion of voltammetric curves becomes negligible. This property enables voltammetric experiments to be conducted in poorly conducting media, such as organic solvents, and even in the absence of supporting electrolyte.

Classical experiments performed with microelectrodes derive from the mass transport regimes and include steady-state voltammetry, fast scan cyclic voltammetry and

chronoamperometry. A key decision to make in microelectrode experiments is the choice of the timescale since this determines the diffusion regime. In the next few lines, a simple analysis based on the chronoamperometric response to a spherical electrode (equation (11.2.14)) is used to provide guidelines for the choice of timescale.

Comparing the two terms in equation (11.2.14) yields the time t_{planar} below which the response is controlled by planar diffusion and the time $t_{\text{spherical}}$ above which the response is controlled by spherical diffusion:

$$t_{\text{planar}} \ll \frac{r_0^2}{\pi D_o} \quad (11.2.60)$$

$$t_{\text{spherical}} \gg \frac{r_0^2}{\pi D_o} \quad (11.2.61)$$

Extending this analysis to all geometries, any microelectrode has therefore a characteristic diffusion time $t_{\text{diffusion}}$ given by

$$t_{\text{diffusion}} \approx \frac{(\text{characteristic dimension})^2}{D} \quad (11.2.62)$$

and the rule of thumb is that the response will be under planar diffusion if the experimental time is much less than $t_{\text{diffusion}}$ or under spherical diffusion (for a sphere, quasi-hemispherical for a microdisc and hemicylindrical for a microband) if the experimental time is greater than $t_{\text{diffusion}}$. Figure 11.12 summarises the relationship between the timescale, the corresponding diffusion field and the chronoamperometric and voltammetric responses.

Since at short times, a microelectrode behaves as a conventional electrode, all the theories developed for potential steps and potential sweeps at large electrodes are applicable. Conversely, at long times, the theories developed for steady-state techniques are applicable. However, the geometry of the electrode determines the expression for the limiting current. The most important ones are given in Table 11.3. For microbands and microcylinders, the current reaches a quasi-steady state. This is a consequence of the infinite length of the electrode relative to its characteristic dimension.

For the sphere, hemisphere and disc electrodes, the limiting current is proportional to the characteristic length. This has led to one of the classical experiments with a microdisc electrode where steady-state voltammograms are recorded for microdiscs of different radii and the limiting current is plotted against the radius of the electrodes. If the electrochemical process is diffusion controlled, the plot should be linear and yield the diffusion coefficient of the reactant. This is analogous to recording the limiting current for various rotation rates on a rotating disc electrode. However, the drawback is that one needs to fabricate different microdisc electrodes to perform this experiment.

Overall, microelectrodes offer three key advantages: (1) high rate of steady-state mass transport, (2) decreased ohmic drop distortion and (3) decreased double layer charging

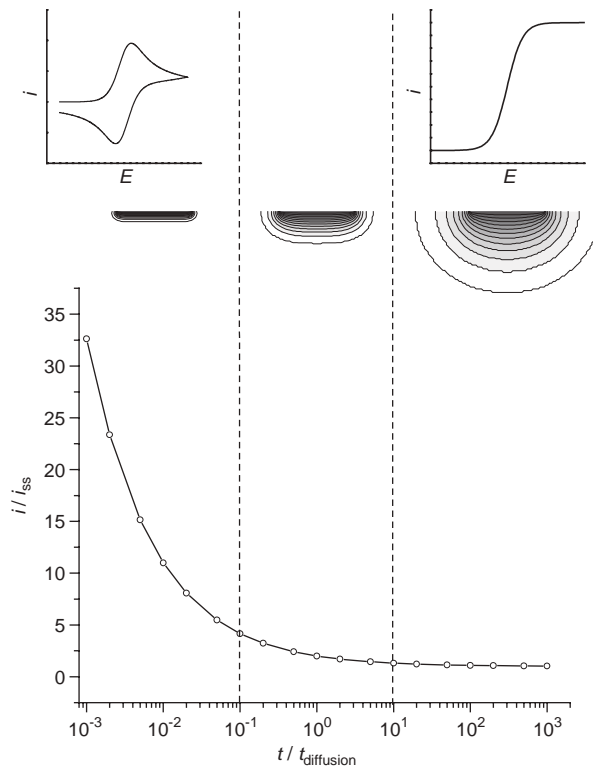


Figure 11.12 Current transient to a microdisc. The dashed lines have been arbitrarily drawn at $t_{\text{planar}} = t_{\text{diffusion}}/10$ and $t_{\text{spherical}} = 10 \times t_{\text{diffusion}}$. The grey scale contour lines, simulated concentration maps, illustrate the shape of the diffusion layer for each regime. The corresponding transient and steady-state voltammetric responses are also indicated.

Table 11.3

Expression for the limiting current at various microelectrode geometries

Geometry	Characteristic length	Steady-state current	
Sphere	r_0	$i_{ss} = 4\pi nFD_oC_o^*r_0$	(11.2.63)
Hemisphere	r_h	$i_{ss} = 2\pi nFD_oC_o^*r_h$	(11.2.64)
Disc	a	$i_{ss} = 4nFD_oC_o^*a$	(11.2.65)
Band ^a	w	$i_{ss} = \frac{2\pi nFD_oC_o^*l}{\ln((64D_o t)/w^2)}$	(11.2.66)
Cylinder ^a	r_c	$i_{ss} = \frac{4\pi nFD_oC_o^*l}{\ln((4D_o t)/r_c^2)}$	(11.2.67)

^a l is the length of the electrode.

distortion. This has led to simpler experiments (e.g. steady state instead of transient measurements) and easier data analysis (e.g. no need to correct for ohmic drop), and enabled electroanalytical experiments on to microsecond timescale (voltammetry up to MV s^{-1}). In all the following cases, microelectrodes should be considered:

- when a high current density is obtained: namely high concentrations of reactants, short time experiments and high rate processes (electron transfer or homogeneous kinetics);
- where a steady-state measurement is desirable;
- where access to sub-millisecond timescale is required, e.g. for high rate processes (electron transfer or homogeneous kinetics);
- where electroanalytical measurements need to be performed in poorly conducting media, even in absence of supporting electrolyte.

For additional information, consult references (34–37), and Chapter 6 of this handbook.

11.2.5 Rotating disc electrodes

The rotating disc electrode (RDE) is the classical hydrodynamic electroanalytical technique used to limit the diffusion layer thickness. However, readers should also consider alternative controlled flow methods including the channel flow cell (38), the wall pipe and wall jet configurations (39). Forced convection has several advantages which include: (1) the rapid establishment of a high rate of steady-state mass transport and (2) easily and reproducibly controlled convection over a wide range of mass transfer coefficients. There are also drawbacks: (1) in many instances, the construction of electrodes and cells is not easy and (2) the theoretical treatment requires the determination of the solution flow velocity profiles (as functions of rotation rate, viscosities and densities) and of the electrochemical problem; very few cases yield exact solutions.

The RDE consists of a disc (e.g. of Pt, Ni, Cu, Au, Fe, Si, CdS, GaAs, glassy carbon and graphite) set into an insulating (PTFE) surround. The electrode is rotated about its vertical axis (Figure 11.13), typically between 400 and 10,000 rpm. The theory for the hydrodynamics at the RDE (40–42) assumes that the electrode is uniformly accessible and affords a precise and reproducible control of the convection and diffusion of reactant to the electrode. Hence, the RDE can be used to study the kinetics of interfacial processes.

The theoretical treatment yields the concentration profile of reactant towards the RDE and defines a layer with thickness δ_0 where diffusion is the sole mode of mass transport (Figure 11.14)

$$\delta_0 = 4.98 D_0^{1/3} v^{1/6} \omega^{-1/2} \quad (11.2.68)$$

where ω is the rotation rate in rpm.

From the concentration profile is derived an expression for the limiting current, known as the Levich equation:

ω in rpm:

$$i_l = 0.201 n F A D_0^{2/3} v^{-1/6} C_0^* \omega^{1/2} \quad (11.2.69)$$

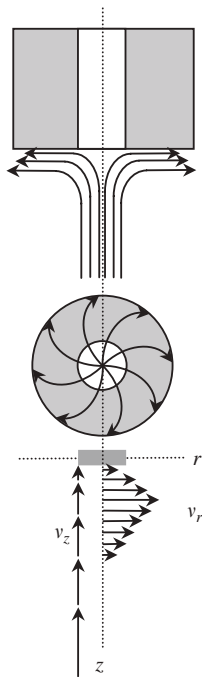


Figure 11.13 Streamlines for flow and vector representation of fluid velocities near a rotating disc electrode.

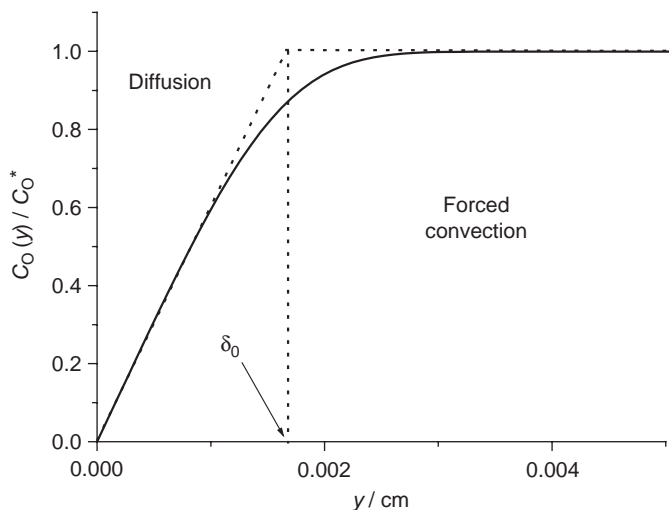


Figure 11.14 Steady-state concentration profile at the RDE, showing the well-stirred bulk where convection dominates and the thin stagnant layer at the electrode surface where diffusion dominates. δ_0 is the diffusion layer thickness. $D_O = 10^{-5} \text{ cm}^2 \text{ s}^{-1}$, $v = 0.01 \text{ cm}^2 \text{ s}^{-1}$ and $\omega = 100 \text{ Hz}$.

ω in rad s⁻¹:

$$i_l = 0.621nFAD_O^{2/3}v^{-1/6}C_O^*\omega^{1/2} \quad (11.2.70)$$

ω in Hz:

$$i_l = 1.554nFAD_O^{2/3}v^{-1/6}C_O^*\omega^{1/2} \quad (11.2.71)$$

Classically, the limiting current is reached by recording a linear sweep voltammogram at a low scan rate (1–10 mV s⁻¹). Under such mass transport conditions, the current–voltage curve is a sigmoidal wave analogous to that found with a spherical microelectrode under steady-state conditions. So the same criteria apply to analyse the shape of the curve. Whereas a range of microelectrodes with different radii is needed to obtain a range of steady-state mass transfer coefficients, the RDE simply needs a range of rotation rates. Hence, the classical RDE experiment consists in recording a series of linear sweep voltammograms at a low scan rate for a range of rotation rates. The Levich equation predicts that a plot of the limiting current vs. the square root of the rotation rate should be a straight line passing through the origin with a slope determined by the number of electrons, the geometric area of the electrode, the diffusion coefficient, the bulk concentration O and the kinematic viscosity of the solution, v .

When the redox process is reversible, the shape of the wave should not depend on ω . Hence, at any potential, the current should, like the limiting current, be proportional to $\omega^{1/2}$. If the shape of the curve depends on ω , then the redox process is kinetically limited. In this case, one can measure the current at fixed potentials along the voltammogram and for each potential plot the inverse of the current vs. $\omega^{1/2}$. This is known as a Koutecký–Levich plot and follows the Koutecký–Levich equation:

$$\frac{1}{i} = \frac{1}{i_K} + \frac{1}{0.201FAD_O^{2/3}v^{-1/6}C_O^*\omega^{1/2}} \quad \text{with } \omega \text{ in rpm} \quad (11.2.72)$$

where i_K is the kinetically controlled current that would be obtained for $\omega^{-1/2} = 0$, i.e. for an infinite rotation speed where the mass transfer would be so efficient that the surface concentration of C_O would be equal to C_O^* . Thus, a plot of $1/i$ vs. $\omega^{-1/2}$ should be linear and extrapolation to $\omega^{-1/2} = 0$ should yield i_K . By repeating this plot for different potentials along the voltammogram, it is possible to determine the kinetic parameters k_0 and α ; see Chapter 9 in reference (2).

One of the most important refinements of the RDE is the rotating ring disc electrode (RRDE) where the central disc is surrounded by an insulating ring, and then by a secondary annular working electrode. The purpose of this configuration is to perform steady-state generation–collection experiments. This is analogous to the reversal techniques, double potential steps or transient cyclic voltammetry but without the problems inherent to transient methods. Typically, the disc acts as the generator while the ring acts as the collector. The disc need not be an electrode and it is possible to study interfacial processes on the disc by electrochemically detecting the products with the ring. Interested readers should refer to reference (40). The geometry of the RRDE is critical to the quality of the results and good ring–disc assemblies are difficult to make.

11.2.6 Small amplitude perturbations and impedance methods

Most, if not all, of the classical experiments considered so far involve large amplitude perturbations of the electrode–solution interface. That is, in a typical voltammetric experiment, the electrode is subjected to a potential ramp often spanning several hundred millivolts (from a potential where no current flows to one where a mass transport-controlled reaction occurs on the electrode surface) and representing several orders of magnitude in electrochemical driving force. As a consequence, the current–potential response is nonlinear (Figure 11.15) and it is customary to analyse the voltammogram in terms of a few key values: E_{pa} , E_{pc} , $E_{1/4}$, $E_{1/2}$, $E_{3/4}$, i_{pa} , i_{pc} or i_r . Similarly, in chronoamperometry, the potential step amounts to a large perturbation and the current–time response is nonlinear.

Another methodology consists in applying small amplitude perturbations where the steps or sweeps are sufficiently small to yield a linear current–potential relationship (Figure 11.15). This approach is at the heart of electrochemical impedance methods.

Electrochemical impedance experiments comprise the following steps: (1) the electrochemical cell is subjected to a small amplitude periodic (usually sinusoidal, although square waves can be used) electrical perturbation (Figure 11.16); (2) its electrical response

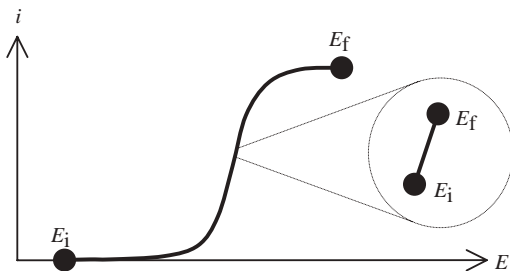


Figure 11.15 A large amplitude perturbation, here a potential sweep to a mass transport-controlled region, yields a nonlinear current–potential relationship. In contrast, a small amplitude perturbation, a few mV between E_i and E_f , yields a linear relationship between current and potential.

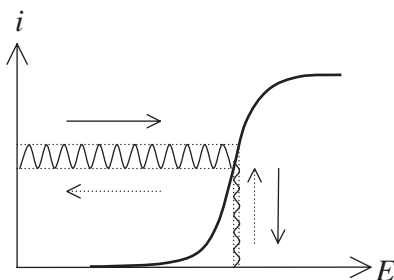


Figure 11.16 Solid arrows: an AC current is applied to the electrode and an AC potential response is obtained. Dashed arrows: an AC potential is applied to the electrode and an AC current is obtained. In both cases, the i – E relationship is recorded over a range of frequencies. Because of the small amplitude used, the current is proportional to the potential and the response is also sinusoidal. The perturbation is shown here around $E_{1/2}$ for the clarity of the drawing.

is acquired over a range of perturbation frequencies; (3) an equivalent electrical circuit is worked out; (4) components of the equivalent circuit are related to key physical or chemical characteristics of the electrochemical system.

As for conventional electrical circuits, the electrochemical impedance of the electrochemical cell is defined as

$$Z_{\text{cell}} = \frac{E_{\text{cell}}}{i_{\text{cell}}} \quad (11.2.73)$$

where E_{cell} is the voltage across the cell and i_{cell} the current circulating through the cell. Alternatively, the admittance is defined as

$$Y_{\text{cell}} = \frac{1}{Z_{\text{cell}}} = \frac{i_{\text{cell}}}{E_{\text{cell}}} \quad (11.2.74)$$

where Z is akin to a generalised resistance and has units of Ω , whereas Y is analogous to a conductance and has units of Ω^{-1} or Siemens. By definition, Z and Y are ratios of AC signals and thus each will have a phase and an amplitude. To facilitate interpretation, both are written as complex numbers in Cartesian or polar coordinates.

The experimental configuration commonly used is shown in Figure 11.17. Alternatively, one may use a low-pass filter and a lock-in amplifier to obtain the DC part, AC part and phase of the cell response.

The key step in electrochemical impedance experiments is the construction of an equivalent circuit that mimics the electrical behaviour of the cell. For this, it is necessary to consider the different ways in which the ionic charges are involved in the passage of current.

Between the electrodes, the solution behaves as an ionic conductor with a resistance, R_Ω , known as the ohmic solution resistance. At the electrode–solution interface, some of the ions are used to adjust the ionic atmosphere until the charge balance between the electrode surface and the solution is reached. Electrically, this is equivalent to the charge or discharge of a capacitor with capacitance C_d , known as the double layer capacitance. Simultaneously, i.e. in parallel, redox species undergo an electron transfer with the electrode; this yields the faradaic current whose magnitude reflects the rate of arrival of the reactants (the rate of mass transport) and the rate of the electron transfer process. Electrically, this is equivalent to two resistors in series: one for the kinetics of the electron

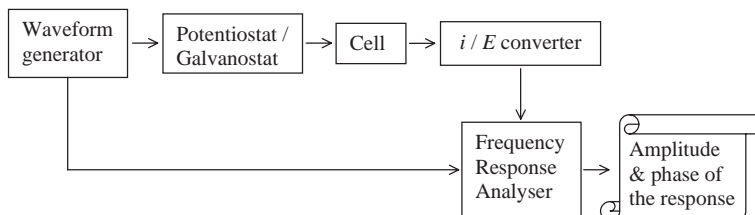


Figure 11.17 The common experimental arrangement for electrochemical impedance experiments relies on the use of a frequency response analyser to derive the Cartesian or polar coordinates of the impedance and admittance.

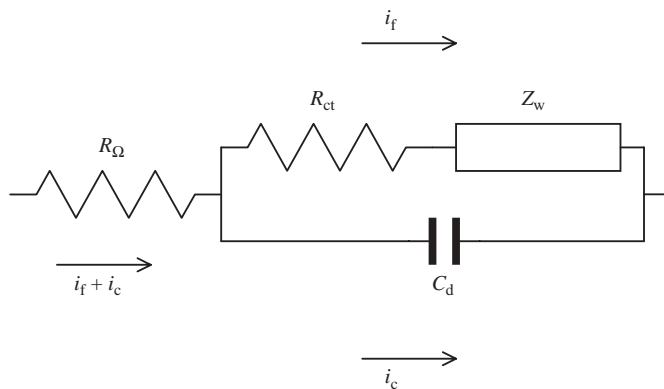


Figure 11.18 The equivalent circuit for a simple reversible electron transfer. R_Ω , the Ohmic solution resistance; R_{ct} , the charge transfer resistance; Z_w , the Warburg impedance or mass transfer resistance; C_d , the double layer capacitance; i_c , the charging current; i_f , the faradaic current.

transfer process, R_{ct} , known as the charge transfer resistance and one for the rate of mass transport, Z_w , known as the Warburg impedance. Pulling all this together, the simplest electrical equivalent circuit consists of four components connected as shown in Figure 11.18.

The solution resistance is determined by the solution conductivity and the geometry of the cell, namely the distance between the electrodes and the cross-sectional area of solution linking the electrodes. The double layer capacitance reflects the electrostatic interplay between the electrode and the electrolyte and depends on the electrode area and nature and the electrolyte ionic strength and permittivity. Together, R_{ct} and Z_w make up the faradaic impedance. R_{ct} reflects the charge transfer kinetics and can be thought of as the ratio of overpotential to current in absence of mass transfer limitation. R_{ct} goes through a maximum at the equilibrium potential; hence, it is best to perturb the electrochemical system around this value. There, the current–potential relationship can be linearised, and R_{ct} is found to be inversely related to the exchange current, i_0 :

$$R_{\text{ct}} = \frac{RT}{nF i_0} \quad (11.2.75)$$

The mass transfer impedance depends on the mode of mass transport within the cell. For semi-infinite linear diffusion, Z_w is a complex number whose real and imaginary parts depend on the perturbation frequency:

$$Z_w = \sigma\omega^{-1/2} - j\sigma\omega^{-1/2} \quad (11.2.76)$$

with

$$\sigma = \frac{RT}{n^2 F^2 A \sqrt{2}} \left(\frac{1}{C_O^* D_O^{1/2}} + \frac{1}{C_R^* D_R^{1/2}} \right) \quad (11.2.77)$$

and

$$\omega = 2\pi f \quad (11.2.78)$$

Combining the impedance of the four components gives the overall impedance of the cell:

$$Z_{\text{cell}} = Z_{\text{Re}} + jZ_{\text{Im}} \quad (11.2.79)$$

with

$$Z_{\text{Re}} = R_{\Omega} + \frac{R_{\text{ct}} + \sigma\omega^{-1/2}}{(C_d\sigma\omega^{1/2} + 1)^2 + \omega^2 C_d^2 (R_{\text{ct}} + \sigma\omega^{-1/2})^2} \quad (11.2.80)$$

and

$$Z_{\text{Im}} = -\frac{\omega C_d (R_{\text{ct}} + \sigma\omega^{-1/2})^2 + \sigma\omega^{-1/2} (C_d\sigma\omega^{1/2} + 1)}{(C_d\sigma\omega^{1/2} + 1)^2 + \omega^2 C_d^2 (R_{\text{ct}} + \sigma\omega^{-1/2})^2} \quad (11.2.81)$$

The frequency response of the cell is represented by plotting $-Z_{\text{Im}}$ vs. Z_{Re} . This is known as a Nyquist plot (Figure 11.19). Alternatively, Bode plots ($\log(|Z|)$) and phase angle vs. log(frequency) or $\log(Z_{\text{Re}})$ and $\log(Z_{\text{Im}})$ vs. log(frequency)) may be used.

Figure 11.19 is best understood by considering the dominant impedance for various frequency limits as shown in Table 11.4.

It is usual to extract the following information from the impedance diagram:

- R_{Ω} from the high frequency intercept on the real axis;
- R_{ct} from the diameter of the circle;
- C_d from the frequency at the maximum of the circle.

Increasingly complex equivalent circuits are used to model a wide range of electrochemical processes (e.g. corrosion, adsorption or porous electrodes) and to facilitate analysis, commercial impedance software includes libraries of equivalent circuits which can be

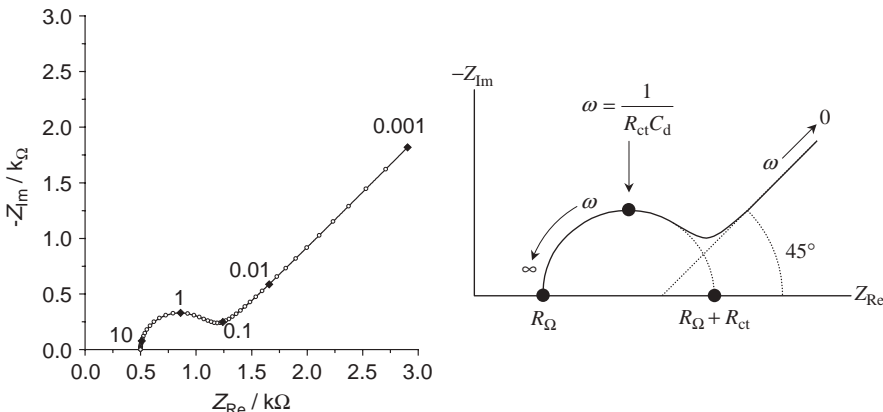


Figure 11.19 (a) Nyquist plot calculated from equations (11.2.80) and (11.2.81) with $R_{\Omega} = 500 \Omega$, $R_{\text{ct}} = 600 \Omega$, $T = 298 \text{ K}$, $C_d = 2 \times 10^{-4} \text{ F}$, $n = 1$, $A = 1 \text{ cm}^2$, $D_O = 7.2 \times 10^{-6} \text{ cm}^2 \text{ s}^{-1}$, $D_R = 6.5 \times 10^{-6} \text{ cm}^2 \text{ s}^{-1}$ and $C_O = C_R = 1 \text{ mM}$. Numbers by points are frequencies in Hz. (b) Key features of an impedance diagram.

Table 11.4

Impedance-frequency dependence and equivalent circuit for a typical electrochemical cell

Frequency	Equivalent circuit	Impedance diagram
$\omega \rightarrow 0$		
$\omega \approx 1/R_{ct}C_d$		
$\omega \rightarrow \infty$		

The dotted lines indicate the least resistive current path.

fitted to the experimental impedance data. However, users should resist the temptation to improve the fit by adding new components to the circuit. Instead, the values of some of the components should be backed up by other electrochemical experiments. Electrochemical impedance methods should be considered as complementary techniques to large amplitude methods. One of their main advantages is to provide a complete electrochemical response over a wide timescale. For in depth reviews and early articles, readers should consult references (1, 43–52).

11.3 SIMULATIONS

With the availability of significant desktop computing power and of electrochemical modelling software, the possibility of simulating electrochemical experiments is no longer restricted to the programming aficionados. For this reason, the present chapter covers the basic principles and applications of numerical simulations of electrode reactions. The section starts with a series of questions, continues with a consideration of simulation principles and finishes with an example.

11.3.1 Electrochemical simulations—a few questions

11.3.1.1 Why use a simulation?

- (1) To predict the electrochemical response when the problem has no known or simple analytical solution, e.g. cyclic voltammetry, microelectrodes, coupled chemical reactions, etc.

- (2) To test a proposed model against experimental results and derive experimental quantities.
- (3) To learn or teach the principles of a technique, e.g. the evolution of concentration profiles during a cyclic voltammogram.

11.3.1.2 What do they do?

Typically, an electrochemical simulation models the transport of the reactant from the bulk to the electrode surface, the transfer of electrons at the electrode/solution interface and the transport of the product away from the electrode. Depending on the complexity of the electrochemical process, the simulation may account for the rate of electron transfer kinetics, the possibility and rate of preceding or following chemical reactions, the possibility and rate of adsorption processes and even combinations of different forms of mass transport (planar or spherical diffusion, convection and migration). In other words, the simulation performs a series of actions which mimic the sequence of events thought to occur in the electrode reaction.

11.3.1.3 How is a simulation put together?

Traditionally, a simulation is constructed as follows: (1) the real world problem is analysed and cast in terms of mathematical expressions (e.g. the differential equations for mass transport and the initial and boundary conditions for what happens at the electrode surface and in the bulk); (2) the expressions are then rewritten in dimensionless form; (3) the continuous variables (typically, concentration, space and time) are discretised; (4) the differential equations and boundary conditions are discretised; (5) an algorithm is chosen and a program written in Fortran, Pascal, Basic or C; (6) the simulation is tested with conditions yielding a known solution; (7) finally, the simulation is applied to the conditions of interest.

Physical approaches not requiring the numerical solution of the differential equations have also been developed. For example, an “atomistic” model considers the cell as a domain filled with a population of particles and diffusion is simulated by the random walk of the particles within the domain (53, 54). The current is computed by counting the number of particles that reach the electrode per unit time. Convection and migration can even be included. Another model, the “box” method used in the early days of electrochemical simulation (55), divides the solution in thin slabs (boxes wherein the concentration is assumed to be uniform) and calculates the movement of species between slabs using Fick’s first law of diffusion. Although more intuitive, these approaches are in fact equivalent to solving the transport equation.

11.3.1.4 How are they used?

It was common to run the simulation for a range of dimensionless parameters and produce working curves and case diagrams. The experimental data were then cast in dimensionless form and analysed by comparison with the simulated working curves. The tendency is now to move towards a direct fitting of simulated data to experimental data by adjusting the

simulation parameters and running the simulation in real time until a fit is obtained. This is made possible by the computing power available nowadays and is in contrast to conventional procedures where an analytical expression is fitted to the experimental data.

The “home-made” simulation is still required for demanding situations (e.g. voltammetry at a microdisc electrode) but for most problems, DigiSim (56–61), a commercial simulation software, and DigiElch (62), a free equivalent software, offer a much simpler alternative. An electrochemical simulator operates as a black box requiring almost no prior knowledge about numerical simulations of electrode reactions. The user may exploit it as a virtual instrument to predict a theoretical response for a given set of conditions, as an analytical tool to fit experimental results to a model and derive experimental parameters or as a learning or even a teaching tool. At the click of the mouse, the software offers an array of simulation conditions: (1) a range of electrode geometries (planar and spherical); (2) a range of mass transports (semi-infinite diffusion, finite diffusion and convection); (3) single or multiple electron transfer reactions; (4) first- and second-order-coupled chemical reactions; (5) a dynamic display of concentration profiles during cyclic voltammetry; (6) the possibility to import experimental data files for comparison and least-squares fitting with simulated data. DigiElch even includes 2D simulations for microdiscs and microband electrodes. Other free softwares are available (63, 64), including a site for online data analysis and simulations (65).

11.3.2 Basic principles of an electrochemical simulation

Although a simulator may be taken as a black box, the user will soon find that some basic knowledge of the principles of electrochemical simulations is essential. A simple simulation will now be described to highlight the fundamental principles of electrochemical modelling. For additional information, readers should consult Britz’s excellent book (66) and Speiser’s extensive review (67).

The following assumptions are made: (1) the electrode is planar and the reaction is a fast electron transfer; (2) only O is present in the cell initially; (3) the diffusion coefficients of O and R are identical; (4) the potential of the electrode is stepped from a value where no reaction occurs to one where the reaction is diffusion controlled; (5) the objective is to predict the current transient and the concentration profiles as a function of time. Under these conditions, the latter should be given by equation (11.2.5) and the former by equation (11.2.7). Using the following definitions:

Dimensionless concentration:

$$c = \frac{C_o}{C_o^*} \quad (11.3.1)$$

Dimensionless distance:

$$X = \frac{x}{\delta} \quad (11.3.2)$$

Dimensionless time:

$$T = \frac{t}{\tau} \quad (11.3.3)$$

Dimensionless current:

$$\Psi = \frac{i\delta}{nFAD_0C_o^*} \quad (11.3.4)$$

Diffusion layer thickness:

$$\delta = \sqrt{D_o \tau} \quad (11.3.5)$$

where τ is a characteristic time of the experiment (e.g. the duration of the experiment); the transport equation (11.2.1), the initial condition (equation (11.2.2)), the boundary conditions (equations (11.2.3) and (11.2.4)) and the current (equation (11.2.6)) are recast in dimensionless form to avoid unnecessary runs of the simulation.

$$\frac{\partial c(X, T)}{\partial T} = \frac{\partial^2 c(X, T)}{\partial X^2} \quad (11.3.6)$$

$$c(X \geq 0, 0) = 1 \quad (11.3.7)$$

$$c(\infty, T > 0) = 1 \quad (11.3.8)$$

$$c(0, T > 0) = 0 \quad (11.3.9)$$

$$\Psi = \left. \frac{\partial c}{\partial X} \right|_{X=0, T>0} \quad (11.3.10)$$

Using finite difference approximations (66), the discrete form of equation (11.3.6) is obtained:

$$\frac{c_i^{k+1} - c_i^k}{\Delta T} = \frac{c_{i+1}^k - 2c_i^k + c_{i-1}^k}{\Delta X^2} \quad (11.3.11)$$

where c_i^k is the discretised dimensionless concentration at location i along the profile and time k equivalent to $C_o(x, t)$ in the usual units. Rearranging yields:

$$c_i^{k+1} = c_i^k + \frac{\Delta T}{\Delta X^2} (c_{i+1}^k - 2c_i^k + c_{i-1}^k) \quad (11.3.12)$$

or

$$c_i^{k+1} = \frac{\Delta T}{\Delta X^2} c_{i+1}^k + \left(1 - 2 \frac{\Delta T}{\Delta X^2} \right) c_i^k + \frac{\Delta T}{\Delta X^2} c_{i-1}^k \quad (11.3.13)$$

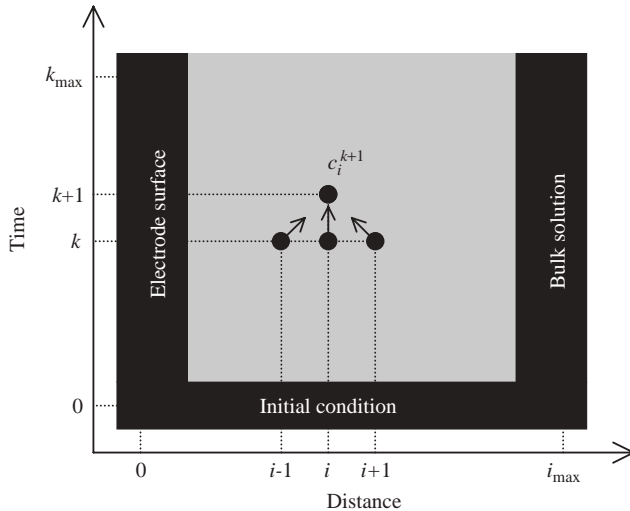


Figure 11.20 Schematic representation of the explicit finite difference algorithm. The grey region indicates unknown concentrations, whereas the black regions indicate known concentrations. Starting with $k = 0$, the unknown concentrations c_i^{k+1} are calculated from the known values of c_{i-1}^k , c_i^k and c_{i+1}^k . Iterating from $i = 1$ to $i_{\max-1}$ yields the concentration profile at $k = 1$. The procedure is repeated to compute all the concentrations profiles until k_{\max} .

All the concentrations on the RHS correspond to the present and are known. Thus, it is possible to calculate the concentration in the future, c_i^{k+1} . This scheme is known as explicit finite difference or EFD and works as shown in Figure 11.20. The ratio $\Delta T/\Delta X^2$ is akin to a dimensionless or model diffusion coefficient and should be as large as possible to make the simulation efficient. However, it cannot be greater than 0.5 or the scheme becomes unstable and produces negative concentrations. In practice, a value of 0.45 is chosen. This is one of the main limitations of EFD and other more efficient algorithms are available (66). Increasing i_{\max} and k_{\max} improves the resolution of the discretisation and therefore the accuracy of the simulation but at the expense of computing time. With the desktop computers available nowadays, this is no longer a limitation.

The current at time k is calculated by discretising equation (11.3.10):

$$\Psi^k = \frac{c_1^k - c_0^k}{\Delta X} \quad (11.3.14)$$

Thus, equations (11.3.13) and (11.3.14) provide the means to calculate the current value and concentration profile for each time iteration. See Figure 11.21 for an example of simulation codes. With $\Delta T/\Delta X^2 = 0.45$, the scheme converges rapidly with current values accurate to 5% after 25 iterations (Figure 11.22). The algorithm is rather simple and yet very powerful. For example, to simulate the transient current for a double potential step, it is simply a matter of changing the surface concentration while the simulation

```

' c(i) : concentration
' cnew(i) : new concentration
' cur : current
' dt : time increment
' dx : space increment
' i : counter for space increments
' imax : number of space increments
' k : counter for time steps
' kmax : number of time steps
' mdc : model diffusion coefficient
' tim : time
Dim c(1000), cnew(1000)
kmax = 1000
mdc = 0.45
dt = 1 / kmax
dx = Sqr(dt / mdc)
imax = CInt(6 * Sqr(mdc * kmax))

For i = 0 To imax + 1
    c(i) = 1
Next i
c(0) = 0
For k = 1 To kmax
    cur = (c(1) - c(0)) / dx
    tim = k / kmax
    ' output tim and cur here
    For i = 1 To imax
        cnew(i) = c(i) + mdc * (c(i - 1) - 2
                                   * c(i) + c(i + 1))
    Next i
    For i = 1 To imax
        c(i) = cnew(i)
    Next i
Next k

```

Figure 11.21 Typical codes used to simulate the current transient for a diffusion-controlled reaction on a planar electrode. Written in Visual Basic as found in a spreadsheet macro. For a given time t , diffusion does not affect the concentration profile beyond a distance equal to $6\sqrt{Dt}$, hence the relationship linking i_{\max} to k_{\max} .

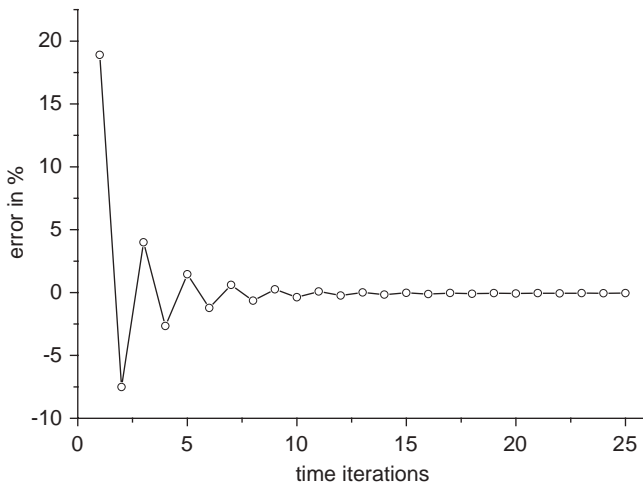


Figure 11.22 Convergence plot for the explicit finite difference algorithm.

is running. The concentration profile gradually adjusts to the new boundary condition and the current follows the characteristic feature of a double pulse experiment (Figure 11.23). Compared to the theoretical treatment, the simulation is exceedingly simple. Similarly, incorporation of potential sweep, heterogeneous or homogeneous kinetics is not difficult and the algorithm can be tailored to simulate complex electrochemical problems.

Many different numerical simulations have been reported, often more accurate and more efficient than EFD. Some include two-dimensional mass transport but they are outside the

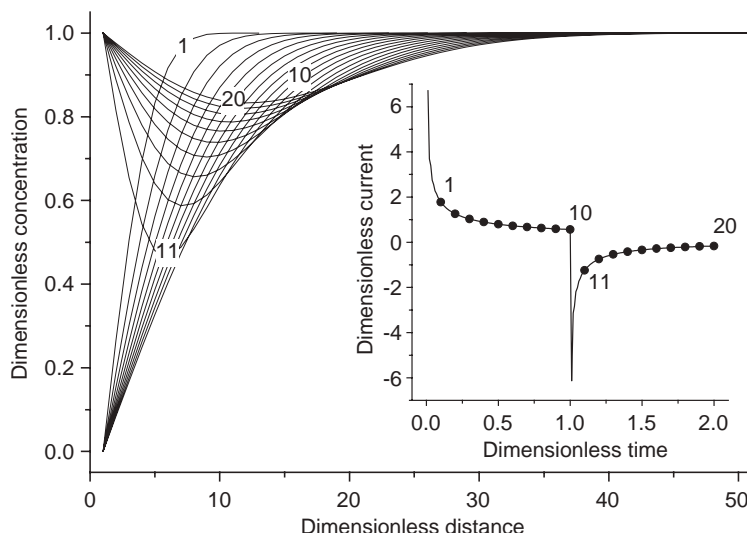


Figure 11.23 Simulated concentration profiles and current transient for a double potential step at a planar electrode under diffusion control. The profiles were taken at the times indicated by the corresponding numbers on the transient.

scope of this chapter and interested readers should consult references (55, 66, 67). The fact is that EFD remains the simplest algorithm and offers the easiest route to implementing complex mechanisms and electrochemical techniques. Since computer power is no longer an issue, EFD's inefficiency is not a concern anymore and interested readers should try to write their own simulation.

11.4 TROUBLE SHOOTING ELECTROCHEMICAL EXPERIMENTS: A CHECKLIST

11.4.1 Checking the results

Electrochemical experiments are often carried out in similar conditions and it is easy to check whether the magnitude of a result is in agreement with expectations. Table 11.5 presents a list of the parameter values typically used to check whether the experimental results obtained have the correct order of magnitude. Many incidents can occur in the course of an electrochemical experiment and the remainder of this section aims to identify the most common causes of problems, as well as how to recognize and correct them.

11.4.2 No current response

Assuming the instruments are turned on, no current indicates that the electrochemical circuit is incomplete. Check the quality of the wires and of the connections. A broken wire at

Table 11.5

Values used to check the magnitude of experimental results.

Quantity	Value	Conditions
C_d	20 $\mu\text{F}/(\text{cm}^2 \text{ real area})$	Pt electrode
D_O, D_R	$10^{-5} \text{ cm}^2 \text{ s}^{-1}$	Aqueous solution
i_l	0.4 nA/mM/(μm radius)	Microdisc electrode, $n = 1$
i_l	$10 \mu\text{A}/(\text{cm}^2 \text{ geometric area})/\text{mM}/\text{rpm}^2$	RDE, $n = 1$, aqueous solution
i_p	$200 \mu\text{A}/(\text{cm}^2 \text{ geometric area})/\text{mM}$	Voltammetry, $n = 1$, $v = 0.1 \text{ V s}^{-1}$
$Q_{\text{monolayer}}$	$200 \mu\text{C}/(\text{cm}^2 \text{ real area})$	Pt electrode
R_Ω	$1 \Omega \text{ cm}/(\text{cm radius})^{-1}$	Spherical electrode, 0.5 M NaCl

the back of a rusty crocodile clip is not uncommon. Ensure that the electrodes are fully immersed in the solution. Test the electrochemical circuit by replacing the electrochemical cell with a resistive dummy cell. Connect the WE connector to one end of the resistor, the CE and RE to the other side and run a potential sweep. The current–voltage plot obtained should be purely ohmic: that is, a straight line through the origin with a gradient equal to the inverse of the resistance of the dummy cell. Should this be the case, then the problem lies with the electrochemical cell. Check that the internal connections within the WE, CE or RE are intact. With microelectrodes, it is common to find that the microwire is loose and no longer in electrical contact with the main wire. If the problem is not obvious, replace each electrode in turn to identify the culprit. If the problem does not lie with the electrochemical cell, simply replace each lead/connection/equipment in turn until the problem is resolved.

11.4.3 Potential shift

First, using a DVM, check the potential difference between the WE and the RE. An unexpected potential shift in the current response is likely due to the reference electrode. If a problem with the RE is suspected, run a voltammogram with a pseudo-reference (e.g. Ag or Pt wire). To test the faulty RE, place it in an electrolyte and measure its potential against a commercial RE of the same type. The potential difference between them should be less than 5 mV and stable. Major sources of error in a RE can come from either the electrode being stored in the wrong solution or the presence of a bubble in the electrode. If in doubt, empty the solution from the electrode and replace with fresh solution. A freshly made RE needs time to equilibrate, so store it in the same solution as the internal one and check its potential against a commercial RE. After 24 h, the difference should be less than 5 mV and stable. If it is not, then dismantle the electrode and recondition it (e.g. for an SCE ensure that the internal solution is saturated in KCl). With non-aqueous solvents, it is not advised to use a RE with an aqueous internal solution; instead, use a quasi-RE with an internal redox standard, such as ferrocene.

11.4.4 Currents lower than expected

If the current–voltage curve obtained is correct in shape, but not in magnitude, then the most probable cause is the working electrode. The WE is very susceptible to fouling and requires regular cleaning. Polymers or adsorbed species can easily block the surface, so the electrode should be polished on a polishing pad covered with damp alumina powder (or diamond paste), starting with a high grain size (approximately 1 μm) and reducing down to approximately 0.05 μm , rinsing off between grain sizes. Some electrodes can also be reconditioned by potential cycling in 1 M H_2SO_4 between oxygen and hydrogen evolutions. For example, once cleaned, a Pt electrode should present its typical “fingerprint” (Figure 11.9). Other problems that affect working electrodes include a poor seal between the glass and the electrode, a poor connection between the electrode wire and the connecting wire or the electrode recessing over time (especially in cases where the electrode is much softer than the glass, e.g. carbon fibre electrodes). Diffusion-controlled currents are very sensitive to temperature changes (D increases by 1–2% $^{\circ}\text{C}^{-1}$), so to enable comparison between data recorded at different times (morning vs. afternoon and summer vs. winter), any diffusion-controlled experiment should be thermostated to within 1 $^{\circ}\text{C}$.

11.4.5 Slanted voltammogram

If the correct shape is seen, but is slanted slightly, then this implies that there is an added resistance in the circuit. The most common reason for this is a bubble inside the RE. This creates a discontinuity in the conductivity of the reference electrode filling solution. The RE should be reconditioned as mentioned above.

11.4.6 Noisy current

This is a particular problem with microelectrodes where the current is typically a few nA. The noise is likely due to the mains and appropriate shielding is required. The cell should be placed inside a grounded Faraday cage. The electrochemical circuit should consist of shielded cables (e.g. BNC) and the instruments should be grounded avoiding ground loops. If possible, battery-operated instruments (e.g. current followers) should be used. A common problem is the use of a thermostatic water bath with a pumped water circuit and a jacketed cell. The water circuit transmits the mains noise which is easily picked up by the WE by coupling through the glass walls. Any mains powered instrument, stirrer or heating mantle, should be removed from the Faraday cage or replaced with battery-operated ones.

11.4.7 Other common problems

- Ohmic distortion:* Increase supporting electrolyte concentration, reposition Luggin capillary, use a microelectrode, decrease reactant concentration or use iR compensation.

- (b) *Double layer charging*: Reduce the WE area and lower the scan rate.
- (c) *Migration*: Increase supporting electrolyte concentration.
- (d) *Natural convection*: Work under 30 s.
- (e) *Oxygen reduction*: Purge with N₂ or better, Ar.
- (f) *Electrode contamination*: Use ultra-pure water and ultra-pure reagents.
- (g) *Chloride contamination*: Use SMSE instead of SCE.
- (h) *Bad cell geometry*: Position CE opposite WE and ensure CE area is greater than WE area.
- (i) *Poor WE geometry*: Avoid geometries with corners.
- (j) *Offset and linearity*: Calibrate instruments.

REFERENCES

1. D. D. Macdonald, *Transient Techniques in Electrochemistry*, Plenum Press: New York, 1977.
2. A. J. Bard, L. R. Faulkner, *Electrochemical Methods: Fundamentals and Applications*, Wiley: New York, 2001.
3. R. Greef, R. Peat, L. M. Peter, D. Pletcher, J. Robinson, *Instrumental Methods in Electrochemistry*, Ellis Horwood: Chichester, 1985.
4. F. G. Cottrell, *Z. Phys. Chem.* **42**, 385 (1903).
5. M. Abramowitz, I. A. Stegun, *Handbook of Mathematical Functions*, Dover Publications, Inc.: New York, 1970.
6. J. Koutecky, *Collection Czech. Chem. Commun.* **21**, 433 (1956).
7. D. D. Macdonald, *Transient Techniques in Electrochemistry*, Plenum Press: New York, 1977.
8. W. M. Smit, M. D. Wijnen, *Recueil des Travaux Chimiques des Pays-Bas et de la Belgique* **79**, 5 (1960).
9. T. Kambara, *Bull. Chem. Soc. Jpn.* **27**, 529 (1954).
10. J. Koutecky, *Collection Czech. Chem. Commun.* **21**, 433 (1956).
11. G. C. Barker, *Anal. Chim. Acta* **18**, 118 (1958).
12. F. M. Kimmerle, J. Chevalet, *J. Electroanal. Chem. Interfacial Electrochem.* **21**, 237 (1969).
13. A. J. Bard, L. R. Faulkner, *Electrochemical Methods: Fundamentals and Applications*, John Wiley & Sons, Inc.: New York, 2001.
14. W. M. Schwarz, I. Shain, *J. Phys. Chem.* **69**, 30 (1965).
15. H. Girault, *Analytical and Physical Electrochemistry*, EPFL Press: Lausanne, 2004.
16. K. B. Oldham, *J. Electroanal. Chem.* **313**, 3 (1991).
17. K. B. Oldham, J. C. Myland, C. G. Zoski, A. M. Bond, *J. Electroanal. Chem.* **270**, 79 (1989).
18. E. Laviron, *J. Electroanal. Chem.* **100**, 263 (1979).
19. R. Bilewicz, K. Wikiel, R. Osteryoung, J. Osteryoung, *Anal. Chem.* **61**, 965 (1989).
20. J. Osteryoung, *Acc. Chem. Res.* **26**, 77 (1993).
21. A. M. Bond, *Modern Polarographic Methods in Analytical Chemistry*, Marcel Dekker: New York, 1980.
22. E. P. Parry, R. A. Osteryoung, *Anal. Chem.* **37**, 1634 (1965).
23. J. B. Flato, *Anal. Chem.* **44**, 75A (1972).
24. R. A. Osteryoung, J. Osteryoung, *Philos. Trans. R. Soc. Lond. A Math. Phys. Eng. Sci.* **302**, 315 (1981).
25. K. B. Oldham, E. P. Parry, *Anal. Chem.* **40**, 65 (1968).
26. J. Osteryoung, J. O'Dea, *Electroanalytical Chemistry*, A. J. Bard, Ed., Marcel Dekker: New York, 1986, Vol. 14, p. 209.

27. G. C. Barker, I. L. Jenkins, *Analyst* **77**, 685 (1952).
28. J. H. Christie, J. A. Turner, R. A. Osteryoung, *Anal. Chem.* **49**, 1899 (1977).
29. J. A. Turner, J. H. Christie, M. Vukovic, R. A. Osteryoung, *Anal. Chem.* **49**, 1904 (1977).
30. J. J. O'Dea, J. Osteryoung, R. A. Osteryoung, *Anal. Chem.* **53**, 695 (1981).
31. L. Ramaley, M. S. Krause, Jr., *Anal. Chem.* **41**, 1362 (1969).
32. J. Wang, *Stripping Analysis: Principles, Instrumentation, and Applications*, VCH: Dearfield Beach, FL, 1985.
33. M. I. Montenegro, M. A. Queirós, J. L. Daschbach, Eds., *Microelectrodes: Theory and Applications*, Kluwer Academic Publishers: Dordrecht, 1991.
34. R. M. Wightman, *Anal. Chem.* **53**, 1125A (1981).
35. M. Fleischmann, S. Pons, D. R. Rolison, P. P. Schmidt, Eds., *Ultramicroelectrodes*, Datatech Systems Inc.: Morganton, NC, 1987.
36. R. M. Wightman, D. O. Wipf, *Electroanal. Chem.* **15**, 267 (1989).
37. K. Stulik, C. Amatore, K. Holub, V. Marecek, W. Kutner, *Pure Appl. Chem.* **72**, 1483 (2000).
38. P. R. Unwin, R. G. Compton, in *Comprehensive Chemical Kinetics*, R. G. Compton, A. Hamnett, Eds., Elsevier: Amsterdam, 1989, Vol. 29, p. 173.
39. J. W. Albery, C. C. Jones, A. R. Mount, in *Comprehensive Chemical Kinetics*, R. G. Compton, A. Hamnett, Eds., Elsevier: Amsterdam, 1989, Vol. 29, p. 129.
40. W. J. Albery, M. L. Hitchman, *Ring-Disc Electrodes*, Clarendon: Oxford, 1971.
41. V. G. Levich, *Physicochemical Hydrodynamics*, Prentice-Hall: Englewood Cliffs, NJ, 1962.
42. J. Newman, in *Electroanalytical Chemistry*, A. J. Bard, Ed., Marcel Dekker: New York, 1973, Vol. 6, p. 187.
43. D. D. Macdonald, *Electrochim. Acta* **35**, 1509 (1990).
44. J. R. Macdonald, *Electrochim. Acta* **35**, 1483 (1990).
45. F. Mansfeld, *Electrochim. Acta* **35**, 1533 (1990).
46. C. Gabrielli, M. Keddam, H. Takenouti, *Electrochim. Acta* **35**, 1553 (1990).
47. I. D. Raistrick, *Electrochim. Acta* **35**, 1579 (1990).
48. R. Oltra, M. Keddam, *Electrochim. Acta* **35**, 1619 (1990).
49. J. R. Macdonald, *Electrochim. Acta* **38**, 1883 (1993).
50. D. D. Macdonald, in *Techniques for Characterization of Electrodes and Electrochemical Processes*, J. R. S. Ravi Varma, Ed., Wiley: New York, 1991, Chapter 11.
51. F. Mansfeld, W. J. Lorenz, in *Techniques for Characterization of Electrodes and Electrochemical Processes*, R. Varma, J. R. Selman, Eds., Wiley: New York, 1991, Chapter 12.
52. C. Gabrielli, in *Physical Electrochemistry Principles, Methods, and Applications*, I. Rubinstein, Ed., Marcel Dekker: New York, 1995, Chapter 6.
53. G. Nagy, Y. Sugimoto, G. Denuault, *J. Electroanal. Chem.* **433**, 167 (1997).
54. G. Nagy, G. Denuault, *J. Electroanal. Chem.* **433**, 175 (1997).
55. S. W. Feldberg, in *Electroanalytical Chemistry, A Series of Advances*, A. J. Bard, Ed., Marcel Dekker: New York, Vol. 3, 1969.
56. M. Rudolph, D. P. Reddy, S. W. Feldberg, *Anal. Chem.* **66**, A589 (1994).
57. M. Rudolph, *J. Electroanal. Chem.* **314**, 13 (1991).
58. M. Rudolph, in *Physical Electrochemistry Principles, Methods, and Applications*, I. Rubinstein, Ed., Marcel Dekker: New York, 1995, p. 81.
59. M. Rudolph, *J. Electroanal. Chem.* **338**, 85 (1992).
60. W. Luo, S. W. Feldberg, M. Rudolph, *J. Electroanal. Chem.* **368**, 109 (1994).
61. M. Rudolph, *J. Electroanal. Chem.* **375**, 89 (1994).
62. M. Rudolph, <http://www.digielch.de/index.html>, 2004.
63. C. Nervi, http://lem.ch.unito.it/chemistry/esp_manual.html, 1998.

64. L. Biesniasz, <http://www.cyf-kr.edu.pl/~nbbienia/elsim3ad.html>, 1996.
65. R. G. Compton, J. A. Alden, <http://physchem.ox.ac.uk/~rgc/datan/datan.htm>, 1998.
66. D. Britz, *Digital Simulation in Electrochemistry*, Springer-Verlag: Berlin, Heidelberg, 1988.
67. B. Speiser, in *Electroanalytical Chemistry, A Series of Advances*, A. J. Bard, I. Rubinstein, Eds., Marcel Dekker: New York, 1996, Vol. 19, p. 1.

This page intentionally left blank

– 12 –

Scanning Electrochemical Microscopy

Fu-Ren F. Fan¹, José Fernandez¹, Biao Liu¹, and Janine Mauzeroll²

¹The University of Texas at Austin, Austin, TX, USA

²Laboratoire d'Électrochimie Moléculaire, Université Paris 7-Denis Diderot, France

12.1 INTRODUCTION AND PRINCIPLES

This chapter is devoted to a concise discussion of various techniques and applications of scanning electrochemical microscopy (SECM) (1). SECM is one of the scanning probe microscopies (SPM) (2) in which three-dimensional images of surfaces are obtained by scanning a small ultramicroelectrode (UME, Chapter 6) tip across a surface (usually termed “the substrate”) and recording an appropriate response. To understand the operation and response of the SECM, it is necessary to review briefly the behavior of a very small UME in an electrochemical cell. More detailed discussions of UMEs are available (Chapter 6 of this handbook). Consider a UME disk immersed in a solution containing an electrolyte and an electroactive species, Ox, as well as counter and reference electrodes. When a potential, sufficiently negative of the formal potential of the redox couple (Ox/Red), is applied to the UME, the reduction of Ox occurs at the UME at a diffusion-controlled rate, and a cathodic current passes through the UME. The current decays as a diffusion layer of Ox builds up around the electrode and attains rather quickly a steady-state value, $i_{T,\infty}$, that depends on the concentration of Ox, C^* , and its diffusion coefficient, D , and is given by (3)

$$i_{T,\infty} = 4nFDaC^* \quad (12.1.1)$$

in which n is the number of electrons involved in the electrode reaction, F is the Faraday constant, and a is the radius of the UME. The steady-state current results from the constant flux of Ox to the electrode surface driven by an expanding, essentially hemispherical, diffusion layer around the electrode (Figure 12.1). In SECM, it is the perturbation of the tip current when the tip is brought to within a few tip diameters of a surface, which constitutes the SECM response.

Consider first when the tip is brought close to an insulating substrate (Figure 12.2a). The steady-state current flowing through the tip, i_T , will now be smaller than $i_{T,\infty}$ because the insulating substrate partially hinders the diffusion of Ox to the tip. Clearly, the closer the tip is to

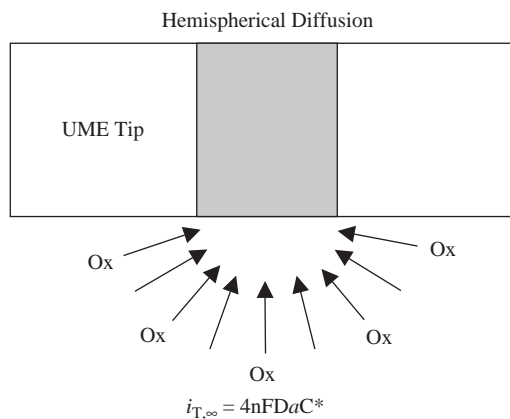


Figure 12.1 Steady-state hemispherical diffusion at an ultramicroelectrode (UME) disk.

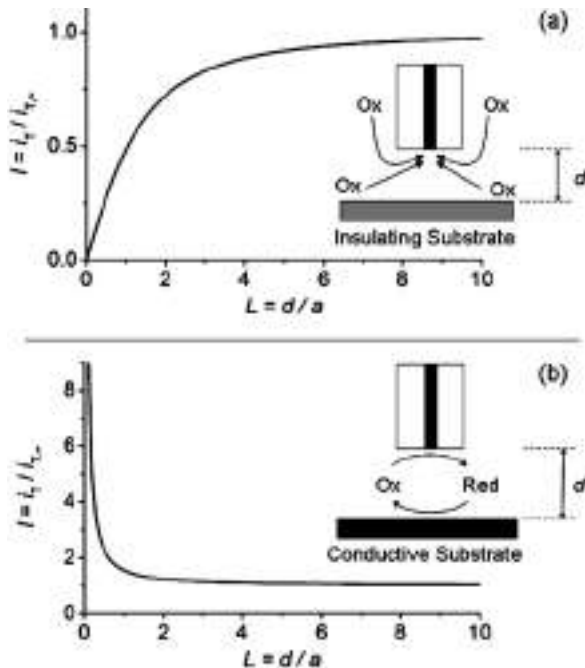


Figure 12.2 SECM approach curves on insulating (a) and conductive (b) substrates. Negative feedback is observed on an insulating substrate and positive feedback is observed on a conductive substrate.

the insulator surface, the smaller i_T will be, and with $i_T \rightarrow 0$ as the tip–substrate separation, d approaches 0. This effect is termed “negative feedback.” However, when the tip is close to a conductive substrate at which Red can be oxidized back to Ox, then a flux of Ox from substrate to tip occurs, in addition to some flux of Ox to the tip from the bulk solution (Figure 12.2b). This results in $i_T > i_{T,\infty}$. This flux of Ox from substrate to tip causes an increase in

i_T as d decreases; this is termed “positive feedback.” Thus, the magnitude of i_T compared with $i_{T,\infty}$ is governed by the nature of the substrate and by the tip–substrate spacing. The actual general situation can be more complicated than those two limiting cases described above, for example, when the rate of the Red \rightarrow Ox + e⁻ reaction on the substrate is governed by the rate of heterogeneous electron-transfer kinetics rather than the rate of mass transfer (diffusion) of Red to the substrate. This situation will be dealt with in Section 12.4.1.

In addition to the amperometric feedback mode described above, other amperometric operation modes are also possible. For example, in the substrate generation/tip collection (SG/TC) mode, i_T is used to monitor the flux of electroactive species from the substrate and vice versa for the tip generation/substrate collection (TG/SC) mode. These operation modes will be described in Section 12.3.1.3 and are useful in studies of homogeneous reactions that occur in the tip–substrate gap (see Section 12.4.2) and also in the evaluation of catalytic activities of different materials for useful reactions, e.g., oxygen reduction and hydrogen oxidation (see Section 12.4.3). In addition to the amperometric methods, other techniques, e.g., potentiometric method is also applicable for SECM and will be discussed in Section 12.3.2. We will also update the techniques suitable for the preparation of SECM amperometric tips in Section 12.3.1.1 and potentiometric probes in Section 12.3.2.2.

The SECM can also be used as an imaging device (see Section 12.3.3), as an electrochemical tool for studies of surface reactivity of thin films (see Section 12.4.4) and as a high-resolution fabrication tool (see Section 12.4.5). Finally, the SECM can be adapted to probe the transport activity of biological systems like single cells, the ion transport across channels and enzyme activity (see Section 12.4.6).

12.2 INSTRUMENTATION

As SECM instrumentation has been extensively and thoroughly discussed in Chapter 2 of reference (1) and there are also commercial instruments (e.g., CH Instruments, Heka, and Uniscan) on the market, we mainly focus on experimental aspects encountered in imaging and tip positioning with SECM. Readers who are interested in the design of an SECM instrument can refer to that chapter. We also intend to include here an up-to-date account of the newly developed combined techniques so that interested individual investigators may appreciate the design of SECM-related techniques for their specific applications.

12.2.1 Basic SECM apparatus

An illustration of the SECM instrument is shown in Figure 12.3. An important aspect of the SECM is the positioning system, which includes the positioning elements, translation stages, and motor controllers. Equally important is the data acquisition system, which starts with the use of a bipotentiostat to amplify the tip signal. After amplification, the signal is acquired with an analog-to-digital converter (ADC) and stored on a computer which is also used to send out (through the interface modules) the controlling signals for bipotentiostat and controllers for positioning elements and translation motors. Computer software is required to control the positioning and data acquisition system as well as to display and analyze the SECM data. Other important accessories of an SECM are the probe mount

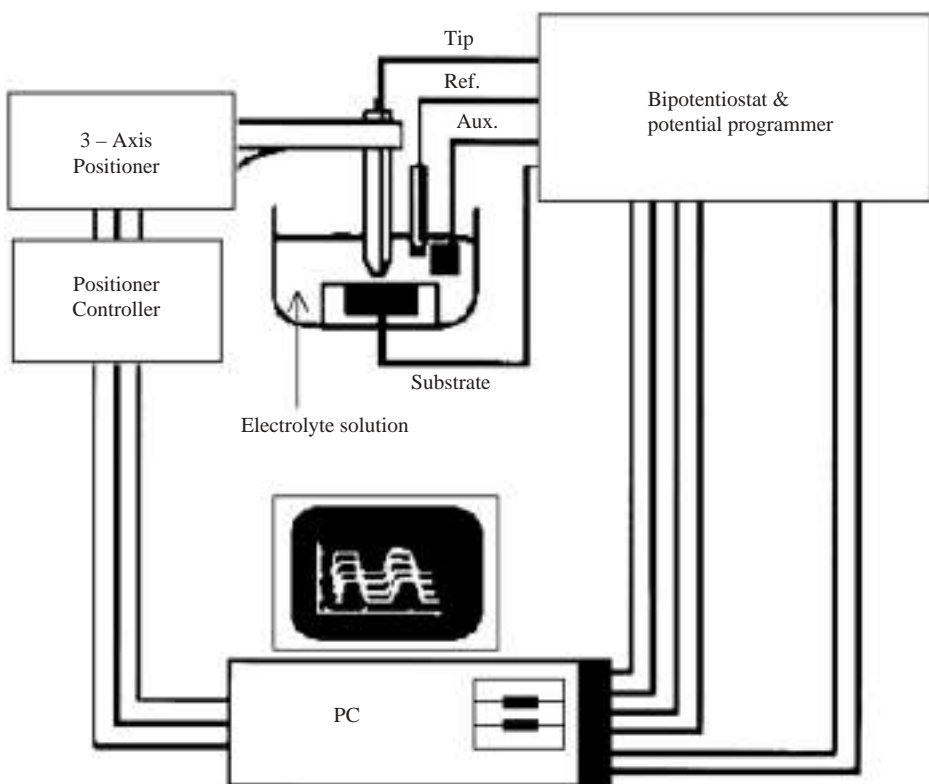


Figure 12.3 A diagram of the SECM instrument.

system and electrochemical cells, which will be described in individual sections for different experiments. If a near-field ($d < 100$ nm) SECM experiment is performed, a vibration isolation system is required.

The SECM apparatus currently used in this laboratory is the model 900 SECM (CH Instruments) specifically designed for SECM experiments. The model 900 includes the cell and the probe positioner as well as a computer, a motor controller, and a bipotentiostat. Lateral probe scans as large as 2.5 cm are accomplished by two inchworm (or step motors for model 900B) driving crossed-roller-bearing translator stages. Vertical motion is provided by mounting the probe directly to the shaft of the third inchworm or a 3-axes piezoelectric block (for model 900B), which is mounted on the z-stage driven by the third motor. The 3-axes piezoelectric block can be used for fine positioning and scan, which eliminate the effect of the clamping step on the shaft movement of the inchworm motor and thus provide smooth movement. The electrochemical cell is stationary and mounted on an adjustable tilting platform to compensate for the substrate tilt. Open-loop motor control is used, and software calibration corrects scan rate, axis, and direction-dependent effects on the probe motion. The data acquisition system and bipotentiostat of the CH series-900 SECM are microprocessor based and communicate with the PC controller via

a serial data link. The bipotentiostat is suitable for analytical voltammetry and has current measurement sensitivity in the pA range. Adjustable second-order Bessel filters provide noise reduction and prevent aliasing by the ADC, which has at least 20 bits of resolution.

The software for the model series-900 SECM runs on the Windows operating system and provides all the controls necessary for positioning the probe in three dimensions and setting parameters for various electrochemical techniques. The software also supports a wide range of electrochemical experiments, graphical displays, and data processing. During probe scanning, either amperometric or potentiometric signals can be recorded. Other software features include a probe approach curve routine that automatically stops the probe when the current reaches a set level and that automatically slows the speed of approach as the probe approaches the substrate surface, helping to prevent crashing the tip. SECM imaging is normally operated at constant height mode. Graphics output during imaging and postscan is by gray-scale or color-coded plots. Further data and graphical manipulation must be done outside the main program with commercially available software packages. Closed-loop or shear force-based positioning systems as described below are also available in CH Instruments, Uniscan, or Heka apparatus.

12.2.2 Combining SECM with other techniques

Combining SECM with other techniques, such as atomic force microscopy (AFM), near-field scanning optical microscopy (NSOM), and electrogenerated chemiluminescence (ECL), greatly increases the difficulty of the experiment and presents challenging problems in tip preparation. However, obtaining information from two or more different techniques at the same time and at the same location can greatly increase the power of SECM (e.g., by providing independent topographical or optical data during the SECM scan).

12.2.2.1 AFM/SECM

AFM measurements made during an SECM experiment allow for an independent determination of the zero distance ($d = 0$, if the tip is not recessed) and aid in the positioning of the tip. Moreover, this combination of techniques opens the way to experiments in which changes in topography are studied by AFM as a reactant is generated electrochemically at the tip.

Several similar studies have already been reported. For example, Ludwig and coworkers (4) used a piezoelectric element attached to the tip shaft for dithering and measured the modulation by noting changes in the Fresnel diffraction pattern created with an illuminating laser beam focused on the lower part of the electrode on a split photodiode. The probe remains stationary to maintain the laser and photodiode alignment, while the substrate is scanned to make images. In the initial experiment, the probe was a 1.5-cm long section of a pulled glass capillary containing a 25- μm -diameter Pt disk electrode. The long-pulled section is necessary to produce the flexibility required for oscillation. Modulation amplitude in this experiment is about 1–2 μm , which is several orders larger than that normally used in NSOM. The large modulation amplitudes can produce a proportionately larger range of shear mode so that the probe–substrate distance, d , is in the μm range when shear force damping is observed. The significant perturbation of the solution near the tip can be cumbersome, especially if the tip is largely immersed in solution.

The existing SECM theory requires some modifications, as the mass transfer now is no longer purely diffusional.

An alternative is to use a cantilever-based AFM and modify the cantilever/tip to behave as an SECM tip. A conventional (not a conductive-probe AFM) cantilever is nonconductive and must be metallized to establish a conductive path to the tip (e.g., by evaporating or sputtering a thin film ($\sim 300 \text{ \AA}$) of Pt) and then the entire conductive surface except the very end of the tip was insulated from the contacting solution. Such an arrangement was used to study a KBr crystal undergoing dissolution (5). Although the AFM imaging was not affected significantly by the metallization, the SECM performance of the tip was poor because of difficulties with simultaneously providing good tip insulation and tip configuration.

A different approach is to construct a special cantilever-type SECM tip (6). A 50- μm diameter Pt wire was bent and etched electrochemically, then flattened and insulated with electrophoretic paint. It was then epoxied to a commercial AFM chip based on the procedures as shown in Figure 12.4 (6a). Another approach used micromachining techniques (e.g., focused ion beam (FIB) and etching) to modify a silicon nitride-insulated Au-coated sharp silicon AFM cantilever into a dual AFM/SECM tip, with a UME ring surrounding the AFM probe (6b). The cantilever mount was additionally protected by an insulating varnish to prevent scratching of the silicon nitride layer. These modified cantilevers could

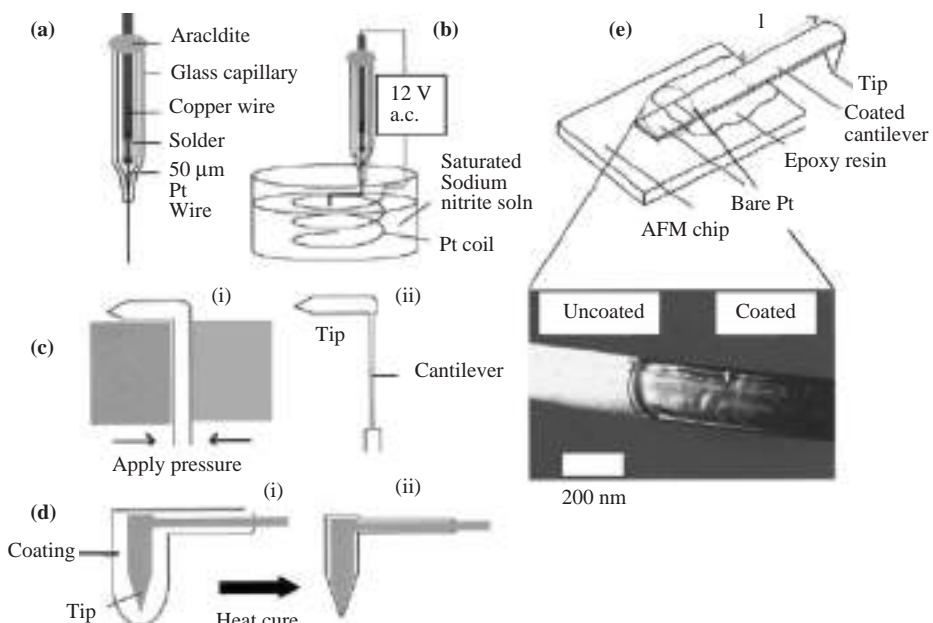


Figure 12.4 Procedures involved in constructing an AFM/SECM tip: (a) Pt microwire inserted in holder; (b) electrochemical etching to a fine point; (c) compression to form cantilever component; (d) insulation of electrode and cantilever with electrophoretic paint followed by heating to expose the very end of the tip; and (e) attachment to a commercial AFM chip. (Adapted from reference (6a).)

then be used to replace conventional AFM cantilever used in a commercial AFM and allow for AFM and SECM measurements.

An alternative approach is the use of a tuning fork attached to an insulated SECM tip (7, 8). The SECM tip can be prepared by the procedures described in Section 12.3.1.1. A tuning fork-based SPM combined with electrochemical techniques can then be used for both topographic imaging and SECM measurements. A key issue in the application of AFM/SECM is the ability to obtain good quantitative approach curves for both insulators and conductors that agree with the theoretical treatment.

12.2.2.2 NSOM/SECM

NSOM is a SPM for obtaining high-resolution optical images and performing spectroscopic measurements. By using a fiber optic probe that has been pulled down to a very small tip (radius of curvature < 100 nm) and scanned along the sample surface in the near-field regime, one can obtain images whose resolution is governed by the tip diameter and placement rather than the usual diffraction limits that govern a conventional optical microscope (9). A typical NSOM tip is coated with aluminum to minimize the loss of light in passing from the laser source to the tip. For an NSOM tip to be also useful in SECM experiments, the metal coating should be electrochemically inert, such as Au or Pt, and an insulating layer must be added (usually by electrophoretic paint deposition) such that only the conducting metal ring at the end is exposed to the solution. To make NSOM tips that have a pinhole free metal layer, which promotes total internal reflection, and a pinhole free insulating layer, which yields the ring geometry, is challenging. The quality of the NSOM/SECM tip can be evaluated by lowering the tip from the air into the test solution and recording the current as the tip is immersed deeper into solution (10).

There have been several reports of the use of commercial NSOM with a W-tip coated with varnish for SECM and photoelectrochemical experiments (11). However, no SECM approach curves for these tips have been shown. Most recently, Lee and coworkers (10, 12) have demonstrated the combined tuning fork-based NSOM/SECM technique to simultaneously obtain topographic, electrochemical, and optical images of an interdigitated array electrode. Although the resolution is still on the order of μm , with the construction of a smaller tip an improved spatial resolution should be possible, leading to NSOM combined with SECM and simultaneous topography.

12.2.2.3 ECL/SECM

An alternative approach to obtain optical images with SECM is through light generation via an ECL process at the tip. The principle and various techniques of ECL are described in Chapter 13 of this handbook. Light generation at UMEs for a scanning microscope can be accomplished either by the radical ion annihilation approach (in aprotic solvents) (13) or by a coreactant route (also applicable in aqueous solutions) (14, 15). A schematic diagram showing the basic concepts of ECL generation is shown in Figure 12.5. ECL is generated at the tip as it is scanned in the XY plane above the sample to be imaged and collected by a detector, e.g., a photomultiplier tube (PMT) beneath the sample. An image is obtained by plotting the detector response as a function of XY position. The first experiments that used this technique (13, 14) (electrode radii were $\sim 1\text{--}10 \mu\text{m}$) relied on measurements with

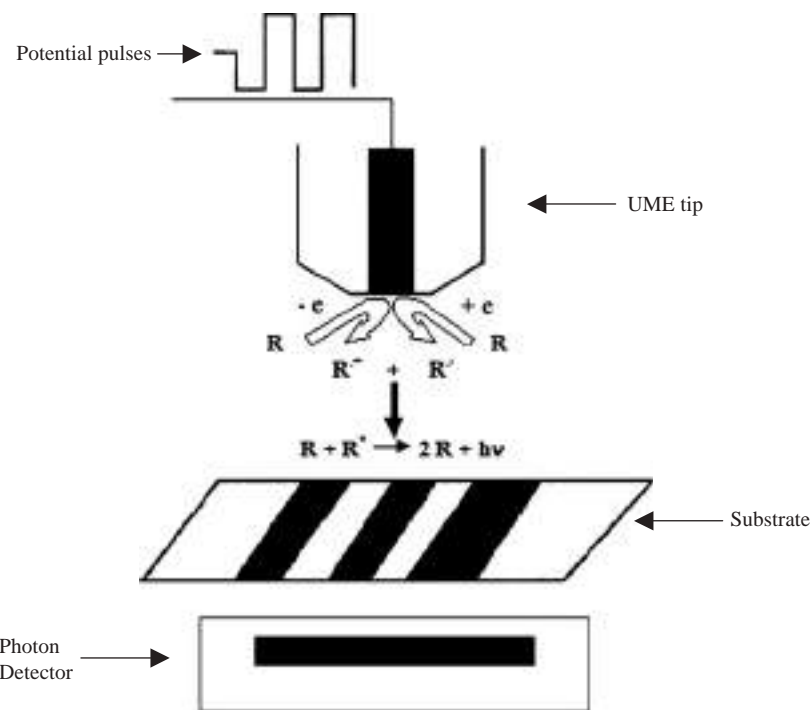


Figure 12.5 Schematic diagram for ECL generation at an SECM tip for optical imaging. (Adapted from reference (14).)

similar d values and did not display high-resolution capabilities. However, the resolution obtainable by this technique, like various scanning probe techniques, depends on the UME radius and the distance, as demonstrated in later experiments (15, 16).

Maus and coworker (16) developed an interesting technique by decreasing the size of the ECL light source but still generating sufficiently strong ECL intensity (≥ 1.8 pW) for high-resolution ECL imaging based on high-frequency alternating pulses on a conical carbon fiber electrode in benzonitrile (BN) containing 25 mM 9,10-diphenylanthracene (DPA) and 10 mM TBAPF₆. Square wave potentials that produce the radical cation of DPA and radical anion of BN were applied to the electrode at different frequencies. At low frequencies (e.g., 200 Hz), ECL occurred along the entire noninsulated region. As the frequency is increased, the ECL intensity increases. At higher frequencies, the area of the cone yielding the ECL emission diminishes. At the highest frequency (20 kHz), the ECL is supported only at the apex of the cone. Based on this phenomenon, a bare cone-shaped carbon fiber electrode can be used as a small light source. Submicrometer ECL light sources with similar submicrometer resolution can be achieved with this kind of technique. The results obtained so far with an ECL-based tip light source are quite promising, particularly for optical imaging of samples immersed in solution. However, to be widely applied as a laser-based NSOM used in optical imaging, the resolution, stability and intensity of ECL, and the operation speed need to be improved. Regardless of these problems, the

ECL/SECM technique can probe ECL generation restricted to small domains (e.g., biological molecules) with high spatial resolution.

12.3 METHODS AND OPERATIONAL MODES

12.3.1 Amperometric methods

SECM amperometric methods are based on the measurement of electrode currents (tip and substrate, i_T and i_S , respectively) as a function of various parameters, including tip–substrate distance (d) and tip or substrate potentials (E_T or E_S). Irrespective of the system studied (e.g., an electrode, an inert surface, a catalyst, or a living organism), the probe tip is a necessary component to perform any SECM experiment. In all cases, the amperometric tip is a UME that can be positioned in close proximity to another surface. There are two amperometric operation modes: feedback and generation/collection modes. The preparation and characterization of commonly used amperometric tips of different geometries as well as their operation modes will be described in this section.

12.3.1.1 Fabrication and characterization of amperometric tips

SECM amperometric tips are UMEs (see Chapter 6) in which insulating sheaths have been sharpened to a tip size below 10 times the effective radius, a , of a UME. As the UME tip needs to approach the substrate surface to within a normalized distance $L = 0.2$ ($L = d/a$) to observe significant change in its response, sharpening of the insulating sheath is necessary to prevent the edge of the insulating sheath from hampering the approach in the event of a slight tilt of the probe (and/or substrate). Because it is relatively easy to fabricate, the inlaid disk is the most commonly used SECM tip. However, other tip geometries, such as hemispheres, cones, and rings (Figure 12.6) are also used for some less extensive but specific applications.

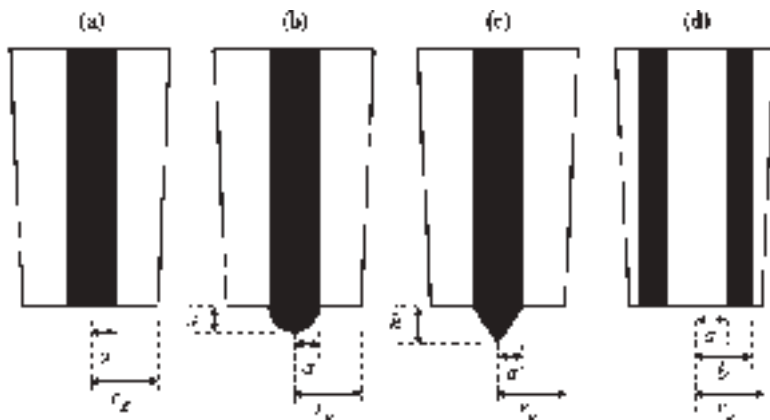


Figure 12.6 Schematic of common tip geometries: disk (a) hemisphere (b) conical (c) and ring (d).

The fabrication of inlaid disk SECM tips (Figure 12.6a) has been described in detail in a recent review by Fan and Demaille in Chapter 3 of reference (1). Tips of varied materials like Pt, Au, and carbon can be prepared by using the conventional heat sealing and pulling methods, which are described in Section 6.3 in Chapter 6 of this handbook. Other than these techniques, there are other procedures that can be used to prepare disk-shaped SECM tips. A method widely used involves the coating of conductive fibers (metals, carbon) with insulating polymer layers (17–19). Anodic or cathodic electrophoretic deposition of polymer paints (e.g., polyacrylic acid, PAAH) is a procedure that has received widespread uses for preparing carbon and Pt disk (or flattened hemispheroid) UME tips (17, 18). The electrode fiber is immersed in an aqueous solution of the paint monomer, concentric to a Pt helix-coil counterelectrode. A positive or negative tip bias (2–7 V) is applied for 30–60 sec against the counterelectrode to evolve O₂ or H₂ with concomitant acidification or alkalinization of the electrode surface, respectively. Anodic paints will precipitate when the electrode surface is acidified, while cathodic paints will do so on alkalinized surfaces, forming a thick (~200 nm) polymeric layer covering the entire electroactive surface. After curing the layer at 140–180 °C, it becomes stable in most aqueous media, although it is unstable in most organic solvents. During curing, the layer contracts to expose the very end of the electrode and it forms a round-shaped aperture and leaves the UME disk slightly recessed. The procedure may be repeated to ensure the total insulation of the lateral walls. Sometimes, polishing may be necessary. This technique was successfully used to fabricate Pt (17) and carbon (18) tips with diameters below 100 nm. Fibers of these materials were etched down to the desired dimension either by electrochemical or thermal methods (1). These tips are only appropriate for aqueous media.

Spherical and hemispherical tips (Figure 12.6b) are less frequently used. The use of hemispherical tips is mostly related to cases where Hg UMEs are needed to extend the tip potential window to more negative values by increasing the H₂ evolution overpotential (20, 21). Controlled fabrication of hemispherical Hg tips has been performed by attaching a small Hg drop to a Pt or Ir UME disk by electrodeposition of Hg from HgNO₃ solutions (21–23), or by contacting a spinning UME tip with an Hg pool (20). Finite conical-shaped tips (Figure 12.6c) are the other preferred UME geometry for SECM amperometric probes. In fact, the optimal tip geometry is a cone with a small *H* value (*H* = *h/a*), since it is possible to reach a tip–substrate distance *L* = 0 with no misalignment problems in the tip approach. The most common procedure for the fabrication of conical tips is by etching metal or carbon fibers to a sharp point and coating them with an insulating layer, such as the previously described electrophoretic paint (6, 24–26), except at the very apex (1). With this procedure, very small insulating sheath thicknesses (low RG, where RG = *r_g/a*; *r_g* is the outer radius of the insulating sheath) can be obtained. A recent variation involves the heat sealing of etched fibers into glass capillaries (27) for making conical tips with RG values up to 5.

Ring UME tips (Figure 12.6d) have received attention only recently because of the increased interest in the combination of SECM with other techniques such as AFM (6) and optical microscopy (10). Fabrication of ring UMEs involves several steps:

- (i) A cylindrical bar is coated with a layer of the metal electrode, for example, by vacuum evaporation or sputtering.
- (ii) It is further insulated with a polymer film, as described previously.

Ring tips with an optic fiber core and dual ring-disk tips have been fabricated following this procedure (10, 28). Open-core ring tips, or micropipette ring tips, have also been fabricated recently with this procedure (29). Dual AFM/SECM tips with a UME ring surrounding a sharp silicon AFM probe have been fabricated by FIB-assisted microlithographic techniques (6b).

The first and most important test of the electrochemical performance of a UME is the evaluation of its voltammetric behavior, or cyclic voltammogram (CV). For all the described geometries, UMEs define stable diffusion-controlled limiting currents whose values depend on the geometric parameters of the electrodes, and are tabulated in Chapter 6 of this handbook. A good UME in a well-studied electrochemical system (e.g., ferrocenemethanol solution) will generate an S-shaped CV, with a stable and clearly defined diffusion limiting current, and small double-layer capacitance. For a well-behaved UME to be suitable as an SECM tip, it is further evaluated through the so-called SECM approach curve, as described in the following section.

12.3.1.2 Feedback modes—approach curves

The first question that one may ask is: what is the reason for carrying out an approach curve? The technical aspect of the answer is: (a) to evaluate the geometric characteristics of an SECM UME tip, and (b) to know how close the tip can be positioned with respect to the substrate surface for further experiments. Whatever the reason, the procedure is the same and is described in detail below.

An SECM approach curve (i.e., tip current as a function of distance) allows one to get a very precise value of the tip–substrate distance when the electrode reactions are diffusion controlled. This ability is a consequence of the strong effect that a surface in close proximity to the UME (<5 radii) has on the diffusion-controlled current. Both positive and negative feedback effects have been theoretically treated and it is possible to correlate the experimental approach curves to analytical equations to determine very accurately the position of the tip with respect to the substrate surface. Furthermore, approach curves recorded over a conducting substrate provide an additional measurement of the effective radius of the UME tip, while those recorded over insulators provide information about the effective RG of the tip. Thus, this type of experiment is very useful for the characterization of SECM tips.

Experimentally, approach curves can be recorded in a cell configuration, such as that shown in Figure 12.7a. A clean and polished Pt substrate electrode (~3 mm diameter) shown as “1” in Figure 12.7a, is placed in the hole of a Teflon cell. If the seal between the cell and the substrate electrode is not tight enough, a small quantity of Teflon tape can be used to ensure a snug fit. The Teflon cell is screwed to the SECM metal plate (Figure 12.7a, #2), which is then screwed onto the SECM head such that the cell is over the tip holder (Figure 12.7a, #3). The Teflon cell is filled with a solution containing a well-known redox system, such as 1 mM ferrocenemethanol in 0.1 M KCl solution. The base of the cell has to be inspected to ensure that the substrate electrode is snug and that the solution is not leaking out. A real sample may very likely have a different geometry, e.g., flat sheets, which need to be located at the substrate compartment. In that case, a cell configuration like that shown in Figure 12.7b is used. The substrate is tightened by a base with screws

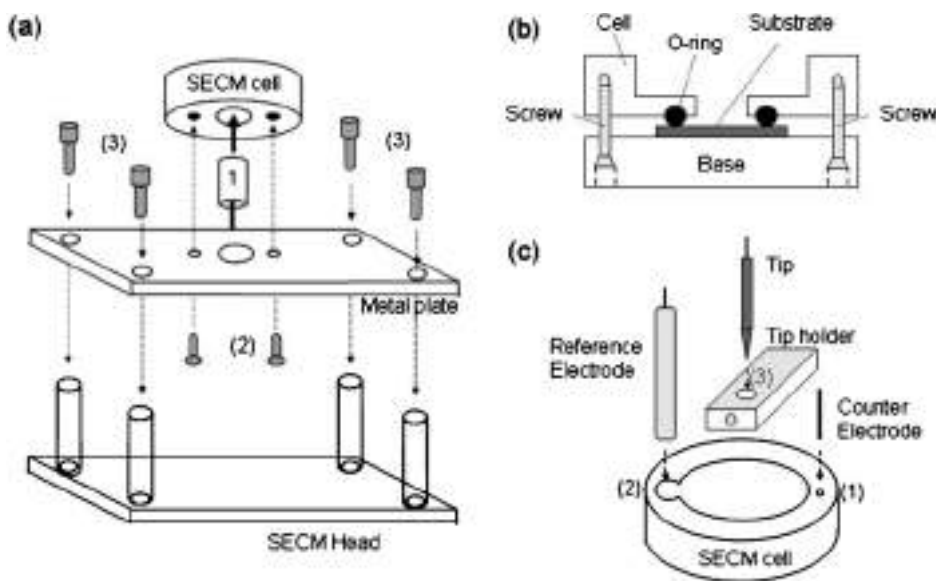


Figure 12.7 (a) Schematic of the SECM cell assembly: inserting the substrate electrode in the SECM cell (1); screwing the cell onto the SECM metal plate (2); and screwing the metal plate onto the SECM head setup. (b) SECM cell for flat substrates. (c) Schematic of electrode setup.

from the bottom of the cell, using a Teflon or FETFE *o*-ring to prevent leakage of electrolyte. The counter (auxiliary) and reference electrodes are placed in their respective slots (Figure 12.7c, #1 and 2), and the UME is placed in the tip holder (Figure 12.7c, #3). Electrical leads are connected to the substrate, counter, reference, and UME tip electrodes.

The tip must be positioned manually about 2 mm above the substrate surface and either over the insulating sheath of the substrate or over the Pt disk electrode. The potential of the tip is held at a value where the mediator reaction occurs under diffusion-controlled condition, e.g., 0.4 V vs. Ag/AgCl for the oxidation of ferrocenemethanol, and a steady-state limiting current is obtained. Usually, a large conductive substrate at open circuit potential will regenerate the mediator by a process called substrate potential driven feedback (30). However, it is a good practice to apply a potential bias (e.g., 0 V vs. Ag/AgCl) for the reduction of tip-generated ferrocenium to carry out the substrate mediator regeneration more effectively. Of course, nonconductive substrates cannot be biased. The tip is then approached to the substrate in a fast and safe manner. A good way to accomplish this is by using a variable scan rate; that is, starting at $\sim 50 \mu\text{m sec}^{-1}$ and then decreasing to $\sim 1 \mu\text{m sec}^{-1}$ when the tip current begins to change because of the SECM feedback effect. A safe point to stop is when i_T changes by about 25% of the $i_{T,\infty}$ value ($I = i_T/i_{T,\infty} = 0.75$ or 1.25 for negative or positive feedback, respectively), which gives a tip–substrate distance $L \cong 1\text{--}2$. If it is necessary to go closer, the tip can be withdrawn with a distance of $L = 10$ from this point and approached again at a slow scan rate, about $1 \mu\text{m sec}^{-1}$. Typical experimental feedback approach curves (i_T vs. d_{exp}) are shown in Figure 12.8a for a 25- μm -diameter tip approached from $\sim 130 \mu\text{m}$ from the substrate. The expected current

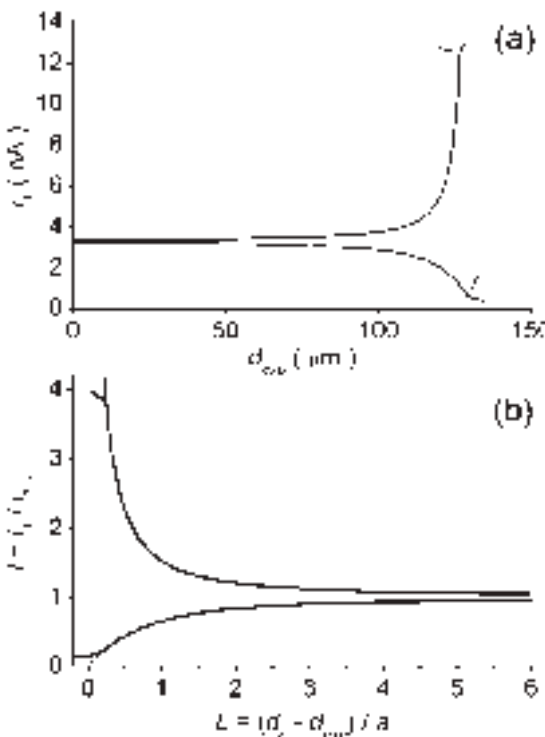


Figure 12.8 (a) Experimental approach curves of a 25- μm Pt tip obtained in a 1 mM ferrocenemethanol–0.1 M KCl solution on a Teflon surface (lower curve) and on a 3-mm Pt electrode (upper curve) at 0 V vs. Ag/AgCl. The tip was polarized at 0.4 V vs. Ag/AgCl. Scan rate: 3 $\mu\text{m sec}^{-1}$. Arrows signal the point where the tip hit the substrate. (b) Best fittings of experimental approach curves (dots) using equations 12.3.1 (lower solid line) and 12.3.2 (upper solid line) with parameters for $RG = 3.04$. $i_{T_i \infty} = 3.29$ nA in both fittings and $d_0 = 131.0$ and 129.3 μm for upper and lower curves, respectively.

for a good tip should increase to at least three times the infinite distance value ($I > 3$) for conductive substrates, or decrease to less than 25% ($I < 0.25$) for insulating surfaces, before the glass sheath of the UME hits the substrate. This event is manifested by a sudden change in the slope of the current vs. distance curve, as it is marked with arrows in the approach curves of Figure 12.8a. If the approach curve is measured just for tip characterization purposes, this is the end of the experiment and the tip can be safely withdrawn and removed from the cell. The quality and geometric characteristics of the tip will be known after fitting the approach curves. If the approach curve is performed to position the tip at a known distance from the substrate, the tip has to be stopped in a previous instance prior to hitting the substrate. The exact tip–substrate distance, corresponding to the end point of the approach curve, can be determined after fitting the measured curve with theoretical equations.

SECM theory, including amperometric feedback mode, has been recently reviewed in Chapter 5 of reference (1). Recent progress in the theoretical description of SECM include

Table 12.1

Dependence of coefficients k_1 , k_2 , k_3 , and k_4 for equations (12.3.1) and (12.3.2) on the tip RG value (37)

RG	k_1	k_2	k_3	k_4
Equation 12.3.1				
15.2	0.37377	1.85113	0.61385	-2.49554
10.2	0.40472	1.60185	0.58819	-2.37294
8.13	0.42676	1.46081	0.56874	-2.28548
5.09	0.48678	1.17706	0.51241	-2.07873
3.04	0.60478	0.86083	0.39569	-1.89455
2.03	0.76179	0.60983	0.23866	-2.03267
1.51	0.90404	0.42761	0.09743	-3.23064
Equation 12.3.2				
10.2	0.72627	0.76651	0.26015	-1.41332
5.1	0.72035	0.75128	0.26651	-1.62091
1.51	0.63349	0.67476	0.36509	-1.42897

the generation of more efficient algorithms (31–33) and the report of approximate analytical expressions (34–36). Analytical approximations of the approach curves obtained by processing simulated data are shown in equations (12.3.1) and (12.3.2) for negative and positive feedback, respectively. The coefficients of these equations depend on the tip RG value and are presented in Table 12.1 (37). Note that the RG has a strong effect on the negative-feedback approach curve, which makes this dependence a good tool to estimate this parameter. The RG effect is much less pronounced in positive-feedback approach curves. To correlate these equations with the experimental curve, it is necessary to normalize the experimental variables according to equations (12.3.3) and (12.3.4). The unknown parameter is d_o , which is the distance between the first point of the experimental approach curve and the substrate surface, which is very close to the last point of the approach curve.

$$I = \frac{1}{k_1 + \frac{k_2}{L} + k_3 \exp\left(\frac{k_4}{L}\right)} \quad (12.3.1)$$

$$I = k_1 + \frac{k_2}{L} + k_3 \exp\left(\frac{k_4}{L}\right) \quad (12.3.2)$$

$$i_T \rightarrow I = i_T / i_{T,\infty} \quad (12.3.3)$$

$$d_{\text{exp}} \rightarrow L = d/a = (d_0 - d_{\text{exp}})/a \quad (12.3.4)$$

$i_{T,\infty}$ can be estimated from the steady-state value measured when the tip is far away from the substrate. However, in the theoretical equations, i_T is, in fact, normalized with respect to $i_{T,\infty}$ for a UME with infinite RG. As the limiting current is affected by the RG value when

it is lower than 10 (37), $i_{T\infty}$ thus has some uncertainty and is treated as a variable parameter during the fitting. For example, Figure 12.8b shows the best fittings of the experimental approach curves shown in Figure 12.8a.

Different strategies to measure approach curves, their theoretical treatment, and the ways to estimate the tip dimensions when using tips having other geometries have been published for hemispherical (21, 38), conical (27), and ring or ring-disk shaped tips (39, 40).

The common characteristic of these tips is that the feedback effect in such cases is much less pronounced than that on disk-shaped tips. For example, the effect of H on conical tip approach curves is shown in Figure 12.9 (27). If H is sufficiently small ($H \leq 0.5$),

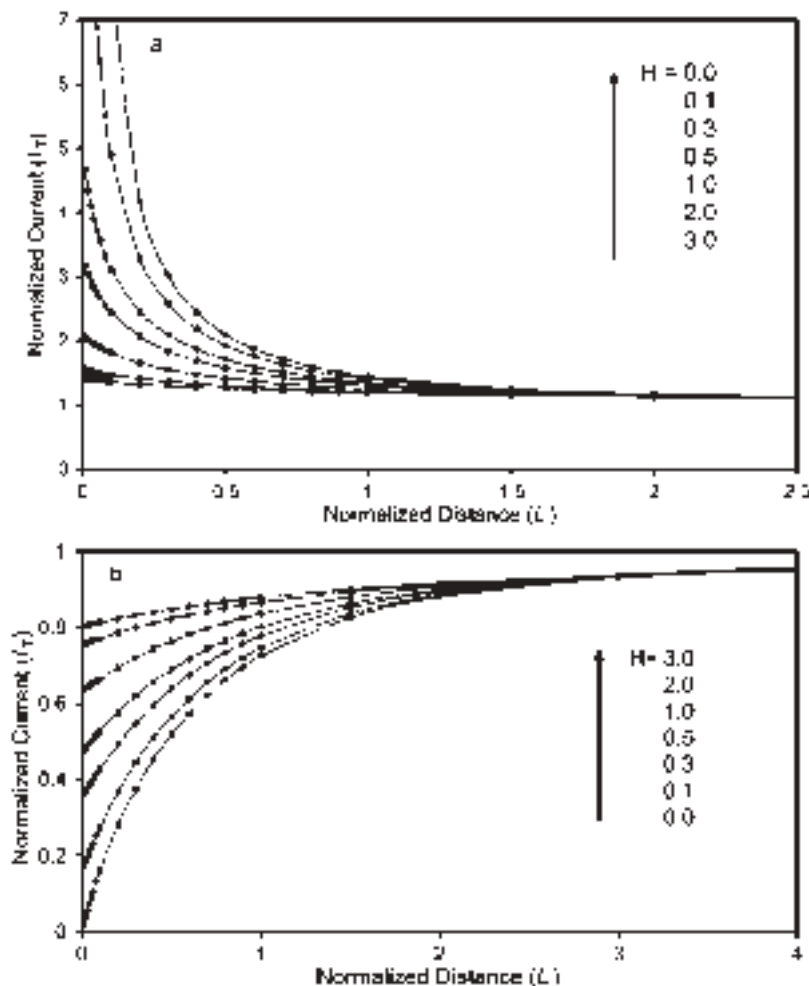


Figure 12.9 Theoretical approach curves of conical tips at (a) a conductive and (b) an insulating substrates for different H values and $RG = 2$ (from reference (27)). Note that the curves for $H = 0$ correspond to a disk UME.

the current at a conical tip is still very sensitive to d . For example, a decrease to $I = 0.5$ or an increase to $I = 3.2$ for negative and positive feedback approach curves, respectively, are expected at the substrate surface for a tip with $H = 0.5$. Thus, a conical tip with a small value of H can closely approach the substrate surface and give substantial feedback.

12.3.1.3 *Generation/collection (G/C) mode*

The generation/collection (G/C) modes constitute a different SECM procedure that expands the applicability of the technique to a wide range of situations. In these modes, the collector (either tip or substrate) works as an amperometric sensor that collects the products produced at the generator surface (either substrate or tip, respectively). Thus, the collector potential is controlled to electrochemically react with the generator-produced species. Typical collector responses used in G/C experiments are (a) voltammetric curves, where the collector potential is swept, and (b) diffusion-controlled limiting current vs. time curves. In contrast to the feedback mode where steady-state responses are monitored, in G/C experiments, the current-time dependence is an important set of data to evaluate. The timescale of most of G/C transient experiments is much wider, possibly up to 100 sec. Moreover, as the tip-substrate distances increase, typical coupling and distortion of transient responses are not significant.

These methods are very useful in situations where the mediator-cycling process that produces the feedback effect is somehow perturbed or just cannot be detected. Furthermore, they can be used for collection efficiency (CE) measurements of reaction products, analogous to other two-electrode geometries, such as rotating ring-disk electrode and microband arrays. Nonetheless, for similar geometric conditions, the spatial and temporal resolutions of the feedback mode are superior to those of G/C methods. Moreover, G/C methods are not useful for precise positioning of the tip, as the measured response is not very sensitive to the tip-substrate distance. Regardless of these limitations, the capabilities of the G/C modes to induce and evaluate processes in micro or even nanometer domains make them very attractive for localized studies. Importantly, G/C experiments can be performed at significant separations (up to $L \approx 20$), which is a major advantage in studies involving the reactivity of surfaces (e.g., reactivity imaging) with significant topographical geometry.

(a) *Substrate generation/tip collection mode*

When the collector is the tip, the mode of operation is called the SG/TC mode; the schematic is shown in Figure 12.10. In this case, the substrate may be any kind of surface that is able to generate a flux of the species to be detected at the tip, such as an electrode generating hydrogen, heterogeneous catalysts producing H_2O_2 , or a living cell pumping out metabolites from stressing agents.

In a SG/TC experiment, the spatial and temporal mapping of concentration profiles of species coming from (or being consumed in) the studied process is performed. Classical theories for linear or hemispherical diffusion that relates concentration vs. time and spatial coordinates (3) can be used to calculate kinetic parameters of chemical and electrochemical processes, as well as mass-transport coefficients. When the substrate is a large surface, linear diffusion of the substrate-generated (or consumed) species is observed, and the

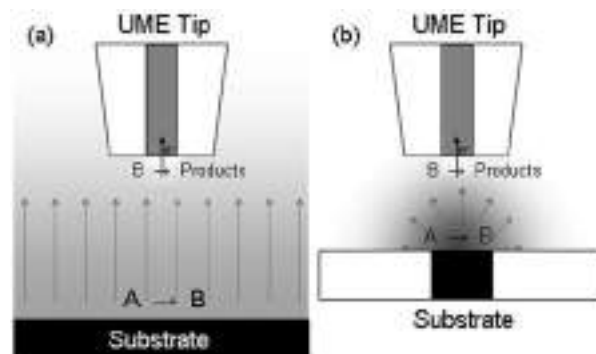


Figure 12.10 Schematic of the SG/TC operation mode applied for studying the reaction $A \rightarrow B$ at the substrate by amperometric detection of B at the tip. (a) The substrate is a large surface (linear diffusion). (b) The substrate is a UME (hemispherical diffusion). Darker gray color indicates higher concentration of B.

diffusion layer does not reach a steady-state situation (Figure 12.10a). If the substrate is a UME disk (diameter $< 30 \mu\text{m}$), hemispherical diffusion of generated species is expected, which provides a quasi-steady-state concentration profile (Figure 12.10b). This latter case is very useful for electrochemical activity imaging of small conductive spots (41).

Systems that are frequently studied by SG/TC include enzymatically patterned surfaces (42). For example, the activity of immobilized *horseradish peroxidase* for reduction of H_2O_2 to water using ferrocenemethanol in solution as an electron-donor can be studied by amperometric detection of ferrocene methanol cations. Furthermore, the oxidation of glucose by oxygen on immobilized *glucose oxidase* can be studied by tip collection (oxidation) of H_2O_2 , the product of oxygen reduction. The tip can be used as an amperometric oxygen sensor (by reducing O_2 to H_2O or H_2O_2) to map O_2 concentration profiles (43). In this way, it is possible to monitor the respiration of living organisms (44, 45), and the catalytic activity for oxygen reduction of electro- and photo-catalysts (46, 47). Transport of ions and molecules through film pores has been thoroughly studied by this technique (see Chapter 9 in reference (1) for a more complete review) in view of future studies of single-pore transport processes in cell membranes. Along this line, SG/TC studies of transport activity of supported cells in a macroscopic fashion have been recently reported (48).

Probably, the main complication of this type of experiment is that the diffusion concentration profile cannot be kept unperturbed during the whole time frame of the measurement, which may be more than a minute. Even using an efficient vibration isolation table, it is very difficult to prevent natural convective processes (3). Another detail to take into account for the interpretation of SG/TC results is the effect that an amperometric tip may have on the concentration profile of the substrate, which is more important for small tip–substrate distances (49).

The CE, defined as $\text{CE}_{\text{SG/TC}} = i_{\text{T}}/i_{\text{S}}$, which is valid only when the substrate is an electrode, is a parameter of limited utility as it depends on the dimension of the substrate and generally is a very small value. In fact, the ratio $J = |i_{\text{T}}/i_{\text{T,S},\infty}|$ is much more useful, where $i_{\text{T,S},\infty}$ is the tip current when it drives the substrate reaction in the bulk solution. When

SG/TC is used in conjunction with the feedback mode, the transient response of J allows the calculation of reaction rate constants for chemical reactions coupled to electrode reactions (50). Another useful ratio is $\gamma = i_{T,SG/TC}/i_{T,feedback}$ calculated at small tip–substrate distances, which allows the ratio between the diffusion coefficients of products and reactants ($\gamma = D_{product}/D_{reactant}$) (51) to be determined.

(b) Tip generation/substrate collection mode

In the TG/SC mode, the collector is the substrate while the tip is used to locally generate species (A), as shown in Figure 12.11a. Thus, the substrate is polarized to catalyze the electrode reaction of a species (A), which is not initially in solution. The tip is positioned in close proximity to the substrate and is controlled to generate A, which will diffuse and reach the substrate surface carrying out the electrode reaction ($A + ne^- \rightarrow B$) of interest. The faradaic substrate current is monitored as a function of time, tip–substrate distance, and substrate potential.

It is important to understand the significance of the background substrate current ($i_{S,B}$) and of the faradaic substrate current ($i_{S,F}$). The background current is the substrate current measured when the tip is not working (i.e., not generating any species). In theory, this current should be null because no solution reaction occurs. In reality, the background current can be so large and unstable that it will be impossible to perform any measurement. The origin of the background current is uncertain. Probably, it arises from the reaction of trace species in solution (e.g., oxygen) or from surface transformations (e.g., oxide electro-generation). It is proportional to the substrate surface area and reactivity. As a rule, any TG/SC experiment should be performed on the smallest possible substrate area, and it should be preceded by a long quiescent time (up to 5 min) so that the substrate background current reaches a stable value. The background current must be measured in a blank experiment (tip off). In contrast, the faradaic current is the current exclusively from the reaction of the tip-generated species. It can be calculated from the substrate current measured when the tip is operating (i_S) minus the background current, $i_{S,F} = i_S - i_{S,B}$.

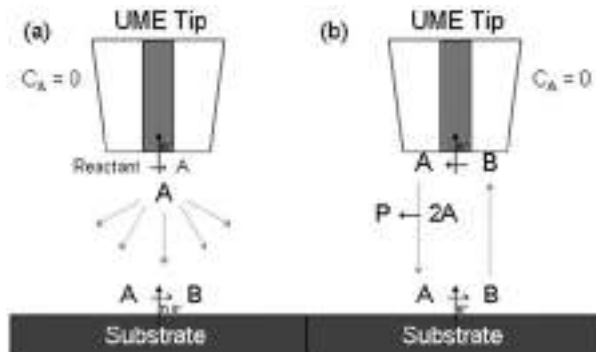


Figure 12.11 (a) Schematic of the TG/SC operation mode applied for studying the reaction $A \rightarrow B$ at the substrate by electro-generating A at the tip by controlling either its potential or its current. (b) Schematic of TG/SC mode combined with feedback mode, applied for studying the kinetics of the chemical reaction $2A \rightarrow P$ in the tip–substrate gap.

At distances of $L < 2$, in the absence of chemical transformation in the tip–substrate gap and when the studied reaction operates under mass-transfer control, all of the tip-generated reactants reach the substrate and undergo the electrode reaction (52). Thus, the CE defined as $CE_{TG/SC} = i_{S,F}/i_T$ is close to 1. Ideally, this means that in the best case, $i_{S,F}$ will be equal to i_T . Note that i_T will never be higher than a few nA, while $i_{S,B}$ (and i_S) may be as high as tens of μ A. Thus, the main drawback of this method is the very low signal-to-background ratio.

This mode has been almost exclusively used in combination with feedback experiments for studying coupled homogeneous chemical reactions following electron-transfer in the tip–substrate gap (53). The CE will be affected by any side reaction in the gap (Figure 12.11b), which makes it a useful parameter to monitor and calculate chemical reaction rates. Only recently was this mode applied to the study of electrode reactions using a constant-current variant of Figure 12.11a (52, 54). The electro-reduction of dissolved oxygen on varied materials was studied using this method. The tip generates a microenvironment of O_2 -saturated solution in a localized region close to the substrate, which allows the construction of an oxygen–reduction I_S vs. E_S curve (polarization curve) for that particular region. By addressing different substrate domains (e.g., spots of different materials, such as Pt and Au supported on a common conductive nonactive surface) and measuring polarization curves on them, it is possible to compare the activity of each of these materials in a single experiment (54). The imaging capability of this mode can be exploited for activity imaging on large arrays of catalyst spots, as will be detailed in Section 12.4.3, because this mode is less dependent on the tip–substrate distance.

12.3.2 Potentiometric method

12.3.2.1 Introduction

This section deals with the fabrication of potentiometric probes and their use in SECM studies. Potentiometric probes (see Chapter 7) can detect many non-electroactive species not accessible to amperometric techniques. They are highly selective and have found widespread application in clinical chemistry, in environmental studies and the food industry. A general review of potentiometric probe fabrication has been presented previously, and several publications have demonstrated the utility of potentiometric probes in SECM studies (55). This section will provide the reader with a highlight of potentiometric probe fabrication techniques taken from the literature. The section will also include a discussion of the basic concepts, fabrication steps, necessary equipment, and characterization of ion-selective micropipettes applied in SECM studies.

Potentiometric detection is based on the detection of a membrane potential across the membrane of a probe electrode. Potentiometric probes measure a membrane potential linearly dependent on the logarithm of the activity of a primary ion. Experimentally, a typical setup would be

Outer-reference || Sample | Membrane | Internal Solution | Internal-Reference
Ion-Selective Electrode

The membranes used in ion-selective electrodes separate two different electrolytes and are not equally permeable to all kinds of ions. At the interface between the two electrolytes, different events contribute to the measured membrane potential. First, a diffusion potential arises from differences in mobility and concentration of ions in contact at the interface, as seen in liquid junctions. Second, a Donnan potential arises when the membrane completely prevents the diffusion of at least one species from solution to the other. Third, the exchange equilibria between the electrolyte and the membrane interface must also be considered to adequately describe the membrane potential of ion-selective electrodes with solid or liquid electrolyte membranes.

When no current is flowing, the measured cell potential (E_{cell}) is the sum of all potential contributions in the cell such that

$$E_{\text{cell}} = E_{\text{IS}} - E_{\text{R}} + E_{\text{J}} \quad (12.3.5)$$

where E_{IS} is the potential of the ion-selective probes, E_{R} is the potential of the reference electrode, and E_{J} is a liquid junction potential between the sample solution and the internal solution of the reference electrode. This junction potential is often eliminated by choosing a supporting electrolyte that closely matches that of the reference electrode.

The resulting cell potential (E_{cell}) describes the relationship between the ion-selective membrane potential and the primary ion activity. When the membrane diffusion potential is zero, the membrane potential is defined by the Nernst equation:

$$E_{\text{cell}} = \text{Const} \pm 2.303RT/z_i F[\log(a_i)] \quad (12.3.6)$$

where Const is a constant that includes activity independent terms of the primary ion, R is the gas constant, T is the absolute temperature, z_i is the charge of the primary ion, F is the Faraday constant, and a_i is the activity of the primary ion in the sample. Specific potentiometric probes should, therefore, present a Nernstian slope of about $59 \text{ mV}/z_i/\text{decade}$ (25°C). To have a relationship dependent on the concentration of the primary ion, the activity coefficient of the primary ion must be known or the experiment must be carried out under dilute conditions.

An ideal analytical sensor should specifically and quantitatively detect a single ion. This would mean that the membrane potential would be affected by only one particular ion in solution. Potentiometric probes are rarely specific to a given ion and are commonly selective to a series of ions. Their response will selectively respond to a certain type of ion but will be affected by the presence of other ions leading to interferences. In the case of a solution with only two types of ions where ion (j) would interfere with the potentiometric response of the primary ion (i), the measured cell potential can be approximated to the Nikolsky–Eisenman equation:

$$E_{\text{cell}} = \text{Const} \pm 2.303RT/z_i F \left[\log \left(a_i + \sum K_{ij}^{\text{pot}} (a_j)^{z_i/z_j} \right) \right] \quad (12.3.7)$$

where K_{ij}^{pot} is the selectivity coefficient that weighs the contribution of the interfering ion, a_j is the activity of the interfering ion, and z_j is the charge of the interfering ion. The derivation

of this equation is reported (56); it was derived for a compact ion-exchanger membrane with a fixed concentration of equivalent active sites where an internal diffusion potential occurred.

12.3.2.2 Potentiometric probe fabrication

There are two defining groups of ion-selective electrodes: (a) solid-membrane electrodes (56, pp. 93, 96, 103, 104, 106, 107), and (b) liquid-membrane electrodes (55, pp. 408–413). In the case of solid membranes, a network of ions is immobilized in a support such that the number of active sites remains constant with time. The membranes can be homogenous (single crystal, crystalline structure, or glass) or heterogeneous (where the active sites are imbedded in a polymer matrix). In this case, the selective compound can be of opposite charge of the primary ion or a complexing agent of this ion. Liquid membrane electrodes are multicomponent devices whose active agents are ionized ion exchangers or electroneutral ion carriers. The measuring membranes are usually a water immiscible organic phase that contain ionophores and that can separate the sample solution from the internal filling solution. A few examples of potentiometric probe fabrication protocols that can be applied to SECM studies will be presented but the interested reader can refer to other work (57).

(a) Ion-selective glass microelectrodes

Glass-membrane electrodes include H⁺, Na⁺, K⁺, and Ag⁺ selective glass electrodes. The active measuring device in these electrodes is confined inside the inner walls of a pulled glass capillary. The ion selectivity is gained by choosing the appropriate glass composition. For example, glass having a weight composition of (Na₂O(22%); CaO(6%); and SiO₂(72%)) is more selective to H⁺ ions; while a glass with a weight composition of (Na₂O(11%); Al₂O₃(18%); and SiO₂(71%)) is more selective toward Na⁺ ions (56, p. 107). Glass electrodes, like the pH electrode, have a Nernstian linear response to H⁺ up to a pH of ~11–12.

Different techniques can be employed to produce micrometer size pH probes. Generally, a thin ion-selective glass bulb needs to be combined with an insulating microcapillary stem such that the internal filling solution and Ag/AgCl reference electrode can be accommodated. To isolate the ion-selective glass at the end of the microcapillary, two approaches can be used: (a) a closed ion-selective micropipette is isolated at the end of an insulating micropipette. This can be accomplished by pulling an ion-selective micropipette and insulating the stem with an insulating material like a shellac or nail polish. Another option is to seal an ion-selective micropipette into an open-ended insulating microcapillary using a glass/glass joint (55, p. 402) or a sealing wax (55, p. 402). The glass/glass sealed pH sensor can further be pulled down with a laser puller to obtain a pH sensor on the order of 2 μm (55, p. 403). (2) The end of an open-ended microcapillary can also be coated with a thin layer of ion-selective glass (55, p. 402). This procedure can yield single and double barrel electrodes (55, p. 402).

The difficulty in combining glass membranes in SECM applications is that their fabrication is technically challenging. To our knowledge, no glass microelectrode probe has been reported in SECM experiments. As these electrodes have been applied in intracellular pH measurements, their detection limit and response time seem to be adequate for low analyte concentration measurements and seem very promising for SECM applications.

(b) Ion-selective crystalline membrane microelectrodes

Solid-state membrane electrodes include H^+ , F^- , CN^- , Cl^- , I^- , Br^- , H_2S , CN^- , thiourea, Pb^{2+} , Cu^{2+} , and Cd^{2+} selective electrodes. In this category, silver halide and silver sulphide electrodes are found. The macroscopic ion-selective electrodes made with these systems have been applied in many fields, such as medicine, food industry, and environmental studies (56, pp. 93, 96, 103, 104) but their full potential has not yet been exploited in terms of SECM studies.

Antimony microdisc electrodes used as a pH-measuring probe have been reported in SECM studies. A detailed protocol for fabrication of these tips has been published (58). Briefly, a thick-walled capillary (o.d., 10 mm; i.d., 1 mm) is filled with melted antimony using suction. The antimony filled capillary is then pulled down sequentially using glass blowing techniques or a resistor coil until a Sb microdisc (o.d., 20–30 μm ; i.d., 2–3 μm diameter) is obtained. This microdisk fiber is then mechanically glued at the end of a pulled glass capillary with silver-epoxy together with a copper wire, which serves as contact.

An Ag/Ag^+ microelectrode has been used in SECM studies to measure Ag^+ and Cl^- profiles (59). To build a Ag/Ag^+ microindicator electrode, a 1-cm long 50 μm diameter Ag wire is soldered onto a large connection wire and then inserted into the end of a Pasteur pipette. Quickset epoxy resin is then rapidly forced up as far inside the capillary as possible. Once set, the tip is sequentially sharpened to form a pencil like shape. The radius of the insulator (glass and/or epoxy resin) should be about five times that of the Ag wire. The geometry of the Ag/Ag^+ microelectrode has no direct influence on the measured potential, but it allows for a closer approach to the substrate and reduces shielding. The Ag/Ag^+ microelectrodes can also be converted into Ag/AgCl microelectrodes by briefly anodizing the Ag microelectrode in 1 mM HCl solution. The Ag/Ag^+ microelectrodes can be used to probe Ag^+ concentration profiles, while the Ag/AgCl microelectrodes can be used to monitor Cl^- concentration profiles.

(c) Ion-selective liquid membrane microelectrodes

Liquid-membrane electrodes include classical ion-exchange, liquid ion-exchange, and electroneutral ionophore-based liquid membrane electrodes. Of particular interest are systems where the ion-exchanging compounds are dissolved macrocyclic compounds that have a strong selectivity to alkali metals. The stability of the formed complexes in nonpolar solvents far exceeds that found in water and allows for the fabrication of membrane-free micropipettes where the nonpolar/water interface is the membrane. Unfortunately, this leads to higher resistance than that exhibited by crystalline micropipettes and requires the addition of lipophilic salt to the nonpolar solvent to decrease the pipette resistance.

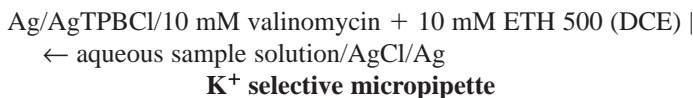
Most macrocycles used in the design of these electrodes are uncharged and have common properties, such as the formation of complexes with univalent ions and the ability to transport these ions across lipid membranes. The complexes have a polar cavity where the complexed ion sits and an outer lipophilic envelop that allows dissolution of the ion into the nonpolar solvent. There is a wide range of applicable macrocyclic ligands, including depsipeptides (valinomycin, enniatins A, B, and C), macrotretolides (nonactin, monactin, dinactin, and trinactin), cyclic peptides (gramicidin S and tyrocidin A), cyclic polyethers (for example, dicyclohexyl-18-crown-6 isomers, dicyclohexyl-14-crown-4, and dibenzo- x -crown- y , where (x, y) : (18, 6); (21, 7); (24, 8); (30, 10); and (60, 20)), and also some

acyclic compounds (nigericin and monensin) (56, p. 149; 55, pp. 408–413). The great advantage of using these electroneutral-based ion-selective electrodes is that their fabrication protocol differs little from one cocktail to the other.

Generally, ion-selective liquid membrane micropipettes are made from a similar procedure. The capillaries are cleaned and pulled to the desired dimensions. The interior of the pipette is silanized prior to the addition of the ion-selective cocktail. The silanization reagent concentration and time of reaction are important as the glass hydrophobicity prevents the outer aqueous solution from being drawn into the pipette. The cocktail solution is loaded from the pulled end of the pipette by capillary action and using light suction. The internal filling solution is back filled and the reference electrode (often 100 μm Ag/AgCl wire) is secured to the pipette with silicon rubber or parafilm. Two detailed fabrication protocol are given below and have been chosen on the basis that they have previously been used in potentiometric SECM studies.

Ca^{2+} ionophore sensor (60). To make Ca^{2+} -selective SECM tips, borosilicate glass capillaries (1.5-mm o.d., 0.75-mm i.d., 100-mm length) are pulled using a laser or resistor puller. The resulting micropipettes should have a 1-cm long flexible taper. Polishing of the micropipettes using a beveler coated with 1- μm sized alumina particles leads to smooth and clean openings with diameters ranging from 5 to 20 μm . The inner wall of the micropipette is then silanized using hexamethyldisilazane prior to being filled with a Ca^{2+} -selective liquid membrane solution like Ca^{2+} -ionophore, ETH129. The micropipette is back-filled with an internal electrolyte solution containing CaCl_2 . The reference electrode, Ag/AgCl, is finally inserted as an internal electrode.

K^+ ionophore sensor (61). To make K^+ -selective SECM tips, borosilicate capillaries (o.d./i.d.: 1.0/0.58 mm) are cleaned in a 1:1 (v/v) mixture of concentrated sulfuric acid and 30% hydrogen peroxide overnight, washed and dried at 120 °C for 30 min. Using a laser-based pipette puller, patch clamp type pipettes are produced (orifice radius = 0.7–20 μm). The inner wall of each pipette is silanized with a toluene solution of trimethylchlorosilane (5–100% v/v). The solution is removed from the pipette after 5–30 min, emptied using a syringe, and then connected to a vacuum pump to remove any residual silanizing vapor. The experimental system can be represented by the following cell:



To make the K^+ selective micropipette, a 1,2-dichloroethane (DCE) solution of 10 mM valinomycin and 10 mM tetradodecylammonium tetrakis (4-chlorophenyl)borate (ETH 500) is used as ionophore and supporting electrolyte, respectively. Hydrophobic ETH 500 was used in the organic phase to obtain a sufficiently wide potential window and also to avoid an ion-exchange reaction between K^+ in the aqueous phase and the cationic electrolyte in the organic phase. The silanized pipettes are filled with the organic solution through the larger opening with a small (10 μL) syringe. A 0.25-mm silver wire coated with silver tetrakis (4-chlorophenyl) borate (AgTPBCl) by reduction of Ag in a DCE solution of

10 mM tetrabutylammonium tetrakis (4-chlorophenyl) borate and was inserted into each pipette. The top of the pipette was then closed with parafilm.

(d) Equipment requirements

A standard one electrode configuration for potentiometric measurements consists of the potentiometric electrode connected to a voltage follower and the reference electrode connected to electrical ground. To improve noise level and drift, a differential potentiometric mode can be carried out using a high-sensitive potentiometer in a three-electrode configuration consisting of the SECM potentiometric probe and two independent external references. For example, the potential difference between the potentiometric micropipette and a large inert Pt electrode (ΔE_{tip}) is compared with the potential difference between a large reference electrode of the same nature as the potentiometric micropipette and the Pt electrode (ΔE_{ref}). The Pt wire is connected to the electrical ground of the electronic circuit. High-input impedance operational amplifiers (150 fA input bias current) are used as voltage followers to buffer the input of the three electrodes (micropipette and two references). The followers should be positioned as close as possible to the electrodes. The potential differences are then compared with a precision unit-gain differential amplifier. The resulting amplified output ($\Delta E_{\text{out}} = \Delta E_{\text{tip}} - \Delta E_{\text{ref}}$) is proportional to the primary ion activity under the proper experimental conditions (60b). In such an instrument, circuit design and proper insulation connection wires are critical to limit the leakage currents. As such, the SECM head and the potentiometric circuit should be located inside a Faraday cage (55).

To perform potentiometric SECM, one needs to combine a high impedance voltmeter as described above with an SECM (homebuilt or commercial). The use of amperometric mode SECM is still desirable as it can be used to position the pipette and determine the tip–substrate distance. A more detailed discussion concerning the positioning of potentiometric probes and the acquisition of approach curves will be presented in the next section.

12.3.2.3 Potentiometric probe characterization

To characterize potentiometric probes, one must evaluate their response function, selectivity coefficient, response time, and ohmic drop. The response function of a potentiometric probe is a calibration curve of the measured membrane potential with the log of the concentration (or activity) of the primary ion must be acquired. To use concentration values, the activity coefficients must be known and many of them are tabulated. Another option is to use (when possible) dilute solutions such that the activity coefficients maybe neglected.

The measured slope of the response function should be close to $59 \text{ mV/z}_i/\text{decade}$. At low primary ion concentrations, the potentiometric response can reach a steady state that can be due to impurities in the water or due to the presence of potentially interfering ions. The lower limiting value of the micropipette response at low primary ion activity can also be taken as the background for the SECM approach curves. In certain circumstances, the addition of different chelators (HEDTA, NTA, and EGTA) can be added to try to limit the effect of interfering metal ions.

Typically, ion-selective micropipettes can be used in a concentration range of 10^{-1} to 10^{-5} M and have a detection limit of about 10^{-6} M . As they can drift easily it is importance

that a calibration curve be performed following an experiment and compared with the initial one. This drift occurs as a result of changes in the surface structure of solid-membrane electrodes when in contact with the electrolyte and to the dissolution of the ion exchanger in liquid-membrane electrodes.

The selectivity coefficient provides fundamental information concerning the impact of various interfering ions on the performance of a given ion-selective electrode. The weaker the interference of a given ion with the primary ion, the lower is the value of the selectivity coefficient. The determination of the selectivity coefficients assumes that the behavior of the ion-selective electrode follows a nernstian behavior. As the electrode often deviates from nernstian behavior, the selectivity coefficient is often only semi-quantitative. The coefficient is dependent on the concentration of both the primary ion and the interfering ion. To determine the selectivity coefficient, a plot of the ion-selective potential vs. the logarithm of the concentration of the primary ion is obtained at a given concentration of interfering ion. This graph ideally presents two linear portions for two ions of identical charge. The intercept of these two regions is the selectivity coefficient. Many of the selectivity coefficients are tabulated and can be substituted but it should be emphasized that these coefficients roughly determine the region in which the electrode exhibits nernstian behavior and is an indication of where they can be used reliably.

The response time of an electrode describes the ion-selective electrode's sensitivity to ion activity changes. The response time is a sensitive parameter defined as the time taken by the experimental setup to reach a chosen percent of the final cell voltage following a given change in the activity of the primary ion. This definition is specific to a given experimental setup as the time response of the micropipette will vary with the type of micropipette used, the particular experimental conditions, the electronics, and the method used to cause the primary ion activity change. In terms of macro ion-selective electrode, common response times would be on the order of seconds (56, p. 70); while for ion-selective micropipettes, response times on the order of 10 ms have been reported (60). The response time of the electrode is of particular interest when close proximity measurements are made.

Liquid membrane ion-selective electrodes have a high internal resistance (10^8 – 10^{11} Ω), which requires the use of a high-impedance voltmeter. Micropipettes with ion-exchangers tend to have impedance in the lower range, while those made with an electroneutral carrier usually exhibit impedances of 10^{11} Ω. Such high resistances require the use of a high-impedance voltage device that has an input impedance of at least 10^{13} Ω. This is necessary to avoid errors in the current input bias. Practically, the maximum current passing through the electrode multiplied by the largest resistance should not exceed 0.5 mV such that an error less than 2% is obtained on the measured activity of the primary ion (55, p. 422). Finally, to avoid contamination of the membrane potential by potentials occurring across the glass, the electrode shaft should be properly shielded.

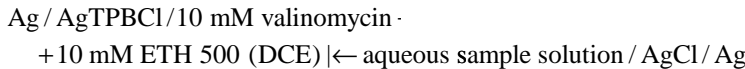
12.3.2.4 SECM potentiometric measurements

To use potentiometric probes in SECM, it must be possible to exactly evaluate the tip-substrate distance. Different methods to evaluate the distance dependence are presented

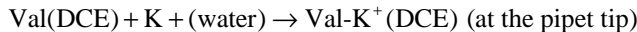
below. None of these methods can be applied unilaterally as they are applicable to a limited number of experimental conditions or require the use of very special instrumental setups.

- (1) Metal oxide electrodes have amperometric and potentiometric capabilities. Sb/SbO₂ electrodes can first be approached to a surface in amperometric mode using the oxygen reduction reaction (ORR). The electrode is then properly conditioned for potentiometric measurements by forming an adequate antimony oxide layer. This electrode can then be used to monitor local pH changes either in feedback or generation/collection mode. This ideal positioning and detection situation can only be applied to metal oxide electrodes because they can use dissolved oxygen as a redox couple for the initial positioning.
- (2) A double barrel tip having one amperometric UME and one potentiometric probe can also be designed. To do so, theta capillaries are usually pulled down and then further modified. Fabrication of a dual barrel electrode is technically challenging. To prepare an electroneutral ionophore probe on one side of the dual barrel electrode, one of the pipette tubes must be silanized. To prevent silanization of the other compartment, nitrogen is flushed through during the silanization process. The choice of amperometric material is also limited as conventional resistance or flame sealing would also seal the end of the potentiometric probe. Liquid gallium has been used but has a limited active potential window (62). The two tips must also be separated by the smallest distance possible so that no significant error is made between the area under the amperometric probe and the potentiometric probe.
- (3) For silver halides potentiometric sensors, the tip-to-substrate separation can be evaluated based on changes of solution resistance. A fixed dc potential between an AgCl micropipette and a AgCl auxiliary/reference electrode is applied and the steady-state current that passes through them is measured. This current corresponds to the formation of AgCl at the tip and dissolution of AgCl at the auxiliary electrode. This system can be modeled by an equivalent electronic circuit. As the AgCl micropipette approaches the substrate, the solution resistance increases and presents a response similar to that observed under amperometric positive feedback experiments. As with the amperometric approach curves, the solution resistance approach curves can be fitted to a derived theory to extract the true tip–substrate distance (63).
- (4) An ac impedance technique based on changes in solution resistance is also available and has been applied to enzyme-coated microelectrodes (64). In this case, a sinusoidal potential is applied between the electrode and the auxiliary electrode. The measured sinusoidal current is sent to a frequency response analyzer that monitors the change of the real impedance with distance to the substrate. Using equivalent circuits, a theoretical approach curve can be obtained and fitted to the experimental solution resistance profiles with distance.
- (5) Techniques 3 and 4 cannot usually be applied to electroneutral ion carrier micropipettes that have large electrode resistance. For systems under steady-state conditions, the change in concentration profile with tip–substrate distance can be used to determine the tip–substrate separation. A theory to that effect is available (58).

- (6) The case of K⁺ selective ionophore microelectrodes is of particular interest as the cell:



can be used in conventional voltammetric and SECM studies. At the water/DCE interface, a facilitated ion-transfer reaction occurs as follows:



The ion-transfer processes at the microinterface between two immiscible electrolyte solutions (micro-ITIES) at the pipette tip are polarizable. The voltage, ΔE , applied between the Ag/AgTPBCl electrode inside the pipette and the Ag/AgCl electrode in the aqueous phase provides the driving force for the ion transfer process. A voltammogram for K⁺ transfer can be obtained. At sufficiently negative bias, a steady-state current is obtained and is associated with the K⁺ transfer from water to DCE internal solution of the pipette. As seen with amperometric UMEs, the observed steady-state current is limited by spherical diffusion of K⁺ in the outer aqueous phase to the pipette's mouth. For conditions where *the valinomycin far exceeds the K⁺ concentration*, the steady-state current varied linearly with K⁺ concentration and conventional approach curves of normalized current with normalized distances can be obtained.

- (7) A nonelectrochemical distance control for SECM tips that permits simultaneous acquisition of topographic and electrochemical information can be used (4, 65). Briefly, two piezoelectric plates are attached to the shaft of the SECM tips. One of the plates vibrates the tip at resonance and the second plate detects the amplitude and phase of the tip oscillation. This technique can also constantly regulate the tip to sample separation during imaging experiments.

12.3.2.5 Conclusions, limitations, and prospects

The SECM potentiometric mode makes use of ion-selective micropipettes. These devices increase the range of detectable species by SECM but are technically very challenging to make and must be calibrated before and after experiments. The electronic requirements to acquire good data are very specific and must include a means to adequately evaluate the tip–substrate distance. Potentiometric detection remains underexploited in SECM studies and has great promise in terms of biological applications.

12.3.3 Imaging

In this section, we illustrate the application of SECM for topographic and chemical imaging. The operational principle and methodology of SECM imaging is described in Section 12.3.3.1. One example of constant height SECM imaging in bulk liquid environments is demonstrated in Section 12.3.3.2. Of particular interest is the use of SECM to perform

chemical imaging; for example, to observe differences in electrocatalytic activity of oxygen reduction or hydrogen oxidation on different materials. This will be discussed very briefly in Section 12.3.3.3. A more detailed discussion will be given in Section 12.4.3. SECM imaging for systems including enzymatic sites, corrosion pits, and other artificial patterns will also be described in individual sections.

12.3.3.1 Principle and methodology of SECM imaging

A three-dimensional SECM image is obtained by scanning the tip in the XY plane and monitoring the tip and/or substrate current as a function of tip location. This is the so-called constant height mode (1). The current image obtained can be converted into a plot of Z-height, i.e., d vs. XY position via a (i_T vs. d) calibration plot. The current image can be presented in gray scale, where high values of current are shown in light colors and small values as dark colors, or in color code. As mentioned previously, the resolution attainable with SECM is largely governed by the tip size and the distance between tip and sample. With a very small diameter tip (e.g., diameter < 100 nm), scanning the tip in close proximity to the substrate surface (e.g., 100 nm above the surface), and measuring the current becomes very difficult due to stray vibrations. Irregularities in the sample surface can cause a tip crash. Thus, for high resolution, SECM must be carried out in the constant current mode (1), as is often used with STM, where the distance is adjusted by a feedback loop to the z -piezo to maintain i_T constant. This is straightforward when the sample is either all conductive or all insulating, as the piezo feedback can be set to counter a decrease in tip current by either moving the tip closer (conductor) or farther away (insulator).

For samples that contain both types of regions, a method of recognizing the nature of the substrate must be available for designing the feedback loop. One approach is to modulate the motion of the tip normal to the sample surface and record di_T/dz . This is the so-called tip position modulation (TPM) technique (66). The use of TPM can improve the sensitivity and resolution of the SECM image and provide a method of distinguishing between conductive and insulating areas on the substrate surface being examined. Another more universal technique is the combined AFM/SECM technique as described in Section 12.2.2.1 topographic and SECM images to be obtained simultaneously if a proper tip is prepared.

12.3.3.2 Constant height imaging

We present one example, of a polycarbonate membrane to illustrate the important factors affecting the resolution of topographic SECM images. Figure 12.12 shows a series of constant height SECM images of polycarbonate filtration membranes having a nominal average pore size of $\sim 14 \mu\text{m}$. These images were taken with Pt disk tips immersed in a $\text{KCl}/\text{K}_4\text{Fe}(\text{CN})_6$ solution. As shown in frames A–C, which are the current images taken with a 10- μm -diameter Pt disk located at different distances, the resolution of SECM images increases with decreasing distance. The gray scales of the image taken at a normalized distance ($L = d/a$) of 2.4 (frame A) are diffuse and not uniformly distributed, indicating significant overlap between the diffusion fields of the electroactive mediator around individual pores. Decreasing d to a normalized distance of 0.26 (frame C) resolves individual pores almost completely, although the apparent pore size is slightly larger than the

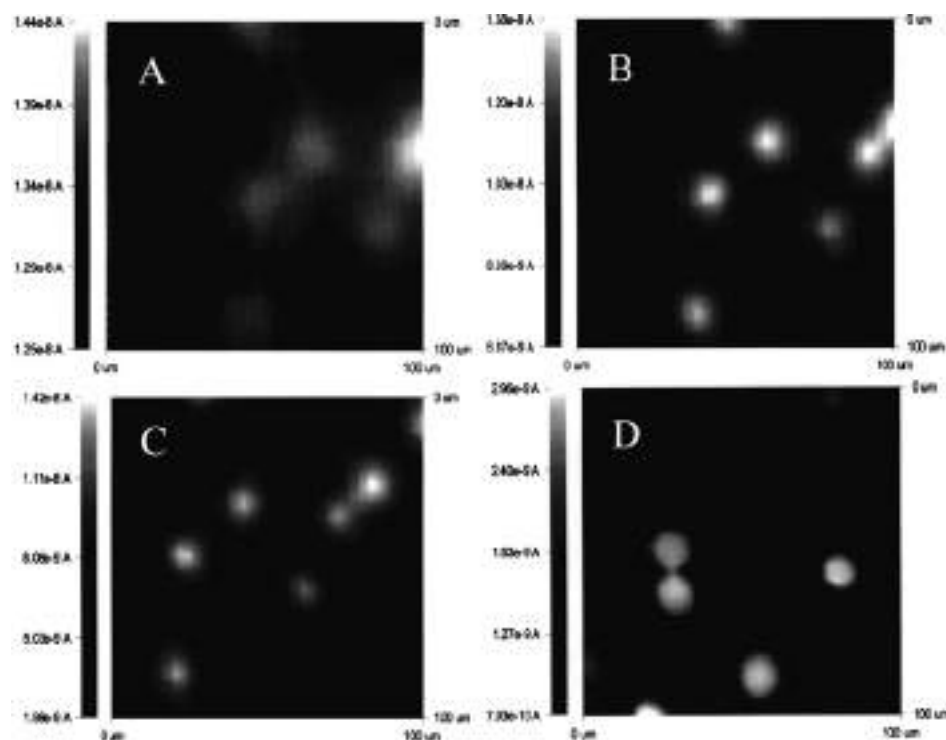


Figure 12.12 A series of constant-height SECM images of polycarbonate filtration membranes having a nominal average pore size of $\sim 14 \mu\text{m}$. The scan size of each image is $100 \mu\text{m} \times 100 \mu\text{m}$. These images were taken with a CH series-900 SECM unit at Pt disk tips immersed in a solution containing $\text{K}_4\text{Fe}(\text{CN})_6$ as the redox mediator and KCl as the supporting electrolyte. Images A–C for a 10- μm diameter Pt tip were taken at different normalized distances, L . $L = 2.4$ (A); 1.0 (B); 0.25 (C). Image D shows one SECM image of the same membrane taken with a smaller tip (2 μm diameter) at a normalized distance of 1.

nominal value and the gray scale of the image near the pores is still not uniformly distributed. Frame D shows the same membrane imaged with a smaller tip (2 μm diameter) at different location from that for frames A–C and at a normalized distance of 1. As can be seen, not only are individual pores well resolved, but also the apparent pore size is fairly close to the nominal value and the gray scale of the image near the pores is more uniformly distributed than that shown in frames A–C.

12.3.3.3 Chemical imaging

Reaction rate imaging is unique to SECM and clearly illustrates its “chemical imaging” capability. By proper choice of solution components to control the tip reaction and the electrochemistry at the substrate/solution interface by varying the electrode potential, differential reaction rates at various surfaces can be probed. For example, the location of enzyme sites in a membrane or organelle, where a particular reaction is catalyzed, can be

seen. Such enzymatic systems will be discussed in Section 12.4.6.2. Here, we choose another important reaction, the ORR on different materials in 0.5 M H₂SO₄, to demonstrate the capability of SECM for chemical imaging. Figure 12.13 shows several constant height images obtained by the TG/SC mode for ORR on smooth Pt (127-μm diameter, left rear) and Au (100-μm diameter, right front) disks embedded in glass (54). During imaging, two electrodes are held at the same potentials. In the region of potentials where the ORR is totally under diffusion control on both metals ($E_S \leq 0.1$ V vs. hydrogen reference electrode (HRE)), there are no significant differences between the i_S values coming from each disk (see frame a), indicating no significant difference in the activity of oxygen reduction on both electrodes. In the range of $0.1 < E_S < 0.4$ V, the difference in electrocatalytic activity between Pt (still very active) and Au (losing substantial activity) is clearly seen (see frame b). At higher potentials ($E_S \geq 0.4$ V), the activity of Au is essentially zero,

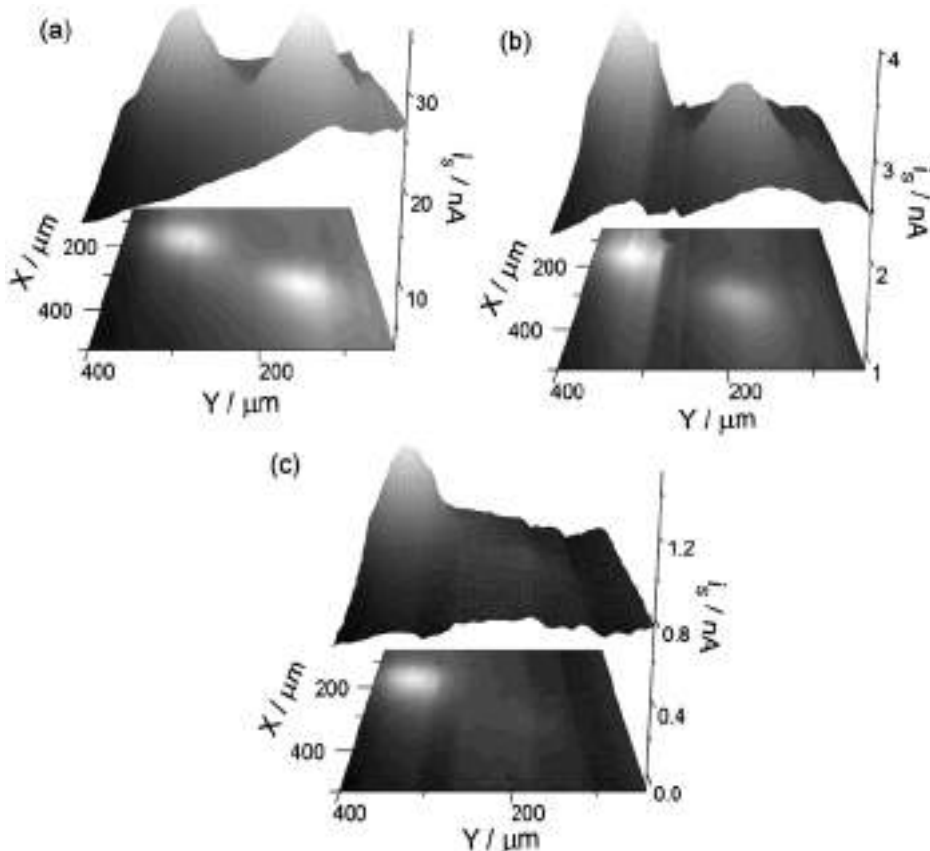


Figure 12.13 ORR images in 0.5 M H₂SO₄ obtained by the TG/SC mode of smooth Pt (127-μm diameter, left rear) and Au (100-μm diameter, right front) disks electrically connected and embedded in glass: scan rate = 300 $\mu\text{m sec}^{-1}$; $d = 30 \mu\text{m}$; $i_T = 15 \text{nA}$; $E_S = 0.1$ (a), 0.2 (b), 0.4 (c) V vs. hydrogen reference electrode (HRE). (Adapted from reference (54).)

while Pt still continues reducing oxygen (see frame c). When E_s is positive of 0.8 V, both Pt and Au lose activity. Note that the background current also varied slightly during the scan and depended on the substrate potential. These results clearly demonstrate the chemical imaging capability of SECM and can be used to visually identify materials with different electrocatalytic activity for the ORR.

12.4 APPLICATIONS

12.4.1 Heterogeneous kinetics

It was shown in Section 12.3 that SECM approach curves allow one to obtain a very precise estimation of the tip–substrate distance and the tip geometric properties, either using negative or positive feedback. In fact, both events are limiting cases of the situation where the reaction at the substrate has a finite reaction rate (Figure 12.14a). If the reaction rate is very small, regeneration of tip reactant is negligible and the substrate behaves as an inert surface, so the approach curve resembles that of hindered diffusion. In contrast, if the substrate reaction is fast enough that it operates under mass-transfer control, total positive feedback occurs and the approach curve is insensitive to the reaction rate. When the tip approaches a substrate with a finite reaction rate, the approach curve may look as one of those shown in Figure 12.14b, depending on the value of the rate constant. This sensitivity of SECM approach curves on the substrate reaction rate, one of the most interesting

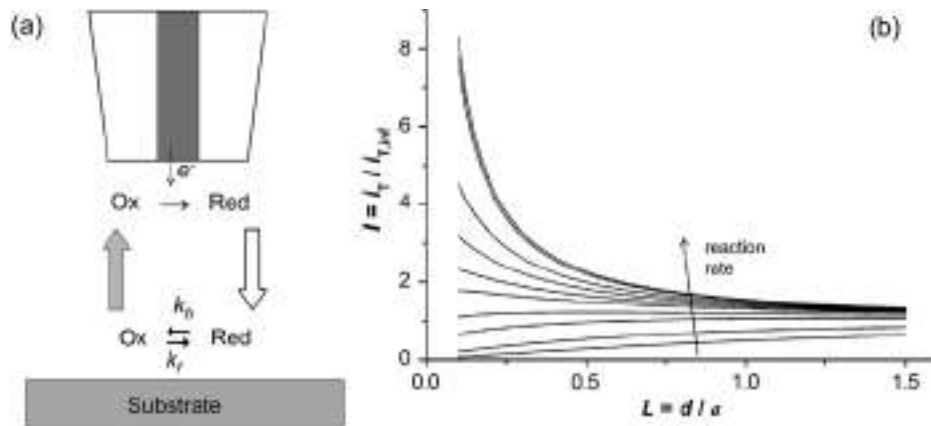


Figure 12.14 (a) Schematic of the feedback process when the substrate reaction ($\text{Red} \rightleftharpoons \text{Ox}$) operates under kinetic control. The tip electrode reaction ($\text{Ox} + e^- \rightarrow \text{Red}$) operates under diffusion control. The flux of Ox that feedbacks the tip (gray arrow) depends on the values of k_f and k_b , the forward (reduction) and backward (oxidation) rate constants of the substrate reaction. (b) Typical kinetically controlled approach curves, where the reaction rate at the substrate increases from bottom to top. Bottom and top dashed lines are curves obtained on substrates that are insulating (negative feedback) and conductive operating under diffusion control (positive feedback), respectively.

properties of SECM, makes this technique a very powerful tool for the kinetic studies of heterogeneous reactions.

The correlation of an experimental “kinetic-controlled” approach curve with a theoretical model allows one to calculate the rate constant of the substrate reaction. To perform this operation, models involving quasireversible and irreversible (reverse reaction neglected) substrate reactions governed by a single-step Butler–Volmer equation were developed by Bard *et al.* (67) using numerical methods. Simulated values of I vs. L for different rate constants and substrate potentials are tabulated in Table 12.2 (67). Although it is time consuming and not very accurate, a procedure to correlate these models with experimental approach curves is by manual comparison of experimental and simulated values. This procedure was used, e.g., to study the kinetics of the $\text{Ru}(\text{NH}_3)_6^{3+}/\text{Ru}(\text{NH}_3)_6^{2+}$ couple (67), and for studies of electron-transfer processes across the liquid/liquid interface (68–70). The most common procedure for processing kinetic approach curves is through the use of an approximate analytical equation (equations (12.4.1)–(12.4.5)) (71). This equation was derived from the correlation of I - L - κ working curves simulated for a quasireversible electron-transfer reaction at the substrate, where $\kappa = ka/D$ (where D is the diffusion coefficient of tip reactant). The parameter k is the rate constant of the quasireversible reaction at the substrate, which for an electrode reaction is given by equation (12.4.6), where k° is the standard rate constant and E° is the standard potential. This equation is valid in the range of distances $0.1 \leq L \leq 1.5$ and for values of rate constants in the interval $0.01 \leq \kappa \leq 1000$.

From Figure 12.14b, it can be noted that the region of highest sensitivity of these equations with respect to the value of κ is in the interval, $0.1 \leq L \leq 0.5$. Thus, an important factor to perform reliable kinetic studies by SECM is the quality of the tip, which needs to be able to approach until the end of this distance interval.

$$I = I_s \left(1 - \frac{I_T^{\text{ins}}}{I_T^C} \right) + I_T^{\text{ins}} \quad (12.4.1)$$

$$I_T^{\text{ins}} = \frac{1}{0.15 + 1.5358/L + 0.58 \exp(-1.14/L) + 0.0908 \exp\left(\frac{L-6.3}{1.017L}\right)} \quad (12.4.2)$$

$$I_T^C = 0.78377/L + 0.3315 \exp(-1.0672/L) + 0.68 \quad (12.4.3)$$

$$I_s = \frac{0.78377}{L+1/\kappa} + \frac{0.68 + 0.3315 \exp(-1.0672/L)}{1+F(L,\kappa)} \quad (12.4.4)$$

$$F(L,\kappa) = \frac{(11/\kappa L) + 7.3}{110 - 40L} \quad (12.4.5)$$

$$k = k^\circ \exp\left[\frac{(1-\alpha)nF(E-E^\circ)}{RT}\right] \quad (12.4.6)$$

There is no analytical equation for a quasireversible substrate reaction. In fact, quasireversible reactions have been studied by means of approximate analytical models for the

Table 12.2

Normalized steady-state tip current ($I = i_T/i_{T,\infty}$) computed as a function of L for a quasi-reversible substrate reaction with different values of dimensionless rate constant ($\kappa = k^\circ a/D$) and dimensionless substrate potential ($E_1 = nF\eta/RT$) (67). The Butler–Volmer relations for the forward (reduction) and backward (oxidation) rate constants are $k_f = k^\circ \exp(-\alpha E_1)$; $k_b = k^\circ \exp[(1-\alpha)E_1]$; where α is the transfer coefficient

		E_1																					
		$\kappa = 25$			$\kappa = 5$			$\kappa = 1$			$\kappa = 0.5$			$\kappa = 0.1$			$\kappa = 0.05$			$\kappa = 0.001$			
L		0.0	0.585	2.926	0.0	1.171	4.682	0.0	2.341	7.803	0.0	3.902	9.754	0.0	7.803	11.71	0.0	7.803	13.66	0.0	15.61	21.4	
0.1	3.71	4.79	7.66	2.40	3.84	7.38	1.00	2.42	7.39	0.68	2.62	7.67	0.21	3.25	6.95	0.17	2.07	7.31	0.11	2.04	7.30		
0.2	2.12	2.74	4.20	1.66	2.62	4.22	0.93	2.05	4.24	0.72	2.22	4.32	0.24	2.59	4.10	0.19	1.89	4.22	0.14	1.86	4.21		
0.5	1.16	1.48	2.20	1.07	1.62	2.26	0.84	1.61	2.28	0.69	1.72	2.29	0.49	1.87	2.25	0.43	1.60	2.27	0.36	1.60	2.27		
0.8	0.89	1.14	1.68	0.85	1.30	1.74	0.78	1.39	1.76	0.68	1.49	1.76	0.60	1.58	1.75	0.57	1.44	1.76	0.50	1.44	1.76		
1.0	0.81	1.03	1.51	0.79	1.18	1.57	0.72	1.31	1.58	0.67	1.40	1.58	0.61	1.47	1.57	0.60	1.37	1.58	0.55	1.37	1.58		
1.5	0.70	0.89	1.32	0.69	1.03	1.35	0.68	1.18	1.36	0.67	1.27	1.36	0.66	1.31	1.35	0.66	1.26	1.36	0.67	1.26	1.36		
2.0	0.66	0.82	1.21	0.65	0.96	1.24	0.66	1.12	1.25	0.66	1.19	1.25	0.70	1.22	1.25	0.73	1.20	1.25	0.78	1.20	1.25		
5.0	0.63	0.78	1.05	0.64	0.90	1.08	0.65	1.01	1.08	0.66	1.06	1.08	0.74	1.07	1.08	0.79	1.07	1.08	0.92	1.07	1.08		

case where the tip reaction operates under kinetic control and the substrate reaction is mass transfer controlled (72, 73). This case has limited applicability as the electrode studied must be prepared as a UME tip. However, recently Zoski *et al.* published an approximate theory to describe SECM approach curves for quasireversible reactions based on a model combining ideal thin-layer cell geometry at close distances and linear diffusion at large tip–substrate distances (35). Although it is still approximate, this model yields a set of analytical equations that are useful for treatment of approach curves under kinetic control with a quasireversible substrate reaction. It also considers the possibility that the reaction at the substrate modifies the concentration profile of reactant in solution, the so-called shielding effect, which occurs when the backward reaction at the substrate is significant (35).

To illustrate the procedure for measuring and fitting kinetically controlled approach curves, the study of the electro-oxidation of Fe^{2+} to Fe^{3+} (equation (12.4.7), $E^\circ = 0.55 \text{ V}$ vs. Ag/AgCl) on glassy carbon, which is considered irreversible, will be described (67).



The SECM experimental setup is identical to that described in Section 12.3.1 for measuring regular approach curves. In this example, a carbon fiber tip (in this example, a 10- μm diameter tip) is the amperometric probe that drives the reaction $\text{Fe}^{3+} + \text{e}^- \rightarrow \text{Fe}^{2+}$. At $E_T = -0.5 \text{ V}$ vs. Ag/AgCl, the reaction is diffusion controlled on a carbon tip in de-aerated 10 mM $\text{Fe}(\text{NO}_3)_3$ /1 M H_2SO_4 as shown in the CV of Figure 12.15a. A large glassy carbon disk (e.g., 3-mm diameter) can be used as a substrate, with a typical CV in this solution shown in Figure 12.15b. In this CV, the oxidation of Fe^{2+} occurs at $E_S > 0.6 \text{ V}$ vs. Ag/AgCl. Thus, a good range of potentials to study this reaction is $0.6 \leq E_S \text{ vs. Ag/AgCl (V)} \leq 1.3$,

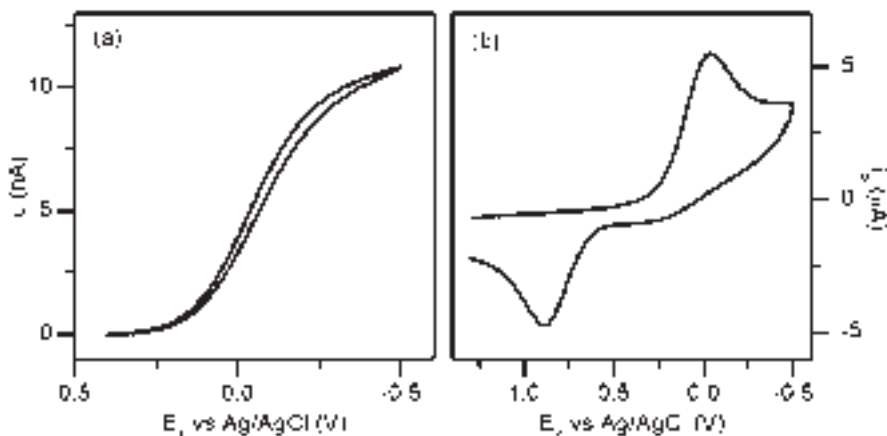


Figure 12.15 Typical cyclic voltammograms (CV) of (a) a carbon-fiber tip (10- μm diameter) and (b) a glassy carbon substrate disk (3-mm diameter) in deaerated 10 mM $\text{Fe}(\text{NO}_3)_3$ in 1 M H_2SO_4 . The steady-state reduction current and the reduction peak observed on the tip and disk CVs, respectively, correspond to the 1e^- reduction of Fe^{3+} to Fe^{2+} . The anodic peak observed on the disk CV comes from the 1e^- oxidation of surface-generated Fe^{2+} .

or $0.05 \leq \eta$ (V) ≤ 0.75 , where $\eta = E_s - E^\circ$. Reference and counter electrodes may be Ag/AgCl and a Pt wire, respectively.

The tip must be positioned at a tip–substrate distance $L \cong 5\text{--}8$ ($d \cong 25\text{--}40 \mu\text{m}$, $a = 5 \mu\text{m}$), from where the kinetic approach curves at different potentials will be measured. The tip can be positioned using a positive-feedback approach curve (see Section 12.3.1) by applying a sufficiently anodic potential to the substrate ($E_s = 1.4$ V vs. Ag/AgCl). When the tip is positioned at the initial place, approach curves at different substrate potentials in the range under study can be measured. For example, applying a substrate potential of 0.6 V vs. Ag/AgCl, the tip is approached at $1 \mu\text{m sec}^{-1}$ and stopped when a change in the slope is observed. After the data is stored, the tip is withdrawn the approached distance, the electrode potential is changed to the next value (e.g., 0.7 V), and a new approach curve is measured. This procedure is repeated to scan the complete desired range of substrate potentials.

Fitting of the curves with equation (12.4.1) involves finding the offset distance (d_o) and the value of κ simultaneously. The value of d_o will affect the conversion of the experimental i_T vs. d_{exp} curve into the normalized curve I vs. L (see Section 12.3.1) that will be correlated with equation (12.4.1). A strategy to perform this operation is to plot equation (12.4.1) for different values of κ , and try to overlap the experimental I vs. L curve to one of these curves by manually changing the value of d_o . Once a good estimation of d_o is obtained, it is possible to perform a fine analytical fitting to find a more accurate value of κ . Figure 12.16 shows a family of approach curves measured for the electro-oxidation of Fe^{2+} to Fe^{3+} on glassy carbon (equation (12.4.7)) at different potentials, correlated with

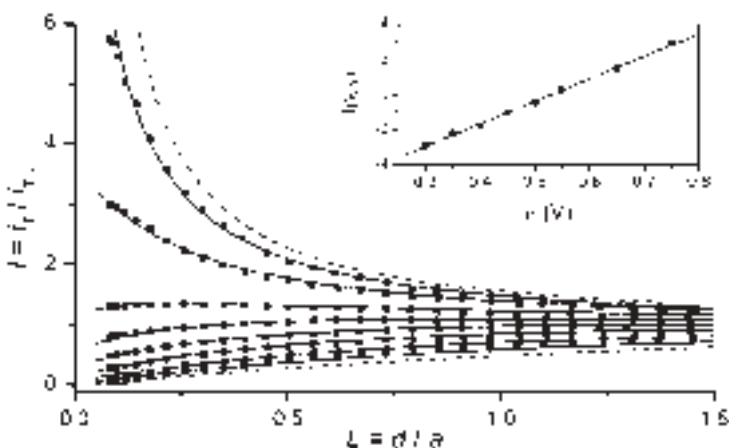


Figure 12.16 Experimental approach curves (■) for the $\text{Fe}^{2+}/\text{Fe}^{3+}$ oxidation reaction measured on glassy carbon. The tip (10- μm diameter carbon fiber disk, RG $\cong 10$) was held at a potential of -0.5 V vs. Ag/AgCl while the substrate was held at various potentials from $\eta = 0.3$ V to $\eta = 0.75$ V from bottom to top. Solid lines are the best fittings using equation 12.4.1 for the rate constant values plotted in the inset graph as a function of η (●). Dashed lines are negative and positive feedback approach curves. Linear fit of $\ln(\kappa)$ vs. η (solid line in inset graph) gives an intercept value $\ln(k^0 a/D) = -6.1$ and a Tafel slope $RT/[(1 - \alpha)nF] = 81$ mV/dec, parameters that lead to a standard rate constant $k^0 = 2 \times 10^{-5} \text{ cm sec}^{-1}$ and a transfer coefficient $\alpha = 0.7$.

equation (12.4.1) for different values of κ . Then, by plotting $\ln(\kappa)$ vs. η (Tafel plot), it is possible to calculate kinetic parameters, such as the Tafel slope and standard rate constant, as shown in the inset of Figure 12.16. Several electrode reactions, such as oxygen reduction (74), hydrogen oxidation (75–77), electron-transfer reactions across liquid/liquid interfaces (78, 79) and on semiconductor thin films (80), and heterogeneous catalyzed reactions (81, 82) have been studied with this procedure.

12.4.2 Homogeneous chemical reactions

SECM is also useful for studying short-lived electrogenerated intermediates and determining the rate of a homogeneous reaction coupled to an electron-transfer reaction at an electrode. In this case, the small volume between the tip and substrate can be considered as a tiny electrochemical cell. The transient time by diffusion between the tip and substrate is $d^2/2D$. Thus, with $d = 0.1 \mu\text{m}$, this time is $\sim 10 \mu\text{sec}$. This represents the approximate half-life of electrogenerated species that can be detected in this arrangement. For a first-order homogeneous reaction following electron transfer (ET), this allows measurement of rate constants on the order of 10^5 sec^{-1} , while for second-order reactions with reactant concentrations of 1 mM, rate constants on the order of $10^8 \text{ M}^{-1} \text{ s}^{-1}$ are attainable. The application of SECM for studies of homogeneous chemical reactions has been discussed in detail in Chapter 7 of reference (1). It is beyond the scope of this section to provide a detailed description of the mechanics of the numerical methods that have been used to treat the general SECM problems involving coupled homogeneous kinetics. Instead, we focus on two cases for more detailed descriptions.

SECM theory has been developed for the following processes involving homogeneous chemical reactions coupled to ET: a first-order irreversible reaction (E_rC_i mechanism) (50, 83), a second-order irreversible dimerization (E_rC_{2i} mechanism) (53, 84) and ECE/DISP processes (85). If both heterogeneous processes at the tip and substrate electrodes are rapid (at extreme potentials of both working electrodes) and the chemical reaction (rate constant, k_c) is irreversible, the SECM response is a function of a single kinetic parameter $\kappa = \text{const } k_c/D$, and its value can be extracted from I_T vs. L dependencies. In the first two cases, the system of differential equations was solved numerically using the alternating-direction implicit (ADI) finite-difference method. The theory was presented in the form of two-parameter families of working curves. These curves represent steady-state tip current or CE as functions of κ and L . We present here some generalizations of the theory, along with analytical approximations for the working curves. To understand this approach, we first consider a positive feedback situation with a simple redox mediator without homogeneous chemistry involved and with both tip and substrate processes under diffusion control. The total normalized steady-state tip current, given by equation (12.3.2), can be represented as the sum of two terms:

$$I_T = I_f + I_T^{\text{ins}} \quad (12.4.8)$$

where I_f is the normalized feedback current coming only from the substrate and I_T^{ins} is the normalized current due to the hindered diffusion of the electroactive species to the tip from

the bulk of solution, which is the tip current observed under the “negative feedback” situation and is given by equation (12.3.1). The substrate current is

$$I_S = I_f + I_d \quad (12.4.9)$$

where I_d is the dissipation current (i.e., the current due to the flux of species not reaching the tip). It was shown that I_S/I_T is more than 0.99 at $0 < L \leq 2$ (i.e., for any L within this interval the tip and substrate currents are essentially equal to each other) (53). Thus,

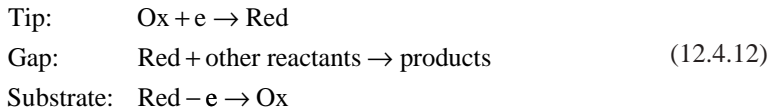
$$I_d = I_T^{\text{ins}} \quad (12.4.10)$$

and

$$I_d / I_S = I_T^{\text{ins}} / I_T = f(L) \quad (12.4.11)$$

where $f(L)$ can be computed for any L from equations (12.3.1) and (12.3.2).

For an electrochemical process followed by an irreversible homogeneous reaction of any order,



One can write

$$I'_T = I'_f + I_T^{\text{ins}'} \quad (12.4.13)$$

$$I'_S = I'_f + I'_d \quad (12.4.14)$$

$I_T^{\text{ins}'}$ is not affected by the occurrence of the homogeneous reaction in equation (12.4.12). Thus, $I_T^{\text{ins}'} = I_T^{\text{ins}}$. As the species O are stable, the fraction of these species arriving at the tip is also not affected by the homogeneous reaction in equation (12.4.12), the relation $I'_d / I'_S = f(L)$ still holds. Thus,

$$\begin{aligned} I'_T &= I_T^{\text{ins}'} + I'_S = I'_d \\ &= I_T^{\text{ins}} + I'_S[1 - f(L)] \end{aligned} \quad (12.4.15)$$

That is, for an SECM process with an irreversible following homogeneous chemical reaction of any order, a plot of I'_T vs. I'_S should be linear with a slope equal to $1 - f(L)$ and an intercept equal to I_T^{ins} . Thus, the TG/SC mode of the SECM for these mechanisms is equivalent to the feedback mode and any quantity, I'_T , I'_S , or the CE, I'_T / I'_S , can be calculated from equation (12.4.15) for a given L if any other of these quantities is known.

For mechanisms with following irreversible reactions, one can expect the CE to be a function of a single kinetic parameter, κ . If this parameter is known, the SECM theory for this mechanism can be reduced to a single working curve.

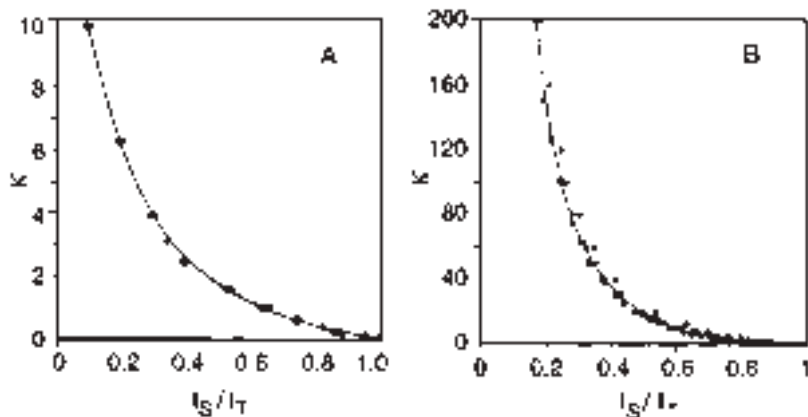


Figure 12.17 Kinetic parameter κ as a function of the collection efficiency (CE) (I'_S/I'_T). (A) E_rC_i mechanism; $\kappa = k_c d^2/D$, solid line was computed from equation (12.4.16), triangles are simulated data from reference (83). (B) E_rC_{2i} mechanism; $\kappa = C^* k_c d^3/aD$, solid line was computed from equation 12.4.17, squares are simulated data from reference (53). (Adapted from reference (84b).)

One has $\kappa = k_c d^2/D$ for an E_rC_i mechanism (83) and $\kappa = k_c d^3 C^*/(aD)$ for an E_rC_{2i} mechanism (53). Figure 12.17A shows the working curve, κ vs. the CE, along with the simulated data for an E_rC_i mechanism. The numerical results fit the analytical approximation (83):

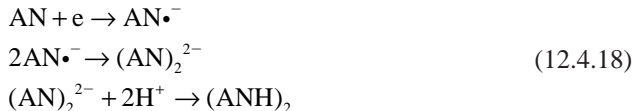
$$\kappa = 5.608 + 9.347 \exp(-7.527x) - 7.616 \exp(-0.307/x) \quad (12.4.16)$$

in which $x = I'_S/I'_T$, within about 1% (84b). For the E_rC_{2i} mechanism, the simulated data can be fitted to (53):

$$\kappa = 104.87 - 9.948x - 185.89/\sqrt{x} + 90.199/x + 9.389/x^2 \quad (12.4.17)$$

with an accuracy of ~5–10%, provided $0.3 \leq x \leq 0.9$ (84b). The invariability of k_c computed from experimental points would assure the validity of the results.

To illustrate this technique, consider the dimerization of the acrylonitrile anion radical ($AN\cdot^-$) in DMF (84a). As shown in Figure 12.18A, the proposed reaction mechanism, an E_rC_{2i} , is



As shown in Figure 12.18B, the voltammogram for the reduction of AN in a DMF/0.1 M TBAPF₆ solution at a gold tip ($a = 2.5 \mu\text{m}$) shows a reduction wave at -2.0 V vs. a silver quasi-reference electrode (AgQRE). The tip-generated species, $AN\cdot^-$, is so unstable that when tip is far away from the Au substrate (60-μm diameter), no oxidation current

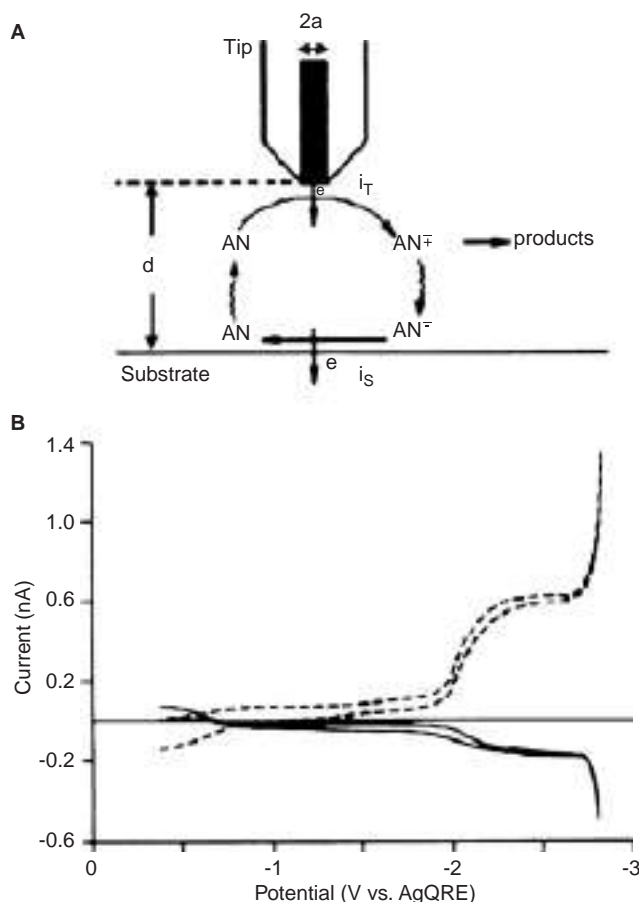


Figure 12.18 SECM TG/SC voltammograms. (A) The tip ($a = 2.5 \mu\text{m}$) was spaced $\sim 1.4 \mu\text{m}$ from a $60\text{-}\mu\text{m}$ diameter gold electrode held at a potential of -1.75 V vs. a silver QRE (AgQRE). (B) The tip potential was scanned at 100 mV sec^{-1} to produce a voltammogram (dashed line) for the reduction of acrylonitrile, AN (1.5 mM) in 0.1 M TBAPF_6 . The substrate current (solid line) shows the oxidation of the radical anion of AN generated at the tip. (Adapted from reference (84a).)

above the background current at the substrate was detected. However, when the tip is close ($\sim 1.5 \mu\text{m}$) to the substrate, held at a potential of -1.75 V vs. AgQRE, where AN^\bullet^- is oxidized, one sees a wave for the oxidation of the radical anion as the tip is scanned through the reduction wave (see Figure 12.18B). By studying the dependence of the CE on d , the rate constant of reaction (12.4.18) was found to be $6 \times 10^7 \text{ M}^{-1}\text{s}^{-1}$.

It is also possible to carry out SG/TC experiments. However, this approach to studies of homogeneous kinetics is less straightforward, since the usually larger substrate electrode does not attain a steady-state condition and also the CE for this case, is much less than unity, even in the absence of a homogeneous kinetic complication (50). However, this mode has been used to study concentration profiles above a substrate (86). SECM has also

been used to investigate more complex chemical reactions sandwiched between successive ETs, as in ECE/DISP scheme (85) discussed in Chapter 7 of reference (1).

12.4.3 Catalytic activity

12.4.3.1 Imaging of catalytic activity by G/C modes

In previous sections, it was shown that the SECM feedback response is highly sensitive to the intrinsic activity of the substrate material for the evaluated reaction. This fact allows one to perform kinetic studies of reactions and to determine reaction rate constants, via analysis of approach curves on varied types of materials. In Section 12.3.3, it was shown that it is also possible to image the chemical activity of heterogeneous surfaces using the sensitivity of tip current to reaction rate. Two main drawbacks of the feedback-based methodology restrict its applicability to a narrow region of conditions. The first one, which was already discussed in Section 12.3.1, is the necessity of using low mediator concentration to observe the feedback effect. The second and also important for activity imaging is the simultaneous dependence of current on activity and tip–substrate distance. Thus, to obtain SECM images that reflect only the activity of the material free of morphological effects, the catalytic surfaces must be very smooth. Moreover, the tilt of the sample, which is important when large areas are imaged, should be carefully controlled.

It was pointed out that other SECM configurations, such as the G/C modes, allow one to address systems and conditions that are inaccessible by using the feedback mode. In Section 12.3.1.3, the G/C modes were described, but very little was said about their imaging capabilities. In fact, these modes are very convenient for imaging catalytic activity of various surfaces. They have the important advantages that they are insensitive to morphological effects and are independent of feedback restrictions. The imaging abilities of these modes are discussed below, mainly focusing on their capacity to image electro-catalytic activity.

12.4.3.2 Imaging by substrate generation/tip collection mode

In this mode, the tip behaves as a passive sensor probing the concentration profile of the product of a process occurring at the substrate. The imaging capability of this mode was mainly exploited to image activity of biological materials (microorganisms, enzymes) (45, 87, 88), corrosion (89) and transport processes across membranes (Chapter 9 of reference (1)). It can also be used to image the concentration profile of oxygen photosynthetically generated from plant leaves (90) and that of electro-generated (or consumed) species at a substrate array of microelectrodes (46), as it was recently done by Zoski *et al.* to establish the quality of individually addressable electrodes (41). In that work, the rate of the reaction studied (oxidation of ferrocenemethanol) was mainly defined by the quality of each individual microelectrode, although it may be dependent on the nature of the electrode if a material-sensitive reaction is imaged. This is, for example, the case of hydrogen evolution reaction (HER) in acidic medium, which can be studied at low overpotentials (η) by this method as illustrated in Figure 12.19a. The substrate is held at a potential to reduce H^+ to H_2 at a value sufficiently small to avoid bubble formation, and the tip is

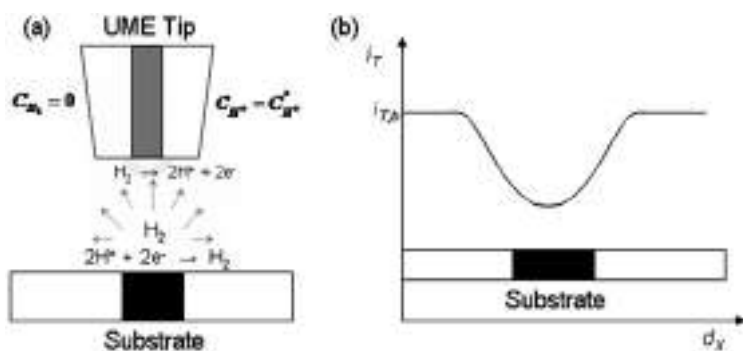


Figure 12.19 (a) Scheme of the SG/TC mode for imaging activity of catalyst spots for the HER. (b) Expected behavior of the tip current during a SG/TC long-direction scan over a catalyst spot when imaging the activity for the HER.

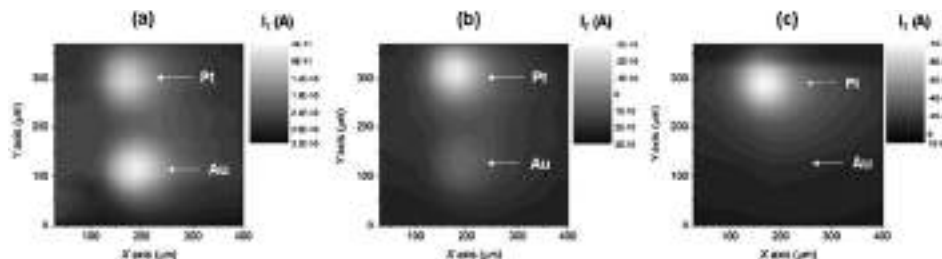


Figure 12.20 SG/TC images of activity for the HER obtained using a 25- μm Pt tip as an amperometric probe of the H_2 concentration profile ($E_T = 0.2$ V vs. HRE), over a substrate containing 100- μm diameter Pt (top) and Au (bottom) disks polarized simultaneously at -0.005 (a), -0.025 (b), and -0.065 (c) V vs. HRE. Solution: 0.5 M H_2SO_4 . The tip current scale can be read at the top right corner of each graph.

held at a potential where the substrate-generated H_2 is oxidized back to H^+ . As the reaction at the tip is diffusion controlled, the tip current is proportional to the concentration of H_2 . In contrast, the concentration profile of H_2 around the substrate disk is a function of its electrocatalytic activity for HER. Thus, the mapping of this profile using the tip current provides a visual image of the activity of the substrate material for this reaction. Although the concentration profile changes in time, it reaches quasi-steady-state hemispherical diffusion in a short time if the substrate electrode is sufficiently small. The expected behavior of the tip current during the long-direction (X) scan is shown in Figure 12.19b. An anodic contribution (negative current) is added to the background tip current during the oxidation of the substrate-generated H_2 . Successive long-direction scans at varied positions in Y generate an image of the H_2 concentration profile.

As an example, Figure 12.20 shows the SG/TC images of activity for the HER of a substrate consisting of two 100- μm diameter disks, one Au (bottom) and the other Pt (top), polarized both simultaneously at three different potentials. At the lowest overpotential

($\eta = 0.005$ V), both metals look poorly active, which is verified by the low tip current. When η increases to 0.025 V, it is seen that the activity increases much faster on Pt than on Au (due to a larger Tafel slope), evidenced by a higher concentration of H₂ around the Pt disk. At $\eta = 0.065$ V, the activity of Pt is so high compared with Au that it is only possible to see the Pt response. At higher η , H₂ bubbles are formed on Pt, warping the concentration profile.

12.4.3.3 Imaging by tip generation/substrate collection mode

This mode has rarely been used for imaging purposes (91) until recently, when a constant tip current was used to generate a constant flux of reactant (54). Two important facts are highlighted: very high scan rate (up to 600 $\mu\text{m sec}^{-1}$) and large tip–substrate distance (up to 50 μm). The effects of these two variables are much less pronounced for this case than for the feedback images. This TG/SC mode was used to image the activity of different materials for the ORR in acidic medium performing as shown in Figure 12.21a. The approach is also valid for other reactions, such as hydrogen oxidation. The substrate potential is held at a potential where oxygen is reduced to water. As the solution initially contains no oxygen, the substrate current is negligible. When a tip is placed close to the substrate and a constant oxidation current is applied to the tip, water is oxidized to oxygen on the UME and a constant flow of oxygen is generated at the tip. The tip current must be sufficiently small to prevent the saturation of the solution by oxygen and the subsequent formation of bubbles. When oxygen reaches the substrate surface, it is reduced at a reaction rate that depends on the substrate potential and its electrocatalytic activity. The substrate current is governed by the flow of oxygen from the UME tip, reacting at the substrate and being lost by lateral diffusion toward the bulk solution (54). The expected behavior of the substrate current in a long-direction (X) scan is shown in Figure 12.21b. In this case, a reduction current (positive) is added to the background current when the substrate reduces the tip-generated oxygen. Successive scans at different positions in Y recording the substrate current produce an image of the substrate material activity for the ORR.

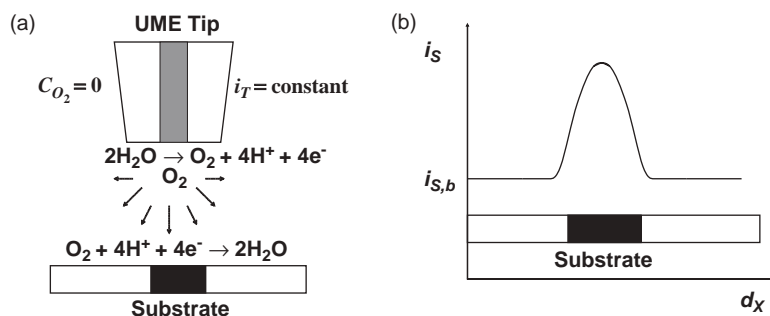


Figure 12.21 (a) Scheme of the TG/SC mode for imaging activity of catalyst spots for the ORR in acidic medium. (b) Expected behavior of the substrate current during a TG/SC long-direction scan over a catalyst spot when imaging the activity for the ORR.

12.4.3.4 Activity screening of electrocatalysts

There is a recent interest in rapid electrochemical techniques that are able to provide information about activity of a large number of electrode materials in a short period of time (92). At present, the most popular methods capable of rapid screening of electrode activity include fluorescent techniques (93) and individually addressable arrays of electrodes (94). As a technique for chemical activity imaging, SECM was applied to characterize systems in sub-micrometer ranges in varied areas including catalysis, corrosion, and microbiology. This ability was only recently exploited to analyze electrode reactions of interest in electrocatalysis, when Bard *et al.* and Hillier *et al.* addressed the study of hydrogen oxidation (75, 76) and oxygen reduction (74) by feedback SECM. After that, Hillier *et al.* (95, 96) used feedback SECM to screen the activity of arrays of individually addressable binary Pt–Ru and ternary Pt–Ru–Mo band electrodes for hydrogen oxidation. That was done by scanning a Pt tip over a 20-mm length array of catalytic bands, using the couple H^+/H_2 as mediator (Figure 12.22). In this study, it was rapidly demonstrated that Pt–Ru (10–50% Ru) and importantly Pt–Ru–Mo (10–25% Mo) mixtures present low overpotentials for hydrogen oxidation in the presence of CO.

Particle size effects of highly dispersed supported catalysts (Pt) on the hydrogen oxidation reaction were evaluated by the same authors using this technique (97). Moreover, electrocatalysts for oxidation of methanol were screened using a technique called scanning differential electrochemical mass spectrometry (98, 99). This method uses a capillary probe scanned over the array that allows the intake and detection by mass spectrometry of products generated locally on each electrode.

Bard *et al.* are using SECM in G/C mode to screen the activity of binary and ternary metallic arrays for electro-reduction of oxygen (54, 100, 101). They used the TG/SC described in Section 12.4.3.1 to image the activity of both multi-metallic and ‘wired’ enzyme catalyst spots deposited on single glassy carbon substrates (Figures 12.23 and 12.24). Different from the previous approach, the spots do not need to be individually connected

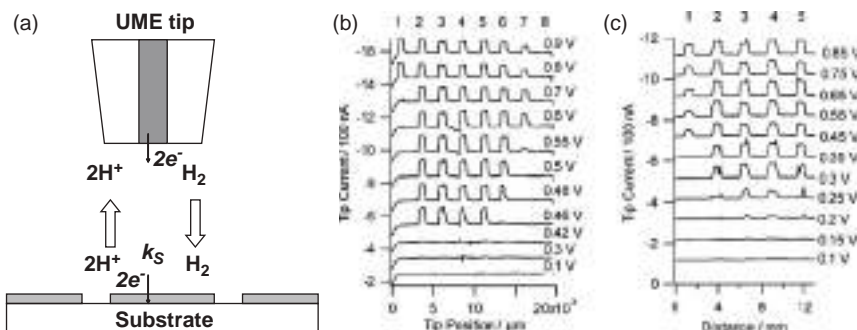


Figure 12.22 (a) Schematic of the SECM feedback mode using the H^+/H_2 couple to image activity of catalyst arrays for hydrogen oxidation. SECM scans over CO-poisoned Pt–Ru (b) and Pt–Ru–Mo (c) band electrodes in 10 mM H_2SO_4 –0.1 M Na_2SO_4 , at a tip–substrate distance of 15 μm . The tip was held at -1.0 V vs. HRE to reduce H^+ under diffusion control. (Adapted from reference (96).)

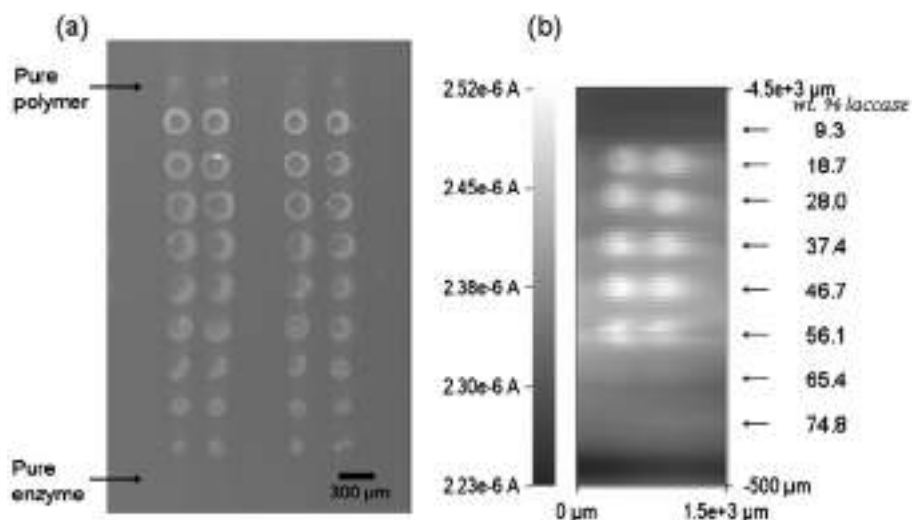


Figure 12.23 (a) SEM photograph of two arrays of ‘wired’ laccase containing different compositions of enzyme and polymer (PAA-PVI-[Os(tpy)(dme-bpy)Cl]^{1+/2+}). (b) TG/SC SECM image of activity for the ORR obtained on one of the arrays shown in (a) polarized at 0.4 V vs. Ag/AgCl using a tip current of -240 nA and a scan rate of $300\text{ }\mu\text{m sec}^{-1}$. The most active spot composition is observed at a wt.% laccase = 46.7.

as the O_2 -generating tip addresses each spot at a time. With this technique, the optimization of the composition of “wired” enzymes used as O_2 -cathodes in biofuel cells was performed in one single experiment, as shown in Figure 12.23 (101).

Furthermore, using this method on bi- and trimetallic catalysts it was found that Pd–Co and Pd–Co–Au electrodes (10–20% Co) present much lower overpotential for the ORR when compared with the pure components, as shown in the images of Figure 12.24 (100). This fact was further verified on rotating disk electrodes of these combinations. With the idea of making this methodology useful for a wider variety of reactions, efforts to replace the reactant-generating tip by a micropipette dispenser tip are being pursued (29). This tip would allow small volumes (a few pLs) of reactant solution to be dispensed locally on a substrate with the simultaneous monitoring of the substrate current.

12.4.4 Surface reactivity

12.4.4.1 Electron transfer on self-assembled monolayers

Understanding and controlling charge transport through molecular films of nanometer thickness is important in several areas including molecular electronics and elucidating ion and electron transport mechanisms through membranes involved in biological systems (102, 103). Self-assembled monolayers (SAMs) of organic molecules have been widely used as the model systems in this type of study. The easy preparation, high stability, and

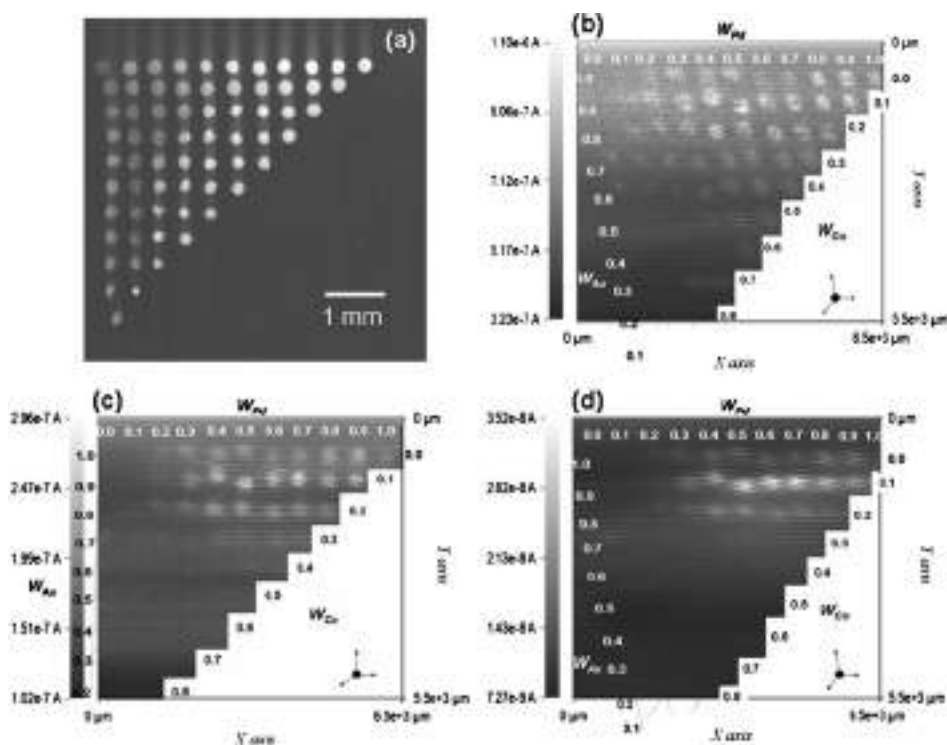


Figure 12.24 (a) SEM photograph of a Pd–Au–Co ternary array. Top left corner is pure Au, top right is pure Pd and bottom left is Co. (b)–(d) SECM TG/SC images of oxygen reduction activity measured on Pd–Au–Co arrays in 0.5 M H_2SO_4 . Tip–substrate distance: 30 μm , tip current = –160 nA, scan rate = 50 μm each 0.2 sec, E_S = 0.4 V (b), 0.6 V (c), and 0.75 V (d) vs. HRE. W_M is the atomic ratio of metal M in the spot.

the almost unlimited possibility of introducing functional groups in the monolayer make SAMs suitable models for investigating charge transport across molecular films (104).

SECM has been used for the studies of ET through monolayers supported at solid/liquid (105, 106), liquid/liquid (107–109) and air/water interfaces (110). In the case of a solid/liquid interface, the rates of ET mediated by monolayer-attached redox moieties and direct ET through the film as well as the rate of a bimolecular ET reaction between the attached and dissolved redox species have been measured using SECM (105). The monolayer may contain redox centers (Figure 12.25a) or simply act as a blocking layer (Figure 12.25b).

In Figure 12.25a, ET occurs via a bimolecular reaction between a dissolved redox species generated at the tip (R) and redox centers attached to the SAM (M^+) followed by the electron tunneling; while in Figure 12.25b, it occurs by direct tunneling between the dissolved species, R , and the electrode. Finally, the charge transfer may occur through pinhole defects in the film. A theoretical model has been developed attempting to independently measure the rates of all of these processes (105). According to the model, provided an appropriate mediator is used and the mediator concentration is high such that the bimolecular ET is

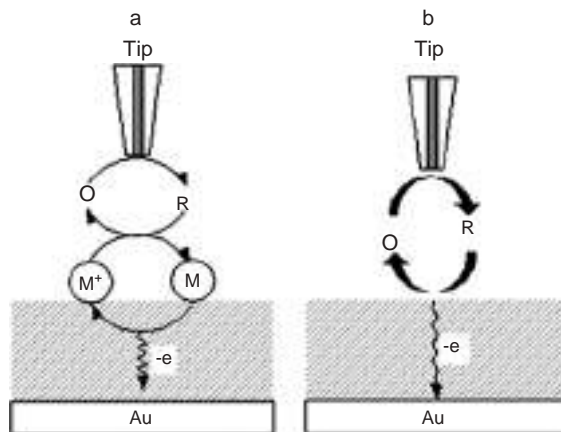


Figure 12.25 Schematic view of the processes involved in the SECM measurements of ET across an electroactive SAM. (a) Mediated ET; (b) direct electron tunneling through monolayer. M and M^+ represent the reduced and oxidized forms of the monolayer bound redox moieties, respectively.

much faster than the ET through the monolayer, the rate constant of electron tunneling through the monolayer, k_b , is determined by equation (12.4.19):

$$k_b \approx k_{\text{eff}} C^*/\Gamma^* \quad (12.4.19)$$

where C^* is the bulk concentration of the redox mediator in solution, Γ^* is the surface coverage of the monolayer-bound redox centers, and k_{eff} is the effective rate constant obtained by fitting an experimental SECM approach curve to SECM theory.

When the tip is very close to the substrate, i.e., $L \ll 1$, L is the normalized tip–substrate distance ($L = d/a$, where d is the distance between the tip and the substrate and a is the tip radius), the mass transfer coefficient $m_o \sim D/d$, where D is the diffusion coefficient, and the upper limit for measurable k_{eff} is $\sim 5m_o = 5D/d$ (1). The tip can be brought down to an $L \approx 0.1$. Thus, for a 1- μm radius tip, $d = 10^{-5}$ cm. Assuming a typical diffusion coefficient $D = 10^{-5} \text{ cm}^2 \text{ sec}^{-1}$, $\Gamma^* \sim 10^{-11} \text{ mol cm}^{-2}$ and $C^* = 2 \times 10^{-4} \text{ mol cm}^{-3}$, the upper limit for measurable k_b is $\sim 10^8 \text{ sec}^{-1}$, calculated using equation (12.4.19). If a nanometer-sized tip is used, a faster ET can be measured.

In contrast, if the bimolecular ET is slow compared with a electron tunneling reaction, and/or the concentration of the redox mediator in solution is low, the following equation holds:

$$k_{\text{Ox}} \approx k_{\text{eff}} (k_b + k_f) / k_b \Gamma^* \quad (12.4.20)$$

where k_{Ox} is the bimolecular ET rate constant ($\text{mol}^{-1} \text{ cm}^3 \text{ sec}^{-1}$), k_b and k_f are backward and forward electron tunneling rate constants (sec^{-1}), respectively. Thus, the bimolecular rate constant for ET between the monolayer-bound and dissolved redox species can be determined based on equation (12.4.20). For a 1- μm radius tip, the upper limit for measurable k_{Ox} is $10^{11} \text{ mol}^{-1} \text{ cm}^3 \text{ sec}^{-1}$ (or $10^8 \text{ M}^{-1} \text{ sec}^{-1}$).

If the redox mediator is a hydrophobic species, the ET at the monolayer or bilayer modified electrodes may not occur by tunneling, but rather by diffusion through the pinholes with ET at the free sites of the electrode. This was confirmed by SECM studies of ET reactions of ferrocenemethanol at tetradecanethiol SAMs on the gold surface and at the bilayer formed by phospholipid adsorption on the first tetradecanethiol layer (106).

The quantitative SECM measurements of the heterogeneous ET at SAM modified electrodes also allows one to study the kinetics of SAMs formation on an electrode and to estimate the surface coverage and the average size of the defects in the monolayer film. For example, SECM, chronoamperometric, and cyclic voltammetric measurements suggested that the surface coverage is > 99.3 and > 99.9% for C₁₄SH and C₁₈SH monolayer, respectively (106, 111) and the defects in the C₁₈SH film are smaller than 0.5 μm (111).

SECM was also used to study kinetics of heterogeneous ET across a monolayer of lipid adsorbed at the interface between two immiscible electrolyte solutions (107–109). The adsorption of phospholipids at the interface significantly decreases the rate of interfacial ET between two redox couples (one in each phase). The fraction of the interfacial area covered with lipid can be evaluated from the measured heterogeneous rate constants (k_f). The driving force dependencies of interfacial ET rates were linear, with a transfer coefficient of $\alpha = 0.5$ when the driving force for ET (ΔG°) was not too high and leveled off to the diffusion-controlled rate at larger overpotentials. For even higher ΔG° , inverted region behavior was observed, as expected from Marcus theory (107). The rate of ET decreased with the number of methylene groups in the hydrocarbon chain of adsorbed lipid suggesting that the ET reaction does not occur at defect sites in the lipid monolayer. For the monolayer consisting of two different types of lipids (e.g., phospholipids with saturated and polyconjugated hydrocarbon chains), the observed ET rate was at least two times faster through films with conjugated chains compared with those with saturated chains (108). SECM imaging of the lipid monolayer at the liquid/liquid interface also revealed the formation of micrometer-sized domains in the monolayer (108, 109).

12.4.4.2 Corrosion and passivation

SECM is ideally suited to investigating corrosion processes as the probe UME can be used to simultaneously initiate ET reactions at the phase boundary and to monitor the response. The capability of imaging with high spatial resolution enables SECM to be a powerful tool to study the structure–activity relationship. It is especially advantageous that SECM can be used in solution under exactly the same conditions at which metal corrodes. To date, SECM has been successfully used to study the corrosion of metals and alloys, such as steel, Fe, Ti, Al, Ta, and Sn (89, 112). Some important issues, such as identifying pitting precursor sites, probing the kinetics of oxide growth and breakdown, and mapping the electronic properties of oxide films have been addressed using SECM.

Both feedback and SG/TC modes of SECM can be used to spatially resolve the electroactive sites on the metal, as illustrated schematically in Figure 12.26. In the feedback mode (Figure 12.26A), the metal substrate is bathed in a solution containing a redox mediator, R. A UME tip, poised at a potential to oxidize R at a diffusion-controlled rate, is brought close to the substrate and scanned over the substrate surface. The substrate is poised at a potential such that the tip-generated species, O, is reduced back to R at the electroactive sites.

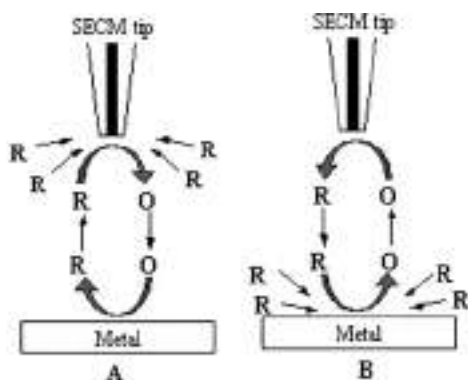


Figure 12.26 SECM feedback (A) and substrate generation/tip collection (B) mode used in the corrosion study.

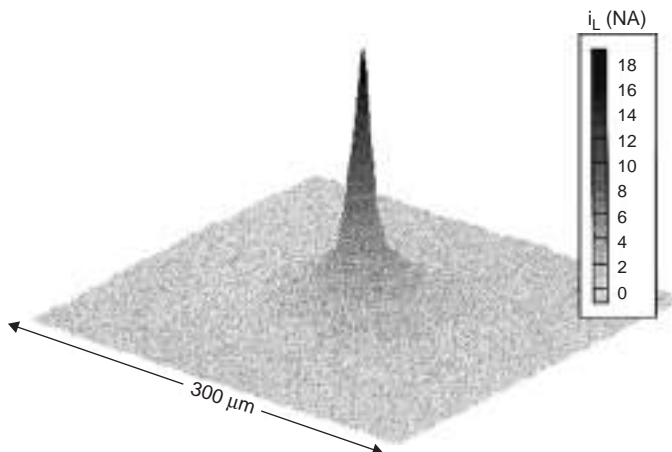


Figure 12.27 A $300 \mu\text{m} \times 300 \mu\text{m}$ SECM image of an electroactive site on Ti/TiO₂ surface obtained in a solution containing 50 mM KBr and 10 mM H₂SO₄. (Adapted from reference (89).)

The tip current is recorded as a function of the tip position in the x, y plane. When the tip scans above electroactive sites, higher tip currents will be observed because positive feedback occurs at these sites. Thus, SECM mapping of the substrate surface should allow one to identify electroactive sites on the metal surface. The feedback mode has been used to study the heterogeneous redox activity of aluminum alloys, such as AA2024. The SECM image showed locally high redox activity, which was attributed to second phase, intermetallic inclusions (112).

In the SG/TC mode (Figure 12.26B), the redox mediator, R, is oxidized at the electroactive sites on the substrate surface. A UME tip, brought close to the substrate and poised at a potential to reduce the substrate-generated O back to R, is scanned over the substrate surface. Thus, the areas of high electroactivity correspond to the increased cathodic tip current, measured as a function of tip position in the x, y plane. Figure 12.27 shows

a three-dimensional SECM image of an electroactive site on titanium surface obtained in the substrate generation/tip collection mode. The redox mediator used in the study was Br^- (89). Other redox mediators, such as $\text{Fe}(\text{CN})_6^{4-}$, I^- , $\text{Ru}(\text{NH}_3)_6^{3+}$, and nitrobenzene have also been used at the substrate generation/tip collection mode to map the electroactivity on steel and metal surfaces. Subsequent examination of the active sites by a range of techniques (energy dispersive X-ray analysis, SEM, and confocal laser microscopy) revealed that the active sites are usually associated with the location of impurity inclusions.

Localized corrosion usually involves change in pH and chloride ion concentration around corrosion pits. Therefore, potentiometric SECM tips can be used to study corrosion processes. When a pH microsensor was used as the SECM tip for the *in situ* measurements during localized corrosion of stainless steel, it was found that pH decreases at the pit initiation stage and increases during pit growth and repassivation (113).

Alternating current scanning electrochemical microscopy (AC-SECM) was recently used to detect precursor sites for localized corrosion on lacquered tinplates (114). AC-SECM utilizes the effect of an increasing (decreasing) solution resistance as the SECM tip approaches an insulator (conductor) for mapping domains of different conductivity/electrochemical activity on surfaces immersed in electrolytes. It was demonstrated that AC-SECM could be used to visualize microscopic cracks and holes in the coating of the lacquered tinplates.

A probe consisting of an optical fiber coated with gold was used as the SECM tip to image simultaneously the electrochemical and photoelectrochemical activity of pitting precursor sites on an oxide film (11b, 115) by combining SECM with scanning photoelectrochemical microscopy (116). It was found that the area of high electrochemical activity is correlated with lower substrate photocurrent in the area.

SECM was also used to initiate pitting on steel and aluminum and to examine the pit growth and corrosion products (112a, 112b). In these studies, the UME tip was used to generate aggressive Cl^- ions in close proximity to stainless steel and aluminum surfaces. The tip and substrate current were then monitored to detect corrosion events. Fluctuations in the tip and substrate current were observed, which were indicative of the breakdown of the passive film and pit initiation on the metal. SECM and CV measurements provided evidence that the large tip current fluctuations observed were caused by the reduction of Fe^{2+} , which was released from the iron surface in the breakdown of the passive film of iron.

12.4.5 Patterning

Due to the small size of the scanning tip, the versatility of tip material, and the various modes of operation, SECM has been used as a tool for the fabrication of microstructures on varieties of substrates. SECM microfabrication is based on tip-induced chemical and electrochemical reactions at the solid/liquid interfaces. So far, SECM has been used for depositing metals and other inorganic materials, etching metals and semiconductors, electropolymerizing conducting polymers, and forming patterns of organic and biomolecules (117, 118).

12.4.5.1 Metal deposition and etching

Metals such as gold, copper, silver, palladium, and cobalt may be deposited locally to form microstructures using SECM working in different modes (30, 119). In one of these modes,

the so-called direct mode, the tip, and the substrate are used as the working and counter electrodes, respectively. The electric field is focused between the tip and the substrate by bringing the tip in close proximity to the conductive substrate in a similar manner as STM. The electric field drives the electrochemical reactions at the tip and substrate, resulting in direct deposition or etching of metals. This mode requires that the tip should be very close to the substrate. To control the distance between the tip and the substrate, the substrate can be coated with a thin film of ionically conductive polymer. The tip is biased vs. the substrate. When the tip touches the polymer film, faradaic current passes through the film. The tip current is a function of the tip position in the polymer. A constant current is maintained using an electronic feedback loop to adjust the penetration of the tip into the polymer. Therefore, the tip–substrate distance can be controlled. One example of this mode is the deposition of metals in ionically conductive polymers, such as Nafion and poly(4-vinylpyridine) (119a, 119b). By changing the sign of the potential between the tip and the substrate, high-resolution deposition and etching of Au, Cu, and Ag were accomplished. The widths of the patterns were in the submicron range.

The feedback mode of SECM has also been used for metal deposition and etching. Etching via SECM feedback is straightforward, as shown in Figure 12.28. A UME tip, which is immersed in a solution containing a redox couple, e.g., $\text{Fe}(\text{phen})_3^{2+}$ (phen = 1,10-phenanthroline), is moved close to a substrate to be etched (Cu in this case). The potential of the UME is controlled so that the redox couple is oxidized at the tip at a diffusion-controlled rate. When the tip is far away (several tip diameters) from the substrate surface, a constant steady-state current is established within several seconds. However, as the tip is brought close to the substrate, i.e., within a few tip radii, an increase in the steady-state current (a positive feedback) is observed due to the regeneration of the redox mediator via ET reaction between the strong oxidant generated at the tip and Cu. As a result, copper dissolution occurs, which is limited to the diffusion range of the oxidized mediator. As the feedback current depends on the tip–substrate separation, the distance between the tip and the substrate can be determined and controlled by measuring the changes in the tip current. The resolution of the etched patterns is governed by the tip

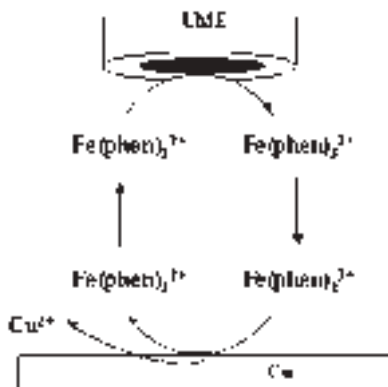


Figure 12.28 Principles of copper etching by the SECM in the feedback mode.

diameter and tip–substrate distance (120, 121). Other parameters affecting the etching size and shape include the concentration of the redox couple and the electrolysis time.

The species generated at the tip may drive the reduction of metal ions, resulting in deposition of the metal on the substrate. Gold (AuCl_4^-) and palladium (PdCl_4^{2-}) structures are fabricated in this way and incorporated into a polymer film. $\text{Ru}(\text{NH}_3)_6^{2+}$, generated at the tip through the reduction of $\text{Ru}(\text{NH}_3)_6^{3+}$, diffuses to the substrate and drives the reduction of AuCl_4^- and PdCl_4^{2-} to their respective metals (119c). In another example, deposition of silver on gold is accomplished by oxidizing nitrite at the tip to lower the pH in the tip–substrate gap and introduce dissociation of $\text{Ag}(\text{NH}_3)_2^+$ in the solution. The free Ag^+ ions are then reduced on a negatively biased gold surface (122).

Fine silver lines can also be formed on a nonconducting substrate like a AgCl film. In this case, hydroquinone generated at the tip diffuses to an AgCl film and reduces silver cations in the vicinity of the AgCl film to form silver patterns (123). Under appropriate conditions, the line width fell below the diameter of the tip used. The high resolution resulted from the reaction of free Ag^+ ions in solution with hydroquinone such that the hydroquinone flux is focused on the AgCl film surface. This system is an example of a “chemical lens” that focuses the flux of the reactive species on the substrate surface. In this example, Ag^+ ions act as the “focusing” agent.

Another approach to metal deposition involves formation of metal ions by anodic dissolution of a microelectrode made of the same metal to be deposited (119d–119f, 124). In one example, gold patterns were fabricated in this way on indium tin oxide (124). The Au UME was anodically dissolved in bromide-containing solution to form AuBr_4^- ions, which diffused to the negatively biased indium tin oxide substrate and were reduced to form micropatterns of Au.

12.4.5.2 Semiconductor etching

Similar to the metal etching, strong oxidants can be locally generated at the tip and used for etching semiconductors. One example is the etching of a GaAs wafer by tip-generated bromine (121). Bromine, generated through the oxidation of bromide at the tip, serves as an oxidant as well as the tip–substrate distance indicator, as the positive feedback is observed as the tip approaches the GaAs wafer. The parameters that affect the etching size and shape include the tip size, the distance between the tip and the substrate, and the electrolysis time. High-resolution etching of GaAs was also accomplished by the direct mode of SECM (125). Other semiconductors etched using SECM include CdTe, GaP, and Si. An interesting result from these studies was that while injection of holes into n-type semiconductors by tip-generated oxidants can effectively etch the semiconductor; injection of holes into p-type semiconductors does not lead to etching. The explanation given by the researchers is that while the injected charge can remain on the surface of n-type semiconductors leading to efficient etching, fast diffusion of the charge into the bulk of p-type semiconductors blocked the etching.

Etching resolution can be improved by using the confined etchant layer technique (CELT), which has been demonstrated by Tian and coworkers in their studies of silicon surface etching (126). The surface of silicon was etched by tip-generated bromine in a solution containing HBr. H_3AsO_3 was added into the etching solution to introduce a scavenging

reaction between H_3AsO_3 and bromine. The lateral diffusion of the etchant around the tip was suppressed by the scavenging reaction. As a result, etching pits on silicon matched closely to the tip size. This technique should be particularly useful for the slow surface etching.

12.4.5.3 Deposition of conducting polymers

Deposition of conducting polymers can be accomplished by either direct or feedback modes of SECM. In an earlier study, SECM was used to deposit polyaniline on a Pt substrate by scanning a UME tip in thin, ionically conductive Nafion films coated on the Pt surface (127). Anilinium ions were incorporated into Nafion films and the Pt substrate was biased positively, which caused the electropolymerization of aniline. The resolution of the polyaniline deposition is controlled by the tip size, the thickness of Nafion films, and the electric field distribution.

The electropolymerization of pyrrole was achieved on a gold substrate in aqueous solution (128). A potential pulse was applied to the gold substrate to obtain a high concentration of pyrrole radical cations and pyrrole oligomers within the tip–substrate gap, leading to a fast chain propagation reaction so that the chain length will reach the critical value for precipitation. Using a 10- μm diameter tip, the width of the polypyrrole lines were 50–60 μm . The aspect ratio of the microscopic deposits can be changed by controlling the tip–sample distance with an optical detection system independent from the electrochemical processes. A polypyrrole tower as high as 400 μm , with diameters of about 80 μm were fabricated (129) using this technique.

Polymerization can also be induced by the tip via an oxidation reaction. This working mode was demonstrated by Heinze and coworkers (122). The monomer 2,5-bis (1-methyl-pyrrol-2yl)-thiophene (NSN) was first deposited on ITO by thermal evaporation. The micropatterning was performed in an aqueous solution containing bromide. The tip oxidizes bromide to bromine, which diffuses to the surface and reacts with the monomer to form patterns of poly-NSN. The remaining monomers were removed by organic solvents. This technique can also be applied to nonconducting substrates.

The feedback mode was used to deposit polyaniline on gold, platinum, and carbon surfaces by applying a positive potential to the substrate and consuming protons at the tip to locally increase the pH in the gap between the tip and the substrate. The increased alkalinity shifts the oxidation potential of the monomer cathodically such that polymerization occurs at the substrate potential (130).

12.4.5.4 Patterning of biological molecules

SECM has been particularly promising for microfabrication and detection of biological molecules, mainly due to the mild patterning conditions and various modes of operation (see also Section 12.4.6.2.3). In contrast, conventional photolithographic techniques are usually limited due to the photoresists, organic solvents, and strong acids and bases that are necessary and are harmful to biological molecules.

Patterning of glucose oxidase was performed using a tip to electrochemically desorb alkanethiols from a SAM on a gold substrate (131). Cystamine was adsorbed on the exposed patterns of the gold surface and periodate-oxidized glucose oxidase was covalently

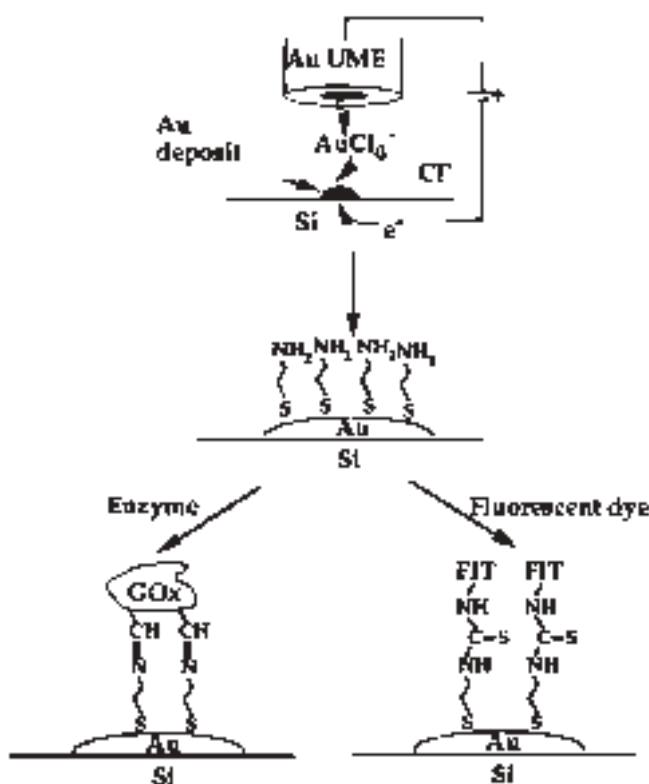


Figure 12.29 Schematic representation of the approach for attaching organic and biological molecules onto surfaces using the SECM. (Adapted from reference (132).)

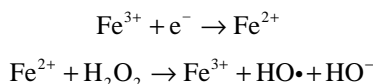
attached to the amino groups of cystamine. The enzyme activity was imaged by detection of hydrogen peroxide in the generation/collection mode.

In another method, gold patterns were deposited on silicon wafers with SECM as a result of the controlled anodic dissolution of a gold microelectrode, as described above (Section 12.4.5.1). The gold patterns were further used as microsubstrates for assembling cystamine monolayers to which either glucose oxidase or fluorescein isothiocyanate was immobilized (FIT) (Figure 12.29). The activity of the enzyme patterns was imaged using the SECM in the generation/collection mode (132).

Another approach to micropatterning of glucose oxidase is based on the fabrication of microstructures of conductive polymers (133). In this case, patterns of functionalized polypyrrole were formed on gold using the approach described above (Section 12.4.5.3). Glucose oxidase was then covalently immobilized to the polypyrrole through the reactions between the terminal amino groups of the deposited polymer and the aldehyde groups at the surface of periodate-oxidized glucose oxidase. The enzyme patterns were imaged using the enzyme-mediated positive feedback mode of SECM. The technique developed in this study could be used as a generic method for patterning of surfaces with organic and biological molecules, such as enzymes and proteins.

SECM was used for the fabrication of diaphorase-patterned surfaces (134). Diaphorase, a flavin enzyme, was immobilized on glass surfaces. The oxidation of Br^- or Cl^- at the tip generated a reactive species, which deactivated the enzyme molecules on glass forming unreactive patterns. The circular and linear patterns were then imaged by SECM based on the detection of catalytic current of ferrocenylmethanol coupled with oxidation of DADH.

Diaphorase patterns were also fabricated on the substrates immobilized with SAMs of different alkylsilane derivatives. A hydroxyl radical is generated at an SECM tip in a solution containing H_2O_2 and Fe^{3+} by Fenton's reaction:



The hydroxyl radicals react with the SAMs and locally change the chemical and physical properties of the monolayer surface. Diaphorase patterns are then formed on the substrates by physical adsorption onto the hydrophobic area or by chemical linkage to the hydroxyl radical-attacked area (Figure 12.30). Diaphorase activity can be visualized using SECM by detecting the diaphorase-catalyzed current of ferrocenylmethanol coupled with the oxidation of reduced nicotinamide adenine dinucleotide (135). The size of the hydroxyl-radical-attacked area, which determines the resolution of the enzyme patterns, is affected by different factors, including the tip size, the concentration of Fe^{3+} , and the potential pulse period for generation of the hydroxyl radical.

SECM has been used to attach biotin on the surface of a carbon electrode (136). In the direct-write mode, biotin hydrazide is oxidized at the SECM tip to generate a reactive species that attaches to the carbon surface. The biotinylated region reacts further with a fluorescent avidin and can be imaged with a fluorescence microscope. Controlling the tip and substrate potential is critical in the formation of biotin patterns. The distance between the tip and the substrate surface and the speed at which the probe tip is moved are other major factors that affect the formation and resolution of patterns. The SECM probe tip can also be used as an electrochemical "eraser" cleaning off the surface attached biotin and leaving clean spots on the surface of a globally derivatized carbon surface (136).

After biotin patterns are formed on the electrode surface, biotin/avidin chemistry can be used for selective attachment of avidin-labeled biomolecules. Thus, the technique based on simple micromodification of the surface of a carbon electrode will allow the fabrication of biosensors that can potentially be tailor-made for a variety of applications.

12.4.6 Biological applications

12.4.6.1 Introduction

SECM can be used to probe transport activity of biological systems, such as single cells, ion transport across channels, and enzyme activity. Experimentally, cells, enzymes, or ion channels are immobilized and a small size electrode (micron to nanometer size) is positioned a few microns above. By stimulating these samples with an oxidative stress agent (by the action of the substrate and cofactors, or by the presence of ions), biological

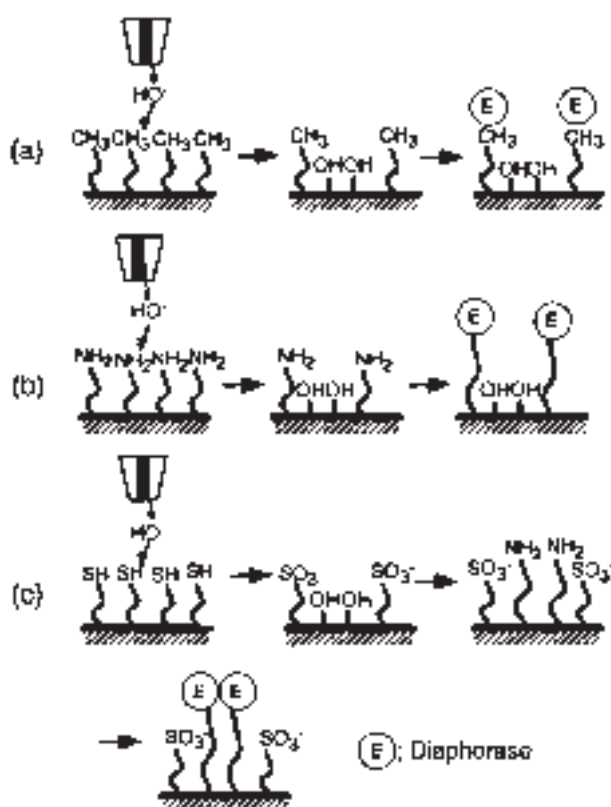


Figure 12.30 Schematic representation of micropatterning of diaphorase at SAM-immobilized glass surfaces by electrogenerated hydroxyl radicals. (a) Diaphorase is physically adsorbed onto the hydrophobic area. (b) Diaphorase is covalently bound to the unattacked area to give a negative pattern. (c) Diaphorase is covalently bound to the hydroxyl-radical-attacked area to give a positive pattern. (Adapted from reference (135).)

metabolites, enzyme catalytic activity, and ion transport can be studied using SECM. The molecules and ions released or regenerated diffuse to the nearby tip electrode where they are detected as a current. The rate of transport or kinetic information related to these transport events can be extracted from the measure current.

This section highlights biological applications of SECM with emphasis on experimental requirements, and the difficulties/limitations involved in applying SECM to biological systems. Specifically, enzymes, ion channels, and cellular systems are considered.

(a) Collection mode vs. feedback mode of SECM

When studying biological systems, one can choose between feedback and G/C (generation/collection) mode. In general, the negative feedback mode may be used to evaluate the tip-substrate distance as well as to locate biological samples based on changes in topography or blocking of a conductive layer by biofilms. Such measurements yield little information

concerning the biological activity of the substrate. Although negative feedback imaging has recently been used to image new growths emerging from PC12 dopamine releasing immortal rat cells (137), positive feedback and G/C measurements are the preferred SECM mode used in biological studies. G/C experiments use the tip electrode as a passive sensor that does not significantly perturb local concentrations. This differs from feedback experiments where the tip-generated species are actively involved in a surface reaction. As the G/C mode is independent of the substrate process, it is very flexible and different selective tips, such as amperometric, enzyme-modified, or ion-selective electrodes can be used. The quantitative characterization of this mode is often done using numerical simulations or through the development of experimentally specific models that do not reach the level of generality or ease of applicability that the feedback treatments have attained. In fact, G/C experiments often rely on independent feedback measurements for the evaluation of distances by using passive mediators or dual-barrel electrodes (138).

G/C experiments are governed by the uncontrolled mass transport of the biological specimen because, unlike the feedback experiment, they do not localize the reaction under the electrode. This implies that feedback experiments benefit from better lateral resolution and are more suited for imaging experiments. However, the G/C mode can detect lower analyte concentrations than the feedback mode because it does not have a significant background current coming from the dissolved mediator in solution. If, for example, the minimum catalytic rate, k_{cat} , of immobilized enzymes measured in the G/C mode was compared with that of the feedback mode, the G/C experiments could measure a k_{cat} three orders of magnitude faster than that obtained via the feedback study (139). When deciding on which SECM mode to use in a biological experiment, the importance of imaging resolution against detection limits should be weighed.

12.4.6.2 Enzymatic systems

(a) Equipment and handling requirements

Enzymes are robust biological systems. They can be stored in the refrigerator or in the freezer for extended periods of time. Their activity under homogenous or immobilized conditions can be measured spectroscopically and electrochemically (140–142). There are no special equipment needs for SECM studies as the solid support modification is often done on electrodes or glass slides that can easily be combined with a conventional SECM setup. Most of the equipment needs are related to the patterning or immobilization of the enzymes onto solid supports.

(b) Enzyme systems

There is considerable literature where SECM has been used in enzymatic studies (139). Table 12.3 outlines the enzymes studied, the SECM mode used, and relevant references. These studies showed that enzyme activity could be studied using SECM and often, catalytic rates could be extracted.

The advantage of studying enzymes is that they can be regenerated by known substrates. Although they might be influenced by the enzyme turnover rate, the enzymatic substrate can sustain a level of activity that is harder to find in other interesting biological systems.

Table 12.3

Examples of enzyme activity studies using SECM

Feedback mode studies		Collection generation mode studies	
Enzyme	Reference	Enzyme	Reference
Glucose oxidase	(143–146)	Glucose oxidase	(64, 131)
NADH-cytochrome <i>c</i> reductase	(144)	Urease	(147, 148)
Diaphorase	(134)	NADPH-dependent oxidase	(149)
Horseradish peroxidase	(150)	Horseradish peroxidase	(151)
Nitrate reductase	(152)	Alkaline phosphatase	(153)
		NAD ⁺ -dependent alcohol dehydrogenase	(154)

In antibody (150) or DNA hybridization studies, there are a finite number of events that can be detected. SECM, therefore, must turn to tagging strategies to enhance the detected signal. Recent DNA hybridization studies, for example, employed a silver staining technique to increase sensitivity that allowed detection of 30 amol of material per analyzed spot (155). This is a spectacular and unique example that is not representative of common electroactive tagging methods, which generally cannot compete with the sensitivity of current fluorescent tagging methods. There is, however, great promise in combining the SECM measurements with selective fluorescent tags in biological studies (156).

(c) SECM imaging of enzyme features

Enzyme-mediated feedback can be used to image enzyme patterns. To successfully image enzymatic features, tip fouling from oxide formation or adsorption from solution constituents must be avoided. The enzyme reaction at the substrate must not be inhibited by solution species. It must also be able to sustain a level of regeneration activity of the mediator that can compete with its mass transport from the bulk electrode to the tip. In the case of a glucose oxidase catalyzed reaction, a digital simulation of the positive feedback observed from this enzyme quantitatively expresses this limitation (143).

Micropatterning of enzymes has received a lot of attention because of its potential use in integrated biochemical devices, such as biosensors (see also Section 12.4.5). As the conventional lithographic techniques employ organic solvents, photoresists and conditions often unsuited for biological systems, many groups have employed different microfabrication techniques. These include enzyme-modified patterned monolayers, enzyme-modified polymer microstructures, enzyme-modified metal microstructures, and enzyme-modified insulator microstructures. A good review of the characterization of enzyme structures activity using SECM is already available (42).

An example of such patterning protocols is a piezoelectric driven dispenser able to eject picoliter-sized droplets based on the impulse movement of a piezoelectric element and a specially designed nozzle (Figure 12.31) or glass capillary (29). Using this technique, drops of enzyme solution having around 100 pL volumes can be dispensed onto a substrate following each current pulse applied on the piezoelement using a function generator. Using a positioning device like a xyz stage or a plotter system, the microdispenser or

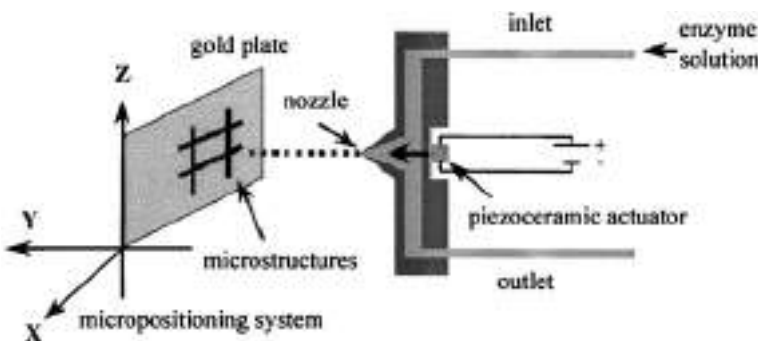


Figure 12.31 Schematic representation of the flow-through microdispenser, gold plate, and positioning system used to obtain enzyme microstructures.

the substrate can be moved to obtain the needed enzyme pattern. Silicon wafers coated with Au (1000 Å), high quality HOPG, polymer films, and glass slides can all be used as substrates.

To immobilize enzymes on these substrates, different strategies can be adopted. In the case of glucose oxidase, catalase or multi-enzyme patterns, a drop of enzyme solution can be dispensed on SAMs of di (*N*-succinimidyl)-3, 3'-dithiodipropionate on Au (157). The formation of amide bonds between the activated ester headgroup of the SAM and the amino groups on the protein shell then takes place. Droplets of enzyme solution containing a cross-linker, such as poly(ethylene glycol) (400) diglycidyl ether (PEGDGE) can also be dispensed on clean Au plates. Polymer matrices in which the dispensed drops of enzyme are on the surface of the polymer have also been used on Au plates.

In another example applied to diaphorase patterning, microcover glasses were immersed into a 3-amino-propyl triethoxysilane/benzene solution and then patterned in three different ways (156). First, using a glass capillary (i.d. 40 mm), a diaphorase and glutaraldehyde solution is drop spotted onto the aminosilanized glass substrate. Second, a diaphorase solution is spin-coated onto the aminosilanized glass substrate, left to dry, and subjected to laser-induced patterning. Third, the SECM probe can deactivate regions of a spin-coated diaphorase substrate as above by generating highly reactive species (HOBr) at the nearby tip.

Such imaging efforts are important because they prove that SECM may be used to pattern enzymes (Figure 12.32), optimize enzyme architectures, and characterize miniaturized multi-sensor arrays. Patterning of enzymes on surfaces and the long scanning distances of SECM make this an attractive option for enzyme activity assays. In order for them to be used to extract enzyme kinetics, however, a significant amount of work remains to be done.

(d) Enzyme-mediated approach curves

The diffusion-controlled feedback response at conductive and insulating surfaces, for simple solution redox couples, are represented by *normalized* current and distance plots commonly referred to as approach curves. In these situations, the approach curves for different redox couples and electrode radii can be superimposed. In the case of enzyme-mediated

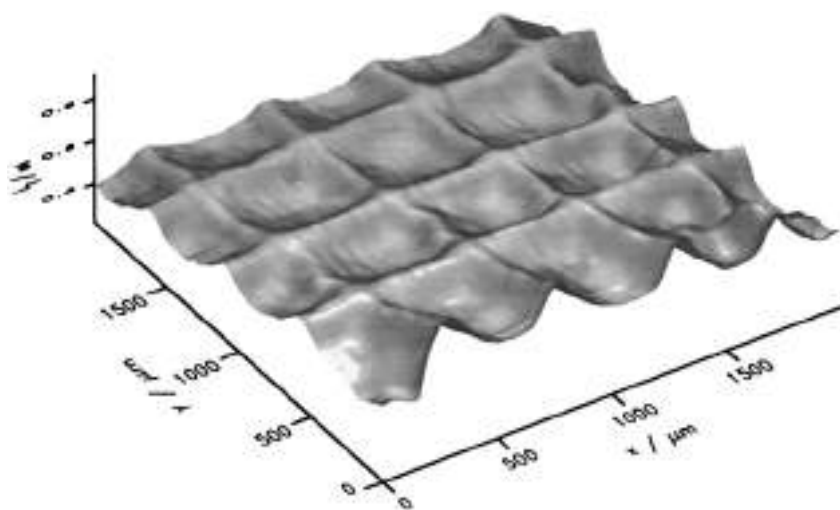


Figure 12.32 SECM image of a GOX grid structure. Each line has a width of $\sim 100 \mu\text{m}$, and the distance between two lines is $500 \mu\text{m}$. Solution dispensed to obtain the structure: 8.8 mg mL^{-1} Vinnapas EP 16 and 1.2 mg mL^{-1} GOX.

feedback curves, the magnitude of the current observed may depend on the enzyme turnover rate, the kinetics of the reaction between the redox couple and the enzyme, the flux of mediator to the enzyme surface, the enzyme surface coverage and the flux of the substrate to the enzyme surface. In the case of glucose oxidase, for example, it was shown that, under conditions of high glucose concentration (substrate saturation), the feedback current depended on the enzyme turnover rate of glucose, the kinetics of the sacrificial electroactive mediator (or enzyme cofactor) and the flux of the mediator to the enzyme. All of these added complications make a complete theoretical treatment of enzyme kinetics using SECM challenging.

(e) Importance of enzyme attachment methods

When enzymes are adsorbed onto a conductive substrate, the surface coverage of the enzyme on the substrate can be evaluated based on the catalytic currents using cyclic voltammetry (142) or by spectroscopic means (140). On an insulating substrate such as a membrane, there is no simple mathematical relationship between the surface coverage of biomolecules and the inhibition of the faradaic current that would be measured by SECM. It is, therefore, necessary to have a quantifiable means to evaluate the surface coverage of immobilized active enzyme if one wishes to extract and compare kinetic information using SECM.

In the past, Matsue *et al.* have discussed this issue in a study related to the characterization of diaphorase-patterned surfaces by SECM. Using a digital simulation based on the explicit finite difference method that considered the heterogeneous enzyme reaction at the substrate, they generated steady-state current vs. distance profiles that depended on the surface concentration of the enzyme. Using these working curves, they quantified the surface concentration of the active immobilized diaphorase (134). Using, the electrochemical

oxidation of bromide or chloride at the SECM tip, they generated highly reactive species that selectively deactivated regions of the enzyme layer. By comparing the approach curves from a deactivated region to that of an untouched region, they showed that the surface concentration of the enzyme for the deactivated region was about half of that for the untreated region.

Bard *et al.* have also presented digital simulations to extract the kinetics of membrane and surface-bound glucose oxidase from feedback measurements (143). Their model included a description of the heterogeneous turnover of the mediator oxidant by immobilized glucose oxidase under a large excess of D-glucose concentrations. The limiting cases of the feedback response obtained for large and small mediator oxidant concentrations are treated. They applied this model to experimental approach curves taken from glucose oxidase immobilized in an albumin/glutaraldehyde hydrogel and showed that, at low mediator concentrations, a clear discrimination for the zero-order kinetic behavior was obtained. Their results clearly showed that the feedback response depended on the amount of immobilized enzyme, but did not quantify this relationship. They also treated the limiting cases of enzyme kinetics, but no complete SECM theoretical treatment is available at present. What is really needed is an accessible general SECM theory that can be applied to different enzymes that would facilitate comparison of results among different groups.

12.4.6.3 Ion channels

(a) Equipment and handling requirements

The special equipment requirements in SECM ion channel studies stem from lipid handling and storage problems. To perform SECM studies with ion channels, one must learn to work with lipids. Stock phospholipid solutions in organic solvents should be stored in glass containers (less than -20°C) and the cap or closure for the vial should be lined with Teflon. When working with lipids, one should avoid contact with polymer or plastic containers (polystyrene, polyethylene, polypropylene, etc.) as impurities often leach out from such materials. Glass, stainless steel, or Teflon syringes and vials should be used to transfer and store lipids. Finally, the phase transition, miscibility, ionization constants of phospholipids, and critical micelle concentrations should always be kept in mind when working with a new lipid (158).

To facilitate and maintain lipid organization, specialized Teflon SECM cells and unusual UME arrangements have to be used. In bilayer lipid membrane (BLM) systems, for example, Teflon cells adapted to the SECM instrument usually have to be made to uniformly distribute the pressure above and below the BLM (Figure 12.33). Also, to visualize the formation of the BLM, the use of an angled microscope combined to a television facilitates the approach of the UME to the BLM (159).

For studies involving air/water interface monolayers or Langmuir-Blodgett techniques, a submarine UME is required. Such an electrode is immersed in the solution and approached to the layer from below (110, 160). The submarine electrode consists simply of a conventional UME of the desired metal and size that is fixed to a glass J tube by Teflon tape or Epoxy (Figure 12.34).

(b) Previous work

The diversity of membrane structures and transport mechanisms studied by SECM demonstrates the utility of this technique for studies of membrane transport (61, 157, 159, 161–163).

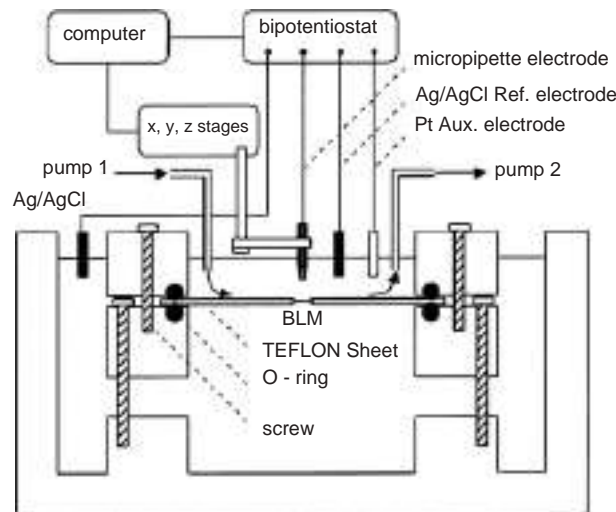


Figure 12.33 Schematic diagram of SECM apparatus and a cell for the preparation of horizontally oriented BLM.

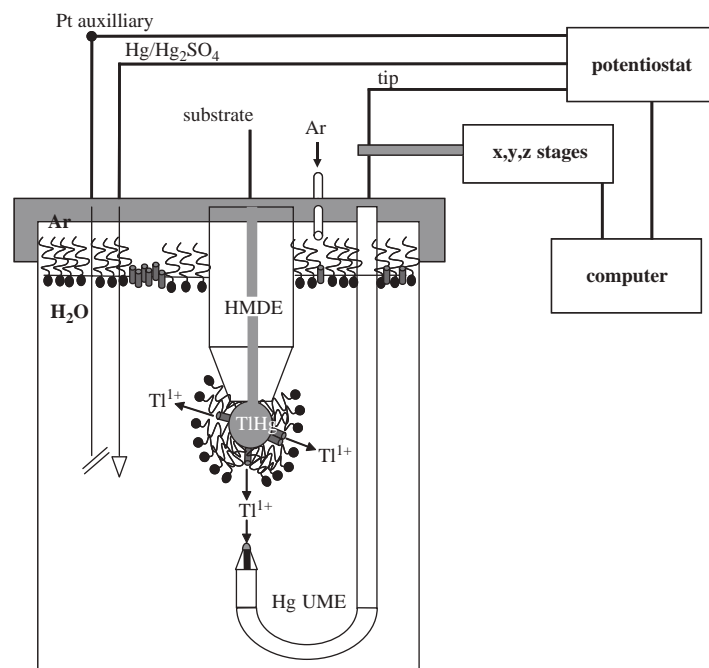


Figure 12.34 Schematic diagram of an ion channel SECM experiment where a submarine UME is used. (Adapted from reference (20).) (for colour version: see colour section at the end of the book).

As described below, potentiometric and amperometric methods have been used to study ion channels. The K⁺ transport across gramicidin channels imbedded in a horizontally supported BLM was studied potentiometrically, for example. In this study, a K⁺ selective micropipette was used to acquire approach curves and measure the transport of K⁺ across the gramicidin channel. The ion-selective micropipette electrodes consisted of silanized pulled borosilicate capillaries (i.d. 0.7–20 µm) filled with a solution of 10 mM valinomycin and 10 mM ETH 500 in dichloroethane. Characterization of the electrodes was accomplished via the steady-state tip current for K⁺ (0.05–0.3 mM). The tips were then used in the SECM feedback and generation/collection modes to study K⁺ transfer through gramicidin channels imbedded in a horizontal BLM of glycerol monooleate.

The difficulty with this measurement is controlling the time at which the ion transport occurs. To have a controlled release of the ion of interest, an amperometric approach can also be used but requires the use of Tl(I) as a surrogate for K⁺. Ion transport across gramicidin channels imbedded in a dioleoylphosphatidylcholine (DOPC) monolayer adsorbed onto a Tl/Hg amalgam can be used as a membrane system. This arrangement allows one to control the release of Tl(I) into gramicidin channels by preconcentration of the Tl as an amalgam on a hanging mercury drop electrode (HMDE) with controlled oxidation of the amalgam using a potential step. An Hg/Pt submarine UME positioned close to the membrane collects the generated Tl(I) following its diffusion from the gramicidin. The tip collection response is a transient current that is fitted to numerical simulations based on finite element method or also to empirical theories. The results (21) agree well with experiments and other reported work (51). An apparent rate constant for the transport of Tl(I) from the amalgam HMDE through the channel can also be extracted (20).

(c) *Problems to tackle*

Knowing the ion channel surface coverage is important to extract the true transport rates rather than apparent rates. When the channels are adsorbed on a conductive electrode, this value can be extracted from cyclic voltamograms (164). On an insulator surface, however, this task becomes harder. As individual channels have distinct opening probabilities and are in equilibrium between the active and inactive forms, evaluating ion channel coverage remains difficult.

To reach imaging capabilities of a single channel, the lateral resolution of SECM needs to be improved and the formation of a substrate where isolated channels are present relative to the size of the electrode needs to be accomplished. Serious consideration also has to be given to current detection limitations.

12.4.6.4 *Cellular systems*

(a) *Equipment and handling requirements*

Though SECM studies on live cells can be performed without the use of an inverted microscope, the rough positioning of the UME over the cells is greatly facilitated if one is used. Also, the use of fluorescent viability dyes is often possible when the inverted microscope has fluorescent capabilities. This allows for simultaneous determination of cellular viability before and after the experiment. Optical micrographs of the UME positioning over the cells can also be acquired. They provide independent proof that the

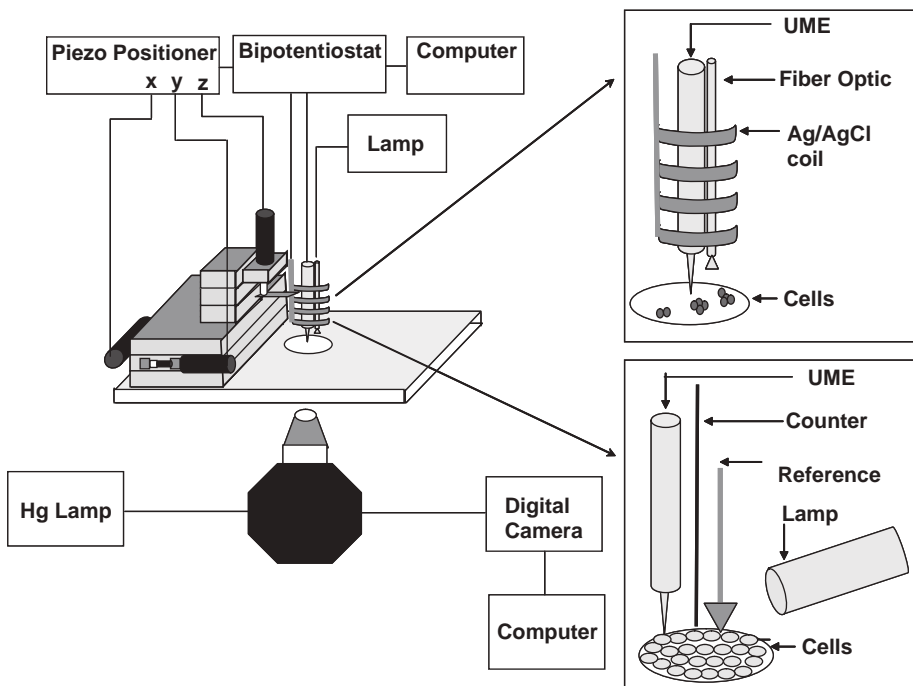


Figure 12.35 Schematic representation of a combined SECM and inverted microscope setup. (for colour version: see colour section at the end of the book).

detected signal originates from the cells themselves and can also monitor the adhesion of the cells onto the substrate during imaging.

The SECM instrument can easily be accommodated to most inverted microscopes. By disassembling the instrument and replacing the bottom plate by a machined piece for the microscope, the SECM head can be installed on the side of the microscope. The height of the z-piezo often prevents the use of the illumination tower but a side halogen lamp or combined UME-fiber optic bundled can be used instead (see Figure 12.35). The UME holder must also be modified and lowered closer to the microscope optics. This can be achieved by the addition of a long cylindrical spacer between the z-piezo and the tip holder (165).

Biological systems are fragile and complex. They require a very controlled environment both for handling and culture conditions. As this type of research is multidisciplinary, cooperation between groups is recommended. Adhesion properties of specific cells, special electrolyte requirements, temperature, humidity, and other environmental concerns important in the design of the SECM experiments are better addressed by specialists.

Examples of live cell systems. Until very recently, little work had been done on live cells. The earliest was the study of photosynthesis on the leaves of *Tradescantia fluminensis*

based on oxygen reduction profiles (90, 166) and the study of resorption of osteoclasts on bone slices using a Ca^{2+} potentiometric sensor (167). Since then, a significant body of work on full cellular studies has been published.

Live cell studies have monitored respiration rate changes using oxygen reduction profiles for different cell types (44, 138, 168–170). In these experiments, oxygen is present in solution and is consumed by the living organism. Close to the cells, more oxygen is consumed and a lower oxygen reduction current is measured. The differences in oxygen reduction currents are in the ranges of 10 pA to nA. Studies have shown that the respiration rate of *in vitro* bovine embryos in the morula developmental stage are related to their quality and viability. Embryos having a higher respiration rate in the morula stage were shown to grow into larger and healthier embryos at subsequent developmental stages. Such information could be useful in supplementing the morphological data used to assess which embryos are to be used in bovine insemination.

Work has also been reported on human breast cells (171) and *Rhodobacter sphaeroides* (172). In these studies, the feedback mode of SECM was used to look at the regeneration reaction of different mediators when exposed to cells. These studies provide useful information about the permeability of the membrane to a wide variety of redox couples. A theoretical treatment enabled kinetic information about these processes (173) to be extracted. SECM has also been used to distinguish between normal and malignant human breast cells (174) with corroboration by optical and fluorescence microscopy measurements.

Other studies have focused on export pump activity of yeast and human liver cells when exposed to quinone oxidative stress. Quinones are readily transported into cells where they retain the ability to redox cycle, impose oxidative stress and form covalent adducts with important cellular species. To cope with oxidative stress, cells have enzymatic and nonenzymatic defenses, like antioxidants, that will limit the stress and damage. For example, glutathione (GSH) is the major nonprotein sulfhydryl present in cells (175) and it detoxifies cells by sacrificially reacting with quinones to limit the irreversible modification of cellular macromolecules. The thioether conjugates formed can then be degraded to other substances or actively removed from the intracellular media using an ATP-dependent pump. In the case of the menadione–glutathione conjugate, the conjugate remains intact and is transported into the extracellular media via the GS-X pump in cells (176, 177). From SECM responses, an apparent rate of transport for the uptake of menadione was extracted (48). Detection of this biological metabolite was also possible in single human liver cell. The cellular detoxification process was observed and imaged for both isolated and monolayer cultured cells (165).

(b) Problems to tackle

The difficulty in working at the interface of two fields like SECM and biology lies in the identification of a biologically relevant problem to address. To do so, one must often rely on collaborations. Now that ground work has been reported in full cellular SECM studies, there is a need to establish general methodologies to compare the SECM results between groups, to develop better numerical simulations adapted to the complexity of the biological system, and to apply SECM in a possible combinatorial setting.

12.4.6.5 Future directions

SECM can be applied to imaging and kinetic studies of biological systems. Ground work on enzymes, ion channels, and cellular system has been reported and demonstrates SECM capabilities. To use SECM in diagnostic assays, nucleic acid analysis, biosensor, bioremediation or other biotechnological processes, SECM needs to be applied quantitatively to different biological systems. There is also a need for the development of accessible kinetic theories, the development of controlled substrate methodologies, and the fabrication of smaller well-characterized UMEs that would increase the lateral resolution of SECM.

REFERENCES

1. A. J. Bard, M. V. Mirkin, Eds., *Scanning Electrochemical Microscopy*, Marcel Dekker: New York, 2001.
2. D. Bonnell, Ed., *Scanning Probe Microscopy and Spectroscopy, Theory, Techniques, and Applications*, Wiley-VCH: New York, 2001.
3. A. J. Bard, L. R. Faulkner, *Electrochemical Methods, Fundamentals and Applications*, John Wiley & Sons, Inc.: New York, 2001, p. 174.
4. M. Ludwig, C. Kranz, W. Schuhmann, H. E. Gaub, *Rev. Sci. Instrum.* **66**, 2857 (1995).
5. J. V. Macpherson, P. R. Unwin, A. C. Hillier, A. J. Bard, *J. Am. Chem. Soc.* **118**, 6445 (1996).
6. (a) J. V. Macpherson, P. R. Unwin, *Anal. Chem.* **72**, 276 (2000). (b) C. Kranz, G. Friedbacher, B. Mikaihoff, A. Lugstein, J. Smoliner, E. Bertagnolli, *Anal. Chem.* **73**, 2491 (2001).
7. (a) P. L. James, P. J. Moyer, L. F. Garfias-Mesias, W. H. Smyrl, *J. Electrochem. Soc.* **145**, L64 (1998). (b) M. Buchler, S. C. Kelley, W. H. Smyrl, *Electrochem. Solid-State Lett.* **3**, 35 (2000).
8. F.-R. F. Fan, A. J. Bard, Unpublished experiments.
9. (a) M. A. Paesler, P. J. Moyer, *Near-Field Optics: Theory, Instrumentation and Applications*, Wiley: New York, 1996. (b) E. Betzig, J. K. Trautman, *Science* **257**, 189 (1992).
10. Y. Lee, A. J. Bard, *Anal. Chem.* **74**, 3626 (2002).
11. G. Shi, L. F. Garfias-Mesias, W. H. Smyrl, *J. Electrochem. Soc.* **145**, 3011 (1998). (b) P. L. James, N. Casillas, W. H. Smyrl, *J. Electrochem. Soc.* **143**, 3853 (1996).
12. Y. Lee, Z. Ding, A. J. Bard, *Anal. Chem.* **74**, 3634 (2002).
13. R. G. Maus, E. M. McDonald, R. M. Wightman, *Anal. Chem.* **71**, 4944 (1999).
14. F.-R. F. Fan, D. Cliffel, A. J. Bard, *Anal. Chem.* **70**, 2941 (1998).
15. Y. Zu, Z. Ding, J. Zhou, Y. Lee, A. J. Bard, *Anal. Chem.* **73**, 2153 (2001).
16. R. G. Maus, R. M. Wightman, *Anal. Chem.* **73**, 3993 (2001).
17. J. J. Watkins, J. Chen, H. S. White, H. D. Abruna, E. Maisonnaute, C. Amatore, *Anal. Chem.* **75**, 3962 (2003).
18. S. Chen, A. Kucernak, *Electrochem. Commun.* **4**, 80 (2002).
19. P. Sun, Z. Zhang, J. Guo, Y. Shao, *Anal. Chem.* **73**, 5346 (2001).
20. J. Mauzeroll, M. Buda, A. J. Bard, F. Prieto, M. Rueda, *Langmuir* **18**, 9453 (2002).
21. J. Mauzeroll, E. A. Hueske, A. J. Bard, *Anal. Chem.* **75**, 3880 (2003).
22. I. Ciani, D. P. Burt, S. Daniele, P. R. Unwin, *J. Phys. Chem. B* **108**, 3801 (2004).
23. J. Golas, Z. Galus, J. Osteryoung, *Anal. Chem.* **59**, 389 (1987).
24. J. L. Conyers, H. S. White, *Anal. Chem.* **72**, 4441 (2000).
25. T. H. Treutler, G. Wittstock, *Electrochim. Acta* **48**, 2923 (2003).

26. A. G. Güell, I. Díez-Pérez, P. Gorostiza, F. Sanz, *Anal. Chem.* **76**, 5218 (2004).
27. C. G. Zoski, B. Liu, A. J. Bard, *Anal. Chem.* **76**, 3646 (2004).
28. P. Liljeroth, C. Johans, C. J. Slevin, B. M. Quinn, K. Kontturi, *Electrochim. Commun.* **4**, 67 (2002).
29. (a) D. A. Walsh, J. L. Fernández, A. J. Bard, C. G. Zoski, manuscript in preparation. (b) D. A. Walsh, J. Fernandez, J. Mauzeroll, A. J. Bard, *Anal. Chem.* **77**, 5182 (2005).
30. J. V. Macpherson, C. J. Slevin, P. R. Unwin, *J. Chem. Soc., Faraday Trans.* **92**, 3799 (1996).
31. Q. Fulian, A. C. Fisher, G. Denuault, *J. Phys. Chem. B* **103**, 4393 (1999).
32. O. Sklyar, G. Wittstock, *J. Phys. Chem. B* **106**, 7499 (2002).
33. T. Nann, J. Heinze, *Electrochim. Acta* **48**, 3975 (2003).
34. J. Galceran, J. Cecilia, E. Companys, J. Salvador, J. Puy, *J. Phys. Chem. B* **104**, 7993 (2000).
35. C. G. Zoski, J. C. Aguilar, A. J. Bard, *Anal. Chem.* **75**, 2959 (2003).
36. L. Rajendran, S. P. Ananthi, *J. Electroanal. Chem.* **56**, 113 (2004).
37. J. L. Amphlet, G. Denuault, *J. Phys. Chem. B* **102**, 9946 (1998).
38. Y. Selzer, D. Mandler, *Anal. Chem.* **72**, 2383 (2000).
39. Y. Lee, S. Amemiya, A. J. Bard, *Anal. Chem.* **73**, 2261 (2001).
40. P. Liljeroth, C. Johans, C. J. Slevin, B. M. Quinn, K. Kontturi, *Anal. Chem.* **74**, 1972 (2002).
41. C. G. Zoski, N. Simjee, O. Guenat, M. Koudelka-Hep, *Anal. Chem.* **76**, 62 (2004).
42. G. Wittstock, *Fresenius J. Anal. Chem.* **370**, 303 (2001).
43. M. Carano, K. B. Holt, A. J. Bard, *Anal. Chem.* **75**, 5071 (2003).
44. T. Kaya, M. Nishizawa, T. Yasukawa, M. Nishiguchi, T. Onouchi, T. Matsue, *Biotechnol. Bioeng.* **76**, 391 (2001).
45. H. Shiku, T. Shiraishi, S. Aoyagi, Y. Utsumi, M. Matsudaira, H. Abe, H. Hoshi, S. Kasai, H. Ohya, T. Matsue, *Anal. Chim. Acta* **522**, 51 (2004).
46. R. C. Engstrom, B. Small, L. Kattan, *Anal. Chem.* **64**, 241 (1992).
47. S. M. Fonseca, A. L. Barker, S. Ahmed, T. J. Kemp, P. R. Unwin, *Chem. Commun.* **8**, 1002 (2003).
48. J. Mauzeroll, A. J. Bard, *Proc. Natl. Acad. Sci. U.S.A.* **101**, 7862 (2004).
49. R. C. Engstrom, R. M. Wightman, E. W. Kristensen, *Anal. Chem.* **60**, 652 (1988).
50. R. D. Martin, P. R. Unwin, *J. Chem. Soc., Faraday Trans.* **94**, 753 (1998).
51. R. D. Martin, P. R. Unwin, *Anal. Chem.* **70**, 276 (1998).
52. J. L. Fernández, A. J. Bard, *Anal. Chem.* **76**, 2281 (2004).
53. F. Zhou, P. R. Unwin, A. J. Bard, *J. Phys. Chem.* **96**, 4917 (1992).
54. J. L. Fernández, A. J. Bard, *Anal. Chem.* **75**, 2967 (2003).
55. G. Denault, G. Nagy, K. Tóth, in "Scanning Electrochemical Microscopy", A. J. Bard, M. V. Mirkin, Eds., Marcel Dekker, Inc.: New York, 2001, pp. 397–444.
56. J. Koryta, *Ion-Selective Electrodes*, Cambridge University Press: Cambridge, 1975.
57. D. Amman, *Ion-Selective Microelectrodes: Principle, Design & Application*, Springer Verlag: New York, 1986.
58. B. R. Horrocks, M. V. Mirkin, D. T. Pierce, A. J. Bard, G. Nagy, K. Tóth, *Anal. Chem.* **65**, 1213 (1993).
59. (a) M. H. Troise-Frank, G. Denuault, *J. Electroanal. Chem.* **354**, 331 (1993). (b) M. H. Troise-Frank, G. Denuault, *J. Electroanal. Chem.* **379**, 405 (1994).
60. (a) G. Denuault, M. H. Troise-Frank, L. M. Peter, *Faraday Discuss.* **94**, 23 (1992). (b) M. Etienne, A. Schulte, S. Mann, G. Jordan, I. D. Dietzel, W. Schuhmann, *Anal. Chem.* **76**, 3682 (2004).
61. S. Amemiya, A. J. Bard, *Anal. Chem.* **72**, 4940 (2000).
62. C. Wei, A. J. Bard, G. Nagy, K. Tóth, *Anal. Chem.* **67**, 1346 (1995).
63. C. Wei, A. J. Bard, I. Kapui, G. Nagy, K. Tóth, *Anal. Chem.* **68**, 2651 (1996).
64. B. R. Horrocks, D. Schmidtke, A. Heller, A. J. Bard, *Anal. Chem.* **65**, 3605 (1993).
65. (a) A. Hengstenberg, C. Kranz, W. Schuhmann, *Chem. Eur. J.* **6**, 1547 (2000). (b) A. Hengstenberg, A. Blöchl, I. D. Dietzel, W. Schuhmann, *Angew. Chem. Int. Ed.* **40**, 905 (2001).

66. D. O. Wipf, A. J. Bard, *Anal. Chem.* **64**, 1362 (1992).
67. A. J. Bard, M. V. Mirkin, P. R. Unwin, D. O. Wipf, *J. Phys. Chem.* **96**, 1861 (1992).
68. Z. Ding, B. M. Quinn, A. J. Bard, *J. Phys. Chem. B* **105**, 6367 (2001).
69. A. L. Barker, P. R. Unwin, J. Zhang, *Electrochem. Commun.* **3**, 372 (2001).
70. P. Liljeroth, B. M. Quinn, K. Kontturi, *Langmuir* **19**, 5121 (2003).
71. C. Wei, A. J. Bard, M. V. Mirkin, *J. Phys. Chem.* **99**, 16033 (1995).
72. M. V. Mirkin, T. C. Richards, A. J. Bard, *J. Phys. Chem.* **97**, 7672 (1993).
73. W. Miao, Z. Ding, A. J. Bard, *J. Phys. Chem. B* **106**, 1392 (2002).
74. B. Liu, A. J. Bard, *J. Phys. Chem. B* **106**, 12801 (2002).
75. J. Zhou, Y. Zu, A. J. Bard, *J. Electroanal. Chem.* **491**, 22 (2000).
76. K. Jambunathan, B. C. Shah, J. L. Hudson, A. C. Hillier, *J. Electroanal. Chem.* **500**, 279 (2001).
77. C. G. Zoski, *J. Phys. Chem. B* **107**, 6401 (2003).
78. M. Tsionsky, A. J. Bard, M. V. Mirkin, *J. Phys. Chem.* **100**, 17881 (1996).
79. Z. Zhang, Y. Yuan, P. Sun, B. Su, J. Guo, Y. Shao, H. H. Girault, *J. Phys. Chem. B* **106**, 6713 (2002).
80. S. K. Haram, A. J. Bard, *J. Phys. Chem. B* **105**, 8192 (2001).
81. Y. Selzer, I. Turyan, D. Mandler, *J. Phys. Chem. B* **103**, 1509 (1999).
82. J. L. Fernández, C. Hurth, A. J. Bard, unpublished results.
83. For example, P. R. Unwin, A. J. Bard, *J. Phys. Chem.* **95**, 7814 (1991).
84. For example, (a) F. Zhou, A. J. Bard, *J. Am. Chem. Soc.* **116**, 393 (1994). (b) D. A. Treichel, M. V. Mirkin, A. J. Bard, *J. Phys. Chem.* **98**, 5751 (1994).
85. C. Demaille, P. R. Unwin, A. J. Bard, *J. Phys. Chem.* **100**, 14137 (1996).
86. R. C. Engstrom, T. Meany, R. Tople, R. M. Wightman, *Anal. Chem.* **59**, 2005 (1987).
87. (a) T. Wilhelm, G. Wittstock, *Angew. Chem. Int. Ed.* **42**, 2248 (2003). (b) C. Zhao, J. K. Sinha, C. Ajith Wijayawardhana, G. Wittstock, *J. Electroanal. Chem.* **561**, 83 (2004).
88. B. Liu, W. Cheng, S. A. Rotenberg, M. V. Mirkin, *J. Electroanal. Chem.* **500**, 590 (2001).
89. S. B. Basame, H. S. White, *J. Phys. Chem. B* **102**, 9812 (1998).
90. M. Tsionsky, Z. G. Cardon, A. J. Bard, R. B. Jackson, *Plant Physiol.* **113**, 895 (1997).
91. C. Lee, J. Kwak, F. C. Anson, *Anal. Chem.* **63**, 1501 (1991).
92. T. E. Mallouk, E. S. Smotkin, in "Handbook of Fuel Cells—Fundamental and Applications", W. Vielstich, A. Lamm, H. A. Gasteiger, Eds., John Wiley & Sons: Hoboken, NJ, 2003, Vol. 2, Part 3, p. 334.
93. E. Reddington, A. Sapienza, B. Gurau, R. Viswanathan, S. Sarangapani, E. S. Smotkin, T. E. Mallouk, *Science* **280**, 1735 (1998).
94. S. Guerin, B. E. Hayden, C. E. Lee, C. Mormiche, J. R. Owen, A. E. Russell, *J. Comb. Chem.* **6**, 149 (2004).
95. S. Jayaraman, A. C. Hillier, *J. Comb. Chem.* **6**, 27 (2004).
96. S. Jayaraman, A. C. Hillier, *J. Phys. Chem. B* **107**, 5221 (2003).
97. S. Jayaraman, A. C. Hillier, *Langmuir* **17**, 7857 (2001).
98. K. Jambunathan, A. C. Hillier, *J. Electrochem. Soc.* **150**, E312 (2003).
99. K. Jambunathan, S. Jayaraman, A. C. Hillier, *Langmuir* **20**, 1856 (2004).
100. J. L. Fernández, D. A. Walsh, A. J. Bard, *J. Am. Chem. Soc.* **127**, 357 (2005).
101. J. L. Fernández, N. Mano, A. Heller, A. J. Bard, *Angew. Chem. Int. Ed.* **43**, 6355 (2004).
102. I. Willner, E. Katz, *Angew. Chem. Int. Ed.* **39**, 1181 (2000).
103. M. A. Fox, *Acc. Chem. Res.* **32**, 201 (1999).
104. H. O. Finklea, in "Electroanalytical Chemistry", A. J. Bard, I. Rubinstein, Eds., Marcel Dekker: New York, 1996, Vol. 19, pp. 109–335.
105. B. Liu, A. J. Bard, M. V. Mirkin, S. E. Creager, *J. Am. Chem. Soc.* **126**, 1485 (2004).

106. C. Cannes, F. Kanoufi, A. J. Bard, *J. Electroanal. Chem.* **547**, 83 (2003).
107. M. Tsionsky, A. J. Bard, M. V. Mirkin, *J. Am. Chem. Soc.* **119**, 10785 (1997).
108. M.-H. Delville, M. Tsionsky, A. J. Bard, *Langmuir* **14**, 2774 (1998).
109. B. Liu, M. V. Mirkin, *J. Phys. Chem. B* **106**, 3933 (2002).
110. J. Zhang, C. J. Slevin, C. Morton, P. Scott, D. J. Walton, P. R. Unwin, *J. Phys. Chem.* **105**, 11120 (2001).
111. F. Forouzan, A. J. Bard, M. V. Mirkin, *Isr. J. Chem.* **37**, 155 (1997).
112. (a) D. O. Wipf, *Colloids Surf. A* **93**, 251 (1994). (b) J. W. Still, D. O. Wipf, *J. Electrochem. Soc.* **144**, 2657 (1997). (c) C. H. Paik, H. S. White, R. C. Alkire, *J. Electrochem. Soc.* **147**, 4120 (2000). (d) M. Buchler, J. Kermino, F. Guillaume, W. H. Smyrl, *J. Electrochem. Soc.* **147**, 3691 (2000). (e) I. Serebrennikova, H. S. White, *Electrochem. Solid-State Lett.* **4**, B4 (2001). (f) I. Serebrennikova, S. Lee, H. S. White, *Faraday Discuss.* **121**, 199 (2002). (g) N. Casillas, S. Charlebois, W. H. Smyrl, H. S. White, *J. Electrochem. Soc.* **141**, 636 (1994). (h) S. B. Basame, H. S. White, *Anal. Chem.* **71**, 3166 (1999). (i) S. B. Basame, H. S. White, *Langmuir* **15**, 819 (1999). (j) Y. Zhu, D. E. Williams, *J. Electrochem. Soc.* **144**, L43 (1997). (k) D. E. Williams, T. F. Mohiuddin, Y. Zhu, *J. Electrochem. Soc.* **145**, 2664 (1998). (l) J. C. Seegmiller, D. A. Buttry, *J. Electrochem. Soc.* **150**, B413 (2003).
113. H. Tanabe, T. Misawa, *J. Mater. Sci. Lett.* **17**, 551 (1998).
114. B. B. Katemann, C. G. Inchauspe, P. A. Castro, A. Schulte, E. J. Calvo, W. Schuhmann, *Electrochim. Acta* **48**, 1115 (2003).
115. N. Casillas, P. L. James, W. H. Smyrl, *J. Electrochem. Soc.* **142**, L16 (1995).
116. R. Peat, A. Riley, D. E. Williams, L. M. Peter, *J. Electrochem. Soc.* **136**, 3352 (1989).
117. D. Mandler, in "Scanning Electrochemical Microscopy", A. J. Bard, M. V. Mirkin, Eds., Marcel Dekker: New York, 2001, pp. 593–627.
118. B. R. Horrocks, in "Encyclopedia of Electrochemistry", A. J. Bard, M. Stratmann, Eds., Wiley-VCH, 2003, Vol. 3, pp. 444–490.
119. (a) O. E. Hüsser, D. H. Craston, A. J. Bard, *J. Vac. Sci. Technol. B* **6**, 1873 (1988). (b) O. E. Hüsser, D. H. Craston, A. J. Bard, *J. Electrochem. Soc.* **136**, 3222 (1989). (c) D. Mandler, A. J. Bard, *J. Electrochem. Soc.* **137**, 1079 (1990). (d) E. Ammann, D. Mandler, *J. Electrochem. Soc.* **148**, C533 (2001). (e) Y. Yatziv, I. Turyan, D. Mandler, *J. Am. Chem. Soc.* **124**, 5618 (2002). (f) O. D. Abril, D. Mandler, P. R. Unwin, *Electrochem. Solid-State Lett.* **7**, C71 (2004).
120. D. Mandler, A. J. Bard, *J. Electrochem. Soc.* **136**, 3143 (1989).
121. D. Mandler, A. J. Bard, *J. Electrochem. Soc.* **137**, 2468 (1990).
122. K. Borgwarth, C. Ricken, D. G. Ebbling, J. Heinze, *Ber Bunsenges Phys. Chem.* **99**, 1421 (1995).
123. C. Hess, K. Borgwarth, C. Ricken, D. G. Ebbling, J. Heinze, *Electrochim. Acta* **42**, 3065 (1997).
124. S. Meltzer, D. Mandler, *J. Electrochem. Soc.* **142**, L82 (1995).
125. C. W. Lin, F.-R. Fan, A. J. Bard, *J. Electrochem. Soc.* **134**, 1038 (1987).
126. Y. B. Zu, L. Xie, B. W. Mao, Z. W. Tian, *Electrochim. Acta* **43**, 1683 (1998).
127. Y. M. Wuu, F.-R. Fan, A. J. Bard, *J. Electrochem. Soc.* **136**, 885 (1989).
128. C. Kranz, M. Ludiwig, H. E. Gaub, W. Schumann, *Adv. Mater.* **7**, 38 (1995).
129. C. Kranz, H. E. Gaub, W. Schumann, *Adv. Mater.* **8**, 634 (1996).
130. L. Zhou, D. O. Wipf, *J. Electrochem. Soc.* **144**, 1202 (1997).
131. G. Wittstock, W. Schumann, *Anal. Chem.* **69**, 5059 (1997).
132. I. Turyan, T. Matsue, D. Mandler, *Anal. Chem.* **72**, 3431 (2000).
133. G. Wittstock, H. Wohlschläger, W. Schumann, *Electrochim. Acta* **42**, 3105 (1997).
134. H. Shiku, T. Takeda, H. Yamada, T. Matsue, I. Uchida, *Anal. Chem.* **67**, 312 (1995).
135. H. Shiku, I. Uchida, T. Matsue, *Langmuir* **13**, 7239 (1997).
136. W. B. Nowall, D. O. Wipf, W. G. Kuhr, *Anal. Chem.* **70**, 2601 (1998).

137. J. M. Liebetrau, H. M. Miller, J. E. Baur, S. A. Takacs, V. Anupunpisit, P. A. Garris, D. O. Wipf, *Anal. Chem.* **75**, 563 (2003).
138. T. Yasukawa, T. Kaya, T. Matsue, *Anal. Chem.* **71**, 4637 (1999).
139. B. R. Horrocks, G. Wittstock, in "Scanning Electrochemical Microscopy", A. J. Bard, M. V. Mirkin, Eds., Marcel Dekker: New York, 2001, pp. 445–519.
140. T. Sawaguchi, T. Matsue, I. Uchida, *Bioelectrochem. Bioenerg.* **29**, 127 (1992).
141. B. Limoges, J. Moiroux, J.-M. Savéant, *J. Electroanal. Chem.* **521**, 1 (2002).
142. B. Limoges, J. Moiroux, J.-M. Savéant, *J. Electroanal. Chem.* **521**, 8 (2002).
143. D. T. Pierce, P. R. Unwin, A. J. Bard, *Anal. Chem.* **64**, 1795 (1992).
144. D. T. Pierce, A. J. Bard, *Anal. Chem.* **65**, 3598 (1993).
145. C. Kranz, G. Wittstock, H. Wohlschläger, W. Schuhmann, *Electrochim. Acta* **42**, 3105 (1997).
146. C. A. Wijayawardhana, G. Wittstock, H. B. Halsall, W. R. Heineman, *Anal. Chem.* **72**, 333 (2000).
147. B. R. Horrocks, M. V. Mirkin, D. T. Pierce, A. J. Bard, *Anal. Chem.* **65**, 1213 (1993).
148. B. R. Horrocks, M. V. Mirkin, *J. Chem. Soc. Faraday Trans.* **94**, 1115 (1998).
149. C. E. M. Berger, B. R. Horrocks, H. K. Datta, *J. Endocrinol.* **158**, 311 (1998).
150. H. Shiku, T. Matsue, I. Uchida, *Anal. Chem.* **68**, 1276 (1996).
151. H. Shiku, Y. Hara, T. Matsue, I. Uchida, *J. Electroanal. Chem.* **438**, 187 (1997).
152. J. Zaumseil, G. Wittstock, S. Bahrs, P. Steinrücke, *Fresenius J. Anal. Chem.* **367**, 352 (2000).
153. G. Wittstock, K. J. Yu, H. B. Halsall, T. H. Ridgway, W. R. Heineman, *Anal. Chem.* **67**, 3578 (1995).
154. Y. N. Antonenko, P. Pohl, E. Rosenfeld, *Arch. Biochem. Biophys.* **333**, 225 (1996).
155. J. Wang, F. Song, F. Zhou, *Langmuir* **18**, 6653 (2002).
156. D. Oyamatsu, N. Kanaya, H. Shiku, M. Nishizawa, T. Matsue, *Sens. Actuators B* **91**, 199 (2003).
157. S. Gáspár, M. Mosbach, L. Wallman, T. Laurell, E. Csöregi, W. Schuhmann, *Anal. Chem.* **73**, 4254 (2001).
158. John R. Silvius, "Thermotropic Phase Transitions of Pure Lipids in Model Membranes and Their Modifications by Membrane Proteins", in *Lipid-Protein Interactions*, John Wiley & Sons, Inc.: New York, 1982.
159. S. Amemiya, Z. Ding, J. Zhou, A. J. Bard, *Electro. Chem.* **483**, 7 (2000).
160. C. J. Slevin, J. A. Umbers, J. H. Atherton, P. R. Unwin, *J. Chem. Soc., Faraday Trans.* **92**, 5177 (1996).
161. E. R. Scott, H. S. White, J. B. Phipps, *J. Membr. Sci.* **58**, 71 (1991).
162. J. V. Macpherson, M. A. Beeston, P. R. Unwin, N. P. Hughes, D. Littlewood, *J. Chem. Soc., Faraday Trans.* **91**, 1407 (1995).
163. E. R. Scott, J. B. Phipps, H. S. White, *J. Invest. Dermatol.* **104**, 142 (1995).
164. A. Nelson, *J.Biophys.* **80**, 2694 (2001).
165. J. Mauzeroll, T. J. Monks, O. Owhadian, A. J. Bard, *Proc. Natl. Acad. Sci. U.S.A.* **101**, 17582 (2004).
166. R. B. Jackson, M. Tsionsky, Z. G. Cardon, A. J. Bard, *Plant Physiol.* **111**, 354 (1996).
167. C. E. M. Berger, H. Rathod, J. I. Gillespie, B. R. Horrocks, H. Datta, *J. Bone Miner. Res.* **16**, 2092 (2001).
168. M. Nishizawa, K. Takoh, T. Matsue, *Langmuir* **18**, 3645 (2002).
169. Y. Takii, K. Takoh, M. Nishizawa, T. Matsue, *Electrochim. Acta* **48**, 3381 (2003).
170. H. Shiku, T. Shiraishi, H. Ohya, T. Matsue, H. Abe, H. Hoshi, M. Kobayashi, *Anal. Chem.* **73**, 3751 (2001).
171. B. Liu, S. A. Rotenberg, M. V. Mirkin, *Proc. Natl. Acad. Sci. U.S.A.* **97**, 9855 (2000).
172. C. Cai, B. Liu, M. V. Mirkin, H. A. Frank, J. F. Rusling, *Anal. Chem.* **74**, 114 (2002).

173. L. Biao, S. A. Rotenberg, M. V. Mirkin, *Anal. Chem.* **74**, 6340 (2002).
174. W. Feng, S. A. Rotenberg, M. V. Mirkin, *Anal. Chem.* **75**, 4148 (2003).
175. D. J. Reed, M. J. Meredith, “Cellular Defense Mechanisms Against Reactive Metabolites”, in *Bioactivation of Foreign Compounds*, M. W. Anders, Ed., Academic Press: New York, pp. 71–108.
176. D. Keppler, *Free Radic. Biol. Med.* **27**(9/10), 985 (1999).
177. H. Sies, *Free Radic. Biol. Med.* **27**(9/10), 916 (1999).

– 13 –

Electrogenerated Chemiluminescence

Wujian Miao

The University of Southern Mississippi, Hattiesburg, Mississippi, USA

13.1 CONCEPTS AND HISTORY

Electrogenerated chemiluminescence (also called electrochemiluminescence and abbreviated ECL) is the process where species generated at electrodes undergo electron-transfer reactions to form excited states that emit light. In other words, ECL is a kind of luminescence produced by electrode reactions (1). A typical ECL system would involve a solution containing ECL precursors in a solution with supporting electrolyte in an electrochemical cell with either a single working electrode using an alternating potential, or two separate electrodes in close proximity to each other by holding one electrode at a reductive potential and the other at an oxidative potential (2). The first detailed ECL studies were described in the middle of 1960s (3–5), although reports concerning light emission during electrolysis date back to the 1920s (6, 7). After about 40 years study, ECL has now become a very powerful analytical technique and been widely used in the areas of, e.g., immunoassay, food and water testing, and biowarfare agent detection (8). ECL has also been successfully exploited as a detector of flow injection analysis (FIA), HPLC, capillary electrophoresis (CE), and micro total analysis (μ TAS) (9). A time line showing various events in the development of ECL is illustrated in Figure 13.1 (10).

Various topics on ECL have been thoroughly reviewed (9, 25–57), and the first ECL monograph (8) was also published recently. In the monograph, an overview and brief history of ECL, both the experimental and theoretical aspects of ECL, a review of the behavior of coreactants, organic molecules, and metal chelates, together with the application of ECL in immunoassay, flow injection, liquid chromatography, CE, and light production and display devices are extensively presented.

13.2 TYPES OF LUMINESCENCE

In addition to ECL, light can be generated by a wide variety of luminescent processes (Table 13.1). Of them, both ECL and chemiluminescence (CL) involve the production of

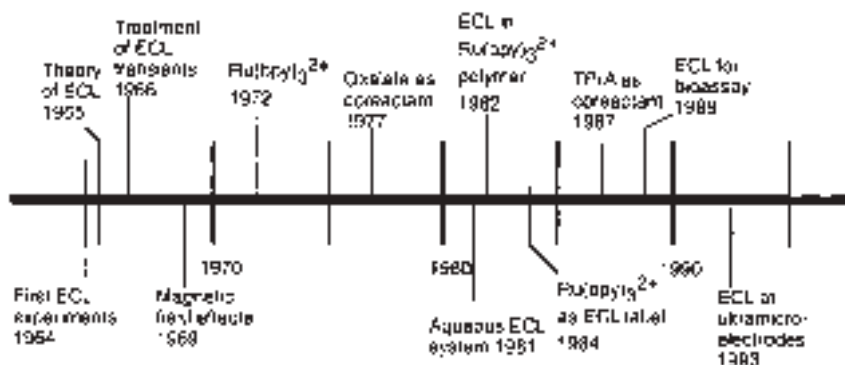


Figure 13.1 Time line of ECL. 1964–1965: First experiments (3–5); 1965: Theory (11) ; 1966: Transients (12, 13); 1969: Magnetic field effects (14); 1972: Ru(bpy)₃²⁺(15); 1977: Oxalate (16); 1981: Aqueous (17); 1982: Ru(bpy)₃²⁺ polymer (18); 1984: Ru(bpy)₃²⁺ label (19); 1987: Tri-n-propylamine (TPrA) (20, 21); 1989: Bioassay (22, 23); 1993: Ultramicroelectrodes (24) (from reference (8)).

Table 13.1

Different types of luminescence^a

Luminescence type	Caused by	References
Photoluminescence (PL)	Photo-excitation of compounds	(58–60)
CHEMILUMINESCENCE (CL)	Chemical excitation of compounds	(58–82)
Electrochemiluminescence (ECL)	Electrogenerated chemical excitation	(9, 25–57)
Radiochemiluminescence	Radiation-induced chemical excitation	(83–88)
Lyoluminescence	Excitation induced by dissolution of an irradiated or other energy-donating solid	(89, 90)
Sonoluminescence	Excitation of compounds by ultrasonication, either by energy transfer from the intrinsic SL centers of water or by chemical excitation by hydroxyl radicals and atomic hydrogen	(91–110)

^aModified from reference (46)

light by species that can undergo highly energetic electron-transfer reactions; however, luminescence in CL is initiated by the mixing of necessary reagents and often controlled by the careful manipulation of fluid flow. In contrast, luminescence in ECL is initiated and controlled by changing an electrode potential. Figure 13.2 schematically describes the general principles of photoluminescence (PL), CL, and ECL. As an analytical technique, the advantages of CL over PL, and ECL over CL are listed in Table 13.2.

13.3 FUNDAMENTAL REACTIONS

13.3.1 Ion annihilation ECL

Classical ECL involves the formation of an excited state as a result of an energetic electron transfer between electrochemically generated species, often radical ions, at the surface of

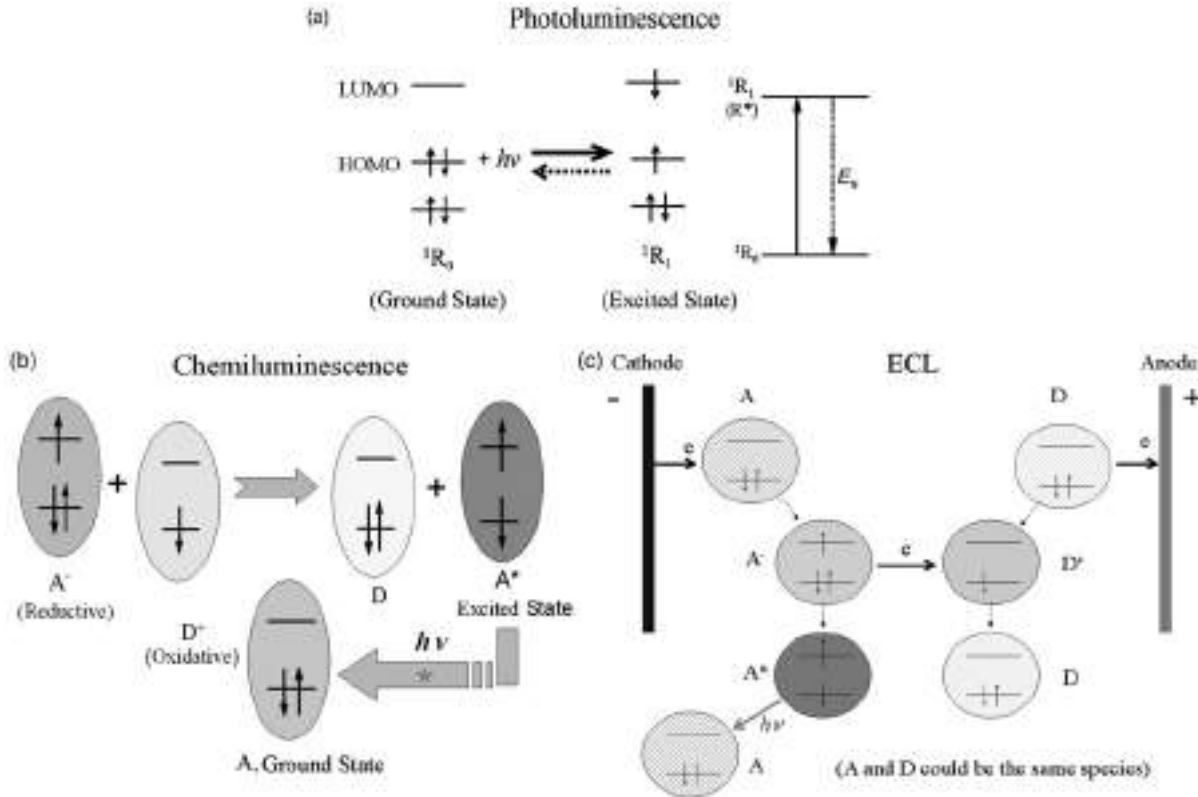


Figure 13.2 Schematic diagrams showing the general principles of (a) Photoluminescence, (b) Chemiluminescence, (c) ECL. (for colour version: see colour section at the end of the book).

Table 13.2

Comparison of photoluminescence (PL), chemiluminescence (CL) and electrochemiluminescence (ECL), in terms of an analytical technique

Advantages of CL over PL	Advantages of ECL over CL
1. No light source needed	1. ECL reactions are localized spatially and temporally and controllable
2. No scattered light	2. Application is possible through turnover of reactions
3. No interference from luminescent impurities	

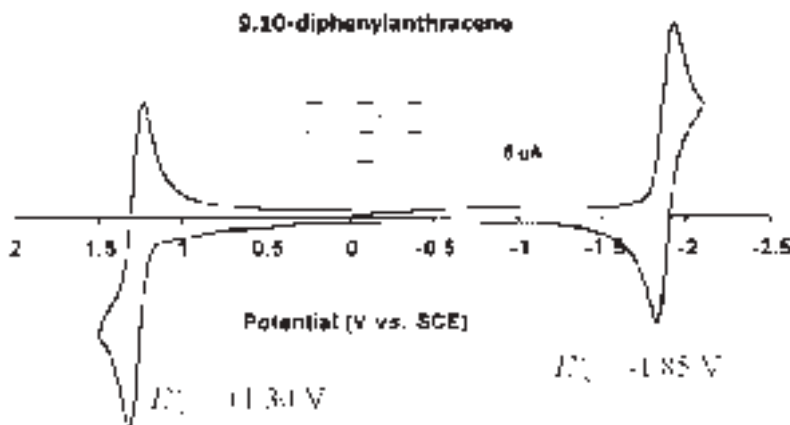
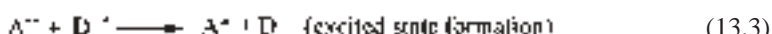


Figure 13.3 Cyclic voltammogram of 1 mM DPA in MeCN containing 0.1 M TBAP at a 2 mm in diameter Pt disk electrode at a scan rate of 200 mV/s (modified from reference (112)).

an electrode. As shown in Figure 13.2c, species A accepts one electron from the cathode to form $A^{-\bullet}$, and species D loses one electron at the anode to form $D^{\bullet+}$. When $A^{-\bullet}$ and $D^{\bullet+}$ diffuse away from the electrodes and come together, $A^{-\bullet}$ transfers one electron to $D^{\bullet+}$ to produce a neutral species D and the excited state A^* . A^* immediately emits light ($h\nu$) and returns to its ground state.

Scheme 13.1 summarizes the reaction sequence of the above processes, where A and D could be the same species, e.g., a polycyclic aromatic hydrocarbon (PAH) such as 9,10-diphenylanthracene (DPA, Figure 13.3) (111, 112).

**Scheme 13.1**

13.3.1.1 Criteria for efficient ion annihilation occurring

For a given chemical species, three criteria are generally required for efficient ion annihilation ECL to occur (10): (i) stable radical ions of the precursor molecules in the electrolyte of interest (as seen in the CV response, e.g., DPA in Figure 13.3), (ii) good PL efficiency of a product of the electron-transfer reaction, which often can be evaluated from the fluorescent experiment, and (iii) sufficient energy in the electron-transfer reaction to produce the excited state (see below for details).

13.3.1.2 Energy requirements, S-route, T-route, and ST-route

The total energy of the ion annihilation reaction (equation (13.3)) is primarily governed by the difference between the thermodynamic potential for oxidation (equation (13.2)) and reduction (equation (13.1)) obtained from the cyclic voltammogram (Figure 13.3) with correction of entropy effects as

$$-\Delta H^0 = (E_a^0 - E_c^0) - T\Delta S^0 \quad (13.5)$$

The value of $T\Delta S^0$ is usually estimated as 0.10 (± 0.1 eV) (5, 113, 114). Since

$$E^\circ = E_p \pm 1.109RT/F = E_p \pm 28.5 \text{ mV at } 298 \text{ K} \quad (13.6)$$

Equation (13.5) is often expressed using CV peak potentials (E_p in volts),

$$-\Delta H^0 = (E_{pa} - E_{pc}) - 0.16 \quad (13.7)$$

If $-\Delta H^0 > E_s$, where E_s (in eV) is the energy gap between the excited singlet state of energy and the ground state of energy (Figure 13.2a), and often determined from the fluorescence spectrum, the ion annihilation reaction can produce an excited singlet state species. Such reactions are sometimes called *energy-sufficient*, and the reaction is said to follow the S-route. A typical example of the energy-sufficient system is the $\text{DPA}^{+\bullet}/\text{DPA}^{-\bullet}$ system (111, 112).

If $E_s > -\Delta H^0 > E_T$, where E_T is excited triplet state of energy, the annihilation reaction energy can produce the triplet state species ${}^3\text{A}^*$, with excited single production occurring via triplet-triplet annihilation (TTA) (Scheme 13.2). Such reactions are called *energy-deficient*, and the reactions are said to follow the T-route. Typical examples of the energy-deficient system are $\text{TMPD}^{+\bullet}/\text{DPA}^{-\bullet}$ and $\text{TMPD}^{+\bullet}/\text{AN}^{-\bullet}$ ($\text{TMPD} = N,N,N',N'$ -tetramethyl *p*-phenylenediamine and $\text{AN} = \text{anthracene}$) (14, 114). The efficiency of direct emission from ${}^3\text{A}^*$ is usually low in a solution phase because of the long radiative lifetime of ${}^3\text{A}^*$ and its quenching by radical ions or other species, such as molecular oxygen.

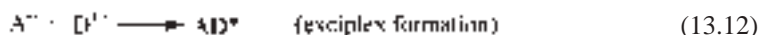


Scheme 13.2

If $-\Delta H^0$ is nearly marginal to E_s , the T-route can contribute to the formation of ${}^3\text{A}^*$ in addition to the S-route, and the reactions are said to follow the ST-route. A typical system with such a route is the rubrene anion-cation annihilation (115–117).

13.3.1.3 Excimers, exciplexes, and E-route

In addition to the formation of singlet and triplet excited states, ion annihilation reactions can lead to the direct formation of excimers (excited dimers) and exciplexes (excited complexes). In most cases, the participating molecules must be able to align so that there is significant π -orbital overlap; thus this occurs mostly among planar PAHs such as pyrene and perylene (118–120). Other reactions such as TTA process can also lead to the formation of excimers and/or exciplexes (121). The reactions associated with the formation of excimers and exciplexes are said to follow the E-route. The relevant reactions are summarized in Scheme 13.3.



Scheme 13.3

Excimer or exciplex emission is generally characterized by broad featureless emission red-shifted from the singlet emission of the molecule. Also, the emission wavelength and intensity change with solvent polarity. Emission from the monomer and the excimer are very often observed in the same spectrum. Although excimers and exciplexes can be formed via photo-excitation as observed in fluorescence spectroscopy, they are most likely to form in ECL due to the close proximity of the radical ions in the contact radical ion pair (122).

13.3.2 Coreactant ECL (123)

13.3.2.1 Terms and definitions

Unlike ion annihilation ECL, in which electrolytic generation of both the oxidized and reduced ECL precursors is required, coreactant ECL is generated with a single potential step or one directional potential scanning at an electrode in a solution containing luminophore species in the presence of a deliberately added reagent (coreactant). Depending on the polarity of the applied potential, both the luminophore and the coreactant species can be first oxidized or reduced at the electrode to form radicals, and intermediates formed from the coreactant then decompose to produce a powerful reducing or oxidizing species that reacts with the oxidized or reduced luminophore to produce the excited states that emit light. Since highly reducing intermediate species are generated after an electrochemical oxidation of a coreactant, or highly oxidizing ones are produced after an electrochemical reduction, the corresponding ECL reactions are often referred to as “oxidative-reduction” ECL and “reductive-oxidation” ECL, respectively (17, 124). Thus, a coreactant is a species that, upon electrochemical oxidation or reduction, immediately undergoes chemical decomposition to form a strong reducing or oxidizing intermediate that can react with an oxidized or reduced ECL luminophore to generate excited states. Another difference between annihilation and coreactant ECL is that, in annihilation ECL, all starting species can be regenerated after light

emission, while in coreactant ECL, only luminophore species can be regenerated and the coreactant is consumed via the ECE (2) reactions.

13.3.2.2 Advantages of coreactant ECL over ion annihilation ECL

1. The use of a coreactant can make ECL possible even for some fluorescent compounds that have only a reversible electrochemical reduction or oxidation.
2. Even with solvents for ECL that have a narrow potential window so that only a reduced or oxidized form of a luminophore can be produced, e.g., tris(2,2'-bipyridine) ruthenium(II), $\text{Ru}(\text{bpy})_3^{2+}$ ($\text{bpy} = 2,2'$ -bipyridine), in aqueous solutions, it is still possible to generate ECL by use of a coreactant.
3. When the annihilation reaction between oxidized and reduced species is not efficient, the use of a coreactant may produce more intense ECL.

13.3.2.3 Criteria for a good coreactant (123)

The following six criteria are generally required for a good coreactant compound:

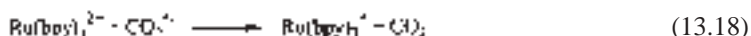
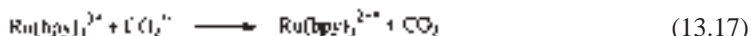
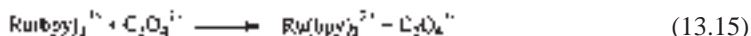
1. *Solubility.* The coreactant should be reasonably soluble in the reaction media, because the ECL intensity is generally proportional to the concentration of the coreactants.
2. *Stability.* The intermediate species generated electrochemically and chemically should be sufficiently stable to allow appreciable reaction with the ECL precursor.
3. *Electrochemical properties.* The coreactant should be easily oxidized or reduced with the luminophore species at or near the electrode, and undergo a rapid chemical reaction to form an intermediate that has sufficient reducing or oxidizing energy to react with the oxidized or reduced luminophore to form the excited state.
4. *Kinetics.* The reaction rate between the intermediate and the oxidized, or reduced luminophore species must be rapid (43).
5. *Quenching effect.* The coreactant and its redox products should not be good quenchers of the ECL compound's luminescence (43).
6. *ECL background.* The coreactant itself should not give any ECL signal over the potential range scanned.

13.3.2.4 Typical coreactant ECL systems and their mechanisms

Although there are a wide variety of molecules that exhibit ECL, the overwhelming majority of publications concerned with coreactant ECL and its analytical applications are based on chemistry involving $\text{Ru}(\text{bpy})_3^{2+}$, or closely related analogs as the emitting species (8), because of their excellent chemical, electrochemical, and photochemical properties even in aqueous media and in the presence of oxygen (125). As a result, much of this section concerns $\text{Ru}(\text{bpy})_3^{2+}$ /coreactant ECL systems.

(a) Oxalate ($\text{C}_2\text{O}_4^{2-}$) system

This was the first account of coreactant ECL system reported in the literature by Bard's group in 1977 (16), and is a classical example of "oxidative-reduction" ECL. The ECL mechanism of this system was proposed to be as in Scheme 13.4 (17).



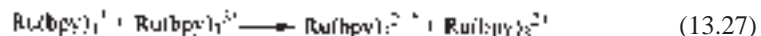
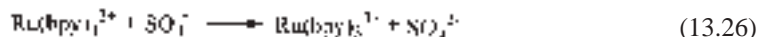
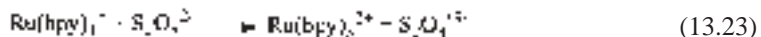
Scheme 13.4 (from reference (123)).

Firstly, the Ru(bpy)_3^{2+} is oxidized at the electrode to the Ru(bpy)_3^{3+} cation. This species is then capable of oxidizing the oxalate ($\text{C}_2\text{O}_4^{2-}$) in the diffusion layer close to the electrode surface to form an oxalate radical anion ($\text{C}_2\text{O}_4^{\bullet-}$). This breaks down to form a highly reducing radical anion ($\text{CO}_2^{\bullet-}$, $E^\circ = -1.9$ V vs. NHE (126)) and carbon dioxide. The reducing intermediate then either reduces the Ru(bpy)_3^{3+} complex back to the parent complex in an excited state, or reduces Ru(bpy)_3^{2+} to form Ru(bpy)_3^{+} that reacts with Ru(bpy)_3^{3+} to generate the excited state Ru(bpy)_3^{2+*} , which emits light with $\lambda_{\text{max}} \sim 620$ nm.

In aqueous solutions, the ECL intensity of the Ru(bpy)_3^{2+} /oxalate system has been reported to have a maximum at \sim pH 6 (17), and also to be essentially constant from pH 4–8 (19, 127) at macro-electrodes and from pH 5–8 at ultramicroelectrodes (128).

(b) Peroxydisulfate (persulfate, $\text{S}_2\text{O}_8^{2-}$) system

This was the first example of so called “reductive-oxidation” coreactant ECL system reported in the literature (124, 129). Because Ru(bpy)_3^{+} is unstable in aqueous solutions and $(\text{NH}_4)_2\text{S}_2\text{O}_8$ has a low solubility in MeCN solutions, the MeCN–H₂O mixed solutions were chosen to produce intense ECL emission (124). Scheme 13.5 summarizes the possible pathways for the production of Ru(bpy)_3^{2+*} when $\text{S}_2\text{O}_8^{2-}$ is used as the coreactant, in which the strongly oxidizing intermediate $\text{SO}_4^{\bullet-}$, generated during reduction of $\text{S}_2\text{O}_8^{2-}$, has a redox potential of $E^\circ \geq 3.15$ V vs. SCE (130).

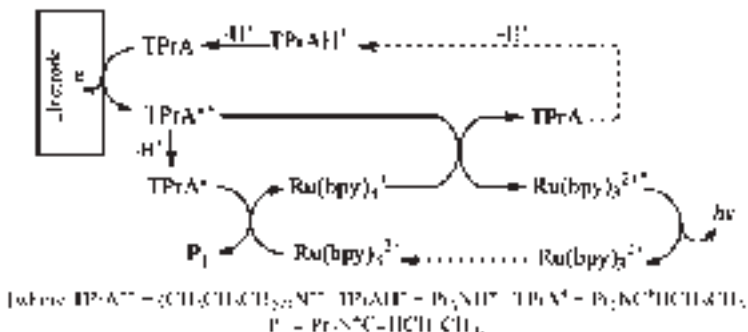


Scheme 13.5 (from reference (123)).

It is believed that persulfate ion is a coreactant of Ru(bpy)_3^{2+} ECL as well as an effective quencher of the excited state Ru(bpy)_3^{2+*} (124, 131). As a result, the ECL intensity of the $\text{Ru(bpy)}_3^{2+}/\text{S}_2\text{O}_8^{2-}$ system was found to be a function of $\text{S}_2\text{O}_8^{2-}$ concentration, and for 1 mM Ru(bpy)_3^{2+} solution the maximum ECL intensity was obtained at 15–20 mM $\text{S}_2\text{O}_8^{2-}$ (124).

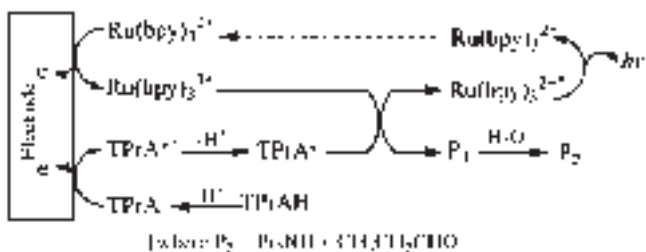
(c) *Tri-n-propylamine (TPrA) system*

The majority of ECL applications reported so far involve $\text{Ru}(\text{bpy})_3^{2+}$ or its derivatives as an emitter (or label) and TPrA as a coreactant, because the $\text{Ru}(\text{bpy})_3^{2+}/\text{TPrA}$ system exhibits the highest ECL efficiency and this system forms the basis of commercial systems for immunoassay and DNA analysis (132, 133). The ECL mechanism of this reaction is very complicated and has been investigated by many workers (20, 21, 134–138). Generally, the ECL emission of this system as a function of applied potential consists of two waves (Figure 13.4). The first occurs with the direct oxidation of TPrA at the electrode, and this wave is often merged into the foot of the second wave when relatively high concentrations of $\text{Ru}(\text{bpy})_3^{2+}$ (~mM) are used. The second wave appears where $\text{Ru}(\text{bpy})_3^{2+}$ is oxidized (137, 138). Both waves are associated with the emission from $\text{Ru}(\text{bpy})_3^{2+*}$ (138). The relative ECL intensity from the first wave is significant, particularly in dilute $\text{Ru}(\text{bpy})_3^{2+}$ solutions ($<\sim \mu\text{M}$) containing ~ 0.1 M TPrA. Thus, the bulk of the ECL signal obtained in this system with low concentrations of analytes, as in immunoassays and DNA probes with $\text{Ru}(\text{bpy})_3^{2+}$ as an ECL label, probably originates from the first ECL wave. Scheme 13.6 summarizes the mechanism of the first ECL wave, where cation radical species $\text{TPrA}^{\bullet+}$ formed during TPrA oxidation is a sufficiently stable intermediate with a half-life of ~ 0.2 ms that it can oxidize $\text{Ru}(\text{bpy})_3^{2+}$ (formed from the reduction of $\text{Ru}(\text{bpy})_3^{2+}$ by TPrA $^{\bullet}$ free radical) to give $\text{Ru}(\text{bpy})_3^{2+*}$ (137).



Scheme 13.6 (from reference (137)).

The mechanism of the second ECL wave follows the classic “oxidative-reduction” coreactant mechanism (Section 13.3.2.1), where oxidation of TPrA generates a strongly reducing species TPrA $^{\bullet}$ ($E_{\text{P}_1/\text{TPrA}}^{\circ} \approx -1.7$ V vs. SCE (112)). This oxidation can be via a “catalytic route” where electrogenerated $\text{Ru}(\text{bpy})_3^{2+}$ reacts with TPrA as well as by direct reaction of TPrA at the electrode described by both Scheme 13.7 and Scheme 13.8 (137):



Scheme 13.7 (from reference (137)).

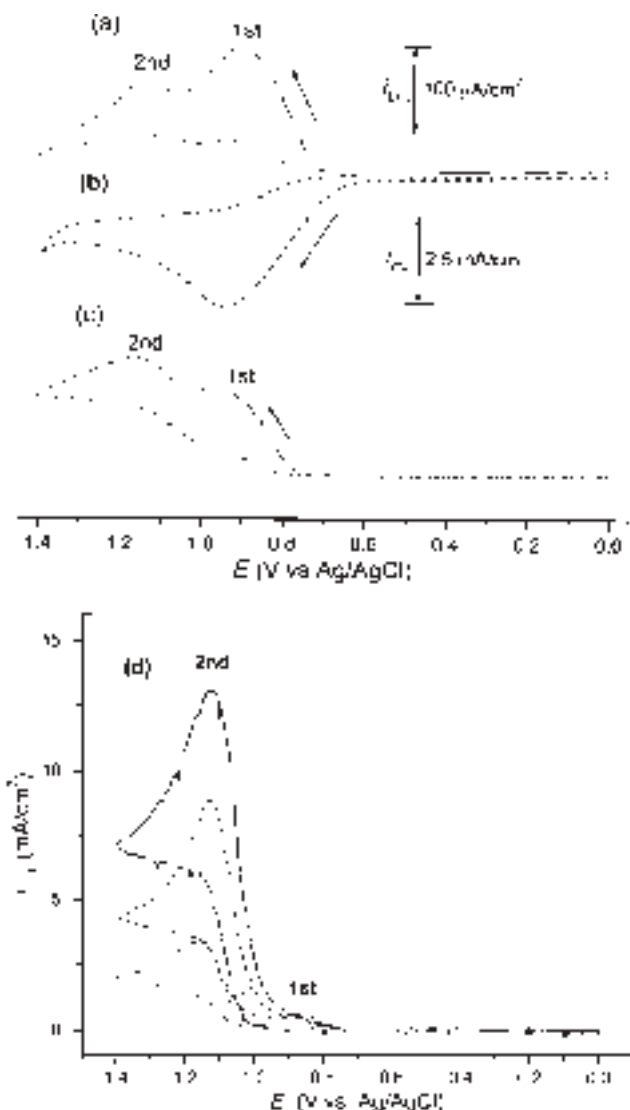
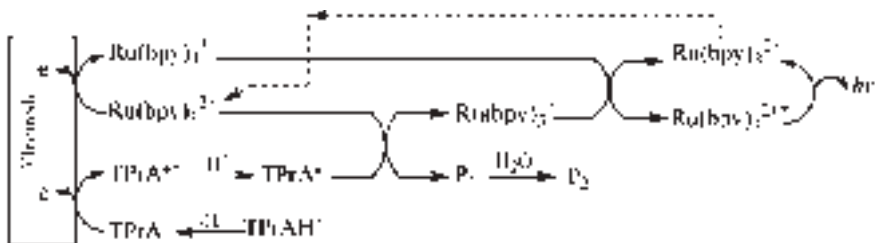
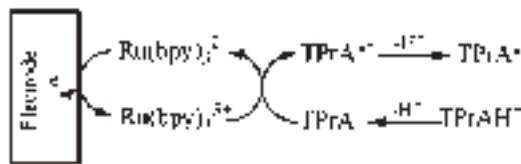


Figure 13.4 (a) ECL, (b) cyclic voltammogram of 1.0 nM Ru(bpy)₃²⁺ in the presence of 0.10 M TPrA with 0.10 M Tris/0.10 M LiClO₄ buffer (pH = 8) at a 3 mm diameter glassy carbon electrode at a scan rate of 50 mV/s. (c) As (a) but with 1.0 μM Ru(bpy)₃²⁺. The ECL intensity scale is given for (c) and should be multiplied by 100 for (a). (d) The first and the second ECL responses in 0.10 M TPrA (0.20 M PBS, pH = 8.5) with different Ru(bpy)₃²⁺ concentrations: 1 mM (solid line), 0.50 mM (dashed line), 0.10 mM (dotted line), and 0.05 mM (dash-dotted line), at a 3 mm diameter glassy carbon electrode at a scan rate of 100 mV/s (from reference (137)).



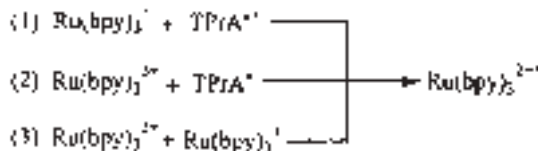
Scheme 13.8 (from reference (137)).

The “catalytic route” involving homogeneous oxidation of TPrA with $\text{Ru}(\text{bpy})_3^{3+}$ is shown in Scheme 13.9 (137). The contribution of this process to the overall ECL intensity, depends upon the $\text{Ru}(\text{bpy})_3^{2+}$ concentration, and is small when relatively low concentrations of $\text{Ru}(\text{bpy})_3^{2+}$ are used (134).



Scheme 13.9 (from reference (137)).

The excited state of $\text{Ru}(\text{bpy})_3^{2+}$ can be produced via three different routes (Scheme 13.10): (i) $\text{Ru}(\text{bpy})_3^{3+}$ oxidation by $\text{TPrA}^{\bullet+}$ cation radicals, (ii) $\text{Ru}(\text{bpy})_3^{3+}$ reduction by TPrA^{\bullet} free radicals, and (iii) the $\text{Ru}(\text{bpy})_3^{3+}$ and $\text{Ru}(\text{bpy})_3^{2+}$ annihilation reaction.



Scheme 13.10 (from reference (123)).

The nature of a working electrode surface can significantly affect the ECL intensity produced from the $\text{Ru}(\text{bpy})_3^{2+}/\text{TPrA}$ system. Among Au, Pt, and glassy carbon (GC) electrodes, GC exhibits the strongest ECL response. The ECL intensity also depends on the solution pH (20, 44) (Figure 13.5), with dramatic increases at $\sim \text{pH} > 5.5$ and a maximum value at pH 7.5. Usually, pHs higher than 9 should not be used, since $\text{Ru}(\text{bpy})_3^{3+}$ generated at the electrode could react with hydroxide ions to produce a significant ECL background signal (139).

(d) Pyruvate/Ce(III) system

Upon anodic oxidation, ECL can be generated from an acidic solution containing pyruvate, Ce(III), and $\text{Ru}(\text{bpy})_3^{2+}$ species (17). The strong oxidant Ce(IV) produced from the oxidation of Ce(III) at the Pt electrode can oxidize pyruvate, resulting in the formation of the strongly reducing intermediate $\text{CH}_3\text{CO}^{\bullet}$. This species behaves in a similar way to

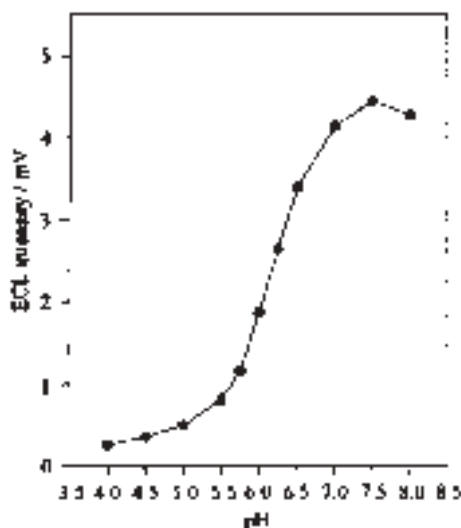
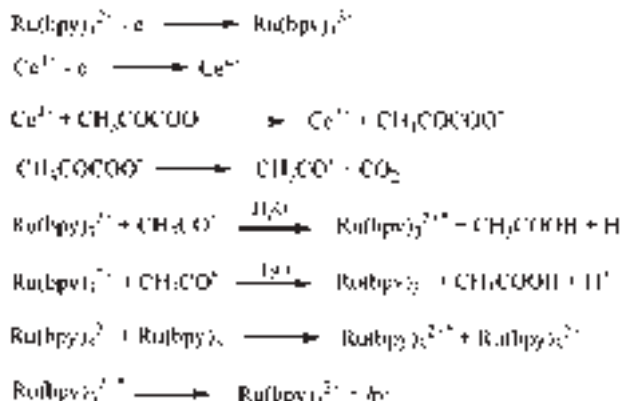


Figure 13.5 Effect of pH on the ECL intensity from the reaction of $\text{Ru}(\text{bpy})_3^{2+}$ with TPrA (from reference (42)).

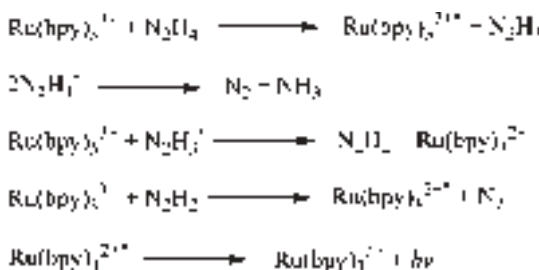
$\text{CO}_2^{\bullet-}$, and participates in electron-transfer reactions with $\text{Ru}(\text{bpy})_3^{3+}$ and $\text{Ru}(\text{bpy})_3^{2+}$, as shown in Scheme 13.4 for oxalate, to produce ECL. The reaction mechanism of this system is summarized in Scheme 13.11.



Scheme 13.11 (from reference (123)).

(e) Hydrazine (N_2H_4) system (140–143)

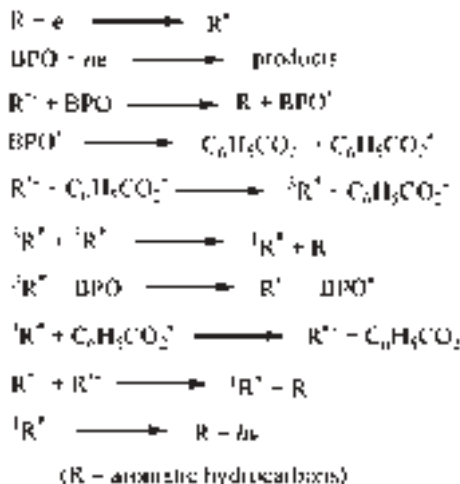
Scheme 13.12 summarizes the ECL mechanism of $\text{N}_2\text{H}_4/\text{Ru}(\text{bpy})_3^{2+}$ system, in which the reactions between $\text{Ru}(\text{bpy})_3^{3+}$ and N_2H_4 , and between $\text{Ru}(\text{bpy})_3^{3+}$ and N_2H_2 were believed to be about 1% and about 99% efficient, respectively (140).



Scheme 13.12 (from reference (123)).

(f) Benzoyl peroxide (BPO) system

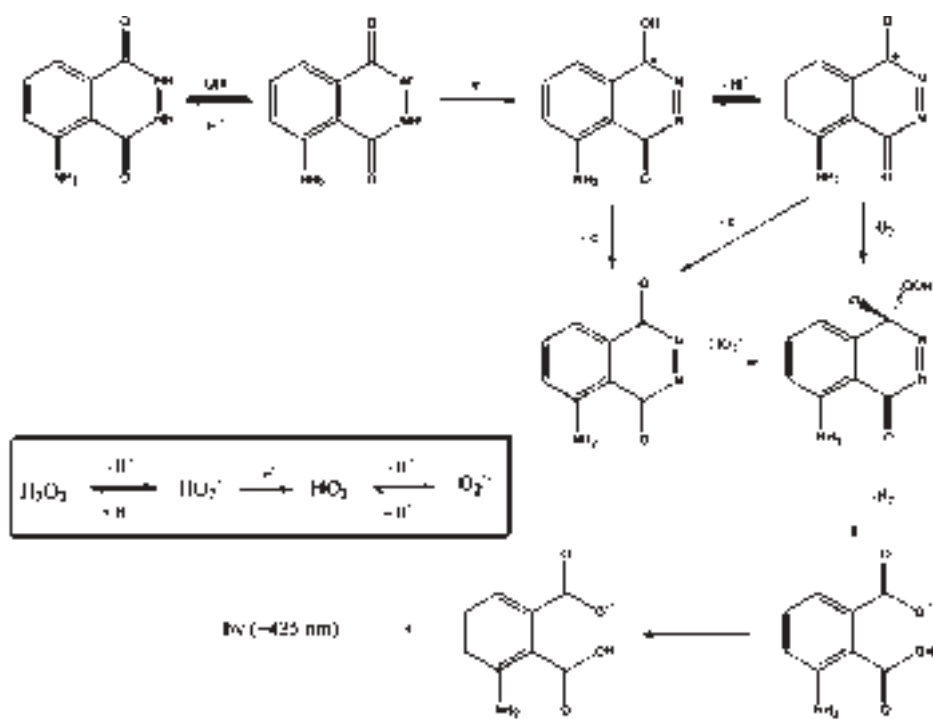
Benzoyl peroxide (BPO) can be used as a coreactant, because, like persulfate, BPO can produce a reactive oxidizing agent, benzoate radical ($\text{C}_6\text{H}_5\text{CO}_2^\bullet$), after it is reduced. The newly formed benzoate radical is energetic enough to react with some cation radicals to form the excited states, since the redox potential value for $\text{C}_6\text{H}_5\text{CO}_2^\bullet/\text{C}_6\text{H}_5\text{CO}_2^-$ couple ($> +1.5$ V vs. SCE) (144), is quite positive. Akins et al. (145, 146) demonstrated that ECL of various aromatic hydrocarbons, such as 9,10-DPA, rubrene, fluoranthene, and anthracene, can be generated in the presence of BPO, after the electrode was brought to a potential of -1.90 V vs. SCE. The ECL mechanism proposed by Akins et al. was considered to be energy-deficient (Scheme 13.13), although the energy-sufficient route may also exist (144).



Scheme 13.13 (from reference (123)).

(g) Luminol/Hydrogen peroxide system

The ECL reaction of luminol (5-amino-2,3-dihydro-1,4-phthalazinedione) with hydrogen peroxide in alkaline medium is similar to the CL of luminol triggered by chemical oxidation (34, 147). The general accepted mechanism is shown in Scheme 13.14. In alkaline solution luminol deprotonates to form an anion, which then undergoes electrochemical oxidation to produce a diazaquinone. This species is further oxidized by peroxide or superoxide to give 3-aminophthalate in an excited state that emits light at ~ 425 nm.



Scheme 13.14 (from reference (54)).

13.4 EXPERIMENTAL SETUP

The basic components of an ECL instrument include an electrical energy supply for the ECL reaction at an electrode within an electrochemical cell and an optical detector for the measurement of either the emitted light intensity or its spectroscopic response. Although certain types of ECL instruments are now commercially available (Section 13.4.3.2), most of the ECL studies reported in the literature were carried out in “home-made” ECL instruments.

13.4.1 Electrochemical media

Before the first aqueous ECL was reported in 1981 (17), all ECL studies were almost exclusively carried out in organic media. In these cases, the purity of the solvent/supporting electrolyte is very crucial, because trace amounts of water, and oxygen can significantly affect the ECL production by either disabling the generation of both reductive and oxidative ECL precursor species at the electrode or quenching the newly formed excited state species. As a result, the apparatus is constructed to allow transfer and degassing of solvent on a high-vacuum line or in an inert-atmosphere box (2).

Commonly used electrolytes, such as tetra-*n*-butylammonium perchlorate (TBAP), tetra-*n*-butylammonium fluoborate (TBABF₄), tetra-*n*-butylammonium hexafluorophosphate (TBAPF₆), tetraethylammonium perchlorate (TEAP), can be purchased from

“Sigma-Aldrich” (www.sigmaaldrich.com) as “electrochemical grade” reagents. They normally can be used as received, but recrystallization is sometimes needed (148). These electrolytes are hydroscopic and must be dried *in vacuo* for 24–48 h at 90–100°C (149). The dried lots should be kept in a desiccator or in a dry box. Solvents are also often required to be dried and purified. Detailed discussions on solvent and electrolyte drying and purification can be found from the literature (150). Although many anhydrous high-purity (spectrophotometric and HPLC grade) solvents are commercially available (e.g., from Sigma-Aldrich, EM, Burdick and Jackson), caution must be taken while handling the solvents. They should be isolated from the atmosphere during storage, and all solutions should be prepared inside an oxygen-free dry box and sealed in an appropriate airtight electrochemical cell for measurements carried out outside the dry box (149).

Oxygen-free solvents can be also obtained by treating them via an “auxiliary vessel” connected to a vacuum line before transferring to electrochemical cells (Figure 13.6) (114). This device is said to be particularly useful for vigorous ECL studies and to offer the best compromise between convenience, flexibility, and effectiveness in handling materials (149).

The simplest way to remove oxygen from the solvent is to bubble the solvent with an inert gas, e.g., high-purity N₂ or Ar. Since oxygen has a high solubility in organic solvents with respect to aqueous media, long bubbling time is often required. In order to avoid the

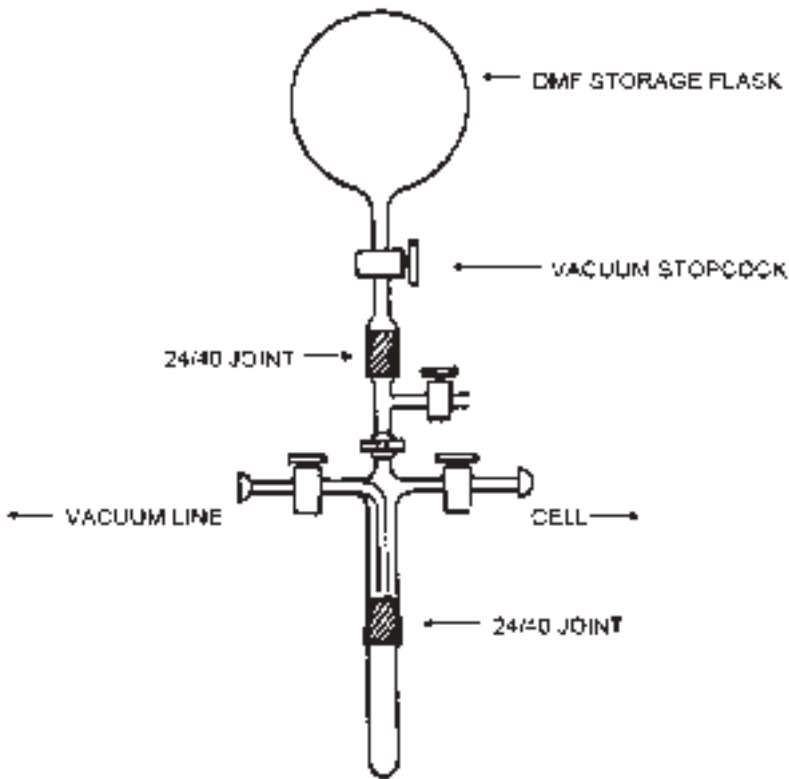


Figure 13.6 Auxiliary vessel for oxygen-free ECL solution preparation (from reference (114)).

solvent loss and to keep the solution concentration unchanged, a bubbler containing the solvent of interest is frequently needed to be connected between the inlet of inert gas and the solvent cell.

Table 13.3 lists the commonly used solvent-supporting electrolyte systems for ECL study.

13.4.2 Cell design and electrodes

Several types of cells with three conventional electrodes have been used for ECL studies. The most commonly used ECL cell for ion annihilation study in Bard's group at the University of Texas at Austin is shown in Figure 13.7a. This type of cell can be easily fabricated from an ACE (www.aceglass.com) internal threaded glass connector

Table 13.3

ECL solvent-supporting electrolytes systems (modified from reference (149))

Solvent	Supporting electrolyte	Potential range (V vs. SCE, at Pt)	Remarks
Acetonitrile	TBABF ₄ , TBAP, TEAP, TBAPF ₆	−1.8 to +2.8	Good stability for both radical anions and cations; potential range strongly depends upon purification
Benzonitrile	TBABF ₄	−1.8 to +2.5	Similar to acetonitrile in terms of ion stabilities; commercial spectro-grade solvent can be used without purification
<i>N,N</i> -Dimethylformamide	TBAP	−2.8 to +1.5	Good stability for radical anions; poor for cations; difficult to purify and tends to decompose or hydrolyze on standing
Dimethylsulfoxide	TEAP	−1.8 to +0.9	Purified by vacuum distillation, collecting the middle 60%; can be stored on molecular serves; limited positive potential range
Methylene chloride	TBAP	−1.7 to +1.8	Excellent stability of cations; limited negative potential range; easily purified; quite resistive
Propylene carbonate	TEAP	−2.5 to +2.0	Purified by reduced pressure distillation at 120–130°C, collect the middle 60% fraction; potential range depends greatly on purity; good stability for radical cation
Tetrahydrofuran	TBAP	−3.0 to +1.4	Excellent stability of anions; easily purified and dried with alkali metals; limited positive potential range; quite resistive
Acetonitrile-benzene mixed solvent (1.5:1 to 4:1)	TBABF ₄ , TBAP, TBAPF ₆	−2.3 to +2.0	Better solubility for some aromatic compounds; quite resistive, depending on the ratio of benzene to acetonitrile

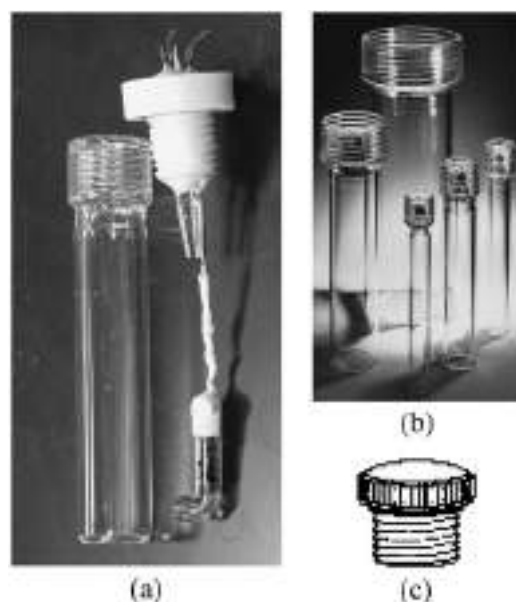


Figure 13.7 (a) Commonly used cell for annihilation ECL study, (b) which can be fabricated from ACE glass internal threaded connectors, (c) Teflon or PTFE plugs. (for colour version: see colour section at the end of the book).

(Figure 13.7b) by flame sealing of the tube bottom and a suitable-sized Teflon or ACE PTFE plug (Figure 13.7c). Three metal wires for electrode potential connections are pierced through the plug and sealed with an epoxy or “Torr-seal” sealant.

For coreactant ECL studies, e.g., in aqueous $\text{Ru}(\text{bpy})_3^{2+}/\text{TPrA}$ solution, degassing is often unneeded. Thus, Fisherbrand glass tool-neck vials (www.fishersci.com) are frequently used as ECL cells. When ECL experiments are carried out at a wafer-type electrode, such as indium tin oxide (ITO), Au/Si (151) and highly oriented pyrolytic graphite (HPOG) (152), the effective area of the electrode can be controlled by using a cell similar to that shown in Figure 13.8. The electrode surface exposed to the electrolyte solution containing a coreactant should face the window of the photo-detector.

ECL has been widely used as a detector in FIA, liquid chromatography, and CE (153). Figure 13.9 displays schematic diagrams of a FI-ECL flow-through thin-layer cell (154) and an ECL cell coupled with separation capillary for end-column mode CE detection (155). In addition to millimeter order-sized working electrodes, a microelectrode ($w = 2 \mu\text{m}$, $l = 2.5 \text{ cm}$) was also constructed by sealing a piece of platinum foil between two microscope slides with epoxy into an ECL flow cell (Figure 13.10) (24). This type of cell has been employed in high-frequency ECL studies. The reduced time scale enables reaction kinetics to be accessed and affords a means for investigating ECL without rigorously purifying solvents or working on a vacuum line or in a dry box (24).

A flow cell system based on ORIGIN technology for ECL assays employing magnetic beads is shown in Figure 13.11 (133).

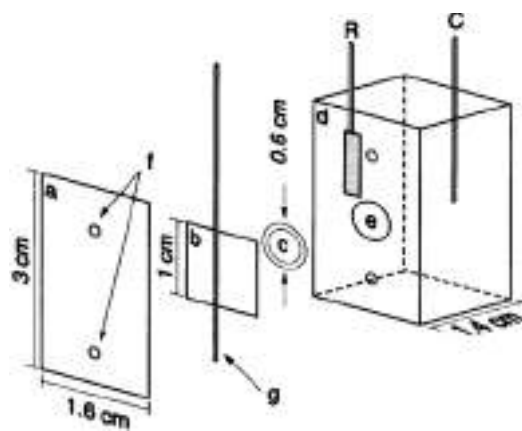


Figure 13.8 Schematic diagram of the cell used for ECL and electrochemical measurements designed so that the edges of the electrode are not exposed to the solution: (a) Plexiglas sheet; (b) working electrode; (c) O-ring; (d) Plexiglas cell; (e) hole exposing the working electrode to the solution; (f) screw holes; (g) copper wire (from reference (152)).

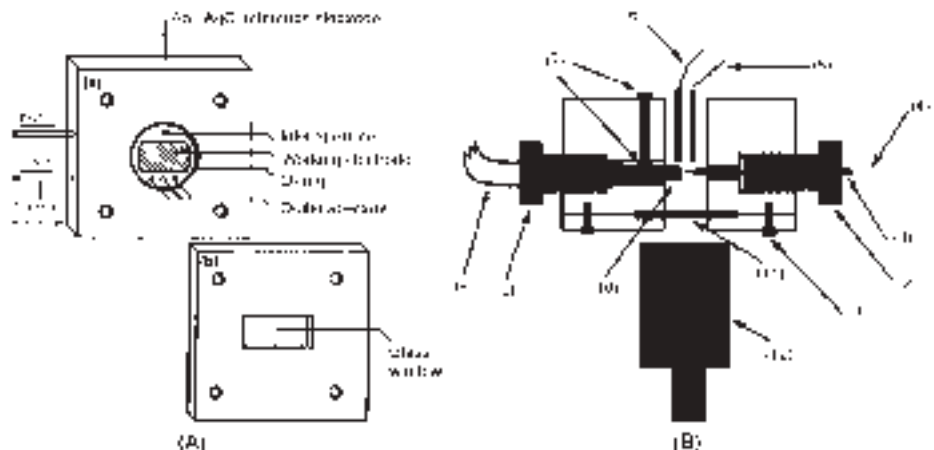


Figure 13.9 Schematic diagrams of (A) a FI-ECL flow-through thin-layer cell. (a) Cell body; (b) Cell cover window, and (B) an ECL cell coupled with separation capillary for end-column mode. (1) Stainless-steel holding screw; (2) PVC capillary holder; (3) stainless-steel tube; (4) separation capillary; (5) reference electrode; (6) counter electrode; (7) nylon screws for alignment; (8) working electrode cable; (9) PVC electrode holder; (10) working electrode; (11) optical glass window; (12) PMT (from references (154, 155)).

For ECL spectral recording, it is generally required that the working electrode be aligned so that its surface faces the slit of a monochromator. A J-shaped electrode serves such a purpose when an airtight “normal” ECL cell (Figure 13.7a) is used. Alternatively, a “small” ECL cell that fits a spectrometer cuvette holder can be fabricated. As shown in

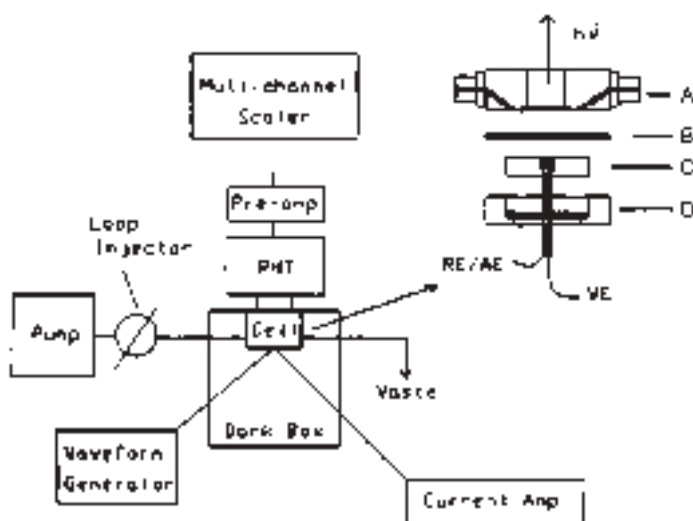


Figure 13.10 Simplified block diagram of ECL flow cell and equipment: (A) stainless-steel cell body housing an optical window; (B) polyethylene spacer; (C) epoxy-encased microelectrode; (D) stainless-steel electrode retainer (from reference (24)).

Figure 13.12 (156), this special cell features a large-area working electrode made from Pt foil or coil and is capable of being evacuated to less than 10^{-5} Torr. The concentric counter electrode is located ~4 cm above the working electrode and is out of the field of view of the photo-detector, so its emission remains undetected. An Ag/AgCl (KCl, sat.) aqueous reference electrode with a non-aqueous salt bridge is fitted into the working/electrode support.

Three types of electrode configurations are commonly used in ECL study: single, dual, and rotating ring disk electrodes (RRDE). In the case of a single electrode, an AC potential, such as multi-step or pulse potential is applied scanning between the redox potential of the particular species desired. Dual electrode configurations, such as shown in Figure 13.2c and a micro-double band electrode (157), use DC potentials for the continuing generation of reductive species at the cathode and oxidative species at the anode. Since the dual electrodes are placed in close proximity (~<100 μ m apart), annihilation ECL takes place in the region where the newly produced anion and cation species meet because of diffusion and/or electro-hydrodynamic convection. A RRDE can also be regarded as a dual electrode, in which the ring or the disk may be set at a potential to produce the oxidized species and the disk or the ring set to produce a reduced species. The species produced at the disk are swept away and react with the species at the ring. Thus, a ring of light (ECL) is expected to be observed around the internal region of the ring.

The nature of the working electrode, i.e., material and surface properties, can significantly affect the ECL production (158). Most commonly used electrode materials include Pt (159), Au (151), GC (137), HPOG (152), ITO (160), and heavily boron-doped diamond (161, 162). It is generally accepted that a Pt electrode gives the highest ECL intensity for

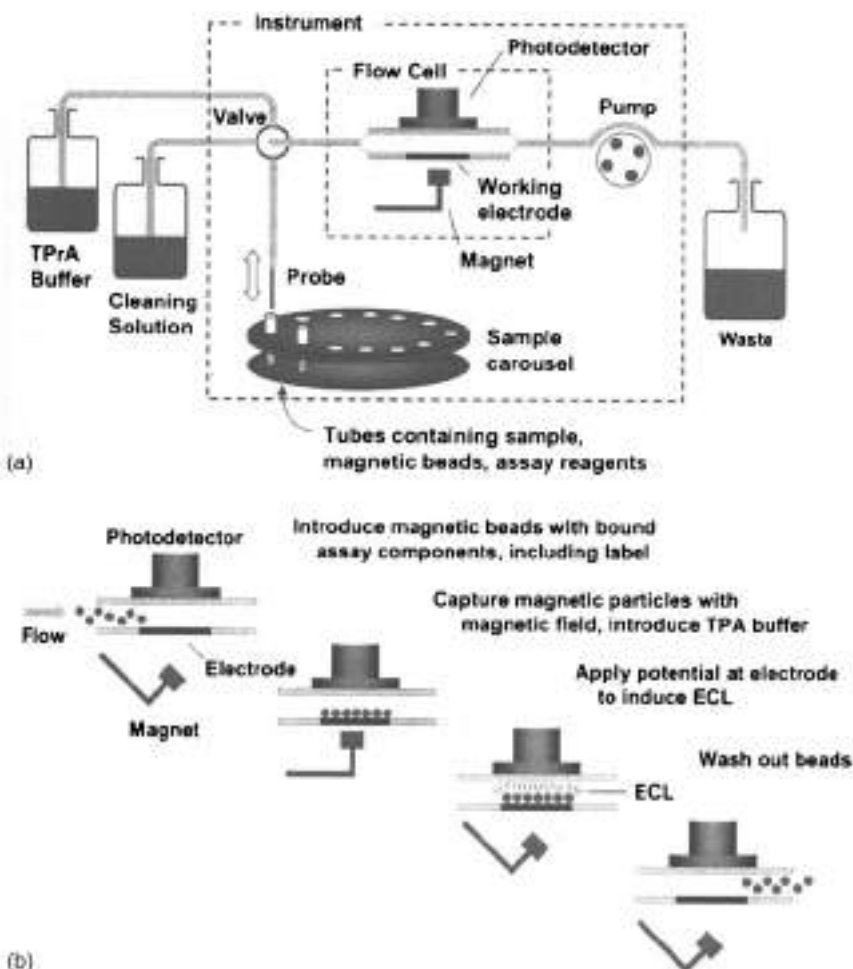


Figure 13.11 (a) Components of a flow system based on ORIGIN technology, (b) Generic process for measuring magnetic bead-based ECL assays in flow cell (from reference (133)).

organic ECL systems, such as those in MeCN media, while a GC electrode is the best for aqueous ECL generation, such as for aqueous $\text{Ru}(\text{bpy})_3^{2+}/\text{TPrA}$ systems.

13.4.3 Light detection and ECL instrumentation

13.4.3.1 Light detection

In ECL studies, photodiodes, photomultiplier tubes (PMT), and charged coupled device (CCD) cameras are the three most commonly used light detectors. Of them, PMT provide the most sensitive means of detecting light, and are capable of detecting single photons. There are generally two different kinds of light detection modes required in ECL: ECL intensity measurements and ECL spectral recording. The first one is mainly used for

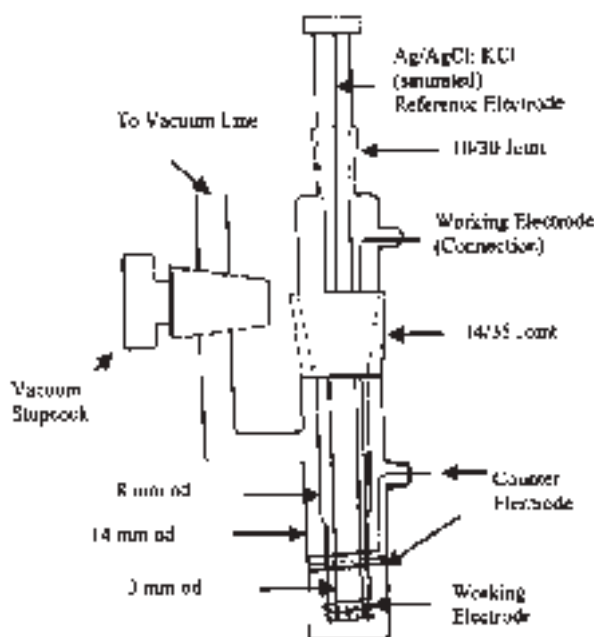


Figure 13.12 ECL cell designed to fit a spectrometer cuvette holder and to be capable of being evacuated to less than 10^{-5} Torr (from references (149, 156)).

quantitative analysis of a given analyte (emitter) or its related species, and the second one is usually used for qualitative analysis. Since ECL signals are often very weak and different emitters have different emitting wavelengths, the selection of ECL light detectors (e.g., types of PMT) and the control of ECL experimental conditions, (e.g., the operating temperature of the detector), are two critical factors that require serious consideration when designing ECL experiments.

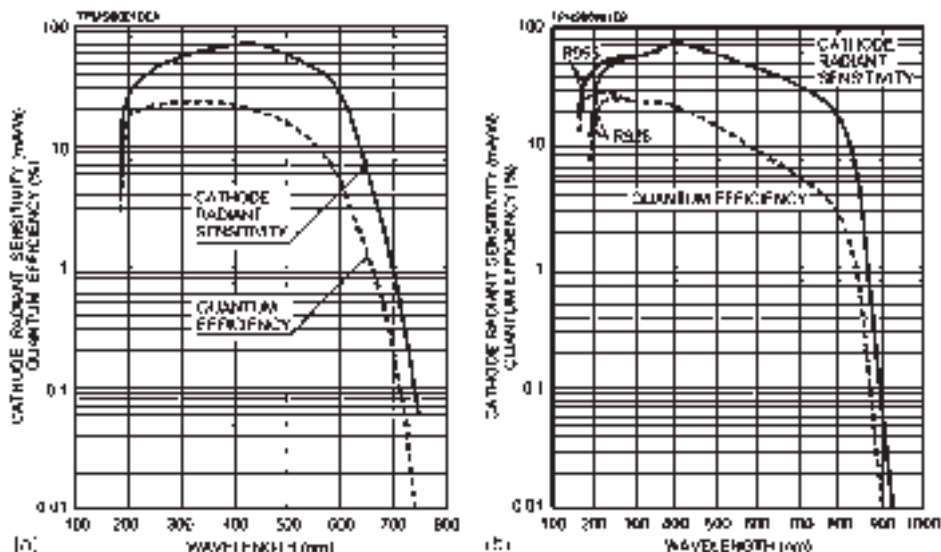
Although a wide range of PMT are commercially available, Hamamatsu (www.hamamatsu.com) R4240 and R928 PMT are perhaps the most popular ones used for ECL studies. Hamamatsu R4220 features extremely high cathode sensitivity, high gain, and low dark current. The R928 features extremely high quantum efficiency, high current amplification, good S/N ratio and wide spectral response from UV to near infrared. Table 13.4 lists the specifications of these two types of PMT. Their typical spectral responses are shown in Figure 13.13.

The solid curves of Figures 13.13a and b show the percent cathode radiant sensitivities of the peak sensitivities at each wavelength over the useful spectral range of the devices. Cathode radiant sensitivity is the amount of current leaving the photocathode divided by the incident radiant power at a given wavelength, usually the wavelength of peak response (see Table 13.4). The dashed curves provide the percent quantum efficiencies at each wavelength. Cathode quantum efficiency may be defined as the average number of photoelectrons emitted per incident photons. The cathode quantum efficiency, QE, in percent at any given wavelength can be calculated from the following formula:

$$QE = S(1239.5/\lambda)(100) \quad (13.28)$$

Table 13.4Hamamatsu R4220 and R928 specifications (from www.hamamatsu.com)

Parameters	R4220	R928
Spectral response	185–710 nm	185–900 nm
Wavelength of maximum response	410 nm	400 nm
Window material	UV glass	UV glass
High cathode sensitivity	At 410 nm	At 400 nm
Luminous	100 μ A/Im	250 μ A/Im
Radiant	70 mA/W	74 mA/W
High anode sensitivity (at 1000 V)	At 410 nm	At 400 nm
Luminous	1200 A/Im	2500 A/Im
Radiant	8.4×10^5 A/W	7.4×10^5 A/W
Gain	1.2×10^7	1.0×10^7
Low dark current	0.2 nA	3 nA
Time response	1.2–22 ns	1.2–22 ns
Anode current sensitivity	0.1% (current hysteresis), 1% (voltage hysteresis)	0.1% (current hysteresis) 1% (voltage hysteresis)

**Figure 13.13** Typical spectral responses of (a) Hamamatsu R4220 and (b) R928 PMT (from www.hamamatsu.com).

where S is the cathode radiant sensitivity at the wavelength λ in amperes per watt, and λ is the wavelength in nanometers. For example, from Table 13.4, the absolute cathode sensitivities for R4220 and R928 are 0.070 A/W at 410 nm, and 0.074 A/W at 400 nm, respectively. The percent quantum efficiencies of them can be calculated as: QE (R4220, 410 nm) = $0.070(1239.5/410)(100) = 21.2$, and QE (R928, 400 nm) = $0.074(1239.5/400)(100) = 22.9$, which, as expected, are consistent with the data shown in Figures 13.13a and b, respectively.

The wavelength of peak response and the long-wavelength cutoff are primarily functions of photocathode material. The short-wavelength cutoff is primarily a function of the window material. Each window material has its characteristic cutoff region that varies from about 300 nm for commonly used lime glass to 105 nm for lithium fluoride. For UV glass window used for R4220 and R928, the short-wavelength is around 185 nm (Table 13.4 and Figure 13.13).

Comparing Figure 13.13a with Figure 13.13b, it is clear that R928 PMT covers a much wider spectral range than R4220 does. If a cutoff cathode radiant sensitivity of 10% is chosen, the “effective spectral response range” for R4220 and R928 would be about 190–630 nm and 185–820 nm, respectively. In this respect, R928 PMT is certainly better than R4220 used for the detection of ECL generated from $\text{Ru}(\text{bpy})_3^{2+}$ species, since, as shown in Figures 13.20 and 13.22, the $\text{Ru}(\text{bpy})_3^{2+}$ ECL spectrum covers a spectral range of about 550 to 800 nm.

Current flows in the anode circuit of a PMT even when the tube is operated in complete darkness. The DC component of this current is called the anode dark current, or simply the dark current. This current and its resulting noise component usually limit the lower level of PMT light detection; as a result, the anode dark current value is nearly always given as part of the data for any tube.

For extremely weak ECL measurements, such as in the ECL spectral recording experiments, the PMT may be cooled down to a certain low temperature so that a much lower dark current with respect to that obtained at room temperature can be achieved. This may be accomplished by using a cooled PMT housing on the basis of thermoelectric, compressor, dry ice, or liquid nitrogen cooler series (www.photocool.com). A typical temperature characteristic of dark current for Hamamatsu R928 is shown in Figure 13.14. The dark current, hence the noise level, is approximately reduced to 1/3 of the previous value for each 10 °C drop in temperature.

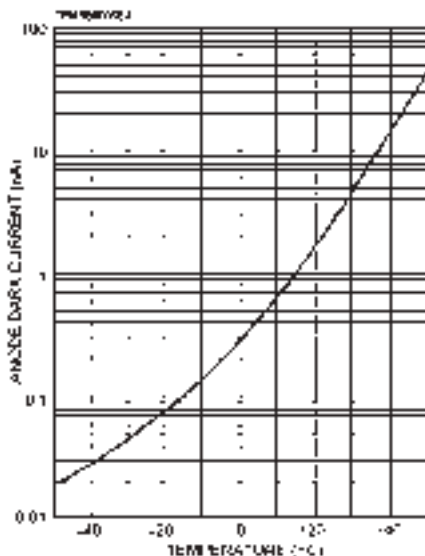


Figure 13.14 Typical temperature characteristic of dark current for Hamamatsu R928 (at 1000 V after 30 min storage) (from www.hamamatsu.com).

13.4.3.2 Commercial ECL instruments

ECL instrumentation has been commercially available from IGEN International Inc. (now BioVeris) since 1994 on the basis of ORIGEN technology (163). The first commercial ECL instrument was the ORIGEN analyzer (Figure 13.15A), which is adapted to measure ECL labels ($\text{Ru}(\text{bpy})_3^{2+}$ or its derivatives) present on the surface of magnetically responsive beads in the presence of TPrA (Figure 13.11). The beads are coated with binding reagents and are used as assay supports in solid-phase binding assays, which are pre-designed so that the amount of label on the beads is correlated with the amount of analyte in a sample. Figure 13.15 shows several examples of commercial flow cell-based ECL instruments (133).

Unlike ECL instruments based on ORIGEN technology, the Sector HTS Imager, and Sector PR Reader instruments (Figures 13.15H and I) use disposable screen-printed carbon ink electrodes within the wells of multiwell plates. Each well contains several binding domains that react with specific targets. ECL is generated using $\text{Ru}(\text{bpy})_3^{2+}$ analogs and TPrA or similar coreactants, and the light is collected with either a CCD camera (Sector HTS Imager) or a series of photodiodes (Sector PR Reader) (Figure 13.16) (133).

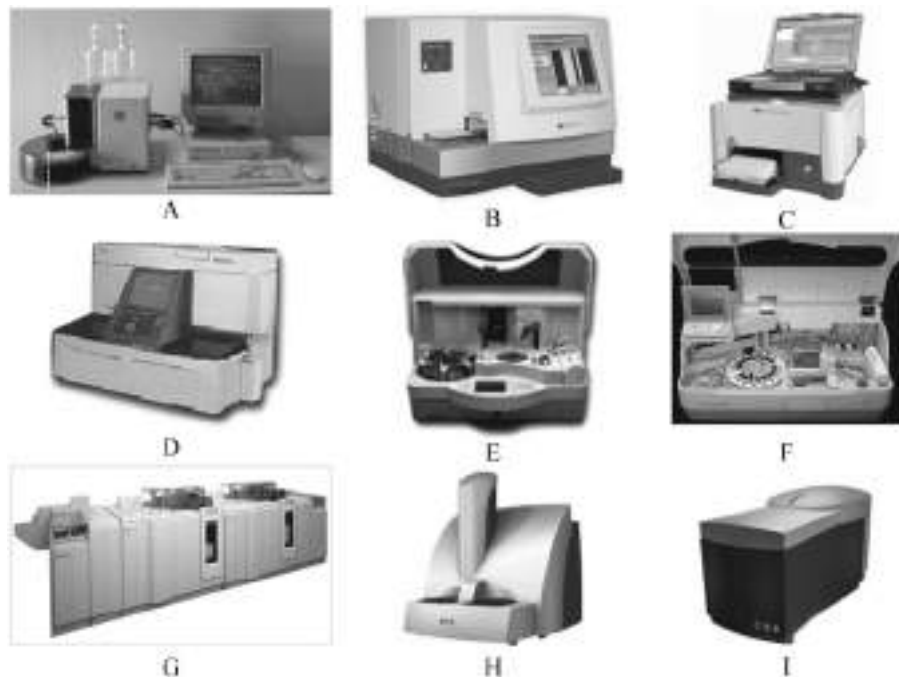


Figure 13.15 Commercial flow cell-based ECL instrumentation. (A) The ORIGEN 1.5, (B) M series M-384 analyzer by Igen International (now BioVeris, www.bioveris.com), (C) M-1 analyzer by Igen International, (D) PicoLumi by Eisai, Japan, (E) Elecsys 1010, (F) Elecsys 2010, (G) the MODULAR system containing E-170 immunoassay module by Roche Diagnostics (www.roche-diagnostics.com), (H) Sector HTS Imager, and (I) Sector PR Reader by Meso Scale Discovery (meso-scale.com) (modified from reference (133)).

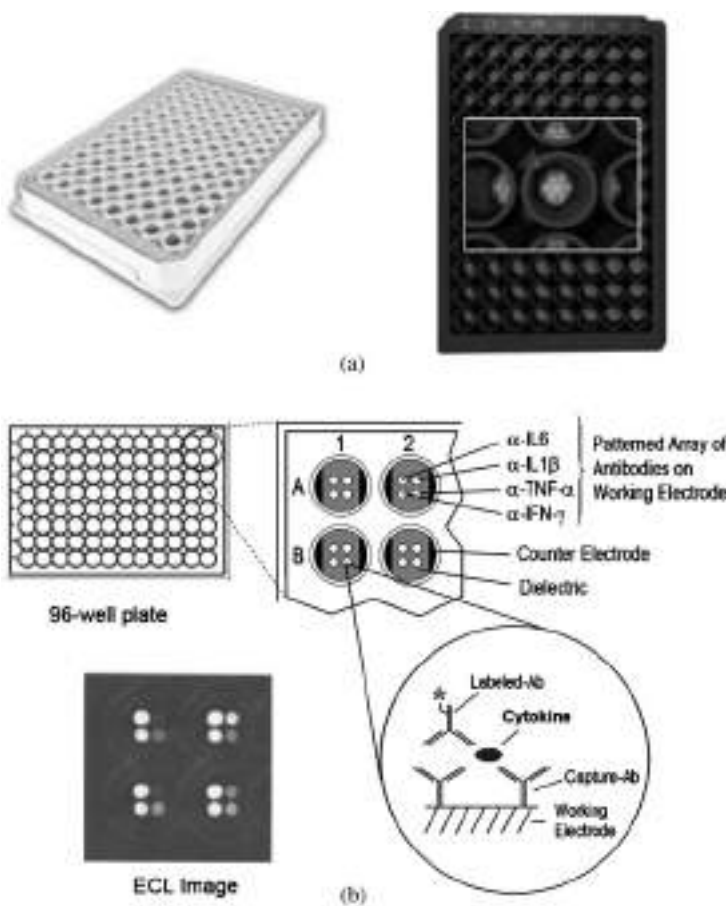


Figure 13.16 (a) Pictures of Meso Scale Discovery multi-spot plates with seven binding domains in each well of the 96-well plates. (b) Schematic diagram of a multi-spot plate assay for four human cytokines. Each spot within each well of the 96-well plate contains capture antibody specific for one cytokine. Inset shows an image of the ECL emitted from assays in four wells using samples with varying concentrations of cytokines (from reference (133)).

A commercial CE ECL system fabricated in Changchun Institute of Applied Chemistry, Chinese Academy of Science has been recently reported (9).

13.4.3.3 Other ECL setups for emitted light intensity measurements

The basic components of a home-made ECL instrument for ECL intensity measurement generally consist of a potentiostat, an electrochemical cell, a light detector, and a data acquisition system. Many recently produced computer-based potentiostats, such as CH660A (CH Instruments, Austin, Texas, www.chinstruments.com), Autolab PGSTAT100 (Autolab Electrochemical Instruments, the Netherlands, www.ecochemie.nl), have external signal

recording functions, which can be used to record/collect the ECL signals along with the electrochemical responses obtained at the surface of the working electrode. When an old model or home-made potentiostat combined with a potential function generator is used for the ECL experiment, the LabVIEW software and related hardware (National Instruments, Austin, Texas, www.ni.com) may be used to control the devices, collect all the desired data to a computer, and display them on the screen. In most cases, light detection is made by a bare PMT (e.g., Hamamatsu R4240 or R928) that is applied with a high voltage (~ -500 to -1000 V) using a high voltage power supply (e.g., Brandenburg Photomultiplier Power Supply). The light signal (as photocurrent) can be measured with a high sensitive electrometer (e.g., Keithley 6517, 6514 electrometer, Keithley, Cleveland, Ohio, www.keithley.com) and converted to a voltage (normally in the range of ± 2 V) that is collected/recorded to the computer. A schematic diagram of an ECL instrumental setup is illustrated in Figure 13.17. The PMT and the electrochemical cell must be placed in a light-tight box to avoid any environmental light interference. Alternatively, ECL light can be measured, converted and then collected to a computer using a PMT module system (www.hamamatsu.com). The PMT module is basically comprised of a PMT to convert light to electrical signals, a high voltage power supply circuit, and voltage divider circuit to distribute the optimum voltage to each dynode, all assembled in a single compact case. Examples of using PMT modules with AD converters and collecting data to a PC are shown in Figure 13.18.

In addition, ECL experiments can also be carried out using a commercial fluorescence spectrometer coupled with an electrochemical instrument with the excitation function of the fluorimeter disabled. For example, one can have the three electrodes fitted into a standard fluorescence cuvette so that the entire cell system fits into the sample compartment of the spectrometer. The electrodes should be arranged so that the working electrode faces the detection window of the emission monochromator. ECL intensity can be measured either at

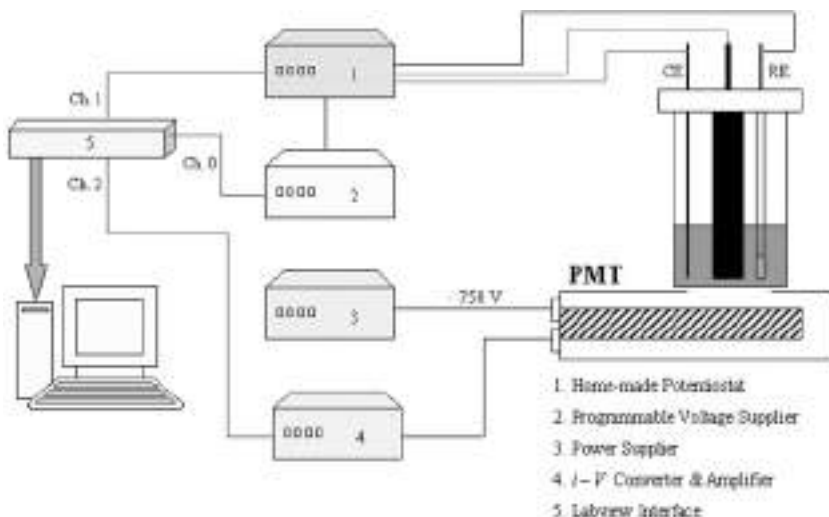


Figure 13.17 Schematic diagram of an ECL instrumental setup. (for colour version: see colour section at the end of the book).

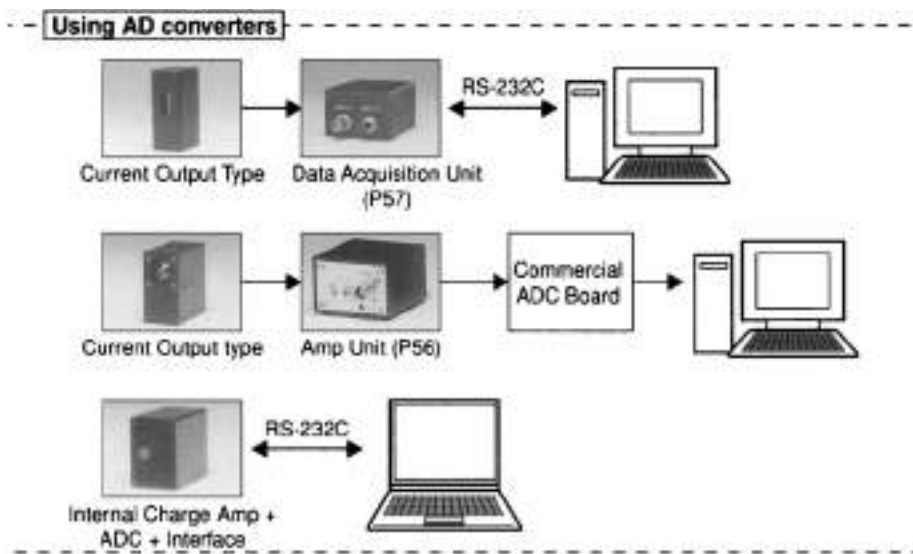


Figure 13.18 Constitution examples of PMT modules with AD converters (from www.hamamatsu.com).

a specific wavelength or over a range of wavelengths. In the latter case, the overall ECL intensity may be integrated from the ECL spectra. Because of the space limitation of the electrochemical cell and the small slit of the emission monochromator etc., the operation of fluorimeter-based ECL measurements may be not as convenient as the other systems mentioned above, and the ECL signals obtained could also be relatively weak.

13.4.3.4 Instrumentation of ECL spectral recording

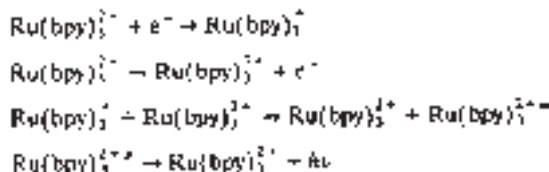
ECL spectra are mainly measured in two ways. The first one is based on a commercial fluorimeter (see Section 13.4.3.3) with a PMT as a light detector. The second way is to use a CCD camera as the light detector. Because the ECL signal is generally very weak, and the acquisition of the signal is often carried out from seconds to minutes, elimination of the background signal (or dark current, Figure 13.14) by cooling down the temperature of the detector is often required. The ECL spectral recording instrument in Bard's Lab at the University of Texas at Austin consists of a potentiostat, a Chemspec 100S spectrometer (American Holographic, Littleton, MA), a Photometrics CH260 CCD camera (Photometrics, Tucson, AZ) cooled to $\sim -105^{\circ}\text{C}$ with liquid nitrogen, and a data acquisition system. The spectrometer is calibrated using an Hg (Ar) spectral calibration lamp (e.g., Oriel Instruments, Stratford, CT, www.orient.com). The whole experimental setup is housed in a dark room, and all lights from, e.g., computer, potentiostat, are all properly covered to avoid any possible interference to the ECL spectra. It is generally believed that the light detecting sensitivity of a CCD camera (even in low temperatures) is much less sensitive than a PMT operated even at room temperature. For example, a 25–30 nA ECL photocurrent was readily measured with a potentiostat/Keithley 6517/Hamamatsu R4220

instrumental setup at room temperature, but the ECL spectrum from the same solution using the exactly same electrochemical parameters was almost impossible to record with the Chemspec 100S spectrometer/Photometrics CH260 CCD camera cooled to -105°C configuration when light integration time was less than 30 min.

13.5 TYPES OF EXPERIMENTS

13.5.1 Ion annihilation ECL: $\text{Ru}(\text{bpy})_3^{2+}$ and derivatives

There have been a number of studies of ECL of $\text{Ru}(\text{bpy})_3^{2+}$ in aprotic media (15, 164–168). For example, in MeCN solutions the excited $\text{Ru}(\text{bpy})_3^{2+*}$ is produced by ion annihilation reaction (Scheme 13.1) between $\text{Ru}(\text{bpy})_3^{+}$ and $\text{Ru}(\text{bpy})_3^{3+}$, as outlined in Scheme 13.15.



Scheme 13.15

As discussed in Section 13.3.1.1, one of the criteria for efficient annihilation ECL generation is that both anion and cation radicals formed from the ECL precursor must be stable in the electrolyte of interest, which can be verified by cyclic voltammetry. Figure 13.19 shows the CV behavior of $\text{Ru}(\text{bpy})_3^{2+}$, $\text{Ru}(\text{dp-bpy})_3^{2+}$, and $\text{Ru}(\text{dp-phen})_3^{2+}$ in MeCN containing 0.1 M TBABF₄ at a Pt electrode (166). Clearly, these three compounds have very similar electrochemical responses, and their first oxidation and reduction products are all stable. Not surprisingly, the ECL was readily generated by repetitive potential cycling between E_p^{a} and E_p^{c} at a suitable frequency of, e.g., 10 Hz (Figure 13.20). It is evident that the emission of the two diphenyl compounds is higher than that of the non-substituted $\text{Ru}(\text{bpy})_3^{2+}$. The wavelengths for the emission peaks for all complexes, giving in Table 13.5, are similar, with $\text{Ru}(\text{dp-bpy})_3^{2+}$ shifted to the red compared with the other two.

The relative ECL efficiencies of these compounds can be measured on the basis of the integrated light intensity under the emission curve for a double-pulse experiment (Table 13.5). The ECL efficiencies can be calculated relative to the ECL quantum efficiency of $\text{Ru}(\text{bpy})_3^{2+}$, which is ~5% in MeCN (168, 169). The ECL quantum efficiency is defined as the ratio of the number of photons emitted to the number of annihilations between the 3^+ and the 1^+ forms of the ruthenium complex. The number of annihilations is somewhat smaller than the number of moles of reactant generated during a pulse, as calculated from the integrated current (170, 171). However, this difference is the same for all three complexes, so that, in estimating the relative efficiencies, the following equation can be employed:

$$\phi_{\text{ECL}} = \frac{\int_0^t Idt}{\int_0^t idt(N_A / F)} \quad (13.29)$$

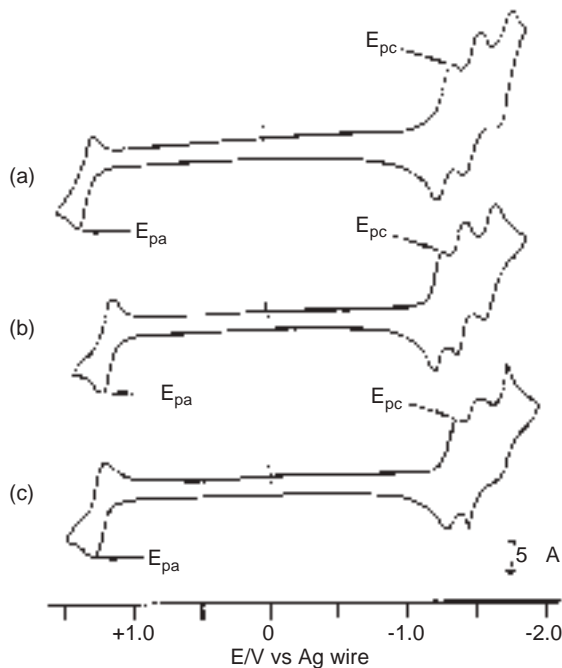


Figure 13.19 Cyclic voltammograms of (a) 1.0 mM $\text{Ru}(\text{bpy})_3^{2+}$, (b) 1.0 mM $\text{Ru}(\text{dp-bpy})_3^{2+}$, and (c) 1.0 mM $\text{Ru}(\text{dp-phen})_3^{2+}$ obtained from MeCN containing 0.1 M TBABF_4 at a 0.03 cm^2 Pt disk electrode. All the solution preparations and cell preparations were conducted in the glove-box under a helium atmosphere (from reference (166)).

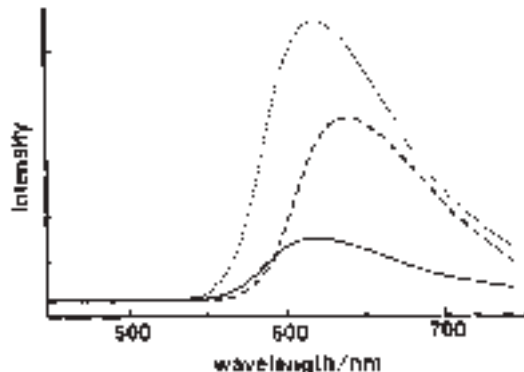


Figure 13.20 ECL spectra of $\text{Ru}(\text{bpy})_3^{2+}$ (—), $\text{Ru}(\text{dp-bpy})_3^{2+}$ (----), and $\text{Ru}(\text{dp-phen})_3^{2+}$ (.....). The solutions contained 0.10 M TBABF_4 in MeCN. Intensities shown have been normalized to the concentrations of the complexes. Exposure time = 2 s (from reference (166)). The experimental setup used was very similar to that described in Section 13.4.3.4 when a cooled CCD camera is used as the light detector.

Table 13.5

Emission maximum, integrated intensity, integrated current, ECL and photoluminescence efficiencies in MeCN at 25°C (from reference (166))^a

Compounds	λ_{max} (nm)	Integrated intensity (arbitrary units)	Integrated current (one cycle)/μC	ECL efficiency ϕ_{ECL}	Photoluminescence efficiency ϕ_{l}
Ru(bpy) ₃ ²⁺	616	363 (± 33)	17.6	0.05 ^b 0.089 ^c	0.075 ^b
Ru(dp-bpy) ₃ ²⁺	635	761 (± 70)	14.1	0.14	0.31 ^c
Ru(dp-phen) ₃ ²⁺	615	1723 (± 153)	18.1	0.24	0.37 ^d

^aExcept for those cited from the references, each of the values in this table is the average of at least five experimental trials.

^bFrom reference (168).

^cIn ethanol + methanol (4:1 v/v) solution at 20°C (172).

^dIn ethanol + methanol (4:1 v/v) solution at 20°C (173).

where I is the intensity in photons per second, i is the current in amperes (Coulombs per second), F is Faraday's constant and N_A is Avogadro's constant. Since the same electrode was used for each experiment and concentration of the test solutions were approximately the same, the charge passed for each compound was about the same, as shown in the integrated current values in Table 13.5.

13.5.2 Coreactant ECL of Ru(bpy)₃²⁺/TPrA system in aqueous solutions

Since the first report on the CL of Ru(bpy)₃³⁺ with aliphatic amines (21), followed by the ECL study of the Ru(bpy)₃²⁺ with TPrA as a coreactant (20), a wide range of ECL fundamental research and analytical applications involving Ru(bpy)₃²⁺ or its derivatives have been reported (8). The Ru(bpy)₃²⁺ (or its derivatives) with TPrA exhibit the highest ECL efficiency, and the relevant experiments can be carried out in an aqueous solution with a relatively wide range of pH (Figure 13.5) in the presence of oxygen. Consequently, this system is well suitable for ECL demonstrations (174, 175), as well as for ECL instrumental setup examinations.

Typically, 10–100 mM of TPrA in 0.10 M phosphate buffer (PBS) with a pH value of 7–8 can be prepared by dissolving the appropriate amount of phosphate salt and TPrA in water, and adjusting the pH of the TPrA–phosphate mixture with a concentrated H₃PO₄, HCl or HClO₄ solution while the mixture is stirred magnetically. Initially, the TPrA floats on the top, and a large number of small “oil drops” are distributed in the “solution” mixture after stirring. These “oil drops” should totally disappear (completely dissolved) once the solution pH approaches 7–8. Since the ECL intensity is proportional to the concentration of TPrA, a high concentration of TPrA–PBS buffer solution is always recommended. However, in the pH range of 7–8, 100 mM of TPrA is almost the saturated value. Care must be taken when using an ultrasonic bath to accelerate the TPrA dissolution, because TPrA may partially evaporate during the process. Similarly, the prepared TPrA–PBS solution should be kept in a well-sealed bottle. On the other hand, a mM Ru(bpy)₃²⁺ aqueous

solution can be prepared readily from solid $\text{Ru}(\text{bpy})_3\text{Cl}_2 \cdot 2\text{H}_2\text{O}$, and kept in the dark. Only μM levels of $\text{Ru}(\text{bpy})_3^{2+}$ in TPrA–PBS solutions are needed for ECL experiments. Instead of phosphate buffer, Tris- LiClO_4 can be also used as the buffer electrolyte, and the ECL responses in both buffers are essentially the same (137).

GC, Au, and Pt are all good for ECL studies of the $\text{Ru}(\text{bpy})_3^{2+}$ /TPrA system, but GC gives the best ECL responses (Figure 13.4). When Cl^- and ClO_4^- containing PBS buffer is used, unusual ECL behavior of $\text{Ru}(\text{bpy})_3^{2+}$ /TPrA system may be observed at Au electrodes. For example, the second ECL peak could completely disappear. This is probably associated with the generation of gold chloride/perchlorate complexes at the surface of the electrode after a positive potential is applied, although the exact mechanism is still under investigation. Before each experiment, the electrode should be carefully polished with a $\sim 0.3\text{--}0.05\text{ }\mu\text{m}$ alumina slurry and rinsed thoroughly with water, because $\text{Ru}(\text{bpy})_3^{2+}$ molecules can be very strongly adsorbed onto the electrode surface (and the wall of the electrochemical cell) (152), resulting in the generation of significant amount of ECL background. Either chromic acid or alcoholic KOH cleaning solution can be used to clean $\text{Ru}(\text{bpy})_3^{2+}$ contaminated electrodes and glassware.

Several types of reference electrodes can be used in the ECL study: SCE, $\text{Ag}/\text{AgCl}/\text{Cl}^-$ (saturated or 3 M KCl) are two typical examples. Quasi reference electrodes, i.e., Pt wire and Ag wire, are also suitable, but their potentials need to be calibrated immediately after the experiment with an added fully reversible redox reagent, e.g., ferrocene methanol, as an internal potential standard.

Control experiments are always helpful for verifying possible problems from the electrochemical cell and for understanding the ECL mechanism. No ECL should be observed in the absence of either $\text{Ru}(\text{bpy})_3^{2+}$ or TPrA. As shown in Figure 13.4, when nM to μM of $\text{Ru}(\text{bpy})_3^{2+}$ in 0.10 M Tris/0.10 M LiClO_4 , pH = 8, were used, two separated ECL waves are observed. The initial ECL signal starts at potentials where the direct oxidation of TPrA at the GC electrode occurs (Figures 13.4a–c), and reaches a first maximum at a potential of about 0.90 V vs. Ag/AgCl , about 50 mV less positive than the peak potential for TPrA oxidation, and well before $\text{Ru}(\text{bpy})_3^{2+}$ oxidation. The second ECL signal has a peak potential value of 1.14 V vs. Ag/AgCl , in the potential region of the direct oxidation of $\text{Ru}(\text{bpy})_3^{2+}$ at a GC electrode (138). The corresponding TPrA oxidation CV is essentially the same as that in Figure 13.4b. Note that even with a high concentration of $\text{Ru}(\text{bpy})_3^{2+}$ ($\sim\text{mM}$), the ECL signal first appears in a potential range less positive than that for the oxidation of $\text{Ru}(\text{bpy})_3^{2+}$. However, the initial ECL signal is relatively small compared to the large one.

Linear relationships were found between the ECL peak intensities and both TPrA and $\text{Ru}(\text{bpy})_3^{2+}$ concentrations for the first as well as the second ECL wave in certain concentration ranges (20, 134, 136–138).

ECL spectra of aqueous $\text{Ru}(\text{bpy})_3^{2+}$ /TPrA system are also easy to record, because of the strong ECL response and the insensitivity of the system to oxygen. Figure 13.21 shows a mercury lamp spectrum measured with the CCD camera-based ECL spectral recording apparatus described in Section 13.4.3.4. For good experimental setup, at least four sharp peaks with the peak wavelengths of 404.86, 435.83, 546.07, and 578.01 nm are expected to be observed. The measured Hg spectrum quality depends on several factors: slit sizes of the monochromator and the lamp, Hg lamp and other optics alignment, exposure time,

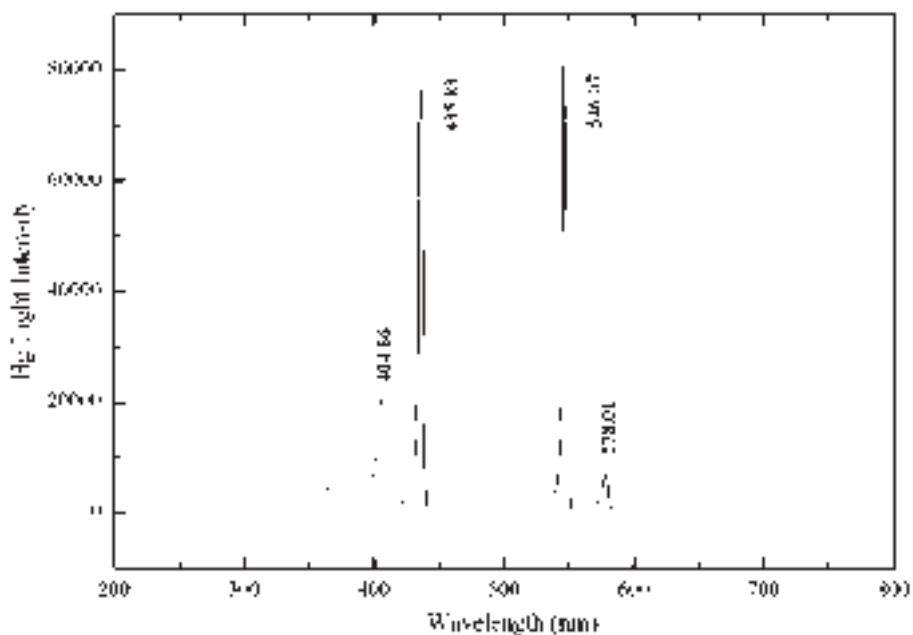


Figure 13.21 Hg lamp spectrum used to calibrate the CCD-based ECL spectral recording instrument. The operating temperature of the CCD camera was -108°C . Exposure time ~ 30 ms.

CCD camera cooling temperature, and the CCD camera focus control etc. A typical method for ECL generation and spectrum recording is to use repetitive pulsing potential scanning between the oxidation potential of $\text{Ru}(\text{bpy})_3^{2+}/\text{TPrA}$ (e.g., 1.2 V vs. Ag/AgCl , see Figure 13.4) and 0 V vs. Ag/AgCl at a frequency of ~ 10 Hz. The wavelength of the measured ECL spectrum is calibrated with a previously measured mercury spectrum (Figure 13.21). An example of $\text{Ru}(\text{bpy})_3^{2+}/\text{TPrA}$ ECL spectrum obtained from a J-shaped Pt electrode (Figure 13.7a) with pulsing potential scanning between 1.2 and 0 V vs. Ag/AgCl is shown in Figure 13.22. As expected, the maximum emissions from the annihilation and coreactant $\text{Ru}(\text{bpy})_3^{2+}$ ECL are essentially the same (Figure 13.20/Table 13.5 and Figure 13.22).

13.6 APPLICATIONS

A wide range of ECL-based applications have been developed in the last two decades, in which coreactant $\text{Ru}(\text{bpy})_3^{2+}/\text{TPrA}$ system has been overwhelmingly used. This section will list some of the most important/interesting ECL applications in tables, and readers who are interested in particular application aspects are encouraged to consult the relevant references cited (see Tables 13.6–13.13).

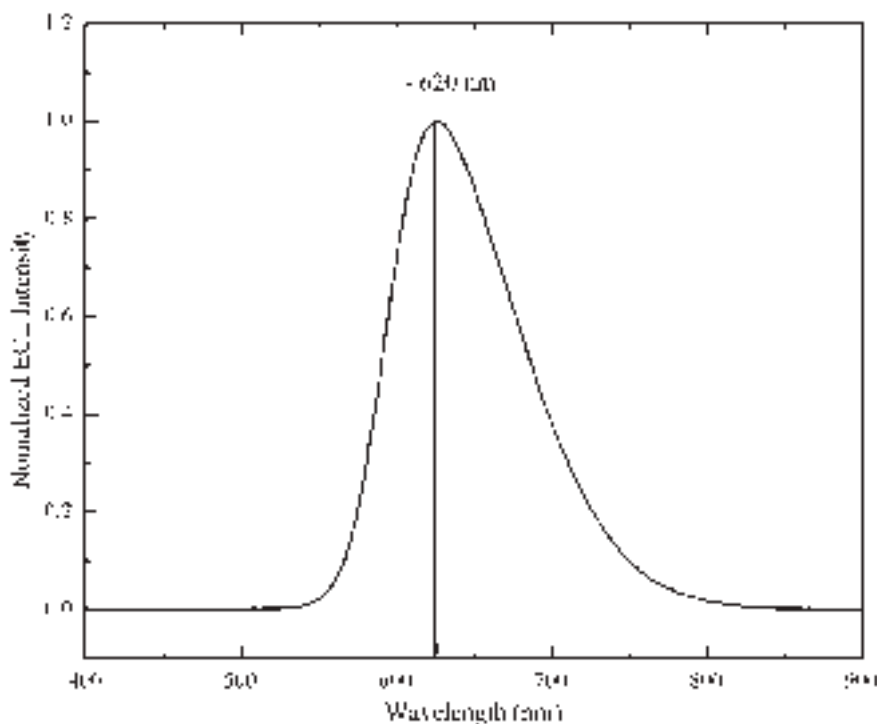


Figure 13.22 Normalized ECL spectrum obtained from 1 mM $\text{Ru}(\text{bpy})_3^{2+}$ –10 mM TPrA–0.1 M PBS buffer (pH 7.0) solution with a 3 mm in diameter J-shaped Pt electrode. The electrode potential was pulsed between 0 and 1.2 V vs. Ag/AgCl at a frequency of 10 Hz for 30 s. The CCD camera was operated at -108°C .

13.6.1 Applications of $\text{Ru}(\text{bpy})_3^{2+}$ ECL: determination of oxalate and organic acids

Table 13.6

Applications of $\text{Ru}(\text{bpy})_3^{2+}$ ECL for the determination of oxalate and organic acids
(adapted from reference (176))

Analyte	Comments	Matrix	Limit of detection	Reference
Oxalate	Batch method, linear range 1.0×10^{-6} to 1.0×10^{-4} M	Synthetic	Not stated	(177)
Oxalate	FIA, linear for oxalate up to 10^{-6} M, recoveries for oxalate ranged between 97% and 105%, standard derivation 2.3%	Urine	0.3 pmol	(178)
Oxalate	Fibre optic based sensor $\text{Ru}(\text{bpy})_3^{2+}$ immobilized on a Nafion modified electrode	Urine, vegetables	3×10^{-5} M	(179)

(Continued)

Table 13.6 (Cont.)

Analyte	Comments	Matrix	Limit of detection	Reference
Oxalate	FIA immobilized Ru(bpy) ₃ ²⁺ in Nafion	Synthetic	1×10^{-6} M, limited by background	(127)
Oxalate	Batch method, fibre optic sensor with (a) Ru(bpy) ₃ ²⁺ immobilized in Nafion and (b) Ru(bpy) ₃ ²⁺ modified in carbon paste electrode	Synthetic	(a) 3×10^{-5} M, (b) 2×10^{-5} M	(180)
Oxalate	Sonochemical enhancement of Ru(bpy) ₃ ²⁺ emission	Synthetic	Not determined	(181)
Oxalate	LC for determination of oxalate FIA	Urine, plasma	$< 1 \times 10^{-6}$ M	(182)
Oxalate	<i>In situ</i> and external Ru(bpy) ₃ ³⁺ generation comparison	Synthetic	External generation 1.0 μ M, <i>in situ</i> solution 0.5 μ M, <i>in situ</i> immobilized 1.0 μ M	(183)
Oxalate	Ion-pair LC with Ru(bpy) ₃ ²⁺ included in mobile phase	Urine, blood plasma	0.1×10^{-6} M	(184)
	Batch, fibre optic probe	Synthetic	0.5×10^{-6} M	(185)
Pyruvate	<i>In situ</i> oxidation of pyruvate to CH ₃ CHO [•] by electrogenerated Ce(IV)	Synthetic	3.1×10^{-7} M	(186)
Ascorbic acid	Ion-pairing LC	Soft drinks, fruit juice	2 pmol (20 μ L injection)	(187)

13.6.2 Applications of Ru(bpy)₃²⁺ ECL: determination of amines

Table 13.7Applications of Ru(bpy)₃²⁺ ECL for the determination of amines (adapted from reference (176))^a

Analyte	Comments	Limit of detection	Reference
Cyclic tertiary amines	FIA Solanidine, lincomycin, ergotamine, aconitine	Not stated	(188)
Alicyclic amine	FIA, linear ranges estimated at two orders of magnitude	1-ethylpiperidine 1.8 pmol, 1-methylpyrrolidine 0.7 pmol, <i>N</i> -ethylmorpholine 0.8 pmol, sparteine 0.5 pmol, nicotine 0.4 pmol, lincomycin 0.3 pmol, atropine 1.5 pmol, and diphenidol 1.0 pmol	(189)
Primary amines	FIA, LC, cyclization to form thiomorpholine with divinylsulfone	18 alkyl amines evaluated for relative intensities, no detection limits given	(190)
Reduced nicotinamide adenine dinucleotide (NADH) and phosphate (NADPH)	FIA, LC, linear range from 0.10 to 40 pmol	NADH 30 fmol NADPH 31 fmol	(191)

Table 13.7 (Cont.)

Analyte	Comments	Limit of detection	Reference
Alkylamines	FIA, immobilized Ru(bpy) ₃ ²⁺ in Nafion working range TPrA 1×10 ⁻⁶ to 1×10 ⁻³ M, antibiotics evaluated	TPrA 1×10 ⁻⁸ M	(127)
Reduced nicotinamide adenine dinucleotide	FIA, immobilized Ru(bpy) ₃ ²⁺ in Nafion working range TPrA 1×10 ⁻⁶ to 1×10 ⁻³ M	NADH 1×10 ⁻⁶ M	(127)
Primary amines	LC, pre-column derivatization with divinylsulfone (cyclo-addition)	Propylamine 30 pmol, 3-aminopentane 1 pmol	(192)
Tripropylamine	FIA, log linear calibration over three orders of magnitudes	140 µg/L (~1 µM)	(193)
Tripropylamine, proline	Capillary electrophoresis	TPrA 3.7×10 ⁻⁵ M, Proline 1.3×10 ⁻⁵ M	(194)
Tripropylamine	Sub-µL ECL detector	TPrA <5×10 ⁻¹³ M	(195)

^aAll matrixes were synthetic.

13.6.3 Applications of Ru(bpy)₃²⁺ ECL: determination of amino acids

Table 13.8

Applications of Ru(bpy)₃²⁺ ECL for the determination of amino acids
(adapted from reference (176))

Analyte	Comments	Limit of detection	Reference
Tryptophan	FIA	Not stated	(178)
Tryptophan, and indole derivatives	FIA	Tryptophan 3×10 ⁻¹¹ mol	(196)
Tryptophan ^a	Ligand exchange chiral LC, calibration for D- and L-tryptophan linear for both enantiomers in the range 2–200 (injected), 96% recovery for spiked samples	Both enantiomers 0.2 pmol	(197)
Amino acids, and phenyl thiohydantoin (PTH) derivatized amino acids	FIA, LC, for leucine linear response range 2–3 orders of magnitudes, reproducibility 5% (<i>n</i> = 27)	Proline 5×10 ⁻⁹ M, leucine 45×10 ⁻⁹ M, aspartic acid 90×10 ⁻⁹ M, serine 1.1×10 ⁻⁹ M	(198)
D- and L-amino acids	Chiral LC, pre-column derivatization	fmol range (10 µL injection)	(199)
Dansyl amino acid	FIA, LC, pre-column derivatization with dansyl chloride, working curve (dansyl glutamine) 5–250 mM, RSD (<i>n</i> = 3) 1.5–4.5%	Dansyl chloride 1.0 mM, dansyl alanine 0.1 mM	(200)

(Continued)

Table 13.8 (Cont.)

Analyte	Comments	Limit of detection	Reference
Dansyl amino acids	Ion-pair LC with Ru(bpy) ₃ ²⁺ included in mobile phase	Dansyl glutamine 0.1 μM (Ru(bpy) ₃ ²⁺ in mobile phase), dansylated glutamine 0.2 μM (Ru(bpy) ₃ ³⁺ post-column)	(184)
Indoxyl derivatives	LC, detection limits using FIA	Indoxyl sulfate 2.3 pmol, indoxyl phosphate 3.1 pmol, indoxyl acetate 1.7 pmol, indoxyl 1,3-diacetate 0.4 pmol, indoxyl β-D-glucoside 0.0015 pmol, indoxyl β-D-galactoside 0.0015 pmol, indoxyl β-D-glucuronide 0.0023 pmol, tryptophan 0.25 pmol	(201)
Proline	FIA, various modes of Ru(bpy) ₃ ³⁺ generation	External generation 0.5 μM, <i>in situ</i> solution 0.5 μM, <i>in situ</i> immobilized 1.0 μM	(183)

^aThe matrix was blood plasma.

13.6.4 Applications of Ru(bpy)₃²⁺ ECL: determination of pharmaceuticals

Table 13.9

Applications of Ru(bpy)₃²⁺ ECL for the determination of pharmaceuticals
(adapted from reference (176))

Analyte	Comments	Matrix	Limit of detection	Reference
Oxprenolol	FIA, linear range from 0.0001 to 0.04 mM	Synthetic	35 nM	(202)
Codeine, heroin, detromethorphan	FIA, calibration range from 0.1 to 1.0 μM	Synthetic	Codeine 15×10 ⁻⁹ M, heroin 45×10 ⁻⁹ M, detromethorphan 44×10 ⁻⁹ M	(203)
Amitriptyline	FIA, calibration range from 0 to 40 μM	Synthetic	3.0×10 ⁻⁷ M	(204)
Amethocaine (tetracaine), bupivacaine, lignocaine (lindocaine), prilocaine, and procaine	FIA	Lignocaine in local anaesthetic preparation	Bupivacaine and procaine 5×10 ⁻⁸ M, lignocaine 7×10 ⁻⁸ M	(205)
β-Lactam antibiotics and β-lactamases	ORIGEN analyzer	Untreated milk and crude bacterial broth culture	β-Lactamase I from <i>B. cereus</i> using penicillin G as a substrate 25 pmol/L	(206)
Erythromycin	Microbore LC Ru(bpy) ₃ ²⁺ in mobile phase	Synthetic, blood plasma, urine	In synthetic standard 0.01 μM, in urine 0.05 μM, in blood plasma <0.10 μM,	(207)

Table 13.9 (Cont.)

Analyte	Comments	Matrix	Limit of detection	Reference
β -Blockers (acebutolol, alprenolol, oxprenolol, propranolol, tomolol, nadolol, labetolol)	Capillary electrophoresis	Synthetic	Oxprenolol 2 μM	(208)

13.6.5 Applications of $\text{Ru}(\text{bpy})_3^{2+}$ ECL: determination of $\text{Ru}(\text{bpy})_3^{2+}$ **Table 13.10**

Applications of $\text{Ru}(\text{bpy})_3^{2+}$ ECL for the determination of $\text{Ru}(\text{bpy})_3^{2+}$
(adapted from reference (176))

Analyte	Comments	Matrix	Limit of detection	Reference
$\text{Ru}(\text{bpy})_3^{2+}$	Oxalate and peroxodisulfate coreactants	Synthetic and liver tissue extract	$\sim 10^{-8} \text{ M}$ with oxalate, $\sim 10^{-13} \text{ M}$ with peroxodisulfate (with deoxygenation)	(19)
$\text{Ru}(\text{bpy})_3^{2+}$	Peroxodisulfate coreactants	Synthetic	$\sim 4.3 \times 10^{-8} \text{ M}$	(209)
$\text{Ru}(\text{bpy})_3^{2+}$	TPrA coreactant, ORIGEN analyzer I	Synthetic	10 pM	(20)
$\text{Ru}(\text{bpy})_3^{2+}$	Micro-fabricated ECL cell, TPrA coreactant	Synthetic	$\sim 10^{-9} \text{ M}$	(210)

**13.6.6 Applications of $\text{Ru}(\text{bpy})_3^{2+}$ ECL in capillary electrophoresis
(CE) and micro-total analysis (μTAS)****Table 13.11**

Applications of $\text{Ru}(\text{bpy})_3^{2+}$ ECL in CE and μTAS (modified, reference (9))

Analyte	Separation channel (μm)	Matrix	Limit of detection	Electrochemical system	Reference
Proline, valine, phenylalanine	75	Standard soln. ^a	0.2 μM , 0.7 μM , 0.5 μM	Two-electrode system	(211)
Diphen-hydramine	25	Rabbit plasma, urine	$2 \times 10^{-8} \text{ M}$	Three-electrode system	(212)
Tramadol, lidocaine	25	Urine	$6 \times 10^{-8} \text{ M}$, $4.5 \times 10^{-8} \text{ M}$	Three-electrode	(213)
Procyclidine	25	Urine	$1 \times 10^{-9} \text{ M}$	Three-electrode	(214)
Proline, histidine	50	Standard soln.	1 μM	DC battery	(215)

(Continued)

Table 13.11 (Cont.)

Analyte	Separation channel (μm)	Matrix	Limit of detection	Electrochemical system	Reference
TPrA, proline	21	Standard soln.	$2-5 \mu\text{M}$	DC battery (1.5 V)	(216)
TPrA, lidocaine	75	Urine	$5 \times 10^{-11} \text{ M}$, $2 \times 10^{-8} \text{ M}$	Three-electrode	(155)
TPrA	75	Standard soln.	$1 \mu\text{M}$ (TPrA) with $\text{Ru}(\text{bpy})_3^{2+}$ immobilized	Three-electrode	(217)
Proline, oxalic acid	75	Degradation soln. of pHPP ^b	1 mM (Proline), Not given	Three-electrode system	(218)
Proline, valine, phenylalanine	50	Standard soln.	1.2, 50, 25 μM	Three-electrode	(219)
$\text{Ru}(\text{bpy})_3^{2+}$	60×20 chip	Standard soln.	$5 \times 10^{-6} \text{ M}$	Voltage required to obtain ECL reaction from the electric field in separation channel	(220)
$\text{Ru}(\text{phen})_3^{2+}$, proline	15×48	Standard soln.	$6 \times 10^{-6} \text{ M}$, 1.2 μM	Three-electrode	(221)

^aWith field decoupler.^bpHPP: *p*-hydroxyphenylpyruvic acid.

13.6.7 Application of $\text{Ru}(\text{bpy})_3^{2+}$ ECL: determination of clinical analytes

Table 13.12

Summary of clinical assays using ECL detection (adapted from reference (133))

Analyte	Application	Detection method	Reference
I. Assays for ECL labels			
<i>A. Immunoassays</i>			
AFP, α -fetoprotein	Tumor, fertility	TPrA, $\text{Ru}(\text{bpy})_3^{2+}$	(222, 223)
Anti-Borna disease antibodies	Infectious disease	TPrA, $\text{Ru}(\text{bpy})_3^{2+}$	(224–226)
β -Amyloid peptide	Alzheimer's disease	TPrA, $\text{Ru}(\text{bpy})_3^{2+}$	(227)
CA (cancer antigen) 15-3	Tumor marker	TPrA, $\text{Ru}(\text{bpy})_3^{2+}$	(223, 228)
CA (cancer antigen) 19-9	Tumor marker	TPrA, $\text{Ru}(\text{bpy})_3^{2+}$	(223)
CA (cancer antigen) 72-4	Tumor marker	TPrA, $\text{Ru}(\text{bpy})_3^{2+}$	(229)
CA (cancer antigen) 125 II	Tumor marker	TPrA, $\text{Ru}(\text{bpy})_3^{2+}$	(230, 231)
CEA, carcinoembryonic antigen	Tumor marker	TPrA, $\text{Ru}(\text{bpy})_3^{2+}$	(223, 232)
β -Crosslaps	Bone	TPrA, $\text{Ru}(\text{bpy})_3^{2+}$	(233, 234)
C-Telopeptides	Bone	TPrA, $\text{Ru}(\text{bpy})_3^{2+}$	(235)
Anti-CMV antibodies	Infectious disease	TPrA, $\text{Ru}(\text{bpy})_3^{2+}$	(236)
Cytokeratin 19	Tumor marker	TPrA, $\text{Ru}(\text{bpy})_3^{2+}$	(237)
CKMB, creatine kinase	Cardiac	TPrA, $\text{Ru}(\text{bpy})_3^{2+}$	(232, 238)
C-Reactive protein (CRP)	Cardiac	TPrA, $\text{Ru}(\text{bpy})_3^{2+}$	(151, 239)
Cytomegalovirus	Infectious disease	TPrA, $\text{Ru}(\text{bpy})_3^{2+}$	(238)
Des- γ -carboxy prothrombin	Tumor marker	TPrA, $\text{Ru}(\text{bpy})_3^{2+}$	(240, 241)

Table 13.12 (Cont.)

Analyte	Application	Detection method	Reference
Estradiol	Reproductive Endocrinology	TPrA, Ru(bpy) ₃ ²⁺	(242)
Ferritin	Anemia	TPrA, Ru(bpy) ₃ ²⁺	(223)
FSH, follitropin	Reproductive Endocrinology	TPrA, Ru(bpy) ₃ ²⁺	(242)
HCG (human chorionic Gonadotropin)	Reproductive Endocrinology	TPrA, Ru(bpy) ₃ ²⁺	(232, 243)
HBsAg, hepatitis B virus surface antigen	Infectious disease	TPrA, Ru(bpy) ₃ ²⁺	(244–247)
HAsAg, hepatitis A virus surface antigen	Infectious disease	TPrA, Ru(bpy) ₃ ²⁺	(248)
HIV-1 p7 antigen	Infectious disease	TPrA, Ru(bpy) ₃ ²⁺	(249)
IgE, immunoglobulin E	Allergy	TPrA, Ru(bpy) ₃ ²⁺	(250)
Insulin	Diabetes mellitus	TPrA, Ru(bpy) ₃ ²⁺	(251, 252)
IL(Interleukin)-18 binding Protein	Sepsis	TPrA, Ru(bpy) ₃ ²⁺	(253)
IL(Interleukin)-2	Immune system	TPrA, Ru(bpy) ₃ ²⁺	(254)
IL(Interleukin)-4	Immune system	TPrA, Ru(bpy) ₃ ²⁺	(254)
IL(Interleukin)-6	Immune system	TPrA, Ru(bpy) ₃ ²⁺	(223)
IL(Interleukin)-8	Immune system	TPrA, Ru(bpy) ₃ ²⁺	(223)
IL(Interleukin)-10	Immune system	TPrA, Ru(bpy) ₃ ²⁺	(254, 255)
IL(Interleukin)-10	Immune system	TPrA, Ru(bpy) ₃ ²⁺	(253)
Interferon-γ	Immune system	TPrA, Ru(bpy) ₃ ²⁺	(254)
LH, lutropin	Reproductive Endocrinology	TPrA, Ru(bpy) ₃ ²⁺	(242)
Osteocalcin	Bone	TPrA, Ru(bpy) ₃ ²⁺	(235)
Pancreatic phospholipase A2	Pancreatic diseases	Terbium chelate	(256)
PTH (parathyroid hormone)	Ca metabolism	TPrA, Ru(bpy) ₃ ²⁺	(257)
Prolactin	Reproductive Endocrinology	TPrA, Ru(bpy) ₃ ²⁺	(242)
PSA (prostate specific antigen)	Tumor marker	TPrA, Ru(bpy) ₃ ²⁺	(232, 258–260)
Serum interferon-α	Immune system	TPrA, Ru(bpy) ₃ ²⁺	(253)
T4, thyroxine	Thyroid function	TPrA, Ru(bpy) ₃ ²⁺	(232, 237, 261, 262)
T3, triiodothyronine	Thyroid function	TPrA, Ru(bpy) ₃ ²⁺	(232, 261, 263)
TSH (thyroid stimulating hormone)	Thyroid function	TPrA, Ru(bpy) ₃ ²⁺	(232, 261, 263)
TSH	Thyroid function	Terbium chelate	(264)
Testosterone	Reproductive Endocrinology	TPrA, Ru(bpy) ₃ ²⁺	(242, 263)
Troponin	Myocardial Infarction	TPrA, Ru(bpy) ₃ ²⁺	(232, 238, 257, 265–267)
Tumor necrosis factor-α	Immune function	TPrA, Ru(bpy) ₃ ²⁺	(268)
<i>B. Molecular assays</i>			
Apo 8–100 gene mutation	Metabolism	TPrA, Ru(bpy) ₃ ²⁺	(269)
Astrovirus	Infectious disease	TPrA, Ru(bpy) ₃ ²⁺	(270)
Coxsackievirus B3 RNA	Infectious disease	TPrA, Ru(bpy) ₃ ²⁺	(271)
CMV DNA	Infectious disease	TPrA, Ru(bpy) ₃ ²⁺	(272)
Dengue virus RNA	Infectious disease	TPrA, Ru(bpy) ₃ ²⁺	(273)
Enterovirus	Infectious disease	TPrA, Ru(bpy) ₃ ²⁺	(274)
Epstein–Barr virus DNA	Infectious disease	TPrA, Ru(bpy) ₃ ²⁺	(275)
Foot-and-mouth disease	Infectious disease	TPrA, Ru(bpy) ₃ ²⁺	(276)
HIV-1 RNA	Infectious disease	TPrA, Ru(bpy) ₃ ²⁺	(277, 278)
HIV DNA	Infectious disease	TPrA, Ru(bpy) ₃ ²⁺	(278–281)

(Continued)

Table 13.12 (Cont.)

Analyte	Application	Detection method	Reference
HPIV-1/2/3	Infectious disease	TPrA, Ru(bpy) ₃ ²⁺	(282)
Influenza virus RNA	Infectious disease	TPrA, Ru(bpy) ₃ ²⁺	(283–285)
mRNA	Tumor marker	TPrA, Ru(bpy) ₃ ²⁺	(286–289)
Prothrombin gene mutation	Venous thromboembolism	TPrA, Ru(bpy) ₃ ²⁺	(290)
St. Louis encephalitis	Infectious disease	TPrA, Ru(bpy) ₃ ²⁺	(291)
Varicella-zoster virus DNA	Infectious disease	TPrA, Ru(bpy) ₃ ²⁺	(292)
West Nile virus RNA	Infectious disease	TPrA, Ru(bpy) ₃ ²⁺	(293)
ΔF508 deletion	Cystic fibrosis	TPrA, Ru(bpy) ₃ ²⁺	(293)
<i>C. Other</i>			
Heavy metals	Toxicology	TPrA, Ru(bpy) ₃ ²⁺	(294)
Potassium	Electrolytes	TPrA, Ru(bpy) ₃ ²⁺	(294)
Sodium	Electrolytes	TPrA, Ru(bpy) ₃ ²⁺	(295)
II. Assays for coreactants			
Carbon dioxide	Blood gases	NADH, Ru(bpy) ₃ ²⁺	(296)
Cholesterol	Lipids	Oxalate, Ru(bpy) ₃ ²⁺	(296)
Ethanol	Toxicology	NADH, Ru(bpy) ₃ ²⁺	(296, 297)
Glucose	Diabetes mellitus	NADH, Ru(bpy) ₃ ²⁺	(296, 297)
Lactate	Exercise	NADH, Ru(bpy) ₃ ²⁺	(297)

13.6.8 Applications of Ru(bpy)₃²⁺ ECL: analytes associated with food, water, and biological agents

Table 13.13

ECL-based assays for food, water, and biological threat agents (adapted from reference (133))

Analyte	Sample matrix	Assay method ^a	Detection limit	Reference
<i>Cryptosporidium parvum Oocysts</i>	Water	NASBA RNA amplification, ECL probe detection, NucliSens reader	About five viable oocysts per sample	(298)
	Turbid water	IA, ORIGEN analyzer	50 viable oocysts/mL	(299)
	Highly turbid water	LA, ORIGEN analyzer	1 oocyst/mL	(300)
	Karst water	IA, ORIGEN analyzer	5 oocysts/mL	(301)
<i>Escherichia coli</i> O157	Creek water	IA, ORIGEN analyzer	25 cells/mL, 1–2 viable cells/mL after concentration	(302)
	Drinking water	NASBA mRNA amplification, ECL probe detection. NucliSens reader	40 viable cells/mL	(303)
	Feces	PATHIgen IA, ORIGEN analyzer	1×10^5 CFU/g	^b
	Various food matrices	PATHIgen IA, ORIGEN analyzer	100 cells/sample, more sensitive than culture methods	^b

Table 13.13 (Cont.)

Analyte	Sample matrix	Assay method ^a	Detection limit	Reference
Campylobacter	Ground beef	IA, Origin analyzer	100x as sensitive a commercial dipstick	(304)
	Ground beef, chicken, fish, milk, juices, serum, water	IA, Origin analyzer	1000–2000 cells/mL	(305)
	Various food and Environmental water matrices	IA, Origin analyzer	Not reported	(306)
	Feces	PATHIgen IA, ORIGEN analyzer	1×10^4 CFU/g	^b
	Poultry samples	PATHIgen IA, ORIGEN analyzer	Comparable to culture methods	^b
		PATHIgen IA, ORIGEN analyzer	5×10^5 CFU/g	^b
Salmonella	Feces	PATHIgen IA, ORIGEN analyzer	1 CFU/100 cm ²	^b
	Surface swabs	PATHIgen IA, ORIGEN analyzer	81% positive predictive value vs. culture	^b
	Poultry house drag swabs	PATHIgen IA, ORIGEN analyzer	Equivalent sensitivity to culture methods	^b
	Various food matrices	PATHIgen IA, ORIGEN analyzer	1000–2000 cells/mL	(305)
	Ground beef, chicken, fish, milk, juices, serum, water	IA, Origin analyzer		
		Environmental surface	1 CFU/100 cm ²	^b
<i>Listeria monocytogenes, Staphylococcus aureus, enterotoxins</i>	Buffer, milk, ground beef, let-tuce, potato salad	PATHIgen IA, ORIGEN analyzer	10 pg/mL for SEB	^b
	Buffer, various food matrices	IA, ORIGEN analyzer	5–50 ng/mL (SEA, B, C ₁ , C ₂ , C ₃ , D, E)	^b
	Serum, tissue, buffer, urine	IA, ORIGEN analyzer	1 pg/mL for SEB	(307)
	Buffer	IA, ORIGEN analyzer	~0.5 pg/mL	(308)
	Soil	IA, ORIGEN analyzer	10 ⁵ spores	(306, 309)
	Buffer	LA, ORIGEN analyzer	100 spores	(310)
<i>Bacillus anthracis</i>	Buffer	IA, ORIGEN analyzer	1000 CFU/mL	(308)
	Specific DNA		Not reported	(151)
	Buffer	IA, ORIGEN analyzer	~5 pg/mL	(310)
	Buffer	IA, ORIGEN analyzer	4 pg/mL	(308)
	Cholera toxin	IA, ORIGEN analyzer	~0.5 pg/mL	(310)
	Buffer	IA, ORIGEN analyzer	2 pg/mL	(308)
Botulinus A toxin	Buffer	IA, ORIGEN analyzer	~5 pg/mL	(310)
	Buffer	IA, ORIGEN analyzer	0.5 pg/mL	(308)
Ricin toxin	Buffer	IA, ORIGEN analyzer		
	Buffer	IA, ORIGEN analyzer		

^aIA = Immunoassay.^bCourtesy of Igen International, Inc. (Now BioVeris).

ACKNOWLEDGMENTS

The support of this work by the University of Southern Mississippi via New Faculty Start-up Funding and the College of Science and Technology Dean's Research Initiative Program is gratefully acknowledged.

REFERENCES

1. A. D. McNaught, A. Wilkinson, IUPAC, Eds., *IUPAC Compendium of Chemical Terminology*, 2nd ed., Blackwell Science Inc.: Oxford, UK, 1997.
2. A. J. Bard, L. R. Faulkner, *Electrochemical Methods: Fundamentals and Applications*, John Wiley & Sons, Inc.: New York, 2001.
3. D. M. Hercules, *Science (Washington, DC, United States)* **145**, 808 (1964).
4. K. S. V. Santhanam, A. J. Bard, *J. Am. Chem. Soc.* **87**, 139 (1965).
5. R. E. Visco, E. A. Chandross, *J. Am. Chem. Soc.* **86**, 5350 (1964).
6. R. T. Dufford, D. Nightingale, L. W. Gaddum, *J. Am. Chem. Soc.* **49**, 1858 (1927).
7. N. Harvey, *J. Phys. Chem.* **33**, 1456 (1929).
8. A. J. Bard, Ed., *Electrogenerated Chemiluminescence*, Marcel Dekker, Inc.: New York, 2004.
9. X.-B. Yin, S. Dong, E. Wang, *Trends Anal. Chem.* **23**, 432 (2004).
10. A. J. Bard, in *Electrogenerated Chemiluminescence*, A. J. Bard, Ed., Marcel Dekker, Inc.: New York, 2004, Chap. 1.
11. R. A. Maus, *J. Phys. Chem.* **43**, 2654 (1965).
12. S. W. Feldberg, *J. Am. Chem. Soc.* **88**, 390 (1966).
13. S. W. Feldberg, *J. Phys. Chem.* **70**, 3928 (1966).
14. L. R. Faulkner, A. J. Bard, *J. Am. Chem. Soc.* **91**, 209 (1969).
15. N. E. Tokel, A. J. Bard, *J. Am. Chem. Soc.* **94**, 2862 (1972).
16. M.-M. Chang, T. Saji, A. J. Bard, *J. Am. Chem. Soc.* **99**, 5399 (1977).
17. I. Rubinstein, A. J. Bard, *J. Am. Chem. Soc.* **103**, 512 (1981).
18. H. D. Abruna, A. J. Bard, *J. Am. Chem. Soc.* **104**, 2641 (1982).
19. D. Ege, W. G. Becker, A. J. Bard, *Anal. Chem.* **56**, 2413 (1984).
20. J. K. Leland, M. J. Powell, *J. Electrochem. Soc.* **137**, 3127 (1990).
21. J. B. Noffsinger, N. D. Danielson, *Anal. Chem.* **59**, 865 (1987).
22. A. J. Bard, G. M. Whitesides, *US Patent 5, 221, 605*, 1993.
23. G. F. Blackburn, H. P. Shah, J. H. Kenten, J. Leland, R. A. Kamin, J. Link, J. Peterman, M. J. Powell, A. Shah, D. B. Talley, *Clin. Chem. (Washington, DC, United States)* **37**, 1534 (1991).
24. M. M. Collinson, R. M. Wightman, *Anal. Chem.* **65**, 2576 (1993).
25. A.-M. Andersson, R. H. Schmehl, *Mol. Supramol. Photochem.* **7**, 153 (2001).
26. A.-M. Andersson, R. H. Schmehl, *Electron Transfer in Chemistry* **1**, 312 (2001).
27. Anon, *Indian J. Clin. Biochem.* **13**, 129 (1998).
28. N. R. Armstrong, R. M. Wightman, E. M. Gross, *Annu. Rev. Phys. Chem.* **52**, 391 (2001).
29. V. Balzani, A. Juris, *Coord. Chem. Rev.* **211**, 97 (2001).
30. A. J. Bard, F.-R. F. Fan, *Acc. Chem. Res.* **29**, 572 (1996).
31. A. J. Bard, S. M. Park, *Exciplex*, *Proc. Meet.*, 305 (1975).
32. R. C. Beier, L. H. Stanker, *Recent Res. Dev. Agric. Food Chem.* **4**, 59 (2000).
33. F. Bolletta, S. Bonafede, *Pure Appl. Chem.* **58**, 1229 (1986).
34. K. A. Fahnrich, M. Pravda, G. G. Guilbault, *Talanta* **54**, 531 (2001).
35. L. R. Faulkner, R. S. Glass, *Chem. Biol. Gener. Excited States*, 191 (1982).

36. R. D. Gerardi, N. W. Barnett, S. W. Lewis, *Anal. Chim. Acta* **378**, 1 (1999).
37. J. Gonzalez Velasco, *Electroanalysis* **3**, 261 (1991).
38. J. Gonzalez Velasco, *Bull. Electrochem.* **10**, 29 (1994).
39. G. M. Greenway, *Trends Anal. Chem.* **9**, 200 (1990).
40. A. Kapturkiewicz, *Adv. Electrochem. Sci. Eng.* **5**, 1 (1997).
41. P. T. Kissinger, *J. Pharm. Biomed. Anal.* **14**, 871 (1996).
42. A. W. Knight, *Trends Anal. Chem.* **18**, 47 (1999).
43. A. W. Knight, G. M. Greenway, *Analyst (Cambridge, United Kingdom)* **119**, 879 (1994).
44. A. W. Knight, G. M. Greenway, *Analyst (Cambridge, United Kingdom)* **121**, 101R (1996).
45. A. V. Kukoba, A. I. Bykh, I. B. Svir, *Fresenius J. Anal. Chem.* **368**, 439 (2000).
46. S. Kulmala, J. Suomi, *Anal. Chim. Acta* **500**, 21 (2003).
47. W. Y. Lee, *Mikrochim. Acta* **127**, 19 (1997).
48. U. Mitschke, P. Bauerle, *J. Mater. Chem.* **10**, 1471 (2000).
49. A. Nabi, M. Yaqoob, M. Anwar, *Lab. Rob. Autom.* **11**, 91 (1999).
50. T. A. Nieman, *J. Res. National Bureau of Standards (United States)* **93**, 501 (1988).
51. T. A. Nieman, in *Chemiluminescence and Photochemical Reaction Detection in Chromatography*; J. W. Birks, Ed., VCH: New York, NY, 1989, Ch. 4.
52. S.-M. Park, D. A. Tryk, *Rev. Chem. Intermed.* **4**, 43 (1980).
53. M. M. Richter, *Opt. Biosens.* 173 (2002).
54. M. M. Richter, *Chem. Rev. (Washington, DC, United States)* **104**, 3003 (2004).
55. M. L. Tortorello, D. Stewart, *New Techniques in the Analysis of Foods (Proceedings of an American Chemical Society Symposium on New Techniques in the Analysis of Foods)*, Las Vegas, NV, Sept. 7–11, 1997, 91 (1998).
56. J. M. Zaleski, C. Turro, R. D. Mussell, D. G. Nocera, *Coord. Chem. Rev.* **132**, 249 (1994).
57. M. Zhou, J. Heinze, K. Borgwarth, C. P. Grover, *Chem. Phys. Chem.* **4**, 1241 (2003).
58. P. B. Oldham, M. E. McCarroll, L. B. McGown, I. M. Warner, *Anal. Chem.* **72**, 197R (2000).
59. R. A. Agbaria, P. B. Oldham, M. McCarroll, L. B. McGown, I. M. Warner, *Anal. Chem.* **74**, 3952 (2002).
60. A. M. Powe, K. A. Fletcher, N. N. St. Luce, M. Lowry, S. Neal, M. E. McCarroll, P. B. Oldham, L. B. McGown, I. M. Warner, *Anal. Chem.* **76**, 4614 (2004).
61. R. J. Aitken, M. A. Baker, M. O'Bryan, *J. Androl.* **25**, 455 (2004).
62. J. Sherma, *J. AOAC Int.* **87**, 20A (2004).
63. K. Jacobson, P. Eriksson, T. Reitberger, B. Stenberg, *Adv. Polym. Sci.* **169**, 151 (2004).
64. A. Roda, P. Pasini, M. Mirasoli, E. Michelini, M. Guardigli, *Trends Biotechnol.* **22**, 295 (2004).
65. A. M. Jimenez, M. J. Navas, *J. Hazard. Mater.* **106**, 1 (2004).
66. L. J. Kricka, *Anal. Chim. Acta* **500**, 279 (2003).
67. A. Roda, M. Guardigli, E. Michelini, M. Mirasoli, P. Pasini, *Anal. Chem.* **75**, 462A (2003).
68. A. Roda, M. Guardigli, P. Pasini, M. Mirasoli, *Anal. Bioanal. Chem.* **377**, 826 (2003).
69. F. Li, C. Zhang, X. Guo, W. Feng, *Biomed. Chromatogr.* **17**, 96 (2003).
70. J. S. Gaffney, N. A. Marley, *Conference on Atmospheric Chemistry: Urban, Regional, and Global Scale Impacts of Air Pollutants*, 4th, Orlando, FL, United States, Jan. 13–17, 2002, 1 (2002).
71. D. O. Shah, C. D. Chang, J. L. Stewart, *BIOforum Europe* **7**, 44 (2003).
72. N. I. Butkovskaya, D. W. Setser, *Int. Rev. Phys. Chem.* **22**, 1 (2003).
73. W. Qin, *Anal. Lett.* **35**, 2207 (2002).
74. Y.-M. Liu, J.-K. Cheng, *J. Chromatogr. A* **959**, 1 (2002).
75. R. A. W. Stott, in *Protein Protocols Handbook*; J. M. Walker, Ed., Human Press: Totowa, NJ, 2002, Part 156.
76. A. M. Garcia-Campana, W. R. G. Baeyens, L. Cuadros-Rodriguez, F. A. Barrero, J. M. Bosque-Sendra, L. Gamiz-Gracia, *Curr. Org. Chem.* **6**, 1 (2002).

77. M. Yamaguchi, H. Yoshida, H. Nohta, *J. Chromatogr. A.* **950**, 1 (2002).
78. R. Creton, L. F. Jaffee, *BioTechniques* **31**, 1098 (2001).
79. G. Gubitz, M. G. Schmid, H. Silviaeh, H. Y. Aboul-Enein, *Crit. Rev. Anal. Chem.* **31**, 167 (2001).
80. J. Arnhold, in *Chemiluminescence at the Turn of the Millennium*; S. Albrecht, T. Zimmermann, H. Brandl, Eds., Schweda-Werbedruck GmbH: Dresden, Germany, 2001, pp. 85–94.
81. C. Kuyper, R. Milofsky, *Trends Anal. Chem.* **20**, 232 (2001).
82. L. Rychla, J. Rychly, in *Polymer Analysis and Degradation*; A. Jimenez, G. E. Zaikov, Eds., Nova Science Publishers Inc.: Huntington, NY, 2000, pp. 123–134.
83. K. Papadopoulos, T. Triantis, D. Dimotikali, J. Nikokavouras, *J. Photochem. Photobiol. A: Chem.* **131**, 55 (2000).
84. K. Papadopoulos, J. Lignos, M. Stamatakis, D. Dimotikali, J. Nikokavouras, *J. Photochem. Photobiol. A: Chem.* **115**, 137 (1998).
85. G. L. Sharipov, R. A. Sadikov, in *Issled. Obl. Khim. Vysokomol. Soedin. Neftekhim*; S. R. Rafikov, Ed., Akad. Nauk SSSR: Ufa, USSR, 1977, pp. 52–53.
86. G. M. Avakyan, T. M. Avakyan, *Biologicheskii Zhurnal Armenii* **8**, 9 (1972).
87. T. M. Avakyan, L. G. Stepanyan, *Biofizika* **17**, 712 (1972).
88. F. Bistolfi, *Panminerva Medica* **42**, 69 (2000).
89. G. T. Reynolds, *J. Lumin.* **54**, 43 (1992).
90. C. D. Kalkar, *Radiat. Phys. Chem.* **34**, 729 (1989).
91. M. Ashok Kumar, F. Grieser, *Chem. Phys. Chem.* **5**, 439 (2004).
92. V. H. Arakeri, *Curr. Sci.* **85**, 911 (2003).
93. T. V. Prevenslik, *Ultrasonics* **41**, 313 (2003).
94. M. P. Brenner, S. Hilgenfeldt, D. Lohse, *Rev. Mod. Phys.* **74**, 425 (2002).
95. M. A. Margulis, I. M. Margulis, *Ultrason. Sonochem.* **9**, 1 (2002).
96. H. Mitome, *Jpn. J. Appl. Phys., Part 1: Regular Papers, Short Notes & Review Papers* **40**, 3484 (2001).
97. D. Hammer, L. Frommhold, *J. Mod. Opt.* **48**, 239 (2001).
98. T. Lepoint, F. Lepoint-Mullie, *Adv. Sonochem.* **5**, 1 (1999).
99. D. Lohse, S. Hilgenfeldt, *Festkoerperprobleme* **38**, 215 (1999).
100. I. V. Ostrovskii, O. A. Korotchenkov, T. Goto, H. G. Grimmeiss, *Phys. Rep.* **311**, 1 (1999).
101. P. T. Greenland, *Contemp. Phys.* **40**, 11 (1999).
102. B. A. DiDonna, T. A. Witten, J. B. Young, *Physica A: Statistical and Theoretical Physics (Amsterdam)* **258**, 263 (1998).
103. S. M. Cordry, L. A. Crum, *Luminescence of Solids*, 343 (1998).
104. S. Putterman, *Phys. World* **11**, 38 (1998).
105. K. S. Suslick, *Proceedings - IEEE Ultrasonics Symposium*, 523 (1997).
106. F. Macintyre, *Ultrason. Sonochem.* **4**, 85 (1997).
107. T. J. Matula, R. A. Roy, *Ultrason. Sonochem.* **4**, 61 (1997).
108. J. D. N. Cheeke, *Can. J. Phys.* **75**, 77 (1997).
109. B. P. Barber, R. A. Hiller, R. Loefstedt, S. J. Putterman, K. R. Weninger, *Phys. Rep.* **281**, 65 (1997).
110. L. A. Crum, *Phys. Today* **47**, 22 (1994).
111. F. E. Beideman, D. M. Hercules, *J. Phys. Chem.* **83**, 2203 (1979).
112. R. Y. Lai, A. J. Bard, *J. Phys. Chem. A.* **107**, 3335 (2003).
113. L. R. Faulkner, A. J. Bard, *Electronal. Chem.* **10**, 1 (1977).
114. L. R. Faulkner, H. Tachikawa, A. J. Bard, *J. Am. Chem. Soc.* **94**, 691 (1972).
115. H. Tachikawa, A. J. Bard, *Chem. Phys. Lett.* **26**, 246 (1974).
116. A. Pighin, B. E. Conway, *J. Electrochem. Soc.* **122**, 619 (1975).
117. N. Periasamy, K. S. V. Santhanam, *Proc. Indian Acad. Sci. Sec. A.* **80**, 194 (1974).

118. B. Fleet, G. F. Kirkbright, C. J. Pickford, *J. Electroanal. Chem. Interfac. Electrochem.* **30**, 115 (1971).
119. A. Weller, K. Zachariasse, *Chem. Phys. Lett.* **10**, 197 (1971).
120. T. C. Werner, J. Chang, D. M. Hercules, *J. Am. Chem. Soc.* **92**, 5560 (1970).
121. J. T. Maloy, A. J. Bard, *J. Am. Chem. Soc.* **93**, 5968 (1971).
122. E. A. Chandross, J. W. Longworth, R. E. Visco, *J. Am. Chem. Soc.* **87**, 3259 (1965).
123. W. Miao, J.-P. Choi, in *Electrogenerated Chemiluminescence*, A. J. Bard, Ed., Marcel Dekker, Inc.: New York, 2004, Chap. 5.
124. H. S. White, A. J. Bard, *J. Am. Chem. Soc.* **104**, 6891 (1982).
125. A. Juris, V. Balzani, F. Barigelletti, S. Campagna, P. Belser, A. Von Zelewsky, *Coord. Chem. Rev.* **84**, 85 (1988).
126. J. Butler, A. Henglein, *Radiat. Phys. Chem.* **15**, 603 (1980).
127. T. M. Downey, T. A. Nieman, *Anal. Chem.* **64**, 261 (1992).
128. F. Kanoufi, A. J. Bard, *J. Phys. Chem. B.* **103**, 10469 (1999).
129. F. Bolletta, M. Ciano, V. Balzani, N. Serpone, *Inorg. Chim. Acta* **62**, 207 (1982).
130. R. Memming, *J. Electrochem. Soc.* **116**, 785 (1969).
131. F. Bolletta, A. Juris, M. Maestri, D. Sandrini, *Inorg. Chim. Acta* **44**, L175 (1980).
132. A. J. Bard, J. D. Debad, J. K. Leland, G. B. Sigal, J. L. Wilbur, J. N. Wohlsadter, in *Encyclopedia of Analytical Chemistry: Applications, Theory and Instrumentation*; R. A. Meyers, Ed., John Wiley & Sons: New York, 2000, p. 9842.
133. J. D. Debad, E. N. Glezer, J. K. Leland, G. B. Sigal, J. Wohlsadter, in *Electrogenerated Chemiluminescence*; A. J. Bard, Ed., Marcel Dekker, Inc.: New York, 2004, Chap. 8.
134. E. M. Gross, P. Pastore, R. M. Wightman, *J. Phys. Chem. B.* **105**, 8732 (2001).
135. L. He, K. A. Cox, N. D. Danielson, *Anal. Lett.* **23**, 195 (1990).
136. F. Kanoufi, Y. Zu, A. J. Bard, *J. Phys. Chem. B.* **105**, 210 (2001).
137. W. Miao, J.-P. Choi, A. J. Bard, *J. Am. Chem. Soc.* **124**, 14478 (2002).
138. Y. Zu, A. J. Bard, *Anal. Chem.* **72**, 3223 (2000).
139. D. M. Hercules, F. E. Lytle, *J. Am. Chem. Soc.* **88**, 4745 (1966).
140. D. M. Hercules, *Acc. Chem. Res.* **2**, 301 (1969).
141. D. M. Hercules, F. E. Lytle, *Photochem. Photobiol.* **13**, 123 (1971).
142. B. Li, Z. Zhang, X. Zheng, C. Xu, *Chem. Anal. (Warsaw)* **45**, 709 (2000).
143. J. E. Martin, E. J. Hart, A. W. Adamson, H. Gafney, J. Halpern, *J. Am. Chem. Soc.* **94**, 9238 (1972).
144. E. A. Chandross, F. I. Sonntag, *J. Am. Chem. Soc.* **88**, 1089 (1966).
145. D. L. Akins, R. L. Birke, *Chem. Phys. Lett.* **29**, 428 (1974).
146. T. D. Santa Cruz, D. L. Akins, R. L. Birke, *J. Am. Chem. Soc.* **98**, 1677 (1976).
147. A. R. Bowie, M. G. Sanders, P. J. Worsfold, *J. Biolumin. Chemilumin.* **11**, 61 (1996).
148. H. O. House, E. Feng, N. P. Peet, *J. Org. Chem.* **36**, 2371 (1971).
149. F. R. F. Fan, in *Electrogenerated Chemiluminescence*, A. J. Bard, Ed., Marcel Dekker, Inc.: New York, 2004, Chap. 2.
150. A. J. Fry, in *Laboratory Techniques in Electroanalytical Chemistry*, P. T. Kissingerand, W. R. Heineman, Eds., Marcel Dekker, Inc.: New York, 1996, Chap. 15.
151. W. Miao, A. J. Bard, *Anal. Chem.* **75**, 5825 (2003).
152. X.-H. Xu, A. J. Bard, *Langmuir* **10**, 2409 (1994).
153. N. D. Danielson, in *Electrogenerated Chemiluminescence*, A. J. Bard, Ed., Marcel Dekker, Inc.: New York, 2004, Chap. 9.
154. F. Li, H. Cui, X.-Q. Lin, *Anal. Chim. Acta* **471**, 187 (2002).
155. W. Cao, J. Liu, X. Yang, E. Wang, *Electrophoresis* **23**, 3683 (2002).
156. L. R. Faulkner, D. J. Freed, *J. Am. Chem. Soc.* **93**, 2097 (1971).
157. J. E. Bartelt, S. M. Drew, R. M. Wightman, *J. Electrochem. Soc.* **139**, 70 (1992).

158. Y. Zu, A. J. Bard, *Anal. Chem.* **73**, 3960 (2001).
159. W. Miao, A. J. Bard, *Anal. Chem.* **76**, 5379 (2004).
160. X. Zhao, T. You, H. Qiu, J. Yan, X. Yang, E. Wang, *J. Chromatogr. B: Anal. Technol. Biomed. Life Sci.* **810**, 137 (2004).
161. K. Honda, T. Noda, M. Yoshimura, K. Nakagawa, A. Fujishima, *J. Phys. Chem. B* **108**, 16117 (2004).
162. K. Honda, M. Yoshimura, T. N. Rao, A. Fujishima, *J. Phys. Chem. B* **107**, 1653 (2003).
163. H. Yang, J. K. Leland, D. Yost, R. J. Massey, *Biotechnology* **12**, 193 (1994).
164. R. S. Glass, L. R. Faulkner, *J. Phys. Chem.* **85**, 1160 (1981).
165. J. D. Luttmer, A. J. Bard, *J. Phys. Chem.* **85**, 1155 (1981).
166. P. McCord, A. J. Bard, *J. Electroanal. Chem. Interfac. Electrochem.* **318**, 91 (1991).
167. N. E. Tokel-Takvoryan, R. E. Hemingway, A. J. Bard, *J. Am. Chem. Soc.* **95**, 6582 (1973).
168. W. L. Wallace, A. J. Bard, *J. Phys. Chem.* **83**, 1350 (1979).
169. K. Itoh, K. Honda, *Chem. Lett.* **1**, 99 (1979).
170. D. Laser, A. J. Bard, *J. Electrochem. Soc.* **122**, 632 (1975).
171. R. Bezman, L. R. Faulkner, *J. Am. Chem. Soc.* **94**, 3699 (1972).
172. M. J. Cook, A. P. Lewis, G. S. G. McAuliffe, V. Skarda, A. J. Thomson, J. L. Glasper, D. J. Robbins, *J. Chem. Soc., Perkin Trans. 2: Phys. Org. Chem.* **8**, 1293 (1984).
173. P. C. Alford, M. J. Cook, A. P. Lewis, G. S. G. McAuliffe, V. Skarda, A. J. Thomson, J. L. Glasper, D. J. Robbins, *J. Chem. Soc., Perkin Trans. 2: Phys. Org. Chem.* **5**, 705 (1985).
174. E. Bolton, M. M. Richter, *J. Chem. Educ.* **78**, 641 (2001).
175. C. Alexander, J. McCall, M. M. Richter, *Chemical Educator (Electronic Publication)* **3**, No pp. given (1998).
176. R. D. Gerardi, N. W. Barnett, A. W. Lewis, *Anal. Chim. Acta* **378**, 1 (1999).
177. I. Rubinstein, C. R. Martin, A. J. Bard, *Anal. Chem.* **55**, 1580 (1983).
178. K. Uchikura, *Bunseki Kagaku* **39**, 323 (1990).
179. N. Egashira, H. Kumasako, K. Ohga, *Anal. Sci.* **6**, 903 (1990).
180. N. Egashira, *Proc. Electrochem. Soc.* **93**, 674 (1993).
181. D. J. Walton, S. S. Phull, D. M. Bates, J. P. Lorimer, T. J. Mason, *Ultrasonics* **30**, 186 (1992).
182. D. R. Skotty, T. A. Nieman, *J. Chromatogr. B* **665**, 27 (1995).
183. W.-Y. Lee, T. A. Nieman, *Anal. Chem.* **67**, 1789 (1995).
184. D. R. Skotty, W.-Y. Lee, T. A. Nieman, *Anal. Chem.* **68**, 1530 (1996).
185. J. P. Preston, T. A. Nieman, *Anal. Chem.* **68**, 966 (1996).
186. A. W. Knight, G. M. Greenway, *Analyst (Cambridge, United Kingdom)* **120**, 2543 (1995).
187. X. Chen, M. Sato, *Anal. Sci.* **11**, 749 (1995).
188. K. Uchikura, *Chromatography* **11**, 102 (1990).
189. K. Uchikura, M. Kirisawa, *Anal. Sci.* **7**, 803 (1991).
190. K. Uchikura, M. Kirisawa, *Chromatography* **12**, 56 (1991).
191. K. Uchikura, M. Kirisawa, *Chromatography* **13**, 257 (1992).
192. K. Uchikura, M. Kirisawa, A. Sugii, *Anal. Sci.* **9**, 121 (1993).
193. A. W. Knight, G. M. Greenway, E. D. Chesmore, *Anal. Proc.* **32**, 125 (1995).
194. J. A. Dickson, M. M. Ferris, R. E. Milofsky, *J. High Resolut. Chromatogr.* **20**, 643 (1997).
195. A. Arora, A. J. de Mello, A. Manz, *Anal. Commun.* **34**, 393 (1997).
196. K. Uchikura, M. Kirisawa, *Chem. Lett.*, 8, 1373 (1991).
197. K. Uchikura, M. Kirisawa, *Anal. Sci.* **7**, 971 (1991).
198. W. A. Jackson, D. R. Bobbitt, *Anal. Chim. Acta* **285**, 309 (1994).
199. K. Uchikura, M. Kirisawa, *Chromatography* **15**, 232 (1994).
200. W.-Y. Lee, T. A. Nieman, *J. Chromatogr.* **659**, 111 (1994).
201. K. Uchikura, S. Asami, *Chromatography* **16**, 320 (1995).

202. G. M. Greenway, P. J. Knight, *Anal. Proc.* **32**, 251 (1995).
203. G. M. Greenway, A. W. Knight, P. J. Knight, *Analyst (Cambridge, United Kingdom)* **120**, 2549 (1995).
204. S. J. L. Dolman, G. M. Greenway, *Anal. Commun.* **33**, 139 (1996).
205. A. W. Knight, G. M. Greenway, *Anal. Commun.* **33**, 171 (1996).
206. P. Liang, R. I. Sanchez, M. T. Martin, *Anal. Chem.* **68**, 2426 (1996).
207. J. S. Ridlen, D. R. Skott, P. T. Kissinger, T. A. Nieman, *J. Chromatogr. B* **694**, 393 (1997).
208. G. A. Forbes, T. A. Nieman, J. V. Sweedler, *Anal. Chim. Acta* **347**, 289 (1997).
209. L. S. Kuhn, A. Weber, S. G. Weber, *Anal. Chem.* **62**, 1631 (1990).
210. Y. T. Hsueh, R. L. Smith, M. A. Northrup, *Proc. Electrochem. Soc.* **95**, 117 (1995).
211. X. Wang, D. R. Bobbitt, *Anal. Chim. Acta* **383**, 213 (1999).
212. J. F. Liu, W. D. Cao, X. R. Yang, E. K. Wang, *Talanta* **59**, 453 (2003).
213. W. Cao, J. Liu, H. Qiu, X. Yang, E. Wang, *Electroanalysis* **14**, 1571 (2002).
214. X. Sun, J. Liu, W. Cao, X. Yang, E. Wang, Y. S. Fung, *Anal. Chim. Acta* **470**, 137 (2002).
215. M.-T. Chiang, C.-W. Whang, *J. Chromatogr. A* **934**, 59 (2001).
216. M.-T. Chiang, M. C. Lu, C.-W. Whang, *Electrophoresis* **24**, 3033 (2003).
217. W. Cao, J. Jia, X. Yang, S. Dong, E. Wang, *Electrophoresis* **23**, 3692 (2002).
218. G. N. Chen, Y. W. Chi, X. P. Wu, J. P. Duan, N. B. Li, *Anal. Chem.* **75**, 6602 (2003).
219. X.-J. Huang, S.-L. Wang, Z.-L. Fang, *Anal. Chim. Acta* **456**, 167 (2002).
220. A. Arora, J. C. T. Eijkel, W. E. Morf, A. Manz, *Anal. Chem.* **73**, 3282 (2001).
221. H. Qiu, J. L. Yan, X. H. Sun, J. F. Liu, W. D. Cao, X. R. Yang, E. K. Wang, *Anal. Chem.* **75**, 5435 (2003).
222. Y. Namba, M. Usami, O. Suzuki, *Anal. Sci.* **15**, 1087 (1999).
223. N. Yilmaz, A. B. Erbagci, A. S. Aynacioglu, *Acta. Biochim. Polon.* **48**, 775 (2001).
224. K. Fukuda, K. Takahashi, Y. Iwata, N. Mori, K. Gonda, T. Ogawa, K. Osonoe, M. Sato, S.-I. Ogata, T. Horimoto, T. Sawada, M. Tashiro, K. Yamaguchi, S.-I. Niwa, S. Shigeta, *J. Clin. Microbiol.* **39**, 419 (2001).
225. Y. Horii, N. P. Garcia, D. Noviana, F. Kono, T. Sawada, T. Naraki, K. Yamaguchi, *J. Vet. Med. Sci./The Jpn. Soc. Vet. Sci.* **63**, 921 (2001).
226. K. Yamaguchi, T. Sawada, S. Yamane, S. Haga, K. Ikeda, R. Igata-Yi, K. Yoshiki, M. Matsuoka, H. Okabe, Y. Horii, Y. Nawa, R. W. Waltrip, II, K. M. Carbone, *Ann. Clin. Biochem.* **38**, 348 (2001).
227. O. E. Khorkova, K. Pate, J. Heroux, S. Sahasrabudhe, *J. Neurosci. Methods* **82**, 159 (1998).
228. P. Stieber, R. Molina, D. W. Chan, H. A. Fritzsche, R. Beyrau, J. M. G. Bonfrer, X. Filella, T. G. Gornet, T. Hoff, W. Inger, G. J. Van Kamp, D. Nagel, K. Peisker, L. J. Sokoll, F. Troalen, M. Untch, I. Domke, *Clin. Chem. (Washington, DC, United States)* **47**, 2162 (2001).
229. X. Filella, S. Friese, H. J. Roth, S. Nussbaum, B. Wehn, *Anticancer Res.* **20**, 5229 (2000).
230. W. Hubl, D. W. Chan, H. E. Van Ingen, H. Miyachi, R. Molina, X. Filella, L. Pitzel, A. Ruibal, J. C. Rymer, G. Bagnard, I. Domke, *Anticancer Res.* **19**, 2727 (1999).
231. H. E. Van Ingen, D. W. Chan, W. Hubl, H. Miyachi, R. Molina, L. Pitzel, A. Ruibal, J. C. Rymer, I. Domke, *Clin. Chem. (Washington, DC)* **44**, 2530 (1998).
232. W. Stockmann, W. Bablok, P. Lupp, *Wiener Klinische Wochenschrift* **110**, 10 (1998).
233. T. Seck, I. Diel, H. Bismar, R. Ziegler, J. Pfeilschifter, *Bone (New York, NY, United States)* **30**, 217 (2002).
234. R. Okabe, K. Nakatsuka, M. Inaba, T. Miki, H. Naka, H. Masaki, A. Moriguchi, Y. Nishizawa, *Clin. Chem.* **47**, 1410 (2001).
235. K. Scheunert, S. Albrecht, V. Konnegen, G. Wunderlich, W. Distler, in *Chemiluminescence at the Turn of the Millennium*; S. Albrecht, T. Zimmermann and H. Brandl, Eds., Schweda-Werbedruck GmbH: Dresden, 2001, p. 347.

236. M. Ohlin, M. Silvestri, V. A. Sundqvist, C. A. Borrebaeck, *Clin. Diagn. Lab. Immunol.* **4**, 107 (1997).
237. M. Sanchez-Carbayo, A. Espasa, V. Chinchilla, E. Herrero, J. Megias, A. Mira, F. Soria, *Clin. Chem. (Washington, DC)* **45**, 1944 (1999).
238. G. Klein, M. Kampmann, H. Baum, T. Rauscher, T. Vukovic, K. Hallermayer, H. Rehner, M. Mueller-Bardorff, H. A. Katus, *Wiener Klinische Wochenschrift* **110**, 40 (1998).
239. W. Miao, A. J. Bard, *Anal. Chem.* **76**, 7109 (2004).
240. A. Shimizu, K. Shiraki, T. Ito, K. Sugimoto, T. Sakai, S. Ohmori, K. Murata, K. Takase, Y. Tameda, T. Nakano, *Int. J. Mol. Med.* **9**, 245 (2002).
241. T. Sassa, T. Kumada, S. Nakano, T. Uematsu, *Eur. J. Gastroenterol. Hepatol.* **11**, 1387 (1999).
242. N. Gassler, T. Peuschel, R. Pankau, *Clin. Lab. (Heidelberg)* **46**, 553 (2000).
243. V. Ehrhardt, G. Assmann, O. Batz, C. Biegelmayer, C. Muller, D. Neumeier, H. J. Roth, A. Veys, J. P. Yvert, *Wiener klinische Wochenschrift* **110 Suppl 3**, 61 (1998).
244. Y. Kobayashi, M. Hayakawa, Y. Fukumura, *Igaku Yakugaku* **42**, 749 (1999).
245. S. Kashiwagi, J. Hayashi, T. Asai, J. Nishimura, N. Arai, M. Kanashima, Y. Asai, *Igaku Yakugaku* **40**, 119 (1998).
246. M. Takahashi, H. Hoshino, Y. Ohuchi, S. Ryan, K. Shimoda, K. Yachuda, J. Tanaka, K. Yoshizawa, K. Hino, S. Iino, *Igaku Yakugaku* **40**, 483 (1998).
247. B. Weber, A. Bayer, P. Kirch, V. Schluter, D. Schlieper, W. Melchior, *J. Clin. Microbiol.* **37**, 2639 (1999).
248. See www.rochediagnostics.com
249. M. P. De Baar, K. H. M. Van der Horn, J. Goudsmit, A. De Ronde, F. De Wolf, *J. Clin. Microbiol.* **37**, 63 (1999).
250. L. Kobrynski, L. Tanimune, N. A. Pawlowski, S. D. Douglas, D. E. Campbell, *Clin. Diagn. Lab. Immunol.* **3**, 42 (1996).
251. A. Liebert, L. Beier, E. Schneider, P. Kirch, *Chemiluminescence at the Turn of the Millennium*, 2001, p. 341.
252. R. Sapin, V. Le Galudec, F. Gasser, M. Pinget, D. Grucker, *Clin. Chem.* **47**, 602 (2001).
253. D. Novick, B. Schwartzburg, R. Pinkus, D. Suissa, I. Belzer, Z. Sthoeger, W. F. Keane, Y. Chvatchko, S. H. Kim, G. Fantuzzi, C. A. Dinarello, M. Rubinstein, *Cytokine* **14**, 334 (2001).
254. S. V. Sennikov, S. V. Krysov, T. V. Injelevskaya, A. N. Silkov, L. V. Grishina, V. A. Kozlov, *J. Immunol. Methods* **275**, 81 (2003).
255. S. J. Swanson, S. J. Jacobs, D. Mytych, C. Shah, S. R. Indelicato, R. W. Bordens, *Developments in Biological Standardization* **97**, 135 (1999).
256. J. Kankare, K. Haapakka, S. Kulmala, V. Nanto, J. Eskola, H. Takalo, *Anal. Chim. Acta* **266**, 205 (1992).
257. D. Hermsen, L. Franzson, J. P. Hoffmann, A. Isaksson, J. M. Kaufman, E. Leary, C. Muller, K. Nakatsuka, Y. Nishizawa, H. Reinauer, W. Riesen, H.-J. Roth, T. Steinmuller, T. Troch, P. Bergmann, *Clin. Lab. (Heidelberg, Germany)* **48**, 131 (2002).
258. X. H. Xu, R. B. Jeffers, J. Gao, B. Logan, *Analyst* **126**, 1285 (2001).
259. A. W. Butch, D. Crary, M. Yee, *Clin. Biochem.* **35**, 143 (2002).
260. A. Haese, T. Dworschack Robert, P. Piccoli Steven, J. Sokoll Lori, W. Partin Alan, W. Chan Daniel, *Clin. Chem.* **48**, 944 (2002).
261. P. B. Luppa, S. Reutemann, U. Huber, R. Hoermann, S. Poertl, S. Kraiss, S. Von Buelow, D. Neumeier, *Clin. Chem. Lab. Med.* **36**, 789 (1998).
262. R. Sapin, J.-L. Schlienger, F. Gasser, E. Noel, B. Lioure, F. Grunenberger, B. Goichot, D. Grucker, *Clin. Chem. (Washington, DC, United States)* **46**, 418 (2000).
263. M. Sanchez-Carbayo, M. Mauri, R. Alfayate, C. Miralles, F. Soria, *Clin. Biochem.* **32**, 395 (1999).

264. S. Kulmala, M. Hakansson, A. M. Spehar, A. Nyman, J. Kankare, K. Loikas, T. Ala-Kleme, J. Eskola, *Anal. Chim. Acta* **458**, 271 (2002).
265. O. Hetland, K. Dickstein, *Clin. Chem.* **44**, 1348 (1998).
266. J. Ishii, T. Ishikawa, J. Yukitake, Y. Nagamura, M. Ito, J. H. Wang, Y. Kato, S. Hiramitsu, S. Inoue, T. Kondo, S. Morimoto, M. Nomura, Y. Watanabe, H. Hishida, *Clin. Chim. Acta, Int. J. Clin. Chem.* **270**, 183 (1998).
267. P. O. Collinson, B. Jorgensen, C. Sylven, M. Haass, F. Chwallek, H. A. Katus, M. Muller-Bardorff, U. Derhaschnig, M. M. Hirsch, R. Zerback, *Clin. Chim. Acta* **307**, 197 (2001).
268. E. Moreau, J. Philippe, S. Couvent, G. Leroux-Roels, *Clin. Chem.* **42**, 1450 (1996).
269. K. R. Klingler, D. Zech, K. Wielckens, *Clin. Lab. (Heidelberg)* **46**, 41 (2000).
270. J. H. Tai, M. S. Ewert, G. Belliot, R. I. Glass, S. S. Monroe, *J. Virol. Methods* **110**, 119 (2003).
271. K. N. Reetoo, S. A. Osman, S. J. Illavia, J. E. Banatvala, P. Muir, *J. Virol. Methods* **82**, 145 (1999).
272. R. Boom, C. Sol, J. Weel, Y. Gerrits, M. de Boer, P. Wertheim-van Dillen, *J. Clin. Microbiol.* **37**, 1489 (1999).
273. S. J. Wu, E. M. Lee, R. Putvatana, R. N. Shurtliff, K. R. Porter, W. Suharyono, D. M. Watts, C. C. King, G. S. Murphy, C. G. Hayes, J. W. Romano, *J. Clin. Microbiol.* **39**, 2794 (2001).
274. J. D. Fox, S. Han, A. Samuelson, Y. Zhang, M. L. Neale, D. Westmoreland, *J. Clin. Virol.* **24**, 117 (2002).
275. S. J. C. Stevens, M. B. H. J. Vervoort, A. J. C. Van den Brule, P. L. Meenhorst, C. J. L. M. Meijer, J. M. Middeldorp, *J. Clin. Microbiol.* **37**, 2852 (1999).
276. R. A. Collins, L.-S. Ko, K. Y. Fung, L.-T. Lau, J. Xing, A. C. H. Yu, *Biochem. Biophys. Res. Commun.* **297**, 267 (2002).
277. B. van Gemen, R. van Beuningen, A. Nabbe, D. van Strijp, S. Jurriaans, P. Lens, T. Kievits, *J. Virol. Methods* **49**, 157 (1994).
278. T. E. Schutzbank, J. Smith, *J. Clin. Microbiol.* **33**, 2036 (1995).
279. J. H. Kenten, S. Gudibande, J. Link, J. J. Willey, B. Curfman, E. O. Major, R. J. Massey, *Clin. Chem. (Washington, DC, United States)* **38**, 873 (1992).
280. H. Yu, J. G. Bruno, T. C. Cheng, J. J. Calomiris, M. T. Goode, D. L. Gatto-Menking, *J. Biolumin. Chemilumin.* **10**, 239 (1995).
281. J. J. Oprandy, K. Amemiya, J. H. Kenten, R. G. Green, E. O. Major, R. Massey, *Technical Advances in AIDS Research in the Human Nervous System (Proceedings of an NIH Symposium on Technical Advances in AIDS Research in the Human Nervous System)*, Washington, DC, Oct. 4–5, 1993, 281 (1995).
282. S. Hibbitts, A. Rahman, R. John, D. Westmoreland, J. D. Fox, *J. Virol. Methods* **108**, 145 (2003).
283. R. A. Collins, L.-S. Ko, K.-Y. Fung, K.-Y. Chan, J. Xing, L.-T. Lau, A. C. H. Yu, *Biochem. Biophys. Res. Commun.* **300**, 507 (2003).
284. R. A. Collins, L.-S. Ko, K.-L. So, T. Ellis, L.-T. Lau, A. C. H. Yu, *J. Virol. Methods* **103**, 213 (2002).
285. S. Shan, L.-S. Ko, R. A. Collins, Z. Wu, J. Chen, K.-Y. Chan, J. Xing, L.-T. Lau, A. C.-H. Yu, *Biochem. Biophys. Res. Comm.* **302**, 377 (2003).
286. I. Miyashiro, C. Kuo, K. Huynh, A. Iida, D. Morton, A. Bilchik, A. Giuliano, D. S. B. Hoon, *Clin. Chem. (Washington, DC, United States)* **47**, 505 (2001).
287. C. D. O'Connell, A. Juhasz, C. Kuo, D. J. Reeder, D. S. B. Hoon, *Clin. Chem. (Washington, DC)* **44**, 1161 (1998).
288. B. Taback, A. D. Chan, C. T. Kuo, P. J. Bostick, H.-J. Wang, A. E. Giuliano, D. S. B. Hoon, *Cancer Res.* **61**, 8845 (2001).
289. D. S. B. Hoon, C. T. Kuo, S. Wen, H. Wang, L. Metelitsa, C. P. Reynolds, R. C. Seeger, *Am. J. Pathol.* **159**, 493 (2001).

290. A. Gellings, G. Holzem, K. Wielckens, K. R. Klingler, *Laboratoriumsmedizin* **25**, 26 (2001).
291. R. S. Lanciotti, A. J. Kerst, *J. Clin. Microbiol.* **39**, 4506 (2001).
292. M. D. de Jong, J. F. Weel, T. Schuurman, P. M. Wertheim-van Dillen, R. Boom, *J. Clin. Microbiol.* **38**, 2568 (2000).
293. H. J. Stern, R. D. Carlos, T. E. Schutzbanks, *Clin. Biochem.* **28**, 470 (1995).
294. B. D. Muegge, M. M. Richter, *Anal. Chem.* **74**, 547 (2002).
295. R. Y. Lai, M. Chiba, N. Kitamura, A. J. Bard, *Anal. Chem.* **74**, 551 (2002).
296. F. Jameison, R. I. Sanchez, L. Dong, J. K. Leland, D. Yost, M. T. Martin, *Anal. Chem.* **68**, 1298 (1996).
297. A. F. Martin, T. A. Nieman, *Biosens. Bioelectron.* **12**, 479 (1997).
298. A. J. Baeumner, M. C. Humiston, R. A. Montagna, R. A. Durst, *Anal. Chem.* **73**, 1176 (2001).
299. J. L. Call, M. Arrowood, L. T. Xie, K. Hancock, V. C. Tsang, *J. Parasitol.* **87**, 203 (2001).
300. Y. M. Lee, P. W. Johnson, J. L. Call, M. J. Arrowood, B. W. Furness, S. C. Pichette, K. K. Grady, P. Reeh, L. Mitchell, D. Bergmire-Sweat, W. R. Mackenzie, V. C. Tsang, *Am. J. Trop. Med. Hyg.* **65**, 1 (2001).
301. E. Kuczynska, G. Boyer Douglas, R. Shelton Daniel, *J. Microbiol. Methods* **53**, 17 (2003).
302. D. R. Shelton, J. S. Karns, *Appl. Environ. Microbiol.* **67**, 2908 (2001).
303. J. Min, A. J. Baeumner, *Anal. Biochem.* **303**, 186 (2002).
304. C. G. Crawford, C. Wijey, P. Fratamico, S. I. Tu, J. Brewster, *J. Rapid Methods Autom. Microbiol.* **8**, 249 (2000).
305. H. Yu, J. G. Bruno, *Appl. Environ. Microbiol.* **62**, 587 (1996).
306. H. Yu, J. G. Bruno, *Biomed. Prod.* **20**, 20 (1995).
307. T. M. Kijek, C. A. Rossi, D. Moss, R. W. Parker, E. A. Henchal, *J. Immunol. Methods*, **236**, 9 (2000).
308. H. Yu, J. W. Raymonda, T. M. McMahon, A. A. Campagnari, *Biosens. Bioelectron.* **14**, 829 (2000).
309. J. G. Bruno, H. Yu, *Appl. Environ. Microbiol.* **62**, 3474 (1996).
310. D. L. Gatto-Menking, H. Yu, J. G. Bruno, M. T. Goode, M. Miller, A. W. Zulich, *Biosens. Bioelectron.* **10**, 501 (1995).

– 14 –

Spectroelectrochemistry

Tia E. Keyes and Robert J. Forster

National Centre for Sensor Research, School of Chemical Sciences,
Dublin City University, Dublin 9, Ireland

14.1 INTRODUCTION

Electrochemistry can provide both thermodynamic and kinetic information on a range of chemical processes driven by electron transfer. However, electrochemistry can rarely unequivocally identify electroactive species; the molecular identity of a new electrogenerated material is typically inferred from the measured physical properties of a known standard system. In addition, electrochemistry provides only limited and indirect information on structural changes accompanying redox events.

In the past two decades, spectroelectrochemical techniques (i.e., tandem spectroscopic and electrochemical methods) have been exploited across diverse applications ranging from inorganic and organic chemistry to biochemistry. Spectroscopically acquired molecular information under potential control, including vibrational frequencies, molar absorptivities, luminescence intensities, and electronic or magnetic resonance frequencies, are now routinely available. Such combinations of electrochemical and spectroscopic techniques have contributed to the elucidation of electron transfer reaction mechanisms and to the understanding of fundamental molecular states at interfaces. For example, spectroelectrochemistry can yield clues to the mechanism of photoinduced electron transfer processes by providing static products which mirror those that are produced only fleetingly in transient spectroscopy (1).

There is extensive literature on applications of spectroelectrochemistry and the myriad of cell designs and techniques which have been applied. We focus here on the most common optical techniques that are performed *in situ* and those which can be undertaken under ambient conditions. By focusing in this way on optical methodologies we exclude a range of important non-optical techniques such as mass spectrometry, EPR, and NMR and those which require specialized conditions such as ultra high vacuum including X-ray and photoelectron methods. Details of these experiments and methods can be found in the literature (2). This chapter gives insight into experimental considerations for qualitative and quantitative spectroelectrochemical measurements and outlines common applications. We

focus on the use of spectroelectrochemistry in elucidating mechanisms and intermediates in electrode reactions rather than in elucidation of interfacial structure.

Conventional spectroelectrochemistry involves bulk electrolysis of an analyte in a low volume cell combined with simultaneous or subsequent *in situ* spectroscopic investigation. The key point is that investigations are *in situ* with spectroscopic studies undertaken within an electrochemical cell that is under potential control. Spectroelectrochemical experiments are frequently qualitative and are used to structurally characterize an intermediate redox state. Quantitative measurements can be experimentally challenging because they require rigorous geometric arrangement of the cell to avoid problems such as iR drop and low current densities as a consequence of the relative size of the working electrode and its orientation with respect to the other electrodes.

The spectroelectrochemical cell design is critically dependent on the spectroscopic technique being used. Parameters such as cell orientation with respect to optical source and detector and electrode transparency are dictated by how the optical changes are interrogated (i.e., whether through light transmission as in electronic spectroscopy or light scattering as in Raman spectroscopy). Most cells follow the conventional three-electrode configuration: with reference and auxiliary electrodes and a working electrode on which the optical path is generally trained. Another common feature of spectroelectrochemical methods is the requirement for small reagent volumes in order to minimize the time required for the cell to reach equilibrium at a given applied potential. Small solution volumes can also minimize background interference from solvent and electrolyte. Thin layer cells are consequently common in spectroelectrochemistry and these are described below. We begin by examining how light interacts with a solid electrode material.

14.2 LIGHT TRANSMISSION AND REFLECTION AT AN ELECTRODE SURFACE

Light striking a dielectric interface can undergo a number of processes, the most important of which are reflection, absorption, and scattering. In a spectroscopic experiment, the intensity of light incident on a surface, I_0 , is compared to that which has been transmitted through the medium, $T = I_0/I$, scattered from the medium $S = I_s/I_0$ or reflected from the medium, where $R = I_r/I$. A material's optical parameters (i.e., reflectivity, transmissivity, and absorptivity) are described by the Fresnel equations which define these properties in terms of the materials refractive index, n' , where $n' = n_r + ik_i$ or complex dielectric constant $\epsilon' = \epsilon_r + ik_i$. These two parameters are interrelated since $n' = \sqrt{\epsilon'}$. Fresnel also describes the incident angle dependent intensity reflection coefficients and transmission coefficients for the electric field vectors of light which are perpendicularly (s) and parallel (p) polarized relative to the plane of incidence (when light is incident, but not normal on a surface) (3). In other words, the intensities of the s and p-polarized components of reflected light varies and depends on the angle of the incident beam. The dominant processes in light interaction at an interface are reflection, transmission, and elastic scattering of light. Inelastic scattering, as in the case of Raman scattering, is a much weaker phenomenon. Figure 14.1 shows common optical geometries for transmission and reflectance measurements used in optical spectroelectrochemistry. Optical transmission

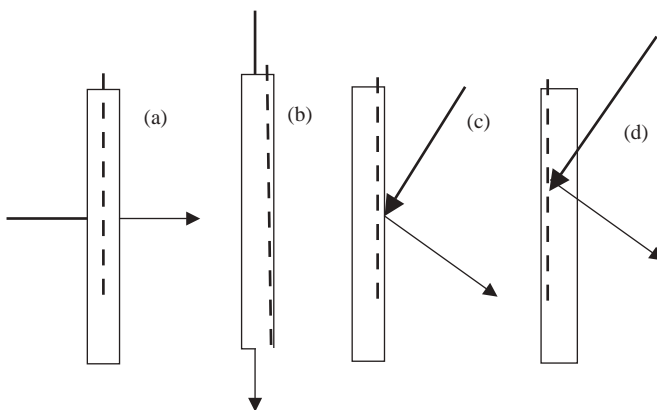


Figure 14.1 Common optical configurations for spectroelectrochemical cells showing path of incident light (thick line) and detected light (thin line) in (a) transmission mode normal to the electrode and (b) transmission mode parallel to the electrode, internal (c) and external (d) reflectance modes. The dashed line represents the electrode solution interface.

experiments are the most common optical arrangement. They are based on the measurement of the wavelength-dependent decrease in the intensity of incident light, I_0 , following its passage through an absorbing medium. In a conventional absorbance experiment, the optical arrangement minimizes the contribution of scatter and reflection from the sample so that the main contribution to the decrease in I_0 arises from absorption; therefore absorbance $A = -\log(I/I_0)$ or $-\log(T)$.

In absorbance or transmission measurements in spectroelectrochemistry, scattering and reflection must also be minimized to provide an optimum signal-to-noise ratio. Since the working electrode generally presents a reflective surface, minimizing scatter and reflection can prove challenging and lead to distortions of the optical signal in an absorbance experiment. The use of optically transparent electrodes (OTEs) in which the incident light is perpendicular or normal to the electrode surfaces significantly reduces such interferences. An alternative transmission arrangement directs the optical path parallel to the electrode (Figure 14.1b).

In a reflectance experiment, incident light reflected from a sample at a surface R_2 is measured and compared to light reflected from a bare surface, R_1 . The differential reflectance, $\Delta R/R_1$, where ΔR is $R_2 - R_1$, is the difference in reflectance between a clean surface and that on which the analyte is placed. In a spectroelectrochemical experiment, it may indicate the difference in reflectance in the absence and presence of applied potential. Since this is a differential value, it is frequently very small and therefore it is important to limit background contributions to the signal.

14.3 ELECTRONIC SPECTROSCOPY

Electronic spectroelectrochemistry is the most commonly reported form of spectroelectrochemistry due to its ease of use, low cost, and its value in obtaining both quantitative and qualitative information on electrochemical processes. Electronic spectroscopy addresses

the transitions that occur between electronic states within a target analyte. Such transitions generally occur in the ultra-violet or visible region (190–700 nm of the electromagnetic (EM) spectrum) or less frequently in the near infrared (NIR), ~700–3000 nm. Electrochemistry directly addresses the valence electrons of a given species through oxidation or reduction and changes in these electronic states are naturally reflected in the associated electronic spectroscopy. Therefore, UV-vis-NIR or electronic spectroelectrochemistry is valuable for elucidating the nature of electronic changes induced by a redox process. UV-vis spectrometers conventionally operate in a transmission mode, where absorbance is expressed in terms of percentage transmittance where $A = \log(100/\%T) = 2.000 - \log(\%T)$ is the measured absorbance. Absorbance is directly related to an absorbing species concentration according to the Beer–Lambert Law, $A = \varepsilon c L$, where L is the path length through the sample, c is the concentration of the absorbing species, and ε is the molar absorptivity or extinction coefficient.

14.3.1 Transmittance spectroscopy and optically transparent cell materials

Transmission electronic spectroscopy, the most facile and readily available spectroscopic technique for investigating electrochemical reactions, became possible due to the availability of OTEs. The underlying principle is that the working electrode, usually solid, is optically transparent. This means that it transmits more than 50% of incident light within the wavelength region of interest.

Prerequisites of working electrode materials for OTEs include optical transparency, amenable potential windows, and stability towards electrolyte and solvent. There are broadly two types of OTE materials in common use:

14.3.1.1 Thin conducting film electrodes

Thin metal films include vapor deposited or sputtered Au, Ag, or Pt on transparent substrates such as glass, quartz, or plastic. On quartz, an optical window ranging from 220 nm through the visible and NIR spectral regions is possible, whereas glass or plastic substrates are useful only in the visible and to a variable extent, in the NIR region. The deposition of metal films of Pt and Au typically requires an undercoating of transition metal (ca. 5 nm), such as W or Ti to improve adhesion and to stabilize the conducting metal film. Another useful approach in stabilizing such thin metal films on glass or quartz is to silylate the substrate with mercaptotrimethoxysilane. The thiol group binds the metal and stabilizes the metal film. This is particularly important in the case of gold which is vulnerable to damage from friction and produces very robust transparent electrode materials (4). The metal film must be sufficiently thin (i.e., less than ~200 nm thick) to maintain optical transparency. A drawback then is that the metal film can be poorly conducting.

Thin films of transparent metal oxide semiconductor (e.g., indium tin oxide and fluorine doped tin oxide) deposited on a transparent medium are finding increasing application because thick films can be used due to the optical transparency of metal oxides in the visible region of the spectrum and there are fewer problems with resistance than for thin metal films. The drawback to these materials is that they do not transmit ultra violet

wavelengths and are thus limited to optical studies in the visible and NIR spectral regions. High levels of dopant can also reduce their optical transmittance.

Diamond electrodes are finding increasing application in transmission spectroelectrochemical methods (5). Optically transparent diamond electrodes are fabricated in a number of ways. Chemical vapor deposited diamond (CVD) is the most common form. Polycrystalline diamond can be grown on metal substrates and then separated for use as an optical window (6). Thin film diamond can be deposited on optically transparent substrates (7, 8). Conducting diamond film has been used as a transparent electrode for attenuated total reflectance infrared (ATR-IR) spectroscopy (9). High purity diamond has an excellent optical transparency, transmitting from ~225 nm (where it has a bandgap absorption) to the far IR (typically >50% transparency). However, diamond is a poor conductor and requires doping (e.g., with boron) to produce a useful electrode material. Unfortunately, the optical properties are degraded by doping and the available wavelength range and transparency are considerably reduced. Even so, diamond possesses a wide potential window, is resistant to fouling, and can tolerate extreme solvent conditions.

14.3.1.2 Minigrid electrodes

Semi-transparent materials in the form of minigrids or meshes of conducting materials have found extensive application in UV-vis and UV-vis-NIR spectroelectrochemistry. These are metals which are primarily commercially available as meshes (e.g., gold, platinum, or platinum–rhodium alloy) but porous reticulated vitreous carbon and other less common metals and alloys such as Hg coated gold have also been used (10, 11). The optical transparency of the minigrid depends on the dimensions of the crossbars and the pitch of the mesh but overall the transparency is 50% or greater. The very large surface areas and conductivity of these materials means exhaustive electrolysis can be achieved very quickly. The dimensions of the micromesh, pore size, and wire thickness is important in determining the diffusion behavior at a mesh electrode. A simulation of cyclic voltammetry at a minigrid Pt electrode was recently reported; useful limits were given for electrode dimensions within which thin layer behavior is maintained (12).

The auxiliary and reference electrodes in electronic and other spectroelectrochemical experiments are similar to those used in conventional electrochemical cells. They must be small enough to fit into the cell without complicating its construction. Common auxiliary electrodes are small platinum wires, paddles, or coils. Reference electrodes (see Chapter 4) are frequently Ag/Ag⁺ or AgCl because these can be miniaturized. In non-quantitative applications, silver wire coated with AgCl or a simple silver wire as a pseudo reference (quasi-reference electrode, QRE) can be used. However, commercially available aqueous and non-aqueous Ag/Ag⁺ in which the electrode is separated from the analyte solution via a frit are preferable because they are more stable. The majority of electronic spectroelectrochemical experiments are conducted using OTEs in either thin layer (finite) or semi-infinite diffusion regimes.

14.3.2 Thin layer spectroelectrochemistry

A challenge in using bulk electrolysis to generate redox states for *in situ* spectroscopic investigations is to minimize the time for exhaustive electrolysis. The most common

approach uses large working electrode area-to-solution volume ratios to create efficient convective mass transfer. An extensive range of optically transparent thin layer electrode (OTTLE) spectroelectrochemical designs have been used for transmission experiments in electronic spectroelectrochemistry (13–16). Some simple OTTLE designs for electronic spectroscopy for static and flow cells are shown in Figure 14.2.

In the simplest approach, a short path length quartz cuvette is constructed either with a reservoir at the top or side arms into which the counter and reference electrodes can be placed.

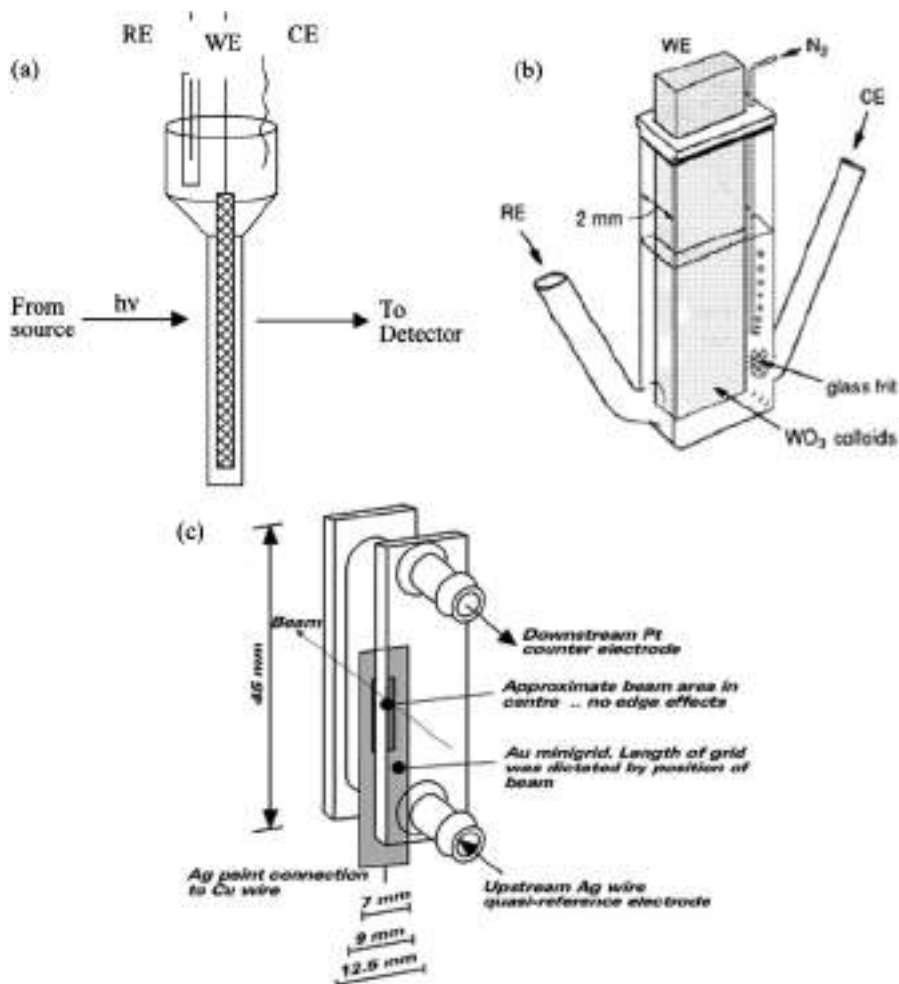


Figure 14.2 OTTLE cells for UV-vis-NIR spectroscopy (a) employing a metal mesh electrode and conventional thin layer cuvette with reservoir for counter and reference electrodes, (b) a thin layer cuvette with side arms for counter and reference electrodes, reproduced with permission of American Chemical Society, (c) a thin layer flow cell. Reprinted with permission from reference (16). Copyright 1989 and 1993, American Chemical Society.

A common arrangement for thin layer geometry is to sandwich the solution between glass and an ITO electrode using a Teflon or Kapton spacer; such cells are now commercially available. For a thin layer arrangement, the cell width through which the excitation beam is directed ranges between 50 and 250 μm and the electrolysis rate is controlled by finite diffusion.

At short electrolysis times when mass transport occurs via linear diffusion, the approximate time, t , required to fully electrolyze the cell is given by

$$t = \delta^2 / \pi D \quad (14.1)$$

where δ is the thin layer thickness and D is the diffusion coefficient of the analyte. Taking a typical diffusion coefficient of $1 \times 10^{-5} \text{ cm}^2 \text{ sec}^{-1}$, equation (14.1) predicts that a 25 μm path length of a typical spectroelectrochemical cell (17) can be exhaustively electrolyzed in ~ 200 msec. This relatively rapid electrolysis time can provide the opportunity for the collection of dynamic information. In a system with slow heterogeneous electron transfer, this time can be significantly extended.

The cuvette is usually constructed so that it sits within a conventional spectrometer cell holder or it can be used with a fiber optic spectrometer. The reference and counter electrodes should be sufficiently small to fit into the reservoir or can be soldered to the non-conducting window of the cell. Elimination of oxygen is most frequently achieved by bubbling an inert gas such as argon or nitrogen through the solution prior to electrolysis and maintaining a blanket of inert gas over the solution during electrolysis.

Experimental set-ups have also included the use of milled polyethylene or Teflon stands into which optical windows are incorporated. These are designed to replace the sample holder in conventional spectrometers and may incorporate temperature control through the flow of cooled N_2 . Modern spectrometers have a range of options for cell holders including temperature control. For applications employing thin layer cells with the optical path normal to the electrode, cells such as those shown in Figure 14.2 work well. Because the cell is so narrow in the thin layer arrangement, there is no bulk solution within the optical path and all of the material in this cell geometry lies within the diffusion layer; electrolysis is very rapid, typically occurring within a few tens of milliseconds. This arrangement is used to provide spectral information on an electrochemical system when the reagents have achieved equilibrium at an applied potential. In flow cells based on the OTTLE cell design, the channel electrode geometry consists of a gold minigrid electrode mounted within a thin layer silica cell as shown in Figure 14.2c with a reference electrode positioned upstream and a counter electrode downstream (16). Solution flows into the cell from a reservoir, is electrolyzed, and the spectrum collected. The low cell volume permits exhaustive electrolysis, eliminating contribution from the parent species.

Poor geometric arrangement of auxiliary and reference electrodes relative to the working electrode results in significant and spatially varying iR drop across the surface of the working electrode. This ohmic polarization is a serious problem in conventional bulk electrolysis, and can be difficult to overcome in the OTTLE arrangement (18). It is not important as long as quantitative time-dependent data are not required, the volume of the cell and concentration of the analyte is sufficiently small so that extensive convective mass transfer is not required and sufficient time is allowed for exhaustive electrolysis during each spectroelectrochemical potential step, as given by equation (14.1). For quantitative

measurements, poor geometric arrangement is alleviated by using a sandwich arrangement in which Pt foils, for example, are positioned at either side of the working electrode to regulate current flow and an internal reference point is set to alleviate poor potential control (19). In qualitative studies, bulk electrolysis is used as a means of electrolyzing the sample exhaustively at one or more discrete potentials. There is usually no requirement for kinetic control at the working electrode and a slow response at the counter-electrode, due to its small relative area, is not as critical a consideration as it is for conventional electrode measurements.

Qualitative electronic spectroelectrochemistry using thin layer cells has found broad application across organic and inorganic chemistry. In such an experiment, a complete UV-vis-NIR spectrum is recorded at a fixed potential. The voltammetry of the species in question is obtained first, followed by the spectroscopic signature of the chemical species formed in each redox step using spectroelectrochemistry. Analysis of such voltammograms can provide clues to the nature of intermediate redox states and lead to quantitative information gathered from the resulting spectroscopy on molecular parameters such as electron delocalization in a new species. Investigation of the extent of electronic communication in multinuclear metal complexes has been studied using spectroelectrochemistry in this way and provides information about mixed valence complexes which are frequently inaccessible synthetically. Figure 14.3a illustrates the spectroelectrochemical response of a 2,3,5,6-tetrakis(2-pyridyl)-pyrazine (tppz)-bridged diruthenium complex $\{(\text{L})\text{ClRuII}\}_2(\mu\text{-tppz})](\text{ClO}_4)_2$, where L = 2,2-dipyridylamine, Figure 14.1b (20). Voltammetry demonstrates that the two metal oxidations in this symmetric complex are separated by 380 mV. Such large peak-to-peak separations exceed what would be expected from electrostatic and statistical effects of oxidizing only one side of the complex on the remaining reduced metal center and is generally indicative of metal–metal communication.

Spectroelectrochemistry provides a convenient avenue to assess whether this conclusion is correct by allowing the isolation and spectroscopic study of the mixed valence state. Oxidation of the first metal center results in the formation of the mixed valence Ru(II)Ru(III) ion reflected in the grow-in of a new optical transition centered at 1700 nm ($\epsilon = 2250 \text{ dm}^3 \text{ mol}^{-1} \text{ cm}^{-1}$) and identified as an intervalence charge transfer transition (IVCT). The optical characteristics of such transitions can be analyzed according to the Hush theory (21) and used to estimate the extent of electronic coupling between two metals across the intervening bridge. The full width at half maximum (FWHM) ($\nu_{1/2}$) of the

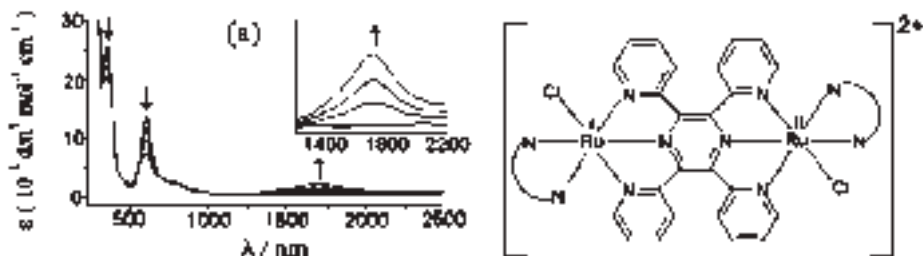


Figure 14.3 UV-vis-NIR spectroelectrochemistry of a mixed valence metal complex, reproduced from reference (20) with permission from The Royal Society of Chemistry.

IVCT band reflects the extent of electronic delocalization between the metal centers and this was measured to be 1390 cm^{-1} . For a compound in which the electron on the reduced metal is localized on that metal, known as a class II system, $\nu_{1/2}$ can be theoretically predicted from the Hush theory and this was estimated to be 3680 cm^{-1} for this complex. The considerably narrower experimental IVCT observed reflects significant delocalization of electron density across the metal centers which is further reflected in the coupling constant, H_{AB} , which was estimated to be 2940 cm^{-1} . On the basis of spectroelectrochemistry, this complex is assigned as a class III or delocalized species in which the mixed valence state is more accurately described as Ru(2.5)-Ru(2.5).

Electronic spectroelectrochemistry can provide insight into the nature of electrochemical intermediates in redox active materials where the identity of each redox step is ambiguous. For example, in metal complexes containing redox active ligands, it may be difficult to distinguish between the metal and ligand-based redox processes by electrochemistry alone.

Figure 14.4 shows the electronic spectroelectrochemistry of a dinuclear ruthenium complex bridged via a hydroquinone linker (22).

Voltammetry of this complex showed three reversible oxidation waves at 0.13, 0.54, and 1.32 V vs. SCE. On the basis of electrochemistry alone, it was difficult to assign the redox responses as being metal or hydroquinone bridge based. UV-vis-NIR spectroelectrochemistry shown in Figure 14.4 confirmed that the first two oxidation steps were hydroquinone bridge based. The metal to ligand charge transfer (MLCT) persisted through the first two oxidation steps and new NIR transitions associated with semiquinone to metal charge transfer and quinone to metal charge transfer were observed. As for the dinuclear complexes described above, the bandwidth of these new transitions revealed different extents of delocalization of electron density across the molecule for each oxidation state.

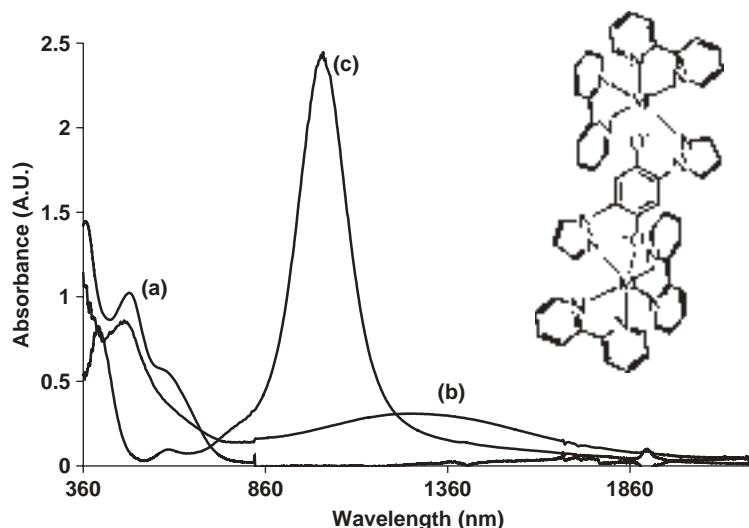


Figure 14.4 Electronic spectroelectrochemistry of $[\text{Ru}(\text{bpy})_2]_2(\text{Pqyr})]^{4+}$ (inset) (a) at open circuit potential and on application of (b) 0.3 V and (c) 0.8 V versus SCE.

Spectroelectrochemistry reveals that the semiquinone state is highly localized whereas there is considerable mixing of quinone and metal states. Such information is impossible to extract from electrochemical measurements alone.

One of the most useful quantitative experiments in thin layer spectroelectrochemistry is the Nernst plot which leads to accurate values for the formal redox potential $E^{\circ'}$ and the number of electrons, n , transferred during an electrochemical reaction. For reversible electrochemistry, the following reaction



exhibits Nernstian behavior. In a thin layer cell, electrolysis equilibrium is achieved rapidly thus ensuring that the concentrations of oxidized and reduced species in solution and at the interface are the same. Then

$$E_{\text{applied}} = E^{\circ'} + \frac{RT}{nF} \ln \frac{[\text{O}]}{[\text{R}]} \quad (14.2)$$

In a Nernst plot, a series of potentials encompassing the peak potentials of the redox process under interrogation are applied sequentially and spectra collected when the system has reached equilibrium at each potential. The resulting ratios of the oxidized and reduced form of the reagent are calculated for each potential using the Beer-Lambert law

$$\frac{[\text{O}]}{[\text{R}]} = \frac{(A_i - A_{\text{R}})/\Delta\varepsilon.L}{(A_{\text{O}} - A_i)/\Delta\varepsilon.L} = \frac{A_i - A_{\text{R}}}{A_{\text{O}} - A_i} \quad (14.3)$$

where A_{O} and A_{R} are the absorbances of the fully oxidized and reduced forms of the analyte and A_i is the absorbance at intermediate applied potentials. $\Delta\varepsilon$ is the difference in extinction coefficient between O and R at the monitoring wavelength and L is the path length. Substituting equation (14.3) into the Nernst equation (14.2), leads to equation (14.4)

$$E_{\text{applied}} = E^{\circ'} + \frac{RT}{nF} \ln \frac{A_i - A_{\text{R}}}{A_{\text{O}} - A_i} \quad (14.4)$$

Plots of E_{applied} versus $\ln(A_i - A_{\text{R}})/(A_{\text{O}} - A_i)$ are linear for reversible systems; $E^{\circ'}$ is determined from the intercept and n from the slope. Because the spectra are measured under equilibrium conditions, iR drop is unimportant to the measurement. This description of $E^{\circ'}$ determination assumes that the two redox forms of the analyte have discrete absorbance spectra which do not overlap. It is also possible to assess $E^{\circ'}$ for more complex systems in which spectra are not well resolved through deconvolution of the contributions to the composite spectra. Spectropotentiostatic measurements of this type have been applied to multi-redox steps in supramolecular systems containing several of the same chromophore units undergoing sequential redox steps. Distributions of redox species can be estimated using iterative algorithms based on the Nernst equation to obtain $E^{\circ'}$ values for each step (23).

Chronoabsorptometry has been used extensively in protein electrochemistry to obtain kinetic information on heterogeneous electron transfer rates for forward and reverse reactions. Heterogeneous electron transfer in such systems is often kinetically slow due to

inaccessibility of the redox center which can be embedded deeply within a protein structure. The small volumes used in thin layer cells makes them amenable to biological studies where only limited amounts of reagent are available. Chronoabsorptometry has provided insight into structure–function relationships in complex biological systems which would not have been possible through electrochemistry alone. Single potential step chronoabsorptometry, asymmetric double potential step chronoabsorptometry, and cyclic potential scan chronoabsorptometry are used in assessing kinetic parameters for heterogeneous electron transfers in complex and sometimes irreversible systems (24).

Indirect electrochemical methods are used to investigate a site which may be embedded in a macromolecular structure, making direct heterogeneous electron transfer at the electrode impossible. Smaller redox active species, electron transfer mediators, are then employed which diffuse to the redox active site in the biomolecule, undergo a homogeneous electron transfer, and then diffuse to the electrodes to undergo oxidation or reduction. These mediators are ideally spectroscopically silent in the region of interest and possess suitable thermodynamic characteristics to undergo facile electron transfer with the redox active site, without participating in any interfering interactions with the target molecule (25). This method has found use in protein electrochemistry. Figure 14.5 illustrates an example of a Nernst plot taken from absorbance data for the mediated spectroelectrochemistry of recombinant ferric soybean leghemoglobin (26) a (rLb), an oxygen binding heme protein, in its free form and when bound to nicotinate (rLb-N). The objective of the study was to examine the influence of alterations in axial ligand structure on the redox properties of the heme. Replacement of the water in (rLb) with nicotinamide, resulted in a cathodic shift of 95 mV in the heme reduction potential.

Detailed spectroelectrochemical studies on myoglobin and hemoglobin were undertaken using the same potentiopspectrometric methodology but with $\text{Ru}(\text{NH}_3)_6\text{Cl}_2$ as the electron transfer mediator (27). The Nernst plots for these metalloproteins were shown to be sensitive indicators of alterations to the heme environment where sensitivity to aerobic and anaerobic conditions has provided important insights into heme binding of O_2 (28).

14.3.3 Spectroelectrochemistry: semi-infinite linear diffusion

Exhaustive electrolysis can be achieved within a short period of time in spectroelectrochemistry under semi-infinite diffusion conditions, even in the absence of convective mass transport. In these cells, the solution layer is thicker than that in the OTTLE cell and on application of potential the diffusion layer does not extend over the entire optical path.

For quantitative spectroelectrochemistry, chronocoulometric experiments are performed in semi-infinite diffusion spectroelectrochemical cells such as that shown in Figure 14.6 (29). An adjustable cell capable of both finite and semi-infinite diffusion conditions has also been reported which permits both thin layer and semi-infinite diffusion conditions to be selected (30). Typically, transparent film electrodes such as ITO are employed as the working electrode to avoid complicated diffusion parameters associated with a minigrid. Application of a potential step leads to a time-dependent response which is reflected in absorption changes. Assuming that the detector is set to monitor absorbance at a region where only the product, P , of the electrolysis absorbs, the absorbance change dA across a

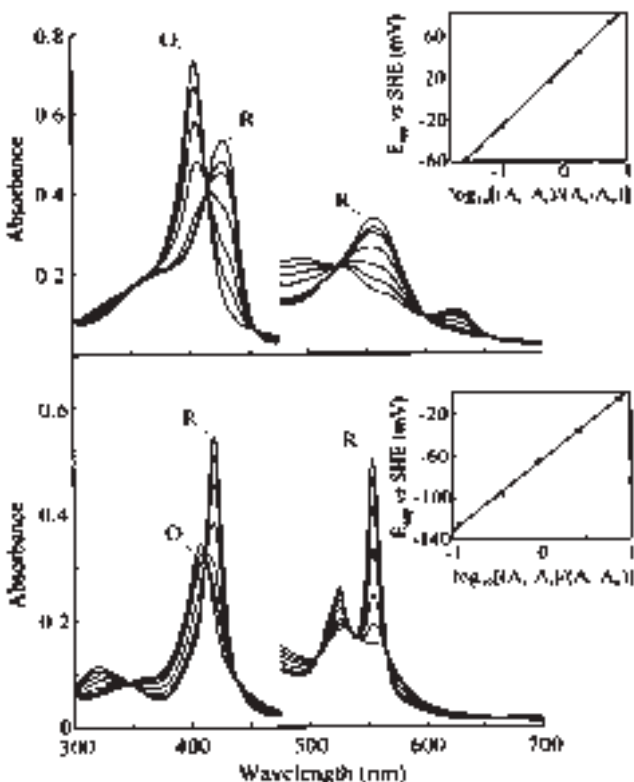


Figure 14.5 Thin layer spectroelectrochemical data for rLb (top) and rLb-N (bottom) at various applied potentials, E_{app} (mV vs. SHE). Fully oxidized (O) and fully reduced (R) spectra for each derivative are indicated. The insets show fits of the absorbance data at 403.5 nm (for rLb) and 419.5 (for rLb-N) to the Nernst equation. Absorbance values in the visible region (475–700 nm) have been multiplied by a factor of five. Conditions: sodium phosphate, pH 5.40, 25.0 °C, $\mu = 0.10$ M for rLb; sodium phosphate, pH 5.42, 10 mM nicotinic acid, 25.0 °C, $\mu = 0.10$ M for rLb-N. Reproduced from reference (26) with permission of Blackwell Publishing.

cross sectional area of thickness dx which is uniformly irradiated is $dA = \varepsilon_p c(x, t) dx$, where c_p is the concentration of P and ε_p its extinction coefficient, the integrated total absorbance A is

$$A = \varepsilon_p \int_0^\infty c_p(x, t) dx \quad (14.5)$$

Assuming the product P is stable, this integral represents the total concentration of P per unit area, which is equal to Q/nFA . Q , the charge passed during the electrolysis, is described by the integrated Cottrell or Anson equation. Therefore

$$A = \frac{2\varepsilon_p C_0^* D_0^{1/2} t^{1/2}}{\pi^{1/2}} \quad (14.6)$$

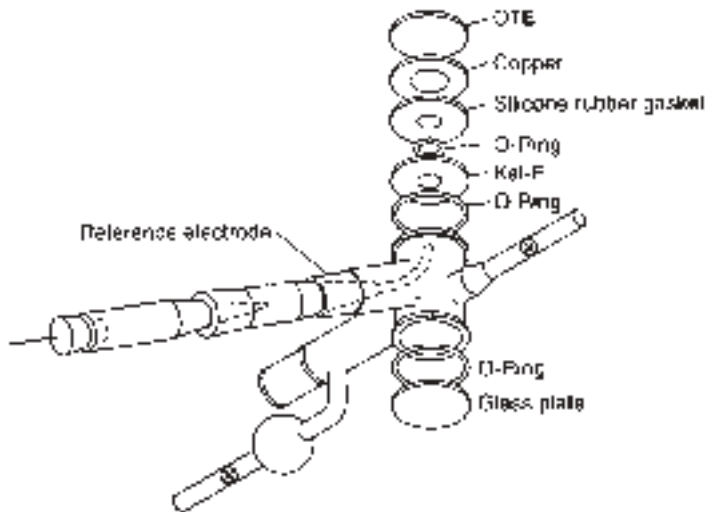


Figure 14.6 Sandwich cell for semi-infinite diffusional spectroelectrochemistry. Reproduced from reference (29) with permission of Blackwell Publishing.

where C_0^* is the bulk concentration of the precursor species and D_0 is the diffusion coefficient of this reagent. Plots of absorbance versus $t^{1/2}$ should be linear and once the extinction coefficient is known, can be used to determine D_0 . In practice, this means that in transmittance mode, with the incident light normal to the electrode surface, the absorbance contains contributions from reagent within and outside of the diffusion layer.

Spectroelectrochemical cells employing OTTE and semi-infinite diffusion dimensions work well as long as the material under investigation and its redox product have sufficient absorption cross sections to give reasonable a signal-to-noise ratio. The ideal absorbance working range is 0.3–1 AU because this range is least susceptible to interference from stray light and other noise.

14.3.4 Long optical pathway thin layer cells (LOPTLC)

For materials with low molar absorptivities, the use of thin layer cells is not practical because the concentrations required to achieve measurable absorption spectra using the thin cell regime may be prohibitive. Long optical path thin layer cells (LOPTLC) are useful in these circumstances (31, 32). In such a cell, the optical path runs parallel to the working electrode as demonstrated in Figure 14.1b. The advantages of this method are that the electrode, which is not in the optical path, can be opaque and lower concentrations of reagents can be used because of the increased sensitivity arising from the long optical path. Disadvantages include the electrolysis time which is often compromised in such cells. Additionally, because the incident light is not directed through the electrode, equations (14.5) and (14.3) no longer apply, so such cells are not suitable for dynamic studies. As described, the absorbance spectrum reflects the integral of the absorption of all species along the light

path. As the light is directed through a path in front of the working electrode and assuming the cell is symmetric along its length, this arrangement monitors the same set distance from the electrode, usually in the diffuse layer. This means that if the electrochemical reaction is anything other than a purely diffusive process, the parallel cell arrangement can lead to different spectral information than observed for the conventional optical path. This is particularly true for semi-infinite diffusion regimes where the absorbance spectrum from the conventional arrangement will simultaneously contain contributions from bulk, diffuse layer, and interface.

For example, a bidirectional thin layer cell was used to compare visible spectral data simultaneously collected for incident light normal to and parallel with the working electrode (Figure 14.7) (33) for a spectroelectrochemical study of the electropolymerization of 4,4'-bis(methylthio)-2,2'-bithiophene in acetonitrile. Significant spectral discrepancies were observed between the two optical arrangements as shown in Figure 14.7(ii). This was

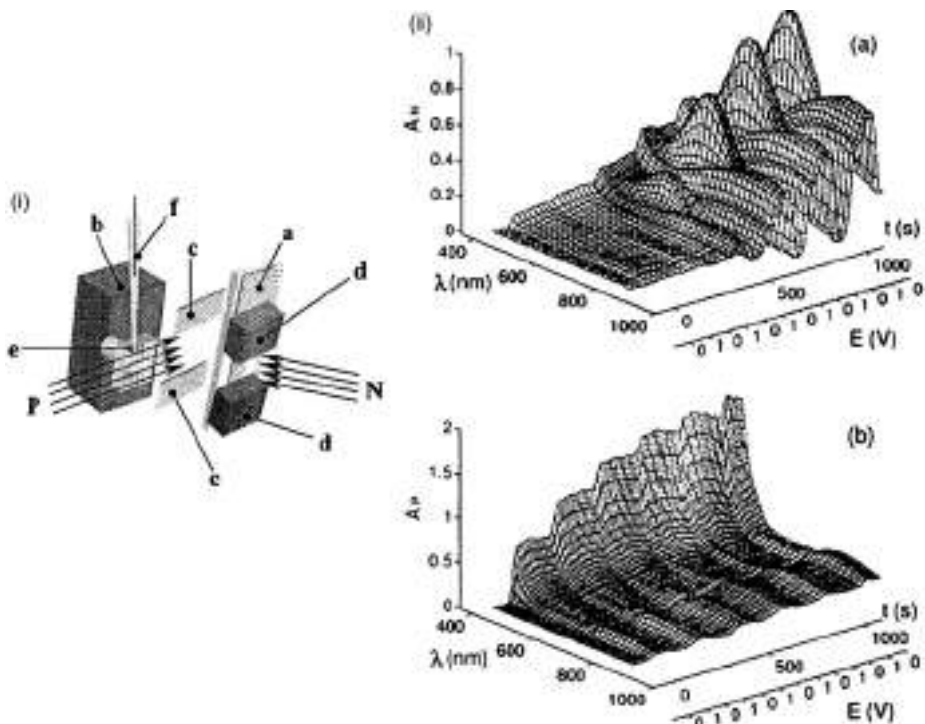


Figure 14.7 (i) Schematic diagrams (3D, front and side views) of a bidirectional thin layer spectroelectrochemical cell. (a) Gold-sputtered working electrode; (b) epoxy resin piece; (c) spacers; (d) epoxy resin brackets; (e) circular window, diameter 3 mm; (f) reference electrode; (g) counter electrode. (N) Normal and (P) parallel-beam incident light paths. (ii) 3D plot of absorbance, potential time and wavelength obtained during electropolymerization of 0.005 mol L^{-1} of 4,4'-bis(methylthio)-2,2'-bithiophene in acetonitrile with TBAPF_6 0.1 M as the supporting electrolyte. Display of six scans at $v = 0.01 \text{ V sec}^{-1}$; $\omega = 220 \mu\text{m}$; and $l = 3 \text{ mm}$. (a) Normal-beam signal, (b) parallel-beam signal. Reprinted with permission from reference (33). Copyright 2001, American Chemical Society.

attributed to a complex electrochemical process that involved interfacial adsorption of the polymer in addition to diffusion-controlled electrolysis. A spectral response which included both the adsorption and diffusive processes was obtained in the normal optical arrangement, whereas the spectra from a parallel beam arrangement contained contributions from the diffuse species only. This example serves to highlight that caution must be exercised in the interpretation of data from parallel beam arrangements in complex electrochemical processes.

14.3.5 Reflectance spectroscopy

The majority of electronic spectroelectrochemical studies are based on transmission experiments interrogating solution phase analytes. Reflectance spectroscopy is particularly important in studies of thin films, solid deposits, or self-assembled mono- and multilayers at reflecting surfaces. The two most commonly applied techniques of reflectance spectroscopy are external reflectance and attenuated total reflectance (ATR).

14.3.5.1 External reflectance spectroscopy

In external differential reflectance spectroscopy, light incident on an opaque, reflective interface may be partially reflected and partly absorbed. The reflected light is detected and this contains the intensity of the incident beam minus components of the light absorbed by material at the interface. In UV-vis reflectance spectroscopy, the intensity of the reflected light is divided by the intensity of the incident beam according to equation (14.6). The reflectance is typically normalized at each potential against a blank electrode or thin layer at the electrode containing only electrolyte and this normalized differential reflectance, $\Delta R/R$, is plotted against wavelength. Both specular and diffuse reflectance occur concurrently and both have been used in UV-vis reflectance spectroelectrochemistry. Specular reflectance requires mirror like surfaces and the reflectance is dependent on the angle of the incident light; this phenomena is well understood and described by the Fresnel equations. Specularly reflected light is polarized and highly anisotropic (i.e., specularly reflected light is emitted only over a limited range of angles with respect to the incident beam). Variable angle specular reflectance spectroscopy provides useful information about film homogeneity and thickness (2). Diffuse reflectance occurs principally from rough or granular surfaces and is isotropic. Specular and diffuse reflectance are experimentally distinguished through control of the angle of detection (or incident beam). The majority of reflectance reports for electronic spectroelectrochemistry study specular reflectance using highly polished metal electrodes as the interface. Highly polished carbon is also used.

Reflectance accessories are available on modern UV-vis spectrometers and many are available which allow for variation of the incident angle for separation of specular reflectance and diffuse reflectance. Reflectance UV-vis has found application in spectroelectrochemistry of thin films, polymer modified electrodes, and surface adsorbates such as self-assembled mono- and multilayers. A number of cell designs have been applied and these are generally designed to fit into commercial reflectance attachments. A thin film reflectance cell is shown in Figure 14.8 (34). The electrode was fabricated by anodization of a thin layer

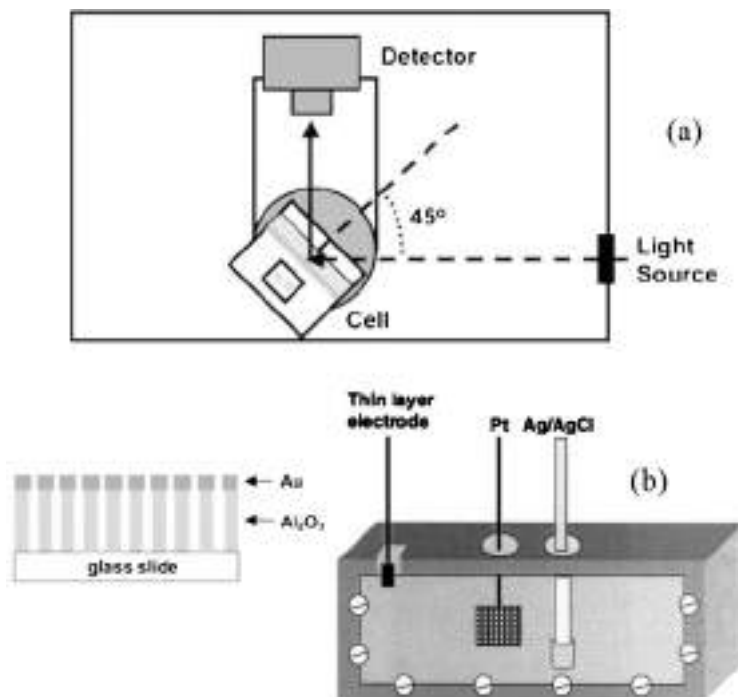


Figure 14.8 Schematic of spectroelectrochemical experiment (a) and employing a thin layer optically reflective thin layer cell. (b) Side profile of the optically reflective thin layer electrode. Reproduced from reference (34) with permission from Wiley.

of aluminum sputtered onto a plain glass microscope slide to create a 750 nm thick transparent porous alumina film. A thin film of gold was then sputtered on top of the alumina film. The reflective gold layer retained the pores of sub-optical wavelength dimensions and filled with analyte solution; despite this, the surface remained specularly reflective. This cell was used in a study which combined specular reflectance spectroscopy and chronoamperometry to determine the onset of water reduction from shifts in the interference fringes of the specularly reflected light from the electrode surface.

A thin layer cell for specular reflectance measurements with temperature control is shown in Figure 14.9 (35, 36), where the cell is surrounded by a hollow brass heat exchanger. The temperature of the cell was controlled using an external heating:cooling circulator which pumped low viscosity silicone oil through the hollow brass heat exchanger surrounding a three-electrode cell. Polished Pt or Au foil soldered on a brass post served as the working electrode and a circular 0.5 mm Ag wire, placed 0.5 mm outside the perimeter of the working electrode, was used as pseudo-reference electrode. A platinum wire held beyond the perimeter of the working electrode was used as the auxiliary electrode. This cell was designed for use in a commercial reflectance attachment for both electronic and IR instruments.

External reflectance spectroscopy has been used in the study of proton coupled electron transfers at a dinuclear ruthenium complex $[(\text{phen})_2\text{Ru}(\text{tatpp})\text{Ru}-(\text{phen})_2]^{4+}$ (Figure 14.10) (37).

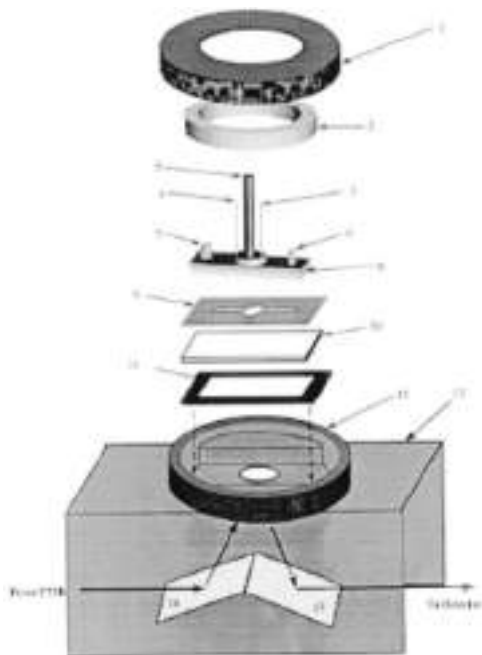


Figure 14.9 Thin layer cell for temperature controlled specular reflectance spectroelectrochemistry. (1) Tightening brass cap (threaded inside). (2) Teflon or brass washer required to tighten the cell. (3) Working electrode (a brass rod with platinum foil soldered to the base). (4) Auxiliary electrode: platinum wire with the tip made flush to the Teflon base of the cell. (5) Pseudo-reference electrode: silver wire, also made flush to the Teflon. (6, 7) Luer lock type injection ports. (8) Cell body, top part aluminum, lower part Teflon. (9) Teflon spacer which determines the path length of the cell. (10) Calcium fluoride window. (11) Rubber gasket. (12) Hollow brass cell body. (13) Two mirror reflectance accessory (Nicolet FT-30). (14, 15) Mirrors. Reproduced from reference (35) with permission from Elsevier.

Both difference and differential reflectance spectroelectrochemistry were used in this study. In the difference mode, the reflectance (R) data were acquired during square-wave modulation with the potential limits of the square-function selected to encompass the redox wave being probed. Conventional $\Delta R/R$ versus wavelength spectra result. Differential reflectance–potential profiles show the spectral changes that occur for an electrochemical species as a function of a small amplitude potential perturbation. The monitoring wavelength, which is associated with an absorbance of the target analyte, is held constant. Lock-in detection of the changes in the reflected intensity of this wavelength off the working electrode surface as a function of AC potential (11 Hz) modulation was monitored, after demodulation, as a function of the DC electrode potential. The optical signal generated by such AC modulation is expressed as

$$\frac{1}{R} \frac{\delta R}{\delta E} = -\frac{1}{R} \frac{\delta A}{\delta c_{int}} \left| \frac{\delta c_{int}}{\delta E} + \frac{1}{R} \frac{\delta R}{\delta q} \frac{\delta q}{\delta E} \right|_{AuER} \quad (14.7)$$

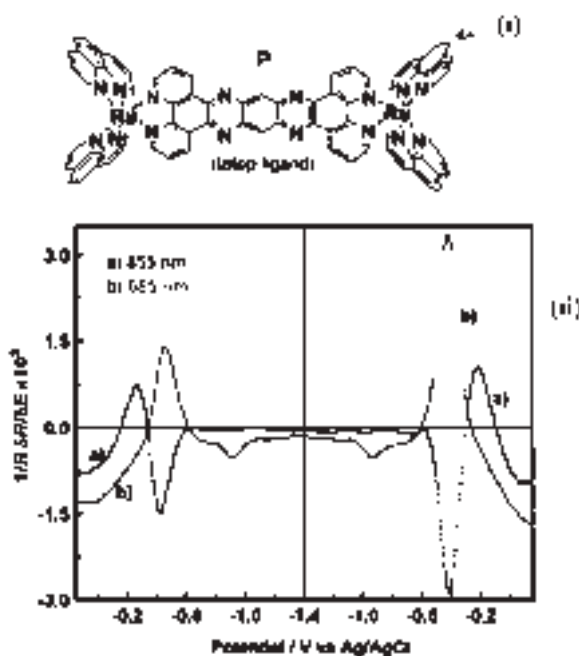


Figure 14.10 (i) Structure of $[(\text{phen})_2\text{Ru}(\text{tatpp})\text{Ru}-(\text{phen})_2]^{4+}$ and (ii) in-phase differential reflectance versus potential curves for 3.5×10^{-5} M P at pH 11 during a cyclic linear potential scan at 2 mVs^{-1} on a polycrystalline gold disk electrode. Two wavelengths were used to monitor the singly and doubly reduced products from P: (a) 855 nm and (b) 685 nm. The switch potential, -1.35 V , was used to separate the plot in two halves. Reproduced from reference (37) with permission from Wiley.

where E is the electrode potential, A is the optical absorbance, R the reflectance, and δc_{int} is the modulation of the interfacial concentration. An example of an optical response using this method is shown in Figure 14.10 for the study of $[(\text{phen})_2\text{Ru}(\text{tatpp})\text{Ru}-(\text{phen})_2]^{4+}$. These electroreflectance studies were used to characterize the interfacial reaction occurring with AC voltammetry and led to the identification of the redox products and their pH dependence to generate a scheme of squares for the protonation states of the various redox states of $[(\text{phen})_2\text{Ru}(\text{tatpp})\text{Ru}-(\text{phen})_2]^{4+}$.

The increasing availability of fiber optic probes and microscope objectives on conventional spectroscopic instrumentation have improved the sensitivity and versatility of reflectance spectroelectrochemical measurements. These features have reduced the need for special spectroelectrochemical cells to fit into reflectance accessories and in the case of fiber optic instruments, can reduce the costs of spectroelectrochemical measurements considerably.

Fiber optic spectrometers with reflectance probes build an additional degree of flexibility into reflectance spectroelectrochemical measurements. Fiber optic reflectance probes are typically made of multiple fiber optics which direct the light from the source to the sample surrounding one or more fiber optics which collect the reflected light and direct it to the detector. These fibers are usually combined within a single cable which is bifurcated

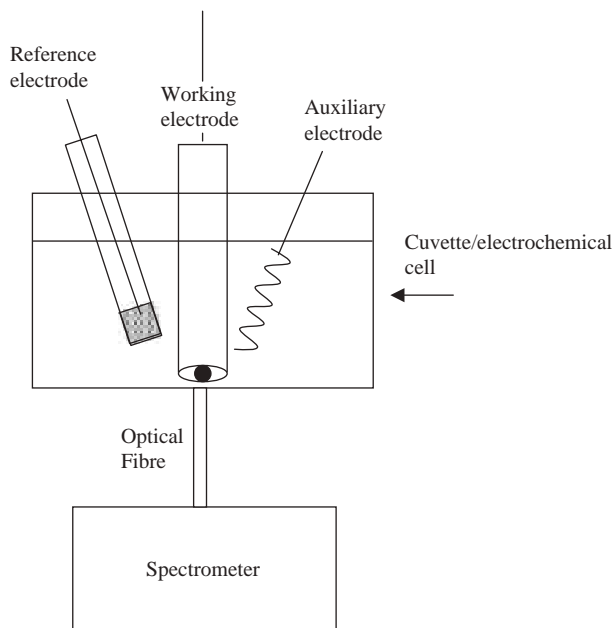


Figure 14.11 Fiber optic spectroelectrochemical arrangement for electronic spectroscopy. A conventional electrochemical cell is combined with a fiber optic spectrometer in which the optical fiber is directed in front of the working electrode at the bottom of the cell.

at one end to connect the respective detector and illumination fibers separately to the light source and detector. A reflectance spectroelectrochemical configuration with a fiber optic probe is shown in Figure 14.11. This configuration is simple and highly versatile for both semi-infinite and thin layer configurations (30). A highly polished working electrode is placed very close to the optical window to generate thin film conditions. The fiber optic probe is oriented directly in front of the electrode where it directs the monitoring light normal to the electrode and collects the reflected light at the same angle for specular reflectance.

The growing use of microscopy in spectroscopic methods has had a significant impact on both the versatility of reflectance spectroscopy and sensitivity as a result of the increased capacity to focus onto the electrode solution interface. An example of a spectroelectrochemical cell for diffuse reflectance spectroscopy in which an optical microscope fiber is optically coupled to a spectrometer is shown in Figure 14.12. The optical geometry imposed by the use of the microscope means that the angle between the incident and detected beams is zero and this, combined with the use of crossed polarizers, eliminates specular reflectance making it possible to use the Kubelka–Munk function for quantifying optical measurements. This arrangement was used in the study of electrochromic responses of solid silver octacyanomolybdate (IV/V) deposited on a graphite electrode in contact with a silver nitrate solution (38). In this arrangement, a microscope objective was used to focus the incident beam onto the electrode. Because the film was

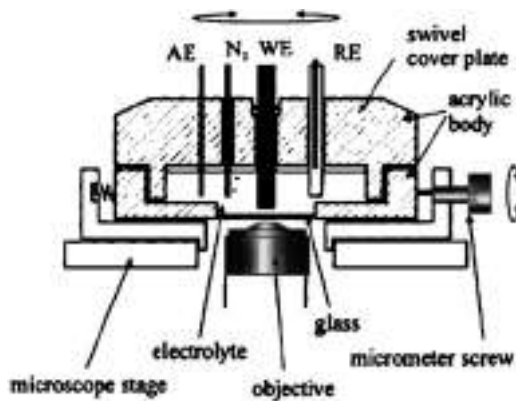


Figure 14.12 Spectroelectrochemical cell for UV-vis reflectance studies using a microscope. Reproduced from reference (38) with kind permission of Springer Science and Business Media.

immobilized on the electrode, small volumes were not necessary in contrast to the OTTLE experiment.

14.3.5.2 Internal reflectance spectroscopy

The drawback in conventional absorbance and reflectance measurements is that their sensitivity relies strongly on the extinction coefficient of the analyte. If this is low then only thick films or highly concentrated solutions can be detected at an electrode surface using these methods. For increased sensitivity at a surface layer, external reflectance and UV-vis ATR spectroelectrochemistry can be used. This latter method, for thin films at least, can provide spectra which are very similar to transmission spectra. In ATR, a beam of light incident on a surface is bent normal from the surface as it passes from a higher to lower refractive index material; the beam is said to undergo internal reflection. A high refractive index crystal and a high angle of incidence must be used. Germanium is a commonly used ATR material. In ATR, the total reflection of a light beam at a transparent electrode/solution interface is obtained when the incident light is directed through the electrode toward the solution at an incident angle that exceeds the critical angle θ_c according to

$$\theta_c = \arcsin\left(\frac{n_1}{n_2}\right) \quad (14.8)$$

where n_1 and n_2 are refractive indices of the transmitting and incident media respectively. This propagates an evanescent wave perpendicular to the internally reflected beam through the electrolyte with a penetration depth d :

$$d = \frac{\lambda}{4\pi(n_1^2 \sin^2 \theta - n_1^2)^{1/2}} \quad (14.9)$$

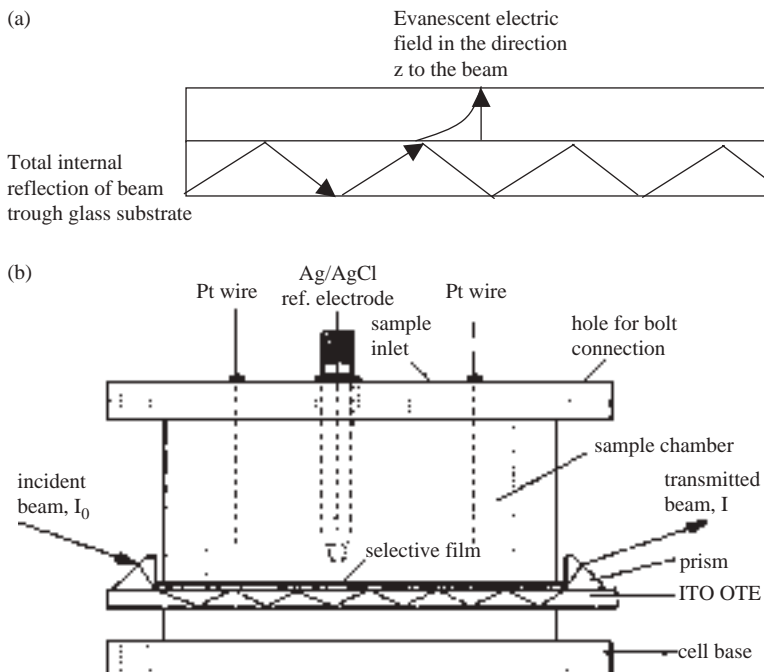


Figure 14.13 (a) Schematic showing light incident on a substrate undergoing total internal reflection and the evanescent field of the totally reflected light which propagates through the adjacent media. (b) A spectroelectrochemical cell for attenuated total reflectance spectroelectrochemical cell. Reprinted with permission from reference (39). Copyright 1997, American Chemical Society.

where θ is angle of incidence within the substrate, Figure 14.13a. This method offers significant sensitivity in the interfacial region where the evanescent field propagates, particularly for cells with multiple reflectances. The penetration depth of the evanescent wave depends on the excitation wavelength but is typically of the order of 500–1000 Å this means that it is strictly limited to interrogation of the interfacial region.

Figure 14.13b shows a spectroelectrochemical cell for ATR which illustrates the concept (39). The spectroelectrochemical cell was an optically transparent electrode made of ITO deposited on glass. The incident light was coupled into the ITO glass slide of the spectroelectrochemical cell with a coupling prism and a high viscosity refractive index standard fluid spanned the prism–ITO glass gap. The light propagated by internal reflection through the slide was collected into a prism at the detector end of the slide and directed by fiber optic into the detector. This arrangement was investigated as a charge selective sensor by immobilizing a thin film of a silica sol-gel poly(dimethyldiallyl ammonium chloride) composite over the ATR element.

A consideration in spectroelectrochemical cell design in ATR is that the working electrode must be transparent. Typically metal or metal oxide deposited thin films on the germanium reflection element and are used as the working electrode. As described in Section 14.3.1,

poor conductance can present a problem for thin film electrodes. Nonetheless, this method can provide significant sensitivity and selectivity for optical changes localized at the electrode solution interface and has found application in studies of conducting polymer films and self-assembled monolayers (40, 41). In a related approach, spectroelectrochemical responses in less than 1% of an equivalent monolayer at adsorbed films of Prussian blue on an ITO electroactive integrated optical waveguide (EA-IOW) (42) have been reported. An advantage of this method lies in its immunity to perturbation of the surrounding solution due to the low penetration depth of the radiation into the solution phase making it amenable to spectroelectrochemical measurements in moving media (43). Internal reflection methods have been exploited extensively in IR studies, as discussed in Section 14.6.1, where solvent interference is particularly important.

14.4 LUMINESCENCE SPECTROELECTROCHEMISTRY

14.4.1 Steady-state luminescence spectroelectrochemistry

Luminescence spectroscopy (fluorescence or phosphorescence) is one of the relatively under explored areas of spectroelectrochemistry. This is surprising given the high sensitivity and selectivity of this technique, but may be due to the experimental difficulties in achieving 90° orientation between excitation and detector. Reports employing this spectroelectrochemical method have been increasing.

In a conventional luminescence experiment, the detector and excitation source must be maintained at a 90° angle to one another in order to limit the amount of excitation light reaching the detector. To achieve this requirement, a square clear sided cuvette is needed as shown in Figure 14.14a. The use of such a square cuvette as a cell for spectroelectrochemistry is not easily adaptable to the thin layer or semi-diffusion cell arrangements conventionally used in UV-vis spectroscopy. Two approaches have been taken to circumvent this problem. First, a thin layer cell comparable to that used in an OTTLE experiment, where the cell is positioned at a 45° angle relative to the excitation source and detector, can be used as shown in Figure 14.14b.

Such an arrangement is analogous to the OTTLE experiment described for electronic spectroscopy. The working electrode is frequently a wire mesh such as gold, platinum, or a

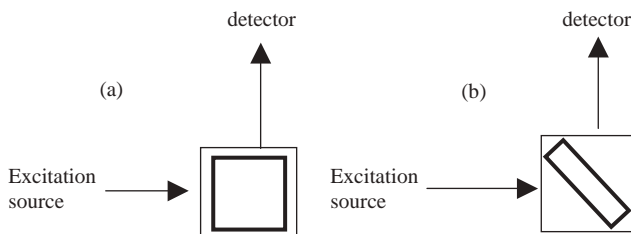


Figure 14.14 Orientation of cuvette in (a) conventional luminescence spectrometer. (b) Spectroelectrochemical experiment employing a thin cell.

rhodium–platinum alloy. This and the 45° angle of the cuvette, particularly if orientation of the cuvette is not exact, can lead to significant spectral scattering of the excitation source resulting in serious interference from stray light in the resulting emission spectroscopy. In addition, small alterations to the angle of the cuvette can lead to lack of reproducibility in the luminescence signal between experiments. This can be overcome by careful placement of the cell in the spectrofluorimeter. A simple solution is to use a PTFE insert in the instrument cuvette holder which is milled to hold the spectroelectrochemical cell securely and reproducibly at a 45° angle. This is a simple method which works well.

There are a number of options for using a fluorescence cell in the conventional 90° orientation. One 90° cell incorporated a chair shaped gold coated Teflon electrode milled to fit into a conventional fluorescence cuvette. The large Teflon insert provided was also milled to support the reference and auxiliary electrodes at the bottom of the cell. The size of the insert significantly reduced the volume of the cell permitting use of 90° excitation and detection (44). Another 90° oriented cell is shown in Figure 14.15 (45) where a quartz

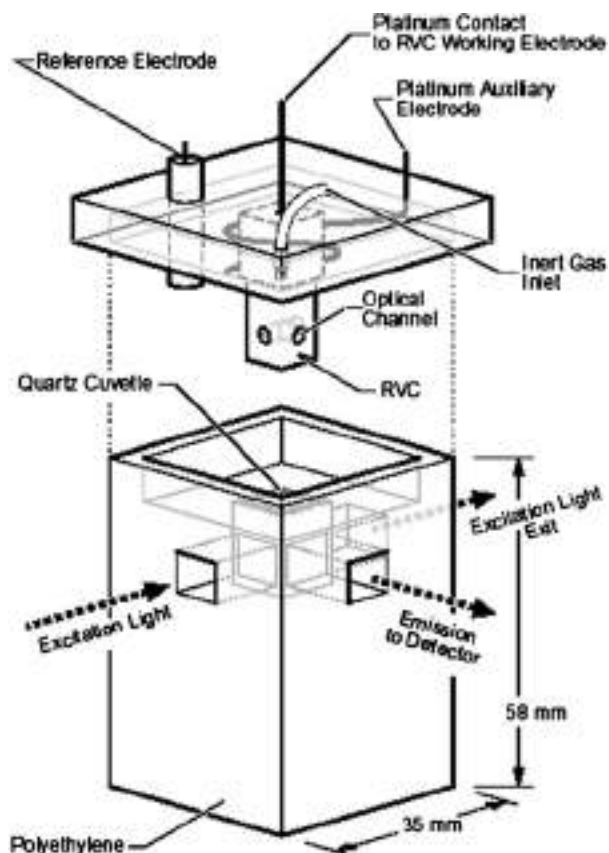


Figure 14.15 Low volume spectroelectrochemical cell for luminescence, reprinted from reference (45b) with kind permission of Prof. J. R. Kirchhoff and Bioanalytical Services Incorporated.

optical cell is housed in the lower part of a milled PTFE block which fits snugly into the spectrometer cell holder like a conventional cell.

The upper part of the arrangement houses the auxiliary and reference electrodes. The shaped optical channels were drilled into the lower portion of the cell configuration to permit a 90° angle between excitation and emission pathways and a long optical path for better sensitivity. A reticulated carbon electrode was used as the working electrode. This use of a non-metal electrode may be advantageous in avoiding luminescence quenching which can occur at a metal surface. The large volume of this cell led to exhaustive electrolysis times of up to 25 min depending on the arrangement used.

Nernst plots analogous to those in UV-vis spectroelectrochemistry are achievable using luminescence spectroelectrochemistry in which the concentrations of oxidized and reduced species are obtained by using the luminescence quantum yields of the analyte according to

$$\frac{[\text{Ox}]}{[\text{Red}]} = \frac{(I_{\text{red}} - I)/\phi L}{(I - I_{\text{ox}})/\phi L} = \frac{I_{\text{red}} - I}{I - I_{\text{ox}}} \quad (14.10)$$

$$E_{\text{applied}} = E^{\circ'} + \frac{RT}{nF} \ln \left(\frac{I_{\text{red}} - I}{I - I_{\text{ox}}} \right) \quad (14.11)$$

where I_{red} , I_{ox} , and I are the luminescence intensities of the analyte at potentials where it is fully reduced, fully oxidized, and at intermediate potentials respectively. ϕ is the luminescence quantum yield and L is the path length. Substitution of equation (14.10) to the Nernst equation leads to equation (14.11) indicating that a plot of E_{applied} versus $\ln(I_{\text{red}} - I)/(I - I_{\text{ox}})$ will yield $E^{\circ'}$ from the intercept and n from the slope. Such a Nernst plot was constructed for rhodamine 6G at a 4,4-bipyridine modified gold electrode using a 90° thin layer cell. Good agreement was found between the spectroelectrochemically derived value for the formal potential of the rhodamine 6G (-0.787 V) and that obtained from cyclic voltammetry (-0.791 V) (46).

In the simplest spectroscopic description of the Nernst equation, the two redox states should not emit in the same spectral region. Since it is unusual for a single species to emit in two different oxidation states, this requirement is usually fulfilled in emission measurements and is a distinct advantage over absorbance measurements. In many instances, however, the oxidized or reduced form of the analyte can quench the luminescent precursor leading to lower intensity values. This can lead to serious errors in the apparent concentrations of the oxidized and reduced species and therefore the values derived from the Nernst plots.

The strength of spectroelectrochemistry lies in its ability to achieve states which are frequently inaccessible synthetically. An example of such a species is $[\text{Re}(\text{dmpe})_3]^+$, where dmpe is 1,2-bis(dimethylphosphino) ethane (47). This d⁶ Re(I) complex is colorless and non-luminescent. As Figure 14.16 shows, oxidation resulted in the formation of the d⁵ Re(II) complex which exhibited an absorbance at 530 nm and an intense emission at 593 nm; the luminescence quantum yield exceeded that of the well-known $[\text{Ru}(\text{bpy})_3]^{2+}$ complex.

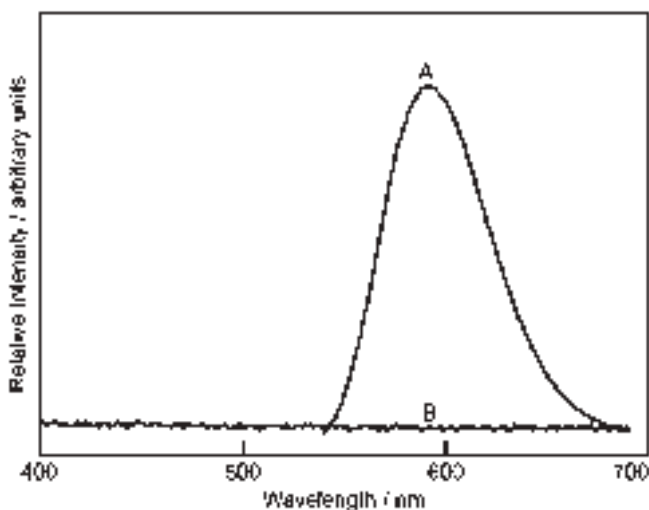


Figure 14.16 Uncorrected emission spectra of 0.14 mM. (A) $[\text{Re}(\text{dmpe})_3]^{2+}$, $\lambda_{\text{ex}} = 530 \text{ nm}$; and (B) $[\text{Re}(\text{dmpe})_3]^+$, $\lambda_{\text{ex}} = 220 \text{ nm}$ in acetonitrile with 0.1 M $(n\text{-Bu})_4\text{NPF}_6$ in the luminescence spectroelectrochemical cell. Reprinted with permission from reference (47). Copyright 1994, American Chemical Society.

14.4.2 Time-resolved luminescence spectroelectrochemistry

Time-resolved luminescence spectroelectrochemistry (TRLS) is less common than but complementary to luminescence spectroelectrochemistry. TRLS can be used to monitor the lifetime of a luminescent species, provided it is sufficiently long-lived. TRLS may be useful in studying the photophysics of an electroactive species to understand its temporal behavior under application of potential and can be used to provide a unique perspective on the electrochemical interface.

The two most common methods for studying luminescent lifetimes are time correlated single photon counting and flash photolysis. Single photon counting has not been used with spectroelectrochemical studies due to instrumental difficulties associated with the need for complete light tightness. Laser flash photolysis methods have been used in spectroelectrochemical studies (48, 49). A typical instrumental set-up for nanosecond TRLS is shown in Figure 14.17.

A pulsed light source (e.g., a neodymium YAG laser) is set up at a right angle to the detector which may be a fast photodiode or more complex detection device such as an intensified charge coupled device (iCCD) or diode array. The iCCD or diode array offers significant advantages because it allows a complete emission spectrum (spectral range for a typical iCCD of about 250 nm) to be obtained within times as short as 10 nsec, but also permits collection of a steady-state spectrum. This means that both static and dynamic fluorescence studies can be carried out simultaneously using a single instrument. The gate width (i.e., the exposure time of the iCCD) for time-resolved measurements, controlled using a delay generator, is never more than 5% of the excited state lifetime. The step size

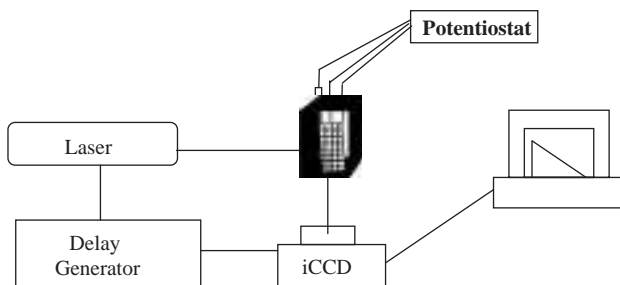


Figure 14.17 Schematic of instrumental layout for nanosecond flash photolysis for collection of luminescence lifetime.

(i.e., the time between the acquisition of discrete spectra) is typically between 2 and 5% of the excited state half-life. For steady-state spectra, the gate width is set to at least six times the lifetime and no temporal steps are required.

An example which highlights both the steady-state and time-resolved aspects of luminescence spectroelectrochemistry is shown in Figure 14.18. This study reported a dinuclear ruthenium (II) complex bridged by dianionic bridge shown in the inset of the figure (49).

In this system the metals are bound through N,N coordination to the pyridine and triazole and O,N coordination to the triazole and phenolate. In its native state the dinuclear compound is weakly emissive with a lifetime of 50 nsec. The mixed valence complex was prepared *in situ* electrochemically through oxidation of the O,N bound metal. Electronic spectroelectrochemistry suggested the metals were weakly coupled. Oxidation of the first metal lead to strong luminescence from the complex which was reflected in its increased lifetime of 130 nsec. This luminescence is reversibly switched on at 0.3 V and reversibly switched off by application of 1.3 or 0 V. This study was carried out using a thin layer OTTLE cell which was held using an insert at a 45° angle to the detector and light source. Time-resolved spectroscopy was carried out using the methodology described in Figure 14.17. The use of an intensified iCCD meant that both the full luminescence spectrum and the lifetime of the complex could be determined with one instrument operated in different time domains (50).

14.5 VIBRATIONAL SPECTROELECTROCHEMISTRY

Vibrational spectroelectrochemistry has now almost superseded UV-vis spectroelectrochemistry as the most commonly reported method. Because vibrational spectroscopy can give structural information, it has found extensive application in the study of the double layer, redox products in solution, and surface adsorbed species. The two most prevalent vibrational spectroscopies applied to spectroelectrochemistry are Infrared and Raman. Though the underlying mechanism and theory of each technique is fundamentally different, both methods give detailed vibrational information which may be used in spectroelectrochemistry to determine and monitor structural changes accompanying electrochemical

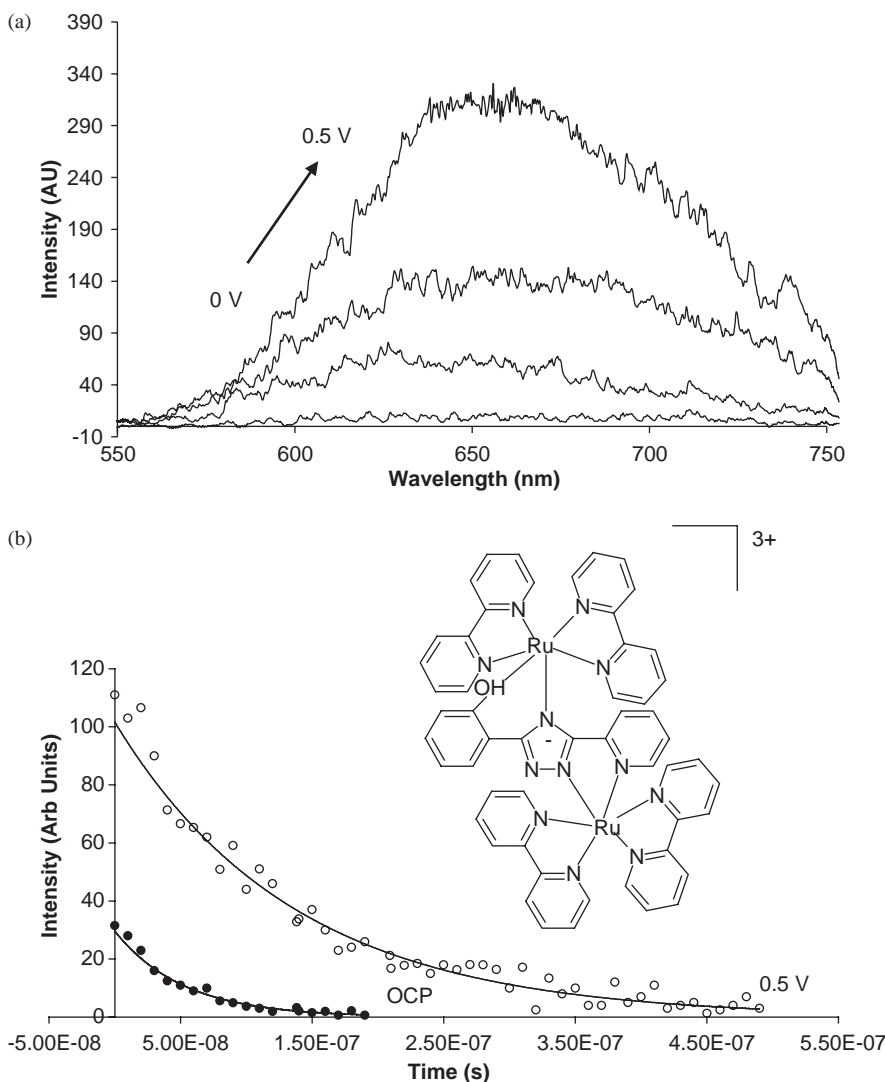


Figure 14.18 (a) Luminescence spectroelectrochemistry and (b) time resolved luminescence spectroelectrochemistry of mixed valence state of dinuclear ruthenium complex, shown in inset. Experiments were conducted in dry acetonitrile containing 0.1 M TEABF₄ as supporting electrolyte. Emission spectra were collected using iCCD with gate width at 500 nsec. Luminescent decays, collected using iCCD with gate width at 20 nsec. Reproduced from reference (49) with permission from the Royal Society of Chemistry.

processes. In electronic spectroscopy, the majority of spectroelectrochemical experiments are conducted in the transmission mode; for infrared spectroelectrochemistry, the reflectance mode is mainly used. Since Raman is a scattering technique, it is fundamentally suited to interfacial measurement.

14.5.1 IR spectroelectrochemistry

The infrared (IR) region of the EM spectrum lies between 50 and 10^4 cm^{-1} . Absorption of IR light by a molecule occurs when the electric field of an incident photon is resonant with the frequency of a vibrational mode. In order to be excited in this way (i.e., IR active) the vibration must elicit a change in the permanent electric dipole in the molecule. Modern IR spectrometers are Fourier transform IR (FTIR) instruments in which an interferometer interrogates the IR transmission of a sample at all wavelengths simultaneously. The operation of the FTIR technique is described extensively elsewhere (51). In short, an interferometer is composed of a beamsplitter and two flat mirrors, one fixed and one movable. The beamsplitter splits the incident analyzing laser source into two optical beams. One beam reflects off the fixed mirror while the second beam reflects off the movable mirror which moves within a path of millimeters from the beamsplitter. The two reflected beams are recombined when they meet at the beamsplitter as an interference pattern or interferogram. This interference pattern arises as a consequence of the displacement of the moving mirror. The interferogram is then directed through the sample compartment where, if a sample is present, components of the interferogram are transmitted or absorbed by the sample. The interferogram that reaches the detector is then transformed to spectral information using the FT. An advantage of the FT method applied to spectroelectrochemistry is its speed, which permits rapid spectral collection particularly in difference experiments where, for example, the applied potential is modulated. IR spectroscopy, like electronic spectroscopy, is commonly conducted in the transmission mode. Due to large solvent background, particularly in aqueous environments as a consequence of the large permanent dipole of water, the use of transmission in IR spectroelectrochemistry is relatively uncommon, although there are a number of reports on transmission cells (52–54). Reflectance methods are more commonly used for spectroelectrochemistry, the most common of which are ATR, external reflectance, and infrared reflection absorption spectroscopy (IRRAS). In general, the IR signal in spectroelectrochemistry is collected and distinguished from the signal in the absence of applied potential by using a difference method or a modulation method. IR spectroelectrochemistry is an extensive area; a number of reviews are available (55–57).

14.5.1.1 Internal reflectance

In internal reflection spectroelectrochemistry, the working electrode is a reflective metal surface which behaves like a mirror directing the specularly reflected incident light through the solution to the detector. Because the path length must be very small, the surface of the working electrode should be as flat as possible to minimize solvent contribution. A metal electrode polished to a mirror finish is usually used. A common IR spectroelectrochemical cell is shown in Figure 14.19 (58). The cell construction is syringe-like. A mirror-like working electrode, frequently a 5–10 mm diameter gold or platinum disk, is adhered to the end of a plunger. Gold is most commonly used because it has excellent IR reflectance; however, it has a limited potential window. Electrical connection is made at the back of the working electrode and the wires run through the hollow plunger body. A luggin reference electrode and auxiliary are placed within a few millimeters of the

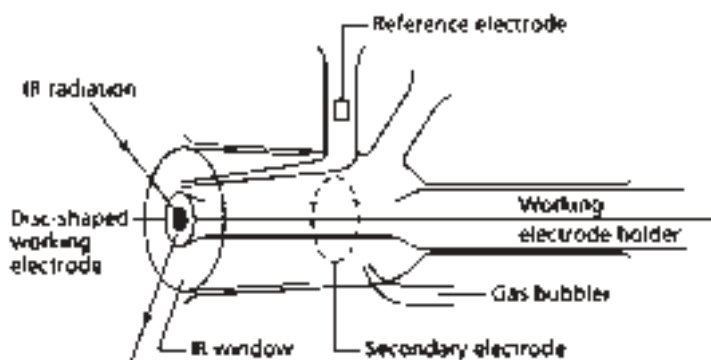


Figure 14.19 IR spectroelectrochemical cell for external reflectance. Reproduced from reference (58) with permission from Elsevier.

working electrode. The bottom of the cell is a flat window of appropriate optical material. The plunger is forced close to the window to form a thin layer of electrolyte between the working electrode and the window. In this configuration, incident light is directed through the optical window onto the thin film of solution compressed between the optical window and working electrode. The light is then reflected from this surface towards the detector. The material used for the optical window is critical because it must simultaneously transmit IR light and be stable toward the solvent system used (which is frequently aqueous). Silicon, calcium fluoride, zinc sulfide, and zinc selenide are commonly used materials for the optical window in the IR spectroelectrochemical cell.

In aqueous systems the electrode may be sealed onto the glass plunger using epoxy resin. Because most epoxy resins are unsuitable for organic solvents, the metal is usually sealed directly to the glass. The solvent and electrolyte are typically present in large excess over the analyte and will frequently have a significant IR absorbance. Correction for this background IR contribution is best achieved by modulation of the applied potential, polarization of the incident light, or by using a difference method. SNIFTIRS (subtractively normalised interfacial Fourier transform infrared spectroscopy) is a difference technique developed for spectroelectrochemistry. SNIFTIRS involves collection of a successive series of interferograms (59) at two potential limits, E_1 and E_2 , where E_1 is a reference potential typically corresponding to a potential at which no faradaic process occurs and E_2 corresponds to the potential at which the analyte redox step occurs. The step between E_1 and E_2 is cycled until an acceptable signal-to-noise ratio is obtained. If R_1 and R_2 are the reflectances measured at E_1 and E_2 respectively, the change of reflectivity $\Delta R/R$ is given as $(R_2 - R_1)/R_1 = R_2/R_1 - 1$. This method has been developed for a commercial FTIR spectrometer (60). The SNIFTIRS method has been used for the *in situ* detection of electro-generated intermediates in the double layer or species adsorbed at the electrode surface. For example, the SNIFTIRS of self-assembled monolayers of short chain alkyl thiols terminated with ferrocene (Fc) at Au(111) surfaces has been reported. Figure 14.20 shows representative SNIFTIRS spectra for these monolayers (61). Using p-polarized light and exploiting the surface selection rule described below, orientational changes in the ferrocene moieties could be detected on oxidation of the ferrocene groups in the monolayers. This

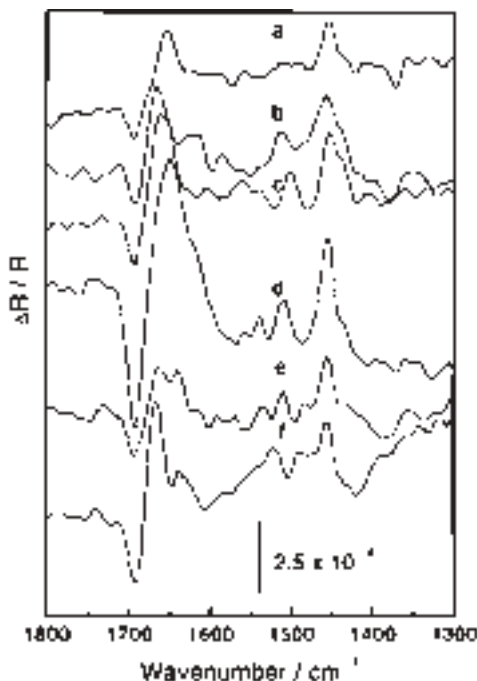


Figure 14.20 SNIFTIRS spectra in the region 1300–1800 cm^{-1} for a single crystal gold(111) disc electrode modified with FcC_3 (a), FcC_4 (b), FcC_5 (c), FcC_6 (d), FcC_8 (e), and FcC_{10} (f), obtained at 650 mV using p-polarized radiation. The reference spectrum for each monolayer was obtained at 200 mV. Reproduced from reference (61) with permission from Elsevier.

was attributed to rotation of the ferrocene groups towards a position where the plane of the cyclopentadienyl rings moves to a position normal to the surface of the electrode (61).

Infrared reflection absorption spectroscopy (IRRAS) has also been applied to electrochemical measurements. This method is interesting because of the additional selection rules it confers to the method which can be exploited for detailed structural assignment. IRRAS involves the rapid and continuous modulation of the polarization of the infrared light between s and p polarization states using a photoelastic modulator. The potential at the electrode is fixed at a chosen voltage during this process. For incident s-polarized light (perpendicular to the plane of reflection), the reflected beam is out-of-phase with the incident beam and they destructively interfere to produce a node in the electric field at the surface. This means there is no electric field at the surface to interact with the molecular dipole of the adsorbate. For p-polarized light (parallel to the plane of reflection) the two fields are in phase. This means that s-polarized radiation interacts only with species in solution, while p-polarized radiation interacts with both surface and solution species. Subtracting the s- and p-polarized spectra produces a spectrum which only shows bands associated with species in the interfacial region and eliminates any contribution from solvent or electrolyte. In addition, because the exciting radiation at the surface is p-polarized, only those modes with a dipole moment perpendicular to the metal surface can interact

with the electric field of IR radiation. This is known as the metal surface selection rule for IR spectroscopy, Figure 14.21.

Figure 14.22 shows a IRRAS spectroelectrochemical *in situ* study of *trans*-[NBu₄][RuX₄(CNXyl)₂] (X = Cl or Br, Xyl = 2,6-dimethylphenyl) (62). These materials undergo temperature dependent electrochemically induced isomerization reactions involving reductive elimination of a halide ion. In Figure 14.22a, the potential of the working electrode was stepped to 0.50 V and single scan IR spectra were collected following the step at 2-min intervals. Reduction of *trans*-[RuCl₄(CNXyl)₂] is indicated by increasing negative absorbance at 2154 cm⁻¹. In Figure 14.22b, re-oxidation is achieved at $E_{app} = 0.50$ V where the band at 2076 cm⁻¹ collapses and another grows at 2176 cm⁻¹.

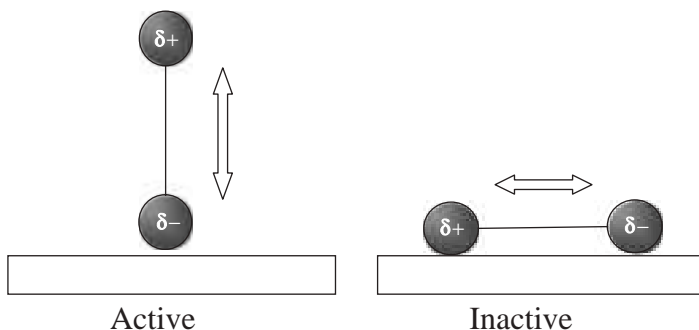


Figure 14.21 Schematic illustrating surface metal selection rule for IR spectroscopy. Only vibrational modes with a dipole moment component perpendicular to the metal surface can interact with the electric field of IR radiation (i.e., the stretching mode on the left is IR active whereas that on the right is not).

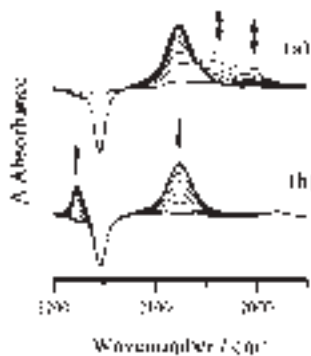


Figure 14.22 Changes in the IR difference absorption spectra accompanying (a) reduction of *trans*-[NBu₄][RuCl₄(CNXyl)₂] in an IRRAS cell at 293 K at -0.5 V. The horizontal line at zero absorbance corresponds to the initial spectrum (i.e., that of *trans*-[RuCl₄(CNXyl)₂]⁻) prior to electrolysis, ratioed against itself. (b) Reoxidation of *trans*-[NBu₄][RuCl₄(CNXyl)₂] at +0.5 V. Reproduced from reference (62) by permission of The Royal Society of Chemistry.

14.5.1.2 External reflectance

Electronic reflectance spectroscopy and attenuated total internal reflection (ATR) cells provide significant improvement in discrimination of background and interfacial signals because ATR minimizes penetration of the monitoring beam into the solvent. The mechanism of ATR is described in Section 14.3.2. The cell design for external reflectance IR methods is similar to those described for electronic spectroscopy. The total internal reflection component, which doubles as a working electrode, must be made of high refractive index material which is also IR transparent. A prism or parallel plate made from semiconductor material can be used as the ATR element as can silicon or germanium because they have good IR transparency. The ATR element may be coated with a thin layer of gold (for IR transparency). A balance must be achieved between the conductivity of the film and its optical transparency because the IR beam must penetrate the metallic layer to reach the sample. Alternatively, at moderate doping levels semiconductors such as silicon and germanium can be used as both ATR element and electrode, although, doping reduces the transparency of the material (57).

Figure 14.23 shows an example of an ATR a cell for FTIR spectroscopy (63). A thin layer of gold (10–15 nm) on a right-handed silicon prism serves as the working electrode. The prism was clamped to the electrochemical cell which was rotated so that the position of the electrochemical cell permitted an angle of incidence of the infrared beam of 45°. The detector, which was liquid nitrogen-cooled mercury cadmium telluride, was oriented so that the angle between the incident and reflected beams was 90°. The cell was used to study step-scan double-modulation (phase and electrochemical potential) ATR FT-IR spectrometry experiments using the ferricyanide redox couple to explore digital signal processing as an alternative to two lock-in amplification for demodulation of optical at two modulation frequencies.

The main advantages of ATR for IR arise from the fact that the IR EM field decays exponentially from the ATR surface into solution. This means that only a very thin film material in direct contact with the electrode is interrogated. This leads to limited solvent

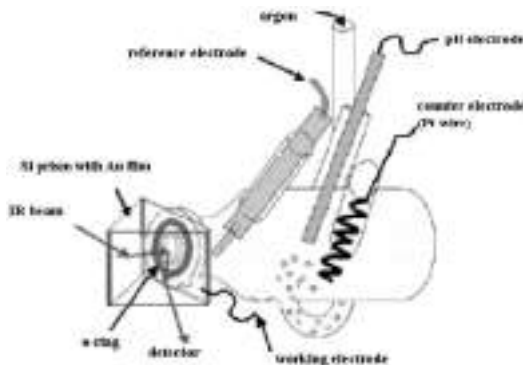


Figure 14.23 Schematic of IR ATR spectroelectrochemical cell. Reproduced from reference (63) with permission from Elsevier.

contribution to the signal and also as multiple reflections occur, the sensitivity to interfacial species is increased.

A number of practical limitations for IR attenuated ATR have been highlighted. Theoretical and experimental refraction have been found to differ substantially and these differences have been attributed to the difference in optical properties of the thin metal layers and the bulk, due to either non-ideal geometric arrangement of the atoms or through compositional changes caused by inter-diffusion of the phases in the process of film formation (64).

14.5.2 Raman spectroelectrochemistry

In Raman spectroscopy the inelastic scattering of light incident on an analyte is investigated. Light is inelastically scattered when there is an exchange of energy between an incoming photon and the analyte molecule. This leads to the emission of a second photon with a different frequency, ν to the incident photon, ν_0 . Therefore, Raman is fundamentally a two photon process. The frequency of the Raman scattered photon may be greater than that of the incident photon (i.e., $\nu_0 + \nu$) known as anti-Stokes Raman scatter, or less than that of the incident photon, $\nu_0 - \nu$, known as Stokes Raman scatter. In each instance the $\Delta\nu$ corresponds to vibrational quanta. The Raman effect is fundamentally weak with between only 1 in 10^8 and 10^{11} molecules in a sample scattering inelastically. Figure 14.24 illustrates the mechanism of Raman scattering which originates from electronic excitation into a “virtual” state.

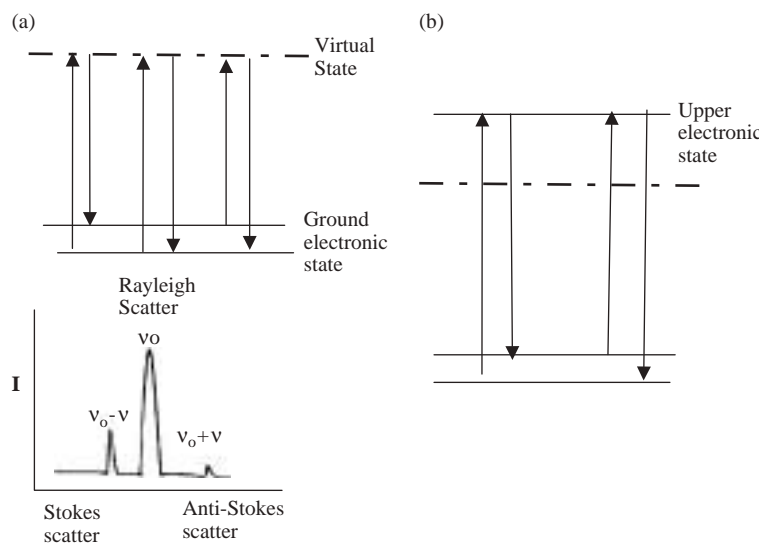


Figure 14.24 Schematic illustration of the concept of Raman excitation. (a) Conventional Raman spectroscopy: excitation to a virtual state leads to reemission of a photon of the same frequency as the excitation source, Rayleigh scattering, or inelastic scattering where the reemitted photon has greater (Anti-Stokes) or less energy (Stokes) than the incident photon. (b) Resonance Raman conditions: the frequency of the incident photon matches or is close to the energy of an optical absorbance, resulting in scatter which originates from an excited electronic state.

The most probable Raman process is Stokes scatter because this originates from a ground vibrational level $v = 0$, the most likely state to be populated at room temperature. After excitation to a virtual level, the scattered photon is released and the molecule returns to a higher vibrational level, $v = 1$. Therefore, $\Delta v = v_0 - v = 1$ corresponds to a vibrational quantum. Anti-Stokes is the weaker process because it involves excitation from the higher ground state vibrational level which is usually poorly populated at room temperature. Thus Raman spectroscopy is usually conducted on Stokes radiation. Similar to IR spectroscopy, vibrational information is gleaned from the Raman experiment although the selection rules for each process are quite different. The selection rule for Raman spectroscopy states that for a given molecular vibrational mode to be Raman active it must cause a change in a component of the molecular polarizability. This is substantially different from the selection rule for IR spectroscopy. Thus for highly symmetric molecules, a vibration which is IR active is frequently excluded from being Raman active. For example, molecules with large permanent dipoles (such as water) that are strongly IR active tend to be difficult to polarize and therefore have weak Raman signals. This offers a substantial advantage of Raman over IR spectroscopy for electrochemical studies because it is possible to study reactions *in situ* in aqueous or polar media without the significant background interference which makes IR so difficult. Additionally, since excitation is usually conducted in the visible region in Raman, there is no requirement for special IR transmissible optical windows such as the alkali salt windows required in IR. However, because of inherent signal weakness, Raman spectroscopy requires the use of high power monochromatic light sources and sensitive detection. With the increasing availability of affordable laser sources and sensitive detection by CCDs, the popularity of this technique has soared.

Raman spectroelectrochemistry has been reviewed in detail (65, 66). The type of cell used for spectroelectrochemistry depends to some extent on the optical layout of the Raman experiment. The main optical layouts in conventional Raman spectroscopy are front incident and collection mode, 180° backscattering, and ATR mode. For most solution phase applications of Raman spectroelectrochemistry, a three-electrode cell for bulk electrolysis is used and a number of such cells have been described (67). The conventional OTTLE cell described for electronic spectroscopy can be used in Raman spectroelectrochemistry. However, this cell can suffer from solvent interference in non-aqueous media. Thin layer cells like those described for IR are also frequently used (66).

An interesting approach uses the immersion cell shown in Figure 14.25 which has been used to study self-assembled monolayers and interfacial structure using Raman spectroscopy (68, 69). In this approach a slowly rotating electrode is in partial contact with a droplet of analyte solution. The laser samples a portion of the electrode that has been rotated through and out of this solution drop, and which retains a thin film of the solution on the order of tens of angstroms thickness on its surface. The interfacial solvent species in this layer retains any preferred orientation that occurred *in situ*. Electrical contact is maintained with the working electrode through the droplet. This approach minimizes the amount of bulk solvent sampled leading to reduced background interference. Because the electrode is turned during the Raman study, local heating due to the incident laser is minimized.

A more recent advance in Raman spectroscopy which has increased its versatility is Raman confocal microscopy. In confocal microscopy, out-of-focus information, which contributes to the overall image in conventional microscopy, is eliminated by means of a

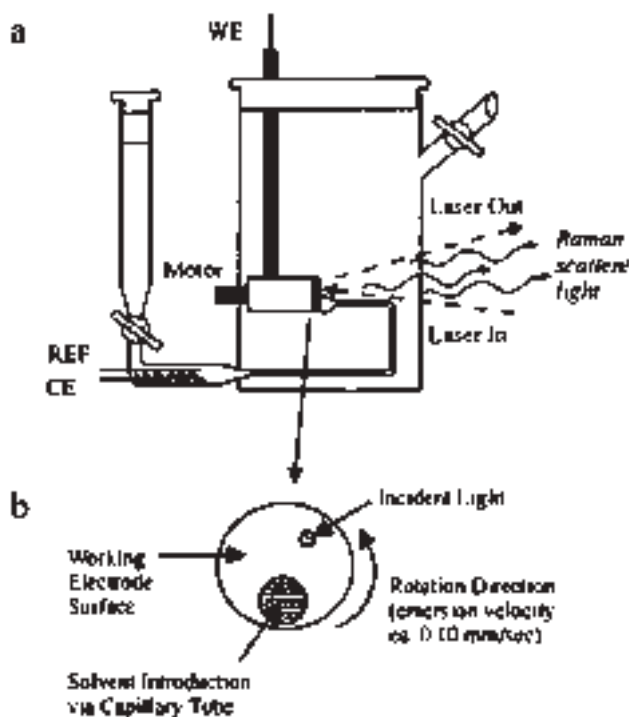


Figure 14.25 (a) Schematic of Raman spectroelectrochemical emersion cell. Reference electrode (Ag wire), (CE) counter electrode (Pt wire), (WE) working electrode (Ag disk); (b) front view of working electrode surface. Reprinted with permission from reference (69). Copyright 1997, American Chemical Society.

confocal “pinhole” aperture which lies in front of the image plane, Figure 14.26. This acts as a spatial filter permitting only the in-focus portion of the light to be imaged. In Raman spectroscopy this permits discrimination of Raman scatter from outside the plane of focus of the laser thus limiting the portion of the sample interrogated to a tiny volume and allowing depth profiling with a resolution of 1–2 μm .

The spatial resolution in a confocal Raman microscope is typically sub-micron. Confocal microscopy improves the axial and lateral resolution of Raman spectroscopy permitting Raman imaging and has improved fluorescence rejection, which can hinder conventional Raman experiments. This tiny sample volume allows the same kind of selectivity as does using a thin layer method in spectroelectrochemistry. The fine depth control and very narrow sample volume means that background contributions from solvent/electrolyte and background fluorescence interferences can be eliminated. A rotating disk electrode for Raman electrode spectroelectrochemistry has also been described for fast bulk electrolysis at a large area Pt electrode which achieved bulk electrolysis of a 5 mL solution in less than 6 min (70). The spectroelectrochemical set-up using this method provides the ability to interrogate very limited volumes, thus reducing background interference.

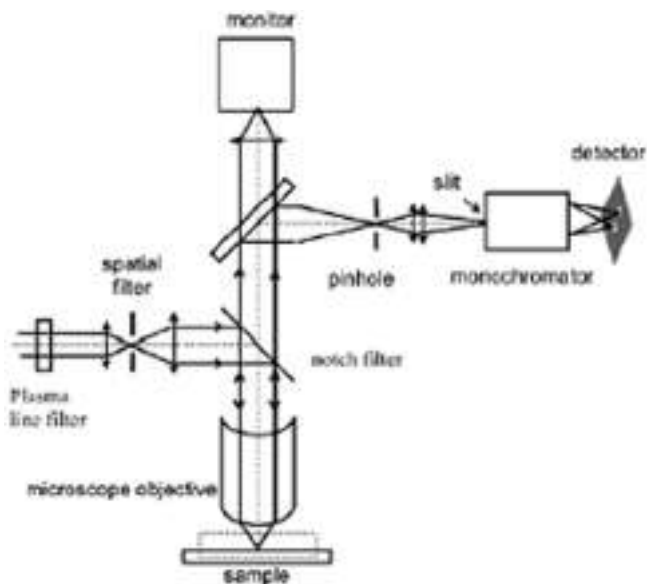


Figure 14.26 Instrumental set-up for confocal Raman microscopy. Reproduced from reference (66) with permission from Wiley-VCH.

Raman spectroelectrochemistry can provide detailed information about structural changes which accompany an electrochemically induced process in solution. In addition, confocal methods are increasingly being used on surfaces, interfaces, and in thin solid films. Because confocal microscopy is a scattering rather than a transmission technique, it can be used for electrochemical studies at solid electrodes and is a valuable means of probing the electrode/solution interface. An L bend microscope objective can be used with the cell shown in Figure 14.27. In this arrangement the working electrode is inserted into the side of a conventional cuvette. Typically a methacrylate cuvette into which a hole has been bored is used for visible excitation. The cell is sealed against leakage with a rubber o-ring or wax. A thin layer of solution is then compressed between the cuvette window and the electrode. For monolayers or thin films, the compression of the electrode to the window is not required. The auxiliary and reference electrodes and the solution may be degassed and a blanket of inert gas may be maintained over the top of the cell during spectral acquisition.

The precise focusing of the confocal method can be used to obtain good signal intensities from Raman of thin films deposited onto electrode surfaces and this limits spectral contributions from background solvent or electrolyte or the cell material. This cell has been used with confocal Raman microscopy for studying the spectroelectrochemistry of thin solid films and self-assembled monolayers (71, 72). For example, Figure 14.28 shows the Raman spectroelectrochemistry for solid crystalline films of hydroquinone 3,5-bis (2-pyridyl)-1,2,4-triazole co-crystal adhered to a glassy carbon working electrode using the cell shown in Figure 14.27. Reversible oxidation of the hydroquinone moiety could be mapped through Raman spectroscopy.

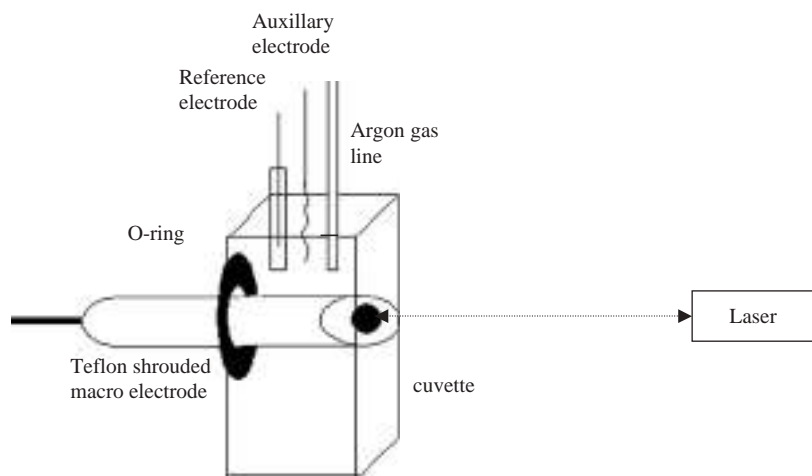


Figure 14.27 Spectroelectrochemical cell for Raman. (a) Simple thin layer set-up for Raman spectroelectrochemistry for use with solid films or monolayers and suitable for use with backscattering and microscope geometries.

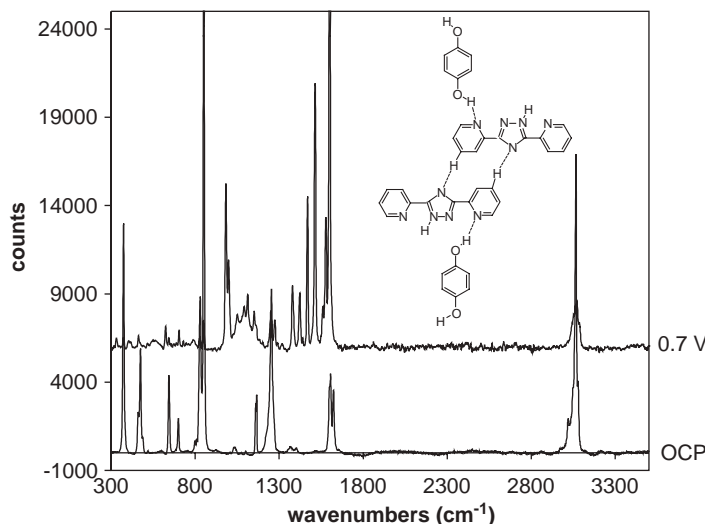


Figure 14.28 Confocal Raman spectroelectrochemistry of a thin surface layer of solid films of HQBpt (inset) on a glassy carbon electrode (A) at open circuit potential, (B) at +0.700 V. The supporting electrolyte was aqueous 0.1 M LiClO_4 . Reprinted with permission from reference (71). Copyright 2001, American Chemical Society.

The overriding drawback of Raman spectroscopy is that Raman scatter is fundamentally a weak phenomenon. Resonance Raman spectroscopy and surface enhanced Raman spectroscopy (SERS) are two methods which can be exploited in a spectroelectrochemical experiment to enhance the signal and increase the selectivity of the signal.

14.5.2.1 Resonance Raman spectroscopy

In resonance Raman spectroscopy (73), the Franck Condon modes of a chromophore can be resonantly enhanced by up to seven orders of magnitude by using excitation wavelengths that are coincident with the absorbances under interrogation. The theory behind this condition is complex (74) and beyond the scope of this chapter. Employing the resonance condition in spectroelectrochemistry provides a unique and powerful opportunity to unequivocally identify new optical transitions resulting from electrode reactions.

In terms of experimental set-up, the methods described for conventional Raman spectroscopy apply. Typically a number of laser excitation wavelengths are required to elucidate overlying transitions. Figure 14.29 illustrates the utility of this technique for $[M(bpy)_2(\text{box})]^+$, where bpy is 2,2-bipyridyl, box is 2-(2-hydroxyphenyl)benzoxazole, and M is either Ru or Os which are coordinated through a N of the benzoxazole and through the phenolate O. For these metal complexes, the assignment of the oxidation steps was unclear, but electrochemical and UV spectroelectrochemical behavior suggested that the first oxidation was metal based. Resonance Raman of the native complex suggested the highest energy occupied molecular orbital, HOMO, lay on the phenolate suggesting that this should be site of the most cathodic oxidation (75). The inset of Figure 14.29 shows the electronic spectroelectrochemistry observed for the first oxidation step of the ruthenium complex which resulted in loss of the visible MLCT transition with the development of a new optical transition in the NIR.

Resonance Raman spectroelectrochemistry was carried out on $[Ru(bpy)_2(\text{box})]^+$ and the osmium analogue in which the bipyridyl units were perdeuteriated $[Os(d_8\text{-bpy})_2(\text{box})]^+$ by holding the cell potential beyond the first oxidation step for each sample. The resonance Raman spectra of $[Ru(bpy)_2(\text{box})]^{2+}$ and $[Os(bpy)_2(\text{box})]^{2+}$ are in essence analogous. This implies that the bipyridyl unit does not participate in the new optical transition in the oxidized complex and therefore confirmed that for both M(bpy) containing complexes the NIR band is a phenolate (π) to M(III) ($d\pi$) ligand to metal charge transfer LMCT transition. This example also serves to illustrate how a simple synthetic modification such as deuteration can yield detailed information on electron transfer processes. If the bipyridyl unit were involved in the optical transition, shifts of between 30 and 60 cm^{-1} would have been observed between the deuterated and non-deuteriated spectra.

14.5.2.2 Surface enhanced Raman spectroscopy

Surface enhanced Raman spectroscopy (SERS) is becoming an increasingly popular technique for probing interfacial structure in electrochemical reactions. It has been exploited to study adsorbate structure and orientation changes on application of potential and to interrogate the interfacial distribution of solvent and ions. The mechanism of SERS has been described in detail (76, 77) and is only broadly outlined here. The intensity of a Raman signal is proportional to the square of the magnitude of any incident EM field. SERS exploits this sensitivity by using the enhanced EM field at a roughened metal surface to achieve significantly enhanced Raman scattering of the vibrational modes of adsorbates. Up to 10^{14} signal enhancements have been reported for silver in conditions where “hot particles” of magnitude of ~100 nm appear (78). The origin of this enhancement is still debated, but is believed to draw on two contributions: EM and chemical enhancements.

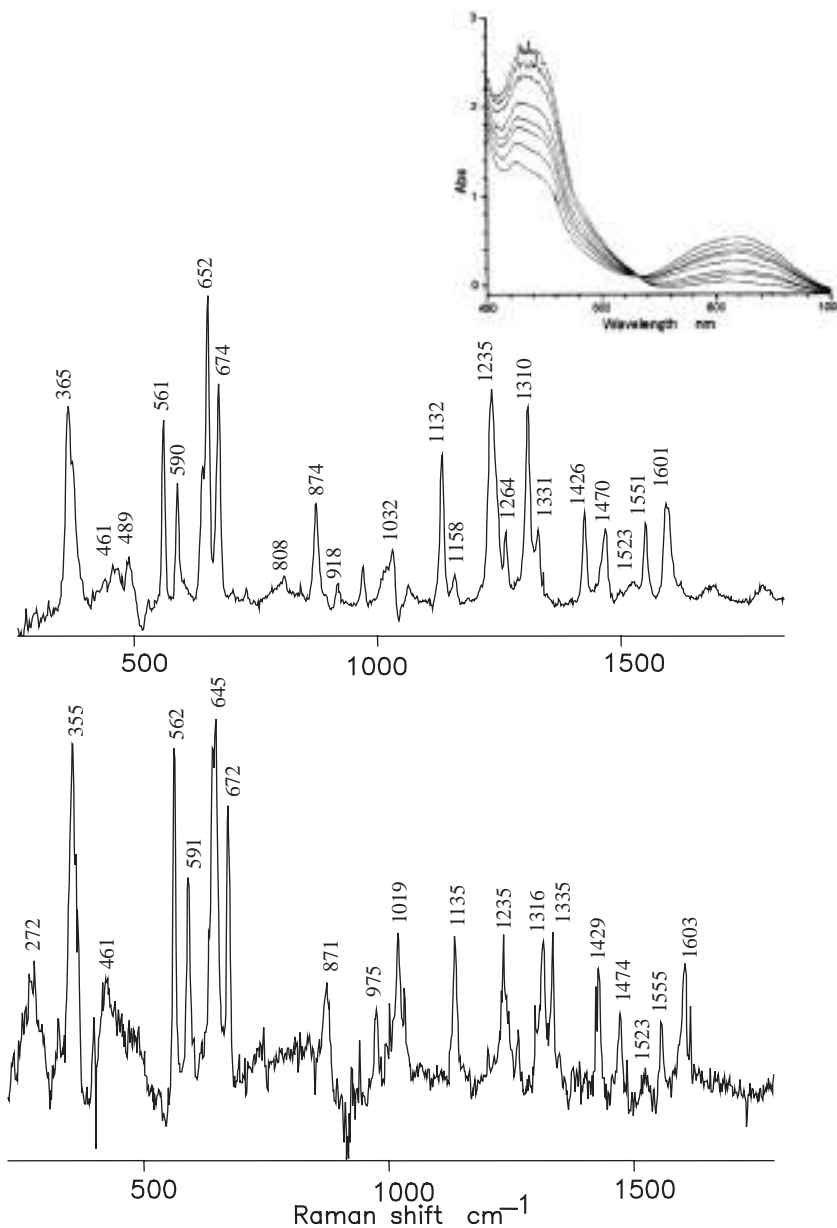


Figure 14.29 Controlled potential spectroscopy of (a) $[\text{Ru}(\text{bpy})_2(\text{box})]^+$ electronic spectroscopy, (b) $[\text{Ru}(\text{bpy})_2(\text{box})]^+$ resonance Raman spectroscopy in dichloromethane, excited at 785 nm, (c) resonance Raman of $[\text{Os}(\text{d}_8\text{-bpy})_2(\text{box})]^+$ in dichloromethane, excited at 785 nm, the applied potential in each instance was 0.5 V versus Ag/AgCl and the electrolyte was 0.1 M TeabF₄. Reproduced from reference (75) by permission of The Royal Society of Chemistry.

The former is best understood and arises when the incident photon excites plasmons at the metal surface thus augmenting, through energy transfer from the plasmons, the electric field experienced by the analyte molecules. The chemical enhancement mechanism remains controversial. It is thought that as a consequence of the perturbation of the adsorbate states on substrate binding that excited states induced at the metal undergo a charge transfer to the adsorbate enhancing the Raman scatter.

SERS enhancement is largely limited to the coinage and alkali metals: Ag, Au, Cu, Na, Li, K. In principle all metals should be capable of enhancement and Pd and Pt, Rh, and Ru will produce enhancements with UV excitation (79). The difficulty lies in the availability of accessible laser lines. UV lasers are expensive and their associated optic constraints make instrumentation expensive. Herein lies the main limitation for the use of SERS in spectroelectrochemistry. The best SERS enhancements reported are for Ag and Au, but these metals, particularly Ag, have very limited working potential windows. This has been overcome by depositing overlayers of platinum group metals such as Pt on a SERS active substrate such as silver or gold, using a range of methods including constant current deposition (80) and electrochemical replacement of an underpotential-deposited copper or lead monolayer with a Pt-group metal cation (81, 82). This method works with relatively little loss of enhancement because the EM field enhancement mechanism operates over several nanometers. The requirement for roughened surfaces for optimal SERS enhancement is well established (83). Surface roughness should be on the order of between 10 and 200 nm and the surface morphology is critical in dictating the quality of SERS achieved. Theory dictates that the highest SERS enhancements of electric field will be achieved where the surface roughness has the highest curvature (84). A range of methods have been explored for development of SERS substrates including electrochemical, chemical, and laser-induced roughening of metal surfaces, immobilization of metal particles onto an etched or modified substrate, vapor deposition, metal nanoparticle assembly via lithography (85), colloidal metal nanoparticles, and electrodeposition over polystyrene nanospheres which can be used to create highly reproducible surface structures (86). All of these methods leave the metal surface with small metal particles or aggregates of particles that behave as rough surface features. Electrochemical roughening is a useful method of surface roughening (87). Typical roughening procedures involve sequential oxidative and reductive cycles (ORC). For gold or silver this is achieved in Cl^- electrolyte (88, 89). Figure 14.30 shows the effect of electrochemical surface roughening of gold.

In general, this method produces stable surface morphologies that give good levels of signal enhancement which depend inherently on the number of oxidation reduction cycles conducted. Figure 14.31 illustrates the impact of increasing ORC on surface roughness, R , for a gold electrode (90). In this study, the SERS intensity of a pyrazine adsorbate ring-breathing mode (ca. 1016 cm^{-1}) was used as a measure of the impact of surface morphology on SERS signal enhancement. The intensity of this mode reached a maximum between 20 and 30 ORCs. AFM studies indicated that roughness features with an average size of approximately 100 nm corresponded to this strongest SERS signal.

SERS has found application across a broad range of electrochemical investigations, including studies of morphological changes associated with redox states (91). It has been used to dynamically determine molecular orientation, and to characterize the structure of

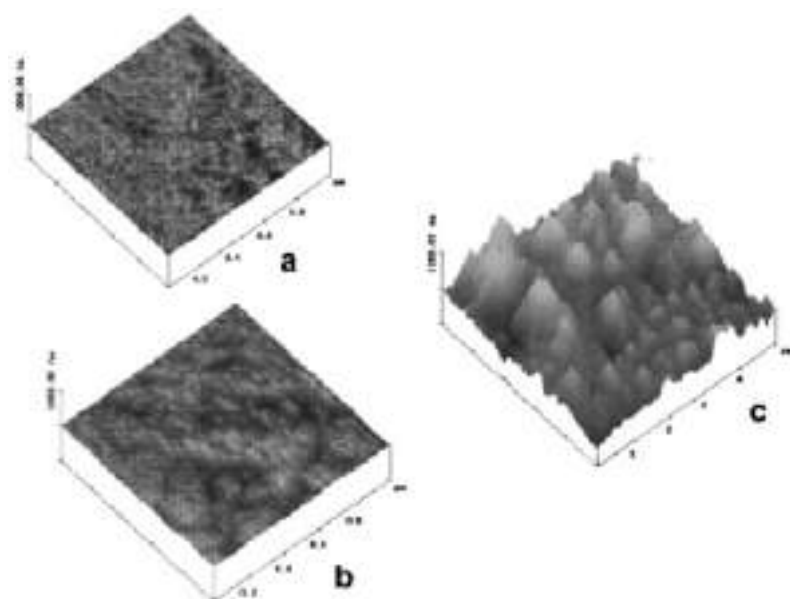


Figure 14.30 Contact mode AFM images of roughened gold electrodes following oxidation reduction cycling (ORC) in 0.1 M KCl (a) $R = 0.7$ (five ORCs); (b) $R = 3.1$ (20 ORCs); (c) $R = 10.5$ (60 ORCs). Reprinted with permission from reference (90). Copyright 1998, American Chemical Society.

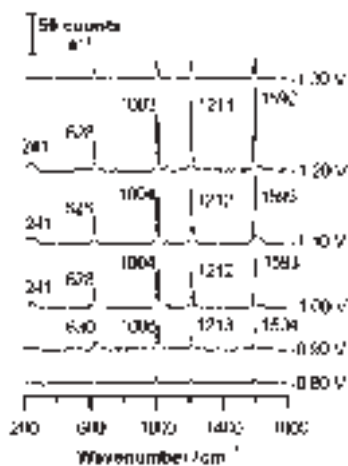


Figure 14.31 The potential-dependent SERS spectra of adsorbed pyridine from a cobalt electrode in 10^{-2} M pyridine/0.1 M NaClO₄. The electrode was roughened electrochemically. The laser excitation line was 632.8 nm. Reproduced from reference (86) with permission from the Royal Society of Chemistry.

adsorbate and how this influences heterogeneous electron transfer (92). Studies focusing on the potential dependence of SERS spectra for water and hydroxyl ions on silver have demonstrated the feasibility of probing solvent molecules within the inner layer of the interface, as well as those associated with the solvation shells of adsorbed cations (93, 94). The comparative power of IRRAS and Raman methods in probing the interfacial layer have been discussed and the power of SERS in probing this environment arises from: (a) much less restrictive selection rules than IRRAS which is subject to the surface selection rule that dictates that only adsorbed species with dipole moments perpendicular to the surface are IR active; (b) greater sensitivity due to EM and chemical enhancement; (c) wider optical ranges (95). Although IRRAS methods can also benefit from surface plasmon enhancement (96), the effect is considerably weaker than for SERS. The surface selection rules for IR spectroscopy are not necessarily a disadvantage because they can yield clues to orientation of adsorbates on surfaces. Although both SERS and IRRAS have their merits, combination of both techniques to study a single surface can lead to unprecedented structural insights.

14.6 OUTLOOK

Spectroelectrochemistry continues to provide unique insights into interfacial reaction and redox processes. Electrochemical methods continue to find partners across a diverse range of spectroscopic methods, both optical and non-optical. As spectroscopic methods continue to develop and improvements in light focusing and collection optics improve, increasing use of imaging is likely. The increasing use of microscopes as optical elements in spectroelectrochemistry leads to the possibility of imaging, which will compliment and may be used in tandem with existing electrochemical methods. For example, epifluorescence imaging of potential-dependent adsorption and desorption at an electrode interface has been described (97) and wavelength-dispersive multispectral imaging of ion-selective membranes have been reported (98). Imaging of spectroelectrochemical and interfacial processes will inevitably extend to IR and Raman methods as well. In particular, the use of confocal optics is likely to find increasing use in spectroelectrochemical studies, particularly in interfacial studies as a result of the ability of this arrangement to selectively interrogate very small sample volumes. Z-piezo control on many confocal microscopes will allow depth resolved studies into the diffusion layer and beyond. Combination of less common spectroscopic methods such as circular dichroism have been applied to spectroelectrochemical methods and this is likely to increase, particularly in studies of biological materials where conformational changes in response to an electric field or potential responses can be monitored.

Scanning near field optical microscopy (SNOM), developed in the 1990s, combines the advantages of conventional scanning probe methods for topological information and the advantages of optical imaging for structural information, and permits the optical imaging of materials and structures beyond the optical diffraction limit. This method utilizes a scanning probe reminiscent of that used in other scanning probe methods; the critical difference is that the micromachined probe tip acts as a nanoscale light source. The tiny distances between probe and sample are in the near field, which means that the optical resolution of the image is not restricted as conventional far-field imaging is by the diffraction limit.

SNOM can be applied in a range of modes including transmission, reflectance, and emission. Such techniques are likely to be coupled to electrochemical studies in the future. The spatial resolution of such imaging makes the possibility of interrogating potential control of single molecules a reality.

REFERENCES

1. E. Wolcan, M. R. Feliz, G. T. Ruiz, M. P. Juliarena, R. O. Lezna, *J. Electroanal. Chem.* **101**, 533 (2002).
2. R. J. Gale, Ed., *Spectroelectrochemistry, Theory and Practise*, Plenum Press: New York, 1988.
3. G. R. Fowler, *Introduction to Modern Optics*, Dover: New York, 1989.
4. C. A. Goss, D. H. Charych, M. Majda, *Anal. Chem.* **63**, 85 (1991).
5. (a) J. Stotter, J. Zak, Z. Behier, Y. Show, G. M. Swain, *Anal. Chem.* **74**, 5924 (2002). (b) M. Hupert, A. Muck, R. Wang, J. Stotter, Z. Cvackova, S. Haymond, Y. Show, G. M. Swain, *Diamond Relat. Mat.* **12**, 1940 (2003).
6. J. K. Zak, J. E. Butler, G. M. Swain, *Anal. Chem.* **73**, 908 (2001).
7. J. Stotter, S. Haymond, J. K. Zak, Y. Show, Z. Cvackova, G. M. Swain, *Interface* **12**, 33 (2003).
8. J. Stotter, J. Zak, Z. Behler, Y. Show, G. M. Swain, *Anal. Chem.* **74**, 5924 (2002).
9. H. B. Martin, P. W. Morrison, *Electrochem. Solid State Lett.* **4**, E17 (2001).
10. P. A. Flowers, M. A. Maynor, D. E. Owens, *Anal. Chem.* **74**, 720 (2002).
11. M. L. Meyer, T. P. DeAngelis, W. R. Heineman, *Anal. Chem.* **49**, 602 (1977).
12. Y. Zhy, G. Cheng, S. Dong, *Electroanalysis* **12**, 10736 (1999).
13. D. A. Scherson, S. Sarangapani, F. L. Urback, *Anal. Chem.* **57**(7), 1501 (1985).
14. D. Collison, F. E. Mabbs, E. J. L. McInnes, K. J. Taylor, A. J. Welch, L. J. Yellowlees, *J. Chem. Soc., Dalton Trans.* **3**, 329 (1996).
15. X. Q. Lin, K. M. Kadish, *Anal. Chem.* **57**(7), 1498 (1985).
16. (a) M. B. G. Pilkington, B. A. Coles, R. G. Compton, *Anal. Chem.* **61**, 1787 (1989). (b) I. Bedja, S. Hotchandani, P. V. Kamat, *J. Phys. Chem.* **97**, 11064, (1993).
17. A. T. Hubbard, F. C. Anson, *Electroanal. Chem.* **4**, 129 (1970).
18. T. Chen, S. J. Dong, Y. W. Xie, *J. Electroanal. Chem.* **379**, 239 (1994).
19. R. G. Compton, J. Winkler, D. J. Riley, S. D. Bearpark, *J. Phys. Chem.* **98**, 6818 (1994).
20. N. Chanda, B. Sarkar, J. Fiedler, W. Kaim, G. K. Lahiri, *Dalton Trans.* **18**, 3550 (2003).
21. (a) N. S. Hush, *Prog. Inorg. Chem.* **8**, 391 (1967). (b) M. B. Robin, P. Day, *Adv. Inorg. Radiochem.* **10**, 247 (1967).
22. T. E. Keyes, R. J. Forster, P. M. Jayaweera, C. G. Coates, J. J. McGarvey, J. G. Vos, *Inorg. Chem.* **37**, 5925 (1998).
23. H. E. Toma, K. Araki, *Curr. Org. Chem.* **6**, 21 (2002).
24. S. Dong, J. Niu, T. Cotton, *Methods Enzymol.* **246**, 701 (1995).
25. M. L. Fultz, R. Durst, *Anal. Chim. Acta* **140**, 1 (1982).
26. N. Patel, D. K. Jones, E. L. Raven, *Eur. J. Biochem.* **267**, 2581 (2000).
27. C. Taboy, C. Bonaventure, A. Crumbliss, *Methods Enzymol.* **353**, 187 (2002).
28. C. Taboy, K. M. Faulkner, D. Kraiter, C. Bonaventure, A. Crumbliss, *J. Biol. Chem.* **275**, 39048 (2000).
29. N. Winograd, T. Kuwana, *Electroanal. Chem.* **7**, 1 (1974).
30. J. Salbeck, *J. Electroanal. Chem.* **340**, 169 (1992).
31. M. Shi, X. Gao, *Electroanalysis* **2**, 471 (1990).
32. N. J. Simmons, M. D. Porter, *Anal. Chem.* **69**, 2866 (1997).

33. J. López-Palacios, A. Colina, A. Heras, V. Ruiz, L. Fuente, *Anal. Chem.* **73**, 2883 (2001).
34. P. G. Miney, M. V. Schiza, M. L. Myrick, *Electroanalysis* **16**, 113 (2004).
35. I. S. Zavarine, C. P. Kubiak, *J. Electroanal. Chem.* **495**, 106 (2001).
36. M. G. Hill, J. P. Bullock, T. Wilson, P. Bacon, C. P. Blaine, K. Mann, *Inorg. Chim. Acta* **226**, 61 (1994).
37. N. R. de Tacconi, R. O. Lezna, R. Konduri, F. Ongeri, K. Rajeshwar, F. M. MacDonnell, *Chem. Eur. J.* **11**, 4327 (2005).
38. U. Schröder, F. Scholz, *J. Solid State Electrochem.* **1**, 62 (2001).
39. Y. Shi, A. F. Slaterbeck, C. J. Seliskar, W. R. Heineman, *Anal. Chem.* **69**, 3679 (1997).
40. J. Tarabek, P. Rapti, M. Kalbac, L. Dunsch, *Anal. Chem.* **76**, 19, 5918 (2004).
41. I. T. Bae, M. Sandifer, Y. W. Lee, D. A. Tryk, C. N. Sukenik, D. A. Scherson, *Anal. Chem.* **67**, 24, 4508 (1995).
42. D. R. Dunphy, S. B. Mendes, S. S. Saavedra, N. R. Armstrong, *Anal. Chem.* **69**, 3086 (1997).
43. S. Simison, A. Pellicano, D. J. Schiffrian, *J. Chem. Soc., Faraday Trans.* **94**, 3439 (1998).
44. M. J. Simone, W. R. Heineman, G. P. Kreishman, *Anal. Chem.* **54**, 2382 (1982).
45. (a) Y. F. Lee, J. R. Kirchoff, *Anal. Chem.* **65**(23), 3430 (1993). (b) J. R. Kirchoff, *Curr. Sep.* **16**, 1 (1997).
46. J.-S. Yu, T.-Y. Zhou, *J. Electroanal. Chem.* **504**, 89 (2001).
47. Y. F. Lee, J. R. Kirchhoff, *J. Am. Chem. Soc.* **116**, 3599 (1994).
48. Z. Ding, R. G. Wellington, P. F. Brevet, H. H. Girault, *J. Phys. Chem.* **100**, 10658 (1996).
49. T. E. Keyes, B. Everard, C. Brady, J. G. Vos, *Dalton Trans.* **15**, 2341 (2004).
50. R. J. Forster, T. E. Keyes, *J. Phys. Chem.* **102**, 10004 (1998).
51. J. M. Hollas, *Modern Spectroscopy*, Wiley: Chichester, UK, 1996.
52. K. M. Kadish, X. H. Mu, X. Q. Lin, *Electroanalysis* **1**, 35 (1989).
53. M. Krejcik, M. Danek, F. Hartl, *J. Electroanal. Chem. Interfacial Electrochem.* **317**, 179 (1991).
54. F. Hartl, H. Luyten, H. A. Nieuwenhuis, G. Schoemaker, *Appl. Spectrosc.* **48**, 1522 (1994).
55. T. Iwasita, F. C. Nart, *Prog. Surf. Sci.* **55**, 271 (1997).
56. K. Ashley, S. Pons, *Chem. Rev.* **88**, 673 (1988).
57. J.-N. Chazalviel, B. H. Erne, F. Maroun, F. Ozanam, *J. Electroanal. Chem.* **502**, 180 (2001).
58. A. Bewick, K. Kunitatsu, S. Pons, J. W. Russell, *J. Electroanal. Chem.* **160**, 47 (1984). (b) S. Pons, *J. Electroanal. Chem.* **150**, 495 (1983).
59. C. Korzeniewski, S. Pons, *J. Vac. Sci. Tech. B* **3**, 1421, (1985).
60. J. D Mozo, M. Dominguez, E. Roldan, J. M. Rodrigues Mellado, *Electroanalysis* **12**, 767 (2000).
61. A. S. Viana, A. H. Jones, L. M. Abrantes, M. Kalaji, *J. Electroanal. Chem.* **500**, 290 (2001).
62. J. P. al Dulaimi, A. M. Bond, R. J. H. Clark, N. C. Harden, D. G. Humphrey, *J. Chem. Soc., Dalton Trans.* **12**, 2541 (2002).
63. D. A. Brevnon, E. Hutter, J. H. Fendler, *Appl. Spectrosc.* **2**, 58 (2004).
64. B. W. Johnson, J. Bauhofer, K. Doblhofer, B. Pettinger, *Electrochim. Acta* **37**(12), 2321 (1992).
65. W. Plieth, G. S. Wilson, G. C. de la Fe, *Pure Appl. Chem.* **70**, 1395 (1998).
66. Z. Q. Tian, B. Ren, "Raman Spectroscopy of Electrode Surfaces", in *Encyclopedia of Electrochemistry, Instrumentation and Electroanalytical*, A. J. Bard, M. Stratmann, P. R. Unwin, Eds., Wiley-VCH: Weinheim, 2003, Vol. 3, pp. 572–659.
67. (a) I. C. G. Thanos, *J. Electroanal. Chem.* **200**, 23 (1986). (b) A. J. McQuillan, P. J. Hendra, M. Fleischmann *J. Electroanal. Chem.* **65**, 933 (1975).
68. M. H. Schoenfisch, J. E. Pemberton, *Langmuir* **15**, 509 (1999).
69. J. E. Pemberton, A. Shen, *Phys. Chem. Chem. Phys.* **1**, 5671 (1999).
70. Q. Hu, A. S. Hinman, *Anal. Chem.* **72**, 3233 (2000).
71. T. E. Keyes, R. J. Forster, A. M. Bond, W. Miaou, *J. Am. Chem. Soc.* **123**, 2877 (2001).
72. R. J. Forster, T. E. Keyes, A. M. Bond, *J. Phys. Chem. B* **104**, 27, 6389 (2000).

73. We refer here to vibronic resonance Raman spectroscopy.
74. D. A. Long, *The Raman Effect*, Wiley: Chichester, UK, 2002.
75. T. E. Keyes, D. Leane, R. J. Forster, C. G. Coates, J. J. McGarvey, J. G. Vos, *Inorg. Chem.* **41**, 5721 (2002).
76. Z.-Q. Tian, B. Ren, D.-Y. Wu, *J. Phys. Chem. B* **106**, 37 (2002).
77. A. Campion, P. Kambhampati, *Chem. Soc. Rev.* **27**, 241 (1998).
78. (a) D. J. Maxwell, S. R. Emory, S. M. Nie, *Chem. Mater.* **13**(3), 1082 (2001). (b) S. Nie, S. R. Emory, *Science* **275**, 1102 (1997).
79. (a) Z. Q. Tian, B. Ren, D. Y. Wu, *J. Phys. Chem. B* **106**, 9463 (2002).
80. S. Zou, M. J. Weaver, *Anal. Chem.* **70**, 2387 (1988).
81. M. F. Mrozek, Y. Xie, M. J. Weaver, *Anal. Chem.* **73**, 5953 (2001).
82. M. F. Mrozek, S. A. Wasileski, M. J. Weaver, *J. Am. Chem. Soc.* **123**, 12817 (2001).
83. T. R. Jensen, M. D. Malinsky, C. L. Haynes, R. P. Van Duyne, *J. Phys. Chem. B* **104**, 10549 (2000).
84. M. Moskovits, *Rev. Mod. Phys.* **57**, 783 (1985).
85. L. A. Dick, A. D. McFarland, C. L. Haynes, *J. Phys. Chem. B* **106**, 853 (2002).
86. K. Kneipp, H. Kneipp, I. Itzkan, R. R. Dasar, M. S. Feld, *Chem. Rev.* **99**, 2957 (1999).
87. D. Y. Wu, Y. Xie, B. Ren, J. W. Yan, B. W. Mao, Z. Q. Tian, *Phys. Chem. Commun.* **18**, 1 (2001).
88. P. Gao, D. Gosztola, L-W. H. Leung, M. J. Weaver, *J. Electroanal. Chem.* **233**, 211 (1987).
89. S. Byahu, T. E. Furtak, *Langmuir* **7**, 508 (1991).
90. A. G. Brolo, D. E. Irish, G. Szymanski, J. Lipkowski, *Langmuir* **14**, 517 (1998).
91. Y.-Y. Song, Z.-D. Gao, J. J. Kelly, X.-H. Xia, *Electrochem. Solid State Lett.* **8**, 10, C148 (2005).
92. L. A. Dick, A. J. Haes, R. P. Van Duyne, *J. Phys. Chem. B* **104**, 11752 (2000).
93. Z. Q. Tian, B. Ren, *Ann. Rev. Phys. Chem.* **55**, 197 (2004).
94. Y. X. Chen, S. Z. Zou, K. Q. Huang, Z. Q. Tian, *J. Raman Spectrosc.* **29**, 749 (1998).
95. M. J. Weaver, *Top. Catal.* **8**, 65 (1999).
96. R. Kellner, B. Mizaihoff, M. Jakusch, H. D. Wanzenböck, N. Weissenbacher, *Appl. Spectrosc.* **5**, 495 (1997).
97. J. Shepherd, Y. Yang, D. Bizzotto, *J. Electroanal. Chem.* **524**, 54 (2002).
98. R. E. Gyurcsányi, E. Lindner, *Anal. Chem.* **77**, 2132 (2005).

This page intentionally left blank

Part Four

APPLICATIONS

This page intentionally left blank

– 15 –

Determination of Electrode Kinetics

Michael V. Mirkin

Department of Chemistry and Biochemistry,
Queens College—CUNY, Flushing, NY 11367, USA

15.1 INTRODUCTION TO KINETIC MEASUREMENTS

This chapter is concerned with measurements of kinetic parameters of heterogeneous electron transfer (ET) processes (i.e., standard heterogeneous rate constant k° and transfer coefficient α) and homogeneous rate constants of coupled chemical reactions. A typical electrochemical process comprises at least three consecutive steps: diffusion of the reactant to the electrode surface, heterogeneous ET, and diffusion of the product into the bulk solution. The overall kinetics of such a multi-step process is determined by its slow step whose rate can be measured experimentally. The principles of such measurements can be seen from the simplified equivalence circuit of an electrochemical cell (Figure 15.1).

According to Figure 15.1, electrons can be transferred across the electrode/solution interface via two parallel pathways, i.e., the faradaic process, which is represented by the charge transfer resistance and diffusion (Warburg) impedance connected in series, and the charging/discharging of the electrical double layer. In both cases, the current flows through solution, which is represented by the ohmic resistance R_s . The second pathway is important only if the electrode potential (or surface area) is changed rapidly, as in chronoamperometry, fast-scan voltammetry, or polarography. In this case, the kinetic parameters can be determined only after separating faradaic current from the double layer charging current. Under steady-state conditions, the charging current is negligibly small and the range of accessible kinetic parameters is determined by the values of R_{ct} , Z_w , and R_s . Clearly, the charge transfer resistance can be measured accurately only if it is much larger than the solution resistance. The R_{ct} value is inversely proportional to the standard rate constant of the charge transfer (CT) reaction, k° . Therefore, the magnitude of solution resistance is less important when relatively slow kinetics (i.e., $k^\circ \ll 0.1$ cm/sec) is measured. In contrast, fast electrode kinetics (e.g., $k^\circ > 0.1$ cm/sec) can be studied if the ohmic potential drop is either very small (e.g., at ultramicroelectrodes (UMEs) under steady-state conditions) or fully compensated.

Another requirement for successful measurement of heterogeneous kinetics is that R_{ct} must be at least comparable to Z_w , i.e., the overall process must not be diffusion controlled.

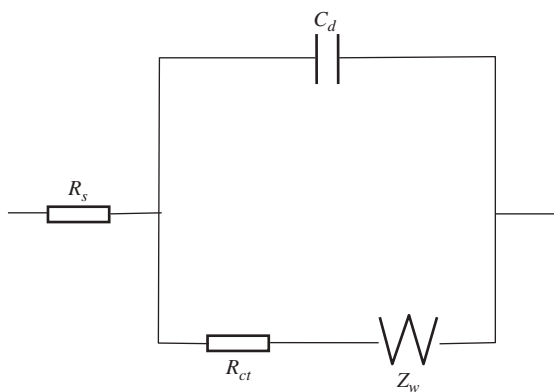


Figure 15.1 Equivalent circuit model of a simple electrochemical process. R_s is the solution resistance, R_{ct} is the charge transfer resistance, Z_w is the Warburg impedance, and C_d is the double layer capacitance.

When the ET rate is much slower than that of the mass transfer, the process is practically irreversible, and the determination of the kinetic parameters is relatively straightforward (see Section 2.1.1 in reference (1) for the discussion of electrochemical reversibility). In contrast, when the mass transfer and ET rates are comparable, the process is quasi-reversible and the kinetic analysis is more complicated.

The mass transfer rate can be expressed in terms of the mass transfer coefficient m . For uniformly accessible electrodes, the mass transfer coefficient can be defined as

$$m = i_1 / (nFAc^\circ) \quad (15.1)$$

where i_1 is the characteristic mass transfer current for a specific electrochemical method, e.g., diffusion limiting current in polarography or peak current in linear sweep voltammetry (2), n is the number of transferred charges, F is the Faraday constant, A is the electrode surface area, and c° is the bulk concentration of the reactant.

There are many ways to increase the mass transfer rate, e.g., by employing fast convection in hydrodynamic techniques or by applying high-frequency perturbation in impedance measurements. In this chapter, we will focus on two approaches: steady-state techniques and transient methods. In the former case, the high mass transfer rate is achieved by decreasing a suitable geometric parameter, e.g., the UME radius or the thickness of a thin-layer cell. However, to investigate fast heterogeneous reactions ($k^\circ \geq 1 \text{ cm/sec}$) under steady-state conditions one has to fabricate submicrometer-sized devices, which is not straightforward. In contrast, transient measurements are based on quick perturbation of electrochemical equilibrium and monitoring of the response on a sufficiently short experimental time scale. In this way, high mass transfer rates can be obtained with macroscopic electrodes or micrometer-sized UMEs. Unfortunately, the problems caused by resistive potential drop in solution and charging current, which are more significant at shorter times, often hamper the applications of transient techniques to fast kinetic measurements.

The kinetic parameters of a coupled homogeneous chemical reaction can be determined electrochemically as long as they affect the magnitude of the measured signal. Because of the large variety of possible multi-step processes, it is not easy to define the limits of measurable

homogeneous rate constants (they are typically described by kinetic zone diagrams applicable to specific mechanisms; see Chapter 12 in reference (1)). Generally, the time window of the electrochemical experiment should match the time scale of the homogeneous reaction. Thus, the need for a high mass transfer rate and the problems caused by uncompensated solution resistance and double layer charging current discussed above are equally important for studies of fast coupled chemical reactions.

In this chapter, we focus on extraction of kinetic parameters from experimental dependences generated by several widely used electrochemical methods. It is presumed that the reader is familiar with the fundamentals of those methods as well as with the basics of electrode kinetics discussed in the previous chapters of this handbook and in standard electrochemistry texts (1, 3).

15.2 HETEROGENEOUS ELECTRON TRANSFER: TRANSIENT METHODS

15.2.1 Linear sweep and cyclic voltammetry

The mass transfer coefficient in linear sweep voltammetry and cyclic voltammetry is directly proportional to the square root of the potential scan rate $v^{1/2}$. Accordingly, the apparent reversibility of an ET reaction under voltammetric conditions is determined by the value of the dimensionless parameter $\Lambda = k^\circ \sqrt{RT / FDv}$ (4), and the kinetic zones can be specified as follows:

Reversible: $\Lambda > 15$

Quasireversible: $15 \geq \Lambda \geq 10^{-2(1+\alpha)}$

Irreversible: $\Lambda < 10^{-2(1+\alpha)}$

Assuming common parameter values ($T = 298$ K, $D = 10^{-5}$ cm²/sec, and $\alpha = 0.5$), the quasi-reversibility limits can be defined in terms of k° and v : $0.3v^{1/2} \geq k^\circ \geq 2 \times 10^{-5}v^{1/2}$, where the unit of k° cm/sec and of v is in V/sec. In theory, by increasing v , one can render a completely reversible (Nernstian) electrode reaction quasi-reversible and even irreversible (i.e., totally controlled by ET kinetics) in order to determine its kinetic parameters. Practically, this approach is limited by the simultaneous increases in the double layer charging current and resistive potential drop in solution.

It is relatively easy to extract the kinetic parameters of a one-step irreversible ET reaction from a linear sweep voltammogram obtained at a large, e.g., mm-sized electrode (see Chapter 6 for discussion of the differences between macro- and microelectrode behaviors). The transfer coefficient α can be found from the slope of the linear dependence of the peak current vs. square root of the potential scan rate (i_p vs. $v^{1/2}$):

$$i_p = 2.99 \times 10^5 \alpha^{1/2} A c D^{1/2} v^{1/2} \quad (15.2)$$

The same parameter can also be found from the difference between the peak potential E_p and the half-peak potential:

$$\alpha = \frac{47.7 \text{ mV}}{|E_p - E_{p/2}|} \text{ (at } 25^\circ\text{C}) \quad (15.3)$$

where $E_{p/2}$ is the potential where the current equals one half of the peak value. The standard rate constant of a one-electron reduction reaction can be found from equation (15.4):

$$E_p = E^\circ - \frac{RT}{\alpha F} \left[0.78 - \ln \frac{D_o^{1/2}}{k^\circ} + 0.5 \ln \frac{\alpha Fv}{RT} \right] \quad (15.4)$$

where E° is the formal potential and D_o is the diffusion coefficient of oxidized species.

The task to measure quasi-reversible kinetic parameters is more common than the analysis of completely irreversible voltammograms. The method developed by Nicholson (5) for extraction of standard rate constants from quasi-reversible cyclic voltammograms (CVs) has been most frequently used (and misused) during the last four decades. The method of Nicholson became so popular because of its extreme simplicity. The only required experimental parameter is the difference of two peak potentials, $\Delta E_p = |E_{pa} - E_{pc}|$, where E_{pa} and E_{pc} are the potentials of the anodic and cathodic peaks, respectively. Nicholson showed that ΔE_p is a function of the single dimensionless kinetic parameter,

$$\psi = \frac{(D_o / D_R)^{\alpha/2} k^\circ}{(\pi D_o v F / RT)^{1/2}} \quad (15.5)$$

After measuring the ΔE_p value, one can use Table 15.1 to find the corresponding value of ψ (5). When the transfer coefficient is within the range $0.3 < \alpha < 0.7$, which is most common for simple ET reactions, the ΔE_p value is essentially independent of α . Moreover, the diffusion coefficients of oxidized and reduced species are typically similar. Therefore $(D_o / D_R)^{\alpha/2} \approx 1$, and the k° value can be easily calculated from equation (15.5).

Although Nicholson's method has been used extensively to determine the rate constants of quasi-reversible ET reactions, it must be employed judiciously to avoid getting totally

Table 15.1

Variation of ΔE_p with ψ at 25 °C

Ψ	ΔE_p (mV)
20	61
7	63
6	64
5	65
4	66
3	68
2	72
1	84
0.75	92
0.5	105
0.35	121
0.25	141
0.10	212

misleading results. The most common source of error is the uncompensated ohmic potential drop, which may increase the peak separation and produce severe underestimation of the rate constant. Also a ΔE_p value can be extracted from any cyclic voltammogram including a distorted curve whose shape significantly deviates from the theory. Such deviations may be caused by a number of factors including adsorption, charging current, etc. Therefore, it may be safer to fit the entire voltammogram to the theory (e.g., by using DigiSim program discussed in Section 15.4.3) than to use the values of two peak potentials. Alternatively, the results of Nicholson's analysis can be validated by calculating theoretical curves using the determined parameter values and comparing them to experimental voltammograms obtained at different scan rates.

In addition to analysis of CVs obtained at macroscopic planar electrodes, the approaches discussed above are applicable to fast-scan voltammetry at UMEs. The faradaic response of an UME is essentially equivalent to that of a "large" planar electrode if $v \gg RTD/nFa^2$ (for discussion, see reference (1, p. 232)), where a is the radius of a UME. At high sweep rates, a very high mass transfer rate can be obtained, and the problems associated with the resistive potential drop and charging current are less severe for UMEs than for macroelectrodes. By carefully choosing the experimental conditions to keep both factors under control, and using background subtraction, one can obtain ultra-fast CVs—e.g., up to 1 MV/sec (6)—in a good agreement with the theory and use them to determine fast heterogeneous rate constants (Figure 15.2).

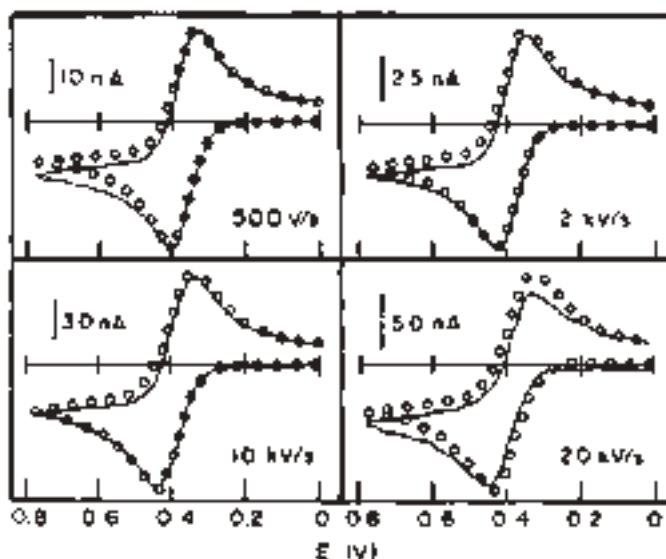


Figure 15.2 Voltammograms with background current subtracted for the oxidation of 2 mM ferrocene in acetonitrile containing 0.6 M tetraethylammonium perchlorate obtained at a 5- μm -radius gold disk electrode. Solid lines: experimental data. Open circles: simulated data for $k^\circ = 3.1 \text{ cm/sec}$ and $\alpha = 0.5$. Reprinted with permission from reference (7). Copyright 1988 American Chemical Society.

15.2.2 Sampled-current voltammetry

A large number of potential-relaxation and current-relaxation techniques have been developed in 1950s–1980s for fast kinetic measurements (8). The later advances in UMEs resulted in a less frequent use of relaxation techniques in kinetic experiments. Because of the space limitations, only one large-perturbation method (sampled-current voltammetry) and one small-perturbation technique (alternating current voltammetry) will be considered.

In sampled-current voltammetry, a sigmoidal current vs. potential curve is obtained by applying several potential steps (from the rest potential to the desired value) to the working electrode and recoding current at the same sampling time ($t = \tau$) after the beginning of each step. The mass transfer coefficient in this method is inversely proportional to $\tau^{1/2}$, so that the given electrode process can be fully reversible at a long sampling time, quasi-reversible at shorter τ , and irreversible at very short sampling times. As discussed above, the practical limit for τ is determined by the resistive and capacitive effects, which impair short-time measurements at macroelectrodes.

Equation (15.6) describes the shape of a sampled-current voltammogram for a general case of a quasi-reversible ET reaction:

$$\frac{i}{i_d} = \frac{F_1(\lambda)}{1 + \xi\theta_1} \quad (15.6)$$

where i_d is the Cottrell current, $\xi = \sqrt{D_o/D_R}$, $\theta_1 = \exp[RT/F(E - E^\circ)]$, $F_1(\lambda) = \pi^{1/2}\lambda\exp(\lambda^2)\operatorname{erfc}(\lambda)$,

$$\lambda = \frac{k_f\tau^{1/2}(1 + \xi\theta_1)}{D_o^{1/2}} \quad (15.7)$$

and $k_f = k^\circ \exp[-\alpha nF(E - E^\circ)/RT]$ for a reduction reaction following Butler–Volmer kinetics.

The kinetic zones in sampled-current voltammetry are determined by the value of the kinetic parameter $\lambda^\circ = k^\circ\tau^{1/2}(1 + \xi)/D_o^{1/2}$, and the quasi-reversibility region can be expressed as $10^{-2\alpha} \leq \lambda^\circ \leq 2$ (for details, see reference (1, p. 196)).

The most general way to determine kinetic parameters from sampled-current voltammetry is to fit an experimental i/i_d vs. E dependence to the theory [equation (15.6)] using k° , α , and E° as adjustable parameters. This can be done using a number of commercially available programs, e.g., TableCurve 2D.

Alternatively, one can determine k_f point-by-point by calculating $F_1(\lambda)$ from the experimental i/i_d values using equation (15.6), and then finding λ either numerically or from the table of F_1 function. Once λ is determined, one can use equation (15.7) to calculate k_f for a given E , provided that both D_o and E° values are known. α and k° can be found from the slope and the intercept of the linear $\ln k_f$ vs. E plot, respectively.

In the case of a totally irreversible voltammogram, equation (15.6) is simplified to yield

$$\frac{i}{i_d} = F_1(\lambda) \quad (15.8)$$

where $\lambda = k_f \tau^{1/2} / D_0^{1/2}$. Although the kinetic parameters can be found either by curve fitting or calculated point-by-point using equation (15.8), simpler analytical expressions can be used in this case. k° and α can be found from the intercept and the slope of the $E_{1/2}$ vs. $\ln(\tau^{1/2})$ dependence, respectively:

$$E_{1/2} = E^\circ + \frac{RT}{\alpha F} \ln \left(\frac{2.31k^\circ \tau^{1/2}}{D_0^{1/2}} \right) \quad (15.9)$$

Alternatively, from the difference of two quartile potentials $|E_{3/4} - E_{1/4}|$, where $E_{1/4}$ and $E_{3/4}$ are the potential values at which $i = \frac{1}{4}i_d$ and $i = \frac{3}{4}i_d$, respectively, one can find α using Tomeš criterion:

$$|E_{3/4} - E_{1/4}| = 45.0 \text{ mV}/\alpha \quad (15.10)$$

When α is determined, equation (15.9) can be used to calculate k° .

15.2.3 Ac voltammetry

Ac voltammetry is one of the techniques based on the analysis of faradaic impedance. A low-amplitude sinusoidal voltage (E_{ac}) is applied to the working electrode, which is also biased at some dc potential (E_{dc}) with respect to the reference electrode. Because of the difference in the time scale, the ac component of the total current can be readily separated from the dc component. The kinetic parameters can be extracted either from the amplitude of ac current, which is measured as a function of E_{dc} , or from the phase angle between the ac current and ac voltage, ϕ .

There are several modifications of this technique. In ac polarography, which employs a dropping mercury working electrode, E_{dc} is changed step-wise (one step per drop lifetime) and the diffusion layer is completely renewed after every drop fall. In linear sweep ac voltammetry, the working electrode is stationary, and E_{dc} is a linear function of time. However, when the sweep rate is slow, the polarographic and voltammetric responses are quite similar, and we will neglect the difference between those two modifications. For more details, one should consult Chapter 10 in reference (1) and the review articles cited therein.

The equivalent circuit corresponding to an uncomplicated electrochemical reaction (i.e., a one-step CT process) is shown in Figure 15.1. An important advantage of ac voltammetry is that it allows relatively easy evaluation of the solution resistance (R_s) and double layer capacitance (C_d). These elements can be separated from the Z_w and R_{ct} components, which together make faradaic impedance. Without simplifying assumptions, the analysis of faradaic impedance even for a simple ET reaction is rather complicated (9). The commonly used assumptions are that the dc and ac components of the total current can be uncoupled, and the dc response is Nernstian because of the long dc time scale. The latter assumption is reasonable because ac voltammetry is typically used to measure fast electrode kinetics. The ac response of the same electrochemical process may be quasi-reversible on the much shorter ac time scale. Quasi-reversible ac voltammograms are bell-shaped,

and at the high-frequency limit both the peak potential and the peak current become independent of ac frequency, according to equations (15.11a) and (15.11b):

$$E_p = E_{1/2} + \frac{RT}{F} \ln \frac{1-\alpha}{\alpha} \quad (15.11a)$$

$$I_p = \frac{F^2 A k^\circ c^\circ \Delta E \zeta^\alpha}{RT} (1-\alpha)^{(1-\alpha)} \alpha^\alpha \quad (15.11b)$$

Although it is possible to determine α from the peak potential [equation (15.11a)] and then use its value to find k° from equation (15.11b), it is more common to extract the kinetic parameters from the phase angle ϕ . The dependence of $\cot\phi$ on the ac frequency (ω) and dc potential is given by equation (15.12), which is valid for both quasi-reversible and irreversible ET kinetics:

$$\cot\phi = 1 + \frac{(2D_R \zeta^\beta \omega)^{1/2}}{k^\circ} \frac{1}{e^{(1-\alpha)F(E_{dc} - E_{1/2})/RT} [1 + e^{-F(E_{dc} - E_{1/2})/RT}]} \quad (15.12)$$

Kinetic parameters can be determined by fitting experimental $\cot\phi$ vs. $(E_{dc} - E_{1/2})$ dependences obtained at different ac frequencies to equation (15.12) (10).

At $E_{dc} = E_{1/2}$, equation (15.12) is simplified to yield

$$\cot\phi = 1 + \frac{(0.5D_R \zeta^\beta \omega)^{1/2}}{k^\circ} \quad (15.13)$$

Assuming $D_o \cong D_R$, one can find the standard rate constant from the slope of the linear $\cot\phi$ vs. $\omega^{1/2}$ plot (Figure 15.3).

More recently, ac voltammetry was carried out at μm -sized UMEs to further diminish the effect of the resistive potential drop in studies of fast ET reactions (11). These experiments yielded kinetic parameters for several rapid electrode processes in agreement with the results obtained by steady-state techniques.

15.3 HETEROGENEOUS ELECTRON TRANSFER: STEADY-STATE METHODS

15.3.1 Steady-state voltammetry

There are several ways of obtaining a time-independent (steady-state or pseudo-steady-state) voltammogram. For example, in classical polarography, the current is time dependent, but by measuring it at a same fixed moment during the lifetime of each drop one can obtain a pseudo-steady-state current-potential curve, i.e., a polarogram. True steady-state voltammograms are obtained at a rotating disk electrode, as well as with thin-layer electrochemical cells, and at various UMEs, e.g., microdisks, rings, and spherical caps (12). Steady-state voltammetry is one of the best techniques for studying fast electrochemical kinetics. Its important advantages over the transient methods include the absence of the limitations caused by the charging current (and also ohmic potential drop in the case of UME

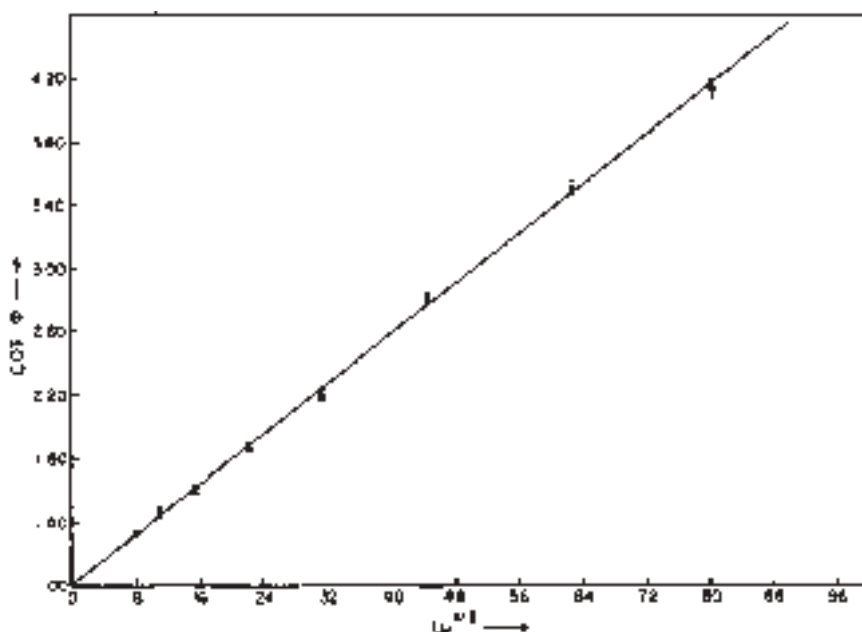


Figure 15.3 Frequency dependence of phase angle with 3.36 mM TiCl_4 in 0.2 M $\text{H}_2\text{C}_2\text{O}_4$. $\Delta E = 5.00 \text{ mV}$, $E_{dc} = -0.290 \text{ V}$ vs. SCE, $T = 25^\circ\text{C}$. Reprinted with permission from reference (10). Copyright 1963 American Chemical Society.

experiments), insensitivity to low levels of reactant adsorption, relative simplicity of data acquisition, high accuracy, and reproducibility of the results.

Unlike transient methods, the theory for steady-state techniques is relatively simple. Equation (15.14) describes the shape of a steady-state voltammogram at any uniformly accessible working electrode (i.e., when the surface concentrations and diffusion fluxes of redox species are uniform over the entire electrode surface):

$$\frac{i}{i_d} = \frac{1}{\theta + 1/\kappa} \quad (15.14)$$

where $\theta = 1 + \exp[nF(E - E^\circ)/RT]m_o/m_r$, $\kappa = k^o \exp[-\alpha nF(E - E^\circ)/RT]/m_o$. The mass transfer coefficients of oxidized and reduced species, m_o and m_r , can be calculated from equation (15.1).

No general analytical expression similar to equation (15.14) is available for a steady-state current vs. potential curve at an electrode whose surface is not uniformly accessible. An exception is a microdisk electrode for which an analytical approximation (15.15) provides an accurate description of a quasireversible steady-state voltammogram (13)

$$\frac{\partial i}{i_d} = \left[1 + \frac{\pi}{\kappa' \theta} \frac{2\kappa' \theta + 3\pi}{4\kappa' \theta + 3\pi^2} \right]^{-1} \quad (15.15)$$

where $\kappa' = (\pi a k^\circ / 4 D_0) \exp[-\alpha n F (E - E^\circ') / RT]$ and a is the disk radius.

If the process is totally irreversible, equation (15.14) is simplified as follows:

$$\frac{i}{i_d} = \frac{1}{1 + 1/\kappa} \quad (15.16)$$

The kinetic analysis in this case is rather straightforward. The transfer coefficient can be determined directly from the difference of two quartile potentials

$$\alpha = 56.4 \text{ mV}/|E_{3/4} - E_{1/4}| \quad (15.17)$$

Next, one can use equation (15.16) to obtain κ for a specific potential value and calculate $k^\circ = \kappa m_0 \exp[\alpha n F (E - E^\circ') / RT]$. To use this approach one needs the formal potential value E°' , which may not be readily available for a totally irreversible reaction.

For quasi-reversible processes, both kinetic parameters, k° and α , and also the formal potential can be determined from the differences of quartile potentials, $\Delta E_{1/4} = |E_{1/2} - E_{1/4}|$ and $\Delta E_{3/4} = |E_{3/4} - E_{1/2}|$ (14). To obtain the parameter values, one has to carefully measure the diffusion limiting current and find the quartile potential values (for reliable determination of a fast rate constant, the uncertainty in both $\Delta E_{3/4}$ and $\Delta E_{1/4}$ values should be ≤ 0.5 mV). Two extensive tables are available in reference (14) for uniformly accessible electrodes and for the microdisk geometry. The k° , α , and E°' values can be found in the table cell corresponding to the experimentally determined $\Delta E_{1/4}$ and $\Delta E_{3/4}$. This method provides two useful diagnostic criteria: (i) the inequality $|\Delta E_{3/4}| > |\Delta E_{1/4}|$ holds true for any undistorted quasi-reversible voltammogram; and (ii) reliable values of kinetics parameters can only be obtained if $\Delta E_{1/4} \geq 30.5$ mV and $\Delta E_{3/4} \geq 31$ mV (otherwise the voltammogram is essentially Nernstian). For a microdisk electrode, the upper limit for the measurable rate constant can be estimated as $k^\circ \leq 5D/a$. Taking $D = 10^{-5}$ cm/sec, this limit is ~ 0.5 cm/sec for a 1-μm-radius UME.

The advantages and disadvantages of the three-point method are similar to those of the Nicholson's method discussed above. The analysis is very fast and simple, and requires no calculations. On the other hand, from the $\Delta E_{1/4}$ and $\Delta E_{3/4}$ values alone one cannot detect imperfections in the shape of the voltammogram caused by uncompensated resistance, electrode surface fouling, and other experimental problems. An alternative approach is to fit the entire experimental voltammogram to either equation (15.14) or equation (15.15) using a suitable curve-fitting computer program.

15.3.2 Scanning electrochemical microscopy (SECM)

Scanning electrochemical microscopy (SECM) (see Chapter 12) combines useful features of UMEs and thin-layer cells. The mass transfer rate in SECM is a function of the tip-substrate distance d . For an UME far from a substrate, the mass transfer coefficient, $m \sim D/a$, while for the tip near a conductive substrate ($d < a$), $m \sim D/d$. By decreasing the tip-substrate distance, the mass transport rate can be increased sufficiently for quantitative characterization of the ET kinetics, preserving the advantages of steady-state methods, i.e., the absence of problems associated with ohmic drop, adsorption, and charging current. For example, with

$D = 10^{-5}$ cm²/sec, $d = 0.1$ μm corresponds to $m = 1$ cm/sec. This gives the upper limit for the determinable rate constant of about 10 cm/sec.

SECM theory has been developed for extraction of kinetic parameters of heterogeneous ET reactions occurring at both tip and substrate electrodes. If the mediator regeneration at the substrate is diffusion-controlled, the finite kinetics at the tip can be extracted from steady-state tip voltammograms (15). Conversely, when the tip process is diffusion-controlled, the finite kinetics at the substrate can be extracted from the tip current vs. distance curves (16). For the former situation, two approximate equations have been proposed for calculating the tip current at any potential and separation distance values (15). However, more recent simulations (17) showed that both equations in reference (15) are not very accurate and may yield underestimated k° values. Equation (15.18) is a significantly better approximation:

$$I_T(E, L) = \frac{0.78377}{L(\theta + 1/\kappa)} + \frac{0.68 + 0.3315 \exp(-1.0672/L)}{\theta \left[1 + \frac{\pi}{\kappa\theta} \frac{2\kappa\theta + 3\pi}{4\kappa\theta + 3\pi^2} \right]} \quad (15.18)$$

where $\kappa = \pi k^\circ a \exp[-\alpha nF(E - E^\circ)/RT]/(4D_O I_T^c)$ and $\theta = 1 + \exp[nF(E - E^\circ)/RT]D_O/D_R$, E is the tip potential, $L = d/a$ is the normalized tip/substrate separation distance, and I_T^c is the normalized tip current for the same L and a diffusion-controlled positive feedback at a conductive substrate

$$I_T^c = 0.68 + 0.78377/L + 0.3315 \exp(-1.0672/L) \quad (15.19)$$

At a constant L , equation (15.18) describes a quasi-reversible steady-state voltammogram of a reduction reaction at the tip. Kinetic parameters can be determined either by fitting steady-state voltammograms to this equation or by using the three-point method (14) and assuming uniform accessibility of the tip surface, as discussed in the previous section. In this way, the kinetics of the fast oxidation of ferrocene at a Pt tip electrode was measured (15). The reproducible standard rate constant value (3.7 ± 0.6 cm/sec) was obtained at different tip/substrate distances (Figure 15.4). Thus, one can check the validity of the experimental results and the reliability of the kinetic analysis.

While the mass transfer rate in Figure 15.4 increased with a decrease in the tip-substrate separation, the heterogeneous rate constant and transfer coefficient remained constant within the range of experimental error.

The rate constant of an irreversible heterogeneous reaction occurring at the substrate (k_f) can be extracted by fitting an experimental current-distance curve to equation (15.20) (16):

$$I_T(L) = I_S(1 - I_T^{\text{ins}}/I_T^c) + I_T^{\text{ins}} \quad (15.20a)$$

$$I_S = 0.78377/L(1 + 1/\Lambda) + [0.68 + 0.3315 \exp(-1.0672/L)]/[1 + F(L, \Lambda)] \quad (15.20b)$$

where I_T^c and I_T^{ins} are given by equations (15.19) and (15.21), respectively; I_S is the normalized kinetically controlled substrate current; $\Lambda = k_f d/D$, and $F(L, \Lambda) = (11/\Lambda + 7.3)/(110 - 40L)$

$$I_T^{\text{ins}} = 1/(0.15 + 1.5385/L + 0.58 \exp(-1.14/L) + 0.0908 \exp[(L - 6.3)/(1.017L)]) \quad (15.21)$$

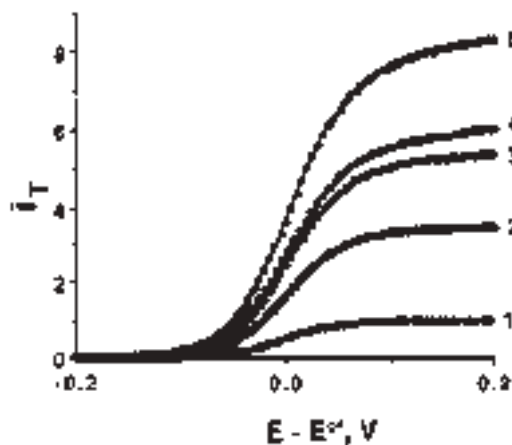


Figure 15.4 Tip steady-state voltammograms for the oxidation of 5.8 mM ferrocene in 0.52 M TBABF₄ in acetonitrile at a 1.08- μ m-radius Pt tip. Solid lines calculated from equation (15.25) in reference (15). Tip/substrate normalized separation decreases are $L = \infty$ (1), 0.27 (2), 0.17 (3), 0.14 (4), and 0.10 (5). Reprinted with permission from reference (15). Copyright 1988 American Chemical Society.

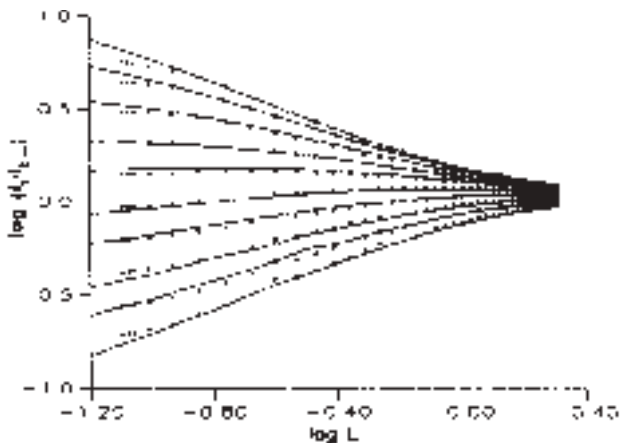


Figure 15.5 SECM current vs. distance curves for the Fe(III)/Fe(II) system (symbols) and the best theoretical fits to the data (solid curves). The tip (5.5- μ m-radius carbon fiber electrode) was held at a potential of -0.6 V, while the GC substrate electrode was held at various potentials, 300–750 mV, positive of the formal potential (50 mV increments). Reprinted with permission from reference (18). Copyright 1992 American Chemical Society.

Figure 15.5 shows a family of the SECM approach curves obtained at different substrate potentials. Fe³⁺ was reduced at a carbon fiber tip, and the product of this reaction (Fe²⁺) was reoxidized at a glassy-carbon substrate. The rate of the irreversible oxidation of Fe²⁺ increased with increasing substrate potential (from the bottom to the top curve).

A heterogeneous rate constant value corresponding to the specific substrate potential was extracted by fitting each current-distance curve to the theory.

The radius of the portion of the substrate surface participating in the SECM feedback loop can be evaluated as $r \geq a + 1.5d$ (18). Thus at small tip-substrate separations (e.g., $L \leq 2$), a large substrate behaves as a virtual UME of a size comparable with that of the tip electrode. The SECM allows probing local kinetics at a small portion of the macroscopic substrate with all of the advantages of microelectrode measurements.

One should keep in mind that equations (15.19)–(15.21) are valid for $RG = 10$. Deviations of the experimental approach curves from theory can be expected when a tip with a very small RG (e.g., < 3) is used and the kinetics is relatively slow (i.e., $k_f \leq D/d$).

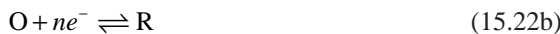
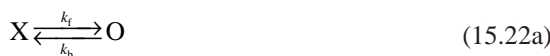
15.4 PROCESSES WITH COUPLED HOMOGENEOUS REACTIONS

15.4.1 Linear sweep and cyclic voltammetry

Since the 1960s, cyclic voltammetry has been the most widely used technique for studies of electrode processes with coupled chemical reactions. The theory was developed for numerous mechanisms involving different combinations of reversible, quasi-reversible, and irreversible heterogeneous ET and homogeneous steps. Because of space limitations, we will only consider two well-studied examples— C_rE_r (i.e., first-order reversible reaction preceding reversible ET) and E_rC_i (i.e., reversible ET followed by a first-order irreversible reaction)—to illustrate general principles of the coupled kinetics measurement. A detailed discussion of other mechanisms can be found in Chapter 12 of reference (1) and references cited therein, including a seminal publication by Nicholson and Shain (19).

The kinetic analysis of a complicated electrochemical process involves two crucial steps: the validation of the proposed mechanism and the extraction of the kinetic parameter values from experimental data. In cyclic voltammetry, the variable factor, which determines the mass transfer rate, is the potential sweep rate v . Therefore, the kinetic analysis relies on investigation of the dependences of some characteristic features of experimental voltammograms (e.g., peak potentials and currents) on v . Because of the large number of factors affecting the overall process rate (concentrations, diffusion coefficients, rate constants, etc.), such an analysis may be overwhelming unless those factors are combined to form a few dimensionless kinetic parameters. The set of such parameters is specific for every mechanism. Also, the expression of the potential and current as normalized (dimensionless) quantities allows one to generalize the theory in the form of dimensionless working curves valid for different values of kinetic, thermodynamic, and mass transport parameters.

In the C_rE_r process, an electroinactive species X is converted into the oxidized species O via reversible chemical reaction (15.22a) preceding reversible ET (15.22b):



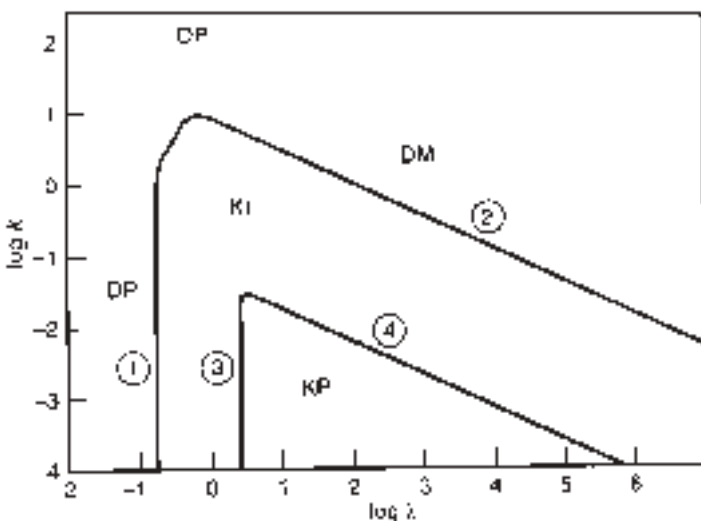


Figure 15.6 Zone diagram for C_rE_r process. The zones are DP, pure diffusion; KI, intermediate kinetics; KP, pure kinetics; and DM, diffusion modified by equilibrium constant of preceding reaction. Adapted with permission from reference (20). Copyright 1963 Pergamon Press.

The appropriate dimensionless kinetic parameters are $K = k_f/k_b$ and $\lambda = (RT/nF)[(k_f + k_b)/v]$. Using these parameters, the voltammetric behavior of a C_rE_r process can be summarized in a zone diagram (Figure 15.6).

The small $\log \lambda$ (i.e., large v) values in Figure 15.6 correspond to the pure diffusion regime (DP). In this zone, reaction (15.22a) is slow on a short experimental time scale and does not significantly affect the concentrations of the redox species in the electrode proximity. The chemical kinetics is too slow to be measured. At higher λ values (smaller v), the process shifts to the intermediate kinetic zone (KI), where the response is under mixed diffusion/kinetic control. By further decreasing the sweep rate, one can reach the pure kinetic zone (KP). Finally, if the sweep rate is slow and the equilibrium constant, K is sufficiently large (zone DM), reaction (15.22a) comes to equilibrium. The process behavior is diffusion-controlled, but the current magnitude depends on the K value.

These features can also be seen in a family of working curves calculated for $K = 10^{-4}$ (Figure 15.7) (20). When $\lambda \leq 0.1$, the process is diffusion-controlled, i.e., E_p is independent of the sweep rate, and $i_p \sim v^{1/2}$. $0.1 \leq \lambda \leq 1$ corresponds to the KI zone, where the voltammograms gradually change from peak-shaped to sigmoidal. Sigmoidal (S-shaped) curves obtained for $1 \leq \lambda \leq 100$ represent the KP zone. The current is independent of v , and at extreme potentials it reaches the plateau value

$$i_L = nFAD^{1/2}c^\circ K(k_f + k_b)^{1/2} \quad (15.23a)$$

The “half-plateau” potential of such a voltammogram (i.e., the potential at which $i = 0.5i_L$) is

$$E_{p/2} = E^\circ - \frac{RT}{2nF}(\ln \lambda + 0.554) \quad (15.23b)$$

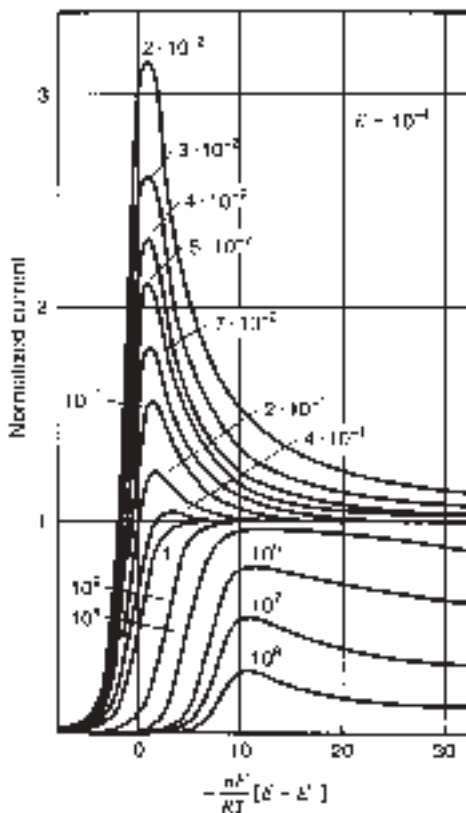


Figure 15.7 Dimensionless linear sweep voltammograms of $C_r E_r$ process calculated for different values of λ shown on each curve and $K = 10^{-4}$. Adapted with permission from reference (20). Copyright 1963 Pergamon Press.

At $\lambda \geq 1000$, the mixed diffusion/kinetic control becomes apparent again (KI zone), and finally, the DM zone is reached at very low scan rates ($\lambda \geq 10^6$).

The kinetic analysis of a $C_r E_r$ process requires a series of experimental voltammograms obtained at various scan rates. The changes in the voltammogram shape with v similar to those shown in Figure 15.6 would be indicative of the $C_r E_r$ mechanism. The next step is to fit the experimental voltammograms to theoretical curves that can be produced by digital simulation (see Section 15.4.3) or generated from the current function tabulated in reference (19), and to extract the rate constant values. The k_f and k_b values are constant and independent of v thus confirming the validity of the proposed mechanism.

The k_f and k_b values can also be determined from a sigmoidal voltammogram obtained under complete kinetic control. Using equation (15.23b), one can obtain λ from the $E_{p/2}$ of such a curve and use it to calculate the sum of two rate constants, $k_f + k_b$. Then, equation (15.23a) can be used to find K from the plateau current. With both λ and K known, the calculation of k_f and k_b is straightforward.

The kinetic behavior of a E_rC_i process



is determined by the single dimensionless kinetic parameter, $\lambda = (RT/nF)(k/v)$, and the corresponding zones are

KP (pure kinetic control): $\lambda > 5$

KI (intermediate kinetic zone): $5 \geq \lambda \geq 0.1$

DP (pure diffusion control): $\lambda < 0.1$

A dramatic effect of v on the voltammogram shape can be seen in Figure 15.8.

In the DP zone (e.g., at $\lambda = 0.01$), the following reaction is too slow to be detected, and the corresponding voltammogram is essentially indistinguishable from CVs of a simple, diffusion-controlled ET. At a lower v (e.g., $\lambda = 0.1$; KI zone), reaction (15.24b) becomes sufficiently fast to compete with diffusion. A significant fraction of species R is converted to electroinactive X before being reoxidized at the electrode surface during the potential sweep in the reverse (anodic) direction. Hence, the decreased height of the reverse peak. The disappearance of the reverse peak at slower v ($\lambda = 10$ or 500; KP zone) is typical of an irreversible chemical reaction following the ET step.

The value of λ , and subsequently the rate constant of reaction (15.24b), can be obtained by measuring the difference between the peak potential and $E_{1/2}$. The following equation shows that in the KP region this quantity is a linear function of $\ln v$:

$$E_p - E_{1/2} = \frac{RT}{2nF}(\ln \lambda - 1.56) \quad (15.25)$$

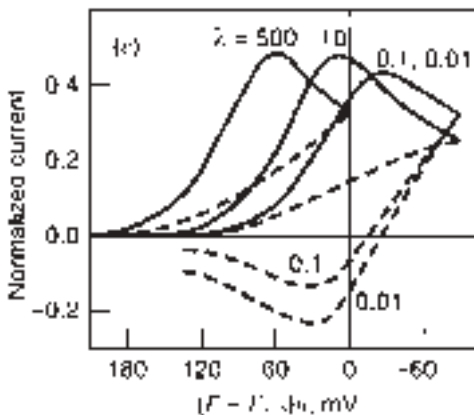


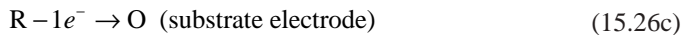
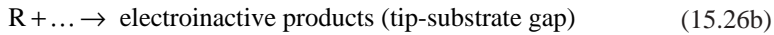
Figure 15.8 Dimensionless cyclic voltammograms of E_rC_i process calculated for different values of λ shown on each curve. Reprinted with permission from reference (19). Copyright 1964 American Chemical Society.

Alternatively, λ can be found from the ratio of the reverse and forward voltammetric peaks (i_{pa}/i_{pc}) using a working curve presented in reference (19).

15.4.2 Scanning electrochemical microscopy (SECM)

Unlike heterogeneous kinetics measurements, which typically employ the feedback mode of the SECM operation (see Chapter 12), homogeneous rate constants are often determined using the tip generation/substrate collection (TG/SC) mode. A TG/SC experiment includes simultaneous measurements of both tip and substrate currents (i_T and i_S). For a one-step heterogeneous ET at steady-state, these quantities are almost identical, if L is not very large (the collection efficiency, i_S/i_T , is more than 0.99 at $L \leq 2$). Under these conditions, the tip-generated species predominantly diffuse to the large substrate, rather than escape from the tip-substrate gap. For a process with a coupled chemical reaction, there are large differences between i_S and i_T , and both quantities provide important kinetic information.

Under TG/SC conditions, the homogeneous chemical reaction competes with diffusion in the tip/substrate gap. For example, consider an ET process followed by an irreversible homogeneous reaction of any order



If both heterogeneous processes at the tip and substrate are rapid (at extreme potentials of both electrodes), the overall process rate is controlled either by diffusion in the gap or by the rate of homogeneous chemical reaction (15.26b). If that reaction is slow, the process is diffusion-controlled, the i_T vs. d curves follow the positive feedback theory, and $i_S/i_T \rightarrow 1$ at short separation distances. If reaction (15.26b) is very fast, most species R get converted to electroinactive products before reaching the substrate. Hence, the very low substrate current, and $i_S/i_T \rightarrow 0$. Between these two extreme cases, the kinetics of reaction (15.26b) can be determined by measuring the collection efficiency as a function of L . A family of theoretical working curves showing the collection efficiency as a function of the dimensionless rate constant (K) is shown in Figure 15.9. As one can expect, i_S/i_T increases with decreasing L and K .

The TG/SC theory was developed for several mechanisms; E_rC_{2i} (ET followed by second-order irreversible dimerization of the product) (21), E_rC_i (22), and more complicated ECE/DISP mechanisms involving two ET steps (23). In all cases, the kinetics have to be found by fitting the experimental approach curves to theoretical curves generated by numerically solving two-dimensional diffusion equations. These procedures are rather complicated, and here we consider only the determination of E_rC_i and E_rC_{2i} rate constants based on analytical approximations (24). A comprehensive discussion of the SECM studies of coupled chemical reactions is available (25).

For each mechanism, i_S/i_T is determined by the single dimensionless parameter κ . In case of the E_rC_i mechanism, $\kappa = k_c d^2/D$; and for E_rC_{2i} , $\kappa = c^\circ kd^3/aD$. Two analytical approximations can be used to relate κ to collection efficiency (24)

$$\kappa = 5.608 + 9.347 \exp(-7.527x) - 7.616 \exp(-0.307/x) \quad (E_rC_i) \quad (15.27a)$$

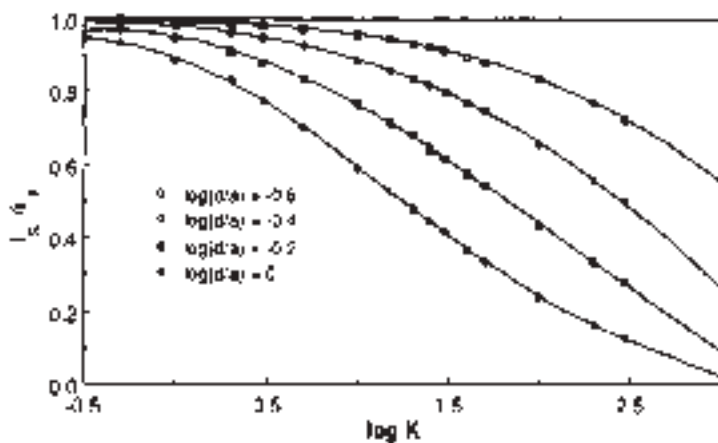


Figure 15.9 Simulated SECM collection efficiency (i_S/i_T) vs. K dependences for the E_rC_{2i} mechanism. The tip/substrate separation distances corresponding to each curve are shown. $K = ka^2c^0/D$. Reprinted with permission from reference (21). Copyright 1992 American Chemical Society.

and

$$\kappa = 104.87 - 9.948x - 185.89/x^{1/2} + 90.199/x + 0.389/x^2 \quad (E_rC_{2i}) \quad (15.27b)$$

where $x = i_S/i_T$. The collection efficiency values most suitable for determination of k are those between about 0.2 and 0.8.

To find the collection efficiency experimentally, one has to measure both i_S and i_T values as functions of d . This is possible if the substrate current is produced only by oxidation/reduction of species generated at the tip (i.e., $i_S = 0$ at large d). If the substrate current cannot be measured accurately, the collection efficiency can be calculated from the experimental tip current vs. distance curve using equation (15.28):

$$i_S/i_T = (1 - I_T^{\text{ins}}/I_T)/[1 - f(L)] \quad (15.28)$$

which can be derived from equation (15.20a); $f(L) = I_T^{\text{ins}}/I_T^c$.

Most other electrochemical techniques employed for homogeneous kinetics studies are also based on the generation/collection scheme. Among them is the rotating ring-disk method (the employed probe comprises concentrical disk generator and ring collector electrodes), which has been very popular before the introduction of UMEs (26). A more recent and powerful approach employing arrays of parallel microband electrodes has been reviewed in reference (27).

15.4.3 Simulations and curve fitting

The theory for most systems involving coupled chemical reactions is rather complicated. Analytical approximations are available only for a limited number of relatively simple processes. “Semi-analytical” solutions based on infinite series, integral equations, tabulated

functions, etc., are available for some systems (see reference (19) for several useful examples of such solutions). In general—especially for multi-dimensional UME diffusion problems—numerical solution of partial differential equations is required to generate theoretical curves; this complicates the extraction of the kinetic parameters from experimental data.

Since Feldberg's pioneering publication (28), many approaches to numerically solving electrochemical diffusion problems—"digital simulation"—have been developed to treat various mechanisms and electrode geometries. A more recent trend has been from developing new algorithms to using commercially available simulation packages. Typical advantages of the commercial packages are computational efficiency, versatility, and ease of use. For example, modifying the system geometry or changing the reaction sequence typically takes only a few minutes using commercial software, while a similar task may not be straightforward for a home-written simulation program.

In macroelectrode electrochemistry, where the diffusion problem is typically one-dimensional (either linear, spherical, or cylindrical), a powerful DigiSim program (Bioanalytical Systems, West Lafayette, IN) allows one to treat various mechanisms without doing any calculus or computer programming (29). The program is designed mainly for CV simulations, but potentiostatic transients can also be obtained. To generate a theoretical curve using DigiSim, one only needs to type in chemical equations of the related electrochemical/homogeneous reactions and the values of rate constants, diffusion, coefficients, and other parameters. The simulation results include concentration profiles of all species involved at any time moment, and current vs. time dependences. The effects of the double layer charging and the resistive potential drop in solution can be included. A typical example of data simulated using DigiSim for the E_qC_r mechanism is shown in Figure 15.10. The possibilities to consider simultaneously concentration profiles and CVs and to see curves corresponding to different parameter values in the same graph facilitate the mechanistic analysis.

Another important feature of DigiSim is automated curve fitting. An experimental voltammogram can be imported and fitted to the theory generated for the chosen mechanism and geometry. Figure 15.11 shows the fit between the experimental and theoretical CVs obtained for the square scheme, which involves two ET steps coupled with two homogeneous reactions.

To fit the data, one inputs the values of all known parameters (e.g., formal potentials, concentrations, diffusion coefficients) and uses the unknown quantities as adjustable parameters. For a relatively simple mechanism (e.g., one-step ET or EC), the number of fitting parameters is small, and DigiSim can easily find the best fit and determine the unique values of adjustable parameters. However, for a relatively complicated mechanism like the one pictured in Figure 15.11A, the number of fitting parameters is large (e.g., six rate constants, two transfer coefficients), and it may not be possible for DigiSim to find the unique best fit. Moreover, the shape of the theoretical voltammogram may be determined largely by the values of a few kinetic parameters with a weak dependence on the rest of them. If this is the case, the determined values of such parameters are highly uncertain. To ensure that the results are meaningful, one has to fit a number of experimental CVs obtained for a wide range of sweep rates.

Several commercially available simulation packages can be used to simulate two-dimensional or three-dimensional UME and SECM problems, from relatively simple and

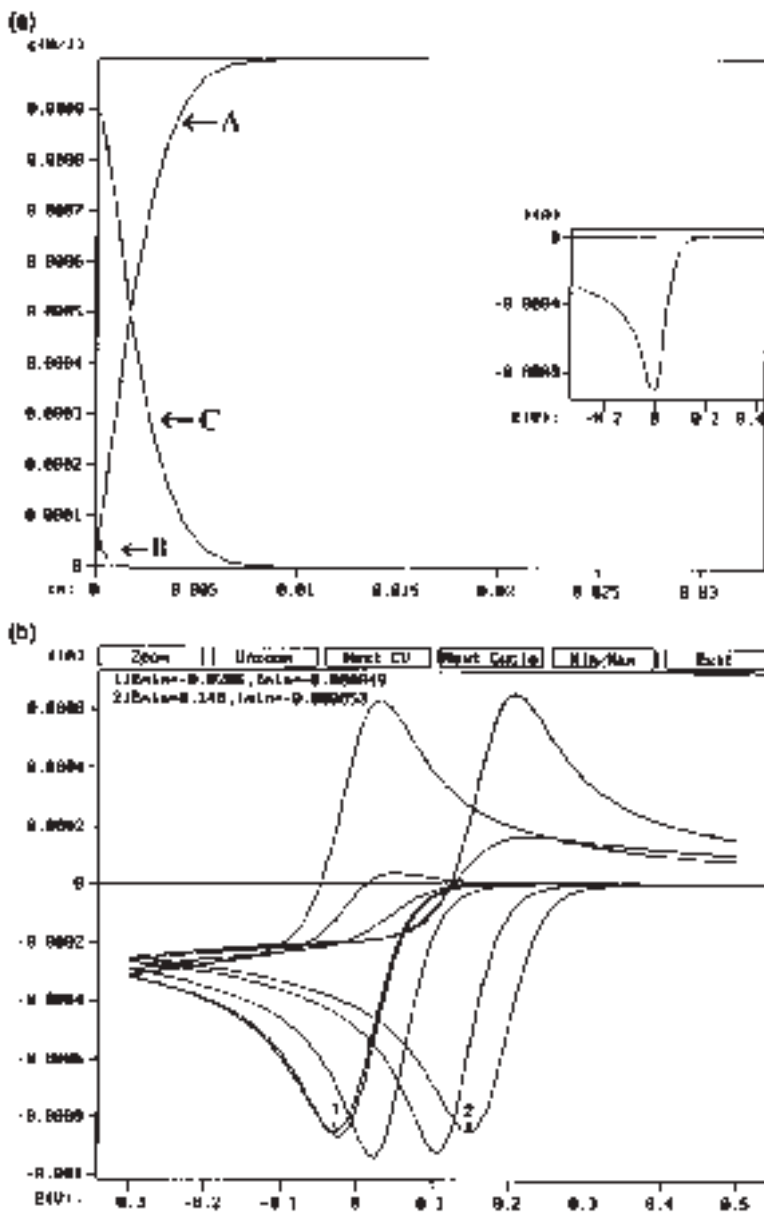


Figure 15.10 (a) Concentration profiles and (b) cyclic voltammograms at a large planar electrode simulated for the E_qC_r mechanism $[A + 1e^- \xrightleftharpoons[k_b]{k_f} B, B \xrightleftharpoons[k_b]{k_f} C]$. $A = 1 \text{ cm}^2$, $E^\circ = 0 \text{ V}$, $K = 1000$ (equilibrium constant), $D_A = D_B = D_C = 10^{-5} \text{ cm}^2/\text{sec}$, $v = 1 \text{ V/sec}$, $c_A^\circ = 1 \text{ mM}$, $c_B^\circ = c_C^\circ = 0$. (a) $k^0 = 1 \text{ cm/sec}$, $k_f = 100 \text{ sec}^{-1}$, $E = -0.3 \text{ V}$. (b) $k^0 = 10^4 \text{ cm/sec}$; $k_f = 0, 10, 1000, 10^6$, and 10^{10} sec^{-1} . Arrow 1 marks the reduction peak of the CV with $k_f = 0$; arrow 2 marks the reduction peak of the CV with $k_f = 10^{10} \text{ sec}^{-1}$. Reprinted with permission from reference (29). Copyright 1994 American Chemical Society.

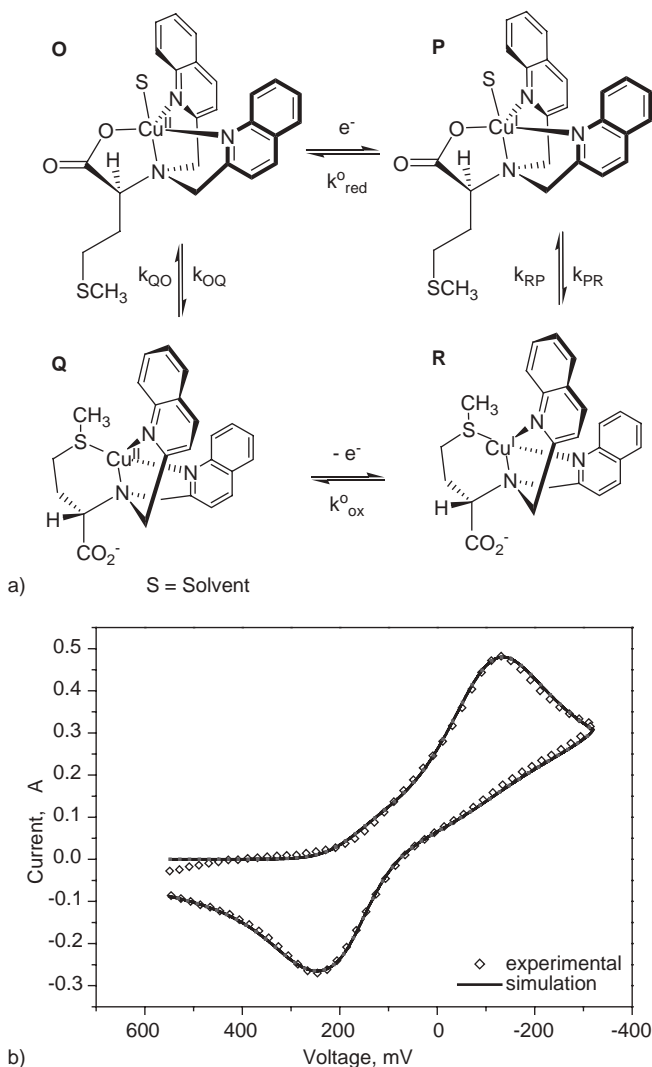


Figure 15.11 (A) Square mechanism: electron-induced ligand reorganization results in an inversion of the chromophore orientation ($k_{\text{red}, \text{ox}}^0$ = rate of electron transfer, $k_{\text{PR}, \text{QQ}}^0$ = forward rate of reaction, $k_{\text{RP}, \text{QQ}}^0$ = reverse rate of reaction); and (B) corresponding experimental voltammogram and the best theoretical fit obtained by DigiSim at $v = 60$ mV/sec. Reprinted with permission from reference (30). Copyright 2005 American Chemical Society.

inexpensive FlexPDE software package (PDE Solutions Inc., Antioch, CA) to more complicated and versatile FEMLAB (COMSOL, Inc., Burlington, MA) to very complicated, powerful and expensive Flux Expert (Simulog, Guyancourt, France). Unlike DigiSim, all these packages are general solvers of partial differential equations rather than electrochemical simulators. Thus, they are suitable for modeling a broad range of physico-chemical

problems involving mass transfer, fluid dynamics, electrostatics, etc. However, unlike DigiSim, the user has to write pertinent differential equations and specify the geometry of his problem. Simulating more complicated systems (e.g., coupled two-phase systems or three-dimensional geometries) may be challenging.

REFERENCES

1. A. J. Bard, L. R. Faulkner, *Electrochemical Methods: Fundamentals and Applications*, 2nd ed., John Wiley & Sons: New York, 2001.
2. Z. Galus, *Fundamentals of Electrochemical Analysis*, 2nd ed., Harwood & PWN: New York, 1994.
3. H. H. Girault, *Analytical and Physical Electrochemistry*, Marcel Dekker: New York, 2004.
4. H. Matsuda, Y. Ayabe, *Z. Electrochem.* **59**, 494 (1955).
5. R. S. Nicholson, *Anal. Chem.* **37**, 1351 (1965).
6. R. M. Wightman, D. O. Wipf, *Acc. Chem. Res.* **23**, 64 (1990).
7. D. O. Wipf, E. W. Kristensen, M. R. Deakin, R. M. Wightman, *Anal. Chem.* **60**, 306 (1988).
8. A. M. Bond, *Modern Polarographic Methods in Analytical Chemistry*, Marcel Dekker: New York, 1980.
9. H. Matsuda, *Z. Electrochem.* **62**, 977 (1958).
10. D. E. Smith, *Anal. Chem.* **35**, 610 (1963).
11. K. Winkler, A. Baranski, *J. Electroanal. Chem.* **346**, 197 (1993).
12. A. M. Bond, K. B. Oldham, C. G. Zoski, *Anal. Chim. Acta* **216**, 177 (1989).
13. K. B. Oldham, C. G. Zoski, *J. Electroanal. Chem.* **256**, 11 (1988).
14. M. V. Mirkin, A. J. Bard, *Anal. Chem.* **64**, 2293 (1992).
15. M. V. Mirkin, T. C. Richards, A. J. Bard, *J. Phys. Chem.* **97**, 7672 (1993).
16. C. Wei, A. J. Bard, M. V. Mirkin, *J. Phys. Chem.* **99**, 16033 (1995).
17. P. Sun, M. V. Mirkin, *Anal. Chem.* in press (2006).
18. A. J. Bard, M. V. Mirkin, P. R. Unwin, D. O. Wipf, *J. Phys. Chem.* **96**, 1861 (1992).
19. R. S. Nicholson, I. Shain, *Anal. Chem.* **36**, 706 (1964).
20. J.-M. Savéant, E. Vianello, *Electrochim. Acta* **8**, 905 (1963).
21. F. M. Zhou, P. R. Unwin, A. J. Bard, *J. Phys. Chem.* **96**, 4917 (1992).
22. P. R. Unwin, A. J. Bard, *J. Phys. Chem.* **95**, 7814 (1991).
23. C. Demaille, P. R. Unwin, A. J. Bard, *J. Phys. Chem.* **100**, 14137 (1996).
24. D. A. Treichel, M. V. Mirkin, A. J. Bard, *J. Phys. Chem.* **98**, 5751 (1994).
25. P. R. Unwin, in *Scanning Electrochemical Microscopy*, A. J. Bard, M. V. Mirkin, Eds., Marcel Dekker: New York, 2001, p. 241.
26. W. J. Albery, M. L. Hitchman, *Ring-Disk Electrode*, Oxford University: Oxford, 1971.
27. C. Amatore, in *Physical Electrochemistry: Principles, Methods, and Applications*, I. Rubinstein, Ed., Marcel Dekker: New York, 1995, p. 131.
28. S. W. Feldberg, in *Electroanalytical Chemistry*, A. J. Bard, Ed., Marcel Dekker: New York, 1969, Vol. 3, p. 228.
29. M. Rudolph, D. P. Reddy, S. W. Feldberg, *Anal. Chem.* **66**, 589A (1994).
30. H. S. Barcena, B. Liu, M. V. Mirkin, J. W. Canary, *Inorg. Chem.* **44**, 7652 (2005).

Metal Deposition

16.1 ELECTRODEPOSITION OF NANOSTRUCTURES AND MICROSTRUCTURES ON HIGHLY ORIENTED PYROLYTIC GRAPHITE (HOPG)

Reginald M. Penner

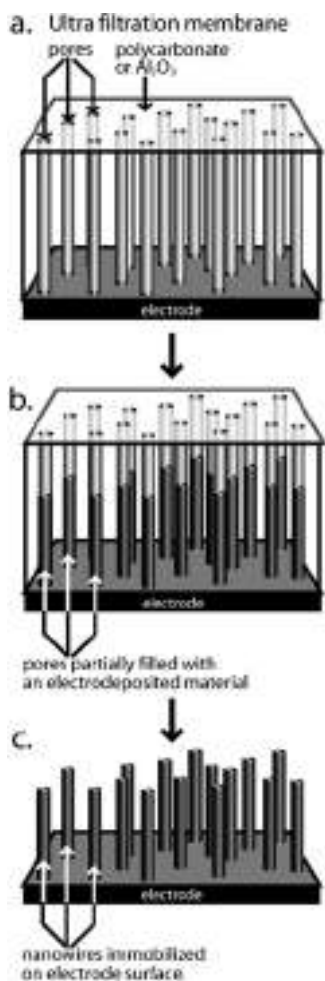
University of California, Irvine, CA, USA

16.1.1 Introduction and perspective

In spite of the exquisite control of reaction rate and duration afforded by electrochemical methods, electrodeposition has hardly been used for preparing nanomaterials. An exception to this generalization is the synthesis of nanoparticles and nanorods using the template synthesis method pioneered by Martin (1–6), Moskovits and co-workers (7–9), and Searson and co-workers (10–16). Template synthesis (Scheme 16.1.1) involves the electrodeposition of materials into the pores of ultrafiltration membranes (e.g., Nuclepore® and Anopore™) that have uniform, cylindrical, or prismatic pores of a particular size.

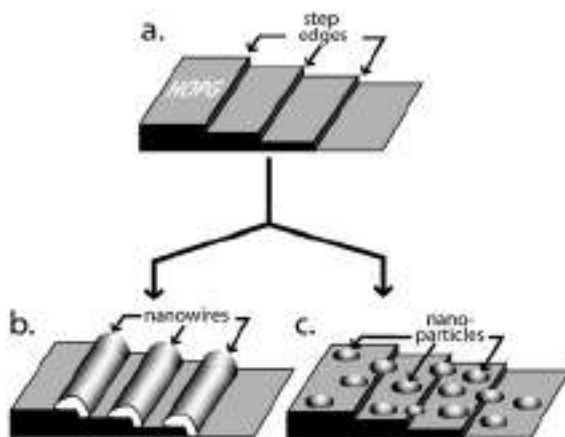
Dissolution of the membrane material exposes arrays of cylinders that are attached at one end to a conductive electrode. Template synthesis can be used to prepare size-monodisperse particles or cylindrical wires that are up to 50 µm in length and 15 nm to 5.0 µm in diameter. Template synthesis is the most popular method for preparing nanostructures of various materials using electrodeposition. Its primary disadvantage is that commercial templates are usually less than 50 µm in thickness and this places an upper limit on the length of the nanowires that can be obtained.

We have sought to develop a “templateless” scheme for preparing nanoparticles and nanowires using electrodeposition (17, 18). The methods we have developed are based on electrodeposition onto highly oriented pyrolytic graphite electrodes (HOPG), as shown in Scheme 16.1.2. HOPG basal plane surfaces are coordinately saturated and have a low surface free energy (19). On such low-energy surfaces, simple energetic arguments (20) can be used to show that deposition processes will prefer a Volmer–Weber (or VW) (21) mechanism. VW growth involves the prompt appearance of three-dimensional islands on the



Scheme 16.1.1 Template (e.g., AnoporeTM and Nuclepore[®]) synthesis of nanowires using electrodeposition.

graphite surface. VW growth can be contrasted with Frank–Van der Merwe (FV) growth which involves the atomic layer-by-layer deposition of a material. Intermediate between these two extremes is Stanski–Krastanov (SK) growth in which a deposition process occurs initially via a layer-by-layer process but which transitions to three-dimensional growth after several layers are deposited (20). Often at noble metal electrodes (e.g., gold and platinum), the electrodeposition of a less noble metal is preceded by the electrodeposition of one or more “underpotentially” deposited (or UPD) metal monolayers just as in the SK growth mechanism. These UPD monolayers do not form on the HOPG basal plane. This “non-wetting” behavior is observed because the system (defined in an electrodeposition experiment as the solution + the deposited material + HOPG) can minimize its energy by minimizing the area of the interface between the deposited material and the HOPG surface (20).



Scheme 16.1.2 Two schemes for generating nanowires (b) or nanoparticles (c) on an HOPG electrode (a).

Our unconventional approach presents two main synthetic challenges: the first is to identify the factors affecting the shape of electrodeposited islands and to manipulate these to favor the production of billions of nanostructures that are identical in shape (e.g., hemispherical islands vs. nanowires, as shown in Schemes 16.1.2b and c). The second challenge is to understand the mechanism by which nanostructures “coarsen”, or become increasingly heterogeneous in size during growth, so that dimensionally uniform nanostructures can be synthesized. In order for this strategy to be generally useful, these two problems must be addressed for a variety of electrodeposited materials. In this section, progress toward this objective is summarized.

16.1.2 HOPG: seeing electrodeposited metal nano- and microparticles

Some of the first *in situ* STM images of electrodes published by Sonnenfeld and Schardt in 1986 (22) showed silver electrodeposits on HOPG. The conclusion of that paper, reinforced by subsequent work (23–25), was that the electrodeposition of silver proceeded by a Volmer–Weber mechanism characterized by prompt 3D growth of silver islands. It was also concluded (23, 24) that the nucleation of silver islands occurred at defects present on the HOPG surface. This was an entirely reasonable conclusion that was supported by the *in situ* STM data.

Our efforts in this area were initiated in 1995 with investigations of the electrodeposition of silver (26, 27) and, soon thereafter, platinum (28) nanoparticles on HOPG surfaces. The primary characterization tool employed in these experiments was *ex situ* non-contact atomic force microscopy (NC-AFM). In the silver work, HOPG electrode surfaces were examined by NC-AFM after the application of large amplitude potentiostatic pulses with amplitudes of -100 to -500 mV (vs. Ag/Ag⁺) and durations of 10–50 msec in dilute silver-plating solutions. These images looked dramatically different from the

STM images acquired previously. Specifically, they showed the presence of silver nanoclusters that were just 30–50 Å in diameter. These nanoclusters are present at a much higher density— 10^9 – 10^{10} cm $^{-2}$ —than the silver nanostructures seen by *in situ* STM in previous studies. The NC-AFM images for platinum, shown in Figure 16.1.1, were very similar.

Since coulometry showed that much less than one atomic layer of silver or platinum was present on these surfaces, these NC-AFM images were consistent with a Volmer–Weber mechanism of deposition, but they contradicted the prior STM work because they showed that the nucleation of these metals occurred readily on defect-free terraces. Why were these nanoparticles not observed in the earlier STM experiments?

Our explanation for these conflicting results is that metal nanoclusters that nucleate on defect-free regions of the HOPG surface interact weakly with the surface and are easily dislodged and removed from terraces by the action of the scanning STM tip. Metal particles that nucleate at steps and other defects are more strongly attached to the surface and many of these are not scraped off the surface during STM imaging. Thus, the STM images show only those particles that interact strongly enough with defects to resist the lateral forces applied to them by the STM tip during imaging. It is likely, but unproven, that *in situ* STM imaging (carried out in electrolyte solutions) is more perturbing than *ex situ* STM in air or vacuum because the solvent provides for efficient viscous coupling of tip motion to electrodeposited structures present on the surface. The tapping action of the NC-AFM tip, in contrast, is apparently much less perturbing with the result that metal particles located on terraces are accurately rendered without being displaced.

These experiments proved the value of NC-AFM for characterizing electrodeposits on HOPG and other surfaces. Beyond this, the NC-AFM data demonstrated that a high density of size-similar ($\text{RSD}_{\text{height}}$ of $\approx 30\%$ (26, 28)) metal nanoparticles could be prepared by electrodeposition at large overpotentials (>100 mV) on HOPG surfaces and that the particle diameter could be controlled by adjusting either the pulse amplitude or its duration. One puzzling observation was related to the size dispersion of these metal nanoparticles. The standard deviation of the particle diameter increased with the mean diameter of the particles. Typical particle height histograms for platinum nanoparticles, for example, are shown in Figure 16.1.2.

Subsequent work carried out over the next 2 years (18, 29–32) revealed the origin of this “coarsening” and also led to techniques for minimizing it, as discussed in the next section.

16.1.3 Brownian Dynamics simulations: understanding particle size distribution broadening

The observation of size heterogeneity for electrodeposited micro- or nanostructures is often attributed to “progressive nucleation”, a scenario in which individual particles begin growing at different times, and therefore grow for a range of different durations. Colloid chemists have understood for a long time that “instantaneous nucleation” (33)—in which the initiation of nanoparticle growth is separated in time from the subsequent growth of these particles—is essential for the synthesis of size-monodisperse colloid particles (34).

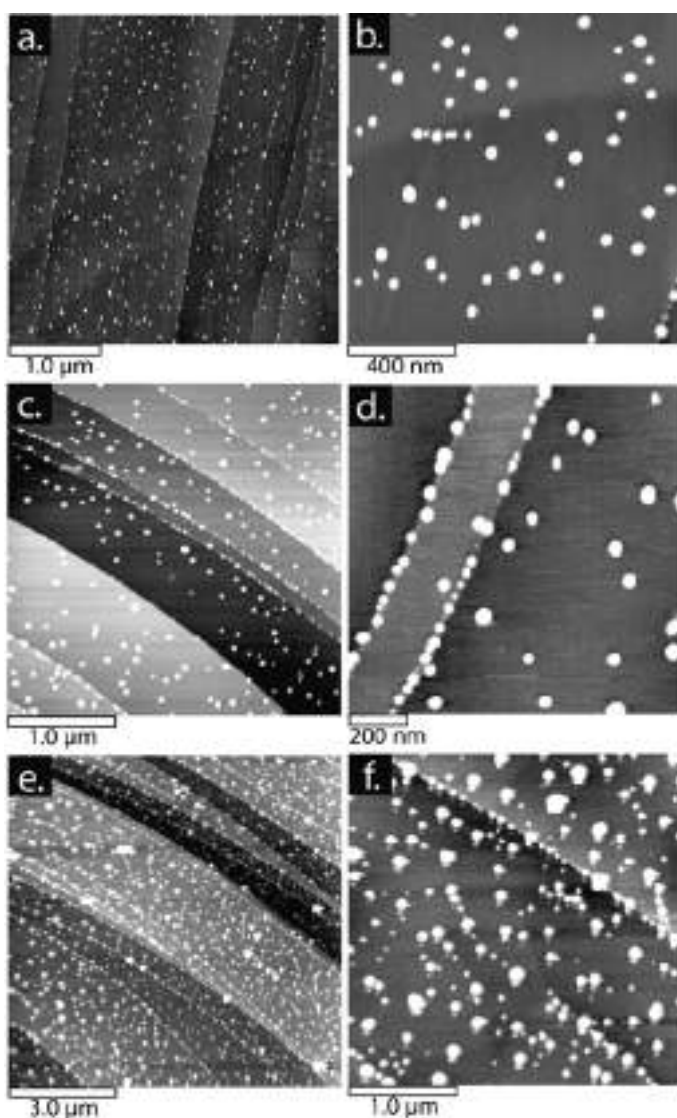


Figure 16.1.1 NC-AFM images of an HOPG surface after the application of potentiostatic plating pulses with a voltage of -600 mV vs. mercurous sulfate reference electrode. (a and b) Pulse duration = 10 msec and deposition charge = $4.84 \mu\text{C cm}^{-2}$. The mean particle height on this surface was $25 \pm 9 \text{ \AA}$. (c and d) Pulse duration = 50 msec platinum pulse and deposition charge = $37.6 \mu\text{C cm}^{-2}$. The mean particle height on this surface was $52 \pm 9 \text{ \AA}$. (e and f) Pulse duration = 100 msec platinum pulse and deposition charge = $77.1 \mu\text{C cm}^{-2}$. The mean particle height on this surface was $72 \pm 27 \text{ \AA}$. In both (e) and (f), a “double tip” imaging artifact, manifest as a smaller “particle” observed below each larger one, is present. Reference (28). Reprinted with permission of the American Chemical Society.

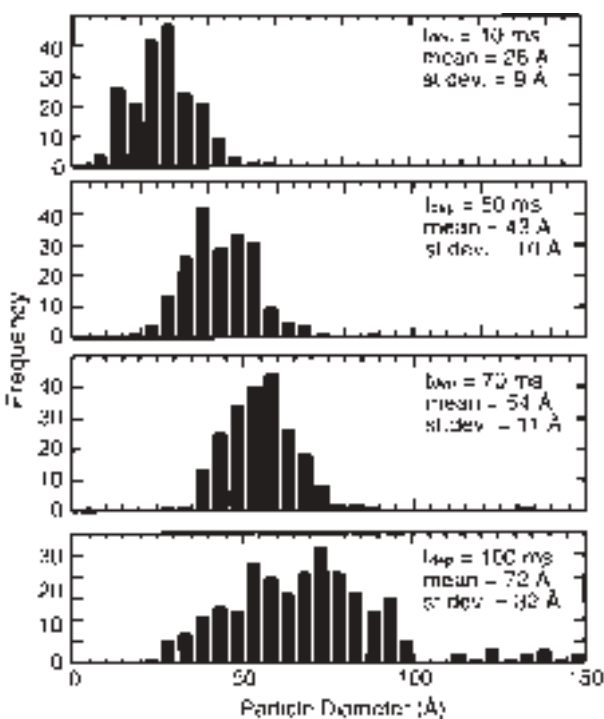


Figure 16.1.2 Histograms of particle heights for platinum nanoparticles prepared by potentiostatic pulse on HOPG surfaces. Heights were measured from NC-AFM images. Data for four different surfaces prepared using the conditions specified on the diagram. Reprinted with permission of the American Chemical Society.

Instantaneous nucleation is a necessary but insufficient condition for preparing dimensionally uniform nanoparticles on an electrode surface. The reason, shown schematically in Figure 16.1.3 (29, 31), is that the growth rates of individual particles can be inversely related to their proximity to other particles on the electrode surface.

If a particular particle is located in proximity to other growing particles (within 10 particle radii, r_o), it can be deprived of reactant relative to particles that are located in relative isolation on the surface. This means that even when nanoparticles nucleate instantaneously, a distribution of growth rates can exist for individual particles on the surface. This deleterious phenomena, which we have termed “interparticle diffusional coupling” or IDC, does not occur for the growth of colloid particle suspensions because particles are constantly moving during growth and they typically do not persist in proximity to other particles.

Brownian Dynamics computer simulations (30, 32) facilitate the study of IDC by eliminating other possible mechanisms of particle coarsening. Since IDC occurs when the depletion layers for adjacent particle overlap, a simple strategy for minimizing IDC is to shrink the radii of these depletion layers. Experimentally, this is accomplished by reducing the particle growth rate, as shown schematically in Figure 16.1.3 (middle and bottom). The

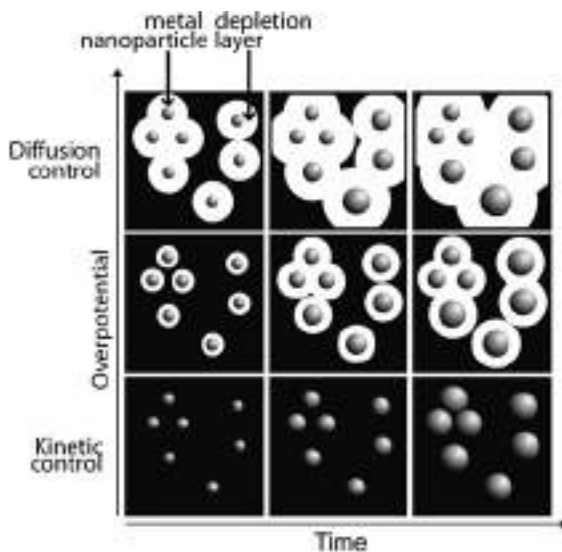


Figure 16.1.3 Schematic diagram depicting the effect of interparticle diffusion coupling (or IDC) on particle size dispersion at three deposition rates: diffusion control (top), activation control (bottom), and an intermediate reaction rate (middle). Reprinted with permission of the American Chemical Society.

results of computer experiments in which the effect of growth rate on the development of particle size heterogeneity can be seen are shown in Figure 16.1.4.

In a Brownian Dynamics simulation, the growth of individual particles is explicitly modeled using a simulation “box” like that shown in Figure 16.1.4a (30). In the experiments documented in Figure 16.1.4, 200 particles were first grown rapidly for a short interval so that a significant size distribution developed. This distribution, characterized by a standard deviation of the particle radius, $\sigma_r = 0.095 \text{ nm}$, was then grown in a range of overpotentials between -1 mV (very slow) and -200 mV (fast; nearly diffusion controlled). σ_r is plotted vs. the mean particle radius, $\langle r \rangle$, at each of these overpotentials in Figure 16.1.4b. Over the entire range of overpotentials explored here, σ_r increased linearly as a function of $\langle r \rangle$, and the slope $d\sigma_r/dr$ was higher at $\eta_{dep} = -200 \text{ mV}$ by a factor of 8 as compared with $\eta_{dep} = -1 \text{ mV}$ (Figure 16.1.4c) (30). A more detailed analysis of these simulation data (described in reference (30)) revealed that the mechanism of particle coarsening seen in Figure 16.1.4b is IDC, and that the reduction of the growth rate effectively decouples nearby particles and permits them to grow more nearly at the same rate.

16.1.4 “Slow-growth” electrodeposition: dimensionally uniform metal nano- and microparticles

In metal particle growth experiments, the “slow growth” strategy shown to be effective in Brownian Dynamics simulations can be implemented using a two-step procedure (18, 29, 31).

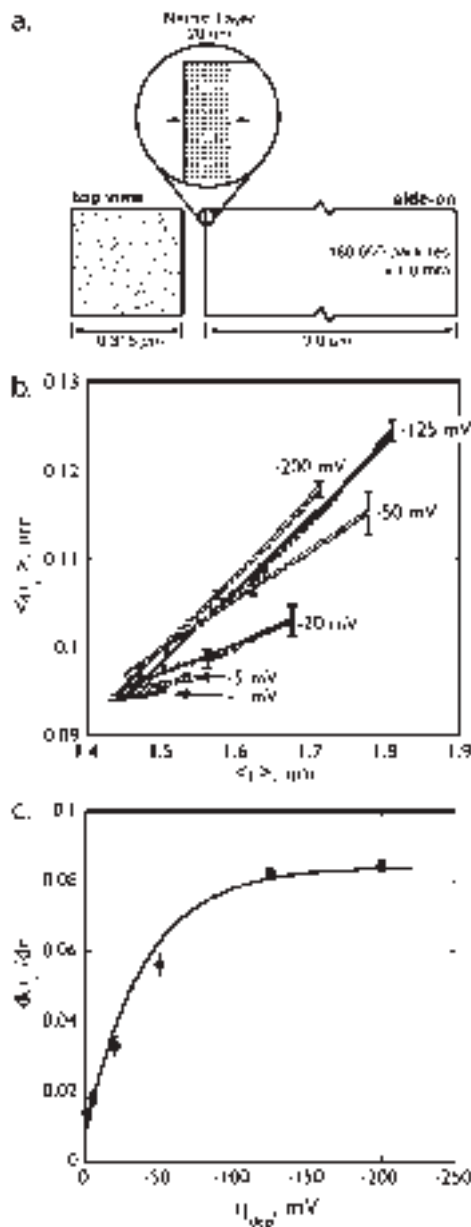


Figure 16.1.4 (a) A simulation box for the simulation by Brownian Dynamics of the growth of 200 silver nanoparticles. (b) The standard deviation of the particle radius, s_r , vs. the mean radius, $\langle r \rangle$, for simulations at six deposition overpotentials, h_{dep} , as indicated. Solid lines are the results of linear least-squares analysis for each h_{dep} . The error bars in this plot represent ± 1 sec for the s_r obtained from three or four replicate simulations conducted at each h_{dep} . (c) Plot of the coarsening rate, ds/dr , obtained from the straight lines plotted in (b). The error bars in this plot represent ± 1 sec for ds/dr obtained from three or four replicate simulations conducted at each h_{dep} . Reprinted with permission of the American Chemical Society.

Preparation of our electrode surface involves cleaving a crystal of ZYA-grade HOPG (source: GE Advanced Ceramics, Inc.) using adhesive tape to expose a clean, basal plane surface. This crystal is then placed in Teflon® electrode holder that masks the edges of the crystal, and exposes a small ($3\text{--}5\text{ mm}^2$) circular area to an aqueous metal-plating solution having $[M^{n+}] \approx 1\text{--}5\text{ mM}$. This solution also contains an electrochemically inert supporting electrolyte, such as NaF, and other additives, specified in Table 16.1.1, are also sometimes included. Metal nanoparticles are nucleated by applying a very negative voltage pulse with η_{dep} of up to -1.0 V and a duration of $5\text{--}50\text{ msec}$. This nucleation pulse produces a one-dimensional ensemble of metal nanoparticles, or “seeds”, arrayed along each step edge on the HOPG surface. These seeds are then grown (without further nucleation) at an overpotential in the range from -5 to -75 mV . Typical results for the growth of silver particles prepared using $\eta_{dep} = -70\text{ mV}$ are shown in Figure 16.1.5.

Particle size histograms for such particles (Figure 16.1.5a) show a relative standard deviation (RSD_{dia}) of $6\text{--}33\%$. Silver particles with a mean diameter of $2.0\text{ }\mu\text{m}$, prepared by

Table 16.1.1

Metal nanoparticle/nanowire growth solutions and potentials^a

Material	Plating solution(s)/comments ^b	Growth potential ^c	References
Silver	1–5 mM Ag^+ in 0.10–0.30 M NaF (pH ≈ 5), NaCH_3COO (pH ≈ 6.5), NaNO_3 (pH = 1–2), and/or Na_2SO_4 (pH = 1–2) Silver nanoparticles have also been obtained from acetonitrile solutions containing: 1 mM AgClO_4 and 0.1 M LiClO_4 Nanowire growth (in aqueous solutions only) is promoted by the addition of saccharine (1 mM). Of the metals listed here, silver presents the most difficulties for synthesizing nanowires	−180 to −60 mV vs. Ag^0/Ag^+	(18, 29, 31, 37, 40)
Platinum	Aqueous 1–5 mM PtCl_6^{2-} in 0.10–0.30 M HCl	150 to −30 mV vs. MSE	(18, 29)
Nickel	1–10 mM $\text{Ni}(\text{NO}_3)_2$ or NiSO_4 0.1–0.2 M NaCl, 0.2 M NH_4Cl , pH = 7.5–8.5, or Na_2SO_4	−900 mV vs. SCE	(18, 29, 37)
Gold	1–5 mM AuCl_3 , 0.1 M NaCl Nanowire growth is promoted by the addition of saccharine (1 mM)	560–600 mV vs. SCE	(18, 29, 37)
Copper	1 mM CuSO_4 , 0.1 M K_2SO_4 or Na_2SO_4	−5 to 20 mV vs. $\text{Cu}^0/\text{Cu}^{2+}$	(18, 29, 37)
Palladium	2 mM Pd^{2+} , 0.1 M HCl or 0.1 M HClO_4	300–450 mV vs. SCE	(17, 36, 41)
Cadmium	10 mM CdF_2 , 0.1 M NaF (particles) 5 mM CdCl_2 , 6 mM Na_2EDTA , 0.5 M NaCl, 0.5 M NH_4Cl buffered at pH = 8.5 using $\text{NH}_3\text{H}_2\text{O}$ (nanowires)	−770 mV (particles) −1150 mV (nanowires) vs. SCE	(29, 42)

^aThe selection between nanoparticles and nanowires is decided by the electrode preparation procedure and the nucleation conditions as described in the text. All experiments involved “slow growth” of particles or nanowires.

^bAll solutions aqueous, and prepared with nanopure water ($\rho > 18\text{ M cm}$).

^cMSE: saturated mercurous sulfate reference electrode; SCE: saturated calomel reference electrode.

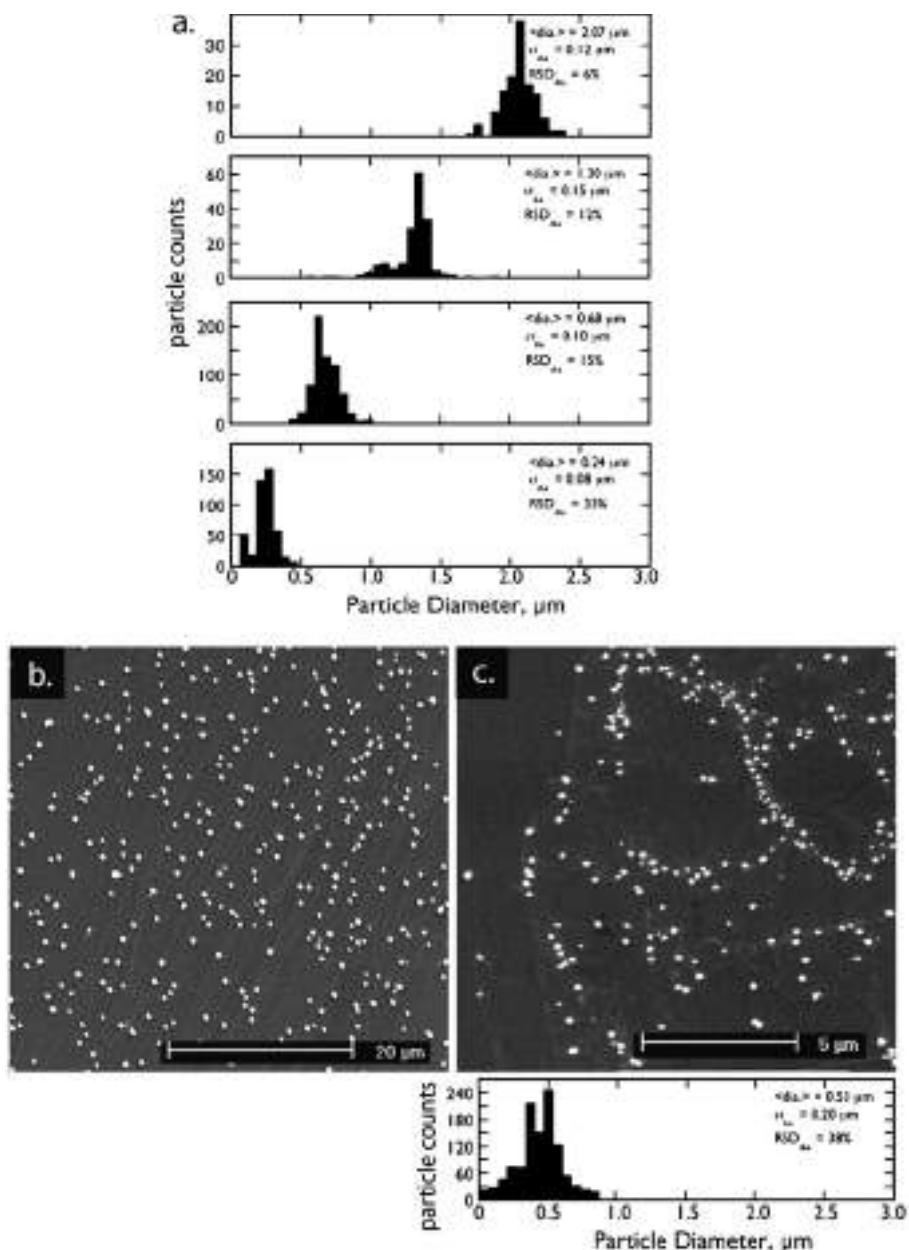


Figure 16.1.5 (a) Particle size histograms for silver particles prepared using η_{dep} of -70 mV and deposition durations of: 500 msec (bottom), 5.0 sec, 30 sec, and 120 sec (top). (b) An SEM image of silver particles prepared by “slow growth” using $\eta_{\text{dep}} = -70$ mV and a growth duration of 120 sec. (c) An SEM image of silver particles prepared by growth at diffusion control ($\eta_{\text{dep}} = -500$ mV) and a growth duration of 150 msec. The histogram corresponding to the sample shown below this image is plotted below it. Reprinted with permission of the American Chemical Society.

growth at $\eta_{dep} = -70$ mV for 120 sec, are shown in the SEM image of Figure 16.1.5b. By comparison, growth at $\eta_{dep} = -500$ mV for 150 msec produces particles like that shown in Figure 16.1.5c. Two important differences can be discerned: first, the nucleation pulse employed in a slow growth experiment produces a high, and uniform, density of particles on the graphite surface. A careful examination of this image reveals that particles in densely nucleated regions of the surface are noticeably smaller than those nucleated in sparse regions of the surface. This inverse correlation between the number density of particles and the particle diameter is clear evidence for IDC. The RSD_{dia} for this surface (38%) was approximately twice as large as for silver particles of the same diameter prepared by slow growth ($RSD_{dia} \approx 16\%$). One should not be convinced of the generality of the slow growth approach based on the data shown in Figure 16.1.5 because silver is a special case, exhibiting excellent reversibility and the fastest heterogeneous electron transfer kinetics of any metal (35).

We have studied a range of different metals and metal oxides with widely varying degrees of electrochemical reversibility and electrodeposition kinetics. In contrast to silver, many important noble metals and metal oxides electrodeposit irreversibly. In Figure 16.1.6a, for example, irreversible cyclic voltammograms acquired in plating solutions for MoO₂ (a metallic oxide of molybdenum) and platinum are compared with the reversible CVs seen for silver.

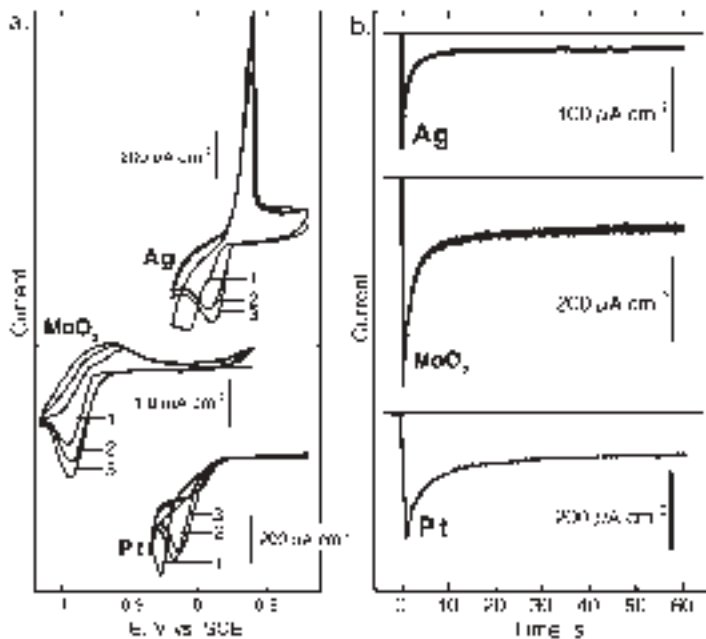


Figure 16.1.6 (a) Cyclic voltammograms for an HOPG electrode immersed in plating solutions containing Ag^+ (20 mV sec^{-1} in 1 mM AgClO_4 , 0.1 M LiClO_4 , acetonitrile), MoO_4^{2-} (20 mV sec^{-1} in $1.0 \text{ mM MoO}_4^{2-}$, 1.0 M NaCl , $1.0 \text{ M NH}_4\text{Cl}$, $\text{pH} = 7.5-8.5$), and PtCl_6^{2-} (30 mV sec^{-1} in 1 mM PtCl_6^{2-} , 0.1 M HCl). (b) Current-time transients for the electrodeposition of silver, molybdenum dioxide, and platinum using the deposition solutions indicated in (a). Reprinted with permission of Elsevier.

For all three systems, the growth phase of a particle slow growth experiment is characterized by a constant current, as shown in Figure 16.1.6b. In addition to MoO₂ and platinum, we also prepared nano- and micro-particles of copper, nickel, cadmium, and gold. Representative SEMs of particles prepared by slow growth are shown in Figure 16.1.7.

The particles in these images range from 100 nm in diameter (Cd) to more than 2 μm (Cu), but for all of these metals, particles ranging in size from 50 nm to 2 μm with a comparable degree of size monodispersity have been obtained. These data support the conclusion that

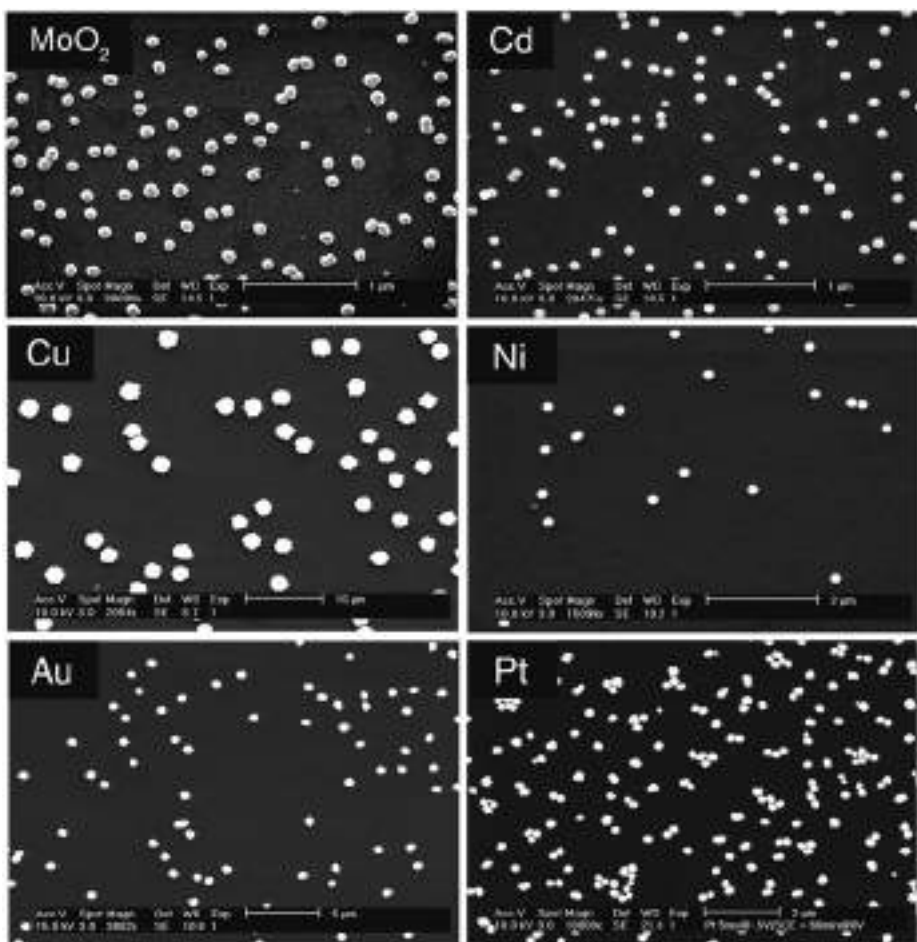


Figure 16.1.7 Scanning electron micrographs of metal particles prepared using the slow growth method. The composition of the plating solutions employed for the electrodeposition of these metal particles is listed in Table 16.1.1. The deposition current density observed in each experiment was as follows: (MoO₂) 180–140 $\mu\text{A cm}^{-2}$, (Cd) 40–60 $\mu\text{A cm}^{-2}$, (Cu) 40–60 $\mu\text{A cm}^{-2}$, (Ni) 240–260 $\mu\text{A cm}^{-2}$, (Au) 30–40 $\mu\text{A cm}^{-2}$, and (Pt) 5–100 $\mu\text{A cm}^{-2}$. Reprinted with permission of the American Chemical Society and Elsevier.

the slow growth method for obtaining particles size selectively is a general one for a variety of metals and at least one metal oxide (i.e., MoO_2).

16.1.5 Electrodeposition of metal nanowires

A variant of the slow growth method for obtaining dimensionally uniform metal nanoparticles can be used to prepare metal nanowires, as shown in Scheme 16.1.2b (17, 18, 36–39). Nanowires are obtained instead of nanoparticles when the nucleation of the electrodeposited material occurs preferentially at the step edges present on the HOPG surface. Nucleation at step edges is enhanced by oxidizing them immediately prior to the application of the nucleation pulse. This oxidation can conveniently be carried out electrochemically in the metal-plating solution at a potential of ≈ 0.8 V vs. SCE for 5 sec, typically. On such pre-oxidized surfaces, the nucleation pulse that is normally applied in a slow growth experiment produces a high density of metal nuclei—usually in excess of $10 \mu\text{m}^{-1}$ —on step edges. Initially, these nanoparticles have a diameter of 1 nm or so. This means that the nucleation pulse produces a disconnected 1D array of metal nanoparticles at step edges—not a continuous nanowire. Nanowires are obtained during the subsequent growth phase as these nuclei coalesce into an electrically continuous wire that has a minimum diameter usually in the 30–70 nm range.

The behavior of copper is typical of that for many other metals including gold, platinum, palladium, nickel, and cadmium (37). Shown in Figure 16.1.8 is the pulse program employed for nanowires growth and the cyclic voltammogram for an aqueous copper-plating solution containing 2.0 mM $\text{CuSO}_4 \cdot 5\text{H}_2\text{O}$ and 0.1 M Na_2SO_4 .

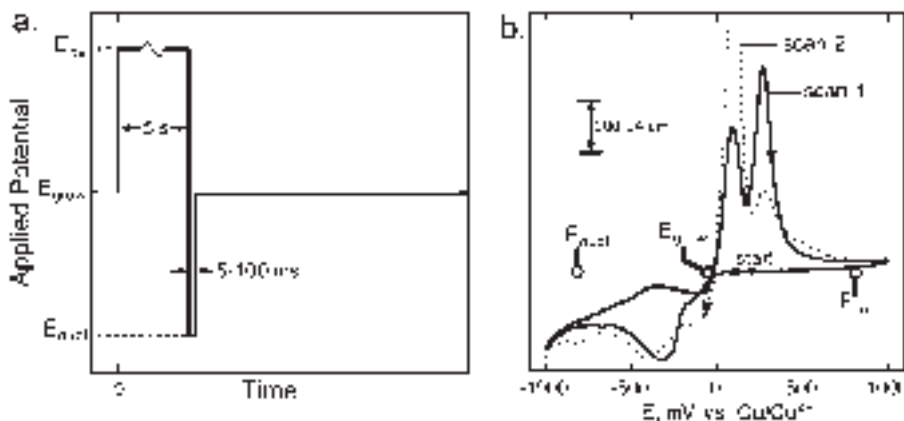


Figure 16.1.8 (a) Triple voltage pulse used to prepare metal nanowires in this study. (b) Cyclic voltammograms of a copper-plating solution at an HOPG electrode showing the values for E_{ox} , E_{nucl} , and E_{grow} typically used for the preparation of copper nanowires. The solution was aqueous 2.0 mM $\text{CuSO}_4 \cdot 5\text{H}_2\text{O}$, 0.1 M Na_2SO_4 . Two oxidation waves seen at $+100$ mV_{SCE} and $+350$ mV_{SCE} are assigned to copper stripping ($+100$ mV_{SCE}) and oxidation of Cu^0 to CuO ($+350$ mV_{SCE}). Reprinted with permission of the American Chemical Society.

Nanowire growth was accomplished by pre-oxidizing the HOPG surface at +0.80 V vs. SCE, applying a nucleation pulse of $-0.8\text{ V} \times 5\text{ msec}$, and then growing at -5 mV vs. SCE for between 100 sec and 40 min. As shown in the scanning electron micrographs of Figure 16.1.9, the nanowires obtained range in diameter from 70 nm to more than 300 nm.

These polycrystalline nanowires possess a unique morphology, consisting of single crystalline metal grains arranged in series along the step edge, that is a direct consequence of the growth mechanism.

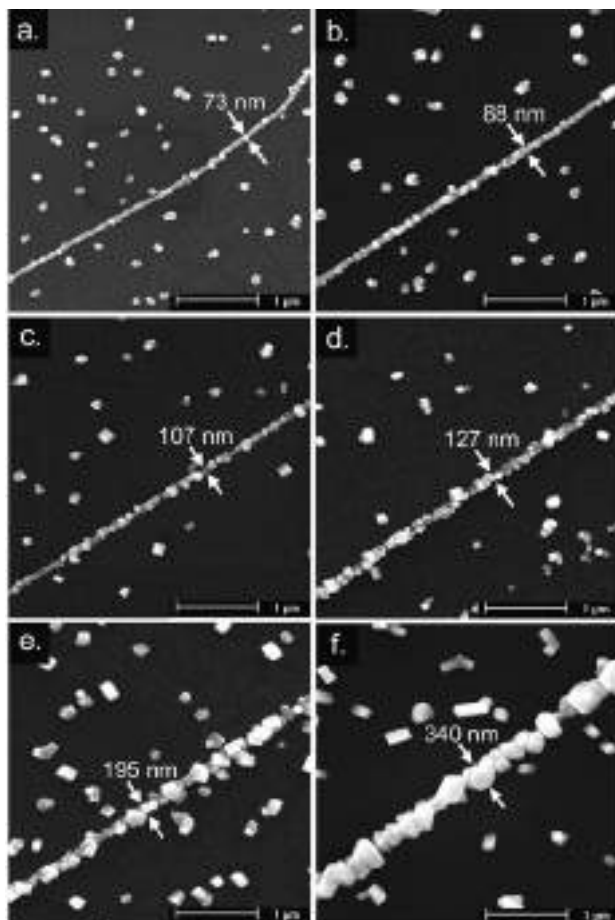


Figure 16.1.9 Scanning electron micrographs of copper nanowires. These nanowires were electrodeposited from the solution indicated in Table 16.1.1, using $E_{\text{nuc}} = -800\text{ mV}_{\text{SCE}}$ and $E_{\text{grow}} = -5\text{ mV}_{\text{SCE}}$. The growth times employed in each experiment were: (a) 120 sec, (b) 180 sec, (c) 300 sec, (d) 600 sec, (e) 900 sec, and (f) 2700 sec. Reprinted with permission of the American Chemical Society.

As in the slow growth experiments described earlier involving particles, nanowire growth is characterized by a constant deposition current. The transport of metal ions under these conditions occurs under conditions of mixed diffusion and convection control and a simple growth law can be derived (18):

$$r(t) = \sqrt{\frac{2i_{\text{dep}} t_{\text{dep}} V_m}{\pi n F l}} \quad (16.1.1)$$

In this equation, t_{dep} is the total deposition duration, V_m is the molar volume of the electrodeposited metal, and l is the total length of metal nanowires on the graphite surface. Equation (16.1.1) assumes a hemicylindrical nanowire geometry. As shown in Figure 16.1.10, the radii of the electrodeposited copper nanowires, measured from SEM data like that of Figure 16.1.1, increased in proportion to $t^{1/2}$ as predicted by equation (16.1.1). A similar relationship is obtained for other metals, including gold, silver, and nickel, as shown in Figure 16.1.10.

We have termed this method of nanowire growth Electrochemical Step Edge Decoration or ESED. In recent work, we have demonstrated that ESED can be applied to materials other than metals. Specifically, ESED seems to provide a general method for synthesizing nanowires composed of a variety of technologically interesting compounds including $\beta\text{-MnO}_2$ (43) (a lithium ion intercalation compound), MoS_2 (44) (an indirect-gap semiconductor), CdS (44) (a direct-gap semiconductor), and Bi_2Te_3 (45)

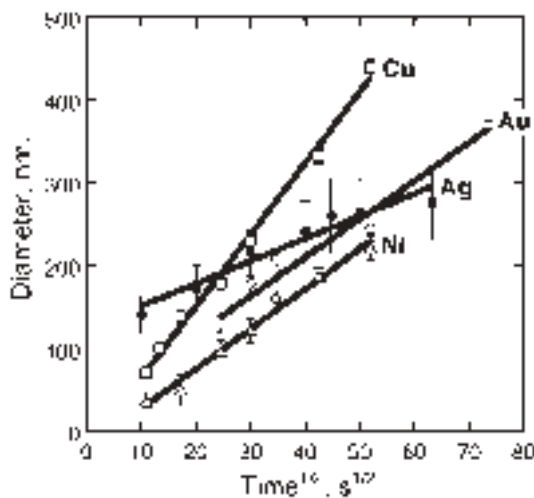


Figure 16.1.10 Nanowire diameter vs. (deposition time) $^{1/2}$ for the growth of nanowires composed of four metals as indicated. Each series of experiments for a particular metal were performed using a single graphite crystal in order to limit the variation in the step edge density from experiment to experiment (see equation (16.1.1)). This crystal was cleaved before each experiment to expose a fresh, clean graphite surface. Error bars for each data point are twice the standard deviation for the mean particle diameter as measured from SEM images. Reprinted with permission of the American Chemical Society.

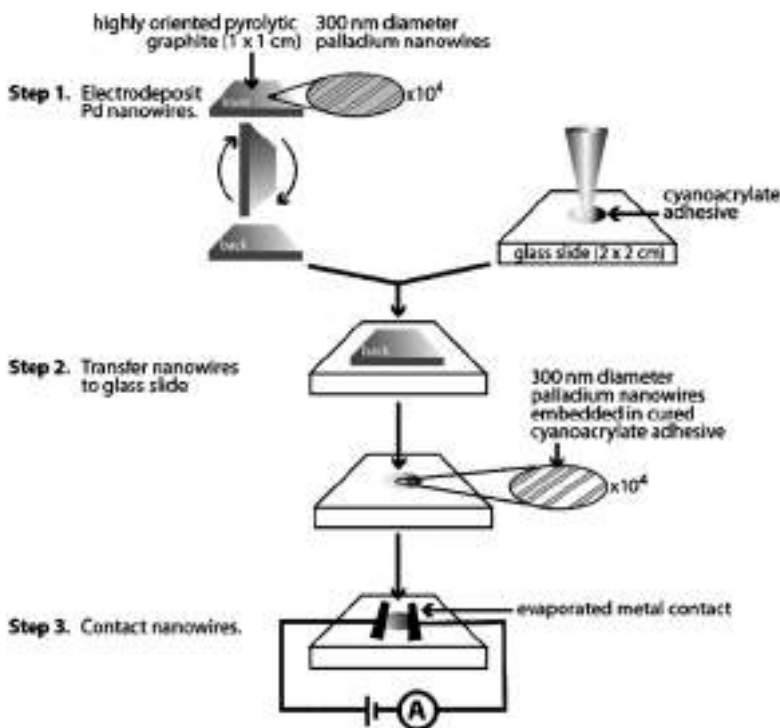


Figure 16.1.11 Schematic diagram of the method for transferring nanowires (palladium in this case) from an HOPG surface on which they are synthesized onto a second surface for characterization and/or device fabrication. Reprinted with permission of the American Chemical Society.

(a thermoelectric material). Relative to competing methods, such as template synthesis (Scheme 16.1.1), ESED has two important advantages. First, much longer nanowires with lengths of a millimeter or more can be prepared. Second, these nanowires can be transferred from the HOPG surface onto the surface of an insulator. This is accomplished by embedding the nanowires in a film of adhesive (usually a cyanoacrylate) dispersed on another surface composed of glass, semiconductor, polymer, etc., as shown schematically in Figure 16.1.11.

After the adhesive hardens, the graphite surface can be separated from the insulator surface and the nanowires are presented at the surface of the adhesive layer. This ability to transfer nanowires onto various surfaces simplifies the characterization of the nanowires by TEM, and it facilitates the fabrication of devices such as chemical sensors.

REFERENCES

1. C. A. Foss, M. J. Tierney, C. R. Martin, *J. Phys. Chem.* **96**, 9001 (1992).
2. C. J. Brumlik, C. R. Martin, *J. Am. Chem. Soc.* **113**, 3174 (1991).

3. C. J. Brumlik, V. P. Menon, C. R. Martin, *J. Mater. Res.* **9**, 1174 (1994).
4. C. R. Martin, *Science* **266**, 1961 (1994).
5. C. R. Martin, *Adv. Mater.* **3**, 457 (1991).
6. C. A. Foss, G. L. Hornyak, J. A. Stockert, C. R. Martin, *J. Phys. Chem.* **98**, 2963 (1994).
7. D. N. Davydov, J. Haruyama, D. Routkevitch, B. W. Statt, D. Ellis, M. Moskovits, J. M. Xu, *Phys. Rev. B* **57**, 13550 (1998).
8. C. K. Preston, M. Moskovits, *J. Phys. Chem.* **97**, 8495 (1993).
9. D. Routkevitch, T. Bigioni, M. Moskovits, J. M. Xu, *J. Phys. Chem.* **100**, 14037 (1996).
10. P. C. Searson, R. C. Cammarata, C. L. Chien, *J. Electron. Mater.* **24**, 955 (1995).
11. T. M. Whitney, J. S. Jiang, P. C. Searson, C. L. Chien, *Science* **261**, 1316 (1993).
12. K. Liu, K. Nagodawithana, P. C. Searson, C. L. Chien, *Phys. Rev. B* **51**, 7381 (1995).
13. K. Liu, C. L. Chien, P. C. Searson, Y. Z. Kui, *Appl. Phys. Lett.* **73**, 1436 (1998).
14. K. Liu, C. L. Chien, P. C. Searson, *Phys. Rev. B* **58**, R14681 (1998).
15. K. Liu, C. L. Chien, P. C. Searson, Y. Z. Kui, *IEEE Trans. Magn.* **34**, 1093 (1998).
16. G. Oskam, J. G. Long, A. Natarajan, P. C. Searson, *J. Phys. E Appl. Phys.* **31**, 1927 (1998).
17. E. C. Walter, M. P. Zach, F. Favier, B. J. Murray, K. Inazu, J. C. Hemminger, R. M. Penner, *Chemphyschem* **4**, 131 (2003).
18. R. M. Penner, *J. Phys. Chem. B* **106**, 3339 (2002).
19. I. Morcos, *J. Chem. Phys.* **57**, 1801 (1972).
20. A. Zangwill, *Physics at Surfaces*, Cambridge University Press: Cambridge, 1988.
21. M. Volmer, A. Weber, *Z. Phys. Chem.* **119**, 277 (1926).
22. R. Sonnenfeld, B. C. Schardt, *Appl. Phys. Lett.* **49**, 1172 (1986).
23. L. Vazquez, A. H. Creus, P. Carro, P. Ocon, P. Herrasti, C. Palacio, J. M. Vara, R. C. Salvarezza, A. J. Arvia, *J. Phys. Chem.* **96**, 10454 (1992).
24. R. T. Pötzschke, C. A. Gervasi, S. Vinzelberg, G. Staikov, W. J. Lorenz, *Electrochim. Acta* **40**, 1469 (1995).
25. K. Itaya, E. Tomita, *Surf. Sci.* **201**, L507 (1988).
26. J. V. Zoval, R. M. Stiger, P. R. Biernacki, R. M. Penner, *J. Phys. Chem.* **100**, 837 (1996).
27. J. V. Zoval, P. Biernacki, R. M. Penner, *Anal. Chem.* **68**, 1585 (1996).
28. J. V. Zoval, J. Lee, S. Gorer, R. M. Penner, *J. Phys. Chem.* **102**, 1166 (1998).
29. H. Liu, F. Favier, K. Ng, M. P. Zach, R. M. Penner, *Electrochim. Acta* **47**, 671 (2001).
30. R. M. Penner, *J. Phys. Chem. B* **105**, 8672 (2001).
31. H. Liu, R. M. Penner, *J. Phys. Chem. B* **104**, 9131 (2000).
32. J. L. Fransaer, R. M. Penner, *J. Phys. Chem. B* **103**, 7643 (1999).
33. Nucleation is termed “instantaneous” when the interval over which nucleation occurs is much smaller than the total duration of growth.
34. V. K. LaMer, R. H. Dinegar, *J. Am. Chem. Soc.* **72**, 4847 (1950).
35. J. D. Porter, T. O. Robinson, *J. Phys. Chem.* **97**, 6696 (1993).
36. E. C. Walter, F. Favier, R. M. Penner, *Anal. Chem.* **74**, 1546 (2002).
37. E. C. Walter, B. J. Murray, F. Favier, G. Kaltenpoth, M. Grunze, R. M. Penner, *J. Phys. Chem. B* **106**, 11407 (2002).
38. M. P. Zach, K. Inazu, K. H. Ng, J. C. Hemminger, R. M. Penner, *Chem. Mater.* **14**, 3206 (2002).
39. M. P. Zach, K. H. Ng, R. M. Penner, *Science* **290**, 2120 (2000).
40. B. J. Murray, E. C. Walter, R. M. Penner, *Nano Lett.* **4**, 665 (2004).
41. F. Favier, E. C. Walter, M. P. Zach, T. Benter, R. M. Penner, *Science* **293**, 2227 (2001).
42. Q. Li, R. M. Penner, *Nano Lett.* **5**, 1720 (2005).
43. Q. G. Li, J. B. Olson, R. M. Penner, *Chem. Mater.* **16**, 3402 (2004).
44. Q. Li, J. T. Newberg, E. C. Walter, J. C. Hemminger, R. M. Penner, *Nano Lett.* **4**, 277 (2004).
45. E. J. Menke, Q. Li, R. M. Penner, *Nano Lett.* **4**, 2009 (2004).

16.2 TEMPLATE DEPOSITION OF METALS

Paolo Ugo and Ligia Maria Moretto

Department of Physical Chemistry, University of Venice,
Santa Marta 2137, 30123 Venice, Italy

16.2.1 Introduction

Template synthesis is a relatively simple and easy procedure which has made the fabrication of rather sophisticated nanomaterials accessible to almost any laboratory. Template synthesis requires access to instrumentation capable of metal sputtering and electrochemical deposition. The characterization of the fabricated nanostructures can be done using instrumental techniques including spectrophotometry, voltammetry, optical microscopy, atomic force microscopy, and electronic microscopies (scanning electron microscopy (SEM) and transmission electron microscopy (TEM)).

The method is based on the simple but effective idea that the pores of a host material can be used as a template to direct the growth of new materials. Historically, template synthesis was introduced by Possin (1) and refined by Williams and Giordano (2) who prepared different metallic nanowires with widths as small as 10 nm within the pores of etched nuclear damaged tracks in mica. It was further developed by Martin's group (3–5) and followed by others (6) with the number of examples and applications (7) continually increasing. The nanoporous membranes usually employed as templates are alumina or track-etched polymeric membranes which are widely used as ultrafiltration membranes. Recently, metal nanostructures have also been obtained using the pores created by self-assembly in block copolymer structures under the influence of electric fields and high temperatures (8, 9).

The first part of this section focuses on the main characteristics and fabrication techniques used for obtaining templating membranes and depositing metal nanostructures by suitable electroless and electrochemical procedures. Methods such as sol–gel (10–12) or chemical vapor deposition (10, 13), which have been used primarily for the template deposition of carbon, oxides, or semiconducting-based materials, will not be considered here in detail. The second part of the section focuses on the electrochemical properties of the fabricated nanomaterials with emphasis on the characteristics and applications of nano-electrode ensembles (NEEs).

16.2.2 Templating membranes

16.2.2.1 Alumina membranes

Aluminum oxide films with regular pore distribution can be formed by electrooxidation of high-purity aluminum substrates in acidic electrolytes (14, 15). The structure of the oxide film consists of a uniform array of parallel alumina cells packed hexagonally, each containing a nearly cylindrical pore. The uniform diameter of the pores is a consequence of the

equilibrium between the growth rate of the alumina and its dissolution in the acidic electrolyte. The hexagonal self-order of the pores can be explained by the repulsive forces due to the volume expansion associated with the anodization process (14). By appropriate selection of the process conditions, films with pore diameters between <10 nm up to $2\ \mu\text{m}$, pore density between 10^8 and 10^{11} pores cm^{-2} , and film thickness up to $200\ \mu\text{m}$ can be prepared (16).

The electrolysis of aluminum is carried out in a two-electrode cell. The anode is usually a high-purity (99.9% or even 99.99%) aluminum sheet. The metal surface must be carefully cleaned via chemical or electrochemical polishing (17). After degreasing in 1:2:1 ethanol–dichloromethane–acetone solution (17), the aluminum surface is cleaned by immersion in NaOH (1 M (18) or 0.05 M (17)), followed by rinsing in distilled water, and then electropolished using one of the following typical experimental conditions:

- **Potentiostatic control:** Applied potential 20–21 V for 2–5 min in 61% perchloric acid–95% ethanol (19/81, v/v) at $2\ ^\circ\text{C}$ (18, 19).
- **Galvanostatic control:** Current density of $75\ \text{mA cm}^{-2}$ (or $125\ \text{mA cm}^{-2}$ (20)) in a 2:3 (v/v) phosphoric/sulfuric acid solution in 1% glycerol at 70 – $80\ ^\circ\text{C}$ (17).

According to Hornyak *et al.* (17), the electropolished aluminum is rinsed immediately in distilled water (often with the aid of a strong stream of distilled water to remove the tenacious gelatinous oxide layer), immersed in concentrated nitric acid for 10 min, rinsed and left to dry in air. Well-polished aluminum should present a shiny/mirror-like surface; accurate polishing is crucial for obtaining high-quality aluminum oxide membranes.

The pre-treated aluminum is then anodized potentiostatically or galvanostatically in a thermostatically controlled bath (14, 16, 21). Potentials from 10 to 160 V and current densities from 10 to $30\ \text{mA cm}^{-2}$ are usually applied; however, for high pore spacing, voltages as high as 700 V have been used (22). The electrolyte is typically 15% sulfuric acid ($10\ ^\circ\text{C}$), 4% phosphoric acid ($24\ ^\circ\text{C}$), 2% oxalic acid ($24\ ^\circ\text{C}$), or 3% chromic acid ($38\ ^\circ\text{C}$) (14); the temperature ranges from 38 to $0\ ^\circ\text{C}$ and even lower (18, 23).

The cathode used for the anodization of aluminum consists of a large plate of aluminum, lead, platinum, or stainless steel.

As shown in Table 16.2.1, the pore diameter is proportional to the DC potential or the current density used. The thickness of the porous aluminum oxide increases linearly with

Table 16.2.1

Conditions used for the electrochemical preparation of nanoporous alumina membranes

Applied potential (V)	Pore diameter (nm)	Pore density ($\times 10^9\ \text{cm}^{-2}$)
30	52 ^a	30 ^d
20	32 ^b	56 ^d
15	22 ^b	83 ^d
10	16 ^c	

^aIn 4% oxalic acid, reference (17).

^bIn 10% sulfuric acid, reference (17).

^cIn 15% sulfuric acid, reference (17).

^dFrom reference (14).

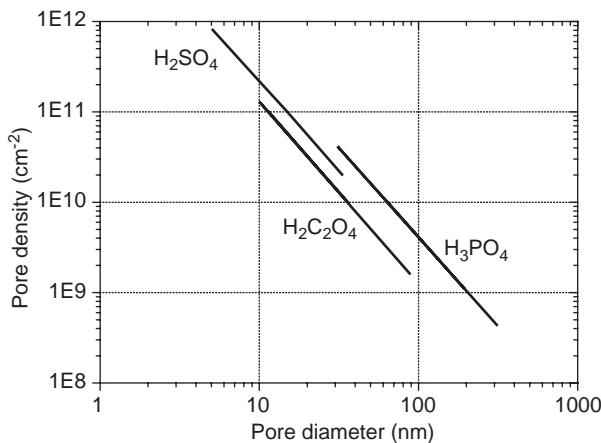


Figure 16.2.1 Pore density vs. pore diameter in alumina nanoporous membranes prepared in the three electrolytes indicated. Reproduced with permission from <http://www.synkera.com/>. (for colour version: see colour section at the end of the book).

the anodization time at a given voltage and temperature and can be adjusted from 0.1 to 10 µm. The pore spacing varies with the applied potential and the electrolyte pH; the effect of the applied voltage on pore density for films formed in 15% sulfuric acid at 10 °C is presented in the last column of Table 16.2.1.

As shown in Figure 16.2.1, there is a bi-logarithmic linear relationship between the pore density and the pore diameter.

The growth of the oxide layer is such that it advances into the aluminum phase with simultaneous formation and dissolution of the oxide to form the pores. During the pore formation, the aluminum anode material is never directly exposed to the solution since it is always coated by a relatively thin (10–100 nm) non-porous insulating oxide layer called the “barrier layer” (see Figure 16.2.2A). Various procedures can be used to separate the unoxidized aluminum from the porous oxide layer (14, 24). The most widely used is the so-called voltage reduction sequence (VRS) developed by Furneaux *et al.* (22). VRS entails the stepwise reduction of the potential so that a progressive reduction of the pore diameter is produced at the bottom of the pore (see Figure 16.2.2).

After formation of this highly porous layer, the electrode is immersed into an acidic detachment solution, typically 25% sulfuric acid or phosphoric acid, which causes the rapid dissolution of the interfacial oxide. This process is faster in the areas indented by the smaller and smaller branched pores. Under such conditions, the acid can readily access the Al electrode so that H₂ gas is evolved; when the H₂ bubbles coalesce, the process is completed. The Al electrode is then rinsed by immersion in water and dried in air. The porous alumina membrane is finally collected by sliding an index card between the alumina layer and the Al electrode. The two faces of the detached alumina membrane are not equivalent; the face that was detached from the Al electrode surface contains remnants of the interfacial oxide layer. However, these remnants can be

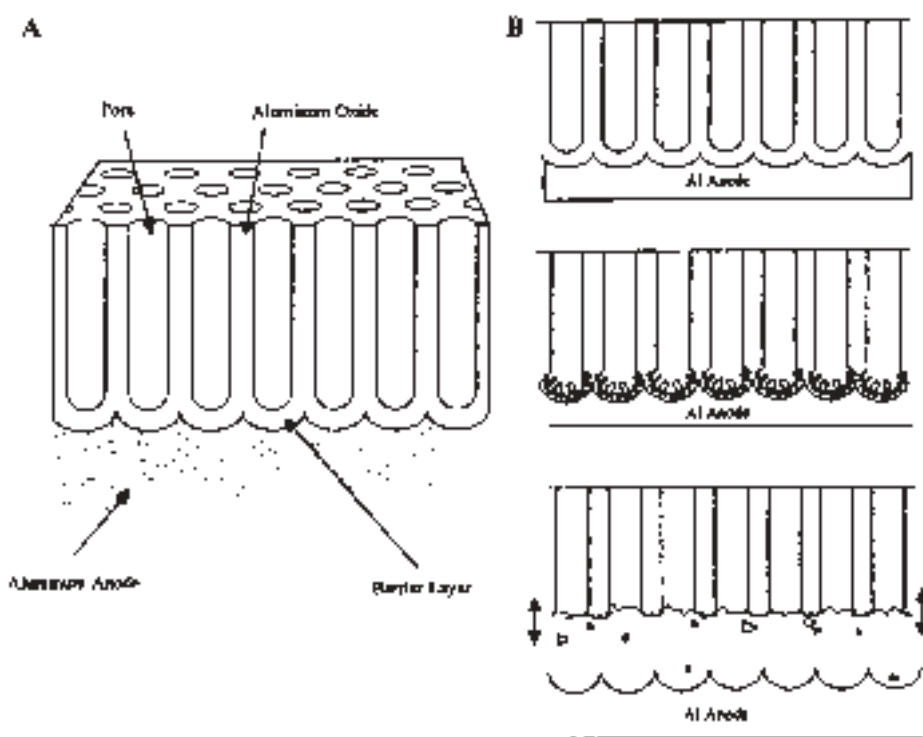
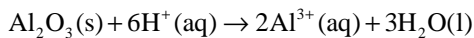


Figure 16.2.2 (A) Schematic drawing of the porous anodic aluminum oxide layer that is formed during aluminum anodization. (B) Steps involved in the detachment of the aluminum oxide layer from bulk aluminum by using the voltage reduction sequence. Top: growth of the primary pores; middle: voltage reduction and infiltration of barrier layer by branched pore network; bottom: dissolution of branched network region of the porous film and separation from aluminum anode. Reproduced with permission from reference (25).

removed by floating the membrane on the surface of a 0.2 M KOH solution in ethylene glycol. Such a procedure tends to make both faces of the membrane essentially equivalent (17). Another procedure to separate the porous film from the Al electrode is by immersing the anodized foil in a saturated aqueous HgCl_2 solution. This results in the amalgamation of aluminum along the $\text{Al}_2\text{O}_3/\text{Al}$ interface and delamination of the oxide layer. The remaining part of the insulating barrier layer is then etched away with 0.025 M NaOH solution (26).

Note that both of these approaches induce isotropic chemical etching with concomitant enlargement of pore size. Very recently, Mallouk and coworkers (20) proposed a new method to penetrate and detach the barrier layer by applying a reverse bias voltage (-3.5 to -5V) immediately after the completion of the anodization; both anodization and reverse bias are carried out in the same 3% H_2SO_4 solution. When H_2 bubbles are observed, the bias voltage is reduced until no more bubbles are detected; the process takes a few minutes. It was postulated (20) that the application of a reverse bias voltage in acidic

solution results in an increase of the local H⁺ concentration, thus promoting the dissolution of the oxide barrier layer by the following reaction:



The reverse bias method was applied successfully to both bulk aluminum and thin aluminum layers deposited on Ti/Si_xO/Si wafers (20).

Recently, Mozalev *et al.* (27) detached the alumina film from the residual aluminum foil by dipping in an HCl–CuCl₂ solution, until the aluminum metal was completely dissolved. The pores of the alumina film were protected with gelatine gel and the oxide barrier layer was finally dissolved with 5% NaOH from the bottom side of the film. This method allows the complete removal of the barrier layer without introducing discontinuities in the pore network across the membrane.

Freestanding alumina microporous membranes are commercially available, for example, from AnoporeTM or Synkera Technologies Inc. The rather limited number of pore sizes available limits a wider use of the commercial alumina membranes as templates so that many research groups still prefer to prepare their own membranes.

16.2.2.2 Track-etched polymer membranes

Nanoporous polymeric membranes can be prepared by the track-etch method. This method involves tracking a film of solid material (polymer) with a beam of high-energy particles to create damage tracks in the film. Such tracks are then etched into monodisperse pores by exposure to an alkaline etching solution. The time the material is exposed to the tracking particles determines the number of tracks (and thus pores), while the etching time (as well as the composition of the etching solution) determines the size of the pores (28, 29).

Polymeric materials used for the production of track-etched membranes include poly(ethylene terephthalate) (PET), polycarbonate (PC), polyimide (Kapton), polypropylene, polyvinylidene fluoride, and CR-39 (allyl diglycol carbonate) (29). The most widely used are PET, PC, and Kapton.

PET presents a high etch ratio that allows the production of membranes with a wide range of pore diameters. The membranes are relatively hydrophilic, rather stable to acids and organic solvents, and biologically inert. However, PET-tracked membranes require UV irradiation before etching. The membrane is exposed to UV light with maximum intensity at 320 nm for approximately 30 min. The UV treatment leads to saturation of the damage in the tracks so that further storage of the samples in air or illumination with visible light does not change the etching behavior (30).

PC is the material used for preparing the majority of commercially available track-etched membranes. It is characterized by high sensitivity to tracking and it does not require UV sensitization. However, PC is soluble in organic solvents and has low wettability in aqueous solutions. Its hydrophilicity can be increased by impregnation with polyvinylpyrrolidone (29).

Kapton foils are also used to produce nanoporous track-etched membranes (31, 32). Track-etched membranes are commercially available as filtration membranes with pore

diameters ranging from as small as 10 nm to as large as 10 μm and pore densities between 10^7 and 10^9 pores cm^{-2} . Track but not etched nanoporous membranes are also commercially available, for example, from Osmonics (50 tracks cm^{-2}) or from Whatman (10^7 tracks cm^{-2}).

(a) *Tracking*

There are two basic methods of producing latent tracks in the polymer foils to be transformed into porous membranes. The first method is based on the irradiation with fragments from the fission of heavy nuclei such as californium, bismuth, or uranium (33) of energy 11.4 MeV per nucleon (30, 34). Typical energy losses of the fission fragments are about 10 keV nm^{-1} . The fission fragments coming from a thin layer target have an almost isotropic angle distribution. To create an array of latent tracks penetrating the foil, a collimator is normally used. The advantages of this tracking method are: (a) good time stability of the particle flux and (b) relatively low cost. The limitations of the method are: (a) contamination of the tracked foil with radioactive products (“cooling” of the irradiated material is needed, which usually takes few months); (b) limited thickness of the membrane to be tracked; (c) limited possibilities of controlling the angle distribution of the tracks; (d) fragments of different masses and energies produce tracks with different etching properties (29).

The second method is based on the use of ion beams in accelerators (29). The intensity of the ion beam should be at least 10^{11} sec^{-1} . To irradiate large areas, a scanning beam is normally used. The advantages of the ion beam accelerator tracking method are: (a) no radioactive contamination of the material when the ion energy is below the Coulomb barrier; (b) identity of the bombarding particles gives tracks with the same etching properties; (c) large range of high-energy particles makes possible the tracking of thicker membranes; (d) better conditions for producing high-density ($>10^9 \text{ cm}^{-2}$) track arrays; (d) particles heavier than fission fragments can be used (^{238}U , for example); (e) it is easier to control the impact angle and produce arrays of parallel tracks or create some particular angular distributions for getting rid of merging pores (29).

Very recent advances have shown that it is possible to control the number and the geometric distribution of tracks with an ion beam (35). The sample is covered by a metallic mask with a hole of small diameter (0.1 mm) so that the ions can penetrate the film only within a small area. By registering the ions passing through the film and shutting down and moving the membrane after one single ion has passed through (31, 34), it is possible to obtain single pore membranes or membranes with geometrically patterned arrays of tracks (and pores). The limitations of the ion beam accelerator method are: (a) relative instability of the particle flux and (b) higher cost than irradiation.

In the past decade, a decrease in the popularity of reactor-based irradiation facilities and an increase in the use of accelerated ion beams were observed (29). With the use of ion beams from accelerators, it is easier to control the impact angle for getting rid of merging pores of the kind shown in Figure 16.2.3A (29).

(b) *Chemical etching*

Chemical etching is the process of pore formation during which the damaged zone of a latent track is removed and transformed into a hollow channel (pore) (29, 33). The most

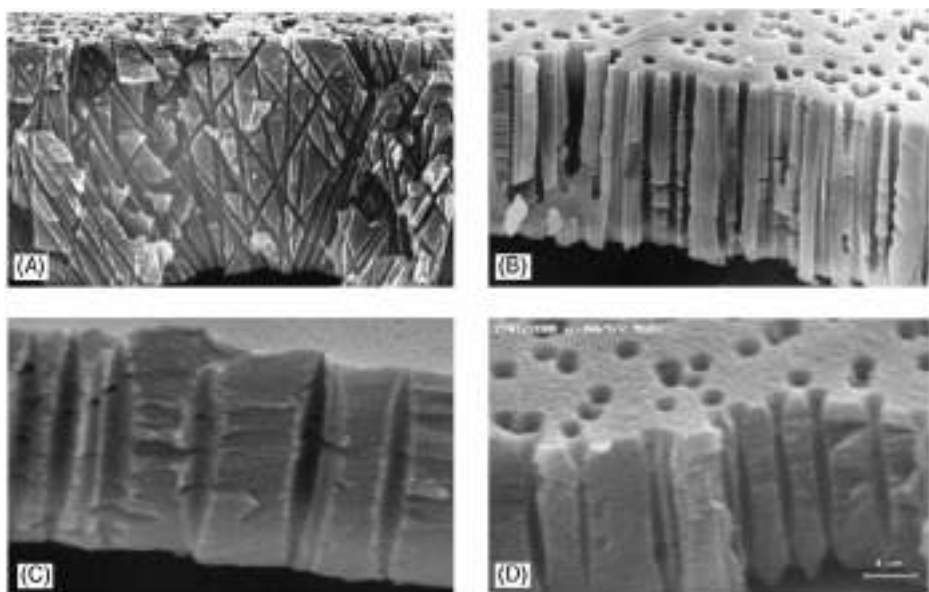


Figure 16.2.3 Porous structures produced in thin polymeric films using various methods of irradiation and chemical treatment: (A) cross-section of a polycarbonate membrane with cylindrical non-parallel pore channels; (B) polypropylene with slightly conical (tapered toward the center) parallel pores; (C) poly(ethylene terephthalate) with cigar-like pores; (D) poly(ethylene terephthalate) with “bow-tie” pores. Reprinted with permission from reference (29).

widely used etching agents are alkali solutions (KOH or NaOH) although the etching of polyimide (Kapton) requires an oxidizing agent such as NaClO (31, 32). The simplest description of the kinetics of the etching process is based on two parameters: the bulk etch rate (V_B) and the track-etch rate (V_T). While V_B depends on the material, the etchant composition, and the temperature, V_T depends on additional parameters such as sensitivity of the material, irradiation, post-irradiation conditions, and etching conditions (29). Etching with KOH or NaOH on both sides of the tracked membrane generates pores with a symmetric shape that are typically cylindrical or cigar-like (see Figure 16.2.3).

The formation of cigar-like-shaped pores has been explained by two hypotheses (36): (a) further exposure by electrons generated in the secondary electron cascade caused by the impact of the high-energy particle and (b) an acceleration of the etching rate caused by the etching products, which are more concentrated inside the pores. It was shown that perfectly cylindrical pores could be obtained if a special PC film (PC^+) is used instead of standard PC films (36).

It was recently shown that strict control of the etching conditions allows one to control the shape of the pores, obtaining, for example, funnel-like or conically shaped pores (30). Conical pores can be obtained by asymmetric etching with oxygen plasma of initially cylindrical pores (37), or by performing an asymmetric chemical etching, so that $V_B > V_T$, with the ratio changing throughout the thickness of the membrane. Asymmetric etching of

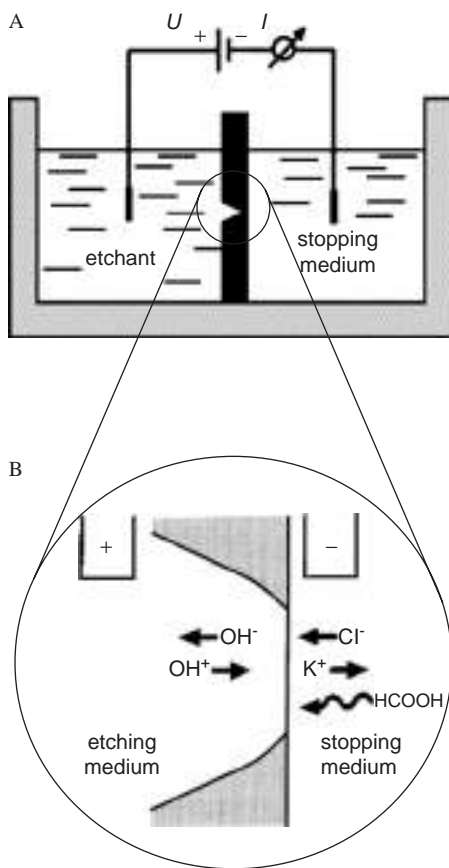


Figure 16.2.4 (A) Scheme of the experimental set-up with the etching cell for asymmetric pore etching. (B) Direction of electromigration and diffusion during break-through under stopping electric field conditions (30). (→) Migration and (~>) diffusion direction. Adapted with permission from references (30, 34).

tracked membranes was first described three decades ago (38). It is based on the treatment of an ion-irradiated sample with an etchant on one side, while the opposite face is in contact with a stopping medium that neutralizes the etchant as soon as it perforates the sample. This method was modified recently by applying an additional electric field (34). The application of the electric field allows one to detect the instant of pore break-through and, additionally, to protect the etched cone pore from further chemical attack. The scheme of the apparatus used for the asymmetric etching is shown in Figure 16.2.4A.

For asymmetric etching of PC or PET, one side of the membrane is put in contact with an alkaline etching solution, usually 9 M NaOH or KOH, and the other side is in contact with the stopping medium, typically a weak acid solution such as 1 M HCOOH in 1 M KCl (30). For asymmetric etching of polyimide (Kapton), the etching solution is NaClO

(with 13% active chlorine) while the stopping medium is a suitable reducing agent such as 1 M KI (39). A potential of some tens of volts is applied across the membrane by two Pt electrodes. As shown in Figure 16.2.4A, a positive potential is applied to the electrode in the etching solution, while the electrode in the stopping solution is at a negative potential. As shown in Figure 16.2.4B, if a positive potential is applied from the alkali (etchant) side during the break-through, the OH^- anions are pulled out of the pore which accelerates the stopping process. It was demonstrated (30) that electrostopping at voltages around 1 V is more efficient in producing conical pores than chemical stopping alone.

The application of a potential across the membrane is stopped as soon as a monitoring ammeter records an increase in the current that passes through the membrane up to reaching a pre-set value, typically 1 mA (40). The membrane is then immediately immersed (both sides) in the stopping medium, thus blocking the asymmetric etching. At the end of the process, conical nanopores of controlled shape are obtained (37, 40). It was also shown that the addition of alcohols (such as methanol, ethanol, or propanol) to the etch solution allows further control of the etching rate (24) and the V_B/V_T ratio (40, 41).

16.2.2.3 Comparison between alumina and track-etched polymer nanoporous membranes

Track-etched membranes are flexible with a smooth surface while alumina films are brittle and rather rough. Another difference is the pore density which is typically 10^9 pores cm^{-2} for track-etched membranes compared to 10^{11} pores cm^{-2} for alumina membranes (42). Alumina membranes are therefore interesting as templates for producing high-density nanomaterials. Track-etched membranes are more suitable for obtaining low-density nanomaterials, for example, in the fabrication of NEEs where low nanoelectrode densities are often desired. As shown in Figure 16.2.3, a problem with track-etched membranes is the fact that the pores are not always parallel to each other. Their shape is not always cylindrical and pore positions are randomly distributed unless special procedures are applied (43). For alumina membranes, depending on the method used to separate the membrane from the aluminum, the pores on the side of the barrier layer can be branched into smaller pores (see Figure 2 in reference (44)).

16.2.3 Template deposition of metals

16.2.3.1 Electrochemical deposition

Electrochemical deposition of metals in the pores of templating membranes requires that one side of the membrane be in direct contact with a metallic layer. This can be produced by plasma or vacuum deposition of a metal layer on one side of the membrane (25) and requires that the membrane film be robust enough to tolerate this kind of manipulation. The thickness of the conductive layer is typically 100–1000 nm (45–47). The metal which produces the conductive layer can be the same or different from the one that will provide the final template structure. In electrochemical template deposition, the coated film is placed in an electrochemical cell where the template membrane acts as the cathode and a counter electrode is the anode. The deposition can be carried out under galvanostatic or

potentiostatic conditions. In the case of track-etched PC, it was recently shown that the addition of 1–2% gelatin to the plating solution improves the wettability of the nanoporous membrane, thus improving the reproducibility of the electrodeposition step (45, 48–50).

Final products of the electrochemical deposition are solid nanoparticles, typically nanowires and not hollow structures (e.g., nanotubes or nanocapsules). The electrochemical process is based on the progressive growth and filling of the pores starting from the bottom metallic layer and proceeding progressively toward the open end of the templating pore.

Figure 16.2.5B summarizes the steps for electrochemical growth of continuous metal wires for use as micro- or nanoelectrodes, for example. To form smaller template nanoparticles or nanowire segments, procedure 1–2–5–6 is used. For this latter case, sputtering and

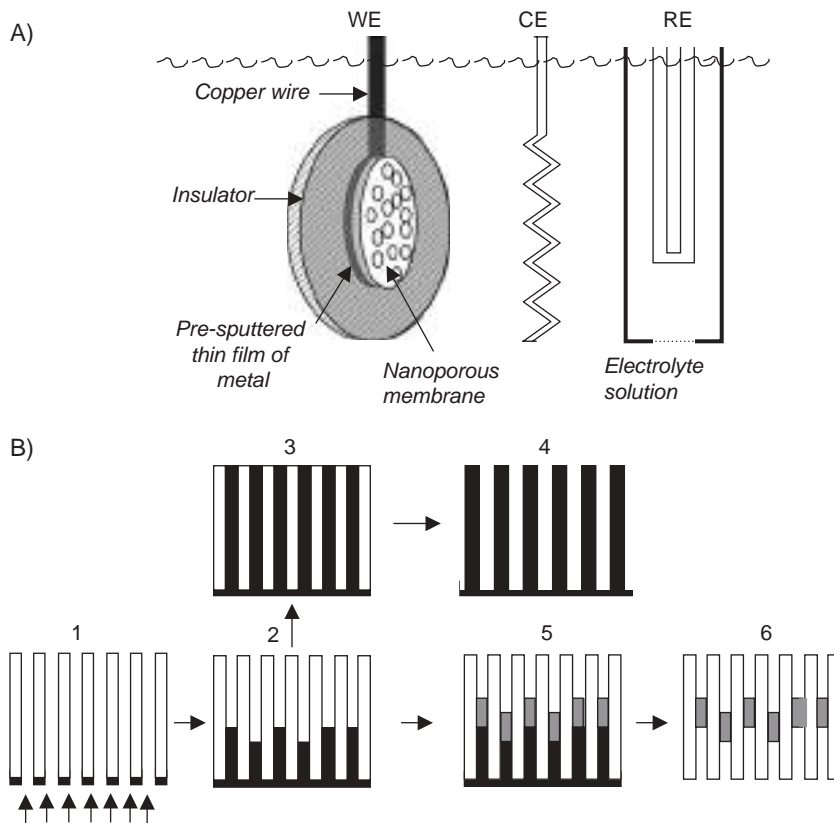


Figure 16.2.5 Electrochemical template deposition of metals: (A) scheme of the electrochemical cell and (B) sequence of the growth of the template for the preparation of single metal continuous nanowires (sequences 1–4) or segmented nanoparticles (sequences 1, 2, 5, and 6). Detailed steps: (1) metal sputtering to provide a conductive layer for the subsequent electrodeposition; (2) electrodeposition of the same metal to form the fibers; (3) growth of the fibers; (4) etching of the template; (5) electrodeposition of another metal; (6) composite structure after the etching of the foundation metal. Part (B) redrawn with permission from reference (25).

the first growth of nanowires are performed with an etchable metal such as silver which acts as a foundation for the deposition of the metal of interest to be deposited in a desired amount in a second step as shown in Figure 16.2.5B-5 (15). The silver foundation is then etched away with nitric acid leaving the nanoparticles or nanowire segments composed of the second metal (gold, for example) in the pores of the template (Figure 16.2.5B-6). A similar procedure is also used for fabricating multilayered nanowires composed of cylindrical segments of different metals such as Ni/Cu (51), Co/Cu (52), or Au/Sn (50). Table 16.2.2 summarizes examples of template electrochemical deposition of nanowires, nanoparticles, or nanowire segments.

16.2.3.2 Electroless deposition of metals

Electroless metal deposition involves the use of chemical reducing agents to plate a metal from a solution onto a surface (68). The key requirement for this process is to arrange the chemistry so that the kinetics of homogeneous electron transfer from the reducing agent to the metal ion is very slow. A catalyst that accelerates the rate of metal ion reduction is then applied to the surface to be coated. In this way, the metal ion is reduced at the surface incorporating the catalyst so that only this surface is coated with the desired metal. The thickness of the metal film deposited can be controlled by changing the plating time (7).

The principles of electroless deposition in templates are exemplified for Au deposition developed in Martin's laboratory for the template fabrication of NEEs, nanotubes, and other shaped gold nanomaterials (5, 7). The electroless plating of gold (5) consists of three steps: (i) "sensitization" with Sn^{2+} ; (ii) reduction of Ag^+ to produce discrete Ag metal nanoparticles; (iii) galvanic displacement of Ag particles by reduction of gold followed by auto-catalytic reduction of more Au.

Detailed conditions for Au electroless deposition include (5, 69):

- (i) After wetting for 2 h in methanol, the PC membrane is sensitized with Sn^{2+} by immersion into a solution 0.026 M in SnCl_2 and 0.07 M in trifluoroacetic acid in 50:50 methanol/water as the solvent for 45 min.
- (ii) After rinsing with methanol for 5 min, the sensitized membrane is immersed for 10 min in 50 mL of 0.029 M $\text{Ag}[(\text{NH}_3)_2]\text{NO}_3$. This solution is prepared by a dropwise addition of concentrated NH_4OH from a burette (1 mL or less will be needed) to a 0.029 M AgNO_3 aqueous solution. With a careful, dropwise addition, a brown precipitate will appear and then disappear with further addition of NH_4OH . At the first disappearance of the brown precipitate, the $\text{Ag}[(\text{NH}_3)_2]\text{NO}_3$ solution is ready.
- (iii) The membrane is then immersed into an Au plating bath (volume ~ 20 mL) composed of 7.9×10^{-3} M $\text{Na}_3\text{Au}(\text{SO}_3)_2$, 0.127 M Na_2SO_3 , and approximately 0.6 M formaldehyde (1 mL of formaldehyde 37% solution in water is added); the pH of the plating bath is around 11–11.5 for nanowires, which is lowered to 8 for nanotubes (see below). Note that the Au electroless bath component is typically obtained by 1:40 dilution of commercial plating baths, such as Oromerse SO Part B (Technic Inc.) which contains 0.4 troy ounces of gold in 200 mL (1 troy ounce = 31.1035 g of gold), that is, 0.316 M in $\text{Na}_3\text{Au}(\text{SO}_3)_2$ (5).
- (iv) After 15 h of electroless deposition, an additional 0.2 mL of formaldehyde is added.

Table 16.2.2

Conditions and materials used for the electrochemical template deposition of metals

Metal deposited	Templating membrane	Electrodeposition conditions	Nanomaterial obtained	Note	References
Au	Mica (track-etched)	Commercial Au electroplating solution, pH = 6, $T = 60^\circ\text{C}$, potential step up to a constant current value, or Au–Ag alloys electroplating solution, pH = 8–9	Wires ($\phi = 8$ nm for commercial bath and 20 nm for Au–Ag alloy bath)		(2)
Au	Alumina	Commercial electroless bath (Orotemp 24, Technic Inc.), galvanostatic ($0.8\text{--}1.2 \text{ mA/cm}^2$), two-compartment cell	Wires (microhole array); $\phi \sim 200$ nm		(53)
Au	Alumina	0.32 M Au(I) cyanide, 0.26 M citric acid, 0.65 M KOH, pH = 5–6, potentiostatic	Nanorods, $\phi = 12\text{--}22$ nm, length = 39–729 nm		(54)
Au	Alumina	12 g/L HAuCl ₄ , 160 g/L Na ₂ SO ₃ , 5 g/L EDTA, 30 g/L K ₂ HPO ₄ , 0.5 g/L CoSO ₄ , pH = 9.0, potentiostatic, 0.8 V	Wires ($\phi = 45$ nm)		(55)
Au	Polycarbonate	0.32 M gold(I)cyanide + 0.26 M citric acid, 0.65 M KOH, pH = 5–6, potentiostatic: –1.0 V vs. SCE	Wires	Wire diameter even three times the nominal diameter of the membrane	(47)
Au	Alumina	Commercial Au electrodeposition bath (Orotemp Technic Inc.); deposition at –2.5 V	Au nanowires ($\phi < 10$ nm)	Electrodeposition takes advantage of penetration of aluminum oxide barrier layer by reverse bias voltage	(20)
Au, Ag, Cu, Ni, Co, Rh	Polycarbonate	Electrodeposition from suitable baths added with 1–2% gelatin to improve polycarbonate wettability	Au, Ag, Cu single-crystalline nanowires; Ni, Co, Rh polycrystalline nanowires		(45)
Co	Crystalline bisphenol-A polycarbonate	CoSO ₄ bath, three-electrode cell, room temperature	Wires, $\phi = 70$ and 10 nm	Wires “toothpick” shape	(56)

(Continued)

Table 16.2.2 (Cont.)

Metal deposited	Templating membrane	Electrodeposition conditions	Nanomaterial obtained	Note	References
Co	Alumina	40 g/L $\text{CoSO}_4 \cdot \text{H}_2\text{O}$, 40 g/L H_3BO_3 , 20 g/L ammonium citrate, pH = 3.5, $T = 50^\circ\text{C}$, current density: 0.3–0.8 mA/cm ² , two-electrode cell	Wires, $\phi \sim 100$ nm		(57)
Co	Polycarbonate	400 g/L $\text{CoSO}_4 \cdot 7\text{H}_2\text{O}$ + 40 g/L H_3BO_3 , potentiostatic: -1.1 V vs. Saturated Calomel Electrode	Wires, $\phi \sim 10$ –200 nm	Wire diameter even three times the nominal pore diameter	(47)
Co	Polycarbonate	0.1 M H_3BO_3 + 5×10^{-2} M CoSO_4 , potentiostatic, applying a sequence of pulses (-1.3 and -0.8 V), three-electrode cell	Cigar-shaped monocristalline wires ($\phi \approx 60$ nm)		(58)
Co	Polycarbonate	0.1 M H_3BO_3 + 0.1 M CoSO_4 , potentiostatic, applying a sequence of pulses (-1.5 and -0.8 V), three-electrode cell	Wires or nanotubes	The nanotubes are obtained changing the pulse cycles	(59)
Co	Polycarbonate	20 g/L H_3BO_3 + 252 g/L $\text{CoSO}_4 \cdot 7\text{H}_2\text{O}$ + 7 g/L NaCl, pH = 3.6, potentiostatic	Arrays of nanowires		(60)
Cu	Polycarbonate	0.6 M CuSO_4 + H_2SO_4 (pH = 2), potentiostatic, -0.4 V vs. Cu ref.	Wires	“Foundation” film of Pt-Pd	(61)
Cu	Polycarbonate	125 g/L $\text{CuSO}_4 \cdot 5\text{H}_2\text{O}$ + H_2SO_4 up to pH = 1.0, potentiostatic: -0.2 V vs. SCE	Wires	Wire diameter even three times the nominal pore diameter	(47)
Fe	Polycarbonate	0.1 M H_3BO_3 + 5×10^{-2} M FeSO_4 , potentiostatic, applying a sequence of pulses (-1.3 and -0.8 V), three-electrode cell	Cigar-shaped monocristalline wires or tubes ($\phi \approx 60$ nm)	Short deposition time produced mainly nanotubes	(58)
Fe	Polycarbonate	0.1 M H_3BO_3 + 0.1 M FeSO_4 , potentiostatic, applying a sequence of pulses (-1.3 V/0.1 sec, cell off/2 sec), three-electrode cell	Nanotubes		(59)
Ni	Alumina	270 g/L $\text{NiSO}_4 \cdot 7\text{H}_2\text{O}$, 40 g/L $\text{NiCl}_2 \cdot \text{H}_2\text{O}$, 40 g/L H_3BO_3 , pH = 3.6, $T = 50^\circ\text{C}$, current density: 0.3–0.8 mA/cm ²	Wires, $\phi \sim 100$ nm		(57)

Ni	Alumina	$300 \text{ g/L } \text{NiSO}_4 \cdot 6\text{H}_2\text{O}$, $45 \text{ g/L } \text{NiCl}_2 \cdot 6\text{H}_2\text{O}$, $45 \text{ g/L } \text{H}_3\text{BO}_3$, pH = 4.5, T = 35 °C, constant current pulses	Wires, magnetic material	(62)
Ni	Polycarbonate	$515 \text{ g/L } \text{Ni}(\text{H}_2\text{NSO}_3)_2 \cdot 4\text{H}_2\text{O}$ + $20 \text{ g/L } \text{NiCl}_2 \cdot 6\text{H}_2\text{O}$ + $20 \text{ g/L } \text{H}_3\text{BO}_3$, pH = 3.4, potentiostatic: -1.2 V vs. SCE	Wires	Wire diameter even three times the nominal pore diameter (47)
Pd	Alumina	$1 \times 10^{-3} \text{ M } (\text{NH}_4)_2\text{PdCl}_4$ + 50 mM LiCl + 50 mM LiSO ₄ , four-electrode mode	Nanoparticles ($\phi \approx 3\text{--}5 \text{ nm}$)	Deposition at the polarized interface between aqueous solution and 1,2-dichloroethane (63, 64)
Pt	Alumina	$1 \times 10^{-3} \text{ M }$ ammonium tetrachloroplatinate + 50 mM LiCl + 50 mM LiSO ₄ , four-electrode mode	Nanoparticles ($\phi \approx 3\text{--}5 \text{ nm}$)	Deposition at the polarized interface between aqueous solution and 1,2-dichloroethane (63, 64)
Sn	Polycarbonate	$0.1 \text{ M } \text{Sn}_2\text{SO}_4$ + 2% gelatin, pH = 1 with H ₂ SO ₄ , E _{applied} = -80 mV	Single crystal nanowires	Super conducting material with nanoscopic effects on electric transport properties (48)
Sn	Alumina	$7 \text{ g/L } \text{SnCl}_2 \cdot 2\text{H}_2\text{O}$ + $25 \text{ g/L } \text{Na}_3\text{C}_6\text{H}_5\text{O}_7 \cdot 2\text{H}_2\text{O}$, potentiostatic, -0.8 V (vs. Ag/AgCl saturated), Sn wires annealed in the air give SnO ₂ wires	Sn and SnO ₂ nanowires array	(65)
Au/Sn	Polycarbonate	Sequential electrodeposition of Au and Sn using conditions as in references (20, 45) for Au and reference (48) for Sn	Striped Au/Sn/Au nanowires	(50)
Bi ₂ Te ₃	Alumina	HTeO ₂ + 25 mM, Bi(NO ₃) ₃ ·5H ₂ O 33 mM, galvanostatic deposition, 3.5 mA/cm ²	Nanowires	(66)
Bi ₂ Te ₃	Alumina	1 M HNO ₃ + elemental Bi and Te, three-electrode cell, potentiostatic (E < -0.45 V vs. Hg/Hg ₂ SO ₄)	Wires	(67)

(Continued)

Table 16.2.2 (Cont.)

Metal deposited	Templating membrane	Electrodeposition conditions	Nanomaterial obtained	Note	References
Co/Cu	Polycarbonate	Sulfate bath: 10^{-3} M Cu, 0.5 M Co, potentiostatic pulsed (-0.2 and -0.9 V)	Co/Cu multilayered wires	Giant magnetoresistance	(52)
Ni/Cu	Polycarbonate	2 M Nickel sulfamate, 0.02 M copper sulfate, 0.5 M boric acid, room temperature, pH = 3.5–4.0; potentiostatic pulsed; for Cu: -0.80 V; for Ni: -1.90 V vs. SCE	Multilayered wires ($\phi = 60\text{--}80$ nm, 5 μm length)		(51)
NiFe	Alumina	6 g/L $\text{FeSO}_4 \cdot 7\text{H}_2\text{O}$, 218 g/L $\text{NiSO}_4 \cdot 7\text{H}_2\text{O}$, 40 g/L H_3BO_3 , pH = 3.6, current density: 0.3–0.8 mA/cm ² , two-electrode cell	Magnetic nanowires		(57)

- (v) Deposition is carried out for 9 h more to give a total of 24 h of electroless deposition.
- (vi) The membrane is removed from the plating solution, rinsed with water, and immersed for approximately 6 h in 10% HNO₃ to eliminate traces of tin or silver.
- (vii) The membrane is then rinsed with water and dried in air.

Note that if the plating procedure is stopped after a relatively short time, Au nanotubes are formed within the pores (70–73). To fill the pores completely and obtain nanowires, the electroless plating process must proceed for about 24 h as described above (5). In order to slow the kinetics of the deposition, the process is performed between 0 and 5 °C.

In contrast to electrochemical template deposition, in the electroless method, the growth of the metal layer starts from the sensitized/activated sites located on the pore walls and progresses from the pore walls toward the center of the pore. This is the reason why stopping the deposition at short times results in hollow metal nanomaterials such as nanotubes (70). In fabricating Au nanotubes, it is also important to control the size of the gold particles that are deposited on the pore walls. This is achieved by controlling the pH of the deposition bath at a value around 10, for example, by adding carbonate buffer (73). After completion of the deposition, it is possible to separate the nanowires or nanotubes from the template membrane (see Section 16.2.3.3) or to keep them in the template. By keeping metal nanotubes in the membrane, it is possible to obtain separation membranes with metallized pores (71, 72) which can be further functionalized chemically by resorting to thiol chemistry (73), for example. In contrast, NEEs can be fabricated from the continuous metal nanowires which are kept inside the template membrane.

Examples of nanomaterials obtained by template electroless deposition of metals are listed in Table 16.2.3.

A new method for the chemical deposition of carbon/gold composite nanotubes in alumina templates has been proposed recently (79). It is based on the impregnation of the template pores with diluted hydrogen tetrachloroaurate (HAuCl₄)/acetone solutions and subsequent thermolysis. Gold(III) is reduced, whereas the solvent acetone is oxidized. The results are nanotubes whose walls consist of gold nanocrystals supported by amorphous carbon. The authors report that when the template pores have a diameter smaller than 180 nm, single crystal gold nanowires are obtained.

An elegant way to obtain nanotubes made of preformed metal nanoparticles (named nanoparticle nanotubes (NPNT)) has been reported recently by Rubinstein and coworkers (80). Their method is based on the assembly of gold or silver nanoparticles on the pore walls of a silane-treated alumina template. Following a published procedure (81), the silyl groups of 3-aminopropyl trimethoxysilane react with the hydroxyl groups on the alumina surface (80), thus leaving the amine groups available for binding the metal nanoparticles. The particles self-assemble and coalesce at room temperature within the pores to form the NPNTs.

16.2.3.3 Separation from the template

When the goal of the deposition is to obtain freestanding nanostructures in the form of nanowires, nanotubes, or nanocones, then the nanomaterial must be separated from the templating membrane. Track-etched membranes can be dissolved by using suitable organic solvents such as CH₂Cl₂ for PC (3, 47) or 1,1,1,3,3-hexafluoro-2-propanol (HFIP) for

Table 16.2.3

Examples of conditions and materials used for the electroless template deposition of metals

Metal deposited	Templating membrane	Electroless conditions	Nanomaterial obtained	References
Au	Polycarbonate	Sensitization: 0.026 M SnCl_2 + 0.07 M trifluoroacetic acid, 50/50 methanol/water; activation: 0.029 M AgNO_3 ; Au deposition: 7.79×10^{-3} M $\text{Na}_3\text{Au}(\text{SO}_3)_2$ + 0.127 M Na_2SO_3 + 0.625 M formaldehyde; temperature $\sim 0^\circ\text{C}$	Wires	(5)
Au	Polycarbonate	The same as reference (5), but with a different deposition time and at pH = 10 controlled with 0.025 M $\text{NaHCO}_3/\text{H}_2\text{SO}_4$	Nanotubes	(73)
Au	Home-etched polycarbonate (37) or poly(ethylene terephthalate) (40) with conical pores	Same as above and in reference (73)	Nanocones	(37, 40)
Ag	Polycarbonate	1st step: 0.026 M SnCl_2 + 0.07 M trifluoroacetic acid; 2nd step: 2.3 g AgNO_3 + 1.9 mL NH_4OH + 22.7 mL H_2O ; 3rd step: 7.95 g $\text{KNaC}_4\text{O}_6\text{H}_4$ + 0.57 g MgSO_4 + 18.2 mL H_2O , temperature = 35°C	Nanotubes	(74)
Cu	Polycarbonate	Pre-activation: SnCl_2 10 g/L + 10 mL/L HCl; activation: PdCl_2 0.1 g/L + 10 mL HCl; deposition: $\text{CuSO}_4 \cdot 5\text{H}_2\text{O}$ 10 g/L + NaOH 12 g/L (pH = 12.1) + tartaric acid 18 g/L (complexing agent) + formaldehyde 10 mL/L (reducing agent)	Tubes: cylindrical, cigar-shaped, conical; $\phi_{\text{external}} = 300\text{--}2000\text{ nm};$ $\phi_{\text{internal}} = \text{function of deposition time}$	(75)
Pd	Polycarbonate, alumina	Ammonium tetrachloropalladate + decamethylferrocene in 1,2-dichloroethane	Nanoparticles	(76)
Ni-P	Polycarbonate	Sensitization: 0.026 M SnCl_2 + 0.07 M trifluoroacetic acid, methanol/water solution; activation: 0.25 g/L PdCl_2 + 1.0 g/L HCl; Ni plating: $\text{Na}_2\text{PO}_2 \cdot 2\text{H}_2\text{O}$ 20 g/L, $\text{NiSO}_4 \cdot 6\text{H}_2\text{O}$ 40 g/L, $\text{NaC}_6\text{H}_5\text{O}_7 \cdot 2\text{H}_2\text{O}$ 100 g/L, NH_4Cl 50 g/L; NH_4OH (pH adjustment)	Ni-P tubules electrode array; internal diameter $\approx 180\text{ nm};$ wall thickness $\approx 20\text{ nm};$ length 2 μm	(77)
Co–Fe–P	Alumina	Sensitization: SnCl_2 10 g/L; activation: PdCl_2 1 g/L; plating: $\text{CoSO}_4 \cdot 7\text{H}_2\text{O}$ 20 g/L + $\text{FeSO}_4 \cdot 7\text{H}_2\text{O}$ 5 g/L + $\text{NaH}_2\text{PO}_2 \cdot 2\text{H}_2\text{O}$ 25 g/L + $\text{KNa}(\text{C}_4\text{H}_4\text{O}_6) \cdot 4\text{H}_2\text{O}$ (Rochelle salt) 60 g/L at 80–85 $^\circ\text{C}$	Nanowire arrays	(78)

PET (40). Polymers can also be etched by treatment with oxygen plasma (82). Dissolution of alumina templates is easily achieved by immersion in strong alkali such as 5 M KOH or NaOH (20).

16.2.4 Morphological and optical properties

16.2.4.1 SEM-TEM studies

Scanning or transmission electron microscopy (SEM or TEM, respectively) are typically used for performing morphological characterization of nanomaterials obtained by template synthesis. The resolution of the images is improved if the nanomaterial is separated from the host membrane.

As an example, Figure 16.2.6 shows SEM and TEM images of nanostructures produced in PC templates. Figure 16.2.6A images 30 nm nanofibers of an NEE still in the

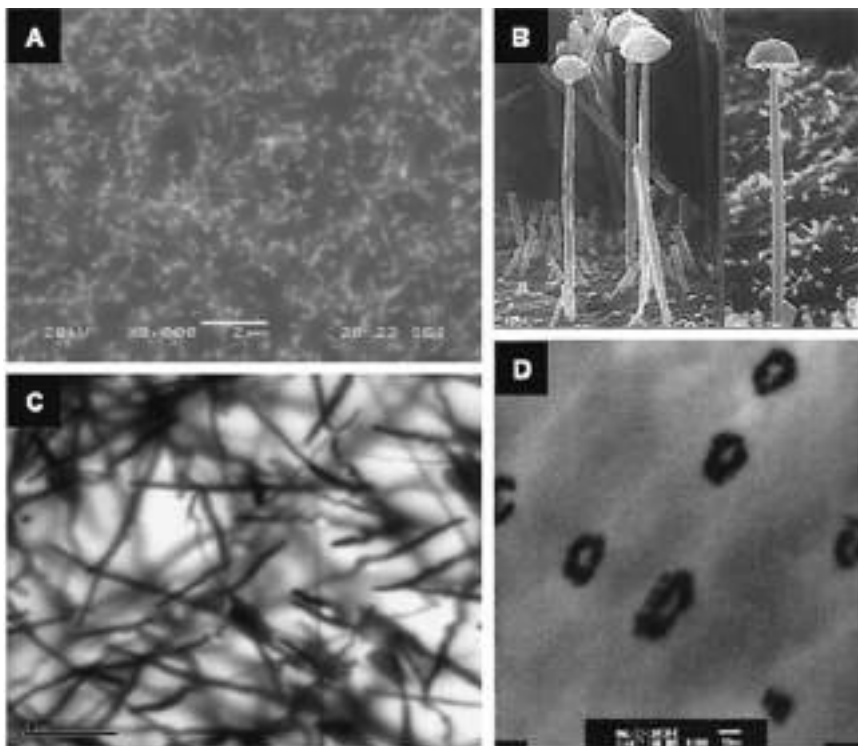


Figure 16.2.6 (A) SEM image of the surface of an Au-NEE, in PC template, pore diameter 30 nm; (B) SEM image of Ni wires, template pore diameter 80 nm, after dissolution of the PC membrane; (C) TEM image of an Au-NEE, template pore diameter 30 nm with the nanofibers still embedded in the polycarbonate; (D) TEM image of a microtomed section of a PC membrane after deposition of Au tubes within the pores of the membrane. Reprinted with permission from reference (83) for (A) and (C), reference (47) for (B), and reference (5) for (D).

polymer membrane. The surface gold layers present on both sides of the membrane at the end of the deposition step have been removed before the SEM analysis. This image clearly shows the surface of the nanodisks emerging from the PC template. The fading lines behind the nanodisks are the traces of the nanofibers that grew inside the membrane. The observation of such traces is related to the partial transparency of the PC template to the electron beam. The nanofibers are not aligned parallel, but have a considerable angular distribution as a consequence of the angles of the original trajectories of the tracks used to sensitize the membrane before etching of the pores in the membrane production (47). Figure 16.2.6B shows that more detailed images are obtained after the removal of the guest membrane by dissolution with CH_2Cl_2 ; in this case, the nickel nanowires have a curious mushroom shape (47). Figure 16.2.6C shows that information about the inner structure of the nanofibers inside PC templates can be obtained by TEM without removal of the guest membrane thanks to the transparency of the PC to electron beams (83). However, some distortion and artifacts cause apparent whirling and bending of the fibers and are attributed to possible interactions between the e-beam and the polymer. High-resolution TEM images of nanowires isolated from template membranes (51, 63) also permit the study of the structure and crystallinity of the nanofibers. Finally, Figure 16.2.6.D demonstrates that microtomy can also be used to characterize templated nanostructures, in this case, gold nanotubes of 30 nm diameter in PC (5).

16.2.4.2 Optical properties

Nanometals have interesting optical properties, whether they are inside the host template or liberated from it. For example, suspensions of nanoscopic Au particles can be pink, purple, or blue, depending on the diameter of the particles. These colors arise from the plasmon resonance absorption of the nanometal particle (25). Membranes containing Au nanowires also show this plasmon resonance band, and as a result, such membranes can show a wide variety of colors (42). This absorption in the visible region, typically between 400 and 800 nm for 10–30 nm diameter particles, provides an interesting optical approach to characterizing Au nanowires (5).

One attractive feature of host templates such as porous anodic alumina is the parallel alignment of the pores. This feature permits the straightforward interpretation of the plasmon resonance spectra of non-spherical metal particles that are prepared within such pores. Figure 16.2.7A shows the plasmon resonance spectra of a series of gold nanorod/porous alumina composite films measured with light incident normal to the film surface (23, 84).

Since the rods are also aligned perpendicular to the film surfaces, the electric field of the light is incident only along the diameter (or short axis) of the rods. Thus, only one plasmon resonance band appears in each spectrum (the transverse resonance). An increase in the aspect ratio (length/diameter) of the particles causes a blue shift in the maximum of the plasmon resonance absorption (17). The change in the incidence angle (θ) modifies the spectrum (see Figure 16.2.7B): as θ increases, a second spectral band grows in corresponding to the long-axis resonance. Converse to the transverse resonance case, the wavelength maximum of the longitudinal resonance increases with increasing particle aspect ratio (23, 85).

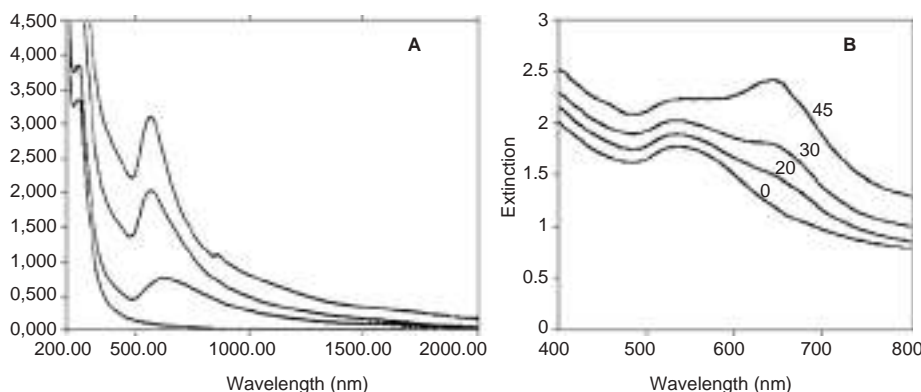


Figure 16.2.7 UV-vis spectra of oriented Au nanoparticle composites. (A) Normal incidence spectra of 60 nm diameter Au rods in alumina membrane; particle aspect ratios: (1) blank; (2) 1; (3) 3.38; (4) 5.28. (B) Polarization spectra of Au nanorods (diameter = 30 ± 4 nm; length = 54 ± 4 nm) in host alumina membrane at different incident angles θ , indicated in the graph and measured in degrees relative to membrane normal surface. Adapted with permission from references (23, 84).

The spectra resulting from the aqueous dispersion of the nanorods removed from the host template show two plasmon resonance bands: a strong one at long wavelengths due to the long-axis resonance and a weaker one at shorter wavelengths that originates from the transverse resonance (85).

All of these optical features are useful in characterizing the shape and spatial distribution of the nanostructures.

16.2.5 Electrochemistry with template nanomaterials: nanoelectrode ensembles

Nanoelectrode ensembles (NEEs) (see also Chapter 10 of this handbook) are nanotech-based electroanalytical tools which find application in a variety of fields ranging from electroanalysis to sensors (86) and electronics (7). They are fabricated by growing metal nanowires in the pores of a template, typically a PC nanoporous membrane. The density of the pores in the template determines the number of Au-disk nanoelectrode elements per cm^2 of NEE surface and, correspondingly, the average distance between the nanoelectrode elements. Such electrode systems proved to be valuable tools for trace determinations and kinetics studies by simply using cyclic voltammetry (CV) (5, 69, 86, 97).

The NEE fabrication procedure used in our laboratory is described below and is based on that reported in reference (5) apart from minor modifications such as positioning of the copper tape (see below and reference (83)). A scheme of an NEE is presented in Figure 16.2.8; specific details on the construction can be found in the original papers (5, 83) as well as in recent reviews (7, 86, 87). The starting material is a piece of golden PC membrane with

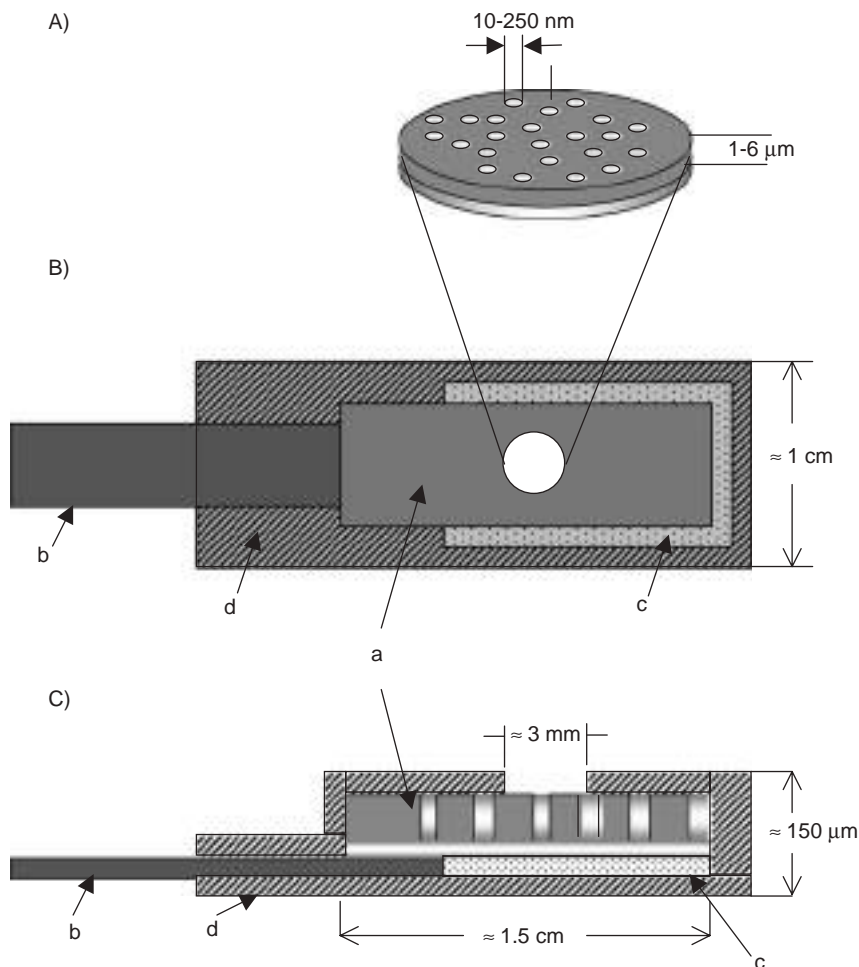


Figure 16.2.8 Scheme of an Au-NEE prepared using a track-etched polycarbonate membrane as template (A). Particular of the section of the active area; (B) top view; (C) section of the all NEE ready for use as working electrode. (a) Track-etched golden membrane; (b) copper adhesive tape with conductive glue to connect to instrumentation; (c) aluminum adhesive foil with non-conductive glue; (d) insulating tape. Note: Some dimensions are only indicative and not in scale.

gold within the pores and on both faces of the membrane; this membrane, named Au/Au-PC/Au, is the final product of the Au electroless deposition process. In particular, a 5×6 mm piece of the Au/Au-PC/Au membrane is first affixed to a 6×15 mm piece of adhesive aluminum foil tape. The Au/Au-PC/Au membrane is placed on the Al foil tape such that the Au film covering the rough face of the membrane is down (i.e., against the adhesive). A rectangular strip (6×40 mm) of copper foil with a conductive adhesive is affixed to the lower Au-coated surface of the Au/Au-PC/Au membrane between the Au on the rough face

of the membrane and the Al foil. The copper foil is positioned such that it covers only about 1 mm of the 6 mm length of the Au/Au-PC/Au membrane. This copper foil tape acts as a current collector and working electrode lead for the NEE. The upper Au surface layer from the portion of the Au/Au-PC/Au membrane not covered by the Cu foil tape is then removed by simply applying and then removing a strip of Scotch tape. Removal of the Au surface layer exposes the disk-shaped ends of the Au wires within the pores of the membrane. These nanodisks will become the active electrode elements. At this point, the NEE assembly is heat-treated at 150 °C for 15 min. This procedure produces a water-tight seal between the Au nanowires and the pore walls. Finally, strips of strapping tape are applied to the lower and upper surfaces of the assembly to insulate the Al and Cu foil tapes. A hole (diameter of 3 mm) is punched into the upper piece of tape prior to the placement on the assembly. This hole defines the geometric area (A_{geom}) of the NEE. All the nanoelectrodes in the NEE are connected to each other, so that they all experience the same applied potential.

Track-etched polymer membranes are preferred for NEE fabrication over alumina membranes because track-etched membranes are not brittle and they have smaller pore densities. From an electroanalytical viewpoint, the latter is an important feature since it reduces the interactions between individual nanoelectrode elements (see below).

16.2.5.1 Current signals of nanoelectrode ensembles

From a voltammetric viewpoint, an NEE is a large assembly of very small ultramicroelectrodes confined in a rather small space. As shown in Figure 16.2.9, NEEs can exhibit three distinct voltammetric response regimes depending on the scan rate or distance between the nanoelectrode elements (88, 89; see also Chapter 10 of this handbook)—(A) *Total Overlap Regime*: when radial diffusion boundary layers overlap totally (slow scan rates and/or small distance between nanoelectrodes); (B) *Pure Radial*: when the nanoelectrodes behave independently (higher scan rates, larger distances between nanoelectrodes; (C) *Linear*: when the nanoelectrodes behave as isolated planar electrodes (very high scan rates).

The transition from the Total Overlap to the Pure Radial Regime has been demonstrated experimentally as a function of the template pore density (88). For electroanalytical applications, the most advantageous regimes are the Total Overlap and the Pure Radial Regimes because they give high faradaic-to-capacitive current ratios (90). The diffusion regime usually observed at NEEs fabricated from commercial track-etched membranes is the Total Overlap Regime (5).

Relevant geometric parameters that define the behavior of NEEs include:

(i) **Total geometric area (A_{geom})**: Overall area (nanodisks plus bare membrane area) of the ensemble exposed to the sample solution; typical values for this parameter range from 0.008 to 0.580 cm² (91). A_{geom} is determined by the dimension of the hole punched into the insulator (see Figure 16.2.8).

(ii) **Active area (A_{act})**: Area of the metal nanoelectrode elements alone. It can be calculated by the pore density (p), the average radius of the pores (r), and the geometric area, according to the following equation:

$$A_{\text{act}} = \pi r^2 p A_{\text{geom}} \quad (16.2.1)$$

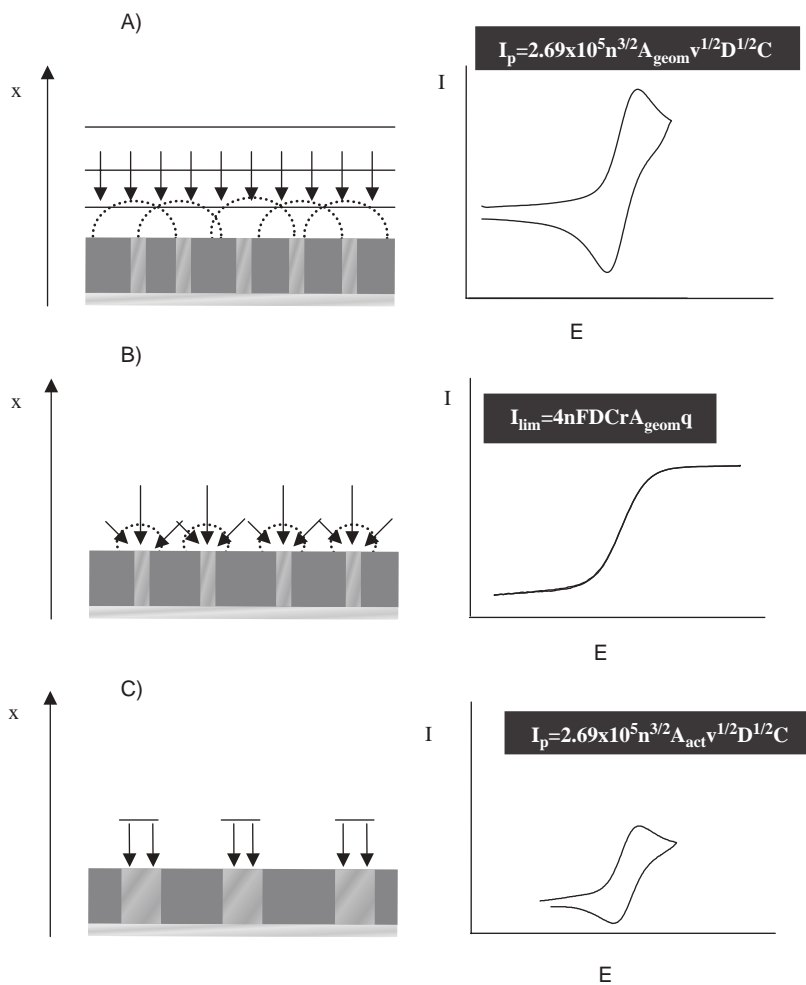


Figure 16.2.9 Schematic drawing of the different diffusional regimes at NEE: (A) Total Overlap; (B) Pure Radial; (C) Linear active. The scan rate or the distance between the nanodisk elements increases from (A) to (C). Relevant equations for peak currents (A and C) and plateau current (B) refer to reversible redox systems. A_{act} is the active area (nanodisk surface), A_{geom} is the total geometric area of the ensemble (nanodisks and insulator), q is the nanodisk density (disk cm^{-2}), and all other symbols have their usual meaning. Reprinted with permission from reference (86). (for colour version: see colour section at the end of the book).

(iii) **Fractional electrode area (f):** It is defined as the ratio between active and geometric areas:

$$f = \frac{A_{\text{act}}}{A_{\text{geom}}} \quad (16.2.2)$$

By substitution of equation (16.2.1), it can be easily calculated also as:

$$f = \pi r^2 p \quad (16.2.3)$$

The faradaic peak current at an NEE operating in the Total Overlap Regime for a reversible redox system obeys the Randles–Sevcik equation (5):

$$i_p = 2.69 \times 10^5 n^{3/2} A_{\text{geom}} D^{1/2} C^* v^{1/2} \quad (16.2.4)$$

where i_p is the peak current (A), A_{geom} is the geometric area of the ensemble (cm^2), D is the diffusion coefficient ($\text{cm}^2 \text{ sec}^{-1}$), C^* is the redox species bulk concentration (mol cm^{-3}), and v is the scan rate (V sec^{-1}).

At the same NEE, the double-layer charging current (i_C) is proportional to the area of the electrode elements (active area, A_{act}) (92, 93):

$$i_C = v C_{\text{dl}} A_{\text{act}} \quad (16.2.5)$$

where C_{dl} is the double-layer capacitance of the metal nanodisks of the NEE. Typical i_C values will be in the range of 1 and 2 nA (based on a C_{dl} value between 20 and 40 $\mu\text{F cm}^{-2}$ (93), a gold NEE with $A_{\text{geom}} = 0.079 \text{ cm}^2$, pore density = $6 \times 10^8 \text{ pore cm}^{-2}$, average pore radius = $1.5 \times 10^{-6} \text{ cm}$, and scan rate (v) = 0.1 V sec^{-1}).

Faradaic-to-capacitive current ratios at an NEE and a conventional electrode with the same geometric area are related by equation (16.2.6) (86):

$$\left(\frac{i_F}{i_C} \right)_{\text{NEE}} = \left(\frac{i_F}{i_C} \right)_{\text{conv}} \left(\frac{A_{\text{geom}}}{A_{\text{act}}} \right) = \left(\frac{i_F}{i_C} \right)_{\text{conv}} \left(\frac{1}{f} \right) \quad (16.2.6)$$

This ratio is larger at the NEE than that at the conventional electrode by a factor that is the reciprocal of the fractional electrode area f . Since typical f values for NEEs are between 10^{-3} and 10^{-2} , i_F/i_C ratios at NEEs can be 2–3 orders of magnitude higher than the ratios at conventional electrodes of the same geometric area. Thus, detection limits at NEEs are 2–3 orders of magnitude lower than that at regular electrodes (5, 68, 69).

From a practical viewpoint, the values given for the faradaic peak currents and for the double-layer charging currents calculated by equations (16.2.4) and (16.2.5) can be used to discriminate between “good” and “bad” NEEs. In our laboratory, from a commercial PC nanoporous membrane of 47 mm diameter, we prepare a rather large number (typically around 30) of NEEs, which are then selected on the basis of the agreement between theoretical and experimental i_F and i_C values. The latter can be obtained from the cyclic voltammogram recorded in supporting electrolyte alone (5; 92, p. 18) and the former by recording the CV in solution containing a known concentration of a reversible redox probe of known diffusion coefficient. From the CVs with and without the redox probe we select as “good NEEs” those that are characterized by $i_{F(\text{exp})} = i_{F(\text{theor})}(1 \pm 0.2)$ and $i_{C(\text{exp})} = i_{C(\text{theor})}(1 \pm 0.5)$, where $i_{F(\text{exp})}$ and $i_{C(\text{exp})}$ are the faradaic and double-layer charging currents measured experimentally, and $i_{F(\text{theor})}$ and $i_{C(\text{theor})}$ are values calculated by equations (16.2.4) and (16.2.5). Figure 16.2.10 reports typical experimental CVs (dotted and dashed lines) recorded at “good” (part A) and “bad” NEEs (part B). The comparison with the simulated CV curves (full lines in the same figure) allows one to immediately distinguish good ensembles from bad ones. Note that the two experimental curves in part B show the features typical for two kinds of defects which can be produced during the NEEs preparation.

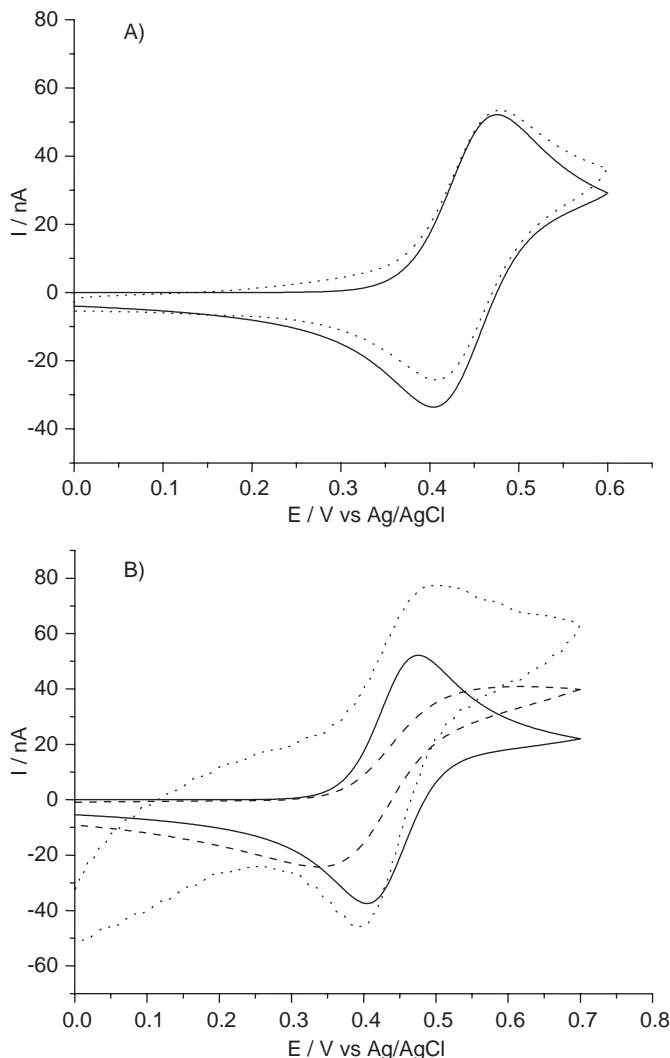


Figure 16.2.10 Comparison between digital simulations (—) and experimental CVs; the experimental curves refer to (A) (···) a “good” NEE; (B) (··· and - - -) a “bad” NEE. Experimental conditions: 10^{-2} M NaNO₃, 6×10^{-6} M (ferrocenylmethyl)-trimethylammonium hexafluorophosphate, $A_{\text{geom}} = 0.07$ cm², scan rate 50 mV sec⁻¹. Additional parameters used for the digital simulation (run with CH Instruments software): $E^\circ = 0.44$ V, $k^\circ = 0.007$ (which is really k_{app}° , see equation (16.2.8)), and $D = 4 \times 10^{-6}$ cm² sec⁻¹ (94).

The dotted-line voltammogram indicates that this NEE is affected by a large capacitive current, which was probably produced by poor sealing between the nanowires and the surrounding PC insulator and/or by heavy scratches or abrasions of the PC membrane caused by improper handling of the NEE. The dashed-line voltammogram shows a radial diffusive contribution to the overall signal and a current smaller than the theoretical one. This

suggests larger distances between and a smaller number of nanoelectrode elements with respect to expected values, possibly due to not all of the pores being filled by gold in the final NEE. The number of NEEs that satisfy the above criteria ranges typically from 25 to 40% in a batch of NEEs obtained from one PC membrane.

16.2.5.2 Electron transfer kinetics

A distinctive feature of NEEs is that electron transfer kinetics appear slower than those at conventional electrodes (5). In fact, NEEs behave as electrodes with a partially blocked surface (PBE). According to the model elaborated by Amatore *et al.* (95), the current response at a PBE is identical to that at a bare electrode of the same overall geometric area but with a smaller apparent standard rate constant for the electron transfer which decreases as the coverage with the blocking agent increases. Such an apparent rate constant (k°_{app}) is related to the true standard charge transfer rate constant (k°) and the fraction of blocked surface (ϑ) by the following relationship (95):

$$k^{\circ}_{app} = k^{\circ}(1 - \vartheta) \quad (16.2.7)$$

Considering that $\vartheta = (A_{geo} - A_{active})/A_{geo}$, then equation (16.2.7) can be easily converted into:

$$k^{\circ}_{app} = k^{\circ}f \quad (16.2.8)$$

where f is the fractional electrode area, defined by equation (16.2.2).

In CV at a conventional electrode, the reversibility depends on both k° and the scan rate, while at an NEE, it depends on k°_{app} and the scan rate (5). At a conventional electrode, a redox system gives a reversible voltammetric pattern when $v^{1/2} \leq (k^{\circ}/0.3)$ (see p. 239 in reference (92)). At NEEs, equation (16.2.8) suggests that, for a certain redox couple, the scan rate that defines the transition between reversible and quasi-reversible behavior will be placed at a lower value than that at conventional electrodes. Note that such a boundary scan rate will decrease with decreasing f .

From a mechanistic viewpoint, this behavior means that with NEEs characterized by small f values (for example, very small diameter nanodisks and/or very small pore densities), it is experimentally easier to measure large k° values (5, 69, 94). Values of k°_{app} are measured typically by CV operating within a scan rate range where the redox system behaves quasi-reversibly (92, 93). By the analysis of the ΔE_p dependence on the scan rate (93) and by using suitable working curves (96), k° values are readily obtained. At NEEs, quasi-reversible behavior is observed at scan rates 2–3 orders of magnitude lower than those at conventional electrodes (depending on f). What is measured experimentally under such conditions is really the smaller k°_{app} value, which is converted into the larger k° by equation (16.2.8) (69, 94).

16.2.5.3 Electroanalysis with NEEs

The potential window accessible at gold disk NEEs (Au-NEEs) has been studied in detail (5, 69). It was shown that the limit at negative potentials is determined by the hydrogen evolution reaction and depends on the solution pH (69). The limit at positive potentials is

given by the formation of gold oxide. NEEs are typically used at low analyte concentrations (typically from 10^{-5} to lower than 10^{-9} M) (5, 69) so that faradaic peak current signals can be on the order of a few nA down to a few pA. Therefore, relatively high electronic amplification of the current signal is required. By operating with suitable amplification levels at pH around 7 and micromolar (or lower) analyte concentrations, the potential window accessible at Au-NEEs is limited approximately to the range between -0.750 and $+0.800$ V vs. Ag/AgCl. Such limits can change with the nature of the metal of which the nanoelectrode is made, but no precise information is available up to now for materials different from gold.

The ability of NEEs to furnish well-resolved cyclic voltammograms has allowed researchers to develop sensitive methods for trace determination of redox species characterized by relatively fast electron transfer kinetics and an electroactivity range within the above-mentioned potential window. As explained in Section 16.2.5.2, the high sensitivity of NEEs to electron transfer kinetics causes the observation of a perfectly reversible electrochemical behavior only to very fast redox couples, while for “sluggish” redox couples, quite flattened voltammetric patterns are recorded. In addition to the application for trace electroanalysis at well-known reversible redox probes such as ferrocene derivatives or ruthenium complexes (5, 97), Figure 16.2.11 shows that NEEs can be used for CV at micromolar concentration levels of more complex redox systems such as organic mediators like phenothiazines (azure B in Figure 16.2.11B), methylviologen (69) (not shown), or the heme-protein cytochrome *c* (see Figure 16.2.11A). Note that for these redox systems, k^o values are 8×10^{-3} cm sec $^{-1}$ for azure B (69) and >0.1 cm sec $^{-1}$ for cytochrome *c* (98).

The cytochrome *c* case is noteworthy because at NEEs, well-resolved CVs are obtained in diluted solutions of the protein both with and without promoters such as 4,4'-bipyridyl typically used for promoting cytochrome *c* electrochemistry (99–101). These promoters are generally required to avoid adsorption/denaturation (83, 102, 103) of cytochrome *c* on the Au surface. However, such an adsorption is concentration dependent so that lowering the cytochrome *c* solution concentration below the adsorption limit (possible at NEEs thanks to their lower detection limit) can overcome adsorption-related problems. A similar situation has been reported for the adsorption of some organic dyes such as the phenothiazines (69).

Recently, it was shown that by etching only a layer of the templating membrane, it is possible to fabricate ensembles of 3D nanowires instead of 2D nanodisks (82, 104). The partial etching can be performed by either oxygen plasma (82) or partial dissolution of the PC using a mixture of ethanol and dichloromethane (105). The use of nanowire ensembles together with suitable redox indicators (104, 106, 107) has been demonstrated to be useful for improving the sensitivity for the electrochemical detection of DNA duplexes. This example illustrates how NEEs can be used advantageously for advanced bio-electroanalytical sensing.

16.2.6 Conclusions and prospects

The use of nanoporous membranes as templates constitutes an attractive and practical methodology for the fabrication of nanomaterials characterized by high aspect ratios, ranging from relatively simple nanomaterials made of just one component, such as metal nanowires

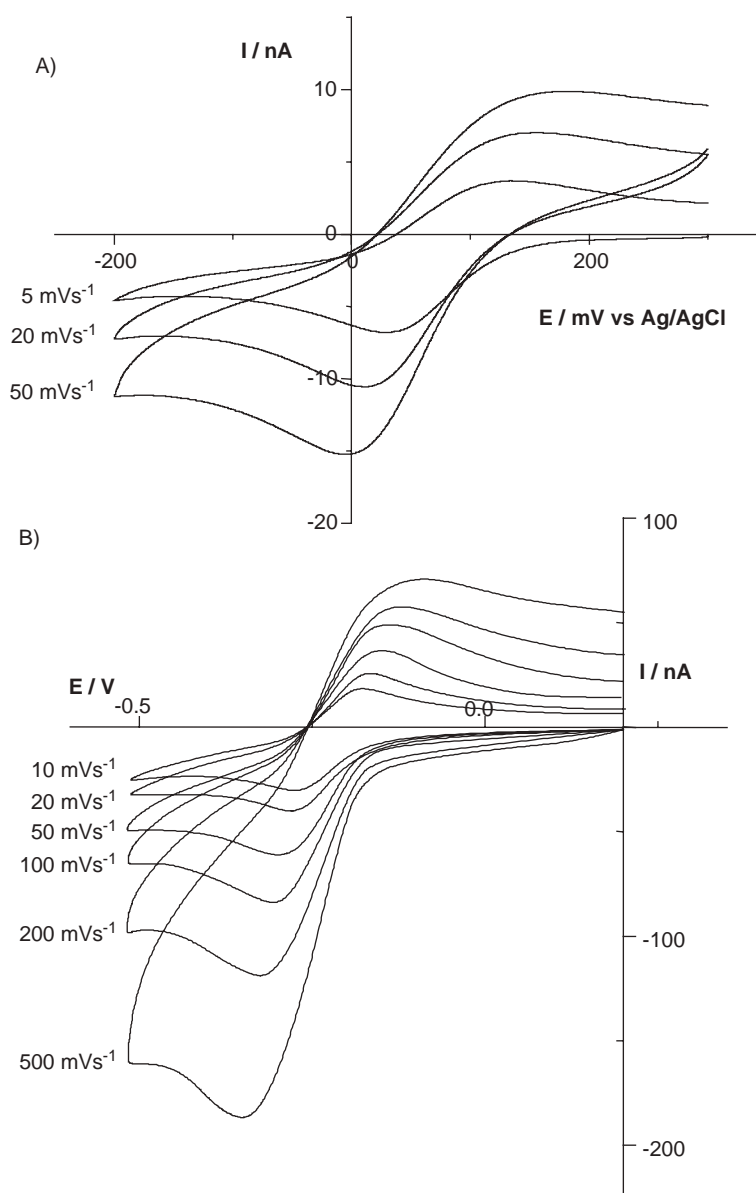


Figure 16.2.11 CVs recorded at Au-NEEs in: (A) 5×10^{-6} M cytochrome *c* and (B) 5×10^{-6} M azure B; scan rates as indicated in the figure; supporting electrolyte in both cases: 10^{-2} M phosphate buffer at pH = 7.4; nominal diameter of the Au nanodisks = 30 nm; disks' density = 6×10^8 disks cm^{-2} . Reprinted with permission from reference (83) for (A) and reference (69) for (B).

and nanotubes, to more complex structures such as nanotubes of nanoparticles, nanotubes in nanotubes, or segmented nanowires.

The description presented here focused mainly on metal-based nanomaterials. However, the same principles can find application and extension to the preparation of nanostructures made of organic polymers, oxides, and salts.

It is reasonable to think that such a membrane-based approach to the synthesis of nanomaterials will find wider application due to the fact that it allows easy fabrication and rapid screening of the properties of new and unusual nanomaterials.

Template synthesis has made accessible to almost any electrochemical laboratory the fabrication of electrode systems with critical dimensions in the nanometer domain. Future research efforts will likely be devoted to fundamental studies aimed at better understanding the effects related to decreasing the size of electrodes to dimensions comparable or smaller than the dimensions of the double- and diffusion layers. From a practical and application perspective, the next frontier will focus on the development of methods and materials that allow one to better control the size, spatial distribution, and addressability of the single nanoelectrode elements in rather complex arrays or ensembles.

REFERENCES

1. G. E. Possin, *Rev. Sci. Instrum.* **41**, 772 (1970).
2. W. D. Williams, N. Giordano, *Rev. Sci. Instrum.* **55**, 410 (1984).
3. R. M. Penner, C. R. Martin, *Anal. Chem.* **59**, 2625 (1987).
4. J. F. Cheng, C. R. Martin, *Anal. Chem.* **60**, 2163 (1988).
5. V. P. Menon, C. R. Martin, *Anal. Chem.* **67**, 1920 (1995).
6. K. Uosaki, K. Okazaki, H. Kita, H. Takahashi, *Anal. Chem.* **62**, 652 (1990).
7. C. R. Martin, D. T. Mitchell, in *Electroanalytical Chemistry, A Series of Advances*, A. J. Bard, I. Rubinstein, Eds., Marcel Dekker: New York, 1999, Vol. 21, p. 1.
8. T. Thurn-Albrecht, J. Schotter, G. A. Kästle, N. Emley, T. Shibauchi, L. Krusin-Elbaum, K. Guarini, C. T. Black, M. T. Tuominen, T. P. Russel, *Science* **290**, 2126 (2000).
9. E. Jeoung, T. H. Galow, J. Schotter, M. Bal, A. Ursache, M. T. Tuominen, C. M. Stafford, T. P. Russel, V. M. Rotello, *Langmuir* **17**, 6396 (2001).
10. B. B. Lakshmi, C. J. Patrissi, C. R. Martin, *Chem. Mater.* **9**, 2544 (1997).
11. C. J. Patrissi, C. R. Martin, *J. Electrochem. Soc.* **146**, 3176 (1999).
12. N. Li, C. R. Martin, B. Scrosati, *J. Power Sources* **97–98**, 240 (2001).
13. G. Che, K. B. Jirage, E. R. Fisher, C. R. Martin, H. Yoneyama, *J. Electrochem. Soc.* **144**, 4296 (1997).
14. J. W. Diggle, T. C. Downie, C. W. Goulding, *Chem. Rev.* **69**, 365 (1969).
15. A. Despic, V. P. Parkhutik, in *Modern Aspects of Electrochemistry*, J. O. Bockris, R. E. White, B. E. Conway, Eds., Plenum Press: New York, 1989, Vol. 20, p. 401.
16. A. T. Shawaqfeh, R. E. Baltus, *J. Membr. Sci.* **157**, 147 (1999).
17. G. L. Hornyak, C. J. Patrissi, C. R. Martin, *J. Phys. Chem. B* **101**, 1548 (1997).
18. P. Bocchetta, C. Sunseri, A. Bottino, G. Capannelli, G. Chiavarotti, S. Piazza, F. D. Quarto, *J. Appl. Electrochem.* **32**, 977 (2002).
19. Y. Piao, H. Lim, J. Y. Chang, W.-Y. Lee, H. Kim, *Electrochim. Acta* **50**, 2997 (2005).
20. M. Tian, S. Xu, J. Wang, N. Kumar, E. Wertz, Q. Li, P. M. Campbell, M. H. W. Chan, T. E. Mallouk, *Nano Lett.* **5**, 697 (2005).

21. G. Paternarakis, *J. Electroanal. Chem.* **404**, 69 (1996).
22. R. C. Furneaux, W. R. Rigby, A. P. Davidsons, *Porous Films and Methods Forming Them*, USA, Patent number 4,687,551 (1987).
23. J. C. A. Foss, G. L. Hornyak, J. A. Stockert, C. R. Martin, *J. Phys. Chem.* **98**, 2963 (1994).
24. Z. Zhang, D. Gekhtman, M. S. Dresselhaus, J. Y. Ying, *Chem. Mater.* **11**, 1659 (1999).
25. C. A. Foss, Jr., in *Metal Nanoparticles, Synthesis, Characterization and Applications*, D. L. Feldheim, J. C. A. Foss, Eds., Marcel Dekker: New York, 2002, p. 119.
26. T. Parpaleis, J. M. Laval, M. Majda, C. Bourdillon, *Anal. Chem.* **64**, 641 (1992).
27. A. Mozalev, S. Magaino, H. Imai, *Electrochim. Acta* **46**, 2825 (2001).
28. C. C. Harrell, S. B. Lee, C. R. Martin, *Anal. Chem.* **75**, 6861 (2003).
29. P. Apel, *Radiat. Meas.* **34**, 559 (2001).
30. P. Y. Apel, Y. E. Korchev, Z. Siwy, R. Spohr, M. Yoshida, *Nucl. Instrum. Methods Phys. Res. B* **184**, 337 (2001).
31. C. Trautman, W. Bruchle, R. Spohr, J. Vetter, N. Angert, *Nucl. Instrum. Methods Phys. Res. Sect. B* **111**, 70 (1996).
32. L. Klintberg, M. Lindberg, G. Thornell, *Nucl. Instrum. Methods Phys. Res. Sect. B* **184**, 536 (2001).
33. R. L. Fleisher, P. B. Price, R. M. Walker, *Nuclear Tracks in Solids: Principle and Applications*, University of California Press: Berkley, CA, 1975.
34. Z. Siwy, P. Apel, D. Baur, D. D. Dobrev, Y. E. Korchev, R. Neumann, R. Spohr, C. Trautmann, K.-O. Voss, *Surf. Sci.* **532**, 1061 (2003).
35. R. Spohr, *Methods and Device to Generate a Predetermined Number of Ion Tracks*, Germany, Patent number DE 2951376C2 (1983).
36. E. Ferain, R. Legras, *Nucl. Instrum. Methods B* **174**, 116–122 (2001).
37. N. Li, S. Yu, C. C. Harrell, C. R. Martin, *Anal. Chem.* **76**, 2025 (2004).
38. C. P. Bean, W. De Sorbo, US Patent 3,770,532-19731 106 (9 February 1968).
39. Z. Siwy, D. Dobrev, R. Neumann, C. Trautmann, K. Voss, German and US patent, registration on 26.02.2002, no. 102 08 023.2, Verfahren zur Herstellung von Nanostrukturen in Membranen und Asymmetrische Membran, *Appl. Phys. A* **76**, 781 (2003).
40. P. Scopece, L. A. Baker, P. Ugo, C. R. Martin, *Nanotechnology* **17**, 3951 (2006).
41. V. A. Oleinikof, Y. V. Tolmachyova, V. V. Berezhkin, A. I. Vilensky, B. V. Mchedlishvili, *Radiat. Meas.* **25**, 713 (1995).
42. C. R. Martin, *Science* **266**, 1961 (1994).
43. L. D.-D. Pra, E. Ferain, R. Legras, S. Demoustier-Champagne, *Nucl. Instrum. Methods Phys. Res. B* **196**, 81 (2002).
44. P. Ugo, L. M. Moretto, G. A. Mazzocchin, P. Guerriero, C. R. Martin, *Electroanalysis* **10**, 1168 (1998).
45. M. Tian, J. Wang, J. Kurtz, T. E. Mallouk, M. H. W. Chan, *Nano Lett.* **3**, 919 (2003).
46. W. Kautek, S. Reetz, S. Pentzien, *Electrochim. Acta* **40**, 1461 (1995).
47. C. Schönenberger, B. M. I. v. d. Zande, L. G. J. Fokkink, M. Henny, C. Schmid, M. Krüger, A. Bachtold, R. Huber, H. Birk, U. Staufer, *J. Phys. Chem. B* **101**, 5497 (1997).
48. M. L. Tian, J. Wang, J. Snyder, J. Kurtz, Y. Liu, P. Schiffer, T. E. Mallouk, M. H. W. Chan, *Appl. Phys. Lett.* **83**, 1620 (2003).
49. J. Wang, M. Tian, T. E. Mallouk, M. H. W. Chan, *J. Phys. Chem. B* **108**, 841 (2004).
50. J. G. Wang, M. L. Tian, T. E. Mallouk, M. H. W. Chan, *Nano Lett.* **4**, 1313 (2004).
51. L. Wang, K. Yu-Zhang, A. Metrot, P. Bonhomme, M. Troyon, K. Ounadjela, A. Fert, *Thin Solid Films* **288**, 86 (1996).
52. L. Piraux, J. M. George, J. F. Despres, C. Leroy, E. Ferain, R. Legras, *Appl. Phys. Lett.* **65**, 2484 (1994).

53. C. J. Brumlik, C. R. Martin, K. Tokuda, *Anal. Chem.* **64**, 1201 (1992).
54. B. M. I. v. d. Zande, M. R. Böhmer, L. G. J. Fokkink, C. Schönenberger, *Langmuir* **16**, 451 (2000).
55. X. Y. Zhang, L. D. Zhang, Y. Lei, L. X. Zhao, Y. Q. Mao, *J. Mater. Chem.* **11**, 1732 (2001).
56. L. Piraux, S. Dubois, S. D. Champagne, *Nucl. Instrum. Methods Phys. Res. B* **131**, 357 (1997).
57. H. Chiriac, A. E. Moga, M. Urse, T.-A. Óvári, *Sens. Actuators A* **106**, 348 (2003).
58. J. Verbeeck, O. I. Lebedev, G. Van Tendeloo, L. Cagnon, C. Bougerol, G. Tourillon, *J. Electrochem. Soc.* **150**, E468 (2003).
59. G. Tourillon, L. Pontonnier, J. P. Levy, V. Langlais, *Electrochim. Solid State Lett.* **3**, 20 (2000).
60. T. M. Whitney, J. S. Jiang, P. C. Searson, C. L. Chien, *Science* **261**, 1316 (1993).
61. Y. Konishi, M. Motoyama, H. Matsushima, Y. Fukunata, R. Ishii, Y. Ito, *J. Electroanal. Chem.* **559**, 149 (2003).
62. K. R. Pirota, D. Navas, M. Hernández-Vélez, K. Nielsch, M. Vásquez, *J. Alloys Compd.* **369**, 18 (2004).
63. M. Platt, R. A. W. Dryfe, E. P. L. Roberts, *Electrochim. Acta* **49**, 3937 (2004).
64. M. Platt, R. A. W. Dryfe, E. P. L. Roberts, *Electrochim. Acta* **48**, 3037 (2003).
65. M. Zheng, G. Li, X. Zhang, S. Huang, Y. Lei, L. Zhang, *Chem. Mater.* **13**, 3859 (2001).
66. S. A. Sapp, B. Lakshmi, C. R. Martin, *Adv. Mater.* **11**, 402 (1999).
67. A. L. Prieto, M. S. Sander, M. S. M. González, R. Gronsky, T. Sands, A. M. Stacy, *J. Am. Chem. Soc.* **123**, 7160 (2001).
68. M. Paunovic, M. Schlesinger, *Fundamentals of Electrochemical Deposition*, Electrochemical Society Series, Wiley-Interscience: New York, 1998.
69. B. Brunetti, P. Ugo, L. M. Moretto, C. R. Martin, *J. Electroanal. Chem.* **491**, 166 (2000).
70. M. Wirtz, C. R. Martin, *Adv. Mater.* **15**, 455 (2003).
71. K. B. Jirage, J. C. Hulteen, C. R. Martin, *Science* **278**, 655 (1997).
72. J. C. Hulteen, K. B. Jirage, C. R. Martin, *J. Am. Chem. Soc.* **120**, 6603 (1998).
73. K. B. Jirage, J. C. Hulteen, C. R. Martin, *Anal. Chem.* **71**, 4913 (1999).
74. S. Demoustier-Champagne, M. Delvaux, *Mater. Sci. Eng. C* **15**, 269 (2001).
75. B. Bercu, I. Enculescu, R. Spohr, *Nucl. Instrum. Methods B* **225**, 497 (2004).
76. R. A. W. Dryfe, A. O. Simm, B. Kralj, *J. Am. Chem. Soc.* **125**, 13014 (2003).
77. Y.-L. Tai, H. Teng, *Chem. Mater.* **16**, 338 (2004).
78. X. Y. Yuan, G. S. Wu, T. Xie, Y. Geng, Y. Lin, G. W. Meng, L. D. Zhang, *Solid State Sci.* **6**, 735 (2004).
79. P. Göring, E. Pippel, H. Hofmeister, R. B. Wehrspohn, M. Steinhart, U. Gösele, *Nano Lett.* **4**, 1121 (2004).
80. M. Lahav, T. Sehayek, A. Vaskevich, I. Rubinstein, *Angew. Chem. Int. Ed.* **42**, 5576 (2003).
81. C. A. Goss, D. H. Charych, M. Majda, *Anal. Chem.* **63**, 85 (1991).
82. S. Yu, N. Li, J. Wharton, C. R. Martin, *Nano Lett.* **3**, 815 (2003).
83. P. Ugo, N. Pepe, L. M. Moretto, M. Battagliarin, *J. Electroanal. Chem.* **560**, 51 (2003).
84. M. L. Sandrock, C. D. Pibel, F. M. Geiger, C. A. Foss, Jr., *J. Phys. Chem. B* **103**, 2668 (1999).
85. N. A. F. Al-Rawashdeh, M. L. Sandrock, C. J. Seugling, C. A. Foss, Jr., *J. Phys. Chem. B* **102**, 361 (1998).
86. (a) P. Ugo, L. M. Moretto, F. Vezzà, *Chemphyschem* **3**, 917 (2002). (b) P. Ugo, L. M. Moretto, F. Vezzà, in *Sensors Update*, H. Baltes, G. K. Fedder, J. G. Korvink, Eds., Wiley-VCH: Weinheim, 2003, Vol. 12, p. 121.
87. P. Ugo, in *Encyclopedia of Sensors*, C. A. Grimes, E. C. Dickey, M. V. Pishko, Eds., American Scientific Publishers: Stevenson Ranch, USA, 2006, Vol. 8, p. 67.
88. J. C. Hulteen, V. P. Menon, C. R. Martin, *J. Chem. Soc. Faraday Trans.* **92**, 4029 (1996).
89. I. F. Cheng, L. D. Whiteley, C. R. Martin, *Anal. Chem.* **61**, 762 (1989).

90. C. Amatore, in *Physical Electrochemistry*, I. Rubinstein, Ed., Marcel Dekker: New York, 1995, p. 131.
91. L. M. Moretto, N. Pepe, P. Ugo, *Talanta* **62**, 1055 (2004).
92. A. J. Bard, L. Faulkner, *Electrochemical Methods*, Wiley: New York, 2000.
93. R. Greef, R. Peat, L. M. Peter, D. Pletcher, J. Robinson, *Instrumental Methods in Electrochemistry*, Ellis Horwood Ltd.: Chichester, UK, 1985.
94. E. Sabatani, J. Rubinstein, *J. Phys. Chem. B* **91**, 6663 (1987).
95. C. Amatore, J. M. Saveant, D. Tessier, *J. Electroanal. Chem.* **147**, 39 (1983).
96. R. S. Nicholson, *Anal. Chem.* **37**, 1351 (1965).
97. P. Ugo, L. M. Moretto, S. Bellomi, V. P. Menon, C. R. Martin, *Anal. Chem.* **68**, 4160 (1996).
98. H. A. O. Hill, Y. Nakagawa, F. Marken, R. G. Compton, *J. Phys. Chem.* **100**, 17395 (1996).
99. M. J. Eddowes, H. A. O. Hill, *J. Chem. Soc. Chem. Commun.* 771 (1977).
100. P. M. Allen, H. A. O. Hill, N. J. Walton, *J. Electroanal. Chem.* **178**, 69 (1984).
101. M. J. Eddowes, H. A. O. Hill, *J. Am. Chem. Soc.* **101**, 4461 (1979).
102. T. Sagara, H. Murakami, S. Igarashi, H. Sato, K. Niki, *Langmuir* **7**, 3190 (1991).
103. T. Sagara, K. Niwa, A. Sone, C. Innen, K. Niki, *Langmuir* **6**, 254 (1990).
104. R. Gasparac, B. J. Taft, M. A. Lapierre-Devlin, A. D. Lazareck, J. M. Xu, S. O. Kelly, *J. Am. Chem. Soc.* **126**, 12270 (2004).
105. K. Krishnamoorthy, C. G. Zoski, *Anal. Chem.* **77**, 5068 (2005).
106. E. Finot, E. Bourillot, R. Meunier-Prest, Y. Lacroute, G. Legay, M. Cherkaoui-Malki, N. Latruffe, O. Siri, P. Braunstein, A. Dereux, *Ultramicroscopy* **97**, 441 (2003).
107. J. Li, H. T. Ng, A. Cassell, W. Fan, H. Chen, Q. Ye, J. Koehne, J. Han, M. Meyyappan, *Nano Lett.* **3**, 597 (2003).

16.3 SINGLE PARTICLE DEPOSITION ON NANOMETER ELECTRODES

Anthony Kucernak

Department of Chemistry, Imperial College London, London SW7 2AZ, UK

16.3.1 Introduction

This section describes the electrochemical deposition of single particles onto electrodes of nanometer dimensions. Methods for producing sharp tips from a range of materials have been discussed in previous sections of this work and by Melmed (1), and more recently with specific reference to electrochemical systems (2–4). Arrigan has given a review of some of the applications to which such insulated electrodes have been put (5). This section will consider both the *deposition* of material on nanometer-sized electrodes and the uses of such composite systems. The use of these nanoelectrodes in studying biological systems and enzymes will not be covered. There are a number of methods which in principle allow the formation of a nanoelectrode-film/particle composite (Figure 16.3.1):

- (a) direct physical contact of electrode to particle;
- (b) electrochemical deposition of particle or film;
- (c) electrophoretic deposition of particles.

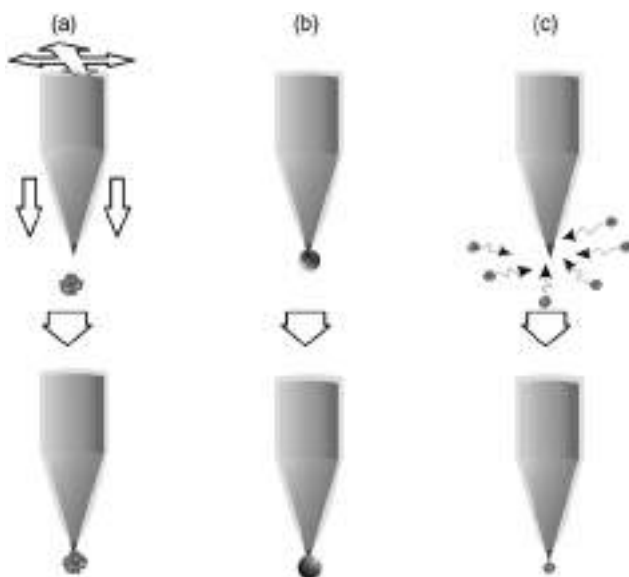


Figure 16.3.1 Three different approaches which can be used to create a nanoelectrode/single particle composite electrode: (a) “spearing” of a particle; (b) single particle nucleation and growth; (c) electrophoretic deposition.

All of these approaches have been applied to electrodes with dimensions on the micron scale. For instance, physical contact between microelectrodes and individual particles of materials has been used to study materials used in lithium-based (6, 7) and nickel-based batteries (8–10); microelectrodes have been extensively used to study single nucleation and growth on a range of substrates (11–13); and electroactive particles have been electrophoretically deposited onto microelectrodes (14, 15). Increasingly, such approaches are also being used to make composite electrodes utilizing substrates with radii $<1\text{ }\mu\text{m}$.

16.3.2 Electrode selection

The choice of electrode material, its morphology, and the method of insulation depends critically on the desired use of the electrode system, and is somewhat limited in choice due to the small number of systems which have been studied. Currently available nanometer-sized electrodes are either conical in shape and composed of Pt (2, 3, 16, 17), Ag (18), W (19), or carbon (20, 21) or disk-like and composed of Pt, Ag (22, 23), or Au (24) or even liquid—that is, the junction formed at the interface between two immiscible electrolytes (25).

In order to reduce the magnitude of background currents, it is important to insulate all of the electrodes apart from the working tip. Electrode insulation may be glass—formed by translating the tip at 0.1 mm s^{-1} through a molten glass bead held in a Pt heating

coil (2, 3) or by heating and pulling a glass capillary using a laser-based micropipettete puller so that both the electrode material and the glass sheath are greatly reduced in diameter (22, 23). It may be a polyimide—produced by heating the electrode body while the electrode is immersed in dimethyl acetamide containing 1,2,4,5-benzenetetracarboxylic anhydride and 4,4'-diaminodiphenyl (26); or it may be a ptfe-like substance—produced by either dipping in a ptfe-like precursor (Cytop, Asahi Glass Co. Ltd.) (27–31) or photopolymerization of a ptfe-like precursor material (32). Commonly because of the ease of insulation, it is an electrophoretic paint (16, 17, 20, 21, 33).

Direct physical contact with a particle is made difficult in the nanoscopic regime because of the difficulty in imaging the particle system. For electrodes and particles in the micron-size domain, it is possible to use optical microscopes to see the particles and, using micromanipulators, move the electrode so that it is in contact with the particle (8–10, 34, 35). Using optical microscopy to guide the making of contact between particles and electrodes with radii $<1\text{ }\mu\text{m}$ may be difficult unless the particle is $>1\text{ }\mu\text{m}$ in size, although having a conical-shaped electrode may be beneficial to allow ‘spearing’ of the particle (19). Conically shaped and suitably insulated electrodes of suitable materials are increasingly being used as probes in AFM, STM, and SECM. Utilizing these techniques, a suitable particle can be imaged and then the tip can be used to make contact with that particle in order to perform electrical experiments on it.

Deposition of particles through electrochemical deposition requires a suitable substrate and electrochemical system which shows a suitable nucleation density. Although many studies of single-particle nucleation and growth have been undertaken on microelectrodes, many of those studies have been on systems which are not of major commercial relevance, presumably because the nucleation density of commercially relevant electrochemical systems (e.g., Au on Ni) is too high to afford single nucleation and growth, even on microelectrodes. The use of nanoelectrodes of suitable materials will allow a significant growth of understanding of nucleation and growth of a diverse number of systems. A special case of single nucleation and growth is the production of potentiometric electrodes in which the electrode material is typically one which can be easily anodized to produce the requisite electrochemical couple—thus, an Ag electrode can be anodized in 0.1 M KCl (18) or 0.01 M KI + 0.1 M KNO_3 (22) to make Ag/AgCl or Ag/AgI nanoreference electrodes; a W electrode can be anodized in 2.0 M H_2SO_4 to produce a surface WO_3 layer in order to produce a pH-sensitive electrode (36).

In the following sections, the discussion focuses on electrochemical deposition of particles, as this is the most developed method for producing single particle on electrode composites.

16.3.3 Electrodeposition of particles: electrokinetic vs. diffusion control

Early work on single particle nucleation and growth involved the use of either Pt or carbon microelectrodes on which was deposited a material which had a suitably low nucleation density, for instance, Ag, Hg, or Cu (11–13). Later work expanded this to look at other systems such as PbO_2 on carbon (37), or PbSO_4 on Pb (34). Working with single particles allows analysis of the electrokinetics of deposition without the complication due to overlap of growing particles or their diffusion spheres.

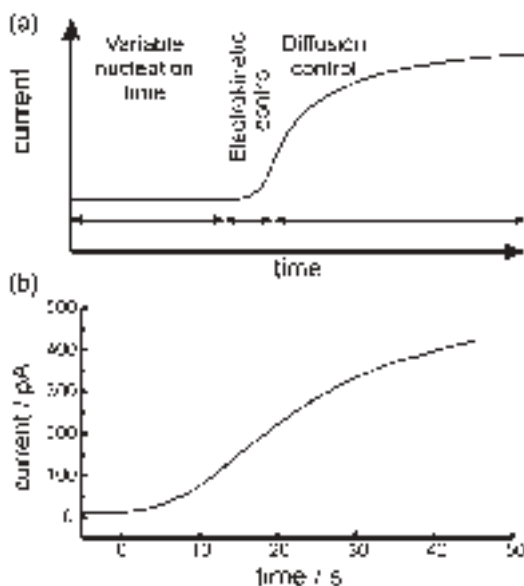


Figure 16.3.2 Different stages of nucleation and growth of single electrodeposited particles: (a) cartoon showing the different phases of particle growth and (b) current–time transient for the electrodeposition of a single Pt nuclei on a carbon electrode of radius 5 nm from a solution composed of 0.1 M H₂SO₄ + 0.001 M H₂PtCl₆ at a potential of 0.27 V (vs. SCE).

The growth of a single particle during single nucleation and growth is commonly preceded by an induction period (Figure 16.3.2).

This induction period is described as being due to the required formation of a nucleus of critical size. The formation of new nuclei is a result of aggregation of small atom clusters due to surface diffusion along the electrode surface (38). The small clusters may also dissolve into the solution. A stable growing center can only be formed when a cluster contains enough atoms and exceeds a critical size. The size of that stable nucleus is around 1 nm diameter, corresponding to about 30–40 atoms (38). Once such a stable nucleus is formed, spontaneous growth can then easily proceed. Measurement of the stochastic nature of induction times during single nucleation/growth has already been performed on microelectrodes (12, 37), although such measurement on nm-sized electrodes is complicated by the difficulty in producing large number of electrodes with exactly the same geometry required for such studies.

After the induction period, growth of the particle may be measured by following the current transient. Typically, analyses of current transients during the single nucleation and growth of a particle have been performed either at low overpotentials so that growth is assumed under electrokinetic control (34)

$$i(t) = FHK^3 n V_M^2 t^2 \quad (16.3.1)$$

or at larger overpotentials where it is assumed that the growth is under diffusion control (39)

$$i(t) = \frac{1}{2} FHn(2DC^*)^{3/2} V_M^{1/2} t^{1/2} \quad (16.3.2)$$

where H is a geometric factor related to the shape of the growing particle ($H = 4\pi$ for hemispherical particles); K (mol cm⁻² s⁻¹) is the rate of the electrocrystallization process; n is the number of electrons involved in the deposition process; V_M is the molar volume of the material being deposited; and D and C^* are the diffusion coefficient and concentration of the precursor in the surrounding solution.

However, the situation is somewhat more complicated when considering deposition on nanometer-sized electrodes. Because of the small surface area of the substrate electrodes, the growth transients can be followed from a very early stage, as shown in Figure 16.3.2. The growing particles will act as microelectrodes in their own right, and for such microelectrodes, the mass transport coefficient for species i is

$$m_i = \frac{D_i}{r} \quad (16.3.3)$$

where r is the radius of the growing particle. Table 16.3.1 plots the mass transport coefficient and the equivalent rotation rates required to produce those same mass transport coefficients in a rotating disk experiment for a range of different particle sizes. It is clear that for particles with radii $\leq 1 \mu\text{m}$, the mass transport coefficients are larger than the kinetic rate constants which might be expected for metal reductions (for comparison, the hexacyanoferrate redox couple, $\text{Fe}(\text{CN})_6^{3-/-4-}$, has a kinetic rate constant of $0.14\text{--}0.18 \text{ cm s}^{-1}$ in KCl solution (27)). This suggests that for small particles, it is very difficult to have the particles grow under pure diffusion control, and that virtually all particles initially grow under electrokinetic control.

This is illustrated in Figure 16.3.2, where it can be seen that at short times, the current grows quadratically with time—only at longer times does the current start showing a $t^{1/2}$ dependence as would be expected for diffusion-controlled growth.

Table 16.3.1

Comparison of mass transport coefficient for particles of different sizes

r (nm)	m (cm s ⁻¹)	w (rpm)
1	100	2.48×10^{11}
10	10	2.48×10^9
100	1	2.48×10^7
1000	0.1	2.48×10^5
10,000	0.01	2480

Note: Also shown are the disk rotation rates required to produce the same mass transport coefficient in a rotating disk experiment. Calculations assume $D = 1.00 \times 10^{-5} \text{ cm}^2 \text{ s}^{-1}$ and $v = 0.01 \text{ cm}^2 \text{ s}^{-1}$.

A more complete analysis of single particle and growth suggests that under combined electrokinetic and diffusion control, and taking into account the concentration overpotential due to depletion of reactant at the surface, the radius and current associated with the growth of a particle as a function of time should follow (40)

$$r(t) = \frac{\sqrt{A^2 + 8ABV_M t} - A}{2C} \quad (16.3.4)$$

$$i(t) = \frac{ABFHn \left(\sqrt{A^2 + 8ABV_M t} - A \right)^2}{2C^3 \sqrt{A^2 + 8ABV_M t}} \quad (16.3.5)$$

$$A = c_\infty DFn$$

$$B = \frac{j_0^2}{Fn} \left(\exp\left(\frac{2\alpha nF\eta}{RT}\right) - \exp\left(\frac{(2\alpha-1)nF\eta}{RT}\right) \right)$$

$$C = j_0 \exp\left(\frac{\alpha nF\eta}{RT}\right)$$

The latter equation predicts a crossover from approximate t^2 dependence to $t^{1/2}$ dependence, and can be used for extracting various parameters from the current transients. A current transient simulated using this equation is shown in Figure 16.3.3.

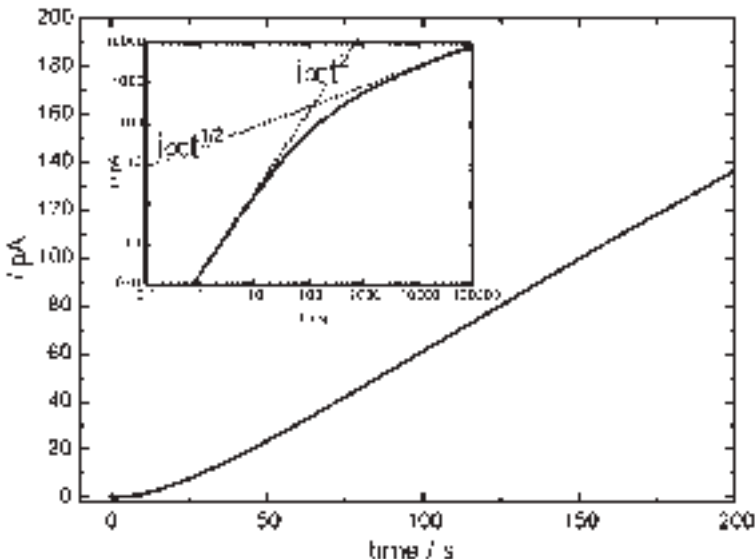


Figure 16.3.3 Simulated current transient using equation (16.3.5) for the growth of single particle. Inset: double-log axis plot of the same transient showing limiting electrokinetic ($i \propto t^2$) and diffusion ($i \propto t^{1/2}$) control. $n = 1$; $DC^* = 5 \times 10^{-12} \text{ mol cm}^{-1} \text{ s}^{-1}$; $j_0 = 1 \times 10^{-5} \text{ A cm}^{-2}$; $T = 298 \text{ K}$; $\eta = 0.2 \text{ V}$.

16.3.4 Nucleation exclusion zones: modeling particle growth

Standard electrochemical theory has been applied to the growth of single particles on microelectrodes, for instance, looking at the stochastic nature of induction times during single nucleation/growth (12, 37). Some modification from standard electrochemical theory is typically required for these very small electrodes because of geometric effects, violation of electroneutrality (41), and even changes to the double-layer structure at interfaces with high curvature (20). For instance, when dealing with the cone-shaped electrodes mentioned above, standard approaches are based on disk or hemispherical electrodes. Mirkin *et al.* have performed some work on establishing what differences are expected from this change of geometry, although this work is predominantly targeted at SECM work (42).

The production of single nuclei is somewhat helped by the formation of ‘nucleation exclusion zones’ around the growing particles (43–45). In the area surrounding a growing particle, there will be a reduction in the concentration of precursor, and this will reduce the probability of nucleating a new particle. Milchev *et al.* have derived an equation for the stationary nucleation rate around a growing stable cluster (46, 47).

This approach then allows a useful set of conditions under which single particle nucleation and growth are favored (40). The distance from a growing particle within which the nucleation rate decreases by an amount J_{rel} of the value on the unperturbed surface is

$$\rho(t) = \frac{\left(\sqrt{A^2 + 8ABV_M t} - A\right)^3}{16Dc_\infty V_M C^3 t (1 - J_{\text{rel}}^{1/1+n_k})} \quad (16.3.6)$$

where A , B , and C are defined above, and n_k is the number of atoms above which a nucleus becomes stable, and is expected to be about 30–40 atoms (38). We can put this in a dimensionless form by dividing by the radius of the electrode

$$\frac{\rho(t)}{r(t)} = \frac{\left(\sqrt{A^2 + 8ABV_M t} - A\right)^2}{8Dc_\infty V_M C^2 t (1 - J_{\text{rel}}^{1/1+n_k})} \quad (16.3.7)$$

Figure 16.3.4 shows a set of plots displaying the radius of a growing particle as a function of time and overpotential, and the corresponding size of the nucleation exclusion zone as a ratio to the actual size of the particle. When the growth of the particle is under electrokinetic control, the nucleation exclusion zone is always within a few radii of the growing particle. This means that under electrokinetic control, it is quite possible that other particles can nucleate and grow at other points on the electrode, unless the area of the electrode is very small. In contrast, when the particle is growing under diffusion control, the nucleation exclusion zone can extend some distance from the growing particle.

In the limit when $8BV_M t \gg A$ (i.e., long time, large j_0 , and small $c_\infty D$), equation (16.3.7) simplifies to

$$\frac{\rho(t)}{r(t)} = \frac{1 - \exp(-nF\eta / RT)}{1 - J_{\text{rel}}^{1/1+n_k}} \quad (16.3.8)$$

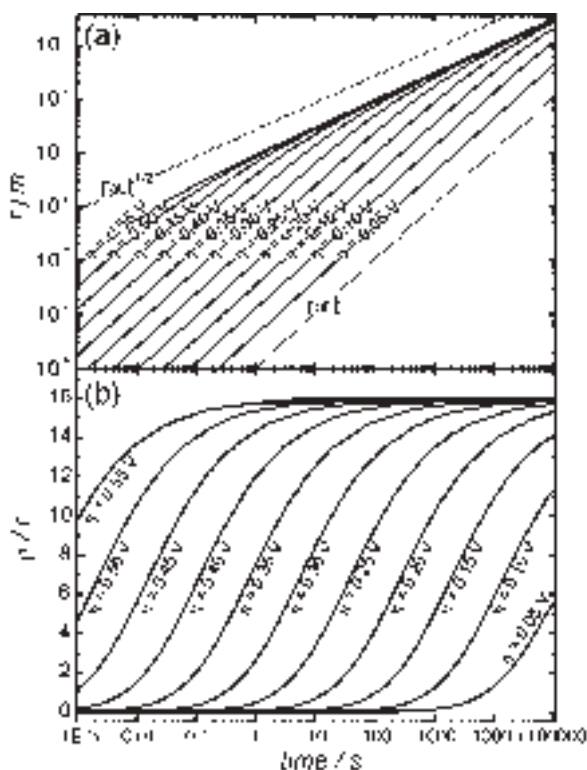


Figure 16.3.4 Variation of the size of a growing particle as a function of applied overpotential and time calculated using equation (16.3.4) (a). Lines corresponding to the limiting cases of diffusion limiting growth ($r \propto t^{1/2}$) and electrokinetic growth ($r \propto t$) are also shown. (b) Variation of the size of the nucleation exclusion zone nucleation for the cases mentioned in (a) calculated using equation (16.3.7). The size of the nucleation exclusion zone is shown as a ratio to the radius of the particle. $n = 1$; $DC^* = 5 \times 10^{-12} \text{ mol cm}^{-1} \text{ s}^{-1}$; $j_0 = 1 \times 10^{-5} \text{ A cm}^{-2}$; $T = 298 \text{ K}$; $J_{\text{rel}} = 0.1$; $n_k = 35$.

For most applicable overpotentials, the numerator becomes 1 and the nucleation exclusion zone extends a distance $(1 - J_{\text{rel}}^{1/(1+n_k)})^{-1}$ particle radii from the growing particle—that is, the size of the nucleation exclusion zone is sensitively dependent upon the size of the critical nucleus. For realistic values of J_{rel} (0.1—corresponding to a reduction of nucleation probability by a factor of 10) and n_k (35), this corresponds to a value of $\rho(t)/r(t)$ of 16—that is, the nucleation probability is reduced by at least a factor of 10 within a 16 radii distance from the growing particle when that particle is growing under diffusion control.

These results suggest important criteria for maximizing the likelihood for producing single particles—growth of particles should be on small electrodes (maybe no more than $\sim 10 \times$ the radius of the intended particle), and at high overpotentials and low concentrations. Where these conditions cannot be met, the electrode size must be decreased so that it is similar in size to the particle which is being created.

16.3.5 Examples of systems

Guo *et al.* have examined the growth of silver particles at the water/dichloroethane interface formed at the end of a ~0.5 µm radius pipette, and interpreted the current transients in terms of diffusion-limited growth of multiple non-interacting particles (25). Chen and Kucernak have followed the single nucleation and growth of Pt particles on carbon electrodes with radii from several hundred nm down to <5 nm. Single nucleation and growth under conditions of high overpotential are seen with electrodes up to a few hundred nm in radii, whereas under less extreme conditions, where electrokinetic control would be expected, single nucleation and growth are only reproducibly seen when the electrode radius <5 nm (40). The resulting Pt/carbon composite electrodes have been used to study the hydrogen oxidation reaction (48) and the oxygen reduction reaction (49).

Electrodeposition of silver particles on single wall nanotubes (SWNT) has been used as an aid to visualization of the SWNTs, although the deposition transients have not been analyzed (50, 51).

Finally, one interesting approach to depositing small nm-sized clusters on suitable substrates has been developed in which the first step is the deposition of metal onto an SECM tip prior to transfer to a surface. The approach utilizes the local creation of a concentration cell during the local dissolution of metal from the tip to nucleate and grow a particle on the adjacent surface. The approach has been utilized for the growth of Ag on C (52), Co growth on Au, and Pb on Si (53, 54).

REFERENCES

1. A. J. Melmed, *J. Vac. Sci. Technol. B* **9**, 601 (1991).
2. R. M. Penner, M. J. Heben, N. S. Lewis, *Anal. Chem.* **61**, 1630 (1989).
3. R. M. Penner, M. J. Heben, T. L. Longin, N. S. Lewis, *Science* **250**, 1118 (1990).
4. C. J. Slevin, N. J. Gray, J. V. Macpherson, M. A. Webb, P. R. Unwin, *Electrochim. Commun.* **1**, 282 (1999).
5. D. W. M. Arrigan, *Analyst* **129**, 1157 (2004).
6. M. Nishizawa, H. Koshika, I. Uchida, *J. Phys. Chem. B* **103**, 192 (1999).
7. M. Nishizawa, H. Koshika, R. Hashitani, T. Itoh, T. Abe, I. Uchida, *J. Phys. Chem. B* **103**, 4933 (1999).
8. H. S. Kim, T. Itoh, M. Nishizawa, M. Mohamedi, M. Umeda, I. Uchida, *Int. J. Hydrogen Energy* **27**, 295 (2002).
9. A. Palencsar, D. A. Scherson, *Electrochim. Solid State Lett.* **6**, E1 (2003).
10. A. Palencsar, D. A. Scherson, *Electrochim. Solid State Lett.* **8**, A328 (2005).
11. G. Hills, A. K. Pour, B. Scharifker, *Electrochim. Acta* **28**, 891–898 (1983).
12. B. Scharifker, G. Hills, *J. Electroanal. Chem.* **130**, 81 (1981).
13. G. Gunawardena, G. Hills, B. Scharifker, *J. Electroanal. Chem.* **130**, 99 (1981).
14. D. J. Caruana, A. Heller, *J. Am. Chem. Soc.* **121**, 769 (1999).
15. T. de Lumley-Woodyear, D. J. Caruana, C. N. Campbell, A. Heller, *Anal. Chem.* **71**, 394 (1999).
16. J. L. Conyers, H. S. White, *Anal. Chem.* **72**, 4441 (2000).
17. J. J. Watkins, J. Y. Chen, H. S. White, H. D. Abruna, E. Maisonnaute, C. Amatore, *Anal. Chem.* **75**, 3962 (2003).
18. N. J. Gray, P. R. Unwin, *Analyst* **125**, 889 (2000).

19. Q. F. Shi, L. J. Rendek, W. B. Cai, D. A. Scherson, *Electrochim. Solid State Lett.* **6**, E35 (2003).
20. S. Chen, A. Kucernak, *J. Phys. Chem. B* **106**, 9396 (2002).
21. S. L. Chen, A. Kucernak, *Electrochim. Commun.* **4**, 80 (2002).
22. Y. H. Shao, M. V. Mirkin, G. Fish, S. Kokotov, D. Palanker, A. Lewis, *Anal. Chem.* **69**, 1627 (1997).
23. B. B. Katemann, T. Schuhmann, *Electroanalysis* **14**, 22 (2002).
24. D. H. Woo, H. Kang, S. M. Park, *Anal. Chem.* **75**, 6732 (2003).
25. J. D. Guo, T. Tokimoto, R. Othman, P. R. Unwin, *Electrochim. Commun.* **5**, 1005 (2003).
26. P. Sun, Z. Q. Zhang, J. D. Guo, Y. H. Shao, *Anal. Chem.* **73**, 5346 (2001).
27. K. Dokko, M. Umeda, T. Itoh, I. Uchida, *Electrochim. Commun.* **2**, 717 (2000).
28. K. Dokko, S. Horikoshi, T. Itoh, M. Nishizawa, M. Mohamedi, I. Uchida, *J. Power Sources* **90**, 109 (2000).
29. K. Dokko, M. Nishizawa, S. Horikoshi, T. Itoh, M. Mohamedi, I. Uchida, *Electrochim. Solid State Lett.* **3**, 125 (2000).
30. K. Dokko, M. Mohamedi, Y. Fujita, T. Itoh, M. Nishizawa, M. Umeda, I. Uchida, *J. Electrochem. Soc.* **148**, A422 (2001).
31. K. Dokko, Q. F. Shi, I. C. Stefan, D. A. Scherson, *J. Phys. Chem. B* **107**, 12549 (2003).
32. B. Liu, J. P. Rolland, J. M. DeSimone, A. J. Bard, *Anal. Chem.* **77**, 3013 (2005).
33. J. Abbou, C. Demaille, M. Druet, J. Moiroux, *Anal. Chem.* **74**, 6355 (2002).
34. L. J. Li, M. Fleischmann, L. M. Peter, *Electrochim. Acta* **34**, 459 (1989).
35. M. Mohamedi, T. Sato, T. Itoh, M. Umeda, I. Uchida, *J. Electrochem. Soc.* **149**, A983 (2002).
36. K. Yamamoto, G. Y. Shi, T. S. Zhou, F. Xu, M. Zhu, M. Liu, T. Kato, J. Y. Jin, L. T. Jin, *Anal. Chim. Acta* **480**, 109 (2003).
37. M. Fleischmann, L. J. Li, L. M. Peter, *Electrochim. Acta* **34**, 475 (1989).
38. F. Gloaguen, J. M. Leger, C. Lamy, A. Marmann, U. Stimming, R. Vogel, *Electrochim. Acta* **44**, 1805 (1999).
39. G. J. Hills, D. J. Schiffrian, J. Thompson, *Electrochim. Acta* **19**, 657 (1974).
40. S. Chen, A. Kucernak, *J. Phys. Chem. B* **107**, 8392 (2003).
41. C. P. Smith, H. S. White, *Anal. Chem.* **65**, 3343 (1993).
42. M. V. Mirkin, F. R. F. Fan, A. J. Bard, *J. Electroanal. Chem.* **328**, 47 (1992).
43. B. R. Scharifker, J. Mostany, A. Serruya, *Electrochim. Acta* **37**, 2503 (1992).
44. I. Markov, A. Boynov, S. Toshev, *Electrochim. Acta* **18**, 377 (1973).
45. A. Milchev, E. Vassileva, V. Kertov, *J. Electroanal. Chem.* **107**, 323 (1980).
46. W. S. Kruijt, M. Sluytersrebbach, J. H. Sluyters, A. Milchev, *J. Electroanal. Chem.* **371**, 13 (1994).
47. A. Milchev, W. S. Kruijt, M. Sluytersrebbach, J. H. Sluyters, *J. Electroanal. Chem.* **362**, 21 (1993).
48. S. L. Chen, A. Kucernak, *J. Phys. Chem. B* **108**, 13984 (2004).
49. S. L. Chen, A. Kucernak, *J. Phys. Chem. B* **108**, 3262 (2004).
50. D. P. Burt, N. R. Wilson, J. M. R. Weaver, P. S. Dobson, J. V. Macpherson, *Nano Lett.* **5**, 639 (2005).
51. B. M. Quinn, C. Dekker, S. G. Lemay, *J. Am. Chem. Soc.* **127**, 6146 (2005).
52. W. Li, G. S. Hsiao, D. Harris, R. M. Nyffenegger, J. A. Virtanen, R. M. Penner, *J. Phys. Chem.* **100**, 20103 (1996).
53. W. Schindler, D. Hofmann, J. Kirschner, *J. Electrochem. Soc.* **148**, C124 (2001).
54. W. Schindler, P. Hugelmann, A. Hugelmann, F. Kartner, *J. Electroanal. Chem.* **522**, 49 (2002).

Electrochemistry in Small Places and at Novel Interfaces

17.1 ELECTROCHEMISTRY IN AND AT SINGLE BIOLOGICAL CELLS

Nathan J. Wittenberg and Andrew G. Ewing

Pennsylvania State University, Department of Chemistry,
University Park, PA 16802

17.1.1 Electrochemistry at the cell membrane–solution interface

In nature, secretory cells are thought to release chemical messengers to the extracellular space through a process called exocytosis. Many different electrochemically detectable substances are released from a variety of cell types by this process. Chemical release by exocytosis is a complex process that involves the fusion of a membrane bound vesicle filled with a chemical messenger with the plasma membrane (Figure 17.1.1A).

The initiation of this process is triggered by a cascade of biochemical processes, which are being studied extensively by numerous research groups (1–4). Depolarization of the plasma membrane and a rise in intracellular calcium levels are hallmarks of the initiation of the exocytotic process.

Electrochemical detection of exocytosis from single, isolated cells is typically carried out in amperometric or voltammetric mode (see Chapter 11). This is accomplished by placing a carbon fiber microelectrode (UME, see Chapter 6) at the surface of a cell by micromanipulation and holding it at a constant potential for amperometric experiments, or rapidly sweeping the potential for voltammetric experiments. Amperometric experiments require the electrode be held at high enough potentials to oxidize released molecules in a diffusion-limited fashion. In the amperometric mode, the resulting current vs. time trace exhibits a characteristic current transient corresponding to the release and subsequent oxidation of the contents of a single vesicle (Figure 17.1.1B). By integrating the current transient it is possible via Faraday's Law to determine the number of neurotransmitter molecules released in each event ($N = Q/nF$ where N is the number of moles detected, Q is

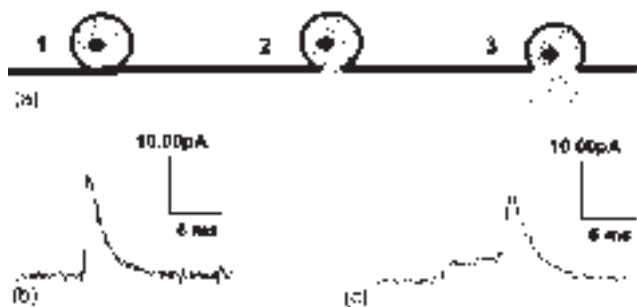


Figure 17.1.1 (A) A schematic representation of a neurotransmitter filled vesicle fusing with the plasma membrane and releasing its contents to the extracellular space. (B) An amperometric spike recorded from a PC12 cell undergoing exocytosis. (C) An amperometric spike displaying a “foot” corresponding to leakage of neurotransmitter through the fusion pore. Reproduced with permission from reference (36).

the charge integrated under the current transient, n is the number of electrons transferred in the oxidation reaction, and F is the Faraday constant). Using background subtracted fast scan cyclic voltammetry it is possible to determine the neurotransmitter identity and concentration at the electrode surface as a function of time (5, 6). Exocytosis and its electrochemical detection has been thoroughly reviewed (7–10).

In addition to exocytosis of neurotransmitters, other chemical processes can be monitored electrochemically, including insulin release from pancreatic cells (11–14), monitoring of cellular respiration (15, 16), drug efflux from cells (17), and determination of cholesterol content in the plasma membrane of a single cell (18), among others. Recently scanning electrochemical microscopy (SECM, see Chapter 12) (19, 20) has been employed to probe cellular activity with respect to electroactive molecules at the plasma membrane–solution interface (21–24). In the following sections we review significant advances in electrochemical monitoring of exocytosis and other processes at the cell membrane/solution interface.

17.1.1.1 Detection of biogenic amine release

A number of chemical messengers released by neurons, neuroendocrine, and immune response cells are electrochemically active. These include dopamine, epinephrine, norepinephrine, and serotonin, all of which can be oxidized at moderate potentials. Development of electrochemical methods for detection of neurotransmitters began with the work of Adams (25) and has progressed to the point where it is now possible to detect the release of neurotransmitters from a single vesicle, as demonstrated by Wightman and coworkers (26, 27). In those experiments a carbon fiber UME 5 μm in diameter was placed adjacent to a bovine adrenal chromaffin cell isolated in a culture dish and the cell was stimulated to release neurotransmitters either by chemical or mechanical means. Individual current transients corresponding to the release of roughly 5 attomoles of catecholamine were resolved on the millisecond timescale. The results from those experiments were highly significant because they were the first demonstration that current transients recorded from stimulated cells correspond to the release of the oxidizable content from a single vesicle.

The bovine adrenal chromaffin cells used by Wightman et al. typically release roughly 5 attomoles of detectable epinephrine and norepinephrine. Efforts have been made to detect smaller numbers of molecules released via exocytosis to the point where it has been reported that the release of 4700 and 6000 molecules can be detected per event from release of a small portion of transmitter in a vesicle (28, 29).

The first demonstration of zeptomole detection was shown by Chen et al. (30) for amperometric detection of dopamine during exocytosis at PC12 cells. The average single PC12 vesicle from this study contained 190 zeptomole of catecholamine. Using previous electron microscopy data (31) that estimated the average vesicular radius to be 74 nm, the concentration of catecholamine in a single vesicle was estimated to be 0.11 M. Chen et al. reported a limit of detection of 31 zeptomole with the amperometric technique, which is within the range needed to detect exocytosis at mammalian neurons. Mammalian neurons contain between 1.8 and 96.4 zeptomole of catecholamine in a synaptic vesicle (32).

Among the smallest amounts of detected release reported was from the Retzius cell of the leech *Hirudo medicinalis* which synthesizes, stores, and releases serotonin. Bruns and Jahn detected release from two populations of vesicles (large and small) from this cell type, with the current transients from the small population averaging 3.0 fC in area and 595 μ sec wide, while the larger vesicles had an average area of 47.4 fC and width of 3.66 msec (28). Earlier reports by Chow et al. and Alvarez de Toledo et al. were among the first to describe electrochemical detection of discrete stages of exocytosis, specifically the release of chemical messenger through the fusion pore in the adrenal chromaffin and mast cells (33, 34). The fusion pore forms shortly after the vesicle fuses with the plasma membrane and soluble messenger is free to diffuse through the pore, resulting in a small current rise (termed a “foot”) before the main current spike that results from completed exocytosis. A current spike exhibiting a foot is shown in Figure 17.1.1C. Chow et al. reported an average foot duration of 8.26 msec, an average foot area of 34 fC, and an average foot amplitude of 7.17 pA. Since the discovery of this prespike feature, many groups have tried to elucidate the physiological significance of neurotransmitter release through the fusion pore (35, 36). One prominent example is the electrochemical detection of rapid opening and closing of the fusion pore known as flicker (29). A rapid succession of transient dopamine release from ventral midbrain neurons was detected amperometrically giving rise to the idea that dopaminergic neurons regulate the amount of dopamine released by controlling the flicker rate as well as the number of flickers per event.

Both the Wightman and Ewing groups have exploited the minute dimensions of micro-electrodes (UME, see Chapter 6) to explore zones of exocytotic release on chromaffin and differentiated PC12 cells. Zerby and Ewing used 5 μ m diameter carbon fiber UME to probe local zones of dopamine exocytosis at PC12 cells that were induced to sprout varicose neurites via exposure to neuronal growth factor (NGF) (37). These experiments showed that quantal size from differentiated PC12 cell varicosities is not significantly different from undifferentiated PC12 cell quantal size, and exocytotic events were absent from the cell body of the NGF treated cells. For detection of localized exocytosis at bovine adrenal chromaffin cells Schroeder et al. used a carbon fiber UME that was flame etched to 1- μ m diameter for greater spatial resolution (38). The smaller electrode dimension allowed two electrodes to be placed directly on the cell and simultaneous recordings to be carried out. These experiments showed that distinct zones of exocytosis exist and are

spatially persistent on the minute time scale. Also, there are zones where no release occurs and these do not change position on the scale of minutes.

Certain cell types, in particular chromaffin and mast cells, are known to synthesize and release more than one messenger molecule. Chromaffin cells synthesize, store, and release epinephrine and norepinephrine, while mast cells synthesize and release serotonin and histamine. In an attempt to determine if corelease of these molecules takes place in chromaffin cells, Pihel *et al.* used fast scan cyclic voltammetry with a scan rate of 800 V/sec repeated every 16.7 msec at a 5- μm diameter carbon fiber UME (6). Expanded potential scan limits were employed to distinguish epinephrine from norepinephrine, because a second oxidation wave is present at large positive potentials for the oxidation of epinephrine *o*-quinone, an amine, to the imine form of the molecule. The second oxidation wave made it possible to determine whether an individual release event was attributable to epinephrine or norepinephrine. The results from this study suggest that the majority of chromaffin cells release either norepinephrine or epinephrine. However, 17% of the cells observed released both epinephrine and norepinephrine, and each secretory vesicle contained either epinephrine or norepinephrine, but in general not both.

Mast cells are immune response cells that are found distributed throughout the body. Mast cells synthesize, store, and release both histamine, a neurohormone, and serotonin, a common neurotransmitter. In mast cells, histamine is found in much greater abundance than serotonin. By some reports there is an average of 140–240 fmol of histamine and 2–24 fmol of serotonin per cell (39, 40). Previous data have suggested that histamine and serotonin are coreleased from single vesicles in mast cells; however, the evidence for this was indirect. Using electrochemically pretreated carbon fiber electrodes and a high positive potential scan limit, two oxidative waves for histamine were observed, as well as an oxidation wave for serotonin (5). This allowed the simultaneous detection of the two analytes, leading to the conclusion that both histamine and serotonin are released from the same vesicles in mast cells.

17.1.1.2 *Electrochemical detection of insulin release*

Insulin is another biochemically relevant molecule that can be detected electrochemically at the cell surface. It is released by exocytosis from pancreatic β cells. Insulin, however, is not detected at an untreated carbon fiber electrode, so a chemically modified electrode is used to catalyze the oxidation of the disulfide bonds that are present in the insulin molecule. Initially Kennedy and coworkers used an electrochemically deposited composite thin film of ruthenium oxide and cyanoruthenate (41, 42). The film was deposited by placing a clean carbon fiber electrode in a solution of KCl, RuCl₃, and K₄Ru(CN)₆ at pH 2. Then the electrode potential was cycled between +0.47 and +1.07 V (vs. SSCE) at 50 mV/sec for 25 min. This approach proved useful as amperometric detection of single events was possible from both human and rat pancreatic β cells (12, 43). However, the ruthenium oxide/cyanoruthenate modified electrode was not stable over long periods of time under physiological conditions. Therefore an alternative ruthenium oxide catalytic film was developed resulting in an insulin sensitive electrode that was stable over many hours (44). Using amperometry and these two types of chemically modified electrodes, Kennedy's group has determined that serotonin loaded into β cell vesicles is coreleased with insulin (14). In addition, Kennedy and

coworkers demonstrated that the insulin receptor can function with positive feedback, stimulating β cells to secrete insulin in response to an insulin stimulus (13).

17.1.1.3 Combined electrochemical/electrophysiological measurements: patch amperometry

Although electrochemical methods alone are powerful tools for the detection and analysis of single exocytotic events, they can be combined with electrophysiological methods such as patch clamp, for example, to provide more detailed information about the events. This technique is known as patch amperometry. Patch amperometry is typically accomplished by inserting a carbon fiber, which functions as the electrochemical sensor, into a glass patch clamp pipette and performing cell attached voltage clamp experiments simultaneously with electrochemical experiments. This is shown in Figure 17.1.2A.

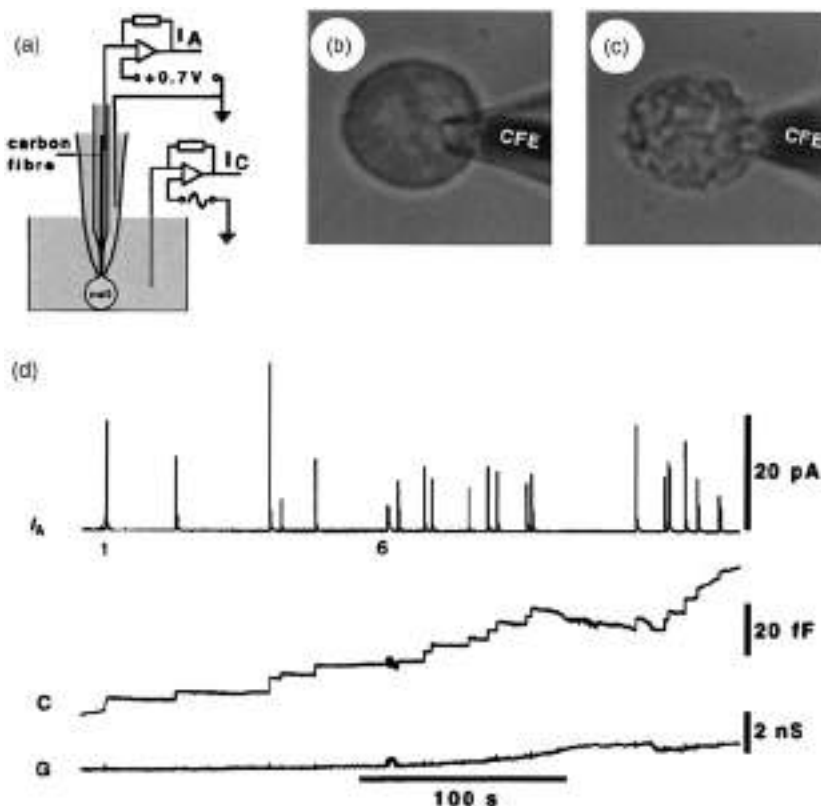


Figure 17.1.2 (A) Arrangement of a CFE inside a patch pipette. I_A , Amperometric current; I_C , sine wave current used to measure capacitance changes. (B), (C) Chromaffin cell with attached patch pipette containing CFE at the beginning (B) and end (C) of the experiment. (D) Recording from this cell shows amperometric transients (top), associated capacitance steps (middle), and conductance trace (bottom). Reproduced with permission from reference (45).

This configuration allows simultaneous monitoring of membrane capacitance as well as detection of the opening of individual fusion pores and the monitoring of catecholamine release kinetics from the same vesicle (45). Membrane capacitance is directly proportional to membrane area; therefore discrete jumps in capacitance signify fusion of individual vesicles with the plasma membrane and allow estimation of the size of the fusing vesicles (Figure 17.1.2D). These experiments were used with currently accepted models of the structure of the fusion pore to estimate the diameter of the pore preceding full release in chromaffin cells to be less than 3 nm. Additionally, this technique was used to determine that release of transmitter through the pore in adrenal cells is much faster than release through the pore of mast cells. In other studies on mast cells, Tabares *et al.* demonstrated that the size of the initial fusion pore does not determine the rate of neurotransmitter efflux during the early or late stages of full exocytotic release (46). This technique has also been used to elucidate the coregulation of vesicle membrane area and the amount of neurotransmitter contained in vesicles in response to pharmacological treatment (47). Patch amperometric experiments have reinforced the conclusion put forth by Colliver *et al.* that neurotransmitter concentration in vesicles remains constant when vesicles are induced to grow or shrink by drug treatment (48). While the cell attached configuration is the most prevalent configuration, patch amperometry has also been applied to excised membrane patches, thereby allowing control over the environment on both sides of the plasma membrane (49).

17.1.1.4 *Electrochemical determination of cholesterol in the plasma membrane*

Devadoss *et al.* (18) have developed a cholesterol oxidase modified electrode that has been used to detect cholesterol in the plasma membranes of *Xenopus* oocytes. A platinum electrode modified with a lipid bilayer containing cholesterol oxidase (50) is operated in the amperometric mode and placed adjacent to an oocyte (Figure 17.1.3A–B).

As the electrode moves closer to the cell surface, the amperometric current rises (Figure 17.1.3C). When the electrode is placed in contact with the cell surface, cholesterol is extracted from the membrane and moves across the thin membrane layer and partitions into the electrode-supported enzyme-modified lipid bilayer. Subsequent enzyme catalyzed oxidation of cholesterol by molecular oxygen produces hydrogen peroxide which is oxidized at the platinum electrode and detected. This is an efficient and simple method to determine cholesterol levels in the plasma membrane of cells which should find applicability in determining the role cholesterol plays in the organization of cellular membranes (51).

17.1.1.5 *Scanning electrochemical microscopy (SECM) at single cells*

Scanning electrochemical microscopy (SECM, see Chapter 12) is another microelectrode technique that has been used at the cellular surface. Briefly, with SECM a microelectrode (UME, see Chapter 6) functions as a scanning probe that detects local electrochemical activity. When the UME is rastered over a sample, electrochemical data is recorded at multiple positions and an image is constructed based on the local electrochemical properties of the area of interest. SECM has been thoroughly reviewed (19, 20, 52, Chapter 12 of this

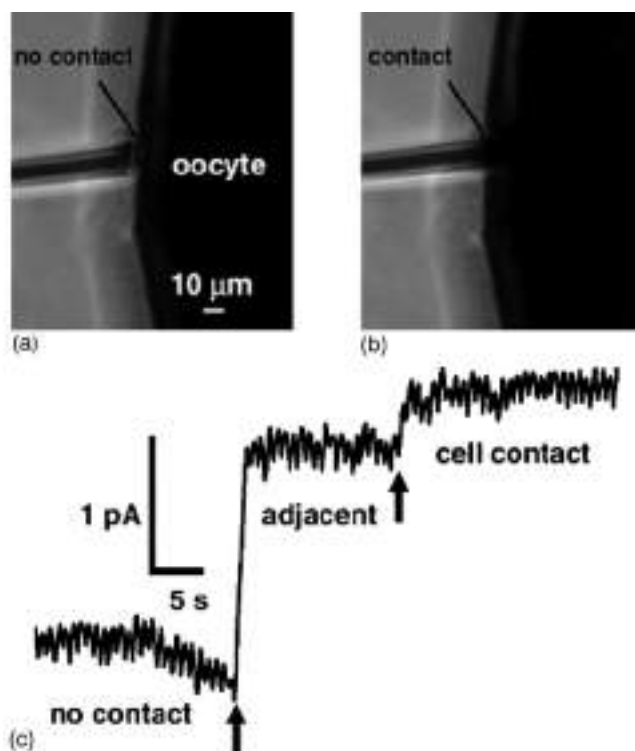


Figure 17.1.3 Photographs and amperometric detection of cholesterol in the plasma membrane of a *Xenopus* oocyte. Photographs showing the electrode (A) positioned about 5 μm from the plasma membrane and (B) contacting the plasma membrane. (C) Amperometric data for detection of cellular cholesterol at a microelectrode (11.5- μm diameter) modified with a lipid bilayer membrane containing cholesterol oxidase. No contact (Figure 17.1.3A): baseline data; no cholesterol detection. Adjacent: data for positioning the electrode within about 1 μm of (or partially touching) the plasma membrane. Cell contact: data for contacting the oocyte plasma membrane. Arrows indicate the approximate times of changing the electrode position. The buffer was 0.1 M sodium phosphate, pH 6.5. The electrode potential was 800 mV vs. NHE. Reproduced with permission from reference (18).

handbook). A cellular property than can be assessed by SECM is membrane permeability. In one such permeability study, algal protoplasts were incubated in solutions of redox active molecules and redox current was monitored as a function of the distance between the microelectrode and the cell (53). These types of curves are known as approach curves. Molecules resulting in lower current at close approach were determined to have lower permeability with respect to the cellular membrane because the membrane hindered diffusion of the molecules to the microelectrode surface. Cellular redox activity can also be probed with the scanning electrochemical microscope, as demonstrated by Liu and coworkers (54). This study focused on measuring the rate and assessing the pathway of transmembrane charge transfer. Additionally, an electrochemical image of cellular redox activity showed that the periphery of cells had the highest redox activity while the area occupied

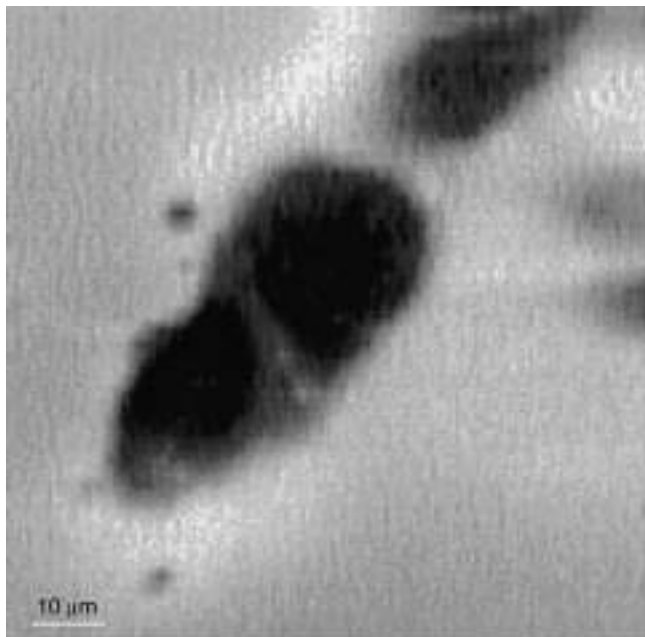


Figure 17.1.4 Normal human breast (MCF-10A) cells imaged by the SECM with a 1- μm -radius Pt tip and 40 μM 1,2-naphthoquinone as mediator. Reproduced with permission from reference (54).

by the nucleus had the lowest activity, due to the impermeability of the nuclear membrane to the redox mediator (Figure 17.1.4).

In a subsequent study, Liu *et al.* used SECM to image the local pH around groups of cells, noting that surrounding pH differs for cells in different metastatic stages (55). Liebetrau and coworkers used negative feedback SECM to image differentiation of PC12 exposed to nerve growth factor, which initiates cellular neurite outgrowth (56). With this technique it was possible to image neurites 1–2 μm in width and observe cellular surface morphology not apparent with a light microscope. In a follow-up study Kurulugama *et al.* used constant-height mode SECM to monitor topographical changes and faradaic current simultaneously (55). This allowed imaging of cellular morphology (seen as an impedance change) concurrent with amperometric monitoring of neurotransmitter release. This approach to imaging and amperometry has the potential to determine spatiotemporal dynamics of exocytosis *in vitro*. SECM has been employed in numerous other investigations of cellular surfaces and function including studies of redox activity and respiration of bacteria (16, 58), respiration activity of single bovine embryos (15, 59), and the permeability of bovine cartilage to various molecules (60, 61).

17.1.2 Electrochemistry at lipid bilayer membranes

Processes occurring at the cellular surface are of great interest to biologists and biophysicists. However, the plasma membrane surface of a cell is quite complex because the

membrane is not a homogeneous structure. It is a bilayer structure formed by a wide variety of lipids, is imbedded with proteins, decorated by carbohydrates, and supported by cytoskeletal elements. Numerous processes crucial to cellular survival occur at the plasma membrane including exocytosis and endocytosis as well as ionic transport via ion channels. Many of these processes are the result of a number of proteins acting in concert with the lipid bilayer in a complex symbiotic relationship. A model system was developed by Bangham in the 1960s in an effort to exclude influences from proteins and focus on the role of lipid bilayer properties in cellular membrane processes (62). Planar lipid bilayers were the first manifestation of a system to model the cellular surface and the unmodified varieties of these membranes have similar resistance and capacitance values to cell membranes (63, 64). The composition of bilayer lipid membranes can be altered to make them more conductive. This is accomplished by insertion of lipophilic molecules into the membrane that form channels or increase the permeability to certain ions (64). By doping lipid bilayers with lipophilic electron donors (e.g., ferrocene or tetrathiafulvalene) or acceptors (e.g., 7,7,8,8-tetracyanoquinodimethane) membranes can function as working electrodes (65, 66). Membrane modified electrodes (67, 68) have been suggested as a platform for biosensor development and have proved useful in development of enzyme electrodes.

Since lipid bilayer membranes have physical and electrical properties quite similar to those of cellular membranes, they are useful for constructing simple models of cells. The most efficient cellular model is the liposome, which is a spherical lipid bilayer. Liposomes can range in diameter from a few nanometers to hundreds of micrometers (depending on preparation method) and have found application in fields varying from drug delivery (69–73) to cosmetics (74, 75). Recently technology has been developed by Orwar and coworkers that allows transformation of single liposomes into networks of multiple liposomes with lipid membrane nanotube connections (76–78). Networks of this sort have been suggested as a new generation of microfluidics. However, it is the ability to manipulate liposomes into biologically relevant geometries that is of interest to the biological electrochemist. To mimic exocytosis, the process of cellular chemical secretion, a network of two liposomes can be constructed (79). This model system can be used to study the dependency of electrochemical response on electrode size and can be used to model neurotransmitter efflux from synapses *in vivo* (80).

17.1.2.1 *Electrochemistry at a liposome-based artificial cell*

Exocytosis is a complex process that involves protein–protein and protein–lipid interactions, membrane fusion, and release of neurotransmitter. A model system that mimics this process in a protein free fashion is advantageous to study the role of the lipid bilayer in exocytosis. A totally lipidic system is useful to study the effects of altered membrane physical properties, typically accomplished by altering the components that form the membrane. Thus an “artificial cell” composed of two liposomes with a lipid membrane nanotube connection and one inside the other (Figure 17.1.5) was developed (79).

The liposome inside a liposome configuration is analogous to a vesicle inside a secretory cell during the last stages of the release process. Microelectroporation (77) assisted insertion and careful micromanipulation of a micropipette is required for formation of the artificial cell. Briefly, a micropipette filled with the redox molecule of choice (typically catechol) is positioned next to a surface immobilized giant unilamellar vesicle (GUV) with

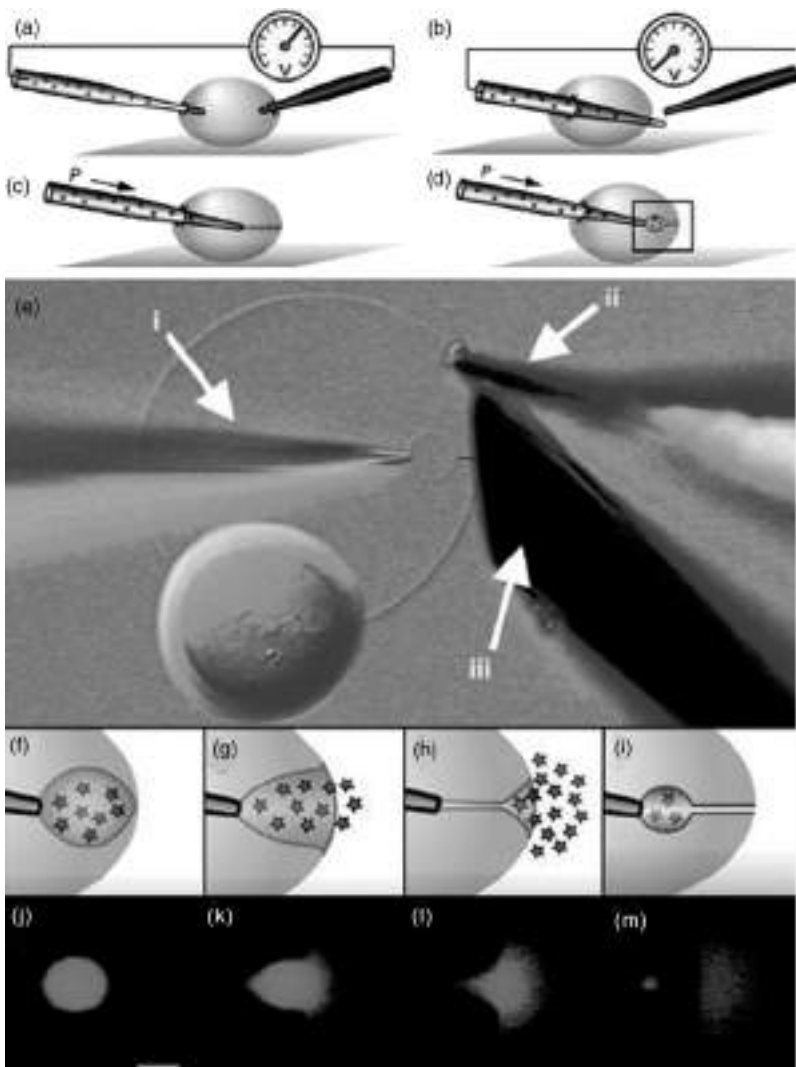


Figure 17.1.5 Formation and release of vesicles in an artificial cell. (A–D) Schematics of a microinjection pipette electroinserted into the interior of a unilamellar liposome and then through the opposing wall, pulled back in to the interior, followed by spontaneous formation of a lipid nanotube and formation of a vesicle from flow out of the tip of the micropipette. (E) Nomarski image of a unilamellar liposome, with a multilamellar liposome attached as a reservoir of lipid, microinjection pipette (i), electrode for electroinsertion (ii), and 30- μm diameter amperometric electrode beveled to a 45° angle (iii). A small red line depicts the location of the lipid nanotube, which is difficult to observe in the computer image with a 20 \times objective, illustrating a vesicle with connecting nanotube inside a liposome. (F–I) Fluid injection at a constant flow rate results in growth of the newly formed vesicle with a simultaneous shortening of the nanotube until the final stage of exocytosis takes place spontaneously and a new vesicle is formed with the attached nanotube. (J–M) Fluorescence microscopy images of fluorescein-filled vesicles showing formation and final stage of exocytosis matching the events in F–I. (Scale bar represents 10 μm .) Reproduced with permission from reference (79). (for colour version: see colour section at the end of the book).

an attached multilamellar vesicle. At the opposite side of the vesicle is the electroporation counter electrode. When a voltage pulse is applied across the GUV, the membrane is transiently destabilized, allowing insertion of the micropipette. The micropipette is then translated across the interior of the GUV and a voltage is applied again, allowing the micropipette to exit the distal side of the GUV. The micropipette is rapidly withdrawn into the interior with part of the membrane adhered to the tip. This forms a nanotube and when solution flows from the micropipette a small vesicle begins to form. When the vesicle has grown to the size where it nearly contacts the larger exterior vesicle, the geometry is exactly like that of a cell undergoing exocytosis. There is a small vesicle fused to a larger vesicle with an aqueous pore connecting the vesicular contents with the extracellular space. At this point in the artificial cell, the interior vesicle empties its content to the surrounding solution in a process that resembles exocytosis. The nanotube remains adhered to the pipette tip, however, allowing successive release events without pipette reinsertion. The size of the fusing vesicle can be adjusted by varying the distance from the pipette tip to the large vesicle membrane, and release from vesicles ranging from 4 μm in diameter to larger than 30 μm has been measured.

Monitoring the material released is accomplished by amperometrically detecting the redox molecule contained in the smaller interior vesicle as it is released. Typically a carbon fiber electrode measuring 33 μm in diameter is employed for amperometric detection. The resulting current transient appears qualitatively similar to those recorded at living secretory cells, such as mast cells, chromaffin cells, and PC12 cells (Figure 17.1.6A–B).

The difference in time scale, amplitude, and area of the artificial cell current spike is due to the fact that the vesicle is larger and contains more electroactive molecules than those in living cells. However, release from the smallest vesicles measured (approximately 4 μm diameter) is similar in time to events measured from the large vesicles of the beige mouse mast cell which average 700 nm in diameter (81). In Figure 17.1.6C, the relationship between vesicle radius and full width at half maximum (half-width) is shown for experiments with artificial cells. The fit is nearly perfectly cubic, meaning that release kinetics scale linearly with vesicle volume.

An interesting feature of this system is the transport or leakage of catechol through the nanotube prior to full release. This can be thought of as analogous to neurotransmitter leakage through the fusion pore formed before full release in living cells (33, 34). Transpore catechol transport is apparent on the amperometric traces as a prespike rise in current, which in live cells is termed a “foot” (Figure 17.1.7A–B).

This transport was characterized at artificial cells as a function of vesicle size and as a function of the pressure applied to the micropipette used to inflate the vesicles (Figure 17.1.7C–E). The pressure applied to the inflation micropipette correlates with the flow rate of catechol solution from the micropipette. The duration of the foot is strongly dependent on vesicle size for larger vesicles (size of vesicle just before release), and is also dependent on the flow rate. However, the number of molecules detected during the foot portion of the event (foot area) is not dependent on solution flow rate. The ratio of area to the duration of the foot is dependent on both vesicle size and flow rate. These electrochemical data coupled with models of membrane and fluid dynamics lead to cogent explanation of leakage through the membrane nanotube (Figure 17.1.7F). As the vesicle is inflated, additional membrane required to accommodate the growing volume is drawn along the nanotube thus

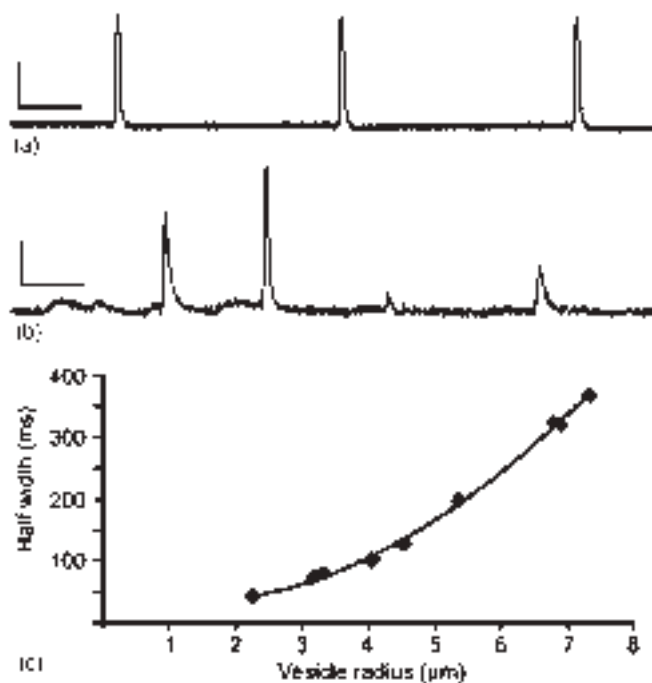


Figure 17.1.6 Amperometric monitoring of repeated exocytosis events at artificial cells and cells. (A) Amperometric detection of continuous exocytosis of three vesicles from an artificial cell (scale bars are 40 pA and 3000 msec). (B) Amperometric detection of dopamine exocytosis from a PC12 cell (scale bars are 10 pA and 40 msec). (C) Plot of half-width vs. vesicle radius for vesicles fusing from an artificial cell where the vesicle radius has been the only parameter varied in the experiment. Reproduced with permission from (79).

inducing shear flow of the solution inside the nanotube. Opposing shear flow is Poiseuille flow resulting from the pressure difference across the nanotube. As the interior vesicle is inflated, its volume grows at a constant rate, whereas the rate of surface area growth slows as the vesicle grows larger. Thus, shear flow has a high velocity when the vesicle is small and slows as the surface area to volume ratio decreases. Additionally, as the vesicle grows the nanotube connecting it to the larger vesicle shrinks, Poiseuille flow velocity increases as the nanotube shortens, and outward flow begins to dominate. When Poiseuille flow overcomes shear flow, catechol solution is transported out of the nanotube and is amperometrically detected as a prespike foot.

In this sense, transport through the nanotube is analogous to leakage through an elongated fusion pore in living cells. Intravesicular pressure and membrane transfer through the fusion pore have been suggested previously as significant driving forces for exocytosis (82–85). Finally, the most significant finding from this work is that membrane mechanics alone seem to be sufficient to drive exocytosis-like behavior at biological time scales without protein intervention.

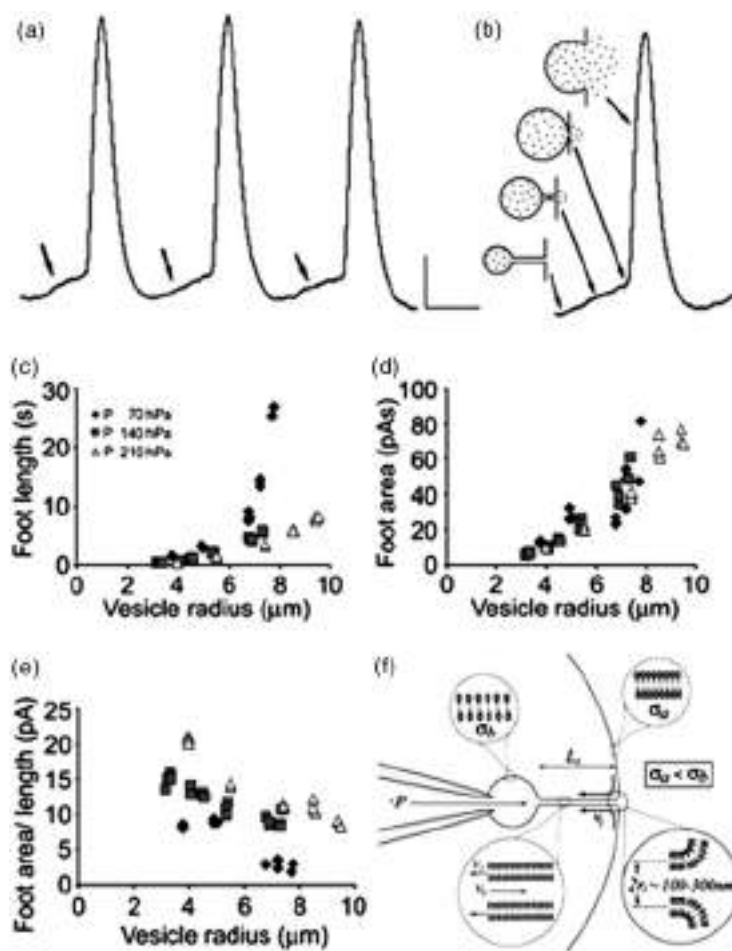


Figure 17.1.7 Amperometric monitoring of release via an artificial fusion pore. (A) Amperometric detection of release from a 5-μm radius vesicle showing prespike feet (arrows), indicating catechol transport through the lipid nanotube or fusion pore. (B) Time correlation of vesicle growth, transport of transmitter through the lipid nanotube, and the final stage of exocytosis with amperometric detection. (C–E) Plots of foot length (C), foot area (D), and the ratio of foot area over foot length (E) observed with amperometry for vesicles fusing with an artificial cell at three different pressures used to inflate the vesicles. (F) Schematic model of the factors affecting flow in the vesicle and nanotube of the artificial cell. Reproduced with permission from reference (79).

17.1.2.2 Modeling a synapse with the liposome-based artificial cell

In a separate set of experiments, the artificial cell model was used to develop models of coulometric efficiency as a function of electrode size and to determine the size of the space between the electrode and the membrane (80). In this case, coulometric efficiency is defined as the ratio of the total number of molecules detected from a vesicle to the total

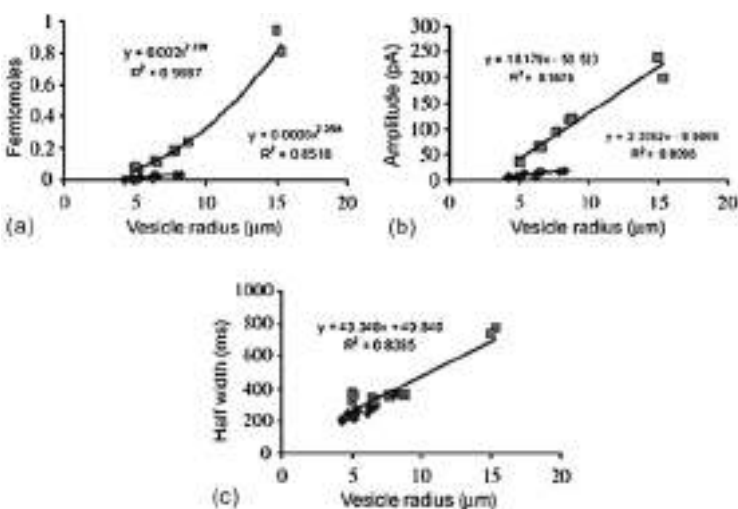


Figure 17.1.8 Amperometric data for fusion of vesicles of varying size at beveled 5- (♦) and 33-μm (■) electrodes: (A) the amount of catechol observed at each electrode, (B) the amplitude of each current transient, and (C) the half-width of each transient vs. the radius of vesicles undergoing exocytosis. Each data set has been curve fit to observe the trend in the data as indicated. Reproduced with permission from reference (80). (for colour version: see colour section at the end of the book).

number of molecules released by the vesicle. These studies employed two different size electrodes (5 and 33 μm diameter) to detect release and compared the electrochemical responses as a function of electrode and vesicle size. When a vesicle is released from the artificial cell, its size relative to the detection electrode is a strong determinant of the amount of vesicular content detected as well as the spike amplitude (Figure 17.1.8A–B). However, the measured kinetics of release is not affected by the size of the electrode used for detection (Figure 17.1.8C).

To model coulometric efficiency and determine the size of the electrode membrane gap, a simple geometric representation of the system was devised (Figure 17.1.9). The space between the electrode and the membrane was modeled as a cylinder and the ratio of the vesicle volume to cylinder volume determines the coulometric efficiency. If the vesicular volume is smaller than the cylinder volume, 100% oxidation is expected.

For a 33-μm electrode, the best fit of the data is obtained when the height of the cylinder is 300 nm suggesting that even when the electrode is in direct contact with the membrane there is a small volume of solution trapped between the electrode and the membrane. Moreover, even for somewhat smaller vesicles a significant portion of the released molecules escape undetected. This is probably caused by solution flow out of the membrane-electrode gap due to volume limitation and not diffusion (i.e., the volume of the gap cannot accommodate the total volume of liquid released from the vesicle).

The first model presented in this work was quite simplistic and did not take into account the distinct stages of release that are characteristic of the artificial cell model. Therefore a second model was proposed with distinct stages of release and each stage was represented as having a distinct geometric shape (Figure 17.1.10).

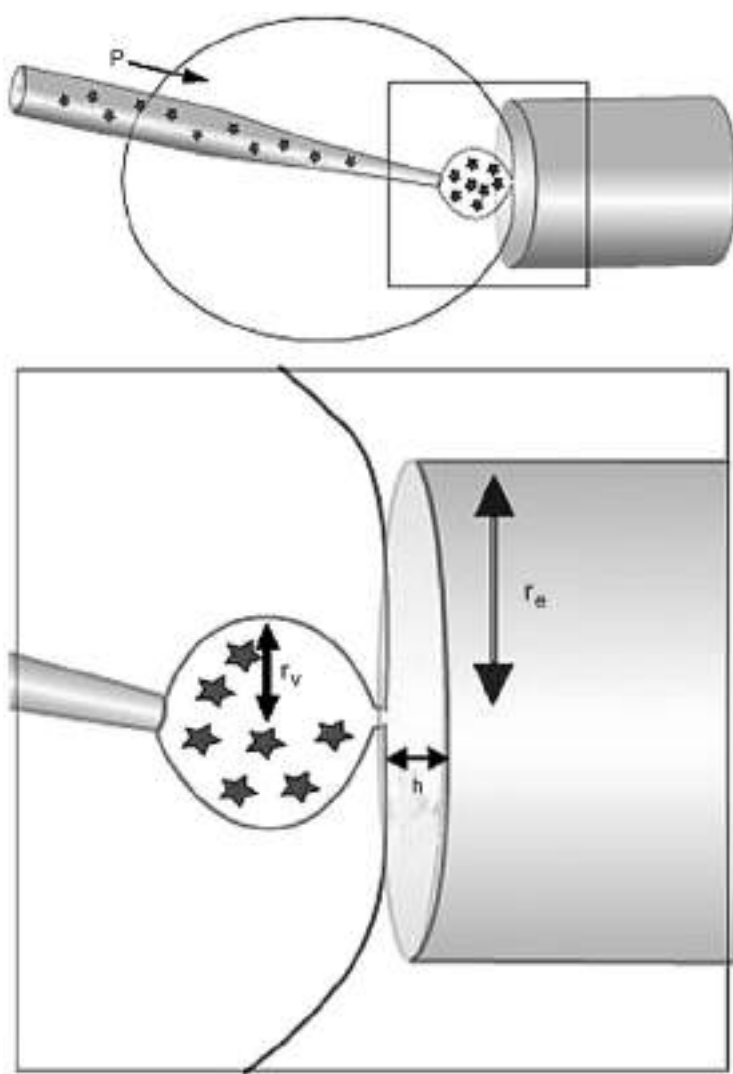


Figure 17.1.9 Simple model of coulometric efficiency for artificial exocytosis. This first-stage model assumes that the efficiency of oxidation for material released is simply the ratio of the membrane–electrode space (calculated as $\pi r_e^2 h$) over the volume of the vesicle ($4 \pi r_v^3/3$). This assumes that all the catechol that is present in the membrane–electrode space after exocytosis will be oxidized, but also that only catechol in the solution that fits in this volume will be oxidized. Reproduced with permission from reference (80). (for colour version: see colour section at the end of the book).

In the first stage of release the nanotube begins to dilate and at this stage some vesicular material escapes the vesicle as revealed by fluorescence imaging of release events (Figure 17.1.10B). The next stage is characterized by a membrane structure that is between a spherical vesicle and a frustum (Figure 17.1.10C). The final stage is after full release

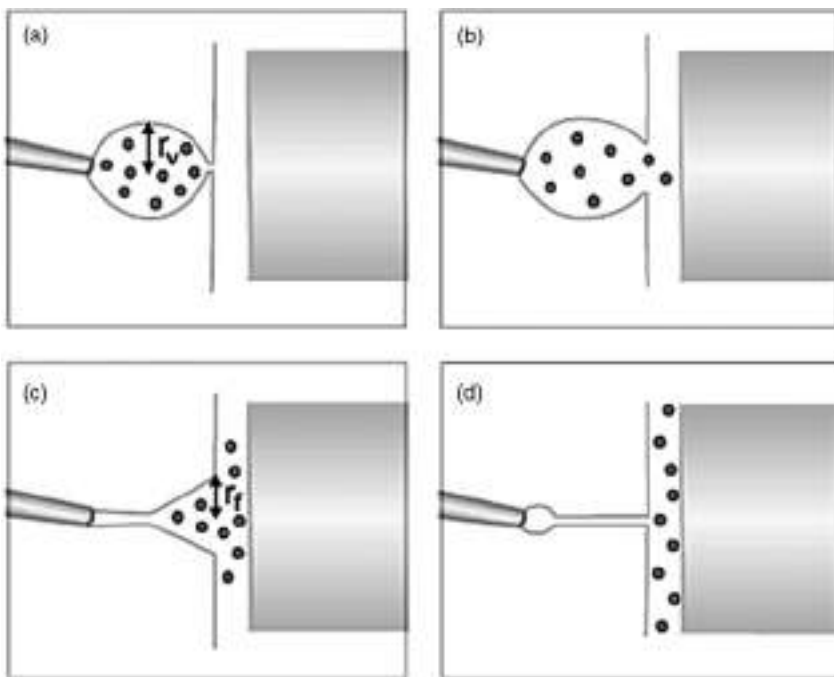


Figure 17.1.10 A more complete model of the release process during exocytosis based on the fluorescence observations. This model assumes that as the vesicle opens, it has a transitory period where mass transport of catechol to the electrode is via diffusion from a frustum with opening r_f defined the value of r_v . Catechol diffusing to the electrode is oxidized. After exocytosis is complete, the membrane-electrode space is filled with solution from the inside of the vesicle and catechol present continues to be oxidized as in the thin-layer representation of Figure 17.1.9. Reproduced with permission from reference (80). (for colour version: see colour section at the end of the book).

when the small vesicle has become fully incorporated into the larger liposome membrane and the nanotube remains attached to the pipette tip (Figure 17.1.10D). During the time the vesicle is in the frustum state (calculated as twice the spike half-width for each vesicle) the charge passed is estimated from the integrated Cottrell equation

$$Q_{\text{frustum}} = \frac{2nFAD^{1/2}C^*t^{1/2}}{\pi^{1/2}} \quad (17.1.1)$$

where n is the number of electrons transferred in the electrochemical reaction, F is Faraday's constant, A is the effective electrode area which is taken to be the area defined by the opening of the frustum or the electrode area, which ever is smaller, D is the diffusion coefficient ($6 \times 10^{-6} \text{ cm}^2/\text{sec}$), C^* is the concentration of catechol in the vesicle, and t is the time the frustum is open, taken to be twice the peak half-width. During the next stage, after full exocytosis, the charge passed by oxidation of catechol in the electrode-membrane space is given by the equation

$$Q_{\text{space}} = nFC'\pi r_e^2 h \quad (17.1.2)$$

where r_e is the average radius of the beveled electrode and h is the distance between the membrane and the electrode. C' is the concentration of the remaining unoxidized catechol in the membrane–electrode space and is calculated by subtracting the number of moles oxidized during the previous (frustum) stage by the equation

$$C' = \frac{[C * (V_v + V_{\text{flow}})] - 2AD^{1/2}C * t^{1/2} / \pi^{1/2}}{V_v + V_{\text{flow}}} \quad (17.1.3)$$

where V_v is the volume of the vesicle and V_{flow} is the volume of flow out of the pipette during the release event. Flow during the event is calculated by dividing the vesicle volume by the time between events to get a volume flow rate in cm^3/sec then multiplying by twice the event half-width. Combining Faraday's Law ($N = Q/nF$) and the integrated Cottrell equation, $Q = 2nFAD^{1/2}C * t^{1/2}/\pi^{1/2}$ the number of moles oxidized during the frustum stage is given by $N = 2AD^{1/2}C * t^{1/2}/\pi^{1/2}$.

Oxidation of all the catechol in the vesicle prior to release results in the following coulometric charge

$$Q_{\max} = nFC * (V_v + V_{\text{flow}}) \quad (17.1.4)$$

Thus the predicted coulometric efficiency is the ratio of the sum of the charge from the two stages of opening over Q_{\max} . The resulting equation that predicts percent coulometric efficiency is given as

$$\% \text{ Coulometric Efficiency} = 0.38[(0.25Q_{\text{frustum}} + Q_{\text{space}})/Q_{\max}] \times 100 \quad (17.1.5)$$

Only 25% of the Cottrell equation is used in the final expression to correct for the diminished diffusion in the narrowing frustum. This model correctly predicts the shape of the percent coulometric efficiency vs. vesicle radius; however, the predicted magnitude is 2.6 times larger than that observed. To correct this a factor of 0.38 has been applied to the theoretical prediction. Experimental data, predicted coulometric efficiency, and the best fit of the experimental data is shown in Figure 17.1.11.

The discrepancy in magnitude leading to the 0.38 correction term may arise from numerous factors. One possible explanation is that the detection electrode may not always be centered over the release site, resulting in a greater than expected escape of undetected catechol. Also, solution flow due to the distention of the vesicle membrane may lead to loss of material and the reduced oxidation efficiency. The calculation for charge passed during the frustum stage assumes mass transport by diffusion only, but it seems that the changing membrane geometry may lead to solution flow causing molecules to escape the membrane–electrode gap without being oxidized. In cell-to-cell communication, it is assumed that diffusion is the predominant mass transport process, but this model shows that convective flow is likely to play an important role in mass transport over short distances.

Applying this model to exocytosis in biological systems permits the prediction of coulometric efficiency for any size electrode if the vesicle size is known. Two cell types commonly used in exocytosis experiments, adrenal chromaffin and PC12 cells, have average vesicle radii of 99 and 125 nm, respectively (33, 48). The model set forth here predicts

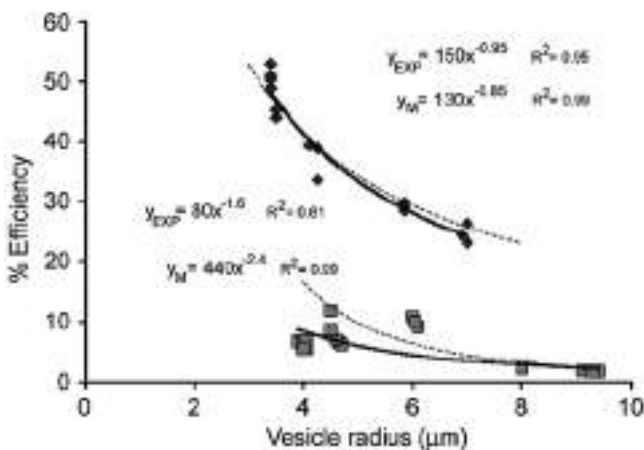


Figure 17.1.11 Coulometric efficiencies for a data set obtained with a beveled 33-μm electrode (♦) compared to data obtained with a 5-μm electrode (■) for release of catechol measured from a range of vesicle sizes. This is compared to the theoretical coulometric efficiencies for these electrode dimensions calculated with the conditions outlined in Figure 17.1.5 and with the model discussed in the text (dashed lines). These are compared to each set of experimental data, which are shown with best-fit equations (thick lines). The equations for all lines, and their correlation coefficients, are given with the symbols y_{exp} for experimental data sets and y_m for the modeled efficiencies with that for the 5-μm electrode to the left and that for the 33-μm electrode to the right. Reproduced with permission from reference (80). (for colour version: see colour section at the end of the book).

100% coulometric efficiency for amperometric experiments employing 5 μm electrodes at adrenal chromaffin and PC12 cells. In contrast, for cell types that release larger vesicles, such as the beige mouse mast cells, the model predicts less than 100% coulometric efficiency. In fact, for beige mouse mast cells (average vesicle radius is 1.35 μm) coulometric efficiency at a 5 μm electrode is predicted to be 47% and for the largest mast cell vesicles (vesicle radii as large as 2 μm) coulometric efficiency drops to 25%. The model predicts that even 33 μm electrodes will not quantitatively oxidize all material released from beige mouse mast cell vesicles. Most cellular experiments performed to date use a 5 or 10 μm electrode for detection. Therefore it is doubtful, based on this model, that measurements made on cells releasing large vesicles are quantifiable with the assumption of 100% coulometric efficiency.

The data gathered with the artificial cell system shows that under certain conditions much of the released catechol will escape the membrane–electrode space undetected. Also the model suggests that in addition to diffusion, solution flow is a significant mode of mass transport of neurotransmitter in synapses. This system can be used to model what happens in a synapse *in vivo*. The membrane–electrode space can be considered analogous to the synaptic cleft and the detection electrode can be thought of as the post-synaptic membrane which has receptors that “capture” the released neurotransmitter. If a synapse is considered to be a 20-nm gap between cells and the average diameter of the post-synaptic surface is 100 nm, then 70% of the volume of a 100-nm diameter vesicle will be pumped directly to the extrasynaptic space during release. This agrees with recent *in vivo* work that suggests

that at dopamine and serotonin synapses much of the neurotransmitter escapes the synapse following exocytotic release (86, 87). There are still many experimental models to examine before a thorough understanding of exocytosis is achieved. However, the models presented here provide a means to simplify the experiments and to examine the effect of membrane mechanics and structure on exocytotic release measured with amperometry.

17.1.3 Electrochemistry in small drops and vials

Many of the intriguing problems yet to be solved in biology and medicine require the chemical analysis of minute amounts of material in constricted geometries. The study of photosynthesis, cellular metabolism, and neurotransmission, to name a few, all require chemical analyses in tiny volumes. Electrochemical methods employing microelectrodes are perfectly suited to analyze small volumes, provided the analytes of interest are electrochemically active, which is the case with many neurochemical analytes. Neurotransmitters such as dopamine, serotonin, epinephrine, and norepinephrine are easily oxidized at moderate potentials. The study of these molecules *in vivo* and *in vitro* may lead to breakthroughs in the treatment of neurological disorders such as Parkinson's disease and Alzheimer's disease, as well as depression and anxiety related disorders. Detection and analysis of these molecules, however, is not always easily accomplished due to a wide variety of interferences and due to the volume-limited nature of the measurement, which may have confounding effects on the electrochemical response. For these reasons many groups have devised model systems employing small volume droplets and vials, some even in the picoliter regime, to investigate electrochemical responses in confined geometries. In this section we review the techniques and results for detection of small amounts of analytes in small drops and vials, as well as some biological applications of these techniques.

17.1.3.1 Fabrication of microvials

Exploration of electrochemical behavior in small volume containers requires fabrication methods capable of defining micrometer size structures from a suitable substrate. Initially, Bowyer *et al.* (88) sandwiched silver and platinum foil between layers of Tefzel film and glass to form an electrochemical cell with auxiliary, reference and working band electrodes, the smallest of which measured 4 μm thick. This electrochemical cell was used to investigate the differential pulse, normal pulse, and cyclic voltammetric behavior of ferrocence in aqueous solutions with volumes ranging from 2 mL to 50 nL.

More recently, however, photolithography has been employed to define and fabricate vials with a capacity as small as 1 picoliter (89, 90). Small vials, described by Clark *et al.* have been fabricated using silicon template photolithographically, then transferring the template pattern into polystyrene using a hot press method. This results in arrays of transparent microvials. An alternative approach to producing transparent sample vials has been taken by Bratten and coworkers whereby a polyimide chamber is photolithographically defined on a transparent glass slide (91–93). These structures differed from those of Clark and Ewing in that the reference, auxiliary, and working electrodes were formed by *in situ* gold deposition on the bottom surface of the container.

A third method of vial fabrication uses a combination of screen printing and laser ablation (94, 95). Briefly, carbon ink was screen printed through a patterned stencil onto a ceramic substrate. An insulating dielectric ink was screen printed on top of the carbon layer and a Ag/AgCl ink was printed on top of the dielectric ink. A final layer of dielectric ink was printed on the outermost layer. The carbon and Ag/AgCl layers eventually form, after laser ablation, the working and reference electrodes of the device. Formation of the vials was accomplished by Kr-F excimer laser ablation at 248 nm and resulted in vial with a volume of 7.2 nL. Figure 17.1.12 shows scanning electron micrographs of the three types of vials described above.

There are two prominent electrochemical detection schemes when working in small volume vials. The simplest method is to use micromanipulators to position the working and reference electrodes into the vial. This is the approach taken by Clark and Ewing, as well as some groups conducting biological electrochemical experiments in microvials, which will be discussed later in this section. Secondly, electrodes can be formed *in situ* in the chambers by traditional microfabrication and photolithography techniques (91–93, 96) or by a combination of screen printing and laser ablation (94–95). The drawback to some of these fabrication methods is that the materials that form the sides and bottom of the vials are not always the same. This could lead to differential adsorption of analytes and erroneous voltammograms.

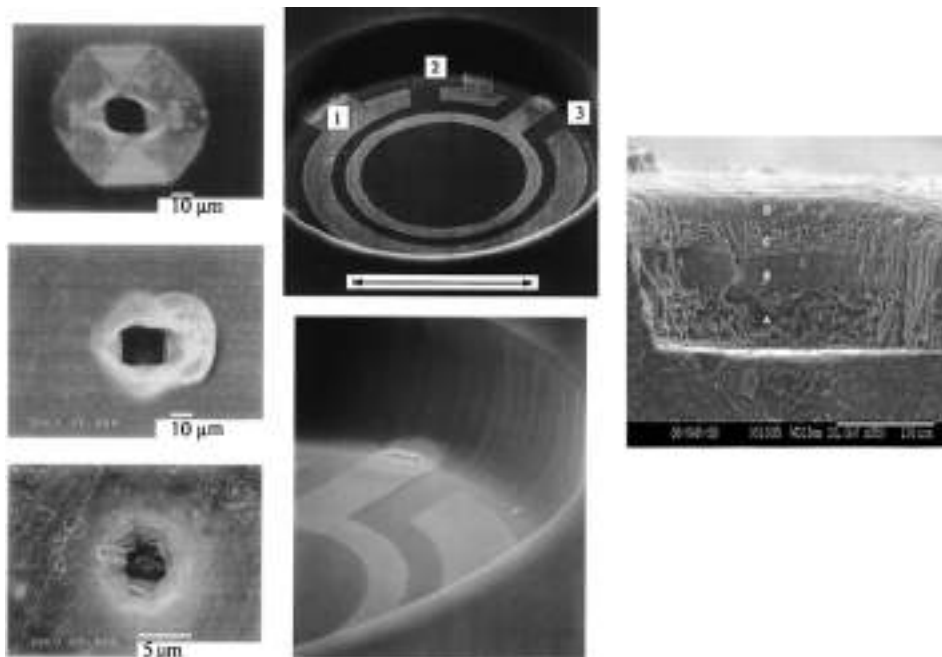


Figure 17.1.12 Scanning electron micrographs of three types of microvials. The leftmost images are polystyrene microvials fabricated with a hot press method. The center images are vials photolithographically defined polyimide wells. The rightmost image is a vial prepared by ink jet printing followed by laser ablation. Reproduced with permission from references (89, 91, 94).

17.1.3.2 Microscopic droplets

Performing electrochemistry in small volumes does not require that the sample container be defined by solid boundaries. By directly depositing a droplet on a substrate (or electrode), the need for access to photolithographic equipment is circumvented. Gratzl and coworkers have directly deposited microscale droplets on a flat polystyrene substrate resulting in sample volumes as small as 75 pL (97, 98). These experiments required that both the working and reference electrode be positioned in the sample by micromanipulation. The reference electrode used in these experiments was a Ag/AgCl reference inserted in a modified diffusional microburet (DMB). A DMB is essentially a glass micropipette that has a diffusion membrane in the tip allowing diffusional delivery of reagents contained within the pipette.

A second method of droplet formation involves modifying the surface of the working electrode with a small droplet of the solution to be examined. This method has the advantage that the droplet does not have to contain any deliberately added supporting electrolyte as the droplet-coated electrode is inserted in an immiscible conductive solution to perform the analysis. The electrochemistry of electrode immobilized droplets has been thoroughly reviewed by Banks *et al.* (99).

Whether investigating redox reactions in small drops or microvials, one of the main considerations is sample handling since evaporation can significantly change analyte concentration as well as solution pH and viscosity. Evaporation is proportional to surface area to volume ratio of the sample solution, which is quite large for small samples. Thus, total evaporation can occur in seconds for picoliter aqueous samples. Evaporation can be minimized by coating the sample with a membrane lid (100), saturating the experimental headspace with water (88), or covering the sample with a saturated hydrophobic liquid such as heptane (101) or glycerol (89).

17.1.3.3 Electrochemical response in small volume samples

The examination of the voltammetric response at carbon fiber UMEs as a function of microvial volume was undertaken by Clark *et al.* (89). The experimental volume was varied from about 4 nL to as little as 1 pL. For a 5 μm diameter electrode, the voltammograms of ferrocenecarboxylic acid did not vary as a function of sample volume. The shape of the voltammograms was sigmoidal which is expected for disk microelectrodes scanned at slow rates (1–1000 mV/sec) under steady-state conditions (102). The half wave potential measured in the microvials was identical to that of ferrocenecarboxylic acid in bulk solution and the current value also matched the expected value. In addition, Clark *et al.* performed voltammetry with a 1 μm diameter flame etched carbon fiber electrode in a 1 pL vial; however, no deviation from bulk solution behavior was apparent.

More detailed analyses of microdisk electrode behavior has been provided by both Clark and Ewing (90) as well as Kashyap and Gratzl (101). The work by Clark *et al.* was done in picoliter vials while the work by Kashyap *et al.* was carried out in picoliter droplets, and in these experiments the researchers investigated the sample volume, voltammetric scan rate, and analyte concentration dependence of the electrochemical response. Clark and Ewing showed that the voltammetric response as a function of scan rate displayed some interesting characteristics (Figure 17.1.13).

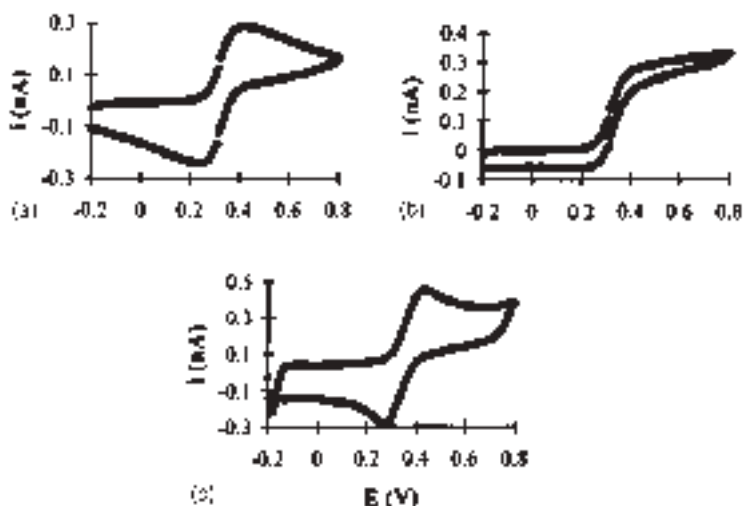


Figure 17.1.13 Cyclic voltammograms of 1.0 mM ferrocenecarboxylic acid in a 16-pL vial. The scan rates are (A) 0.1, (B) 1.0, and (C) 10 V/sec. Carbon fiber working electrodes are 5 μm in diameter. Reproduced with permission from reference (90).

At the highest scan rate (10 V/sec, Figure 17.1.13C) the voltammetric peak shape was not significantly different from that observed in bulk solution. At an intermediate scan rate (Figure 17.1.13B) the voltammogram was sigmoidal, similar to bulk solution voltammograms at the same scan rate with microelectrodes. However, a significant deviation from bulk solution behavior is apparent when a voltage is scanned slowly (0.1 V/sec, Figure 17.1.13A) in a 16-pL vial. Unlike in bulk solution where voltammograms obtained at slow scan rate with microelectrodes are sigmoidal, voltammograms obtained at slow scan rate in picoliter vials are peak shaped and display a large current increase on the reverse (reduction) wave. In general, the data for fast and intermediate scan rates follow microelectrode theory, and the data for slow scan rates can be described as quasi-thin layer behavior.

Peak shaped voltammograms at slow scan rates only appeared in smaller vials (16 pL or less) and can be explained by comparison of diffusion in bulk solution vs. diffusion in microvials. In microvials the diffusion profile to the electrode is altered due to the vial boundaries. Thus, depletion of electroactive molecules near small electrodes can be achieved in the smallest vials. In bulk solution the amount of molecules reduced at a microelectrode is negligible compared to the bulk analyte concentration. But, in a 16-pL vial the data show that 21% of the total analyte in solution is oxidized by a 5- μm electrode scanned at 0.1 V/sec. These data suggest that bulk electrolysis in microvials can be easily implemented to determine the total amount of analyte present in a vial.

Experiments in microvials also reveal an increase in current on the reverse wave for slow scan rates. After ruling out any effect from interactions between the analytes and the microvial surface, a diffusion-based explanation was formulated. By determining the concentration dependence of the ratio of reduction currents in microvials and bulk solution

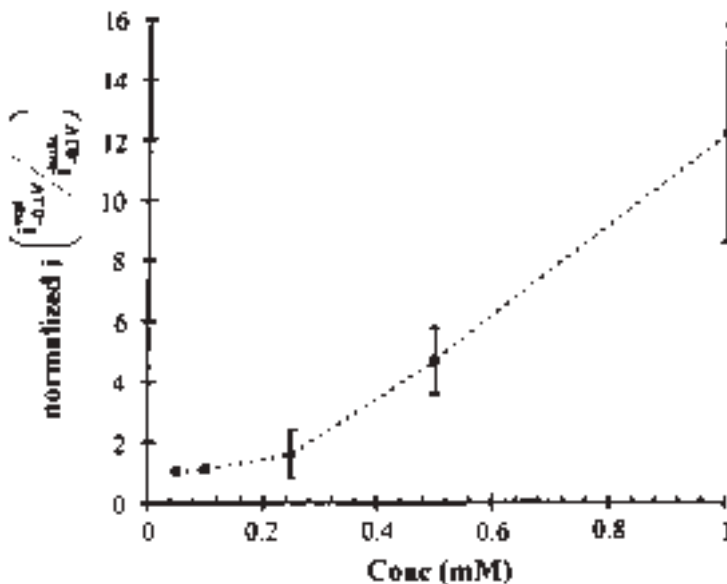


Figure 17.1.14 Normalized reduction current as a function of concentration. Concentration range is from 0.05 to 1.0 mM. Scan rate is 0.2 V/sec, and the vial size is 7 pL. Error bars indicate the mean \pm standard deviation. Reproduced with permission from reference (90).

($i_{\text{vial}}/i_{\text{bulk}}$) (Figure 17.1.14) in a 16-pL microvial it was determined that diffusion of the oxidized species away from the electrode is restricted.

Unlike experiments in bulk solution where the oxidation product at a UME diffuses away prior to the reverse scan, in a microvial, the oxidation product is restricted by the vial boundaries and forms a depletion layer that can be re-reduced. The increase in the ratio $i_{\text{vial}}/i_{\text{bulk}}$ with higher concentration occurs because more oxidized molecules are produced in the vicinity of the electrode at higher concentrations and are available for reduction on the reverse scan. Reducing the size of the microvials has a related effect on the ratio $i_{\text{vial}}/i_{\text{bulk}}$. When the vial size is decreased, diffusion of oxidized species is further restricted thus maintaining a more concentrated depletion layer near the electrode resulting in increased $i_{\text{vial}}/i_{\text{bulk}}$. These experiments demonstrate that the characteristics of the diffusion/depletion layer, which is dependent on the ratio of the sizes of the sample microvial and the electrode, is the largest determining factor on the voltammetric response.

17.1.3.4 Biological applications of electrochemistry in microvials

Microvials are attractive environments for single cell experiments due to their limited volumes and the possibility to create integrated devices with electrodes fabricated by photolithographic techniques inside the vials. Such studies include the monitoring of purine release during cardiac cell ischemia (93), monitoring metabolic flux due to stress response (103), and monitoring dopamine transport into cells (104). Microvials with spatially distinct electrodes have been fabricated by Dias *et al.* and have been used to determine the

spatial distribution of exocytosis events on the surface of adrenal chromaffin cells (96). In a study by Troyer and Wightman, HEK-293 cells transfected to express the dopamine transporter were placed in vials ranging from 100 to 200 pL (104). Dopamine was then injected into the vials and the rate of clearance of dopamine by the cell was monitored with fast scan rate cyclic voltammetry. Monitoring dopamine concentration change with time allows the calculation of the kinetics of the dopamine transporter, specifically the initial transport rate, V_{\max} . Using the single cell microvial approach, V_{\max} was determined to be 55 ± 17 amol/sec-cell. In populations of cells, V_{\max} was determined to 18.9 ± 1.4 amol/sec-cell by rotating disk electrode voltammetry (105) (see Chapter 11). The discrepancy in V_{\max} measured by competing techniques may be due to the difference in the cell volume/solution ratio. In microvial experiments, this ratio is larger indicating that there is less extracellular volume per cell and thus fewer dopamine molecules are transported into the cell. Fewer transported molecules generally prevents the cytosolic concentration from reaching a high enough concentration for reverse transport to occur. However, in some cells in microvial experiments, reverse transport did occur as determined by a nonzero dopamine concentration plateau. Cells exhibiting this behavior were not taken into account in the calculation of V_{\max} because the calculated V_{\max} from these experiments appeared lower.

17.1.4 Intracellular electrochemistry

Extracellular measurements are powerful tools for elucidating mechanisms of cellular secretion. However, to gain information on cellular synthesis and storage of various molecules, measurements in the cell cytoplasm are necessary. Microseparation techniques, such as capillary electrophoresis, with electrochemical detection schemes are useful in measuring and identifying neurotransmitters from whole cells as well as from samples of cell cytoplasm (106, 107). Voltammetric methods have also been used to monitor neurotransmitters inside single cells. Invertebrate cells are typically chosen for intracellular studies because they are generally much larger than their mammalian counterparts, allowing the use of larger electrodes and detection of larger amounts of analyte.

17.1.4.1 Intracellular voltammetry

Early studies by Meulemans *et al.* used differential pulse voltammetry (see Chapter 11) to measure the concentration of electroactive drugs in the cytoplasm of cholinergic neurons of *Aplysia californica* and to determine rates of cellular uptake and clearance (108). Another report by Meulemans *et al.* described a needle tipped glass insulated platinum electrode for detection of intracellular serotonin in metacerebral neurons from *Aplysia* (109). Again differential pulse voltammetry was used to measure intracellular concentration of serotonin after cell stimulation, after injection of serotonin into the cell, and after extracellular treatment with tryptophan, a serotonin precursor. Serotonin concentration in resting untreated cells was determined to be 0.94 ± 0.61 mM. Chen *et al.* have also used platinum electrodes with multiple pulse voltammetry to measure dopamine levels in the giant dopamine neuron of *Planorbis corneus* (110).

Monitoring neurotransmitters as well as oxygen in cytoplasm can be accomplished using carbon ring and platinized carbon ring microelectrodes (111–113). In the giant dopamine neuron of *Planorbis*, baseline dopamine concentration was below the limit of detection. However, after membrane permeabilization, the total dopamine content of the cell was determined. The ratio of the total dopamine content to the detection limit lead the authors to conclude that roughly 98% of cellular dopamine is bound and not available for detection in the cytoplasm (114). Intracellular oxygen levels are proportional to glucose metabolism and have been determined with platinized carbon ring electrodes (113). The platinization of the electrode is important since oxygen is not detected at a bare carbon ring electrode. Inside the giant dopamine neuron of *Planorbis* the measured oxygen concentration was found to be 0.032 ± 0.004 mM. Oxygen transport into the cell has also been evaluated with this experimental setup by bathing the neuron sequentially in oxygen free, air saturated, and oxygen saturated solutions. As expected, intracellular oxygen was lowest when the cell was surrounded by oxygen free solution and highest when bathed in oxygen saturated solution. After only a few minutes following a pulse of exposure to these solutions, oxygen levels returned to baseline levels presumably due to oxygen consumption for cellular respiration and metabolism.

In addition to neurotransmitters and oxygen, intracellular glucose has also been measured. The detection scheme for glucose relies on an enzyme modified platinized carbon ring microelectrode that is $2\text{ }\mu\text{m}$ in diameter (115, 116). In the presence of glucose and oxygen, glucose oxidase will oxidize glucose resulting in gluconolactone and hydrogen peroxide which is oxidized at the platinized electrode. These ultra small enzyme electrodes displayed a response time to the presence of glucose as low as 270 msec and the characteristic response time of an electrode was linearly proportional to the electrode diameter. Other groups have used different enzymes and coupling chemistries to make *in vivo* measurements with microelectrodes (117–119).

17.1.4.2 Intracellular patch electrochemistry

As with extracellular measurements, intracellular measurements can be made by combining electrophysiological and electrochemical techniques (120). For intracellular measurements, the initial patch electrochemical setup is in the cell attached configuration. However, after some time additional suction is applied to the patch pipette, the membrane is ruptured and the whole cell configuration is attained (Figure 17.1.15). Disruption of the membrane allows oxidizable intracellular content to diffuse to the UME where it is detected in either the amperometric or voltammetric mode.

In the amperometric mode all easily oxidized molecules (including catechols) are detected whereas in the voltammetric mode catecholamines can be preferentially measured. Because membrane capacitance is recorded simultaneously, it is possible to determine if exocytosis is taking place and how it affects cytosolic catecholamine concentration in real time. Figure 17.1.16 shows representative voltammetric data for intracellular patch electrochemistry.

Effects of drug treatment on cytosolic levels of catecholamines and total oxidizable species were also investigated. Reserpine, an inhibitor of the vesicular monoamine transporter (this transporter loads vesicles with catecholamines), had no effect on the amount

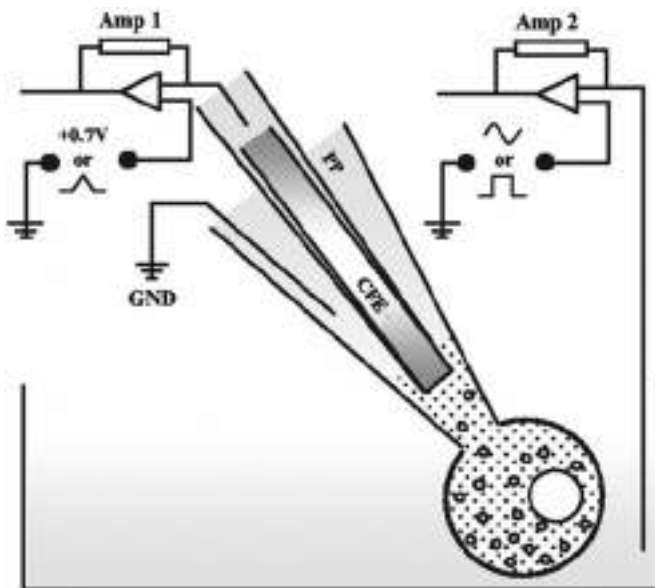


Figure 17.1.15 Schematic diagram of the intracellular patch electrochemistry setup. Amp 1, Amp 2, Amplifiers; GND, electric ground; CFE, carbon fiber electrode; PP, patch pipette. Reproduced with permission from reference (120).

of catecholamines but increased total oxidizable species by four or five times. A transient five-fold increase in cytosolic catecholamines and slow increase in total oxidizable species was observed when cells were treated with amphetamine.

17.1.5 Conclusions

Significant advances in biological analysis with electrochemical methods have been made. At the cellular surface, amperometry and voltammetry are effective in measuring chemical secretion with detection of fewer than 5000 molecules possible. Inroads into electrochemical analysis of the lipid composition are possible with enzyme modified electrodes. Scanning probe methodologies are emerging for topographic and metabolic imaging of live cells, and combined electrophysiological and electrochemical measurements are shedding new light on the biochemistry and biophysics of exocytosis. Liposome-based systems mimic exocytosis without protein intervention and have been useful in elucidating the role membrane properties play in exocytosis. They can also be used to model mass transport of neurotransmitter molecules in synapses. Electrochemical analyses in small droplets and microvials are effective methods for determining electrochemical responses in volume-limited samples. Microvials have also been used as cellular chambers for analysis of chemical secretion and transport. Advances in intracellular electrochemistry have lead to greater understanding of cellular metabolism of drugs and cellular neurotransmitter synthesis and

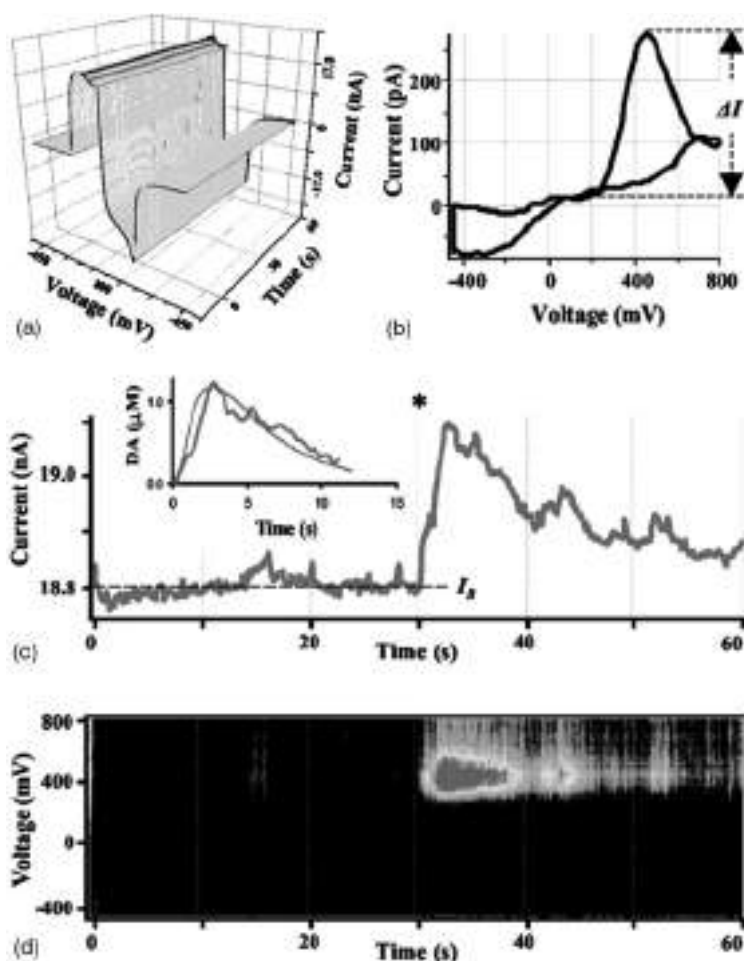


Figure 17.1.16 Analysis of cyclic voltammetry recordings from a single rat chromaffin cell. (A) A representative recording shown as a three-dimensional matrix of data. Red and blue lines represent samplings of the current at 400 and 0 mV, respectively. (B) Voltammogram of catecholamines released during the same recording. A subtraction was made between 10 consecutive averaged I-V profiles at 10 sec from those at 33 sec. Dashed line indicates ΔI , the height of DA oxidation peak. (C) Current sampled at 400-mV oxidation potential. The asterisk indicates a time when the patch was disrupted by suction and a whole-cell configuration was attained. The inset shows a random walk fit (green) of the sampled current trace (red) using $15\text{ M}\Omega$ access resistance, $8\text{ }\mu\text{m}$ cell radius, $60\text{ }\mu\text{m}$ distance between the CFE and the pipette tip, and $6.7\text{ }\mu\text{M}$ cytosolic catecholamine concentration. (D) Pseudo-three-dimensional representation of approximate voltammograms of intracellular metabolites encountering the CFE during the recording, in which the intensity of color ("Planet Earth" color table) indicates the current at a given voltage and time. Reproduced with permission from reference (120). (for colour version: see colour section at the end of the book).

storage. Intracellular patch amperometry may prove valuable in elucidating the coupling of the neurotransmitter synthesis, storage, and release processes.

REFERENCES

1. J. Monck, J. Fernandez, *Neuron* **12**, 707 (1994).
2. R. Jahn, T. Lang, T. C. Sudhof, *Cell* **112**, 519 (2003).
3. R. Jahn, T. C. Sudhof, *Annu. Rev. Biochem.* **68**, 863 (1999).
4. R. Jahn, T. C. Sudhof, *Annu. Rev. Neurosci.* **17**, 219 (1994).
5. K. Pihel, S. Hsieh, J. W. Jorgenson, R. M. Wightman, *Anal. Chem.* **67**, 4514 (1995).
6. K. Pihel, T. Schroeder, R.M Wightman, *Anal. Chem.* **66**, 4532 (1994).
7. R. A. Clark, A. G. Ewing, *Mol. Neurobiol.* **15**, 1 (1997).
8. E. R. Travis, R. M. Wightman, *Annu. Rev. Biophys. Biomol. Struct.* **27**, 77 (1998).
9. D. M. Cannon, Jr., N. Winograd, A. G. Ewing, *Annu. Rev. Biophys. Biomol. Struct.* **29**, 239 (2000).
10. G. Chen, A. G. Ewing, *Crit. Rev. Neurobiol.* **11**, 59 (1997).
11. J. M. Finnegan, K. Pihel, P. S. Cahill, L. Huang, S. E. Zerby, A. G. Ewing, R. T. Kennedy, R. M. Wightman, *J. Neurochem.* **66**, 1914 (1996).
12. L. Huang, H. Shen, M. A. Atkinson, R. T. Kennedy, *Proc. Natl. Acad. Sci. U.S.A.* **92**, 9608 (1995).
13. C. A. Aspinwall, J. R. Lakey, R. T. Kennedy, *J. Biol. Chem.* **274**, 6360 (1999).
14. C. A. Aspinwall, L. Huang, J. R. Lakey, R. T. Kennedy, *Anal. Chem.* **71**, 5551 (1999).
15. H. Shiku, T. Shiraishi, S. Aoyagi, Y. Utsumi, M. Matsudaira, H. Abe, H. Hoshi, S. Kasai, H. Ohya, T. Matsue, *Anal. Chim. Acta*, **522**, 51 (2004).
16. T. Kaya, D. Numai, K. Nagamine, S. Aoyagi, H. Shiku, T. Matsue, *Analyst* **129**, 529 (2004).
17. H. Lu, M. Gratzl, *Anal. Chem.* **71**, 2821 (1999).
18. A. Devadoss, J. D. Burgess, *J. Am. Chem. Soc.* **126**, 10214 (2004).
19. A. J. Bard, G. Denuault, C. Lee, D. Mandler, D. O. Wipf, *Acc. Chem. Res.* **23**, 357 (1990).
20. M. V. Mirkin, B. Horrocks, *Anal. Chim. Acta*, **406**, 119 (2000).
21. M. V. Mirkin, B. Liu, S. A. Rotenberg, *Methods Enzymol.* **352**, 112 (2002).
22. T. Yasukawa, T. Kaya, T. Matsue, *Electroanalysis* **12**, 653 (2000).
23. J. Mauzeroll, A. J. Bard, *Proc. Natl. Acad. Sci. U.S.A.* **101**, 7862 (2004).
24. J. Mauzeroll, A. J. Bard, O. Owhadian, T. J. Monks, *Proc. Natl. Acad. Sci. U.S.A.* **101**, 17582 (2004).
25. R. N. Adams, *Anal. Chem.* **48**, 1126A (1976).
26. D. J. Leszczyszyn, J. A. Jankowski, O. H. Viveros, E. J. Dilberto, Jr., J. A. Near, R. M. Wightman, *J. Biol. Chem.* **265**, 14736 (1990).
27. R. M. Wightman, J. A. Jankowski, R. T. Kennedy, K. T. Kawagoe, T. J. Schroeder, D. J. Leszczyszyn, J. A. Near, E. J. Dilberto, Jr., O. H. Viveros, *Proc. Natl. Acad. Sci. U.S.A.* **88**, 10754 (1991).
28. D. Bruns, R. Jahn, *Nature* **377**, 62 (1995).
29. R. G. Staal, E. V. Mosharov, D. Sulzer, *Nat. Neurosci.* **7**, 341 (2004).
30. T. K. Chen, G. Luo, A. G. Ewing, *Anal. Chem.* **66**, 3031 (1994).
31. D. Schubert, M. LaCorbiere, F. G. Klier, J. H. Steinbach, *Brain Res.* **190**, 67 (1980).
32. A. Dahlstrom, J. Haggendal, T. Hokfelt, *Acta Physiol. Scand.* **67**, 289 (1966).
33. R. H. Chow, L. von Ruden, E. Neher, *Nature* **356**, 60 (1992).
34. G. Alvarez de Toledo, R. Fernandez-Chacon, J. M. Fernandez, *Nature* **363**, 554 (1993).
35. S. Choi, J. Klingauf, R. W. Tsien, *Philos. Trans. R. Soc. Lond. B Biol. Sci.* **358**, 695 (2003).

36. L. A. Sombers, H. J. Hanchar, T. L. Colliver, N. Wittenberg, A-S. Cans, S. Arbault, C. Amatore, A. G. Ewing, *J. Neurosci.* **24**, 303 (2004).
37. S. E. Zerby, A. G. Ewing, *Brain Res.* **712**, 1 (1996).
38. T. J. Schroeder, J. A. Jankowski, J. Senyshyn, R. W. Holz, R. M. Wightman, *J. Biol. Chem.* **269**, 17215 (1994).
39. U. Wingren, A. Wasteson, L. Enerback, *Int. Arch. Allergy Appl. Immunol.* **70**, 193 (1983).
40. W. M. Prucell, D. L. Cohen, T. H. Hanahoe, *Int. Arch. Allergy Appl. Immunol.* **90**, 382 (1989).
41. J. Cox, T. Gray, *Anal. Chem.* **61**, 2462 (1989).
42. J. Cox, T. Gray, *Electroanalysis* **2**, 107 (1990).
43. R. T. Kennedy, L. Huang, M. A. Atkinson, P. Dush, *Anal. Chem.* **65**, 1882 (1993).
44. W. Gorski, C.A. Aspinwall, J. R. Lakey, R. T. Kennedy, *J. Electroanal. Chem.* **425**, 191 (1997).
45. A. Albillos, G. Dernick, H. Horstmann, W. Almers, G. Alvarez de Toledo, M. Lindau, *Nature* **389**, 509 (1997).
46. L. Tabares, M. Lindau, G. Alvarez de Toledo, *Biochem. Soc. Trans.* **31**, 837 (2003).
47. L. W. Gong, I. Hafez, G. Alvarez de Toledo, M. Lindau, *J. Neurosci.* **23**, 7917 (2003).
48. T. L. Colliver, S. J. Pyott, M. Achalabun, A. G. Ewing, *J. Neurosci.* **20**, 5276 (2000).
49. G. Dernick, G. Alvarez de Toledo, M. Lindau, *Nat. Cell Biol.* **5**, 358 (2003).
50. A. Devadoss, J. D. Burgess, *Langmuir* **18**, 9617 (2002).
51. K. Simons, E. Ikonen, *Science* **290**, 1721 (2000).
52. A. J. Bard, M. V. Mirkin, Eds., *Scanning Electrochemical Microscopy*, Marcel Dekker: New York, NY, 2001.
53. T. Yasukawa, I. Uchida, T. Matsue, *Biochim. Biophys. Acta* **1369**, 152 (1998).
54. B. Liu, S. A. Rotenberg, M. V. Mirkin, *Proc. Natl. Acad. Sci. U.S.A.* **97**, 9855 (2000).
55. B. Liu, W. Cheng, S. A. Rotenberg, M. V. Mirkin, *J. Electroanal. Chem.* **500**, 590 (2001).
56. J. M. Liebetrau, H. M. Miller, J. E. Baur, S. A. Takacs, V. Anupunpisit, P. A. Garris, D. O. Wipf, *Anal. Chem.* **75**, 563 (2003).
57. R. T. Kurulugama, D. O. Wipf, S. A. Takacs, S. Pongmayteegul, P. A. Garris, J. E. Baur, *Anal. Chem.* **77**, 1111 (2005).
58. C. Cai, B. Liu, M. V. Mirkin, H. A. Frank, J. F. Rusling, *Anal. Chem.* **74**, 114 (2002).
59. H. Shiku, T. Shiraishi, H. Ohya, T. Matsue, H. Abe, H. Hoshi, M. Kobayashi, *Anal. Chem.* **73**, 3751 (2001).
60. M. Gonsalves, A. L. Barker, J. V. Macpherson, P. R. Unwin, D. O'Hare, C. P. Winlove, *Biophys. J.* **78**, 1578 (2000).
61. M. Gonsalves, J. V. Macpherson, D. O'Hare, C. P. Winlove, P. R. Unwin, *Biochim. Biophys. Acta*, **1524**, 66 (2000).
62. A. D. Bangham, *Chem. Phys. Lipids* **64**, 275 (1993).
63. M. Montal, P. Mueller, *Proc. Natl. Acad. Sci. U.S.A.* **69**, 3561 (1972).
64. R. B. Gennis, *Biomembranes: Molecular Structure and Function*, Springer-Verlag: New York, NY, 1989.
65. H. Tien, *J. Phys. Chem.* **88**, 3172 (1984).
66. H. Tien, *Bioelectrochem. Bioenerg.* **13**, 299 (1984).
67. P. Krynski, H. Tien, A. Ottova, *Biotechnol. Prog.* **15**, 974 (1999).
68. H. Tien, S. Wurster, A. Ottova, *Bioelectrochem. Bioenerg.* **42**, 77 (1997).
69. O. Medina, Y. Zhu, K. Keiremo, *Curr. Pharm. Des.* **10**, 2981 (2004).
70. R. Mainardes, L. Silva, *Curr. Drug Targets* **5**, 449 (2004).
71. D. Meisner, M. Mezei, *Adv. Drug Deliv. Rev.* **16**, 75 (1995).
72. A. Chonn, P. Cullis, *Curr. Opin. Biotechnol.* **6**, 698 (1995).
73. N. Maurer, D. Fenske, P. Cullis, *Expert Opin. Biol. Ther.* **1**, 923 (2001).
74. D. Lasic, *Trends Biotechnol.* **16**, 307 (1998).

75. P. Aikens, S. Friberg, *Curr. Opin. Colloid Interface Sci.* **1**, 672 (1996).
76. A. Karlsson, R. Karlsson, M. Karlsson, A. S. Cans, A. Stromberg, F. Ryttsen, O. Orwar, *Nature* **409**, 150 (2001).
77. M. Karlsson, K. Nolkrantz, M. Davidson, A. Stromberg, F. Ryttsen, B. Akerman, O. Orwar, *Anal. Chem.* **72**, 5857 (2000).
78. M. Karlsson, K. Sott, A. S. Cans, A. Karlsson, R. Karlsson, O. Orwar, *Langmuir* **17**, 6754 (2001).
79. A. S. Cans, N. Wittenberg, R. Karlsson, L. Sombers, M. Karlsson, O. Orwar, A. G. Ewing, *Proc. Natl. Acad. Sci. U.S.A.* **100**, 400 (2003).
80. A. S. Cans, N. Wittenberg, D. Eves, R. Karlsson, A. Karlsson, O. Orwar, A. G. Ewing, *Anal. Chem.* **75**, 4168 (2003).
81. L. J. Breckenridge, W. Almers, *Proc. Natl. Acad. Sci. U.S.A.* **84**, 1945 (1987).
82. C. Amatore, Y. Bouret, E. R. Travis, R. M. Wightman, *Biochimie* **82**, 481 (2000).
83. C. Amatore, Y. Bouret, E. R. Travis, R. M. Wightman, *Angew. Chem. Int. Ed.* **39**, 1952 (2000).
84. J. R. Monck, G. Alvarez de Toledo, J. M. Fernandez, *Proc. Natl. Acad. Sci. U.S.A.* **87**, 7804 (1990).
85. Y. A. Chizmadzhev, D. A. Kumenko, P. I. Kuzmin, L. V. Chernomordik, J. Zimmerberg, F. S. Cohen, *Biophys. J.* **76**, 2951 (1999).
86. M. A. Bunin, R. M. Wightman, *J. Neurosci.* **18**, 4854 (1998).
87. M. A. Bunin, R. M. Wightman, *Trends Neurosci.* **22**, 377 (1999).
88. W. Bowyer, M. Clark, J. Ingram, *Anal. Chem.* **64**, 459 (1992).
89. R.A Clark, P.B Heitpas, A. G. Ewing, *Anal. Chem.* **69**, 259 (1997).
90. R.A Clark, A. G. Ewing, *Anal. Chem.* **70**, 1119 (1998).
91. C. D. T. Bratten, P. H. Cobbold, J. M. Cooper, *Anal. Chem.* **69**, 253 (1997).
92. C. D. T. Bratten, P. H. Cobbold, J. M. Cooper, *Chem. Commun.* **4**, 471 (1998).
93. C. D. T. Bratten, P. H. Cobbold, J. M. Cooper, *Anal. Chem.* **70**, 1164 (1998).
94. J. C. Ball, D. L. Scott, J. K. Lumpp, S. Daunert, J. Wang, L. G. Bachas, *Anal. Chem.* **72**, 497 (2000).
95. J. C. Ball, J.K. Lumpp, S. Daunert, L. G. Bachas, *Electroanalysis*, **12**, 685 (2000).
96. A. F. Dias, G. Dernick, V. Valero, M. G. Yong, C. D. James, H. G. Craighead, M. Lindau, *Nanotechnology* **13**, 285 (2002).
97. M. Gratzl, C. Yi, *Anal. Chem.* **65**, 2085 (1993).
98. C. Yi, M. Gratzl, *Anal. Chem.* **66**, 1976 (1994).
99. C. E. Banks, T. J. Davies, R. G. Evans G. Hignett, A. J. Wain, N. S. Lawrence, J. D. Wadhawan, F. Marken, R. G. Compton, *Phys. Chem. Chem. Phys.* **5**, 4053 (2003).
100. M. Jansson, A. Emmer, J. Roeraade, U. Lindberg, B. Hok, *J. Chromatogr.* **626**, 310 (1992).
101. R. Kashyap, M. Gratzl, *Anal. Chem.* **70**, 1468 (1998).
102. R. M. Wightman, D. O. Wipf in *Electroanalytical Chemistry*, A. J. Bard, Ed., Marcel Dekker: New York, NY, Vol. 15, 1998.
103. T. Yasukawa, A. Glidle, J. M. Cooper, T. Matsue, *Anal. Chem.* **74**, 5001 (2002).
104. K. P. Troyer, R. M. Wightman, *Anal. Chem.* **74**, 5370 (2002).
105. C. Earles, J. O. Shenk, *Synapse*, **33**, 230 (1999).
106. T. M. Olefirowicz, A. G. Ewing, *J. Neurosci. Methods* **34**, 11 (1990).
107. T. M. Olefirowicz, A. G. Ewing, *Anal. Chem.* **62**, 1872 (1990).
108. A. Meulemans, B. Poulain, G. Baux, L. Tauc, D. Henzel, *Anal. Chem.* **58**, 2088 (1986).
109. A. Meulemans, B. Poulain, G. Baux, L. Tauc, *Brain Res.* **414**, 158 (1987).
110. T. K. Chen, Y. Y. Lau, D. K. Y. Wong, A. G. Ewing, *Anal. Chem.* **64**, 1264 (1992).
111. Y. Y. Lau, J. B. Chien, D. K. Y. Wong, A. G. Ewing, *Electroanalysis* **3**, 87 (1991).
112. Y. Y. Lau, D. K. Y. Wong, A. G. Ewing, *Microchem. J.* **47**, 308 (1993).
113. Y. Y. Lau, T. Abe, A. G. Ewing, *Anal. Chem.* **64**, 1702 (1992).

114. J. B. Chien, R. A. Wallingford, A. G. Ewing, *J. Neurochem.* **54**, 633 (1990).
115. T. Abe, Y. Y. Lau, A. G. Ewing, *J. Am. Chem. Soc.* **113**, 7421 (1991).
116. T. Abe, Y. Y. Lau, A. G. Ewing, *Anal. Chem.* **64**, 2160 (1992).
117. P. Pantano, W. G. Kuhr, *Anal. Chem.* **65**, 623 (1993).
118. P. Pantano, T. H. Morton, W. G. Kuhr, *J. Am. Chem. Soc.* **113**, 1832 (1991).
119. P. Pantano, W. G. Kuhr, *Electroanalysis* **7**, 405 (1995).
120. E. V. Mosharov, L. W. Gong, B. Khanna, D. Sulzer, M. Lindau, *J. Neurosci.* **23**, 5835 (2003).

17.2 SINGLE MOLECULE ELECTROCHEMISTRY

Fu-Ren F. Fan

The University of Texas at Austin, Texas, USA

17.2.1 Introduction

The detection of single molecules, their characterization, and their chemical and physical manipulation are within current scientific capability and are of significant interest. A number of electrochemical techniques have been used in recent years to detect single molecules or ions and to study single electron-transfer events. We focus here on a few topics involving these processes. These include trapping an electroactive molecule in solution between a small ultramicroelectrode (UME, see Chapter 6) tip and a conductive substrate in a scanning electrochemical microscope (SECM, see Chapter 12). In this arrangement, the tip current represents repeated collisions and electron transfer of the molecule with the tip. An alternative approach is to use electrogenerated chemiluminescence (ECL, see Chapter 13) in which the product of the electron transfer of the electroactive molecules reacts to form an excited state that emits a photon, which can be detected with a time-resolved single photon counter. The third approach is to utilize very small UME or nanoparticles to study quantized double layer charging associated with single electron-transfer events. The final approach we illustrate is the deposition of molecules, particularly polymers or macromolecules of biological interest, on a mica surface and subsequent imaging of the surface topology with a highly sensitive SECM or scanning tunneling microscope (STM). This technique requires the use of a high relative humidity (RH) to form a thin film of water on the mica surface that allows electrochemical reactions to take place and produce a faradaic current (~1 pA).

17.2.2 Special topics

17.2.2.1 Scanning electrochemical microscopy (SECM) and single molecule electrochemistry

(a) Operational principles

Trapping of a molecule in solution and detection of the electrolysis current are carried out with SECM (1). The principle and various techniques of SECM have been described in

Chapter 12 of this handbook. We describe here only very briefly how this technique can be used to study the electrochemistry of a single molecule and its underlying operational principle. Detailed discussions on earlier SECM works can be found in reference (1) and the literature cited therein.

SECM is based on observing the electrolysis current of an electroactive species, A, at a very small (nm–μm) electrode (an UME or SECM tip, see Chapter 6) to form a product, A⁺, as shown in the following oxidation reaction



in which e is the electron charge. The current that flows represents the flux A to the electrode as it diffuses to the tip. The presence of a surface near the tip can affect the tip current, i_T , in two ways. When the tip is close to the surface, diffusion is blocked; this causes a decrease in the current. If, however, the product of the tip reaction A⁺ can be reduced back to A at the surface, then an additional flux of A to the tip occurs (termed positive feedback), and the tip current is increased compared to the tip current when it is far away from the surface, $i_{T,\infty}^0$. If the tip is a conductive disk in an insulating plane, the tip radius a can be found from the following equation (2)

$$i_{T,\infty}^0 = 4nFDC * a \quad (17.2.2)$$

where D is the diffusion coefficient of A, C* is its concentration, and F is Faraday's constant.

Current instrumentation does not allow measurement of the charge or current from single electron-transfer events at an electrode. To detect a single molecule electrochemically, one must provide some amplification process. In the SECM experiment, illustrated schematically in Figure 17.2.1, this amplification is provided by the positive feedback process, i.e., the repeated conversion of A to B at the tip and B to A at the substrate as the molecule, in the oxidized or reduced state, shuttles back and forth between the tip and substrate. Since the transport between the tip and the substrate is by diffusion, the transit time, τ , between the two electrodes separated by a distance d is about $d^2/2D$, in which D is the diffusion coefficient of A. If $d = 10$ nm and $D = 10^{-5}$ cm²/sec, then $\tau = 5 \times 10^{-8}$ sec or the molecule cycles 10⁷ times per second. If each cycle results in the exchange of one electron (1.6×10^{-19} C), then an average current of about 1.6 pA will flow. Thus, positive feedback provides a 10-million-fold amplification that results in a readily measurable current. It is necessary to trap the molecule within the small pocket of solution in the gap between the tip and substrate for a sufficient time to make the measurement possible, which is governed by the time constant of the picoammeter.

(b) Tip fabrication and experimental methods

The single-molecule trapping experiments require a tip with a diameter on the order of 10–20 nm and the particular geometry that results from the procedures used in the tip preparation. The ultramicrotips used in this experiment were prepared by insulating an electrochemically sharpened Pt–Ir (80:20) wire (0.250-mm diameter) by passing it through molten Apiezon wax or polyethylene based on the procedure used by Nagahara *et al.* (3). The insulated tip was then mounted on the SECM in a cell containing a redox electrolyte

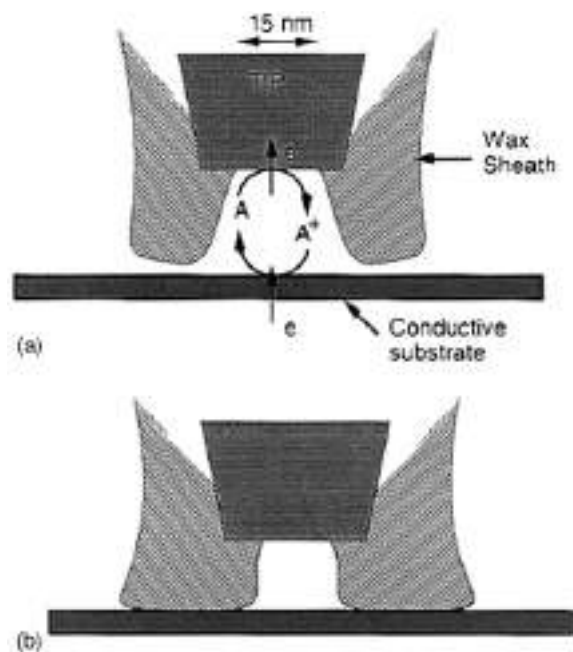


Figure 17.2.1 (A) Idealized diagram of the trapping of molecule A that is oxidized at the tip electrode. The product A^+ is reduced at the substrate. (B) Schematic diagram of the effect of compressing wax tip coating against substrate. Adapted with permission from reference (8).

(e.g., 2 mM [(trimethylammonio)methyl]ferrocene (Cp_2FeTMA^+) in 1.0 M $NaNO_3$). The success of the tip insulation was checked by cyclic voltammetry in this solution. For a well-insulated tip, i_T , during an initial scan, was less than 50 fA. The very end of the tip was then exposed in the SECM by the following procedure. The potentials of the tip and a conductive substrate (e.g., indium tin oxide (ITO)) were biased at suitable values (e.g., 0.60 V vs. SCE for the tip and -0.20 V for the substrate) with the SECM operated in the constant-current mode (e.g., with a reference current of 10 pA). As the well-insulated tip approached the surface of the substrate, the onset of an enhanced current flow caused the z-piezo to retract the tip. This process produced a hole in the tip insulation at the point of closest approach of tip to substrate, while leaving most of the tip still insulated. The exposed area of the tip was estimated from the steady-state tip current with the tip far away from the substrate (equation 17.2.2). The basic instrument used in this experiment is a custom-built scanning probe microscope (SPM) (4) capable of both STM and SECM measurements with a current sensitivity of 50 fA for SECM experiments. The electrochemical cell contained a Pt counter electrode and an SCE as the reference electrode.

(c) Experimental results and data analyses

SECM approach tip current vs. distance curve. The SMD experiment, as stated above, requires a tip of small diameter that is slightly recessed within the soft insulating sheath.

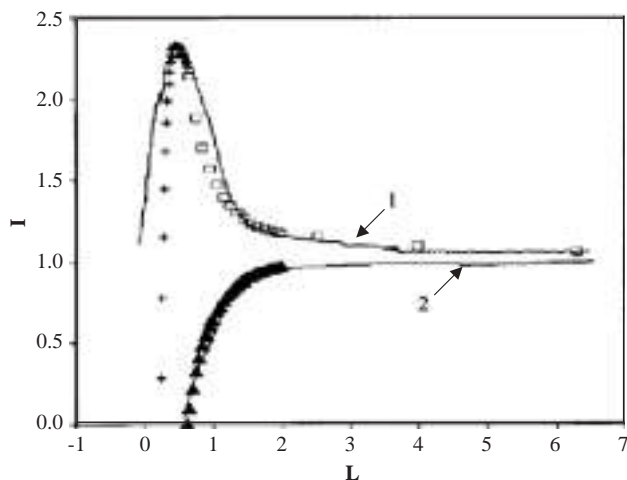
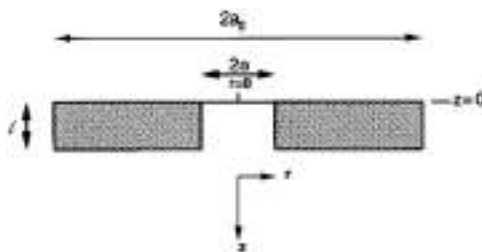


Figure 17.2.2 Dependence of tip current (normalized to $i_{T,\infty}$) on relative tip displacement (normalized to tip radius) over a conductive n-TiO₂ substrate ($E_S = -0.7$ V vs. SCE), curve 1, and an insulating n-TiO₂ substrate ($E_S = 0.0$ V vs. SCE), curve 2, in a solution containing 2 mM Cp₂FeTMA⁺ and 1.0 M NaNO₃. The tip was biased at 0.60 V vs. SCE. The tip moved to the substrate surface at a rate of 38 Å/sec. Solid curves are experimental data and symbols are theory. Squares: Simulated data for conducting substrate; pluses: calculated data based on equation 17.2.4; triangles: simulated data for insulating substrate. Fitting parameters: $a = 45$ nm, $a_0 = 67$ nm, $l = 28$ nm, and $D = 5.0 \times 10^{-6}$ cm²/sec. Experimental $i_{T,\infty}$ is equal to 9.0 pA. Adapted with permission from reference (8).

While it is not possible to remove the tip after preparation from the SECM cell and examine it by electron microscopy, information about the exposed area of the tip and the shapes of the tip and insulating sheaths can be obtained indirectly from SECM approach curves where i_T is measured as a function of tip–substrate spacing, d , as the tip is moved toward the substrate. Tips with correct configuration show approach curves similar to those shown in Figure 17.2.2. These curves were obtained with a solution containing 2 mM Cp₂FeTMA⁺ and 1.0 M NaNO₃, with the tip biased at 0.6 V vs. SCE (where Cp₂FeTMA⁺ oxidation is diffusion-controlled). In the experiment shown in curve 1, the n-TiO₂ substrate (a semiconductor) was biased at -0.7 V vs. SCE (a potential well negative of its flat-band potential, $V_{fb} \sim -0.25$ V vs. SCE), so that Cp₂FeTMA²⁺ generated at the tip was rapidly reduced back to Cp₂FeTMA⁺ at the n-TiO₂ surface, since it is operated in the accumulation region and acts as a conductor. A similar approach curve was also observed for the same solution and ITO substrate (5). When the n-TiO₂ substrate is biased at a potential positive of V_{fb} (e.g., 0 V vs. SCE), the n-TiO₂ surface becomes insulating (it is now operated in the depletion region). The negative feedback approach curve is shown in curve 2. Hence, experiments can be carried out with the same tip and solution without making any changes, while the conductance of an n-TiO₂ substrate is controlled by adjusting bias potential.



Scheme 1

Different from an inlaid microdisk electrode with $i_{T,\infty}^0$ expressed in equation 17.2.2, a recessed disk-shaped electrode with the geometry shown in Scheme 1, $i_{T,\infty}$ is given by an approximate equation

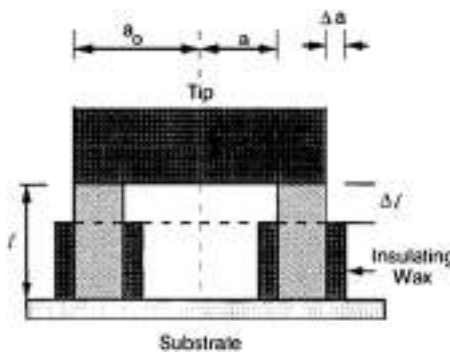
$$i_{T,\infty} = \left[\frac{\pi a}{(4l + \pi a)} \right] i_{T,\infty}^0 \quad (17.2.3)$$

in which l is the recessed depth of the disk electrode. $i_{T,\infty}$ can also be obtained by digital simulation as a function of $L = l/a$ (as tabulated in Table 1 of reference (8)). For the normalized tip current ($I_T = i_{T,\infty}/i_{T,\infty}^0$), the difference between the value calculated by the approximate analytical equation (equation 17.2.3) and the simulated value is less than 3.4%, when $l > 0.2a$.

The shape of the approach curve also depends on the tip shape. For a coplanar disk, the tip current, i_T , increases monotonically with decreasing d for a conductive substrate and diffusion-controlled reactions at tip and substrate (6). For a recessed disk, the SECM positive feedback process starts to become significant when the tip approaches a conductive n-TiO₂ substrate (biased at -0.7 V vs. SCE) to within a few tip diameters (curve 1 of Figure 17.2.2). The agreement between experimental and simulated data (for $l = 0.62a$, $a = 45$ nm) is reasonably good up to a distance $d \sim l$, at which point the insulating sheath starts to compress against the substrate. Different from an inlaid disk electrode, with a recessed disk, i_T increases to reach a maximum and then decreases as the tip comes even closer before showing a large increase (not shown in curve 1 of Figure 17.2.2) presumably because of the occurrence of electron tunneling between tip and substrate. Although this current decrease might be attributed to heterogeneous kinetic effects on the electron-transfer reactions (7), this behavior was observed at even more extreme tip or substrate potentials for various substrates and other redox couples. We thus believe that this region of current behavior is associated with the deformation of the soft insulating sheath as it is press against the substrate at very small distance as shown in Figure 17.2.1B.

Consider an idealized thin-layer cell as shown in Scheme 2, where we assume that the insulating wax flows inward and outward by equal amounts as it is compressed against the substrate, the steady-state current of the thin-layer cell confined by the disk, substrate, and insulating sheath is given by the following equation (8),

$$I_{TLC} = \left\{ \frac{\pi [2la^2 - \Delta l(a_0^2 + a^2)]}{[8a(l - \Delta l)^2]} \right\} i_{T,\infty}^0 \quad (17.2.4)$$



Scheme 2

where a is the initial disk radius, a_0 is the initial outer radius of the insulating sheath before the compression occurs, and Δl is the change of the recessed depth of the disk electrode during compression. As implied in equation 17.2.4, if $a_0 < \sqrt{3}a$, the tip current will increase to reach a maximum at Δl equal to $l(3a^2 - a_0^2)/(a_0^2 + a^2)$ and then decrease as the tip approaches even closer to the surface of the substrate; otherwise, it will reach the maximum at $\Delta l = 0$. As shown in curve 1 of Figure 17.2.2, there is some discrepancy between the experimental curve and the theoretically calculated data based on equation 17.2.4, perhaps because Δl is not exactly equal to the nominal tip displacement due to the finite compressibility of the insulating wax and deviations from the assumed idealized model. With a diffusion coefficient of Cp_2FeTMA^+ of 5×10^{-6} cm²/sec, the theoretical fit of the experimental approach curve yields $a = 45$ nm, $a_0 = 67$ nm, and $l = 28$ nm.

When the n-TiO₂ substrate is in its insulating state (e.g., biased at 0 V vs. SCE), the approach curve is that shown in curve 2 of Figure 17.2.2. Here the approach behavior of a recessed tip is similar to that of a usual inlaid disk electrode and decreases monotonically with decreasing distance.

Fluctuation of the tip current at small distances. Figure 17.2.3A shows an experiment with a water soluble ferrocene derivative, Cp_2FeTMA^+ , as the species oxidized at the tip to produce the ferrocenium form that is then reduced at the conductive ITO substrate (5). In this experiment, the tip (radius ~10 nm) was brought to a position where the approach curve was near its minimum current value, estimated as about 10 nm. At the concentration (~2 mM) of electro active species employed, the resultant volume under the tip would contain, on the average, one molecule of Cp_2FeTMA^+ . When the current at the tip is recorded with time, one finds fluctuations of the current (on top of the noise signal on the order of 0.2 pA), which were interpreted to indicate the presence of zero, one, or two molecules. This finding is clarified by examining the data by autocorrelation and probability density function (PDF) analyses (Figure 17.2.3B and C) as discussed below. The time correlation function (TCF) (or autocorrelation function) analysis indicated multiple fluctuation processes with the frequencies on the order of a few tenths of a Hertz. The PDF contains several bell-shaped peaks. The most probable tip currents at the given cell parameters and concentrations are spaced 0.5 (± 0.1 pA) apart. These fluctuation amplitudes of the tip current-time series correspond quite well with the contribution to the current expected for

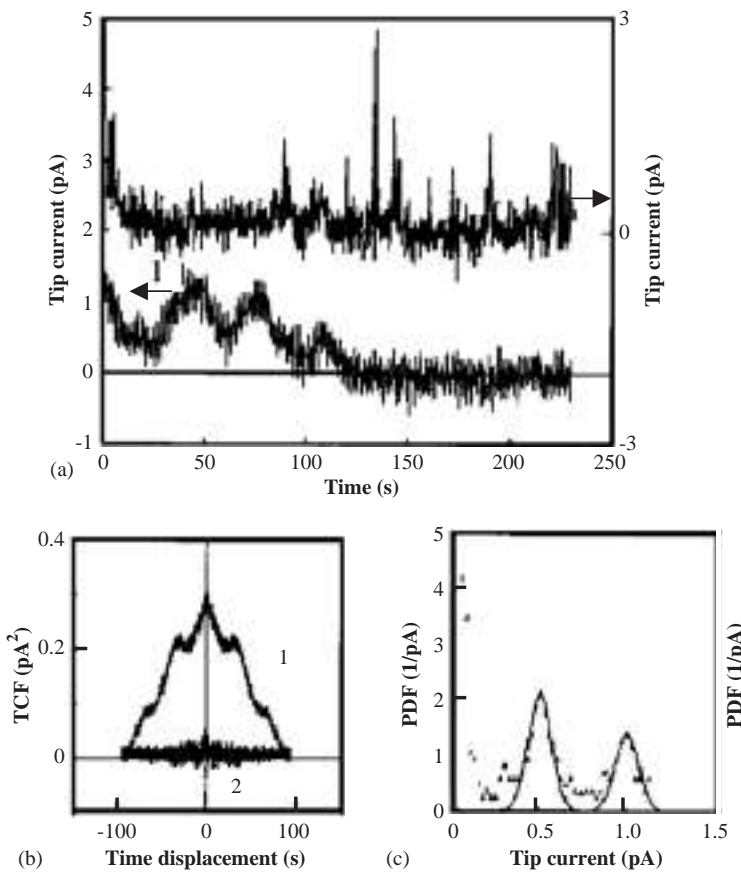


Figure 17.2.3 (A) Curve 1: Tip current with time for a solution of 2 mM $\text{Cp}_2\text{FeTMA}^+$ and 2.0 M NaNO_3 with a Pt–Ir tip at 0.55 V vs. SCE and an ITO substrate at –0.3 V; $d \sim 10$ nm. Curve 2: Time series of the tip current for d within the tunneling range in a solution containing only 2.0 M NaNO_3 ; tip radius ~ 7 nm. Data sampling rate was 0.4 sec per point. (B) Corresponding time correlation function. (C) Probability density function of time series 1 in (A). Adapted with permission from reference (8).

a single molecule in a thin-layer cell of that geometry. Control experiments with the tip at longer and closer distances to the ITO and with two different species that oxidize at two different potentials are consistent with this interpretation (5).

We compare the fluctuation behavior of the i_T on both conductive and insulating substrates by using an n-TiO₂ electrode as the substrate. As found in the previous studies, the fluctuation intensity in i_T was strongly dependent on the distance and the conductance states of the substrate. To ensure that we were measuring two different fluctuation behaviors at the same distance, we used the same substrate, n-TiO₂, held at a fixed distance and changed in conductance simply by varying its bias potential. When the tip was far away from the substrate surface (e.g., $d/a > 2$), as expected, only a very small fluctuation in i_T was observed when the substrate was either conductive (biased at –0.7 V vs. SCE) or

insulating (biased at 0.0 V vs. SCE) (see Figure 17.2.4A). When the tip approached the recessed depth of the disk electrode (i.e., $d < 1$), considerable fluctuation in i_T was observed when the substrate was conductive, while i_T was essentially zero and its fluctuation was negligibly small when the substrate was insulating (see Figure 17.2.4B). This suggests that the positive feedback of the SECM is responsible for the high amplification of the i_T . When the tip was moved even closer to the surface of the substrate, i_T decreased because of the decrease of the active area of the electrode (as discussed in the previous section), but the relative fluctuation of i_T intensified (see Figure 17.2.4C).

In spite of the lack of sufficient knowledge of the basic mechanisms of the fluctuation phenomena, a limited description of the general shape of the current fluctuation is of interest. Assuming that the redox molecule diffuses inside the TLC with a constant diffusion coefficient, there are at least two possibilities which might cause i_T to change with time: (1) changes in d and the electrode area, for example, because of temperature fluctuations and (2) fluctuations in the number of molecules inside the TLC, N . The probability of large step or quantized change in d without changing N is small. A continuous change in d without changing N cannot cause a stepwise fluctuation in i_T , either; however, it might account for a slow drift of the TLC current. We cannot rule out the possibility that the electric field in the gap may affect the observed behavior, especially at very small supporting electrolyte concentration, which will be discussed later. In the work described here, however, a high concentration of supporting electrolyte was employed.

Data analyses. Exact mathematical descriptions of the data shown in Figures 17.2.3A and 17.2.4C are difficult in the absence of a better understanding of the processes causing the large current fluctuations and of the microscopically detailed cell geometry. However, one can analyze the results by taking the data to be non-deterministic or random. In cases where no explicit mathematical equations can be written for the microscopic pictures of the time histories produced by a random phenomenon, statistical procedures are usually used to define the descriptive properties of the data (9, 10). Three of the basic statistical properties for describing random data, i.e., TCF, spectral density function (SDF), and PDF, for the time series in Figure 17.2.4C are shown in Figure 17.2.5. Those for the time series in Figure 17.2.3A are shown in Figure 17.2.3B and C (see the discussion below). The TCF is a measure of time-related properties in the data that are separated by fixed time delays and is defined as

$$\text{TCF}(\tau) = \lim_{T \rightarrow \infty} \frac{1}{T} \int_0^T x(t)x(t+\tau)dt \quad (17.2.5)$$

in which τ is the time delay and T is the available record length or some desired portion of the record length. The SDF of $x(t)$ is related to TCF through Fourier transformation and is given by

$$\text{SDF}(f) = 4 \int_0^\infty \text{TCF}(\tau) \cos(2\pi f \tau) d\tau \quad (17.2.6)$$

in which f is the frequency. Both TCF and SDF provide information on the rate of fluctuation in a time history record.

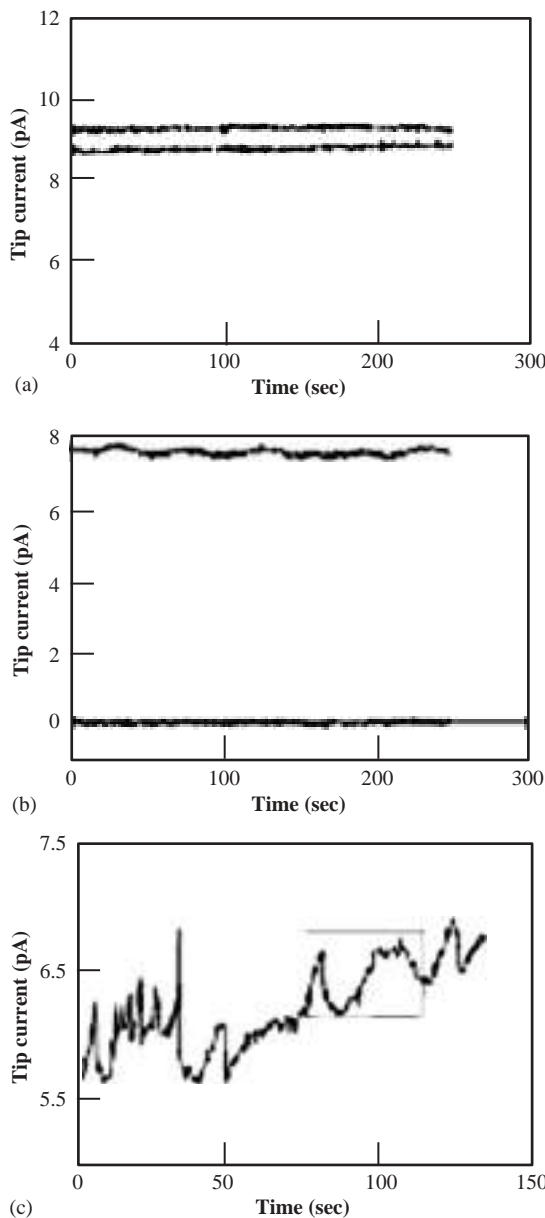


Figure 17.2.4 Time evolution of the tip current observed at a tip potential $E_T = 0.6$ V and a n-TiO₂ substrate potential $E_S = -0.7$ V (curve 1) or 0.0 V (curve 2) vs. SCE for various distances in a solution containing 2 mM Cp₂FeTMA⁺ and 1.0 M NaNO₃. The data sampling rate was 0.4 sec per point. (A) With tip far away from the substrate; (B) $d \sim 13$ nm, which gave an average steady-state current of ~ 7.6 pA when $E_S = -0.7$ V vs. SCE; (C) $d \sim 11$ nm, which gave an average steady-state tip current of ~ 6.1 pA. Adapted with permission from reference (8).

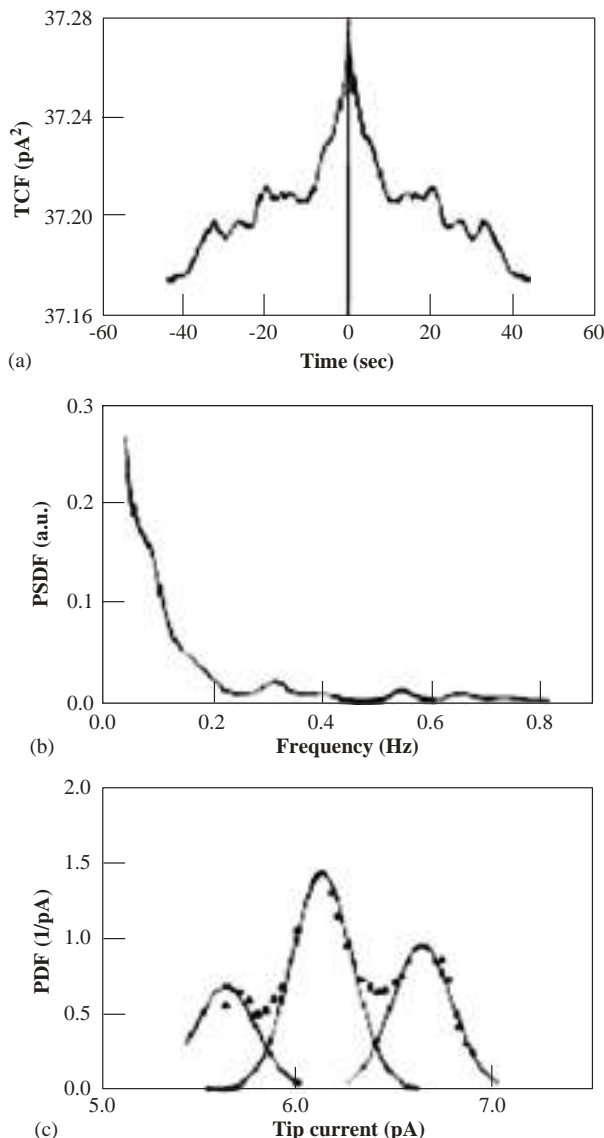


Figure 17.2.5 (A) Time correlation function, (B) power spectral density function, and (C) probability density function of the time series in Figure 17.2.4C. Adapted with permission from reference (8).

As shown in Figure 17.2.5A, the coherence of the data is high, and TCF indicates that several fluctuation processes occur at frequencies on the order of a few tenths of Hertz. Parallel to the TCF, the SDF of the time series is fairly broad and contains several peaks at frequencies on the order of fractions of Hertz (Figure 17.2.5B). From the autocorrelation of the time series at zero and infinite time displacement, a mean square i_T of 37.3

(pA)² and a mean i_T of 6.1 pA can be obtained, respectively. A mean tip current of 6.1 pA is consistent with the estimate from Figure 17.2.4B, which shows that i_T fluctuates around 6 pA with fluctuating amplitude of about 0.5 pA. A more accurate analysis is based on the PDF, which describes the probability that the data will assume a value within some defined range at any instant of time. In equation form, it is defined as follows:

$$\text{PDF} = \lim_{\Delta x \rightarrow \infty} \frac{\text{Prob}[x < x(t) < x + \Delta x]}{\Delta x} = \lim_{\Delta x \rightarrow 0} \left[\lim_{T \rightarrow \infty} \frac{T x}{T} \right] \quad (17.2.7)$$

in which $\text{Prob}[x < x(t) < x + \Delta x]$ is the probability that $x(t)$ assumes a value within the range between x and $(x + \Delta x)$, and $T x$ is the total amount of time that $x(t)$ falls inside the range $(x, x + \Delta x)$ during an observation time T . As shown in Figure 17.2.5C, the PDF of the time series of Figure 17.2.4C contains several Gaussian peaks. The most probable tip currents are spaced 0.5 pA apart, with a standard deviation of ~0.1 pA.

Some statistical methods have also been applied to analyze the i_T time series observed on a different conductive ITO substrate (as shown in Figure 17.2.3A). This series was obtained using a tip with a much smaller radius ($a \sim 7$ nm) than that used in Figure 17.2.4 so that the average i_T was much smaller than that shown in Figure 17.2.4C for comparable tip–substrate spacing and the same concentration of electroactive species; however, similar fluctuation amplitude in i_T was observed in both cases. The TCF of the series (see Figure 17.2.3B) also shows that multiple fluctuation processes with fluctuating frequencies in the range of fractions of hertz are involved. The probability density plot shown in Figure 17.2.3C again is characterized by a stepwise transition character of the fluctuation of i_T . Thus, the fluctuation pattern of i_T is apparently not strongly dependent on the substrate as long as the heterogeneous electron-transfer kinetics on the substrate is fast.

It is interesting to notice that the current fluctuations mapped as the PDF will be related to the probability of the number of molecules in the tip–substrate gap as a function of solution composition. At a solution concentration of 2 mM for a solution volume of 10^{-18} cm³, for example, the actual occupancy is one molecule. However, the actual occupancy, because of fluctuation, is governed by the Poisson distribution (10),

$$P_b(m) = (b^m / m!) \exp(-b) \quad (17.2.8)$$

in which $P_b(m)$ is the probability of m molecules occupying the solution volume when the average occupancy is b . Thus, for $b = 1$, $P_b(0) = 0.368$, $P_b(1) = 0.368$, and $P_b(2) = 0.184$. The distribution shown in Figure 17.2.3C approaches this, favoring slightly less than an average of one molecule per gap volume.

17.2.2.2 Electrogenerated chemiluminescence (ECL) on microelectrodes; single electron-transfer events

(a) Introduction and principles

Electron-transfer theories (11) predict that the highly exothermic production of the ground states proceeds in the inverted region. This allows the formation of the excited state to be kinetically competitive with other non-radiative pathways which are predicted to occur near the diffusion-controlled limit. Time-resolved fluorescence quenching has commonly

been used to measure the rates to form the separated radical ions and ground state donor and acceptor molecules in the photoinduced electron-transfer reactions (12). The back electron-transfer rate to reform the emitting excited state, however, is not readily accessible from such experiments. This value can be obtained from ECL (13) providing the ECL efficiency and total rate of ion annihilation (k_{annih}) are known. The principle and various techniques of ECL are described in Chapter 13 of this handbook, and detailed discussions can be found in reference (13) and the literature cited therein.

(b) *Experimental methods*

As carried out in Collinson's experiments discussed below, high-speed electrochemical and photon-detection techniques were used to monitor the real time rate of ECL generation of several compounds, e.g., 9, 10-diphenylanthracene, DPA. In these experiments, a microelectrode in a flow cell is continuously stepped between the oxidation and reduction potentials of DPA to alternatively generate the radical ions. The cation and anion radicals react in a thin plane at a point where the inward and outward fluxes meet and subsequently produce light. The ECL intensity was monitored with a Hamamatsu 4632 PMT. A high-voltage power supply (Bertan Series 230) applied -800 V to the PMT. The PMT signal was amplified by a fast preamplifier (EG&G Ortec VT120A, 150 MHz bandpass, 200 gain) and the output was directed to the discriminator of a multichannel scaler (EG&G Ortec T-914). The discriminator level was set at -600 mV. A Wavetek Model 143 function generator applied a symmetric square wave to a silver counter electrode and triggered the multichannel scaler. The microelectrode was connected to a current amplifier. Particularly worth stressing is that these short-time steps (or high square-wave frequencies) are not suitable for larger electrodes because the current during the step is dominated by double-layer charging and the electrode potential does not follow the applied potential step waveform.

(c) *Results and data analyses*

In order to ensure that the electrode potentials are chosen so that the cation and anion radicals are produced at a diffusion-controlled rate at all frequencies, following frequency selection of the square wave, the cathodic and anodic potentials were adjusted so that they roughly correspond to those of the redox potentials for the generation of the cation and anion radicals (14). Figure 17.2.6 shows two cycles of the potential waveform applied to a gold disk (radius = 5 μm) and the resulting luminescence from a 0.6 mM DPA solution. Two pulses of light are observed from each cycle. When the potential is stepped positive, the cation radical reacts with the anion radical formed on the previous step in a reaction zone lying near the electrode surface. The light increases sharply as the diffusion layers meet and then decays as the reactants are depleted. If the cation and anion radicals are stable during the time scale of the experiment, equal-size light pulses should be obtained on the forward and reverse steps. Increasing the frequency of the applied square wave usually results in more equivalent luminescent curves. As shown in Figure 17.2.6, at ~ 1 kHz, a slightly smaller pulse of light is observed when the electrode is stepped from a negative to a positive potential, indicating that the DPA anion is less stable than the cation on this time scale. At ~ 20 kHz, both the cation and anion radical are stable as evident from the equivalent light pulses.

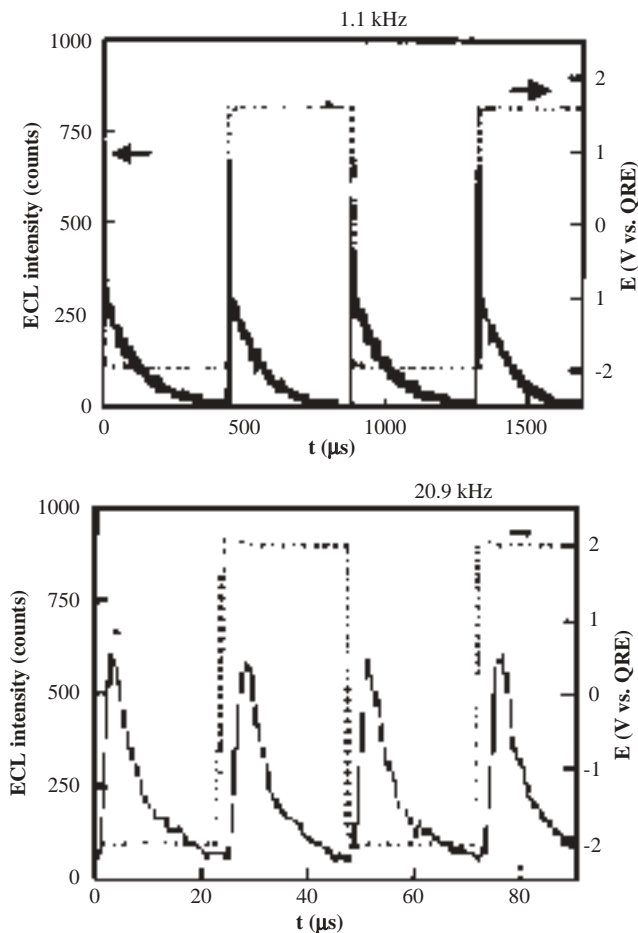


Figure 17.2.6 Potential waveform with the corresponding ECL curves from 0.6 mM DPA at a gold disk ($\text{radius} = 5 \mu\text{m}$) in acetonitrile containing 0.2 M TBAPF_6 at two different frequencies. The ordinate represents the number of counts collected during 1- μsec time bins. The luminescence curves were summed 100 times. Adapted with permission from reference (14a).

When the dimensionless kinetic parameter, $\lambda_k = k_{\text{annih}} t_f C^*$, approaches infinity, the reaction layer is an infinitely thin parallel plane which moves nearly linearly away from the electrode surface with time. This plane of light broadens and becomes Gaussian-like as λ_k decreases. When λ_k drops below 1000, i.e., when t_f and C^* are significantly reduced, the transfer from diffusion to kinetic control begins and distinct changes in the width and the shift in the peak maximum of the ECL-time curves become apparent. The k_{annih} can be theoretically evaluated from the characteristic shapes of ECL-time curves in dilute solutions and at reduced step times (cf. Chapter 3 of reference (13) for detailed theoretical discussion on ECL). For illustration, we show only some comparisons of the simulated curves

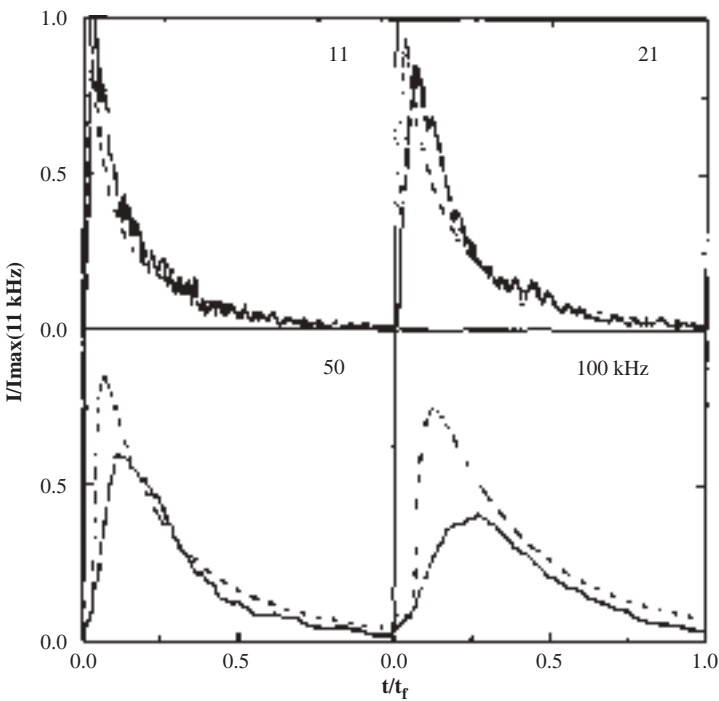


Figure 17.2.7 Normalized ECL from 0.38 mM DPA in acetonitrile containing 0.1 M TBAPF₆ at a Pt disk (radius = 1 μm) (solid lines) and corresponding simulated curves (dashed lines) as a function of frequency of potential pulse. Simulations for $k_{\text{annih}} = 2 \times 10^{10}/\text{M}\cdot\text{s}$ and double-layer charging time constant, RC_d , of 0.10 μsec . Adapted with permission from reference (14b).

to the experimental data with a k_{annih} of $2 \times 10^{10}/\text{M/sec}$ in Figure 17.2.7 (14). Roughly agreeing with experimental observations, the simulation predicts certain features in the data such as the delay time in the initial ECL and the diminished amplitude and increased breadth of the ECL curve with decreasing step time. The delay time is due to the electrochemical time constant (the product of the double-layer capacitance and the uncompensated solution resistance) whereas the diminished amplitude and increased breadth are due to the finite ECL kinetics. The simulation, however, does not predict the slow rise in emission or the substantially lower amplitude evident in Figure 17.2.7 as the step time is decreased from 48 to 5 μsec . Similar results were obtained with Au or Pt disk electrodes (radius = 3–10 μm), with different solvents, and with half the electrolyte concentration.

However, the shape of the ECL curve is dependent on the concentration of DPA. At higher concentration, e.g., 5.8 mM, distinct oscillation in the ECL intensity can be observed on the decaying emission. These features have been attributed to the direct interaction of the emission with the metal electrode due to the close proximity of the light-emitting species to the metal electrode surface (15). These effects were least apparent with carbon-fiber microelectrodes due to their low reflectivity and density of states. In this case,

diffusion-controlled k_{annih} of $2 \times 10^{10}/\text{M/sec}$ was measured for DPA in acetonitrile and $4 \times 10^9/\text{M/sec}$ for DPA in propylene carbonate, a more viscous solvent.

In a later experiment (16), the DPA concentration was decreased to 15 μM and the temporal resolution to the nanosecond regime. In this case, an unsymmetrical waveform (a 500 μsec anodic pulse followed by a 50 μsec cathodic pulse) was used. The emission occurred predominantly during the shorter cathodic pulse (Figure 17.2.8) as the electro-generated radical anion diffused into the sea of DPA radical cations generated in the anodic pulse. When the photons were counted over 1 sec intervals, no evidence for individual reaction events was observed. The ensemble average of the counts detected during 1000 cathodic voltage pulses also masked individual reaction events but revealed that the luminescence approached steady-state (Figure 17.2.8D). When events during a single cathodic pulse were viewed with greater temporal resolution (i.e., bin size of 5 nsec), photons

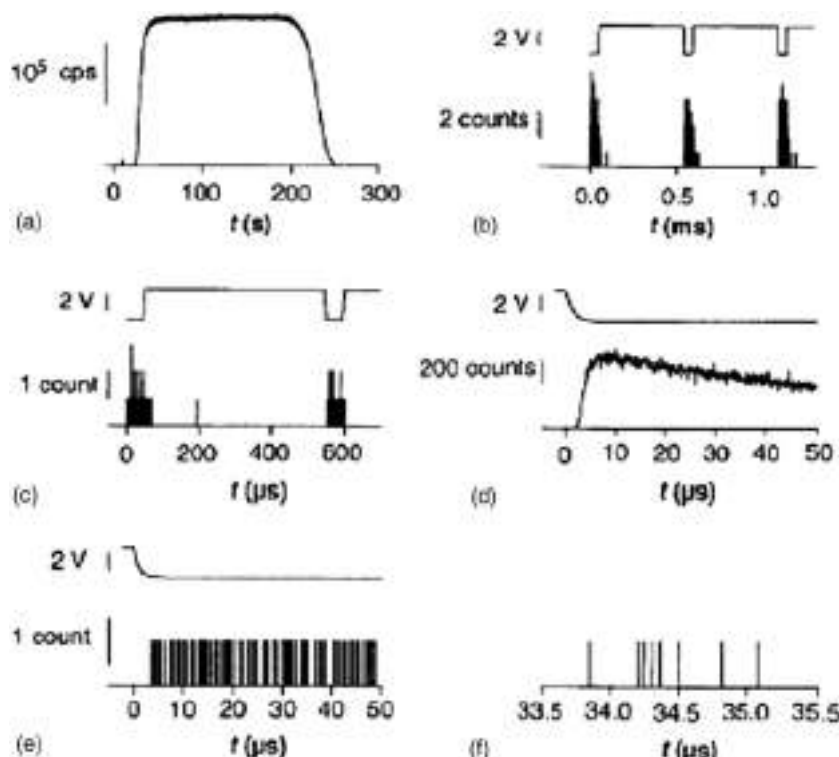


Figure 17.2.8 Temporal resolution of single reaction events. (A) Chemiluminescence from a bolus of 15 μM DPA in acetonitrile containing 0.1 M TBAPF₆. The electrode was a gold disk (radius = 5.4 μm) pulsed from 1.7 to -2.1 V at 550- μsec intervals. Data collected during the time interval between 50 and 200 sec have been expanded through a successive decrease in the bin size from 1 sec (A) to 1 μsec (B), 100 nsec (C and D), and 5 nsec (E and F). The double-layer capacitance (14 pF) and the solution resistance (75 k Ω) were used to calculate the rise time of the voltage pulses shown in (D) and (E). The curve shown in (D) is an ensemble average of events measured during 1000 cathodic pulses. Adapted with permission from reference (16).

resulting from individual reactions were revealed (Figure 17.2.8E and F). Virtually no background photons were detected so the corrections were unnecessary. Thus, the individual photon counts shown in Figure 17.2.8E and F, resulted from single chemical reactions between individual DPA radical ions in solution.

The stochastic nature of these events was characterized in two ways. First, a histogram of the time between individual photons was constructed (Figure 17.2.9A). Such a histogram for random events should be an exponential whose frequency, f , gives the mean rate of the events (10). The value of f from the exponential was in excellent agreement with the mean rate of photon arrival obtained by ensemble averaging data from repetitive cathodic pulses. Second, the data followed a Poisson distribution. The measured value of f should be a function of the generation rate and diffusion of the radical ions, the rate and efficiency of the light-producing chemical reaction, as well as the photon collection efficiency. At concentrations greater than 20 μM , f , normalized by concentration and electrode area, was essentially constant (inset, Figure 17.2.9B). The ratio of the mean photon rate (accounting for the detection efficiency) and the mean rate of generation of radical anions during each cathodic pulse directly yields the probability of a reaction generating a photon, i.e., the ECL quantum yield, Φ_{ecl} . At the high concentrations, this ratio yields a value of Φ_{ecl} of 6%, in good agreement reported values for DPA in acetonitrile. At lower concentrations, the normalized value of f decreases (inset, Figure 17.2.9B).

17.2.2.3 Coulomb staircase (CS) in electrochemistry

(a) Electrode potential and double-layer structure effects on voltammetric behavior of nanoelectrodes

All of the experiments described in Section 17.2.2.1 were carried out with a high concentration of supporting electrolyte so that electric field effects on the movement of the electroactive molecules were negligible. However, at low electrolyte concentrations, electric migration effects, in addition to diffusion, should be important; i.e., when the electroactive molecules make a significant contribution to the ionic strength, their movement to maintain electroneutrality (and double-layer charge equilibrium) contributes to their flux and hence to the current (17). We have performed several sets of SECM experiments to address this problem (18). The first involves oxidative voltammetric measurements on a positively-charged species ($\text{Cp}_2\text{FeTMA}^+$) at various gap separations d . The second experiment compared the limiting tip current for the oxidation of a positively-charged species ($\text{Cp}_2\text{FeTMA}^+$), a singly negatively-charged species ($\text{Cp}_2\text{FeCOO}^-$), and a doubly negatively-charged species ($\text{Fe}(\text{CpCOO}^-)_2$). This experiment was carried out by biasing the tip potential (E_T) at a constant value, e.g., 0.6 V vs. a platinum quasireference electrode (PtQRE), to obtain a limiting anodic i_T . i_T was then monitored while the substrate potential (E_S) was scanned.

As shown in Figure 17.2.10, when the tip ($a \sim 18$ nm) was fairly far away from the ITO substrate, a steady-state plateau-shaped cyclic voltammogram (CV) was obtained for the oxidation of $\text{Cp}_2\text{FeTMA}^+$ in an aqueous solution containing no supporting electrolyte. When the tip was brought to a distance within the range where i_T started to decrease significantly with decreasing d , a steady-state, somewhat peak-shaped voltammogram was obtained (curve 2). The dramatic decrease in i_T with decreasing distance,

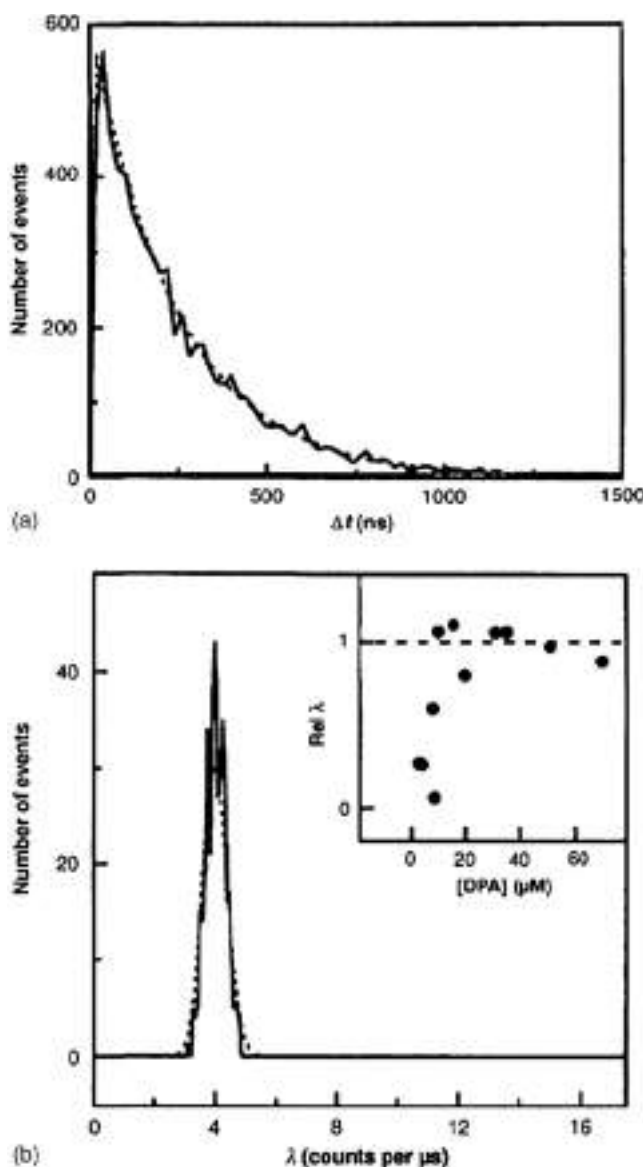


Figure 17.2.9 ECL time series in acetonitrile solution containing 31 μM DPA. (A) Histogram (7000 interevent times and a bin size of 20 nsec) of interarrival times and (B) histogram (375 voltage pulses and a bin size of 0.8 counts per microsecond). The counts used were from the last 25 μsec of the voltage pulse where the emission rate is pseudo-steady state. Dashed line: (A) exponential fit to data with rate of 205 counts per 50 μsec and (B) Poisson fit to data with rate of 200 counts per 50 μsec . Other conditions are same as in Figure 17.2.8. Insert: Plot of relative f values (f normalized by DPA concentration and electrode area and given as a ratio of the highest value) obtained from Poisson distribution. Data were obtained with electrodes of radii of 5.4 or 2.5 μm . Adapted with permission from reference (16).

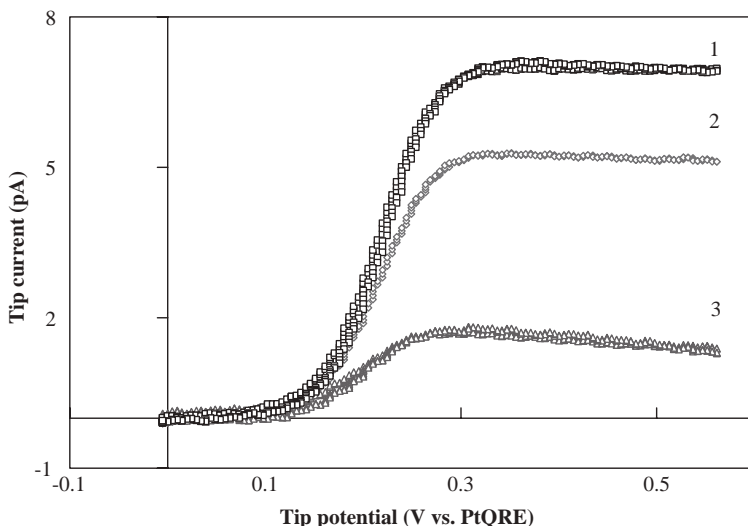


Figure 17.2.10 SECM tip cyclic voltammograms of 2 mM $\text{Cp}_2\text{FeTMA}^+$ in an aqueous solution containing no supporting electrolyte at a Pt tip ($a \sim 18$ nm) at three different gap separations. Curve 1: Tip held far away from the substrate (ITO) surface. Curve 2: Tip at a distance within the range where the tip current started to decrease with decreasing distance. Curve 3: Tip closer to the surface as compared with curve 2. Tip potential scan rate 5 mV/sec for all cases. $E_s = -0.3$ V vs. PtQRE. (for colour version: see colour section at the end of the book).

as discussed previously, is mainly due to diffusion to the tip being hindered by the insulating sheath and by the decrease in the effective tip radius as the tip is pushed against the ITO substrate. The peaking became more evident as the tip was brought even closer to the surface (curve 3). No evident peaking under such conditions was observed in the presence of 1.0 M NaNO_3 .

The results of the second experiment are shown in Figure 17.2.11A. When the tip was far away from the ITO surface, i_T , as expected, was essentially independent of E_s in the potential range studied. However, at small d , a significant increase in the limiting i_T with $\text{Cp}_2\text{FeTMA}^+$ (or decrease with $\text{Cp}_2\text{FeCOO}^-$ and $\text{Fe}(\text{CpCOO}^-)_2$) was observed when E_s was scanned toward more negative potentials. The higher the charge of the species, the more significant was the effect (compare green-triangle curve (curve 3) with blue-circle curve (curve 4)). The overall qualitative behavior of the experimental tip current as a function of E_s is consistent with that predicted by a simplified model (19), based on the consideration of both the effect of charge on mass transfer coefficient (2) and the effect of space charge associated with excess or deficiency of the electroactive species in the gap region (Figure 17.2.11B).

(b) CS at nanoelectrodes

Operational principles and experimental methods. It is of interest to consider whether the effect of a single electron-transfer event might ultimately be detected at electrodes or interfaces. The problem is to detect the difference a single electron makes in the measured signal

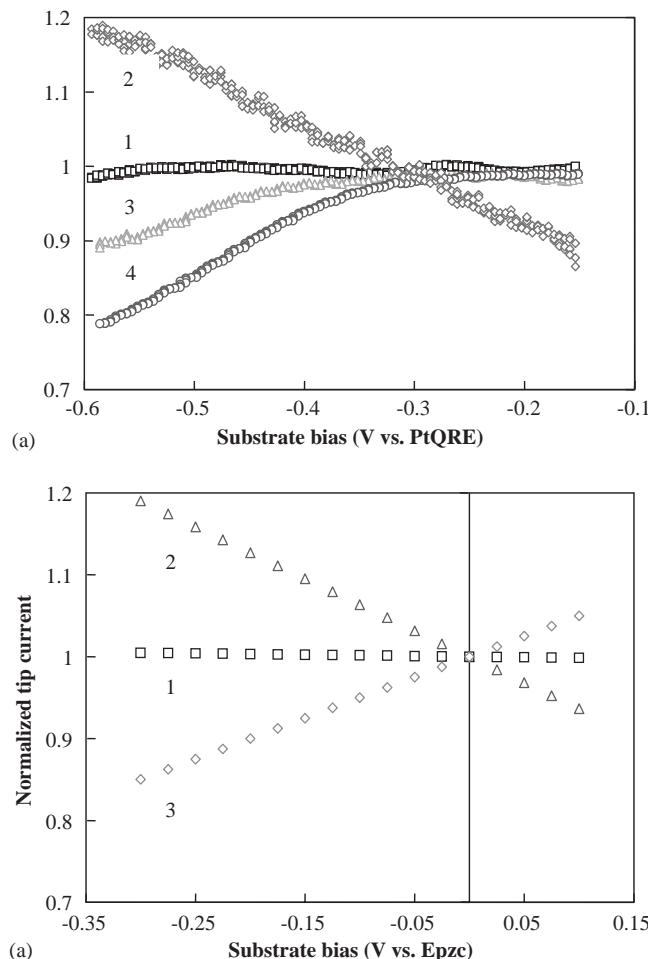


Figure 17.2.11 (A) Tip limiting current at $E_T = 0.6$ V vs. PtQRE as a function of the substrate potential, E_S , for different charged species. Curve 1: 2 mM $C_pFeC_pCOO^-$ in 1.0 M $NaNO_3$. Curve 2: 2 mM Cp_2FeTMA^+ , no supporting electrolyte. Curve 3: 2 mM $C_pFeC_pCOO^-$, no supporting electrolyte. Curve 4: 2 mM $Fe(C_pCOO^-)_2$, no supporting electrolyte. All limiting currents are normalized with respect to the limiting tip current of curve 1 at $E_S = -0.3$ V vs. PtQRE. Substrate potential scan rate: 5 mV/sec. (B) Normalized theoretical tip current as a function of E_S , with respect to the tip current at $E_S = E_{pzc}$ (the potential of zero charge) of ITO. Curve 1: 1 mM Cp_2FeTMA^+ in 1.0 M $NaNO_3$. Curve 2: 1 mM Cp_2FeTMA^+ only. Curve 3: 1 mM $C_pFeC_pCOO^-$ only. (for colour version: see colour section at the end of the book).

above noise level. Such single electron events are seen at two tunnel junctions formed by very small metal or semiconductor structures (quantum dots) at low temperatures in so called “Coulomb blockade” (CB) or “Coulomb staircase” (CS) experiments (20, 21). When an external voltage scan is applied to this two-junction system, an i - V characteristic

showing discrete steps is obtained. The semiclassical model of the CS takes account only of coulombic interactions and yields a peak spacing (or step width) of

$$\Delta V_{\text{p-p}} = \frac{e}{C} \quad (17.2.9)$$

in which C is the capacitance of the junction having higher electron-transfer rate (20, 21).

In an analogous electrochemical experiment, consider the double-layer capacitance, C_d , of an electrode with an area of 1000 nm^2 . If the differential capacitance per unit area near the (electrode/solution) interface is the same as that ($\sim 10 \mu\text{F}/\text{cm}^2$) for a typical larger electrode, then its capacitance would be $\sim 10^{-16}$ farad. The change of a charge corresponding to one electron would produce a voltage change (e/C_d) of $\sim 1.6 \text{ mV}$. If a suitable high input impedance device is available, such a charge step would be measurable. One can achieve such a structure in an electrochemical system by using a nanometer-scale electrode (nanode) immersed in a solution containing a redox couple. A schematic representation of two (electrode/solution) interfaces coupled in series through a solution for measurements is shown in Figure 17.2.12 (22). A voltage is applied to the (cell/electrometer) system and the current flowing through the interface system is monitored in a voltage measurement mode with an electrometer, as shown in Figure 17.2.12A. Current was found from the potential drop across the nominally 200-Tohm internal resistance at the most sensitive voltage setting. The leads were connected in the guard mode with the inner shield connected to the ungrounded electrode lead. The cell was placed inside a grounded Faraday cage. All current or voltage measurements were carried out at room temperature ($25.0 \pm 0.5^\circ\text{C}$) in a deaerated solution with an electrometer (Keithley). The Ir-Pt nanodes used in this experiment were prepared and characterized by the procedures described in Section 17.2.2.1.2. As shown in Figure 17.2.12B, each interface is characterized by a double-layer capacitance (C_d) and charge-transfer resistance (R_f) and thus mimics a tunnel junction which is connected in series to the electrometer. The redox molecules in the solution serve as donors and acceptors for electron transfer and also as charge carriers for ionic conduction between two interfaces.

Another approach to the single electron charging phenomenon is through a coulostatic-type experiment based on a single nanode as shown in Figure 17.2.12C. In this experiment, the

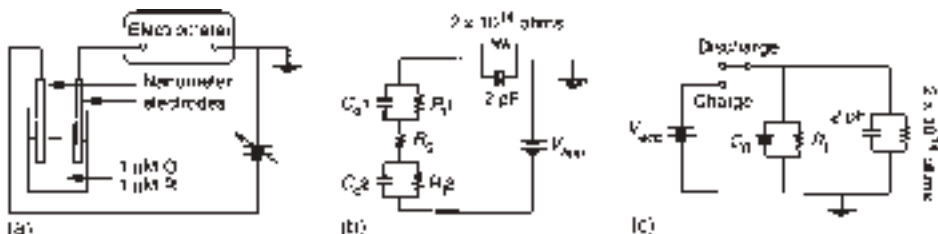


Figure 17.2.12 (A) Experimental setup for the current or voltage measurements. (B) Schematic representation of two (electrode/solution) interfaces coupled in series through the solution. C_d , double-layer capacitance; R_f , faradaic impedance of each interface; R_s , solution resistance; V_{app} , voltage source. The electrometer has an input impedance of $\sim 2 \times 10^{14} \Omega$ and a shunt capacitance of $2 \mu\text{F}$. (C) Schematic representation of the experimental setup for the coulostatic experiment. Adapted from reference (22).

other electrode was a saturated calomel electrode (SCE) or a large Pt quasireference electrode (PtQRE, area $\sim 0.2 \text{ cm}^2$). The two electrodes were immersed in a cell containing the $\text{Fe}(\text{CN})_6^{4-}/\text{Fe}(\text{CN})_6^{3-}$ couple. The potential of the nanode was displaced by $\sim 85 \text{ mV}$ from the equilibrium potential when this voltage was applied for 30–60 sec between the two electrodes. After the applied voltage was switched off, the cell voltage, measured with a high input impedance electrometer, relaxed back to the equilibrium value. Because the input impedance of the electrometer is not higher than the faradic impedance of the (nanode/solution) interface, the discharge of the cell voltage is convoluted by the input RC of the electrometer.

Results and discussion. In Figure 17.2.13, we show experimental data for a two-interface system consisting of two electrodes with radii of 2.5 and 3.2 nm about 2.5 cm apart in a solution containing 1 μM each of $\text{Cp}_2\text{FeTMA}^+$, $\text{Cp}_2\text{FeTMA}^{2+}$, NH_4^+ , and SO_4^{2-} , and 2 μM PF_6^- . The $i-V$ characteristic in the low-bias region (Figure 17.2.13A) exhibits a staircase shape, and the differential conductance (di/dV) (Figure 17.2.13B) consists of a series of peaks. The peak spacing, corresponding to the step width of the CS, is 65 (± 6) mV. The step heights of the staircase show some variation but were typically ~ 60 attoamperes (aA or 10^{-18} A). The general shape of the staircase was reproducible, although sharp change in the current at some voltage locations sometimes occurred. The step width was independent of data sampling rate, voltage scan rate ($< 20 \text{ mV/sec}$), and the concentration of the redox couple as long as it was low. The data in Figure 17.2.13 give a calculated C_d of $\sim 2.5 \times 10^{-18} \text{ farad}$, which is close to the expected C_d of an electrode of radius 2.8 nm, if we assume a double-layer capacitance of $\sim 10 \text{ } \mu\text{F/cm}^2$. At a higher bias voltage ($> 0.3 \text{ V}$), the current attains a diffusion-limited plateau of $\sim 530 \text{ aA}$ (Figure 17.2.13C). This corresponds to only about 3300 collisions per second of electroactive molecule ($\text{Cp}_2\text{FeTMA}^+$) with the electrode. A current staircase is observed in the low-bias region where the electron transfer is kinetically controlled. Similar $i-V$ curves were also observed at similar experimental conditions by Watkins and White (23).

A staircase $i-V$ curve is also observed for another redox couple with the same pair of electrodes in a solution containing 10 μM $\text{K}_4\text{Fe}(\text{CN})_6$ and 10 μM $\text{K}_3\text{Fe}(\text{CN})_6$. The estimated step height for this $\text{Fe}(\text{CN})_6^{4-}/\text{Fe}(\text{CN})_6^{3-}$ solution is $< 7 \text{ aA}$, even though the concentration of the electroactive species is 10 times that of the ferrocene couple. The estimated staircase width is $0.07 \pm 0.01 \text{ V}$, which is near the value seen with the ferrocene couple. This result is consistent with the predictions of the semiclassical CS model and the much slower heterogeneous electron-transfer kinetics. On the basis of the semiclassical model of the CS, the step height (Δi_{cs}) is, to the first approximation, inversely proportional to the charge-transfer resistance, R_f , at the interface. R_f controls the charge-transfer kinetics of the electrochemical system, and Δi_{cs} is given by (21, 22)

$$\Delta i_{cs} = \frac{e}{[R_f(C_d 1 + C_d 2)]} \quad (17.2.10)$$

R_f at low overpotential is given by

$$R_f = \left(\frac{RT}{F} \right) \left[\frac{1}{(nFAk_s C^*)} \right] \quad (17.2.11)$$

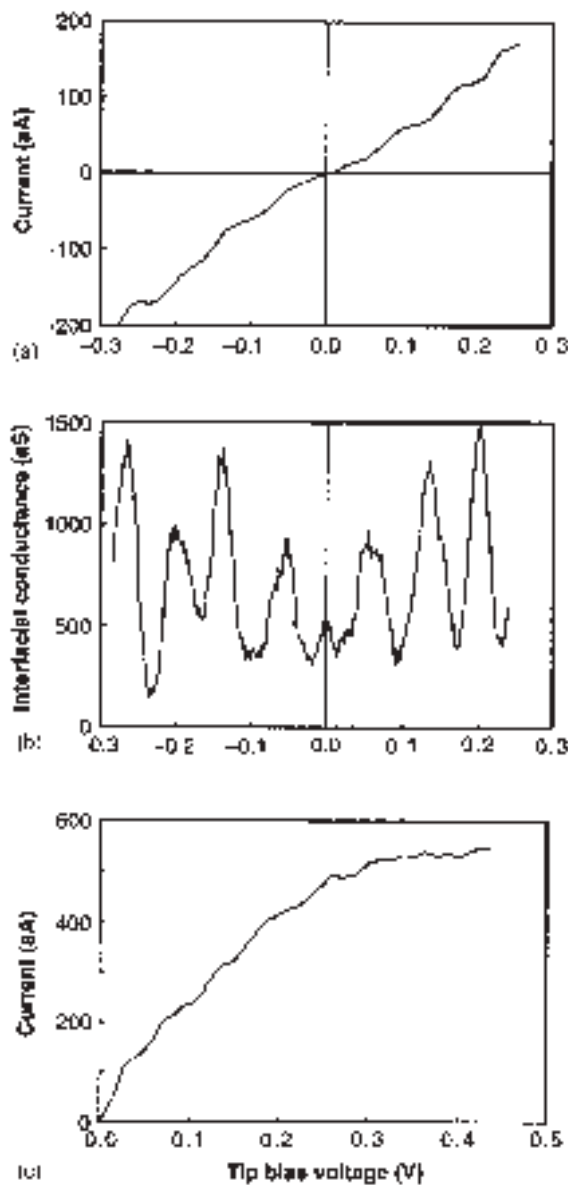


Figure 17.2.13 (A) Experimental i – V characteristic of a two-interface system consisting of a pair of electrodes with radii of 2.5 and 3.2 nm immersed in a deaerated solution containing 1 μM each of $\text{Cp}_2\text{FeTMA}^+$, $\text{Cp}_2\text{FeTMA}^{2+}$, NH_4^+ , and SO_4^{2-} , and 2 μM PF_6^- . (B) The corresponding differential conductance ($d\text{i}/d\text{V}$) – V plot. (C) i – V curve taken to more positive potentials. Adapted from reference (22).

in which R is the gas constant, T is the absolute temperature, k_s is the heterogeneous electron-transfer rate constant, and A is the electrode area. Thus, the step height depends on A , k_s , C^* , and C_d , whereas the step width depends mainly on C_d as given by equation (17.2.9). The results shown here suggest that k_s for the $\text{Fe}(\text{CN})_6^{4-}/\text{Fe}(\text{CN})_6^{3-}$ couple is at least two orders of magnitude smaller than that for the $\text{Cp}_2\text{FeTMA}^+/\text{Cp}_2\text{FeTMA}^{2+}$ couple, which has a $k_s = 2.5 \text{ cm/sec}$ as calculated from $\Delta i_{cs} = 60 \text{ aA}$, $C_d1 + C_d2 = 4.4 \times 10^{-18} \text{ farad}$, $C^* = 1 \mu\text{M}$, and $A = 2.0 \times 10^{-13} \text{ cm}^2$. We should point out that the $i-V$ curve at low bias (e.g., $<0.3 \text{ V}$) for a pair of large Pt microdisk electrodes with radii of 5 and $12.5 \mu\text{m}$ in the same solutions is smooth and linear, since the coulomb energy of one electron for electrodes of this size is very small ($<50 \text{ nV}$). At higher bias voltage, the current is expected to reach a diffusion-limited plateau.

Figure 17.2.14 shows the results of the coulostatic-type experiment. Curve a of Figure 17.2.14A shows the observed uncorrected cell voltage (V_u) as a function of discharge time for an electrode (effective radius $\sim 7 \text{ nm}$). A distorted staircase can be seen over an envelope of a smooth discharge background. Curve b shows the smooth discharge curve for a larger disk microelectrode (radius, $1 \mu\text{m}$). This discharge curve is nearly coincident with the background discharge curve (V_m) associated with the shunt capacitance of the electrometer alone. V_{corr} (V_u after correction for V_m based on the relation $V_{corr} = 2V_u - V_m$) is shown in Figure 17.2.14B. As shown in this figure, when the discharge time is longer than 200 sec, successive stepwise discharge steps become apparent and clearly resolved. The step height was $\sim 9 \text{ mV}$. The step near the starting portion of the discharge curve (between 100 and 200 sec) may be a two-electron step that is not well resolved. These data suggest that the temporal relation of the voltage of the electrochemical system, V_{corr} , can be represented as

$$V_{corr} = n(t) \left(\frac{e}{C_d} \right) + \text{terms independent of } n(t) \quad (17.2.12)$$

in which $n(t)$ is a step function, representing the discrete number of electron gained by the electrode during the discharge process.

(c) CS on nanoparticles

The quantization of double-layer capacitance charging has also been observed on monolayer-protected cluster (MPC) in solutions and is one of the most interesting solution electrochemical properties of alkanethiolate MPCs (24). The capacitance is associated with the double layer formed around an MPC dissolved in an electrolyte solution, upon electronic charging of the core (Figure 17.2.15a). Because of the small capacitance of an MPC, charging of the tiny capacitor by single electrons occurs in potential intervals (as given by equation (17.2.9)) that exceed $k_B T$, in which k_B is the Boltzmann constant. These potential intervals are readily observable in voltammetry (Figure 17.2.15b) of MPC solutions. The discretized (one electron) double layer charging steps are smeared out when the MPC core sizes are not mono-disperse or are too large (25). MPC quantized double layer charging is formally analogous to classical CS experiments on single MPCs, but the equivalent circuits are different (26, 27). The spacing of the current peaks on the potential axis in Figure 17.2.15b reflects the underlying nature of the MPC core charging process (24).

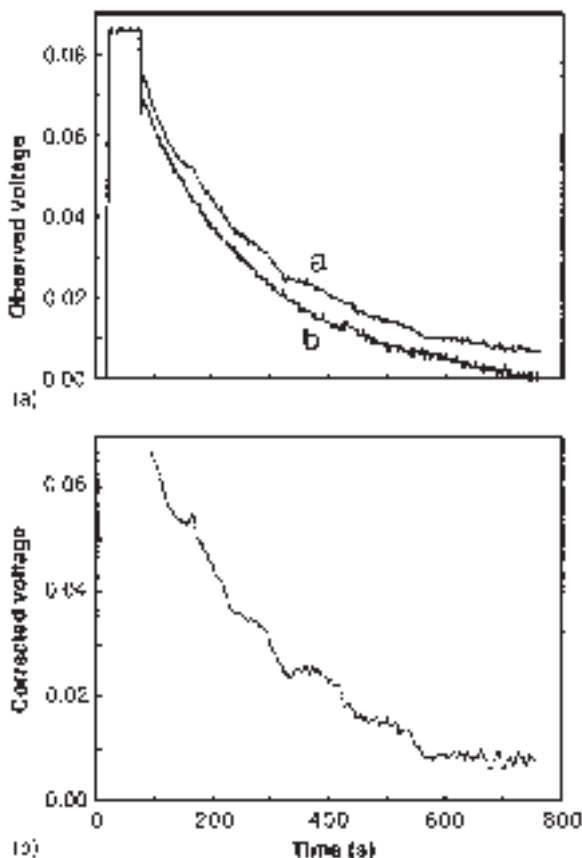


Figure 17.2.14 (A) Curve a: Discharge curve (V_u) of an electrode (radius, 7 nm) in a deaerated solution containing 2 μM each of $\text{K}_4\text{Fe}(\text{CN})_6$ and $\text{K}_3\text{Fe}(\text{CN})_6$ after biasing at 85 mV vs. the equilibrium cell voltage, V_0 , for 60 sec. Curve b: The corresponding curve for a microdisk electrode (radius, 1 μm) (shifted down by 4.8 mV for clarity). (B) Corrected discharge curve (V_{corr}) based on the relation $V_{\text{corr}} = 2V_u - V_m$. V_m is the background discharge curve of the shunt capacitance of the electrometer. Adapted from reference (22).

An even peak spacing signifies a metal-like core whose charging is controlled by electrostatic principles. The evolution of molecule-like properties when the MPC core is very small is seen as a wide spacing between the two current peaks adjacent to the MPC potential-of-zero charge (E_{pzc} , ca. -0.2 V vs. Ag/AgCl). It is important to understand that one-electron double layer charging peaks in MPC solutions are formally analogous to those produced by traditional redox reactions (e.g., oxidation of ferrocene). The double layer charging of MPCs is kinetically fast (demonstrably controlled by mass transport (25, 26)), so that the profile of working electrode current vs. average potential of MPC cores in the adjacent solution is determined by traditional combinations of the Nernst equation

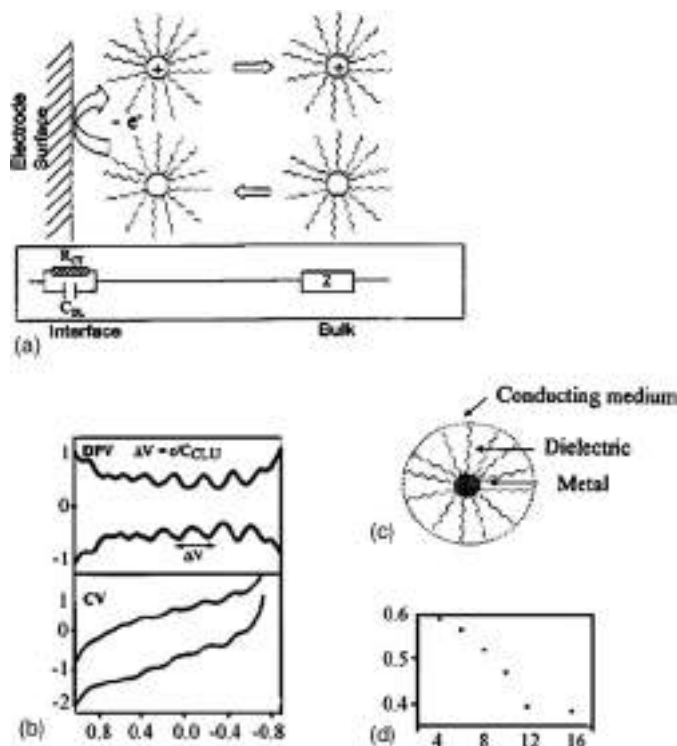


Figure 17.2.15 (a) Cartoon of quantized double layer charging of neutral MPCs (with PZC core potential) diffusing from bulk solution to an electrode/solution interface with a potential $E_{\text{pzc}} \pm e/C_d$; all MPC cores are charged to that potential by \pm a single electron. The MPCs then diffuse back into the solution. Box: Equivalent circuit, which determines current flow, in which R_{CT} and C_d are interfacial charge-transfer resistance (between electrode and MPC) and electrode double-layer capacitance, respectively, and Z is MPC diffusional Warburg impedance. (b) Cyclic voltammogram (bottom) and differential pulse voltammogram (top) of hexanethiolate Au MPC, in CH_2Cl_2 at a 1.6 mm diameter Au working electrode. (c) Cartoon of the concentric sphere capacitor model used in describing MPC capacitance. (d) Average MPC capacitance vs. chain length. Adapted with permission from reference (24).

with mass transport relationships. Each core charging step has a “formal potential”, which is referenced to the E_{pzc} is (25)

$$E_{z,z-1}^0 = E_{\text{pzc}} + (z - 1/2)(e/C_d) \quad (17.2.13)$$

where $E_{z,z-1}^0$, the formal potential of the $z/(z-1)$ charge state “couple”, corresponds to the differential pulse voltammetry (DPV) peak currents (Figure 17.2.15b) and C_d is the double-layer capacitance of the MPCs. z is signed such that $z > 0$ and $z < 0$ correspond to core “oxidation” and “reduction”, respectively. Insofar as C_d is potential independent, which seems to be so for potentials not far removed from E_{pzc} , this relation predicts a linear plot of $E_{z,z-1}^0$ vs. charge state, with C_d determined from its slope. Recent studies (28, 29) of the monolayer chain length dependence of C_d show that it varies with the

dielectric thickness in remarkable agreement with a simple concentric sphere capacitor model (Figure 17.2.15c and d). The simple model predicts no dependence in C_d on solvent or electrolyte changes.

It is interesting to point out that the charges stored on MPC cores can be used for chemical reactions. One can electrolytically store charge on MPCs in solutions (30); these solutions can be dried and reconstituted with minimal loss of the MPC core charge upon re-dissolution. Charges can also be stored on MPCs using chemical reactions. Charged MPCs can be used as quantitative redox reagents. For example, without a drying step, the titration of an ethyl ferrocene solution with oxidatively charged MPCs has been demonstrated. Charged MPCs can also undergo electron-transfer reactions with themselves, as shown by observing equilibrium potentials in solution mixtures of differently charged MPCs.

17.2.2.4 *Electrochemistry in humid environments*

Most SECM measurements are carried out with the sample under a thick liquid layer with a tip that must be sheathed in an insulator in order to achieve high resolution. SECM measurements can also be carried out within a thin layer of water that forms on the surface of a sample in air. In this case very high resolution can be attained using tips without insulation (e.g., the usual uninsulated W or Pt–Ir tips) because the tip area is defined by the small part of the tip that touches the liquid layer (31, 32). Studies of mica surfaces, polymer films, and some biological samples as described below are possible by this technique. With this mode, it is also possible to fabricate small metal structures in polymer films as demonstrated previously (33). High-resolution electrochemical deposition of silver nanostructures on mica surfaces in humid air was also achieved (32).

(a) *Gas/liquid/solid interface*

Theory (34) predicts that high-resolution imaging surface topologies of non-conducting bulk materials, especially biological specimens by scanning tunneling microscopy (STM) is possible. The realizability of this technique relies mainly upon surface condensation of water molecules on the specimens and substrate (35), with the measured current carried by ions rather than tunneling electrons. As a tip is brought into contact with the water layer (Figure 17.2.16) with an appropriate bias voltage between tip and substrate and with a sufficient concentration of ions, a measurable current proportional to the contact area should occur. Before the contact breaks, there is a column of water, called a bridge (34), at the tip/water layer/water vapor interface. When the constant current mode is used, the feedback mechanism will keep the tip-surface distance, d , and thus the contact area constant, provided the thickness of the water film is approximately uniform. Therefore, the altitude of the tip provides information about the surface topology of the specimen. According to theoretical calculation, the resolution is on the order of nanometers, strongly dependent on the humidity and temperature, and independent of specimen thickness. At nanometer resolution, this mode of operation will be useful in imaging surface structures of biological macromolecules and polymer thin films, as will be discussed below.

We should note that a previous report (36) also described “gas phase electrochemistry” in a thin film of liquid on an insulator surface, in agreement with the mechanism we describe here.

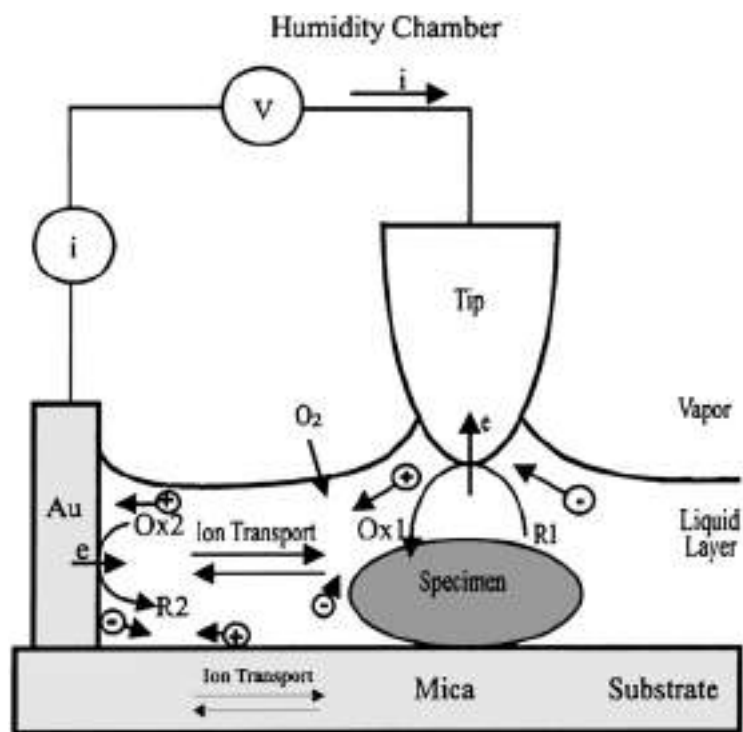


Figure 17.2.16 Schematic diagram for the SECM chamber with controlled humidity, and the electrochemical processes that control the current. The tip was located laterally ca. 1–2 mm away from Au counter electrode. For illustration purposes, the thickness of the liquid layer is exaggerated to accommodate equations for various electrochemical processes. V : Voltage bias between the tip and Au contact; i : current flow through the tip. R and Ox represent the reduced and oxidized forms of an electroactive species. \oplus and \ominus represent cations and anions in the liquid layer and in the mica sheet. Adapted from reference (38).

(b) Surface conductance of mica: effect of relative humidity and ion concentration

To obtain information about the surface conductance of a mica substrate, after treatment with a buffer solution that can serve as a source of ions in the condensed liquid layer as a function of RH, the following experiment was carried out. Two 50 nm thick layers of Au separated by ca. 1 mm were deposited on 1×0.8 cm pieces of mica. One small drop ($\sim 10 \mu\text{L}$) of a buffer solution was spread over the gap to cover an area of ca. 0.3×0.8 cm. After partially dried in the ambient for ca. 10 min, the treated (or untreated) mica substrate was then allowed to equilibrate with the atmosphere within the humidity chamber for at least 1 h before the voltammetric experiments were carried out. Figure 17.2.17 shows a series of semilog plots of current–voltage curves for a bare mica substrate at different RH. The measured current was very small (ca. 20 fA at 2 V bias) in a desiccated (anhydrous MgClO_4 as the desiccant, RH < 10%) chamber, while it increased at least five orders of magnitude to ca. 6.9 nA at 93% RH.

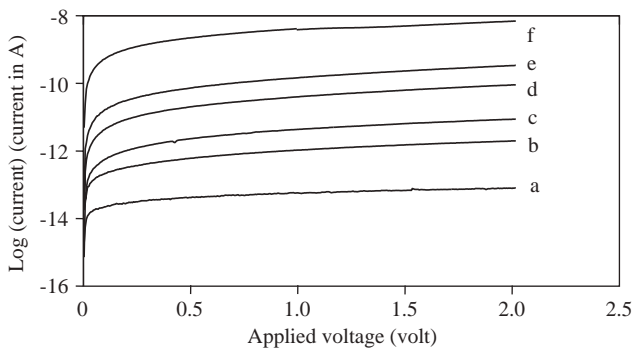


Figure 17.2.17 A series of semilogarithmic plots of i – V curves for a bare mica substrate at different relative humidity, RH: 33% (a); 58% (b); 65% (c); 74% (d); 81% (e); and 93% (f). Adapted from reference (38).

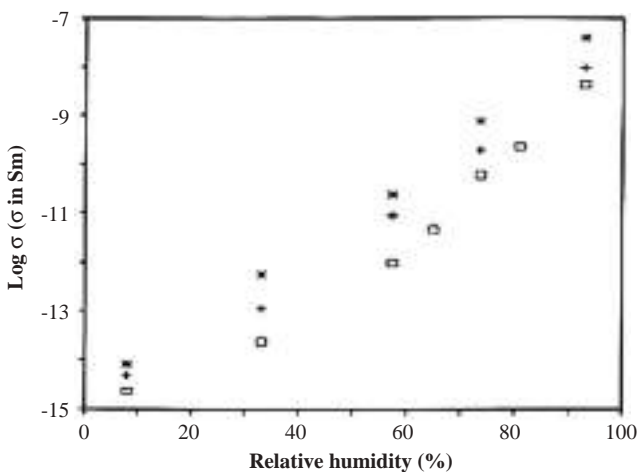


Figure 17.2.18 Conductance values at various RH for the same sheet before (rectangles) and after (asterisks) the treatment with TE or phosphate (pluses) buffer. The conductance was measured as the slope of the i – V curve in the bias range of 1.5–2.0 V. Adapted from reference (38).

Figure 17.2.18 summarizes the conductance values (measured as the slope of the current–voltage curve in the bias range of 1.5–2.0 V) at various RH for the same mica sheet before and after the treatment of Tris/EDTA (TE) buffer [10 mM Tris-HCl (pH 7.6)/1 mM EDTA] or phosphate buffer solution. As shown, the absolute conductance values of the bare mica surface increased slowly at low RH and more rapidly at high RH. Similar behavior was reported previously (35) for the adsorption isotherm measured by ellipsometry, suggesting that the observed conductance is closely related to the amount of water adsorbed on the mica surface. The adsorption isotherm indicates initial weak interaction between water molecule and the mica surface followed by growth of layers of water. The

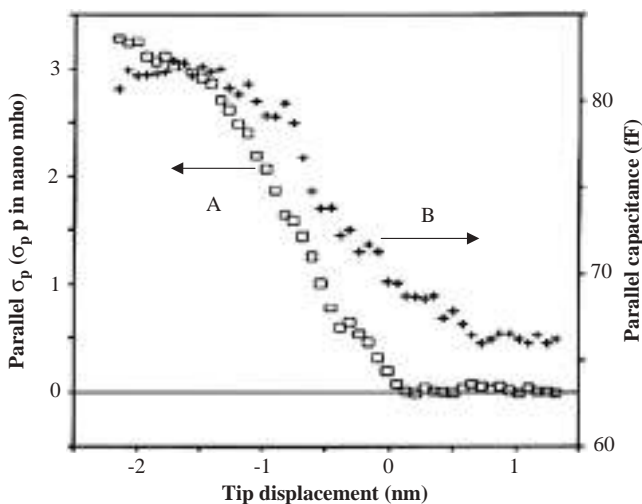


Figure 17.2.19 Typical parallel conductance (A) and parallel capacitance (B) vs. tip displacement curves for a blunt W tip at 100% at 25°C for a mica substrate treated with TE buffer solution. Tip bias was 3 V with respect to the Au counter electrode. The tip approached the substrate surface at 3 nm/sec. Adapted from reference (38).

average thickness of the water layer on a bare mica surface is ca. 0.4 nm at 70% RH. It is interesting to notice that although the surface conductance of the mica substrate was substantially enhanced (one to two orders of magnitude) by the treatment with TE or phosphate buffer solution, similar behavior was observed for the RH dependence of the conductance. The enhanced conductance could be attributed to the increased ion concentration in the thin electrolyte film on the mica substrate, which in turn can affect the thickness and structure of the water layer that forms on it. The conductance on untreated mica can probably be attributed to the presence of a small amount of ionic species that exist or desorb from the mica or are included in the liquid layer from the air.

In SECM experiments, when a W or Pt–Ir tip (biased at +3 V) approached the sample at a scan speed of 3 nm/sec, the current remained at zero until it contacted the liquid layer where it increased sharply, showing several orders of magnitude increase over a distance of a few nanometers. Accompanying this sharp increase in the tip current when it contacted the liquid layer, both parallel tip conductance and parallel tip capacitance also increased very rapidly (see Figure 17.2.19). This is characteristic of the occurrence of an electrochemical process and provides the necessary feedback mechanism to control the tip position for high-resolution imaging. As reported previously, this arrangement can be used for imaging (31, 37, 38) and fabrication (33, 39).

(c) Voltammetric behavior

Information about the mechanism of current flow was obtained from current–voltage (i – V) curves under different conditions (31). In these experiments, a rather blunt tip (radius of curvature \sim 10 μm) was brought into contact with the sample and the piezo-feedback was

switched off to avoid changes in the tip–substrate gap during the potential scan. i – V curves for a Nafion film with a Pt–Ir tip show some hysteresis in the range of +1 and –1 V where pA currents flow. Outside this range the curves become linear and are largely independent of scan direction (31). The shape of the curves is consistent with an electrochemical reaction, presumably mainly water electrolysis, at the tip and Au contact. Above this region the current is limited by the resistance of the thin film ($\sim 7.5 \times 10^{11} \Omega$). i – V curves with a blunt Pt–Ir tip on a mica substrate treated with TE buffer solution are more complex and depend on scan history (31). Thus for scans from 0 V to negative tip potential, the i – V relation is fairly linear with the current increasing slightly on each scan. An initial scan of the tip towards positive potentials following these scans is also almost linear. However, on successive positive tip potential scans, a definite peak appears; the current decreases and the peak shifts to less positive potentials on each scan (31). The voltammetric scan is restored if the tip is biased to negative potentials for about 2 min, suggesting that a species, probably H₂, builds up around the tip at negative bias that is depleted during successive anodic tip scans. After a series of scans of the tip to positive potentials, an initial cathodic tip scan shows decreased current, but gradually attains the linear behavior shown in successive cathodic scans (31). For purposes of imaging with a Pt–Ir tip, the current is fairly stable for negative tip bias values; with positive tip bias, oscillations frequently occurred.

As expected for an electrochemical process, the i – V curves also depend upon the tip material. For a blunt W tip on mica treated with TE buffer solution (Figure 17.2.20B), the current is stable and increases almost linearly for positive tip bias, but tends to saturate and shows considerable hysteresis on scan reversal in the negative tip bias region. Thus with a W tip, imaging at positive bias is appropriate. The observed electrochemical behavior also depends on the pretreatment of the insulating substrate like mica. For example, the voltammetric behavior is very different when the mica is simply immersed in water (even for a

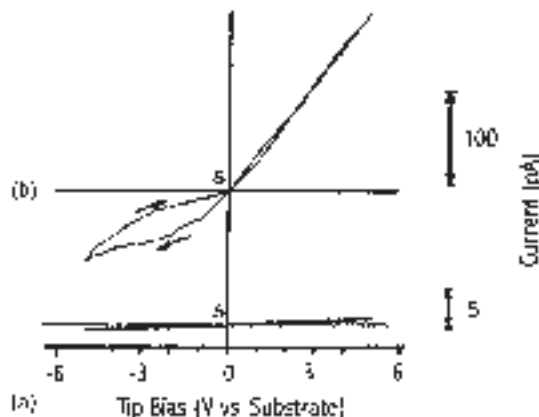


Figure 17.2.20 Typical voltammetric curves in the humidity chamber at 100% RH, 25°C over a bare mica substrate (A) or a mica substrate treated with TE buffer solution (B). Radius of curvature of the W tip is $\sim 10 \mu\text{m}$. In all cases, the voltage was scanned from 0 V (the starting point S) in either direction and then returned to 0 V; the scan rate was 0.2 V/sec. Adapted from reference (38).

few hours) rather than treated with TE buffer solution. Here $i-V$ curves at 100% RH at a W tip (Figure 17.2.20A) shows only very small currents across a region of ± 5 V. For a Ir-Pt tip, the current at 100% RH is at least one order of magnitude smaller for a water-treated sample as compared to one treated with TE buffer solution. The current under these conditions, however, was steady and showed little hysteria (38). At low RH (e.g., 33%), no appreciable current (<0.1 pA) was observed in the region of ± 5 V. Thus pretreatment of the insulating substrate to provide ions in the water layer and thus increase its conductivity appears to be useful. Following treatment with TE buffer solution it appears that sufficient ions remain adsorbed on the mica surface, even after washing, to yield some conductance in the water film that forms on exposure to humid air.

The electrochemical signal observed here could arise from both capacitive charging and faradaic processes. However, charging processes are transient and cannot sustain a true steady direct current. Because the observed $i-V$ curves are perturbed by resistive drops in the solution, one cannot identify with certainty the nature of the faradaic processes at the tip and Au contact. At Pt-Ir, candidate reactions are oxidation of water to O_2 or Cl^- to Cl_2 when TE buffer solution is used, reduction of water or protons to H_2 , reduction of dissolved O_2 or reduction of Cl_2 generated in the oxidation process, and processes involving adsorbed species, e.g., oxidation of EDTA or adventitious impurities. At W, in addition to these processes, oxidation of the W to form the oxide and transiently, reduction of native or electrochemically-generated oxide, are possible. The large and stable currents with a W tip at positive tip bias compared to Pt-Ir (see also the following discussion) suggest that the W oxidation reaction occurs at the tip. Note that the faradaic processes also generate ions that can contribute to the solution conductivity. Ions in the water layer also play an important role in establishing the double layers at both electrodes and providing charge compensation for electrogenerated species. They may also affect the hydrophilicity of the substrate surface and the thickness and structure of the water layer that forms on it.

(d) Imaging of polymers or biological macromolecules

As stated above, on the specimen and the mica substrate, there is normally a thin film of water (a few nanometers or less) at moderate RH. As the tip, biased at a certain voltage, is brought into contact with the film containing a sufficient concentration of ions, a measurable current occurs. When the constant-current mode is used, the feedback mechanism will allow the tip to move up and down to maintain contact in the thin electrolyte layer. The altitude of the tip provides some information about the surface topology of the specimen as shown in the following examples.

Mica surfaces and Nafion thin films. Figure 17.2.21A shows the image of the mica surface obtained in the constant-current mode at a reference tip current of 0.3 pA. The step running diagonally from the lower left corner represents a cleavage plane for a single mica layer, ca. 1 nm high, and the small pieces seen on the lower plane probably represent salt residue or debris left after cleavage. A thin film (~200 nm) of Nafion could also be imaged by this technique. The film was prepared on the mica substrate by spin-coating at 3000 rpm with a photoresist spinner (Headway Research, Garland, TX) from an isopropanol–ethanol (4:1 by volume) solution containing 5% Nafion. The image of this film (Figure 17.2.21B) shows smaller circular domain structures, 1–2 nm diameter, consisting of

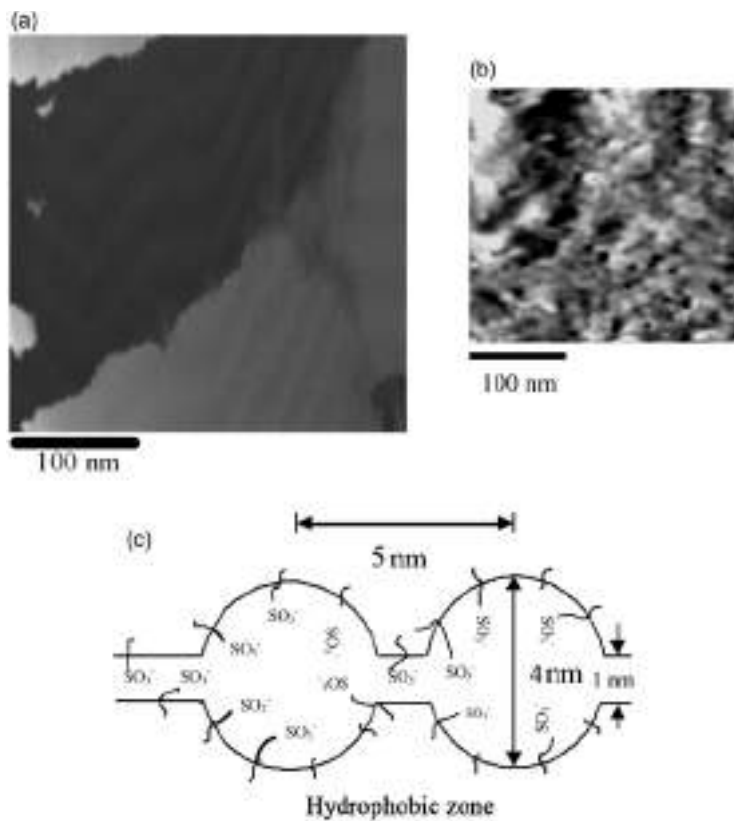


Figure 17.2.21 (A) Image of a mica surface treated with TE buffer solution taken in humid air (80% RH at 25°C) with a sharp W tip at a reference current of 0.3 pA and a tip bias of 3 V. The tip raster rate was 0.25 Hz. The total z-range is 3 nm. (B) Image of a Nafion film on mica taken in humid air (100% RH at 25°C) with a sharp Pt–Ir tip at a reference current of 3 pA and a tip bias of 3 V with respect to the Au counter electrode. The tip raster rate was 0.25 Hz. The image is inverted to enhance the visual effect of the domain structure; the dark region has a higher transient current than the lighter region and is corresponding to the hydrophilic domain. (C) Gierke's cluster model for Nafion membrane. Adapted from reference (31).

a more conductive central zone surrounded by a less conductive region. These structures correspond to those proposed in Gierke's cluster model (Figure 17.2.21C) for a Nafion membrane (40) in which a central hydrophilic domain consisting of backbone ions and water is surrounded by a Teflon-like hydrophobic zone. This image demonstrates that SECM can distinguish between zones of different ionic conductivity in a sample. It also suggests that such an imaging mode does not pose serious limitation on the specimen thickness as long as the surface water film provides a closed circuit for ion conduction.

DNA. As first reported by Guckenberger *et al.* (37), images of DNA on mica could also be obtained in this configuration. DNA on mica was prepared as follows: A small drop

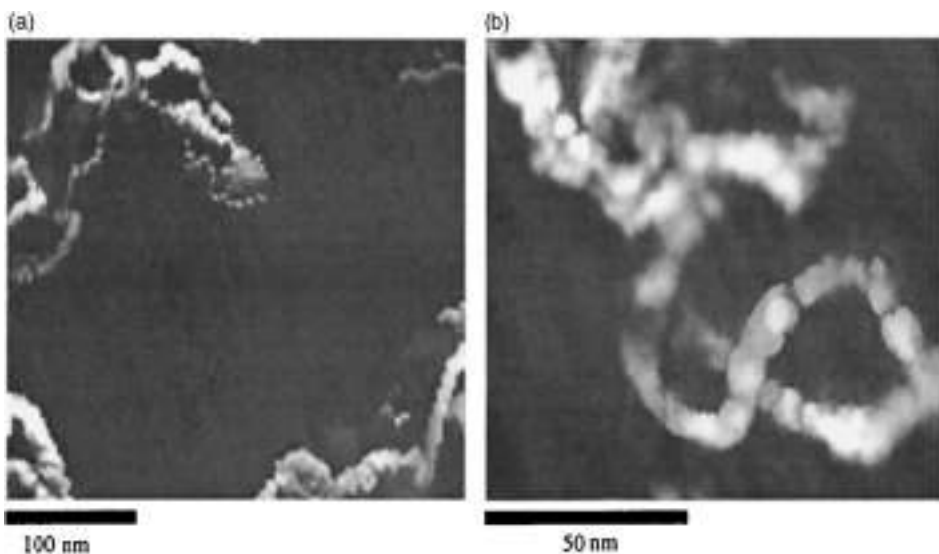


Figure 17.2.22 (A) Constant-current image of fragments of DNA specimen in humid air (80% RH at 25°C). The DNA specimen was deposited on a TE buffer-treated mica substrate. Image was taken with a sharp W tip at a reference current of 0.3 pA and a tip bias of 3 V. The tip raster rate was 0.25 Hz. (B) A high-resolution image of a DNA molecule obtained by scanning over a smaller area. Adapted from reference (38).

(10 μL) of the DNA specimen (2.96 kbp, 21.75 $\mu\text{g/mL}$) in TE buffer solution was placed on mica to cover ca. 1 cm^2 and left to adsorb for ca. 5 min. The sample was then dipped (1 sec) in water, dried for 5 min in air, and dipped again for 1 sec in water. Excess water on the surface was carefully removed with filter paper and the sample was mounted on the SECM/STM and allowed to equilibrate with the atmosphere within the box before the imaging was carried out. Figure 17.2.22A shows corresponding images of several super-coiled DNA molecules on mica. In general, imaging is more stable at positive tip bias if a W tip is used. There is a tendency to lose the image after repeated scans at the same area, presumably due to the depletion of electroactive species at or near the tip and the non-negligible tip–sample interaction. Interestingly, the magnitude of the signal can be partially recovered if there is a short period of waiting time between different frames of imaging. The signal can also be recovered by imaging different areas of the sample. As shown in Figure 17.2.22B, the lateral resolution obtained (4–8 nm) is considerably larger than the expected diameter of DNA (~2.5 nm). Information in the z -axis is limited, due to the lack of a quantitative relation between the charge-transfer rate and the tip–sample distance for this system.

Proteins. In addition to DNA, it is also possible to image antibody (e.g., a mouse monoclonal IgG), enzyme (e.g., glucose oxidase, GOD), and haemocyanin (e.g., keyhole limpet haemocyanin, KLH) molecules by the same technique (38). All of these protein molecules

have characteristic three-dimensional structures and the majority of their surfaces are hydrophilic; thus one can test the applicability of this technique for imaging. A small drop of 10 μL protein solution to cover ca. 1 cm^2 of the mica surface was used for the experiment. A stock solution of GOD (22.5 $\mu\text{g/mL}$) was prepared from a buffer solution containing 24 μM KH_2PO_4 , 170 μM NaCl, and 10 μM NaN_3 . It is important to use low concentrations of protein to minimize aggregate formation. However, for imaging purposes, the protein concentration should be high enough to have a proper coverage of protein molecules on the mica surface. The images were recorded using a W tip. The reference current was 1 pA at a tip bias of 1.5 V (vs. the Au contact).

Figure 17.2.23 shows the image of a group of GOD (MW = 160,000 Da, from *A. niger*) molecules on a mica surface at 81% RH. Most of the molecules show a dimeric structure corresponding to the folded form of the two identical polypeptide chains of the GOD molecules. The monomeric unit is apparently a compact spheroid with approximate dimensions of 8×4 nm. The top-view images of some of the molecules are observed as near circles with diameters of ca. 7 nm, which might represent the third dimension of the spheroidal monomeric unit. Contact between two monomeric units forming the dimer is confined to a long, narrow stretch. The overall dimensions of the GOD molecules are thus approximately $8 \times 7 \times 8$ nm, which are significantly larger than those ($6.0 \times 5.2 \times 7.7$ nm) determined from X-ray crystallographic data on the partially deglycosylated enzyme (41).

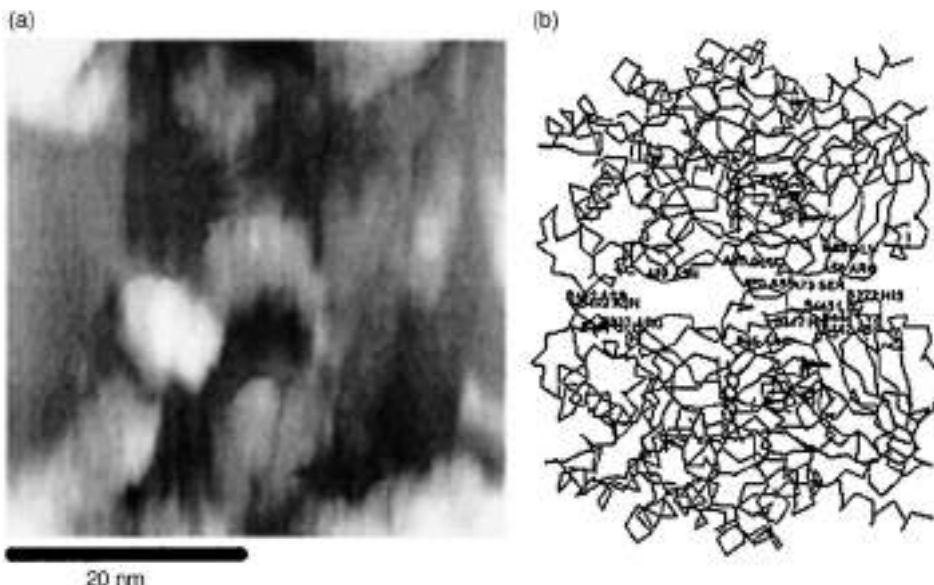


Figure 17.2.23 (A) Constant-current image showing several glucose oxidase molecules on mica substrates treated with phosphate buffer. The images were recorded with a W tip in humid air (80% RH at 25°C). The reference current was 1 pA at a tip bias of 1.5 V. (B) C^z tracing of the dimer structure of a glucose oxidase molecule. Contacts between molecules forming the dimer are confined to a long, narrow stretch. Adapted from reference (38).

The significant increases in size of the DNA and small protein molecules determined by this technique as compared with other techniques are most likely due to the presence of water and salt around the molecules, and the convolution of the non-negligible tip size. They could also be caused by the deformation of the molecules by the tip during imaging, as frequently encountered in SPM images for biological samples (42). It is conceivable that when the dimensions of the specimen are large compared with the tip curvature, the relative deviation due to tip geometry is small. It is also possible to de-convolute the images if one knows the exact tip dimensions and the detailed mechanisms of imaging. One can also minimize the size deviation by optimizing the RH and the salt concentration. In spite of this discrepancy, the overall shapes of the DNA and protein molecules are well reproduced in this experiment and are similar to those determined from other more established techniques. They further indicate that the use of a mica surface, which is atomically flat and can easily be chemically modified, is a suitable substrate for studying protein samples as suggested previously.

17.2.3 Conclusions

These studies have shown that single molecules can be trapped and detected electrochemically at electrodes and single reaction events of reactants generated at electrodes can be observed. These have involved soluble species and UMEs or nanoparticles. It should also be possible to observe single molecules adsorbed on a surface, e.g., self-assembled monolayers (SAMs), if a suitable amplification process can be developed. Such studies would be of use in determining free energies and reaction kinetics with tiny samples. They would also represent the ultimate sensitivity for electroanalytical detection.

Moreover, as with other SMD techniques, there is the expectation that will allow one to uncover phenomena and properties of materials, that are not apparent when one observes processes involving a large number of molecules, as are typical in conventional electrochemical experiments. For example, one can adsorb DNA on a suitably structured surface and detect DNA by itself or after intercalation with other agents. In principle, given sufficient stability of (DNA/intercalate) system, single molecule DNA detection would be possible.

REFERENCES

1. *Scanning Electrochemical Microscopy*, A. J. Bard, M. V. Mirkin, Eds., Marcel Dekker: New York, 2001.
2. A. J. Bard, L. R. Faulkner, *Electrochemical Methods, Fundamentals and Applications*, John Wiley & Sons, Inc.: New York, 2001, p. 174.
3. L. A. Nagahara, T. Thundat, S. M. Lindsay, *Rev. Sci. Instrum.* **60**, 3128 (1989).
4. F.-R. F. Fan, A. J. Bard, *J. Electrochem. Soc.* **136**, 3216 (1989).
5. F.-R. F. Fan, A. J. Bard, *Science* **267**, 871 (1995).
6. A. J. Bard, F.-R. F. Fan, M. V. Mirkin, in *Electroanalytical Chemistry*, A. J. Bard, Ed., Marcel Dekker: New York, 1994, Vol. 18, pp. 243–373.

7. M. V. Mirkin, A. J. Bard, *J. Electroanal. Chem.* **323**, 1 (1992).
8. F.-R. F. Fan, J. Kwak, A. J. Bard, *J. Am. Chem. Soc.* **118**, 9669 (1996).
9. J. S. Bendat, A. G. Piersol, *Random Data Analysis and Measurement Procedures*, 2nd ed., John Wiley and Sons: New York, 1986.
10. N. G. Van Kampen, *Stochastic Processes in Physics and Chemistry*, North Holland: Amsterdam, 1992.
11. R. A. Marcus, *J. Chem. Phys.* **43**, 2654 (1965).
12. See, for example, G. J. Kavarnos, "Fundamental Concepts of Photoinduced Electron Transfer," in *Topics in Current Chemistry*, J. Marray, Ed., Springer-Verlag: New York, 1990, Vol. 156, pp. 21–58.
13. *Electrogenerated Chemiluminescence*, A. J. Bard, Ed., Marcel Dekker: New York, 2004.
14. (a) M. M. Collinson, R. M. Wightman, *Anal. Chem.* **65**, 2576 (1993). (b) M. M. Collinson, R. M. Wightman, P. Pastore, *J. Phys. Chem.* **98**, 11942 (1994).
15. M. M. Collinson, P. Pastore, K. M. Maness, R. M. Wightman, *J. Am. Chem. Soc.* **116**, 4095 (1994).
16. M. M. Collinson, R. M. Wightman, *Science* **268**, 1883 (1995).
17. C. P. Smith, H. S. White, *Anal. Chem.* **65**, 3343 (1993).
18. A. J. Bard, F.-R. F. Fan, *Acc. Chem. Res.* **29**, 572 (1996).
19. F.-R. F. Fan, A. J. Bard (unpublished results).
20. M. Amman, R. Wilkins, E. Ben-Jacob, P. D. Maker, R. C. Jaklevic, *Phys. Rev. B* **43**, 1146 (1991).
21. A. E. Hanna, M. Tinkham, *Phys. Rev. B* **44**, 5919 (1991).
22. F.-R. F. Fan, A. J. Bard, *Science* **277**, 1791 (1997).
23. J. Watkins, H. S. White (private communication).
24. A. C. Templeton, W. P. Wuelfing, R. W. Murray, *Acc. Chem. Res.* **33**, 27 (2000).
25. S. Chen, R. W. Murray, S. W. Feldberg, *J. Phys. Chem. B* **102**, 9898 (1998).
26. S. Chen, R. S. Ingram, M. J. Hostetler, J. J. Pietron, R. W. Murray, T. G. Schaaff, J. T. Khoury, M. M. Alvarez, R. L. Whetten, *Science* **280**, 2098 (1998).
27. R. S. Ingram, M. J. Hostetler, R. W. Murray, T. G. Schaaff, J. T. Khoury, R. L. Whetten, T. P. Bigioni, D. K. Guthrie, P. N. First, *J. Am. Chem. Soc.* **119**, 9279 (1997).
28. J. F. Hicks, A. C. Templeton, S. Chen, K. M. Sheran, R. Jasti, R. W. Murray, J. Debord, T. G. Schaaff, R. L. Whetten, *Anal. Chem.* **71**, 3703 (1999).
29. J. F. Hicks, D. T. Miles, R. W. Murray, *J. Am. Chem. Soc.* **124**, 13322 (2002).
30. J. J. Pietron, J. F. Hicks, R. W. Murray, *J. Am. Chem. Soc.* **121**, 5565 (1999).
31. F.-R. F. Fan, A. J. Bard, *Science* **270**, 1849 (1995).
32. F. Forouzan, A. J. Bard, *J. Phys. Chem. B* **101**, 10876 (1997).
33. D. H. Craston, C. W. Lin, A. J. Bard, *J. Electrochem. Soc.* **135**, 785 (1988).
34. J.-Y. Yuan, Z. Shao, C. Gao, *Phys. Rev. Lett.* **67**, 863 (1991).
35. D. Beaglehole, E. Z. Radlinska, B. W. Ninham, H. K. Christenson, *Phys. Rev. Lett.* **66**, 2084 (1991).
36. Y. Fang, J. Leddy, *J. Electroanal. Chem.* **384**, 5 (1995).
37. R. Guckenberger, M. Heim, G. Ceve, H. Knapp, W. Wiegräbe, A. Hillebrand, *Science* **266**, 1538 (1994).
38. F.-R. F. Fan, A. J. Bard, *Proc. Nat. Acad. Sci. U.S.A.* **96**, 14222 (1999).
39. R. L. McCarley, S. A. Hendricks, A. J. Bard, *J. Phys. Chem.* **96**, 10089 (1992).
40. W. Y. Hsu, T. D. Gierke, *J. Membr. Sci.* **13**, 307 (1983).
41. H. J. Hecht, H. M. Kalisz, J. Hendle, R. D. Schmid, D. Schomburg, *J. Mol. Biol.* **229**, 153 (1993).
42. H. Hansma, J. Hoh, *Annu. Rev. Biophys. Biochem. Struct.* **23**, 115 (1994).

17.3 ELECTROCHEMISTRY AT LIQUID/LIQUID INTERFACES

Yuanhua Shao

College of Chemistry and Molecular Engineering, Peking University,
Beijing 100871, China

17.3.1 Introduction

Charge (electron and ion) transfer at a liquid/liquid (L/L) interface, or at an oil/water (O/W) interface, or at an interface between two immiscible electrolyte solutions (ITIES) is one of the most fundamental physicochemical processes. The study of such soft molecular interfaces by various electrochemical techniques is referred to as electrochemistry at liquid/liquid interfaces. This field has developed quickly over the past 30 years (1–10) due to applications in areas including exploration of mechanisms of phase transfer catalysis, extraction processes and chemical sensing, investigation of solar energy conversion systems, drug release and delivery, and in mimicking the function of biological membranes.

The first work in this field can be traced back to the beginning of last century when Nernst and Riesenfeld carried out experiments at a water/phenol interface in the presence of colored inorganic electrolytes [KI₃, K₂CrO₄, Fe(SCN)₃, etc.]. They were mainly interested in developing suitable methods to evaluate transport numbers in non-aqueous solvents (11). After Cremer (12) pointed out in 1906 the analogy between water/oil/water concentration cells and biological membranes studied by Ostwald (13), interest in this field spread to physiologists and the liquid/liquid interface became a model for the investigation of bioelectrical potentials and currents. In 1939, Verwey and Niessen (14) published the first theoretical paper regarding the electrical double layer and potential distribution at a liquid/liquid interface. In the mid-1950s, Guastalla *et al.* (15) investigated the effect of passing current across the water/nitrobenzene (NB) interface and also began to study electrosorption (which was later found by Blank (16) to be based on a depletion–accumulation effect of surface active electrolytes).

The progress however was rather slow in the first half of the century. This was mainly due to a lack of knowledge of the interfacial structure and associated potential distribution across the interface, and secondly to the inherent difficulty in gathering reliable data due to the presence of *iR* drop caused by the use of an organic solvent. There are two landmarks in the establishment of modern electrochemistry at liquid/liquid interfaces. One is around the end of the 1960s, after recognition that the liquid/liquid interface could be polarized just like the metallic electrode/electrolyte interface. For example, Gavach *et al.* (17–20) first employed modern electrochemical techniques such as chronopotentiometry to investigate ion transfer across liquid/liquid interfaces and used the Modified Verwey–Niessen (MVN) model to rationalize the experimental data (18, 19). The second is around the late 1970s when Samec *et al.* (21, 22) in Prague employed a four-electrode potentiostat with *iR* drop compensation to record the cyclic voltammograms of charge transfer across the liquid/liquid interfaces. Meanwhile, Koryta *et al.* (23–27) established the theoretical background for a series of

electrochemical cells and pioneered the study of facilitated ion transfer by ionophores. The research groups who have shown interest in this field are spread all over the world (28–32).

17.3.2 Fundamentals

17.3.2.1 Thermodynamics of a liquid/liquid interface (33)

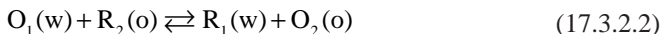
When two electrically conducting phases such as *w* (water) and *o* (organic) are in contact, the partition of the charge carriers (electron and ion) between the two adjoining phases occurs due to the difference in energy of the carriers in both phases. Thus, an interfacial region is built up. Within the interfacial region, the electrical field strength differs from zero and a Galvani potential difference, $\Delta_o^\circ \phi = \phi^w - \phi^o$, is established across the interface. In the case of a metallic electrode/electrolyte interface, the region of excess charge at the interface consists of electrons (or holes) on the metallic side and of ions on the electrolyte side. In the case of a liquid/liquid interface, both charge regions are formed by ions: anions on one side and cations on the other. As a whole, in any case, the interfacial region should be electrically neutral (see Figure 17.3.1).

In general at liquid/liquid interfaces, there are two types of charge partition (3):

- (A) The transfer of an ion M^z with the charge number *z* from phase *w* to phase *o* and the reverse:



- (B) The electron transfer between a redox couple O_1/R_1 in phase *w* and a redox couple O_2/R_2 in phase *o*, can be represented as:



Each of these two heterogeneous charge transfer reactions may be coupled to a series of homogeneous chemical reactions inside phase *w* or *o* or to heterogeneous reactions occurring at the interfacial region (e.g., ion-pair formation and adsorption), so that the interfacial charge transfer may be very complicated. As an example, the transfer of an ion M^+ facilitated by complex formation with a ligand (ionophore) *L* at a liquid/liquid interface may be written as:

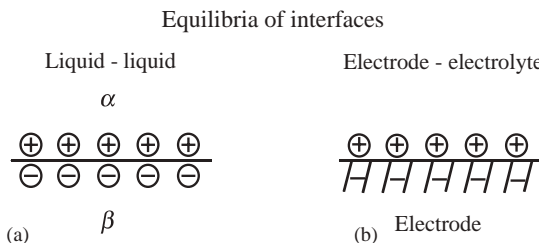


Figure 17.3.1 The equilibria of the interfaces. (a) Liquid/liquid interface; (b) Electrode/electrolyte interface. (Reprinted with permission from (25). Copyright 1979 Elsevier Science).

The conditions for equilibrium of ion (M^z) at a liquid/liquid interface are such that their electrochemical potentials are equal

$$\bar{\mu}_M^w = \bar{\mu}_M^o \quad (17.3.2.4)$$

with

$$\bar{\mu}_M^w = \mu_M^{0,w} + RT \ln \alpha_M^w + zF\phi^w \quad (17.3.2.5)$$

and

$$\bar{\mu}_M^o = \mu_M^{0,o} + RT \ln \alpha_M^o + zF\phi^o \quad (17.3.2.6)$$

where μ_M^0 , α_M and ϕ are standard chemical potentials, activities of M^z and inner potentials in water (w) and organic (o) phases, respectively.

The equilibrium potential difference $\Delta_o^w \phi$ is obtained by combination of the above equations, and is as follows:

$$\begin{aligned} \Delta_o^w \phi &= \phi^w - \phi^o \\ &= (\mu_M^{0,o} - \mu_M^{0,w})/zF + (RT/zF) \ln(\alpha_M^o / \alpha_M^w) \\ &= \Delta_o^w \phi_M^0 + (RT/zF) \ln(\alpha_M^o / \alpha_M^w) \end{aligned} \quad (17.3.2.7)$$

Equation (17.3.2.7) is analogous to the Nernst equation for electrode potential, and $\Delta_o^w \phi_M^0$ is called the standard transfer potential.

The standard Galvani potential difference between the two phases can be further written as:

$$\Delta_o^w \phi_M^0 = -(\mu_M^{0,w} - \mu_M^{0,o})/zF = \Delta G_{tr}^{0,w \rightarrow o}/zF \quad (17.3.2.8)$$

where $\Delta G_{tr}^{0,w \rightarrow o}$ is the standard single ion Gibbs energy of transfer from water to oil. However, this quantity, in contrast to the electrolytes as a whole, is not amenable to direct measurement. For quantitative determination, extra-thermodynamic assumptions must be made. So far, as pointed out by Girault and Schiffrian (34) there are at least six categories of assumptions which have been proposed. The most commonly used is the “TATB assumption” stating that the cation and the anion of tetraphenylarsonium tetraphenylborate (TPAs⁺TPB⁻) have equal standard Gibbs transfer energies for any pair of solvent (25, 26) (see Figure 17.3.2). That is:

$$\Delta G_{tr,TPAs^+}^{0,w \rightarrow o} = \Delta G_{tr,TPB^-}^{0,w \rightarrow o} = \frac{1}{2} \Delta G_{tr,TPAsTPB}^{0,w \rightarrow o} \quad (17.3.2.9)$$

On the basis of this assumption, a scale for standard Gibbs energies of transfer of individual ions from one solvent to another can be obtained using standard Gibbs energy of transfer of a salt which can be calculated from partition coefficients, solubility and voltammetric measurements (9, 10, 33). Similarly, the standard potential difference for individual ions between phase w and o can be evaluated from equation (17.3.2.8). For example, the standard Gibbs energies of transfer of TPAs⁺ and TPB⁻ between water and

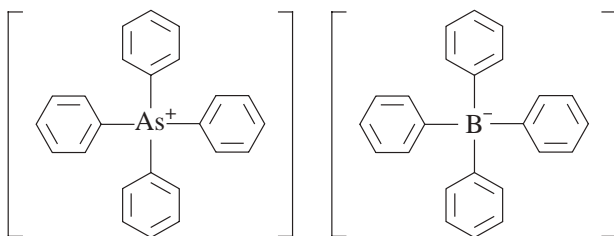


Figure 17.3.2 The structure of TPAsTPB.

1,2-dichloroethane (DCE) are both equal to -35.2 KJ/mol , their corresponding standard potential differences are -365 and 365 mV , respectively (33). Girault and Schiffrian (35) have proposed another way to define the absolute potential scale by using the potential of zero charge (PZC) as the absolute zero point.

It should be noticed that the standard Gibbs transfer energy data commonly used are related to ion transfer between mutually saturated solvents (known as the Gibbs energy of partition), which are different from the data for transfer between pure solvents (known as the Gibbs energy of transfer). These values are in agreement only under circumstances where the ion transferred from water to an organic solvent not hydrated by water present in that solvent (34).

Updated lists of the values of standard Gibbs energies of transfer for various individual ions are given in Professor Hubert H. Girault's website at the EPFL of Switzerland (36). More values can be found in a data survey of Gibbs energy of ion transfer for 57 different solvents published by IUPAC (37). Table 17.3.1 lists some data for W/NB and W/DCE systems.

Liquid/liquid interfaces have been classified as ideal-polarizable interfaces and non-polarizable interfaces (25–27). Let us first discuss the system in which a strongly hydrophilic 1:1 electrolyte B_1A_1 is dissolved in water (e.g., LiCl in water) and a strongly hydrophobic 1:1 electrolyte B_2A_2 is dissolved in an organic solvent [e.g., tetrabutylammonium tetraphenylborate (TBATPB) in NB], as shown in Cell 1:

$$r_1/B_1A_1(w)//B_2A_2(o)/r_2 \quad \text{Cell 1}$$

where r_1 and r_2 represent the reference electrodes which are reversible to either cation (B_1 or B_2) or anion (A_1 or A_2). The situation can be described by the following equations:

$$\Delta_o^w \phi_{B_1}^0 \gg 0 \text{ and } \Delta_o^w \phi_{A_2}^0 \gg 0 \quad (17.3.2.10)$$

$$\Delta_o^w \phi_{B_2}^0 \ll 0 \text{ and } \Delta_o^w \phi_{A_1}^0 \ll 0 \quad (17.3.2.11)$$

It has been demonstrated by Koryta (25, 26) that for such cases, there exists a range of potential differences (potential window) in which $\Delta_o^w \phi$ is controlled by the charge in the double layer rather than by the ion activities (see Figure 17.3.5A). This situation is completely analogous to that of an ideal-polarizable metal/electrolyte interface. We call this case the ideal-polarizable liquid/liquid interface. One of such example is the following

Table 17.3.1

Standard Gibbs energies of transfer and standard potential differences for some ions at the W/NB and the W/DCE interfaces (9, 10, 33)

Ion	$\Delta_o^w G_{tr}^{0,W \rightarrow NB}$ (kJ/mol)	$\Delta_o^w \phi^0$ (mV) W/NB system	$\Delta_o^w G_{tr}^{0,W \rightarrow DCE}$ (kJ/mol)	$\Delta_o^w \phi^0$ (mV) W/DCE system
Li ⁺	38.4	398	55.6	576
Na ⁺	34.4	358	55.9	579
H ⁺	32.5	337	53	549
K ⁺	24.3	252	51.9	538
Rb ⁺	19.9	206	45.8	475
Cs ⁺	15.5	161	37.3	386
TMA ^{+a}	3.4	35	15.4	160
TEA ^{+a}	-5.8	-60	1.8	19
TPA ^{+a}	-15.5	-161	-8.8	-91
TBA ^{+a}	-24.2	-248	-22.2	-230
TPAs ⁺	-35.9	-372	-35.2	-365
F ⁻	44.0	-454	58	-601
Cl ⁻	30.5	-316	51	-528
Br ⁻	28.5	-295	39	-404
I ⁻	18.8	-195	26	-269
ClO ₄ ⁻	8.0	-83	17.0	-176
SCN ⁻	16.0	-176	26	-269
BF ₄ ⁻	11.0	-121	-17.9	185
NO ₃ ⁻	24.4	-253	34	-352
TPB ⁻	-35.9	372	-35.2	365

^aTMA⁺, TEA⁺, TPA⁺, and TBA⁺ are abbreviations of tetramethylammonium, tetraethylammonium, tetrapropylammonium, and tetrbutylammonium, respectively.

electrochemical cell: Ag/AgTPBCl/0.01 M TBATPBCl//0.01 M LiCl + 0.3 M Li₂SO₄/Ag/AgCl (dichloromethane is the organic phase, TPBCl⁻ is tetrakis[4-chlorophenyl]borate), it has an approximately 500 mV potential window, in which other charge transfer processes can be studied electrochemically.

Let us discuss another case shown in Cell 2:

$$r_1/B_3 A_1(w) // B_3 A_2(o) / r_2 \quad \text{Cell 2}$$

Both phases have a common ion B₃ which is transferable across this interface. However, the transfer of the ion A₁ from w to o and that of ion A₂ in the opposite direction are negligible in the potential window. This system is described by the following inequalities:

$$\Delta_o^w \phi_{A_1}^0 \ll 0 \text{ and } \Delta_o^w \phi_{A_2}^0 \gg 0 \quad (17.3.2.12)$$

$$\Delta_o^w \phi_{A_1}^0 \ll \Delta_o^w \phi_{B_3}^0 \ll \Delta_o^w \phi_{A_2}^0 \quad (17.3.2.13)$$

Under these conditions, the potential difference between w and o is determined practically only by the activities of ion B₃ in both phases according to equation (17.3.2.14), if the concentrations of ion B₃ in both phases have suitable values.

$$\Delta_o^w \phi = \Delta_o^w \phi_{B_3}^0 + (RT/z_{B_3} F) \ln(\alpha_{B_3}^o / \alpha_{B_3}^w) \quad (17.3.2.14)$$

We call this case the non-polarizable liquid/liquid interface. One example is as follows: Ag/AgTPB/0.01 M TBATPB//0.01 M TBACl/Ag/AgCl. Here TBA^+ is the common ion in both phases. Usually one studies the charge transfer across the ideal-polarizable liquid/liquid interface and employs a non-polarizable liquid/liquid interface as a reference electrode.

There are over 20 organic solvents which have been tested so far. As pointed out by Koryta (38), the following three requirements have been commonly employed to select the organic solvent:

- (1) The solubilities of solvent in water and water in the solvent must be very small.
- (2) The solvent must be polar to promote sufficient dissociation of the supporting electrolyte and thus maintaining conductivity of the solution.
- (3) The density of the solvent should differ significantly from that of aqueous phase in order to obtain a physically stable liquid/liquid interface.

At present, the most commonly used solvents are NB and DCE. Other solvents which have been considered include, for example, propiophenone (39), 4-isopropyl-1-methyl-2-nitrobenzene (40), dichloromethane (41), *o*-nitrophenyloctyl ether (42). In order to have more flexible choices, organic solvent mixtures have also been employed; for example, NB with chlorobenzene (43), benzonitrile, benzene (44), and tetrachloromethane (45).

During the early days of electrochemical measurements of charge transfer reactions at liquid/liquid interfaces, TBATPB was the most commonly used supporting electrolyte in the organic phase, which usually determined the potential window. In order to widen the potential window, more hydrophobic salts were studied, including:

CVTPB (crystal violet tetraphenylborate) (46);

BTPPATPB (Bis[triphenylphosphoranylidene]ammonium tetraphenylborate) (47);

TPAsDCC (tetraphenylarsonium3,3'-commo-bis[undecahydro-1,2-dicarba-3-cobalta-chosododecarborate]) (48);

TBAPBCl (tetraphenylammonium tetrakis[4-chlorophenyl]borate) (47);

TBAPBF (tetraphenylammonium tetrakis[pentafluorophenyl]borate) (47);

BTPPATPBCl (Bis[triphenylphosphoranylidene]ammonium tetrakis [4-chlorophenyl] borate) (49);

BTPPATPBF (Bis[triphenylphosphoranylidene]ammonium tetrakis[pentafluorophenyl] borate) (49)

have been successfully used recently. Now the limitations of the potential window are mostly due to the transfers of the supporting electrolytes in the aqueous phases while the salts such as BTPPATPBCl is used as the supporting electrolyte in DCE.

17.3.2.2 Interfacial structure

The distribution of the potential at the interfacial region is related to the structure of the interface. Although charge transfer reactions at liquid/liquid interfaces have been studied experimentally using modern electrochemical and spectroscopic methodologies (2, 6), the interpretation of the results has not yet allowed a complete understanding of the kinetic

mechanism. This is due to the fact that any theoretical approach of charge transfer kinetics across the liquid/liquid interface is mainly dependent upon the physical model of the interface considered. The interface between two phases is by nature a molecular interface with its own dynamics. It is obviously hard to define an interfacial structure or thickness. Is the interface sharp or diffuse? The answer to this question is timescale dependent (6). Unlike solid electrodes, the microscopic aspects of the structure of a liquid/liquid interface are not amenable to scanning probing microscopes with atomic resolution. This drawback can be turned into an advantage. Because of interfacial dynamics, the macroscopic properties of liquid/liquid interface are indeed highly reproducible (6). The current views of such interfaces have come from molecular dynamic simulations (50–52). However, it is crucial to point out that the mechanism and kinetics of charge transfer reactions at these interfaces are still not well understood and two of the most commonly used models will be described below.

(a) MVN (Modified Verwey–Niessen) model

The first model of interfacial structure was introduced by Verwey and Niessen (14). It was represented by a space charge region in each phase, one containing an excess of positive charge and the other an equal excess of negative charge. The space charge distribution was described by the Gouy–Chapman theory (20, 53). Gavach et al. (20) in 1977 proposed a modified version of this model assuming the presence of an ion-free layer composed of oriented solvent molecules separating two diffuse layers, as shown in Figure 17.3.3.

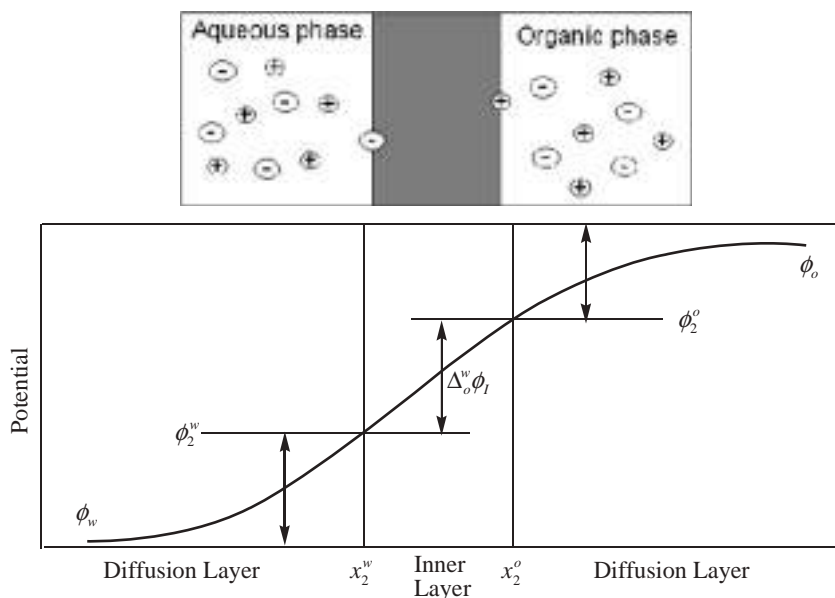


Figure 17.3.3 The modified Verwey–Niessen model and potential distribution. (Reprinted with permission from (20). Copyright 1977 Elsevier Science).

In this MVN model, the Galvani potential difference $\Delta_o^w \phi$ was split into three parts

$$\Delta_o^w \phi = \phi^w - \phi^o = \Delta_o^w \phi_i + \phi_2^o - \phi_2^w \quad (17.3.2.15)$$

where $\Delta_o^w \phi_i = \phi(\chi_2^w) - \phi(\chi_2^o)$ is the potential difference across the inner layer and $\phi_2^o = \phi(\chi_2^o) - \phi^o$ or $\phi_2^w = \phi(\chi_2^w) - \phi^w$ are the potential differences across the diffuse layers in the phases o or w, respectively.

The variation of $d\phi/dx$ in each diffuse layer is given by the classical Poisson–Boltzmann equation, which in case of a 1:1 electrolyte is

$$\left(\frac{d\phi}{dx} \right)_{x_2 < x < x_\infty} = \pm \sqrt{\frac{8RTc}{\epsilon}} \sinh \left[\frac{F}{2RT} (\phi_\infty - \phi_\infty) \right] \quad (17.3.2.16)$$

Since the model assumes the existence of a physical barrier between the two phases, it is possible to define the charge of the diffuse layer by

$$\sigma = \pm \sqrt{8RTc\epsilon} \sinh \left[\frac{F}{2RT} (\phi_2 - \phi_\infty) \right] \quad (17.3.2.17)$$

The electroneutrality of the interface $\sigma^o = -\sigma^w$ leads to two important relations

$$\epsilon^o \left(\frac{d\phi}{dx} \right)_{x=\chi_2^0} = \epsilon^w \left(\frac{d\phi}{dx} \right)_{x=\chi_2^w} \quad (17.3.2.18)$$

and

$$\frac{\sinh[F(\phi_2^w - \phi_\infty^w)/2RT]}{\sinh[F(\phi_2^o - \phi_\infty^o)/2RT]} = -\sqrt{\frac{\epsilon^o c^o}{\epsilon^w c^w}} \quad (17.3.2.19)$$

From equation (17.3.2.19), the potential drop in each diffuse layer can be calculated as a function of the difference $\Delta_o^w \phi - \Delta\phi_i$. Furthermore, the potential drop in the inner layer can also be calculated. The interesting conclusion of this work is that the potential drop across the inner layer was found to be negligible.

(b) GS (Girault–Schiffrin) model

Girault and Schiffrin (54) proposed a new model to explain the interfacial structure according to surface tension (32) and capacitance measurements (55), which have given access to important interfacial quantities such as surface excess concentrations and have shown that there is no inner layer of oriented solvent molecules and consequently no interfacial potential drop (54, 56, 57). They suggested that the interface could be regarded as a mixed solvent layer, no more than of two or three molecular diameter thickness. The model is illustrated in Figure 17.3.4, and shows that the penetration of the ions in the interfacial region depends on their hydrophobicity or hydrophilicity. Hydrophilic ions like potassium or chloride tend not to enter the interfacial region as shown by positive excess concentration of water (Figure 17.3.4A) (54). On the other hand, at the interface between two electrolytes having a common hydrophobic cation (e.g., TBACl/TBATPB), this cation

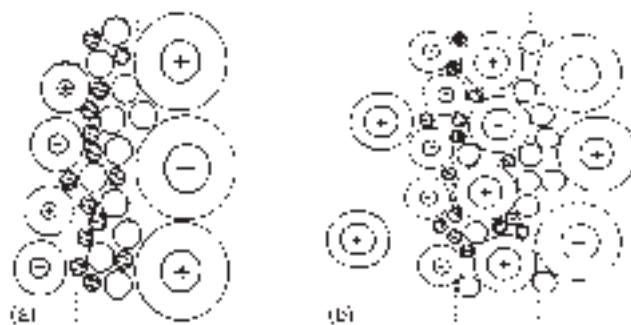


Figure 17.3.4 Mixed solvent model. (A) KCl/TBAPB system (polarizable interface); (B) TBACl/TBAPB system (non-polarizable interface). (Reprinted with permission from (54). Copyright 1985 Elsevier Science).

will freely penetrate the interface to such an extent as to be specifically adsorbed (Figure 17.3.4B). It is expected that the variation of standard chemical potential which represents the Gibbs energy of transfer takes place within this mixed solvent layer.

17.3.3 Charge transfer reactions at liquid/liquid interfaces

One of the characteristics of electrochemistry at liquid/liquid interfaces is the diversity of charge transfer reactions which can be studied by electrochemical methodologies (6). These charge transfer reactions can be classified into three main categories: (a) ion transfer (IT) reaction; (b) facilitated ion transfer (FIT) reaction; (c) electron transfer (ET) reaction.

17.3.3.1 Ion transfer reactions

Ion transfer reactions are perhaps the easiest to investigate. When an ion has a relatively low Gibbs energy of transfer and its value is within the potential window of the experimental system, its transfer can occur while the liquid/liquid interface is polarized. Figure 17.3.5 shows one example. The potential window is about 500 mV (Figure 17.3.5A) and the transfer of acetylcholine (Ac^+) is at the middle of the potential window (Figure 17.3.5B). In contrast to ET reactions at a solid/electrolyte interface, the valence state of the ion does not change so that only the solvation is varied while the transfer is occurring. Since the first report by Gavach *et al.* in 1974 describing the observation of TBA^+ transfer at the polarized W/NB interface, there have been numerous investigations on this subject, ranging from simple inorganic and organic ions to drugs and biomolecules (2, 3, 34, 58, 59). Most of the IT reactions are fast and can be considered as reversible (6).

Equation (17.3.2.7) is the Nernst equation for ion transfer reactions at equilibrium. The resemblance with the classical Nernst equation for redox reactions implies that all of the electrochemical methods for reversible reactions where the Nernst equation is used as a boundary condition for the resolution of Fick's diffusion equations can be directly transposed (6).

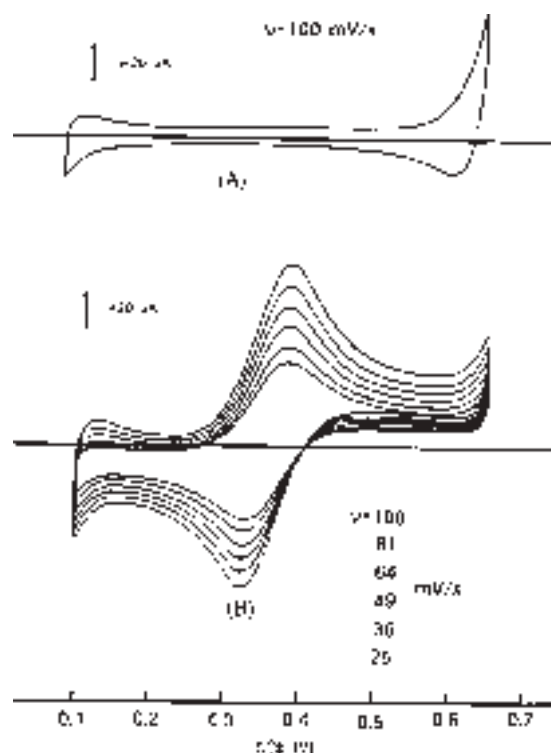


Figure 17.3.5 Voltammograms of the following systems: (A) Aqueous phase: 0.01 M LiCl + 0.3 M Li₂SO₄; (B) aqueous phase: 0.4 mM AcCl + 0.01 M LiCl + 0.3 M Li₂SO₄. Dichloromethane phase: 0.01 M TBATPBCl ((33), page 94).

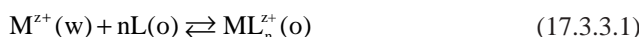
Determination of the rate constant of IT reactions has been a focus in the past 20 years (2, 3, 6). From a phenomenological point of view, an IT reaction includes three major steps:

- (1) Mass transfer in one phase to the interface (mainly diffusion);
- (2) Ion transfer reaction;
- (3) Mass transfer in the other phase away from the interface.

Scanning electrochemical microscopy (SECM) (Chapter 12) is one method that can provide reliable and precise measurement of rate constants of IT reactions (60). Marcus recently formulated the theory for ions transfer reaction at a L/L interface and proposed a mechanism involving initial desolvation of an ion from the first phase, A, and concerted solvation by the second phase, B (61). Although there has been significant experimental progress in this area, the mechanism is still uncertain. Regardless of these mechanistic uncertainties, IT reactions can be used in many applications as will be discussed below.

17.3.3.2 Facilitated ion transfer reactions

When an ion has relatively higher (or lower) Gibbs energy of transfer at a liquid/liquid interface, its transfer wave normally appears outside of the potential window or very near the positive or negative end of the potential window, so that it is difficult to study the simple IT reaction directly. In order to solve such a problem, a ligand which can complex with the ion can be chosen to be put into either phase to lower the Gibbs energy of transfer. Thus, its transfer can be adjusted to be within the potential window. Such a process is called facilitated IT reaction and can be expressed as follows:



Koryta reported the first FIT reaction in 1979 (25), and this method can not only provide the stoichiometric information between the ion and the ligand, thermodynamic and kinetic parameters, but can also have applications in selective amperometric ion sensors, and in electro-assisted solvent extraction across liquid membranes (1, 2, 6, 62). Various ionophores, such as crown ethers, antibiotics, ETH series ionophores and calixarenes, have been used to facilitate cations transfer (1–6). Recently anion transfers facilitated by ionophores have also been observed (63, 64).

In 1991 Girault *et al.* (65) proposed a mechanism for FIT reactions (see Figure 17.3.6). Depending upon the distribution coefficient of the ligand, four possible mechanisms can be outlined as follows:

- (1) Transfer by interfacial complexation (TIC);
- (2) Transfer by interfacial dissociation (TID);
- (3) Transfer followed by organic phase complexation (TOC);
- (4) Aqueous complexation followed by the transfer of the complex (ACT).

In the case of TIC, one has to consider the mass transport of the different reactants to the interface. For a 1:1 complexation reaction with the TIC mechanism where either the ion in

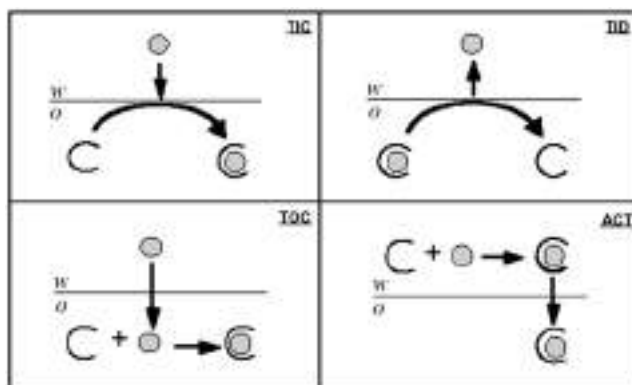


Figure 17.3.6 Mechanisms of the FIT reaction at a liquid/liquid interface. (Reprinted with permission from (65). Copyright 1991 Elsevier Science).

one phase or the ligand in the other phase is in excess with respect to the other, the mass transport problem is equivalent to that of a redox reaction on a solid electrode. For the remaining cases, either numerical simulations or simplifying approximations are required to understand the mass transport problem.

In 1991, Matsuda *et al.* (66) developed the general theory for a FIT reaction. The equations obtained are too complicated to be applied directly even for the simplest case of 1:1 complexation. However, under the following two limiting conditions, i.e., $C_M \gg C_L$ and $C_L \gg C_M$ (C_s are the bulk concentration of metal ion and ligand), the current–potential relationship can be simplified for 1:1 complexation (the following two equations respond to the $C_M \gg C_L$, and a TIC process)

$$\Delta_o^w \phi = \Delta_o^w \phi^{1/2} + \frac{RT}{zF} \ln\left(\frac{I}{I_1 - I}\right) \quad (17.3.3.2)$$

where

$$\Delta_o^w \phi^{1/2} = \Delta_o^w \phi^{0'} - \frac{RT}{zF} \ln \xi + \frac{RT}{zF} \ln \left(\frac{1 + \xi K_{P,L} + K_a^w C_M^w}{K_{P,L} K_a^o C_M^w} \right) \quad (17.3.3.3)$$

In these equations, I_1 is the diffusion limited current, the diffusion coefficients of all transferred species in the aqueous (or in the organic) phase are assumed to be equal to $D_w(D_O)$, and $\xi = (D_O / D_w)^{1/2}$. K_{PL} and K_a are respectively the distribution coefficient of the ligand and the complexation constants in both phases.

The relationship between the cation concentration and the half-wave potential can be discussed based on the following three regions:

- (1) If $1 + \xi K_{P,L} > 20 K_a^w C_M^w$, the half-wave potential will shift about 59 mV when the concentration of cation varies 10-folds. This inequality usually corresponds to the TIC mechanism.
- (2) If $1 + \xi K_{P,L} < 20 K_a^w C_M^w$, the half-wave potential is independent of the concentration of the cation. The complexation constant in the aqueous phase is large and corresponds to the ACT case.
- (3) If $1 + \xi K_{P,L} \sim 20 K_a^w C_M^w$, then the region is a mixture of the preceding two processes and is difficult to be analyzed quantitatively. Matsuda *et al.* further defined another function F_A (65).

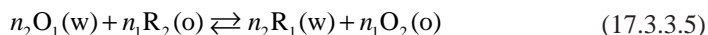
$$\begin{aligned} F_A &= \exp[(zF/RT)(\Delta\phi^{1/2} - \Delta\phi^{0'})] \\ &= (K_a^w / \xi K_a^o K_{P,L}) + [(1 + \xi K_{P,L})/\xi K_a^o K_{P,L}] (1/C_M^w) \end{aligned} \quad (17.3.3.4)$$

If K_{PL} is known, then K_a^w and K_a^o can be evaluated from a plot of F_A vs. $1/C_M^w$. Under the condition of $1 + \xi K_{P,L} > 20 K_a^w C_M^w$, the plot will pass through the origin and K_a^o can be calculated from the slope. For $1 + \xi K_{P,L} < 20 K_a^w C_M^w$, the plot is a straight line and parallel to the abscissa. The intercept on the ordinate is $K_a^w / \xi K_a^o K_{P,L}$. Thus the majority of the thermodynamic parameters can be obtained from a simple liquid/liquid interface experiment.

Molecules with acid–base properties can also be classified as a FIT reaction. For instance, the protonated base BH^+ (neutral B) can be regarded either as a simple cation transfer reaction or as a proton transfer facilitated by the conjugated acid (67, 68). Finally, the FIT by ion-pair formation can also be classified into this category (6).

17.3.3.3 Electron transfer reactions

Electron transfer at a liquid/liquid interface is an example of an interfacial heterogeneous ET reaction occurring between a redox couple in an aqueous phase and another redox couple in an organic phase. The ET occurs either by external polarization of the interface or by the interfacial potential difference represented in equation (17.3.3.5) and schematically shown in Figure 17.3.7 (2, 6).



At equilibrium, the Galvani potential difference is

$$\Delta_{\text{o}}^{\text{w}}\phi = \frac{\mu_{\text{R}_1}^0 - \mu_{\text{O}_1}^0}{n_2 F} + \frac{\mu_{\text{O}_2}^0 - \mu_{\text{R}_2}^0}{n_1 F} + RT \ln \frac{a_{\text{R}_1} a_{\text{O}_2}}{a_{\text{O}_1} a_{\text{R}_2}} \quad (17.3.3.6)$$

In contrast to IT reactions, it is experimentally difficult to study ET reactions at a liquid/liquid interface because there are very few ideal systems. There are normally two requirements for such systems

- (1) The potentials of the redox couples in both phases cannot be very different;
- (2) The reactants and the products in the organic phase cannot be dissolved in the aqueous phase, and will not be transferred across the interface in their ionic forms.

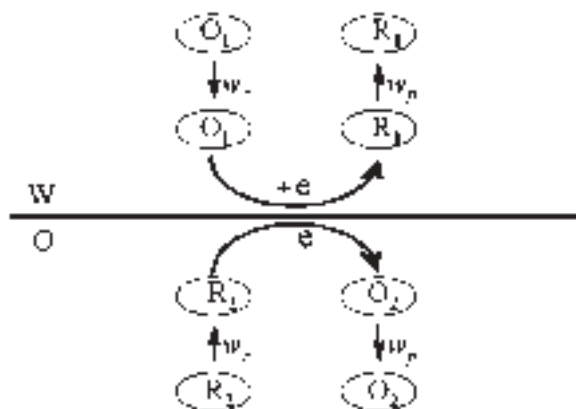


Figure 17.3.7 The schematic diagram of a heterogeneous ET reaction at a liquid/liquid interface.

Guaninazzi *et al.* found in 1975 that copper could be formed at the W/DCE interface under constant-current electrolysis and with CuSO₄ in the aqueous and tetrabutylammonium hexacarbonylvanadate in the organic phase (40). This was the first report of heterogeneous ET reaction at a liquid/liquid interface. Later on, Samec *et al.* and Schiffrin *et al.* investigated this subject systematically (69–73). Bard *et al.* studied heterogeneous ET reactions at a non-polarizable interface by varying concentration ratios of the common ion in both phases using SECM (the ET reactions are driven by the interfacial potential difference) (7, 60, 74–78). Recently, Shao *et al.* combined the three-electrode setup and SECM to probe the heterogeneous ET reactions at a polarizable interface (the interface is polarized by externally applied potential) (79, 80). In the past decade, interest in ET reactions at a liquid/liquid interface has been steadily increasing and many experimental problems have been solved (6, 7, 80).

Key issues in these developments are focused on the dynamics of heterogeneous ET as well as on the effect of the Galvani potential difference. Marcus proposed the theory for ET reactions at the interface between two dielectric media (81–84). Figure 17.3.7 shows the elementary steps involved in interfacial ET processes. The reduction of the species in phase w by the redox couple in phase o requires the diffusion of both species to the interface. The activation energy ΔG_{act} for the overall process is determined by the reorganization energy term λ , the formal Gibbs energy for the elementary ET, $\Delta G^{0'}$, and the work terms for the approach of the reactants, w_r , to the interface and the departure of the product, w_p , away from the interface (6).

$$\Delta G_{\text{act}} = (\lambda + \Delta G^{0'} + w_p - w_r)/4\lambda \quad (17.3.3.7)$$

For outer-sphere ET reactions where no substantial changes in the structure of the redox species are involved, the reorganization energy is dominated by the solvent contribution λ_s . In the case of W/DCE, Girault has solved the expression for λ_s (85).

The dependence of the activation energy on the Galvani potential difference arises mainly from the three remaining parameters in equation (17.3.3.7). $\Delta G^{0'}$ can be obtained from the difference of the electrochemical potential of the redox couples. w_r and w_p depend upon the changes of the solvation energy and ionic atmosphere of the reactants and products. The Galvani potential difference across the interface can effectively induce changes in all these parameters. Therefore, the observed potential dependence of the ET rate constant can arise from two phenomena:

- (1) Variations in the interfacial concentration of the reactants;
- (2) Changes in the free energy of the elementary step (6).

Shao *et al.* recently demonstrated that the dependence of the heterogeneous ET rate constant on the interfacial potential difference (also called driving force) follows the Marcus theory and observed the Marcus inverted region (79, 80).

Another very interesting type of heterogeneous ET reaction involves photo-excitatory dye molecules adsorbed at liquid/liquid interfaces. Such reactions are important for fundamental aspects of photosynthesis and solar energy conversion (86–88).

17.3.4 Methodologies and techniques

From an experimental point of view, the difficulties encountered for electrochemical measurements at a liquid/liquid interface are even more severe than that at a solid/electrolyte interface. This is because of the inherent problems of using organic solvents, such as high iR drop and the difficulty in separating the faradaic and charging currents. Despite these problems, almost all modern electrochemical techniques have been applied to study charge transfer reactions at liquid/liquid interfaces (2). For example, methods including cyclic voltammetry and techniques incorporating novel dropping (or ascending) water electrodes have all been employed (1, 2). Various spectroscopic techniques (87, 89, 90) and computer simulations (50–52) have been used in solving problems in this field in the past decade. SECM has emerged as a popular and powerful technique for obtaining reliable heterogeneous rate constants at a L/L interface (60).

17.3.4.1 Four-electrode system

For all experiments at a large planar liquid/liquid interface (mm- to cm-sized) a four-electrode system is usually adopted. A four-electrode potentiostat must be used in order to compensate the iR drop from both phases. The cell design used is shown in Figure 17.3.8. The interface is not fully planar because of curvature due to surface tension effects. The position of the interface is adjusted close to the organic and aqueous reference Luggin capillaries in order to minimize the influence of iR drop. Two counter electrodes made of platinum

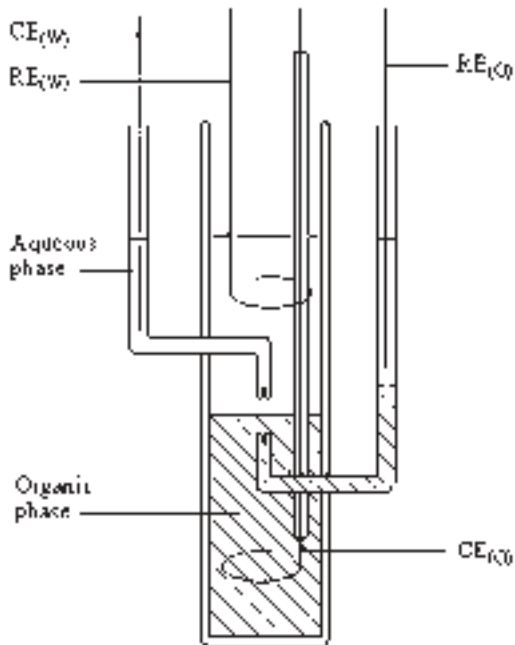


Figure 17.3.8 Schematic diagram of the four-electrode cell.

(wire or plate) are used for passing the current. The two reference electrodes are usually Ag/AgCl or one Ag/AgCl and another Ag/AgX (X = big anion, e.g., TPB⁻) and can be employed to control the external polarization. The majority of early thermodynamic and kinetic data gathered were from such a setup (1, 34).

17.3.4.2 Two-electrode system

A micro–liquid/liquid ($\mu\text{-L/L}$) interface is usually formed either at the tip of a pulled glass micropipet or within a small hole made in a thin membrane (8, 91, 92). Unlike solid ultramicroelectrodes (UMEs), such pipets or holes are easily made. Pipets as small as a few nanometer radii have recently been fabricated using a laser puller (93). Dual-pipets (or θ -pipets) can also be prepared by pulling θ -glass tubing (94–96). Another simple way of producing a $\mu\text{-L/L}$ interface in a microcavity is to chemically dissolve microwire encapsulated within a glass tube (97).

In 1986, Taylor and Girault introduced the $\mu\text{-L/L}$ interface supported at the tip of a micropipet (91). Under certain experimental conditions, the $\mu\text{-L/L}$ interface behaves like an UME. As in classical electrochemistry, which was revolutionized by the development of UMEs, many advantages can be obtained by replacing a large L/L interface with a $\mu\text{-L/L}$ interface. These advantages include minimization of charging current and iR drop, and a significantly increased mass transport rate. Micropipets can also be employed as probes for electrochemical imaging in SECM. The theory and application of electrochemistry at a $\mu\text{-L/L}$ interface has been reviewed (8).

Since the current passed at a $\mu\text{-L/L}$ interface is normally at nA to pA levels, electrochemical measurements can be simplified and a two-electrode system is usually employed. Figure 17.3.9 shows the typical electrochemical cell of a glass U-tube, which contains the organic reference solution in contact with the organic phase. The organic phase is covered with an aqueous layer to limit evaporation of the organic solvent during the experiment.

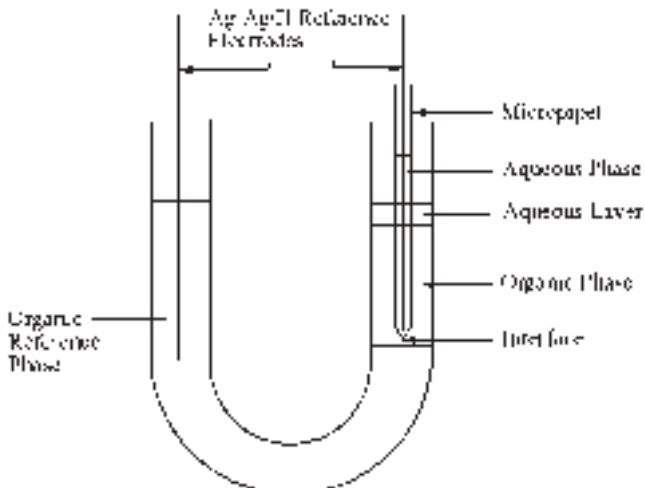


Figure 17.3.9 Schematic diagram of the two-electrode cell.

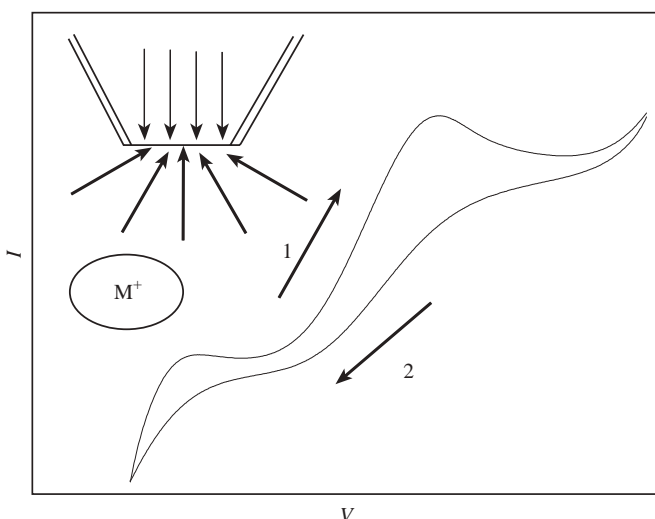


Figure 17.3.10 The asymmetric diffusion field (see the inset) and its corresponding asymmetric cyclic voltammogram at a μ -L/L interface supported at a micropipet. 1 corresponds to linear diffusion and 2 shows the steady-state voltammogram corresponding to hemispherical diffusion.

The specific geometry of the micropipet produces an asymmetric diffusion field, i.e., ion transfer from inside the pipet to outside is confined to a linear diffusion field which can produce a peak-shaped wave in cyclic voltammetry. In the reverse process, the diffusion field is hemispherical, which produces a steady-state wave in cyclic voltammetry (see the inset in Figure 17.3.10). This unique characteristic of micropipets has been used to identify species responsible for limiting the potential window as well as in the development of mechanisms for FIT reactions (47, 65). Dual-pipets have been used in the generation/collection mode for ionic processes, and these have employed to study complicated ET-IT and IT-IT coupling reactions (96).

17.3.4.3 Three-electrode system

Unlike the situation at a solid/electrolyte interface where a three-electrode system is used, four- and two-electrode systems have been widely employed for large and small liquid/liquid interfaces. Most of the four-electrode potentiostats are homemade and only a few instruments with such functions have been commercialized (98). This is probably one of the reasons why this field has not been very popular since most electrochemical laboratories are equipped with a three-electrode potentiostat. In 1998, Anson *et al.* reported that charge transfer reactions at a liquid/liquid interface could also be studied by a three-electrode system with a thin-layer cell (99, 100). Later, Scholz *et al.* reported a three-phase junction setup (101, 102). Shao *et al.* supported a small droplet of aqueous solution (μ L) containing a certain concentration ratio of redox couples on a Pt surface and demonstrated that charge transfer could be studied by a three-electrode setup (103). Girault *et al.* extended this to a supported small droplet of aqueous (organic) phase on the surface of

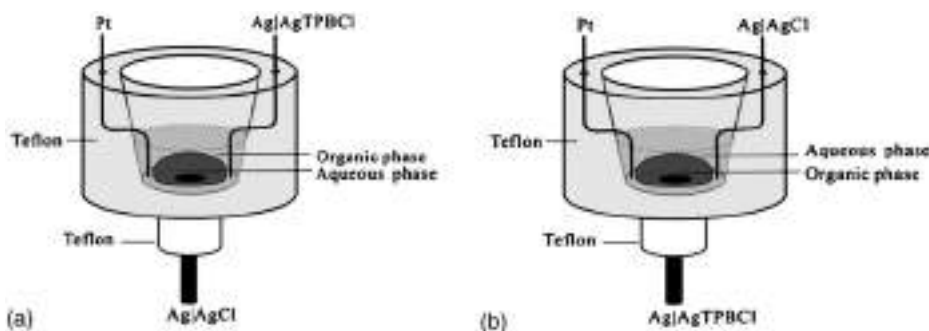


Figure 17.3.11 Schematic presentations of the electrochemical cells for the cases in which r is large (A) or small (B). (Reprinted with permission from (105). Copyright 2003 American Chemical Society).

Ag/AgCl (Ag/AgTPBCl) (104). Figure 17.3.11 shows the schematic representations of electrochemical cells, which can be used to study the phase volume ratio ($r = V_o/V_w$, V_o and V_w are respective organic and aqueous phase volume) effect (105).

For an aqueous droplet supported on a solid (Pt or C) electrode surface, the potential difference at the solid/liquid interface is fixed because the concentration ratio of the redox couples in the droplet is constant and it can be used as a pseudo-reference electrode. It forms a W/O interface when the assembly is immersed in an organic solution. The W/O interface formed between the aqueous droplet and the organic phase can be studied with a three-electrode system. The ET process at the solid/liquid interface and the charge transfer processes at the liquid/liquid interface are coupled as reactions in series. The disadvantage of this setup is the cations associated with the redox couples usually limit the potential window and very few redox couples can be chosen (103). The droplet supported on Ag/AgCl or Ag/AgX (X is a big anion) can function similarly and only needs Cl^- (or X^-) to be present in the aqueous (organic) droplet to fix the potential difference at the solid/liquid interface. In this way one can obtain a wider potential window and study the effect of the phase volume ratio on charge transfer reactions at a L/L interface.

17.3.5 Applications

In the past 10 years, more and more applications of charge transfer reactions at liquid/liquid interfaces have been demonstrated (1–10). The following are some examples.

17.3.5.1 Pharmacokinetics

In pharmaceutical sciences, $\log P$ is an important parameter, which is defined as $\log P = \log(a_i^o/a_i^w)$ (where α is the activity of species i in both phases). Lipophilicity represents the affinity of a compound for a lipidic environment, and has been widely used to design drugs and to assess their performances. It is commonly measured by its partition coefficient in a biphasic system, P . Therefore, $\log P$ is actually related to the difference in

solvation energy between water and the adjacent organic phase, and is then directly related to the Gibbs energy of transfer (6).

Since the Gibbs energy of transfer of a species can be easily determined by cyclic voltammetry at a liquid/liquid interface, numerous compounds of biological interest have been studied in the past 20 years (2). In pharmaceutical sciences, a commonly used $\log P$ is based on an interface between water and *n*-octanol. However, many compounds have very low solubility in *n*-octanol and hydrogen-bonding between water and *n*-octanol exists. These factors make direct electrochemical measurements difficult (107, 108). Girault *et al.* demonstrated that the water/DCE system could be used to replace the water/*n*-octanol system. They transposed the Pourbaix's pH–potential diagrams to include biphasic systems and established the ionic partition diagram which can be used to predict and interpret the transfer mechanism of ionizable species (6, 106, 109). This method consists of measurements of equiconcentration boundaries as a function of the interfacial Galvani potential difference $\Delta_{\text{g}}^{\text{w}}\phi$ and aqueous pH by taking account of the thermodynamic equilibria governing the distribution of the various acid–base forms of the molecule involved in the transfer. Figure 17.3.12 shows the particular case of the anti-arrhythmic drug quinidine. The ionic partition diagram defines the domains of predominance of each species either in the aqueous or in the organic phase and it offers a general and direct visualization of all the transfer mechanisms. The amperometric determination of the pH-lipophilicity profile of drugs by electrochemistry at liquid/liquid interfaces will become an important competitor to the potentiometric two-phase titration which is the most popular technique to date (109).

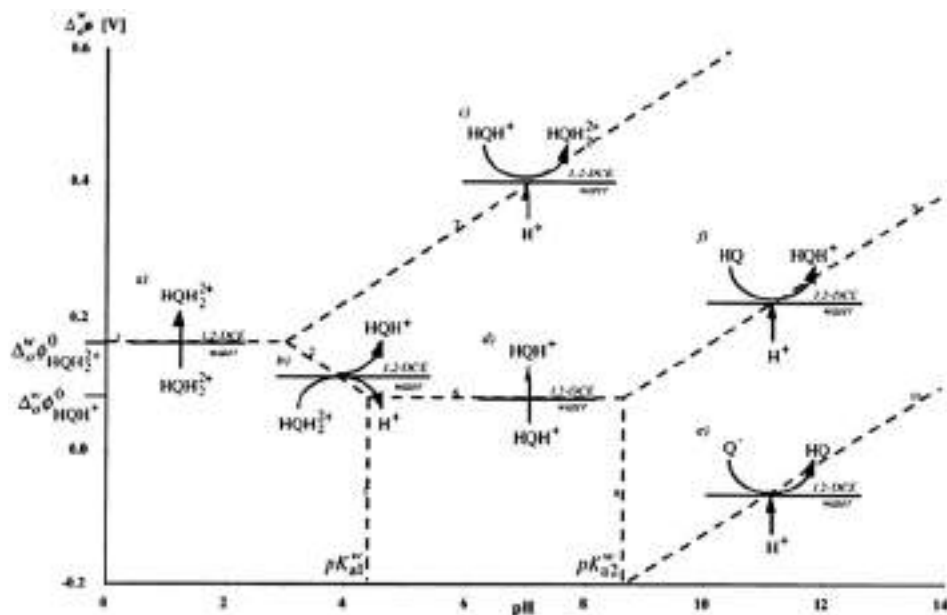


Figure 17.3.12 Ionic partition diagram of quinidine in water/DCE interface at 21°C. (Reprinted with permission from (106). Copyright 1996 American Chemical Society).

17.3.5.2 Amperometric sensors

Since most IT and FIT reactions are reversible and the currents resulting from them are proportional to their concentrations, they can be used to design amperometric ion sensors (5, 6). The main advantage of such an approach is that selectivity may be tailored by the choice of the ionophore and by the polarization potential. The main disadvantages are (1) the mechanical instability of the interface and (2) the large iR drop resulting from the toxic organic phase. It is possible to adopt gel electrolytes to overcome the former and charge transfer reactions at liquid/polymer-gel and agar-gel/liquid interfaces have been successfully applied in designing such amperometric sensors (110–114).

Minimization is the way to circumvent the problems caused by iR drop. One good example is the iondes, which consist of a thin inert polymer layer. They are micro-perforated and covered by a polyvinylchloride-2-nitrophenyloctylether (PVC-NPOE) electrolyte gel and can be incorporated in a flowing cell (Figure 17.3.13). Various ionophores have been put into the gel matrix in order to fabricate amperometric detectors for the measurements of different ions (115–118). Less toxic solvents such as NPOE have been employed to replace toxic NB or DCE (118).

The amperometric sensors based on FIT reactions can determine either ionophore (when metal ion is in excess) or metal ion (when ionophore is in excess). One example is the determination of trace Hg(II) and Pb(II) in water at a macro-L/L interface using stripping voltammetry where the organic phase has excess concentration of suitable ionophore with detection limits as low as 1.6 and 1 ppb, respectively (119).

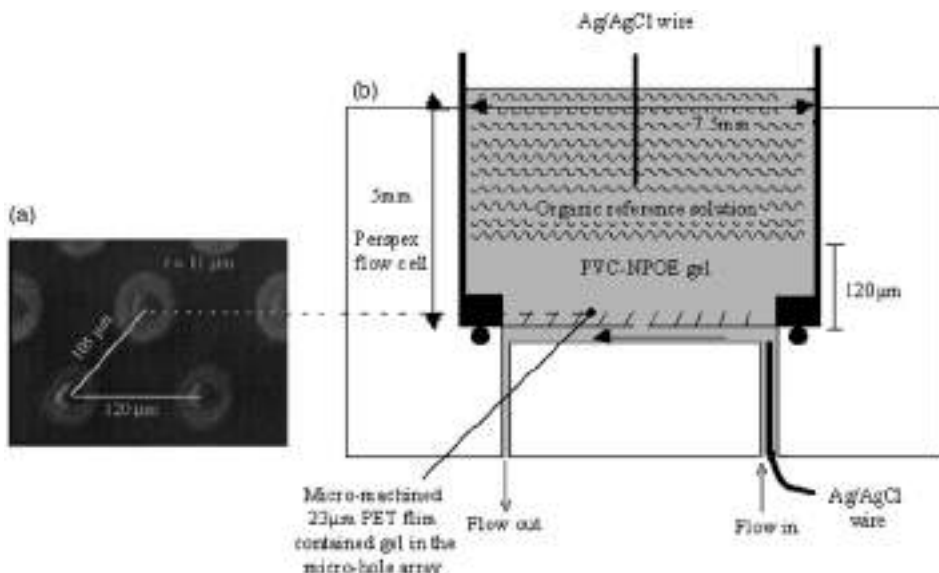


Figure 17.3.13 (a) SEM of the entrance-side holes in an array with PVC-NPOE gel cast at 70 °C. (b) Simplified diagram of the setup for flow experiment. (Reprinted with permission from (118). Copyright 1997 Elsevier Science).

17.3.5.3 Electrochemical imaging

Another important aspect of charge transfer reactions at a L/L interface is that all three types of transfer reactions can be employed to obtain imaging of various kinds of substrates and information about reactivity (5, 60). In a SECM imaging experiment, a micropipet can replace a solid tip and serve as a probe or tip. SECM imaging is obtained by rastering the tip above the substrate, either solid or liquid, and recording the variations in the tip current.

Solomon and Bard reported the first such application (74). The ET between aqueous ferrocyanide inside a micropipet and TCNQ in the outer DCE phase was used for SECM imaging. TCNQ was reduced by ferrocyanide to form TCNQ^- at the tip. The images of surface topography and redox reactivity of parallel platinum bands on the silicon surface were obtained by scanning a micropipet in a horizontal x-y plane just a few micrometers above the substrate surface.

IT-based SECM imaging can be performed with a micropipet containing the same ion (M^+) as that in another phase (120). The IT reaction at the L/L interface can be induced by the depletion of the concentration of this ion in the top solution near the interface caused by the polarization of the micropipet, which can provide positive feedback if the bottom phase has a sufficiently high concentration of M^+ . The images of a 5 μm pore in a polycarbonate membrane were obtained by a 3 μm diameter pipet based on the transfer of tetraethylammonium (TEA^+) across the W/DCE interface.

The SECM positive-negative feedback mode can also be achieved based on FIT reactions at the L/L interface (121). Figure 17.3.14 illustrates the principle. The tip current can be produced by transferring K^+ , facilitated by DB18C6, from the aqueous phase inside the micropipet to the outer DCE phase. When the tip is biased at a sufficiently positive potential, the tip current is limited by the diffusion of DB18C6 to the interface. As the tip approaches the bottom aqueous phase, K^+ is released from the complex and transferred to

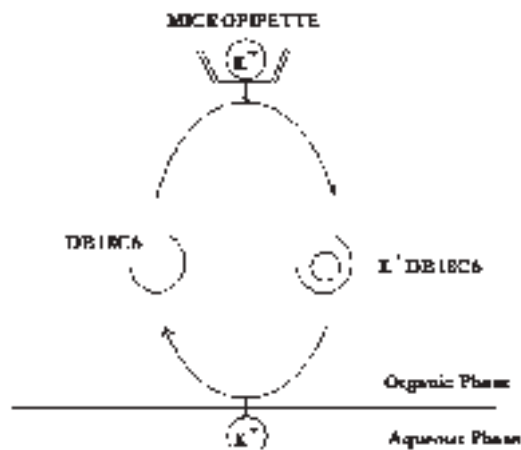


Figure 17.3.14 Schematic diagram of SECM operating in the FIT mode. (Reprinted with permission from (121). Copyright 1997 Elsevier Science).

the aqueous phase. Here DB18C6 serves just as a mediator in the conventional SECM feedback experiments and is regenerated via an interfacial dissociation mechanism. Therefore, the tip current can be enhanced and a positive feedback can be produced. If a solid substrate is probed by this approach, a negative feedback will occur.

This approach has been used to probe K⁺ transfer through gramicidin channels in a BLM (77), and to fabricate micro-patterns on a solid surface (122).

As mentioned in a recent review article by Girault *et al.* (6), potential applications can also be found in the areas of electrocatalysis and solar energy conversion, Marangoni pumps, electro-assisted solvent extraction and thermoelectricity, and phase transfer catalysis (123).

17.3.6 Prospects

Electrochemistry at liquid/liquid interfaces has progressed markedly in the past 30 years. Excellent work on modified liquid/liquid interface with lipids and nanoparticles have been reported (75, 78, 124–127). Droplet electrodes and three-phase junctions have made this field more popular and versatile (102, 103, 128). The ET induced IT reactions at three-phase junction have been employed to obtain the log P of different drugs at W/n-octanol interfaces (102, 129, 130). New and less toxic solvents, such as room temperature ionic liquids (RTILs) have replaced organic solvents to form W/RTIL interfaces (131, 132). However, from a theoretical point of view, the key aspects of potential distribution remain the major challenge. Only a few biological applications have been so far reported based on the techniques developed from this field.

Acknowledgments

This work is supported by the National Natural Science foundation of China (#20235010, #20475003, #20173058, and #20420130137) and special 985 project of Peking University. I appreciate the help of my students Zhong Chen, Zhongwei Liang, Meiqin Zhang in drawing the Figures.

REFERENCES

1. A. G. Volkov, D. W. Deamer, Eds., *Liquid-liquid Interfaces: Theory and Methods*, CRC Press: Boca Raton, FL, 1996.
2. A. G. Volkov, Ed., *Liquid Interfaces in Chemical, Biological, and Pharmaceutical Applications*, Marcel Dekker: New York, 2001.
3. H. H. Girault in *Modern Aspects of Electrochemistry*, J. O' M. Bockris, B. E. Conway, R. E. White, Eds., Plenum: New York, 1993, Vol. 25.
4. P. Vanysek in *Modern Electroanalytical Techniques, Chemical Analysis Series*, P. Vanysek, Ed., John Wiley: New York, 1996, Vol. 139.
5. B. Liu, M. V. Mirkin, *Anal. Chem.* **73**, 670A (2001).
6. F. Reymond, D. Fermin, H. J. Lee, H. H. Girault, *Electrochim. Acta* **45**, 2647 (2000).

7. S. Amemiya, Z. Ding, J. Zhou, A. J. Bard, *J. Electroanal. Chem.* **483**, 7 (2000).
8. B. Liu, M. V. Mirkin, *Electroanalysis* **12**, 1433 (2000).
9. Z. Samec, *Pure Appl. Chem.* **76**, 2147 (2004).
10. P. Vanysek, *Electrochemistry at Liquid-Liquid Interfaces, Lecture Notes in Chemistry*, Springer: Berlin, 1985, Vol. 39.
11. W. Nernst, E. H. Risenfield, *Ann. Phys.* **8**, 600 (1902).
12. M. Cremer, *Z. Biol.* **47**, 562 (1906).
13. W. Ostwald, *Z. Phys. Chem.* **6**, 71 (1890).
14. E. L. W. Verwey, K. F. Niessen, *Phil. Mag.* **28**, 435 (1939).
15. J. Guastalla, *Proc. 2nd Int. Congr. Sur. Act.* **3**, 112 (1957).
16. M. Blank, *J. Colloid. Interface Sci.* **22**, 51 (1966).
17. C. Gavach, T. Mlodnicka, J. Guastalla, *C. R. Acad. Sci. C* **266**, 1196 (1968).
18. C. Gavach, F. Henry, *C. R. Acad. Series C* **274**, 1545 (1972).
19. C. Gavach, F. Henry, *J. Electroanal. Chem.* **54**, 361 (1974).
20. C. Gavach, P. Seta, B. D'Epenoux, *J. Electroanal. Chem.* **83**, 225 (1977).
21. Z. Samec, V. Marecek, J. Koryta, M. W. Khalil, *J. Electroanal. Chem.* **83**, 393 (1977).
22. Z. Samec, V. Marecek, J. Weber, *J. Electroanal. Chem.* **100**, 841 (1979).
23. J. Koryta, P. Vanysek, M. Brazina, *J. Electroanal. Chem.* **67**, 263 (1976).
24. J. Koryta, P. Vanysek, M. Brezina, *J. Electroanal. Chem.* **75**, 211 (1977).
25. J. Koryta, *Electrochim. Acta* **24**, 293 (1979).
26. J. Koryta, *Electrochim. Acta* **29**, 445 (1984).
27. J. Koryta, *Electrochim. Acta* **33**, 189 (1988).
28. O. R. Melroy, B. P. Buck, *J. Electroanal. Chem.* **136**, 19 (1982).
29. Z. Yoshida, H. Freiser, *J. Electroanal. Chem.* **162**, 307 (1984).
30. M. Senda, T. Kakutani, *Hyomen* **18**, 535 (1980).
31. S. Kihara, Z. Yoshida, T. Fujinaga, *Bunseki Kagaku* **31**, E297 (1982).
32. H. H. Girault, D. J. Schiffrin, *J. Electroanal. Chem.* **150**, 43 (1983).
33. Y. Shao, Ph. D. Thesis, Edinburgh University, 1991.
34. H. H. Girault, D. J. Schiffrin in *Electroanalytical Chemistry*, A. J. Bard, Ed., Marcell Dekker: New York, 1989, Vol. 15.
35. H. H. Girault, D. J. Schiffrin, *Electrochim. Acta* **31**, 1341 (1986).
36. <http://lepa.epfl.ch/cgi/DB/InterrDB.pl>.
37. Y. Marcus, *Pure Appl. Chem.* **55**, 977 (1983).
38. J. Koryta, P. Vanysek in *Advances in Electrochemistry and Electrochemical Engineering*, H. Gerischer, C. W. Tobias, Eds., John Wiley: New York, 1981, Vol. 12.
39. J. Guastalla, *J. Chim. Phys.* **53**, 470 (1956).
40. M. Guainazzi, G. Silversti, G. Serravalle, *J. Chem. Soc. Chem. Commun.* **6**, 200 (1975).
41. Z. Samec, D. Homolka, V. Marecek, L. Kavan, *J. Electroanal. Chem.* **145**, 213 (1983).
42. O. Valent, J. Koryta, *J. Electroanal. Chem.* **226**, 1 (1987).
43. P. Vanysek, *Anal. Chem.* **62**, 827A (1990).
44. Z. Koczorowski, I. Paleska, G. Gleblewicz, *J. Electroanal. Chem.* **164**, 201 (1984).
45. Y. Shao, J. A. Campbell, H. H. Girault, *J. Electroanal. Chem.* **300**, 415 (1991).
46. D. Homolka, L. Hung, A. Hofmanova, M. W. Khalil, J. Koryta, V. Marecek, Z. Samec, S. K. Sen, P. Vanysek, J. Weber, M. Janda, I. Stiber, *Anal. Chem.* **52**, 1606 (1980).
47. A. A. Stewart, Y. Shao, C. M. Pereira, H. H. Girault, *J. Electroanal. Chem.* **305**, 135 (1991).
48. T. Wandlowski, V. Marecek, K. Holub, Z. Samec, *J. Phys. Chem.* **93**, 8204 (1989).
49. A. Brown, Ph.D. Thesis, Edinburgh University, 1992.
50. I. Benjamin, *J. Chem. Phys.* **97**, 1432 (1992).
51. I. Benjamin, *Chem. Rev.* **96**, 1449 (1996).

52. I. Benjamin, *Annu. Rev. Phys. Chem.* **48**, 407 (1997).
53. M. Gros, S. Gromb, C. Gavach, *J. Electroanal. Chem.* **89**, 29 (1978).
54. H. H. Girault D. J. Schiffrrin, *J. Electroanal. Chem.* **195**, 213 (1985).
55. Z. Samec, V. Marecek, D. Homolka, *Faraday Discuss. Chem. Soc.* **77**, 197 (1984).
56. H. H. Girault, *Electrochim. Acta* **32**, 383 (1987).
57. H. H. Girault, *J. Electroanal. Chem.* **257**, 47 (1988).
58. M. Senda, *Anal. Sci. Technol.* **8**, 95A (1995).
59. S. Amemiya, X. Yang, T. L. Wazenegger, *J. Am. Chem. Soc.* **125**, 11832 (2003).
60. A. J. Bard, M. V. Mirkin, Eds., *Scanning Electrochemical Microscopy*, Marcel Dekker: New York, 2001.
61. R. A. Marcus, *J. Chem. Phys.* **113**, 1618 (2000).
62. M. Senda, T. Kakiuchi, T. Osakai, *Electrochim. Acta* **36**, 253 (1991).
63. Y. Shao, B. Linton, A. D. Hamilton, S. W. Weber, *J. Electroanal. Chem.* **441**, 33 (1998).
64. T. Shioya, S. Nishizawa, N. Teramae, *J. Am. Chem. Soc.* **120**, 11534 (1998).
65. Y. Shao, M. Osborne, H. H. Girault, *J. Electroanal. Chem.* **308**, 101 (1991).
66. H. Matsuda, Y. Yamada, K. Kanamori, Y. Kudo, Y. Takeda, *Bull. Chem. Soc. Jpn.* **64**, 1497(1991).
67. E. Wang, Z. Sun, *J. Electroanal. Chem.* **220**, 235 (1987).
68. K. Kontturi, L. Murtomaki, *J. Pharm. Sci.* **81**, 970 (1992).
69. Z. Samec, V. Marecek, J. Weber, *J. Electroanal. Chem.* **96**, 245 (1977).
70. Z. Samec, V. Marecek, J. Weber, *J. Electroanal. Chem.* **103**, 11 (1979).
71. Z. Samec, V. Marecek, J. Hovorka, *J. Electroanal. Chem.* **216**, 303 (1987).
72. G. Geblewicz, D. J. Schiffrrin, *J. Electroanal. Chem.* **244**, 27 (1988).
73. V. J. Cunnane, D. J. Schiffrrin, C. Beltran, G. Geblewicz, T. Solomon, *J. Electroanal. Chem.* **247**, 203 (1988).
74. T. Solomon, A. J. Bard, *Anal. Chem.* **67**, 2787 (1995).
75. M. Tsionsky, A. J. Bard, M. V. Mirkin, *J. Am. Chem. Soc.* **119**, 10785 (1997).
76. C. Wei, A. J. Bard, M. V. Mirkin, *J. Phys. Chem.* **99**, 16033 (1995).
77. M. Tsionsky, A. J. Bard, M. V. Mirkin, *J. Phys. Chem.* **100**, 17881 (1996).
78. M. Tsionsky, J. F. Zhou, S. Amemiya, F. Fan, A. J. Bard, R. A. W. Dryfe, *Anal. Chem.* **71**, 4300 (1999).
79. Z. Zhang, Y. Yuan, P. Sun, B. Su, J. Guo, Y. Shao, H. H. Girault, *J. Phys. Chem. B* **106**, 6713 (2002).
80. P. Sun, F. Li, Y. Chen, M. Zhang, Z. Zhang, Z. Gao, Y. Shao, *J. Am. Chem. Soc.* **125** , 9600 (2003).
81. R. A. Marcus, *J. Phys. Chem.* **94**, 1050 (1990).
82. R. A. Marcus, *J. Phys. Chem.* **94**, 4152 (1990).
83. R. A. Marcus, *J. Phys. Chem.* **94**, 7742 (1990).
84. R. A. Marcus, *J. Phys. Chem.* **95**, 2010 (1991).
85. H. H. Girault, *J. Electroanal. Chem.* **388**, 93 (1995).
86. D. J. Fermin, Z. Ding, H. D. Duong, P. F. Brevet, H. H. Girault, *Chem. Comm.* 1125 (1998).
87. D. J. Fermin, Z. Ding, H. D. Duong, P. F. Brevet, H. H. Girault, *J. Phys. Chem. B* **102**, 10334 (1998).
88. D. J. Fermin, Z. Ding, H. D. Duong, P. F. Brevet, H. H. Girault, *Phys. Chem. Chem. Phys.* **1**, 1461 (1999).
89. P. S. Pershan, *J. Chem. Soc. Faraday Discuss.* **89**, 231 (1990).
90. J. Penfold, R. K. Thomas, *J. Phys. A.* **2**, 1369 (1990).
91. G. Taylor, H. H. Girault, *J. Electroanal. Chem.* **208**, 179 (1986).
92. J. A. Campbell, H. H. Girault, *J. Electroanal. Chem.* **266**, 465 (1989).

93. Y. Shao, M. V. Mirkin, *J. Am. Chem. Soc.* **119**, 8103 (1997).
94. Y. Shao, B. Liu, M. V. Mirkin, *J. Am. Chem. Soc.* **120**, 12700 (1998).
95. B. Liu, Y. Shao, M. V. Mirkin, *Anal. Chem.* **72**, 510 (2000).
96. Y. Chen, Z. Gao, F. Li, L. H. Ge, M. Q. Zhang, D. P. Zhan, Y. Shao, *Anal. Chem.* **74**, 6593 (2003).
97. V. J. Cunnane, D. J. Schiffrian, D. E. Williams, *Electrochim Acta* **40**, 2943 (1995).
98. Y. Shao, S. N. Tan, V. Devaud, H. H. Girault, *J. Chem. Soc. Faraday Trans.* **89**, 4307 (1993).
99. C. Shi, F. C. Anson, *J. Phys. Chem. B* **102**, 9850 (1998).
100. T. Chung, F. C. Anson, *Anal. Chem.* **73**, 337 (2001).
101. F. Scholz, S. Komorsky-Lovric, M. Lovric, *Electrochim. Commun.* **2**, 112 (2000).
102. R. Gulaboski, V. Mirceski, F. Scholz, *Electrochim. Commun.* **4**, 277 (2002).
103. S. Ulmeanu, H. Lee, D. J. Fermin, H. H. Girault, Y. Shao, *Electrochim. Commun.* **3**, 219 (2001).
104. V. Gobry, S. Ulmeanu, F. Reymond, G. Bouchard, P. Carrupt, B. Testa, H. H. Girault, *J. Am. Chem. Soc.* **123**, 10684 (2001).
105. M. Zhang, P. Sun, Y. Chen, F. Li, Z. Gao, Y. Shao, *Anal. Chem.* **75**, 4341 (2003).
106. F. Reymond, G. Steyaert, A. Pagliara, P. A. Carrupt, B. Testa, H. H. Girault, *J. Am. Chem. Soc.* **118**, 19511 (1996).
107. G. Caron, A. Pagliara, P. Guillard, P. A. Carrupt, B. Testa, *Helv. Chim. Acta* **79**, 1683 (1996).
108. R. N. Smith, C. Hansch, M. M. Ames, *J. Pharm. Sci.* **64**, 599 (1975).
109. F. Reymond, P. A. Carrupt, B. Testa, H. H. Girault, *Chem. Eur. J.* **5**, 39 (1999).
110. T. Osakai, T. Kakutani, M. Senda, *Bunseki Kagaku* **33**, E371 (1984).
111. T. Kakutani, T. Ohkouchi, T. Osakai, T. Kakiuchi, M. Senda, *Anal. Sci.* **1**, 219 (1985).
112. E. Wang, Z. Sun, *Trends Anal. Chem.* **7**, 99 (1988).
113. V. Marecek, H. Janchenova, M. P. Colombini, P. Papoff, *J. Electroanal. Chem.* **217**, 213 (1987).
114. V. Marecek, M. P. Colombini, *J. Electroanal. Chem.* **241**, 133 (1988).
115. H. J. Lee, C. Beriet, H. H. Girault, *J. Electroanal. Chem.* **453**, 211 (1998).
116. F. Silva, M. J. Sousa, C. M. Pereira, *Electrochim. Acta* **42**, 3095 (1997).
117. H. J. Lee, H. H. Girault, *Anal. Chem.* **70**, 4280 (1998).
118. H. J. Lee, P. D. Beattie, B. J. Seddon, M. D. Osborne, H. H. Girault, *J. Electroanal. Chem.* **440**, 73 (1997).
119. H. Ketano, M. Senda, *Anal. Sci.* **14**, 63 (1998).
120. Y. Shao, M. V. Mirkin, *J. Phys. Chem. B* **102**, 9915 (1998).
121. Y. Shao, M. V. Mirkin, *J. Electroanal. Chem.* **439**, 137 (1997).
122. Y. Yatziv, I. Turyan, D. Mandler, *J. Am. Chem. Soc.* **124**, 5618 (2002).
123. Y. Uchiyama, M. Fujinami, T. Sawada, I. Tsuyumoto, *J. Phys. Chem. B* **104**, 4699 (2000).
124. B. M. Quinn, P. Liljeroth, K. Kontturi, *J. Am. Chem. Soc.* **124**, 12915 (2002).
125. B. M. Quinn, K. Kontturi, *J. Am. Chem. Soc.* **126**, 7168 (2004).
126. R. A. W. Dryfe, A. O. Simm, B. Kralj, *J. Am. Chem. Soc.* **125**, 13014 (2003).
127. B. Su, J. P. Abid, D. J. Fermin, H. H. Girault, H. Hoffmannova, P. Krtil, Z. Samec, *J. Am. Chem. Soc.* **126**, 915 (2004).
128. P. Sun, Z. Zhang, Z. Gao, Y. Shao, *Angew. Chem. Int. Ed.* **41**, 3445 (2002).
129. R. Gulaboski, A. Galland, G. Bouchard, K. Caban, A. Kretschmer, P. A. Carrupt, Z. Stojek, H. H. Girault, F. Scholz, *J. Phys. Chem. B* **108**, 4565 (2004).
130. R. Gulaboski, F. Scholz, *J. Phys. Chem. B* **107**, 5650 (2003).
131. T. Kakiuchi, N. Tsujioka, S. Kurita, Y. Iwami, *Electrochim. Commun.* **5**, 159 (2003).
132. T. Kakiuchi, N. Tsujioka, *Electrochim. Commun.* **5**, 253 (2003).

This page intentionally left blank

Part Five

DATA

This page intentionally left blank

— 18 —

Electrode Potentials

Melissa D. Arning and Shelley D. Minteer

Department of Chemistry, Saint Louis University,
3501 Laclede Ave., St. Louis, MO 63103, USA

18.1 OVERVIEW

The beginning of the chapter is dedicated to charts of operating potential ranges for different solvent/electrolyte/electrode combinations. Operating potentials can act as a guide for determining the maximum and minimum potential to apply to a system. The second half of the chapter includes tables of electrode potentials of organic redox couples, inorganic redox couples, biological redox couples, drugs, vitamins, and neurochemicals. Electrode potentials can be used in conjunction with operating potential ranges to determine the optimal solution/electrode for monitoring a given redox species.

18.2 ESTIMATED POTENTIAL RANGES: AQUEOUS AND NON-AQUEOUS SOLUTIONS

Figure 18.1 shows potential ranges (operating windows) for carbon, platinum, and mercury electrodes in aqueous solutions of common electrolytes. Figure 18.2 shows potential ranges (operating windows) for common organic solvents. Potential ranges are merely a guide and will vary with purity of solvent and electrolyte.

18.3 STANDARD ELECTRODE POTENTIALS: AQUEOUS SOLUTIONS

Table 18.1 contains a selected list of standard electrode potentials of common redox species in aqueous solutions. A more complete list can be found in reference (3) and a discussion on fundamental standard electrode potential concepts can be found in Chapter 1 of this handbook. All standard electrode potentials are vs. NHE and for solutions at room temperature.

18.4 FORMAL ELECTRODE POTENTIALS: APROTIC SOLVENTS

Table 18.2 lists formal electrode potentials for a series of organic redox species in common aprotic solvents. Due to variations in formal potentials with solvent and electrolyte

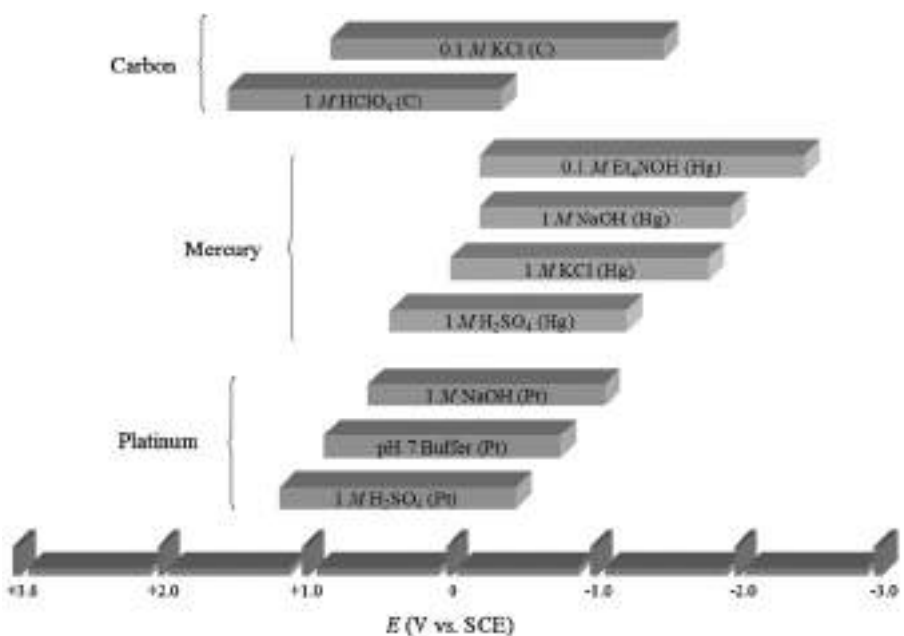


Figure 18.1 Estimated potential ranges in aqueous solutions at 25 °C. (for colour version: see colour section at the end of the book).

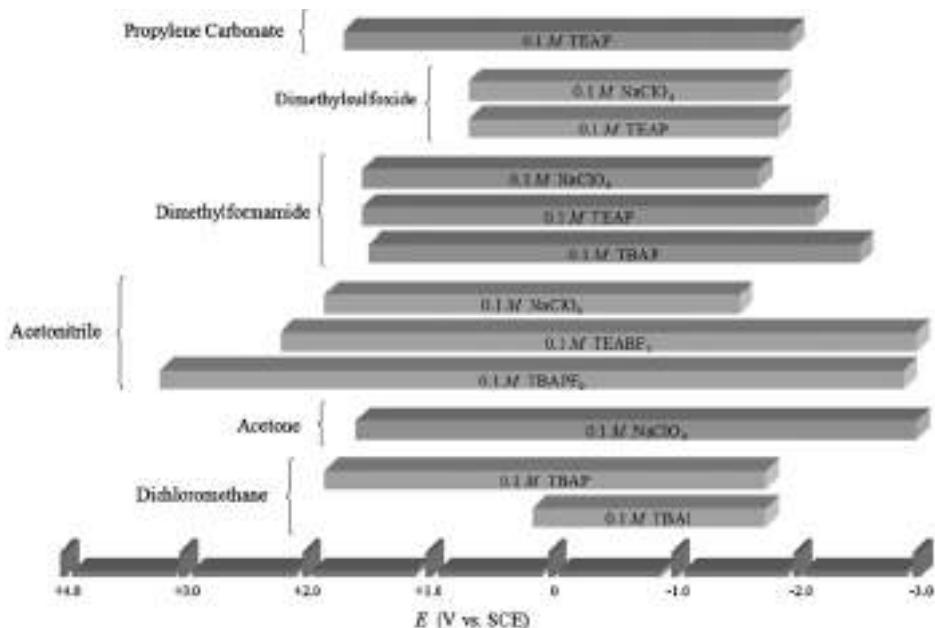


Figure 18.2 Estimated potential ranges at Pt electrodes for non-aqueous solvent/electrolyte solutions. Data from reference (1). (for colour version: see colour section at the end of the book).

Table 18.1

Selected standard electrode potentials (V vs. NHE) in aqueous solution at 25 °C. Data from references (2–4)

Reaction	E^0 (V vs. NHE)
$\text{Ag}^+ + e \rightleftharpoons \text{Ag}$	0.799
$\text{Ag}^{2+} + e \rightleftharpoons \text{Ag}^+$	1.980
$\text{AgBr} + e \rightleftharpoons \text{Ag} + \text{Br}^-$	0.071
$\text{AgCl} + e \rightleftharpoons \text{Ag} + \text{Cl}^-$	0.222
$\text{AgI} + e \rightleftharpoons \text{Ag} + \text{I}^-$	-0.152
$\text{Ag}_2\text{O} + \text{H}_2\text{O} + 2e \rightleftharpoons 2\text{Ag} + 2\text{OH}^-$	0.342
$\text{Al}^{3+} + 3e \rightleftharpoons \text{Al}$	-1.676
$\text{As} + 3\text{H}^+ + 3e \rightleftharpoons \text{AsH}_3$	-0.230
$\text{As(OH)}_3 + 3\text{H}^+ + 3e \rightleftharpoons \text{As} + 3\text{H}_2\text{O}$	0.240
$\text{AsO(OH)}_3 + 2\text{H}^+ + 2e \rightleftharpoons \text{As(OH)}_3 + \text{H}_2\text{O}$	0.560
$\text{Au}^+ + e \rightleftharpoons \text{Au}$	1.830
$\text{Au}^{3+} + 2e \rightleftharpoons \text{Au}^+$	1.360
$\text{Ba}^{2+} + 2e \rightleftharpoons \text{Ba}$	-2.920
$\text{Be}^{2+} + 2e \rightleftharpoons \text{Be}$	-1.970
$p\text{-Benzoquinone} + 2\text{H}^+ + 2e \rightleftharpoons \text{hydroquinone}$	0.699
$\text{Br}_2(\text{l}) + 2e \rightleftharpoons 2\text{Br}^-$	1.060
$\text{Br}_2(\text{aq}) + 2e \rightleftharpoons 2\text{Br}^-$	1.087
$\text{BrO}^- + \text{H}_2\text{O} + 2e \rightleftharpoons \text{Br}^- + 2\text{OH}^-$	0.760
$2\text{HOBr} + 2\text{H}^+ + 2e \rightleftharpoons \text{Br}_2 + 2\text{H}_2\text{O}$	1.600
$2\text{BrO}^{3-} + 12\text{H}^+ + 10e \rightleftharpoons \text{Br}_2 + 6\text{H}_2\text{O}$	1.480
$2\text{BrO}^{4-} + 2\text{H}^+ + 2e \rightleftharpoons \text{BrO}^{3-} + \text{H}_2\text{O}$	1.850
$\text{CO}_2 + 2\text{H}^+ + 2e \rightleftharpoons \text{CO} + \text{H}_2\text{O}$	-0.110
$\text{CO}_2 + 2\text{H}^+ + 2e \rightleftharpoons \text{HCOOH}$	-0.200
$2\text{CO}_2 + 2\text{H}^+ + 2e \rightleftharpoons \text{H}_2\text{C}_2\text{O}_4$	-0.480
$\text{Ca}^{2+} + 2e \rightleftharpoons \text{Ca}$	-2.840
$\text{Cd}(\text{OH})_2 + 2e \rightleftharpoons \text{Cd} + 2\text{OH}^-$	-2.840
$\text{Cd}^{2+} + 2e \rightleftharpoons \text{Cd}$	-0.403
$\text{Cd}^{2+} + 2e \rightleftharpoons \text{Cd(Hg)}$	-0.352
$\text{Ce}^{4+} + e \rightleftharpoons \text{Ce}^{3+}$	1.720
$\text{Cl}_2(\text{g}) + 2e \rightleftharpoons 2\text{Cl}^-$	1.358
$\text{HClO}_2 + 2\text{H}^+ + 2e \rightleftharpoons \text{HOCl} + \text{H}_2\text{O}$	1.680
$\text{HClO} + \text{H}^+ + e \rightleftharpoons \frac{1}{2}\text{Cl}_2 + \text{H}_2\text{O}$	1.630
$\text{ClO}_3^- + 3\text{H}^+ + 2e \rightleftharpoons \text{HClO}_2 + \text{H}_2\text{O}$	1.180
$\text{ClO}_3^- + 2\text{H}^+ + e \rightleftharpoons \text{ClO}_2 + \text{H}_2\text{O}$	1.170
$\text{ClO}_4^- + 2\text{H}^+ + 2e \rightleftharpoons \text{CO}_3^- + \text{H}_2\text{O}$	1.200
$\text{Co}^{2+} + 2e \rightleftharpoons \text{Co}$	-0.277
$\text{Co}^{3+} + e \rightleftharpoons \text{Co}^{2+}$	1.920
$\text{Co}(\text{NH}_3)_6^{3+} + e \rightleftharpoons \text{Co}(\text{NH}_3)_6^{2+}$	0.060
$\text{Co}(\text{phen})_3^{3+} + e \rightleftharpoons \text{Co}(\text{phen})_3^{2+}$	0.330
$\text{Co}(\text{C}_2\text{O}_4)_3^{3-} + e \rightleftharpoons \text{Co}(\text{C}_2\text{O}_4)_3^{4-}$	0.570
$\text{Cr}^{2+} + 2e \rightleftharpoons \text{Cr}$	-0.900
$\text{Cr}^{3+} + 3e \rightleftharpoons \text{Cr}$	-0.740
$\text{Cr}^{3+} + e \rightleftharpoons \text{Cr}^{2+}$	-0.424
$\text{Cr}_2\text{O}_7^{2-} + 14\text{H}^+ + 6e \rightleftharpoons 2\text{Cr}^{3+} + 7\text{H}_2\text{O}$	1.360
$\text{Cs}^+ + e \rightleftharpoons \text{Cs}$	-2.920
$\text{Cu}^+ + e \rightleftharpoons \text{Cu}$	0.520

(Continued)

Table 18.1 (Cont.)

Reaction	E^0 (V vs. NHE)
$\text{Cu}^{2+} + 2\text{CN}^- + e \rightleftharpoons \text{Cu}(\text{CN})_2^-$	1.120
$\text{Cu}^{2+} + e \rightleftharpoons \text{Cu}^+$	0.159
$\text{Cu}^{2+} + 2e \rightleftharpoons \text{Cu}$	0.340
$\text{Cu}^{2+} + 2e \rightleftharpoons \text{Cu}(\text{Hg})$	0.345
$\text{CuCl} + e \rightleftharpoons \text{Cu} + \text{Cl}^-$	0.120
$\text{Cu}(\text{NH}_3)_4^{2+} + 2e \rightleftharpoons \text{Cu} + 4\text{NH}_3$	0.000
$\text{Eu}^{3+} + e \rightleftharpoons \text{Eu}^{2+}$	-0.350
$\frac{1}{2}\text{F}_2 + \text{H}^+ + e \rightleftharpoons \text{HF}$	3.053
$\text{Fe}^{2+} + 2e \rightleftharpoons \text{Fe}$	-0.440
$\text{Fe}^{3+} + 3e \rightleftharpoons \text{Fe}$	-0.040
$\text{Fe}^{3+} + e \rightleftharpoons \text{Fe}^{2+}$	0.771
$\text{Fe}(\text{phen})^{3+} + e \rightleftharpoons \text{Fe}(\text{phen})^{2+}$	1.130
$\text{Fe}(\text{CN})_6^{3-} + e \rightleftharpoons \text{Fe}(\text{CN})_6^{4-}$	0.361
$\text{Fe}(\text{CN})_6^{4-} + e \rightleftharpoons \text{Fe} + 6\text{CN}^-$	-1.160
$2\text{H}^+ + 2e \rightleftharpoons \text{H}_2$	0.000
$2\text{H}_2\text{O} + 2e \rightleftharpoons \text{H}_2 + 2\text{OH}^-$	-0.828
$\text{H}_2\dot{\text{O}}_2 + \text{H}^+ + e \rightleftharpoons \text{HO}\cdot + \text{H}_2\text{O}$	0.710
$\text{H}_2\dot{\text{O}}_2 + 2\text{H}^+ + 2e \rightleftharpoons 2\text{H}_2\text{O}$	1.763
$2\text{Hg}^{2+} + 2e \rightleftharpoons \text{Hg}_2^{2+}$	0.911
$\text{Hg}_2^{2+} + 2e \rightleftharpoons 2\text{Hg}$	0.796
$\text{Hg}_2\text{Cl}_2 + 2e \rightleftharpoons 2\text{Hg} + 2\text{Cl}^-$	0.268
$\text{Hg}_2\text{Cl}_2 + 2e \rightleftharpoons 2\text{Hg} + 2\text{Cl}^-$ (sat'd KCl)	0.242
$\text{HgO} + \text{H}_2\text{O} + 2e \rightleftharpoons \text{Hg} + 2\text{OH}^-$	0.098
$\text{Hg}_2\text{SO}_4 + 2e \rightleftharpoons 2\text{Hg} + \text{SO}_4^{2-}$	0.613
$\text{I}_2 + 2e \rightleftharpoons 2\text{I}^-$	0.536
$\text{I}_3^- + 2e \rightleftharpoons 3\text{I}^-$	0.536
$2\text{HOI} + 2\text{H}^+ + 2e \rightleftharpoons \text{I}_2 + 2\text{H}_2\text{O}$	1.440
$2\text{IO}_3^- + 12\text{H}^+ + 10e \rightleftharpoons \text{I}_2 + 6\text{H}_2\text{O}$	1.200
$\text{IO}(\text{OH})_5 + \text{H}^+ + e \rightleftharpoons \text{IO}_3^- + 3\text{H}_2\text{O}$	1.600
$\text{In}^+ + e \rightleftharpoons \text{In}$	-0.130
$\text{In}^{3+} + 2e \rightleftharpoons \text{In}^+$	-0.440
$\text{In}^{3+} + 3e \rightleftharpoons \text{In}$	-0.340
$\text{K}^+ + e \rightleftharpoons \text{K}$	-2.925
$\text{Li}^+ + e \rightleftharpoons \text{Li}$	-3.045
$\text{Mg}^{2+} + 2e \rightleftharpoons \text{Mg}$	-2.356
$\text{Mn}^{2+} + 2e \rightleftharpoons \text{Mn}$	-1.180
$\text{Mn}^{3+} + e \rightleftharpoons \text{Mn}^{2+}$	1.500
$\text{MnO}_2 + 2\text{H}^+ + 2e \rightleftharpoons \text{Mn}^{2+} + 2\text{H}_2\text{O}$	1.230
$\text{MnO}_4^- + 8\text{H}^+ + 5e \rightleftharpoons \text{Mn}^{2+} + 4\text{H}_2\text{O}$	1.510
$\text{MnO}_4^- + e \rightleftharpoons \text{MnO}_4^{2-}$	0.560
$\text{MoO}_4^{2-} + 4\text{H}_2\text{O} + 6e \rightleftharpoons \text{Mo} + 8\text{OH}^-$	-0.910
$\text{NO}_3^- + 2\text{H}^+ + e \rightleftharpoons \text{NO}_2 + \text{H}_2\text{O}$	0.800
$\text{NO}_3^- + 4\text{H}^+ + 3e \rightleftharpoons \text{NO} + 2\text{H}_2\text{O}$	0.960
$\text{NO}_3^- + \text{H}_2\text{O} + 2e \rightleftharpoons \text{NO}_2^- + 2\text{OH}^-$	0.010
$\text{Na}^+ + e \rightleftharpoons \text{Na}$	-2.714
$\text{Ni}^{2+} + 2e \rightleftharpoons \text{Ni}$	-0.257
$\text{Ni}(\text{OH})_2 + 2e \rightleftharpoons \text{Ni} + 2\text{OH}^-$	-0.720
$\text{NiO}_2 + 2e \rightleftharpoons \text{Ni}^{2+} + 2\text{H}_2\text{O}^-$	1.590
$\text{O}_2 + 2\text{H}^+ + 2e \rightleftharpoons \text{H}_2\text{O}_2$	0.695

Table 18.1 (Cont.)

Reaction	E^0 (V vs. NHE)
$O_2 + 4H^+ + 4e \rightleftharpoons 2H_2O$	1.229
$O_2 + 2H_2O + 4e \rightleftharpoons 4OH^-$	0.401
$O_2 + e \rightleftharpoons O_2^-$	-0.330
$O_2 + H_2O + 2e \rightleftharpoons HO_2^- + OH^-$	-0.080
$O_2 + H^+ + e \rightleftharpoons HO_2^-$	-0.130
$O_3 + 2H^+ + 2e \rightleftharpoons O_2 + H_2O$	2.075
$P + 3H^+ + 3e \rightleftharpoons PH_3$	-0.060
$HPO(OH)_2 + 3H^+ + 3e \rightleftharpoons P + 3H_2O$	-0.500
$HPO(OH)_2 + 2H^+ + 2e \rightleftharpoons H_2PO(OH) + H_2O$	-0.500
$PO(OH)_3 + 2H^+ + 2e \rightleftharpoons HPO(OH)_2 + H_2O$	-0.280
$Pb^{2+} + 2e \rightleftharpoons Pb$	-0.125
$Pb^{2+} + 2e \rightleftharpoons Pb(Hg)$	-0.121
$PbO_2 + 4H^+ + 2e \rightleftharpoons Pb^{2+} + 2H_2O$	1.468
$PbO_2 + SO_4^{2-} + 2H^+ + 2e \rightleftharpoons PbSO_4 + 2H_2O$	1.698
$PbSO_4 + 2e \rightleftharpoons Pb + SO_4^{2-}$	-0.351
$Pd^{2+} + 2e \rightleftharpoons Pd$	0.915
$Pt^{2+} + 2e \rightleftharpoons Pt$	1.188
$PtCl_4^{2-} + 2e \rightleftharpoons Pt + 4Cl^-$	0.758
$PtCl_6^{2-} + 2e \rightleftharpoons PtCl_4^{2-} + 2Cl^-$	0.726
$Ru(NH_3)_6^{3+} + e \rightleftharpoons Ru(NH_3)_6^{2+}$	0.100
$Rb^+ + e \rightleftharpoons Rb$	-2.930
$S + 2e \rightleftharpoons S^{2-}$	-0.447
$2SO_2(aq) + 2H^+ + 4e \rightleftharpoons S_2O_3^{2-} + H_2O$	-0.400
$SO_2(aq) + 4H^+ + 4e \rightleftharpoons S + 2H_2O$	0.500
$S_4O_6^{2-} + 2e \rightleftharpoons 2S_2O_3^{2-}$	0.080
$2SO_4^{2-} + H_2O + 2e \rightleftharpoons SO_3^{2-} + 2OH^-$	-0.940
$2SO_4^{2-} + 4H^+ + 2e \rightleftharpoons S_2O_6^{2-} + 2H_2O$	-0.250
$S_2O_8^{2-} + 2e \rightleftharpoons 2SO_4^{2-}$	1.960
$Sn^{2+} + 2e \rightleftharpoons Sn$	-0.138
$Sn^{4+} + 2e \rightleftharpoons Sn^{2+}$	0.150
$Sr^{2+} + 2e \rightleftharpoons Sr$	-2.890
$Ti^{2+} + 2e \rightleftharpoons Ti$	-1.630
$Ti^{3+} + e \rightleftharpoons Ti$	-0.370
$TiO^{2+} + e \rightleftharpoons Ti^{3+}$	0.100
$Tl^+ + e \rightleftharpoons Tl$	-0.336
$Tl^+ + e \rightleftharpoons Tl(Hg)$	-0.334
$Tl^{3+} + 2e \rightleftharpoons Tl^+$	1.250
$U^{3+} + 3e \rightleftharpoons U$	-1.660
$U^{4+} + e \rightleftharpoons U^{3+}$	-0.520
$UO_2^{+} + 4H^+ + e \rightleftharpoons U^{4+} + 2H_2O$	0.273
$UO_2^{2+} + e \rightleftharpoons UO_2^{+}$	0.163
$V^{2+} + 2e \rightleftharpoons V$	-1.130
$V^{3+} + e \rightleftharpoons V^{2+}$	-0.255
$VO^{2+} + 2H^+ + e \rightleftharpoons V^{3+} + H_2O$	0.337
$VO_2^{+} + 2H^+ + e \rightleftharpoons VO^{2+} + H_2O$	1.000
$Zn^{2+} + 2e \rightleftharpoons Zn$	-0.763
$ZnO_2^{2-} + 2H_2O + 2e \rightleftharpoons Zn + 4OH^-$	-1.285

Table 18.2

Formal electrode potentials (V vs. aq SCE) at 25 °C for hydrocarbons in solvents. Data from references (2, 7)

Compound	Reaction	Solvent	Medium	$E^{\prime\prime}$ (V vs. SCE)
Anthracene	$\text{An} + e \rightleftharpoons \text{An}\cdot^-$	DMF	0.1 M TBAI	-1.920
	$\text{An} + e \rightleftharpoons \text{An}\cdot^-$	MeOH	0.1 M TEAI	-1.920
	$\text{An}\cdot^- + e \rightleftharpoons \text{An}^{2-}$	DMF	0.1 M TBAI	-2.500
Azobenzene	$\text{An}\cdot^+ + e \rightleftharpoons \text{An}$	MeCN	0.1 M TBAP	1.300
	$\text{AB} + e \rightleftharpoons \text{AB}\cdot^-$	DMF	0.1 M TBAP	-1.360
	$\text{AB}\cdot^- + e \rightleftharpoons \text{AB}^{2-}$	DMF	0.1 M TBAP	-2.000
Benzophenone	$\text{AB} + e \rightleftharpoons \text{AB}\cdot^-$	MeCN	0.1 M TEAP	-1.400
	$\text{AB} + e \rightleftharpoons \text{AB}\cdot^-$	PC	0.1 M TBAP	-1.400
	$\text{BP} + e \rightleftharpoons \text{BP}\cdot^-$	MeCN	0.1 M TBAP	-1.880
1,4-Benzoquinone	$\text{BP} + e \rightleftharpoons \text{BP}\cdot^-$	THF	0.1 M TBAP	-2.060
	$\text{BP} + e \rightleftharpoons \text{BP}\cdot^-$	NH ₃	0.1 M KI	-1.230
	$\text{BP}\cdot^- + e \rightleftharpoons \text{BP}^{2-}$	NH ₃	0.1 M KI	-1.760
Chrysene	$\text{BQ} + e \rightleftharpoons \text{BQ}\cdot^-$	MeCN	0.1 M TEAP	-0.540
	$\text{BQ}\cdot^- + e \rightleftharpoons \text{BQ}^{2-}$	MeCN	0.1 M TEAP	-1.400
	$\text{Ch}^{\cdot+} + e \rightleftharpoons \text{Ch}$	MeCN	0.1 M TEAP	1.220
Ferrocene	$\text{Cp}_2\text{Fe}^+ + e \rightleftharpoons \text{Cp}_2\text{Fe}$	MeCN	0.2 M LiClO ₄	0.310
Naphthalene	$\text{N} + e \rightleftharpoons \text{N}\cdot^-$	MeCN	0.1 M TEAP	-2.600
Nitrobenzene	$\text{NB} + e \rightleftharpoons \text{NB}\cdot^-$	MeCN	0.1 M TEAP	-1.150
	$\text{NB} + e \rightleftharpoons \text{NB}\cdot^-$	DMF	0.1 M NaClO ₄	-1.010
	$\text{NB}\cdot^- + e \rightleftharpoons \text{NB}^{2-}$	NH ₃	0.1 M KI	-0.420
Oxygen	$\text{O}_2 + e \rightleftharpoons \text{O}_2\cdot^-$	DMF	0.2 M TBAP	-0.870
	$\text{O}_2 + e \rightleftharpoons \text{O}_2\cdot^-$	MeCN	0.2 M TBAP	-0.820
	$\text{O}_2 + e \rightleftharpoons \text{O}_2\cdot^-$	DMSO	0.1 M TBAP	-0.730
Perylene	$\text{P}\cdot^+ + e \rightleftharpoons \text{P}$	MeCN	0.1 M TEAP	0.850
Phenanthrene	$\text{Ph}\cdot^+ + e \rightleftharpoons \text{Ph}$	MeCN	0.1 M TEAP	1.280
Pyrene	$\text{Py}\cdot^+ + e \rightleftharpoons \text{Py}$	MeCN	0.1 M TEAP	1.360
Ru(bpy) ₃ ⁿ⁺ (RuL ₃ ⁿ⁺)	$\text{RuL}_3^{3+} + e \rightleftharpoons \text{RuL}_3^{2+}$	MeCN	0.1 M TBABF ₄	1.320
	$\text{RuL}_3^{2+} + e \rightleftharpoons \text{RuL}_3^+$	MeCN	0.1 M TBABF ₄	-1.300
	$\text{RuL}_3^+ + e \rightleftharpoons \text{RuL}_3^-$	MeCN	0.1 M TBABF ₄	-1.490
	$\text{RuL}_3^- + e \rightleftharpoons \text{RuL}_3^{2-}$	MeCN	0.1 M TBABF ₄	-1.730
Stilbene	$\text{St}\cdot^+ + e \rightleftharpoons \text{St}$	MeCN	0.1 M NaClO ₄	1.430
Tetracene	$\text{T}\cdot^+ + e \rightleftharpoons \text{T}$	MeCN	0.1 M NaClO ₄	0.770
Tetracyanoquinodimethane	$\text{TCNQ} + e \rightleftharpoons \text{TCNQ}\cdot^-$	MeCN	0.1 M LiClO ₄	0.130
	$\text{TCNQ}\cdot^- + e \rightleftharpoons \text{TCNQ}^{2-}$	MeCN	0.1 M LiClO ₄	-0.290
<i>N,N,N',N'</i> -Tetramethyl- <i>p</i> -phenylenediamine	$\text{TMPD}\cdot^+ + e \rightleftharpoons \text{TMPD}$	DMF	0.1 M TBAP	0.210
	$\text{TTF}\cdot^+ + e \rightleftharpoons \text{TTF}$	MeCN	0.1 M TEAP	0.300
Thianthrene	$\text{TTF}^{2+} + e \rightleftharpoons \text{TTF}\cdot^+$	MeCN	0.1 M TEAP	0.660
	$\text{TH}\cdot^+ + e \rightleftharpoons \text{TH}$	MeCN	0.1 M TBABF ₄	1.230
	$\text{TH}^{2+} + e \rightleftharpoons \text{TH}\cdot^+$	MeCN	0.1 M TBABF ₄	1.740
Tri- <i>N-p</i> -tolylamine	$\text{TH}\cdot^+ + e \rightleftharpoons \text{TH}$	SO ₂	0.1 M TBAP	0.300
	$\text{TH}^{2+} + e \rightleftharpoons \text{TH}\cdot^+$	SO ₂	0.1 M TBAP	0.880
	$\text{TPTA}\cdot^+ + e \rightleftharpoons \text{TPTA}$	THF	0.1 M TBAP	0.980

(see Chapter 1 of this handbook), this table should only be used as a guide. All potentials are for solutions at room temperature and vs. SCE. Table 18.3 lists electrode potentials of common redox species in aprotic solvents. These lists are not comprehensive and additional redox potentials can be found in reference (7). If an exact formal potential value is not needed, then Figure 18.3, a chart of potential ranges for the oxidation and reduction of

Table 18.3

Formal electrode potentials (V vs. aq SCE) at 25 °C for common redox species in solvents.
Data from reference (7)

Redox species	Solvent	Electrolyte	$E^{\circ'} \text{ (V)}$
Theophylline	H ₂ O	HCOONH ₄	0.765
Methyl viologen	H ₂ O	PBS	0.700
Phenanthrene quinone	2-Propanol	PBS	-0.280
Catechol	H ₂ O	PBS	0.600
Hydroquinone	H ₂ O	PBS	0.035
Aspirin/acetilsalicylic acid	MeCN	TBAI	-1.640
Salicylic acid	MeCN	TBAI	-1.540
L-DOPA	DMSO	TEAP	-2.500
Alizarin red S	H ₂ O	MB	0.410
Ferrocenemethanol	MeOH	HClO ₄	0.200

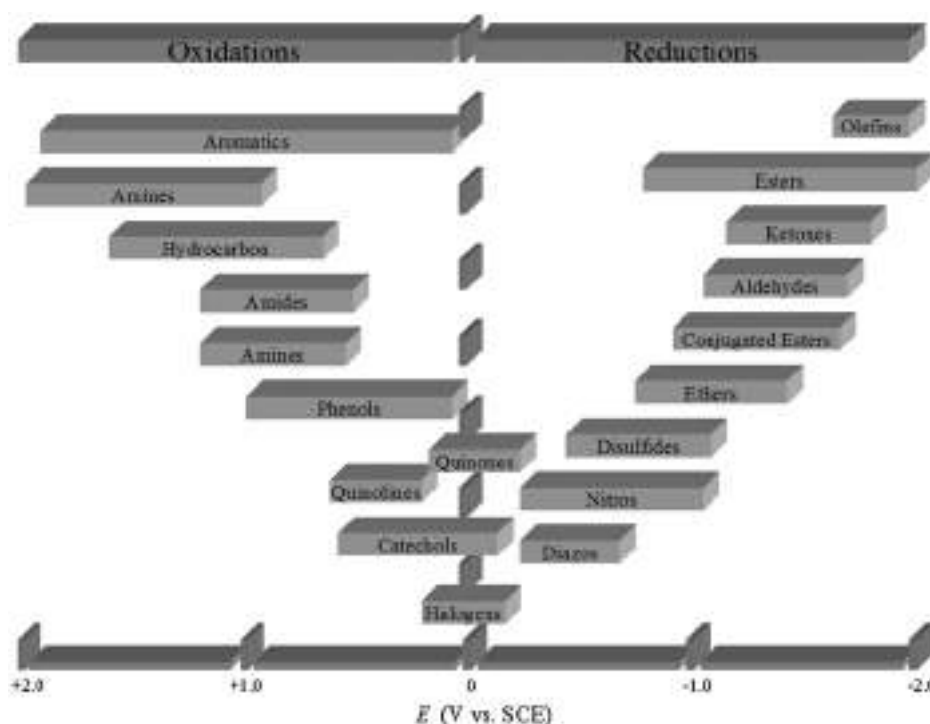


Figure 18.3 Estimated potential range of organic functional groups at 25 °C. Data from references (5, 6). (for colour version: see colour section at the end of the book).

various organic functional groups, can be used to find an approximate potential range for a specific organic functional group.

18.5 FORMAL ELECTRODE POTENTIALS: COMMON ORGANIC MEDIATORS

Table 18.4 is a list of formal electrode potentials (vs. NHE) for common organic mediators at room temperature in aqueous solution of pH = 7. These are popular organic mediators that are often used for sensors and biosensors.

18.6 ELECTRODE POTENTIALS: INORGANIC ONE-ELECTRON COMPLEXES

Table 18.5 lists electrode potentials for common one-electron processes. These redox species are also frequently used as electron transfer mediators in sensors and biosensors.

Table 18.4

Electrode potentials (V vs. NHE) at 25 °C for common organic mediators at pH 7.0. Data from reference (8)

Organic mediator	$E^{\circ'}$ (V vs. NHE)
<i>N,N'</i> -Dimethyl- <i>p</i> -phenylenediamine	0.380
1,4-Benzoquinone	0.280
<i>N,N,N',N'</i> -Tetramethyl- <i>p</i> -phenylenediamine	0.270
2,6-Dichlorophenol indophenol	0.217
1,2-Naphthoquinone-4-sulfonic acid	0.217
Toluylene blue	0.115
Phenazine methosulfate	0.060
Rosinduline 2G	0.080
Phenazine ethosulfate	0.055
Cresyl blue	0.047
Toluidine blue	0.027
Methylene blue	0.011
Tetramethyl- <i>p</i> -benzoquinone	0.005
Indigo-disulfonate	-0.125
Safranine T	-0.289
Neutral red	-0.325
1,1'-Dibenzyl-4,4'-bipyridyl salt	-0.350
1,1'-Ethylene-2,2'-bipyridyl dichloride	-0.350
1,1'-Bis(hydroxyethyl)-4,4'-bipyridyl salt	-0.408
1,1'-Dimethyl-4,4'-bipyridyl dichloride	-0.430

Table 18.5

Formal and standard electrode potentials (V vs. NHE) at 25 °C for inorganic complexes in aqueous solution

Inorganic complexes	E (V vs. NHE)	Reference
$\text{Ni}(\text{bpy})_3^{3+}$	$E^0 = 1.720$	9
$\text{Ru}(\text{bpy})_3^{2+}$	$E^0 = 1.272$	10
$\text{Ru}(\text{phen})_3^{2+}$	$E^0 = 1.220$	11
$\text{Fe}(\text{phen})_3^{2+}$	$E^0 = 1.107$	10
$\text{Fe}(\text{bpy})_3^{2+}$	$E^0 = 1.074$	10
IrCl_6^{2-}	$E^0 = 0.892$	12
$\text{Os}(\text{bpy})_3^{2+}$	$E^0 = 0.844$	10
$\text{Mo}(\text{CN})_8^{4-}$	$E^0 = 0.798$	10
$\text{Co}(\text{oxalate})_3^{3-}$	$E^0 = 0.570$	13
$\text{Ru}(\text{NH}_3)_4(\text{bpy})^{2+}$	$E^0 = 0.520$	14
$\text{W}(\text{CN})_8^{3-}$	$E^0 = 0.510$	15
$\text{Ru}(\text{NH}_3)_5\text{Pz}^{3+}$	$E'^0 = 0.490, 1 \text{ M NaCl}$	16
$\text{Co}(\text{EDTA})^-$	$E^0 = 0.380$	13
$\text{Co}(\text{phen})_3^{3+}$	$E^0 = 0.370$	10
$\text{Co}(\text{bpy})_3^{3+}$	$E^0 = 0.315$	17
$\text{Ru}(\text{NH}_3)_5(\text{py})^{2+}$	$E'^0 = 0.299, 1 \text{ M CF}_3\text{SO}_3\text{H}$	18
$\text{Fe}(\text{dipic})_2$	$E'^0 = 0.278, \text{pH} = 5.15$	19
$\text{Co}(\text{terpy})_2^{3+}$	$E^0 = 0.270$	17
$\text{Ru}(\text{en})_3^{3+}$	$E'^0 = 0.184, 0.1 \text{ M KPF}_6$	20
$\text{Fe}(\text{EDTA})^-$	$E^0 = 0.120$	21
Toluylene blue	$E'^0 = 0.115, \text{pH} = 7$	22
Thionine	$E'^0 = 0.056, \text{pH} = 7$	22
$\text{Ru}(\text{NH}_3)_6^{3+}$	$E'^0 = 0.051, 0.1 \text{ M NaBF}_4$	23
Cresyl blue	$E'^0 = 0.047, \text{pH} = 7$	22
Methylene blue	$E'^0 = 0.011, \text{pH} = 7$	22
$\text{Co}(\text{en})_3^{3+}$	$E'^0 = -0.216, 1 \text{ M NaClO}_4$	20
$\text{Cr}(\text{bpy})_3^{3+}$	$E^0 = -0.250$	24
$\text{Co}(\text{sepalchrate})^{3+}$	$E^0 = -0.300$	25
Neutral red	$E'^0 = -0.325, \text{pH} = 7$	22
Benzylviologen	$E^0 = -0.352$	26

18.7 FORMAL ELECTRODE POTENTIALS: BIOLOGICAL REDOX SPECIES

Table 18.6 lists formal potentials for common protein electron transfer reactions in biologically related systems. Table 18.7 lists standard reduction potentials for biochemical reduction reactions.

18.8 FORMAL ELECTRODE POTENTIALS: COMMON VITAMINS, DRUGS, NEUROCHEMICALS

Table 18.8 lists half-wave potentials or peak potentials for selected vitamins, drugs, and neurochemicals. These potentials are dependent on solvent, solvent purity, and electrolyte and thus should serve only as a guide.

Table 18.6

Reduction potentials (V vs. SCE) for selected biological redox systems at 25 °C in aqueous solution at pH 7. Data from reference (27)

Redox couples	$E^{0'}$ (V vs. SCE)
Laccase Cu ²⁺ /Cu ⁺	0.165
Cytochrome f Fe ³⁺ /Fe ²⁺	0.125
Cytochrome a (mammalian) Fe ³⁺ /Fe ²⁺	0.100
O ₂ /H ₂ O ₂	0.055
Cytochrome c (mammalian) Fe ³⁺ /Fe ²⁺	0.020
Hemoglobin Fe ³⁺ /Fe ²⁺	-0.070
Ubiquinone ox/red	-0.140
Cytochrome b (mammalian) Fe ³⁺ /Fe ²⁺	-0.210
Methylene blue/leukomethylene blue	-0.230
Myoglobin Fe ³⁺ /Fe ²⁺	-0.236
Cytochrome b3 (mammalian) Fe ³⁺ /Fe ²⁺	-0.240
Glucose oxidase ox/red (pH 5.3)	-0.305
Horseradish peroxidase Fe ³⁺ /Fe ²⁺	-0.310
FMN (old yellow enzyme)/FMNH ₂	-0.360
Riboflavin/dehydroriboflavin	-0.448
Glutathione ox/red	-0.470
Adrenodoxin Fe ³⁺ /Fe ²⁺	-0.515
Xanthine oxidase ox/red	-0.534
Flavodoxin ox/red	-0.550
NAD ⁺ /NADH	-0.560
NADP ⁺ /NADPH	-0.564
H ⁺ /½H ₂	-0.660
Ferredoxin (spinach) Fe ³⁺ /Fe ²⁺	-0.668

18.9 ABBREVIATIONS

PBS	phosphate buffer
TBAI	tetrabutylammonium iodide
TBAP	tetrabutylammonium perchlorate
TEAP	tetraethylammonium perchlorate
TEABF ₄	tetraethylammonium tetrafluoroborate
TBAPF ₆	tetrabutylammonium hexafluorophosphate
TEAI	tetraethylammonium iodide
MeCN	acetonitrile
DMF	dimethylformamide
DMSO	dimethylsulfoxide
THF	tetrahydrofuran
MeOH	methanol
PC	propylene carbonate
EtOH	ethanol

Table 18.7

Standard electrode potentials (V vs. NHE) at 25 °C for half-cell reactions of selected biochemical reductions. Data from reference (28)

	E^0
<i>Reduction of carbonyl to aldehyde</i>	
1,3-Diphosphoglycerate + $2e^- \rightarrow$ 3-phosphoglyceraldehyde + HPO_4^{2-}	−0.286
Acetyl-CoA + $2\text{H}^+ + 2e^- \rightarrow$ acetaldehyde + coenzyme A	−0.412
Oxalate + $3\text{H}^+ + 2e^- \rightarrow$ ascorbate	−0.462
Gluconate + $3\text{H}^+ + 2e^- \rightarrow$ glucose	−0.470
Acetate + $3\text{H}^+ + 2e^- \rightarrow$ acetaldehyde	−0.598
<i>Reduction of carbonyl to alcohol</i>	
Dehydroascorbic acid + $\text{H}^+ + 2e^- \rightarrow$ ascorbate	0.077
Glyoxylate + $2\text{H}^+ + 2e^- \rightarrow$ glycolate	−0.090
Hydroxypyruvate + $2\text{H}^+ + 2e^- \rightarrow$ glycerate	−0.158
Oxaloacetate + $2\text{H}^+ + 2e^- \rightarrow$ malate	−0.166
Pyruvate + $2\text{H}^+ + 2e^- \rightarrow$ lactate	−0.190
Acetaldehyde + $2\text{H}^+ + 2e^- \rightarrow$ ethanol	−0.197
Acetoacetate + $2\text{H}^+ + 2e^- \rightarrow$ b-hydroxybutyrate	−0.349
<i>Carboxylation</i>	
Pyruvate + $\text{CO}_2(\text{g}) + \text{H}^+ + 2e^- \rightarrow$ malate	−0.330
a-Ketoglutarate + $\text{CO}_2(\text{g}) + \text{H}^+ + 2e^- \rightarrow$ isocitrate	−0.363
Succinate + $\text{CO}_2(\text{g}) + \text{H}^+ + 2e^- \rightarrow$ a-ketoglutarate + H_2O	−0.673
Acetate + $\text{CO}_2(\text{g}) + \text{H}^+ + 2e^- \rightarrow$ pyruvate + H_2O	−0.699
<i>Reduction of carbonyl with amino</i>	
Oxaloacetate + $\text{NH}_4^+ + 2\text{H}^+ + 2e^- \rightarrow$ aspartate + H_2O	−0.107
Pyruvate + $\text{NH}_4^+ + 2\text{H}^+ + 2e^- \rightarrow$ alanine + H_2O	−0.132
a-Ketoglutarate + $\text{NH}_4^+ + 2\text{H}^+ + 2e^- \rightarrow$ glutamate + H_2O	−0.133
<i>Reduction of C=C</i>	
Crotonyl-CoA + $2\text{H}^+ + 2e^- \rightarrow$ butyryl-CoA	0.187
Fumarate + $2\text{H}^+ + 2e^- \rightarrow$ succinate	0.031
<i>Reduction of disulfide</i>	
Cystine + $2\text{H}^+ + 2e^- \rightarrow$ 2-cysteine	−0.340
Glutathione dimer + $2\text{H}^+ + 2e^- \rightarrow$ 2-glutathione	−0.340
<i>Others</i>	
$\text{FAD}^+ + \text{H}^+ + 2e^- \rightarrow$ FADH	−0.200
$\text{NAD}^+ + \text{H}^+ + 2e^- \rightarrow$ NADH	−0.320

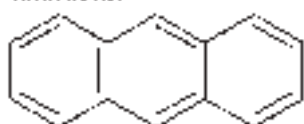
Table 18.8

Half-wave and peak potentials for common vitamins, drugs, and neurochemicals at room temperature

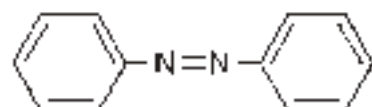
	Solvent	Electrolyte or reference	$E^{\frac{1}{2}}$ (or E_p)	Reference
<i>Vitamins</i>				
Vitamin A/retinol	DMF	TEAI	−2.400	7
Vitamin B2/riboflavin	DMSO	NaClO ₄	−1.020	7
Vitamin B3/Niacin/nicotinic acid	H ₂ O	TEAP	−1.440	7
Folate/folic acid	H ₂ O	NaOH	0.560	7
Vitamin B12/cyanocobalamin	H ₂ O	0.1 M KCN, vs. SCE	−1.120	27
Vitamin C/ascorbic acid	H ₂ O	PBS	$E_p = 0.020$	7
<i>Neurochemicals</i>				
Aspartic acid	DMSO	TEAP	−2.400	7
Glutamic acid	DMSO	TEAP	−2.120	7
Epinephrine/L-adrenaline	H ₂ O	H ₂ SO ₄	$E_p = 0.550$	7
Progesterone	MeCN	TBAI	−1.850	7
Hydrocortisone	EtOH	PBS	−1.300	7
Catechol	H ₂ O	pH = 0	0.792	27
Epinephrine	H ₂ O	pH = 0	0.809	27
Dopamine	H ₂ O	pH = 0, vs. SCE	0.580	27
Dihydroxyphenylalanine	H ₂ O	pH = 0	0.800	27
Epinine	H ₂ O	pH = 0	0.788	27
Norhomoepinephrine	H ₂ O	pH = 0	0.822	27
Adrenalone	H ₂ O	pH = 0	0.909	27
Protocatechinic acid	H ₂ O	pH = 0	0.883	27
6-Hydroxydopamine	H ₂ O	pH = 6.87, vs. SCE	−0.159	27
6-Methoxydopamine	H ₂ O	pH = 6.87, vs. SCE	−0.070	27
<i>Drugs</i>				
Sertraline	H ₂ O	pH = 8, vs. Ag/AgCl	−1.750	29
THC	H ₂ O	PH = 7.02, vs. Ag	1.500	30
Caffeine	H ₂ O	HCOONH ₄	0.850	7
β-Carotene	H ₂ O	vs. Ag wire	0.600	32
Celecoxib	H ₂ O	pH = 7, vs. Ag/AgCl	−1.540	33
Azithromycin	H ₂ O	PH = 6.0 PBS, vs. Ag/AgNO ₃	0.800	34
Acetaminophen	H ₂ O	Acetate buffer, vs. SCE	0.500	35
Ciprofloxacin	H ₂ O	pH = 7.3 PBS, vs. SCE	−1.410	31
Enoxacin	H ₂ O	pH = 7.3 PBS, vs. SCE	−1.350	31
Norfloxacin	H ₂ O	pH = 7.3 PBS, vs. SCE	−1.405	31
Ofloxacin	H ₂ O	pH = 7.3 PBS, vs. SCE	−1.403	31
Pefloxacin	H ₂ O	pH = 7.3 PBS, vs. SCE	−1.435	31

18.10 CHEMICAL STRUCTURES

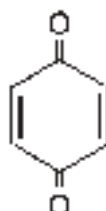
Anthracene



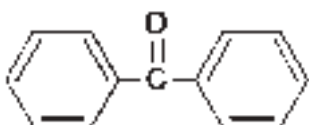
Azobenzene



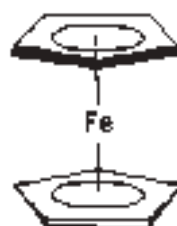
1,4-Benzoquinone



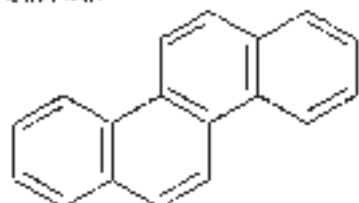
Benzophenone



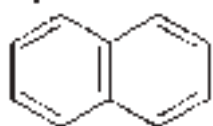
Benzene



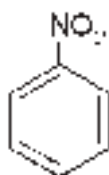
Chrysene



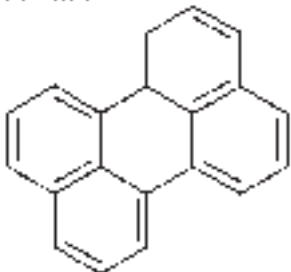
Naphthalene



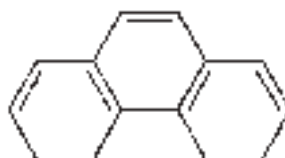
Nitrobenzene

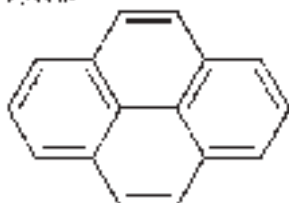
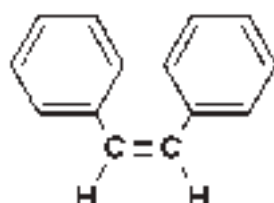
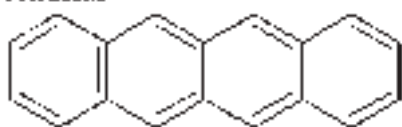
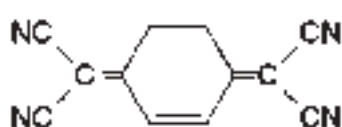
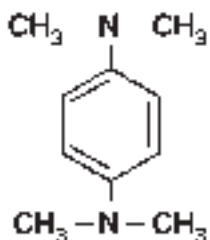
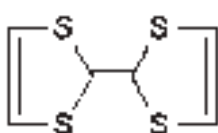
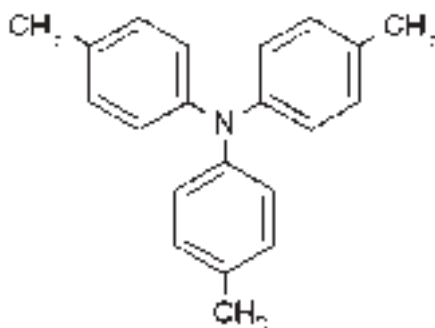
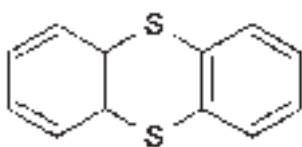


Perylene



Phenanthrene



Pyrene**Stilbene****Tetracene****Tetracyanopropenylmethane****Tetramethylphenylenediamine****Tetrathiafulvalene****Tri-*p*-tolylamine****Thianthrene**

REFERENCES

1. C. K. Mann, *Electroanal. Chem.* **3**, 57 (1969).
2. A. J. Bard, L. R. Faulkner, *Electrochemical Methods: Fundamentals and Applications*, 2nd ed., Wiley: New York, 2001.
3. A. J. Bard, R. Parsons, J. Jordan, *Standard potentials in aqueous solution*, Dekker: New York, 1985.
4. C. M. A. Brett, A. M. O. Brett, *Electrochemistry: Principles, Methods and Applications*, Oxford: Oxford, 1993.
5. D. A. Skoog, F. J. Holler, T. A. Nieman, *Principles of Instrumental Analysis*, 5th ed., Harcourt: Philadelphia, 1998.
6. S. G. Weber, "Chem. Analysis," in *Detectors for Liquid Chromatography*, E. S. Yeung, Ed., Wiley: New York, 1986, Vol. 89.
7. L. Meites, P. Zuman, *Handbook Series in Organic Electrochemistry*, CRC Press: Cleveland, 1977, Vol. 1–2.
8. M. L. Fultz, R. A. Durst, *Anal. Chem. Acta* **140**, 1 (1982).
9. D. H. Macartney, N. Sutin, *Inorg. Chem.* **22**, 3530 (1983).
10. T. Kuwana, in *Electrochemical Studies of Biological Systems*, D. T. Sawyer, Ed., ACS Symposium Series #38, ACS, 1977.
11. A. A. Schilt, *Analytical Applications of 1,10-Phenanthroline and Related Compounds*, Pergamon Press: New York, 1969.
12. F. P. Bossu, K. L. Chellappa, D. W. Margerum, *J. Am. Chem. Soc.* **99**, 2195 (1977).
13. L. Hin-Fat, W. C. E. Higginson, *J. Chem. Soc. A* **2**, 298 (1967).
14. G. M. Brown, N. Sutin, *J. Am. Chem. Soc.* **83**, 3357 (1961).
15. H. Baadsgaard, W. D. Treadwell, *Helv. Chim. Acta* **38**, 1669 (1955).
16. H. S. Lim, D. J. Barclay, F. C. Anson, *Inorg. Chem.* **11**, 1460 (1972).
17. D. Cummins, H. B. Gray, *J. Am. Chem. Soc.* **99**, 5158 (1977).
18. G. M. Brown, H. J. Krentzien, M. Abe, H. Taube, *Inorg. Chem.* **18**, 3374 (1979).
19. G. Anderegg, *Helv. Chim. Acta* **43**, 1530 (1960).
20. E. L. Yee, R. J. Cave, K. L. Guyer, P. D. Tyma, M. J. Weaver, *J. Am. Chem. Soc.* **101**, 1131 (1979).
21. H. J. Schugar, A. T. Hubbard, F. C. Anson, H. B. Gray, *J. Am. Chem. Soc.* **91**, 71 (1969).
22. W. Clark, *Oxidation-Reduction Potentials of Organic Systems*, Williams & Wilkins Co.: Baltimore, 1960.
23. T. Matsubara, P. C. Ford, *Inorg. Chem.* **15**, 1107 (1976).
24. B. S. Brunschwig, N. Sutin, *J. Am. Chem. Soc.* **100**, 7568 (1978).
25. A. M. Sargeson, *Chem. Br.* **15**, 23 (1979).
26. R. C. Prince, S. J. G. Linkletter, P. L. Dutton, *Biochem. Biophys. Acta* **635**, 132 (1981).
27. G. Dryhurst, K. M. Kadish, F. Scheller, R. Renneberg, *Biological Electrochemistry*, Academic Press: New York, 1982.
28. H. A. Krebs, H. L. Kornberg, K. Burton, *Erg. Physiol.* **49**, 212 (1957).
29. M. H. Vela, M. B. Quinaz Garcia, M. C. Montenegro, *Fresenius J. Anal. Chem.* **369**, 563 (2001).
30. U. Backofed, W. Hoffmann, F. Matysik, *Biomed. Chromatogr.* **14**, 49 (2000).
31. M. Warowna-Grzeskiewicz, J. Chodkowski, Z. Fijalik, *Acta Poloniae Pharm.* **52**, 442 (1995).
32. A. L. Suarez-Fernandez, G. Alarnes-Varela, A. Costa-Garcia, *Electrochim. Acta* **44**, 4489 (1999).
33. M. M. Ghoneim, A. M. Beltagi, *Talanta* **60**, 911 (2003).
34. O. A. E. Farghaly, N. A. L. Mohamed, *Talanta* **62**, 531 (2004).
35. C. M. Shearer, K. Christenson, A. Mukherji, G. J. Papariello, *J. Pharm. Sci.* **61**, 1627 (1972).

This page intentionally left blank

– 19 –

Diffusion Coefficients

John E. Baur

Department of Chemistry, Illinois State University,
Normal, IL 61790-4160, USA

19.1 INTRODUCTION

Electrochemical experiments are often designed so that diffusion is the sole form of mass transport. Even in cases where convection and migration occur, diffusion can rarely be ignored as a significant contributor to the overall mass transport. Therefore, theoretical treatments of electrochemical systems that involve mass transport normally require that the diffusion coefficient of the redox species of interest, D , is known. A quick perusal of this or any other electrochemistry text reveals that D is a term in most important equations relating current to solution conditions. Only current arising from non-transport related sources (e.g., double-layer charging and redox reactions of adsorbate layers) are independent of the diffusion coefficient.

Yet despite its importance, values of D are not readily found. This is because the diffusion coefficient of a species in solution depends upon several factors (e.g., temperature, viscosity, electrolyte, etc.), so comprehensive tabulation is impractical. When the diffusion coefficient must be known for a new compound or a new set of conditions, the usual approach is to measure D for the particular species of interest under specified experimental conditions. Making such measurements accurately requires careful characterization and calibration of the measurement system using a species with a known diffusion coefficient under well-defined conditions. Methods for measuring diffusion coefficients are described in this chapter. A tabulation of values of D for commonly used redox species is included at the end of the chapter.

19.2 FUNDAMENTAL EQUATIONS

Simply stated, the diffusion coefficient is the proportionality between flux, $J(x,t)$, and concentration gradient, $\partial C(x,t)/\partial x$, which is mathematically expressed by Fick's first law

(for one dimension):

$$J(x,t) = -D \frac{\partial C(x,t)}{\partial x} \quad (19.1)$$

where x is the distance measured from the electrode surface and t is time. In electrochemistry, flux commonly has units of mol cm⁻² sec⁻¹ and the concentration gradient has units of mol cm⁻⁴, so the diffusion coefficient has units of cm² sec⁻¹. Faradaic current is proportional to flux at the electrode surface, $J(0,t)$:

$$i(t) = -nFAJ(0,t) \quad (19.2)$$

where F is Faraday's constant. Most electrochemical measurements of the diffusion coefficient rely on a measurement of the faradaic current.

Equations (19.1) and (19.2) reveal that at least three other quantities must be accurately known in order to make a reliable measurement of D . These critical variables are the electrode area A (or in the case of ultramicroelectrodes (UMEs) (Chapter 6), the electrode radius r_0), the stoichiometric number of electrons, n , involved in the electron transfer reaction, and the bulk concentration of the redox species, C^* .¹ The electrode area is normally determined electrochemically with equations equivalent to equation (19.2) and using a redox couple having a known diffusion coefficient. This is done because calculations based on manufacturers' nominal dimensions or on optically measured dimensions ignore imperfections in the manufacture, geometry, and local reactivity of the electrode. For existing redox couples the value of n is often known, but for the characterization of a new species n must be experimentally determined. To avoid techniques that in turn rely on knowledge of the diffusion coefficient, coulometric or thin layer methods are preferred for such determinations. Finally, care must be taken to ensure that the redox species, supporting electrolyte, and solvent are of high purity, and that proper volumetric technique is used in preparing solutions so that C^* is accurately known. Because a measured value of D will contain errors associated with each of these experimental variables in addition to the current, without very careful measurements and precisely calibrated instruments and electrodes, it is difficult to accurately determine diffusion coefficients to more than two significant figures.

19.3 GENERAL CONSIDERATIONS

19.3.1 Selection of a technique

The techniques described in this chapter (see Chapter 11 for detailed description of techniques) for the determination of diffusion coefficients are summarized in Table 19.1. Each of these techniques has its own strengths and weaknesses that should be evaluated before selecting a method. One important consideration is the dependence of D on the experimentally measured quantities (e.g., current or electrode dimensions). Under conditions of

¹ C^* does not appear in equation (19.1) or equation (19.2), but the flux at the surface depends on C^* .

Table 19.1

Summary of electrochemical methods for measuring diffusion coefficients

Method	Procedure	Equation	Comments
<i>Methods with $D \propto i$</i>			
Chronoamperometry at disk UME	Measure steady-state current	$D = \frac{i_{ss}}{4nFC^* r_0}$	$RG \geq 100, 4Dt/r_0^2 > 500$ for <2% planar diffusion contribution to i_{ss}
Chronoamperometry at hemispherical UME	Measure steady-state current	$D = \frac{i_{ss}}{2\pi nFC^* r_0}$	$RG \geq 100, Dt/r_0^2 > 800$ for <2% planar diffusion contribution to i_{ss}
Linear scan voltammetry at disk UME	Measure steady-state current	$D = \frac{i_{ss}}{4nFC^* r_0}$	$RG \geq 100$, same time criterion as chronoamperometry, but use $t \approx E_f - E_{1/2} /v$
Linear scan voltammetry at hemispherical UME	Measure steady-state current	$D = \frac{i_{ss}}{2\pi nFC^* r_0}$	$RG \geq 100$, same time criterion as chronoamperometry, but use $t \approx E_f - E_{1/2} /v$
<i>Methods with $D \propto i^{3/2}$</i>			
Rotating disk electrode	Measure limiting current, i_l as a function of rotation rate ω and plot i_l vs. $\omega^{1/2}$	$D = \left(\frac{\text{slope}}{0.62nFAC^* v^{-1/6}} \right)^{3/2}$	Use with $10 < \omega < 10,000$
<i>Methods with $D \propto i^2$</i>			
Chronoamperometry at planar electrode	Measure current as a function of time, plot $i(t)$ vs. $t^{-1/2}$	$D = \frac{(\text{slope})^2 \pi}{(nFAC^*)^2}$	Avoid charging current measurements at short times ($t \leq 10R_s C_d$), avoid long times (convection, edge effects)
Normalized chronoamperometry at disk UME	Measure current as a function of time and normalize by steady-state current. Plot normalized current vs. $t^{-1/2}$	$D = \frac{4r_0^2}{(\text{slope})^2 \pi^3}$	Requires only r_0 ; avoid charging current measurements at short times ($t \leq 10R_s C_d$)

(Continued)

Table 19.1 (Cont.)

Method	Procedure	Equation	Comments
Chronopotentiometry at planar electrode	Measure transition time at several current densities, find average value of τ	$D = \frac{4i_0^2\tau}{\pi(nFC^*)^2}$	Avoid conditions with long transition times (convective effects); less accurate when there are large relative background contributions to the overall current (i.e., low C^* , large C_d , short τ)
Linear scan voltammetry at a planar electrode	Measure peak current as a function of scan rate, plot i_p vs. $v^{1/2}$	$D = \frac{(\text{slope})^2}{n^3 (2.69 \times 10^5 A C^*)^2}$	Nernstian systems only; avoid scan rates with appreciable nonlinear diffusion; should be considered an approximate method

linear diffusion, the current is typically proportional to $D^{1/2}$ (e.g., in chronoamperometry, equation (19.8), and in linear scan voltammetry (LSV), equation (19.17), Chapter 11), or in other words D is proportional to i^2 . Any errors in i (or C^* , A , or n) are thus amplified because of the second-order dependence of the diffusion coefficient on these variables. For the rotating disk electrode (RDE) (Chapter 11), current is proportional to $D^{2/3}$ (equation (19.12)), so D depends on $i^{3/2}$. For steady-state UME techniques (Chapters 6 and 11), the current is directly proportional to D (equations (19.3) and (19.4)). Because of this linear relationship, errors in i (or C^* , A , or n) produce the smallest error in D . Therefore, in most situations, steady-state UME techniques are preferred for determinations of diffusion coefficients. One caveat is that with UMEs it is often more difficult to make accurate measurements of the electrode dimensions (because they are so small), but calibration of the electrode with a system having a known diffusion coefficient can compensate for this uncertainty. Certainly the application of more than one technique will also improve the confidence in the measured value of D .

19.3.2 Electrode

The electrode is a critical component in the electrochemical measurement of diffusion coefficients. The general type of electrode to be used (i.e., UME or conventional electrode, see Chapters 5, 6, and 11 for more detail) has a fundamental impact on the type of measurement to be made. As shown in Figure 19.1a, at a conventional electrode diffusion normally is planar (i.e., comes from essentially one direction toward the electrode surface). With planar diffusion there is a depletion of the redox species close to the surface, resulting in a current that decays with time. As such, under planar diffusion control the current is measured as a function of time. With an RDE, forced convection causes efficient, steady-state transport of species to the electrode surface (Figure 19.1b) and time-independent current results. With

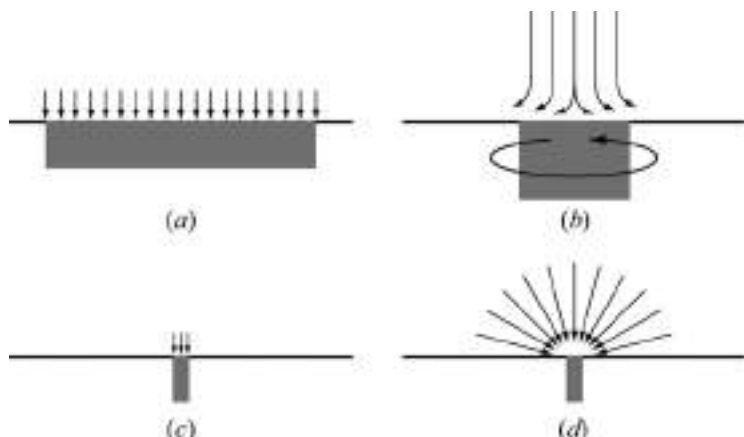


Figure 19.1 Mass transport to electrodes of different types. (a) Planar diffusion to a macroelectrode, (b) convection to a rotating disk electrode, (c) planar diffusion to a microdisk electrode at short times, (d) radial diffusion to a microdisk electrode at long times.

UMEs, planar diffusion occurs at short times because the diffusion distance is small compared to the electrode dimensions (Figure 19.1c). At longer times the current becomes time-independent as radial diffusion dominates (Figure 19.1d). For diffusion coefficient measurements with UMEs, the steady-state current is normally measured, although some techniques utilize both short- and long-time current measurements.

The electrode selected for the measurement of a diffusion coefficient should be closely inspected for defects and non-idealities. Figure 19.2 depicts several possible non-idealities: poor electrode seals, irregular geometry, thin insulators, eccentricities, and protrusions, all of which contribute to errors in the measured current. If the electrode is poorly sealed (Figure 19.2a), solution can creep between the conductor and insulator, increasing both the apparent electrode capacitance (C_d) and the geometric area. Because the ratio of perimeter to surface area for a UME is large, this type of defect is typically more problematic for a UME than for a conventional electrode. Irregular or elongated geometries (Figure 19.2b) are also problematic for UMEs because the current is dependent on electrode radius and a true circular or spherical geometry is assumed. In contrast, for pure planar diffusion the

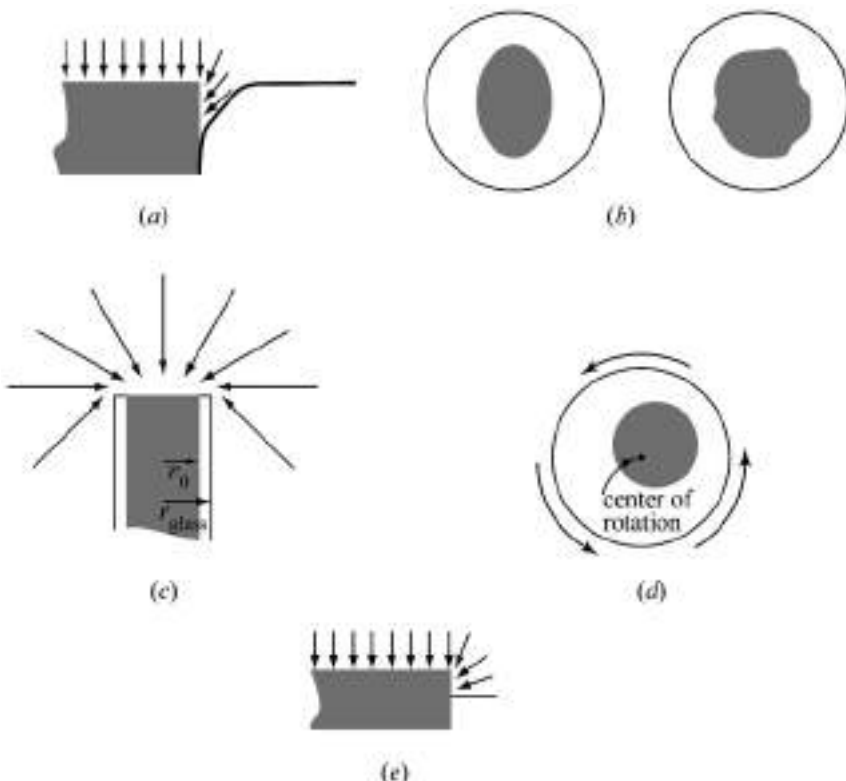


Figure 19.2 Electrode features causing deviations from theoretical behavior. (a) Crack or poor seal at electrode-insulator boundary, (b) elongated and irregular electrode geometries, (c) UME with a thin insulator, (d) RDE in which the disk is not centered on the axis of rotation, (e) electrode protrusion from the plane of the insulator.

current is only dependent on area (not geometry), so such irregularities are typically not important. Thin insulators (Figure 19.2c) are especially problematic for UMEs at long times because molecules can diffuse from behind the plane of the electrode, causing the measured current to be higher than the theoretical current. Eccentricities (Figure 19.2d) are most problematic for RDEs; an electrode not centered on the axis of rotation will exhibit a positive deviation from the theoretical current. Protrusions (Figure 19.2e) are problematic for any type of electrode, as they give increased areas and can have unusual diffusional or hydrodynamic behaviors near the edges. While electrochemical measurements of electrode areas can correct some of these non-idealities, the presence of such defects can potentially cause measurements to deviate significantly from theory. It is therefore of vital importance that electrodes used for measurements of diffusion coefficient are free of such defects.

19.3.3 Electrochemical system

Before attempting to measure diffusion coefficients, some basic information regarding the electrochemical behavior of the redox species must be known. This is particularly important for newly prepared compounds. First, one should evaluate the reversibility of the electron transfer reaction. Certain techniques, such as LSV, can only be applied to measure diffusion coefficients for nernstian systems. Second, the presence of any coupled homogeneous reactions should be established. The current for each technique is often dependent on such reactions, thus making measurements of the diffusion coefficient unreliable. Finally, the adsorption of reactants or products can produce faradaic current that can greatly affect the measurement of the diffusion coefficient. For example, measurement of the critical time in chronopotentiometry is less reliable when adsorption is present. For these reasons, the electrochemical behavior of the compound must be factored into the selection of a technique.

Background measurements of blanks should always be subtracted when making careful diffusion coefficient measurements. Such corrections can often minimize charging current, instrumental offsets, and other background contributions to the measured current. Care must be taken, however, that the condition of the electrode does not change between measurements of the blank and the redox species.

Finally, before measuring the diffusion coefficient of a new compound, the technique and equipment should be tested using at least one standard compound (see tables of D at the end of this chapter for common test compounds). In this way an estimate of the accuracy can be made before measuring the diffusion coefficient of an unknown. If accuracy is a particular concern, the use of more than one technique will improve the reliability of the measurement.

19.3.4 Instrumentation

For the most reliable measurements of D , some general instrumental conditions must be controlled. When using a technique that requires the measurement of a diffusion-limited current (i.e., those described in this chapter with the exception of the RDE technique), all other modes of mass transport must be eliminated. Convection from vibrational agitation of the solution is minimized by conducting the experiment on a vibrationally isolated

workstation. The temperature should be carefully controlled by using a water-jacketed cell to avoid convection due to thermal gradients. Since the diffusion coefficient is a function of temperature, such thermostatic control is also important for calibration. To avoid migration, sufficient supporting electrolyte must be present in solution.² A rule of thumb is that supporting electrolyte concentration should be $100\times$ the concentration of the redox couple. Finally, the amplification factor of the potentiostat (or galvanostat) must be carefully calibrated to minimize errors in the current measurement.

19.4 ELECTROCHEMICAL METHODS

In the following discussion, the specific techniques for measuring diffusion coefficients are listed in order of preference. The selection of a technique will depend on the individual situation and the equipment available to the researcher.

19.4.1 Potential step techniques (chronoamperometry)

Techniques based upon the application of a large amplitude potential step (see Chapter 11) are probably the simplest and most widely applicable methods for measuring D . When using these techniques, it is of vital importance that the potential is stepped from a value where the species of interest is not reduced (or oxidized) to a value where the current is diffusion-controlled (Figure 19.3). Furthermore, the step potential must be selected so that only the redox species is electrolyzed. Cyclic voltammetry (CV) (see Chapter 11) is useful for selecting these potentials. By conducting the experiment in a blank solution, any contributions to the current from extraneous sources can be identified and subtracted from the current measured due to the redox couple. An advantage of chronoamperometric techniques is that species with slow heterogeneous kinetics (see Chapter 15) are amenable to the determination of D , as long as the potential can be stepped to a value where the rate of the electron transfer reaction is large and therefore the process is under diffusion control.

There are limitations to this approach. First, very short and very long times must be avoided. At short times, current arising from the charging of the double layer can cause deviations from theoretical behavior (Figures 19.3a and b). This charging current decays exponentially, so it is normally negligible after several time constants (the product of the uncompensated resistance R_u and the electrode double layer capacitance C_d). In most situations, this corresponds to a few milliseconds (for macroelectrodes) or microseconds (UMEs), and these problems can be avoided by not collecting data during the first 5–10 time constants after the potential step. At long times, convection develops in the solution (from vibrations and/or by density gradients arising from the electrolysis products), causing positive deviations from the theoretical current. These effects can become noticeable in as short as 20–30 seconds, but the exact time depends on the experimental conditions.

²UME techniques have been developed to measure D in solutions with low or no supporting electrolyte. See references (2) and (3).

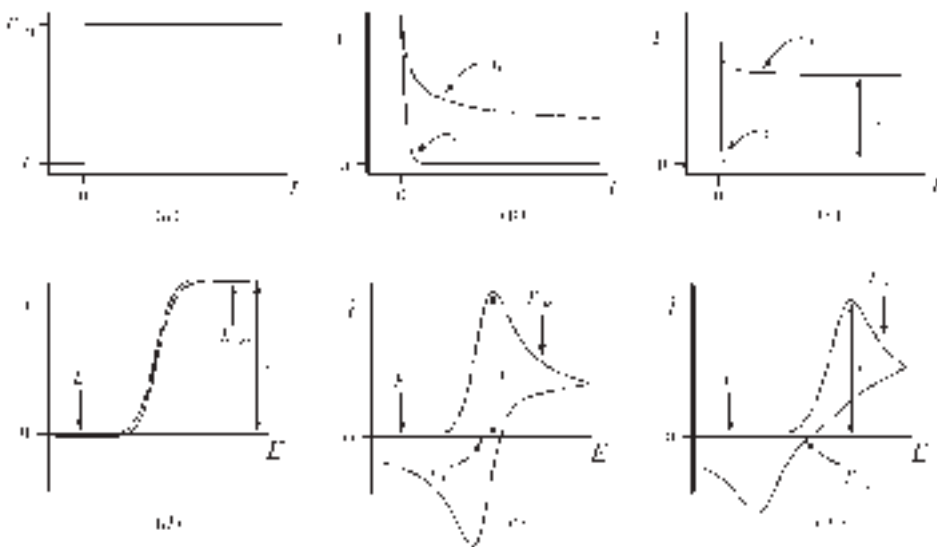


Figure 19.3 Charging current and selection of step potential for chronoamperometry. (a) Potential waveform applied to the electrode in chronoamperometry. At $t = 0$, the potential is stepped from the initial value E_i to a constant value E_{step} . (b) Dependence of faradaic current (i_f) and charging current (i_c) on time for a planar macroelectrode. (c) Dependence of i_f and i_c on time for a UME. (d) Cyclic voltammogram at a UME showing i_{ss} and selection of E_i and E_{step} . (e) Cyclic voltammogram of a reversible redox couple at a macroelectrode showing i_p and $E_{1/2}$ and selection of E_i and E_{step} . (f) Cyclic voltammogram of a quasi-reversible redox couple at a macroelectrode showing i_p and $E_{1/2}$ and selection of E_i and E_{step} .

Convective effects are most notable in solvents with low viscosity such as acetonitrile and dimethylformamide (see Chapter 3).

19.4.1.1 Chronoamperometry at UMEs

Steady-state conditions are typically attained within a few seconds after application of the potential step to a UME (see Chapter 6 for detailed discussions of UMEs). The resulting limiting current, i_{ss} (Figure 19.3c), is linearly dependent on the diffusion coefficient. Rearranging the equations for i_{ss} at hemispherical electrodes (equations (6.1.4.5) and (11.2.64)) and disk electrodes (equations (6.1.4.5) and (11.2.65)) gives expressions for the diffusion coefficient in terms of the experimental variables:

$$D = \frac{i_{\text{ss}}}{2\pi nFC^* r_0} \quad (\text{hemispherical UME}) \quad (19.3)$$

$$D = \frac{i_{\text{ss}}}{4nFC^* r_0} \quad (\text{circular disk UME}) \quad (19.4)$$

It is important to note that these equations only hold for an electrode embedded in an infinite insulating plane (Figures 19.1c and d). Electrodes having thin insulators (such as those used for *in vivo* voltammetry (see Chapter 17) or as SECM tips (see Chapters 6 and 12)) are susceptible to significant diffusion from behind the plane of the electrode (Figure 19.2c), resulting in appreciably larger steady-state currents. Therefore only UMEs having large values of RG ($RG = r_{\text{glass}}/r_0$, where r_{glass} is the radius of the insulation) should be used for diffusion coefficient measurements. Electrodes with $RG \geq 100$ can be assumed to behave as if they are embedded in infinite insulators. For an electrode radius of 5 μm , this means that the overall tip radius should be no less than 0.5 mm.

For careful measurements of the diffusion coefficient, it is critical that the measured current be truly at steady state, otherwise the current will contain a planar diffusion contribution that will produce a larger apparent value of D . At a hemispherical electrode, the Cottrell equation is used to determine the relative contributions of planar and spherical diffusion:

$$i(t) = nFADC * \left[\frac{1}{(\pi Dt)^{1/2}} + \frac{1}{r_0} \right] \quad (19.5)$$

Steady-state conditions are reached when the planar diffusion term of the Cottrell equation (equation 19.5) is insignificant compared to the spherical diffusion term:

$$\frac{1}{(\pi Dt)^{1/2}} \ll \frac{1}{r_0} \quad (19.6)$$

The dimensionless parameter Dt/r_0^2 is a convenient measure of the degree of spherical diffusion and can be used for estimating errors that arise from assuming the measurement is at steady state. For a 1% error (i.e., the spherical diffusion is 100 times the planar contribution), Dt/r_0^2 must be greater than 3200. For a hemispherical electrode with a radius of 5 μm (5×10^{-4} cm) and a molecule with a diffusion coefficient of 1×10^{-5} $\text{cm}^2 \text{ sec}^{-1}$, this corresponds to 80 sec, a time where appreciable convective effects might be present. If a 2% error is acceptable, Dt/r_0^2 must exceed 800, corresponding to a time of only 20 sec, well before convective effects are likely to be significant. A modest decrease in the electrode size greatly reduces the time required to reach steady state; an electrode with a radius of 2.5 μm would have a 1% error at 20 sec and 2% at 5 sec.

Disk UMEs are easier to fabricate than hemispherical UMEs, and are therefore much more commonly used. The Shoup and Szabo equation (1) for chronoamperometry at a disk UME

$$i(\tau) = 0.7854 + 0.8862\tau^{-1/2} + 0.2146 \exp(-0.7823\tau^{-1/2}) \quad (19.7)$$

where $\tau = 4Dt/r_0^2$ and $i(\tau)$ is ratio of the current at time τ to the steady-state current (i_{ss}), can be used to estimate the time required to reach steady state within a given error level. A value of $\tau = 2000$ gives a 1% error and $\tau = 500$ gives a 2% error. For a disk with a radius of 5 μm and a compound with a diffusion coefficient of 1×10^{-5} $\text{cm}^2 \text{ sec}^{-1}$, this corresponds to 50 and 12 sec, respectively. As with the spherical electrode, a decrease of the electrode radius by a factor of 2 (to 2.5 μm) gives a fourfold reduction of these times to 12.5 and 3 sec, respectively.

Another advantage of UME determinations of the diffusion coefficient is that measurements can be made in solutions of low conductivity, i.e. low or no supporting electrolyte (2, 3). Furthermore, double potential step techniques can be useful for determining diffusion coefficients of both D_O and D_R (4). Although these methods are beyond the scope of this chapter, the interested reader is referred to the original literature.

19.4.1.2 Chronoamperometry at macroelectrodes

At a large planar electrode, the diffusion-limited current following the application of a potential step follows the familiar Cottrell equation:

$$i(t) = \frac{nFAD^{1/2}C^*}{\pi^{1/2}t^{1/2}} \quad (19.8)$$

For electrodes with pure linear diffusion, the diffusion coefficient can be calculated from a plot of i vs. $t^{-1/2}$ (Figure 19.4). The slope of the best-fit line is then $nFAD^{1/2}C^*/\pi^{1/2}$, and D can be found from

$$D = \frac{(\text{slope})^2 \pi}{(nFAC^*)^2} \quad (19.9)$$

This is an excellent technique for measuring diffusion coefficients, and it has long been used for this purpose. The classic work of von Stackelberg (5) represents perhaps the most careful study of diffusion coefficients using this method.

The Cottrell equation assumes that planar diffusion is the only contribution to the overall current. However, purely planar diffusion is only achievable with very large electrodes or with shielded electrodes. The current measured with small, unshielded electrodes can exhibit appreciable edge effects, resulting in positive deviations from the Cottrell equation and thus positive errors in the diffusion coefficient. Edge effects are normally manifested at long times (i.e., small values of $t^{-1/2}$). The presence of convection at long times will also be evidenced by a positive deviation of the current. For these reasons, only those data points from the linear portion of the i vs. $t^{-1/2}$ curve should be used for the analysis of D .

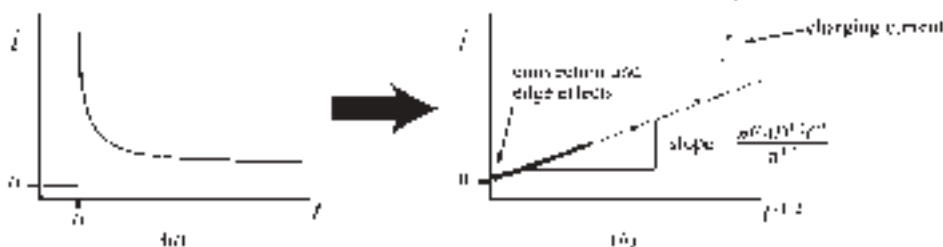


Figure 19.4 Analysis of data for chronoamperometry at a macroelectrode. (a) Raw data, (b) current plotted as a function of $t^{-1/2}$. Note the positive deviations arising from charging current and convection/edge effects.

In theory, spherical macroelectrodes (e.g., mercury drops) could be used to measure the diffusion coefficient. The advantage of mercury drops is that the surface is renewable and therefore electrode fouling can normally be avoided. However, these electrodes are of limited utility because they exhibit both planar diffusion, which predominates at short times, and spherical diffusion, which predominates at very long times. The time required to reach steady state with large spherical electrodes exceeds the time at which convection occurs. Likewise, the time frame for purely planar diffusion is short enough (~ 30 msec for $r_0 = 0.1$ cm, $D = 1 \times 10^{-5}$ cm 2 sec $^{-1}$, and $\leq 1\%$ contribution from spherical diffusion) that no particular advantage is realized by using spherical macroelectrodes to measure D . Hemispherical UMEs, however, are well-suited to steady-state measurements of diffusion coefficients (see above).

19.4.1.3 Normalized chronoamperometry techniques

By normalizing the chronoamperometric response of a UME to the limiting current at steady state, an equation depending only on r_0 , D , and t results (6, 7):

$$\frac{i(t)}{i_{ss}} = 1 + \frac{2r_0}{\pi(\pi D_0 t)^{1/2}} \quad (19.10)$$

A plot of the normalized current as a function of $t^{-1/2}$ gives a straight line with an intercept of 1 and a slope of $2r_0/\pi(\pi D)^{1/2}$. The diffusion coefficient can then be calculated from this slope:

$$D = \frac{4r_0^2}{(\text{slope})^2 \pi^3} \quad (19.11)$$

Note that D is now dependent on the square of the radius, so careful characterization of the UME's dimensions using a test compound is particularly important. An additional advantage of this normalization technique is that because the measurement of i_{ss} and $i(t)$ can occur in the same experiment, calibration errors in the current amplifier are essentially eliminated. An alternative approach is to fit the normalized chronoamperometry data to the Shoup and Szabo equation (equation (19.7)), which only requires knowledge of r_0 .

19.4.2 Rotating disk electrode techniques

The advantage of using the RDE for determining diffusion coefficients is that the measured current is steady state (see Chapter 11). The Levich equation relates the measured current to the experimental parameters:

$$i_l = 0.62nFAC^* D^{2/3} \omega^{1/2} v^{-1/6} \quad (19.12)$$

where ν is the kinematic viscosity. In the determination of diffusion coefficients with an RDE, it is common to change the rotation rate³ (ω in sec^{-1}) and plot i_1 vs. $\omega^{1/2}$. The slope of the resulting best-fit line can be used to determine D :

$$D = \left(\frac{\text{slope}}{0.62nFAC^*\nu^{-1/6}} \right)^{3/2} \quad (19.13)$$

As with chronoamperometry, there are limits to the range of experimental conditions under which equation (19.12) applies, but with the RDE the important parameter is the rotation rate ω . At low values of ω , the hydrodynamic boundary layer becomes large and the assumptions used to derive the Levich equation no longer hold. The lower limit for ω can be found from

$$\omega > 10 \frac{\nu}{r_1^2} \quad (19.14)$$

where r_1 is the electrode radius. At large values of ω , laminar flow is overcome by turbulent flow and again the Levich equation no longer holds. This occurs with Reynolds number Re

$$Re = \frac{\omega r_1^2}{\nu} \quad (19.15)$$

greater than about 10^5 . Thus for a solution with $\nu = 0.009 \text{ cm}^2 \text{ sec}^{-1}$ and $r_1 = 0.15 \text{ cm}$, the Levich equation can in theory be applied over the range of $\omega = 4\text{--}40,000 \text{ sec}^{-1}$, or 40–400,000 rpm. Practically, however, the upper limit is more on the order of 10,000 rpm for real RDEs (8).

Two additional experimental factors are important when the RDE is used to determine diffusion coefficients. First, the Levich equation assumes that the disk is centered on the axis of rotation. Any non-idealities in the construction of the RDE will result in an increase in the measured current, and thus lead to an overestimation of D . Second, edge effects can be present, particularly at very low rotation rates and/or with very small electrodes. These effects will be apparent as non-linearities in the i_1 vs. $\omega^{1/2}$ plot, and therefore rotation rates at which these non-linearities occur should not be used for the determination of the diffusion coefficient.

For more accurate determinations of diffusion coefficients with the RDE, one can apply the Riddiford correction (9), where the constant 0.62 in the Levich equation is replaced by

$$\frac{0.554}{0.8934 + 0.316(D/\nu)^{0.36}} \quad (19.16)$$

For a diffusion coefficient of $1 \times 10^{-5} \text{ cm}^2 \text{ sec}^{-1}$ and a kinematic viscosity of $0.009 \text{ cm}^2 \text{ sec}^{-1}$, the coefficient becomes 0.60, corresponding to a 3% difference from the Levich equation. The application of this correction is problematic, however, because an

³ ω is an angular velocity, so the one revolution is actually 2π , or 1 revolution per second corresponds to $\omega = 2\pi \text{ sec}^{-1}$.

approximate value of D must be known to calculate the coefficient, which is then used to calculate D . Because of this uncertainty, one should expect an error of a few percent in the calculated value of the diffusion coefficient even with the most careful RDE experiment.

19.4.3 Potential sweep techniques

Linear scan voltammetry (LSV) and cyclic voltammetry (CV) (see Chapter 11) are among the most common electrochemical techniques employed in the laboratory. Despite their utility, however, they are not particularly well suited to careful measurements of diffusion coefficients when using electrodes of conventional size. We will briefly discuss techniques for measuring D with LSV and CV, but the reader should be cautioned that these measurements under conditions of planar diffusion (i.e., at conventional electrodes) are probably useful to only one significant digit, and then only for nernstian systems with no coupled homogeneous reactions and with no adsorption. For more reliable results with LSV and CV, UMEs should be used.

For a reversible redox reaction (Figure 19.3e), the diffusion-controlled peak current at a planar electrode (Figure 19.3) is given by (10)

$$i_p = 2.69 \times 10^5 n^{3/2} AC^* D^{1/2} v^{1/2} \quad (19.17)$$

The most straightforward method for determining the diffusion coefficient is to measure the peak current (i_p) at several scan rates (v) and then plot i_p as a function of $v^{1/2}$. The slope of the best-fit line can then be used to calculate D :

$$D = \frac{(\text{slope})^2}{n^3 (2.69 \times 10^5 AC^*)^2} \quad (19.18)$$

It is important to re-emphasize that this equation applies only to reversible reactions. If one wishes to use this method, then steps should be taken to ensure that the system is in fact reversible and has no coupled homogeneous reactions. CV is useful for this purpose (see Chapters 11 and 15).

For irreversible systems ($O + e \xrightarrow{k_f} R$), D could also (in theory) be calculated from an analogous equation (10):

$$i_p = 2.99 \times 10^5 \alpha^{1/2} n^{3/2} AC^* D^{1/2} v^{1/2} \quad (19.19)$$

This equation requires knowledge of the transfer coefficient α , which can be estimated from

$$|E_p - E_{p/2}| = \frac{1.857 RT}{\alpha F} \quad (19.20)$$

However, the errors associated with this determination of α will further decrease the reliability of the measured D . This fact, combined with the limitations of LSV discussed for the

reversible case, means that this technique should not be used other than for an estimation of the diffusion coefficient. For quasi-reversible systems (Figure 19.3*f*), the peak current is a complex function of the heterogeneous rate constant, and therefore a reliable value of the diffusion coefficient cannot be obtained.

Much more accurate measurements of diffusion coefficients can be obtained with LSV or CV using UMEs. These measurements are much less dependent on the electrochemical reversibility of the redox couple. Measurement of the diffusion-limited current from a voltammogram recorded at a microelectrode is demonstrated in Figure 19.3*c*. The concept is identical to that already discussed for chronoamperometry at UMEs; at slow scan rates (i.e., long times) the current becomes steady state as long as the potential is well past $E_{1/2}$. The dependence of D on the steady-state current i_s is given by equation (19.3) for a hemispherical UME and equation (19.4) for a disk UME. The time considerations for CV are the same as those discussed above for chronoamperometry, except that the time is estimated from the scan rate and the difference between the final potential E_f and $E_{1/2}$:

$$t \approx \frac{|E_f - E_{1/2}|}{v} \quad (19.21)$$

Thus for a UME with a radius of 5 μm and $|E_f - E_{1/2}| = 0.3$ V, planar diffusion contributes <2% to the measured current at a scan rate of <20 mV sec⁻¹.

19.4.4 Current step techniques (chronopotentiometry)

In chronopotentiometry, a current is applied to the electrode and the potential changes to a value at which the flux of the electroactive species is sufficient to supply the applied current. After a certain time, the flux of redox species to the surface cannot sustain this current and the potential changes rapidly to a new value at which another species (often solvent or electrolyte) is reduced (or oxidized). This time, termed the transition time τ , follows the Sand equation:

$$\tau^{1/2} = \frac{\pi^{1/2} n F D^{1/2} C^*}{2 i_0} \quad (19.22)$$

where i_0 is the current density (i/A). To calculate diffusion coefficients, the transition times are measured at several current densities, and an average value of D can be calculated from

$$D = \frac{4 i_0^2 \tau}{\pi (n F C^*)^2} \quad (19.23)$$

The two primary advantages of chronopotentiometry are that the measured quantity (τ) is directly proportional to D , and that τ is the same regardless of heterogeneous electrode kinetics (although the break in the $E-t$ curve is less sharp when the reaction is not reversible). The primary disadvantages of chronopotentiometry include some of those

discussed previously for planar electrodes—convection at long times and complications by charging current contributions to the overall current. Convective effects can be minimized as before by choosing current densities such that transition times are no longer than 30–60 sec. The charging current issue is more troublesome, especially under conditions where short transition times occur. The current that flows to charge the double-layer means that the faradaic current differs from the applied current, thus introducing inaccuracies in the measurement of τ . Short transition times, low concentrations, and electrodes having a large capacitance contribute to a higher fraction of the applied current going towards charging current and thus a less accurate determination of diffusion coefficient. Furthermore, the oxidation of the electrode surface or the presence of adsorbed electroactive material can complicate the measurement of the transition times. For these reasons, chronopotentiometry is not commonly used for accurate measurements of diffusion coefficients.

19.4.5 Scanning electrochemical microscopy (SECM) techniques

Scanning electrochemical microscopy (SECM) (see Chapter 12) has unique capabilities that can be exploited for measurements of the diffusion coefficient. Bard introduced a transient SECM technique that allows the determination of D without knowledge of C^* or n (11). The only parameter that must be known is the tip radius a . This technique uses an approximate analytical expression relating a characteristic transition time t_c to the change in tip position above a substrate. From plots of the normalized tip current vs. $t^{-1/2}$, t_c can be determined, and then a working curve is used to calculate D . Although this technique has relatively low precision, it is useful for measuring diffusion coefficients in situations where the concentration is not known or cannot be independently measured. For example, it has been used for measuring diffusion coefficients in non-traditional media such as gels (12).

The diffusion coefficient ratio of a redox couple can also be measured with SECM using an approach developed by Unwin (13, 14). With this technique, the ratio of the steady-state collector current for the substrate generation/tip collection (SG/TC) mode to the steady-state collector current measured in the feedback mode (at the same tip-substrate separation) gives directly the ratio of diffusion coefficients for the redox couple. The advantage of this approach is that no knowledge of the tip-substrate separation, the electrode sizes, or the mediator concentration is required.

Beyond these applications, SECM can also be used to probe diffusional transport in unusual samples because the UME can be placed precisely in the microenvironment of interest. For example, lateral proton diffusion in Langmuir monolayers (15), diffusional transport through porous membranes and dentin (16), and the contribution of diffusion to iontophoretic transport in skin (17) have been investigated using the SECM.

19.5 TABLES OF DIFFUSION COEFFICIENTS

Diffusion coefficients for common test compounds (see Tables 19.2 –19.4).

Table 19.2

Diffusion coefficients of selected inorganic and organometallic compounds. Unless otherwise indicated, data are for 25 °C or room temperature

Compound	Solvent system	$D \times 10^5$ ($\text{cm}^2 \text{ sec}^{-1}$)	Method ^a	Reference
Ag^+	0.1 M KNO_3	1.55	1	5
Cd^{2+}	1.0 M KCl	0.808	1	5
Tl^+	0.5 M KNO_3	1.9	5	18
	0.9 M NaNO_3	1.6	5	18
$\text{Fe}(\text{CN})_6^{3-}$	0.05 M KCl	0.765	1	5
	0.1 M KCl	0.763	1	5
	0.5 M KCl	0.770	1	5
	1.0 M KCl	0.763	1	5
	0.5 M KCl , pH 3.0	0.72	2, 3	19
$\text{Fe}(\text{CN})_6^{4-}$	0.05 M KCl	0.662	1	5
	0.1 M KCl	0.650	1	5
	0.5 M KCl	0.639	1	5
	1.0 M KCl	0.632	1	5
$\text{Ru}(\text{NH}_3)_6^{3+}$	Phosphate buffer, pH 7.0	0.55	1	19
	0.1 M NaTFA	0.67	2	20
Ferrocene (Fc)	0.5 M TBABF_4 in CH_3CN	1.7	2	21
	0.2 M TBACIO_4 in CH_3CN	2.2	2, 3	19
	0.2 M LiClO_4 in CH_3CN	2.4	4	22
	0.1 M TBACIO_4 in CH_3CN	2.2	6	23
	0.1 M TBACIO_4 in CH_3CN	2.7 (40 °C)	2	24
	0.1 M TBACIO_4 in CH_3CN	3.0 (50 °C)	2	24
	0.1 M TBACIO_4 in CH_3CN	3.2 (60 °C)	2	24
Fc^+	0.1 M TBACIO_4 in CH_3CN	1.6	6	14
$\text{Fc}(\text{CO}_2\text{H})$	0.2 M LiClO_4 in CH_3CN	1.1	4	22
	0.1 M NaClO_4 (aqueous)	0.67	2	12
$\text{Fc}(\text{CH}_2\text{CO}_2^-)$	0.1 M LiClO_4 (aqueous)	0.51	2	2
FcTMA^+	0.1 M NaClO_4 (aqueous)	0.66	2	12
FcMeTMA^+	0.1 M TBACIO_4	1.4	2	2
$\text{Fc}(\text{CH}_2\text{OH})_2$	0.1 M NaClO_4 (aqueous)	0.65	2	12
	0.1 M LiClO_4 (aqueous)	0.63	3	25
	0.050 M TMACIO_4 (aqueous)	0.78	2	26
IrCl_6^{2-}	0.5 M K_2SO_4	0.64	5	27
Osmocene	0.2 M LiClO_4 in CH_3CN	2.2	4	22
Ruthenocene	0.2 M LiClO_4 in CH_3CN	2.2	4	22
$\text{Ru}(\text{bpy})_3^{2+}$	0.1 M TEABF_4 in CH_3CN	2.1	7	28
$\text{Fe}(\text{bpy})_3^{2+}$	0.1 M TEABF_4 in CH_3CN	2.1	7	28
$\text{Ru}(\text{acac})_3$	0.1 M TEABF_4 in CH_3CN	2.3	7	28

Abbreviations: TFA, trifluoroacetate; TBA, tetra-*n*-butylammonium; TEA, tetraethylammonium; TMA, trimethylammonium; bpy, 2,2'-bipyridine; acac, acetylacetone.

^a1, chronoamperometry at a shielded planar electrode; 2, steady-state current at a disk UME; 3, normalized chronoamperometry; 4, chronopotentiometry; 5, chronoamperometry at unshielded, planar electrode; 6, scanning electrochemical microscopy (method from reference (23)); 7, rotating disk electrode.

Table 19.3

Diffusion coefficients of selected organic compounds. Unless otherwise indicated, data are for 25 °C or room temperature

Compound	Solvent system	$D \times 10^5$ ($\text{cm}^2 \text{ sec}^{-1}$)	Method ^a	Reference
p-benzoquinone	0.25 M TEACIO ₄ in CH ₃ CN	2.7	1	23
Hydroquinone	0.1 M H ₂ SO ₄	0.73	2	29
Anthracene	0.1 M TEACIO ₄ in CH ₃ CN	2.55	3	30
	0.1 M TBABF ₄ in DMF	1.1	4	31
Anthraquinone	0.1 M TBABF ₄ in DMF	1.0	4	31
Benzophenone	0.1 M TBABF ₄ in DMF	1.0	4	31
Biphenyl	0.1 M TEACIO ₄ in CH ₃ CN	2.48	3	30
Fullerene (C60)	0.5M TBABr in <i>o</i> -dichlorobenzene	0.11	4	32
Fullerene (C70)		0.11	4	32
Naphthalene	0.1 M TEACIO ₄ in CH ₃ CN	2.74	3	30
Perylene	0.1 M TBABF ₄ in DMF	0.84	4	31
TMPD (<i>N,N,N',N'</i> -tetramethylphenylene diamine)	0.1 M TBACIO ₄	2.4	5	24
Ascorbic acid	0.1 M Phosphate, pH 7.4	0.53	6	33
Catechol	0.1 M H ₂ SO ₄	0.66	2	29
(<i>–</i>)-3,4-dihydroxy-norephedrine	0.1 M H ₂ SO ₄	0.66	7	33, 34
3,4-dihydroxy-hydrocinnamic acid	0.1 M H ₂ SO ₄	0.69	7	34
L-DOPA	0.1 M H ₂ SO ₄	0.55	7	33, 34
L-DOPA methyl ester	0.1 M H ₂ SO ₄	0.70	7	34
DOPAC (3,4-dihydroxy-phenylacetic acid)	0.1 M Phosphate, pH 7.4	0.59	6	33
Dopamine	0.1 M Phosphate, pH 7.4	0.60	6	33
	0.1 M H ₂ SO ₄	0.67	7	34
Epinephrine	0.1 M Phosphate, pH 7.4	0.52	6	33
	0.1 M H ₂ SO ₄	0.61	7	34
4-methylcatechol	0.1 M Phosphate, pH 7.4	0.66	6	33
Norepinephrine	0.1 M Phosphate, pH 7.4	0.55	6	33
	0.1 M H ₂ SO ₄	0.62	7	34
Serotonin (5-hydroxy-tryptamine)	0.1 M Phosphate, pH 7.4	0.54	6	33

Abbreviations: TBA, tetra-*n*-butylammonium; TEA, tetraethylammonium.

^a1, scanning electrochemical microscopy (method from reference (23)); 2, hydrodynamic voltammetry with a tubular electrode; 3, tracer diffusion from capillaries; 4, rotating disk electrode; 5, steady-state current at a disk UME; 6, flow injection analysis (a non-electrochemical method); 7, chronoamperometry at unshielded planar electrode.

Table 19.4

Diffusion coefficients of other species of interest. Unless otherwise indicated, data are for 25 °C or room temperature

Compound	Solvent system	$D \times 10^5$ ($\text{cm}^2 \text{ sec}^{-1}$)	Method ^a	Reference
H^+	0.1 M KNO_3	7.9	1	35
	1.0 M KCl	7.3	2	36
	0.1 M NaClO_4 in 0.010–0.060 M HClO_4	7.1	1	37
OH^-	0.1 M Na_2SO_4	5.6	3	38
	1 M KNO_3	4.4	3	39
	0.1 M Na_2SO_4 in 0.2–25 mM OH^-	4.9	1	40
H_2	0.1 M KNO_3	5.0	1	35
O_2	1.0 M KOH	1.6	3	41
	0.025 M H_2SO_4	1.9	3	42
	0.1 M Na_2SO_4	2.5	4	43

^a1, steady-state current at a disk UME; 2, chronoamperometry at a shielded planar electrode; 3, rotating disk electrode; 4, diaphragm diffusion cell.

REFERENCES

1. D. Shoup, A. Szabo, *J. Electroanal. Chem.* **140**, 237 (1982).
2. W. Hyk, A. Nowicka, Z. Stojek, *Anal. Chem.* **74**, 149 (2002).
3. W. Hyk, Z. Stojek, *Anal. Chem.* **74**, 4805 (2002).
4. H. Ikeuchi, M. Kanakubo, *J. Electroanal. Chem.* **493**, 93 (2000).
5. M. von Stackelberg, M. Pilgram, V. Toome, *Z. Elektrochem.* **57**, 342 (1953).
6. S. C. Petrovic, R. H. Hammericksen, *Electroanalysis* **14**, 599 (2002).
7. G. Denuault, M. V. Mirkin, A. J. Bard, *J. Electroanal. Chem.* **308**, 27 (1991).
8. A. J. Bard, L. R. Faulkner, *Electrochemical Methods: Fundamentals and Applications*, 2nd ed., John Wiley & Sons, Inc.: New York, 2001.
9. D. P. Gregory, A. C. Riddiford, *J. Chem. Soc.*, 3756 (1956).
10. R. S. Nicholson, I. Shain, *Anal. Chem.* **36**, 706 (1964).
11. A. J. Bard, G. Denuault, R. A. Friesner, B. C. Dornblaser, L. S. Tuckerman, *Anal. Chem.* **63**, 1282 (1991).
12. F.-R. F. Fan, *J. Phys. Chem.* **102**, 9777 (1998).
13. R. D. Martin, P. R. Unwin, *Anal. Chem.* **70**, 276 (1998).
14. R. D. Martin, P. R. Unwin, *J. Electroanal. Chem.* **439**, 123 (1997).
15. J. Zhang, P. R. Unwin, *Phys. Chem. Chem. Phys.* **4**, 3814 (2002).
16. S. Nugues, G. Denuault, *J. Electroanal. Chem.* **408**, 125 (1996).
17. B. D. Bath, E. R. Scott, J. B. Phipps, H. S. White, *J. Pharm. Sci.* **89**, 1537 (2000).
18. M. Kakihana, H. Ikeuchi, G. P. Sato, K. Tokuda, *J. Electroanal. Chem.* **108**, 381 (1980).
19. J. E. Baur, R. M. Wightman, *J. Electroanal. Chem.* **305**, 73 (1991).
20. D. O. Wipf, E. W. Kristensen, M. R. Deakin, R. M. Wightman, *Anal. Chem.* **60**, 306 (1988).
21. M. V. Mirkin, T. C. Richards, A. J. Bard, *J. Phys. Chem.* **97**, 7672 (1993).
22. T. Kuwana, D. E. Bublitz, G. Hoh, *J. Am. Chem. Soc.* **82**, 5811 (1960).
23. R. D. Martin, P. R. Unwin, *Anal. Chem.* **70**, 276 (1998).
24. S. R. Jacob, Q. Hong, B. A. Coles, R. G. Compton, *J. Phys. Chem.* **103**, 2963 (1999).

25. S. C. Petrovic, W. Zhang, M. Ciszkowska, *Anal. Chem.* **72**, 3449 (2000).
26. W. Miao, Z. Ding, A. J. Bard, *J. Phys. Chem. B* **106**, 1392 (2002).
27. M. R. Deakin, K. J. Stutts, R. M. Wightman, *J. Electroanal. Chem.* **182**, 113 (1985).
28. M. Morita, Y. Tanaka, K. Tanaka, Y. Matsuda, T. Matsumura-Inoue, *Bull. Chem. Soc. Japan* **61**, 2711 (1988).
29. L. R. Sharma, R. K. Kalia, *J. Chem. Eng. Data* **22**, 39 (1977).
30. T. A. Miller, B. Prater, J. K. Lee, R. N. Adams, *J. Am. Chem. Soc.* **87**, 121 (1965).
31. S. U. Pedersen, T. B. Christensen, T. Thomasen, K. Daasbjerg, *J. Electroanal. Chem.* **454**, 123 (1998).
32. B. Miller, J. M. Rosamilia, G. Dabbagh, A. J. Muller, R. C. Haddon, *J. Electrochem. Soc.* **139**, 1941 (1992).
33. G. Gerhardt, R. N. Adams, *Anal. Chem.* **54**, 2618 (1982).
34. S. A. Nowinski, D. M. Anjo, *J. Chem. Eng. Data* **34**, 265 (1989).
35. J. V. Macpherson, P. R. Unwin, *Anal. Chem.* **69**, 2063 (1997).
36. M. von Stackelberg, M. Pilgram, *Coll. Czech. Chem. Commun.* **25**, 2974 (1960).
37. J. Zhou, Y. Zu, A. J. Bard, *J. Electroanal. Chem.* **491**, 22 (2000).
38. M. Breiter, K. Hoffmann, *Z. Elektrochem.* **64**, 462 (1960).
39. R. Landsberg, W. Geissler, S. Mueller, *Z. Chem.*, **1**, 169 (1961).
40. B. Liu, A. J. Bard, *J. Phys. Chem. B* **106**, 12801 (2002).
41. C. P. Winlove, K. H. Parker, R. K. C. Oxenham, *J. Electroanal. Chem.* **170**, 293 (1984).
42. V. G. Levich, *Physicochemical Hydrodynamics*, Prentice-Hall: Englewood Cliffs, NJ, 1962.
43. G. W. Hung, R. H. Dinius, *J. Chem. Eng. Data* **17**, 449 (1972).

Liquid Junction Potentials

Robert A. W. Dryfe

School of Chemistry, University of Manchester, Oxford Road,
Manchester M13 9PL, UK

20.1 TYPES OF LIQUID JUNCTIONS

20.1.1 Interfacial potentials without electrolyte transport

Potentiometric methods of electroanalysis (see Chapter 7 of this handbook) depend on the ability of a membrane material to transport either cations or anions selectively. This selective behaviour results in an imbalance of concentrations on either side of the membrane which, in turn, leads to the establishment of a measurable potential difference across the membrane. In the simplest possible analysis, if we consider our membrane to be infinitely thin, or alternatively to have some kind of electrolyte boundary that is infinitely thin, then the equality of electrochemical potential, $\bar{\mu}_i$, in either of the solution phases, α and β , implies that

$$\bar{\mu}_{\alpha,i} = \bar{\mu}_{\beta,i} \quad (20.1.1-1)$$

where i is the ion which is able to partition between the two phases. Thus, from the definition of the electrochemical potential:

$$\mu_{\alpha,i}^0 + RT \ln a_{\alpha,i} + z_i F \phi_{\alpha} = \mu_{\beta,i}^0 + RT \ln a_{\beta,i} + z_i F \phi_{\beta} \quad (20.1.1-2)$$

where μ_i^0 is the standard chemical potential of the ion in a given phase, a is the ion activity, ϕ is the electrical potential of the phase, z is the charge number of the ion, F is Faraday's constant, R is the universal gas constant and T is the absolute temperature.

Hence, the potential difference established across the membrane depends on the ratio of the activities of the ions in phases α and β :

$$\Delta\phi \equiv \phi_{\beta} - \phi_{\alpha} = \frac{RT}{zF} \ln \left(\frac{a_{\alpha,i}}{a_{\beta,i}} \right) \quad (20.1.1-3)$$

where $\Delta\phi$ is the potential difference between phase β and phase α . Towards the end of the chapter, methods to establish stable interfacial potentials between phases that are physically distinct (i.e. do not require separation via a membrane) will be discussed.

The establishment of such interfacial potentials is readily envisaged for cases where the net transport of an electrolyte is prevented because one of its constituents cannot partition. What is perhaps less obvious is that such potentials arise continually within solution phases, even where there is no physical separation into distinct phases. These so-called liquid junction potentials or diffusion potentials play an important role in electrochemical experiments, but because there is no well-defined phase boundary, they are intrinsically more difficult to measure. This chapter discusses how these potentials arise, how they may be calculated, what quantities are associated with them, and how they may be minimised. Finally, interfaces *between* electrolytes (i.e. those interfaces between immiscible electrolyte solutions (ITIES)) and the application of some of the concepts developed earlier in the chapter to “non-standard” electrolyte systems, such as polymer electrolytes and room-temperature ionic liquids, will be discussed.

20.1.2 Interfacial potentials with electrolyte transport

The starting point for the discussion of the potentials that arise within a given electrolyte solution is to return to the Nernst–Planck equation, describing the flux of charge J within an electrolyte (1):

$$J = -\frac{F}{RT} \nabla\phi \sum_j z_j D_j C_j - \sum_j D_j \nabla C_j + v \sum_j C_j \quad (20.1.2-1)$$

which reduces to

$$J = -\frac{F}{RT} \frac{\partial\phi(x)}{\partial x} \sum_j z_j D_j C_j - \sum_j D_j \frac{\partial C_j(x)}{\partial x} + v(x) \sum_j C_j \quad (20.1.2-2)$$

for the one-dimensional case, where x is the relevant spatial co-ordinate. Of the symbols, D_j and C_j are the diffusion coefficient and concentration of ion j , respectively, and v is the velocity of the solution. The terms on the right-hand side of these equations represent fluxes due to migration, diffusion, and convection, respectively.

Equation (20.1.2-1) can be written in terms of the current density, since this quantity is defined as the flux multiplied by $-z_i F$:

$$I = F \nabla\phi \sum_j z_j u_j C_j + F \sum_j z_j D_j \nabla C_j - F v \sum_j z_j C_j \quad (20.1.2-3)$$

where I is the current density (i/A , where A represents electrode area), and u_j is the mobility of each ion. In the limit of infinite dilution, the ionic mobility is related to its diffusion coefficient via the Einstein law (2):

$$u_i = \frac{z_i F D_i}{R T} \quad (20.1.2-4)$$

Note that there is some inconsistency in prior literature regarding the precise definition of ionic mobility, with some authors distinguishing between the competing definitions by referring to an “absolute” and a “conventional” mobility (2). Here, the term mobility refers to the latter quantity, which has dimensions of the form $\text{cm}^2 \text{ s}^{-1} \text{ V}^{-1}$, which is positive (for cations) or negative (for anions).¹ Even if the solution is flowing, the convective term in the above equation will not contribute to the overall current because of the requirement for local electroneutrality. Hence, equation (20.1.2-3) may be re-arranged to give

$$\nabla\phi = \frac{I}{\kappa} - \frac{F}{\kappa} \sum_j z_j D_j \nabla C_j \quad (20.1.2-5)$$

where κ represents the electrolyte conductivity, defined as

$$\kappa = F \sum_j z_j u_j C_j \quad (20.1.2-6)$$

Equation (20.1.2-2) is important because it states that even when no current flows, a potential gradient arises *within* a given solution when the diffusion coefficients of the ions of the electrolyte differ. This condition, which is almost certain to be met for ions of even slightly differing size, means that the summation term in equation (20.1.2-5) is non-zero, so that a potential gradient exists in solution. Physically, the reason for the establishment of the gradient can be understood if we question the assumption made in arriving at equation (20.1.2-5), namely that the solution must be locally electroneutral. Clearly, electroneutrality will be rapidly violated if the ions diffuse through the solution at different rates. However, this imbalance in transport rates sets up the electric field in solution if, for example, the cations move ahead of the anions. The diffusion potential then arises since electroneutrality is, therefore, the brake that acts to restore parity to the solution. Lingane has delineated three types of diffusion potential, depending on the differences between the constituent parts of the electrolyte solution (3). The first potential is considered to arise when the entire solution consists of the same electrolyte, but a difference in activities exists within the solution. If electrodes reversible to one of the ions are introduced, this becomes a “concentration cell”, discussed in Section 20.2.1. The second type of boundary arises where two solutions containing a common ion meet; the common-ion activities in both halves are identical, but each half of the cell contains a different counter-ion. Finally, the third type of diffusion potential, according to the Lingane classification, is established when neither of the conditions of the first and second type is met.

A consequence of this phenomenon arises from further consideration of equation (20.1.2-1). Neglecting the third (convective) term, for the reasons stated above, the current is given by the sum of the migratory and diffusive fluxes. In the case of the bulk electrolyte

¹Allowing mobilities to take negative, or positive, values (dependent on the ionic charge) accounts for the opposing displacements of ions of opposite charge in the presence of an electric field. Although this deviates from the notation adopted in some texts, this approach means equation (20.1.2-6) follows directly from the Nernst–Planck equation. Further, there is no need to introduce the absolute value of the charge number in the definition of the conductivity, since the product $z_i u_i$ will always be positive. The consequence of this is that definitions of parameters such as ionic conductivity and, in turn, transference number must use $z_i u_i$, rather than u_i .

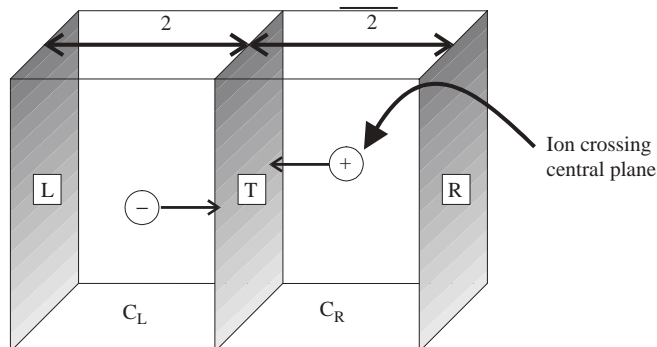


Figure 20.1 Schematic description of charge transport in the bulk of a cell: electroneutrality can be maintained by cations moving from electrode “R” to “L”, or via anions moving in the reverse direction, or by a combination of both processes. The transference number is, essentially, the fraction of charge passed across a virtual reference plane, “T”, in the solution due to a given ion.

solution on addition of an excess of supporting electrolyte (see Chapter 3 of this handbook), the flux of this electrolyte is essentially due to migration alone. Hence, the current density within a region of the bulk solution is given solely by the first term of equation (20.1.2-3). This equation reveals that the fluxes carried by the components of a binary electrolyte will only be equal (or, rather equal and opposite, given their response to an electric field) if the mobilities of the constituent ions are of the same magnitude. As with the discussion of diffusion coefficients, it is extremely unlikely that this condition will be met. Thus, in almost all cases, it is clear that differing fractions of charge will be carried by the components of a given electrolyte solution. This situation may be illustrated schematically for a two-electrode cell illustrated in Figure 20.1. For a given electrolysis process, the excess negative charge generated by the reduction of one equivalent of reactant at the cathode may be compensated by (a) a movement of one equivalent of cations from the bulk of the solution *towards* the cathode; or (b) by movement of one equivalent of anions *away* from the cathode, into the bulk solution. Analogous arguments would hold for the oxidation reaction occurring at the anode. However, a third possibility exists, which will be the more general case: namely that some fraction of the charge balance will be carried out by movement of the cations in one direction *and* the remaining fraction will arise from movement of the anions in the other direction. The important point is, based on the statement about mobilities, that these fractions will *not* necessarily be equal (i.e. the fraction of charge transported by each ion will *not* usually be one-half) but nor will it normally approach zero (or one). This gives rise to the concept of the transference number, defined algebraically below, which is simply the fraction of the current flowing attributable to a particular ion. In summary, the origin of the transference number can be understood by paraphrasing Orwell: “all ions are mobile, but some are more mobile than others”.

The conclusion that charge transport is unequally shared between the constituent ions of an electrolyte may appear to be at odds with the underlying assumption that the solutions remain locally electroneutral, but one can again resolve this objection by consideration of the “membrane” case alluded to in the opening section. If one considers ion transport

within a cation-exchange membrane (e.g. an organic ionomer such as “Nafion” or an inorganic ion-exchanger such as a zeolite (see Section 20.5)), then for an ideal membrane the fraction of charge transported by the cation should approach one. This does not mean that electroneutrality is violated, merely that the anions (or rather the framework charges) are bystanders with zero mobility. The converse case applies to electronic conduction within metals in the case where charge is transported solely by the mobile electrons; again, this does not violate the principle of electroneutrality within the bulk of the metal.

The transference number was defined above as the fraction of current (or current density) attributable to a particular ion:

$$t_i = \frac{I_i}{I} = \frac{I_i}{\sum_j I_j} \quad (20.1.2-7)$$

By definition,

$$\sum_j t_j = 1 \quad (20.1.2-8)$$

As discussed above for the bulk solution where there is no concentration gradient, the current density will arise solely from the first term of equation (20.1.2-3). Combination with equation (20.1.2-7) leads to (2)

$$t_i = \frac{z_i C_i u_i}{\sum_j z_j C_j u_j} \quad (20.1.2-9)$$

Recall that the mobility terms are, by definition, positive for cations and negative for anions. Some further relations are required to complete our definitions of transference numbers (4). The molar conductivity, Λ , of a solution is defined as

$$\Lambda = \frac{\kappa}{C} \quad (20.1.2-10)$$

where C is the electrolyte concentration.

Kohlrausch's law of independent ionic migration states that the molar conductivity at infinite dilution, Λ^0 , is given by the sum of the values for its ionic components, A^{a+} and B^{b-} .

$$\Lambda^0 = v_A \lambda_A^0 + v_B \lambda_B^0 \quad (20.1.2-11)$$

where λ_A^0 is the limiting ionic molar conductivity for ion A and v_A defines its stoichiometry in the electrolyte.

By definition,

$$\lambda_i = z_i u_i F \quad (20.1.2-12)$$

Combining equations (20.1.2-7) and (20.1.2-10) yields

$$t_i = \frac{C_i \lambda_i}{\sum_j C_j \lambda_j} \quad (20.1.2-13)$$

For a binary electrolyte, a combination of equations (20.1.2-11) and (20.1.2-13) leads to

$$t_A = \frac{C_A \lambda_A^0}{C_A \lambda_A^0 + C_B \lambda_B^0} = \frac{v_A \lambda_A^0}{\Lambda^0} \quad (20.1.2-14)$$

Note that the transference numbers defined in terms of ionic conductivity apply, strictly speaking, to infinite dilution where ion–ion interactions are minimal and Kohlrausch’s law holds.

Having defined the relevant quantities, methods of measuring them and appropriate sample calculations are given in the next sections. Note that the subsequent sections are solely concerned with transference parameters of electrolyte solutions. The measurement of transference numbers in ionic crystals is subject to some quite different constraints and is not considered here. This area has been reviewed in reference (5).

20.2 TRANSFERENCE NUMBERS AND CONDUCTIVITY

20.2.1 Experimental methods of determining transference number

The molar conductivity of an electrolyte is the more generally useful quantity since the Kohlrausch law allows its limiting value to be resolved into those of its constituent ions. Comparison between different electrolytes with a common ion therefore allows the determination of an unknown molar conductivity. However, the quantity typically measured is the overall electrolytic conductivity. A way to apportion the conductivity (and hence mobility) to the individual ions of the electrolyte is required. Equation (20.1.2-11) shows that resolution of the molar conductivity into the terms arising from its constituent ions is possible if the transference number of the ion is found. Although this property and the methods developed to measure it may seem rather arcane, it has been of fundamental importance in the understanding of the conductivity and diffusion potentials developed within electrolyte solutions. Experimentally, a number of ways of measuring transference numbers have been developed; these are summarised below.

One important point to make is that the quantity accessed experimentally, in general, is the net transference number for a given species regardless of its exact speciation (6). For complex ions, if the Hittorf method (see below) is used to measure the transport of chloropalladate ions for example, by analysis of the amount of Pd accumulated on an electrode surface, one has no way of distinguishing between the transfer of $[PdCl_4]^{2-}$ and $[PdCl_3]^-$, both of which occur in solution. The existence of rapidly occurring equilibria, which will typically interconvert on time-scales much shorter than the measurement time-scale, means that the net transference of anionic palladium species of whatever form is

measured rather than the transport of a particular species. This general point must be borne in mind for all measurements other than those in simple binary electrolytes (e.g. for aqueous sodium chloride solutions).

The classical methods of experimental transference number determination can be divided into three general groups. The first (the Hittorf method) is essentially an analytical approach, which relates changes in cell composition to the transference numbers of the electrolyte solution. The second group of methods relates the motion of the boundary separating zones of different composition to the transference numbers. The final approach relates the cell potential, which arises from the diffusion potential, to the transference number. Each of these methods is summarised, in turn, below.

20.2.1.1 The Hittorf method

This approach uses a three-compartment cell and relates the change in composition of the anodic and cathodic parts of the cell to the experimental transference number. The crucial assumption is that the composition within the central compartment is not affected by the electrolytically induced changes within the outer compartments. The cell can thus be represented as shown in Figure 20.2.

If, for example, two silver/silver chloride electrodes are bathed in a sodium chloride solution, reduction of an equivalent of silver chloride to silver will be compensated, as explained above, by the ingress of t_+ equivalents of sodium ions and the egress of t_- equivalents of chloride ion. However, one equivalent of chloride has also been gained by electrolysis, so the net change in chloride composition is $(1 - t_-)$, which equals t_+ by equation (20.1.2-8). The reaction will be driven in reverse at the anode. Hence, there will be a net loss of t_+ equivalents of chloride, accompanied by an egress of t_+ ions of sodium. The situation can be extended to more complex electrolyte solutions but the principle remains the same. Key to the method is the analysis of the compositional changes within the outer (electrode) compartments of the cell. The method dates back to 1863; the classical approach to the analysis involved cell designs where outer compartments could be isolated from the inner part of the cell (via stopcocks; see Figure 20.3) and, originally, compositional changes

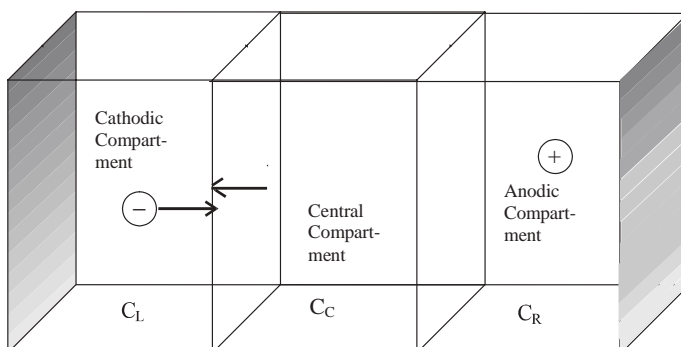


Figure 20.2 Schematic representation of the Hittorf cell. The basis of the method is that the composition of the central compartment is uniform.

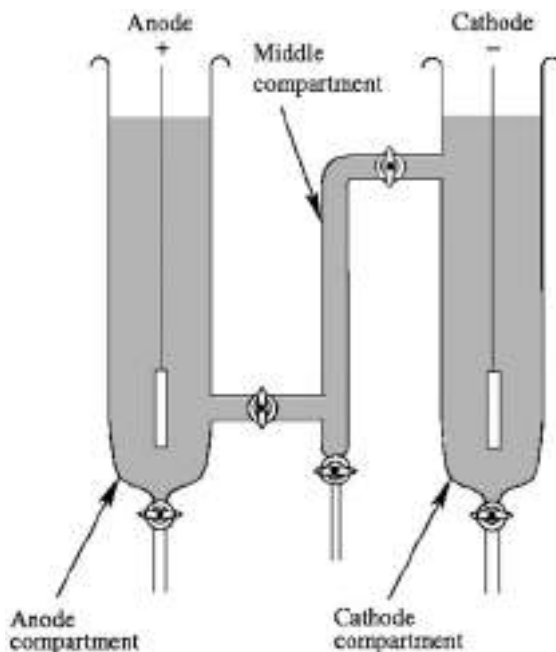


Figure 20.3 Schematic diagram of the Hittorf apparatus for experimental determination of transference numbers. (for colour version: see colour section at the end of the book).

were determined from the net weight change within the outer solutions. *In situ* analytical methods of compositional change, including spectrophotometric and conductometric detection, were subsequently introduced (6), although questions then arise about the locus of the detection process and how representative it may be of the electrolyte concentration within the compartment as a whole.

Much of the early 20th century data on transference numbers, and hence on ionic mobilities, was obtained via this route. One general drawback of the Hittorf method is the requirement, for transference measurements, that all of the charge transfer reported be due to migration. This condition is difficult to satisfy for the Hittorf approach; it is extremely difficult to exclude diffusive (and convective) contributions from the cell. This need highlights a general feature of transference measurements: a compromise often has to be made to achieve maximum possible accuracy. On one hand, passage of a large current in a Hittorf cell maximises compositional changes and hence minimises the error in determining those changes. However, the perturbation imposed on the cell is likely to mean that the parameters extracted correspond in part to the movement of ions through a substantially electrolysed solution of electrolyte rather than through the pristine electrolyte solution.

20.2.1.2 The moving boundary method

This approach requires an observable boundary between the “front” of differing composition and the rest of the cell. The front is established by gravitational stratification between

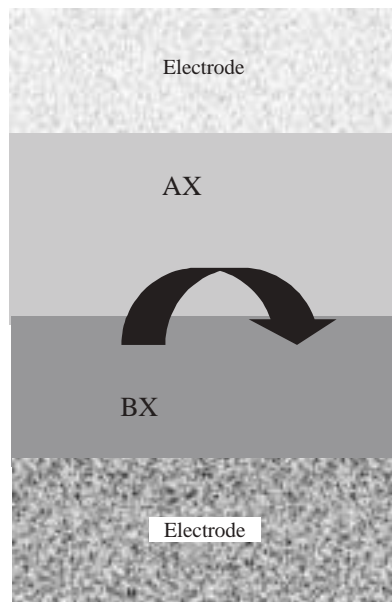


Figure 20.4 Schematic of the moving boundary method. Two stratified solutions retain their compositional boundary because of the differences in mobility of ions A and B.

two compartments of electrolyte solutions, AX and BX. The front is maintained because of the differing mobilities of ions A and B under the applied electric field (see equation (20.1.2-3) and Figure 20.4).

If one equivalent of charge is passed, driving solution AX towards the upper electrode, the boundary will move forward through a volume $V_{A,0}$ and the number of moles of solution displaced is

$$C_A V_{A,0} = \frac{t_A}{z_A} \quad (20.2.1-1)$$

where t_A is the transference number of ion A in electrolyte AX. The above equality holds because of the presence of the common ion, X, on either side of the boundary (i.e. the net movement of the boundary is due to A). The ratio of the volume advanced under passage of one equivalent of charge to the volume generally swept out (V_A) is

$$V_{A,0} = \frac{V_A F}{I t} \quad (20.2.1-2)$$

where t is the duration of the experiment. The transference number found from equations (20.2.1-1) and (20.2.1-2) is

$$t_A = \frac{z_A C_A V_A F}{I t} \quad (20.2.1-3)$$

The key issue here is the extent to which a stable, moving boundary can be obtained and how accurately its progress can be monitored. Boundary observation methods have often employed optical methods. Either the change in absorbance (where an indicator solution may be added at low concentration to one of the solutions) or the change in refractive index can be used to monitor the front. Solution resistance can also be used to probe the moving boundary (by definition, the leading ion A has a mobility higher than that of B). Another analytical route is presented by the thermal gradient arising from the difference in conductivities, due to Joule heating, from the following solution (6).

The Joule heating effect is one of a number of instabilities, including other convective and diffusive interferences, which can disturb the boundary and interfere with measurements. The use of this method is, therefore, complicated in solutions of poor conductivity and requires measurement of transference numbers over a range of electrolysis conditions, with extrapolation to zero current. The general issue of the extent of the perturbation, discussed for the Hittorf technique, also arises here. Errors are minimised by prolonging the measurement time, but the perturbation to the cell (noted above, but also arising from differences in molar volume between the products of the electrolysis reaction) will be maximised therefore raising questions over the extent to which the parameter actually measured corresponds to the parameter sought. The general solution to this problem is the measurement of transference numbers at a variety of electrolysis currents (or electrolysis times) with extrapolation of the variation to zero charge.

Other methods related to the moving boundary method include the indirect moving boundary method (where the concentration in the “trailing edge” behind the boundary is monitored) and the analytical boundary method. The latter approach involves analysis of the compositional change within the moving boundary zone and is a hybrid of the Hittorf and standard moving boundary techniques.

20.2.1.3 Measurements of cell potential

This approach avoids some of the difficulties associated with methods (a) and (b). In contrast to the other methods, which utilise the effect of a charge passed on the composition of the electrode compartments, or on the bulk of the solution, this method relates the cell potential observed in concentration cells to the transference number of the constituent ions. Experimentally, a concentration cell is made by opening the inter-connecting valve between the two solution compartments. Each compartment must contain an electrode that is reversible to one of the ions in the solution. Diffusion will blur the distinction between the solutions once they come into contact and will ultimately homogenize them. However, as explained at the outset of this chapter, diffusion of the more concentrated electrolyte into the more dilute solution will set up a diffusion potential which will essentially act as a brake on the transport of the more mobile ion. If there were no difference in the magnitude of the cationic and anionic mobility, no diffusion potential would arise. Hence, the value of the cell potential reflects the transference numbers of the electrolytes in solution. A way to relate the observed cell potential to the transference number is necessary. A rigorous derivation of the inter-relationship between the two quantities requires recourse to Onsager's equation for the thermodynamics of irreversible systems, which is beyond the scope of this chapter (4). An approximate derivation, which gives the identical final result, can be

obtained by imposing a pseudo-steady-state condition on the electrolyte transport (7). This implies that the diffusive flux balances the migratory flux developed. Another form of the one-dimensional Nernst–Planck equation (20.1.2-2) can be written to describe the counteracting fluxes in the pseudo-steady-state:

$$d\mu_i = RT \ln a_i \approx -Fd\phi \quad (20.2.1-4)$$

where the forces are assumed to apply in one dimension only. Each term can be written as the sum of its ionic components. For every mole passed, the diffusive flux must include the transference number of each ion (normalised for its charge since this is by definition the fraction of current carried by a given ion in response to the electric field see equation (20.1.2-7)). Hence,

$$RT \sum_i \frac{t_i}{z_i} \ln a_i \approx -F d\phi \quad (20.2.1-5)$$

Therefore,

$$d\phi = \frac{-RT}{F} \sum_i \frac{t_i}{z_i} \ln a_i \quad (20.2.1-6)$$

which is the equation resulting from the full Onsager analysis. Equation (20.2.1-6) relates to a differential potential within the solution and must be integrated with respect to the cell length (l) to equal the (measurable) potential difference between the electrodes resulting from the diffusion potentials within the cell. Consequently,

$$\Delta\phi = \frac{-RT}{F} \sum_i \int_0^l \frac{t_i}{z_i} \frac{d(\ln a_i)}{dx} dx = \frac{-RT}{F} \sum_i \int_0^l \frac{t_i}{z_i a_i} \frac{da_i}{dx} dx \quad (20.2.1-7)$$

Deriving the exact solution of this integral requires that a number of assumptions be made. The most general assumption is that solution activities can be replaced by the ionic concentrations, that the transference number is concentration independent and that the concentration varies linearly across the cell. Thus

$$\Delta\phi = \frac{-RT}{F} \sum_i \frac{t_i}{z_i} \ln \frac{C_i(l)}{C_i(0)} \quad (20.2.1-8)$$

which, for a symmetrical ($z:z$) electrolyte, reduces to

$$\Delta\phi = \frac{-RT}{z_i F} (t_+ - t_-) \ln \frac{C_i(l)}{C_i(0)} = \frac{-RT}{z_i F} (2t_+ - 1) \ln \frac{C_i(l)}{C_i(0)} \quad (20.2.1-9)$$

by combination with equation (20.1.2-8). Equation (20.2.1-9) is known as the Planck–Henderson equation. It predicts that when the charge is transported equally by both ions, the cell potential from equation (20.2.1-9) reduces to zero. Likewise, if some part of the solution is only permeable to one ion, there is no net transference and the measured potential collapses to the membrane case discussed in Section 20.1.1.

The above analysis provides a simple route to the measurement of transference numbers from readily measurable quantities. The method may be applied to a wide range of electrolyte solutions (hence a large working range of electrolyte concentrations). The drawback is the rather severe set of approximations made in the derivation of equation (20.1.2-10) which limits the accuracy of the transference numbers derived. More accurate results can be obtained by considering the non-ideality of the electrolytes, to a first approximation by use of the Debye–Hückel limiting law. The fact that the potentials respond to the logarithm of the concentration ratio also reduces the accuracy of this method.

Distinct from the preceding methods is a crude approach to transference number determination. This method relies on the relationship between the mobilities and diffusion coefficients of ions, the Einstein law:

$$u_i = \frac{z_i F D_i}{RT} = \frac{\lambda_i}{z_i F} \quad (20.2.1-10)$$

If the ions' diffusion coefficients are measured independently, the ratio of mobilities and transference numbers can be found (equation (20.1.2-9)). The problem is that the Einstein law is only valid at infinite dilution. This approach to transference number determination is substantially more limited than the schemes detailed above.

20.2.2 Sample calculations of ionic transference numbers

Some reported values of cationic transference numbers are listed in Table 20.3. Conductivity data from Table 20.1 can be used to calculate transference numbers for protons in aqueous nitric acid, for example, from equations (20.1.2-9) and (20.1.2-12):

$$t_{\text{H}^+} = \frac{3.62 \times 10^{-3} \times [1 \times C_{\text{H}^+}]}{3.62 \times 10^{-3} \times [1 \times C_{\text{H}^+}] - 7.40 \times 10^{-4} \times [(-1) \times C_{\text{NO}_3^-}]} = 0.83 \quad (20.2.2-1)$$

since the concentrations of both ions must be equal. Likewise, the transference number for protons in dilute sulphuric acid can be found from

$$t_{\text{H}^+} = \frac{3.62 \times 10^{-3} \times [1 \times C_{\text{H}^+}]}{3.62 \times 10^{-3} \times [1 \times C_{\text{H}^+}] - 8.29 \times 10^{-4} \times [(-2) \times C_{\text{SO}_4^{2-}}]} = 0.81 \quad (20.2.2-2)$$

since the concentration of protons is twice the sulphate concentration. Note that the anomalously high proportion of the current carried by the proton in aqueous solution is evidence of the veracity of the Grotthus mechanism of proton transport.

An illustration of the Hittorf method can be found in an early experimental report of the technique for barium chloride solutions, electrolysed using silver/silver chloride electrodes (8). The 18th run in this study reportedly passed 0.0194 F across the cell, which is schematically described in Figure 20.5.

The composition of the anode compartment following electrolysis was 1.366 wt% of barium chloride, where the compartment contained 120.37 g of solution. The product of

Table 20.1

Selected limiting ionic conductivities in aqueous solution at 298 K. The values are tabulated with cations (left-hand half of table) and anions (right-hand half of table) listed separately. Elemental ions are listed first, in order of increasing atomic mass, with molecular ions following, also in order of increasing mass

Cation	λ^0 (S cm ² mol ⁻¹)	Reference	Anion	λ^0 (S cm ² mol ⁻¹)	Reference
H ⁺	349.8	(11)	F ⁻	55.4	(11)
Li ⁺	38.6	(11)	Cl ⁻	76.4	(11)
Be ²⁺	90.0	(11)	Br ⁻	78.1	(11)
Na ⁺	50.1	(11)	I ⁻	76.8	(11)
Mg ²⁺	106.0	(11)	OH ⁻	198.3	(11)
K ⁺	73.5	(11)	N ₃ ⁻	69.0	(11)
Ca ²⁺	119.0	(11)	CH ₃ CO ₂ ⁻	40.9	(11)
Co ²⁺	110.0	(11)	CO ₃ ²⁻	138.6	(11)
Cu ²⁺	107.2	(11)	NO ₃ ⁻	71.5	(11)
Zn ²⁺	105.6	(11)	C ₂ H ₅ CO ₂ ⁻	35.8	(11)
Rb ⁺	77.8	(11)	FCH ₂ CO ₂ ⁻	44.3	(11)
Sr ²⁺	118.8	(11)	ClO ₃ ⁻	64.6	(11)
Ag ⁺	61.9	(11)	CNCH ₂ CO ₂ ⁻	43.4	(11)
Cs ⁺	77.2	(11)	C ₃ H ₇ CO ₂ ⁻	32.6	(11)
Ba ²⁺	127.2	(11)	C ₂ O ₄ ²⁻	148.2	(11)
La ³⁺	209.1	(11)	ClCH ₂ CO ₂ ⁻	42.2	(11)
Ce ³⁺	209.4	(11)	SO ₄ ²⁻	160.0	(11)
Pr ³⁺	208.8	(11)	H ₂ PO ₄ ⁻	32.3	(21)
Nd ³⁺	208.2	(11)	ClO ₄ ⁻	67.3	(11)
Sm ³⁺	205.5	(11)	C ₅ H ₁₁ CO ₂ ⁻	27.4	(22)
Eu ³⁺	203.4	(11)	C ₆ H ₅ CO ₂ ⁻	32.3	(11)
Gd ³⁺	201.9	(11)	BrO ₃ ⁻	55.7	(11)
Dy ³⁺	196.8	(11)	BrCH ₂ CO ₂ ⁻	39.2	(11)
Ho ³⁺	198.9	(11)	C ₇ H ₁₅ CO ₂ ⁻	23.1	(23)
Tl ⁺	74.7	(11)	P ₂ O ₇ ⁴⁻	380.0	(11)
Pb ²⁺	139	(11)	IO ₃ ⁻	40.5	(11)
Am ³⁺	193.2	(15)	ICH ₂ CO ₂ ⁻	40.6	(11)
Cf ³⁺	191.1	(15)	IO ₄ ⁻	54.5	(11)
NH ₄ ⁺	73.5	(11)	Fe(CN) ₆ ³⁻	302.7	(11)
NCH ₃ H ₃ ⁺	58.7	(11)	Fe(CN) ₆ ⁴⁻	440.0	(11)
N(C ₂ H ₅) ₃ H ₃ ⁺	46.6	(16)	C ₆ H ₂ (NO ₂) ₃ O ⁻	30.4	(11)
N(CH ₃) ₂ H ₂ ⁺	51.8	(11)	P ₃ O ₉ ³⁻	250.8	(11)
N(CH ₃) ₃ H ⁺	47.2	(11)	P ₃ O ₁₀ ⁵⁻	545.0	(11)
N(CH ₃) ₄ ⁺	44.9	(11)	P ₄ O ₁₂ ³⁻	279	(11)
N(C ₂ H ₅) ₂ H ₂ ⁺	36.8	(16)	(C ₆ H ₅) ₄ B ⁻	19.7	(19)
N(C ₂ H ₅ OCH ₃)H ₃ ⁺	39.1	(16)			
Piperidinium	37.5	(16)			
N(C ₃ H ₇ OCH ₃)H ₃ ⁺	41.8	(16)			
Cyclohexylammonium	35.0	(16)			
N(C ₂ H ₅) ₃ H ⁺	31.3	(16)			
N(C ₂ H ₅) ₄ ⁺	32.6	(11)			
N(C ₂ H ₅ OCH ₃) ₂ H ₂ ⁺	29.3	(16)			
N(CH ₃) ₃ C ₆ H ₅ ⁺	34.6	(11)			

(Continued)

Table 20.1 (Cont.)

Cation	λ^0 (S cm ² mol ⁻¹)	Reference	Anion	λ^0 (S cm ² mol ⁻¹)	Reference
Co(NH ₃) ₆ ³⁺	305.7	(11)			
N(C ₃ H ₇) ₄ ⁺	23.4	(11)			
N(C ₄ H ₉) ₄ ⁺	19.4	(11)			
UO ₂ ²⁺	114.0	(17)			
PuO ₂ ²⁺	118.0	(18)			
N(C ₅ H ₁₁) ₃ C ₄ H ₉ ⁺	20.7	(19)			
(C ₆ H ₅) ₄ P ⁺	19.9	(20)			
(C ₆ H ₅) ₄ As ⁺	19.4	(20)			
(C ₆ H ₅) ₄ Sb ⁺	19.1	(20)			

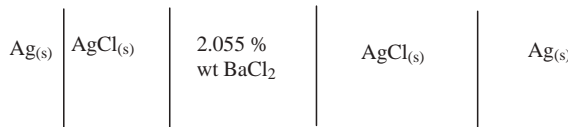


Figure 20.5 Cell used by Jones and Dole (8) for calculation of transference numbers by the Hittorf method. The solution compartment is further sub-divided into sub-compartments (see Figure 20.3), although the composition of each sub-compartment is initially identical.

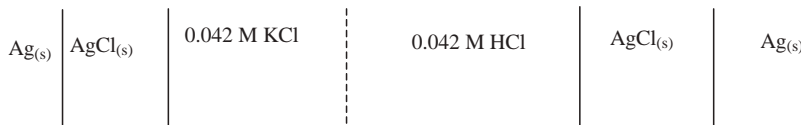


Figure 20.6 Example cell for calculation of transference number by the moving boundary method.

this weight percentage and the weight of solution (g), divided by the molecular mass of the salt (208.27 g mol⁻¹), gives the number of moles of salt remaining in the anode compartment following electrolysis. Hence 7.89×10^{-3} moles of Ba²⁺ ions remained in the anode compartment of the cell after electrolysis. The original Ba²⁺ content, calculated as the product of the weight of solution and its weight percentage pre-electrolysis (2.055 wt%), was 2.47 g. Since this initial BaCl₂ content corresponded to 0.0119 moles, the loss of Ba²⁺ induced by electrolysis was, therefore: $0.0119 - 7.89 \times 10^{-3} = 4.06 \times 10^{-3}$ moles. As explained in the preceding section, the net loss from the anode compartment will be t_+ moles of univalent cation per unit charge passed. For a divalent cation, only half the number of moles need be lost to compensate the charge (compare equation (20.1.2-9)). Thus, the transference number is twice the ratio of moles lost per Faraday passed. In this case,

$$t_{\text{Ba}^{2+}} = \frac{2 \times 4.06 \times 10^{-3} \text{ F}}{1.94 \times 10^{-2} \text{ F}} = 0.419 \quad (20.2.2-3)$$

Likewise, a simple illustration of the moving boundary method can be provided, for example, for the case of electrolysis of the cell denoted in Figure 20.6.

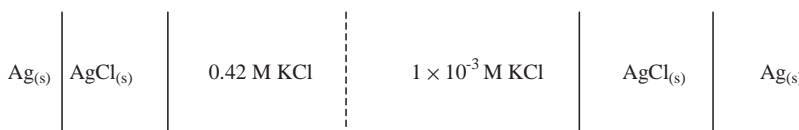


Figure 20.7 Example cell for calculation of transference number by the measurement of cell potential.

The advance of the moving boundary marking the denser, less mobile KCl solution allows the transference number of the potassium ion to be found from equation (20.2.1-3). For a capillary of 0.209 cm inner radius, the displacement of the boundary after 200, 400 and 600 sec was found to be 6.4, 12.9 and 19.2 cm. A constant current of 36.4 mA was maintained. Using the first pair of data, the volume displaced (the cross-sectional area multiplied by the distance the boundary has moved through) is 0.88 cm³:

$$t_{K^+} = \frac{1 \times 4.2 \times 10^{-5} \text{ mol cm}^{-3} \times 0.88 \text{ cm}^3 \times 9.648 \times 10^4 \text{ C mol}^{-1}}{(0.0364 \times 200) \text{C}} = 0.49 \quad (20.2.2-4)$$

Finally, a simple measurement of a diffusion potential allows us to determine the potassium ion transference number as shown in the cell of Figure 20.7.

The measured cell potential was -3.0 mV. Re-arrangement of equation (20.2.1-9) gives

$$\begin{aligned} t_{K^+} &= \frac{1}{2} - \frac{zF\Delta\phi}{2RT \ln\left(\frac{C_i(l)}{C_i(0)}\right)} \\ &= 0.5 - \left(\frac{[1 \times 9.64 \times 10^4 \times (-3) \times 10^{-3}] \text{J mol}^{-1}}{2 \times (8.314 \times 298) \text{ J mol}^{-1} \times (-6.04)} \right) = 0.49 \quad (20.2.2-5) \end{aligned}$$

where the cell potential is defined, following convention, as the potential difference between the right-hand electrode (located at *l*) and the left-hand electrode.

20.2.3 Experimental methods of determining electrolytic conductivity

The electrolyte conductivity can be measured using a conductivity cell which consists of a pair (or pairs) of electrode(s) of known area separated by a constant distance. A simple two-electrode cell can be used. For small excursions of potential, the current response of the cell is proportional to the electrolytic conductance, *L*. The conductivity, *κ* (see equation (20.1.2-3)) is related to *L* via (4, 9)

$$\kappa = L \left(\frac{l}{A} \right) \quad (20.2.3-1)$$

where the quantity in brackets is known as the cell constant and is the ratio of electrode separation, *l*, to the surface area, *A*. The cell constant is initially determined by measuring

the conductance of a solution of known conductivity (dilute aqueous solutions of potassium chloride, for example) before proceeding to measurements on solutions of unknown conductivity. The reciprocal quantities of L and κ are the electrolyte resistance (R) and resistivity, respectively. To minimise the effects of electrolysis, a sinusoidally alternating voltage is imposed upon the cell. An ac bridge arrangement can be employed to determine the resistance of the electrolyte. The resistance is the purely in-phase component of the frequency-dependent complex impedance of the cell, $Z(\omega)$, which is defined as

$$Z(\omega) = R_c - jX_c \quad (20.2.3-2)$$

where R_c and X_c are the resistance and capacitative reactance of the cell, respectively (10). Care must be taken to ensure that the out-of-phase capacitative response does not contribute to the measured signal. Also, the conductivity cell must be designed such that the dominating resistance is that of the electrolyte rather than any interfering resistances due to electrode processes or extraneous resistances from the external circuitry. Electrodes of platinum black electrodes are almost always used. Conductance should be determined at a range of frequencies to ensure that the value derived is constant and therefore free of any artefacts due to capacitative effects.

The essential point with regard to the interpretation of data is that the molar conductivity (see equation (20.1.2-10)) at infinite dilution can be broken down into terms due to the constituent ions. Some knowledge of the transference properties of the individual ions can be used to determine the fraction of electrolyte conductivity attributable to each ion.

20.2.4 Sample calculations relating to electrolytic conductivity

To illustrate the relation between transference numbers and conductivity, the transport number of potassium in dilute potassium chloride solution is used to find the limiting ionic conductivity. On extrapolation to infinite dilution, the molar conductivity of aqueous potassium chloride solution is found to be $149.85 \text{ S cm}^2 \text{ mol}^{-1}$ (11). From equation (20.1.2-14) and the value for t_{K^+} found in Section 20.2.3:

$$\begin{aligned} \lambda_{\text{K}^+}^0 &= t_{\text{K}^+} \Lambda_{\text{KCl}}^0 = t_{\text{K}^+} (\lambda_{\text{K}^+}^0 + \lambda_{\text{Cl}^-}^0) \\ &= 0.49 \times 149.9 = 73.45 \text{ S cm}^2 \text{ mol}^{-1} \end{aligned} \quad (20.2.4-1)$$

The remaining molar conductivity of the potassium chloride solution can be attributed to the chloride anion if one neglects the contribution arising from the auto-ionisation of water. Hence, the limiting ionic conductivity of the chloride anion is $76.42 \text{ S cm}^2 \text{ mol}^{-1}$.

The values of individual ionic conductivities can also be found by comparison between the extrapolated values. For example, the limiting molar conductivity of magnesium chloride is found to be $258.7 \text{ S cm}^2 \text{ mol}^{-1}$. Comparison with the potassium chloride value yields the limiting ionic conductivity of magnesium:

$$\lambda_{\text{Mg}^{2+}}^0 = \Lambda_{\text{MgCl}_2}^0 - \Lambda_{\text{KCl}}^0 + \lambda_{\text{K}^+}^0 - \lambda_{\text{Cl}^-}^0 = 105.9 \text{ S cm}^2 \text{ mol}^{-1} \quad (20.2.4-2)$$

A list of representative limiting ionic conductivity values and related parameters is given in the next section.

The concentration dependence of ionic conductivity has been discussed briefly above. Due to ion–ion interactions, the conductivity per ion falls as the ion concentration is increased. Two specific interactions have been identified: the electrophoretic effect due to the tendency of the ion atmosphere to move in the opposite direction of the ion; and the relaxation effect due to the finite time required for the ion atmosphere to re-arrange itself due to the asymmetry imposed by the electric field. Onsager produced a limiting law that showed that the molar electrolytic conductivity fell with the square root of the ion concentration:

$$\Lambda = \Lambda^0 - (A + B\Lambda^0)C_i^{1/2} \quad (20.2.4-3)$$

The constants A and B are related to the above retarding effects. Exact expressions have been presented for these terms (12, 13). In aqueous solutions at room temperature, the values of A and B are $59.86 \text{ S cm}^2 \text{ mol}^{-1} \text{ M}^{-1/2}$ and $0.2296 \text{ M}^{-1/2}$, respectively. Values for these parameters have also been presented for non-aqueous solutions (7).

With regard to calculation in aqueous solution (for example, using a $1 \times 10^{-3} \text{ M}$ aqueous solution of potassium chloride), equation (20.2.4-3) predicts a molar conductivity of $148.87 \text{ S cm}^2 \text{ mol}^{-1}$. This compares with the experimentally observed value of $146.95 \text{ S cm}^2 \text{ mol}^{-1}$. The agreement diverges increasingly as the ionic concentration is increased. The Onsager equation predicts KCl molar conductivity values of 140.42 and $120.04 \text{ S cm}^2 \text{ mol}^{-1}$ for 0.01 and 0.1 M concentrations, respectively. The experimentally observed values are higher than these values.

Determination of the degree of dissociation of weak electrolytes is a common application of conductivity measurements. This approach will be briefly outlined here with a sample calculation illustrating the utility of the method. From the data presented in the next section, the limiting molar conductivity of acetic acid can be seen to be $389.9 \text{ S cm}^2 \text{ mol}^{-1}$ (from addition of the limiting values for the proton and the acetate ion). At finite concentrations, this weak acid will only be partially deprotonated. The ratio of observed to predicted electrolytic conductivity can be used to determine the degree of dissociation, α . At 0.01 M, the observed molar conductivity of acetic acid was found to be $14.30 \text{ S cm}^2 \text{ mol}^{-1}$. Thus

$$\alpha = \frac{\Lambda_{\text{expt}}}{\Lambda} \approx \frac{\Lambda_{\text{expt}}}{\Lambda^0} = \frac{14.30 \text{ S cm}^2 \text{ mol}^{-1}}{389.9 \text{ S cm}^2 \text{ mol}^{-1}} = 0.0367 \quad (20.2.4-4)$$

The assumption made here is that the solution is sufficiently dilute for the molar conductivity, on complete dissociation at this concentration, to approximate the limiting molar conductivity. Equation (20.2.4-1) can be used to adjust the molar conductivity for ion–ion interactions but this requires knowledge of the ionic concentration, C_i . One approach is to use the initial approximation to α to give an initial C_i value; substitution of the aqueous phase constants into equation (20.2.4-3) gives

$$\Lambda = \{389.9 - [59.8 + (0.2296 \times 389.9)](\alpha C)^{1/2}\} \text{ S cm}^2 \text{ mol}^{-1} \quad (20.2.4-5)$$

The αC term is initially approximated to $0.0367 \times 0.01 \text{ M}$, thus

$$\Lambda = 389.9 - [149.32 \times (3.67 \times 10^{-4})^{1/2}] = 387.0 \text{ S cm}^2 \text{ mol}^{-1} \quad (20.2.4-6)$$

Hence, α can be re-computed and is found to be 0.0369. Repetition of the iteration procedure does not significantly change the value of α indicating that convergence has occurred. More accurate functional forms of the factor relating Λ^0 to Λ have been given (12). The ease with which conductometric titrations can be applied to follow acid–base neutralisation reactions is notable.

The models discussed above hold for aqueous solutions. More complex behaviour is observed in non-aqueous solutions, particularly in media of low polarity. In such cases, extensive ion-pairing is observed. That is, electrically neutral ion-pairs will not contribute to solution conductivity. Conversely, under some conditions charged “triple ions” can form. The formation of such species is clearly favoured by higher concentrations. Thus, in some cases, molar conductivity can increase with ionic activity due to triple ion formation. Theories have been developed to predict the formation constants of such species (14).

20.2.5 Tabulation of parameters related to electrolyte conductance

The limiting values of various ionic conductivities, λ^0 , are given in Table 20.1 for aqueous solutions. Transference numbers for any given electrolyte, for solutions of infinite dilution, can be determined from the data in this table, using equation (20.1.2-13). Similarly, the mobility of an ion can be found by combining data from this table with equation (20.1.2-12).

The temperature and concentration dependence of the transport properties of a number of aqueous electrolytes can be assessed via Tables 20.2 and 20.3. Table 20.2 reports the temperature dependence of limiting ionic conductivities of a number of ions in aqueous solution whereas Table 20.3 gives the concentration dependence of a number of aqueous phase transference numbers.

Parameters for ionic transport in non-aqueous solutions (including pure sulphuric acid) and solvent mixtures are provided below (Tables 20.4–20.9).

Table 20.2

Temperature variation of the limiting ionic conductivities for selected ions in aqueous solution (24)

Cation	$\lambda^0(\text{S cm}^2 \text{ mol}^{-1})$			
	288 K	298 K	308 K	313 K
H^+	300.6	349.8	397	441.4
Na^+	39.8	50.1	61.5	73.8
K^+	59.7	73.5	88.2	103.5
Cl^-	61.4	76.4	92.2	108.9
Br^-	63.1	78.1	94	110.7

Table 20.3

Cationic transference numbers of selected electrolytes in aqueous solution at 298 K (9, 24)

Cation	t_+						
	0.01 M	0.02 M	0.05 M	0.1 M	0.2 M	0.5 M	1.0 M
H ⁺ (in HCl)	0.825	0.827	0.829	0.831	0.834	—	—
Li ⁺ (in LiCl)	0.329	0.326	0.321	0.317	0.311	0.300	0.287
Na ⁺ (in NaCl)	0.392	0.390	0.388	0.385	0.382	—	—
K ⁺ (in KCl)	0.490	0.490	0.490	0.490	0.489	0.489	0.488

Table 20.4

Limiting ionic conductivities of selected ions in methanol at 298 K

Cation	λ^0 (S cm ² mol ⁻¹)	Reference	Anion	λ^0 (S cm ² mol ⁻¹)	Reference
Li ⁺	39.1	(25)	Cl ⁻	52.1	(25)
Na ⁺	45.1	(25)	Br ⁻	56.4	(25)
Mg ²⁺	115.2	(26)	I ⁻	62.6	(25)
K ⁺	47.8	(25)	CH ₃ O ⁻	53.0	(24)
Ca ²⁺	120.0	(26)	NO ₃ ⁻	61.1	(25)
Zn ²⁺	96.0	(25)	ClO ₄ ⁻	71.0	(25)
Rb ⁺	56.1	(25)	C ₆ H ₂ (NO ₂) ₃ O ⁻	47.1	(25)
Sr ²⁺	118	(26)	(C ₆ H ₅) ₄ B ⁻	37.1	(25)
Ag ⁺	50.1	(25)			
Cs ⁺	61.3	(25)			
N(CH ₃) ₄ ⁺	68.7	(25)			
N(C ₂ H ₅) ₄ ⁺	59.6	(27)			
N(C ₃ H ₇) ₄ ⁺	45.3	(27)			
N(C ₄ H ₉) ₄ ⁺	38.9	(27)			
N(C ₅ H ₁₁) ₄ ⁺	34.8	(27)			
N(C ₆ H ₁₃) ₄ ⁺	30.8	(27)			
N(C ₇ H ₁₅) ₄ ⁺	28.8	(27)			

20.3 MINIMIZATION OF LIQUID JUNCTION POTENTIAL

20.3.1 Balancing ionic mobilities

Equations (20.1.2-2) and (20.2.1-7) relate the diffusion potential to mass-transport within the electrolyte and to transference numbers, respectively. If both the transference numbers are equal to one-half in the latter equation, then the diffusion potentials in solution arising from contact of solutions with differing concentrations will be eliminated. The limiting values of the ionic diffusion coefficient are related to their mobility by the Einstein law, equation (20.2.1-10), which provides justification for the argument that balancing the mobilities of the electrolyte's constituent ions will nullify any diffusion potential. This approach to eliminating diffusion potentials clearly suffers from the severe restriction that

Table 20.5

Limiting ionic conductivities of selected ions in ethanol at 298 K

Cation	λ^0 (S cm ² mol ⁻¹)	Reference	Anion	λ^0 (S cm ² mol ⁻¹)	Reference
Li ⁺	17.1	(25)	Cl ⁻	21.9	(25)
Na ⁺	20.4	(25)	Br ⁻	23.9	(25)
Mg ²⁺	101.8	(25)	I ⁻	27.0	(25)
K ⁺	22.2	(25)	C ₂ H ₅ O ⁻	25.4	(24)
Rb ⁺	25.0	(26)	ClO ₄ ⁻	33.6	(24)
Cs ⁺	26.5	(25)	C ₆ H ₂ (NO ₂) ₃ O ⁻	26.3	(24)
N(CH ₃) ₄ ⁺	29.7	(25)			
N(C ₂ H ₅) ₄ ⁺	29.3	(25)			
N(C ₃ H ₇) ₄ ⁺	23.0	(25)			
N(C ₄ H ₉) ₄ ⁺	19.7	(25)			
N(C ₇ H ₁₅) ₄ ⁺	14.0	(25)			

Table 20.6

Limiting ionic conductivities of selected ions in acetonitrile at 298 K

Cation	λ^0 (S cm ² mol ⁻¹)	Reference	Anion	λ^0 (S cm ² mol ⁻¹)	Reference
Li ⁺	79.9	(26)	Cl ⁻	91.6	(28)
Na ⁺	76.9	(25)	Br ⁻	100.7	(25)
Mg ²⁺	189.6	(26)	I ⁻	102.1	(25)
K ⁺	83.6	(25)	NO ₃ ⁻	106.4	(25)
Zn ²⁺	189.6	(26)	BF ₄ ⁻	108.5	(25)
Ag ⁺	86.0	(25)	ClO ₄ ⁻	103.7	(25)
Cs ⁺	87.3	(25)	PF ₆ ⁻	104.0	(25)
N(CH ₃) ₄ ⁺	94.5	(25)	BCl ₄ ⁻	95.2	(28)
N(C ₂ H ₅) ₄ ⁺	85.5	(27)	C ₆ H ₂ (NO ₂) ₃ O ⁻	77.0	(25)
N(C ₃ H ₇) ₄ ⁺	71.1	(27)	BPh ₄ ⁻	58.1	(25)
N(C ₄ H ₉) ₄ ⁺	62.1	(27)			
N(C ₅ H ₁₁) ₄ ⁺	56.5	(27)			
N(C ₆ H ₁₂) ₄ ⁺	51.4	(27)			
N(C ₇ H ₁₅) ₄ ⁺	47.9	(27)			
(C ₆ H ₅) ₄ As ⁺	55.8	(25)			

the experimentalist be limited to combinations of ions with equal and opposite mobility values (or, equivalently, identical ionic conductivities). The data in the preceding section can be used to identify appropriate pairs of ions. The similar limiting ionic conductivities of potassium and chloride explain why this pair of ions is often used to eliminate diffusion potentials (see Section 20.3.2). Likewise, aqueous solutions of potassium nitrate and lithium acetate ought to exhibit minimal diffusion potentials. For non-aqueous media, Table 20.6 shows that diffusion potentials should be negligible in acetonitrile solutions of tetramethylammonium tetrachloroborate or solutions of tetraphenylarsonium tetraphenylborate in the same solvent. The latter observation implies that the effective diameter of the

Table 20.7

Limiting ionic conductivities of selected ions in sulphuric acid at 298 K

Cation	λ^0 (S cm ² mol ⁻¹)	Reference	Anion	λ^0 (S cm ² mol ⁻¹)	Reference
H ⁺	1.08	(29)	HSO ₄ ⁻	170	(29)
Li ⁺	0.64	(29)			
Na ⁺	0.80	(29)			
K ⁺	1.20	(29)			
Ag ⁺	1.59	(29)			
NH ₄ ⁺	1.06	(29)			
H ₃ SO ₄ ⁺	245	(29)			

Table 20.8

Limiting ionic conductivities of cations in nitrobenzene at 298 K

Cation	λ^0 (S cm ² mol ⁻¹)	Reference
Li ⁺	16.3	(26)
Na ⁺	17.8	(26)
N(CH ₃) ₄ ⁺	17.1	(30)
N(C ₂ H ₅) ₄ ⁺	16.2	(30)
N(C ₃ H ₇) ₄ ⁺	13.3	(30)
N(C ₄ H ₉) ₄ ⁺	11.7	(30)

Table 20.9

Cationic transference numbers for sodium chloride and potassium chloride in equimolar mixtures 50:50 of methanol and water (24)

Cation	T_+						
		Limiting value	0.001 M	0.002 M	0.005 M	0.01 M	0.02 M
Na ⁺ (in NaCl)	0.4437	0.4425	0.4421	0.4415	0.4412	0.4412	0.4398
K ⁺ (in KCl)	0.5068	0.5070	0.5071	0.5074	0.5077	0.5085	0.5105

latter pair of ions in non-aqueous solutions is similar and is the basis of the Grunwald assumption used as a reference scale for ion transfer energies (see Section 20.4.1). This approach, while feasible if the experimentalist can tolerate the restriction on electrolytes, is also weakened since it implicitly assumes that the concentration (and temperature) dependencies of the transference numbers are identical. While this may be true for a first approximation, the data of Table 20.9 show that the cationic transference numbers of sodium chloride and potassium chloride display opposite dependencies on concentration in water/methanol mixtures, for example.

20.3.2 The salt bridge

A more general approach to minimising liquid junction potentials is to connect two electrolyte solutions via a salt bridge. The salt bridge is a solution of ions of balanced mobility, such as aqueous phase potassium chloride (see Section 20.3.1). The two solutions are either separated by some kind of “frit” or the salt bridge can consist of a gel of the ions of balanced mobility which should ideally minimise mutual solution contamination. If potassium chloride is used, an excess of this salt over the electrolyte(s) in the other compartments of the cell means the (limited) ion transport at each end of the salt bridge will be dominated by the potassium and chloride ions. This situation is analogous to the use of a supporting electrolyte in voltammetric measurements to ensure that migratory transport in bulk solution has a negligible contribution from the species of interest (see Chapter 3 of this handbook). In the conventional voltammetric case, a concentration ratio of supporting electrolyte to analyte in excess of 100 is normally maintained. The definition of the transference number, equation (20.1.2-9), means that under such conditions at least 99% of the migratory flux will be due to the supporting electrolyte. The establishment of such experimental conditions is important for the analysis of voltammetric data since it is generally assumed that the analyte is transported solely by diffusion. Since the transference number of each end of the salt bridge will be dominated by the potassium and chloride ions and since their mobilities almost cancel, a very low liquid junction potential should be established between the two solutions. Given that the limiting ionic mobilities of potassium and chloride do not sum to zero in aqueous solution, a finite liquid junction potential will be established. Equation (20.2.1-9) can be used to determine the magnitude of this potential, but it is typically of the order of 1–2 mV for most practical KCl salt bridges.

20.4 JUNCTIONS OF IMMISCIBLE LIQUIDS

20.4.1 The non-polarisable liquid/liquid interface

We now return to the example introduced in Section 20.1.1, where two electrolyte solutions α and β were placed in contact and a hypothetical barrier was invoked that prevented the transfer of one of the ions between the phases. Although this example may have seemed obscure, such a system may readily be constructed for the interface between two immiscible electrolyte solutions (ITIES). Such a system can be formed by contacting water with an immiscible organic solvent such as nitrobenzene or 1,2-dichloroethane, as discussed in Section 17.3 in Chapter 17 of this handbook. The two solvents possess a slight mutual solubility. Once the two phases are equilibrated, the system is composed of an organic saturated aqueous phase in contact with a water saturated organic phase. For this reason, measurement of any transport property should always be performed on mutually pre-saturated solutions.

The choice of the organic phase also requires some care. The solubility characteristics with water must be such that two distinct phases form; typically this means that non-polar organic solvents must be employed. However, if the polarity of the organic solvent is too low (such as long-chain alkanes or alcohols), it becomes impossible to dissolve appreciable

amounts of any electrolyte in the organic phase, thus precluding use of these solvents to form electrolyte phases. The choice of organic solvents for liquid/liquid studies is therefore dictated by the need to compromise between the above two opposing factors. A further requirement is that the interface is gravitationally stable. Thus, there must be an appreciable difference in density to form a single stable interface, particularly for measurements at the polarised interface (see next section). A final requirement is that the interface should be chemically stable. This often restricts the usable pH range of the aqueous phase because many of the organic electrolytes are unstable.

To return to the case where one ion is readily solvated by both phases, the equality of the electrochemical potential leads to equation (20.1.1-2). However, equation (20.1.1-3) does not follow from this equation because phases α and β are not composed of the same solvent. Hence, the standard chemical potentials of the partitioning ion in the two phases differ. Thus, equation (20.1.1-3) is replaced by

$$\Delta\phi \equiv \phi_\beta - \phi_\alpha = \frac{\mu_{i,\alpha}^0 - \mu_{i,\beta}^0}{zF} + \frac{RT}{zF} \ln \left(\frac{a_{\alpha,i}}{a_{\beta,i}} \right) \quad (20.3.1-1)$$

By analogy with the Nernst equation, one can define the first term on the right-hand side of equation (20.3.1-1) as the standard potential of transfer of the ion, i , between phases α and β :

$$\Delta\phi_i^0 = \frac{\Delta G_i^0}{zF} = \frac{\mu_{i,\alpha}^0 - \mu_{i,\beta}^0}{zF} \quad (20.3.1-2)$$

The above equations state that when an ion readily partitions, the interfacial potential established is determined, in the first instance, by the standard Gibbs energy of transfer for the ion between the two phases. The second term in equation (20.3.1-1) makes it clear that this potential can be modified by “perturbing” the distribution potential established by the ion from its standard value. This can be achieved by establishing significantly different activities of ion i in the aqueous and organic phases by using differing concentrations of extremely hydrophilic and extremely hydrophobic counter-ions, respectively. An example of such an approach is the use of the tetraphenylarsonium cation as the common-ion in a water/1,2-dichloroethane electrolyte system, with chloride and tetraphenylborate as the respective counter-ions in the aqueous and organic phases (31). In all such cases, the interface is non-polarisable since any attempt to impose an external potential difference (see next section), which is not equal to the distribution potential of the common ion, will be opposed by the common-ion readjusting its relative activities to return the system to equilibrium.

Where both ions of a given univalent electrolyte, AB, have appreciable solubility in phases α and β , an equilibrium salt distribution coefficient, K_{AB} , can be defined as

$$K_{AB} = \frac{a_{\alpha,AB}}{a_{\beta,AB}} = \sqrt{\frac{a_{\alpha,A^+}a_{\alpha,B^-}}{a_{\beta,A^+}a_{\beta,B^-}}} = \sqrt{K_{A^+}K_{B^-}} \quad (20.3.1-3)$$

where the K_i terms on the right-hand side refer to the distribution of the ions. Relating the equilibria for the salt and ions to the free energy changes for transfer of these species:

$$\begin{aligned} -RT \ln K_{AB} &= \frac{-RT}{2} \ln K_{A^+} - \frac{RT}{2} \ln K_{B^-} \\ \Rightarrow \Delta G_{AB}^0 &= \frac{1}{2} (\Delta G_{A^+}^0 + \Delta G_{B^-}^0) \end{aligned} \quad (20.3.1-4)$$

The definition of the standard Gibbs energy of transfer (equation (20.3.1-2)):

$$\Delta\phi = \frac{1}{2} (\Delta\phi_{A^+}^0 + \Delta\phi_{B^-}^0) \quad (20.3.1-5)$$

(i.e., the distribution potential) established by the salt is the mean of the potentials of the individual ions (32).

It is also important to note that the distribution of the common ion(s) accounts for the potential difference established at the liquid/liquid interface. Diffusion potentials can also play a part, but the potential differences derived in the above expressions are equilibrium values arising because of the differences in solvation of the participating ions. As a historical note, some of the earliest experiments on immiscible electrolyte phases were performed with the aim of establishing transport numbers of ions, using a variant of the concentration cell, with an immiscible liquid separating the two aqueous phases (33).

Expressions (20.3.1-4) and (20.3.1-5) show that measurement of the interfacial potential, or alternatively, determination of the distribution coefficient of a salt, can be used to find the standard potential of transfer of a given ion between the immiscible phases in question. As with the determination of the standard potential for redox processes, the issue of the reference scale arises. The potentiometric approach (equation (20.3.1-1)) is straightforward, but requires a way of relating the potential of an appropriate reference electrode in phase α to the potential of the second reference electrode immersed in phase β . The distribution approach (equation (20.3.1-4)) relies on an extra-thermodynamic assumption to resolve the measured salt distribution potential to that of the constituent ions. One of the most commonly used assumptions is that due to Grunwald (34) which states that the standard Gibbs energy of transfer of the tetraphenylarsonium cation is equal to the value for the tetraphenylborate anion (see Section 17.3 in Chapter 17 of this handbook for further details). Given that the transfer potentials are additive (equation (20.3.1-5)), this assumption permits the transfer potentials of other ions to be determined. Although arbitrary, such assumptions are analogous to the assignment of 0.0 V for the standard reduction potential of the proton. Assumptions with a better physical grounding have been presented more recently on the basis of experiments performed using polarised liquid/liquid interfaces (see next section).

Standard Gibbs energies of ion transfer are reported for various ions in Tables 20.10 and 20.11. Values are given for the two most common solvents used with water to form immiscible electrolyte boundaries, namely nitrobenzene and 1,2-dichloroethane.

20.4.2 The polarisable liquid/liquid interface

In contrast to the cells discussed in the previous section, addition of electrolytes CD and EF to phases α and β , respectively, leads to the formation of a polarised liquid/liquid interface

Table 20.10

Standard Gibbs energies of transfer for ions from water to nitrobenzene

Cation	ΔG^0 (kJ mol ⁻¹)	Reference	Anion	ΔG^0 (kJ mol ⁻¹)	Reference
H ⁺	+32.5	(35)	Cl ⁻	+37.0	(36)
Li ⁺	+38.4	(35)	Br ⁻	+28.5	(35)
Na ⁺	+34.5	(35)	I ⁻	+18.8	(35)
Mg ²⁺	+71.4	(35)	NO ₃ ⁻	+24.4	(35)
K ⁺	+24.3	(35)	ClO ₄ ⁻	+8.7	(35)
Ca ²⁺	+68.3	(35)	B(C ₆ H ₅) ₄ ⁻	-35.9	(35)
Rb ⁺	+19.9	(35)			
Sr ²⁺	+67.2	(35)			
Cs ⁺	+15.5	(35)			
Ba ²⁺	+63.3	(35)			
NH ₄ ⁺	+27.4	(35)			
N(CH ₃) ₄ ⁺	+3.4	(35)			
N(C ₂ H ₅) ₄ ⁺	-5.8	(35)			
N(C ₃ H ₇) ₄ ⁺	-15.5	(35)			
N(C ₄ H ₉) ₄ ⁺	-24.2	(35)			
As(C ₆ H ₅) ₄ ⁺	-35.9	(35)			

Table 20.11

Standard Gibbs energies of transfer for ions from water to 1,2-dichloroethane

Cation	ΔG^0 (kJ mol ⁻¹)	Reference	Anion	ΔG^0 (kJ mol ⁻¹)	Reference
H ⁺	+53	(37)	Cl ⁻	+45.4	(36)
Li ⁺	+55.6	(38)	Br ⁻	+38.3	(35)
Na ⁺	+55.9	(38)	I ⁻	+26.4	(35)
K ⁺	+51.9	(38)	ClO ₄ ⁻	+17.2	(35)
Rb ⁺	+45.8	(38)	B(C ₆ H ₅) ₄ ⁻	-33.0	(38)
Cs ⁺	+37.3	(38)			
N(CH ₃) ₄ ⁺	+17.6	(35)			
N(C ₂ H ₅) ₄ ⁺	+4.2	(35)			
N(C ₃ H ₇) ₄ ⁺	-8.8	(35)			
N(C ₄ H ₉) ₄ ⁺	-21.8	(35)			
As(C ₆ H ₅) ₄ ⁺	-32.5	(38)			

if none of the constituent ions transfer readily to the other phase. In terms of equation (20.3.1-2), the standard Gibbs energy of transfer for each ion from its initial phase to the other phase must be considerable (at least 10 kJ mol⁻¹ in practice). The four ions thus function as supporting electrolytes defining a “potential window” with a size determined at the positive end by the lower of the transfer energies of C⁺ or B⁻ and at the negative end by the lower of the transfer energies of D⁻ or A⁺. Suitable candidates for aqueous and organic phase supporting electrolytes may be identified from Table 20.10. For example, a large potential window can be obtained using lithium sulfate as the aqueous phase salt and tetrapentylammonium tetrakis(4-chlorophenyl)borate as the organic phase salt.

The defined potential window can be used to investigate ion and electron transfer processes as discussed in Section 17.3 in Chapter 17 of this handbook where the potential of the ion/electron transfer process must fall within the available window. Experiments can be performed with a two-electrode configuration where currents are sufficiently small, but more generally a four-electrode potentiostat (two reference and two counter electrodes) is required. The experimental procedures required for this type of experiment are discussed in more detail in Section 17.3 in Chapter 17 of this handbook.

20.5 NON-CLASSICAL ELECTROLYTES: POLYMER-BASED ELECTROLYTES AND IONIC LIQUIDS

The preceding sections give an overview of the theoretical framework and experimental techniques required to determine transference numbers and associated properties in electrolyte solutions. The bulk of theoretical developments belong to the early twentieth and even late nineteenth centuries with much of the accurate experimentation being performed during the early/mid twentieth century (aqueous solutions) and mid/late twentieth century (non-aqueous solutions). Although experimental data for what might be termed “classical electrolyte” solutions is still being collected and refined, much of the thrust of current research in this area is in the understanding of ion transport in less conventional electrolyte media. Much of the impetus for this work has stemmed from recent successes in the processing of ionomeric materials for power applications, specifically fuel cells. Polymeric electrolytes, in general, present challenges for the accurate determination of conductivity parameters. Another stimulus for research in non-classical electrolytes has come from successes in the synthesis of air- and water-stable room-temperature ionic liquids. Since these areas are still developing rapidly, it is impossible to present an authoritative statement of the relevant transport parameters. However, a flavour of the recent work in these areas and an indication of likely future developments will be presented.

Polymer electrolytes can be formed by the dissolution of salts within high molecular weight polymers such as polyethylene oxide and its derivatives. This area has been studied widely since their initial discovery in the 1970s because of practical applications deriving from all solid-state electrochemical devices. The low intrinsic conductivity of many polymer electrolytes (ca. 10^{-4} S cm⁻¹ is common, two orders of magnitude lower than moderately concentrated aqueous electrolyte solutions) has hampered their development and considerable effort has been expended towards understanding and ultimately improving on these values. There are various differences that should be considered when comparing ion transport in polymer systems with that in liquid phase electrolytes. One important distinction is the structural heterogeneity intrinsic to many polymers. A thorough knowledge of the phase diagram of the polymer is required to offer a meaningful interpretation of conductivity data. Ionic conductivity has been attributed to the amorphous regions of the polymer. Likewise, the sample history may affect its ion transport properties (39). Two important contrasts with liquid state migratory fluxes have been identified. First, the ion cannot move with a solvation sheath since the (largely translationally immobile) polymer is the solvent. Second, enhanced ion–ion and ion–polymer interactions mean the sensitivity of molar conductivity to concentration changes is enhanced in polymer

electrolytes. Despite the structural complexity of polymer electrolytes compared to liquid electrolyte solutions, one advantage with regard to the experimental determination of transference numbers is that the Hittorf method (Section 20.2.1) can be applied to polymeric species without some of the objections that compromise this method in liquids. Specifically, the low rates of diffusion and absence of convective fluxes in the polymer mean that these factors will exert minimal interferences on the transference numbers determined. Experimental determinations of transference numbers within polymer electrolytes have shown that the bulk of the charge is carried by the anionic species. This is expected from the stronger interactions anticipated between cations and the polymer chain although there are some discrepancies between numbers determined by different techniques. Electrochemical methods can also be employed to deposit conducting polymers, such as polypyrrole and polyaniline, whose charge transfer behaviour is often dictated by the uptake of ions into the polymer framework to re-establish electroneutrality (40, 41).

A related “non-classical” electrolyte system where ion transport properties have received much recent attention are ionomeric materials. The best-known example of this class of materials are the perfluorinated sulphonates which have an anionic backbone and possess a high exchange capacity for protons and alkali metal cations. Recent interest in these particular ionomers stems from potential applications in fuel cells and battery devices. For the anionic polymers, the transference number of the cation tends towards one since anions ought to be charge-excluded (42). The conductivity of these materials towards various ions, notably the proton and alkali metals, has been extensively studied in various solvents (43). Proton-conducting membranes displaying proton conductivities approaching values of $10^{-2} \text{ S cm}^{-1}$ have been reported (44). Correlations have been made of conductivity with various parameters spanning both the structure of the polymer, polymer–solvent interactions and the resultant solvation of the ion under investigation. A general conclusion is that a weakly basic polymer backbone aids conductivity, since it prevents the ions from being held too tightly by the framework (42). Smaller ions (e.g. monovalent metallic cations) generally display much higher conductivity than organic cations, for example (43). Conductivities can be determined using a standard cell of similar design to that employed for liquid electrolytes.

Numerous research groups have investigated the electrochemical properties of room-temperature ionic liquids, an activity driven by their perceived “environmentally friendly” nature and the large potential window they frequently display (45). Although a phase consisting solely of ions may be expected to display high conductivity, the high concentration of charge carriers is offset by the relatively low mobility that arises from the high viscosity of these liquids. Accordingly, conductivity values of the order of $10^{-3} \text{ S cm}^{-1}$ are common, which makes these media closer to electrolyte solutions in nitrobenzene (see Table 20.8) in terms of conductivity. A recent reference has observed proton conductivity in excess of 0.1 S cm^{-1} in a solvent-free ionic liquid which bodes well for future energy storage applications (46). The temperature dependence of the ionic conductivity has been investigated for imidazolium-based ionic liquids but detailed studies of the relationship between ion transport and other liquid properties are still being elucidated (47). High-temperature ionic liquids, such as molten alkali halides, generally have high specific conductivities (greater than 1 S cm^{-1}) although ionic mobility will clearly be enhanced at temperatures of ca. 1000 K (48).

In measuring transport numbers, one point noted in high-temperature ionic liquids (molten salts) is that an appreciable electrolysis of the molten salt leads to a significant change in the liquid's centre of mass due to its pure nature. Attempts to determine transport numbers via the Hittorf approach will generally be highly susceptible to gravitational instabilities in contrast to the situation for polymer electrolytes. An alternative approach is to use the Nernst–Einstein equation (20.2.1-10) to determine ionic mobility from diffusion coefficient measurements and then to find the transport number for the electrolyte (equation (20.1.2-9)). In high-temperature molten salts such as the alkali metal chlorides, cationic transport numbers of 0.7–0.8 have been reported (48).

There will be considerable activity in the optimisation of ion transport parameters within the “non-classical” electrolyte systems discussed in this section. Future prospects for research in this area are likely to involve combination of aspects of the systems referred to above (e.g. the use of room-temperature ionic liquids in conjunction with ionomers) to achieve improvements in performance of energy storage systems.

REFERENCES

1. A. J. Bard, L. R. Faulkner, *Electrochemical Methods: Fundamentals and Applications*, 2nd ed., Wiley: New York, 2001, Chap. 1.
2. J. Newman, in *Advances in Electrochemistry and Electrochemical Engineering*, C. W. Tobias, Ed., Wiley: New York, 1967, Vol. V.
3. J. J. Lingane, *Electroanalytical Chemistry*, 2nd ed., Wiley: New York, 1958.
4. H. H. Girault, *Analytical and Physical Electrochemistry*, EPFL Press: Lausanne, 2004, Chap. 4.
5. F. Bénière, in *Physics of Electrolytes*, J. Hladik, Ed., Academic Press: London, 1972, Vol. I, Chap. 6.
6. M. Spiro, in *Techniques of Chemistry Vol I: Physical Methods of Chemistry*, A. Weissberger, B. W. Rossiter, Eds., Wiley: New York, 1971, Part IIA, Chap. 4.
7. J. O. Bockris, A. K. N. Reddy, *Modern Electrochemistry Part I: Ionics*, 2nd ed., Plenum Press: New York, 1998, Chap. 4.
8. G. Jones, M. Dole, *J. Am. Chem. Soc.* **51**, 1073 (1929).
9. A. J. Bard, L. R. Faulkner, *Electrochemical Methods: Fundamentals and Applications*, 2nd ed., Wiley: New York, 2001, Chap. 4.
10. A. J. Bard, L. R. Faulkner, *Electrochemical Methods: Fundamentals and Applications*, 2nd ed., Wiley: New York, 2001, Chap. 10.
11. R. A. Robinson, R. H. Stokes, *Electrolyte Solutions*, 2nd ed., Butterworths: London, 1959, p. 465.
12. T. Shedlovsky, *J. Am. Chem. Soc.* **54**, 1405 (1932).
13. R. A. Robinson, R. H. Stokes, *Electrolyte Solutions*, 2nd ed., Butterworths: London, 1959, Chap. 7.
14. R. M. Fuoss, *J. Am. Chem. Soc.* **80**, 5059 (1958).
15. B. Fourest, L. R. Morss, G. Blain, F. David, J. M'Halla, *Radiochim. Acta* **69**, 215 (1995).
16. S. T. Lobo, R. E. Robertson, *Can. J. Chem.* **55**, 3850 (1977).
17. G. Marx, W. D. Wittke, *Zeitschrift für Naturforschung A* **32A**, 186 (1977).
18. F. Arndt, G. Marx, *Zeitschrift für Naturforschung A* **36A**, 1019 (1981).
19. J. F. Skinner, R. M. Fuoss, *J. Phys. Chem.* **68**, 1882 (1964).
20. G. Kalfoglou, L. H. Bowen, *J. Phys. Chem.* **73**, 2728 (1969).
21. M. Selvaratnam, M. Spiro, *Trans. Farad. Soc.* **61**, 360 (1965).

22. A. N. Campbell, J. I. Friesen, *Can. J. Chem.* **38**, 1939 (1960).
23. A. N. Campbell, E. M. Kartzmark, G. R. Lakshminarayanan, *Can. J. Chem.* **40**, 839 (1962).
24. B. E. Conway, *Electrochemical Data*, Elsevier: Amsterdam, 1952, Chap. 4.
25. J. I. Padova, in *Modern Aspects of Electrochemistry*, B. E. Conway, J. O. Bockris, Eds., Plenum Press, New York, 1972, Vol. VII, Chap. 1.
26. J. Burgess, *Metal Ions in Solution*, Wiley, New York, 1978, Chap. 4.
27. B. Das, M. Sama, D. K. Hazra, *J. Chem. Eng. Data* **45**, 353 (2000).
28. I. Y. Ahmed, C. D. Schulbach, *Can. J. Chem.* **71**, 2358 (1967).
29. D. P. Sidebottom, M. Spiro, *J. Phys. Chem.* **79**, 943 (1975).
30. M. Della Monica, L. Senatore, *J. Phys. Chem.* **74**, 205 (1970).
31. T. Solomon, A. J. Bard, *J. Phys. Chem.* **99**, 17487 (1995).
32. H. H. J. Girault, D. J. Schiffrin, *Electroanal. Chem.* **15**, 1 (1989).
33. E. H. Riesenfeld, *Ann. Phys.* **8**, 609 (1902).
34. E. Grunwald, G. Baughman, G. Kohnstam, *J. Am. Chem. Soc.* **82**, 5801 (1960).
35. J. Koryta, *Electrochim. Acta* **29**, 445, (1984).
36. Y. Shao, S. G. Weber, *J. Phys. Chem.* **100**, 14714 (1996).
37. A. Sabela, V. Maraček, Z. Samec, R. Fuoco, *Electrochim. Acta* **37**, 231 (1992).
38. Y. Shao, A. A. Stewart, H. H. Girault, *J. Chem. Soc. Farad. Trans.* **87**, 2593 (1991).
39. P. G. Bruce, C. A. Vincent, *J. Chem. Soc. Farad. Trans.* **89**, 3187 (1993).
40. A. J. Bard, L. R. Faulkner, *Electrochemical Methods: Fundamentals and Applications*, 2nd ed., Wiley: New York, 2001, Chap. 14.
41. R. W. Murray, *Acc. Chem. Res.* **13**, 135 (1980).
42. M. Doyle, M. E. Lewittes, M. G. Roelofs, S. A. Perusich, *J. Phys. Chem. B* **105**, 9387 (2001).
43. M. Doyle, M. E. Lewittes, M. G. Roelofs, S. A. Perusich, R. E. Lowrey, *J. Membr. Sci.* **184**, 257 (2001).
44. K. D. Kreuer, A. Fuchs, M. Ise, M. Spaeth, J. Maier, *Electrochim. Acta* **43**, 1281 (1998).
45. M. C. Buzzeo, R. G. Evans, R. G. Compton, *Chem. Phys. Chem.* **5**, 1106 (2004).
46. W. Xu, C. A. Angell, *Science* **302**, 422 (2003).
47. A. B. McEwen, H. L. Ngo, K. LeCompte, J. L. Goldman, *J. Electrochem. Soc.* **146**, 1687 (1999).
48. J. O. Bockris, A. K. N. Reddy, *Modern Electrochemistry Part 1: Ionics*, 2nd ed., Plenum Press: New York, 1998, Chap. 5.

This page intentionally left blank

Subject Index

- 5-amino-2,3-didro-1,4-phthalazinedione, 553
Abrasion and corrosion resistance, 317
Absolute scale, 342
Absorbance, 593
AC Electrokinetics, 184
Ac Voltammetry (ac Polarography), 25
AC voltammetry, 608, 645
Accumulation layer, 349
Acetonitrile, 65, 69, 307
Acid chlorides, 307
Acid/base functionality, 314
Action spectra, 379
Activity
 coefficients, 9
 screening of electrocatalysts, 513
Adlayer, 295, 302–303
Admittance, 275
Adsorption, 12, 704
 capacity, 314
Adsorptive stripping voltammetry, 267
Ag, 296
Alcohols, 307
Alkanethiol, 302
Alkanethiolate, 301
Alumina, 678, 686, 315
Amides, 65
Amines, 307
Amperometric
 feedback mode, 473
 methods, 473
Amperometry, 25, 235
Amplification, 394
Analytical applications, 174
Angular frequency of rotation, 19
Annihilation ECL, 542, 545–547, 557, 559,
 568
Anode, 3, 7
Anodic
 (oxidation) current, 14
 current, 6, 348
 oxidation reaction, 5
 paints, 480
stripping voltammetry (ASV), 266–267
Stripping Voltammetry
 (Stationary/Hydrodynamic), 25
Anodization, 307
Anodized aluminum, 407
Anthracene, 184
Anti-stokes, 623–624
Approach
 curve, 359, 481
 into liquid, 219
Arrays, 391
Artificial Cell, 727
Arylacetates, 307
Aspect ratio, 212
Asymmetric etching, 684
Atomic force microscopy (AFM), 358, 372,
 475
Attenuated total reflectance (ATR), 605
Au, 296, 303
Autocorrelation function, 754
Auxiliary (Counter) Electrode, 7, 595

 γ -butyrolactone, 66
Band
 bending, 344
 gap, 332, 349
 theory, 330
Barium titanate, 315
Barrier
 height, 344
 layer, 680
Based localization of the pore resistance to the
 orifice, 254
Basics, 189
Battery, 3, 7
Becquerel Effect, 329
Behavior of ultramicroelectrodes, 155
Benzonitrile, 65, 69
Benzoyl Peroxide, 553
Bilayer lipid membrane, 530
Bioelectronics, 177
Biogenic Amine Release, 720

- Biological, 297, 310
 molecules, 321
 redox species, 821
 systems, 175
- Biomimetics, 305
- Biomolecule, 310
- Biosensors, 310, 527
- Bis-oxaloborate (BOB), 67
- Bjerrum theory of ion pairing, 60
- Blunt Conical UMEs, 211
- Bode plot, 277
- Boltzmann's constant, 15
- Borates, 67
- Bragg's law, 331
- Brillouin Zone, 331
- Brownian Dynamics Simulations, 664
- Bulk
 concentration, 10
 electrolysis, 12, 25, 257–258
 vs. Surface NO Measurements, 252
- Burstein shift, 379
- Butler–Volmer Equation, 14, 361
- Butyronitrile, 65, 67, 69
- Calcium
 chloride, 69
 sulfate, 69
- Calibration, 100, 252
- Capacitance, 13, 22, 158
- Capacitive currents, 168
- Capillary
 electrophoresis, 541, 557, 565
 tube, 189
- Carbon, 296, 306–307, 316
 electrodes, 114
 fibers, 128
 nanofiber, 218
 nanotubes, 133
 paste, 316
 paste electrodes, 310
- Carbonates, 66
- Carboxylic acid, 307
- Carrier, 262
- Catalysis, 21, 311
- Catalytic activity, 311
- Cathode, 3, 7
- Cathodic
 (reduction) current, 6, 14, 348
 electrophoretic paint, 224
 paints, 480
- reduction reaction, 5
 stripping voltammetry (CSV), 267
- Cation-exchange, 314
- CdS, 353
- Cell
 constructions, 173
 potential, 3, 7, 858
 resistance, 22
 schematic, 4
 time constant, 62
- Cellular detoxification process, 534
- Characterization of NO Microsensors, 252
- Charge mediators, 316
- Charge, 11
 pairs, 349
 step, 25
 transfer, 19
 transfer rate constant, 703
 transfer resistance, 276, 768–769
 transport, 317
- Charged ionophores, 270
- Charging current, 23, 256, 265–266, 268, 276, 835
- Chemical
 bath deposition, 371
 catalysis, 310
 etching, 683
 sensors, 21
- Chemically
 irreversible, 13
 reversible, 13
- Chemiluminescence, 541, 543–544, 570
- Chemisorb, 301
- Chemisorption, 296, 300, 304
- Chromophores, 316
- Chronoabsorptometry, 600
- Chronoamperometric (current-time) response, 157
- Chronoamperometry, 7, 10, 25, 833, 368, 252, 269, 274, 419
- Chronocoulometry, 25, 601
- Chronopotentiometry, 25, 835, 843
- Circular dichroism, 632
- Citrate, 309
- Clarke Oxygen Microelectrode, 243
- Clark-type NO microsensor, 250
- Clay, 296, 308–311
 modified electrodes, 308, 310
- Co-crystal, 626
- Collection efficiency, 487, 489, 508, 655

- Collector/generator, 395
Combinations of sweeps and steps, 265
Commercial Pipette Pullers, 198
Compensated resistance, 24
Complementary error function, 255
Complexation equilibria, 179
Composite Electrodes, 406
Concentration
 gradient, 17, 829
 profiles, 401
Conducting wires, 404
Conductive, 317
 polymer modified electrodes, 321
 polymers, 316, 320
Conductivity, 58
Confined etchant layer technique, 521
Confocal Raman spectroscopy, 422
Conformal mapping techniques, 400
Conical
 electrode, 212
 pores, 684
 ultramicroelectrodes, 211
Constant
 current, 25
 height imaging, 498
 height mode, 475
 potential, 25
Controlled
 charge, 25
 current, 25
 potential, 25
Convection, 17
Convenient Hydrogen Electrode (CHE), 83
Copper, 301
Coreactant ECL, 546–548, 557, 570
Coreactant, 541, 546–549, 553, 557, 564, 570
Cottrell equation, 10, 254, 838
Cottrellian, 419
Coulomb
 blockade, 767
 staircase, 764, 767
Coulometric Titrations, 25
Coulometry, 11, 25
Coulostatic Methods, 25
Covalent, 305
 attachment, 296, 305, 309
 $C_r E_r$, 651
Current, 3
 density, 11
 overpotential equation, 16
 potential characteristic, 15
 reversal, 25
Curve fitting, 656
Cuvette, 597
Cyanuric chloride, 306
Cyclic, 25
 voltammetry, 25, 256, 258–259, 263, 268,
 273, 278, 280, 419, 697, 703, 836
 voltammogram, 195
Cylindrical, 397
 pores, 684
Cytochrome c, 184, 704
1,2-dimethoxyethane(glym), 66
9,10-diphenylanthracene, 184, 544
Dark current, 563
Dead layer, 385
Density gradients, 17
Depletion layer, 385
 thickness, 168
Deposition of conducting polymers, 522
Detection limit, 262, 701
Determination of Cholesterol, 724
Diamond electrodes, 595
Diazonium, 307
 reduction, 307
Dichloroethane, 65
Dichloromethane, 65, 70
Differential
 pulse voltammetry (DPV), 25, 265–266
 pulse voltammograms, 381
 reflectance spectroelectrochemistry, 607
Diffuse
 layer, 23
 reflectance, 605
Diffusion, 10, 17, 251–252, 254, 256,
 259–261, 267–273, 276, 279–284, 286
 coefficient, 10, 701, 829
 control, 711
 fields, 165
 layer, 391, 396
 limited current, 10
 potentials, 850
DigiElch, 280
DigiSim program, 280, 657
Digital simulation, 657
Dimethylformamide (DMF), 65, 70
Dimethylsulfoxide (DMSO), 65
Dip-coating, 317, 319–320, 322
Disk electrodes, 393, 837

- Dissipation current, 507
 Distribution potential, 871
 Disulfide, 301
 Dithionite, 309
 DNA, 297, 549
 analysis, 549
 duplex, 704
 hybridization, 527
 DOS, 340
 Double
 band assembly, 401
 barrel tip, 496
 junction reference electrode, 97
 potential step, 25
 reference electrode, 105
 Double layer
 capacitance, 275–276
 capacity, 256
 charging, 12, 268–269, 287
 charging current, 701
 Drop-casting, 309, 317, 319–320, 322
 Dropping mercury electrode (DME), 34
 Drying agents, 69
 Dual-barrel electrodes, 526
 Dynamic Hydrogen Reference Electrode
 (DHRE), 85
Dynamic methods, 25
 ECE/DISP processes, 506
 Effective
 mass approximation, 337
 masses, 336
 Electric field effects, 764
 Electrical
 charge, 3
 double layer, 23
 Electrically
 conducting diamond, 135
 conductive polymers, 320
 Electroactive, 4
 integrated optical waveguide (EA-IOW),
 612
 species, 10
 tagging methods, 527
 Electroanalytical measurement, 113
 Electrocatalysis, 310, 314, 317
 Electrochemical
 atomic layer epitaxy, 370
 band gap, 380
 cells, 5, 7, 20, 172
 cleaning, 169
 deposition, 369, 686, 709
 detection of NO, 249
 impedance methods, 274, 278
 impedance spectroscopy, 25
 mediator, 7
 polarization, 118
 potential, 341
 Electrochemically
 active, 10
 assisted, 307
 assisted modification, 307
 etched, 212
 etched carbon fiber electrodes, 221
 Electrochemiluminescence (ECL), 410, 541, 544
 Electrochemistry, 3
 in humid environments, 774
 Electrochromism, 317
 Electrode, 3, 7, 369
 area effects, 168
 geometry problems, 160
 kinetics, 15
 modification, 295
 potentials, 813, 820
 response times, 156, 159
 sharpening, 196
 size, 159
 solution interface, 23
 Electrodeposition, 369–370, 408, 661
 Electrogenerated chemiluminescence, 475,
 541, 749
 Electrogravimetry, 11
 Electrokinetic, 711
 Electroless deposition, 371, 409, 688
 bath, 373
 Electrolysis, 3, 25
 Electrolyte, 3, 6, 57
 concentration, 159
 Electrolytic cell, 7, 20
 Electromotive force, 4
 Electron hopping, 319–320
 Electron transfer, 3, 12, 320
 kinetics, 13, 307, 703
 mechanisms, 319
 mediators, 601
 on self-assembled monolayers, 514
 Electron-beam, 414
 Electronic communication, 598

- Electrophoretic
 deposition of an insulating cathodic paint, 231
 deposition, 310
 insulation, 217
 paint, 213
 paint insulation, 218
- Electropolymerization, 321–322
- Electroreflectance, 608
- Ensembles of 3D-nanowires, 704
- Entrapment, 321
- Enzyme, 297, 300, 310
 activity, 524
 turnover rate, 526, 529
- Epifluorescence, 632
- Epitaxial, 375
- $E_q C_r$, 657
- Equilibrium
 constant, 9
 potential, 4, 7, 14
- Equivalence circuit of an electrochemical cell, 639
- Equivalent circuit, 156
- Equivalent electrical circuit, 275
- $E_r C_{2i}$, 655
- $E_r C_i$, 651
- E-route, 546
- Etched
 conical Pt tips, 212
 gold microwire, 230
 Pt UMEs, 213
- Etching, 416
- Ethers, 66
- Ethylene carbonate (EC), 66
- European convention, 6
- Exchange current, 15, 276
- Excimer, 546
- Exciplex, 546
- “Exotic” electrolytes, 67
- Experimental timescale, 164
- Explicit finite difference (EFD), 282–284
- External reflectance, 605
- Extrinsic, 334
- Fabrication, 197
 characterization, 189
 of NO Microsensors, 250
- Faradaic, 7, 349
 current, 11, 22
 electrochemistry, 164
- impedance, 276
 to-capacitive current ratios, 701
- Faraday, 3
 constant, 4
 law, 11
- Fast scan cyclic voltammetry, 268
- $\text{Fe}(\text{CN})_6^{3-}$, 216
- $\text{Fe(OEP)(N-Melm)}_2^+$, 184
- Feedback modes, 481
- Fermi
 dirac distribution function, 332
 dirac statistics, 332
 level, 332, 334
 level pinning, 355
- Ferrocene, 184, 704
- Ferrocenemethanol (FcOH), 196, 219
- Fiber optic, 597
 probes, 608
 reflectance probes, 608
 spectrometers, 608
- Fick’s
 first law of diffusion, 17, 440, 459, 829
 second law, 164
- Finite conical electrode, 215
- Finite diffusion, 597
- Finite-element simulations, 260
- First-order irreversible reaction, 506
- Fission fragments, 683
- Fixed interference method, 274
- Flame Etched Carbon Nanofibers, 217
- Flame etching, 217
- Flat-band potential, 346
- Flow
 electrolysis, 25
 injection analysis, 541, 557
 through cells, 35
- Fluorescence, 612
- Fluorosulfonates, 67
- Fluorosulfonimides, 67
- Flux, 17–18, 829
- Forced convection, 256, 271–272
- Formal
 electrode potentials, 813, 818–821
 potential, 9
 reduction potential, 348
- Forward and reverse rate constants, 15
- Fractional Electrode Area, 700
- Free energy change, 9

- FTIR, 618
- Fuel cells, 7, 21
- Galvanic, 6
 - (Voltaic) Cell, 7, 20
- GaP, 353
- Gas-phase measurement, 244
- Gel, 316
- Generation
 - collection experiments, 453
 - collection (G/C) mode, 486
- Gerischer's model, 343, 357
- Gibbs free energy, 4
- Glass
 - (pyrex and quartz), 33
 - frit, 35
 - membrane electrodes, 491
 - metal seal, 194
 - nano pore electrode, 254
- Glassy carbon (GC), 121
- Gold, 143, 301
 - inlaid disks $\leq 5 \mu\text{m}$ diameter, 197
 - inlaid disks, 189
 - micromesh, 36
 - spherical microelectrodes, 226
- Grain boundaries, 369
- Gramicidin channels, 532
- Graphite packing, 36
- Graphite, 661
- Gratzel cells, 384
- Grid spaces, 400
- Grignard, 307
- Half
 - cell, 5, 7
 - reaction, 4, 7
- Halogenated Organics, 65
- Heat treatment, 118
- Helmholz layer, 345
- Heme, 601
- Hemispherical, 397
 - diffusion, 420
 - electrodes (equations 6.1.4.5, 11.2.64), 837
 - Hg tips, 480
- Hemoglobin, 601
- Heterogeneity, 33
- Heterogeneous
 - electron transfer dynamics, 181
 - kinetics, 501
- rate constant, 14, 347
- reactions, 11
- Hexafluorophosphate, 67
- High
 - aspect-ratio, 404
 - frequency shunt, 105
 - temperature ionic liquids (molten salts), 876
 - voltage single pulse generator, 232
- Highly oriented pyrolytic graphite (HOPG), 115, 661
- Hittorf method, 856
- Hofmeister series, 265
- Homogeneous, 11
 - chemical kinetics, 181, 183
 - chemical reactions, 506
- Hush theory, 599
- Hydrazine, 307, 552
- Hydro-dynamic, 25
- Hydrogen
 - evolution reaction, 510
 - peroxide, 553
 - plasma treatment, 124
- Hydroxyl group, 306–307
- Ideal
 - Nonpolarizable (Depolarized) Electrode, 7
 - Polarizable (Polarized) Electrode, 7
 - polarizable liquid/liquid interface, 788
- Imaging, 632
 - by substrate generation/tip collection mode, 510
 - by tip generation/substrate collection mode, 512
 - fiber, 417
 - of catalytic activity, 510
- Imidazolium $\text{BF}_4^-/\text{PF}_6^-/\text{TFSI}/$ ionic liquids, 67
- Immunoassay, 541, 549, 564
- Impedance, 22
 - methods, 274, 278
 - techniques, 25
- Imprinted
 - polymer modified electrodes, 322
 - polymers, 322
- Impurities, 68
- Indicator Electrode, 8
- Indirect electrochemical methods, 601
- Indium tin oxide (ITO), 147

- Individual electrodes, 392
Individually addressable, 394
Infrared reflection absorption spectroscopy (IRRAS), 618, 620
Inner Helmholtz plane, 23
Insulating sheath thicknesses, 480
Insulin Release, 722
Interdigitated array electrode (IDA), 395
Interdistance spacing, 406
Interface
 (Junction), 3, 7
 between two immiscible electrolyte solutions (ITIES), 870
Interferometer, 618
Interferrogram, 618
Intracellular
 patch electrochemistry, 743
 voltammetry, 742
Intrinsic, 334
Ion, 3
 beam, 414, 683
 by-ion deposition, 372
 channels, 524, 530
 exchange, 308–311, 315, 317, 320
 exchange polymers, 320
 exchange redox polymer modified electrode, 320
 mobility, 60
 pairing, 59
 transport across channels, 524
Ionic conductivity, 317
Ionic site, 262
Ionophore, 262, 316
Ion-selective
 electrode (ISE), 261, 490
 liquid membrane micropipets, 493
 micropipet electrodes, 532
 potential, 495
IR drop, 38
Iron, 309
 oxide, 309
IVCT, 599
- Kel-F, 33
Kinematic viscosity, 19
Kinetic
 parameter, 506, 639
 zones, 641
- Kinetically limited, 19
Kinetics, 12, 14
Koutecký–Levich equation, 453
- Lactone, 66
Langmuir Blodget (LB) films, 376, 297–300, 304, 310
Langmuir, 297–299
 Blodget techniques, 530
Large amplitude perturbations, 274
Laser activation, 117
 based pipette puller, 198
 pulled technique, 199
Layered metal dichalcogenides, 369
Levich equation, 271, 273, 840
Limiting current, 837
Linear, 699
 scan voltammetry, 25, 833
 sweep voltammetry, 235, 258
Linearly Increasing Current, 25
LiPF₆, 66
Lipid, 297
 bilayer membranes, 726
Liquid
 chromatography, 541, 557
 junction potentials, 850
 membrane electrodes, 492
LiTFSI, 66
Lithium
 perchlorate, 71
 salts, 66–67
Lithographic methods, 411
LiTriflate, 66
Low
 aspect-ratio, 403
 conductivity media, 177
 temperature electrochemistry, 68
Luggin capillary, 286
Luminescence, 541–542, 547, 612
 spectroelectrochemistry, 614
Luminescent lifetimes, 615
Luminol, 553
- Manganese oxide, 315
Mass transfer, 12, 17, 19
 coefficient, 10, 18, 516, 640
 limited current, 10, 19
 limiting current, 18
 resistance, 276

- Mass transport, 19, 251–254, 256–263, 267–269, 271, 273–276, 279–280, 283, 391
- Materials, 33
- Mechanical polishing, 121
- Mediation, 310
- Membrane
- potential, 489–490
 - transport, 530
- Menadione-glutathione conjugate, 534
- Mercuric oxide reference electrode, 91
- Mercury, 301
- Sulfate Reference Electrode (MSRE), 89
- Metal
- deposition and etching, 519
 - oxide electrodes, 496
 - surface selection, 621
 - wires, 392
- Method of Nicholson, 642
- Microconical platinum, 36
- Microcontact Printing, 415
- Microdisk, 167
- Microelectrochemical experiments, 173
- Microelectrodes, 391
- applications, 171
 - characterization, 206
 - mass transport regime, 447, 448
 - steady state current, 434, 450
- Micromesh, 595
- Microparticles, 667
- Micropatterning, 523
- Micropatterning of enzymes, 527
- Micropipette beveler, 199
- Microring, 167, 393
- Microscopic Droplets, 739
- Microspheres, 393
- Microvials, 741
- Migration, 12, 17, 251, 279, 287
- Minigrid electrodes, 595
- Mixed valence, 598
- Mobility, 851
- MOCVD, 369
- Model diffusion coefficient, 282–283
- Modeling a Synapse, 731
- Modified electrode, 295–296, 308, 313, 320
- Molar conductivity, 853
- Molecular
- beam epitaxy, 369, 375
 - electronics, 297, 300, 305, 307
- imprinting, 322
- recognition, 297, 310, 314
- Monolayered protected clusters, 381, 771
- MoS₂, 353, 369
- Mott-Schottky, 346
- Moving boundary, 858
- Myoglobin, 601
- Nafion, 67–68
- Nanocrystalline particulate films, 375
- Nanodisk, 254, 699
- Nanoelectrode ensembles, 697
- Nanomaterials, 337
- Nanometer electrodes, 709
- Nanoparticle nanotubes, 693
- Nanoparticles, 661
- Nanoporous membranes, 678
- Nanostructures, 374, 661
- Nanotechnology, 305
- Nanotubes, 693
- Nanowires, 661, 687
- Naphthalene, 184
- Natural convection, 251, 254, 256, 268, 287
- NCE, 88
- Near infra-red (NIR), 594
- Near-field scanning optical microscopy, 475
- Negative feedback, 359, 472, 752
- Nernst
- diffusion layer 451
 - equation, 4, 9, 254, 267
 - plot, 600
 - Planck equation, 17, 850
- Nernstian, 7
- responses, 261
 - system, 421
- Neurochemicals, 821, 824
- Neutral ionophore, 266
- Nikolsky-Eisenman equation, 273, 490
- Nitric
- oxide (NO), 249
 - microsensors, 249
- Nitriles, 65
- N-methylpyrrolidinone (NMP), 65
- NO microsensor, 249
- Nonconducting polymers, 317, 322
- Nonconductive, 317

- Non-faradaic, 8
 current, 12
 time constant, 12
- Non-ideal
 faradaic responses, 168
 microelectrode geometry, 161
 responses, 160
- Non-polarizable liquid/liquid interface, 790
- Non-radiative recombination, 385
- Nonstoichiometric films, 370
- Normal
 Hydrogen Electrode (NHE), 5, 80, 341
 pulse voltammetry (NPV), 265
 Standard Hydrogen Electrode, 8
- Normalized
 chronoamperometry, 840
 distance, 479
 feedback current, 506
 steady-state tip current, 506
- Nucleation exclusion zones, 715
- Numerical techniques, 400
- Nylon, 33
- Nyquist plot, 277
- Ohmic
 distortion, 286
 drop, 267–269, 271
 effects, 163
 losses, 61
 potential drop, 639
 solution resistance, 275–276
- Ohm's law, 22
- Open circuit potential, 4
- Optical
 microscopy, 199, 422
 transparency, 317
- Optically
 transparent electrodes, 594
 transparent thin layer electrode (OTTLE), 596
- Organic
 carbonates, 66
 mediators, 820
- Organometallic
 catalysts, 316
 chemical vapour deposition, 375
- Organosilane, 305–306
- Ortho-dichlorobenzene, 65
- Outer Helmholtz plane, 23
- Overpotential, 8, 10, 14
- Oxalate, 547–548, 573
- Oxidation, 8
 state, 11
- Oxidative
 stress agent, 524, 534
 reduction, 546–547, 549
- Oxidized Species/Oxidizing Agent/Oxidant, 4, 8
- Oxygen, 184
 plasma, 695
 permeable membrane, 244
 reduction reaction, 245, 500, 512
- Packing density, 421
- Partially blocked surface, 703
- Particle growth, 715
- Patch Amperometry, 723
- Patterning of biological molecules, 522
- PC/EC/polyacrylonitrile gel, 67
- PDMS, 415
- Perchlorates, 67
- Perdeuteriated, 628
- Permeability of the membrane, 534
- Peroxydisulphate, 548
- Persulfate, 548
- Phase
 boundaries, 11, 20
 boundary potential, 263
- Phenothiazines, 704
- Phosphorescence, 612
- Phosphorous oxide (P_2O_5), 69
- Photo Mask, 412
- Photocatalyst, 383
- Photoelectrochemical, 378, 384
 (PEC) measurements, 378
- Photoexcitation, 384
- Photolithography, 411
- Photoluminescence, 385, 542–545
- Photomultiplier tube (PMT), 560–563
- Photo-oxidation, 350
- Photoresist, 412
- Photovoltaic, 383
- Physisorption, 296
- Piezoelectric driven dispenser, 527
- Pillared clays, 309
- Piranha solution, 169

- Planar, 397
- Plasma chemical vapor deposition (CVD), 414
- Plasmon resonance, 696
- Plasmons, 630
- Platinum, 143, 189, 197, 301
 - grid, 36
- Poisson distribution, 759, 764
- Polarizability, 624
- Polarization curve, 489
- Polarographic or American convention, 6, 34
- Polishing, 192
 - cloth, 194
 - wheel, 193
- Poly(acrylic acid)(PAAH), 213
- Poly(ethylene terephthalate), 682
- Polycarbonate, 682
- Polycrystalline, 369
- Polyethylene oxide, 67
- Polyethylene-glycol-dimethylether, 67
- Polyimide, 682
- Polyion-selective electrodes, 292
- Polymer, 297, 316–317, 319–322
 - electrolytes, 874
 - modified electrodes, 317, 320–321
- Pore density, 686
- Pore orifice, 255
- Positive feedback, 359, 473, 750
- Potential
 - drop, 24
 - gradient, 17
 - window, 703–704, 788
- Potential step, 10, 25, 431, 432, 436–440, 447–449
 - double, 436, 462, 462
- Potential sweeps, 13, 25, 438, 441
 - experiment for adnorbred species, 443
 - principles, 438
 - steady state experiments, 441
- Potentiometric
 - method, 473
 - probes, 489
 - stripping analysis, 267
- Potentiometry, 8, 25
- Practical reversibility, 14
- Preceding and ensuing reactions, 12
- Preconcentration, 13, 310–311, 316
- Pretreatment, 112
- Primary (non-rechargeable) cell, 21
- Probability density function, 754
- Processes with coupled chemical reactions, 651
- Propylene carbonate(PC), 66, 70
- Proteins, 316
- Protic Solvents, 63
- Pt, 296
 - electrodeposition, 235
 - tip preparation, 255
 - wire, 200
- PTFE gas permeable membrane, 250
- Pulse voltammetry, 265
- Pure Radial, 699
- Purification procedures, 68, 70
- Pursulfate, 553
- Pyrolytic carbon, 228
- Pyrolyzed photoresist films (PPF), 126
- Pyruvate, 551
- Quantized double layer charging, 749, 771
- Quantum
 - dots, 340
 - size effects, 375
 - well, 340
 - wire, 340
 - yields, 614
- Quartile potentials, 648
- Quartz capillaries, 200, 227
- Quasi reference electrode (QRE), 22, 94
- Radial diffusion, 168
- Raman
 - confocal microscopy, 624
 - spectroscopy, 623
- Randles-Sevcik equation, 440, 701
- Random microelectrode arrays, 392
- Rate determining step, 12–13
- RC time costant, 157
- Reaction
 - ion etching, 413
 - rate imaging, 499
 - Rate, 11
- Reactive surfaces, 177
- Rectifying, 352
- Redox, 8, 317
 - couple, 8
 - mediator, 216
 - polymers, 317, 319–320
 - polymer electrodes, 319
 - polymer modified electrodes, 319

- Reduced Species/Reducing Agent/Reductant, 4, 8
Reduction, 8
Reductive-oxidation, 546, 548
Reference
 electrode, 5, 8, 34, 73, 595
 half-cell, 5
Reflectance, 592
 probes, 608
Regular arrays, 393
Resin, 413
Resistivity, 58
Resonance Raman, 628
Respiration rate, 534
Reticulated vitreous carbon (RVC), 36
Reversibility, 13
Reversible system, 9
RF plasma treatment, 123
RG value, 196
Ring UME tips, 480
Room temperature ionic liquids, 68, 875
Rotating disk, 625
 Disc Electrode (RDE), 25, 833, 251, 256, 261, 269, 271–273, 833
 Ring Disc Electrode (RRDE), 25, 273, 559
Rotation rate, 841
Ru (NH_3)₃⁺⁶, 184

Salt bridge, 20, 870
Salts, 66
SAM modified electrodes, 302, 305
Sampled Current Voltammetry, 25, 644
SAMs, 301–302, 304–305
Sand equation, 843
Saturated Calomel Electrode (SCE), 87, 342
Scan rate, 13
Scanning
 Electrochemical Microscopy (SECM), 189, 749, 358, 360, 471, 724, 844, 418, 199, 218, 358, 360
 near field optical microscopy (SNOM), 632
 probe microscopies, 471
 tunneling microscopic (STM), 296, 302
Screen-printing, 309
Sealing, 189
 the Pt tip in glass, 256
SECM
 amperometric tips, 479
 approach curves, 216
 feedback, 235
 microfabrication, 519
Secondary (rechargeable) cells, 21
Second-order irreversible dimerization, 506
Selective Exposure of the spherical end of the microwire, 233
Selectivity coefficient, 273, 490, 495
Self-assembled monolayers (SAMs), 300
Self-assembly, 300–301, 303
 of Gold Nanoparticles, 226
Self-Contained Hydrogen Electrode (SCHE), 83
SEM, 695
Semiconductor
 electrodes, 329
 etching, 521
 films, 369
Semiconductors, 334
Sensing, 317
Sensor, 307, 310, 314, 317, 319, 321, 384
Separate solution method, 273
Shape
 parameter, 167
 selectivity, 311
Sharp Conical UMEs, 213
Sharpened gold microwires, 230
Signal-to-noise ratio, 394
Silane, 306, 316
Silica, 314–315
Silver, 301
 silver cation reference electrode, 93
 silver chloride reference electrode, 92
Silylate, 594
Simulation packages, 657
Simulations, 458, 460
 principles, 460
Single
 electron-transfer events, 749, 759
 molecule electrochemistry, 749
 nuclei, 715
 particle deposition, 709
 particles, 709
 electron events, 767
Size, 311
 quantization effect, 374
 quantized particle, 336–337
Small amplitude perturbations, 274
Small drops and vials, 737

- SNIFTIRS (subtractively normalised interfacial Fourier transform infrared spectroscopy), 619
- S**nSSe₂, 369
- Soft Lithography, 415
- Solar Cells, 381
- Sol-Gel Modified Electrodes, 314, 316–317
- Sol-gel, 297, 314–317
- Solid
- polymer electrolytes, 68
 - state electronic conductivity, 34
 - state membrane electrodes, 492
- Solubility product, 9
- Solution
- conductivity, 13
 - resistance, 12, 33, 60, 256, 275–276
- Solvent Cleaning, 116
- Solvents, 57, 62, 68
- Sonochemical, 407
- Space charge region, 344, 348
- Spark-Induced Melting, 230
- Specific double layer capacitance, 158
- Spectral density function, 756
- Spectroelectrochemical flow cell, 44
- Spectroelectrochemistry, 44
- Specular, 605
- Spherical
- coordinates, 164
 - electrode, 167
 - gold UMEs, 234
 - microelectrodes, 226
 - potential well, 339
- Spin-coating, 309–310, 317, 319–320, 322
- Spontaneous reactions, 4
- Square wave voltammetry (SWV), 25, 265–266
- S-route, 545
- SSCE, 88
- Staircase voltammetry (SCV), 265
- Standard
- electrode potentials, 4, 813, 815, 823
 - Gibbs free energy change, 4
 - heterogeneous rate constant, 15
 - Hydrogen Electrode (SHE), 5, 80
 - potential, 4
 - rate constant, 348
 - reduction potential, 8
 - transfer potential, 787
- Static* method, 25
- Stationary, 25
- Statistical arrays, 398
- Steady state
- current, 195, 471, 834
 - electrochemistry, 183
 - limiting current, 167
 - response, 167
- voltammetric responses of GNEs, 259
- voltammetry, 448, 646
- voltammogram, 194–195
- Step methods, 10
- Stirred Solution/Flow Cell, 25
- STM, 303, 358
- Stokes
- Raman, 623
 - scatter, 624
- Stray capacitance, 162
- Stripping
- analysis, 266–267
 - voltammetry, 310
- Strong electrolytes, 58
- ST-route, 545
- Submarine electrode, 530
- Submicrometer-Sized Spherical Electrodes, 230
- Substrate generation/tip collection mode, 473, 486, 518
- Sulfolane, 65
- Sulfones, 65
- Sulfoxides, 65
- Supporting electrolyte, 8, 18, 57
- Surface
- contamination, 169
 - enhanced Raman spectroscopy (SERS), 628
 - impurities, 161
 - reaction, 10, 12
- Suspended Semiconductor Nanoparticles, 378
- Ta₂O₅, 364
- Tafel Equation, 16
- Tafel plots, 15
- Tafel regions, 17
- TATB assumption, 787
- Teflon, 33
- TEM, 695
- Temperature Effects, 107
- Template, 678
- approaches, 407

- Tetrabutylammonium (TBA), 67
hexafluorophosphate, 71
tetrafluoroborate, 71
- Tetracyanoethylene, 184
- Tetracyanoquinodi-ethane, 184
- Tetraethylammonium (TEA), 67
hexafluorophosphate, 71
tetrafluoroborate, 70
tetraphenylborate, 70
- Tetrafluoroborate, 67
- Tetrahedral amorphous carbon (Ta-C), 140
- Tetrahydrofuran (THF), 66
- Tetraphenylborate salts, 67
- TFSI, 67
- The Hg/Pt ultramicroelectrodes, 235
- Thermal stability, 314
- Thermodynamic reversibility, 14
- Thickness of the Nernst diffusion layer, 19
- Thin
conducting film electrodes, 594
layer cells, 41
metal films, 594
layer cell response, 258
- Thiol, 301
- Thionyl chloride, 307
- Three
dimensional electrode, 417
electrode configuration, 21
point method, 648
- Tight binding, 339
- Time
constant, 157
correlation function, 754
resolved luminescence
spectroelectrochemistry, 615
- Tip
characterization, 218
generation/substrate collection (TG/SC)
mode, 655, 488
position modulation, 498
- Titanium dioxide, 315
- Tomeš criteria, 263
- Topographic and chemical imaging, 497
- Total internal reflection, 622
- Total Overlap, 699
- Track etched membranes, 407
- Track-etch, 682
- Track-Etched Polymer, 686, 699
- Transfer coefficient, 15
- Transference number, 852
- Transient
and steady-state behaviors, 166
techniques, 180
time by diffusion, 506
- Transit time, 750
- Transition time, 843
- Transmission, 592
- Transparent metal oxide, 594
- Transport, 297, 300
- Triethanolamine, 362
- Triflate, 67
- Trifluorotoluene, 65
- Tri-n-propylamine, 549
- Trouble Shooting, 284–285
- T-route, 545
- Tungsten oxide, 315
- Two-electrode, 21
- Ultrafast Electrochemical Techniques, 180
- Ultramicroelectrode fabrication, 200
- Ultramicroelectrodes (UME), 19, 24, 155,
189, 198–199, 359–360, 471, 749,
830
- Ultra-violet, 594
- Uncompensated resistance, 24
- Uniformly accessible working electrode, 647
- UV-vis-NIR, 594
- Vacuum line, 49
- Van der Waals, 299, 301–302, 308
- Vanadium pentoxide, 315
- Variable angle, 605
- Variational methods, 339
- Visible region, 594
- Vitamins, 821, 824
- Voltage
drop, 9, 23
reduction sequence, 680
- Voltaic pile, 3
- Voltammetric, 353
- Voltammetry, 8, 25, 206, 418
amperometry, 13
in pure liquid organics, 179
in the absence of deliberately added
electrolyte, 178
- Voltammograms, 6

- Warburg impedance, 276
Weak electrolytes, 58
Wollaston wire, 189, 197, 198
Working electrode, 5, 8, 34
 WSe_2 , 353, 369
Xerogel, 315
X-ray photoelectron spectroscopy (XPS), 303
X-ray, 414
- Zeolite Modified Electrodes, 311, 313
Zeolites, 297, 311–314
Zinc oxide, 315
Zirconia, 314–315
 $\text{Zn}(\text{TPP})$, 184
 ZnO , 353, 367
Zone
 diagram, 421
 theory, 330

COLOUR SECTION

This page intentionally left blank

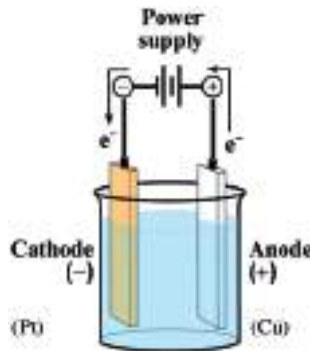


Plate 1 An electrolytic electrochemical cell. (see page 20)

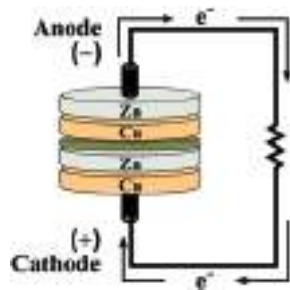


Plate 2 A galvanic electrochemical cell. (see page 21)

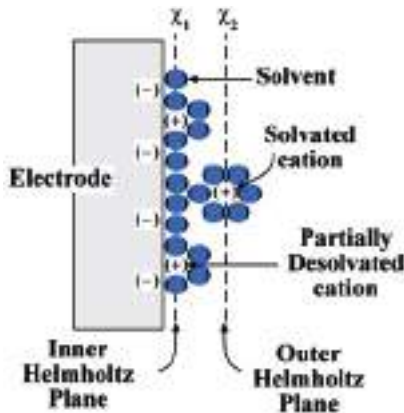


Plate 3 The electrical double layer (adapted from reference (3), with permission). (see page 23)

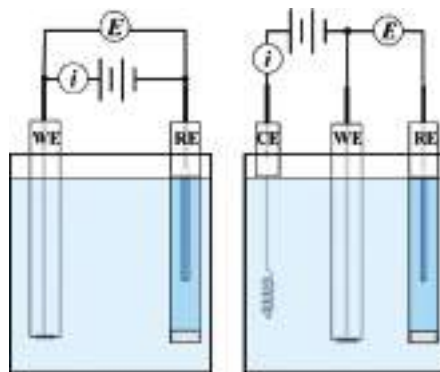


Plate 4 Schematic representation of two-electrode (left) and three-electrode (right) electrochemical cells. (see page 24)



Plate 5 Two-electrode cell for solid-state conductivity measurements. (see page 35)

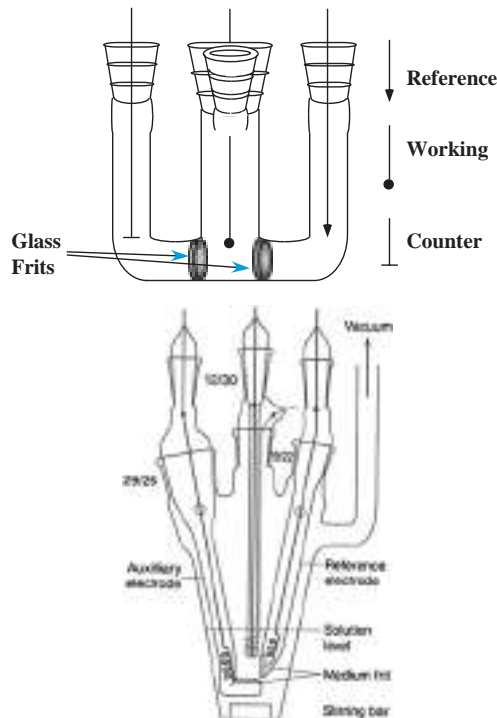


Plate 6 Three-electrode electrochemical cells. Three-compartment cell with (top panel) and without (bottom panel) glass frits (3, 4). (see page 36)

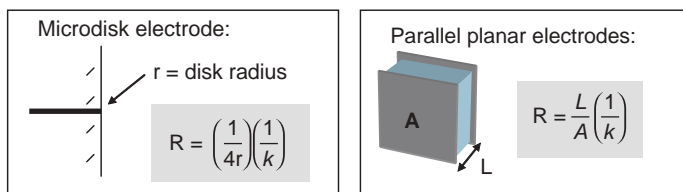


Plate 7 Relationships between solution resistance and cell geometry for two limiting cases of electrodes in contact with electrolytes. (see page 61)

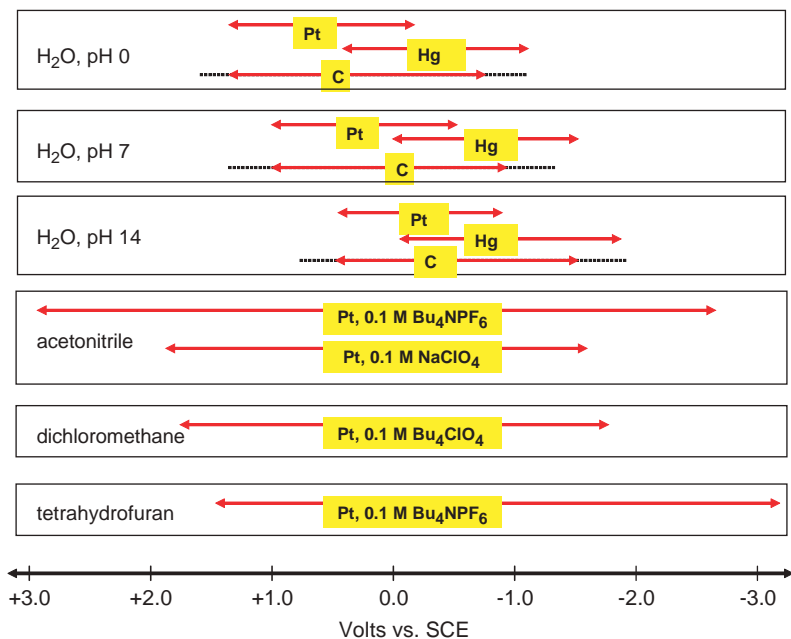


Plate 8 Potential limits for some selected combinations of solvent, electrolyte, and working electrode. Data compiled from Rieger, Electrochemistry, 2nd edition, Chapman & Hall, New York, 1994; Bard and Faulkner, "Electrochemical Methods", Wiley, New York, 1980; and Rocklin, in "A Practical Guide to HPLC Detection", D. Parriott, Ed., Academic Press, San Diego, 1993, Chapter 6. (see page 63)

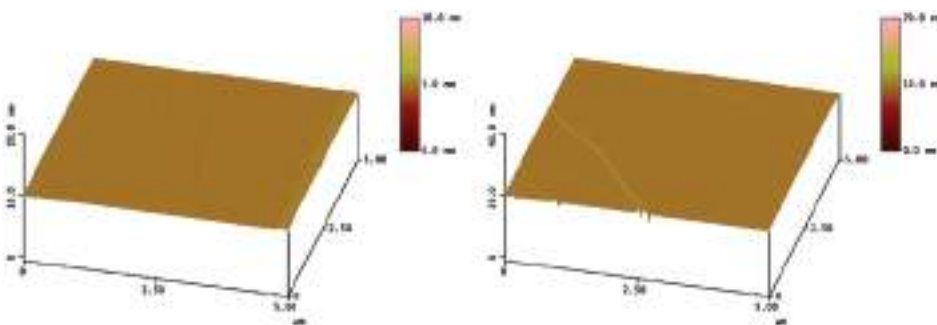


Plate 9 Atomic force micrographs of the basal plane of HOPG after (left) careful layer plane cleavage and (right) damaging cleavage leaving a fracture plane. (see page 117)

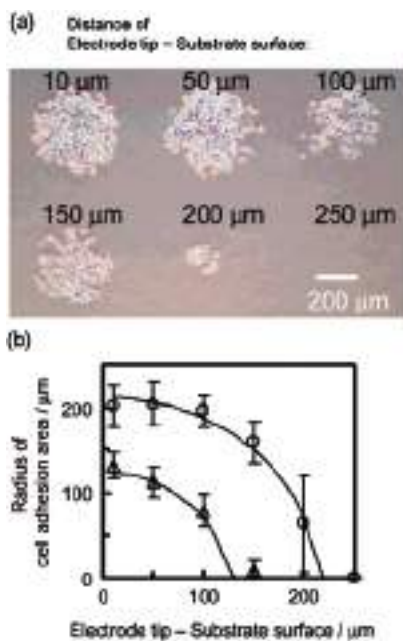


Plate 10 Size of cellular adhesion area at various distances between the electrode tip and the substrate surface during the electrochemical treatment. (a) Phase contrast micrograph of HeLa cells cultured for 24 h on the BSA-coated glass substrate, which was pretreated by a Br – oxidation pulse of 30 sec at the tip–surface distance indicated in the micrograph. (b) Plots of the radius of the cell adhesion area versus the distance of electrode tip–substrate surface for the electrolysis periods of 10 sec (●) and 30 sec (○). Error bars for the plots were calculated from the standard deviation of at least four cellular patterns. Solid curves were calculated assuming a diffusion-limited surface reaction. [Reproduced with permission from H. Kaji, K. Tsukidate, T. Matsue, M. Nishizawa, *J. Am. Chem. Soc.* **126**, 15026 (2004). Copyright 2004, American Chemical Society.] (see page 178)

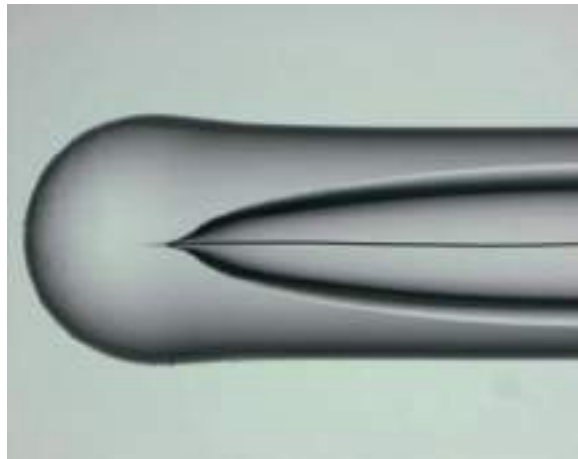


Plate 11 The 25 μm Pt wire is inserted at the base of the cone and remains straight. (see page 191)

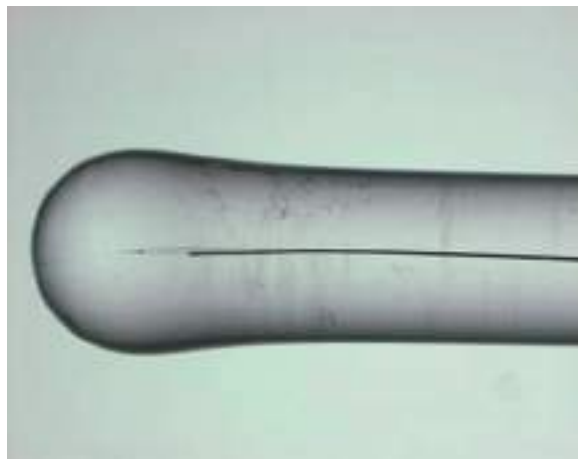


Plate 12 Sealed 25 μm Pt wire in a Pyrex capillary. A small air-pocket is observed at the beginning of the wire but the rest of the body is properly sealed. This is not unusual and can be shaved off during the polishing steps. (see page 193)

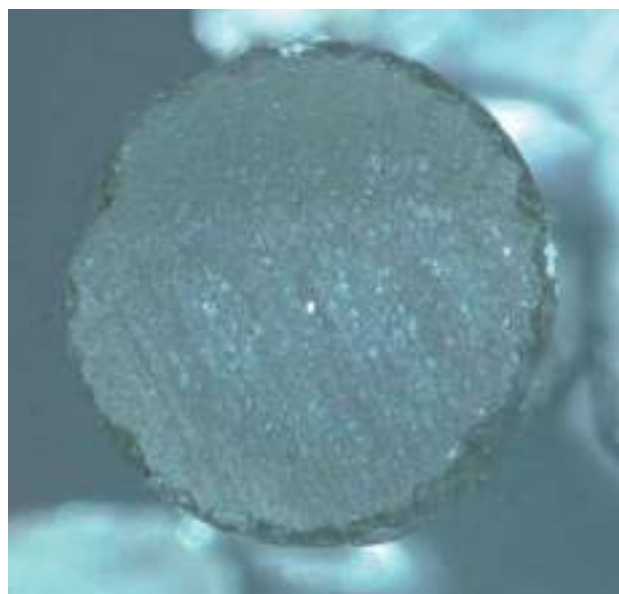


Plate 13 Polished capillary exposing the 25 μm Pt wire at the center. (see page 194)

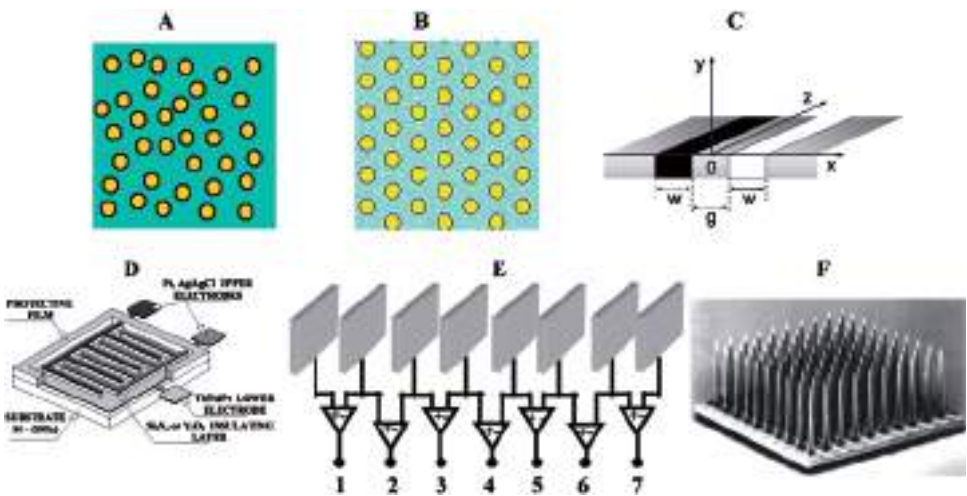


Plate 14 Classification of microelectrodes: (A) random array, (B) ordered array, (C) paired electrode, schematic representation of a double band assembly, (D) interdigitated array, schematic presentation of IDA electrodes vertically arranged (E) linear array, (F) three-dimensional array, Utah electrode array (reprints from reference (28)). (see page 393)

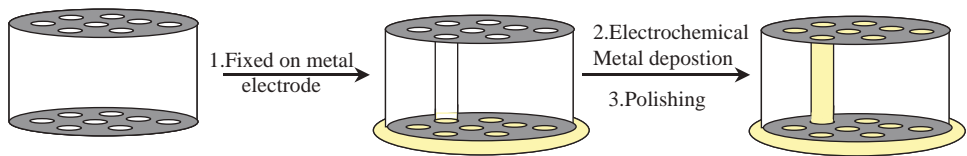


Plate 15 Schematic diagram of the procedure used to prepare the microelectrode array using templates. (see page 407)

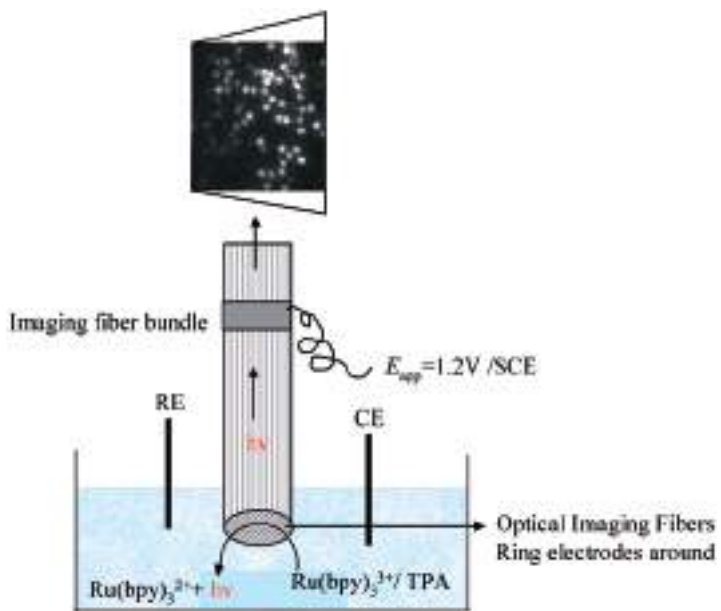


Plate 16 Electrochemiluminescence (ECL) imaging using an opto-electrochemical microring array. (see page 411)

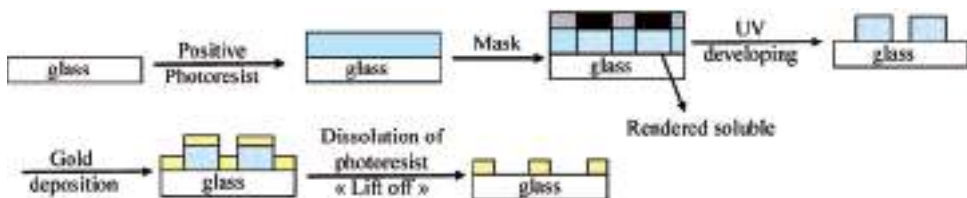


Plate 17 Gold microelectrode array made using photolithography (positive resin) and lift off. (see page 413)

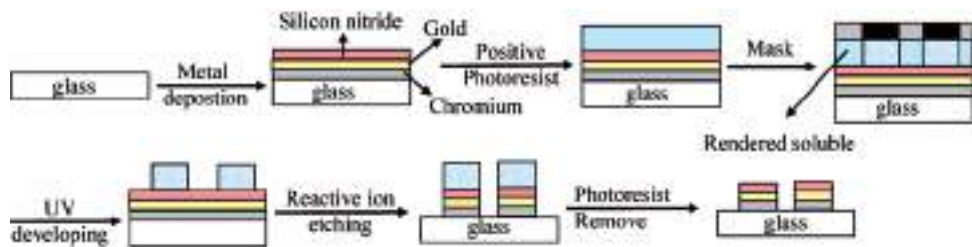


Plate 18 Photolithography and reactive ion etching. (see page 413)



Plate 19 Schematic procedure for micro-contact printing. (see page 415)

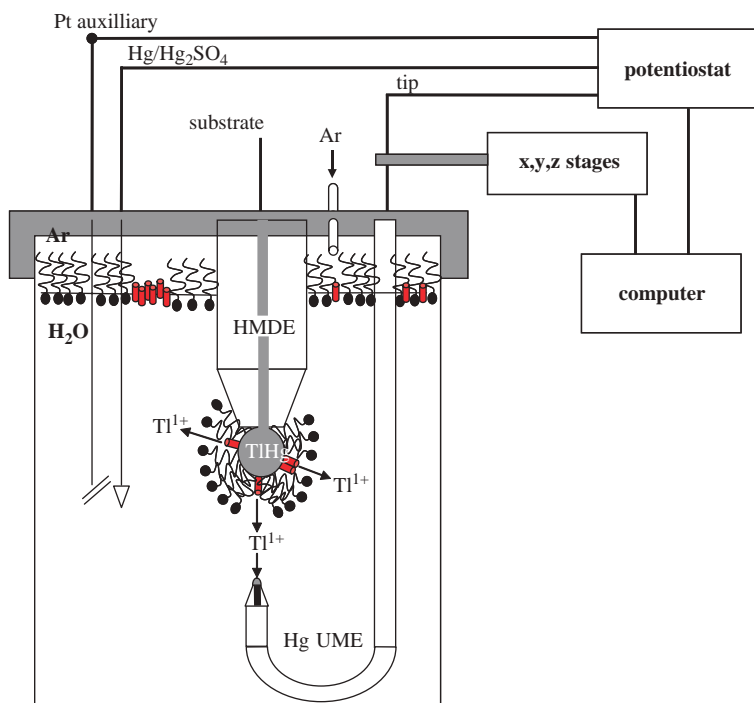


Plate 20 Schematic diagram of an ion channel SECM experiment where a submarine UME is used. (Adapted from reference (20)). (see page 531)

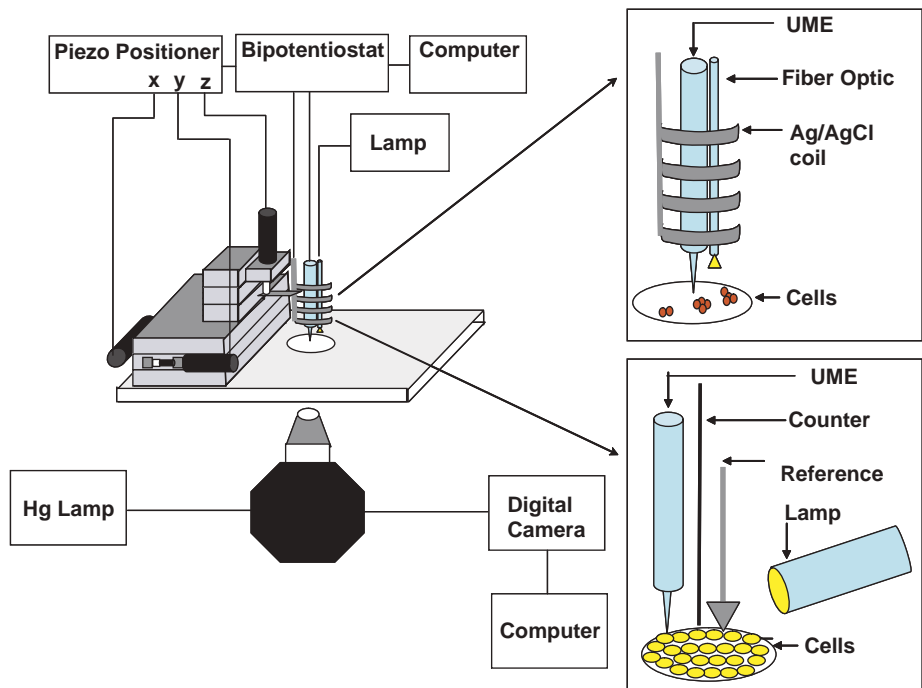


Plate 21 Schematic representation of a combined SECM and inverted microscope setup. (see page 533)

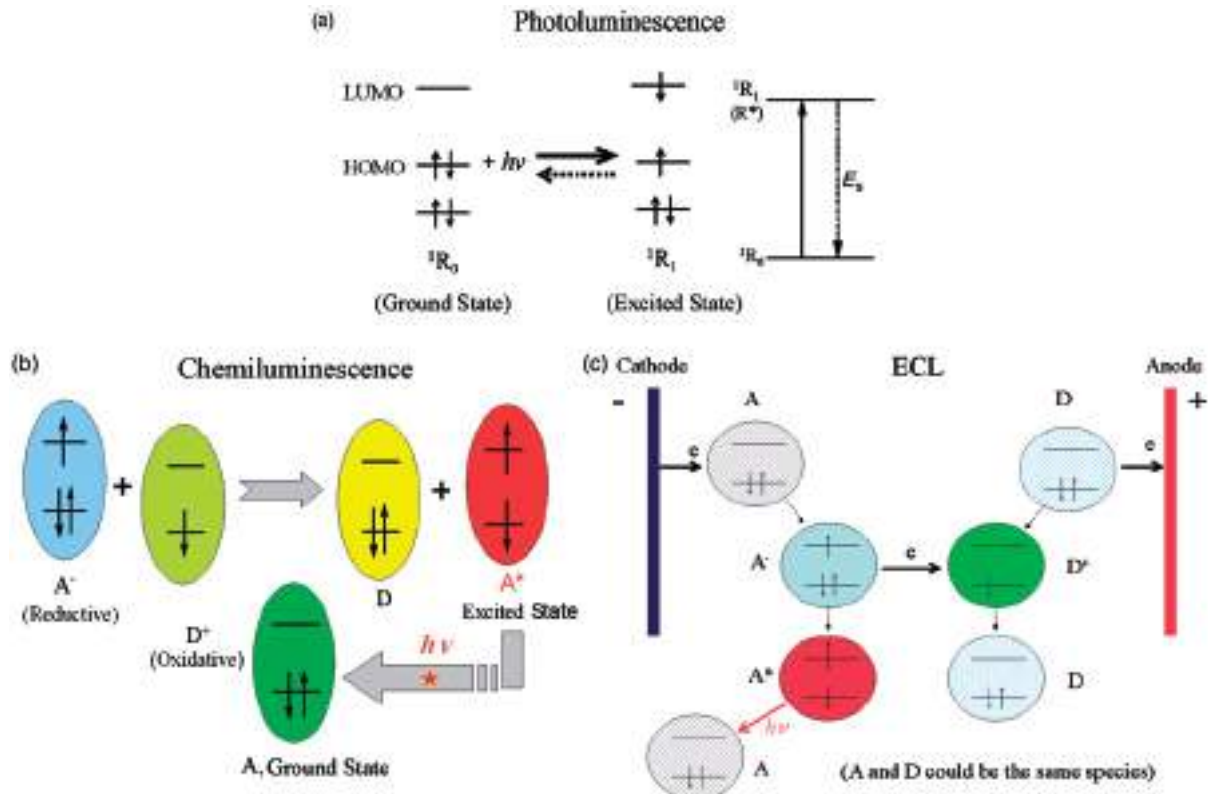


Plate 22 Schematic diagrams showing the general principles of (a) Photoluminescence, (b) Chemiluminescence, (c) ECL. (see page 543)

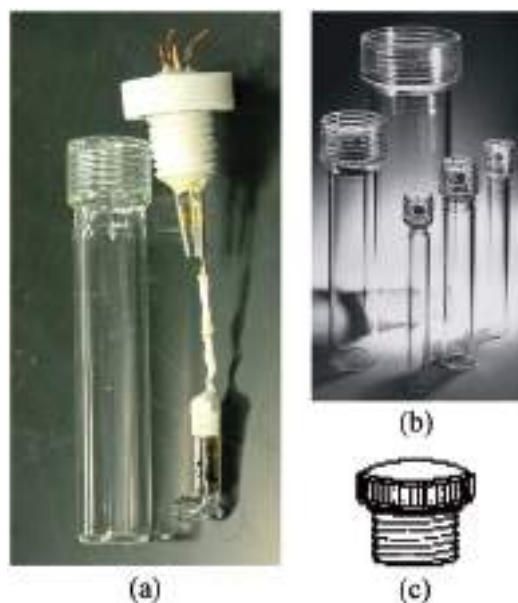


Plate 23 (a) Commonly used cell for annihilation ECL study, (b) which can be fabricated from ACE glass internal threaded connectors, (c) Teflon or PTFE plugs. (see page 557)

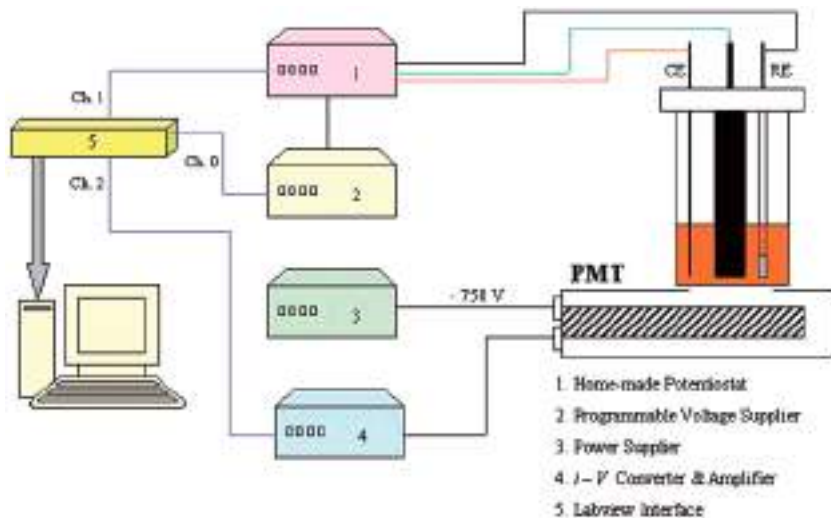


Plate 24 Schematic diagram of an ECL instrumental setup. (see page 566)

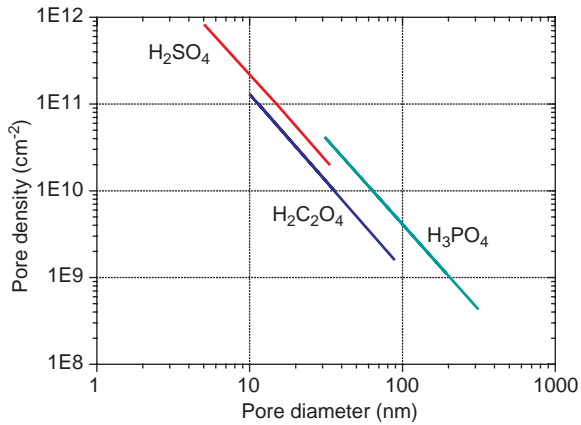


Plate 25 Pore density vs. pore diameter in alumina nanoporous membranes prepared in the three electrolytes indicated. Reproduced with permission from <http://www.synkera.com/>. (see page 680)

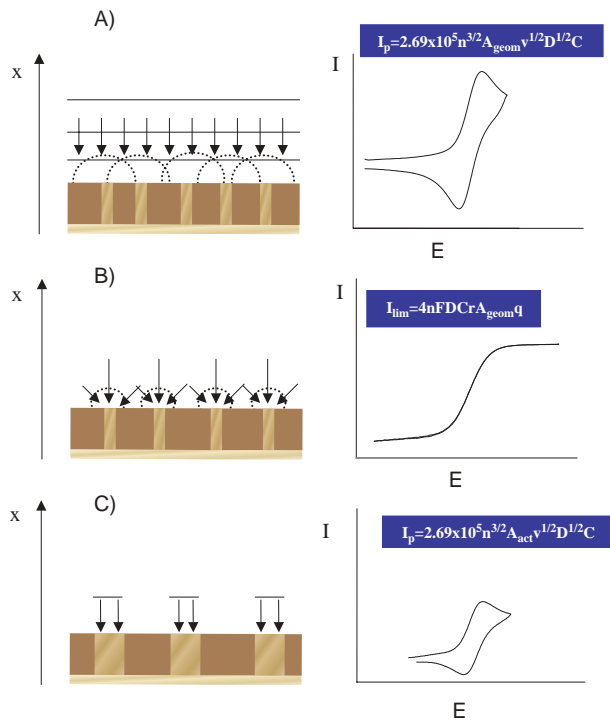


Plate 26 Schematic drawing of the different diffusional regimes at NEE: (A) Total Overlap; (B) Pure Radial; (C) Linear active. The scan rate or the distance between the nanodisk elements increases from (A) to (C). Relevant equations for peak currents (A and C) and plateau current (B) refer to reversible redox systems. A_{act} is the active area (nanodisk surface), A_{geom} is the total geometric area of the ensemble (nanodisks and insulator), q is the nanodisk density (disk cm^{-2}), and all other symbols have their usual meaning. Reprinted with permission from reference (86). (see page 700)

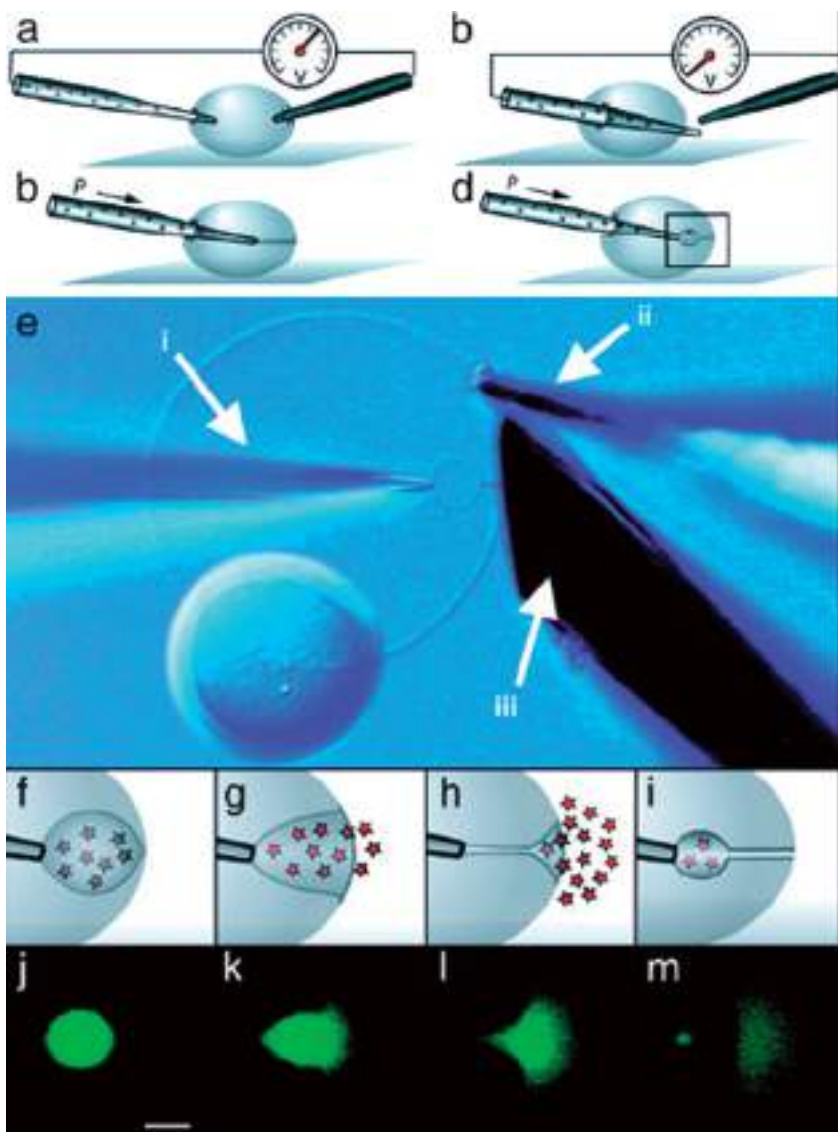


Plate 27 Formation and release of vesicles in an artificial cell. (A–D) Schematics of a microinjection pipette electroinserted into the interior of a unilamellar liposome and then through the opposing wall, pulled back in to the interior, followed by spontaneous formation of a lipid nanotube and formation of a vesicle from flow out of the tip of the micropipette. (E) Nomarski image of a unilamellar liposome, with a multilamellar liposome attached as a reservoir of lipid, microinjection pipette (i), electrode for electroinsertion (ii), and 30- μm diameter amperometric electrode beveled to a 45° angle (iii). A small red line depicts the location of the lipid nanotube, which is difficult to observe in the computer image with a 20 \times objective, illustrating a vesicle with connecting nanotube inside a liposome. (F–I) Fluid injection at a constant flow rate results in growth of the newly formed vesicle with a simultaneous shortening of the nanotube until the final stage of exocytosis takes place spontaneously and a new vesicle is formed with the attached nanotube. (J–M) Fluorescence microscopy images of fluorescein-filled vesicles showing formation and final stage of exocytosis matching the events in F–I. (Scale bar represents 10 μm .) Reproduced with permission from reference (79). (see page 728)

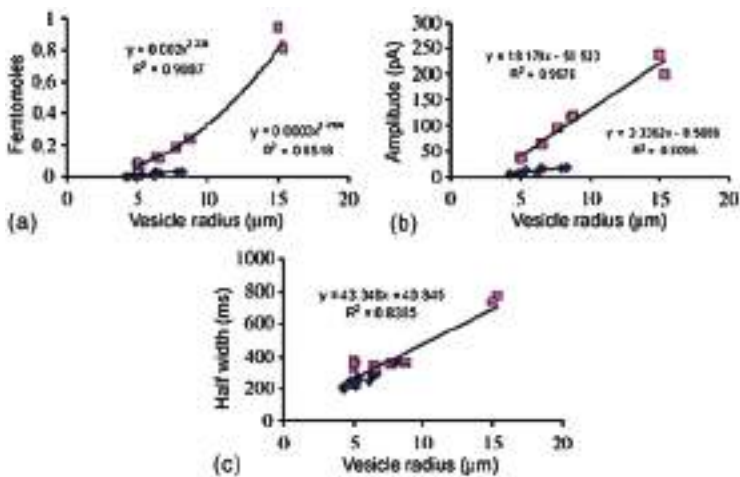


Plate 28 Amperometric data for fusion of vesicles of varying size at beveled 5- (◆) and 33- μm (■) electrodes: (A) the amount of catechol observed at each electrode, (B) the amplitude of each current transient, and (C) the half-width of each transient vs. the radius of vesicles undergoing exocytosis. Each data set has been curve fit to observe the trend in the data as indicated. Reproduced with permission from reference (80). (see page 732)

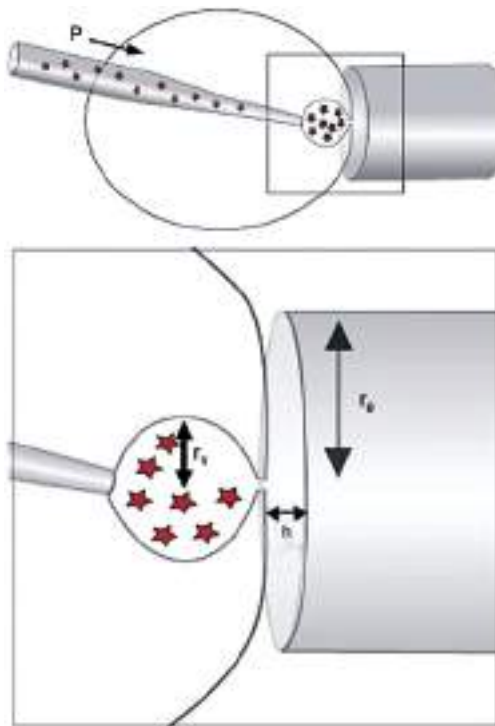


Plate 29 Simple model of coulometric efficiency for artificial exocytosis. This first-stage model assumes that the efficiency of oxidation for material released is simply the ratio of the membrane-electrode space (calculated as $\pi r_e^2 h$) over the volume of the vesicle ($4 \pi r_v^3 / 3$). This assumes that all the catechol that is present in the membrane-electrode space after exocytosis will be oxidized, but also that only catechol in the solution that fits in this volume will be oxidized. Reproduced with permission from reference (80). (see page 733)

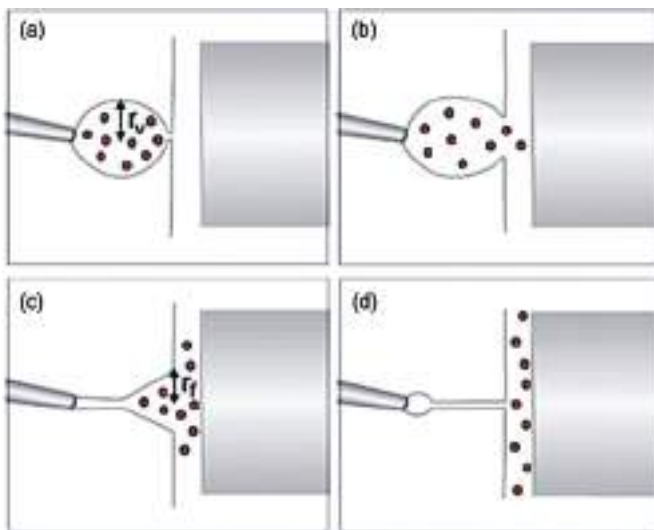


Plate 30 A more complete model of the release process during exocytosis based on the fluorescence observations. This model assumes that as the vesicle opens, it has a transitory period where mass transport of catechol to the electrode is via diffusion from a frustum with opening r_f defined the value of r_v . Catechol diffusing to the electrode is oxidized. After exocytosis is complete, the membrane-electrode space is filled with solution from the inside of the vesicle and catechol present continues to be oxidized as in the thin-layer representation of Figure 17.1.9. Reproduced with permission from reference (80). (see page 734)

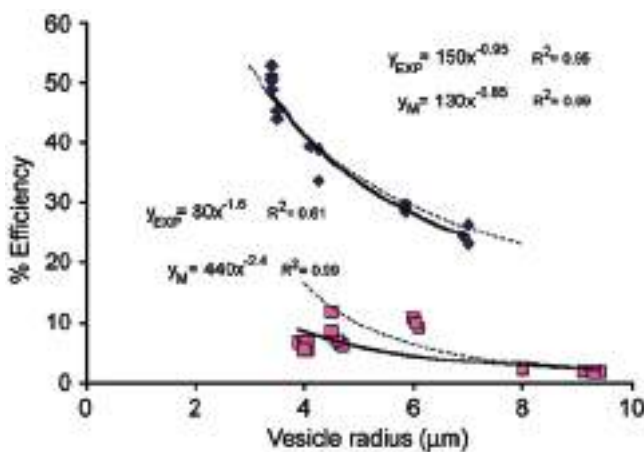


Plate 31 Coulometric efficiencies for a data set obtained with a beveled 33- μm electrode (◆) compared to data obtained with a 5- μm electrode (■) for release of catechol measured from a range of vesicle sizes. This is compared to the theoretical coulometric efficiencies for these electrode dimensions calculated with the conditions outlined in Figure 17.1.6 and with the model discussed in the text (dashed lines). These are compared to each set of experimental data, which are shown with best-fit equations (thick lines). The equations for all lines, and their correlation coefficients, are given with the symbols y_{exp} for experimental data sets and y_m for the modeled efficiencies with that for the 5- μm electrode to the left and that for the 33- μm electrode to the right. Reproduced with permission from reference (80). (see page 736)

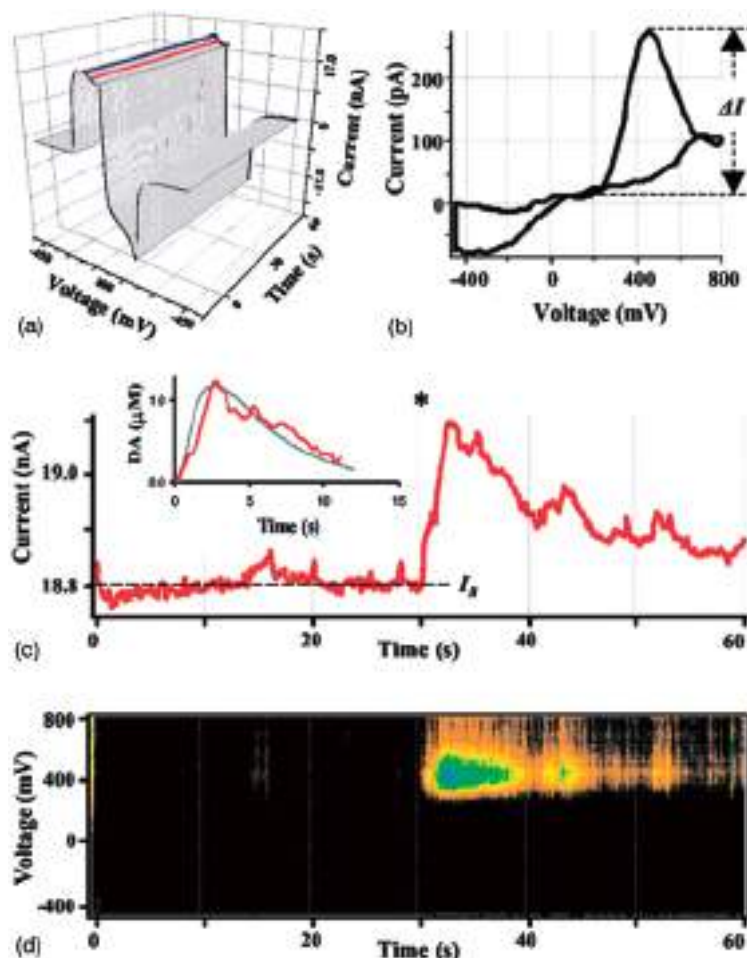


Plate 32 Analysis of cyclic voltammetry recordings from a single rat chromaffin cell. (A) A representative recording shown as a three-dimensional matrix of data. Red and blue lines represent samplings of the current at 400 and 0 mV, respectively. (B) Voltammogram of catecholamines released during the same recording. A subtraction was made between 10 consecutive averaged I–V profiles at 10 sec from those at 33 sec. Dashed line indicates ΔI , the height of DA oxidation peak. (C) Current sampled at 400-mV oxidation potential. The asterisk indicates a time when the patch was disrupted by suction and a whole-cell configuration was attained. The inset shows a random walk fit (green) of the sampled current trace (red) using $15\text{ M}\Omega$ access resistance, 8 μm cell radius, 60 μm distance between the CFE and the pipette tip, and 6.7 μM cytosolic catecholamine concentration. (D) Pseudo-three-dimensional representation of approximate voltammograms of intracellular metabolites encountering the CFE during the recording, in which the intensity of color (“Planet Earth” color table) indicates the current at a given voltage and time. Reproduced with permission from reference (120). (see page 745)

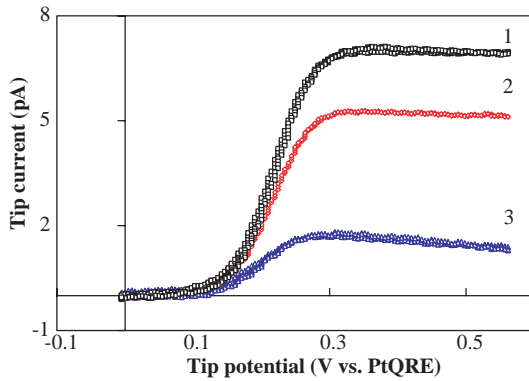


Plate 33 SECM tip cyclic voltammograms of 2 mM $\text{Cp}_2\text{FeTMA}^+$ in an aqueous solution containing no supporting electrolyte at a Pt tip ($\sim 18 \text{ nm}$) at three different gap separations. Curve 1: Tip held far away from the substrate (ITO) surface. Curve 2: Tip at a distance within the range where the tip current started to decrease with decreasing distance. Curve 3: Tip closer to the surface as compared with curve 2. Tip potential scan rate 5 mV/sec for all cases. $E_S = -0.3 \text{ V}$ vs. PtQRE. (see page 766)

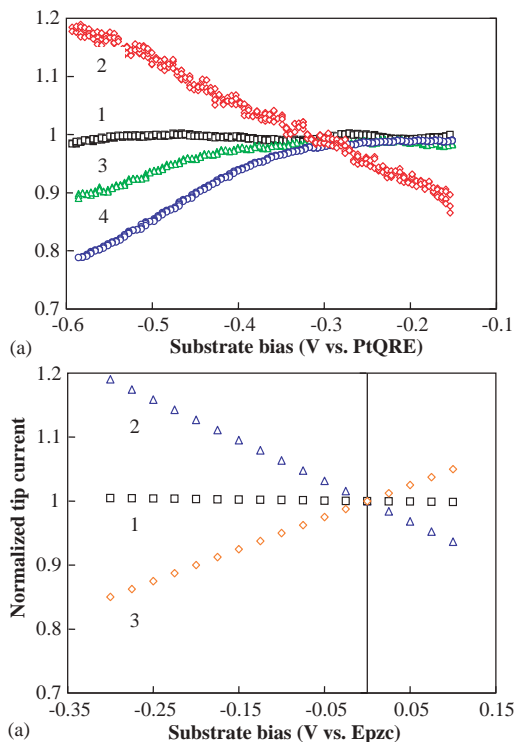


Plate 34 (A) Tip limiting current at $E_T = 0.6 \text{ V}$ vs. PtQRE as a function of the substrate potential, E_S , for different charged species. Curve 1: 2 mM $\text{Cp}_2\text{FeC}_p\text{COO}^-$ in 1.0 M NaNO_3 . Curve 2: 2 mM $\text{Cp}_2\text{FeTMA}^+$, no supporting electrolyte. Curve 3: 2 mM $\text{Cp}_2\text{FeC}_p\text{COO}^-$, no supporting electrolyte. Curve 4: 2 mM $\text{Fe}(\text{C}_p\text{COO}^-)_2$, no supporting electrolyte. All limiting currents are normalized with respect to the limiting tip current of curve 1 at $E_S = -0.3 \text{ V}$ vs. PtQRE. Substrate potential scan rate: 5 mV/sec. (B) Normalized theoretical tip current as a function of E_S , with respect to the tip current at $E_S = E_{pzc}$ (the potential of zero charge) of ITO. Curve 1: 1 mM $\text{Cp}_2\text{FeTMA}^+$ in 1.0 M NaNO_3 . Curve 2: 1 mM $\text{Cp}_2\text{FeTMA}^+$ only. Curve 3: 1 mM $\text{Cp}_2\text{FeC}_p\text{COO}^-$ only. (see page 767)

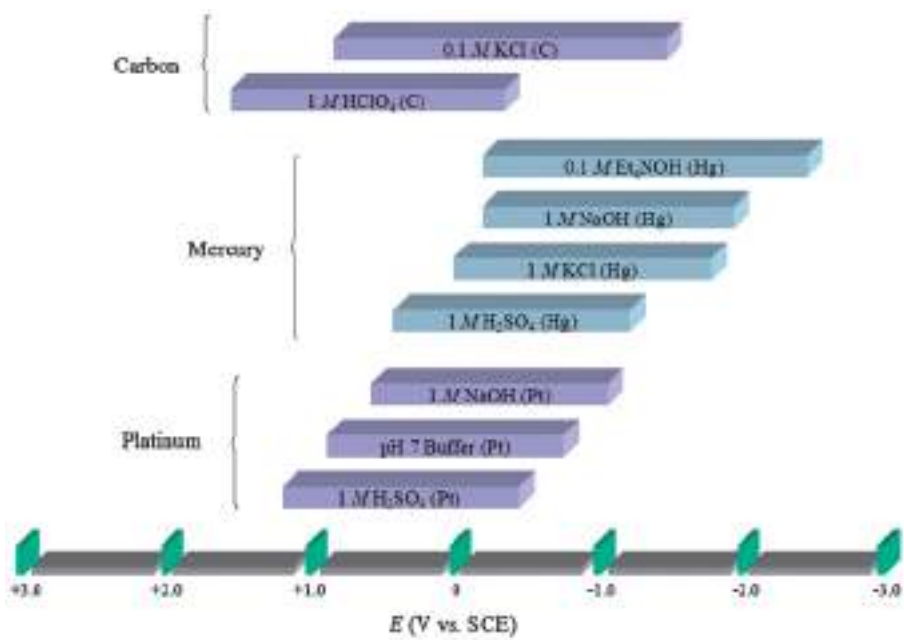


Plate 35 Estimated potential ranges in aqueous solutions at 25 °C. (see page 814)

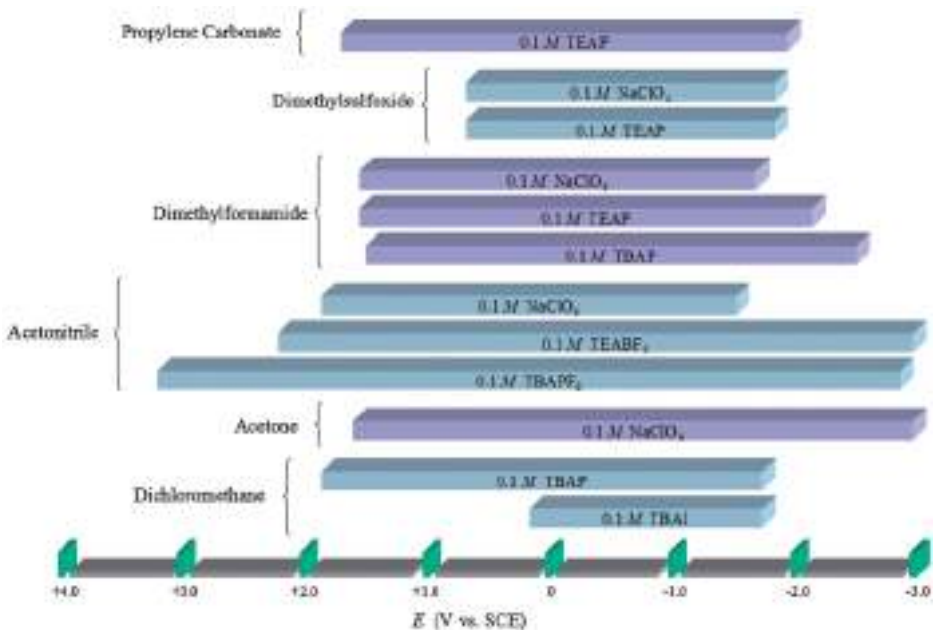


Plate 36 Estimated potential ranges at Pt electrodes for non-aqueous solvent/electrolyte solutions. Data from reference (1). (see page 814)

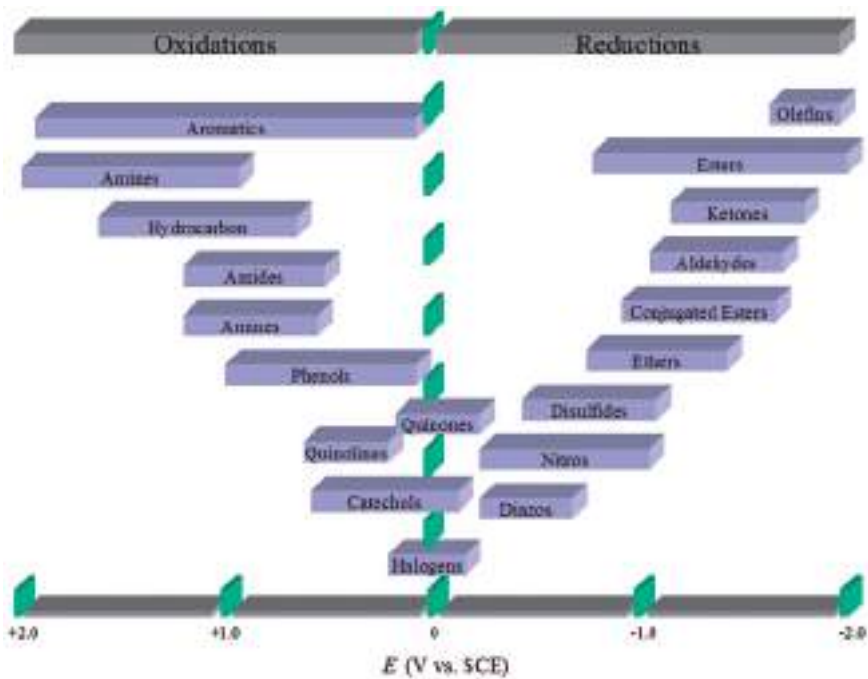


Plate 37 Estimated potential range of organic functional groups at 25 °C. Data from references (5, 6). (see page 819)

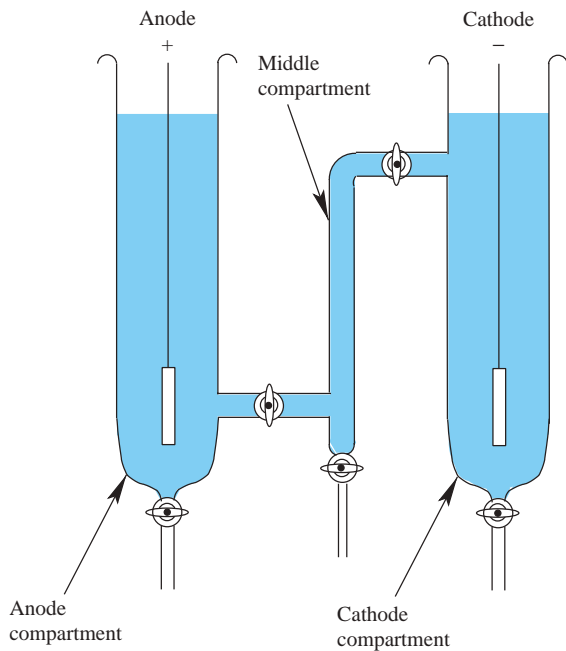


Plate 38 Schematic diagram of the Hittorf apparatus for experimental determination of transference numbers. (see page 856)

This page intentionally left blank